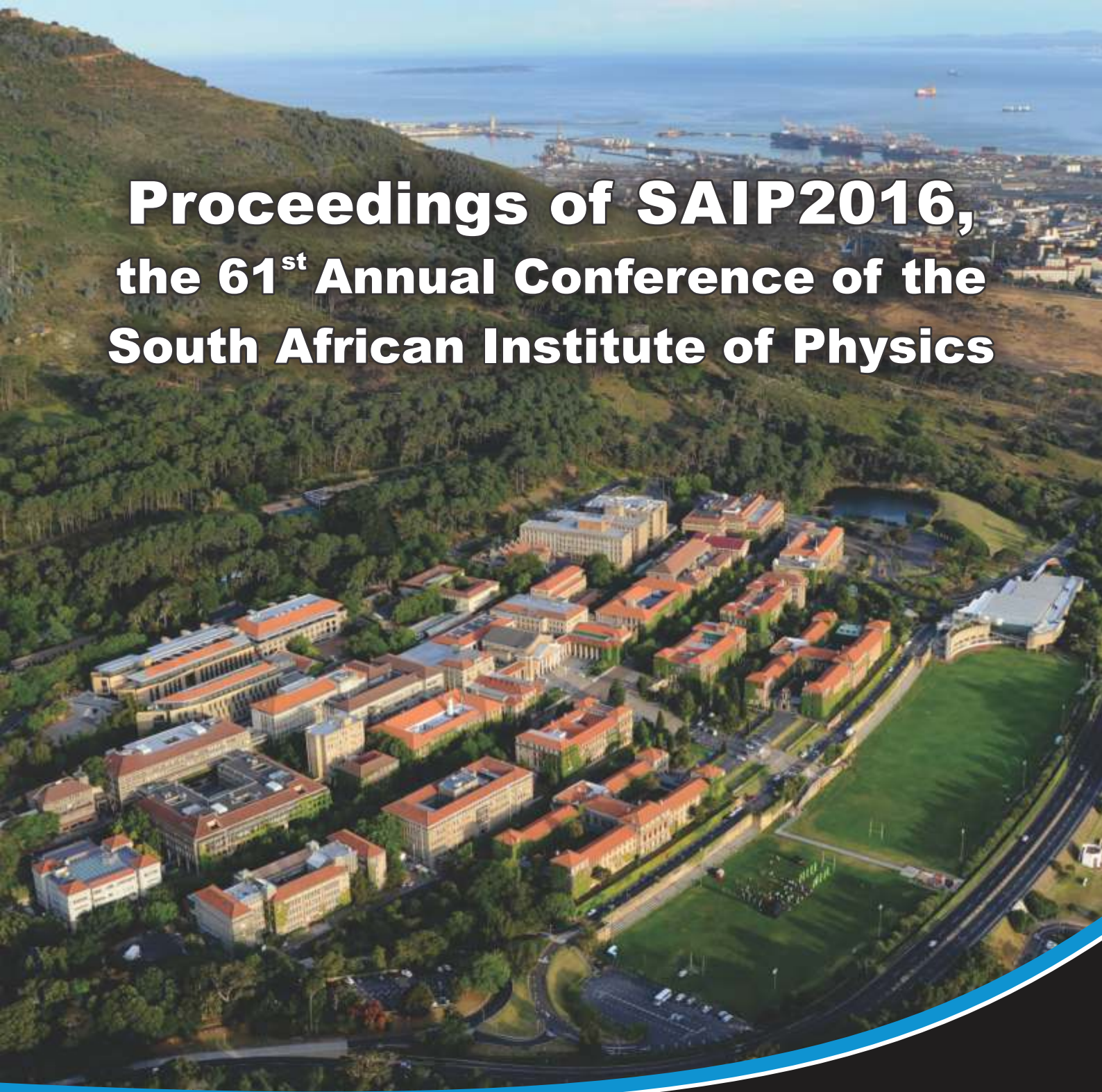
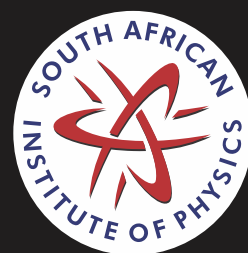


Proceedings of SAIP2016, the 61st Annual Conference of the South African Institute of Physics



Edited by
**Steve Peterson and
Sahal Yacoob**
University of Cape Town



PROCEEDINGS EDITORS: Steve Peterson and Sahal Yacoob

PUBLISHER: The South African Institute of Physics (SAIP)

SAIP COPYRIGHT NOTICE:

Copyright © 2017 by the South African Institute of Physics (SAIP)

The Proceedings of SAIP2016, the 61st Annual Conference of the South African Institute of Physics (SAIP) will only be available electronically on compact disk (CD) and on the SAIP website:

www.saip.org.za.

Permission to make digital or hard copies of part or all of this work for personal or classroom use is granted without fee provided that copies are not made or distributed for profit or commercial advantage and that copies bear this notice and the full citation on the first page. Abstracting with credit is permitted. To copy otherwise, to republish, to post on servers, or to distribute to lists, requires specific permissions and/or a fee. Request permissions from the SAIP Office;

Tel. +27 (0)12 841 2655 / 2627,
Fax +27 (0)86 648 8474,
E-mail info@saip.org.za.

ISBN: 978-0-620-77094-1

SAIP2016

Proceedings of SAIP2016,
the 61st Annual Conference of the
South African Institute of Physics

Hosted by the University of Cape Town

4 July to 8 July 2016
Kramer Law School, Middle Campus
Cape Town
South Africa

Edited By
Steve Peterson and Sahal Yacoob

Table of Contents

Conference Chairs and Committees.....	iii
Message from the Conference Chairperson.....	iv
Message from the Host Editors.....	v
List of Reviewers.....	vii

FULL RESEARCH PAPERS

Division A - Division for Physics of Condensed Matter and Materials

Effect of temperature and CH ₄ /ZrCl ₄ molar ratio on ZrC layers deposited in a vertical-wall CVD system.....	2
<i>S Biira, B A B Alawad, H Bissett, J T Nel, T T Hlatshwayo, P L Crouse and J B Malherbe</i>	
Tunable photoluminescence emission of sol-gel ZnO films prepared by spin coating technique.....	8
<i>E Hasabeldaim, O M Ntwaeaborwa, R E Kroon, E Coetsee and H C Swart</i>	
Pick-off annihilation of delocalized positronium in BaF ₂ at elevated temperatures.....	14
<i>T P Jili, E Sideras-Haddad and D Wamwangi</i>	
Synthesis and characterisation of Y ₂ O ₃ :Bi ³⁺ phosphor material.....	20
<i>E Lee, H C Swart and J J Terblans</i>	
Theory for diffusivity measurements when the temperature is ramped linearly.....	26
<i>J B Malherbe, O S Odutemowo, C C Theron, E G Njoroge, T T Hlatshwayo</i>	
Evolutionary algorithm simulation study of β-MnO ₂ nanoclusters.....	31
<i>P W Masoga, P E Ngoepe and R R Maphanga</i>	
Molecular dynamics studies of Lithium intercalation into amorphous nanostructure of Titanium dioxide.....	37
<i>M G Matshaba, D C Sayle and P E Ngoepe</i>	
Effect of calcination on the structural and magnetic properties of nickel chromite.....	42
<i>P Mohanty, C J Sheppard and A R E Prinsloo</i>	
Role of swift heavy ion irradiation on the structural and magnetic properties of Ti _{0.95} Co _{0.05} O _{2-δ} epitaxial thin films.....	48
<i>P Mohanty, C Rath, C J Sheppard and A R E Prinsloo</i>	
Synthesis and characterization of TiO ₂ doped with Dy ³⁺ ions by sol gel method.....	54
<i>M S Mokoena, M Y A Yagoub, O M Ntwaeaborwa and H C Swart</i>	
Ferromagnetism in magnetic 4f-systems.....	60
<i>V Nolting</i>	
Effect of Annealing Temperature on Optical and Electrical Properties of Sol-Gel ZnO Thin Films.....	66
<i>T K Pathak, H C Swart and R E Kroon</i>	
Spectroscopic investigation of Tm ³⁺ containing Lithium borate glasses.....	72
<i>D D Ramteke and H C Swart</i>	

Characterization of the fine structures associated with E3 defect in GaAs by application of Laplace DLTS	78
<i>F Taghizadeh, K Ostvar, W E Meyer and F D Auret</i>	
Effects of different Ga doping concentration on structural and optical properties of Ga-doped ZnO nanoparticles by precipitation reflux method	82
<i>J Ungula, F B Dejene and H C Swart</i>	
Division B - Nuclear, Particle and Radiation Physics	
NLO Rutherford Scattering and Energy Loss in a QGP.	89
<i>A Khalil and W A Horowitz</i>	
Implementation of the preamplifier response function for the iThemba LABS segmented clover detector	95
<i>T D Bucher, E A Lawrie, O Shirinda, T S Dinoko, J L Easton, N Erasmus, S H Mthembu, W X Mtshali, S P Noncolela</i>	
The search for the Dark Vector Boson via the Higgs Portal	101
<i>S H Connell</i>	
Investigation of the low-lying excitation region in 9B	107
<i>D J Marin-Lámbbari, N J Mukwevho, S Triambak, E H Akakpo, P Adsley, J W Brummer, T Dinoko, S Jongile, M Kamil, N Kheswa, K C W Li, P Z Mabika, S H Mthembu, F Nemulodi, R Neveling, N Orce, P Papka, L Pellegrini, V Pesudo, B Rebeiro, F D Smit, G F Steyn and W Yahia-Chérif</i>	
The search for crystal undulator radiation.	112
<i>D Bosho, M Copeland, F Haffejee, Q Kilbourn, B MacKenzie, C Mercer, A Osato, C Williamson, P Sihoyiya, M Motsoai, M Connell, C A Henning, S H Connell, N L Palmer, T Brooks, J Härtwig, T N Tran Thi, U Uggerhoj and the PEARL Collaboration</i>	
Proton induced radiation damage to the fluorescence capability of plastic scintillators for the Tile Calorimeter of ATLAS.	118
<i>H Jivan, R Erasmus, M Madhuku, B Mellado, G Peters and E Sideras-Haddad</i>	
Estimation of jet-faked muon background in W-boson scattering at $\sqrt{s} = 13$ TeV with the ATLAS detector.	124
<i>L Michael and H McConnell</i>	
Neutron irradiation and light transmission assessment of plastic scintillators of the TileCal section of the ATLAS detector	128
<i>J E Mdhuli, R Erasmus, Y U Davydov, H Jivan, S Liao, C Pelwan, E Sideras-Haddad, B Mellado, G Peters and C Sandrock</i>	
The K600 with CAKE and BaGeL	134
<i>R Neveling, F D Smit, P Adsley, J W Brummer, J Carter, C A Diget, H O U Fynbo, M Freer, N J H Hubbarb, D G Jenkins, M Kamil, M Khumalo, M Kohne, K C W Li, P Z Mabika, D J Marin-Lámbbari, N J Mukwevho, F Nemulodi, P Von Neumann-Cosel, P Papka, L Pellegrini, V Pesudo, B Rebeiro, E Sideras-Haddad, G F Steyn, J A Swartz, S Triambak, I T Usman, C Wheldon, Tz Wheldon and J J van Zyl</i>	

Tracking Electrons Produced by Compton Scatter within a Prompt Gamma Imaging Device.....	140
<i>S W Peterson, M Hillebrand, D Mackin, E Draeger, S Beddar and J Polf</i>	
Investigating prompt gamma emission for a Carbon target using AFRODITE clover detectors.....	146
<i>V Ramanathan, S Peterson, K Li, P Papka, E Lawrie, K Lawrie, J Kiener, S Ouichaoui, W Yahia-Cherif, A Belhout, P Jones, D Moussa, B Hinda, S Damache, A Chafa, M Debabi, K Raju M, T Dinoko and D Bucher</i>	
Estimation of fake rate background in same sign W^+W^+ production at the LHC with ATLAS Detector	152
<i>X Thusini, A Hamilton and S Yacoob</i>	
Constraining hypothetical extensions to the Higgs sector at the LHC.....	158
<i>Stefan Von Buddenbrock, N Chakrabartyb, A S Cornell, D Kar, M Kumar, T Mandal, Bruce Mellado, B Mukhopadhyaya, R G Reeda and X Ruan</i>	
Division C - Photonics	
Photobiomodulation of Isolated Lung Cancer Stem cells.....	165
<i>A Crous and H Abrahamse</i>	
Single-photon probing of plasmonic waveguides.....	170
<i>J Francis and M Tame</i>	
Simulaser, a graphical laser simulator based on Matlab Simulink.....	176
<i>C Jacobs and W Koen</i>	
Nonlinear optical processes in two and multilevel atoms: a theoretical and numerical study	182
<i>M Patel, G De Jager, Z Nkosi and K Govender</i>	
Applying the technique of ultrafast pump-probe spectroscopy on the main plant light-harvesting complex of spinach leaves.....	188
<i>A Singh and T P J Krüger</i>	
Experimental characterisation of a metamaterial optical partial polariser in the quantum regime.....	194
<i>S A Uriri, T Tashima and M S Tame</i>	
Division D1 - Astrophysics	
Existence of anti-Newtonian solutions in fourth-order gravity.....	201
<i>A Abebe</i>	
Calibration of statistical methods used to constrain pulsar geometries via multiband light curve modelling.....	207
<i>M C Bezuidenhout, C Venter, A S Seyffert and A K Harding</i>	

Isotropic energy and luminosity correlations with spectral peak energy for five long Gamma-Ray Bursts.	213
<i>F F Dirirsa and S Razzaque</i>	
Integrability conditions for nonrotating solutions in $f(R)$ gravity.	219
<i>M Elmardi and A Abebe</i>	
New calibration sources for very long baseline interferometry in the 1.4-GHz band.	225
<i>M K Hailemariam, M F Bietenholz, A de Witt and R S Booth</i>	
Ultrahigh-energy neutrino events in current and future neutrino telescopes from nearby Gamma-Ray Bursts.	231
<i>J K Thomas, R Moharana and S Razzaque</i>	
Long-term monitoring of TeV Blazars with the Watcher Robotic Telescope.	237
<i>J P Marais, B van Soelen, R J Britto and P J Meintjes</i>	
Graph theory and pulsar astronomy tie the knot: the use of labeled graph kernels in exploring the pulsar P-P diagram.	243
<i>J Maritz, E Maritz and P Meintjes</i>	
Constraining Lorentz Invariance violation using directional correlations of Gamma-Ray Bursts with IceCube cosmic neutrinos.	249
<i>R Moharana and S Razzaque</i>	
Investigating gamma-ray fluxes from globular clusters.	255
<i>H Ndiyavala, P Krüger and C Venter</i>	
Variability in supersoft X-ray sources RX J0537.7-7034 and RX J0038.6+4020.	261
<i>M M Nyamai, A Odendaal, P J Meintjes and A Udalski</i>	
Identifying new narrow-line Seyfert 1 galaxies and white dwarfs from the second ROSAT all-sky survey catalogue.	267
<i>A Odendaal, T Boller, F Haberl and P J Meintjes</i>	
Investigating the hot gas in active brightest cluster galaxies.	273
<i>A L Ratsimbazafy and S I Loubser</i>	
Correlation study of multi-wavelength transient emission of selected CRTS cataclysmic variables.	279
<i>H Szegedi, A Odendaal and P J Meintjes</i>	
Emission modelling of numerical hydrodynamical simulations with application to active galactic nuclei jets.	285
<i>I P van der Westhuizen, B van Soelen and P J Meintjes</i>	
A comparative timing analysis of Suzaku X-ray data of the nova-like variable system AE Aquarii.	291
<i>H J van Heerden and P J Meintjes</i>	
Solving the radiative transfer equation for maser environments.	297
<i>R van Rooyen and D J van der Walt</i>	

The contribution of photons from the circumstellar disc to gamma-gamma absorption in PSR B1259-63	303
<i>B van Soelen and I Sushch</i>	
Analysis of the rich optical iron-line spectrum of the x-ray variable I Zw 1 AGN 1H0707-495	307
<i>H Winkler and B Paul</i>	
Division D2 - Space Science	
Automated scheduling for a robotic astronomical telescope	313
<i>D Maartens, P Martinez and R van Rooyen</i>	
Near-Earth Object Avoidance Mitigation: Profiting One Rock at a Time	319
<i>G C MacLeod</i>	
Cosmic ray ground level enhancements: Power of the pulse shape	325
<i>O Ogunjobi and R D Strauss</i>	
Ionospheric characterisation of the South Atlantic Magnetic Anomaly using a mobile ship-based dual-frequency GPS Ionospheric Scintillation and Total Electron Content Monitor	331
<i>A Vermeulen, P J Cilliers and P Martinez</i>	
Division E - Education	
Teaching students problem solving with the ‘light bulb effect’ cognitive diagrammatic representation	337
<i>C Albers, D Clerk and D Naidoo</i>	
The development of views on the nature of science of learners in a science enrichment programme	343
<i>V M Baloyi, W E Meyer and E Gaigher</i>	
Understanding of vector addition and subtraction by first year university students: graphical versus algebraic methods	349
<i>E Carleschi</i>	
Termites in our Tests? The role of stigmergy in our examination system	355
<i>D Clerk, D Naidoo and C Albers</i>	
Student difficulties in vectors: foothold ideas	361
<i>I John</i>	
Physical models: A crucial link between reality and mathematical models	367
<i>M Lemmer and R Gunstone</i>	
Shoestring Practicals and the Teaching of Problem Solving	373
<i>D Clerk, D Naidoo and C Albers</i>	
Division F - Applied Physics	
Dose perturbations of unilateral Ti prosthesis in the dosimetry of 6 MV photon beam	380
<i>N Ade and F C P du Plessis</i>	

Radiation Shielding Analysis and Optimisation for the MinPET Kimberlite Sorting Facility using the Monte Carlo Calculation Code, MCNPX.....	386
<i>E M Chinaka, Z Zibi, J van Rooyen, S H Connell and M N Cook</i>	
Using Geant4 to create 3D maps of dosage received within a MinPET diamond sorting facility.....	392
<i>M N H Cook and S H Connell</i>	
A genetic algorithm approach to enhancing the performance of a PET detector array.....	398
<i>M N H Cook and S H Connell</i>	
A method for examining water absorption in sand using fast neutron radiography.....	404
<i>G C Daniels, V Dangendorf, A Buffler and K Tittlemeier</i>	
Effect of atmospheric turbulence on entangled photon field generated by partially coherent pump beam	409
<i>S Joshi, Y Ismail and F Petruccione</i>	
Volume determination of irregular objects by hydrostatic weighing at NMISA.....	415
<i>B Ndlovu and R T Mautjana</i>	
A High Speed OCT System Developed at the CSIR National Laser Centre	421
<i>A Sharma, A Singh, T Roberts, R Ramokolo and H Strauss</i>	
Spark Plasma Sintering of 2507 Duplex Stainless Steel Reinforced with TiC	427
<i>R Sule, P A Olubambi, I Sigalas, J K O Asante and S W Maseko</i>	
Comparison of measurement results obtained from three different calibration systems for performing accelerometer calibration	433
<i>M L Temba and V Tyalimpi</i>	
How local conditions affect solar irradiance and photovoltaic module performance in South Africa	439
<i>H Winkler</i>	
Division G - Theoretical and Computational Physics	
Probing quark gluon plasma in pA collisions.....	446
<i>D M Adamiak and W A Horowitz</i>	
Density functional theory on a lattice: Self-consistent Hartree plus exchange approximation.....	452
<i>K Amouzouvi and D Joubert</i>	
First-principles studies of transition metal defects in a MoS ₂ monolayer.....	457
<i>N F Andriambelaza, R E Mapasha and N Chetty</i>	
Small (q - 1) expansion of the Tsallis distribution and study of particle spectra at LHC	463
<i>T Bhattacharyya, J Cleymans, A Khuntia, P Pareek, R Sahoo</i>	
Quantum Boltzmann evolution of the Quark-Gluon Plasma.....	469
<i>W Grunow and A Peshier</i>	

Energy loss of open strings with massive endpoints in AdS/CFT.....	474
<i>W A Horowitz and A Andrianaivalomahefa</i>	
Are we gauging the pressure correctly?.....	480
<i>G Jackson and A Peshier</i>	
Partition function zeros of adsorbing self-avoiding walks.....	484
<i>E J Janse van Rensburg</i>	
Next-to-leading order electron-quark scattering.....	490
<i>G J Kemp and W A Horowitz</i>	
Evolution of quark masses and flavour mixings in 5D for an $SU(3)$ gauge group.....	495
<i>M O Khojali and A S Cornell</i>	
Short Path Length Energy Loss in the Quark Gluon Plasma.....	501
<i>I Kolbé and W A Horowitz</i>	
Phenomenology of additional scalar bosons at the LHC.....	507
<i>M Kumar, S von Buddenbrock, N Chakrabarty, A S Cornell, D Kar, T Mandal, B Mellado, B Mukhopadhyaya, R G Reed and X Ruan</i>	
Quantum corrections to the kink-antikink potential.....	512
<i>Z Lee and H Weigel</i>	
Two-Higgs doublet model and the LHC.....	518
<i>C Mosomane</i>	
Wilson lines and color-neutral operators in the color glass condensate.....	524
<i>J M Alcock-Zeilinger and H Weigert</i>	

Conference Chairs and Committees

SAIP2016 Conference Chairperson

Roger Fearick, Department of Physics, University of Cape Town

SAIP2016 Division Chairs

Division for Particle and Condensed Matter and Materials Physics:

Japie Engelbrecht (Nelson Mandela Metropolitan University)

Division for Nuclear and Particle Physics:

Simon Mullins (iThemba LABS)

Division for Photonics:

Andrew Forbes (University of the Witwatersrand)

Division for Astrophysics:

Christo Venter (North-West University)

Division for Space Science:

Du Toit Strauss (North-West University)

Division for Physics Education:

Sam Ramaila (University of Johannesburg)

Division for Applied Physics:

Ernest van Dyk (Nelson Mandela Metropolitan University)

Division Theoretical and Computational Physics:

Kristian Müller-Nedebock (Stellenbosch University)

Proceedings Editorial Team

Editors: Steve Peterson and Sahal Yacoob (University of Cape Town)

Online system and Proceedings compilation: Roelf Botha and Juan Grey

Review Panel

Gurthwin Bosman (SUN)

Simon Connell (UJ)

John Bosco Habarulema (SANSA)

Will Horowitz (UCT)

Tom Leadbeater (UCT)

Deena Naidoo (WITS)

Pieter Neethling (SU)

Ernest Van Dyk (NMMU)

Patrick Woudt (UCT)

Message from the Conference Chairperson

The 61st Annual Conference of the South African Institute of Physics was held at the Kramer Law School, Middle Campus, University of Cape Town, from 4 July to 8 July 2016, under the aegis of the Department of Physics and the Department of Astronomy of UCT.

The conference was officially opened on 4 July by DST Chief Director Danny Adams after opening remarks by UCT DVC Research, Danie Visser, and SAIP President, Azwinndini Muronga. The conference was attended by 492 delegates. There were Invited Plenary talks by speakers from South Africa, Germany, Austria, the UK and the USA. These included the Gold Medal address by the 2016 winner, Prof. Manfred Helberg. In addition, there were invited addresses by the 2016 Silver Medal awardees Dr. Angela Dudley and Dr. Shazrene Mohamed. The Conference itself started on 5 July and was preceded on 4 July by two Winter Schools, on the topics “From the Smallest to the Largest Scales: Our Evolving Universe” and “The Biophysics of Cells and Macromolecules”, as well as a Teachers Workshop to encourage school science teachers into the SAIP fold. A feature of the conference was the introduction of the Physics Bowl, a challenge between teams of university students, held on 7 July. A great time was had by all, with the winning team being from the University of Cape Town with second place going to the University of Limpopo. The Conference Banquet was held in the Jameson Memorial Hall on 8 July.

There were a total of 517 scientific contributions presented at the conference, of these 328 being oral presentations and 189 being poster presentations. Of course, the conference would not have been a success without the assistance and commitment of many people: those on the Organising Committee and in the Departments of Physics and Astronomy; the SAIP Division Heads and reviewers whose work has made these Proceedings possible; the SAIP Council and the SAIP Office under Brian Masara, with his team of Dr. Roelf Botha and Juan Grey who supplied vital IT support; and finally the invaluable assistance of the UCT Conference Management Centre under the guidance of Ange Bukasa.

Roger Fearick
Chairperson: SAIP2016 Conference

Message from the Host Editors

As host editors of the 2016 SAIP Proceedings, our job was to supervise and manage the review process and publication of the conference proceedings. The entire process (from submission to publication) was governed by the SAIP Proceedings Guidelines with an effort to emphasize the presence of new scientific material in each of the published proceeding papers. The submission process was supplemented in 2016 by the addition of a Supervisor's Agreement to assist students in producing high-quality submissions.

All submissions were first checked for formatting. Submissions that failed to meet these requirements were returned to authors for their layout to be corrected. Once layout review was complete, it was followed by the peer-review process. The peer-review process followed the SAIP Proceedings Guidelines, which requires that the content of each paper is reviewed by two experts with a PhD in the relevant area of research. If there was differing opinions between reviewers, a third reviewer was called upon to review the paper.

In theory, once a paper is submitted, its publication should be swift but, unfortunately, the reality has been very different. Publication of a proceedings requires as much the goodwill of reviewers as it does the patience of authors. Evaluating papers is onerous and many of our reviewers made commendable efforts to produce detailed and meaningful reports that we are incredibly grateful for. We particularly wish to thank the reviewers who took the time to comment on more than one paper.

We unreservedly apologize for the length of time required to publish these proceedings and are thankful to the many authors who tolerated the delay as we worked to complete the review process. We received 180 papers from the 517 abstracts submitted to the 2016 SAIP Conference. 121 papers completed the required layout criteria and were passed on to reviewers for evaluation. Of these 121 papers, 74% were accepted for publication, a total of 90 papers are included in these proceedings.

In addition, the editors want to thank all authors for submitting their work to 2016 SAIP proceedings. The high-quality scientific content of these proceedings is a reflection of your hard work and the excellent Physics research happening in South Africa.

Special thanks go to the Local Organizing Committee for the 2016 SAIP Conference. Thank you Roger Fearick for your willingness and sacrifice to chair the committee; thank you Andy Buffler and Patrick Woudt for your leadership. And thank you to the rest of the committee members (Mark Blumenthal, Tom Dietel, Tom Jarrett, Gregor Leigh and Heribert Weigert) for the many things that you did. Lastly, thank you to the Physics department staff and students making sure all of the details were handled professionally and quickly.

We would also like to thank the Division Heads for their assistance in assigning appropriate experts for the papers in their fields and their willingness to deliver advice on content when asked.

The editors also thank the Review Panel for helping make the final push towards completion. Your help was invaluable in getting the last reviews and making those final decisions.

Lastly, we would like to thank the SAIP Executive Officer (Brian Masara) and the SAIP IT Team (Roelf Botha, Juan Grey, Lizzy Sathekge and Tebogo Mokhine) for their tireless efforts to support us and teach us the ins and outs of publishing this conference proceedings. Without your help, this would not have been possible.



Steve Peterson and Sahal Yacoob
Host Editors for the 2016 SAIP Proceedings

List of Reviewers

Dr. ALBERS, Claudia	University of Witwatersrand
Prof. ALLIE, Saalih	University of Cape Town
Dr. ASANTE, Joseph	Tshwane University of Technology
Dr. BACKES, Michael	University of Namibia
Prof. BASSET, Bruce	University of Cape Town
Dr. BOSMAN, Gurthwin	Stellenbosch University
Prof. BOTTCHEER, Markus	North-West University
Dr. BUCKLEY, David	South African Astronomical Observatory
Dr. BUTHELEZI, Zinhle	iThemba LABS
Dr. CARLESCHI, Emanuela	University of Johannesburg
Dr. CHANDREYEE, Maitra	Max Planck Institute for Extraterrestrial Physics
Prof. CINTI, Fabio	National Institute for Theoretical Physics
Prof. CLEYMANS, Jean	University of Cape Town
Prof. COMBRINCK, Ludwig	Hartebeesthoek Radio Astronomy Observatory
Prof. CONNELL, Simon	University of Johannesburg
Prof. CORNELL, Alan	University of Witwatersrand
Dr. CROZIER, Jacqui	Nelson Mandela Metropolitan University
Mr. DE BEER, Frikkie	South African Nuclear Energy Corporation
Prof. DE MELLO KOCH, Robert	University of Witwatersrand
Prof. DERRY, Trevor	University of Witwatersrand
Prof. DHLAMINI, Mokhotjwa S.	University of South Africa
Dr. DIALE, Mmantsae	University of Pretoria
Dr. DIETEL, Thomas	University of Cape Town
Prof. DUVENHAGE, Rocco	University of Pretoria
Prof. ENGELBRECHT, Japie	Nelson Mandela Metropolitan University
Dr. ERASMUS, Rudolph	University of Witwatersrand
Prof. FALTENBACHER, Andreas	University of Witwatersrand
Prof. FERREIRA, Stefan	North-West University
Dr. FERRER, Phil	University of Witwatersrand
Prof. FÖRTSCH, Siegfried	iThemba LABS
Prof. GRAHAM, Noah	University of Pretoria
Prof. HABARULEMA, John Bosco	South African National Space Agency
Dr. HOROWITZ, Will	University of Cape Town
Dr. HUTTON, Tanya	University of Cape Town
Dr. ISMAIL, Yaseera	University of Kwa-Zulu Natal
Dr. JOHN, Anslyn	Rhodes University
Prof. JOUBERT, Daniel	University of the Witwatersrand
Dr. KAR, Deepak	University of the Witwatersrand
Prof. KARASTERGIOU, Aris	University of Oxford
Dr. KARSTEN, Aletta	National Metrology Institute of South Africa
Dr. KEMP, Garreth	University of Johannesburg
Dr. KOMIN, Nukri	University of Witwatersrand
Dr. KOTZE, Pieter	South African National Space Agency
Dr. KRIEL, Hannes	Stellenbosch University
Dr. LEADBEATER, Thomas	University of Cape Town

Prof. LEE, Mike	Nelson Mandela Metropolitan University
Prof. MALHERBE, Johan	University of Pretoria
Dr. MALUTA, Nnditshedzeni E.	University of Venda
Prof. MAPHANGA, Regina	Council for Scientific and Industrial Research
Dr. MCBRIDE, Vanessa	University of Cape Town
Prof. MEINTJES, Pieter	University of the Free State
Prof. MEYER, Edson	University of the Free State
Dr. MOEKETSI, Daniel M.	Council for Scientific and Industrial Research
Mr. MOLOI, Sabata	University of South Africa
Prof. MÜLLER-NEDEBOCK, Kristian	Stellenbosch University
Prof. NAIDOO, Deena	University of Witwatersrand
Prof. NEETHLING, Pieter	Stellenbosch University
Dr. NEL, Jacqueline	University of Pretoria
Dr. NNDANGANENI, Rendani	South African National Space Agency
Dr. NOTHNAGEL, Gabriel	South African Nuclear Energy Corporation
Prof. NTWAEABORWA, Odireleng	University of the Free State
Dr. OKOUMA, Patrice	University of Western Cape
Dr. OOZEER, Nadeem	South African Radio Astronomy Observatory
Dr. OSANO, Bon	University of Cape Town
Prof. PAPKA, Paul	Stellenbosch University
Dr. PELLEGRINI, Luna	University of Witwatersrand
Prof. PESHIER, Andre	University of Cape Town
Dr. PETERSON, Stephen	University of Cape Town
Dr. PRAKASH, Ram	Shri Mata Vaishno Devi University
Dr. QUANDT, Alex	University of Witwatersrand
Dr. RAMALIA, Sam	University of Johannesburg
Prof. RATH, Chandana	Indian Institute of Technology
Dr. REDDY, Krish	University of Johannesburg
Prof. ROUX, Stef	University of Witwatersrand
Prof. SCHOLTZ, Frederik	National Institute for Theoretical Physics
Mr. SCHULTZ, Ross	Nelson Mandela Metropolitan University
Dr. SHAFI, Nabiha	University of Witwatersrand
Prof. SHARPEY-SCHAFFER, John F.	University of Western Cape
Dr. SINAYSKIY, Ilya	University of Kwa-Zulu Natal (NITheP)
Mr. SINGH, Vinay	Indian Institute of Technology
Prof. SMITS, Derck	University of Johannesburg
Prof. STAPPERS, Ben	Manchester University, UK
Prof. SWART, Hendrik	University of the Free State
Dr. TAYLOR, Dale	University of Cape Town
Prof. TERBLANS, JJ (Koos)	University of the Free State
Prof. TOUCHETTE, Hugo	National Institute for Theoretical Physics (SU)
Prof. TRIAMBAK, Smarajit	University of Western Cape
Dr. USMAN, Iyabo	University of Witwatersrand
Dr. VALLES, Adam	University of Witwatersrand
Dr. VAN DER HEYDEN, Kurt	University of Cape Town
Mr. VAN DER WALT, Johan	North-West University
Prof. VAN DYK, Ernest	Nelson Mandela Metropolitan University
Dr. VAN SOELEN, Brian	University of the Free State

Prof. VENTER, Christo	North-West University
Dr. VORSTER, Frederik	Nelson Mandela Metropolitan University
Dr. WADIASINGH, Zorawar	North-West University
Dr. WAGENER, Magnus	Nelson Mandela Metropolitan University
Prof. WAMWANGI, Daniel	University of Witwatersrand
Dr. WARMBIER, Robert	University of the Witwatersrand
Mr. WEBSTER, Jason	Stellenbosch University
Prof. WEIGEL, Herbert	Stellenbosch University
Prof. WEIGERT, Heribert	University of Cape Town
Dr. WESTRAADT, Johan	Nelson Mandela Metropolitan University
Dr. WHEATON, Spencer	University of Cape Town
Prof. WHITELOCK, Patricia	South African Astronomical Observatory
Prof. WINKLER, Hartmut	University of Johannesburg
Prof. WOUDT, Patrick	University of Cape Town
Dr. YACOOB, Sahal	University of Cape Town
Dr. ZACHARIAS, Michael	North-West University

*Division A – Division for
Physics of Condensed Matter
and Materials*

Effect of temperature and CH₄/ZrCl₄ molar ratio on ZrC layers deposited in a vertical-wall CVD system

S Biira^{1,2}, BAB Alawad¹, H Bissett³, JT Nel³, TT Hlatshwayo¹, PL Crouse⁴, JB Malherbe¹

¹Department of Physics, University of Pretoria, Pretoria, 0002 South Africa

²Department of Physics, Busitema University, P.O Box 236, Tororo, Uganda

³Applied Chemistry Division, The South African Nuclear Energy Corporation (Necsa), P.O Box 582, Pretoria, 0001 South Africa

⁴Department of Chemical Engineering, University of Pretoria, 0002 South Africa

E-mail address: bsaphina@yahoo.co.uk

Abstract. The synthesis of ZrC layers was performed in an in-house developed, vertical-wall chemical vapour deposition (CVD) system operating at atmospheric pressure. Zirconium tetrachloride and methane were used as zirconium and carbon sources respectively, with an excess of hydrogen as reducing agent. Argon was used to carry the vaporised ZrCl₄ at 300 °C to the reaction chamber. The deposition of ZrC was carried out on graphite substrates at temperatures in the range of 1200 °C –1600 °C. The molar ratio of CH₄/ZrCl₄ was varied from 6.04 to 24.44. Response surface methodology was applied to optimise the process parameters for the deposition of ZrC. A central composite design was used to investigate the effects of temperature and molar ratio of CH₄/ZrCl₄ on the average crystallite size. Quadratic statistical models for crystallite size was established. Scanning electron microscopy (SEM) images show that the coatings became more uniform with increased particle agglomeration as temperature increased.

1. Introduction

The use of ZrC has been proposed as replacement for SiC, or in addition to the standard SiC layer, in TRISO (tristructural-isotropic) layers. This is because ZrC is a better barrier than SiC against Ag diffusion and is more resistant to Pd attack [1,2]. The physical and chemical properties of ZrC layers depend on chemical composition, crystallite size and morphology, orientations of crystal planes, structural defects, porosity, and the presence of impurities. These factors are a function of the methods and conditions used in growing ZrC coatings. Chemical vapour deposition (CVD) produces coatings with very low levels of impurities and low porosity [3]; this is why it is the preferred method. Compared to SiC, little research has been published on the use of ZrC in nuclear reactors. The main reason is that SiC has proven nuclear applications. Another reason for this might be that it is difficult to grow good quality ZrC. This paper reports on the development of a deposition process for the preparation and optimisation of ZrC layers at temperatures ranging from 1200 °C to 1600 °C and CH₄/ZrCl₄ molar ratios ranging from 6.04 to 24.44. After choosing temperature and the CH₄/ZrCl₄ ratio as the dominant variables influencing the properties of ZrC, in order to achieve optimum

conditions for growing ZrC coatings, a statistical experimental design methodology (central composite design) was applied to explore the effects of these variables [4].

2. Experimental

2.1 Apparatus and deposition process

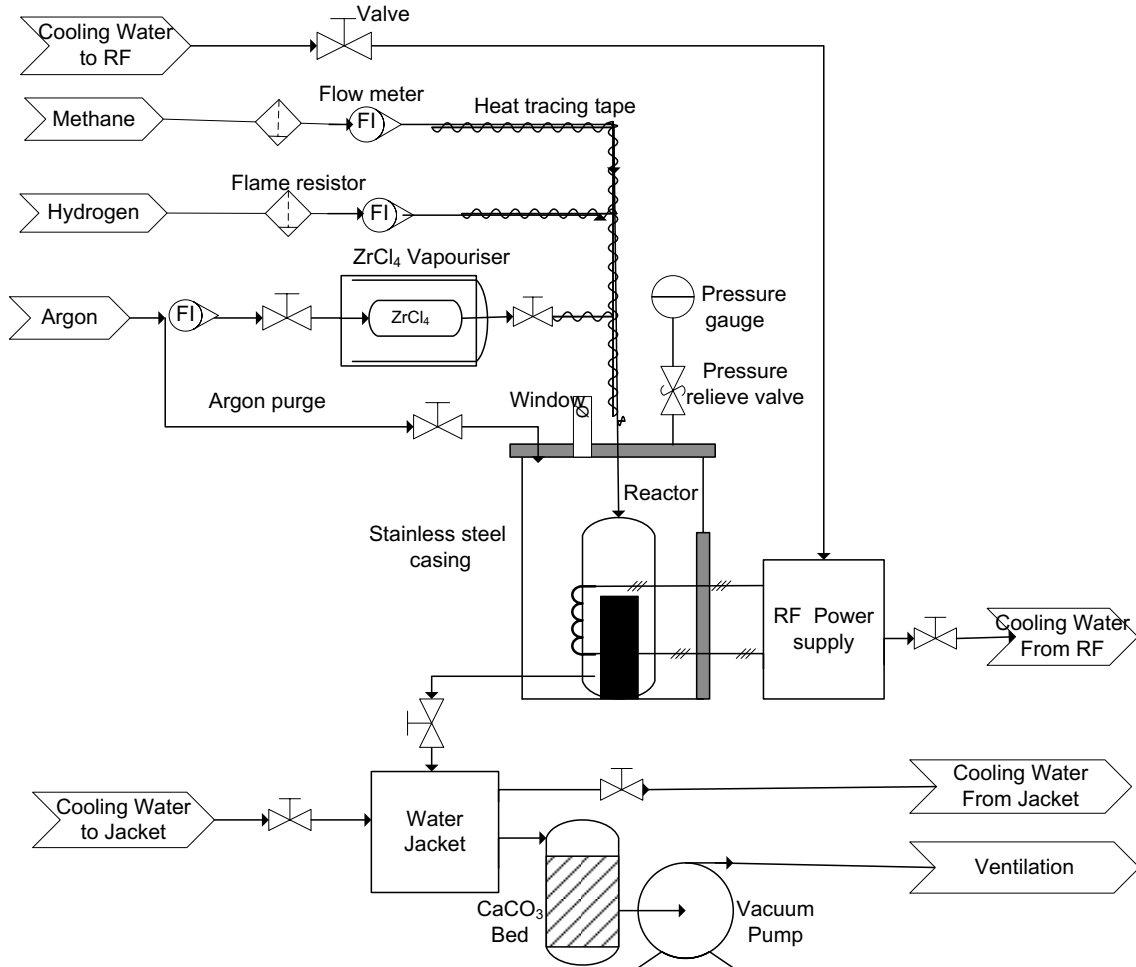


Figure 1. Process and instrumentation diagram for the CVD reactor set-up.

In this study a vertical-wall thermal CVD system illustrated in Figure 1, was developed in-house at The South African Nuclear Corporation (Necsa). It is composed of a 10 kW RF power supply system, a gas supply and delivery system, the reactor system, and an exhaust/scrubber system. ZrC was deposited on graphite substrates from ZrCl₄-Ar-CH₄-H₂ gas mixtures. Methane, hydrogen and argon flow rates were measured by flow meters and directed into the reaction chamber as shown in Figure 1. The deposition was carried out for typically 2 hours at atmospheric pressure. Hydrogen and argon flow rates were constant at 853 sccm and 562 sccm respectively. This gave a 1.0 g/h mass transfer rate of ZrCl₄. Table 1 gives the details of the deposition parameters.

2.2. Design of experiments and response surface methodology

Response surface methodology (RSM) was applied to analyse and model the effect of the independent variables on the response(s) [4]. The ZrC deposition process was investigated using a central composite design (CCD). The temperature (T) and the CH₄/ZrCl₄ molar ratio (M) were chosen as the

independent variables. For this paper, the average crystallite size was selected as the dependent (response) variable. For the purpose of analysing the raw data and testing the goodness of fit of the model, an analysis of variance (ANOVA) was implemented. The details of testing of model adequacy and suitability were explained elsewhere [5]. The 13 experiments and the point types generated, are indicated in Table 1. The experiment was designed and statistical analysis was done using DESIGN-EXPERT® 7.0 [6], which is a commercial statistical software package.

Table 1. Parameters for CVD experiments and average crystallite size.

Exp. Number	Point type	Temperature (°C)	CH ₄ /ZrCl ₄	CH ₄ flow rate (sccm)	Crystallite size (nm)
1	Axial	1400	24.44	43.3	21.8
2	Axial	1400	6.04	10.7	23.9
3	Factorial	1541	8.73	15.5	29.1
4	Factorial	1259	21.75	38.5	28.4
5	Centre	1400	15.24	27.0	31.9
6	Axial	1600	15.24	27.0	34.1
7	Centre	1400	15.24	27.0	32.0
8	Centre	1400	15.24	27.0	34.2
9	Centre	1400	15.24	27.0	33.4
10	Factorial	1259	8.73	15.5	25.8
11	Factorial	1541	21.75	38.5	27.8
12	Centre	1400	15.24	27.0	32.6
13	Axial	1200	15.24	27.0	26.3

3. Results and Discussion

3.1 Crystallographic structure and Phase composition

Figure 2 shows a typical XRD pattern of ZrC coatings deposited at a substrate temperature of 1259 °C at CH₄/ZrCl₄ of 21.7. Ten reflections of ZrC were observed, and matched with the International Centre for Diffraction Data (ICDD) file number 03-065-8833 for the material. They indicate that polycrystalline face-centred cubic structure of the ZrC coating has been deposited. The average crystallite size of the samples was determined from the Scherrer equation [5]. The raw experimental data are presented in Table 1.

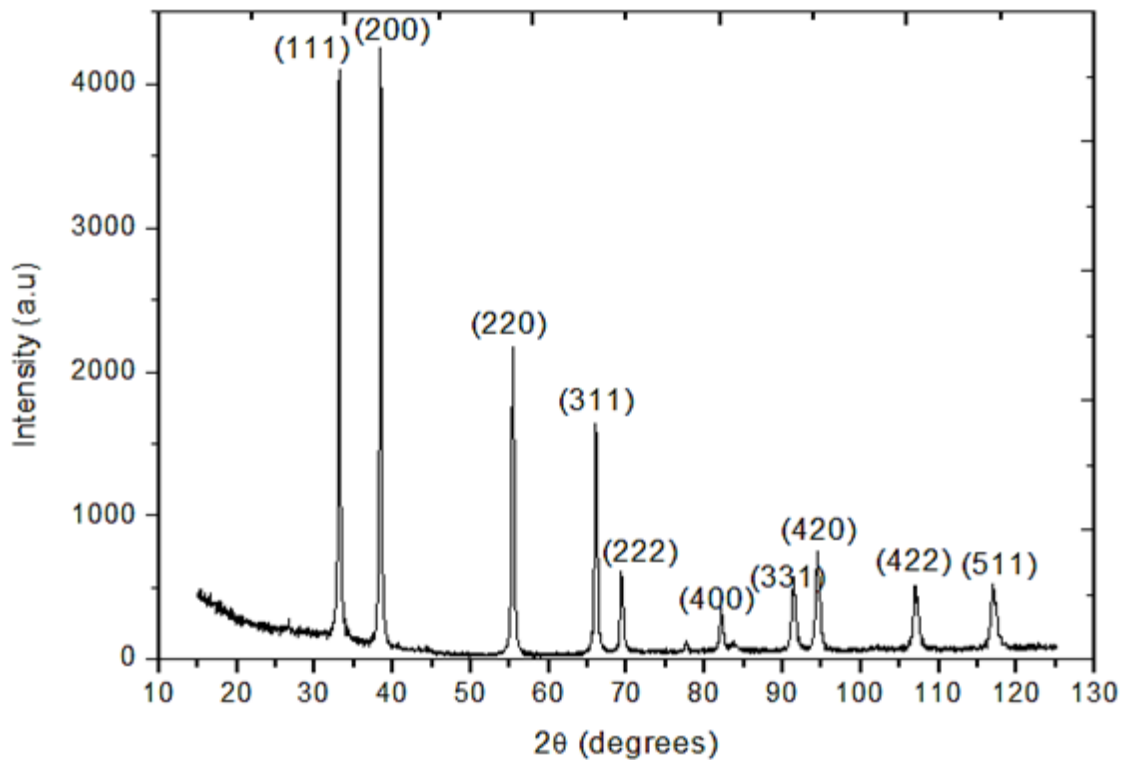


Figure 2. Typical XRD pattern for ZrC deposited at 1259 °C for CH₄/ZrCl₄ molar ratio of 15.23.

3.2.1. Average crystallite size.

The execution of the response surface methodology produced the regression equation (1) which represents the relationship between the crystallite size and the independent variables T (temperature) and M (CH₄/ZrCl₄ molar ratio).

$$D = -129.69 + 0.17T + 4.28M - 1.06 \times 10^{-3} TM - 4.81 \times 10^{-5} T^2 - 8.57 \times 10^{-3} M^2 \quad (1)$$

A quadratic model was found to be statistically significant. The model's corresponding p -value is less than 0.05 (95% confidence). The lack-of-fit is not significant with the F -value and p -value of 4.93 and 0.0787 respectively. The R -squared and adjusted R -squared values are 91% and 85%, indicating that the regression model gives a good description of the relationship between the temperature and CH₄/ZrCl₄, and the crystallite size.

To fully describe the interactions and the quadratic effect of the temperature and CH₄/ZrCl₄ on crystallite size, the response surface analysis was plotted in the contour graph given in Figure 3. The dots represent the experimental values (given in Table 1). The numbers in rectangles denote the value of the response along the given contour given by Equation 1. The integer “5” represents the five replicated centre points. It can be observed that the average crystallite size increases as temperature and CH₄/ZrCl₄ ratios increase. This can be interpreted to be a result of the increasing temperature causing increased atomic mobility which favour crystal growth. There should also be a sufficient CH₄/ZrCl₄ concentration to facilitate the reaction mechanism. It is also observed that as the temperature and CH₄/ZrCl₄ increases further the average crystallite size decreases. The reason for this may be due to increased amount of free carbon which acts as an impurity, retarding ZrC crystal growth.

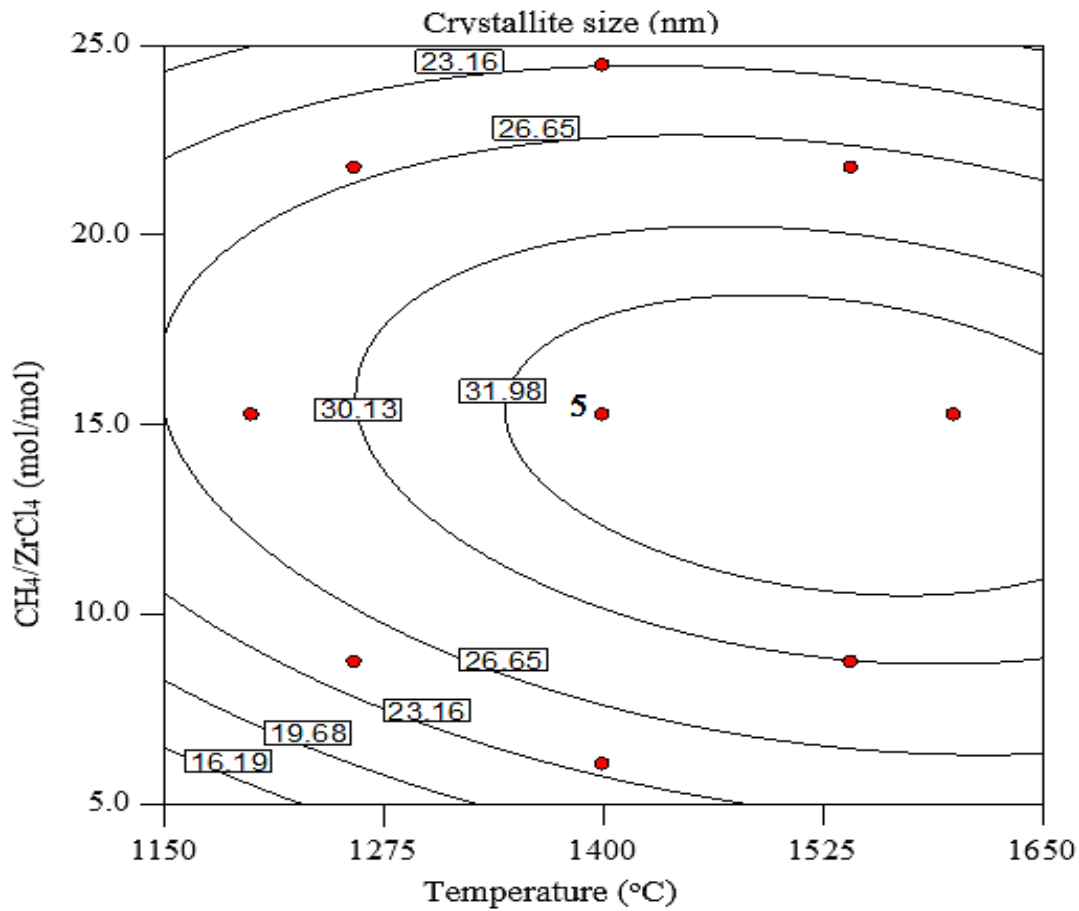


Figure 3. The effect of temperature and CH₄/ZrCl₄ ratio on crystallite size.

3.2 Surface morphology

Figure 4 shows SEM micrographs of ZrC deposited at 1200 °C, 1400 °C and 1600 °C. The CH₄/ZrCl₄ ratio was maintained at 15.23 during deposition. ZrC deposited at 1200 °C shows ball-shaped particles clustering together to form a cauliflower-like shape. Several pores surrounded the cauliflower-like shapes. At 1400 °C the ball-like shapes became bigger and the openings reduce significantly. This might be an indication of small particles agglomerating to form much bigger particles during deposition. When the temperature was increased to 1600 °C, the ball-like shapes became even much bigger than those at 1400 °C. At this point the openings are no longer visible leaving the bottom of the surface looking somehow flat. Some regions of the surface have the particles stacking on top of each like islands. No cracks were visible in all the deposited ZrC. It is therefore clear that the substrate temperature influenced the morphology and the surface uniformity of the ZrC coatings.

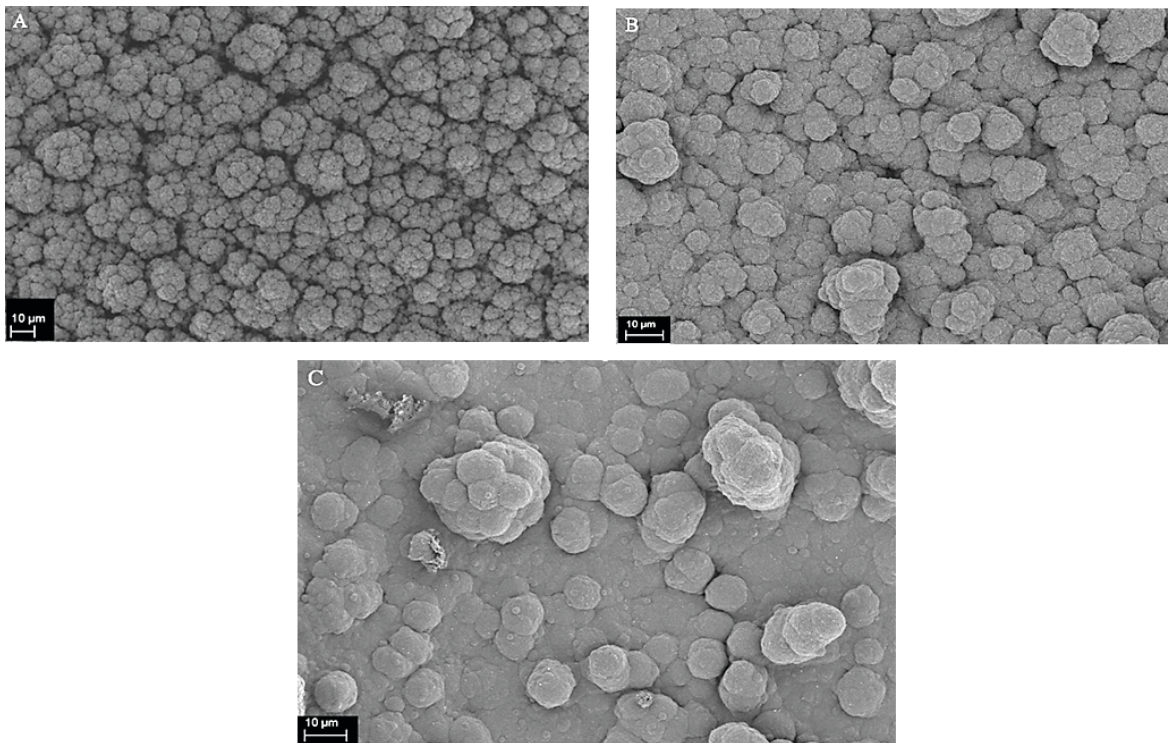


Figure 4. SEM image of the surface morphology of ZrC layers deposited at $\text{CH}_4/\text{ZrCl}_4$ ratio of 15.23 and at A-1200 °C, B-1400 °C and C-1600 °C.

4. Conclusion

ZrC coatings were deposited on graphite substrates at atmospheric pressure using an in-house built vertical CVD system. The experimental raw results were analysed using response surface methodology (RSM) to give a correlation between the crystallite sizes and, substrate temperature and $\text{CH}_4/\text{ZrCl}_4$ ratio. Mathematical regression representations were obtained and are useful in predicting the values of the independent variables for the preparation of ZrC layers with desired average crystallite sizes. The graphical representation further displays the patterns and trends of their behaviour. SEM results showed that particle size and coating uniformity increase with increasing temperature in the range of 1200–1600 °C. This means that to deposit a relatively thick coating high temperatures are required.

5. References

- [1] Malherbe J B 2013 Diffusion of fission products and radiation damage in SiC *J. Phys. D. Appl. Phys.* **46** 473001
- [2] Sawa K and Ueta S 2004 Research and development on HTGR fuel in the HTTR project *Nucl. Eng. Des.* **233** 163–72
- [3] Katoh Y, Vasudevamurthy G, Nozawa T and Snead L L 2013 Properties of zirconium carbide for nuclear fuel applications *J. Nucl. Mater.* **441** 718–42
- [4] Montgomery D C 2008 *Design and analysis of experiments* (John Wiley & Sons)
- [5] Biira S, Crouse P L, Bissett H, Alawad B A B, Hlatshwayo T T, Nel J T, and Malherbe J B 2017 Optimisation of the synthesis of ZrC coatings in an RF induction-heating CVD system using surface response methodology *Thin Solid Films* **624** 61–69
- [6] Stat-Ease 2005 Design expert version 7.0.0 *Stat-Ease Inc*

Tunable photoluminescence emission of sol-gel ZnO films prepared by spin coating technique

E Hasabeldaim, O M Ntwaeaborwa, R E Kroon, E Coetsee and H C Swart
Department of Physics, UFS, Bloemfontein ZA-9300, South Africa

E-mail: swarhc@ufs.ac.za

Abstract. ZnO thin films were successfully synthesized by the sol-gel method using the spin coater technique. The films were annealed at 600 °C in air for two hours and in a H₂ flow for different time periods. The un-annealed film showed an amorphous structure. The c-axis orientation along (002) plane was obtained for the films annealed in air and in the H₂ flow. The crystallite sizes were 47 nm, 44 nm and 38 nm for the films annealed in air and in H₂ for 30 min and 60 min, which were very close to the average particle size obtained from scanning electron microscopy images, confirming the excellent crystallinity of the films. The films (as-prepared and annealed in air) exhibited a broad visible emission as well as a high intense ultraviolet emission. The films annealed in H₂ atmosphere emitted a single greenish emission centred at ~ 511 nm, and this was attributed to oxygen related defects.

1. Introduction

Over the last fifty years, research on metal oxide semiconductors has drawn significant interest because of their optical and electrical potential in electronic devices. ZnO has emerged as a II - VI group compound semiconductor with fascinating properties, the direct wide bandgap (3.37 eV) and the large exciton binding energy (60 meV) of ZnO [1] make it suitable and stable for such application conditions. Furthermore, ZnO has inherent defects which are responsible for its optical properties (visible emission from 400 nm to ~ 750 nm). The interests on ZnO thin films have been considered as a promising route to improve its optical and electrical properties, and to obtain a high quantum efficiency. Excellent crystallinity and particle morphology can easily be adapted by preparing ZnO as a thin film.

Various techniques have been used to fabricate ZnO thin films such as sputtering, pulsed laser deposition, chemical vapour deposition and spray pyrolysis [2]. Amongst these techniques, the sol-gel process is in the forefront in both research and industrial fabrications because of its ease, low cost and above all, the sol-gel process is able to provide homogeneous films, excellent control of the film composition and lower crystallization temperature. These are due to the mixing of liquid precursors. Post-annealing treatments and annealing in reducing atmosphere are some of the laboratory tricks to control the film stoichiometry and to enhance the film structure and morphology in order to obtain required properties.

In this work, sol-gel ZnO films were successfully deposited by using the spin coating technique. The structural and morphological properties were studied by X-ray diffraction (XRD) and scanning electron microscopy (SEM). Although, much research has been done on sol-gel ZnO thin films, different results were obtained in this article. In particular, a single peak of green emission around 500 nm was obtained, which was attributed to oxygen vacancies (V_o).

2. Experimental procedure

Sol-gel ZnO thin films were prepared by using the spin coating technique. Zinc acetate dihydrate ($\text{Zn}(\text{CH}_3\text{COO})_2 \cdot 2\text{H}_2\text{O}$, Alfa Aesar, purity 99.95%) was used as a starting material. Mono-ethanolamine (MEA) and methanol were used as a stabilizer and solvent, respectively. A concentration of 0.2 mol/L zinc precursor solution was prepared by dissolving the zinc acetate dihydrate in the methanol. Mono-ethanolamine was dissolved into the solution. The molar ratio of the MEA:Zn was fixed at 1:1 for all the samples. The final solution was obtained by stirring the mixture for 30 min at room temperature using a magnetic stirrer. The final solution was kept for 48 hours at room temperature of 24 °C. Silicon (100) substrates were used for the film fabrication. The silicon substrate was cleaned ultrasonically for 15 min using acetone to remove the organic contaminations, and then rinsed with ethanol and deionised water, and was then dried by N_2 gas. The solution was dropped onto the silicon substrate, which was rotated at 2500 rev/min for 30 s using the spin coater. After deposition, the films were preheated in air on a hot plate at a temperature of 250 °C for 10 min to evaporate the solvent and remove the organic residuals. The procedures from coating to preheating were repeated 7 times until the desired thickness of ~ 500 nm was obtained. The films were annealed in air at 600 °C for 2 hours using a controlled tube furnace. After annealing at 600 °C, a mixture of H_2 :Ar gas was introduced into the tube furnace. A ratio of 5:95 H_2 :Ar gas was used during the annealing of the films with a flow ratio of 10%. The H_2 /Ar flow was introduced for different annealing times (30 min and 60 min).

For structure and phase analysis, a Bruker X-ray diffractometer (40 kV, 40 mA) with $\text{CuK}\alpha$ (0.15406 nm) was utilized. The scan range was from $2\theta = 15^\circ$ to 100° and steps were 0.0178° . A JEOL JSM-7800F SEM was employed to probe the particle morphology. Photoluminescence (PL) spectra were collected at room temperature with a PMT detector. The films were excited with a He-Cd laser PL system with a 325 nm excitation wavelength.

3. Result and discussion

3.1. XRD and structure analysis

XRD spectra of the sol-gel ZnO films are shown in figure 1. The un-annealed film has an amorphous nature, while the films annealed in different conditions have shown highly c-axis orientation along the (002) plane, which is perpendicular to the substrate surface. It is a common physical phenomenon that ZnO film crystallises by post-annealing treatment. Although the ZnO thin films have been prepared by different methods, the orientation along the c-axis has always been the preferred orientation. This is due to the lower energy of the (002) plane [3]. The crystallite size was estimated by using the well-known Scherrer equation. The crystallite sizes were 47 nm, 44 nm and 38 nm for the films annealed in air, H_2 flow for 30 min and H_2 flow for 60 min, respectively. The crystallite size decreased with increasing time of the H_2 flow. This may be due to the removal of more oxygen atoms from the crystal sites. The peak at $2\theta = 32.86^\circ$ on the films annealed in reducing atmosphere (H_2) for different times is due to the forbidden Si (200) from the substrate that is observed in some cases and not due to changes in the film thickness.

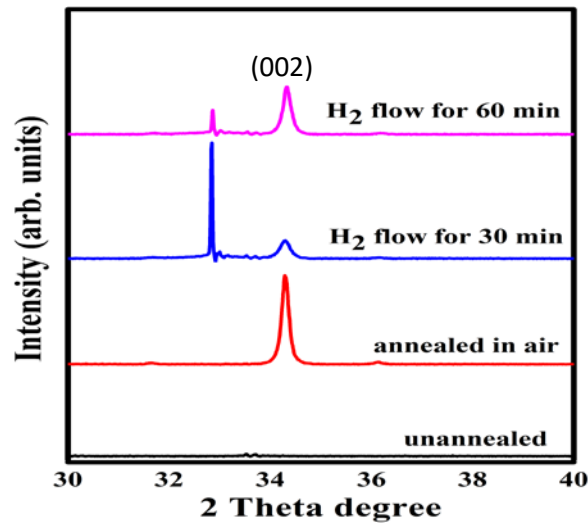


Figure 1. XRD patterns of the films as described in table 1.

3.2. Surface morphology

Figure 2 shows the surface morphology of the sol-gel ZnO films annealed at different conditions. The as-prepared film (un-annealed) showed an amorphous nature as confirmed by XRD results, where no particles were observed, meaning that the film was not crystalline. The films annealed under different conditions (b), (c) and (d) shown spherical particles and their average particles sizes were found to be 42 nm, 28 nm and 46 nm, respectively. Of interest, the particles size computed on the basis of SEM images are in the same order size to the crystallite sizes calculated from XRD (figure 1), hence the annealed films have a high quality of crystallinity. The small differences between the crystallite and the particle size is associated to the un-uniformity of the particle size distribution and the agglomeration of crystallites, however, the obtained bigger crystallite size in comparison to the particle size for the 30 min annealed sample is unexpected and need further investigation. These results have directly contributed into the optical properties of the films, where the films provided a high PL intensity. The particles of the annealed films have a lower particle density compared to the results of Davood Raoufi et al. [4]. Therefore, the films may be porous.

3.3. Photoluminescence properties

Figure 3 shows the PL spectra of the sol-gel ZnO films annealed in different experimental conditions. The un-annealed film figure 3(a) and (de-convoluted in b), exhibited strong excitonic emission around the UV region centred at 379 nm as well as a weak deep level emission centred at 400 nm (blue) and 609 nm (orange), the emission band at 400 nm is probable due to the electron transition from the conduction band or Zn_i to the deeply trapped hole at the zinc vacancies (V_{zn}). The emission at 609 nm arises from the recombination between the photogenerated electron close to the conduction band (Zn_i) and the deeply trapped single ionized oxygen interstitial (O_i) [5]. The weakness of the visible emission on the un-annealed sample means that the film has the lowest concentration of ZnO intrinsic defects. Therefore, the strongest UV emission was due to the lack of competition between the defects and exciton recombination. It is worth noting that with annealing and increasing the reducing atmosphere annealing time, the deep level emission intensity increased while the band to band emission (UV) decreased. Annealing in air and reducing atmosphere introduced more defects in the film structure. The question is, why the un-annealed film contained such low defect concentration? This may be explained by understanding the ZnO structure and the role of annealing temperature on the film structure. ZnO has a non-centrosymmetric hexagonal wurtzite symmetry composed of Zn and O sub-lattices, which are responsible for the generation of the defects. The un-annealed film showed an amorphous structure nature from the XRD pattern (figure 1) which referred to an incomplete crystallization structure,

therefore, no more defects were formed in the film matrix, where the annealed films have well crystallized (XRD (figure 1)), and the defects were generated as confirmed by XRD and their high deep level emission.

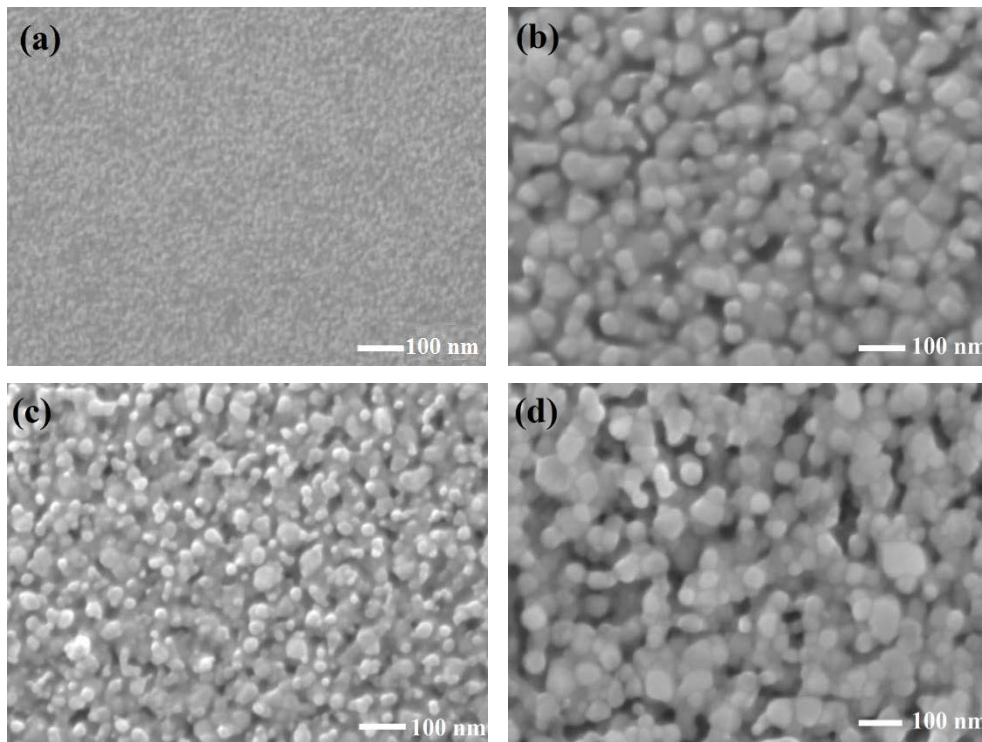
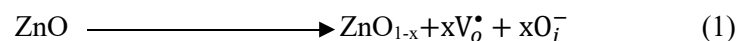


Figure 2. SEM images of the sol-gel ZnO films deposited by spin coating technique, (a) as prepared (un-annealed), (b) annealed in air for two hours at 600 °C, (c) exposed to a H₂ flux for 30 min during annealing, (d) exposed to a H₂ flow for 60 min during annealing.

The un-annealed film may possess residual organic solvents and structural defects which acted as non-radiative recombination centres, and hence the film emitted low defects related emission. After annealing in air at 600 °C, the intensity of the visible emission increased relative to the UV emission, and the violet emission around 400 nm disappeared which was probably due to the disappearance of the Zn_i while a new green emission at 504 nm has appeared. The increasing of the visible emission intensity was due to the film crystallinity, and may be due to the removal of non-radiative centres that came from the residual organic solvents and structural defects. Oxygen vacancies (V_o) are commonly reported defects in ZnO because of their low formation energy, and it is these that are speculated to play a role in the green emission of ZnO [6]. Therefore, Zn_i which caused the blue emission in the un-annealed films may have diffused to form a new V_o in the annealed film. The orange (609 nm) emission of the un-annealed film was red-shifted to 660 nm after the annealing process. The following reaction (1) possibly occurred during the air annealing process:



The oxygen interstitial (O_i) may be also be introduced to the film from the atmospheric oxygen during the annealing process [7]. The shift in the orange emission from 609 nm to 660 nm after annealing in air could be due to the formation of and/or change in local position of the related defects [8]. The peak around 753 nm on the un-annealed film and the film annealed in air is due to the scattered UV second order peak.

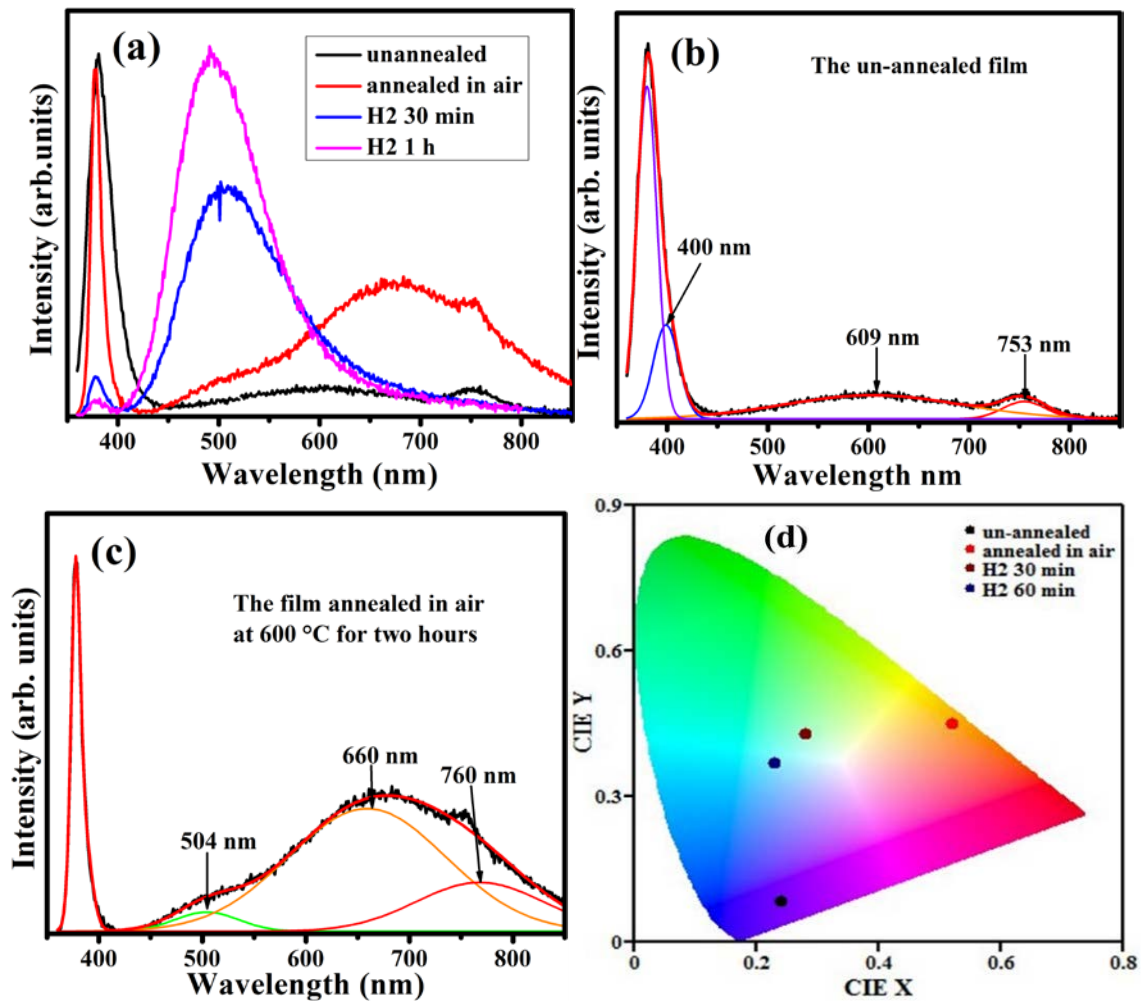


Figure 3. Photoluminescence spectra of (a) the sol-gel ZnO films prepared and annealed in different conditions, (b) De-convoluted peaks of the un-annealed film, (c) De-convoluted peaks of the film annealed in air and (d) CIE colour coordinates.

The film annealed in H₂ for 30 min exhibited a broad green emission peak around 507 nm with a high intensity, while the UV intensity has drastically decreased. The disappearance of orange and red emission is probably due to the removal of some of the oxygen-related defects. H₂ may have reacted with oxygen atoms and ions in the film resulting in the formation of evaporated H₂O or metallic Zn. The film annealed in H₂ for 60 min emitted a higher intensity green emission centred at 500 nm as well as a very weak UV emission, meaning that more/new defects were formed in the film structure leading to an increase in the competition between the defects and the exciton recombination. The blue shift on the green emission after increasing the reducing atmosphere time could be related to a change in the related defects local positions and therefore a shift in the defect level energy position.

Since the photometric characteristics are very important factors in optoelectronic applications, the colour coordinates (X, Y) and the colour correlated temperature (CCT) of the samples were studied by the CIE 1931 software and are displayed in figure 3(d). The CIE coordinate values are important in the sense that they give a quantitative link between the distributions of wavelengths in the electromagnetic visible spectrum, and the physiological perceived colours in the human colour vision. The McCamy equation was used to calculate the parameters which were tabulated in table 1.

$$CCT = -437 n^3 + 3601 n^2 - 6861 n + 5514$$

where $n = (x - x_e)/(y - y_e)$ and the chromaticity epicentre is at $x_e = 0.332$ and $y_e = 0.186$.

Table 1. The colour coordinates (X, Y) and colour correlated temperature (CCT) of the sol-gel ZnO films.

Sample name	X	Y	CCT (K)
Un-annealed	0.24	0.08	1986
Annealed in air	0.52	0.45	2296
H ₂ for 30 min	0.28	0.43	7143
H ₂ for 60 min	0.23	0.37	10497

4. Conclusion

C-axis oriented ZnO thin films were successfully prepared by sol-gel method using the spin coating technique. Structural, morphological and optical properties of the films were studied. The deep level defect related emission of ZnO was discussed. The tuneable green emission with colour coordinates (X = 0.28, Y = 0.43) and (X = 0.23, Y = 0.37) were obtained from the films annealed in H₂ for different times. The results indicate that oxygen vacancies and interstitials are responsible for the green emission. These films are useful for luminescent thin film applications, particularly where green emission is required.

Acknowledgement

This work is supported both by the South African Research Chairs Initiative of the Department of Science and Technology, the National Research Foundation of South Africa (84415) and African Laser Centre (ALC). The PL system used is supported by the rental pool programme of the National Laser Centre (NLC).

References

- [1] Özgür Ü, Alivov Y I, Liu C, Teke A, Reshchikov M, Doğan S and Morkoc H 2005 *J. Appl. Phys.* **98** 041301
- [2] Bao Dinghua, Gu Haoshuang and Kuang Anxiang 1998 *Thin Solid Films* **312** 37
- [3] Natsume Y and Sakata H 2000 *Thin Solid Films* **372** 30
- [4] Raoufi Davood and Raoufic Taha 2009 *Appl. Surf. Sci.* **255** 5812
- [5] Zeng By Haibo, Duan Guotao, Li Yue, Yang Shikuan, Xu Xiaoxia and Cai Weiping 2010 *Adv. Funct. Mater.* **20** 561
- [6] Lin Y, Xie J, Wang H, Li Y, Chavez C, Lee SangYeol, Foltyn S R, Crooker S A, Burrell A K, McCleskey T M and Jia Q X 2005 *Thin Solid Films* **492** 101
- [7] Kumar Vinod, Kumar Vijay, Som S, Yousif A, Singh N, Ntwaeaborwa O M, Avinashi Kapoor and Swart H C 2014 *J. Colloid Interf. Sci.* **428** 8
- [8] Wang Zhenling, Lin Cuikun, Liu Xiaoming, Li Guangzhi, Luo Yan, Quan Zewei, Xiang Hongping and Lin Jun 2006 *J. Phys. Chem. B* **110** 9469

Pick-off annihilation of delocalized positronium in BaF₂ at elevated temperatures

TP Jili^{1,2}, E Sideras-Haddad² and D Wamwangi²

¹Physics Department, University of Zululand, P/B X1001, Kwadlangezwa, 3886, South Africa

²School of Physics, University of the Witwatersrand, P/B 3, Wits, 2050, South Africa

E-mail: jilip@unizulu.ac.za

Abstract. Positron lifetime components and associated intensities in the temperature range 300 – 800 K were measured using standard fast-fast coincidence technique. Two lifetime components were resolved after background and source corrections. The long lifetime component decreases in the temperature range from 500 ps at 300 K to 402 ps at 711 K. This corresponds to a fractional increase in the annihilation rate of 22% in the temperature range 300 K to 693 K. The de-trapping of positronium from the Bloch states followed by annihilation through the ‘pick-off’ process appears to be one of the dominant processes in the long lifetime components in the temperature range. Annihilation rates from positron annihilations with valence and core electrons of the individual atoms of the sample are also calculated using density functional theory in the framework of generalized gradient approximation.

1. Introduction

Positronium which is a hydrogen-like bound state, has two configurations that depend on the relative spins of the positron and electron. The singlet state (S=0, M=0) is referred to as para-positronium (p-Ps), where S is the total spin and M is the z-component quantum number. The triplet states (S=1, M=0, ±1) are referred to as ortho-positronium (o-Ps). Para-positronium emits two gamma photons while ortho-positronium emits three gamma photons. Experimental measurements of positronium annihilations use the two lowest states. These two lowest states are both in ground states (n=1 and L=0) namely ¹S₀ (p-Ps) and ³S₁ (o-Ps). The decay rate of p-Ps ground state, ¹S₀, is calculated as a series of α given by [1]

$$\Gamma(p - Ps \rightarrow \gamma\gamma) = \frac{\alpha^5 m_e}{2} \left[1 - \left(5 - \frac{\pi^2}{4} \right) \frac{\alpha}{\pi} + 2\alpha^2 \ln \frac{1}{\alpha} + 1.73 \left(\frac{\alpha}{\pi} \right)^2 - 3 \frac{\alpha^3}{2\pi} \ln^2 \frac{1}{\alpha} + O\left(\alpha^3 \ln \frac{1}{\alpha}\right) \right] \quad (1)$$

where $\alpha \approx 1/137$

Para-positronium mean lifetime calculated from equation (1) is about 125 ps and more calculations [2-5] are in agreement. The ground state decay rate of the ortho-positronium, ¹S₁, decays into an odd number of photons and is given by [6-7]

$$\Gamma(o - Ps \rightarrow \gamma\gamma\gamma) = \frac{2(\pi^2 - 9)\alpha^6 m_e}{9\pi} \left[1 - 10.28661 \frac{\alpha}{\pi} - \frac{\alpha^2}{3} \ln \frac{1}{\alpha} + B_0 \left(\frac{\alpha}{\pi} \right)^2 - \frac{3\alpha^3}{2\pi} \ln \left(\frac{1}{\alpha} \right) + O(\alpha^3 \ln \alpha) \right] \quad (2)$$

where B_0 is a two-loop coefficient needed to bring theory into an agreement with experiment. The effects of higher order term $O(\alpha^6 m_e)$ are fully discussed elsewhere [8-12]

The mean lifetime of ortho-positronium is about 142 ns [13-14]. The lifetime of ortho-positronium is very long such that it is possible that some processes can take place and disturb the ortho-positronium system before it annihilates. One of the processes known as “pick-off” annihilation involves the positron in the ortho-positronium system colliding and annihilating with one of the electron of the host material but not with the electron that is part of the positronium system [15]. The “pick-off” process is carried out in accordance with the reaction



where e^- is the free electron of conduction band or valence electron of lattice atom

The annihilation rate of Ps in a solid can be written as

$$\Gamma = \kappa\Gamma_o + \Gamma_{pick-off} \quad (4)$$

where $\kappa\Gamma_o$ is self-annihilation rate and $\Gamma_{pick-off}$ is the pick-off annihilation rate. Pick-off annihilation rate can be obtained from a standard Monte Carlo sampling as

$$\Gamma_{pick-off} = \pi r_e^2 c \int n_-(r) n_+ \gamma [n_-(r)] d^3r \quad (5)$$

where $n_-(r)$, $n_+(r)$ are the electron and positron densities respectively and γ is the enhancement factor.

The other process is the conversion of ortho-positronium into para-positronium due to spin-orbit interaction [15]. As soon as the conversion takes place, para-positronium annihilates quickly. Hoydo et al [16-17] suggested that in alkali halide crystals, positronium exist in a free Bloch state at very low temperatures. A simple model proposed by Hoydo et al [23] which include free and trapped states for positrons and positronium is used. The positron lifetimes and their corresponding intensities in the framework of this model are given by

$$I_1 \tau_1 = I_f \tau_f + I_{pPs} \tau_{pPs} + I_{foPs} \tau_{foPs} \quad (6)$$

$$I_2 \tau_2 = I_{t+} \tau_{t+} + I_{toPs} \tau_{toPs} \quad (7)$$

$$I_1 = I_f + I_{pPs} + I_{foPs} \quad (8)$$

$$I_2 = I_{t+} + I_{toPs} \quad (9)$$

where the subscripts f , $t+$, pPs , $foPs$ and $toPs$ refer to the free positron, trapped positron, free para-positronium, free ortho-positronium and trapped ortho-positronium respectively.

More studies on KCl and NaF [18-20] reported a localization of positronium as the temperature rises in the temperature range 9 – 400 K. Alkaline earth halides have a structure close to that of alkali halides. Elefteriades et al [21] measured positron lifetimes in barium fluoride in the temperature range 10 – 293 K. They found an increase in the intensity of a long lifetime component between 12 and 80 K followed by a decrease of intensity from about 63% to 37% in the temperature

range 80 – 293 K. An increase in the positronium formation probability, associated with temperature range 10 – 80 K, was viewed as localization of positronium and they also suggested that a decrease in the second lifetime component intensity from about 63% to 37% was probable due to the de-trapping of localized positronium at temperatures higher than 80 K.

In this work we explore the temperature dependence of annihilation parameters in ionic barium fluoride in the higher temperature range 300 – 800 K. We further study the annihilation rates due to positrons annihilating with valence and core electrons of the individual atoms in barium fluoride in the temperature range using density functional theory in the framework of generalized gradient approximation. We also understand that in alkali earth halide, only anionic vacancies, which are positive, are thermally created and the long positron lifetime measurements would be difficult to attribute to annihilations at defects in the temperature range 300 – 800 K. We have not yet found any literature reporting in this temperature interval using positron annihilation technique.

2. Experiment

Two barium fluoride samples each of surface area 8 mm × 10 mm and thickness of 2 mm and of cleavage [111] were obtained from Goodfellows, Britain. A positron source of activity 15 μCi of ²²NaCl was sealed between two electron-welded nickel foils (density of 8.9 g/cm³) each of thickness 7 μm. The radioactive area was about 16 mm². Sealed positron source was sandwiched between two equal barium fluoride samples in a standard sandwich arrangement. The source-sample-heater arrangement is shown in figure 1

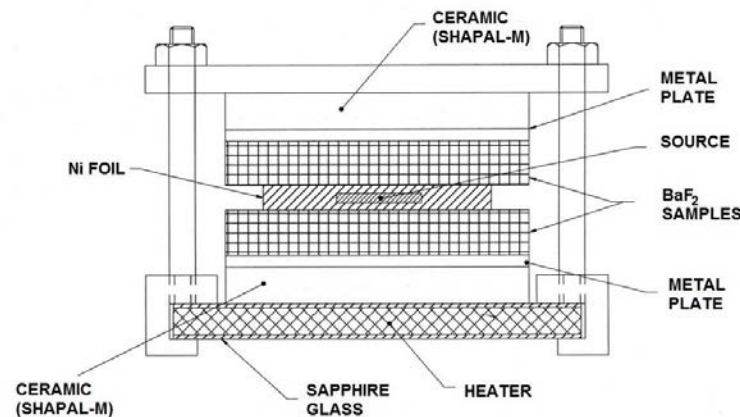


Figure 1. Sample holder system showing the source-sample-heater arrangement.

Annihilation rate measurements were obtained by utilizing a fast-fast coincidence system with two collinear photomultipliers (XP2020) coupled to barium fluoride scintillators. Positron lifetime spectrum in ZnO was accumulated for the calibration of the system. The full width at half maximum (FWHM) of the time resolution was 220 ps of the Gaussian resolution function.

Lifetime spectra were analysed using LIFSPECFIT [22]. A two-component fit was resolved following source correction and background subtraction. Throughout the experiment, the reduced chi-square (χ^2) for most of set data was fairly close to unity.

3. Results and discussions

Barium fluoride is an alkali earth halide of cubic structure of space group Fm3m. Figures 2 and 3 show the long and short positron lifetime components and the corresponding intensities respectively at different temperatures. The long positron lifetime component, as shown in figure 2, decreases

from 500 ps at 300 K to 402 ps at 711 K with a minimum value of 392 ps at approximately 640 K. This corresponds to 22% fractional increase of annihilation rate in the temperature range 300 – 640 K. The measurements were not repeated but the trend seems to be consistent with the measurements carried out by Eleftheriades et al [21] although their range is 30 – 300 K.

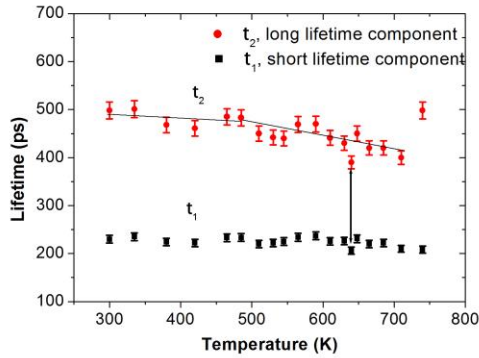


Figure 2. Short and long positron lifetime components in the temperature range 300 – 800 K

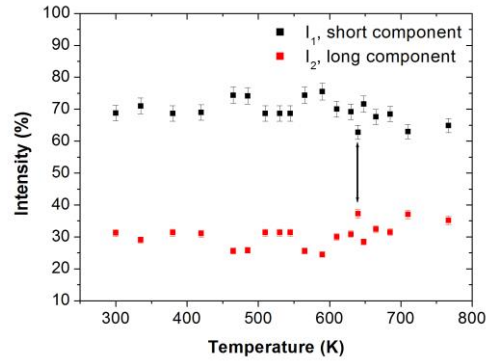


Figure 3. Measured intensities for long and short lifetime components

The “pick-off” annihilations usually take place where the positronium is in a quasistable state [16]. Therefore, in our case in which the temperature range 300 – 711 K is considered, delocalization and the “pick-off” annihilation process is considered. Pick-off process is one of the key processes which explain the observed fractional increase of about 22% in the annihilation rate (or a decrease in long lifetime component) in the temperature range 300 – 640 K. The o-Ps to 2γ radiation is strongly influenced by a high number of electrons more especially, the unpaired electrons of anionic interstitials, which strongly influence or enhance the pick-off process as described in equation 4. When the pick-off process takes place, the delocalized ortho-positronium lifetime is shortened as can be seen from the data in figure 2. It is clear that as the number of anion interstitials increases with temperature, the annihilation rate increases (corresponding to a decrease in the long lifetime component). On the other hand, a large percentage of positrons annihilate in the bulk. It is worth mentioning that although anionic vacancy can find it difficult to trap a positron, there is a probability that it can readily trap an electron (forming an F-center) [24] because of its positive potential which eventually attracts and annihilates with a positron. Barium is an electron-rich atom with 5p and 6s orbitals dominating the fluorine 2p and 2s electrons in terms of high electron density. Using annihilation equations 6-9, we deduce the following annihilation intensities shown in Table 1. The singlet state, p-Ps, which has a very short lifetime of about 125 ps, has 6% intensity whilst the triplet state o-Ps in general has a slightly higher intensity than p-Ps. The lifetime of o-Ps is greatly reduced by the pick-off process with one of the host atom electrons. The two positroniums are different in terms of relative spins between positron and electron within the positronium.

Table 1. Deduced intensities of positrons and positronium in barium fluoride

BaF2		Intensities
Para-positronium	pPs	0.06 ± 0.01
Ortho-positronium	oPs	0.07 ± 0.01
Free positrons	e_f^+	0.56 ± 0.01
Trapped positrons	e_t^+	0.31 ± 0.01

The suggestion is that in the temperature range 300 – 640 K the dominant process is due to the detrapping of previously localized positronium. The temperature range 640 – 711 K shows a slight increase in the annihilation rate corresponding to a decrease slight decrease in the longer lifetime component. Other contributions toward the positron short lifetime component emanate from the

positrons annihilating with valence and core electrons of the individual atoms of the sample. This is achieved through solving Schrodinger equation separately for electrons and positron wavefunctions to obtain positron and electron densities. The annihilation rates are then calculated from

$$\lambda_j = \pi r_0^2 c \int d\mathbf{r} \gamma^{GGA}(\mathbf{r}) n_+(\mathbf{r}) n_j(\mathbf{r}) \quad (10)$$

where r_0 , c , γ^{GGA} , n_+ and n_j are classical radius of electron, speed of light, enhancement factor in the framework of generalized gradient approximation, positron density and electron density in state j respectively

Using the generalized gradient approximation, the positron wavefunction peaks around the barium atom and in the process increasing the annihilation rate probability as shown in figure 4 while positron density around the fluorine atom remains relatively low as shown in figure 5. The pick-off annihilation with valence electrons in barium increases while the annihilation with fluorine valence electrons decreases with temperature as shown in Table 2.

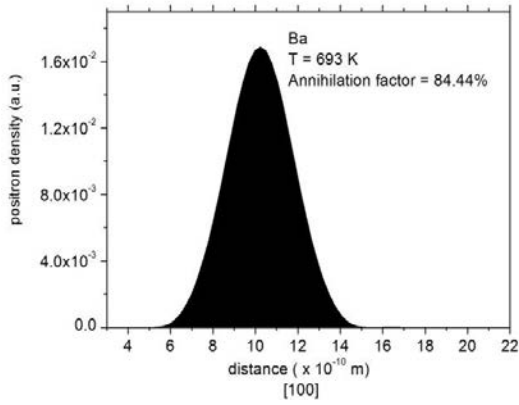


Figure 4. Positron wavefunction density peaks around the barium atom

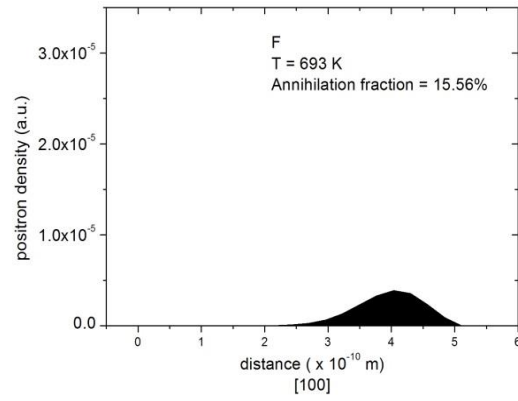


Figure 5. Positron wavefunction density around the fluorine atom

Table 2. Annihilation fractions and rates are calculated in the framework of a generalized gradient approximation.

BaF ₂	λ_{core} (per ns)	λ_{5s} (per ns)	λ_{5p} (per ns)	λ_{6s} (per ns)	Annih. fraction (%)
F-vacancy 300 K					
Ba	0.0053	0.0721	0.6189	3.4563	84.36
F	0.7688				15.64
F-vacancy 580 K					
Ba	0.0051	0.0698	0.6019	3.4257	84.41
F	0.7578				15.59
F-vacancy 693 K					
Ba	0.0049	0.0684	0.5921	3.4084	84.44
F	0.7508				15.56
F- divacancy 693 K					
Ba	0.0052	0.0709	0.6138	3.486	86.57
F	0.6481				13.43

4. Conclusion

We find that the annihilation rate via pick-off annihilation in the temperature range 300 – 750 K primarily due annihilation of ortho-positronium positron with one of the valence electrons of the host atoms, is one of the dominant processes in barium fluoride and as a result the lifetime of o-Ps is highly reduced. The intensity of the long lifetime component is indeed attributed to the annihilation of a delocalized o-Ps through pick-off process. We are also of the view that more positron annihilation data at elevated temperatures greater than 750 K is needed in order to have a complete picture regarding the existence of positronium in barium fluoride since not much is covered of this material in the literature using positron annihilation spectroscopy in the temperatures greater than 600 K. The new proposed region is also of interest since it covers the excess specific heat anomaly in barium fluoride.

Acknowledgements

We gratefully acknowledge financial support from the Research Committee of the University of Zululand and School of Physics at the University of the Witwatersrand. The authors would like to thank Prof Filip Tuomisto and Dr Ilja Makkonen for their support.

References

- [1] Smith C 2002 *Bound State Description in Quantum Electrodynamics and Chromodynamics*, Dissertation, Universite Catholique de Louvain
- [2] Kniel BA and Penin AA 2000 *Phys. Rev. Lett.* **85** 1210
- [3] Czarnecki A, Melnikov K and Yelkhovsky A 1999 *Phys. Rev. Lett.* **83** 1135
- [4] Al-Ramadhan AH and Gidley DW 1994 *Phys. Rev. Lett.* **72** 1632
- [5] Wheeler JA 1946 *Annalen New York Academy Sciences* **48** 219
- [6] Adkins GS 1996 *Phys. Rev. Lett.* **76** 4903
- [7] Lepage GP, Mackenzie PB, Streng KH and Zerwas PM 1983 *Phys. Rev.* **A28** 3090
- [8] Pachucki K and Karshenboim SG 1998 *Phys. Rev. Lett.* **80** 2101
- [9] Czarnecki A, Melnikov K and Yelkhovysk A 1999 *Phys. Rev. Lett.* **82**, 311
- [10] Adkins GS, Fell RN and Mitrikov PM 1997 *Phys. Rev. Lett.* **79** 3383
- [11] Czarnecki A, Melnikov K and Yelkhovsky A 1999 *Phys. Rev.* **A59**, 4316
- [12] Hoang AH, Labelle P and Zebarjad SM 1997 *Phys. Rev. Lett.* **79** 3387
- [13] Vetter RA and Freedman SJ 2002 *Phys. Rev.* **A 66**, 052505
- [14] Vallery RS, Zitzewitz PW and Gidley DW 2003 *Phys. Rev. Lett.* **90** 203402
- [15] Ivanov IA and Mitroy J 2002 *Phys. Rev.* **A 65** 034709
- [16] Hoydo T and Takakusa Y 1977 *J. Phys. Soc. Jpn.* **42** 1065
- [17] Hoydo T and Takakusa Y 1978 *J. Phys. Soc. Jpn.* **45** 795
- [18] Takakusa Y and Hoydo T 1980 *J. Phys. Soc. Jpn.* **49** 2243
- [19] Hoydo T, Kasai J and Takakusa Y 1980 *J. Phys. Soc. Jpn.* **49** 2248
- [20] Kasai J, Hoydo T and Fujiwara K 1983 *J. Phys. Soc. Jpn.* **52** 3671
- [21] Elefteriades CA, Chardalas M, Sp. Dedoussis and Stef. Chalarambous, 1988 *Crys. Res. Technol.* **23** 3 437-440
- [22] LIFSPECFIT 5.1, 1992 *Lifetime spectrum fit version 5.1*, Laboratory of Physics, Technical University of Helsinki
- [23] Hoydo T and Stewart AT 1984 *Phys. Rev.* **29B** 4164
- [24] Hartog HW 1968 *Phys. Stat. Sol.* **25**, K111-K114

Synthesis and characterisation of $Y_2O_3:Bi^{3+}$ phosphor material

E Lee, HC Swart, JJ Terblans

Department of Physics, University of the Free State, PO Box 339, Bloemfontein, 9300, South Africa

Email: LeeE@ufs.ac.za, SwartHC@ufs.ac.za, TerblansJJ@ufs.ac.za

Abstract. Bismuth doped yttrium oxide ($Y_2O_3:Bi^{3+}$) phosphor was synthesised using co-precipitation method. During synthesis, the pH value and Bi^{3+} concentration were varied to study their effects on the luminescent properties of the phosphor. X-ray diffraction patterns showed the phosphor samples had retained its single-phase cubic structure. The crystallite size was determined using the Scherrer equation, which showed that crystallite size was more dependent on the pH during synthesis than that of Bi ion concentration. The photoluminescence spectra revealed two strong excitation bands centred at 330 nm and 390 nm, along with two emission bands one centred at 409 nm and another broad band centred at 489 nm which corresponds to the two sites within the host matrix where Bi ions may occupy. By monitoring the 489 nm emission band intensity, it revealed that the variations in the pH value during synthesis had influenced the luminescent intensity of the phosphor. Altering the Bi^{3+} concentration in the Y_2O_3 host material also influenced the emission intensity of the phosphor, where the maximum intensity was found when the phosphor was synthesised at pH 10 with a Bi^{3+} concentration of 2.0 mol%.

1. Introduction

Solar energy is the most abundant and cleanest source of energy currently available. This led to the invention of photovoltaic (PV) solar cells capable of converting solar energy into electrical energy. Solar cells fabricated from single junction crystalline silicon (c-Si) is the most widely used PV cell but suffers from an efficiency limit of round 29 % [1]. The low conversion efficiency from solar energy to electrical energy results from the mismatch between the solar spectrum and the absorption spectrum of c-Si where the strongest spectral response of c-Si solar cells is around 1000 nm [2-4].

In the past decade, luminescent materials doped with rare-earth elements have been used extensively in the lighting industry, due to the wide range of possible luminescence from ultraviolet (UV) through the visible to the near-infrared (NIR) regions [5, 6]. $RE^{3+}-Yb^{3+}$ ($RE = Tb, Ce, Er$ and Pr) co-doped phosphors are of great interest for down-converting UV photons to NIR photons, used to improve the efficiency of solar cells [7]. Yb^{3+} serves as a suitable acceptor ion as it contains only a single excitation state correlating to an emission at around 1000 nm, very close to the maximum absorption efficiency of c-Si [8, 9]. Lanthanides or rare-earth metals are generally poor at absorbing photons in the UV to blue regions due to their parity forbidden 4f transition [10]. Thus more attention has been placed on metal ions as possible alternatives to the current rare-earth sensitizers [2, 11]. Metal ions such as Bi^{3+} which have a $6s^2$ electron configuration making the $6s^2 \rightarrow 6s6p$ transition an allowed transition [12]. This allowed transitions present in Bi gives rise to much broader excitation and emission bands as compared to rare-earths which are generally narrower [13]. Y_2O_3 phosphor doped with Bi^{3+} ions show a strong emission band between 490 and 510 nm when exposed to UV light [2, 12, 14]. The energy associated

with the visible emission of Bi^{3+} is twice the energy required for the ${}^2\text{F}_{7/2} \rightarrow {}^2\text{F}_{5/2}$ transition of Yb^{3+} and indicates that cooperative energy transfer (CET) from Bi^{3+} to Yb^{3+} could occur [15].

In this study $\text{Y}_2\text{O}_3:\text{Bi}^{3+}$ phosphors were prepared using co-precipitation under different pH values and Bi^{3+} concentrations to investigate their effects on the particle sizes and the luminescent properties.

2. Experimental

2.1. Synthesis of $\text{Y}_{2-x}\text{O}_3:\text{Bi}_x$

$\text{Y}_2\text{O}_3:\text{Bi}^{3+}$ powder phosphor was prepared using the co-precipitation method under various pH values and different doping concentrations. Y_2O_3 (99.99%) and Bi_2O_3 (99.9%) were used as the starting reagents. Stoichiometric amounts of Y_2O_3 and Bi_2O_3 were dissolved in concentrated nitric acid (HNO_3) through heating and stirring until an aqueous solution consisting of $\text{Y}(\text{NO}_3)_3$ and $\text{Bi}(\text{NO}_3)_3$ was obtained. Once the starting material has completely dissolved ammonia (NH_4OH) was added to the acid solution, under vigorous stirring to maintain a pH from 6 to 10 and stirred for a further 2 hours. The white precipitate was collected then washed using ethanol to remove any unreacted materials. The product was placed in an oven at 80°C for at least 12 hours to evaporate the ethanol that was introduced during washing. Using a mortar, the dried mass was crushed before being placed in an annealing furnace for 1 hour at 450°C and finally at 1000°C for 2 hours.

The effect of pH on the luminescence properties of $\text{Y}_2\text{O}_3:\text{Bi}^{3+}$ phosphors were investigated using a spectrometer and showed that samples synthesised under pH 10 displayed the strongest luminescence. Thus all further phosphors were synthesised with pH 10.

2.2. Characterisation

The crystal structure of the powder samples was characterised from x-ray diffraction (XRD) measurements using a Bruker D8 Advance diffractometer with $\text{K}\alpha\text{Cu}$ x-rays (1.54 \AA). The emission and excitation properties of the $\text{Y}_{2-x}\text{O}_3:\text{Bi}_x$ phosphor samples were measured using a Varian Cary Eclipse fluorescence spectrophotometer.

3. Results and discussion

The XRD pattern for $\text{Y}_{1.98}\text{O}_3:\text{Bi}_{2.0\%}$ prepared under different pH conditions are represented in figure 1(a), while figure 1(b) shows the (222) peak shifts of phosphors prepared at different pH values.

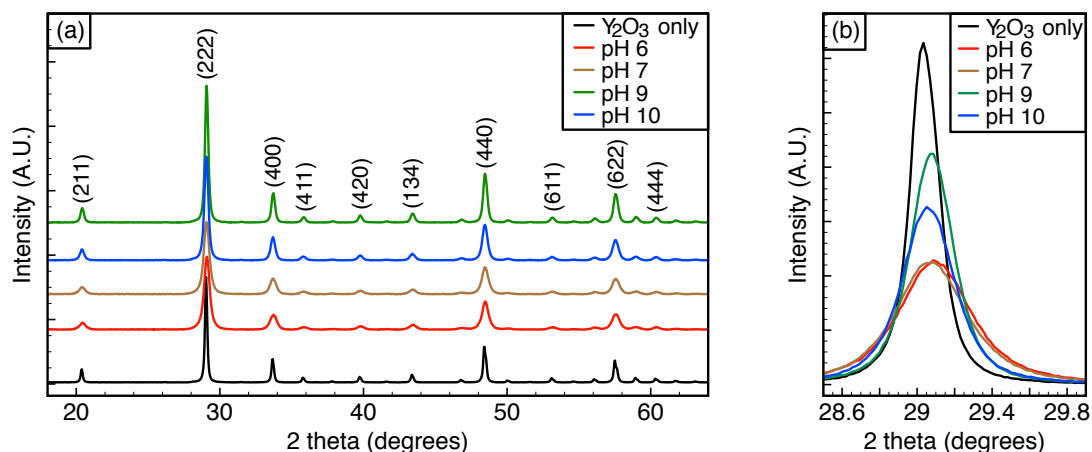


Figure 1 (a) XRD pattern of $\text{Y}_{1.98}\text{O}_3:\text{Bi}_{2.0\%}$ phosphor powder synthesised at pH 6, 7, 9 and 10 along with non-doped Y_2O_3 starting material. (b) The (222) peak shift of $\text{Y}_{1.98}\text{O}_3:\text{Bi}_{2.0\%}$ phosphor as compared to non-doped Y_2O_3 .

The measure XRD patterns correlates well to that of the non-doped Y_2O_3 starting material. From the XRD patterns, it showed that varying the pH value during synthesis did not alter the crystal structure

of the host material as it still resembles a single phase cubic structure. The absence of any additional diffraction peaks suggests that no impurity phases were present. Thus shifts can be attributed to the addition of Bi ions which caused stress and strain within the host matrix.

Figure 2(a) shows both the excitation and emission spectra of a $Y_{1.98}O_3:Bi_{2.0\%}$ phosphor synthesised at pH 6. An illustration of the two occupational site with the Y_2O_3 host matrix is shown in figure 2(b).

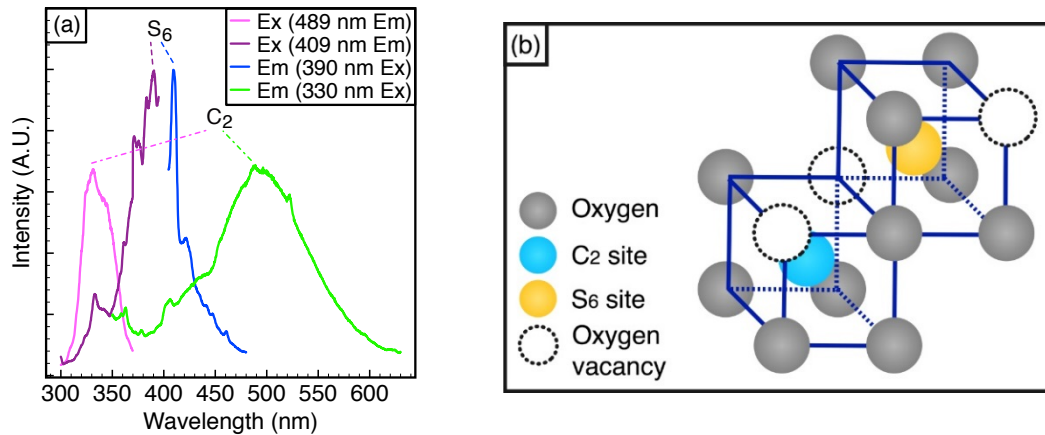


Figure 2: (a) Excitation and emission spectra of $Y_{1.98}O_3:Bi_{2.0\%}$ phosphor due to the C_2 and S_6 occupational sites of Bi ions. (b) Schematic illustration of the C_2 and S_6 sites in cubic Y_2O_3 .

Using an excitation wavelength $\lambda_{ex} = 330$ nm an emission spectrum showing a strong green emission at 489 nm was observed. When exciting at $\lambda_{ex} = 390$ nm a strong blue emission situated at 409 nm was measured. For emission $\lambda_{em} = 489$ nm an excitation band was obtained with the maximum located at 330 nm. Similarly observing at an emission wavelength $\lambda_{em} = 409$ nm an excitation spectrum yielded three excitation bands one located at 330 nm, the second at 370 nm and the strongest peak at 390 nm. The existence of the two emission (409 nm and 489 nm) and excitation (330 nm and 390 nm) bands were a direct result of the two possible sites that the Bi^{3+} ions are able to occupy in the Y_2O_3 host matrix. The emission and excitation bands centred at 489 nm and 330 nm respectively is responsible for the excitation and emission of the Bi^{3+} ion situation in the C_2 site where as the S_6 site correlates to the 409 nm emission and 390 nm excitation bands [2, 11, 16].

Figure 3(a) shows the 489 nm emission and 330 nm excitation spectra of $Y_{1.98}O_3:Bi_{2.0\%}$ phosphor prepared at pH 6, 7, 9 and 10. The effect of pH on the 489 nm emission intensity is shown in figure 3(b).

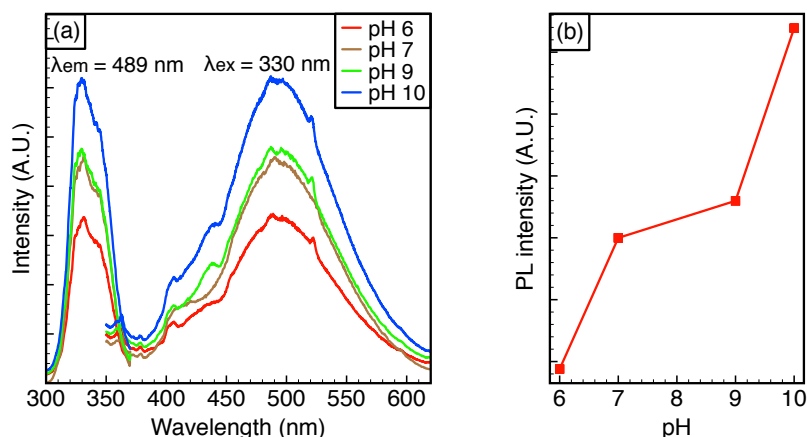


Figure 3: (a) The 330 nm excitation and 489 nm emission spectrum for $Y_{1.98}O_3:Bi_{2.0\%}$ synthesised at varying pH values. (b) PL intensity of 489 nm emission as a function of pH.

While monitoring the emission wavelength $\lambda_{em} = 489$ nm, similar to the sample prepared at pH 6, a broad and intense band centred at 330 nm was observed. Additionally, when the phosphor samples were excited at $\lambda_{ex} = 330$ nm a broad emission band with maximum at around 489 nm was observed. The outer most $6s^2$ electron configuration of Bi^{3+} houses one energy level 1S_0 (ground state) and while in the $6s6p$ configuration (excited state) it splits into four levels 3P_0 , 3P_1 , 3P_2 and 1P_1 in order of increasing energy. Due to the Δj selection rule, transitions from $^1S_0 \rightarrow ^3P_1$ and $^1S_0 \rightarrow ^1P_1$ are allowed transitions whereas transitions $^1S_0 \rightarrow ^3P_0$ and $^1S_0 \rightarrow ^3P_2$ are strictly forbidden. Thus the excitation band at 330 nm and emission band at 489 nm are attributed to the transition from $^1S_0 \rightarrow ^3P_1$ and $^3P_1 \rightarrow ^1S_0$ respectively [2, 17-19].

It can be seen in figure 3 that emission intensity vary sufficiently with variations in the pH with the strongest emission intensity found when the $Y_{1.98}O_3:Bi_{2.0\%}$ phosphor was synthesised at pH 10, therefore further synthesis was conducted at pH 10.

The XRD results for the $Y_{2-x}O_3:Bi_x$ phosphor prepared at varying Bi ion concentrations and at pH 10 are shown in figure 4(a). The results show a single phase cubic structure similar to the structure found when varying pH and the absence of additional peaks shows that no impurity phases had been introduced. The shifts in the main (222) peak shown in figure 4(b) of the cubic structure were due to the stress and strain present in the crystal when Bi ions were introduced into the host matrix.

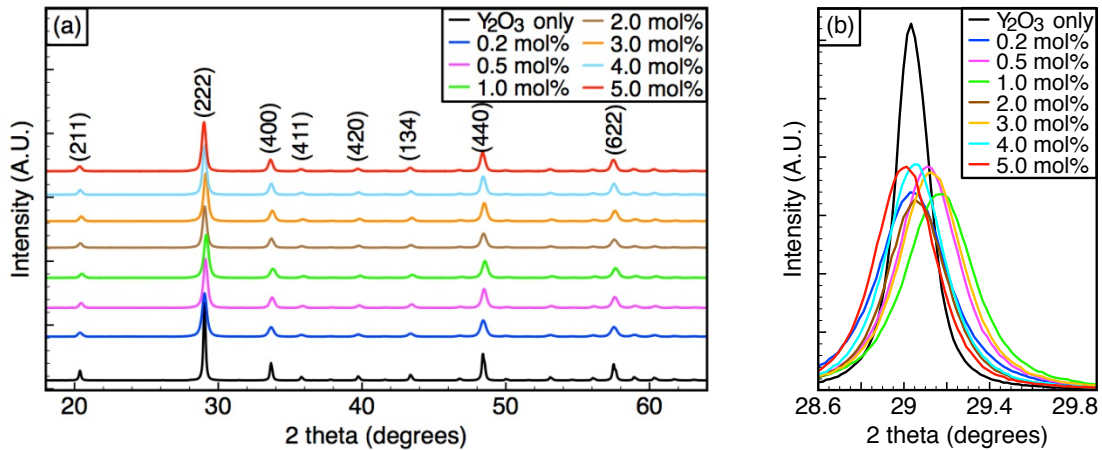


Figure 4: (a) XRD patterns for $Y_{2-x}O_3:Bi_x$ ($x = 0.2, 0.5, 1.0, 2.0, 3.0, 4.0$ and 5.0 mol%) phosphor synthesised using pH 10. (b) The (222) peak shift due to the addition of Bi ions.

The effect of varying pH and Bi concentrations on the crystallite size are shown in figure 5. The crystallite sizes were calculated using the Scherrer equation (1) [20, 21].

$$\tau = \frac{K\lambda}{\beta \cos \theta} \quad (1)$$

τ is the crystallite size, K is the shape factor which has a typical value of 0.9, λ is wavelength of the X-ray used, β is the width of the peak at half its maximum intensity (FWHM) subtracted by the instrumental broadening (measured in radians) and θ is the Bragg angle. To obtain a better approximation of the crystallite size for each sample, all diffraction peaks indexed in Figure 1(a) and 4(a) were used and the average crystallite size for each sample was taken. The Scherrer equation revealed that changes in pH did indeed affect the crystallite size where the crystallite size increased with an increase in pH until a maximum at pH 9 where the size then decreased. In the case of varying Bi concentrations, the crystallite sizes were found to be similar ranging between 21 to 25 nm with no distinct pattern. This suggests that the crystallite size was more dependent on the pH during synthesis than the concentration of Bi dopants.

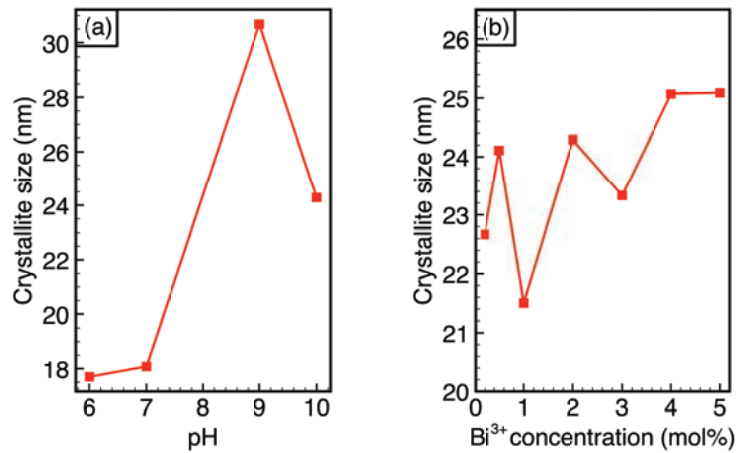


Figure 5: (a) The effect of crystallite size due to the variations in pH during synthesis. (b) Crystallite size as a function of Bi concentration.

The 330 nm excitation and 489 nm emission spectra for varying Bi ion concentrations are represented in figure 6(a). The results showed that the luminescent intensity was also dependant on the Bi ion concentration as shown in figure 6(b).

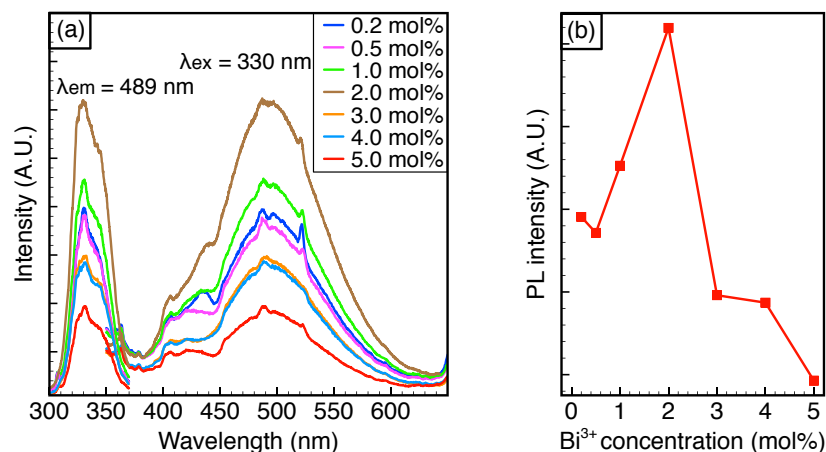


Figure 6: (a) Excitation and emission spectrum for $Y_{2-x}O_3:Bi_x$ phosphor synthesised at varying Bi concentration. (b) PL intensity of 489 nm as a function Bi concentration.

Figure 6 showed that variations in Bi ion concentration does influence the luminescence intensity of the phosphor. Between 0.5 to 2.0 mol% Bi the luminescence increased with an increase in Bi concentration. The luminescent intensity then suddenly decreased between 3.0 to 5.0 mol% Bi. The sharp decrease in intensity was largely due to concentration quenching. Thus the strongest luminescence observed for the $Y_{2-x}O_3:Bi_x$ phosphor was when the phosphor was synthesised at pH 10 and containing a Bi ion concentration of 2.0 mol%.

4. Conclusion

The $Y_2O_3:Bi$ phosphor was successfully synthesised using the co-precipitation method. XRD patterns showed that variations in both the pH and Bi ion concentration did not influence the single phase crystal structure of the Y_2O_3 host material. Utilising the Scherrer equation it revealed that the pH during

synthesis has the strongest influence on the crystallite size of the final phosphor as compared to varying the Bi ion concentration. Photoluminescence showed the two-excitation and emissions bands, which corresponds to the two possible sites (C2 and S6) that Bi ions are able to occupy within the host matrix. While monitoring the 489 nm emission peak it showed that the luminescent intensity was influenced by the pH during synthesis, where an increase in pH showed an increase in the luminescent intensity of the phosphor. The influence of Bi concentration was also demonstrated by observing the 489 nm emission peak, which showed that increasing the Bi ion concentration also lead to an increase in the luminescent intensity until an ion concentration of 2.0 mol%. Thereafter any further increase in the Bi concentration a decrease in the 489 nm emission intensity was observed, due to the effect of concentration quenching. Thus the strongest luminescence was achieved when the $Y_{2-x}O_3:Bi_x$ phosphor was synthesised at pH 10 with an Bi concentration of 2.0 mol%.

Acknowledgments

This research paper is made possible thanks to Prof HC Swart for his guidance through this project, to Prof RE Kroon for his input during PL measurements and Dr S Cronjé for his help in XRD measurements. Funding support is acknowledged to the South African Research Chairs Initiative of the Department of Science and Technology (DST) and the National Research Fund (NRF).

References

- [1] Tiedje T, Yablonovitch E, Cody G D and Brooks B G 1984 *IEEE Transactions on Electron Devices* **31** 711
- [2] Huang X Y, Ji X H and Zhang Q Y 2011 *Journal of the American Ceramic Society* **94** 833
- [3] Saritas M and McKell H D 1987 *Journal of Applied Physics* **61** 4923
- [4] Poruba A, Fejfar A, Remeš Z, Špringer J, Vanecek M, Kocka J, Meier J, Torres P and Shah A 2000 *Journal of Applied Physics* **88** 148
- [5] Feldmann C, Jüstel T, Ronda C and Schmidt P 2003 *Advanced Functional Materials* **13** 511
- [6] Richards B 2006 *Solar Energy Materials and Solar Cells* **90** 1189
- [7] Trupke T, Green M A and Würfel P 2002 *Journal of Applied Physics* **92** 1668
- [8] Li J, Zhang J, Zhang X, Hao Z and Luo Y 2014 *Journal of Alloys and Compounds* **583** 96
- [9] Gao G, Peng M and Wondraczek L 2014 *J. Mater. Chem. C* **2** 8083
- [10] Zhang Q and Huang X 2010 *Progress in Materials Science* **55** 353
- [11] Rambabu U and Han S D 2013 *Ceramics International* **39** 1603
- [12] Jacobsohn L G, Blair M W, Tornga S C, Brown L O, Bennett B L and Muenchausen R E 2008 *Journal of Applied Physics* **104** 124303
- [13] Sun H, Zhou J and Qiu J 2014 *Progress in Material Science* **64** 1
- [14] van de Craats A M and Blasse G 1995 *Chemical Physics Letters* **243** 559
- [15] Xian-Tao W, Jiang-Bo Z, Yong-Hu C, Min Y and Yong L 2010 *Chinese Physics B* **19** 77804
- [16] Avram D, Cojocaru B, Florea M and Tiseanu C 2016 *Opt. Mater. Express* **6** 1635
- [17] Takeshita S, Isobe T, Sawayama T and Niikura S 2009 *Journal of Luminescence* **129** 1067
- [18] Ilmer M, Grabmaier B C and Blasse G 1994 *Chemistry of Materials* **6** 204
- [19] Kumar V, Kumar R, Lochab S and Singh N 2007 *Nuclear Instruments and Methods in Physics Research Section B: Beam Interactions with Materials and Atoms* **262** 194
- [20] Scherrer P 1918 *Göttinger Nachrichten Math. Phys* **2** 98
- [21] Monshi A, Foroughi M and Monshi M 2012 *World Journal of Nano Science and Engineering* **2** 154

Theory for diffusivity measurements when the temperature is ramped linearly

J B Malherbe*, O S Odutemowo, C C Theron, E G Njoroge, T T Hlatshwayo

Department of Physics, University of Pretoria, Pretoria, 0002, South Africa.

* johan.malherbe@up.ac.za

Abstract. Nearly all measurements to determine diffusion coefficients in solids are performed using either isochronal or isothermal measurements. These are usually done using large discrete steps in the annealing temperature. In certain diffusion systems more than one diffusion mechanism may exist in different temperature regimes. The transition temperature between these can be missed when using large temperature steps for annealing. This paper derives the necessary equations for diffusivity measurements where the temperature is ramped linearly and a composition-depth profile is simultaneously performed *in situ*. This yields the diffusion coefficient at small temperature intervals over the whole temperature range.

1. Introduction

In general, nearly all measurements to determine diffusion coefficients in solids are performed using either isochronal or isothermal measurements [1, 2]. Usually, these are done with fairly large discrete steps in temperature, with 100 °C or 50 °C steps being the norm. The diffusion coefficient, at a particular temperature, depends primarily on the microstructure of the substrate, with the type of impurity (i.e. the diffusion species) being of secondary order. When a phase change occurs in the substrate material or when a chemical reaction occurs between the diffusion species and the substrate, the diffusion mechanism usually undergoes a discrete change with a corresponding change in the diffusion coefficient as a function of temperature. When either of these occurs, the large steps in temperature can result in one missing the transition from one diffusion mechanism to another. Consequently, it is often highly desirable to perform *in situ* diffusion measurements during the heating cycle.

Theron [3, 4] developed a method for dealing with the diffusion in the case of a linear increase in temperature and real time analysis. He set up a general rate equation and made the assumption that this rate variable had an Arrhenius temperature behaviour. This resulted in differential equations for standard diffusion limited kinetics and Nernst-Einstein diffusion limited kinetics. These differential equations are solvable in terms of the Exponential Integral for those two cases.

In this paper we also assume a temperature which is ramped linearly while doing simultaneously non-destructive depth profiling (typically with RBS) to determine the diffusion of a diluted species in a homogeneous substrate at small temperature intervals. Analytical equations for such diffusivity measurements are derived.

2. Theory

A key assumption in our theory is that the diffusion coefficient D has an Arrhenius behaviour with respect to the absolute temperature T , i.e.

$$D = D_0 \exp\left(-\frac{E}{k_B T}\right) \quad (1)$$

where E is the activation energy and k_B is the Boltzmann constant [1,2]. This form allows one to calculate the diffusivity D at any temperature; with good accuracy within the temperature range for which (1) was determined, and with reduced accuracy outside this temperature regime. The assumption (1) is also commonly assumed in diffusion studies.

The one-dimensional time-dependent Fick diffusion equation is given by

$$\frac{\partial N}{\partial t} = D \frac{\partial^2 N}{\partial x^2} \quad (2)$$

In solutions to this equation, the diffusion coefficient D usually appears together with the time t as the factor Dt [2,5]. To illustrate this, consider an initial profile of a semi-infinite layer given by

$$\begin{aligned} N(x, 0) &= N_0 \quad \text{for } x < x_0 \\ N(x, 0) &= 0 \quad \text{for } x > x_0 \end{aligned} \quad (3)$$

The solution is given by [2]

$$N(x, t) = \frac{N_0}{2} \operatorname{erfc}\left(\frac{x - x_0}{2\sqrt{Dt}}\right) \quad (4)$$

The Complementary Error Function in (4) is given by [6]

$$\operatorname{erfc} z = 1 - \operatorname{erf} z = 1 - \frac{2}{\sqrt{\pi}} \int_0^z \exp(-t^2) dt \quad (5)$$

The original profile (3) and the diffused profile (4) for model values for the depth scale x and diffusion coefficient D , are illustrated in Figure 1. In practice, the depth profile data of the diffused semi-infinite layer which is annealed for a known time t at a specific temperature T is fitted to equation (4) to give a value for D .

In the different (depending on the boundary values) solutions to (2), the D is taken as a constant value, i.e. it is then a solution of the Fick diffusion equation at a specific temperature T . In the case of a linear increase in temperature with time t there is also a corresponding increase in the D values – cf. equation (1). The cumulative effect of increasing the temperature on the factor Dt can be approximated by the limit of a Riemann integral of infinitesimal small increases in t . Thus, the factor Dt becomes $\int D(t)dt$.

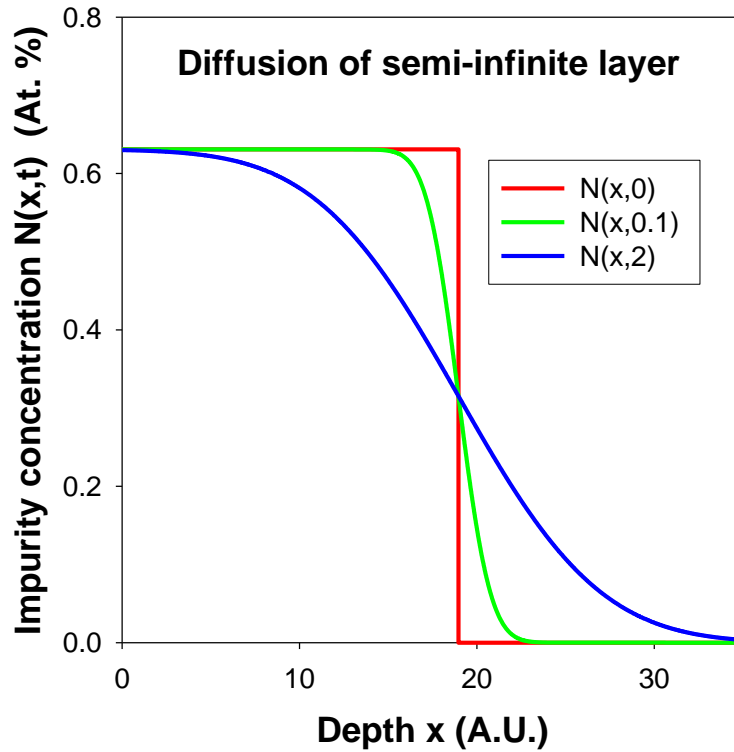


Figure 1. Diffusion of a semi-infinite layer with original profile given by (3) for two different times indicated in the figure.

Using assumption (1), i.e. that over this (limited) temperature range the diffusion coefficient has an Arrhenius behaviour, the integral becomes

$$\int_0^{t_a} D(t)dt = \int_0^{t_a} D_0 \exp\left(-\frac{E}{k_B(T_b + \alpha t)}\right)dt \quad (6)$$

where t_a in the two integral limits is the time at which a measurement is taken, and the absolute temperature is given by the linear function $T = T_b + \alpha t$, where T_b is the temperature at which the ramping started and α is the heating rate. Making two transformations, and integrating by parts give

$$\int_0^{t_a} D(t)dt = \frac{D_0}{\alpha} \left[T \exp\left(-\frac{E}{k_B T}\right) - T_b \exp\left(-\frac{E}{k_B T_b}\right) \right] + \frac{D_0 E}{\alpha k_B} \left[E_1\left(\frac{E}{k_B T_b}\right) - E_1\left(\frac{E}{k_B T_a}\right) \right] \quad (7)$$

where the Exponential Integral function $E_1(x)$ is defined as [6]

$$E_1(x) = \left[\int_x^\infty \frac{\exp(-t)}{t} dt \right] \text{ with } x > 0 \quad (8)$$

with an asymptotic expansion (i.e. $x \gg 1$) given by

$$E_1(x) = \frac{e^{-x}}{x} \left[1 - \frac{1}{x} + \frac{2}{x^2} - \frac{3}{x^3} + \dots \right] \quad (9)$$

Using the first two terms in (9) and after some algebra, one finds that (7) reduces to

$$\int_0^{t_a} D(t)dt = \frac{k_B}{\alpha E} \left[T_a^2 D(T_a) - T_b^2 D(T_b) \right] \quad (10)$$

where $T_a = T_b + \alpha t_a$. Because the diffusion coefficient at the start of the ramping temperature (typically room temperature of 300 K) is extremely small, the last term is approximately zero. Thus

$$\int_0^{t_a} D(t)dt \approx \frac{k_B}{\alpha E} T_a^2 D(T_a) \quad (11)$$

With the notation

$$\int_0^{t_a} D(t)dt = \Delta \quad (12)$$

equation (11) can be written as

$$\frac{k_B}{E} D(T_a) = \alpha \frac{\Delta}{T_a^2} \quad (13)$$

Taking the logarithm and substituting the Arrhenius form of D

$$\ln \frac{k_B}{E} + \ln D_0 - \frac{E}{k_B T_a} = \ln \left(\alpha \frac{\Delta}{T_a^2} \right) \quad (13)$$

Thus from a plot of $\ln \left(\alpha \frac{\Delta}{T_a^2} \right)$ against $\frac{1}{T_a}$, the slope yields the activation energy E and from the intercept D_0 can be obtained, from which the diffusion coefficient D can be calculated via (1).

The increment between successive T_a values depends primarily on the time taken to perform a depth analysis of the diffusing impurity. In practice, for RBS analysis this may result in the increment being of the order of 1 or 2 K. This is small enough to pinpoint the temperature at which the activation energy changes. Since the activation energy E of diffusion represents the average energy needed by a diffusing atom to either pass over or tunnel through the potential barrier between the two semi-equilibrium positions of the atom, a change in the value of E represents two different diffusion mechanisms operating. Information on the exact temperature can provide valuable reference data for DFT (density functional theory) calculation on diffusion traps in a substrate [8, 9].

3. Conclusions

Equations are derived to extract diffusion coefficients at very small temperature intervals from *in situ* real-time non-destructive analysis of an impurity profile in a substrate heated to have a linear increase in temperature of the substrate as a function for time. A key assumption in this

derivation is that the diffusion coefficient over the whole temperature range has an Arrhenius dependence on temperature. The initial temperature must start at a temperature where the diffusion is negligibly low. The solution is given in terms of the Exponential Integral function. Taking the first two terms of the asymptotic power expansion of this function yields an analytical equation from which the diffusion coefficient D at small temperature intervals can be determined.

References

- [1] Heitjans P and Kärger J 2005 *Diffusion in Condense Matter* (Berlin: Springer)
- [2] Boltaks B I 1963 *Diffusion in Semiconductors*, (London: Infosearch Ltd.)
- [3] Theron C C, Mars J A, Churms C L, Farmer J and Pretorius P 1998 *Nucl. Instrum. Meth. Phys. Res.* **B 139** 213
- [4] Theron C C in http://docs.tronsmit.com/index.php/Mathematical_analysis_of_temperature_ramped_data Accessed on 21 Dec. 2015.
- [5] Crank J 1975 *The Mathematics of Diffusion* (Oxford: Clarendon)
- [6] Abramowitz M and Stegun I A 1964 *Handbook of Mathematical Functions*, (Washington: National Bureau of Standards) chapter 7.
- [7] Abramowitz M and Stegun I A 1964 *Handbook of Mathematical Functions*, (Washington: National Bureau of Standards) chapter 5.
- [8] Zheng M J, Swaminathan N, Morgan D and Szlufarska I 2013 *Phys. Rev.* **B 88** 054105
- [9] Jamison L, Sridharan K, Shannon S and Szlufarska I, *J. Mater. Res.* **29** 2781

Evolutionary algorithm simulation study of β -MnO₂ nanoclusters

P W Masoga, P E Ngoepe and R R Maphanga

Materials Modelling Centre, School of Physical and Mineral Sciences, University of Limpopo, Private bag x 1106, Sovenga, 0727, South Africa

E-mail: phalamasoga@gmail.com

Abstract. The increasing demand for high energy density rechargeable batteries has fuelled the interest in the research, development and manufacturing of new battery systems capable of powering high powered machinery as well as rechargeable household appliances. Pyrolusite (β -MnO₂) is the most stable and abundant polymorph of manganese dioxide and a potential cathode material for rechargeable lithium-ion batteries. In this study, a combination of evolutionary algorithm techniques and density functional theory methods are employed to determine the stabilities of MnO₂ nanoclusters across the energy landscape. We investigate the energetics and structural configurations for (MnO₂)_{n=1-6} nanoclusters. The most stable nanoclusters are made of a cubic structure consisting of two manganese and two oxygen atoms for various cluster sizes. The stable structures tend to migrate to more circular compact configurations after geometry optimization using density functional theory. As the temperature is increased from 200K to 1300K, the change in the bond angles and bond distances is measured. An increment of the exterior angles and bonding lengths along with the decrease of the interior angles is observed further emphasizing the migration to a more circular compact configuration.

1. Introduction

The growing demand for energy has caused an increase in scientific research focusing on renewable and rechargeable energy supplies as a way of supplementing the pressure on the rapidly declining fossil fuel reserves. The dependence on fossil fuels as the main source of energy for powering the industrial revolution has contributed considerable damage to the environment [1]. Recent developments in the field of scientific research on energy storage has already begun producing results as evident in the production of electric vehicles (EVs) and hybrid electric vehicles (HEVs) [2]. Among all types of secondary batteries, lithium-ion batteries have attracted the most attention as they are characterized by high energy density and high power density [3]. One of the challenges for improving the performance of lithium-ion batteries to meet increasingly demanding requirements for energy storage is the development of suitable cathode materials [4]

Pyrolusite (β -MnO₂) is regarded as the most stable and abundant polymorph of manganese dioxide. It crystallizes into the rutile crystal structure with three-coordinate oxide and octahedral metal centers. Nanostructuring has been shown to improve the performance of energy storage materials although the mechanisms for this improvement are not fully understood on the atomic-scale. Several nanostructured MnO₂, including nano-crystals of different shapes; nanowires, nanotubes, nanoclusters and nanobelts, have been synthesized and can be used as new materials for battery systems [5, 6]. Experimentally, nanoscaling of cathode materials is still a challenge due to complexities associated with the synthesis and monitoring of reactions occurring at the nanoscale. MnO₂ structures have been simulated and

studied in varying shapes and architectures, that is, nanosheet, nanorod and mesoporous [7]. Consequently, recent advances in computational resources provide options in simulating materials at the nanoscale, thereby shedding light and reducing costs on this very important field of research [8, 9]. In this paper, structural configuration and stability of MnO₂ nanoclusters are investigated using density functional theory, as an approach of refining nanocluster models developed using interatomic potentials. Also the effect of temperature change on nanocluster configuration is investigated.

2. Methodology

Evolutionary algorithms (EA) have been used previously to determine the local minima of desired atomic structures and produced better results compared to other methods [7, 10]. The fundamental idea behind evolutionary algorithms is performing a process that simulates natural selection through survival of the fittest [11, 12]. The method avoids many problems associated with a single starting point by setting up a population of candidate clusters, hence the end product of each EA cycle is a new population of candidate structures [13]. Evolutionary algorithm techniques were used previously to investigate the stability of (MnO₂)_n n=1-4 [14] and a more detailed methodology is presented therein. The multistage configurations procedure for determining the low-energy configurations for MnO₂ clusters is used. In the first EA cycle the candidate structures are configurations in which the ionic coordinates are randomized. In stages 1 and 2, EA make use of the local optimization routines within the GULP program [15] based on Interatomic Potential (IP) method, to relax all newly created structures through breeding or randomization. In stages 3 and 4 of the EA cycle, the better clusters within the final population, as measured by the energy of formation, are selected for analysis or further refinement using a density functional theory (DFT) method.

A multistage procedure is implemented in order to predict the low-energy configurations for neutral, stoichiometric small clusters of MnO₂. For each cluster, n=1 to 6 in the first stage, low-energy stationary points are found on the three different energy hypersurfaces that are defined by interatomic potentials. In EA simulations, the ground-state configuration for a cluster with predefined composition becomes a plausible candidate. In this paper, the all electron density functional theory method with a local numerical orbitals basis set and local optimization techniques as implemented in the CASTEP [16] code were employed to further investigate MnO₂ nanocluster stability trend and temperature effects. Thus, the lowest energy candidate structures, as measured by the energy of formation using the interatomic potential method were subjected to geometry optimization using GGA-PBEsol (stages 3 to 5). The planewave basis set energy cut-off was set at 500 eV. For atomic positions to be considered fully relaxed, the convergence parameters were set as follows: total energy tolerance 1 x 10⁻⁶ eV/atom, maximum force tolerance 0.05 eV/nm and maximum stress component 0.1 GPa. The stable nanoclusters were placed centrally in a 10 x 10 x 10 Å crystal box, large enough to ensure that there were no interactions between the system and its self-image along all the axes within the periodic boundary conditions.

3. Results and Discussions

Geometrical configurations of (MnO₂)_{n=1-6} nanoclusters and their order of stability as determined by the density functional theory are presented. Thus, the structural properties based on atomic configurations as determined by bond lengths and bond angles are discussed along with stability of the nanoclusters. In Figure 1, the most stable nanocluster for each cluster size as measured by formation energy is presented together with bond lengths after optimization. A small letter labels the nanocluster with a number indicating the number of atoms (n), followed by dashed number indicating the stable local minima structures as determined by the evolutionary algorithms sequence (e.g. n1-2). The bond lengths between the atoms in the nanoclusters were measured.

Structure (MnO ₂) _{n=1}	Interatomic potentials (IP) method [17]	Density Functional Theory (DFT) method	DFT Bond Length (Å)
n1-2			Mn1-O1=1.655 Mn1-O2=1.655
n2-2			Mn1-O1=1.652 Mn1-O2=1.801 Mn1-O3=1.802 Mn2-O4=1.651
n3-2			Mn1-O1=1.661 Mn1-O2=1.864 Mn1-O3=1.828 Mn2-O2=1.771
n4-1			Mn1-O1=1.652 Mn1-O2=1.805 Mn1-O3=1.816 Mn2-O2=1.833
n5-1			Mn1-O1=1.649 Mn1-O2=1.773 Mn1-O3=1.848 Mn2-O2=1.905
n6-2			Mn1-O1=1.694 Mn2-O2=1.808 Mn1-O3=1.815 Mn2-O2=1.839

Figure 1: Atomic configurations and bond lengths for (MnO₂)_{n=1-6} nanocluster as predicted by IP (before optimization) and DFT (after optimization) methods.

The interatomic interactions between the manganese and oxygen atoms are classified as follows: Mn1 is encircled in blue while Mn2 is encircled in green. The oxygen atoms are numbered 1, 2, 3, 4 ... with O1 being the first oxygen from the right hand side, followed by O2 as the second oxygen from the right side bonded to Mn1 or Mn2. The same identification was used for O3 and O4. There is a notable decrease in bond length and bond angles of all the nanoclusters after geometry optimization with density functional theory method. The change in bond parameters suggests that the configuration for the nanocluster becomes compact. DFT predicts the bond lengths ranging between 1.655 Å and 1.905 Å for (MnO₂)_{n=1-6}. For n = 1, 2, 3 and 6 the second most stable structures as measured and predicted by interatomic potentials are found to be the most stable structures and this is in agreement with previous studies where a different DFT code, FHI-AIMS was used by Maphanga et al. [17] to refine IP nanocluster structures. On the other hand, n=4 and 5 predict the same nanocluster structures as those predicted by interatomic potentials to be the most stable. DFT predicts the atomic arrangement of the local minima structures to be bending to form a quasi-like isomer for all the systems.

It is evident from the density functional theory techniques that compact ring structures consisting of a cubic structure for the orientation of the two manganese and two oxygen atoms is the most stable and preferred orientation, which correlates with previous studies [9, 18]. Furthermore, experimental photoelectron spectroscopy (PES) studies of isostructural titanium dioxide (TiO₂) nanoclusters by Zhai et al. [19] reported that compact ring structures are the most stable. The predicted most stable MnO₂ nanoclusters have identical bonds between the manganese and oxygen atoms but slightly different bond angles between the manganese and two oxygen atoms for n=1 to n=4. Similar trends have been reported for the isostructural TiO₂ by Hamad [9]. Furthermore, most stable structures adopting compact ring

configurations are in agreement with findings by Woodley et al. [20, 21], which suggested that the smallest clusters preferred shorter average bond distances as opposed to a higher average coordination of the constituent atoms. Thus, nanoclusters prefer compact ring configuration than a linear atomic arrangement. The Mn-O bond lengths decrease slightly after optimization with DFT and the bond angles for the atoms at the outer side (angles at both sides of the Mn1 and Mn2 atoms encircled in blue and green respectively) also decrease. The DFT method predicts a configuration with two-terminal Mn-O bonds. The complexity of the energy landscape increased with the increase in cluster size as seen with the n5-1 and n6-2 nanoclusters where the atoms formed several different bonds after optimization.

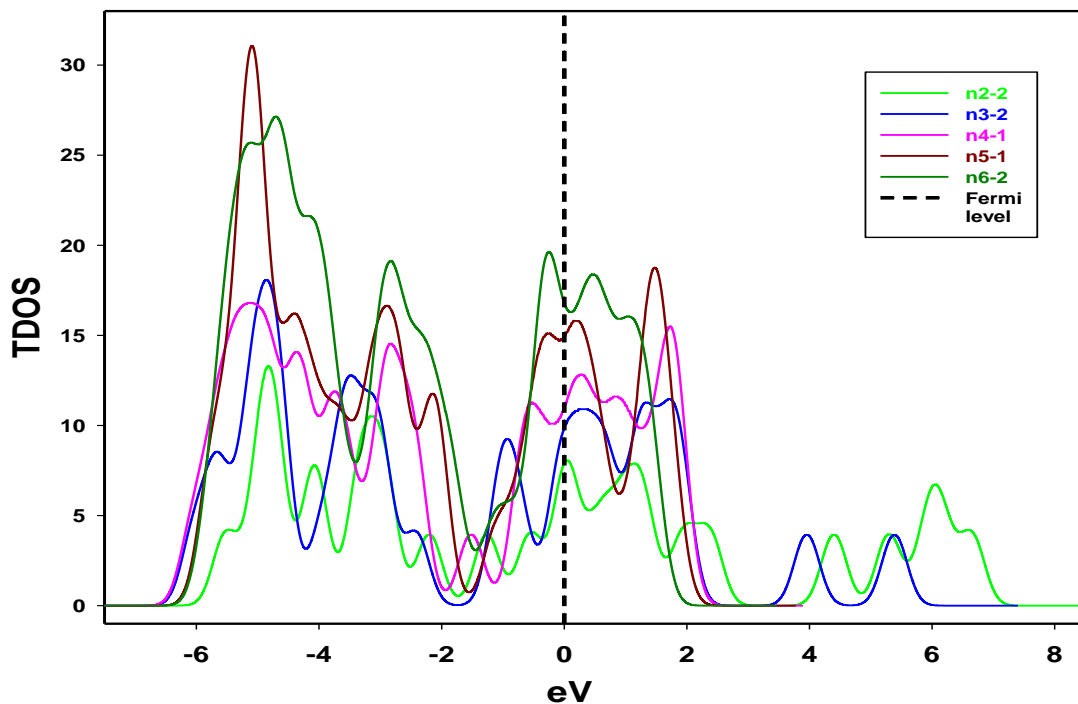


Figure 2: Total density of states for the most stable nanoclusters $(\text{MnO}_2)_{n=2-6}$

Figure 2 shows the total density of states (TDOS) of the five most stable nanoclusters excluding the smallest n1-2 nanocluster with the fewest atoms as compared to the other nanoclusters. From the graph, we observe that as the size of the cluster is increasing, contributions at the Fermi level are also increasing. This is expected as the nanocluster stability increases with the cluster size. It is also observed that the highest peaks on both sides of the Fermi level are moving further away from the Fermi level as the cluster size is increased which shows the varying metallic behavior of the nanoclusters. The density of states for the different stable nanoclusters depict same behaviour; with slight differences on individual atomic contributions due to different coordination numbers and bond lengths for various nanoclusters. Thus, the nanoclusters are predicted to be metallic with the density of states showing no band gap at the Fermi level at ambient pressure. The hybridization of the protruding peaks from the individual atoms leads to the presence of the high peaks on the total DOS. The hybridization of the Mn 3d orbital and the O 2p orbital forming a covalent bond, is mainly due to manganese contributing the majority DOS as it is more reactive and less stable. The highest peak on the valence band corresponds to the n5-1 contributions and is also referred to as the valence band maximum.

Lastly, the effect of temperature on stability of the nanoclusters was investigated using an *ab-initio* molecular dynamics approach. The NVE ensemble using the GGA-PBE functionality in CASTEP was used to determine the effect of temperature change on the nanoclusters. For illustrative purposes, the temperature dependence results for n5-1 nanocluster are presented and shown in Figure 3. It is noted from the graph that, there is a linear increase from 200 K to 500 K. The total energy drops at 600 K,

followed by another linear increase up to 900 K. The nanocluster shows two possible phase transitions at approximately 500 K and 1000 K. As it was observed with the other nanoclusters discussed above, the system is less stable at higher temperatures. The O-Mn-O α angle increases at most temperatures except at 600 K and 900 K, which are the temperatures where phase transitions are observed. Analysis of Mn-O bond lengths revealed a slight change for all the nanoclusters, with the bond lengths ranging from 1.635 Å to 1.949 Å. The experimental melting point of bulk pyrolusite was recorded to be 808 K (535 °C) [22]. The nanoclusters tend to be stable at lower temperatures while depicting a higher disorder at higher temperatures.

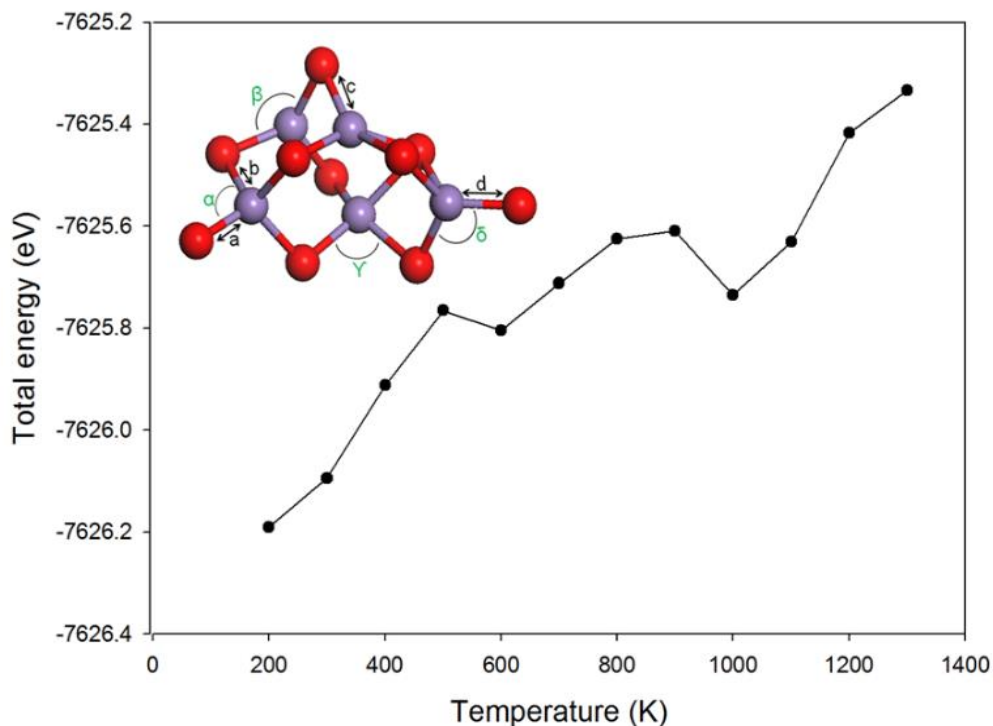


Figure 3: Total energy versus temperature graph for the n5-1 nanocluster.

The stability at low temperatures indicates that there is minimal atomic movement when the temperature is low, hence minimal entropy of the system. The average stable temperature for simulated nanoclusters was calculated to be 300K (26.85 °C). This stable temperature is good as most commercial lithium-ion batteries based on bulk systems show good performance at room temperature 298 K and 333 K.

4. Conclusion

The electronic structure methods were employed successfully to validate the order of stability for previously generated MnO₂ nanoclusters. The plausible nanocluster structures from interatomic potential simulations were refined using density functional theory technique because interatomic potentials are parameterized with reference to bulk crystalline properties and may cause difficulties when applied to clusters where the coordination number and bonding may differ. The most stable nanoclusters are in agreement with those that have been reported previously using FHI-AIMS code, particularly for (MnO₂)_n n= 1-4. Analyzing the basic configurations of the stable nanoclusters, compact ring structures consisting of a cubic structure with two manganese and two oxygen atoms dominate the make-up of the most stable structures. The nanoclusters preferred shorter average bond distances as opposed to a higher average coordination of the constituent atoms. Larger sized structures adopted bubble structures and the bond lengths increased with cation size. The linear configuration was found

to be less favorable for the systems, which explains the migration to a circular compact configuration in the stable MnO₂ nanoclusters. The average stable temperature for the simulated nanoclusters was calculated to be 300K (26.85 °C) which indicated minimal atomic movements at low temperatures.

Acknowledgements

The authors would like to thank the National Research Foundation (NRF) for financial support and South African Centre for High Performance Computing (CHPC) for computing resources.

References

- [1] Hook M and Tang X 2012 *Energy Policy*. **52** 797
- [2] Yamada A, Chung S C and Hinokuma K 2001 *J. Electrochem. Soc.* **148** 224
- [3] Languang L, Xuebing H, Jianqiu L, Jianfeng H and Minggao O 2013 *J. Power Sources*. **226** 272
- [4] Fergus J W 2009 *J. Power Sources*. **195** 939
- [5] Balachanran D, Morgan D and Ceder G 2002 *J. Solid State Chem.* **166**, 91
- [6] Hu CC and Tsou TW 2002 *Electrochimica Acta*, **47**, 3523
- [7] Sayle T X T, Maphanga R R, Ngoepe P E and Sayle D C 2009 *J. Am. Chem. Soc.* **131** 6161
- [8] Tompsett D A, Parker S C and Islam M S 2014 *J. Am. Chem. Soc.* **136** 1418
- [9] Hamad S, Catlow C R A, Woodley S M, Lago S and Mejias J A 2005 *J. Phys. Chem. B.* **109** 15741
- [10] Sugantha M, Ramakrishnan P A, Hermann A M, Warm Singh C P and Ginley D S 2003 *Int. J. Hydrogen Energy*. **28** 597
- [11] Zheng-Jun P 1998 *Evolutionary Algorithm*. Tsinghua University Press, Beijing
- [12] Holland J H 1992 *Sci. Amer.* **66**
- [13] Lian-Jun L 2000 *Int. J. Mod. Phys. C.* **11** 183
- [14] Ngoepe P E, Maphanga R R and Sayle D C 2013 Chapter 9, John Wiley and Sons, LTD, UK
- [15] Gale J D 1997 *J. Chem. Soc.* **93** 629
- [16] Clark S J, Segall M D, Pickard C J, Hasnip P J, Probert M I J, Refson K and Payne M C 2005 *Z. Kristallogr.* **220** 567
- [17] Maphanga R R, Ngoepe P E, Catlow C R A and Woodley S M 2015 *South African Institute of Physics Conference Proceedings*
- [18] Nagarajan V, Saravanakannan R and Chandiramouli 2014 *Int. J. Chem. Tech. Res.* **6** 2962
- [19] Zhai H and Wang L 2007 *J. Am. Chem. Soc.* **129** 3022
- [20] Woodley S M 2011 *Proc. R. Soc. A: Math. Phys. Eng. Sci.* **467** 2020
- [21] Woodley S M 2013 *J. Phys. Chem. C.* **117** 24003
- [22] ChemSpider. Royal Society of Chemistry. Manganese dioxide [Online] Available: <http://www.chemspider.com/Chemical-Structure.14117.html#> [Accessed 21/11/2017]

Molecular dynamics studies of Lithium intercalation into amorphous nanostructure of Titanium dioxide.

¹M. G. Matshaba, ²D. C. Sayle and ¹P. E. Ngoepe

¹Materials Modelling Centre, School of Physical and Mineral Sciences, University of Limpopo, Private Bag X 1106, Sovenga, 0727, South Africa.

²School of Physical Sciences, University of Kent, Canterbury, Kent, CT2 7NZ, United Kingdom.

E-mail: malili.matshaba@ul.ac.za

Abstract. Titanium dioxide (TiO₂) has been confirmed as a safe anode material in lithium ion batteries due to its higher Li-insertion potential, (1.5V) in comparison with commercialised carbon anode materials. Besides being used as an anode material it has a wide range of applications such as photo-catalysis, insulators in metal oxide, dye sensitized solar cells etc. In this work amorphous nanostructure of TiO₂ comprising of 15972 atoms was lithiated with a different concentration of lithium atoms. Simulation of amorphisation and re-crystallisation was employed to attain Li-TiO₂ nanostructures and its microstructures. Molecular dynamics has been performed to crystallise intercalated nanostructure using the computer code DL_Poly. The crystallisation of the materials, starting from amorphous precursors, and the complex microstructure of the material was captured within each structural model including: polymorphic rutile and brookite structures, dislocations, grain boundaries, micro-twinning, vacancies, interstitials, surfaces and morphology. Microstructure depict the lithium atoms situated on the tunnels and vacancies, shows that the material can store and transport lithium during charging and discharging, making it an attractive anode material. Calculated X-Ray diffractions are in accord with the experimental data revealing the presence of brookite and rutile phases.

1. Introduction

The TiO₂ is one of the most extensively studied metal oxide and has been widely used in photocatalysis [1], photosplitting of water [2], photochromic devices [3], gas sensing, dye-sensitized solar cells (DSSCs) (energy conversion) [4] and rechargeable lithium ion batteries (LIBs) (electrochemical storage) [5 - 12]. Over the last two decades, the increasing demand of energy and shifting to the renewable energy resources, has rendered LIBs to be considered as promising alternative and green technology for energy storage applied in hybrid electric vehicles (HEVs), plug-in hybrid electric vehicles (PHEVs), and other electric utilities. TiO₂ is being considered as one of the most attractive anode materials of LIBs owing to the following distinct characteristics: (i) its potential vs. Li^o (~1.5-1.7 V) prevents the plating of metallic lithium at the negative electrode, thus enhancing the safety and extending the life of the cell, (ii) it exhibits relatively high practical capacity (~200 mAh/g), certainly smaller than graphite, but greater than its lithiated form Li₄Ti₅O₁₂, and (iii) it is environmentally benign, abundant, inexpensive and has stable structure. Its most significant advantage, however, is the ability to be charged and discharged at a high current rate (high power). The above-mentioned points are of great importance since large-scale batteries for hybrid electric vehicles and other applications require prolonged life,

improved safety, and reduced cost. In general, the properties of TiO₂ greatly depend on the crystal sizes, phases, exposed facets, and morphologies. We now consider lithium insertion in nanoparticle of anatase TiO₂, which as the size of TiO₂ falls in the nanometers, tends to be more stable than other polymorphs, owing to differences in particle surface tension, size, and shape. A larger Li-ion conductivity is deduced from simulation results for particle size smaller than 20 nm, and lower conductivity for larger nanoparticles.

Simulation of amorphisation and re-crystallisation was employed to attain Li-TiO₂ using the DL_POLY code[13]. We have lithiated nanostructure of TiO₂ with 50 Li atoms. Lithiated nanostructure of TiO₂ is presented in figure 1 below. Charge compensation in the structure is achieved by changing the titanium (4+ oxidation state) closest to the lithium cation into the Jahn-Teller active titanium (3+ oxidation state). This process is repeated for all the lithium ions inserted in the structure.

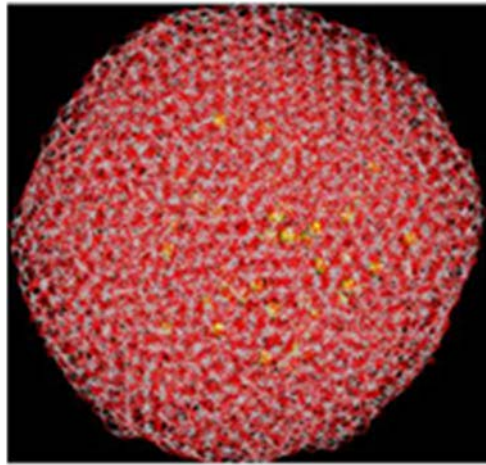


Figure 1. Lithiated amorphous nanostructure of TiO₂ with 50 Li atoms

2. Methodology

The Calculations are based on the Born model of ionic solids, where Ti⁴⁺, Ti³⁺, Li⁺ and O²⁻ ions interact via long-range Coulomb and short range interactions interact via long-range Coulomb and short range interactions. The potentials used in this study were optimized by Matsui [14] for the four polymorphs of TiO₂ (rutile, anatase, brookite and TiO₂ II [α -PbO₂ structure]), and are presented in table 1. The short range interactions are described by Buckingham potentials and the interaction energy takes the form

$$U_{ij} = \frac{q_i q_j}{4\pi\epsilon\epsilon_0 r_{ij}} + A_{ij} \exp\left(-\frac{r_{ij}}{\rho_{ij}}\right) - \frac{C_{ij}}{r_{ij}}$$

Where A_{ij} is the size of the ions, ρ_{ij} is the hardness and C_{ij} is the dispersion parameter. The repulsive interaction between the ions is represented by the first term while the second term is the van der Waals attractive interaction of the ions. All the molecular dynamics simulations were performed using DL_POLY code [13].

Table 1 Buckingham potentials used for lithiated TiO₂

Ion pair (ij)	A _{ij} (eV)	ρ_{ij} (Å)	C _{ij} (eV.Å ⁶)
Ti ³⁺ -O ²⁻	18645.840	0.1950	22.0000
Li ⁺ -O ²⁻	426.48000	0.3000	0.00000
Ti ³⁺ -Ti ⁴⁺	28707.210	0.1560	16.0000
Ti ³⁺ -Ti ³⁺	33883.920	0.1560	16.0000

3. Results and discussion

Lithiated nanostructure of TiO₂ was recrystallised, from the plot of configuration energy which is depicted in figure 2 shows that the nanostructure with lithium atoms has recrystallise. The change of the configuration energy from -2.015×10^5 to -2.043×10^5 eV corresponds to the latent heat of crystallisation and is associated with the transition from an amorphous to a crystalline phase. Beyond 0.6 ns the change in the configuration energy is very small, which indicates that the nanosphere has recrystallised. At 2 ns the energy starts to be near constant which reveals that complete recrystallisation has been achieved.

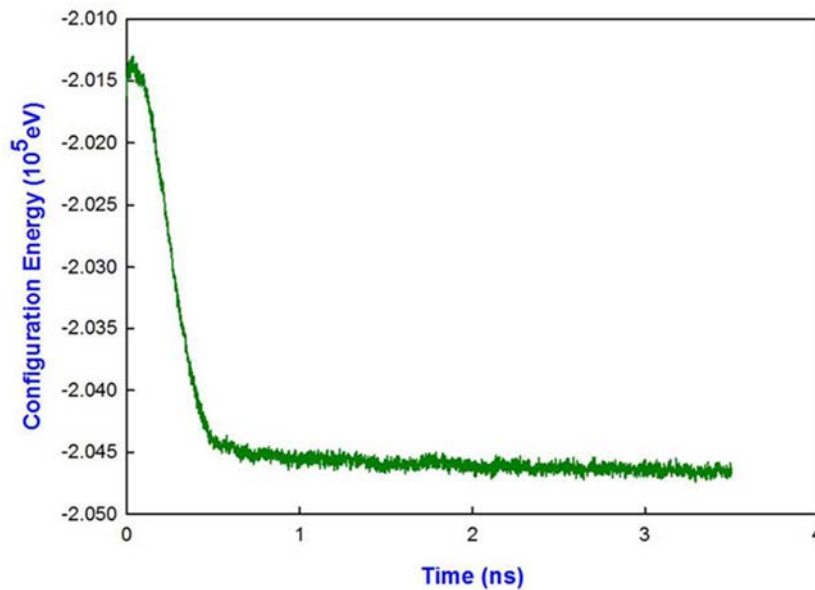


Figure 2. Calculated configuration energy as a function of time for the lithiated nanostructure of TiO₂.

As crystallisation occurs some lithium atoms move out of the nanostructure or away. Our simulation technique divulge that lithium atoms can move away from the nanostructure half the diameter of the nanostructure. Lithium atoms that have moved out of the nanostructure will be captured in electrolyte then transported to cathode material. Recrystallised nanostructure of TiO₂ is depicted in figure 3. Clear patterns are observed on the structure indicating that the nanostructure is recrystallised. We cooled the recrystallised nanostructure gradually by firstly performing MD simulations for 500 ps at temperature of 1500 K, followed by a run for 250 ps at 1000 K, and lastly for 500 ps at temperature of 0 K. Cooled nanostructure of TiO₂ with 50 lithium atoms is shown in figure 3,

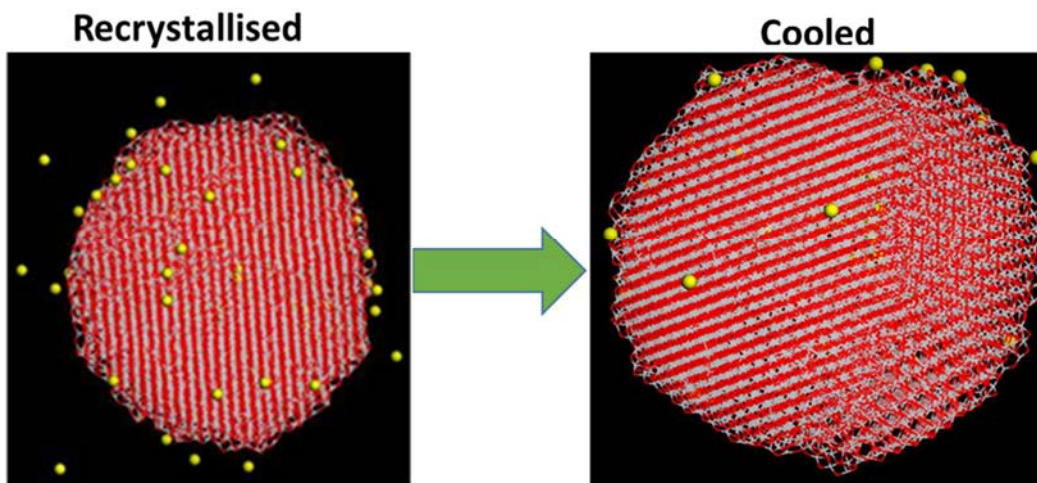


Figure 3. Recrystallised and cooled nanostructure of lithiated TiO₂.

Microstructure was created in order to analyse the positions of lithium atoms inside the nanostructure. The microstructure of nanoparticle of TiO_2 is depicted in figure 4. The blue octahedra correspond to the upper layer of Ti^{4+} and the white adjacent the lower layer and the lithium atoms are represented by yellow balls. The microstructure of the nanostructure shows zigzag tunnels which are associated with the brookite and the straight tunnels that are related to the twinned rutile polymorphs. Few vacancies are observed on the microstructure, and lithium atoms have moved into vacancies of the structure. A good anode requires the nanostructure to store optimum lithium atoms and provide pathways for their transport. Indeed the microstructure of the nanoparticle reflects lithium atoms that are located in the tunnels. A few lithium atoms are located at the edges of the system and those in the nanostructure are positioned in tunnels and have filled existing vacancies.

Simulated X-Ray diffractions depicted in figure 5 shows picks that accord to rutile and brookite polymorphs as compared with the experimental picks [15]. Two peaks just below and above 30° accord with the brookite and $\text{TiO}_2: \alpha\text{-PbO}_2$ structures. At 37° and 57° , observed peaks correspond to all measured structures. Simulated XRDs at 50° has a smooth curve which accords with the rutile structure. At 67° we notice a peak which is in agreement with $\text{TiO}_2: \alpha\text{-PbO}_2$ and rutile polymorphs. This implies that the lithiated TiO_2 nanostructure has a combination of brookite, $\text{TiO}_2: \alpha\text{-PbO}_2$ and rutile structural arrangements.

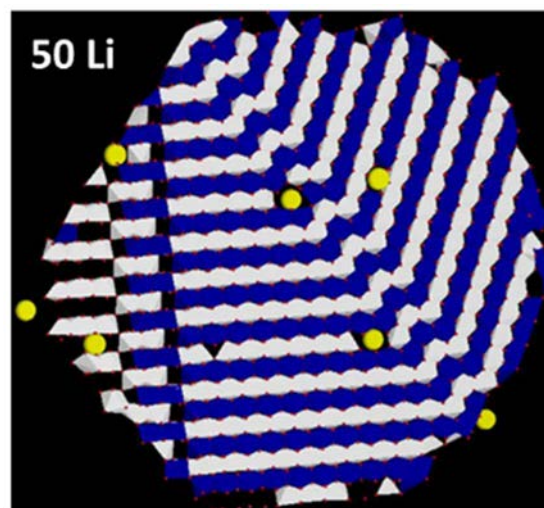


Figure 4. Microstructure of nanostructure of TiO_2 with 50 Li atoms.

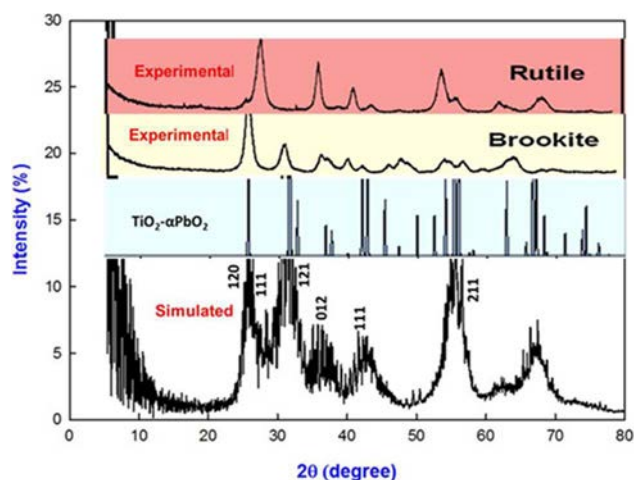


Figure 5. A comparison simulated TiO_2 nanostructure with calculated $\text{TiO}_2: \alpha\text{-PbO}_2$ and experimental [15] XRDs.

4. Conclusion

Amorphisation and recrystallisation technique has been successfully employed to generate nanostructures of TiO₂ with 50 Li atoms. The change of the configuration energy shows an amorphise-crystalline transition and can estimate the latent heat of crystallisation. Their XRDs confirm a brookite structural arrangement and they are accord with those of TiO₂: α -PbO₂. Microstructures of simulated nanostructure concur well on types of TiO₂ polymorphs that are present. Nanostructure of TiO₂ confirms a good anode material.

Acknowledgements

Calculations were performed at Materials Modelling Centre (MMC), University of Limpopo. This work is supported by Department of Science and Technology, National Research Foundation, Pretoria, the Department of Science and Technology HySA Lithium Ion Batteries and Supercapacitors Project, Pretoria and the Centre for High Performance Computing (CHPC) in South Africa.

References

- [1] Schneider J, Matsuoka M, Takeuchi M, Zhang J, Horiuchi Y, Anpo M and Bahnemann D W 2014 *Chem. Rev.* **114** (19) 9919-9986.
- [2] Ni M, Leung M K H, Leung D Y C and Sumathy K A 2007 *Renew. Sust. Energ Rev* **11** (3) 401-425.
- [3] Biancardo M, Argazzi R and Bignozzi C 2005 *Inorg. Chem.* **44** (26) 9619-9621.
- [4] Liu B and Aydil E S 2009 *J. Am. Chem. Soc.* **131** (11) 3985-3990.
- [5] Fujishima A and Honda K 1972 *Nature* **238** 37-38.
- [6] O'Regan B and Gratzel M. 1991 *Nature* **353** 737-740.
- [7] Chen X and Mao S S 2007 *Chem. Rev.* **107** 2891-2959.
- [8] Liu, B, Deng D, Lee J Y and Aydil E S 2010 *J. Mater. Res.* **25** (8) 1588-1594.
- [9] Liu H, Bi Z, Sun X-G, Unocic R R, Paranthaman M P, Dai S and Brown G M 2011 *Adv. Mater.* **23** 3450-3454.
- [10] Liu S, Li J, Shen Q, Cao Y, Guo X, Zhang G, Feng C, Zhang J, Liu Z, Steigerwald M L, Xu D and Nuckolls C 2009 *Angew. Chem. Int. Ed.* **48**, 4759-4762.
- [11] Trascon J M and Armand M 2001 *Nature* 2001 **414** 359-367.
- [12] Wakihara W and Yamamoto O 1998 Wiley-VCH 181-198.
- [13] Smith W and Forster T R. 1996. <http://www.dl.ac.uk/TCSC/Software/DLPOLY>.
- [14] Matsui M and Akaogi M 1991 *Mol. simul.* **6** 239-244.
- [15] Dambournet D Belharouak I and Amine K 2009 *Electrochem. Soc.* 215, No.1.

Effect of calcination on the structural and magnetic properties of nickel chromite

P Mohanty, C J Sheppard and A R E Prinsloo¹

Department of Physics, University of Johannesburg, P. O. Box 524, Auckland Park
2006, South Africa

E-mail: alettap@uj.ac.za

Abstract. The magnetic and structural properties of NiCr₂O₄ synthesized through chemical co-precipitation techniques are reported. *In-situ* high temperature x-ray diffraction (XRD) studies of the as-synthesized NiCr₂O₄ samples measured in air as well as He atmosphere, suggests the phase formation takes place around 800 to 900 °C, suppressing the Cr₂O₃ impurity phase. Upon cooling no change in crystal structure is observed confirming the phase formation process is thermodynamically an irreversible one. The cubic structure of NiCr₂O₄ is retained up to 1100 °C contrary to the reported tetragonal phase observed at such elevated temperature. NiCr₂O₄ samples calcined at 900 °C and 1100 °C respectively, have been used for microstructural and magnetic studies. The particles are found to have a broad size distribution in the micrometer range without any undesired impurities. The Curie temperature (T_C) is found to be 86.5 ± 0.2 K for the sample calcined at 900 °C whereas it is reduced to 74.2 ± 0.08 K for the sample calcined at 1100 °C. For both the samples the magnetic transition observed at 30.2 ± 1.7 K (T_S) remained unchanged, marking the ordering of the antiferromagnetic component below it. The spontaneous magnetization (M_s) values for NiCr₂O₄ calcined at 900 °C and 1100 °C are found to be 0.122 ± 0.002 μ_B /f.u. (at 5 K) and 0.179 ± 0.002 μ_B /f.u. (at 3 K) respectively, that are less than the reported values. Magnetic field dependent magnetization measurements under zero field cooled (M_{ZFC}) and field cooled (M_{FC}) condition show absence of exchange bias effect in these samples at low temperatures.

1. Introduction

The spinel compound NiCr₂O₄ is of the general formula AB_2O_4 and demonstrates ferrimagnetic ordering below the Curie temperature, $T_C = 74$ K [1]. It has a normal spinel structure with magnetic Ni²⁺ and Cr³⁺ ions occupying tetrahedral *A* and octahedral *B* sites, respectively. The structure of NiCr₂O₄ is an elongated tetragonal below 310 K [2]. The magnetic moments of NiCr₂O₄ are comprised of a ferrimagnetic (longitudinal) and an antiferromagnetic (transverse) component [2, 3]. Ordering of both these components occur simultaneously at T_C [3]. Having a normal spinel ferrimagnetic structure with two characteristic magnetic components, NiCr₂O₄ demonstrate different magnetic, as well as structural behaviour when compared to the other members of the chromite family [3]. From specific heat-capacity measurements Klemme *et al.* [4] observed an unknown transition at 29 K for NiCr₂O₄. Later this transition was defined by Tomiyashu and Kagomiya [3] through neutron as well as magnetic measurements. The authors proposed a new magnetic structure below 34 K with a spontaneous

¹ To whom any correspondence should be addressed

magnetization of about $0.3 \mu_B/\text{f.u.}$, in which the B sites are grouped into two sublattices for both the longitudinal and transverse components similar to MnCr_2O_4 and CoCr_2O_4 [3].

In NiCr_2O_4 the structural phase transition from cubic to tetragonal occurs at 310 K due to Jahn-Teller effect on Ni^{2+} ions at tetrahedral site [1]. Earlier results [1, 4] have also shown a further distortion of tetragonal NiCr_2O_4 to an orthorhombic phase, that occurs at the transition temperature $T_N = 65$ K. This transition temperature is quite different from the magnetic transition temperature [5]. Recently, Barman *et al.* [6] have observed an exchange bias effect in NiCr_2O_4 due to anisotropic exchange interaction between the ferrimagnetic and the antiferromagnetic components of the magnetic moment. This exchange bias effect finds important applications such as magnetic read heads and spintronics devices, etc. [7, 8].

Motivated by the concurrent structural and magnetic phase transition in the NiCr_2O_4 compound, the present study gives a detailed investigation of high temperature structural phase changes, as well as the effect of calcination on magnetic properties of NiCr_2O_4 .

2. Experimental

NiCr_2O_4 powders were synthesized using chemical co-precipitation techniques, starting with stock solutions of 0.5 M of nickel nitrate ($\text{Ni}(\text{NO}_3)_2 \cdot 6\text{H}_2\text{O}$) and chromium nitrate ($\text{Cr}(\text{NO}_3)_3 \cdot 9\text{H}_2\text{O}$). The desired amount of chromium nitrate solution was poured into a beaker and stirred using a magnetic stirrer. The required amount of nickel nitrate was then added drop wise to the solution. The mixture was stirred continuously at room temperature for 1 hour, while diluted aqueous ammonia (30 %) solution was added to maintain the pH of 9.8. The precipitates were filtered, washed several times using distilled water, then with acetone and finally with methanol. The precipitated powders were dried overnight on a hot plate and crushed to powder using an agate mortar and pestle.

Structural characterizations of these samples were carried out using a Phillips PAN analytical X-pert Pro X-ray diffractometer utilizing Cu-K_α radiation ($\lambda = 1.54056 \text{ \AA}$). Temperature dependent XRD studies were carried out *in-situ* in a non-ambient Anton Parr HTK 1200 Oven-Chamber under He and air atmosphere. The oven is designed for non-ambient XRD studies measured from room temperature to 1200°C . Data were acquired in a range of $10^\circ \leq 2\theta \leq 80^\circ$, with a waiting time of 10 minutes before each measurement. A hybrid monochromator on the primary beam side of the diffractometer was used to avail a quasi-parallel x-ray beam. This configuration makes the XRD data collection insensitive to height difference of the sample during the course of heating. The sample holder was rotated continuously during the measurement. A JEM-2100 transmission electron microscope (TEM) was used to study the microstructure of the calcined powders. Energy dispersive x-ray spectroscopy (EDS) was carried out using a detector from Oxford attached to the TEM. The magnetic measurements were performed using a 14 T Cryogen Free Physical and Magnetic Measurement System (CRYOGENIC Ltd., UK) with a vibrating sample magnetometer (VSM) insert [9].

3. Results and discussion

The XRD patterns of NiCr_2O_4 particles calcined at 600°C and 900°C are depicted in Fig. 1 (a). The XRD pattern of the dried, as-synthesized NiCr_2O_4 samples (marked 'Raw') show an amorphous nature as shown in Fig. 1 (a). When heated to 600°C , the Cr_2O_3 phase dominate (Fig. 1 (a)), similar to previous reports [10]. Further heating at 900°C , the cubic phase of NiCr_2O_4 is obtained (Fig. 1 (a)). The reflections corresponding to planes (111), (220), (311), (222), (400), (422), (511) and (440) are well matched with the cubic structure of NiCr_2O_4 (ICDD: 89-6615). To observe the phase formation with increasing temperature, *in-situ* temperature dependent XRD was carried out under He as well as air atmosphere up to 1100°C using the dried NiCr_2O_4 powders. Fig. 1(b) depicts the phase evolution of NiCr_2O_4 upon heat treatment under air atmosphere. From this figure it is clear that the NiCr_2O_4 phase formed around 800°C . However, a minute peak is also seen associated with the Cr_2O_3 impurity phase (marked with '*' in Fig. 1(b)). With increasing calcination temperature, the Cr_2O_3 peak intensity reduces, suggesting phase purity enhancement persisting up to 1100°C . The formation of the tetragonal phase of NiCr_2O_4 was previously reported by Ptak *et al.* [10] at a synthesis temperature of 1000°C . However, the

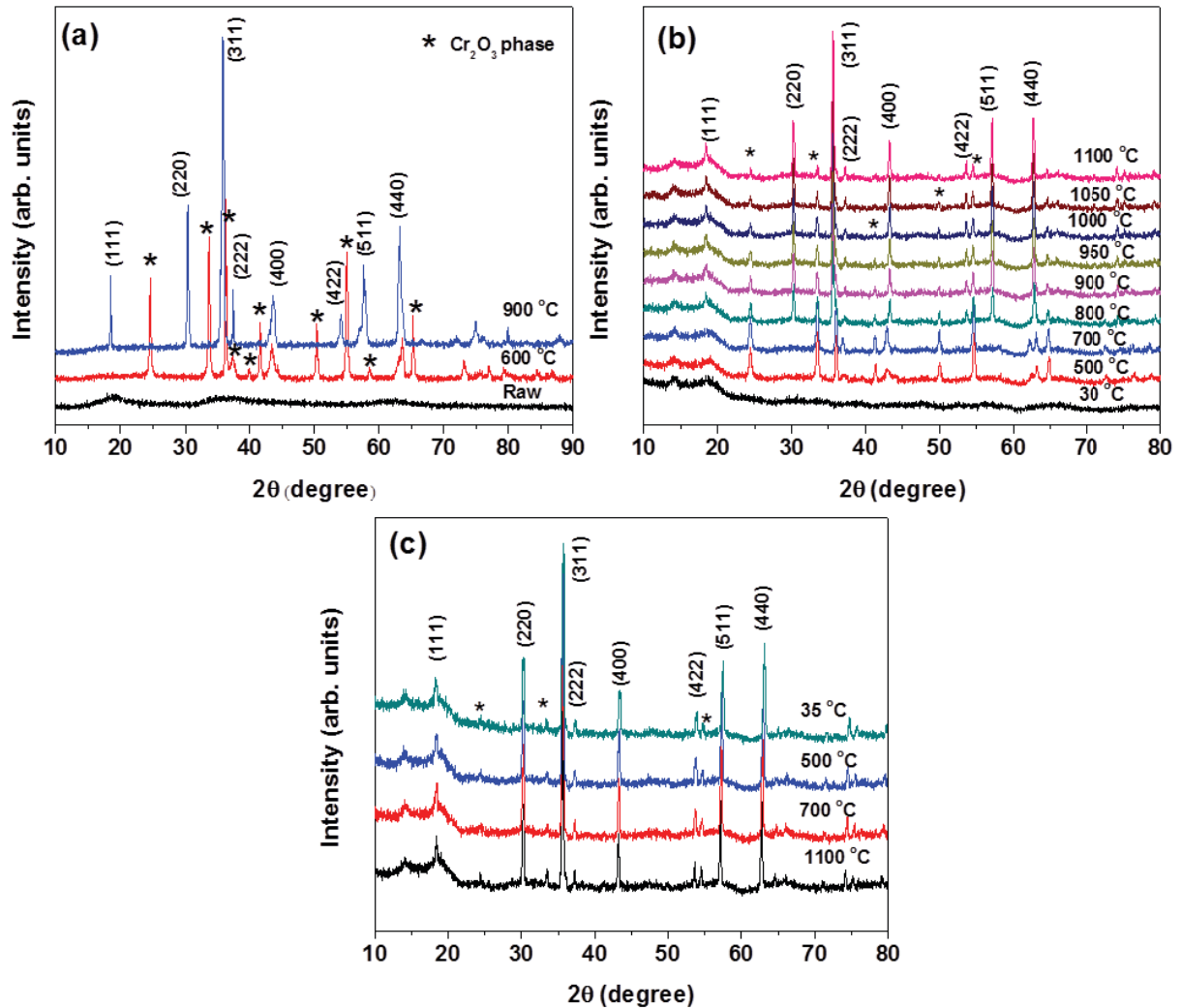


Figure 1. XRD patterns of the NiCr₂O₄ powders synthesized at pH~ 9.8 and measured: (a) *ex-situ*, (b) *in-situ* with increasing temperature up to 1100 °C, (c) during the cooling cycle from 1100 °C to 35 °C. The reflections corresponding to planes (111), (220), (311), (222), (400), (422), (511) and (440) are well matched with the cubic structure of NiCr₂O₄ (ICDD: 89-6615). In these figures ‘*’ mark the peaks indicating the presence of the Cr₂O₃ phase.

present results show that the cubic phase of NiCr₂O₄ is retained up to almost 1100 °C. The XRD patterns of the sample while cooling from 1100 °C to 35 °C was also recorded (Fig. 1(c)). No remarkable difference in the XRD profile was observed. This clearly suggests that the NiCr₂O₄ phase formation process is thermodynamically irreversible. Similar trends in the XRD patterns under heating as well as cooling in He atmosphere was observed (figure not shown).

In order to investigate the effect of calcination on microstructural and magnetic properties, two samples were calcined at 900 °C and 1100 °C in a tubular furnace for 2 hours, respectively. Fig. 2 (a) and (b) shows the TEM images of the NiCr₂O₄ sample calcined at 900 °C and 1100 °C, respectively. Both the micrographs show distribution of particle sizes in the micrometer range, with the largest crystallites having a size of about few micrometers whereas smaller particles fall in the nanometer regime. The presence of bipyramidal structures is clearly seen in the TEM images, characteristic morphology of NiCr₂O₄ (Fig. 2) [10]. The well defined lattice fringes (from high resolution electron microscopy (HREM)) confirm the periodicity of the atoms in the crystal (inset of Fig. 2 (a)). EDS results

of the two samples (see Fig. 2 (c) and (d) and insets therein) confirm the presence of elements Ni, Cr and O without any signatures of foreign impurities. In order to explore the magnetic properties, temperature dependent magnetization measurements were carried out in zero field cooled (M_{ZFC}) and field cooled (M_{FC}) conditions by applying an 0.1 T probing field. For NiCr_2O_4 sample calcined at 900 °C, a decrease in temperature from 300 K both the $M_{ZFC}(T)$ and $M_{FC}(T)$ curves show a rapid increase around 86.5 ± 0.2 K. This is indicative of a paramagnetic to ferrimagnetic transition and termed as the Curie temperature, T_C (Fig. 3 (a)). T_C is obtained from the extrapolation of the linear part of the magnetization to zero as shown in Fig. 3. The value of T_C is higher than the previously reported value of 74 K [1]. However, T_C is found to be 74.2 ± 0.08 K in case of the sample calcined at 1100 °C (Fig. 3(b)), which is in agreement with the reported value. For both the samples, M_{ZFC} shows a sharp peak below T_C . Increasing the temperature up to 27 K, the M_{ZFC} is negative for sample calcined at 1100 °C whereas M_{ZFC} is always positive for the other. The phenomenon leading to negative magnetization has been reported for molecular-based ferrimagnets and is arising due to the change in the direction of the magnetization in the ferromagnetic component at the compensation temperature [11-13]. For spinel compounds, if the sublattice magnetizations M_A and M_B have different temperature dependences, the resultant magnetization changes sign at a temperature known as the compensation temperature [14]. The negative magnetization mostly arises due to the presence of uncompensated spins [15]. In both the samples anomaly in magnetization is observed around 30.2 ± 1.7 K (Fig. 3) termed as T_S , below which ordering of antiferromagnetic component takes place [1, 3]. To gain a deeper understanding of the behaviour of these samples, magnetization as a function of applied magnetic field at various temperatures was measured. Fig. 4 (a) shows the M - H loops of the NiCr_2O_4 sample calcined at 900 °C and measured at temperatures 5, 20, 60 and 70 K. Both coercivity (H_C) as well as remanent magnetization (M_r) decreases with temperature approaching T_C . It is also noted that the magnetization does not saturate

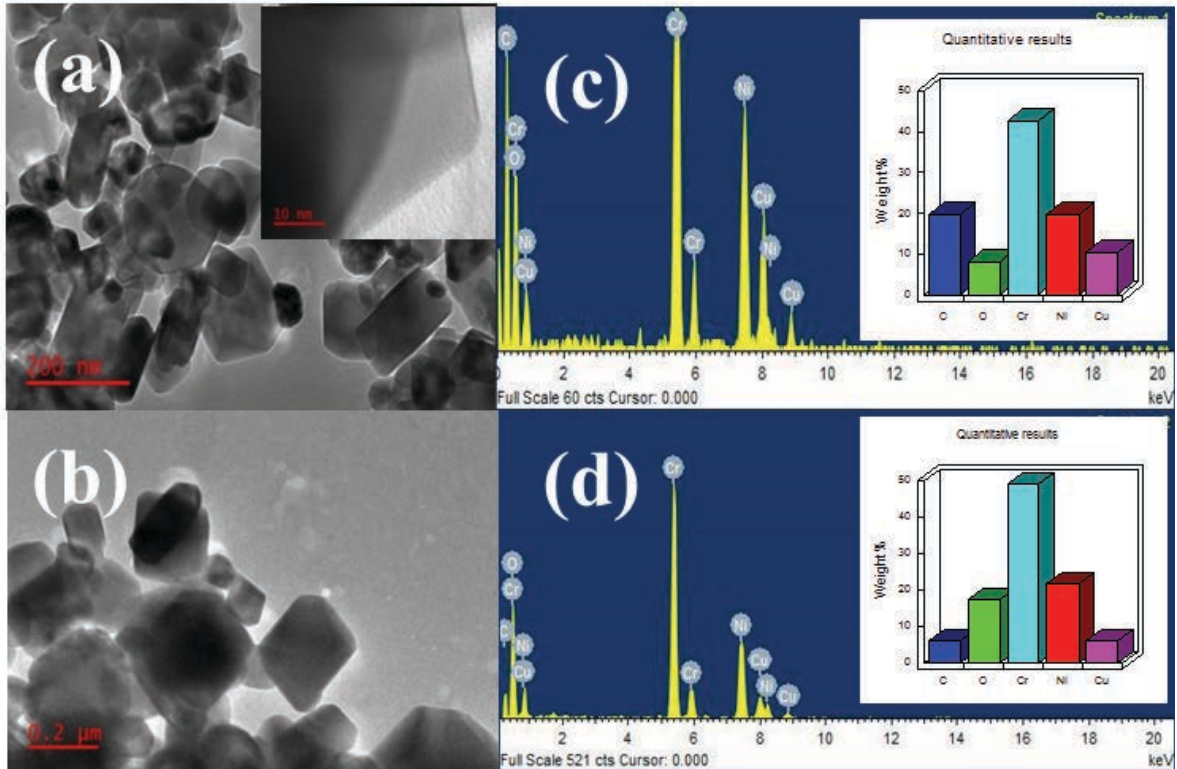


Figure 2. (a) TEM micrograph of NiCr_2O_4 calcined at 900 °C (inset shows the HREM image), (b) TEM micrograph of NiCr_2O_4 calcined at 1100 °C, (c) EDS of NiCr_2O_4 calcined at 900 °C and (d) EDS of NiCr_2O_4 calcined at 1100 °C. The insets of both (c) and (d) depict the elemental distribution.

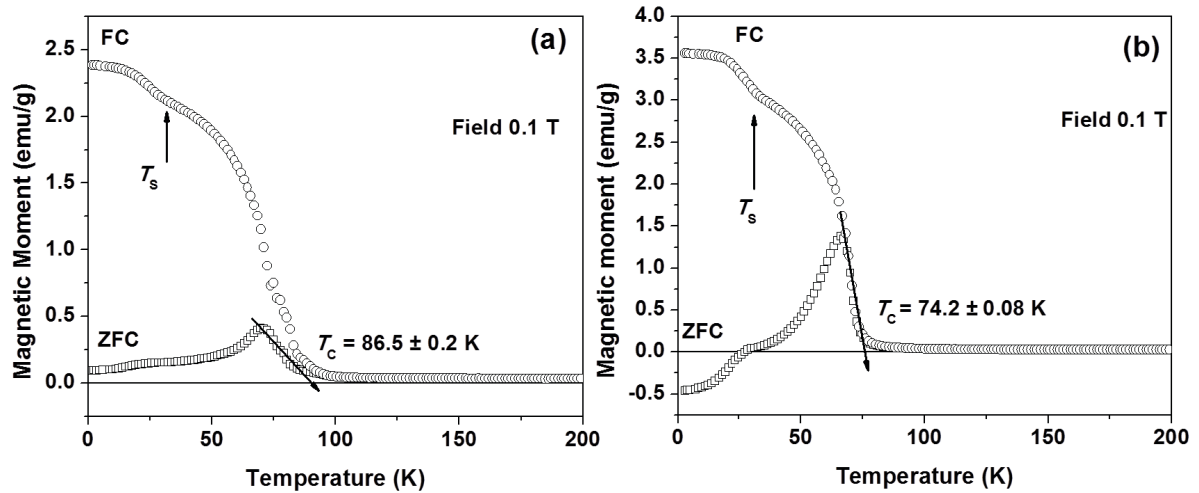


Figure 3. Temperature dependent magnetization under zero field cooled (ZFC) and field cooled (FC) conditions. For the field cooled scenario measurements were done in a 0.1 T applied magnetic field for NiCr_2O_4 samples calcined at (a) 900 °C and (b) 1100 °C.

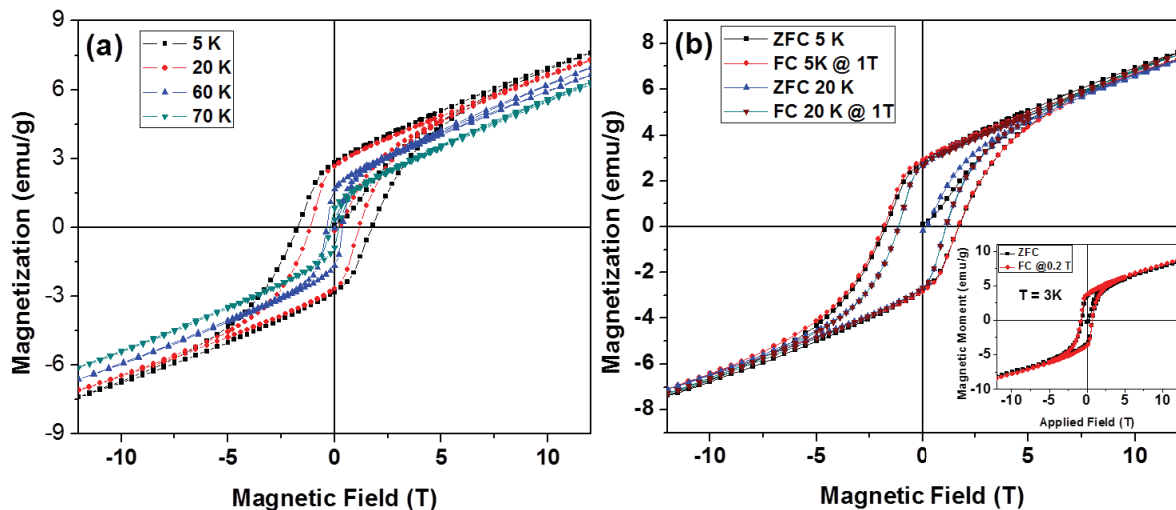


Figure 4. Magnetic field-dependent magnetization at measured at different temperatures for NiCr_2O_4 calcined at 900 °C under: (a) zero field cooled (ZFC) and (b) field cooled (FC) condition. Inset of (b) shows the M - H loop for the sample calcined at 1100 °C at 3 K under ZFC and FC (at 0.2 T) condition.

up to an applied field of 12 T. To obtain spontaneous magnetization (M_s), a linear extrapolation of high field magnetization to zero field is done. The M_s values for NiCr_2O_4 calcined at 900 °C and 1100 °C are found to be $0.122 \pm 0.002 \mu_B/\text{f.u.}$ (f.u. refers to formula unit) at 5 K and $0.179 \pm 0.002 \mu_B/\text{f.u.}$ at 3 K, respectively. These M_s values are less than the previously reported at 5 K by Mufti *et al.* [16] and Tomiyashu and Kagomiya [3], 0.2 and 0.3 $\mu_B/\text{f.u.}$, respectively. In view of the recent observation of exchange bias in NiCr_2O_4 by Barman *et al.* [6], in the present study M - H loops have been traced under 1 T cooling field at 5 K and 20 K as shown in Fig. 4 (b). The inset of Fig. 4 (b) shows the M - H loops of NiCr_2O_4 calcined at 1100 °C and measured under 0.2 T cooling field measured at 3 K. As there is no shifting in the loop for different fields, including for the case of the lowest temperature of 3 K, it suggests the absence of exchange bias phenomenon in the present case.

4. Conclusions

Phases of NiCr₂O₄ samples synthesized through chemical co-precipitation technique were achieved at calcination at 900 °C. *In-situ* temperature dependent x-ray diffraction studies showed no change in the structural phase even up to 1100 °C and the cubic phase was retained contrary to the tetragonal phase reported for the sample calcined at 1000 °C. NiCr₂O₄ samples calcined at 900 °C and 1100 °C were used to investigate the magnetic properties. TEM analyses showed a wide variation of particle sizes of both the samples that mostly contain bipyramidal shaped particles. EDS did not show the presence of any unwanted impurity in the samples. NiCr₂O₄ sample calcined at 1100 °C showed the T_C to be 74.2 ± 0.08 K and T_S equals to 30.2 ± 1.7 K. However, for the sample calcined at 900 °C, T_C was found to be 86.5 ± 0.2 K with T_S unchanged. The negative magnetization in low temperature regime for the 1100 °C sample suggests the presence of uncompensated spins in the material. *M-H* loops measured at various temperatures confirmed the ferrimagnetic nature of the samples. No exchange bias was observed for both the samples even at lowest temperature.

Acknowledgements

Authors acknowledge the financial support from the South African National Research Foundation (Grant numbers: 80928, 93551 and 88080) and the Faculty of Science, University of Johannesburg (UJ), South Africa. The use of facilities at UJ Spectrum is acknowledged.

References

- [1] Ishibashi H and Yasumi T 2007 *J. Magn. Magn. Mater.* **310** e610
- [2] Prince E 1961 *J. Appl. Phys.* **32** 68S
- [3] Tomiyasu K and Kagomiya I 2004 *J. Phys. Soc. Japn.* **73** 2539
- [4] Klemme S and Miltenburg J C 2002 *Phys. Chem. Miner.* **29** 663
- [5] Armbruster T, Lager G A, Ihringer J, Rotella F J and Jorgensen J D 1983 *Z. Krist.* **162** 8
- [6] Barman J, Bora T and Ravi S 2015 *J. Magn. Magn. Mater.* **385** 93
- [7] Tsang C, Fontana R E, Lin T, Heim D E, Speriosu V S, Gurney B A and Williams M L 1994 *IEEE Trans. Magn.* **30** 3801
- [8] Guo S, Liu X H, Cui W B, Liu W, Zhao X G, Li D and Zhang Z D 2009 *J. Appl. Phys.* **105** 064702
- [9] Cryogenic Ltd, 29-30 Acton Park, Industrial Estate, the Vale London, W3 7QE, UK
- [10] Ptak M, Maczka M, Gagor A, Pikul A, Macalik L and Hanuza J 2013 *J. Sol. Stat. Chem.* **201** 270
- [11] Ohkoshi S, Yorozu S, Sato O, Iyoda T, Fujishima A and Hashimoto K 1997 *Appl. Phys. Lett.* **70** 1040
- [12] Mathoniere C, Nuttall C J, Carling S G and Day P 1994 *J. Chem. Soc., Chem. Commun.* **1994** 1551
- [13] Mathonière C, Nuttall C J, Carling S G and Day P 1996 *Inorg. Chem.* **35** 1201
- [14] Néel L 1948 *Ann. Phys.* **3** 137
- [15] Dutta D P, Manjanna J and Tyagi A K 2009 *J. Appl. Phys.* **106** 043915
- [16] Mufti N, Nugroho A A, Blake G R and Palstra T T M 2010 *J. Phys.: Condens. Matter* **22** 075902

Role of swift heavy ion irradiation on the structural and magnetic properties of $\text{Ti}_{0.95}\text{Co}_{0.05}\text{O}_{2-\delta}$ epitaxial thin films

P Mohanty¹, C Rath², C J Sheppard^{1,3} and A R E Prinsloo¹

¹Department of Physics, University of Johannesburg, P. O. Box 524, Auckland Park 2006, South Africa

²School of Materials Science and Technology, Indian Institute of Technology (Banaras Hindu University) Varanasi, Uttar Pradesh 221005, India

E-mail: cjsheppard@uj.ac.za

Abstract. Defects such as oxygen vacancies are found to play a vital role in determining the physical and magnetic properties of $\text{Ti}_{1-x}\text{Co}_x\text{O}_{2-\delta}$. These defects can be created during growth or may be induced by ion irradiation or implantation. In this work, the structural and magnetic properties of epitaxial $\text{Ti}_{0.95}\text{Co}_{0.05}\text{O}_{2-\delta}$ thin films deposited on LaAlO_3 single crystal substrates under dense electronic excitation are discussed. Films were deposited by pulsed laser deposition (PLD) technique. X-ray diffraction (XRD) studies revealed that reflections, beside those corresponding to the planes (004) and (008) of the anatase phase of TiO_2 , are suppressed, indicating epitaxial growth of the films along the *c*-axis. In order to investigate the important role of defects on the physical properties of the thin films, these were irradiated with 100 MeV Ag^{7+} ions with fluences 1×10^{11} , 1×10^{12} and 1×10^{13} ions. cm^{-2} . XRD of the irradiated films indicate successive amorphization of the films with increasing ion dose. The magnetic measurements indicate a significant enhancement in the magnetization of the film irradiated with a fluence of 1×10^{13} ions. cm^{-2} . This unexpected increase in magnetization is explained on the basis of the bound magnetic polaron (BMP) model. The findings suggest the pivotal role of ion irradiation on tailoring the structural as well as the magnetic properties.

1. Introduction

Semiconductor spintronics unites both logic-processing functionalities (electronic charge) of a semiconductor and information-storage functionalities (electronic spin) of a ferromagnetic material. The main obstacle to realize such spintronics devices are the low Curie temperature (T_c) and controversial origin of magnetism in these systems [1].

In oxide based systems, room temperature ferromagnetism (RTFM) was first discovered by Matsumoto *et al.* [2] in Co doped TiO_2 thin films making it a potential diluted magnetic semiconductor (DMS) material. Several models or mechanisms have been used to explain the origin of ferromagnetism in these systems, including the bound magnetic polaron (BMP) model, Ruderman-Kittel-Kasuya-Yosida (RKKY) exchange interaction, Stoner type model and charge transfer mechanisms [3, 4]. All these models or mechanisms could not explain the origin of magnetism satisfactorily. Although the exact mechanism of the magnetic correlation is still unclear, the possible coupling between charge carriers created by defects like oxygen vacancies and magnetic moment is

³ To whom any correspondence should be addressed

unanimously accepted [5]. However, clustering of Co in the TiO₂ matrix resulting in ferromagnetic order is not accepted [6]. Ferromagnetism in Co doped TiO₂ polycrystalline thin films deposited by pulsed laser deposition (PLD) technique refuting the presence of Co clusters in the films has also been reported [7]. Films deposited under low oxygen partial pressure or annealing of the films under reduced atmosphere are found to demonstrate ferromagnetic behaviour at room temperature. Defects like oxygen vacancies also greatly influence the ferromagnetic properties of undoped TiO₂ thin films [8]. The challenge is therefore to create defects in the material systematically.

Ion irradiation used for defect engineering has been employed as a potential tool in material science [9]. Irradiation may dissolve the magnetic clusters in the host lattice and create disorder like amorphization in the system depending on the energy of the incident ion beam [9]. It can also create change in the crystal structure, enhance phase formation and defect annihilation with suitable selection of projectile ion, energy and fluence [10]. The material modification can be complex depending upon the magnitude of electronic energy loss (S_e) as compared with a material-dependent threshold value, S_{eth} , beyond which swift heavy ions (SHI) can create amorphized latent tracks or can induce crystalline-to-crystalline phase transition [11, 12]. Recently, the role of SHI on structural and magnetic properties of Co doped TiO₂ polycrystalline thin films deposited on Si substrates have been reported [13].

To investigate the effect of ion irradiation on epitaxial thin films of Co doped TiO₂, this study utilized *c*-axis oriented LaAlO₃ (LAO) as the substrate, because of the small lattice mismatch it has with TiO₂ [14]. Secondly, owing to the important role of defects in tuning the magnetic property, the thin films were irradiated with 100 MeV Ag⁷⁺ ions with fluences 1×10^{11} , 1×10^{12} and 1×10^{13} ions.cm⁻². The present work focuses on the modification in structural and magnetic properties of Ti_{0.95}Co_{0.05}O_{2- δ} thin films with the use of swift heavy ion irradiation.

2. Experimental

Co doped TiO₂ powdered samples were used to prepare the target for the pulsed laser deposition (PLD) by pressing the samples together in pellets and sintering these at 900 °C for 24 hours. The target was ablated using a *KrF* excimer laser (Lambda Physik COMPex 201 Model, Germany) at constant laser energy of 240 mJ and 10 Hz repetition rate. Commercial LaAlO₃ (LAO) single crystal substrates were used for film deposition. The substrate temperature was maintained at 700 °C during film deposition. Films were fabricated at 10 mTorr oxygen partial pressure. The target was rotated continuously during laser ablation. The deposited films were irradiated with 100 MeV Ag⁷⁺ ions at room temperature using a 15 UD tandem pelletron accelerator at IUAC, New Delhi, India with fluences 1×10^{11} , 1×10^{12} , and 1×10^{13} ions.cm⁻². The magnetic measurements of all the samples were investigated using a superconducting quantum interference device (SQUID) vibrating sample magnetometer (VSM) from Quantum Design in a magnetic field up to 1 T and temperature ranging from 5 to 300 K. Structural characterization was performed using a D8 Advance x-ray diffractometer from Bruker with LynxEye 1D-PSD detector in θ - 2θ geometry. Film thickness and elemental compositions were measured with Rutherford's backscattering spectrometry using stream of α particles (He²⁺). The measured thickness of the pristine film was calculated to be ~ 100 nm.

3. Results and discussion

The XRD pattern of the as deposited thin film indicates the anatase phase of TiO₂, as seen in Fig. 1. All the reflections except (004) and (008) are suppressed due to the epitaxial growth of the film along *c*-axis. After 100 MeV Ag⁷⁺ ion irradiation with fluences 1×10^{11} , 1×10^{12} and 1×10^{13} ions.cm⁻², successive amorphization is clearly seen from the XRD profile shown in Fig. 1.

The interaction of ion beams with material modifies its physical properties. Ion beam irradiation is found to induce defects, anneal pre-existing defects, induce structural phase transformation and also influence the crystallinity of the target material [10]. SHI passes through the surface with velocity comparable to an electron's Bohr velocity and loses its energy while traversing through matter. The

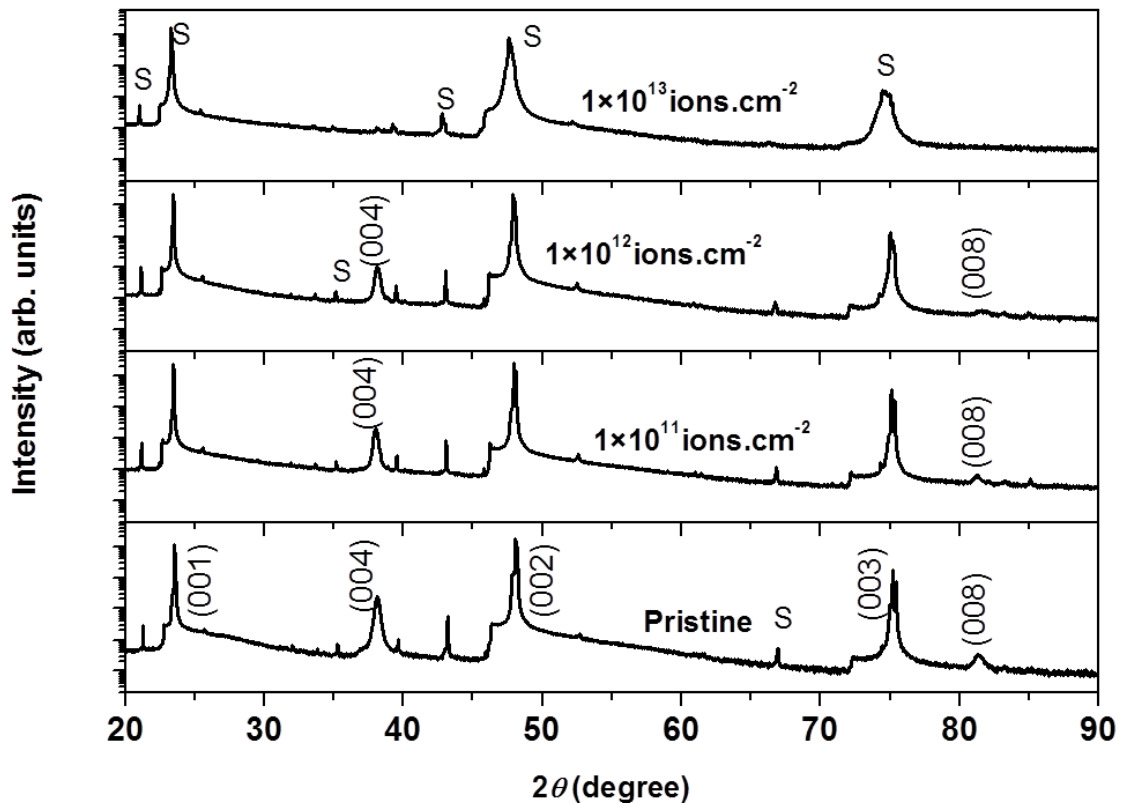


Figure 1. XRD pattern of pristine and irradiated $\text{Ti}_{0.95}\text{Co}_{0.05}\text{O}_{2-\delta}$ thin films deposited at 10 mTorr oxygen partial pressure on LaAlO_3 substrate. The fluence used is indicated in each panel. ‘S’ denotes the reflections related to LaAlO_3 substrate.

total energy loss can be expressed as the contribution of two independent energy loss processes: (i) electronic energy loss, $(dE/dx)_e \sim S_e$, attributed to electronic excitation and ionization due to the inelastic collision with electrons dominating at high energy regime and (ii) nuclear energy loss, $(dE/dx)_n \sim S_n$, due to the elastic collisions with the atoms of the solid with the nuclei of the projectile ion. The former process is dominant for ions in the mega electron volt (MeV) energy range and the latter is valid for ions in the kilo electron volt (keV) energy range. In the present study, the energy of the projectile ions is selected such that it can pass through the film thickness and get buried inside the substrate. The 100 MeV Ag^{7+} ions deposit $\sim 18.16 \text{ keV.nm}^{-1}$ in inelastic collisions (electronic energy loss S_e) with electrons, $\sim 90.86 \text{ eV/nm}$ in elastic collisions (nuclear energy loss S_n) with nuclei as estimated using SRIM (The Stopping and Range of Ions in Matter) simulations code [15]. The projected range of the ions is approximately 9650 Å which is greater than the film thickness i.e. $\sim 1000 \text{ Å}$. Since the threshold for track formation in TiO_2 film is approximately 6.2 keV.nm^{-1} , it is expected that the changes produced in the films are dominantly due to the electronic energy loss [16]. From the XRD it is clear that the film gets completely amorphized at a fluence of $1 \times 10^{13} \text{ ions.cm}^{-2}$, as shown in Fig. 1.

In order to investigate the magnetic properties of the pristine and irradiated films, magnetization measurements as a function of applied magnetic field under zero field cooling (ZFC) and field cooling (FC) conditions, with a probing field of 50 Oe and temperature ranging from 5 to 300 K, were performed. These results are shown in Fig. 2. As Co is a magnetic metal and can contribute to the magnetization of the film in the form of Co clusters instead of substituting the Ti site, it is necessary to determine the Co concentration in TiO_2 . This was performed by using Rutherford’s backscattering

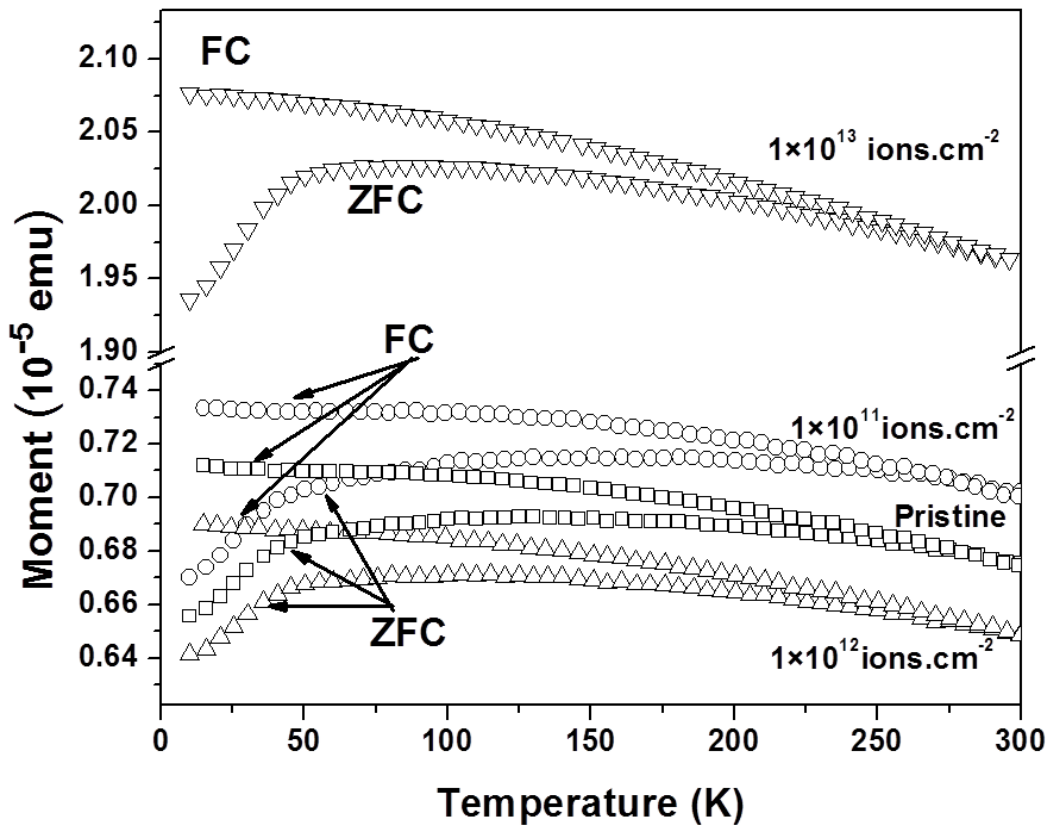


Figure 2. Magnetization as a function of temperature of pristine and irradiated $\text{Ti}_{0.95}\text{Co}_{0.05}\text{O}_{2-\delta}$ thin films deposited at 10 mTorr oxygen partial pressure on LaAlO_3 substrate.

spectrometry (RBS). RBS measurements indicated that the actual Co concentration is 5 atomic %. In order to form Co clusters in TiO_2 matrix, a Co concentration of greater than 7 atomic % is needed [2]. In the measured films the Co concentration is less than the critical concentration and thus the contribution to magnetization because of Co cluster is ruled out. From Fig. 2 it is clear that the magnetization relative to ZFC and FC measurements are irreversible, as the two measurements do not coincide. From Fig. 2 it is also evident that the T_c of the films is above 300 K. Fig. 3 illustrates the magnetization as a function of applied magnetic field at 300 K and 5 K for the pristine as well as irradiated thin films. From the obtained magnetization values the diamagnetic contribution from the LAO substrate was carefully deducted. The magnetization increases with increasing magnetic field and almost saturates. While decreasing the field, the magnetization did not retrace the same path and show a prominent hysteresis for the pristine as well as irradiated thin films. The saturation magnetization (M_s) increases for the fluence $1 \times 10^{11} \text{ ions.cm}^{-2}$. However, it decreases with fluence $1 \times 10^{12} \text{ ions.cm}^{-2}$. Surprisingly, the M_s increased abruptly for the film irradiated with $1 \times 10^{13} \text{ ions.cm}^{-2}$ that shows complete amorphization at this fluence. A similar trend is obtained in $M-H$ behaviour measured at 5 K (see Fig. 3 (b)). Thakur *et al.* [17] reported ferromagnetism in undoped TiO_2 when irradiated with 200 MeV Ag ions with a phase change from anatase to brookite. Sanyal *et al.* [18] reported ferromagnetism with low energy Ar irradiated TiO_2 thin films. In case of Co doped TiO_2 polycrystalline thin films, the saturation magnetization M_s decreases with increasing ion fluence [13]. The decrease in M_s was explained as a consequence of formation of magnetically disordered region around the ion track that does not contribute to the ferromagnetic order [13]. However, in the present

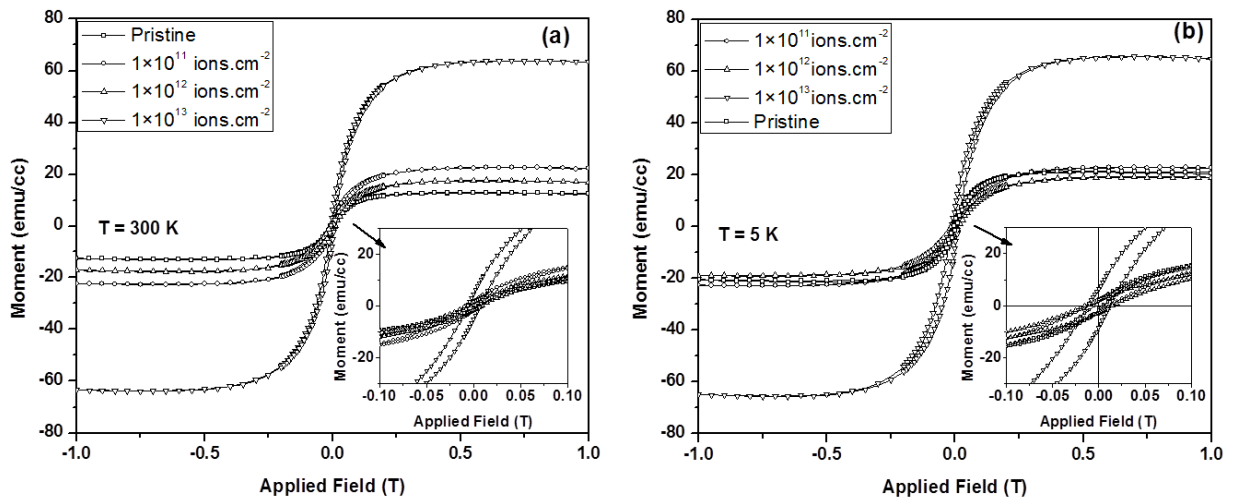


Figure 3. M - H plots for the pristine and irradiated $\text{Ti}_{0.95}\text{Co}_{0.05}\text{O}_{2-\delta}$ thin films deposited at 10 mTorr oxygen partial pressure on LaAlO_3 substrate and measured at temperatures: (a) 300 K and (b) 5 K. The insets show the zoomed view of the hysteresis loops in low field region.

case the M_s is increased with ion irradiation which is quite different from the response of the polycrystalline films towards swift heavy ions.

There are several mechanisms proposed for the observed magnetism in Co doped TiO_2 system: (i) Bound magnetic polaron percolation (BMP) model, (ii) indirect RKKY exchange interaction, and (iii) impurity band exchange model. Among these models or mechanisms BMP and RKKY models are quite convincing. Bound magnetic polarons are formed due to Coulomb and magnetic exchange interactions surrounding a defect like oxygen vacancy [4, 19]. In the BMP model carriers are localized due to electrostatic interaction with some defect [19]. The magnetic polarons are well defined, non-overlapping, isolated entities, only at low carrier densities and sufficiently large temperatures. The size of the polarons increase as the temperature decreases, eventually overlapping with neighbouring BMPs. This overlap causes the alignment of their spins, therefore forming ferromagnetic (FM) clusters. The FM transition takes place when an ‘infinite cluster’ (of the size of the system) is formed, i.e. when the percolation of BMP occurs. The model is valid in the low carrier density regime and when the magnetic impurities are larger than the density of carriers [19]. In case of RKKY model, the itinerant electron plays a vital role. The itinerant electron interacts with the localized moments and tends to order them. For RKKY model to be applicable, the system should have sufficient itinerant electrons. With ion irradiation it has been found that the conductivity of TiO_2 films decreases and films become insulating [20]. Thus, the mechanisms leading to ferromagnetism in these films at lower and higher fluence are definitely different. The competing effect between these two mechanisms leading to ferromagnetic ordering results in the anomaly seen in the magnetization for the intermediate fluence as observed from the M - H measurements at 5 and 300 K. Thus, bound magnetic polaron (BMP) mechanism is mostly dominant for the amorphous film irradiated with fluence 1×10^{13} ions. cm^{-2} demonstrating maximum magnetization.

4. Conclusions

$\text{Ti}_{0.95}\text{Co}_{0.05}\text{O}_{2-\delta}$ thin films were grown on single crystal LaAlO_3 substrates. The anatase phase of the film was retained with ion irradiation. However, the crystallinity degraded with ion irradiation and the films became completely amorphous at fluence 1×10^{13} ions. cm^{-2} . ZFC-FC magnetization revealed prominent bifurcation below 300 K, indicating that the T_c of the film is well above room temperature. Magnetization as a function of applied magnetic field measured at 300 K and 5 K confirms the ferromagnetic behaviour of the films. The M_s initially increased for the film irradiated with fluence

1×10^{11} ions.cm⁻² then decreased for the fluence 1×10^{12} ions.cm⁻² and finally the magnetization increases dramatically for the amorphous film irradiated with fluence 1×10^{13} ions.cm⁻². This unusual increase in the magnetization can be explained on the basis of BMP model.

Acknowledgements

PM gratefully acknowledge Dr. R. J. Choudhary, UGC-DAE Consortium for Scientific Research, Indore, India for the measurement facilities. AREP and CJS acknowledge the financial support of UJ and the NRF (grant number 93551).

References

- [1] Yamada Y, Ueno K, Fukumura T, Yuan H T, Shimotani H, Iwasa Y, Gu L, Tsukimoto, Ilkuhara Y and Kawasaki M 2011 *Science* **332** 1065
- [2] Matsumoto Y, Murakami M, Shono T, Hasegawa T, Fukumura T, Kawasaki M, Ahmet P, Chikyow T, Koshihara S and Koinuma H 2001 *Science* **291** 854
- [3] Janisch R, Gopal P and Spaldin N A 2005 *J. Phys. Condens. Matter* **17** R657
- [4] Coey J M D, Venkatesan M and Fitzgerald C B 2005 *Nat. Mater.* **4** 173
- [5] Sundaresan A, Bhargavi R, Rangarajan N, Siddesh U and Rao C N R 2006 *Phys. Rev. B* **74** 161306(R)
- [6] Manivannan A, Seehra M S, Majumder S B and Katiyar R S 2003 *Appl. Phys. Lett.* **83** 111
- [7] Mohanty P, Mishra N C, Choudhary R J, Banerjee A, Shripathi T, Lalla N P, Annapoorni S and Rath C 2012 *J. Phys. D: Appl. Phys.* **45** 325301
- [8] Mohanty P, Kabiraj D, Mandal R K, Kulriya P K, Sinha A S K and Rath C 2014 *J. Magn. Magn. Mat.* **355** 240
- [9] Kanjilal D 1997 *Vacuum* **48** 979
- [10] Wesch W, Kamarou A and Wendler E 2004 *Nucl. Instrum. Methods Phys. Res. B* **225** 111
- [11] Szenes G 1995 *Phys. Rev. B* **51** 8026
- [12] Benyagoub A 2006 *Nucl. Instrum. Methods Phys. Res. B* **245** 225
- [13] Mohanty P, Singh V P, Mishra N C, Ojha S, Kanjilal D, Rath C 2014 *J. Phys. D: Appl. Phys.* **47** 315001
- [14] Lotnyk A, Senz S, Hesse D 2007 *Thin Solid Films* **515** 3439
- [15] Zeigler J F, Biersack J P and Littmark V 1985 *The Stopping and Range of Ions in Solids* (New York: Pergamon)
- [16] Nomura K-I, Nakanishi T, Nagasawa Y, Ohki Y, Awazu K, Fujimaki M, Kobayashi N, Ishii S and Shima K 2003 *Phys. Rev. B* **68** 064106
- [17] Thakur H, Thakur P, Kumar R, Brookes N B, Sharma K K, Singh A P, Kumar Y, Gautam S and Chae K H 2011 *Appl. Phys. Lett.* **98** 192512
- [18] Sanyal D, Chakrabarti M, Nath P, Sarkar A, Bhowmick D and Chakrabarti A 2014 *J. Phys. D: Appl. Phys.* **47** 025001
- [19] Calderon M J and Sarma S D 2007 *Ann. Phys.* **322** 2618
- [20] Mohanty P, Ph.D. Thesis 2015 *Structure, Magnetic and Transport Properties of Nanostructured $Ti_{1-x}Co_xO_{2-\delta}$*

Synthesis and characterization of TiO₂ doped with Dy³⁺ ions by sol gel method.

M S Mokoena*, M Y A Yagoub, O M Ntwaeaborwa and H C Swart*

¹Department of Physics, University of the Free State, Bloemfontein, ZA9300, South Africa

*Corresponding authors e-mail: swarthc@ufs.ac.za, mokoename@ufs.ac.za

Abstract. Dy³⁺ ions doped in TiO₂ nanophosphor powders were synthesized by the sol-gel method. The prepared samples were characterized by X-ray diffraction (XRD), photoluminescence spectroscopy (PL), ultra-violet visible spectroscopy (UV-Vis), scanning electron microscopy (SEM) and energy dispersive x-ray spectroscopy. The XRD patterns confirmed the tetragonal structure of TiO₂ with the experimental unit cell parameters of $a = b = 3.803\text{\AA}$ and $c = 9.534\text{\AA}$. The average crystallite sizes were estimated by applying the Debye-Scherrer formula and range from 9 to 5 nm. The FE-SEM images showed that the obtained powders surface texture was composed of nanorods. The EDS spectra confirmed the formation of undoped and doped TiO₂ nanophosphors. The UV-Vis diffuse reflectance spectra indicated the absorption bands in the visible region ranging from 460 to 850 nm which originated from the doped nanophosphors. The sharp absorption edge has shifted towards the longer wavelengths with the introduction of Dy³⁺ ions into the TiO₂. The optical band gap of the synthesized nanophosphor powder was determined and ranged from 3.41 to 3.06 eV. The emission bands of the Dy³⁺ ions were observed at 483, 576, 665 and 765 nm, which were assigned to different transitions of the 4f - 4f levels.

1. Introduction

Titanium dioxide is also known as titania or titanium oxide which has a chemical formula of TiO₂ and belongs to the IVB group transition metal oxides. Titania occurs in three common known polymorphs such as anatase (tetragonal), rutile (tetragonal) and brookite (orthorhombic). The above phases are differentiated from one another by their band gap energy and by also their refractive index ($E_g = 3.2$ eV, $n = 2.488$ for anatase, $E_g = 3.0$ eV, $n = 2.608$ for rutile and $E_g = 1.96$ eV, $n = 2.583$ for brookite). Furthermore TiO₂ has a low phonon frequency (<700 cm⁻¹) [1]. Generally the two polymorphs studied are the anatase phase and rutile phase [2]. In addition the rutile phase is considered to be the most stable phase especially at high temperature, while the anatase phase is stable at low temperatures.

Due to the unique properties, titania nanomaterial is considered to be one of the most important metal oxides in the past few years. Many researchers focus on titania due to the wide range of applications in solar cells, photocatalysts, cosmetics, lithium batteries, dye sensitized and chemical sensor and so forth [2, 3]. The applications of rutile and anatase phases will differ because of the different bonding arrangement [2].

Over the past few decades it has been noted that the properties of titania can be modified by doping TiO₂ with lanthanide ions. TiO₂ is one of the more favorable host materials for the incorporation of lanthanide ions due to its interesting properties such as friendly to the environment and its excellent chemical and thermal stabilities. Different researchers have synthesized TiO₂ nanoparticle doped with different lanthanide ions in the past years including TiO₂:Tb³⁺ [4, 5], TiO₂:Sm³⁺ [6, 7], TiO₂:Pr³⁺ [8] and

TiO₂:RE ions [9] for different applications. In addition the presence of rare earth ions in TiO₂ nanocrystalline stabilizes the anatase phase. The Dy³⁺ ion has been chosen to dope TiO₂ because of the fact that Dy³⁺ ions emit light at different ranges in the visible spectrum. There are several methods to synthesize TiO₂ nanoparticle but the focus was on the sol-gel method in this report because it is an inexpensive method and it requires lower temperatures.

The important goals of the present work was to synthesis the titanium oxide nanocrystalline powders by the sol-gel technique at room temperature and also to study the influence of the Dy³⁺ dopant on the structure and optical properties of TiO₂ nanocrystalline powder. The particle size and crystal structure of the synthesized samples were characterized using X-ray diffraction (XRD), surface morphology and chemical composition were determined using scanning electron microscopy (SEM) and energy dispersive x-ray spectroscopy (EDS), respectively, while the emission and excitation of the prepared samples were investigated by using photoluminescence spectroscopy (PL). In addition the optical indirect band gap energies of the prepared samples were obtained by using ultra-violet visible spectroscopy (UV-Vis).

2. Experimental Section

2.1 Synthesis

The undoped and doped TiO₂ nanophosphor powders were prepared by the sol-gel routine at room temperature by using Titanium butoxide (97%, Sigma Aldrich) as the precursor, Ethanol absolute (99.7%, associated chemical enterprise), and Acetic acid ($\geq 99\%$, Sigma Aldrich) as the starting materials and dysprosium (iii) nitrate hydrate (99.9%, Sigma Aldrich) was used as a dopant ion.

Typically, the 25 mL of acetic acid was mixed together with 25 mL of ethanol in a 200 mL beaker and the mixture was stirred for 30 minutes using a magnetic stirrer to obtain the complete esterification solution. Afterwards, the 2.5 mL of titanium butoxide was added into the esterification solution to prepare the undoped nanophosphor. But for the doped nanophosphor a certain volume of titanium butoxide and different concentrations of Dy(NO₃)₃.5H₂O were added simultaneously to the esterification solution. After the addition, the mixture was stirred continuously for an hour to form a sol at room temperature. The sol was aged for 24 hours at room temperature under the vacuum in order to form the white precipitation, and the white precipitations were dried in an oven for 30 minutes at 120°C. The pestle and mortar was used to grind the dried powder obtained from the oven. The grinded nano TiO₂ powder was then transferred into a muffle furnace and calcined at 400°C for 2 hours at a rate of 5°C.min⁻¹.

2.2 Characterization Techniques

The crystallite size and phase of the TiO₂ nanophosphor for all synthesized samples were investigated using XRD patterns that were measured by a Bruker AXS D8 Advanced X-ray diffractometer with Cu K α = 1.5406 Å radiation in the range $2\theta = 20 - 80^\circ$ and a scanning rate of 0.02° .s⁻¹.

The particle morphology and elemental composition of the prepared samples were studied using a Joel JSM-7800F Field Emission equipped with an Oxford Aztec EDS and a Gatan Mono CL4, which was used to identify the elements in the prepared samples. The samples were mounted on carbon tape during the analysis of SEM and EDS.

The optical properties of the synthesized nanophosphor powders were recorded in a scan range of 270 – 850 nm using an ultra violet visible spectrophotometer (Perkin Elmer UV/Vis Lambda 950 powder spectrophotometer) and using a lab-sphere for calibration and standard reference. Furthermore, both excitation and emission spectra of prepared samples were investigated with a Cary Eclipse fluorescent spectrometer using a Xenon lamp as excitation source. All the measurements were done at room temperature.

3. Results and Discussion

3.1 X-ray diffraction (XRD)

The XRD patterns of undoped TiO₂ nanophosphor powder and Dy³⁺ doped TiO₂ nanophosphor powders via sol-gel method are presented in Figure 1. The patterns indicate that the tetragonal phase of TiO₂ has formed and they were indexed according to the JCPDS card number 21-1272 (Anatase) and JCPDS card number 21-1276 (Rutile). The undoped XRD patterns consisted of mixed phases of anatase and a minor content of rutile, while the doped patterns depict that Dy³⁺ ion prevented phase transformation of anatase-rutile by stabilizing only the anatase phase. The same phase was observed for all doped sample without any impurity which may relate to Dy₂O₃ or other phases of Dy in the XRD patterns and therefore this shows that Dy³⁺ ions were well incorporated into the TiO₂ host material.

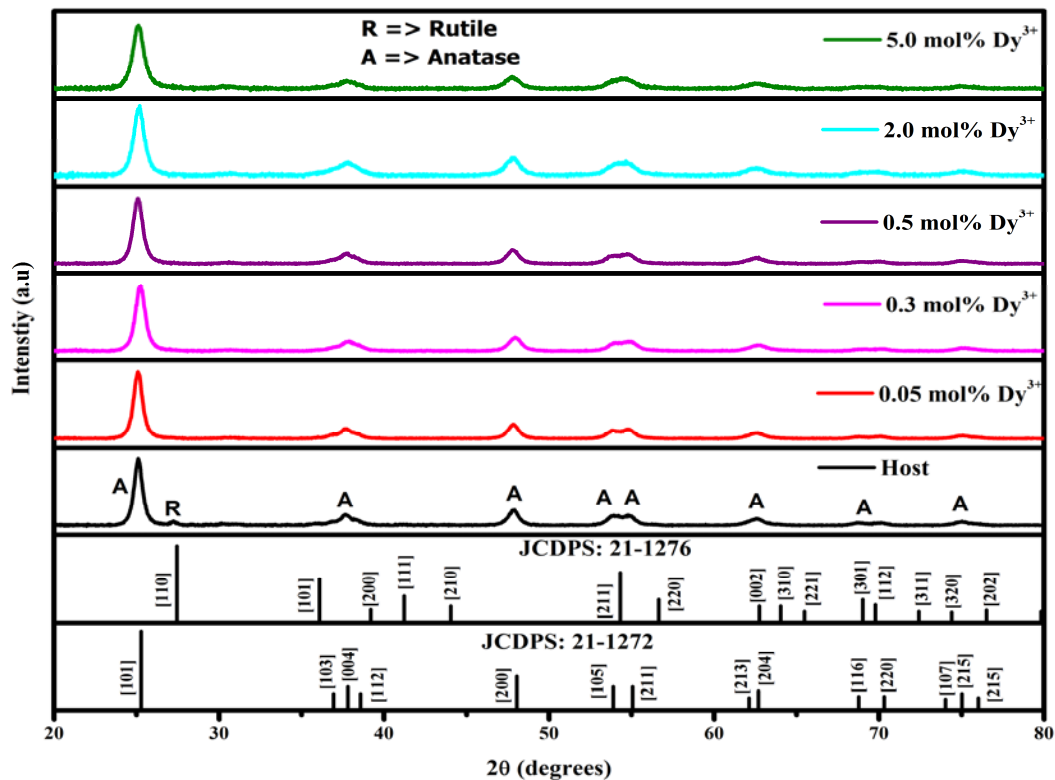


Figure 1: The XRD patterns of the TiO₂: Dy³⁺ nanophosphor powders. (“A” represent anatase phase and “R” represent the rutile phase).

It has been noted that the rutile phase is more stable especially at higher temperatures than the anatase and brookite phases [2], while the anatase phase can be stabilized by introducing dopants into the TiO₂ crystal structure. The XRD of the doped nanophosphor show no visible evidence of the rutile phase in Figure 1, centered at around 27.27°. Fidelus et.al [10] observed the same behavior when TiO₂ was co-doped with Nd³⁺ and Yb³⁺ ions and this effect indicates that the dopant retards the transition of TiO₂ from anatase to rutile phase, therefore stabilizing the anatase phase. The average crystallite sizes of Dy³⁺ doped TiO₂ nanophosphor with different doping concentration were estimated by applying the Debye-Scherrer formula [10, 11].

$$D = \frac{k\lambda}{\beta \cos\theta} \quad (1)$$

where k is constant $k = 0.89$ for spherical nanoparticles, λ is the wavelength X-ray radiation (Cu K α =1.5406 Å), β is the full width at half maximum (FWHM) of the particular peak in radians and θ is the measured Bragg’s angle in degrees. The average crystallite sizes ranged from 9 to 5 nm.

3.2 Scanning electron microscopy and energy dispersive x-ray spectroscopy.

The SEM images and EDS spectrum of synthesized nanophosphor powders are shown in Figure 2 and Figure 3 respectively. The shape morphology was obtained by using FE-SEM as shown in Figure 2 (a) and (b) for undoped TiO_2 and doped TiO_2 with 5.0 mol% of Dy^{3+} respectively. The figure shows that the surface texture was composed of nanorods for both the undoped and doped TiO_2 nanophosphor. This proves that the Dy^{3+} ion did not affect the particle morphology of the synthesized nanophosphors.

The EDS spectra confirm the presence of elements such as Ti, O, and C in the pure synthesized TiO_2 nanophosphor and the same elements in the doped TiO_2 nanophosphor, including the foreign element Dy ion. It thus confirmed that the pure anatase (TiO_2) was synthesized since no other elements were detected as shown in Figure 3 (a) beside Ti and O. The presence of carbon is from the carbon that was used to mount the sample during the analysis of SEM and EDS.

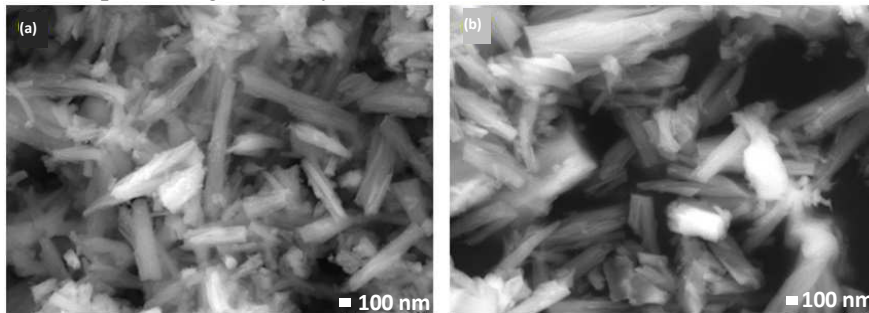


Figure 2: FE-SEM images of the (a) undoped and (b) 5.0 mol% Dy^{3+} doped TiO_2 nanophosphor powders.

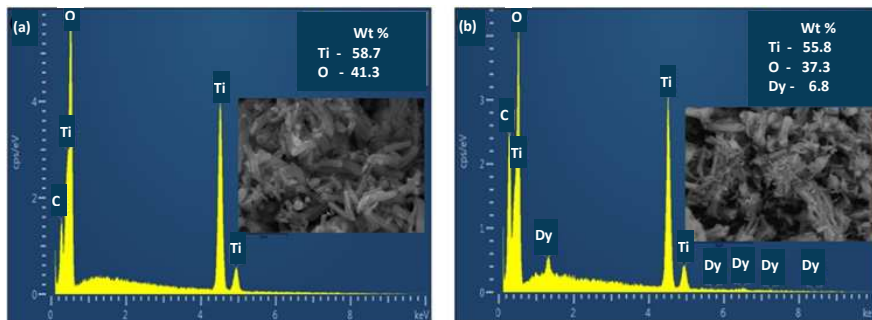


Figure 3: The EDS spectra of the undoped and 5.0 mol% Dy^{3+} doped TiO_2 nanophosphor powders.

3.3 Ultra-violet spectrophotometry

The absorption properties of the prepared samples were obtained from the diffuse reflectance spectra (DRS) as shown in Figure 4(a). It is clear that the absorption bands in a visible region (450 to 850 nm) originated from the doped samples, while for undoped sample there was no sign of absorption bands in that region. The absorption bands centered at 454, 475, 752 and 801 nm originated from the ground $^6\text{H}_{15/2}$ state to different excited states of the Dy^{3+} ion [12]. The sharp absorption edge was observed at ~ 365 nm for the undoped nanophosphor powder, but it shifts towards the longer wavelength after Dy^{3+} was introduced into the TiO_2 matrix. However, this absorption edge is assigned to the intrinsic absorption band of TiO_2 . The optical band gap energy was also calculate by using the Kubelka-Munk remission function [11] and Figure 4 (b) was used to obtain the band gap values, which ranged from 3.41 to 3.06 eV.

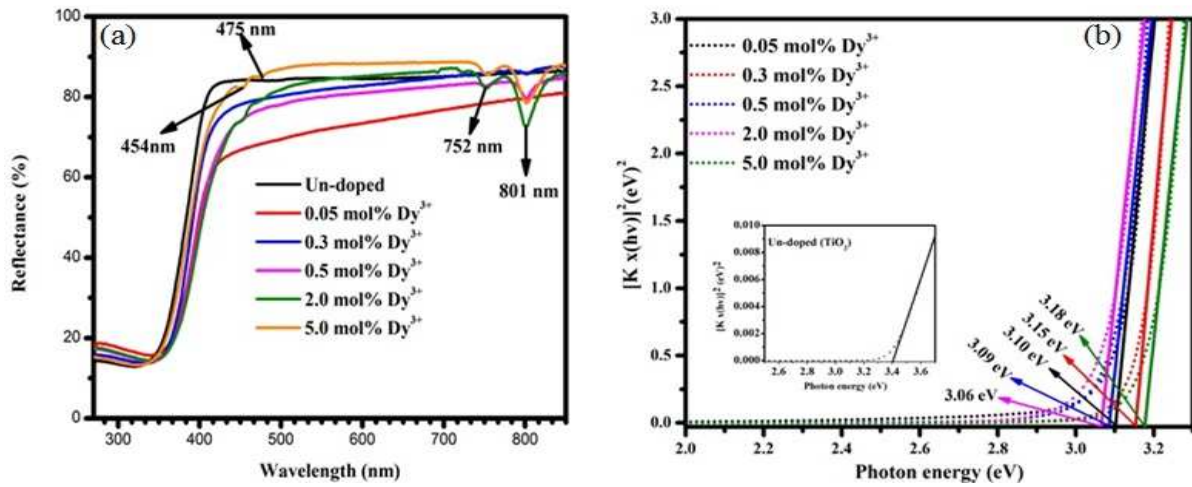


Figure 4: (a) DRS of Dy³⁺ doped TiO₂ nanophosphor and (b) Kubelka Munk transformed reflectance spectra of TiO₂ nanophosphor powders.

Figure 5 illustrates the excitation spectrum of pure TiO₂ nanophosphor and Dy³⁺ doped TiO₂ nanophosphor with different doping concentrations, monitored at an emission wavelength of 576 nm. There were four main excitation peaks with maxima at 392, 428, 453 and 474 nm which were assigned to electronic transition as shown in Figure 5.

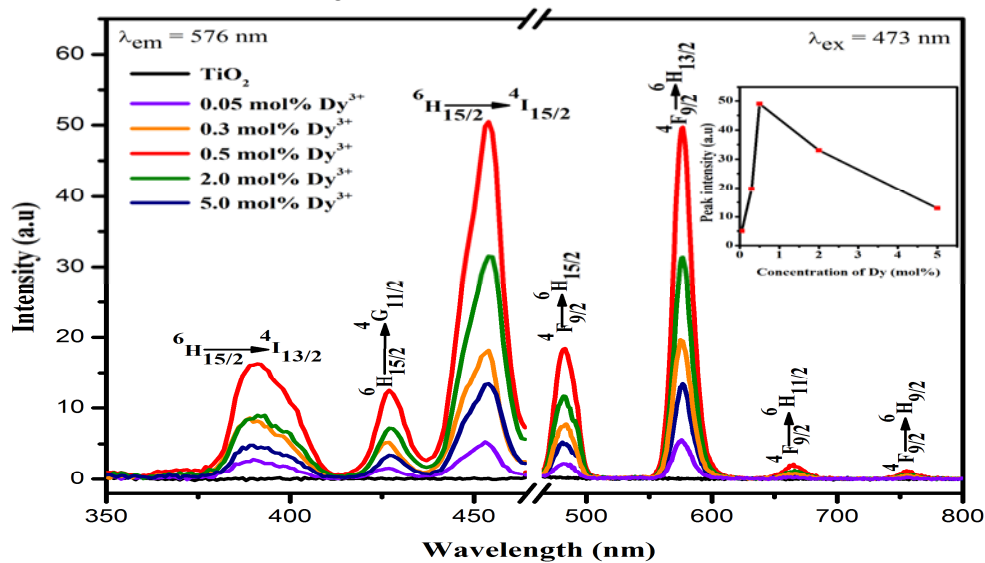


Figure 5: Excitation and emission spectra of Dy³⁺ doped TiO₂ nanophosphor with different doping concentration, (λ_{em} = 576 nm) and (λ_{ex} = 473 nm) respectively. (Inset shows the maximum emission intensity as function of Dy³⁺ concentration).

The emission spectra of Dy³⁺ doped TiO₂ nanophosphor with different doping concentration is also presented in Figure 5, under the excitation wavelength of 453 nm. The four main emission bands were observed with maxima at 483, 576, 665 and 765 nm, which were attributed to the transitions ⁴F_{9/2} → ⁶H_{15/2}, ⁴F_{9/2} → ⁶H_{13/2}, ⁴F_{9/2} → ⁶H_{11/2}, ⁴F_{9/2} → ⁶H_{9/2} of Dy³⁺, respectively [12]. The yellow emission centered at 576 nm has the most intense emission bands for all prepared samples. (The inset shows the intensity as function of Dy³⁺ concentration). The transition at wavelength centered at 576 nm (yellow) ⁴F_{9/2} → ⁶H_{13/2} belongs to the electric dipole transition, while the hypersensitive transition ⁴F_{9/2} → ⁶H_{15/2} at 476 nm band (blue) corresponds to the magnetic dipole of the Dy³⁺ ion.

4. Conclusion

A series of TiO₂ nanophosphor doped with Dy³⁺ were successfully synthesized by sol-gel method. The XRD patterns confirmed the tetragonal structure of TiO₂, although the XRD patterns of undoped nanophosphor consisted of a mixture of anatase and rutile. It was clearly shown that the Dy³⁺ ion played an important role in the crystal structure of TiO₂ because the presence of the Dy³⁺ ions stabilized the anatase phase. The average crystallite sizes were estimated to range from 7 to 9 nm for all samples. The EDS spectra confirmed that the synthesized nanophosphor was pure TiO₂ since no impurity elements were detected in the prepared nanophosphor material. The surface texture was composed of nanorods for pure TiO₂ and doped TiO₂ nanophosphors. The absorption bands in the visible range were observed by using UV-Vis diffuse reflectance spectroscopy. The optical indirect band gap energies of TiO₂ nanophosphor powders were estimated by using the diffuse reflectance spectra to plot the Kubelka-Munk function for an indirect band gap. The estimated band gap energies ranged from 2.92 to 3.13 eV for the doped and undoped nanophosphors. The two major emission bands of Dy³⁺ ion were observed at 483 nm and 576 nm and the maximum emission intensity was obtained when the Dy³⁺ concentration was 0.5 mol%. It was noted that the luminescence intensity depended on the Dy³⁺ ion concentration.

Acknowledgements

This research is supported by the South African Research Chairs Initiative of the Department of Science and Technology and the National Research Foundation of South Africa (grant 84415). The financial support from the University of the Free State is also acknowledged.

5. References

- [1] Brik M G, Anti Z M, Vukovi K, and Drami M D 2015 *Mater. Trans.* **56** 1416.
- [2] Choudhury B and Choudhury A 2013 *Inter. Nano Lett.* **3** 55.
- [3] Masuda Y and Kato K 2009 *J. Ceramic Soc Jap.* **117** 373.
- [4] Wojcieszak D, Kaczmarek D, Domaradzki J, and Mazur M 2013 *Inter. J. Photoenergy* 2013 526140.
- [5] Jia C, Xie E, Peng A, Jiang R, Ye F, Lin H, and T. Xu T 2006 *Thin Solid Films* **496**, 555.
- [6] Kiisk V, Šavel M, Reedo V, Lukner A, and Sildos I 2009 *Phys. Proc.* **2**, 527.
- [7] Reszczyńska J, Esteban D A, and Gazda M 2014 *Fizykochemiczne Problemy Mineralurgii - Physicochemical Problems of Mineral Processing* **50** 515.
- [8] Theivasanthi T and Alagar M 2012 *Nano Biomed. Eng.* **4(2)** 58
- [9] Bahadur N, Jian K, Pasricha R, Govind, Chand S 2011 *Sens. Actuators B Chem.* **159** 112.
- [10] Ogugua S, Swart H C, and Ntwaeaborwa O M 2016 *Physica B* **480**, 131.
- [11] Molefe F V, Koao L F, Dolo J J, and Dejene B F 2014 *Physica B* **439** 185.
- [12] Vishwakarma A K, Jha K, Jayasimhadri M, Sivaiah B, Gahtori B, and Haranath D 2015 *Dalton Trans.* **44**, 17166.

Ferromagnetism in magnetic 4f-systems

V Nolting

Vaal University of Technology, Private Bag X021, Vanderbijlpark 1900, South Africa

volkmarn@vut.ac.za

Abstract. In magnetic 4f-systems electronic and magnetic properties are carried by two different electron groups. They are ferromagnetic insulators and semiconductors respectively and have become important recently due to their applications in spintronics. For their realistic theoretical description the sf-model is used that contains the electron-magnon interaction in the form of an intraatomic exchange coupling between the itinerant conduction and the localized 4f-electrons. The sf-model is solved exactly in the zero bandwidth limit; it turns out that finite band occupations n reduce the saturation magnetization so that $m(T=0, n \neq 0) \leq S$. Furthermore, the Curie temperature T_c depends on band occupation n which is experimentally modeled by doping with suitable impurities. The theoretical calculations are shown to reasonably agree with experimental results.

1. Introduction

Magnetic 4f-systems are compounds containing rare earth atoms and their magnetic properties are due to only partially filled 4f-shells. The incompletely filled 4f-shell is responsible for a permanent magnetic moment that is strictly localized at the lattice site as 4f-wavefunctions of adjacent ions practically do not overlap. However, the two outer 6s-electrons become quasi-free conduction electrons that in metallic 4f-systems move through the entire lattice. An indirect exchange interaction (RKKY interaction) then causes the permanent magnetic moments to align spontaneously below a critical temperature; magnetic 4f-systems are therefore ferromagnetic or antiferromagnetic. Prototypes are the EuX , $X = O, S, Se, Te$ which are insulators or semiconductors respectively and the metallic Gd .

As electronic and magnetic properties of magnetic 4f-systems are caused by two different electron groups several interesting mutual effects are observed. On the one hand, the magnetic moment system is sensitive to changes to the conduction electron density. One consequence of this is that the saturation magnetization $m(T=0, n \neq 0) \leq S$. Here S denotes the spin quantum number of the partially filled 4f-shell. In the case of Eu^{2+} -ions this quantum number is according to Hund's rules $S = 7/2$. On the other hand, the Curie temperature T_c increases with increasing band occupation n and critical temperatures close to room temperature have been observed e.g. in magnetic semiconductors of the type $(Ga, Mn)As$ and in iron based superconductors [1,2]. Here a few percent of the Ga -atoms are replaced by magnetic Mn -ions and the effective coupling between the magnetic moments is similar to that observed in magnetic 4f-systems. This makes such specimen promising examples for the development of spintronic devices. Furthermore, due to the statistical distribution of the Mn -ions interesting phenomena are observed, e.g. spin glass and Kondo behavior, magnetic moment quenching, and a possible coexistence between magnetic order and intermediate valence states [3]. As the temperature dependence of the spin dependent density of states $\rho_\sigma(E)$ is in turn influenced by the magnetization of the 4f-moments drastic conduction band deformations and band splittings have been reported [4].

Magnetic 4f-systems are theoretically described by alternatively the Anderson model [5], a hybridized Kondo lattice model [6], or the sf-model [7]. It is shown in various references (see e.g. reference [8]) that the sf-model describes the coupling between the itinerant conduction electrons and the localized 4f-moments and especially spin exchange processes between the two subsystems in a particularly realistic manner. The detailed understanding of these exchange interactions has recently gained renewed interest in connection with molecular magnetic materials [9]. Even though the sf-model defines a non-trivial many body problem, it can be solved rigorously in certain limiting cases. This provides for a further advantage of the sf-model as the accuracy of approximate solutions can be tested in these limiting cases.

The sf-model is introduced in the following section. In Section 3 both exact and approximate solutions to the many body problem are discussed. Numerical evaluations and corresponding results are presented in Section 4. The paper concludes with a short summary.

2. The Model

The sf-model describes the mutual effects between the two different electron groups in magnetic 4f-systems and is defined by the Hamiltonian

$$H = H_s + H_f + H_{sf}$$

$$H_s = \sum_{ij\sigma} T_{ij} c_{i\sigma}^+ c_{j\sigma} + \frac{1}{2} U \sum_{i\sigma} n_{i\sigma} n_{i-\sigma} \quad (1)$$

Here $c_{i\sigma}^+$ denotes the creation operator for a σ -electron at lattice site R_i , $c_{i\sigma}$ is the corresponding annihilation operator. The operator for the occupation number is then

$$n_{i\sigma} = c_{i\sigma}^+ c_{i\sigma}$$

H_s describes the system of itinerant conduction electrons that are treated as s-electrons and has the well known form of the Hubbard model. Note that the Coulomb interaction is only considered in its simplified intraatomic version, i.e. it only acts if there are two electrons with opposite spin present in the same Wigner-Seitz cell. U is the corresponding Coulomb matrix element: T_{ij} are the hopping integrals. The subsystem of localized magnetic moments is described in a realistic manner by the Heisenberg model

$$H_f = - \sum_{ij} J_{ij} S_i \cdot S_j \quad (2)$$

The spins at R_i and R_j interact via the exchange integrals J_{ij} . The two subsystems are coupled by an sf-exchange, i.e. a local interaction between the 4f-spin S_i and the conduction electron spin σ_i

$$H_{sf} = -g \sum_i \sigma_i \cdot S_i = -\frac{1}{2} g \sum_{i\sigma} (z_\sigma S_i^z n_{i\sigma} + S_i^\sigma c_{i-\sigma}^+ c_{i\sigma}) \quad (3)$$

H_{sf} is an effective operator that simulates the electron-magnon interaction that is responsible for a spontaneous magnetization in magnetic 4f-systems; g is the intraatomic sf-exchange constant. A realistic parameter value for magnetic 4f-systems would be $g = 0.2 \text{ eV}$ [8]. Note that the ratio g/W describes the relative strength of the sf-coupling with $g/W \rightarrow 1$ representing the strong and the limit $g/W \rightarrow 0$ the weak coupling limit.

The Hamiltonian of Eq (1) describes a non-trivial many body problem that is generally not exactly solvable. However, there are a couple of interesting exactly solvable limiting cases that are discussed in Section 3.

3. Exact and approximate solutions

The sf-model is rigidly solved in the zero bandwidth limit [10] and the case ($T = 0, n = 0$) describing one electron in an otherwise empty conduction band [11]. In the zero bandwidth limit the Bloch band degenerates to a single level T_0 that due to the sf-exchange interaction splits into four quasiparticle energies

$$\begin{aligned} E_1 &= T_0 - g S \\ E_2 &= T_0 + g (S + 1) \\ E_3 &= T_0 + U - g (S + 1) \\ E_4 &= T_0 + U + g S \end{aligned}$$

with temperature and particle number dependent spectral weights $\alpha_{i\sigma}(T, n)$ describing the degeneracy of the energy levels E_i . For the general case of finite bandwidths W an alloy analogy may be applied where the alloy consists of four components E_m , $m = 1, \dots, 4$ with concentrations $c_m = \alpha_{m\sigma}(T, n)$ statistically distributed over the entire lattice. This leads to a many body problem that can be solved approximately but selfconsistently within the coherent potential approximation CPA [12]. The CPA calculates an ensemble average where the selfenergy

$$\Sigma_{k\sigma}(E, k) = \Sigma_{k\sigma}(E) \quad (4)$$

becomes wavevector independent. Within the CPA the one particle Green function

$$G_{k\sigma}(E) = \frac{\hbar}{E - \varepsilon(k) + \mu - \Sigma_{k\sigma}(E)} \quad (5)$$

has the typical form of an interacting electron system where the selfenergy represents many particle correlations not contained in a one particle theory. The quasiparticle density of states

$$\rho_{\sigma}(E) = -\frac{1}{\pi} \Im \int_{-\infty}^{+\infty} dx \frac{\rho_0(x)}{E - x - \Sigma_{\sigma}(E)} \quad (6)$$

is in turn calculated from an integral over the free Bloch density of states. Applying Eq (6) to magnetic 4f-systems yields quasiparticle density of states that are considerably deformed and split compared to the free Bloch band. This is discussed further in the next section.

4. Results

We first want to discuss metallic 4f-systems and therefore evaluate Eq (6) as a function of temperature at fixed band occupation n . For the Bloch density $\rho_0(E)$ a simple model version from the tight binding approximation [13] is used. The temperature dependence mainly results from the 4f-magnetization m that is regarded as a parameter and varies from near saturation at $T = 0 K$ to $m(T = T_C) = 0$ according to the usual Brillouin function behavior. The calculation is done to roughly model Gd with $T_C = 238 K$. The remaining set of parameters used are typical for moderate coupling, i.e, $g = 0.2 eV$, $W = 1 eV$. $S = 7/2$. The corresponding results are plotted in Figure 1 below which shows the temperature and spin dependent quasiparticle density of states $\rho_{\sigma}(E)$.

The original Bloch band is for both $\sigma = \uparrow\downarrow$ split into two quasiparticle subbands. The splitting is a consequence of the sf-interaction, i.e. many particle correlations and their effect depends on the relative coupling strength g/W . With decreasing magnetization, i.e. increasing temperature the subbands start to merge until they finally coincide at $T = T_C$. These results imply that the influence of the 4f-moments on the itinerant conduction electrons vanishes above T_C . This view is, however, challenged by the authors of reference [14] who claim that a correlation based exchange splitting between the \uparrow and \downarrow densities of states persists in the paramagnetic phase.

On the other hand, for ferromagnetic insulators and semiconductors, e.g. EuX the Curie temperature $T_C(n = 0)$ for the empty conduction band was previously calculated within the mean field approximation of the Heisenberg model [15] and corresponding results are summarized in Table 1 below.

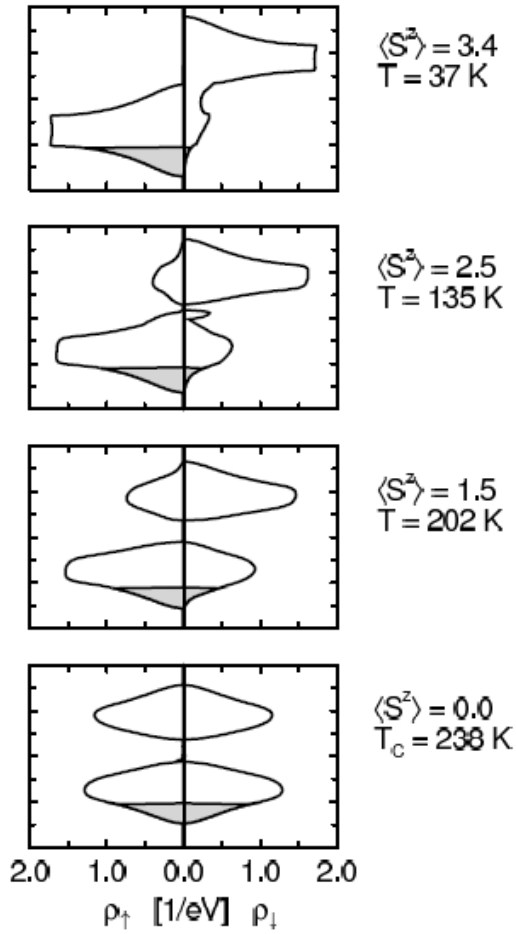


Fig 1: Quasiparticle density of states $\rho_\sigma(E)$ for four different values of the 4f-magnetization $m = \langle S^z \rangle$ and $\sigma = \uparrow\downarrow$.

Table 1: Experimental and theoretical values for the critical temperatures of EuX according to ref [15].

X	Exp value for critical temperature	Theoretical value for critical temperature	Type of magnetization
O	66.8 K	86.6 K	ferromagnetic
S	16.6 K	21.5 K	ferromagnetic
Se	4.6 K	- 4.0 K	metamagnetic
Te	9.6 K	8.5 K	antiferromagnetic

While the calculated values from the MFA are slightly enhanced the Curie temperatures T_c ($n = 0$) generally come out too low, especially with regard to possible applications in electronic devices.

However, with increasing band occupation n , the Curie temperature $T_C(n)$ increases according to the equation

$$\frac{T_C(n)}{T_C(n=0)} = 1 + \frac{S+1-n}{S+1} n^{4/3} \quad (7)$$

Equation (7) is derived from a mean field approximation where the dependence of the exchange integrals on band occupation n is due to the RKKY-interaction [16]. Corresponding numerical results are plotted in Figure 2 below.

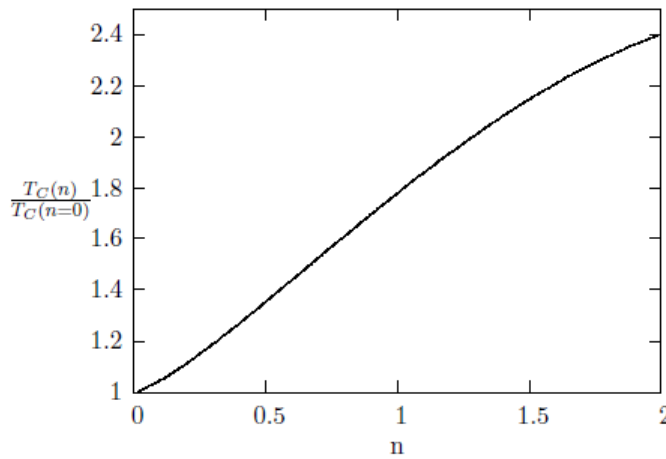


Fig 2: Curie temperature $T_C(n)$ from a mean field approximation of the sf-model.

With increasing band occupation n the Curie temperature T_C of the ferromagnetic 4f-system increases as the RKKY-interaction leads to an effective coupling between the permanent magnetic moments. This increase of T_C on n is experimentally modeled by doping with suitable impurities and similar results have been reported both experimentally [1,2] and theoretically [6, 17]. Furthermore, for large enough band occupations T_C is more than doubled compared to the corresponding value for the empty conduction band. The critical temperature thus becomes close to room temperature which is important regarding possible applications in spintronics. On the other hand, the saturation magnetization decreases from its $n = 0$ value $m(T = 0, n = 0) = S = 7/2$ according to Figure 3 below.

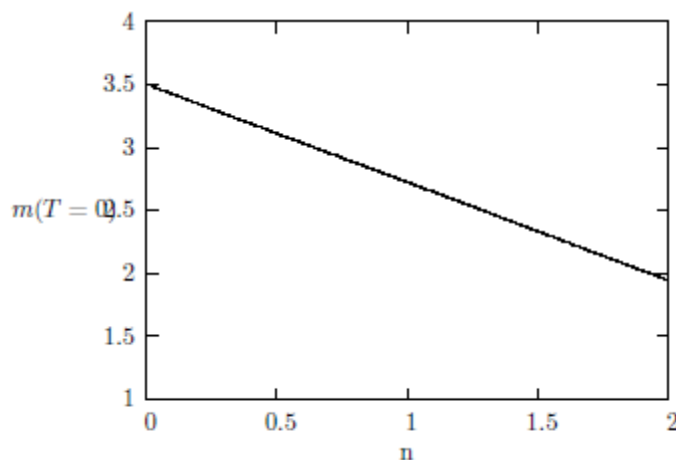


Fig 3: Saturation magnetization $m(T = 0)$ as a function of band occupation n .

This result already follows from the exactly solvable zero bandwidth limit. A \downarrow -electron can even at $T = 0\text{ K}$ exchange its spin with the then antiparallel localized 4f-spin. A bound state of the conduction electron with the spin wave is formed. The corresponding quasiparticle has an infinite lifetime and is known as the magnetic polaron [18]. The consequence of this is a saturation magnetization $m(T = 0, n) \leq S$ in contrast to the Heisenberg model where spin waves only occur at finite temperatures. Spin waves (magnons) are measured by neutron scattering experiments. The magnon-electron interaction on the one hand increases magnetic order, yet on the other hand contributes to the electrical resistivity of magnetic 4f-systems. The authors of reference [19] observe an increase in resistivity of $CeCuAl_3$ with temperature in the magnetically ordered phase in agreement with the theory developed in this paper.

5. Conclusions and Summary

In this paper it is shown that magnetic 4f-systems are reasonably well described within the sf-model that contains an exchange interaction between the localized 4f-spin and the itinerant conduction electron. Using an alloy analogy the spin system is solved within the coherent potential approximation CPA. As a result of correlation effects the conduction band structure becomes temperature dependent while the 4f-magnetization turns out to be sensitive to changes in the conduction electron density. The Curie temperature T_C is enhanced at finite band occupations n with T_C -values close to room temperature being obtained. This makes magnetic 4f-systems suitable for applications in spintronic devices.

Acknowledgment:

The author would like to thank M. Potthoff for carefully perusing the manuscript and acknowledging its valuable summary of the CPA approach to the sf-model.

References

- [1] A H MacDonald, P Schiffer, and N Samarth, Nature Materials 4, 195 (2005)
- [2] K Zhao et al, Nat Commun. 4, 1442 (2013)
- [3] M Matlak and W Nolting, Solid State Comm. 47, 11 (1983)
- [4] W Nolting, J Magn and Magn. Mat 45, 191 (1984)
- [5] P W Anderson, Phys Rev 124, 41 (1961)
- [6] M Hansel, W Nolting, and M Potthoff, Physica B 461, 23 (2015)
- [7] W Nolting, Fundamentals of Many Body Physics, Springer (2009)
- [8] W Nolting, Theoretical Physics, Vol 7, Springer (1997)
- [9] Y Zhang et al, Journal of Physical Chemistry 117, 13194 (2013)
- [10] W Nolting and M Matlak, phys stat sol (b) 123, 155 (1984)
- [11] W Nolting, U Dobil, and M Matlak, J Phys C18, 3687 (1985)
- [12] F Yonezawa and K Morigaki, Prog Theor Phys Suppl 53, 1 (1973)
- [13] R.J. Jellito, J Phys Chem Solids 30, 609 (1969)
- [14] L.M. Sanratskii and J Kubler, Europhysics Letters 23, 661 (1993)
- [15] V Nolting in Proceedings of SAIP2012, edited by J Janse van Rensburg 158 (2014)
- [16] A A Rudermann and C Kittel, Phys Rev 96, 99 (1954)
- [17] V Nolting and W Nolting, phys stat sol (b) 149, 313 (1988)
- [18] A L Kuzemsky, arXiv: 0408404v2 (2004)
- [19] M Klicpera, P Javorsky, and M Divis, J Phys Conf Series 592, 12014 (2014)

Effect of Annealing Temperature on Optical and Electrical Properties of Sol-Gel ZnO Thin Films

Trilok K. Pathak, H.C. Swart and R.E. Kroon

Department of Physics, UFS, Bloemfontein, South Africa

E-mail: KroonRE@ufs.ac.za (Kroon); tpathak01@gmail.com (Pathak)

Abstract. Zinc oxide (ZnO) is a multifunctional material having unique physical properties as well as chemical and photo-stability. In the present work, ZnO thin films were synthesized on indium tin oxide (ITO) coated glass substrates by the sol-gel process using spin coating. The precursor sol was prepared by mixing 2-methoxyethanol and zinc acetate dihydrate and using mono-ethanolamine as stabilizer. After annealing at temperatures of 350 °C, 450 °C or 550 °C, structural, optical and electrical studies were carried out. X-ray diffraction patterns showed the crystalline hexagonal wurtzite structure of the ZnO thin films, while the relative peak intensities showed the formation of a *c*-axis preferential orientation as the annealing temperature increased. Scanning electron microscopy results revealed that a wrinkle-like morphology obtained when annealing at 450 °C was transformed into a fine grain structure after annealing at 550 °C. Optical transmittance of the thin films was about 80% obtained in the range 400-800 nm measured using a UV-vis spectrophotometer. The optical bandgap varied from 3.26 eV to 3.28 eV as calculated using Tauc's plot method. The photoluminescence extended from the UV near band edge emission over the blue region and was influenced by the ITO substrate. The current-voltage characteristics of ZnO films show Ohmic behaviour and the resistivity decreased with increasing annealing temperature. These highly transparent and conducting ZnO thin films can be used in solar cells and optoelectronic devices.

1. Introduction

Zinc oxide (ZnO) is a wide direct bandgap semiconductor with an energy gap of 3.3 eV and a high free exciton binding energy of 60 meV at room temperature which has great applications in the information age [1,2]. Zinc is a cheap and abundant raw material, and ZnO thin films possess unique optical, electrical and semiconducting properties used extensively in applications such as transparent conducting contacts, solar cells, gas sensors, laser diodes, ultraviolet lasers and thin film transistors, etc. ZnO is also attractive for high frequency surface acoustic wave device applications [3]. Despite several approaches adopted for fabricating ZnO thin films, controlling the crystallinity as well as grain size and shape still needs to be further investigated. Therefore, it is essential to investigate optimum conditions for fabrication of highly oriented and transparent ZnO thin films.

ZnO thin films can be produced by different methods such as the sol-gel technique [4,5], chemical vapour deposition [6], pulsed laser ablation [7], spray pyrolysis [8], magnetron sputtering [9] and thermal evaporation [10]. The sol-gel technique has many advantages in preparing ZnO films, such as strong *c*-axis orientation, ease of compositional modifications, large films, simplicity of working principle, low cost, and low annealing temperature. The sol-gel method is therefore prevalent today and ideal for exploratory research. In this work we have used the sol-gel method to deposit ZnO thin films but, regardless of the deposition technique, the annealing effects still remain an open subject for

research. It is interesting to study how the physical properties change with annealing temperature. Bouhssira *et al.* [10] have studied the influence of annealing temperature on the properties of ZnO thin films deposited by thermal evaporation and inferred that the annealing of ZnO thin films allowed obtaining layers with optical transmittance close to 80%. Mosbah *et al.* [11] deposited ZnO thin films by RF sputtering and observed annealing effects on the structural and optical properties. In the present work we have deposited ZnO thin film by the sol-gel method on indium tin oxide (ITO) covered glass substrates. We have focused on the influence of the annealing temperature on the structural, morphological, optical and electrical properties of the ZnO thin films.

2. Experimental details

ZnO thin films were deposited on ITO coated Corning glass substrates by the sol-gel process. The sol was prepared by dissolving 2.195 g of zinc acetate dihydrate (99% purity) in 50 ml of 2-methoxyethanol (solvent) and mixed with mono-ethanolamine (stabilizer) in a 1:1 molar ratio. The solution was stirred using a magnetic stirrer at room temperature for 2 h and then at 60 °C for 1 h. This resulted in a clear solution which was found to be stable and transparent with no precipitate or turbidity after cooling to room temperature. The sol was aged for 72 h at room temperature in order to make it more viscous before using it for spin coating. The ITO covered glass substrates were degreased with acetone by ultrasonic agitation for 10 min and then washed several times by distilled water, and finally methanol. The sol was dropped onto the substrate which was then spun at 2500 rpm for 30 s. The coated substrate was dried at 230 °C for 10 min in air, and the coating process repeated 15 times to increase the thickness. The resulting material was divided into three pieces and annealed in air at a temperature of 350 °C, 450 °C or 550 °C for 1 h to complete the formation of the ZnO thin film. The flow chart of the entire process for synthesis of the ZnO films is schematically drawn in figure 1.

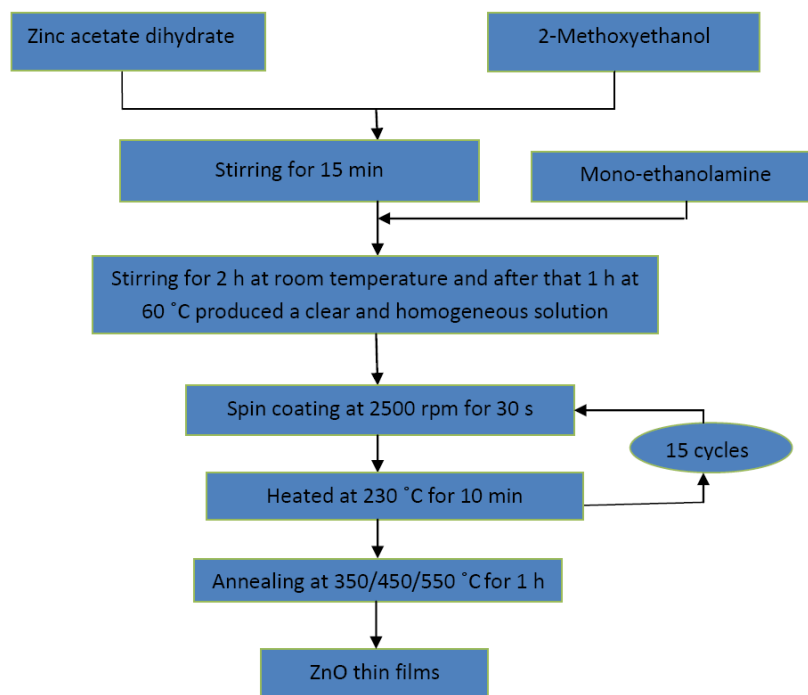


Figure 1. Flow chart for the preparation of ZnO thin films by spin-coating.

Structural, optical and electrical characterization of the ZnO thin films followed. X-ray diffraction (XRD) using a PANalytical X'pert Pro system was used to analyze the crystallographic structure and crystallite size of the films. Scanning electron microscopy (SEM) performed with a Zeiss EVO-40 instrument was used to assess the surface morphology, while a UV-vis spectrophotometer (Schimadzu-3600) was used to measure the transmittance of the samples. The bandgap was determined using Tauc's plot method. Photoluminescence (PL) data was recorded using a

spectrofluorophotometer (Shimadzu RF-5301 pc) and current-voltage (I-V) measurements were made using a Keithley 4200 Semiconductor Characterization System.

3. Results and discussion

3.1. X-ray diffraction analysis

The structure and crystalline quality of the deposited ZnO thin films on ITO coated glass substrates annealed at different temperatures of 350 °C, 450 °C or 550 °C were studied by XRD and the patterns are shown in figure 2(a). The (100), (101), (102) and (002) peaks of ZnO (JCPDS file No. 36-1451) are observed, in addition to several peaks corresponding to ITO occurring at 21.58°, 30.69°, 35.57° and 51.17° which are marked with an asterisk (*) in figure 2(a). The ZnO peaks result from interplanar spacings d_{hkl} given by [12]

$$\left(\frac{1}{d_{hkl}}\right)^2 = \frac{4}{3}\left(\frac{h^2 + k^2 + hk}{a^2}\right) + \frac{l^2}{c^2} \quad (1)$$

for the hexagonal wurtzite structure, where a and c represent the lattice parameters and hkl are the Miller indices. The (100) peak had maximum intensity relative to the (002) peak for the sample annealed at 350 °C, but showed a relative decrease as the annealing temperature was increased. The (002) peak was dominant for the ZnO thin film which was annealed at 550 °C, showing a preferential orientation and indicating that the c -axis of the crystallites is generally perpendicular to the surface of the film.

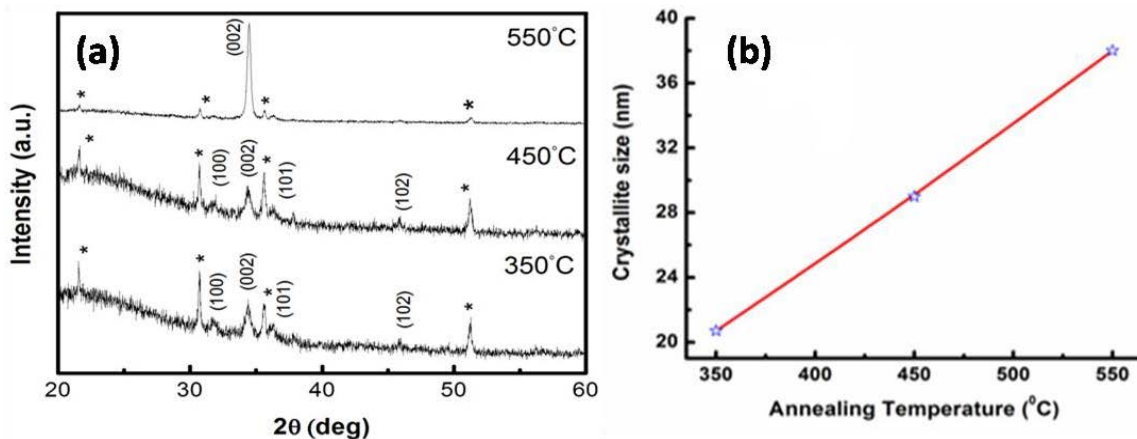


Figure 2. XRD patterns of ZnO thin films annealed at different temperatures. (b) Crystallite size as a function of annealing temperature.

The crystallite size was determined by Scherrer's equation [13]

$$D = \frac{K\lambda}{\beta \sin \theta} \quad (2)$$

where K is a constant taken to be 0.94, λ is the wavelength of X-rays used (0.154 nm for Cu $K\alpha$) and β is the full width at half maximum. The crystallite size was calculated using the (002) peaks which were dominant in all the samples, and it increased from 21 nm to 38 nm with increasing annealing temperature as shown in figure 2(b). A similar result was obtained by Rattana *et al.* [14] on NiO/ZnO heterojunction thin films prepared by the sol-gel method and the increase of the crystallite size with annealing temperature can be explained by the atoms have enough energy to diffuse. The direction perpendicular to the c -axis is the most favourable growth plane for the hexagonal ZnO structure because it has the lowest surface energy [15].

3.2. Surface morphology

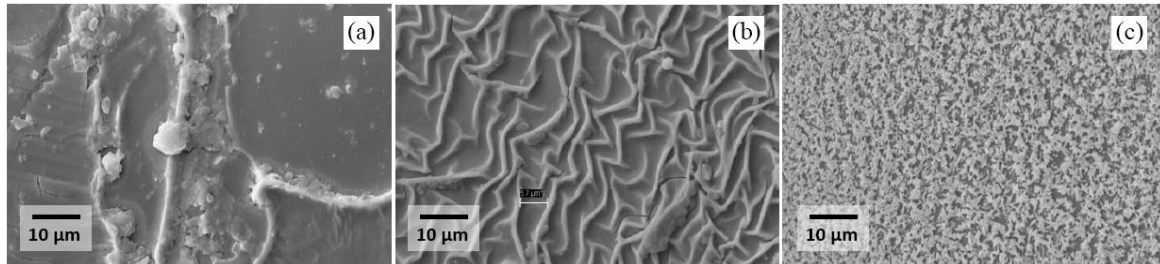


Figure 3. SEM images of the ZnO thin films annealed at (a) 350 °C, (b) 450 °C and (c) 550 °C.

The microstructure and surface morphology of the ZnO thin films were observed using SEM micrographs recorded using an electron accelerating voltage of 20 kV at an original magnification of 4000 times and are shown in figure 3. An irregular morphology is obtained when the annealing temperature is low (350 °C). The microstructure of the film annealed at 450 °C has a wrinkle-like morphology. In contrast, the higher annealing temperature of 550 °C results in a surface of fine grains which is similar to the morphology of Sn doped ZnO thin films observed by Zegadi *et al.* [16]. This is consistent with the improved XRD spectrum for ZnO, suggesting grain growth found for the sample annealed at this temperature.

3.3. Optical and photoluminescence studies

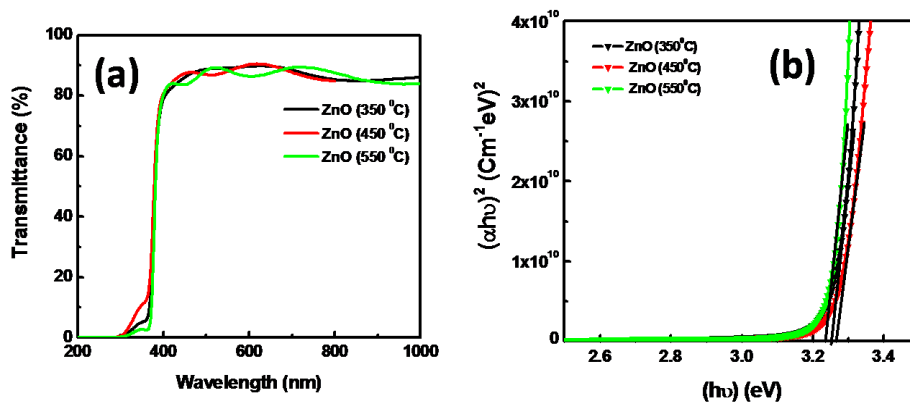


Figure 4. (a) Transmittance, and (b) Tauc's plot of annealed ZnO thin films.

The transmittance measurements were carried out in the range 200 nm - 1000 nm and are shown in figure 4(a). The maximum transmittance, greater than 80%, is observed over the whole visible range and it does not vary greatly with annealing temperature. The dramatic decrease in transmittance in the UV region below 400 nm is due to exciton-related band-to-band absorption of ZnO. The optical bandgap was calculated by considering that for a direct bandgap material the absorption coefficient α can be modelled by [17]

$$(\alpha h\nu)^2 = A(h\nu - E_g) \quad (3)$$

where A is a constant, E_g is the bandgap energy, h is Planck's constant and ν is the frequency of the incident radiation. Therefore the optical bandgap can be estimated by extrapolating the experimental data in a Tauc's plot, figure 4(b), to the horizontal axis. The bandgap has a maximum value 3.28 eV for the sample annealed at 450 °C and is slightly smaller for the sample annealed at 550 °C. This decrease in the bandgap is attributed to the reduction in oxygen vacancies in the thin films when annealed at the higher temperature. Chaabouni *et al.* [18] and Saleh *et al.* [19] found similar results in ZnO thin films deposited by sol-gel and RF sputtering methods respectively.

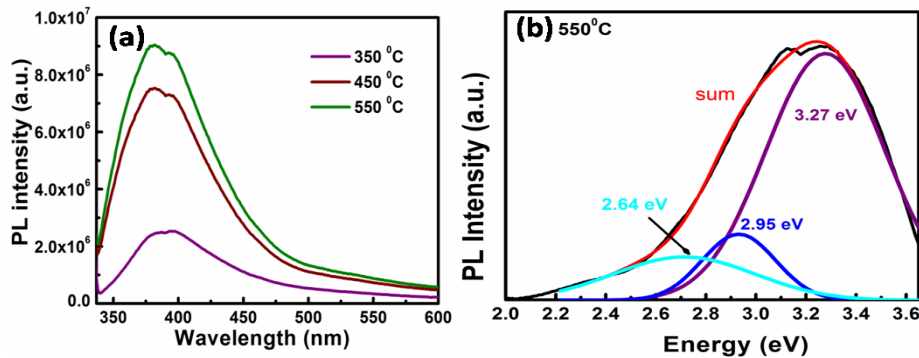


Figure 5. (a) PL spectra of ZnO thin films produced with different annealing temperatures. (b) Deconvolution of the PL emission for the sample annealed at 550 °C.

The PL spectra of the ZnO thin films annealed at different temperatures are shown in figure 5(a). The small cusp-like feature near 390 nm in all the spectra is due to the instrument. Although there is no significant change in the form of the emission, its intensity increased with annealing temperature. Generally the luminescence from ZnO consists of a narrow excitonic emission in the UV region and broad intrinsic defect emission in the visible region, but in this case it consists of a broad emission extending from the UV over to the blue region. In figure 5(b) the emission of the sample annealed at 550 °C is redrawn with a horizontal energy axis and fitted with three Gaussian peaks, namely a high energy peak in the UV region at 3.27 eV (~380 nm) attributed to near band edge emission, a violet peak at 2.95 eV (~420 nm) due to O dangling bonds, together with a weak blue emission at 2.64 eV (~470 eV) originating from Zn and O intrinsic defect emission. Teng *et al.* [20] reported that the near band edge emission of ZnO deposited on ITO by magnetron sputtering was broadened by an unusual (anomalous) component at 410 nm (similar to the violet peak reported here) and suggested this was as a result of O dangling bonds on the ITO surface layer or the interface between the ZnO and ITO. As the annealing temperature was increased, the crystallinity of the ZnO films improved which enhanced the PL intensity.

3.4. Electrical Characterization

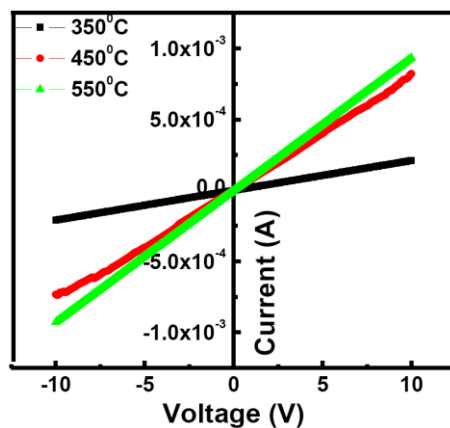


Figure 6. Electrical characterization of ZnO thin films produced at different annealing temperatures.

Few studies have been done of the electrical characterization of ZnO thin films with respect to annealing temperature. In the present work the electrical characteristics of sol-gel ZnO thin films on ITO coated glass substrates produced at different annealing temperatures were measured using a Keithley 4200 semiconductor characterization system. The effect of annealing temperature on the I-V results of the ZnO films is shown in figure 6. The I-V characteristics show good linear (Ohmic) behaviour. Aoun *et al.* [21] deposited ZnO thin films by spray pyrolysis for different substrate temperatures and reported a decrease in resistivity with increasing temperature. In the present work the ZnO thin film annealed at 550 °C showed minimum resistivity and a current of close to 1 mA is obtained for an applied 10 V potential difference, which is larger than for the thin films annealed at

350 °C and 450 °C. The decrease in electrical resistivity may be due to the improved crystallinity and increased crystallite size, as well as the possible reduction in defect concentrations, of the thin films with increased annealing temperature. From the XRD and SEM results it is evident that the films annealed at higher temperature have better crystallinity. As a result of the enhancement of both morphological and structural characteristics of ZnO films, the electrical properties are also improved. Therefore sol-gel ZnO thin films on ITO glass are suitable for optoelectronic devices and buffer layers in solar cells, but require proper annealing at moderate temperature.

4. Conclusion

ZnO thin films were deposited on ITO coated Corning glass substrates using the sol-gel technique and annealed at different temperatures between 350 °C and 550 °C. The films have the hexagonal wurtzite crystalline structure and the (002) diffraction peak was dominant in the ZnO film annealed at 550 °C, indicating preferential orientation of the hexagonal axis perpendicular to the substrate surface. The crystallite size increased from 21 nm to 38 nm with increasing annealing temperature. The transmittance of the films were above 80% in the visible region and the bandgap had a maximum value of 3.28 eV for the sample annealed at 450 °C, which decreased slightly when the maximum annealing temperature of 550 °C was used. The PL emission consisted of near band edge emission near 380 nm, violet emission near 420 nm associated with the ITO/ZnO surface/interface O dangling bonds and a weak blue defect emission at ~470 nm. The I-V characteristics of ZnO films show Ohmic behaviour and the resistivity decreases with increasing annealing temperature. These highly transparent ZnO thin films can be used as a window layer in solar cells and optoelectronic devices.

References

- [1] Janotti A and Van de Walle C G 2009 *Rep Prog. Phys.* **72** 126501
- [2] Ozgu I U, Alivov Ya I, Liu C, Take A, Reshchikov M A, Dogan S, Avrutin V, Cho S J and Morkoc H 2005 *J. Appl. Phys.* **98** 041301
- [3] Saleem M, Fang L, Wakeel A and Kong C Y 2012 *World J. Condens. Matt. Phys.* **2** 10
- [4] Pathak T K, Kumar V, Swart H C and Purohit L P 2016 *Physica B* **480** 31
- [5] Li Y, Xu L, Li X, Shen X and Wang A 2010 *Appl. Surf. Sci.* **256** 4543
- [6] Sen Chien F S, Wang C R, Chain Y L and Wu R J 2010 *Sensor Actuat. Phys. B* **144** 120
- [7] Zhu B L, Zhao X Z, Su F H and Wu X G 2010 *Vacuum* **84** 1280
- [8] Belkhalifa H, Ayed H, Hafdallah A, Aida M S and Ighil R T 2016 *Optik* **127** 2336
- [9] Pathak T K, Kumar R and Purohit L P 2015 *Int. J. ChemTech Res.* **7(2)** 987
- [10] Bouhssira N, Abed S, Tomasella E, Cellier J, Mosbah A, Aida M S and Jacquet M 2006 *Appl. Surf. Sci.* **252** 5594
- [11] Mosbah A, Moustaghfir A, Abed S, Bouhssira N, Aida M S, Tomasella E and Jacquet M 2005 *Surf. Coat. Technol.* **200** 293
- [12] Hasabeldaim E, Ntwaeaborwa O M, Kroon R E and Swart H C 2016 *J. Vacuum Sci. Technol. B* **34** 041221
- [13] Kroon R E 2013 *S. Afr. J. Sci.* **109(5/6)** Art. #a0019
- [14] Rattana T, Suwanboon S, Kedkaew C, Wanichchang K and Choeysuppakat A 2016 *Key Engin. Mater.* **675-676** 225
- [15] Ye J, Gu S, Zhu S, Chen T, Hu L, Qin F, Zhang R, Shi Y and Zheng Y 2002 *J. Cryst. Growth* **243** 151
- [16] Zegadi C, Abdelkebir K, Chaumont D, Adnane M and Hamzaoui S 2014 *Adv. Mater. Phys. Chem.* **4** 93
- [17] Caglar M, Ilcan S and Caglar Y 2009 *Thin Solid Films* **517(17)** 5023
- [18] Chaabouni F, Belgacem J B and Abaab M 2014 *Chin. J. Phys.* **52** 272
- [19] Saleh W R, Saeed N M, Twej W A and Alwan M 2012 *Adv. Mater. Phys. Chem.* **2** 11
- [20] Teng X, Fan H, Pan, Ye C and Li G 2007 *Mater. Lett.* **61** 201
- [21] Aoun Y, Benhaoua B, Benramache S and Gasmi B 2015 *Optik* **126(24)** 5407

Spectroscopic investigation of Tm^{3+} containing Lithium borate glasses

D.D. Ramteke and H. C. Swart*

Department of Physics, University of the Free State, P.O. Box 339, Bloemfontein 9300, South Africa

Email: SwartHC@ufs.ac.za, ddphyvnit@gmail.com

Abstract. In the present study we investigated the spectroscopic properties of Tm^{3+} containing lithium borate glasses as a function of Tm^{3+} concentration. The physical properties were analyzed by using the density and molar volume of the glasses. The Judd-Ofelt theory was used to analyze the experimental data. The main focus of the present study was to study the effect of ion concentration on the emission properties of the glasses. The emission intensity of the glasses increased with the addition of Tm^{3+} ions up to 0.5 mol% and decreased with a further addition due to concentration quenching.

1. Introduction

Ongoing progress in the optical technologies is totally dependent on the rare earth materials in which photons are manipulated by using the change in the host materials or change in the concentration of singly or multi-doped rare earth materials. Glasses are the excellent host for the rare earth ions and their applications play an important role in photonics, nuclear waste management, household and other technologies. Among all rare earth ions Thulium (Tm^{3+}) is the best active ion because of its broad emission range. This emission range cover the applications in telecommunication up to the laser technology. Emission from Tm^{3+} ions at 2 μm is useful in the area of light detection and ranging (LIDAR), remote sensing and in the medical field [1].

The broad emission around 1460 nm is useful for the development of an optical amplifier for applications in fiber-optic communication. By using the 1860 nm emission of Tm^{3+} it is possible to build a mid –infrared laser [2]. Glass hosts can be utilized to attain both these properties. Among the available potential hosts, the lithium borate glasses are very interesting due to their easy formability, wide range of composition and good rare earth solubility [3-5].

The present work was to understand in detail the spectroscopic behavior of Tm^{3+} ions in the lithium borate glasses. We prepared the 27.5 Li_2O : (72.5-X) B_2O_3 : X Tm_2O_3 glasses and analyzed their physical and spectroscopic properties. We also calculated the Judd-Ofelt (J-O) parameters by using the absorption data of the prepared glasses. J-O is a theory in physical chemistry describing the intensity of electron transitions within the 4f shell of rare earth ions in solids and solutions. By using the J-O parameters the estimated values of the radiative transition probabilities, radiative lifetimes of excited states and branching ratios are reported in the present study. Luminescence studies have been performed as a function of mol % of the Tm^{3+} ions.

2. Experimental

The 27.5 Li₂O: (72.5-X) B₂O₃: X Tm₂O₃ (Tm₂O₃ = 0, 0.25, 0.5, 0.75 and 1 mol%) glasses were prepared by the conventional melt quench technique. The appropriate quantity of high purity chemicals were weighed and mixed in an agate mortar by using acetone. The obtained mixture were transferred in an alumina crucible and melted in an electric furnace at 1273 K. To achieve the homogeneity of the melt, the melt was allowed to soak for 1 h with intermediate stirring. Samples of the desired shape were obtained by quenching the melt on the brass molds at room temperature. Samples were immediately transferred to an annealing furnace preheated at 573 K and collected the next day. The prepared sample were labeled as Tm0, Tm1, Tm2, Tm3 and Tm4 according to increasing doping concentration. The density of the samples were measured by the Archimedes principle using the METTLER TOLEDO weighing balance. A LAMBDA 950 Ultra violet/visible/near infra-red (UV/Vis/NIR) spectrophotometer (PerkinElmer) was used to measure the absorption spectra of the glasses. The excitation and emission spectra of the glasses along with the lifetimes were recorded by using an Edinburgh FLS980 system with a 450 W steady state Xe lamp as excitation source. The emission spectra were recorded by using a liquid nitrogen cooled Hamamastu R5509-72 near infrared photomultiplier tube (NIR-PMT) with the response time of 800 ps. The decay analysis were performed by 60 W pulsed microsecond Xe flash lamp and NIR-PMT.

3. Results and Discussion

Fig. 1 shows pictures of the glasses with different concentration of Tm₂O₃. The obtained glasses were colorless with a tint of yellow for the higher concentration Tm₂O₃ glasses and also have good transparency. The absorption spectra were normalized by using the thickness of the samples and concentration of the Tm³⁺ ions in the glass matrix and plotted as absorption cross section as shown in Fig. 2 for the 0.75 mol % Tm₂O₃ as representative. In these spectra five absorption bands centred at 464, 677, 782, 1208 and 1677 nm are assigned to the ³H₆→¹G₄, ³H₆→³F₂+³F₃, ³H₆→³H₄, ³H₆→³H₅ and ³H₆→³F₄ transitions of the Tm³⁺ ions [6]. The wavelength range of the observed transition, mean wavelength ($\bar{\lambda}$) and the integrated cross section ($\int \sigma(\lambda) d\lambda$) were determined and depicted in Table 1. These values were further used to calculate the Judd-Ofelt parameters for the prepared glasses.

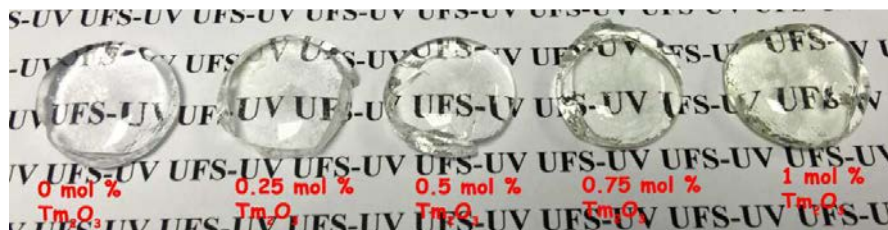


Figure 1. Glasses with different Tm₂O₃ content.

Table 1. Absorption parameters of 0.75 mol % Tm₂O₃ lithium borate glass.

Manifold	Range (nm)	$\bar{\lambda}$ nm	$\int \sigma(\lambda) d\lambda$ (cm ² nm)
¹ G ₄	438-491	464	7.25
³ F ₂ , ³ F ₃	618-726	677	20.14
³ H ₄	733-841	782	21.92
³ H ₅	103-1313	1207	39.04
³ F ₄	1512-1911	1676	82.26

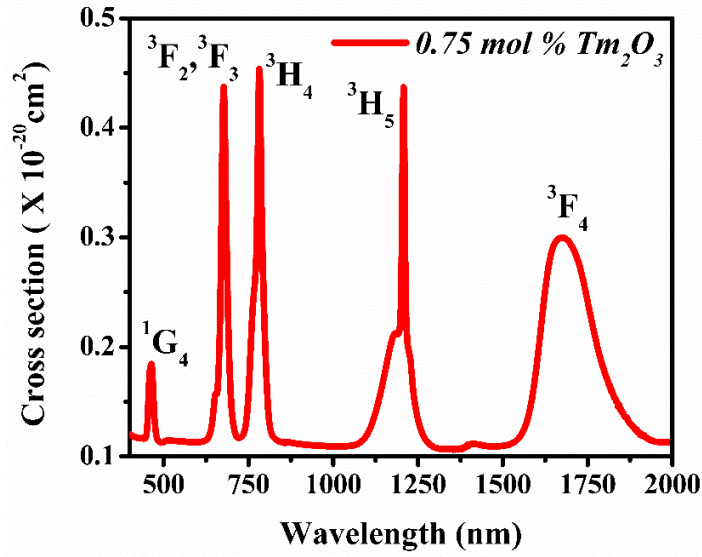


Figure 2. Absorption cross section spectra of 0.75 mol % Tm₂O₃ lithium borate glass.

Table 2. Variation of measured ($S_{measured}^{ED}$), calculated ($S_{calculated}^{ED}$) line strengths ($\times 10^{-20} \text{ cm}^2$) and J-O intensity parameters Ω_i .

Manifold	0.25 mol% Tm ₂ O ₃		0.5 mol% Tm ₂ O ₃		0.75 mol% Tm ₂ O ₃		1 mol% Tm ₂ O ₃	
	$S_{measured}^{ED}$	$S_{calculated}^{ED}$	$S_{measured}^{ED}$	$S_{calculated}^{ED}$	$S_{measured}^{ED}$	$S_{calculated}^{ED}$	$S_{measured}^{ED}$	$S_{calculated}^{ED}$
¹ G ₄	0.60	0.12	0.52	0.1	0.23	0.07	0.26	0.07
³ F ₂ , ³ F ₃	0.81	0.89	0.69	0.77	0.45	0.49	0.41	0.46
³ H ₄	0.76	0.78	0.66	0.69	0.42	0.44	0.41	0.43
³ H ₅	0.88	0.70	0.79	0.61	0.48	0.39	0.48	0.37
³ F ₄	1.29	1.36	1.07	1.13	0.73	0.76	0.71	0.74
$\Omega_2 \times 10^{-20}$	1.43		1.26		0.81		0.85	
$\Omega_4 \times 10^{-20}$	0.62		0.44		0.33		0.29	
$\Omega_6 \times 10^{-20}$	0.64		0.58		0.35		0.34	

By using the J-O theory [7,8] it's possible to calculate the manifold-to-manifold transition probabilities, radiative lifetimes and branching ratios of emission. The accuracy of the J-O parameter depend on accuracy of the absorption measurements. By using the values of integrated cross section, line strength of manifold to manifold electric dipole can be calculated by using the following equation:

$$S_{measured}^{ED} = \frac{3ch(2J'+1)}{8\lambda^2 e^2 \lambda} n \left(\frac{3}{n^2 + 1} \right)^2 \int \sigma(\lambda) d\lambda \quad (1)$$

where n is the refractive index and J' is the total angular momentum, and the other symbols have their usual meaning. By using the values of measured line strength J-O intensity parameters were obtained by solving

the equation for five observed transitions. J-O theory also provides the theoretical expression for line strength which is given by:

$$S_{calculated}^{ED} = \sum_{t=2,4,6} \Omega_t |f^n [SL] J \| U^t \| f^n [S'L'] J|^2 \quad (2)$$

where Ω_t are the Judd–Ofelt parameters, $\| U^t \|$ are the doubly reduced unit tensor operators, S is the spin operator and L is the angular momentum operator for L-S coupling scheme for ground state and first excited state [9]. The obtained values are provided in Table 2. The measured ($S_{measured}^{ED}$) and calculated ($S_{calculated}^{ED}$) line strengths have values relatively close to each other which justify the quality and accuracy of the fitting use in this study. The values or manifold 1G_4 has a very large difference between the calculated and experimental values. This difference may be due to the hypersensitivity of the 1G_4 transition. As the hypersensitive transition is strongly dependent on the host and surrounding and their predicted and experimental values may vary.

The variation of Ω_2 strongly depends on the variation in the covalent bonding. Change in covalency between the Tm^{3+} ions and ligands anions directly affects the values of Ω_2 as it reflects the asymmetry of constituent's ions around the Tm^{3+} ions. Ω_4 and Ω_6 values are the measure of rigidity of the structure in which the rare earth ions are situated [10]. The values of Ω_2 were found to decrease with an increase in the concentration of the Tm^{3+} ions, which confirms an increase in the ionic nature of the bonding in the glasses.

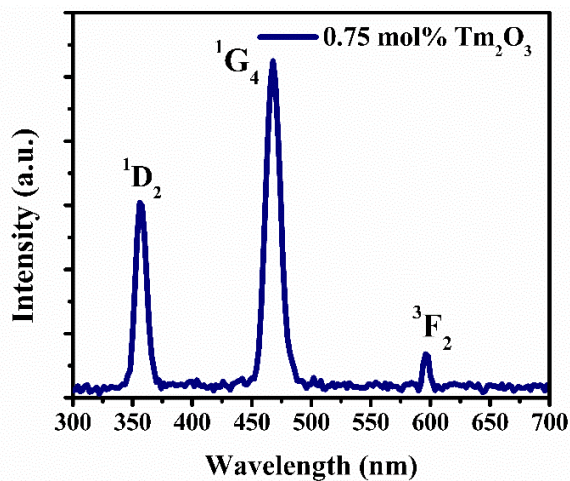


Figure 3 (a). Excitation Spectra of prepared 0.75 mol % Tm_2O_3 containing glass.

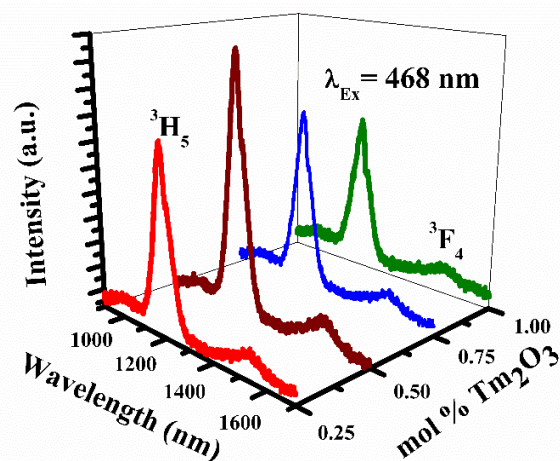


Figure 3 (b). Emission spectra of different mol % Tm_2O_3 glasses.

Fig. 3 (a) shows the excitation spectra of 0.75 mol % Tm_2O_3 containing glasses as representative at an emission wavelength of 1195 nm. The spectra show three excitation bands at 358, 468, and 596 nm from the ground state 3H_6 of the Tm^{3+} to various excited states. These bands are identified as 1D_2 , 1G_4 and 3F_2 after comparing with the literature [2]. Amongst all, the 1G_4 was the most prominent band and it was selected to study the emission properties of the Tm^{3+} ion containing glasses. Fig. 3 (b) shows the emission spectra of glasses for different mol % of Tm^{3+} ions. These spectra contain a prominent band at 1195 nm along with a broad hump at around 1544 nm. These emission bands correspond to the $^3H_4 \rightarrow ^3H_5$ and $^3H_4 \rightarrow ^3F_4$ transitions of the Tm^{3+} ions. Fig. 4 (a) gives the intensity variation of the $^3H_4 \rightarrow ^3H_5$ and $^3H_4 \rightarrow ^3F_4$ transitions as function of composition. It is observed that the emission intensity increased up to 0.5 mol % Tm_2O_3 and decreased with further addition of the Tm^{3+} ions. This effect was due to concentration quenching and came in to effect because of the increase number of Tm^{3+} ions in the glass matrix [11].

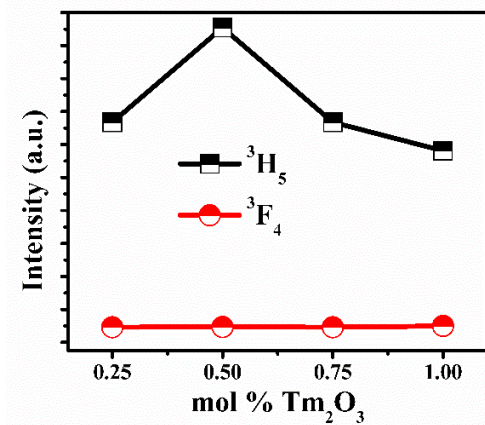


Figure 4 (a). Emission intensity variation with mol % Tm_2O_3 .

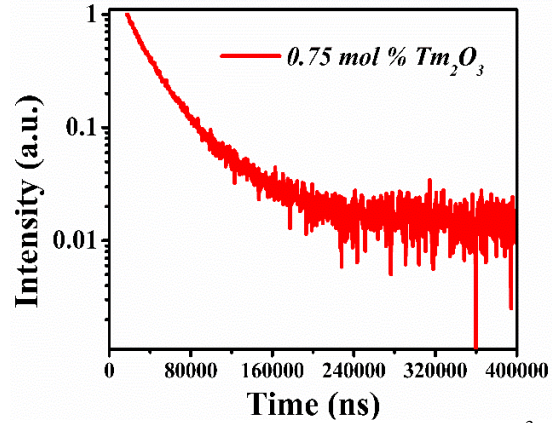


Figure 4 (b) Fluorescence decay profile of the 3H_5 state of the 0.75 mol % Tm^{3+} ion containing glass.

Table 3. Emission band positions (λ_p , nm), effective bandwidths ($\Delta\lambda_{eff}$, cm^{-1}), radiative transition probabilities (A , s^{-1}), peak stimulated emission cross-sections ($\sigma_p \times 10^{-22} cm^2$), branching ratios (β_R) and lifetime (τ_{exp} μs) of 3H_4 state of Tm_2O_3 containing glasses.

SN	Transitions	Parameter	Tm1	Tm 2	Tm 3	Tm 4
1	$^3H_4 \rightarrow ^3H_5$	λ_p	1195	1195	1195	1195
		$\Delta\lambda_{eff}$	193.48	209.48	191.34	204.25
		A	2.2	12.35	9.23	8.2
		σ_p	164	968	668	730
		β_R (exp)	0.49	0.55	0	0.48
		β_R (cal)	0.001	0.01	0.02	0.01
2	$^3H_4 \rightarrow ^3F_4$	λ_p	1544	1544	1544	1544
		$\Delta\lambda_{eff}$	274.73	257.24	242.31	239.14
		A	200	62.8	41	40.56
		σ_p	2943	6922	4915	6075
		β_R (exp)	0.51	0.45	0	0.52
		β_R (cal)	0.11	0.07	0.07	0.07
3	Lifetime (τ_{exp} μs)		53.88	38.61	29.13	22.18

By using the emission spectra of the prepared glasses the values of the branching ratio (β_R), stimulated emission cross-section (σ_p) and effective line width of the transition (λ_{eff}) were calculated by using the following relations [12, 13]:

$$\beta_R(\Psi J, \Psi' J') = \frac{A(\Psi J, \Psi' J')}{A_T(\Psi J)} \quad (3)$$

$$\sigma_p = \frac{\lambda_p^4 A}{8\pi c n^2 \Delta\lambda_{eff}} \quad (4)$$

where A is the transition probability of the upper excited state, A_T is the total transition probability, n is the refractive index, λ_p peak wavelength and λ_{eff} is the effective line width of the transition given by

$$\lambda_{eff} = \frac{1}{I_{max}} \int I(\lambda) d\lambda \quad (5)$$

I is the fluorescence intensity and I_{max} is the maximum intensity. The obtained values are presented in Table 3.

From the table it is clear that the emission cross section (σ_p) has the highest values for the 0.5 mol % Tm_2O_3 containing glasses. The $^3H_4 \rightarrow ^3F_4$ transition has the highest values of σ_p and branching ratio among the observed transitions. A big difference between the theoretical and experimental values was observed, the theoretical calculations, however, does not consider all the processes involved in the excitation and emission. These values are useful in justifying the application of these glasses for lasers. Thus the 0.5 mol % Tm^{3+} ions containing glasses are the best for laser application and telecommunication.

The decay curves of the 3H_4 transition were recorded at room temperature under 468 nm excitation by monitoring the emission at 1195 nm and are showed in Fig. 4(b) for different mol % of Tm_2O_3 . On analyzing these curves it was observed that they were non-exponential in nature after 0.5 mol % Tm^{3+} containing glasses. The measured lifetimes of the 3H_4 state are depicted in Table 3 for the different concentrations of the Tm^{3+} ions. It is clear that the decay times decreased with an increase in Tm^{3+} ion concentration, the shorting of the life time and deviation from the exponential behavior was mainly due to the concentration quenching in the life time of the 3H_4 state. It is therefore clear that there was an energy transfer amongst the Tm^{3+} ions at higher concentrations.

Conclusions

The structural and spectroscopic properties of lithium borate glasses with different concentration of Tm_2O_3 were successfully studied. J-O intensity parameter were calculated for all prepared compositions. Ω_2 intensity parameter decreased with Tm^{3+} ion concentration showing an increase in ionic bonding in the glasses. A decrease in Ω_4 and Ω_6 parameter showed that the rigidity of the glasses decreased with Tm^{3+} ion concentration. Emission spectra of the prepared glasses showed four prominent bands which belongs to the 3F_2 , 3H_4 , 3H_5 and 3F_4 transitions. The emission intensity of the glasses increased up to 0.5 mol % Tm_2O_3 and decreased with further addition.

Acknowledgements

This research is supported by the South African Research Chairs Initiative of the Department of Science and Technology and the National Research Foundation of South Africa (grant 84415). The financial support from the University of the Free State is also acknowledged. The Edinburgh Instruments FLS980 system used in this study was funded by the National Research Foundation of South Africa (Grant EQP14080486021).

References

- [1] Gebavi H, Milanese D, Liao G, Chen Q, Ferraris M, Ivanda M, and Taccheo S 2009 *J. Non-Cryst. Solids* **355(9)** 548.
- [2] Walsh M, Barnes N, Reichle D and Jiang S 2006 *J. Non-Cryst. Solids* **352** 5344
- [3] Ramteke D and Gedam S 2014 *J. Rare Earth* **32** 389.
- [4] Ramteke D, Annapurna K, Deshpande V and Gedam S 2014 *J. Rare Earth* **32 (12)** 1148.
- [5] Ramteke D, Swart H and Gedam S *Physica B* 2016 **438** 49
- [6] Carnall W, Fields P and Rajnak K 1968 *J. Chem. Phys.* **49 (10)** 4424.
- [7] Judd B 1962 *Phys. Rev.* **127**, 750. .
- [8] Ofelt G 1962 *J. Chem. Phys.* **37**, 511.
- [9] Walsh M, Barnes N and Bartolo B 1998 *J. Appl. Phys.* **83** 2772
- [10] Venkatramu V, Babu P, Jayasankar C, Troster T, Sievers W and Wortmann G 2007 *Opt. Mater* **29** 1429.
- [11] Ramteke D, Kumar V and Swart H 2016 *J. Non-Cryst Solids.* **438** 49.
- [12] Dousti M, Ghoshal S, Amjad R, Sahar M, Nawaz F and Arifin R 2013 *Opt. Commun.* **300** 204.
- [13] Seshadri M, Venkata Rao K, Rao J and Ratnakaram Y 2009 *J. Alloys Compd.* **476** 263.
- [14] Suhasini T, Suresh Kumar J, Sasikala T, Jang K, Lee H, Jayasimhadri M, Jeong J, Yi S and Moorthy L 2009 *Opt. Mater.* **31** 1167.

Characterization of the fine structures associated with E3 defect in GaAs by application of Laplace DLTS

Fatemeh Taghizadeh*, Kian Ostvar, Walter E. Meyer, F. Danie Auret

Department of physics, University of Pretoria, Private bag X20, Hatfield 0028, Pretoria

Email: u29255610@tuks.co.za

Abstract. High resolution Laplace deep level transient spectroscopy was used to study the fine structure associated with the radiation induced bi-stable E3 centre in epitaxially grown GaAs. The samples were prepared using n-type GaAs that was doped with silicon to doping densities of 10^{14} cm^{-3} and 10^{15} cm^{-3} , respectively. To introduce the defect, the samples were subjected to MeV electrons emanating from a ^{90}Sr source at room temperature to a total fluence of $2.3 \times 10^{15} \text{ cm}^{-2}$. Laplace DLTS measurements were carried out at 200 K. In addition to the two previously known states, a third stable state of the defect was also observed. It was also observed that at lower doping densities, the concentration of the third state is lower compared to the other two but increased as the doping density increased. From these observations, it was postulated that the existence of the third state could be the result of localized effects due to the close proximity of the E3 and a dopant atom.

1. Introduction

One of the most important contributions to the field of experimental semiconductor physics was the introduction of deep level transient spectroscopy (DLTS) by Lang in 1974 [1]. As a characterization technique, DLTS is capable of providing crucial information regarding the electrical behaviour of deep levels. However, even though the technique surpassed its predecessors in terms of sensitivity at the time of its conception, it still lacked the necessary resolution to reveal hidden fine structures associated with some of the observed deep levels and therefore further study of these structures was not possible at the time. It was only after the introduction of Laplace DLTS by L. Dobaczewski and A.R. Peaker [2], that it became possible to study defects with such level of detail. However, many of the previously identified defects in semiconductors are yet to undergo such studies.

Regardless of their origin, deep and shallow level defects are crucially influential on electrical and mechanical properties of semiconductors and more importantly, semiconductor based devices which can be considered one of the pillars of modern technology. Therefore, any and all efforts at improving current technology must include further and more detailed characterization of semiconductor defects, their effects, structure and their creation and annihilation dynamics. To accomplish this goal, several factors need to be considered. These factors include, but are not limited to, crystal growth methods, doping density, deep level introduction methods, defect annealing dynamics and environmental influences such as magnetic fields and temperature.

The aim of this study was to investigate one of the previously observed deep centers in epitaxially-grown thin film gallium arsenide. Gallium arsenide (GaAs) belongs to a group of semiconductors known as III-V compounds and is important due to its wide band gap, relatively high carrier mobility, etc. These attributes, many of which can be affected by the presence of defects and dopants, have made GaAs a very suitable candidate for application in development of high efficiency solar cells, electro optical devices, ultra-high frequency devices and lasers, just to name a few.

The defect in question for the present study is the E3 center, which is an intrinsic defect present in bulk-grown GaAs, while the E1 and E2 centers have been proposed to be two different charge states of an isolated As vacancy, V_{As} , the E3 was believed to resemble a close $V_{As}-As$ pair [3,4]. However, based on the recent results reported by Schultz [5], the identification of E3 as an arsenic As mono vacancy, agrees more closely with the experimental data.

One method of introducing intrinsic point defects in crystals is through irradiation by alpha and beta particles. For this study, the preferred method of introducing arsenic mono vacancies was to subject GaAs based Schottky diodes to beta radiation emanating from a ^{90}Sr source. The incident electrons which possess energies ranging from 0.1-1 MeV have enough kinetic energy to displace one single atom [3] and therefore the possibility of creating only the desired arsenic vacancy increases while the chance of introducing other more complex types of defects decreases.

2. Experimental procedure

Samples were prepared according to the following procedure: Small rectangular shaped pieces of n-type GaAs were cleaved off as substrates for our samples from various wafers with different doping densities. The pieces were then chemically cleaned and degreased by boiling in trichloroethylene for 3 minutes and then boiling in isopropanol for 3 minutes. Afterwards, the samples were rinsed using deionized water and then chemically etched by being dipped in a solution of $H_2O:H_2O_2:NH_4OH$ with 100:1:3 ratios for 30 seconds. After the etching process, the samples were rinsed in deionized water for the second time and then dipped in a 6 mol.dm^{-3} solution for 60 seconds and then rinsed in deionized water and blow dried by nitrogen gas.

After proper cleaning and etching, the substrates were placed in a resistive evaporation chamber in order to deposit a multi layered ohmic contact (Ni/Au-Ge/Ni) 50/1500/300 nm on one of the surfaces of each substrate. Afterwards, the freshly deposited ohmic contacts were annealed at $450^\circ C$ for 2 minutes in an Ar filled environment.

The substrates were then put through a second cleaning procedure in order to prepare them for Schottky contact deposition. The second cleaning procedure was carried out following the same instruction as for the first one, with only skipping the step involving the dip in a solution of $H_2O:H_2O_2:NH_4OH$. The substrates were then placed in the same deposition chamber and Au Schottky contacts were deposited on to the other surface of the substrate through a metal contact mask.

After the samples were prepared, $I-V$ and $C-V$ measurements were carried out for each sample to obtain information regarding the newly deposited metal contacts. The information thus obtained includes: leakage current, ideality factor and free carrier density which made up the first set of experimental data for this study. The samples were then individually subjected to electron irradiation with each sample being irradiated for a specific duration. After the irradiation, once again $I-V$ and $C-V$ measurements were carried out and the results were compared against the first set of data.

The third part of the experiment, intended to confirm the existence of the defect of interest (E3) in each sample, was performed using conventional DLTS. After the confirmation step, E3 was characterized in each sample and in depth using Laplace DLTS. The goal was to observe the finer structure of E3 and characterize its formation and behaviour in each sample. The obtained results were then compared against each other in an attempt to determine the influence of duration of radiation as well as initial carrier density of each sample on the E3 center.

3. Results and discussion

Figure 1(a) shows the results of I - V measurements for n-GaAs based devices before and after irradiation. Under forward bias, the linearity of the log- I - V plot for unirradiated samples points to the high quality of these devices with an ideality factor of $n = 1.03$. However, after irradiation, the region of the plot between 0 to 0.2 V included a bump which perturbs the linearity of the plot and therefore the ideality factor was reduced to $n = 1.13$. The creation of the bump in the plot is associated with generation-recombination dynamics that take place during the measurement due to irradiation induced defects. By comparing the reverse current, I_R , the irradiated reverse current is higher than the unirradiated current.

Figure 1(b) includes C - V plots for the samples and aims to demonstrate the change in free carrier density as a result of electron irradiation. It can be seen that the slope of the line representing samples after the irradiation process is steeper which suggests a decrease in free carrier density, $N_D = 7.4 \times 10^{14} \text{ cm}^{-3}$ compared to $N_D = 9.7 \times 10^{14} \text{ cm}^{-3}$ for unirradiated samples.

Figure (2) shows both the conventional DLTS and Laplace DLTS spectra. The conventional DLTS spectrum shows three prominent peaks: E1, E2 and E3, which are spaced far from each other in terms of energy levels. These peaks are respectively observable at temperatures close to 30 K, 70 K and 200 K at a rate window of 80 per second. While E3 is identified as a single peak in the conventional DLTS spectrum, once characterization was carried out isothermally and by use of high resolution Laplace DLTS, which revealed that E3 was not a single peak but a combination of three individual peaks (E3a, E3b and E3c).

Figure 3 (a) shows the Arrhenius plots for 3 samples with different carrier density namely 9×10^{14} , 1.9×10^{15} and $9.5 \times 10^{15} \text{ cm}^{-3}$ for E3a, E3b and E3c, respectively. The Arrhenius plot shows three distinct levels. We obtained Arrhenius plots with a high degree of linearity. Activation energy increased with increasing free carrier density for E3a ($E_{0.38}$, $E_{0.37}$ and $E_{0.36}$).

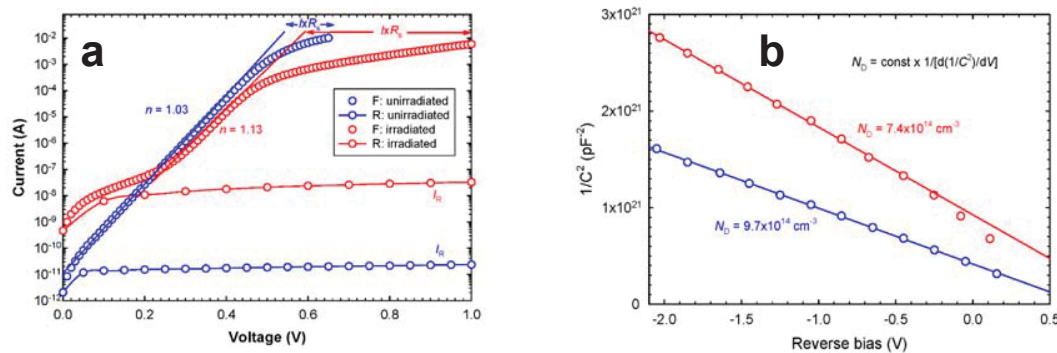


Figure 1. Demonstrates the change in (a) I - V and (b) C - V plots as a result of electron irradiation.

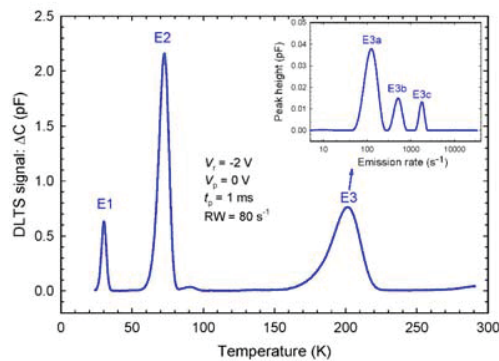


Figure 2. Conventional and Laplace DLTS spectra for E3 peak

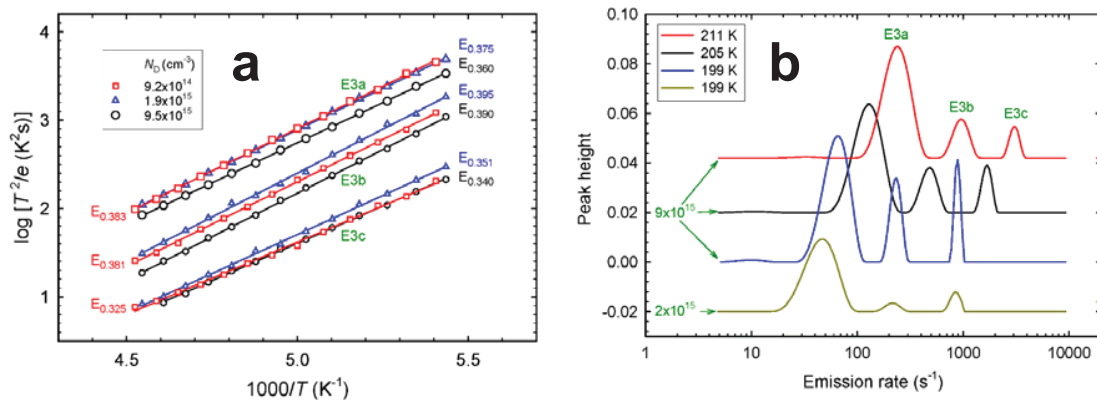


Figure 3. (a) Arrhenius plots associated with constituent peaks of the E3 and (b) the shift in the activation energy of all three constituent peaks as a result of changes in temperature.

Figure 3 (b) demonstrates the change in Laplace DLTS spectra as a result of change in temperature for 2 samples with different carrier densities ($9 \times 10^{15} \text{ cm}^{-3}$ and $2 \times 10^{15} \text{ cm}^{-3}$) at 211, 205 and 199 K. In both samples, all three peaks shifted together to the right in an orderly manner when temperature was raised. This is an indication that the splitting of the defect into three components is reliable.

4. Conclusion

We have shown that irradiating GaAs Schottky diodes, resulted in a higher leakage current and smaller free carrier density. Laplace DLTS demonstrated that the E3 peak has three components, E3a, E3b and E3c, with closely spaced energy levels. All E3 components shifted together when changing the temperature. Arrhenius plots confirmed the three distinct levels of E3 defect and for the main peak (E3a), that the activation energy increased with decreasing free carrier density.

References

- [1] D. V. Lang 1974 Deep-level transient spectroscopy: A new method to characterize traps in semiconductors *J. Appl. Phys.* 45 3023
- [2] L. Dobaczewski, A.R. Peaker, K. Bonde Nielsen 2004 Laplace-transform deep-level spectroscopy: The technique and its applications to the study of point defects in semiconductors *J. Appl. Phys.* 96 4689–4728
- [3] D. Pons, J. C. Bourgoin, A.G. W, A.G. W, A.G.W. and G.G. W, A.L.W. and G.R. D, et al. 1985 Irradiation-induced defects in GaAs *J. Phys. C Solid State Phys.* 18 3839–3871
- [4] F. D. Auret, S.A. Goodman, W.E. Meyer, R.M. Erasmus, G. Myburg 1994 Electronic Properties of Defects Introduced during Electron and Alpha Irradiation of GaAs *Mater. Sci. Forum* 1559–1564.
- [5] P. A. Schultz, P. P, B.H.J. and S.D. Bourgoin J C, P.D. and B.J. C, D.J. and S. M, C.D.J. and C.K. J, et al. 2015 The E 1– E 2 center in gallium arsenide is the divacancy *J. Phys. Condens. Matter.* 27 075801.

Effects of different Ga doping concentration on structural and optical properties of Ga-doped ZnO nanoparticles by precipitation reflux method

J Ungula*¹, F B Dejene¹ and H C Swart²

¹Department of Physics, University of the Free State (QwaQwa Campus), Private Bag X13, Phuthaditjhaba, 9866, South Africa

²Department of Physics, University of the Free State, P.O Box 339, Bloemfontein 9300,

* Corresponding author E-mail: ungulaj@ufs.ac.za

Abstract. Ga-doped ZnO nanoparticles (GZO NPs) were synthesized by the precipitation reflux method. The effects of different Ga doping on the structural, morphological, luminescence and optical properties of GZO NPs were investigated for application as transparent conducting oxides. Structural crystallization was shown to improve with an increase in doping concentration up to 2 mol % as identified by X-ray diffraction. The scanning electron microscopy images showed that the grain sizes increased when increasing the Ga concentration up to 2 mol. % then reduced in size at higher doping concentrations (3-5 mol. %). Photoluminescence results revealed changes in emission peaks of GZO NPs with variation in levels of doping with the highest intensity of the excitonic peak at 2 mol. %. Reflectance of GZO NPs in the UV region was observed to increase up to 2 mol % doping and then reduced at higher doping as determined using an UV-Visible spectrometer. Likewise, an increase in optical band gap from 3.13 to 3.3 eV was observed as the doping concentration increased from 0 to 2 mol. %.

1. Introduction

Ga-doped ZnO (GZO) is an example of ZnO based transparent conducting oxides (TCO) being pursued in the recent time for use as photo anodes in dye-sensitized solar cells (DSSCs), due to its low resistivity, high transmittance, non-toxicity and resource availability [1]. Besides, research has shown that GZO has electrical and optical properties comparable to those of widely employed Indium Tin Oxide TCO and the performance of GZO TCO based DSSCs was found to be superior to fluorine-doped tin oxide based DSSCs under the same growing condition [2].

Doping into the ZnO lattice by replacing Zn^{2+} ions with higher valent ions such as Ga^{3+} , Al^{3+} and In^{3+} is one way to induce dramatic changes in the electrical and optical properties and to obtain thermally stable conductivity in ZnO for solar cells applications. Ga has a similar ionic radius and covalent radius (0.062 and 0.126 nm), as compared to those of Zn (0.074 and 0.134 nm), respectively [3, 4]. Thus, Ga^{3+} can be substituted for Zn^{2+} over a larger doping range compared to other metal dopants in its group, without any lattice distortion.

Many studies on GZO nanostructures have been reported, with many choosing 4 mol % GZO targets, and some others choosing 2, 3, or 5 mol % GZO to obtain thin films and other nanostructures,

which have excellent material properties [5–7]. Gomez and Olvera et al [8] reported a minimum electrical resistivity value of the order of $7.4 \times 10^{-3} \Omega\text{cm}$ and optical transparency of the order of 80 % at 2 mol. % targets. In spite of these reports, it still remains a challenge to achieve high quality of crystalline particles with excellent physical and chemical properties of GZO NPs.

A number of methods for the synthesis of GZO nanopowders have been investigated [9-11]. But unlike some which use complex processes to obtain the samples or demand very high power synthesis conditions in temperature or pressure that makes sizing up of the product a daunting challenge, the precipitation method offers several advantages, which include cost effectiveness, high purity, homogeneity and small crystalline size of its product [12].

In this work, we focus on the optimization of the Ga doping levels in GZO NPs in order to improve the structural, optical and luminescence properties as well as to ensure a large scope of transparency not only in the visible region but also in the near UV region using the precipitation reflux method. To the best of our knowledge, there are only handful of reports in the literature on the synthesis of GZO NPs using this method.

2. Experimental procedure

GZO NPs were synthesized with different Ga^{3+} concentrations. The chemical reagents sodium hydroxide (NaOH), zinc nitrate ($\text{Zn}(\text{NO}_3)_2$) and gallium nitrate hexahydrate ($\text{Ga}(\text{NO}_3)_3 \cdot 6\text{H}_2\text{O}$) were of analytical grade and were used without further purification. In order to dope Ga in ZNPs, five different mol. % doping concentrations (0, 1, 2, 4 and 5) were selected. $\text{Zn}(\text{NO}_3)_2$ was mixed with ($\text{Ga}(\text{NO}_3)_3 \cdot 6\text{H}_2\text{O}$), dissolved in ethanol solvent to make a 0.5 M solution and put in a three-neck glass flask. The solution in the flask was heated under continuous stirring to 70 °C. 10 mg of Polyvinylpyrrolidone was added as a surfactant to reduce agglomeration of nanoparticles during the growth while 2 ml acetic acid was added to ensure both total dissolution of zinc nitrate and to adjust precursor solution to pH of 5.8. A solution of 1 M NaOH was added slowly (dropped for 60 minutes) into the three-neck glass flask containing zinc nitrate-gallium nitrate solution and refluxed under continuous stirring. The suspension formed with the dropping of NaOH was kept stirred for two hours at the same growth temperature and allowed to stand overnight. The material was then filtered and washed several times with deionized water with a pH of 7.5. The washed sample was dried at 60 °C in an oven for one hour and packaged into sample containers.

The characterization of the samples was done by means of a scanning electron microscopy (SEM), energy dispersive X-ray spectroscopy (EDS), X-ray diffraction (XRD), UV-vis spectroscopy and Photoluminescence spectroscopy (PL).

3. Results and Discussion

3.1. XRD analysis

Figure 1(a) shows the XRD diffraction patterns of GZO NPs prepared with different mol. % of Ga^{3+} ions. The patterns consist of broad peaks, which match the common ZnO hexagonal wurtzite structure and are in agreement with the reported values (JCPDS card, No. 79-0205). The XRD results show only diffraction peaks of ZnO without any trace of other diffraction peaks such as $\text{Zn}_{1-x}\text{Ga}_x\text{O}_4$ and Ga_2O_3 . The absence of impurity phases proved that all the gallium ions successfully substituted for the Zn sites in the ZnO lattice when doping ZnO with gallium in this study. This also reveals that it is plausible for the Ga^{3+} to reside on zinc sites in the hexagonal lattice [13]. The average dimensions of crystallite size ‘D’ were estimated from the values of 2θ and β of the XRD peaks using Scherrer’s formula [14].

$$D = \frac{K\lambda}{\beta \cos \theta} \quad (1)$$

where, K is the shape factor, ($K = 0.94$), D is the crystallite size, β is the Full Width at Half Maximum, λ is the wavelength of X-rays used (1.5405 \AA), and θ is the Bragg’s diffraction angle.

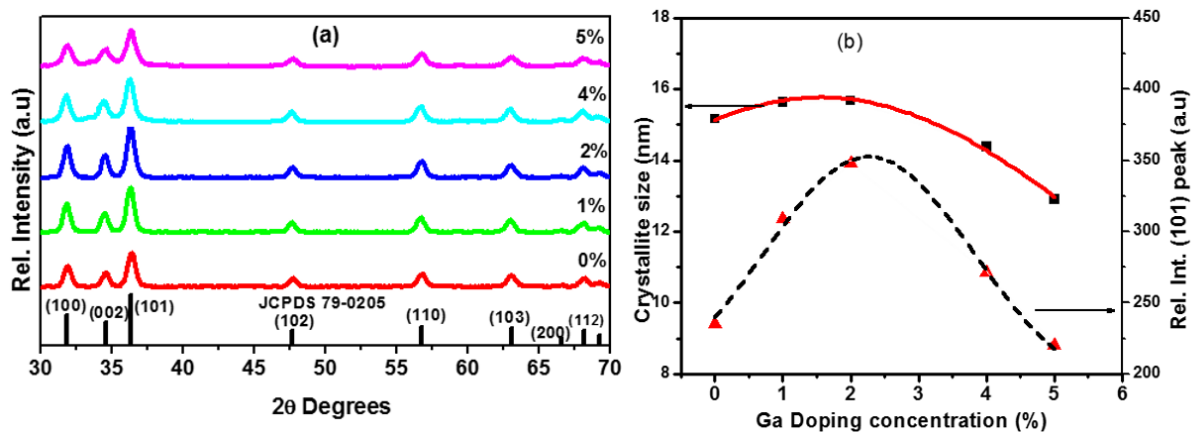


Figure 1: (a) X-ray powder diffraction patterns for GZO NPs prepared at different doping concentrations (b) Crystallite sizes and relative intensity of peak (101) as a function of Ga doping concentrations.

The crystallite sizes D and the relative intensity of peak (101) of the GZO NPs prepared at different concentration of the Ga dopant are plotted in figure 1(b). The D values are 15, 16, 16, 14 and 13 nm for 0, 1, 2, 4 and 5 mol. % doping, respectively. It was observed that a small amount of Ga atoms leads to the improvement in the crystalline quality and increase in crystallite size of the GZO NPs; as indicated by the highest value of D and peak intensity at the 2 mol % Ga doping concentration, but further increase in the Ga atoms results to a decrease in the intensity of the peaks and crystallite sizes. This may be due to the fact that up to 2 mol. % doping, Ga^{3+} ions replace the Zn^{2+} ions in the ZnO lattice but subsequent increase in doping levels may cause Ga^{3+} ions to occupy the interstitial positions in the ZnO lattice. Possibly, higher Ga doping levels could also weaken the crystallinity of GZO NPs due to the formation of stress by the smaller radius of Ga^{3+} ions (0.062 nm) compared with Zn^{2+} ions (0.074 nm).

3.2. SEM analysis

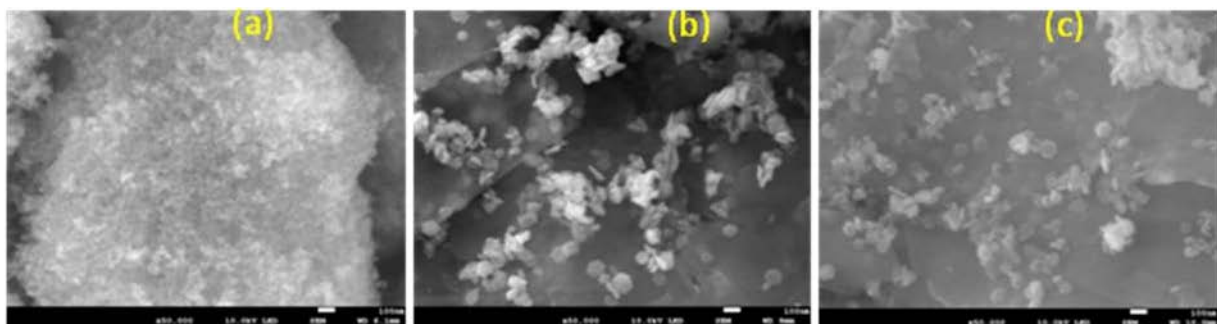


Figure 2: SEM micrographs of GZO NPs synthesized at (a) 0% (b) 2% and (c) 5% doping concentrations.

Figures 2(a-c) show the surface morphology images of the GZO NPs prepared at the different Ga doping concentrations (0, 2 and 5 mol. %). Agglomerated tiny spherical particles were formed at 0 mol. % doping which changed to less dense and dispersed larger hexagonal shaped NPs at 2 % doping. We attribute the reduced density to the formation of large grains as a result of coalescence of the particles with the increase in doping concentration. In the case of doping at 5 mol. % the grain size obtained decreased, which could be due to increasing number of nucleation sites, leading to the

formation of small grains during incorporation of the dopant into the host material [15]. The EDS images of the samples indicated that the collected powder was composed of zinc, oxygen and Ga and the synthesis route produced pure ZnO phases. This high purity of the GZO NPs was further confirmed by the XRD analysis.

3.3. Photoluminescence Analysis

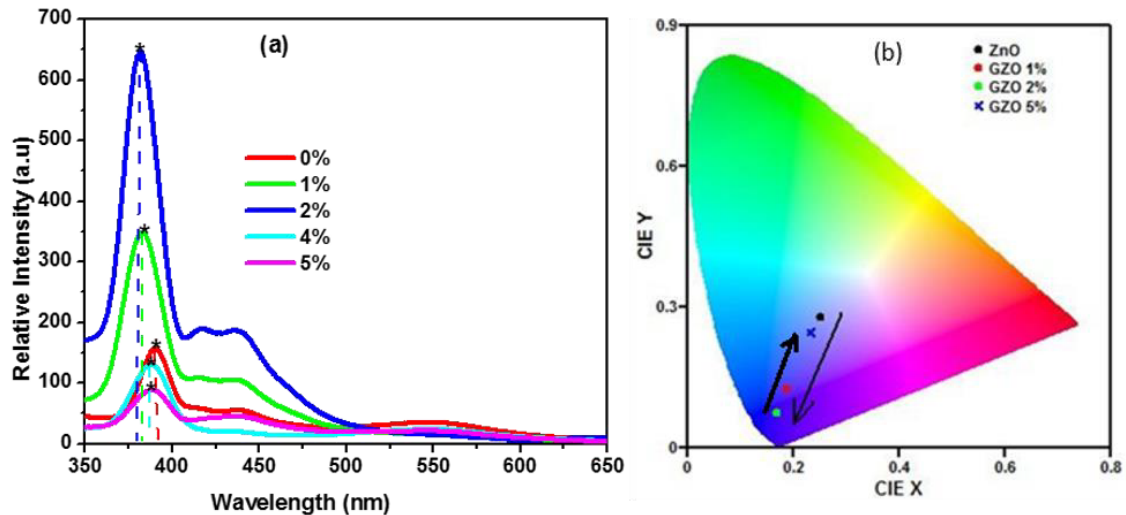


Figure 3: (a) PL emission spectra and (b) Chromaticity diagram depicting the CIE colour co-ordinates for GZO NPs for the different doping concentrations.

The PL spectra of GZO NPs for different Ga doping concentrations are shown in figure 3(a), illustrating the common UV-visible emission due to near band emission (NBE) and deep level defects (DLE) along with blue emission bands around 435 nm and violet peak centred at 415–420 nm. The sharp and strong UV NBE that formed between 380 and 390 nm originated from the free exciton recombination of GZO NPs, while the DLE emissions are associated with oxygen defects [16]. It is also seen, from figure 3(a), that the intensity of the NBE emission increased as the doping concentration increased from 0 to 2 % but reduced with further addition of the Ga dopant. The stronger NBE emission peak intensity in the PL indicates good optical properties of the ZnO NPs, which may be attributed to the reduced concentration of defects and improved crystallinity, in agreement with the XRD results and also as shown by the reduction of the DLE peak emission with an increase in doping concentration to 2 mol%. The quenching of the excitonic peak emission of the GZO NPs after 2 mol% Ga doping concentration was probably due to an enhanced bulk diffusion process, defect generation and migration as a result of the increase in amount of Ga in the ZnO lattice. The violet peak observed in most samples were slightly shifted to larger wavelengths and increased in intensity with the increase in doping concentration to 2 mol%. The source of this violet luminescence at 419 nm (2.96 eV) is probably due to radiative defects related to the interface traps existing at the grain boundaries and emitted from the radiative transition between this level and the valence band [17]. Jeong et al [18] also observed that the violet peak centred at 415–420 nm can be attributed to the Zn vacancies.

The Commission International de l'Éclairage (CIE) chromaticity diagram of the GZO NPs is shown in figure 3(b). The CIE (x, y) colour co-ordinates for 0, 1, 2, 4 and 5 % Ga doping concentrations are (0.25, 0.28), (0.19, 0.13), (0.17, 0.08), (0.28, 0.36) and (0.23, 0.25), respectively. The co-ordinates shift toward the shorter wavelength with the increase in mol % doping concentration but change to longer wavelengths for a further doping increase after 2 mol %. The blue shift of the co-

ordinates with an increase in amount of dopant in the sample is also supported by the PL spectra wavelength shifts.

3.4. Optical properties

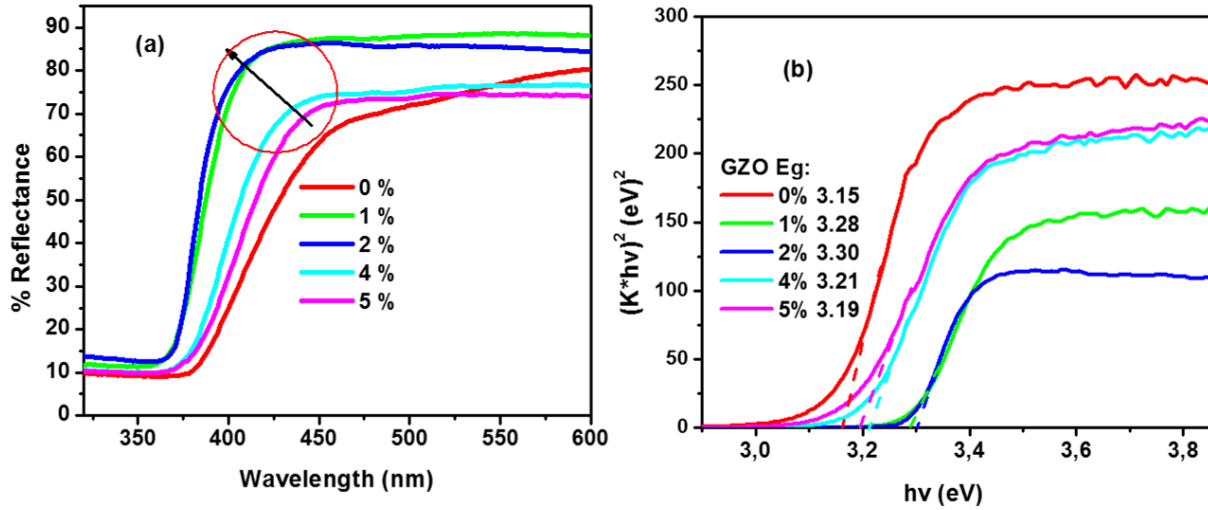


Figure 4: (a) The reflectance spectra and (b) Plot to determine the band gap energy of GZO nanoparticles prepared at various doping concentrations of Ga.

The reflectance spectra of the GZO NPs in the wavelength range of 300–600 nm are shown in figure 4(a). It can be observed that the onset of the band edge absorptions for the samples has blue shifted with the increase in doping concentration from 0 to 2 %, and red shifted with a further increase in the doping concentration confirming the size dependent absorption properties of the GZO NPs. Similarly, the % reflectance in the UV region has increased as the doping levels increased to 2 mol. %, but dropped as the concentrations increased to 5 mol %. Figure 4(b) shows the plot to determine the optical band gap of the ZnO NPs by extrapolating the linear region of the graph of the $(K*hv)^2$ versus hv graph near the onset of the absorption edge to the energy axis. The plots were obtained using the following equation [19].

$$(K*hv)^2 = A(hv - E_g)^2 \quad (2)$$

Where K is reflectance transformed according to the Kubelka-Munk remission function [20],

$$K = \frac{(1-R)^2}{2R} \quad (3)$$

hv is the photon energy, E_g is the optical band-gap energy between the valence band and the conduction band at $n = 2$ for direct transitions and A is a constant, depending on the electron-hole mobility and R is reflectance (%). The optical band gap was found to be 3.15, 3.28, 3.30, 3.21 and 3.19 eV corresponding to the Ga doping ratios of 0, 1, 2, 4, and 5 % respectively as shown in figure 4(b). The band gap values increased slightly with increasing Ga doping concentration to 2 mol %, and then decreased at higher doping. The highest optical band gap, 3.30 eV, was achieved in the GZO NPs doped with 2 mol % Ga due to the increase in carrier concentration, at this moderately doped level, caused by the contribution of Ga^{3+} ions at substitutional sites of Zn^{2+} ions and the higher energy-gap that resulted from the Ga interstitial atoms. The extrapolated absorption onset is slightly blue shifted on increasing the Ga doping concentration. This absorption edge which shifts towards higher energy is associated with an increase of the carrier concentration blocking the lowest states in the conduction band as explained by Burstein-Moss effect [21, 22].

4. Conclusions

The work in this investigation demonstrates that GZO NPs of high quality can be formed at a relatively low temperature (75 °C) by precipitation reflux method by varying the Ga/Zn ratios. It was found that the crystallinity, surface morphology and optical properties of the GZO NPs depend strongly on the Ga doping levels. The XRD results established the synthesis process efficiency, showing only the hexagonal phase pattern and the nanometric behaviour of the crystallites formed. This result shows that GZO NPs prepared at 2 % Ga doping concentration exhibit the best crystal quality. Agglomerated tiny spherical particles were formed at 0 % doping which changed to less dense larger hexagonal shaped NPs at 2 % doping. It was seen that the intensity of the NBE emission increased as the doping concentration increased from 0 to 2 % but reduced with further doping indicative of the superior optical properties at 2 mol. % doping. The highest optical band gap, 3.30 eV, was also achieved in the GZO NPs doped with 2 mol % Ga due to the increase in carrier concentration, at this moderately doped level. The results of this work shows that a 2 mol % Ga-doped ZnO target is most suitable to obtain thin films with fairly good material properties for the use as a photo anode in DSSCs.

Acknowledgement

The financial support from the South African Research Chair Initiative (SARChI) bursary and University of the Free State is highly recognised.

References

- [1] Netrvalova M, Novotny I, Prusakova L, Tvarozek V and Sutta P 2012 *Vacuum* **86** 707–710
- [2] Liu H, Avrutin V, Izyumskaya N, Özgür Ü and Morkoç H 2010 *Superlattices and Microstructures* **48**(5) 458-484.
- [3] Nayak P K, Yang J, Kim J, Chung S, Jeong J, Lee C and Hong Y 2009 *J Phys D: Appl Phys* **42** 035102.
- [4] Yoshino K, Hata T, Kakeno T, Komaki H, Yoneta M, Akaki Y, Ikari T 2003 *Phys Stat Sol (c)* **0** 626.
- [5] Jung K, Choi W K, Yoon S J, Kim H J and Choi J W 2010 *Applied Surface Science* **256** 6219.
- [6] Miyake A, Yamada T, Makino H, Yamamoto N and Yamamoto T 2008 *Thin Solid Films* **517** 1037-1041.
- [7] Nagarani S and Sanjeeviraja C 2011 *American Institute of Physics Conference Proceeding* **1349** 589-590.
- [8] Gomez H and Olvera M de la L 2006 *Mater Sci Eng B* **134** 20–6.
- [9] Du S, Tian Y, Liu H, Liu J, and Chen Y 2006 *Journal of the American Ceramic Society* **89**(8) 2440-2443.
- [10] Chen K J, Fang T H, Hung F Y, Ji L W, Chang S J, Young S J and Hsiao Y J 2008 *Applied surface science* **254**(18) 5791-5795
- [11] Guo J, Zheng J, Song X and Sun K 2013 *Materials Letters* **97** 34-36.
- [12] Chongsri K and Pecharapa W 2015 *Integrated Ferroelectrics* **165**(1) 159-166
- [13] Zhang D H, Yang T L, Ma J, Wang Q P, Gao R W and Ma H L 2015 *Materials Research Express* **2** 9.
- [14] Wagner R S and Doherty C 1996 *J Electroceram Soc* **113** 1300 3 4596.
- [15] Hu J and Gordon RG 1992 *J Appl Phys* **72** 5381.
- [16] Lin B and Fu Z 2001 *Appl Phys Lett* **79** 943.
- [17] Jin B J, Im S and Lee S Y 2000 *Thin Solid Films* **366** 107-110.
- [18] Jeong S H, Kim B S and Lee B T 2003 *Appl Phys Lett* **82** 2625.
- [19] Tauc J, Grigorovichi R and Vancu A 1966 *Phys Status Solidi* **15** 627.
- [20] Duran P, Capel F, Tartaj J and Moure C 2002 *Adv Mater* **14** 137.
- [21] Burstein E 1954 *Physical Review* **93** 632-633.
- [22] Moss T S 1954 *Proceedings of the Physical Society Section B* **67** 775.

*Division B – Nuclear, Particle
and Radiation Physics*

NLO Rutherford Scattering and Energy Loss in a QGP

Abdullah Khalil and W. A. Horowitz

Department of Physics, University of Cape Town, Private Bag X3, Rondebosch 7701, South Africa

E-mail: abdullah@aims.ac.za and wa.horowitz@uct.ac.za

Abstract.

We calculate to next-to-leading order the cross section of a massless electron scattered off of a static point charge in the $\overline{\text{MS}}$ renormalization scheme. Since we use the $\overline{\text{MS}}$ renormalization scheme, our result is valid up to arbitrary large momentum transfers between the source and the scattered electron. We then investigate the importance of the BN vs. KLN theorems in various theories as we work towards computing the NLO corrections to the energy loss of a QCD particle propagating in a quark-gluon plasma.

1. Introduction

The Quark Gluon Plasma (QGP) is believed to be the state of matter in the first few microseconds after the Big Bang [1, 2]. The QGP has been predicted to exist by the Quantum Chromodynamics (QCD) at a very high energy density and very high temperature (~ 180 MeV). The temperature dependence of the energy density in QCD is one of the results of the lattice QCD [3, 4]. Which shows a rapid change of the energy density at the critical temperature (T_c). This rapid change has been interpreted as the change of degrees of freedom in the system. Well below T_c , there are three hadronic degrees of freedom due to the three lightest hadrons: π^+ , π^- and π^0 . Well above T_c , there are $2(N_c^2 - 1) + 2 \times 2 \times N_c \times N_f$ degrees of freedom from the fundamental gluons and quarks of the theory.

Studying the high p_\perp interactions at RHIC and LHC shows that the jet quenching is due to the final state energy loss. The leading-order pQCD calculations give a good estimate for the energy loss [5, 6]. The question now is, what do we expect to find if we include the next-to-leading (NLO) contributions? We wish to check the self-consistency of these pQCD results and to make the pQCD calculation more quantitative. As a first step towards the NLO pQCD calculations, we calculate in this paper the NLO corrections to the elastic scattering of a massless electron scattered off of a static source.

2. The leading term of the scattering cross section

We consider the Lagrangian describing an electron scattered off of a classical source $J^\mu(x) = V^\mu \delta^{(4)}(\vec{x} - \vec{V}x^0)$, where V^μ is the unit time-like velocity vector

$$\mathcal{L} = -\frac{1}{4}F^{\mu\nu}F_{\mu\nu} + \bar{\psi}(i\not{\partial} - m)\psi - e\bar{\psi}\gamma^\mu\psi A_\mu + eJ_\mu A^\mu, \quad (1)$$

The Feynman rules for this Lagrangian will be exactly the same as in the normal QED Lagrangian [7] in addition to that for each external source we write $-ieV^\mu$. Let p and p' to be the momenta of the incoming and the outgoing electrons respectively. The delta function from the source $J^\mu(x)$ ensures the conservation of energy $E_{p'} = E_p = E$ and that the momentum transfer to be $q = p' - p$. Now we write down the amplitude of the leading term using the Feynman rules

$$i\mathcal{M}_0 = \begin{array}{c} p \quad p' \\ \diagdown \quad \diagup \\ \bullet \\ \diagup \quad \diagdown \\ q = p' - p \end{array} = \frac{ie^2}{q^2} \bar{u}^{s'}(p') \gamma^0 u^s(p). \quad (2)$$

We recall the identity $\sum_s u^s(p) \bar{u}^s(p) = \not{p} + m$, the trace technology and the properties of the γ -matrices. The leading term of the differential cross section will be

$$\left(\frac{d\sigma}{d\Omega}\right)_0 = \frac{2\alpha^2}{q^4} (2E^2 - p \cdot p'), \quad (3)$$

where we set the mass of the electron to be zero.

3. Renormalization of the Lagrangian

The NLO diagrams usually contain either fermion or photon loops. These loops require integrations over the loop momentum which usually diverge in 4-dimensions. In order to remove the divergences from our calculations, we first define the divergent parts by using the dimensional regularization to regularize the UV divergences and the mass regularization for the IR divergences. Then we renormalize the Lagrangian using the systematic way of renormalization [7], then we apply the renormalization scheme to get rid of the UV divergences. In this paper, we use $\overline{\text{MS}}$ renormalization scheme to tame the UV divergences as we are dealing with a massless theory [8]. We will follow the calculations of the differential cross section with massive electron while using $\overline{\text{MS}}$ allows us to set $m_e = 0$ safely.

The Dimensional regularization requires replacing the 4-momentum integral by an integral over the momentum in d -dimensions. Which also requires rescaling the electron charge e by the factor $\mu^{\frac{4-d}{2}}$, where μ is any mass scale to ensure that e remains dimensionless [9]. At the end of the calculations, the physics should not depend on this scale.

3.1. Vacuum Polarization

The amplitude for the vacuum polarization is given by

$$i\mathcal{M}_p = \begin{array}{c} p \quad p' \\ \diagdown \quad \diagup \\ \bullet \\ \diagup \quad \diagdown \\ q \quad k \quad k+q \\ \text{loop} \\ q \end{array} = i\mathcal{M}_0 \frac{\alpha}{\pi} \left(\frac{1}{3} \log\left(\frac{-q^2}{\mu^2}\right) - \frac{5}{9} + \mathcal{O}(m^2) \right). \quad (4)$$

The differential cross section due to the interference between the leading and the vacuum polarization amplitudes, neglecting the terms that are in $\mathcal{O}(m^2)$, will be

$$\left(\frac{d\sigma}{d\Omega}\right)_{PL} \approx \left(\frac{d\sigma}{d\Omega}\right)_0 \frac{\alpha}{\pi} \left[\frac{2}{3} \log\left(\frac{-q^2}{\mu^2}\right) - \frac{10}{9} \right]. \quad (5)$$

3.2. Electron Self Energy

The amplitude of the electron-self energy in $\overline{\text{MS}}$ renormalization scheme is given by

$$\Sigma_2(\not{p}) = \frac{\alpha}{4\pi} \left[(\not{p} - 2m) + \int_0^1 dx (4m - 2x\not{p}) \log \left(\frac{\mu^2}{(1-x)m^2 - x(1-x)p^2 + xm_\gamma^2} \right) \right], \quad (6)$$

where m_γ is the mass of the photon to regularize the expected IR divergences from the electron self-energy. The Fourier transform of the two point correlation function of the electron self-energy is given by [7]

$$\int d^4x \langle \Omega | T(\psi(x)\bar{\psi}(0)) | \Omega \rangle e^{ip \cdot x} = \frac{i}{\not{p} - m - \Sigma(\not{p})}. \quad (7)$$

This means that the pole is shifted by $\Sigma(\not{p})$, so the renormalized mass is not the physical mass and the residue of this pole is no longer one [8]. Thus our goal now is to find the correction to the residue and the relation between the renormalized mass m and the physical mass m_e . The physical mass can be given by the position of the pole where we have

$$m_e = m \left[1 + \frac{\alpha}{4\pi} \left(4 + 3 \log \left(\frac{\mu^2}{m^2} \right) \right) + \mathcal{O}(\alpha^2) \right], \quad (8)$$

while the correction of the residue can be given by the derivative of the electron self-energy amplitude at the physical mass. The residue of the pole will be

$$R = 1 + \frac{\alpha}{4\pi} \left[2 \log \left(\frac{m^2}{m_\gamma^2} \right) - \log \left(\frac{\mu^2}{m^2} \right) - 4 \right] + \mathcal{O}(\alpha^2). \quad (9)$$

In contrast to the On-shell renormalization scheme, the value of the residue of the pole is no longer one, where the correction to the residue is in $\mathcal{O}(\alpha)$. Which means we have to multiply the amplitude by the value of $R^{1/2}$ for each external leg, which means that we multiply the differential cross section by R^2 [8]. We note that all the corrections will be in higher orders of α except the leading term. So the only affected term by this correction is the leading term, which becomes

$$\left(\frac{d\sigma}{d\Omega} \right)_L = R^2 \left(\frac{d\sigma}{d\Omega} \right)_0 = \left(\frac{d\sigma}{d\Omega} \right)_0 \left[1 + \frac{\alpha}{\pi} \left(\log \left(\frac{m^2}{m_\gamma^2} \right) - \frac{1}{2} \log \left(\frac{\mu^2}{m^2} \right) - 2 \right) \right] + \mathcal{O}(\alpha^4). \quad (10)$$

The contribution of the self-energy diagram at one loop is zero since the contribution of the diagram due to the self-energy of the incoming electron is exactly the same as the contribution due to the self-energy of the outgoing electron with a relative sign difference.

3.3. Vertex Correction

The amplitude of the vertex correction is given by

$$i\mathcal{M}_V = \begin{array}{c} \text{Diagram: A vertex correction diagram showing an incoming electron with momentum } p \text{ and an outgoing electron with momentum } p'. \text{ A photon with momentum } q \text{ is exchanged between the electron lines. The photon line is wavy and has a cross at its end. The electron lines are solid with arrows. The vertex is a black dot. The photon line is labeled } q \text{ and the electron lines are labeled } p \text{ and } p'. \end{array} = \frac{4i\pi\alpha}{q^2} \bar{u}^{s'}(p') \left(\gamma^0 \cdot F_1(q^2) + \frac{i\sigma^{0\nu}q_\nu}{2m} F_2(q^2) \right) u^s(p), \quad (11)$$

where $F_1(q^2)$ and $F_2(q^2)$ are the form factors, which in the limit $-q^2 \gg m^2$ will be

$$F_1(q^2) \approx \frac{\alpha}{2\pi} \left[-\log \left(\frac{-q^2}{m^2} \right) \log \left(\frac{-q^2}{m_\gamma^2} \right) + \frac{1}{2} \log^2 \left(\frac{-q^2}{m^2} \right) + 2 \log \left(\frac{-q^2}{m^2} \right) - \frac{1}{2} \log \left(\frac{-q^2}{\mu^2} \right) + \frac{\pi^2}{6} \right]. \quad (12)$$

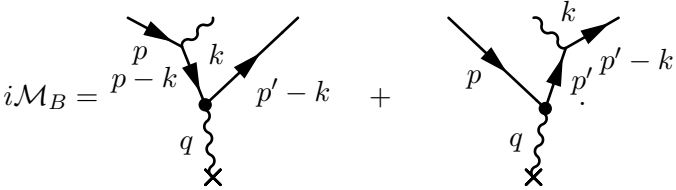
We see that $F_2(q^2)$ is negligible in the limit $m \rightarrow 0$. The differential cross section due to the interference between the vertex and the leading amplitudes will be

$$\begin{aligned} \left(\frac{d\sigma}{d\Omega}\right)_{VL} \approx \left(\frac{d\sigma}{d\Omega}\right)_0 \frac{\alpha}{\pi} \left[-\log\left(\frac{-q^2}{m^2}\right) \log\left(\frac{-q^2}{m_\gamma^2}\right) + \frac{1}{2} \log^2\left(\frac{-q^2}{m^2}\right) \right. \\ \left. + 2 \log\left(\frac{-q^2}{m^2}\right) - \frac{1}{2} \log\left(\frac{-q^2}{\mu^2}\right) + \frac{\pi^2}{6} \right]. \end{aligned} \quad (13)$$

We note that equation (13) contains IR divergences which appear as a single pole when we send m_γ to be zero in addition to the double pole when we set both m_e and m_γ to be zero.

3.4. Bremsstrahlung Correction

The detectors usually can not differentiate between the photon emitted from the vertex and the bremsstrahlung radiation, which require adding the following correction



$$i\mathcal{M}_B = \text{diagram 1} + \text{diagram 2} \quad (14)$$

Equation (14) represents the diagrams describing the bremsstrahlung correction. According to the Bloch-Nordsieck (BN) theorem, one should sum over all emitted soft photons with energy less than the experimental energy resolution (Δ) to get rid of the IR divergences due to the zero mass of the photon [10]. We consider first the final state soft bremsstrahlung diagrams (i.e an emission of a soft photon either from the incoming and/or the outgoing electrons). In this case, we will be able to use the eikonal approximation which allows us to ignore the linear terms in k from the numerator of the amplitude as $|k| \ll |p' - p|$. The amplitude of the final state soft bremsstrahlung will be

$$i\mathcal{M}_B^{f,S} = ie \mathcal{M}_0 \left(\frac{p' \cdot \varepsilon^{r*}}{p' \cdot k} - \frac{p \cdot \varepsilon^{r*}}{p \cdot k} \right). \quad (15)$$

The contribution of the final state soft bremsstrahlung to the differential cross section neglecting the terms that are in $\mathcal{O}(m^2, m_\gamma^2)$ will be

$$\begin{aligned} \left(\frac{d\sigma}{d\Omega}\right)_B^{f,S} \approx \left(\frac{d\sigma}{d\Omega}\right)_0 \frac{\alpha}{\pi} \left[\log\left(\frac{-q^2}{m^2}\right) \log\left(\frac{\Delta^2}{m_\gamma^2}\right) - \log\left(\frac{-q^2}{m^2}\right) \log\left(\frac{E^2}{m^2}\right) + \frac{1}{2} \log^2\left(\frac{-q^2}{m^2}\right) \right. \\ \left. + \log\left(\frac{E^2}{m^2}\right) - \log\left(\frac{\Delta^2}{m_\gamma^2}\right) - \frac{\pi^2}{6} \right]. \end{aligned} \quad (16)$$

The addition of equations (10), (13) and (16) is free of the IR divergences, but we still have another kind of divergences as we send m to be zero which is called the collinear divergence. Where the detector can not differentiate between an electron and an electron associated with a photon emitted or absorbed collinearly with the incoming or the outgoing electrons. Here we have to use the more general theorem made by Kinoshita, Lee and Nauenberg which is known as the KLN theorem stating that one should sum over both emitted and absorbed hard photons within a cone of an angle less than the experimental angular resolution (δ) [11,12]. The contribution of both initial and final state hard bremsstrahlung will be

$$\left(\frac{d\sigma}{d\Omega}\right)_B^H \approx \left(\frac{d\sigma}{d\Omega}\right)_0 \frac{\alpha}{\pi} \left[\log\left(\frac{\delta^2 E^2}{m^2}\right) \left(\log\left(\frac{E^2}{\Delta^2}\right) - \frac{\Delta^2}{2E^2} + \frac{2\Delta}{E} - \frac{3}{2} \right) + \log\left(\frac{\Delta^2}{E^2}\right) - \frac{\pi^2}{3} + \frac{13}{4} \right]. \quad (17)$$

We see that the linear and quadratic terms in Δ can not be ignored as in [12], since it is multiplied by a divergent part producing either a finite piece or divergent piece depending on how small the Δ is. Regarding asking this kind of question we look at similar terms to cancel these suspicious terms. The only way to get similar terms with a relative sign is discussed in [13] by checking the sub-leading collinear divergences from the soft bremsstrahlung which appears beyond the eikonal approximation. Such a calculation requires further work where it should be done carefully as we are interested in the remaining finite pieces from each calculation unlike in [12, 13].

It is obvious that the KLN theorem is the more general form of the BN theorem, but we see that only including the final state soft bremsstrahlung will remove the IR divergences and including both initial and final states hard bremsstrahlung will remove the collinear divergences. Such a treatment with both theorems independently is inconsistent. So we have to include the initial state soft bremsstrahlung which will add more IR divergences that we must take care of. This problem has not been mentioned in [12], while it is been first introduced by [14–16], a more recent discussion can be found in [13]. Where the authors suggest to include the disconnected diagrams to fix the problem. We usually do not add the disconnected diagrams where they describe a non-scattering process. However, the interference between the disconnected diagram with the emission and absorption process produces a fully connected cut diagram. The contribution from adding these diagrams plays an important role in IR cancellation from the initial state as it is shown in [13–16].

Further work needs to be done by including the disconnected diagrams very carefully to get rid of the extra IR divergences from the initial state soft bremsstrahlung and to obtain the remaining finite pieces for the differential cross section.

3.5. Box Correction

The amplitude of the box diagram is given by

$$i\mathcal{M}_{BO} = \begin{array}{c} \begin{array}{ccc} \text{---} & \text{---} & \text{---} \\ & \nearrow & \searrow \\ & \bullet & \bullet \\ & \nwarrow & \nearrow \\ \text{---} & \text{---} & \text{---} \\ \times & & \times \end{array} \\ \begin{array}{c} p \\ k-p \\ k \\ p' \\ p'-k \end{array} \end{array} \quad (18)$$

It is obvious that the box diagram does not contain any ultraviolet divergences, so we do not need to perform the dimensional regularization. We use the trick made by R. Dalitz [17] to simplify the integrals in this diagram. The differential cross section due to the interference between the leading and the box amplitudes will be

$$\left(\frac{d\sigma}{d\Omega}\right)_{BOL} = \frac{\pi\alpha^3 E}{p Q q^2} (p - Q) + O(\alpha^4), \quad Q = |q|. \quad (19)$$

3.6. NLO correction to the differential cross section in Rutherford Scattering

Now we include the NLO contributions mentioned above to the differential cross section without including the initial state soft bremsstrahlung and the sub-leading terms from the soft bremsstrahlung beyond the eikonal approximation (as discussed above, they require more careful work). Since μ is arbitrary, We choose it to be $-q^2$, then we find

$$\begin{aligned} \frac{d\sigma}{d\Omega} = \left(\frac{d\sigma}{d\Omega}\right)_0 & \left[1 + \frac{\alpha}{\pi} \left(\log\left(\frac{\Delta^2}{E^2}\right) \left(1 + \log\left(\frac{-q^2}{E^2\delta^2}\right) \right) + \frac{3}{2} \log\left(\frac{-q^2}{E^2\delta^2}\right) - \frac{\pi^2}{3} + \frac{5}{36} \right. \right. \\ & \left. \left. + \log\left(\frac{\delta^2 E^2}{m^2}\right) \left(\frac{2\Delta}{E} - \frac{\Delta^2}{2E^2} \right) \right] + \frac{\pi\alpha^3 E}{p Q q^2} (p - Q) + O(\alpha^4). \end{aligned} \quad (20)$$

4. Conclusion

In this paper, we calculated the elastic scattering differential cross section, including the next-to-leading order corrections of a massless electron scattered by a classical static point charge. These corrections come from the photon self-energy, vertex, bremsstrahlung and the box diagrams. We found that all UV divergences are absorbed by the counter terms in the $\overline{\text{MS}}$ renormalization scheme. We also saw that unlike most of the renormalization schemes, using $\overline{\text{MS}}$ shows that the contribution from the vacuum polarization correction remains finite in the zero mass limit.

Applying the BN theorem provides the usual cancellation of the IR divergences from the vertex with the one from the final state soft bremsstrahlung. We also note that applying the KLN theorem removes all the collinear divergences by including both initial and final state hard bremsstrahlung. But we still need to add the initial state soft bremsstrahlung correction to stay in the spirit of the more general KLN theorem.

More work to be done by checking the calculations of the soft bremsstrahlung beyond the eikonal approximation as well as including the disconnected diagrams that contribute with the same order of α to get a finite form of the differential cross section; equivalently, we expect a result that is valid up to arbitrary large momentum exchange. Our result also satisfies the Callan-Symanzik equation [18], where it is straightforward to check that the differential cross section at NLO is independent on the mass scale μ .

Acknowledgments

We would like to thank SA-CERN and the South African National Research Foundation (NRF). AK would also like to thank the University of Cape Town (UCT) and the African Institute for Mathematical Sciences (AIMS) for their financial support.

References

- [1] John C Collins and Malcolm J Perry. Superdense matter: neutrons or asymptotically free quarks? *Physical Review Letters*, 34(21):1353, 1975.
- [2] G Baym and SA Chin. Can a neutron star be a giant MIT bag? *Physics Letters B*, 62(2):241–244, 1976.
- [3] Frithjof Karsch, Edwin Laermann, and A Peikert. The pressure in 2, 2+ 1 and 3 flavour QCD. *Physics Letters B*, 478(4):447–455, 2000.
- [4] F Karsch. Lect. notes phys. 583, 209 (2002). *arXiv preprint hep-lat/0106019*, 2002.
- [5] Magdalena Djordjevic and Miklos Gyulassy. Heavy quark radiative energy loss in qcd matter. *Nuclear Physics A*, 733(3):265–298, 2004.
- [6] M Gyulassy, Peter Lévai, and I Vitev. Reaction operator approach to non-abelian energy loss. *Nuclear Physics B*, 594(1):371–419, 2001.
- [7] Michael E Peskin and Daniel V Schroeder. *An introduction to Quantum Field Theory*. Westview, 1995.
- [8] Mark Srednicki. *Quantum Field Theory*. Cambridge University Press, 2007.
- [9] Claude Itzykson and Jean-Bernard Zuber. *Quantum field theory*. Courier Corporation, 2006.
- [10] Felix Bloch and Arnold Nordsieck. Note on the radiation field of the electron. *Physical Review*, 52(2):54, 1937.
- [11] Toichiro Kinoshita. Mass singularities of feynman amplitudes. *Journal of Mathematical Physics*, 3(4):650–677, 1962.
- [12] Tsung-Dao Lee and Michael Nauenberg. Degenerate systems and mass singularities. *Physical Review*, 133(6B):B1549, 1964.
- [13] Martin Lavelle and David McMullan. Initial states: Ir and collinear divergences. *arXiv preprint hep-ph/0607262*, 2006.
- [14] C De Calan and G Valent. Infra-red divergence and incident photons. *Nuclear Physics B*, 42:268–280, 1972.
- [15] Ikuo Ito. Cancellation of infrared divergence and initial degenerate state in qcd. *Progress of Theoretical Physics*, 65(4):1466–1469, 1981.
- [16] T Muta and Charles A Nelson. Role of quark-gluon degenerate states in perturbative quantum chromodynamics. *Physical Review D*, 25(8):2222, 1982.
- [17] RH Dalitz. On higher born approximations in potential scattering. *Proceedings of the Royal Society of London. Series A. Mathematical and Physical Sciences*, 206(1087):509–520, 1951.
- [18] George Sterman. *An introduction to quantum field theory*. Cambridge University Press, 1993.

Implementation of the preamplifier response function for the iThemba LABS segmented clover detector

T. D. Bucher^{1,2}, E. A. Lawrie¹, O. Shirinda^{1,2}, T.S. Dinoko¹, J. L. Easton^{1,3}, N. Erasmus^{1,3}, S. H. Mthembu^{1,4}, W. X. Mtshali^{1,4}, S. P. Noncolela^{1,3}

¹ iThemba LABS, National Research Foundation, P O Box 722, Somerset West 7129, South Africa

² Stellenbosch University, Department of Physics, P/B X1, Matieland 7602, South Africa

³ University of Western Cape, Department of Physics, P/B X17, Bellville 7535, South Africa

⁴ University of Zululand, Department of Physics, P/B X1001, KwaDlangezwa, 3886, South Africa.

E-mail: daphney@tlabs.ac.za

Abstract. In June 2013, iThemba LABS acquired the AGATA detector library (ADL) software to simulate the response of the segmented clover detector for an arbitrary gamma-ray interaction within a germanium crystal. In order to generate realistic pulse shapes that match the measured pulses for a specific position in (x,y,z), the detector characteristics, such as geometry, impurity profile, charge sensitive preamplifier response, cross-talk parameters and crystal orientation, must be measured and implemented into the software in high precision. The implementation of those detector characteristics into the ADL software is in progress. The charge sensitive preamplifier response of crystal A of the iThemba LABS segmented clover detector was measured and implemented into the ADL software. ADL simulated charge collecting signals for crystal A show an excellent agreement with the measured signal.

1. Introduction

The preamplifier represents an interface between the detector and the signal processing electronics. Its basic function is to amplify and shape the small signal from the detector and to transfer it to the electronic chain with the least degradation. Typically, charge sensitive preamplifiers are used for Ge detectors. In a charge sensitive preamplifier, the charge carried by the incoming pulse is first integrated on a capacitor and then removed by a slow discharge through a resistive feedback network. This produces a pulse with a fast leading edge (rise time), corresponding to the charge collection time in the detector, and a slow exponential decay (fall time). In order to preserve as well as possible the information carried in the signal leading edge, a very fast, low noise, low power consumption and stable preamplifier is required. To obtain a fast response, i.e. a signal with short rise time, a large bandwidth (BW) preamplifier is required.

2. iThemba LABS segmented clover detector

The iThemba LABS segmented clover detector consists of four n-type HPGe crystals. The crystals dimensions are; diameter of 60 mm (before tapering) and 90 mm length with depth segmentation at 35 mm. Each crystal is electrically segmented into 8 contacts on the outer surface. This results in a total of 36 electronic channels of which 32 are associated with the outer contacts and 4 with the inner core contacts of the detector.

During γ -ray interaction, all segments and inner core contacts produce a signal with a certain pulse shape. These pulse shapes carry information about the position (x,y,z) of the energy deposition occurred when a γ -ray interacted within the Ge crystal. To make use of this position sensitivity of the detector, we have to create a database of simulated pulse responses for various interaction positions and ensure that the simulated pulse shapes are realistic.

3. Motivation

The determination of the position of a gamma-ray interaction inside a germanium detector uses a database of simulated realistic pulses. This process requires pulse shape analysis and determination of the best match between the measured pulses and the simulated ones. The simulation of pulse shapes for the iThemba LABS segmented clover detector is performed using the AGATA Detector simulation Library (ADL) software [1, 2]. In order to obtain a good match between the measured pulses and the simulated pulses, the default parameters, such as geometry, impurity profile, charge sensitive preamplifier response, cross-talk parameters [3, 4] and crystal orientation, used in the code should be replaced with experimentally measured ones that are specific for the iThemba LABS segmented clover detector.

For each simulated gamma-ray interaction within the germanium, ADL outputs the integrated current signal that reflects the movement of the charges, shown in figure 1 (red). This signal is rising fast and has sharp edges, different from the experimentally observed signal which has smooth edges figure 1 (blue). The difference is caused by the preamplifier response function. What is needed is to measure it, to find a best fitting function for it, to calculate its derivative, to normalise it and then to input it in the ADL. The ADL has a built-in function that convolutes the derivative of the response function with the charge signal. In this work analysis of the detector preamplifier response was performed in order to implement it in the ADL code.

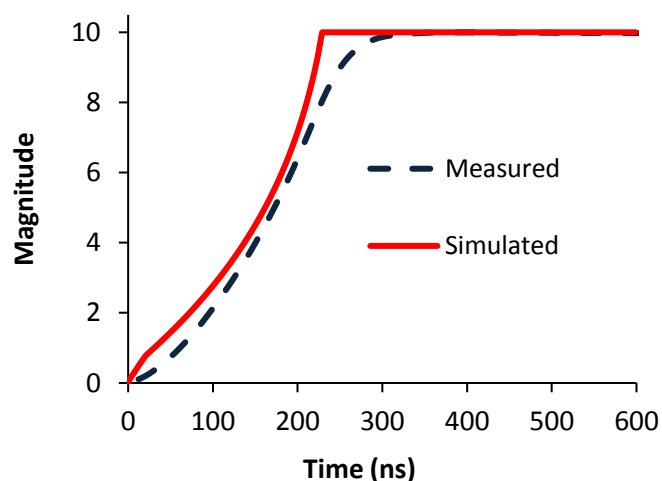


Figure 1. ADL simulated signal without the preamplifier response function (solid) and the experimental measured signal (dash).

4. Experimental measurements

The measurements to extract the detector's preamplifier response for the core signals were done using a pulse generator which produced a step function signal with 5 ns rise-time; see figure 2 (yellow). The pulser was connected to the four test inputs, one for each core of the segmented clover, and the output signals were measured, see figure 2 (blue). This allowed determining the response of the preamplifiers for the four core contacts but not for the segment contacts. As the input signal passes through the preamplifier the sharp edges are smoothed due to the finite bandwidth of the preamplifier [5], and the rise time is increased to ~40 ns. The preamplifier output has under-shoot just before rising and this is a characteristic feature of this charge sensitive PSC823C preamplifier [6].

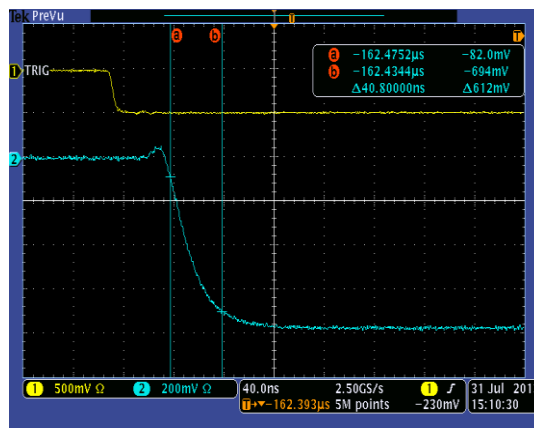


Figure 2. The input pulser (yellow) and the output preamplifier response (blue) signals as observed on an oscilloscope for the core of crystal A.

5. Data analysis and results

Initially, the measured preamplifier response was compared with the function $f(x)$, equation (1), used to fit the AGATA preamplifier response function [7], as shown in figure 3 (black). Then the preamplifier response was fitted with an exponential function $g(x)$, equation (2), see figure 3 (red). Both response functions were found unsatisfactory, because the simulated pulse shapes showed considerable difference from the experimentally measured ones.

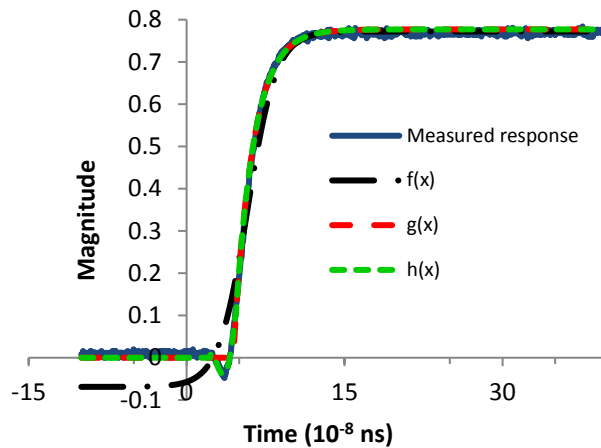


Figure 3. The function $f(x)$ (dash dot) and exponential $g(x)$ (large dash) function were initially used to fit the measured preamplifier response (solid). The function $h(x)$ (small dash) includes both exponential and an undershoot.

$$f(x) = g * \left(\frac{1}{1-c}\right) * \left\{ \frac{1}{1+\frac{1-c}{c} * \exp(-b*t)} - c \right\} * \exp\left(-\frac{t}{t_d}\right), \dots\dots\dots (1)$$

Where b controls the slope, the rise of the signal, and $\frac{1-c}{1}$ shifts the point where the curvature changes, t_d is the decay time of $45\mu s$.

$$g(x) = \begin{cases} a * \exp\left(-\frac{t}{t_d}\right) & \text{for } t > 4.4 \times 10^{-8} \\ 0 & \text{for } t < 4.4 \times 10^{-8} \end{cases} \dots\dots\dots (2)$$

Where a is the gain. To obtain a better agreement a preamplifier response function describing also the undershoot was defined. Two functions, a polynomial of 4th order and an exponential function were employed to fit the preamplifier response signal, as shown in Figure 3 (green). These functions are:

$$h(x) = \begin{cases} (-At^4 + Bt^3 - Ct^2 + Dt - E) & \text{for } t > 2.28 \times 10^{-8} \text{ and } t \leq 4.6 \times 10^{-8} \\ a * \exp\left(-\frac{t}{t_d}\right) & \text{for } t > 4.64 \times 10^{-8} \end{cases} \dots\dots (3)$$

With parameter values: $A = 1.3539E+30$, $B = 2.1716E+23$, $C = 1.1938E+16$, $D = 2.7033E+8$, and $E = 2.1556$. The new preamplifier response function was implemented in the ADL. To test it, a pulser signal was simulated in ADL by selecting an interaction position very close to the electrode such that the rise-time of the signal is as short as that of the pulse generator, about 5 ns; see figure 4 (dash red). ADL convoluted this raw charge with the preamplifier response function; see figure 4 (solid blue) and the simulated signal is in agreement with the measured response function; see figure 4 (dash dot black).

The preamplifier response function for core A of the iThemba LABS segmented clover detector was successfully implemented into the ADL simulation software, see figure 5. It was also ensured the ADL is performing the convolution of the simulated charge signal with the response function correctly.

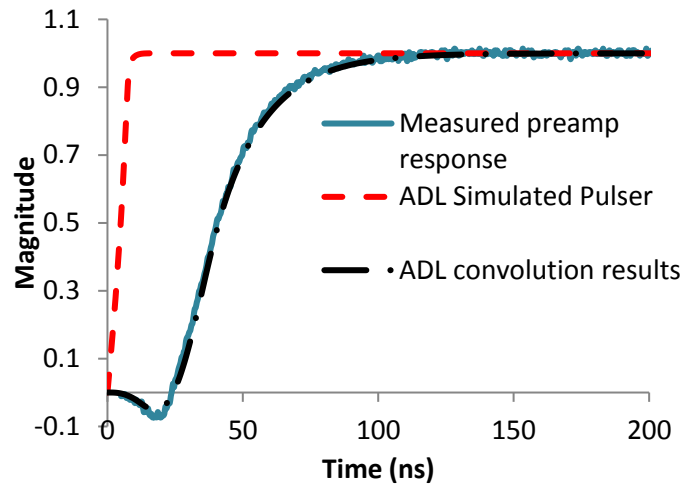


Figure 4. Measured preamplifier response (solid), ADL simulated pulser (dash), and the ADL output of the convolution of charge signal with preamplifier response function (dash dot).

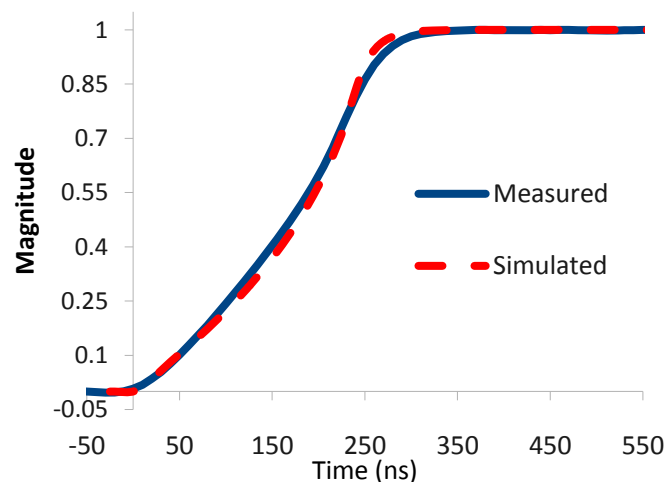


Figure 5. Comparison of the experimentally measured (solid) and simulated signal (dash) for the core of crystal A at a position of $x = 35$, $y = 55$ and $z = 62$ mm.

As a next step the preamplifier response function of a segment was studied. Since one cannot measure directly the preamplifier response function for a segment contact, an alternative method to determine it was used. The comparison of the measured trace for the hit-segment A5 figure 6 (solid blue) and the simulated one assuming that the segment has the same preamplifier response function as the core (solid black) showed a large difference. The observed signal on the segment is rising much slower. To correct for this, a time difference between the core signal and the charge collecting segment signal was calculated. This difference was then added to the preamplifier response function of the core to delay it and have long rising time. With this technique an agreement between the measured pulse and the ADL simulated charge collecting segment was obtained, figure 6 (dash red and the solid blue).

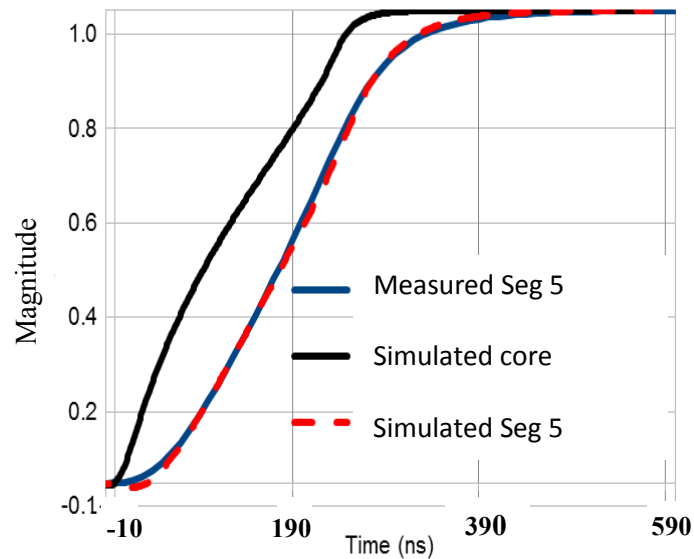


Figure 6. Experimentally measured pulse for hit segment 5 (solid blue), ADL simulated pulse with core preamplifier response function (solid black), and simulated pulse with delayed core preamplifier response function (dash red).

6. Conclusion

The preamplifier response for crystal A was measured with a step function signal of 5 ns rise-time and the core has showed a rise-time of 40ns. The preamplifier response functions for the core and charge collecting segment 5 were successfully implemented on ADL code. For both functions we have obtained an excellent agreement between the measured and simulated charge collecting signals for the core and charge collecting segment crystal A.

Work to determine the response functions of the remaining contacts of crystal A, and of crystals B, C and D, is in progress. Note that the other simulation parameters such as crystal lattice orientation, and electron and hole charge drift velocities of crystal A were experimentally determined and implemented in the ADL to achieve this excellent results [8, 9, 10].

7. References

- [1] Bruyneel, B., Birkenbach, B. & Reiter, P. *Eur. Phys. J. A* **52** 70 (2016)
- [2] B. Bruyneel and B. Birkenbach, AGATA Detector simulation Library (ADL) v. 2.0, <http://www.ikp.uni-koeln.de/research/agata/data/ReadMeADL.pdf>.
- [3] S.P. Noncolela, T.D. Bucher, E.A. Lawrie, T.R.S. Dinoko, J.L. Easton, N. Erasmus, J.J. Lawrie, S.H. Mthembu, W.X. Mtshali, O. Shirinda, J.N. Orce, *A Phys Pol B* **48**, 347 (2017).
- [4] T.D. Bucher, S.P. Noncolela, E.A. Lawrie, T.R.S. Dinoko, J.L. Easton, N. Erasmus, J.J. Lawrie, S.H. Mthembu, W.X. Mtshali, O. Shirinda, J.N. Orce, *Phys. Scr.* **92**, 114004 (2017).
- [5] M. Lauer, PhD thesis, Combined Faculties for the Natural Sciences and for Mathematics of the Ruperto-Carola University of Heidelberg, Germany, 2004
- [6] EURISYS PSC823C Operating Manual, <https://siliconpr0n.org/media/camac/1/PSC823.pdf>
- [7] M. R. Dimmock, PhD thesis, University of Liverpool, Oliver lodge laboratory, 2008
- [8] S. H. MTHEMBU, SAIP 2016, NPRP oral presentation: Crystals Orientation Measurements of the iThemba LABS Segmented Clover Detector.
- [9] T. Dinoko, SAIP 2016 NPRP poster presentation: Orientation of the Ge Crystals of the iThemba LABS Segmented Clover Detector.
- [10] S. Noncolela, SAIP 2016 NPRP poster presentation: Crystal orientation of the iThemba LABS segmented clover detector.

The search for the Dark Vector Boson via the Higgs Portal

SH Connell

University of Johannesburg, Johannesburg, South Africa

E-mail: shconnell@uj.ac.za

Abstract. The Standard Model (SM) is known to be incomplete. The introduction of a Dark Sector via an additional $U(1)_D$ gauge symmetry added to the SM Lagrangian provides a mechanism to introduce much needed new physics without perturbing the already excellent agreement between the SM theoretical description and the Electroweak Precision Observables (EWPO) experimental constraints. The model has a dark vector boson Z_d which can mix with the hypercharge gauge boson with the coupling κ . This opens the Hypercharge Portal which can mediate the fluctuation of a Z to a Z_d , or the decay of the Z_d to SM leptons. If a dark Higgs singlet s also exists, this then breaks the $U(1)_D$, opening the Higgs portal and also allowing for Higgs mass mixing between the SM and dark sectors, described by the Higgs mass mixing parameter, k . Including dark fermionic fields in the Lagrangian allows for long-lived cold Dark Matter candidates. The various connections between the Dark and SM sectors allow descriptions of many key astro-physical phenomena. The Model is therefore a fascinating candidate for new physics beyond the SM. It becomes crucial to search for experimental signatures of this model. This contribution discusses a search for the dark force boson Z_d using its production via the Higgs Portal and its decay back to SM leptons: $H \rightarrow h_d \rightarrow Z_d Z_d \rightarrow 4\ell$. The results from ATLAS Run 1 and the further development of the search for Run 2 are presented.

1. Introduction

Introduction of the hidden or dark sector is a method to extend the Standard Model (SM) [1, 2, 3, 4, 5, 6, 7, 8, 9, 10], to provide candidates for dark matter [11] and dark forces which accommodate both the indirect and the (potential) direct evidence based on astronomical observations or space platform experiments [12, 13, 14]. The hidden or dark sector can be introduced with an additional $U(1)_d$ dark gauge symmetry [5, 6, 7, 8, 9, 10].

This analysis focusses on a Higgs Portal model, which has a Higgs level coupling between the dark sector and the SM. Accordingly, the $U(1)_d$ symmetry is broken by the introduction of a dark Higgs boson, which mixes with the SM Higgs boson [5, 6, 7, 8, 9, 10] with a coupling strength κ . The observed Higgs boson would then be the lighter partner of the new Higgs doublet, which can also decay via the dark sector. We then conceptually allow the decay $H \rightarrow h_d \rightarrow Z_d Z_d$. The dark sector can additionally couple to the SM through kinetic mixing with the hypercharge gauge via the kinetic mixing parameter ϵ . This allows the decay $Z_d \rightarrow \ell\ell$. The current EWPO restrict the hypercharge portal to a greater degree than the Higgs Portal [5, 6, 7, 8, 9, 10, 15, 16]. We can further assume the dark fermions are sufficiently heavy $m_{f_d} < m_{Z_d}/2$, so that the branching ratio for the decay $Z_d \rightarrow \ell\ell$ may be taken as 100%, even though the kinetic mixing parameter ϵ can be set small to be consistent with EWPO, $\epsilon \approx 10^{-4}$, and still satisfy the requirement for prompt decays (a displaced vertex is not observed). The Higgs Portal is opened by the observation of the discovered Higgs at 125 GeV [17, 18, 19] during Run 1 of the Large Hadron Collider (LHC) [20, 21]. This ushers in a new and rich experimental program for physics beyond the SM.

This paper describes an ongoing search for the Higgs bosons decaying to four leptons via two Z_d bosons using pp collision data at $\sqrt{s} = 8$ TeV collected at the CERN LHC with the ATLAS experiment. The Run 1 search used a dataset corresponding to an integrated luminosity of 20.3 fb^{-1} with an uncertainty of 2.8% for $H \rightarrow Z_d Z_d \rightarrow 4\ell$ [22] and was published in [23]. The search is being extended with Run 2 data and also incorporates several extensions and improvements. In essence, same-flavor decays of the Z_d bosons to electron and muon pairs are considered, giving the $4e$, $2e2\mu$, and 4μ final states. Final states including τ leptons are not considered. In the absence of a significant signal, upper bounds are set on the relative branching ratio $\text{BR}(H \rightarrow Z_d Z_d \rightarrow 4\ell)/\text{BR}(H \rightarrow ZZ^* \rightarrow 4\ell)$ as functions of the mass of the dark vector boson m_{Z_d} . The branching ratio limits are used to set upper bounds on the Higgs boson mixing parameters [5, 6]. The search is restricted to the mass range where the Z_d from the decay of the Higgs boson is on-shell, i.e. $15 \text{ GeV} < m_{Z_d} < m_H/2$, where $m_H = 125 \text{ GeV}$. For Run 1, dark vector boson masses below 15 GeV were not considered whereas in the current Run 2 phase, this threshold is dropped to 5 GeV. This low-mass region is also theoretically well motivated [7, 8], and the high p_T of the Z_d boson relative to its mass leads to the phenomenon described as "lepton jets" and requires dedicated treatment [24].

2. Experimental Setup, Monte Carlo Simulation : Signal and backgrounds

The ATLAS detector covers almost the whole solid angle around the collision point with layers of tracking detectors, calorimeters and muon chambers. Further details can be found in [25]. The data are collected using an online three-level trigger system [26] that selects events of interest and reduces the event rate from several MHz to about 400 Hz for recording and offline processing. **Signal** : Samples of Higgs boson production in the gluon fusion (ggF) mode, with $H \rightarrow Z_d Z_d \rightarrow 4\ell$ and were generated for $m_H = 125 \text{ GeV}$ and $15 < m_{Z_d} < 60 \text{ GeV}$ (in 5 GeV steps) in MADGRAPH5 [27] with CTEQ6L1 [28] parton distribution functions (PDF) using the Hidden Abelian Higgs Model (HAHM) as a benchmark signal model [5, 9, 10]. PYTHIA8 [29, 30] and PHOTOS [31, 32, 33] are used to take into account parton showering, hadronization, and initial- and final-state radiation. **Backgrounds** : The background processes follow those used in the $H \rightarrow ZZ^* \rightarrow 4\ell$ measurements [34], and consist of: Higgs boson production via the SM ggF, VBF (vector boson fusion), also WH , ZH , and $t\bar{t}H$ processes with $H \rightarrow ZZ^* \rightarrow 4\ell$ final states, $ZZ^* \rightarrow 4\ell$ Z +jets and $t\bar{t}$ and SM WZ and WW production. There are also backgrounds containing J/ψ and Υ , namely ZJ/ψ and $Z\Upsilon$. Further details may be found in [23].

3. Analysis procedure

The selection of four leptons (e, μ) proceeds in the same way as in the discovery analysis channel $H \rightarrow ZZ^* \rightarrow 4\ell$ as described in [34] and is not described further here. The association of these four leptons into two same flavour opposite sign (SFOS) pairs is different. Instead of the requirement that a primary pair reconstructs back to a Z boson, there is the requirement that the mass difference $\Delta m = |m_{12} - m_{34}|$ is minimised. Here m_{12} and m_{34} are the invariant masses of the first and second pairs associations which achieve this requirement. The mass difference Δm is expected to be minimal for the signal since the two dilepton systems should have invariant masses consistent with the same m_{Z_d} . No requirement is made on Δm ; it is used only to select a unique quadruplet with the smallest Δm . Subsequently, isolation and impact parameter significance requirements are imposed on the leptons of the selected quadruplet as described in Ref. [34]. The 2D dilepton mass distributions are shown in Figs. 1. The ambiguity in lepton pairing is emphasised which is why the Z particle vetos are applied for both pairings.

For the $H \rightarrow Z_d Z_d \rightarrow 4\ell$ search with hypothesized m_{Z_d} , after the impact parameter significance requirements on the selected leptons, four final requirements are applied:

- (1) $115 < m_{4\ell} < 130 \text{ GeV}$ where $m_{4\ell}$ is the invariant mass of the four leptons in the quadruplet.

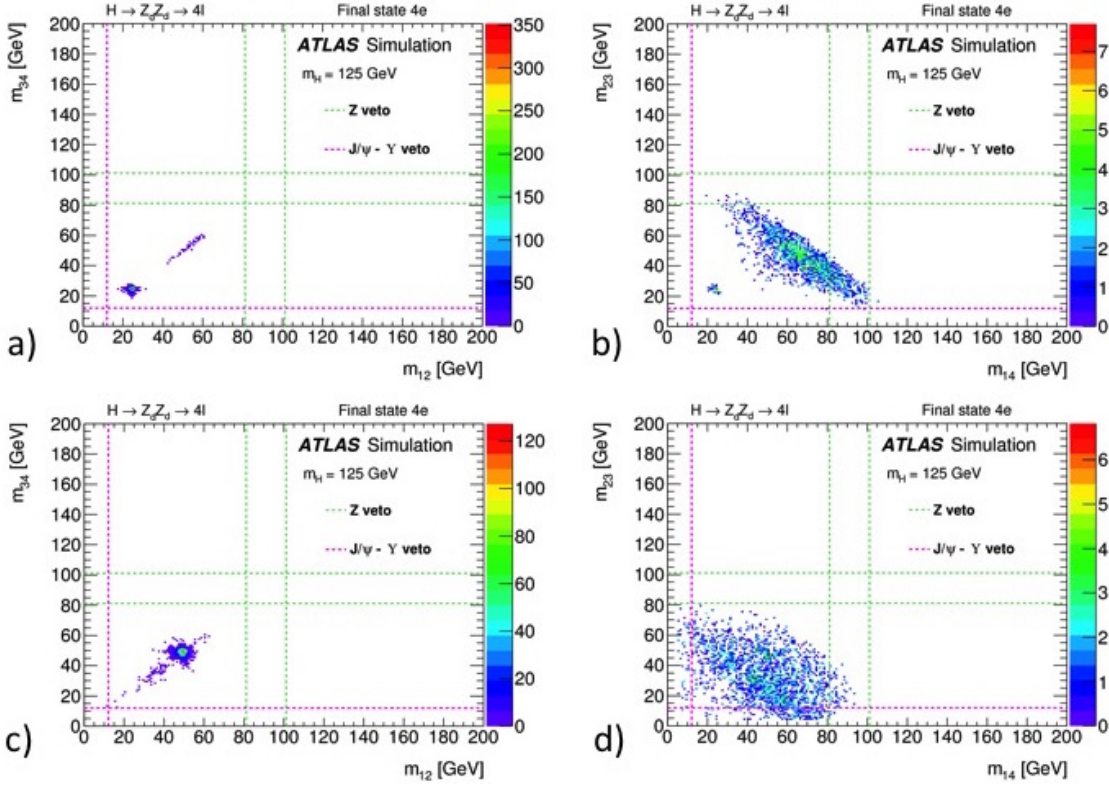


Figure 1. (a), (c) Simulated first pair invariant mass m_{12} as a function of the second pair invariant mass m_{34} and (b), (d) first alternative pair invariant mass m_{14} as a function of the second alternative pair invariant mass m_{23} , for two signal samples (top : $m_{Z_d} = 20$ GeV, bottom : $m_{Z_d} = 50$ GeV), for $m_H = 125$ GeV. These distributions are for the 4e final state. All requirements defining the SR are applied, except the vetoes. The green dashed lines correspond to $m_Z = 10$ GeV, i.e. the region where the Z veto is applied. The pink dashed lines correspond to 12 GeV, i.e. the limit of the $J/\psi - \gamma$ veto.

- (2) Z, J/ψ , and Υ vetoes on all SFOS pairs in the selected quadruplet. The Z veto discards the event if either of the dilepton invariant masses is consistent with the Z-boson pole mass: $|m_{12} - m_Z| < 10$ GeV or $|m_{34} - m_Z| < 10$ GeV. For the J/ψ and Υ veto, the dilepton invariant masses are required to be above 12 GeV.
- (3) the loose signal region requirement: $m_{12} < m_H/2$ and $m_{34} < m_H/2$, where $m_H = 125$ GeV.
- (4) the tight signal region requirement: $|m_{Z_d} - m_{12}| < \delta m$ and $|m_{Z_d} - m_{34}| < \delta m$. The optimized values of the δm requirements are 5/3/4.5 GeV for the 4e/4 μ /2e2 μ final states respectively (the δm requirement varies with the hypothesized m_{Z_d} but the impact of the variation is negligible).

These requirements (1)–(4) define the signal region (SR) of $H \rightarrow Z_d Z_d \rightarrow 4\ell$ that is dependent on the hypothesized m_{Z_d} , and is essentially background-free, but contains small estimated background contributions from $H \rightarrow ZZ^* \rightarrow 4\ell$ and $ZZ \rightarrow 4\ell$ processes.

The analysis exploits the small mass difference between the two SFOS lepton pairs of the selected quadruplet to perform a counting experiment. After the small mass difference requirements between the SFOS lepton pairs, the estimated background contributions, coming from $H \rightarrow ZZ^* \rightarrow 4\ell$ and $ZZ \rightarrow 4\ell$, are small. These backgrounds are normalized with the theoretical calculations of their cross sections. The other backgrounds are found to be negligible. Since there is no significant excess, upper bounds on the signal strength, defined as the ratio of

the $H \rightarrow Z_d Z_d \rightarrow 4\ell$ and $ZZ \rightarrow 4\ell$ rate normalized to the SM $H \rightarrow ZZ^* \rightarrow 4\ell$ expectation are set as a function of the hypothesized m_{Z_d} . In a benchmark model where the SM is extended with a dark vector boson and a dark Higgs boson, the measured upper bounds on the signal strength are used to set limits on the branching ratio of $H \rightarrow Z_d Z_d$ and on the Higgs boson mixing parameter as a function of m_{Z_d} [5, 6].

These backgrounds are further suppressed by the requirements of the tight signal region. The Z +jets and $t\bar{t}$, WW and WZ backgrounds now yield zero events. In the case where the Monte Carlo calculation yields zero expected background events in the tight signal region, an upper bound at 68% CL on the expected events is estimated using 1.14 events [35], scaled to the data luminosity and normalized to the background cross section:

The systematic uncertainties on the theoretical calculations of the cross sections used and the event selection and identification efficiencies are taken into account. The effects of PDFs, α_S , and renormalization and factorization scale uncertainties on the total inclusive cross sections for the Higgs production by ggF, VBF, VH and $t\bar{t}H$ are obtained from Refs. [36, 37]. The renormalization, factorization scales and PDFs and α_S uncertainties are applied to the ZZ^* background estimates. The uncertainties due to the limited number of MC events in the $t\bar{t}$, Z +jets, ZJ/ψ , $Z\Upsilon$ and WW/WZ background simulations are estimated as described in [23]. The luminosity uncertainty [22] is applied to all signal yields, as well as to the background yields that are normalized with their theory cross sections. The detector systematic uncertainties due to uncertainties in the electron and muon identification efficiencies are estimated within the acceptance of the signal region requirements. There are several components to these uncertainties. For the muons, uncertainties in the reconstruction and identification efficiency, and in the momentum resolution and scale, are included. For the electrons, uncertainties in the reconstruction and identification efficiency, the isolation and impact parameter significance requirements, the energy scale and energy resolution are considered.

4. Results

For the Run 1 results, four data events passed the loose signal region requirements, one in the $4e$ channel, two in the 4μ channel and one in the $2e2\mu$ channel. Two of these four events pass the tight signal region requirements: the event in the $4e$ channel and one of the events in the 4μ channel. The event in the $4e$ channel has dilepton masses of 21.8 GeV and 28.1 GeV, and is consistent with a Z_d mass in the range $23.5 \leq m_{Z_d} \leq 26.5$ GeV. The local significance of this event is 1.7σ . For the event in the 4μ channel that passes the tight signal region requirements, the dilepton invariant masses are 23.2 GeV and 18.0 GeV, and they are consistent with a Z_d mass in the range $20.5 \leq m_{Z_d} \leq 21.0$ GeV. The local significance of the 4μ event is 1.7σ . In the m_{Z_d} range of 15 to 30 GeV where four data events pass the loose signal region requirements, histogram interpolation [38] is used in steps of 0.5 GeV to obtain the signal acceptances and efficiencies at the hypothesized m_{Z_d} .

For each m_{Z_d} , in the absence of any significant excess of events consistent with the signal hypothesis, the upper limits are computed from a maximum-likelihood fit to the numbers of data and expected signal and background events in the tight signal regions, following the CL_s modified frequentist formalism [39, 40] with the profile-likelihood test statistic [41, 42]. The nuisance parameters associated to the systematic uncertainties are profiled [23]. The parameter of interest in the fit is the signal strength μ_d defined as the ratio of the $H \rightarrow Z_d Z_d \rightarrow 4\ell$ rate relative to the SM $H \rightarrow ZZ^* \rightarrow 4\ell$ rate:

$$\mu_d = \frac{\sigma \times \text{BR}(H \rightarrow Z_d Z_d \rightarrow 4\ell)}{[\sigma \times \text{BR}(H \rightarrow ZZ^* \rightarrow 4\ell)]_{\text{SM}}}. \quad (1)$$

The systematic uncertainties in the electron and muon identification efficiencies, renormalization and factorization scales and PDF are 100% correlated between the signal and backgrounds. Pseudoexperiments are used to compute the 95% CL upper bound μ_d in each of the final states

and their combination, and for each of the hypothesized m_{Z_d} . The 95% confidence-level upper bounds on the $H \rightarrow Z_d Z_d \rightarrow 4\ell$ rates are shown in the left of Fig. 2 relative to the SM Higgs boson process $H \rightarrow ZZ^* \rightarrow 4\ell$ as a function of the hypothesized m_{Z_d} for the combination of the three final states $4e$, $2e2\mu$ and 4μ .

The simplest benchmark model is the SM plus a dark vector boson and a dark Higgs boson as discussed in Refs. [6, 10], where the branching ratio of $Z_d \rightarrow \ell\ell$ is given as a function of m_{Z_d} . This can be used to convert the measurement of the upper bound on the signal strength μ_d into an upper bound on the branching ratio $\text{BR}(H \rightarrow Z_d Z_d)$. (One has also assumed the SM Higgs boson production cross section and used $\text{BR}(H \rightarrow ZZ^* \rightarrow 4\ell)_{\text{SM}} = 1.25 \times 10^{-4}$ [36, 37]).

abovecaptionskip -12pt The $H \rightarrow Z_d Z_d$ decay can now be used to obtain a m_{Z_d} -dependent

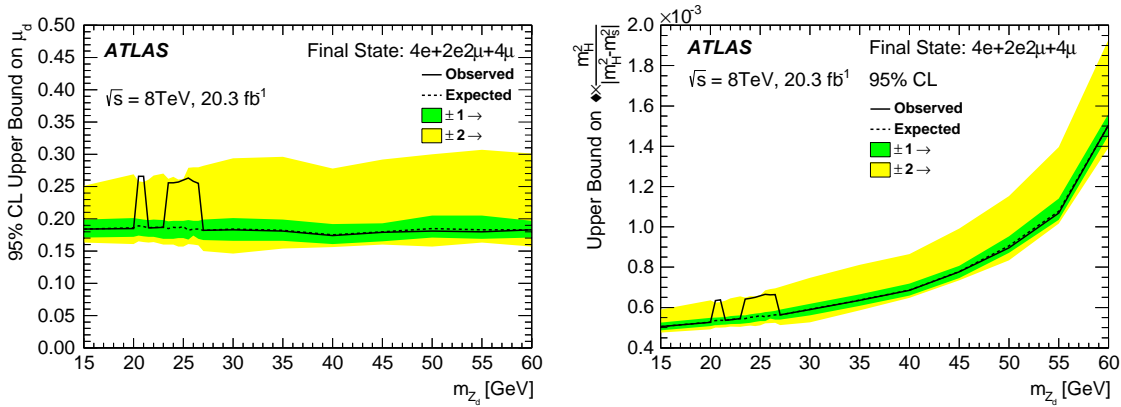


Figure 2. Left : The 95% confidence level upper bound on the signal strength $\mu_d = \frac{\sigma \times \text{BR}(H \rightarrow Z_d Z_d \rightarrow 4\ell)}{[\sigma \times \text{BR}(H \rightarrow ZZ^* \rightarrow 4\ell)]_{\text{SM}}}$ of $H \rightarrow Z_d Z_d \rightarrow 4\ell$ in the combined $4e + 2e2\mu + 4\mu$ final state, for $m_H = 125$ GeV. The $\pm 1\sigma$ and $\pm 2\sigma$ expected exclusion regions are indicated in green and yellow, respectively. Right : The 95% confidence level upper bound on the Higgs mixing parameter $\kappa \times m_H^2 / |m_H^2 - m_S^2|$ as a function of m_{Z_d} , in the combined $4e + 2e2\mu + 4\mu$ final state, for $m_H = 125$ GeV. The $\pm 1\sigma$ and $\pm 2\sigma$ expected exclusion regions are indicated in green and yellow, respectively.

limit on an Higgs mixing parameter κ' [6]. The algebra and rationale are described in reference [23]. Figure 2 shows the upper bound on the effective Higgs mixing parameter as a function of m_{Z_d} : for $m_H/2 < m_S < 2m_H$, this would correspond to an upper bound on the Higgs portal coupling in the range $\kappa \sim (1-10) \times 10^{-4}$.

5. Conclusion

The Run 1 $H \rightarrow Z_d Z_d \rightarrow 4\ell$ search for an exotic gauge boson Z_d that couples to the discovered SM Higgs boson at a mass around 125 GeV in four-lepton events are presented, using the ATLAS detector at the LHC and covers the exotic gauge boson mass range from 15 GeV up to the kinematic limit of $m_H/2$. An integrated luminosity of 20.3 fb^{-1} at 8 TeV is used in this search. One data event is observed to pass all the signal region selections in the $4e$ channel, and has dilepton invariant masses of 21.8 GeV and 28.1 GeV and a local significance of 1.7σ . This $4e$ event is consistent with a Z_d mass in the range $23.5 < m_{Z_d} < 26.5$ GeV. Another data event is observed to pass all the signal region selections in the 4μ channel, and has dilepton invariant masses of 23.2 GeV and 18.0 GeV and a local significance of about 1.7σ . This 4μ event is consistent with a Z_d mass in the range $20.5 < m_{Z_d} < 21.0$ GeV. In the absence of a significant excess, upper bounds on the signal strength (and thus on the cross section times branching ratio) are set for the mass range of $15 < m_{Z_d} < 60$ GeV using the combined $4e$, $2e2\mu$, 4μ final states.

Using a simplified model where the SM is extended with the addition of an exotic gauge boson and a dark Higgs boson, and assuming the SM Higgs production cross section, upper bounds on the branching ratio of $H \rightarrow Z_d Z_d$, as well as on the Higgs portal coupling parameter κ are set in the range $(2\text{--}3) \times 10^{-5}$ and $(1\text{--}10) \times 10^{-4}$ respectively at 95% CL, for $15 < m_{Z_d} < 60$ GeV.

For Run 2, the lower bound on the Z_d mass searched for is dropped from 15 GeV to 0.5 GeV. There are additional improvements in the analysis process. Further details and results to appear later.

6. Acknowledgments

We thank CERN and all associated staff for the very successful operation of the LHC. The support of the National Research Foundation (NRF) and Department of Science and Technology, both of South Africa, is acknowledged. Similar acknowledgements apply for all participating institutions in the ATLAS Collaboration. The crucial computing support from all WLCG partners is acknowledged gratefully.

References

- [1] Fayet P 2004 *Phys.Rev.* **D 70** 023514 (*Preprint hep-ph/0403226*)
- [2] Finkbeiner D P and Weiner N 2007 *Phys.Rev.* **D 76** 083519 (*Preprint astro-ph/0702587*)
- [3] Arkani-Hamed, N et al 2009 *Phys.Rev.* **D 79** 015014 (*Preprint 0810.0713*)
- [4] Dudas, E et al 2012 *J. High Energy Phys.* **1210** 123 (*Preprint 1205.1520*)
- [5] Curtin D, Essig R, Gori S and Shelton J 2015 *J. High Energy Phys.* **1502** 157 (*Preprint 1412.0018*)
- [6] Curtin D et al. 2014 *Phys.Rev.* **D 90** 075004 (*Preprint 1312.4992*)
- [7] Davoudiasl H, Lee H S, Lewis I and Marciano W J 2013 *Phys.Rev.* **D 88** 015022 (*Preprint 1304.4935*)
- [8] Davoudiasl H, Lee H S and Marciano W J 2012 *Phys.Rev.* **D 85** 115019 (*Preprint 1203.2947*)
- [9] Wells J D 2008 (*Preprint 0803.1243*)
- [10] Gopalakrishna S, Jung S and Wells J D 2008 *Phys.Rev.* **D 78** 055002 (*Preprint 0801.3456*)
- [11] Clowe D et al. 2006 *Astrophys.J.* **648** L109–L113 (*Preprint astro-ph/0608407*)
- [12] Adriani, O et al (PAMELA Collaboration) 2009 *Nature* **458** 607–609 (*Preprint 0810.4995*)
- [13] Chang J et al (ATIC Collaboration) 2008 *Nature News* **456** 362
- [14] Aguilar M et al (AMS Collaboration) 2013 *Phys. Rev. Lett.* **110**(14) 141102
- [15] Hook A, Izaguirre E and Wacker J G 2011 *Adv.High Energy Phys.* **2011** 859762 (*Preprint 1006.0973*)
- [16] Hoenic I, Samach G and Tucker-Smith D 2014 *Phys.Rev.* **D 90** 075016 (*Preprint 1408.1075*)
- [17] Englert F and Brout R 1964 *Phys. Rev. Lett* **13** 321–323
- [18] Higgs P W 1964 *Phys. Rev. Lett* **13** 508–509
- [19] Guralnik G S, Hagen C R and Kibble T W B 1964 *Phys. Rev. Lett* **13** 585–587
- [20] ATLAS Collaboration 2012 *Phys.Lett.* **B716** 1–29 (*Preprint 1207.7214*)
- [21] CMS Collaboration 2012 *Phys.Lett.* **B716** 30–61 (*Preprint 1207.7235*)
- [22] ATLAS Collaboration 2013 *Eur.Phys.J.* **C73** 2518 (*Preprint 1302.4393*)
- [23] Wells J D 2015 (*Preprint 1505.07645*)
- [24] ATLAS Collaboration 2014 *J. High Energy Phys.* **1411** 088 (*Preprint 1409.0746*)
- [25] ATLAS Collaboration 2009 (*Preprint 0901.0512*)
- [26] ATLAS Collaboration 2012 *Eur.Phys.J.* **C72** 1849 (*Preprint 1110.1530*)
- [27] Allwell, J et al 2011 *J. High Energy Phys.* **1106** 128 (*Preprint 1106.0522*)
- [28] Lai H L et al. 2010 *Phys.Rev.* **D 82** 074024 (*Preprint 1007.2241*)
- [29] Sjostrand T, Mrenna S and Skands P Z 2006 *J. High Energy Phys.* **0605** 026 (*Preprint hep-ph/0603175*)
- [30] Sjostrand T, Mrenna S and Skands P Z 2008 *Comput.Phys.Commun.* **178** 852–827 (*Preprint 0710.3820*)
- [31] Golonka P and Was Z 2007 *Eur.Phys.J.* **C50** 53–62 (*Preprint hep-ph/0604232*)
- [32] Was Z, Golonka P and Nanava G 2007 *PoS ACAT* 071 (*Preprint 0707.3044*)
- [33] Davidson N, Przedzinski T and Was Z 2010 (*Preprint 1011.0937*)
- [34] ATLAS Collaboration 2015 *Phys. Rev. D* **91** 012006 (*Preprint 1408.5191*)
- [35] Olive, K et al (Particle Data Group) 2014 *Chin.Phys.* **C38** 090001
- [36] LHC Higgs cross section working group 2011 *CERN-2011-002* (*Preprint 1101.0593*)
- [37] LHC Higgs cross section working group 2012 *CERN-2012-002* (*Preprint 1201.3084*)
- [38] Read A L 1999 *Nucl.Instrum.Meth.* **A425** 357–360
- [39] Read A L 2002 *J.Phys.* **G28** 2693–2704
- [40] Cousins R D and Highland V L 1992 *Nucl.Instrum.Meth.* **A320** 331–335
- [41] Cowan G, Cranmer K, Gross E and Vitells O 2011 *Eur.Phys.J.* **C71** 1554 (*Preprint 1007.1727*)
- [42] Cowan G, Cranmer K, Gross E and Vitells O 2013 *Eur.Phys.J.* **C73** 2501 ISSN 1434-6044

Investigation of the low-lying excitation region in ${}^9\text{B}$

D. J. Marín-Lámbarri^{1,2,*}, N.J. Mukwevho¹, S. Triambak^{1,2}, E.H. Akakpo¹, P. Adsley^{2,3}, J. W. Brummer³, T. Dinoko², S. Jongile^{1,2}, M. Kamil¹, N. Kheswa², K.C.W. Li³, P.Z. Mabika¹, S.H. Mthembu¹, F. Nemulodi¹, R. Neveling², N. Orce^{1,2}, P. Papka^{2,3}, L. Pellegri^{2,4}, V. Pseudo^{1,2}, B. Rebeiro¹, F.D. Smit², G.F. Steyn², W. Yahia-Chérif⁵

¹ University of the Western Cape, Department of Physics, Bellville, South Africa

² iThemba Laboratory for Accelerator Based Sciences, Somerset West, South Africa

³ Stellenbosch University, Department of Physics, Stellenbosch, South Africa

⁴ University of the Witwatersrand, School of Physics, Johannesburg, South Africa

⁵ University of Sciences and Technology Houari Boumediene, Algiers, Algeria

E-mail: marinlambarri@gmail.com

* Present address: Instituto de Física, Universidad Nacional Autónoma de México, P.O. Box 20-364, 01000 Cd. México, México

Abstract. A measurement of the ${}^9\text{Be}({}^3\text{He},\text{t}){}^9\text{B}^*$ reaction at 50 MeV was performed. A high-efficiency silicon detector array was used to detect the brake-up particles from excited states in ${}^9\text{B}^*$ in coincidence with the tritons in the high-resolution K600 spectrometer focal plane. The low-lying excitation region in ${}^9\text{B}$ was populated and the different decay channels identified and characterised; these populated excited states were the ground-state $\frac{3}{2}^-$, the 2.36 $\frac{5}{2}^-$, and the 2.75 $\frac{1}{2}^+$. Preliminary analysis are presented regarding the complex observation and characterisation of the first $\frac{1}{2}^+$ in ${}^9\text{B}$.

1. Introduction

The mirror symmetry in the ${}^9\text{Be}/{}^9\text{B}$ isospin doublet has been used to address important phenomena in astrophysics and nuclear structure. For example, the properties of low-lying unbound states in ${}^9\text{Be}$ are important for determining the ${}^4\text{He}(\alpha,\gamma){}^9\text{Be}$ stellar reaction rate, which is a crucial reaction that occurs after core-collapse supernovae and results in the creation of seed nuclei around $A\sim 80$ for the r-process [1]. A revised ${}^4\text{He}(\alpha,\gamma){}^9\text{Be}$ reaction rate was obtained at TRIUMF [2] by studying states in ${}^9\text{B}$ produced via the decay of ${}^9\text{C}$ and using isospin symmetry to deduce the properties of states in ${}^9\text{Be}$, where experimental data was lacking. From a nuclear structure perspective, this mirror nuclei have been described either as a cluster-like Borromean system, where the nuclei are described in a similar configuration as a H_2^+ molecule in which two unbound α -particles are held together by a covalent σ -type neutron or proton [3] or as a ${}^8\text{Be}$ core plus a neutron or proton occupying the sd shell. By determining the Coulomb displacement energies between the analog states in these nuclei will be possible to shed light in the nuclear structure front. Despite the first observation of the unbound ${}^9\text{B}$ nucleus 70 years ago, information on the low-lying excitation region still remains inconclusive [4]. While the astrophysically relevant first $\frac{1}{2}^+$ in ${}^9\text{Be}$ has been well established over several years, at $E_x = 1.684$ MeV with $\Gamma = 0.217$ MeV, there have been discrepancies in both theoretical and experimental attempts

to identify its isobaric analog $\frac{1}{2}^+$ in ${}^9\text{B}$. Calculations with a simple single-particle Woods-Saxon potential model yield a regular Thomas-Ehrman shift, with $E_x(\frac{1}{2}^+; {}^9\text{B}) \approx 1.0$ MeV [5–8]. This result is further validated by microscopic cluster model calculations [9, 10]. An R-matrix calculation on the other hand, yields an inverted Thomas-Ehrman shift with $E_x > 1.7$ MeV [11], due to the analog state in ${}^9\text{Be}$ being above the ${}^8\text{Be}(\text{g.s.}) + s_{\frac{1}{2}}$ neutron threshold. Finally, a revised calculation by Barker [12] using a modified potential yielded the excited $E_x(\frac{1}{2}^+; {}^9\text{B})$ to be either 1.36 or 1.74 MeV. On the experimental side, the results have been far from conclusive as well. A ${}^6\text{Li} + {}^6\text{Li}$ reaction [13] speculates the excitation energy lie between 0.8 - 1.2 MeV, in agreement with a Thomas-Ehrman shift that is expected from solely an s -wave proton. Several other experiments have been performed, reporting a highly discrepant excitation energies ranging from $E_x = 0.7$ to 1.9 MeV [14–20] favoring either a cluster-like configuration or a shell-model configuration. The most recent measurements were performed at Munich [18] and RCNP [20] respectively, employing a transfer reaction with the ${}^9\text{Be}({}^3\text{He}, \text{t}){}^9\text{B}^*$. In the former experiment, a DSSSDs array was placed on the right side of the beam axis and was used to tag α -events from the breakup of ${}^8\text{Be}$ nuclei, while in the latter a triton singles spectrum was obtained using the Grand-Raiden spectrometer at 0° , which was deconvoluted using an elaborate procedure. Both these experiments indicated a resonance around 1.85 MeV which agrees with Barker's R-matrix predictions. However, there is no conclusive information in these experiments that obtain the J^π of the observed 1.85 MeV state.

2. Experimental Details

The experiment was performed at the iThemba LABS cyclotron with a ${}^3\text{He}$ beam at an energy of 50 MeV incident on a $600 \frac{\mu\text{g}}{\text{cm}^2}$ self supporting ${}^9\text{Be}$ target (fabricated at the iThemba LABS). The ${}^9\text{Be}({}^3\text{He}, \text{t}){}^9\text{B}^*$ ($Q = -1.0866 \pm 1$ MeV) reaction of interest populated states in the low-lying excitation region in ${}^9\text{B} < 6$ MeV, above the ${}^8\text{Be} + \text{proton}$ threshold. The triton ejectiles were detected and momentum-analysed at the K600 spectrometer (on a 0° configuration) by a multi-wire chamber positioned at the middle-dispersion focal plane and a plastic scintillator detector, the latter was also used for triggering CAKE (Coincidence Array for K600 Experiments) as well as for particle identification purposes. The high-efficiency silicon detector array CAKE was placed inside the scattering chamber at backward angles and is composed by five MMM-silicon detectors, each segmented into 16 independent concentric strips on the front and 8 sectors on the back, with a solid angle coverage of 26% and was used to detect the products from the decay of excited states in ${}^9\text{B}$.

3. Preliminary Analysis

One of the first steps in the reconstruction of the excited region of interest in any K600 experiment is the identification of that particle of interest in the focal plane as shown in Fig. 1. For the present work, the identification of tritons is vital, as mentioned above, as they were utilised as a trigger for CAKE, and subsequently for the generation of the ${}^9\text{B}$ spectra.

Once the tritons have been identified and momentum-analysed a triton spectrum was generated, in which the triton energies correspond to a specific excitation energy of excited states in ${}^9\text{B}$ as it is shown in Fig. 2.

After the excitation region of interest was identified, a two-dimensional plot was generated in order to find the different decay channels of excited states in ${}^9\text{B}$. For this, the focal plane X position is plotted versus those events detected by CAKE as shown in Fig. 3. A time-gate was placed in order to reduce the background and discard random coincidence. Fig. 4 shows the 3 different decay-channels in the reaction, ${}^8\text{Be}_{\text{g.s.}} + \text{proton}$, the ${}^8\text{Be}_{1\text{st}} + \text{proton}$ and the ${}^5\text{Li} + \alpha$ channel.

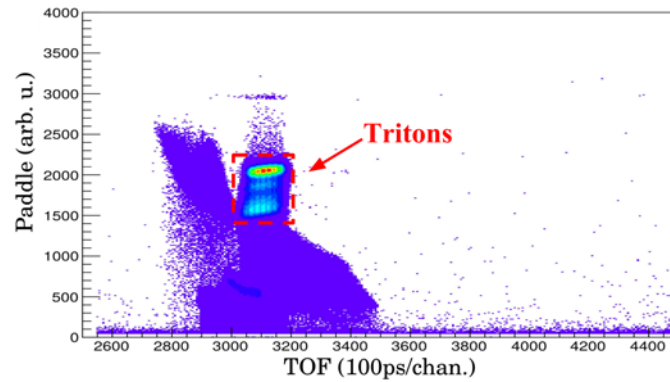


Figure 1. Red dashed-box corresponds to those identified tritons through time-of-flight and energy-loss in the focal plane.

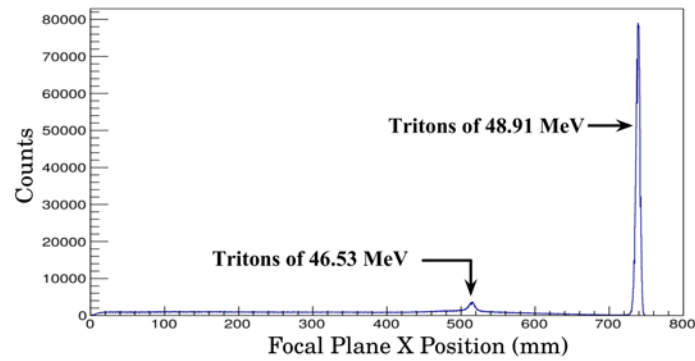


Figure 2. Spectrum of the selected tritons in Fig. 1 corresponding to excited states in ${}^9\text{B}$.

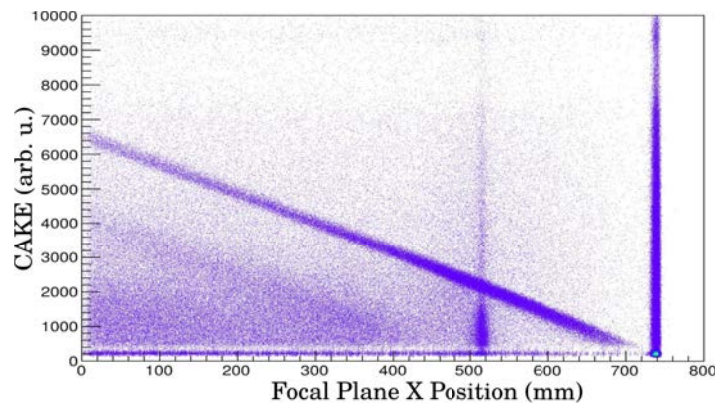


Figure 3. Two-dimensional plot showing triton events at the focal plane versus those detected at the silicon array CAKE.

A calibration of the focal plane was required in order to obtain the precise excitation energy of the populated resonances in ${}^9\text{B}$ (the ground-state, the 2.3 MeV and the 2.7 MeV) as shown in Fig. 5. From this two-dimensional plot, it was possible to generate a gate around the ${}^8\text{Be}_{g.s.} + p$ locus, so the contribution of the sharp 2.3 MeV state was reduced. In Fig. 6 are shown both, the projection of the two-dimensional plot on the x-axis corresponding to the total low-lying

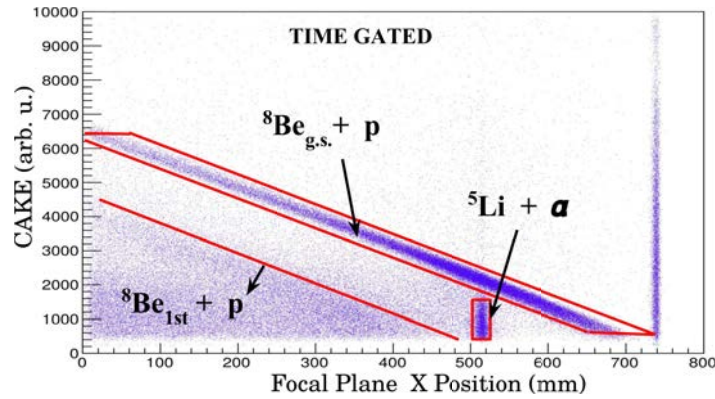


Figure 4. Two-dimensional time-gated plot. From top to bottom, the first diagonal line corresponds to the ${}^8\text{Be}_{g.s.} + p$ decay channel, the second to the ${}^8\text{Be}_{1st} + p$ decay channel and the vertical line to the ${}^5\text{Li} + \alpha$ decay channel.

spectra in ${}^9\text{B}$ and the projection of the gated region around the locus of interest. The latter clearly shows the broad resonances under the sharp 2.3 MeV excited state.

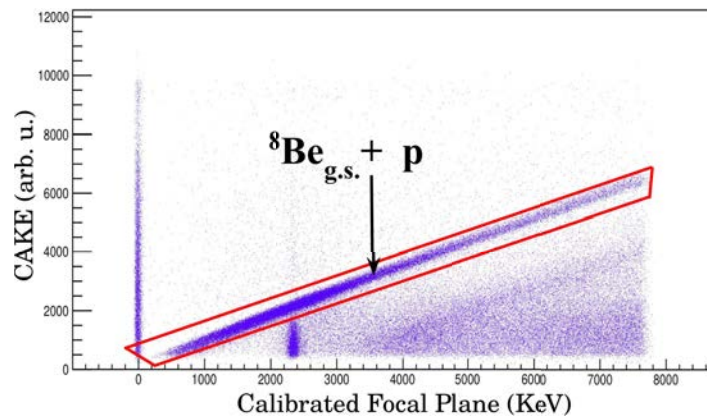


Figure 5. Boron-9 excitation energy versus decay particles detected by CAKE. The ${}^8\text{Be}_{g.s.} + p$ decay channel shown inside the red box.

As shown in Fig. 6, the broad resonance of 2.7 MeV is clearly identified when gating in the ${}^8\text{Be}_{g.s.} + p$, showing the robustness of the coincidence two-dimensional plot, but also it is clear that the identification of a $\frac{1}{2}^+$ state in that range of energy is complicated. As it was mentioned in reference [18], the expected energy of such state should be at or below 1.9 MeV decaying exclusively via the ${}^8\text{Be}_{g.s.} + p$ channel. Further analysis will follow including an angular proton distribution for states of interest, specifically for the first $\frac{1}{2}^+$.

4. Conclusions

An experiment was performed using the ${}^9\text{Be}({}^3\text{He}, t){}^9\text{B}$ transfer reaction at a beam energy of 50 MeV where the low-lying excitation energy region in ${}^9\text{B}$ was populated and identified. The robustness of the detection technique used in the presented work which includes the combination of the K600 and the silicon detector array CAKE for the identification of different decay channels was discussed, being highly efficient in reducing the background and random coincidences. A

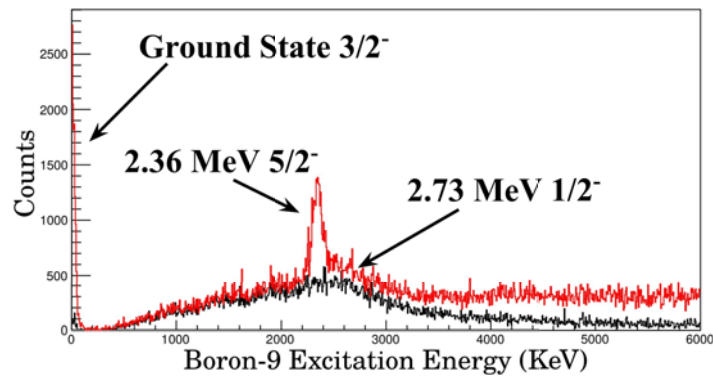


Figure 6. Black color line represents the projection onto the x-axis of Fig. 5 and red line the projection of the gate around the locus of interest showing the broad resonances under the sharp 2.3 MeV peak.

broad energy region below the 2.3 MeV excited state in ${}^9\text{B}$ was identified, which mainly decays through the ${}^8\text{Be}_{g.s.} + p$ channel.

References

- [1] S. E. Woosley and R. D. Hoffman, *Astrophys. J.* 395 (1992) 202.
- [2] L. Buchman *et al.*, *Phys. Rev. C* 63 (2001) 034303.
- [3] W. Von Oertzen, *Z. Phys. A* 354 (1996) 37.
- [4] R. O. Haxby *et al.*, *Phys. Rev.* 1035 (1940) 58.
- [5] R. Sherr and G. Bertsch, *Phys. Rev. C* 32 (1985) 1809.
- [6] R. Sherr, *Phys. Rev. C* 70 (2004) 054312.
- [7] H. T. Fortune and R. Sherr, *Phys. Rev. C* 73 (2006) 064302.
- [8] H. T. Fortune and R. Sherr, *Nucl. Phys. A* 898 (2013) 78.
- [9] P. Descouvemont, *Phys. Rev. C* 39 (1989) 1557.
- [10] K. Arai *et al.*, *Phys. Rev. C* 68 (2003) 014310.
- [11] F. C. Barker, *Aust. J. Phys.* 40 (1987) 307.
- [12] F. C. Barker, *Phys. Rev. C* 79 (2009) 017302.
- [13] T. D. Baldwin *et al.*, *Phys. Rev. C* 86 (2012) 034330.
- [14] M. A. Tiede *et al.*, *Phys. Rev. C* 52 (1995) 1315.
- [15] N. Arena *et al.*, *Europhys. Lett.* 5 (1988) 517.
- [16] M. Bulein *et al.*, *Phys. Rev. C* 38 (1988) 2078.
- [17] W. N. Catford *et al.* *Nucl. Phys. A* 550 (1992) 517.
- [18] C. Wheldon *et al.*, *Phys. Rev. C* 91 (2015) 024308.
- [19] H. Akimune *et al.*, *Phys. Rev. C* 64 (2001) 041305.
- [20] C. Scholl *et al.*, *Phys. Rev. C* 84 (2011) 014308.

The search for crystal undulator radiation

D Boshoff¹, M Copeland¹, F Haffejee¹, Q Kilbourn¹, B MacKenzie¹, C Mercer¹, A Osato¹, C Williamson¹, P Sihoyiya², M Motsoai², M Connell³, CA Henning¹, SH Connell⁴, N L Palmer⁷, T Brooks⁵, J Härtwig^{4,6}, TN Tran Thi⁶, U Uggerhøj⁸ and the PEARL Collaboration⁸

¹St John's College, Houghton, South Africa, ²Barnato Park High School, Berea, South Africa ³King's College London, London, UK ⁴University of Johannesburg, Auckland Park, South Africa ⁵Royal Holloway College, University of London, UK ⁶European Synchrotron Research Facility (ESRF), Grenoble, France ⁷Element Six, Harwell, UK ⁸Århus University, Århus, Denmark ⁹The PEARL Collaboration of the European Commission project H2020-MSKA-RISE-2015

E-mail: shconnell@uj.ac.za

Abstract. The channelling phenomenon applies to the correlated motion of charged particles within a crystal lattice in a direction closely aligned with atomic rows (strings) or crystal planes. When the incident charge particle is highly relativistic, the emitted channeling radiation is boosted by a factor of γ^2 , where γ is the Lorentz factor. Bremsstrahlung may also be coherent for these conditions, and coherent enhancement leads to both quasi monoenergetic peaks and also significant increases in intensity as compared to the normal process. In the special condition that the crystal is periodically bent, such as in a periodic superlattice, one may also have undulator radiation. All of these phenomena are potential sources of MeV and GeV range intense gamma radiation. The latter phenomenon is proposed as potentially the most important source of monochromatic high energy photons. In principle it can also lead to coherent radiation based on the Free Electron Laser (FEL) principle with intensities similar to an extrapolation of what may be obtained at modern light sources. In this contribution we describe a search for crystal undulator radiation using 2.5 – 6.0 GeV positrons incident on a diamond crystal undulator. The experiments were performed at the T9 Beam-line of the Proton Synchrotron at CERN. The experiment was the result of a winning proposal for the 2015 CERN Beam-line for Schools Competition.

1. Introduction

A crystal undulator is similar to a normal undulator [1] as typically found at a synchrotron for the production of extremely brilliant X-ray beams. The difference is that the magnetic lattice is realized by the periodic electrostatic potential of a crystal lattice as seen from the reference frame of an impinging GeV range electron or positron beam. The extremely relativistic incident particle beam has a crystallographically aligned incidence and is captured in a high index crystallographic channel of the crystal superlattice. The crystal lattice undulation period can be in the tens of microns scale. The particle beam will then “see” a many Tesla range periodically varying magnetic field. The larger fields and shorter undulator periods in the crystal undulator as compared to the conventional magnetic lattice undulator are significant. This method could theoretically lead to an MeV range gamma ray laser by the FEL principle.

This paper describes an attempt to commission a tagged photon beamline and then to measure undulator radiation (CUR) at the T9 beam-line of the CERN Proton Synchrotron (PS). The school based authors of this paper developed a successful proposal “Accelerating

Africa” to test a diamond crystal undulator within the CERN Beam-line for Schools [2] project. The goal of the experiment was to search for radiation enhancement effects related to aligned incidence of the positron beam on the diamond superlattice (undulator).

2. Parameters for the diamond crystal undulator

The theoretical feasibility study to produce powerful monochromatic undulator radiation in the gamma ray region by means of a crystal undulator (periodically bent crystal) and ultra relativistic light lepton beams (energy ϵ_{e^+}) impinging on the lattice with incidence aligned to a crystallographic axis is presented in several references [3, 4, 5] and references therein. Figure 1 indicates the trajectory of a charged particle captured in the channeling condition in a low index crystallographic direction. The channelled trajectory has an oscillation within the channel, leading to the emission of channeling radiation (CR, energy ϵ_{ch}). In addition the particle follows the periodic undulations of the lattice, and as such, it will also emit CUR (energy ϵ_u).

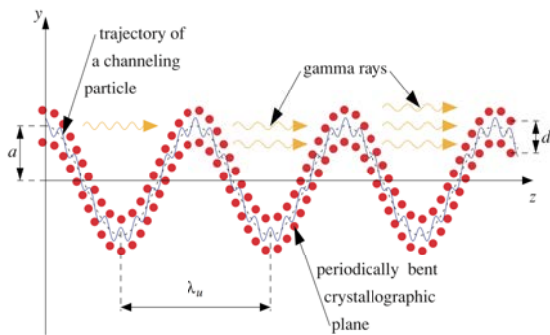


Figure 1: A charged particle captured in a undulating crystal channel [6].

The parameters for a Large Amplitude Long Period (LALP) diamond crystal undulator optimised for the positron beams available at the T9 beamline at the CERN PS are shown in Table 1, where an important condition is $\lambda_u \gg a \gg d$. These symbols are defined in Figure 1. This means $\lambda_u > \lambda_c$ where λ_c is the CR wavelength, so that the CUR will have a lower energy than the CR. There is an alternative scenario known as Small Amplitude Short Period (SASP) where $\lambda_u < \lambda_c$ and where a also has to be small [7]. Table 1 also collects the SASP parameters.

Table 1: Typical physical parameters for a 110 diamond crystal undulator for E_{e^+} few GeV.

Parameter	Value							
ϵ_{e^+} (GeV)	2	3	4	5	6	7	8	9
$L_{e^+}(0)$ (μm)	1059	1563	2061	2553	3042	3528	4012	4493
$L_{e^-}(0)$ (μm)	43	64	86	107	129	150	171	193
ϵ_{ch} (MeV)	9.6	17.6	27.0	37.8	49.7	62.6	76.5	91.3
ϵ_u (MeV) for SASP $\lambda_u = 600$ nm	60	140	240	370	0.52	700	900	1120
ϵ_u (MeV) for LALP $\lambda_u = 10$ μm	2			10				30

For the SASP case, the CUR is of a higher energy than the CR (one source of background). The brehmsstrahlung radiation (BR) has a $1/E_\gamma$ photon energy distribution, which dominates for lower photon energies, so this is the principal source of background, especially for the LALP CUR case. Furthermore, in the SASP case, the undulator layers may be thinner, and therefore, currently, technologically more easily produced. A further effect to consider is the straight crystal dechanneling length $L(0)$, which is much larger for positrons than electrons, but where the overall length should still be minimised. For these reasons, a decision was made to first produce a SASP diamond crystal undulator for positron incidence in the proof of principle experiment.

3. The diamond graded superlattice

Doping diamond with single substitutional atoms of boron dilates the lattice. The boron can be introduced during the growth of synthetic diamond in the Chemical Vapour Deposition (CVD) process in a regulated way, leading to the periodic variation of the lattice constant.

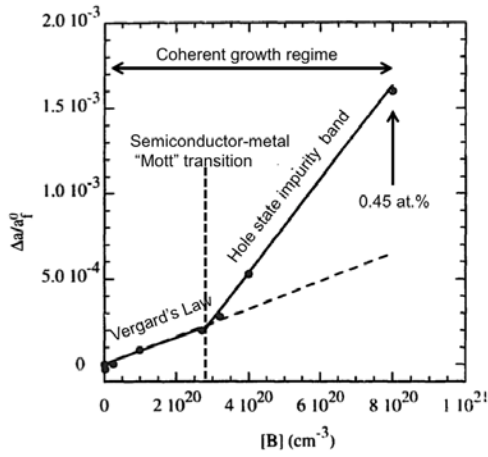


Figure 2: The lattice dilatation due to boron doping in diamond [8].

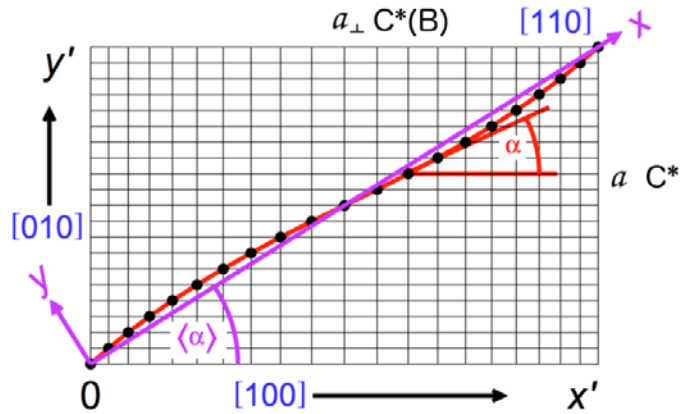


Figure 3: The development of an undulation in the 110 direction due to graded boron doping [9].

The measured lattice dilatation for diamond due to graded boron doping is taken from references [8, 10]. The boron is expected to be uniformly distributed in substitutional sites leading to epitaxial coherent layer growth following the diamond structure up to at least a boron concentration of $C_B = 0.45\%$ (atomic). At first the dilatation effect proceeds based on Vergard's Law, and when the Mott transition is reached, the expansion is faster as the hole state impurity band modifies the Fermi level. Figure 2 quantifies this behaviour. The intrinsic substrate constrains the lattice to an expansion only in the growth direction, as shown in Figure 3. This longitudinal elongation is known as the Poisson effect and can be quantified using the elasticity constants for diamond together with the quantified dilatation behaviour, as well as a model for the progression of the undulator effect, as in the reference [9]. This leads to the determination of the undulation amplitude as a function of the boron doping concentration. This has been done in [9] but also in more detail with direct modelling in [11].

Element Six Technologies prepared a CVD grown diamond crystal undulator with the parameters $\lambda_u \approx 0.6 \mu\text{m}$ and $a \approx 0.4 \text{ \AA}$ with 6 such undulator layers on a $300 \mu\text{m}$ High Pressure High Temperature (HPHT) synthetic diamond type Ib 110 oriented substrate. The diamond undulator was roughly pre-aligned using an on-line X-ray Laue system at the University of Johannesburg and then fine aligned using a highly collimated Bragg condition X-ray Diffraction.

4. Experimental Details

The measurements were performed at the T9 area of the PS at CERN in September 2015. A primary 24 GeV/c proton beam produced a series of secondary beams from a carbon production target, including kaons, pions, muons and electrons and their antiparticles. We have focused on the positrons in the few GeV energy range. Two Cerenkov detectors were set to discriminate the particle identity (PID). A dipole magnet and a collimator set the momentum byte for the experiment. The incident flight path traversed a scintillator (Scint1) for triggering and a second veto scintillator which defined the beam position on the crystal. The first two Delay Wire Chambers (DWC1 and DWC2) provided transverse spatial hit position measurement ($\Delta x \approx 200 \mu\text{m}$). The incident phase space of each particle trajectory could then be measured ($\Delta \theta \approx 500 \mu\text{rad}$). The charged particles could be swept away with the dipole magnet after the crystal position and their momentum reconstructed from their deflection as measured in the third chamber (DWC3). The radiated photon(s) captured in the photon calorimeter (BGO) could be tagged with PID and the momentum of the radiating particle. Calorimetry of the charged particles was performed in a lead glass calorimeter array. Figure 4 illustrates this

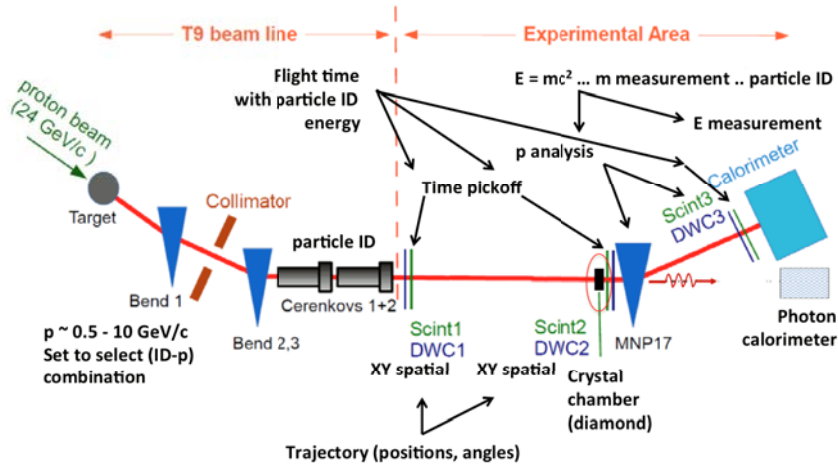


Figure 4: The tagged photon beam-line at the PS-T9 area at CERN (modified from [2]).
discussion.

5. Analysis of Data

5.1. Initial validation

The data was available as an event by event stream in a ntuple which could be processed offline using the ROOT C++ analysis framework [12]. Particle tracking, particle identification, incident angle reconstruction, particle deflection, particle energy and momentum measurement, photon energy measurement, photon tagging could all be successfully established and validated. Some of these steps are described below.

5.2. Drift-chamber commissioning

Figure 5 below left shows the expected linear correlation between the positron hit position for the x-axis on the first two delay wire chambers, DWC1 and DWC2. The full beam envelope has been filtered in reconstructed incident angle phase space to show only those trajectories closely parallel to the ideal central path. The neighbouring plot shows the difference between the actual hit position on the last delay wire chamber, DWC3, and the projected hit position based on the trajectory reconstructed from DWC1 and DWC2. The third DWC3 could be used to measure the deflection and hence reconstruct the momentum of the beam after the dipole MNP17 in Figure 4. A positron which radiated a photon would have a hit in DWC3 with a greater deflection (lower momentum). Gating on positrons which radiated was used indicating the facility had a tagged photon beam-line.

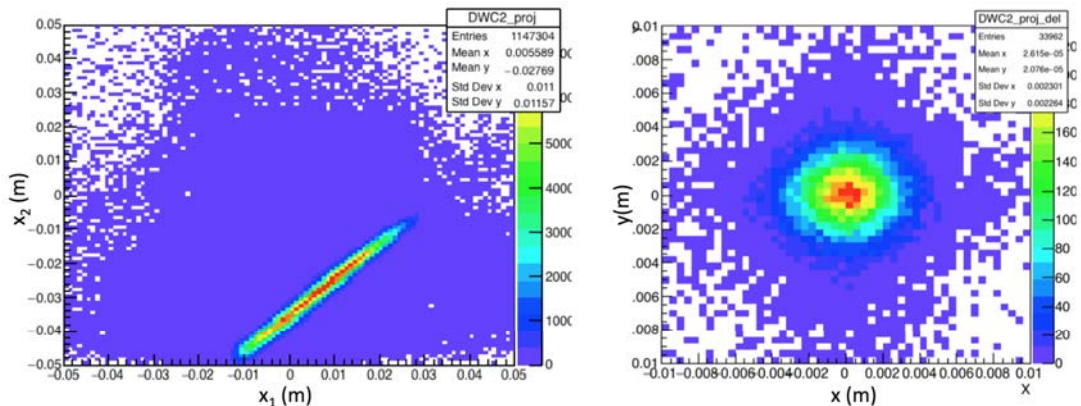


Figure 5: The correlation between x-DWC1 and x-DWC2 (left) and the difference between the actual hit position on DWC3 and the projected hit position based on the trajectory reconstructed from DWC1 and DWC2 (right)

5.3. Event selection and background reduction

The red and black scatter plots in Figure 6 below show the evolution of the beam envelope in DWC1, DWC2 and DWC3 when a elliptic cut is made on the first DWC1. The veto scintillator is next to DWC2, and the operation of this device is clear. The incident angle (θ_x, θ_y) for each particle could be calculated, and a further cut could be made within this two-dimensional phase space, restricting the divergence within the beam envelope. The final plot in Figure 6 is the photon spectrum in the photon calorimeter for a calibration positron beam energy of 1 GeV. All the curves exhibit a positron peak at the nominal beam energy, as well as a broad photon spectrum with the typical $1/E$ shape for bremsstrahlung. A peak due to muons passing through the photon calorimeter with the fixed energy loss of minimum ionising particles is also evident at 0.25 GeV. The bremsstrahlung background could be reduced and the muons could be excluded by the filters described above.

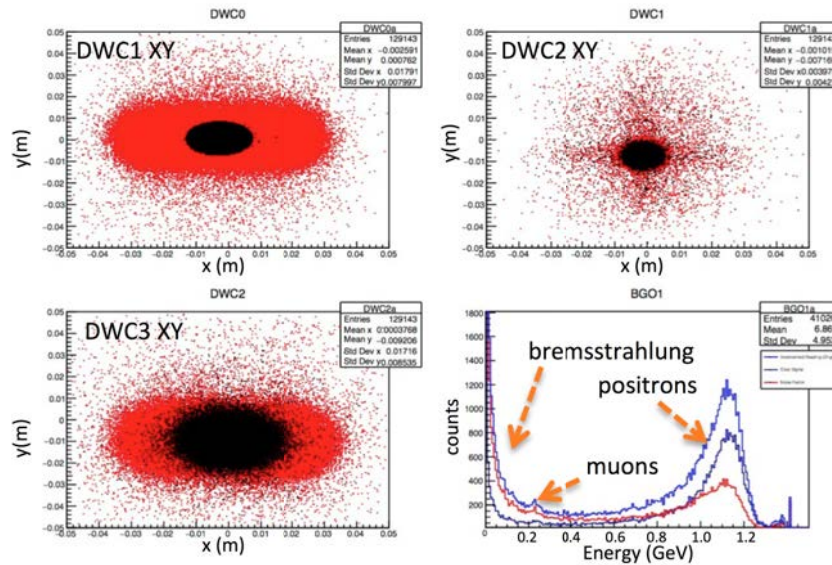


Figure 6: Scatter plots for the three DWCs under the conditions described in the text above. The last plot is the photon spectrum from the photon calorimeter.

5.4. Selection of events aligned to the crystal axis

The critical angle for CR for 6 GeV positrons incident on the 110 axis of diamond is $\theta_c = 86 \mu\text{rad}$.

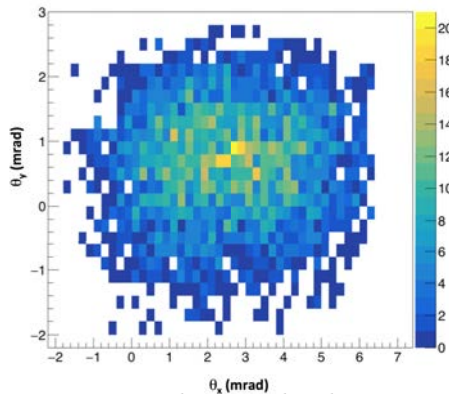


Figure 7: Incident angle phase space.

The two dimensional incident angle phase space plot on the left shows that the useful beam divergence had a range of $\Delta\theta_x = 3 \text{ mrad}$ and $\Delta\theta_y = 6 \text{ mrad}$. The angular resolution is about 0.3 mrad . This was larger than anticipated and would smear out evidence of enhanced yield for aligned radiation phenomena. The incident angle space was scanned for enhanced radiation yields based on CR and coherent enhanced BR, in order to fine-align the diamond to the beam axis. Graphical cuts were placed to define the incident angle phase space leading to aligned or non-aligned radiation phenomena. The Figures 8

(filtering events away from axial / planar incidence) and 9 (filtering events close to axial / planar incidence) below are examples of this, where the former yields the expected flat spectrum for BR.

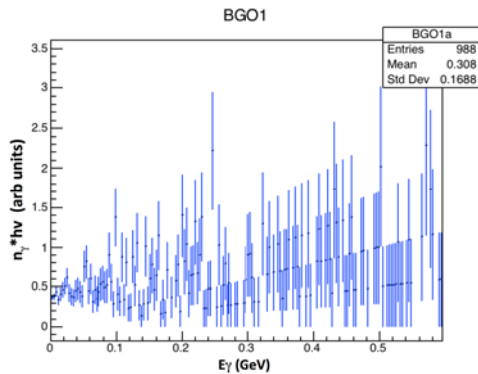


Figure 8: Photon calorimeter selecting for non-aligned incidence events.

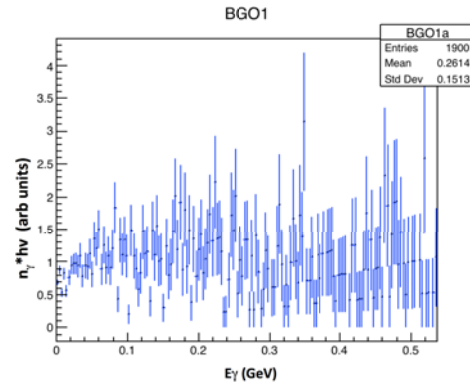


Figure 9: Photon calorimeter selecting for aligned incidence events.

6. Conclusion

In the experiment time available it was possible to successfully commission the T9 beam-line of the CERN PS as a tagged photon beam-line. In this set-up, there was large BR background mostly resulting from beam-air interaction upstream of the target. The DWCs unfortunately had a poor resolution, leading to insufficient angular resolution. Suggestive but inconclusive results were obtained (higher radiation yields for aligned incidence). Nonetheless it was sufficiently promising to show that given certain improvements, the T9 beamline could indeed be expected to perform sufficiently well to search for CUR in a future experiment.

7. Acknowledgements

The authors thank CERN for the successful operation of the T9 beamline of the CERN PS in the CERN Beamline for Science project.

References

- [1] Paroli B and Potenza M 2017 *Advances in Physics X* 2-3 978–1004
- [2] 2015 *CERN Beamline for Schools* URL <http://beamline-for-schools.web.cern.ch>
- [3] Tabrizi M, Korol A V, Solov'yov A V and Greiner W 2007 *Physical Review Letters* **98** 164801
- [4] Korol A V, Solov'yov A V and Greiner W 1998 *Journal of Physics G* **24** L45
- [5] Korol A V, Solov'yov A V and Greiner W 1999 *International Journal of Modern Physics* **E8** 49
- [6] Kostyuk, A et al 2009 *J. Phys. G: Nucl. Part. Phys.* **36** 025107
- [7] Kostyuk A 2013 *Phys. Rev. Lett.* **110** 115503
- [8] Brunet F, Germe P *et al.* 1998 *Diamond and Related Materials* **7** 869–873
- [9] Backe H, Krambrich D and *et al* 2013 *Diamond and Related Materials* **309** 37–44
- [10] Guzmán de la Mata B *et al* 2007 *Diamond and Related Materials* **16** 809–814
- [11] Krause W, Korol A, Solov'yov A and Greiner W 2002 *Nucl. Instrum. Methods A* **483** 455–460
- [12] Brun R and Rademakers F 1997 *Proceedings AIHENP'96 Workshop, Lausanne, Sep. 1996, Nucl. Inst. & Meth. in Phys. Res. A* **389** 81–86 URL <http://root.cern.ch/>

Proton induced radiation damage to the fluorescence capability of plastic scintillators for the Tile Calorimeter of ATLAS

H Jivan^{1,2}, R Erasmus¹, M Madhuku³, B Mellado¹, G Peters¹ and E Sideras-Haddad^{1,2}

¹ University of the Witwatersrand, 1 Jan Smuts Avenue, Braamfontein 2000, Johannesburg.

² DST-NRF Centre of Excellence in Strong Materials.

³ iThemba LABS, North, Empire Road, Braamfontein 2000, Johannesburg.

362863@students.wits.ac.za

Abstract. The Tile Calorimeter of the ATLAS detector relies on plastic scintillators to aid in the energy reconstruction of hadrons, taus, and jets of quarks and gluons that arise from the proton-proton collisions within the Large Hadron Collider of CERN. These scintillators are exposed to harsh radiation environments and therefore sustain damage. In 2018, current plastic scintillators employed in the Gap region of TileCal will be replaced with more radiation tolerant plastics. A series of investigations are currently being conducted into the radiation hardness of several polyvinyl toluene (PVT) and polystyrene (PS) based plastic scintillators which are candidates for the upgrade. In this study, we investigate the damage induced by 6 MeV protons to the light fluorescence capability of 350 μm thick scintillators. Presented here are the results of the damage for proton doses ranging between 800 kGy to 80 MGy conducted using the 6 MV tandem accelerator of iThemba LABS.

1. Introduction

Plastic scintillators are organic materials which undergo luminescence upon interaction with ionizing radiation. They are employed by the Tile Calorimeter of ATLAS, to detect the hadronic particles which result from the proton-proton collisions within the Large Hadron Collider of CERN [1]. Their properties of high light output and high optical transmission ensure that good resolution in measurements can be achieved. Their fast rise and decay times are ideal since fast timing responses are required by the detector. The main problem encountered by plastic scintillators however, is radiation damage incurred due to their interactions with the ionizing particles to be detected. This damage leads to a significant decrease in the light yield of the scintillator and may compromise the detectors performance.

With the LHC gearing up to run proton collisions at increased center of mass energy, with luminosities of a factor of 10 beyond the current design value by 2022, the radiation environment within the ATLAS detector is expected to become much harsher. The Tile Calorimeter has therefore implemented a series of upgrades in order to ensure that the detector performance can be sustained for several years to come. Part of phase two of this upgrade will be implemented in 2018 where scintillators from the GAP region of the Tile Calorimeter will be replaced with more radiation hard

plastics. To aid in the choice of a replacement candidate, a series of investigations which examine the radiation hardness of several commercially available plastic scintillators have been conducted. In this paper, results on the impact of radiation damage to the fluorescence capability of PVT and PS based plastic scintillators is presented.

2. Background

Plastic scintillators generally consist of organic fluors suspended in a polymer base. Ionizing radiation causes the molecular excitations of delocalized π -electrons typically in the base. These may de-excite through several mechanisms [2], i.e. fluorescence, phosphorescence, delayed fluorescence, radiationless internal conversion or vibrational losses. The fluorescence process occurs for transitions from the lowest vibrational first excited state to the ground state whereby energy is emitted in the form of light of a characteristic wavelength. This wavelength ranges around 300-350 nm in general for polymer bases. The base however, tends to have a low fluorescence light yield due to the small Stoke's shift between their excitation and emission ranges.

Primary fluors are thus added in small concentrations (typically < 3% by weight). These are chosen such that their absorption spectra match the emission spectra of the base and generally contain a high quantum yield of the energy transfer transition. Light can be transferred between base and fluor via either radiative re-absorption, or by a non-radiative coulombic interaction called Forster resonance energy transfer. [3]

Forster energy transfer is limited by the distance between the interacting states and is therefore more likely to occur with increasing fluor concentrations until a saturation is reached. Light is then emitted by the fluors at higher wavelengths, generally in the UV range of 350-400 nm. Since this wavelength is still below the peak efficiency of common photomultipliers, a secondary fluor is added at concentrations of < 0.1% by weight. The secondary fluor acts as a wavelength shifter (shifting emission to 400-500 nm) and prevents re-absorption of scintillation light by the primary fluor. It also helps to increase the bulk attenuation length of the emitted light. Energy transfer between the primary and secondary fluors occurs via radiative exchange. [3]

Whilst ionizing radiation may lead to molecular excitations and hence scintillation, prolonged exposure can also cause the breaking of chemical bonds thereby modifying the polymer properties. The optical properties of the scintillator can be effected in two ways, either a decrease in actual scintillation light output due to damage to the fluorescent component, or through a degradation in its transmission character as a result of the formation of optical absorption centres. The change in transmission character further affects the light attenuation length of the scintillator.

In [4], preliminary transmission and Raman studies on 6 MeV proton irradiated PVT samples of 250 μm thickness were presented. The study looked at irradiated doses of ~ 1.8 kGy, 164 kGy and ~ 1 -1.5 MGy. At these doses, an increase in transparency over the wavelength region of 300 - 410 nm was observed for the blue emitting scintillators, whilst an absorptive tint began to form for the green emitting scintillator. In [5], the study was extended to cover doses of approximately 0.8 MGy, 8 MGy, 25 MGy and 80 MGy in 350 μm thick samples where visible discolouration in samples developed. At these higher doses, the absorptive tint shifted to higher wavelengths with increasing dose and could be correlated to free radical production.

3. Methods and materials

The main properties of the scintillators under study are summarised in table 1. The light output is given relative to the light output of anthracene which has the highest known light output amongst all organic scintillators. The scintillator response times are given in terms of the rise time and decay time. The rise time characterizes the sharp increase in intensity of a measured scintillation light pulse, whilst the decay time measures the time taken for the intensity to exponentially drop to $1/e$ of the maximum value. The wavelength at which maximum intensity of light emission occurs is also given.

EJ208 emits at a slightly higher wavelength as compared to the other blue scintillators, whilst EJ260 emits in the green range. These higher wavelength shifting scintillators are marketed for

exhibiting greater radiation tolerance since radiation damage causes the optical attenuation of light across the lower visible wavelength range [6].

Samples cut and polished to dimensions of 5 mm by 5 mm and of 350 ± 30 μm thickness were subjected to 6 MeV proton irradiation using the 6 MV tandem accelerator (operated at 3 MV) at the iThemba LABS, Gauteng. The procedure for irradiations has been described previously in [4] and [5]. The light fluorescence of each plastic scintillator was measured using the LabRAM HR Raman spectrograph. A 229 nm laser with a power of $\sim 3\text{-}5$ mW was employed to provide energy for molecular excitations to occur and thereby prompt light emission through luminescence. At this wavelength, the laser energy is sufficient to be absorbed by the PS or PVT base, and the successive light transfer from base to primary and secondary fluors can occur.

Table 1: Properties of the scintillators under study.

	EJ200	EJ208	EJ260	BC408	UPS923A	TileCal
Manufacturer:	Eljen Technology	Eljen Technology	Eljen Technology	Saint Gobain Crystals	Institute of Scintillating Materials, Kharkiv.	Institute of High Energy Physics, Protvino in association with SIA IChP, Podolsk.
Base	PVT	PVT	PVT	PVT	PS	PS
Primary Fluor	0.3% organic fluors	0.3% organic fluors	0.3% organic fluors	Not available (However, listed as a performance equivalent of EJ200)	2% PTP	1.5% PTP
Secondary Fluor					0.03% POPOP	0.044% POPOP
Light Output (% Anthracene)	64	60	60	64	60	
Wavelength of Max. Emission (nm)	425	435	490	425	425	Not available
Rise Time (ns)	0,9	1	~	0,9	0,9	
Decay Time (ns)	2,1	3,3	9,2	2,1	3,3	
Source	<	[6]	>	[7]	[8]	[9]

Photographs of the LabRAM HR are shown in figure 1. The laser is guided through a series of mirrors and optics in the machine, and is incident on the sample through the Olympus microscope aperture. As the sample fluoresces, the backscattered light is passed through a 150 lines/mm grating and collected by a CCD detector to obtain a differential wavelength spectrum.

The main obstacle to overcome during testing, was the effect of photo-bleaching of the fluorescent light. For excitation wavelengths below 250 nm, photo-bleaching occurs more prominently since the probability of exciting the electron to the triplet state increases. This is a stable state with a long lifetime and can interact with other molecules to produce irreversible covalent modifications. Photo-bleaching therefore results in a decrease to the fluorescence yield since molecules undergo photon induced chemical damage.

The destruction of the molecule is proportional to the emission intensity, the emission time and the number of excitation and fluorescence cycles undergone. In order to reduce the effect of photo-bleaching undergone during testing, the laser was scanned over a 20x20 μm^2 area and the acquisition time was limited to one second per spot tested.

Three spots along the irradiated region and three spots along the un-irradiated regions of each sample were tested in order to gauge the ratio of loss to fluorescence yield over the wavelength range of 350-500 nm.



Figure 1: (a) Back view showing the path travelled by the laser into the LabRAM HR, (b) front view of the spectrograph, (c) enlarged view of the sample undergoing fluorescence

4. Results of fluorescence testing

The fluorescence spectra for EJ200 samples are shown in figure 2. An indication of the visual discolouration of the irradiated spot for the approximate dose exposures are also shown. A similar trend in the loss to fluorescence peak features were observed for the other scintillator types [10].

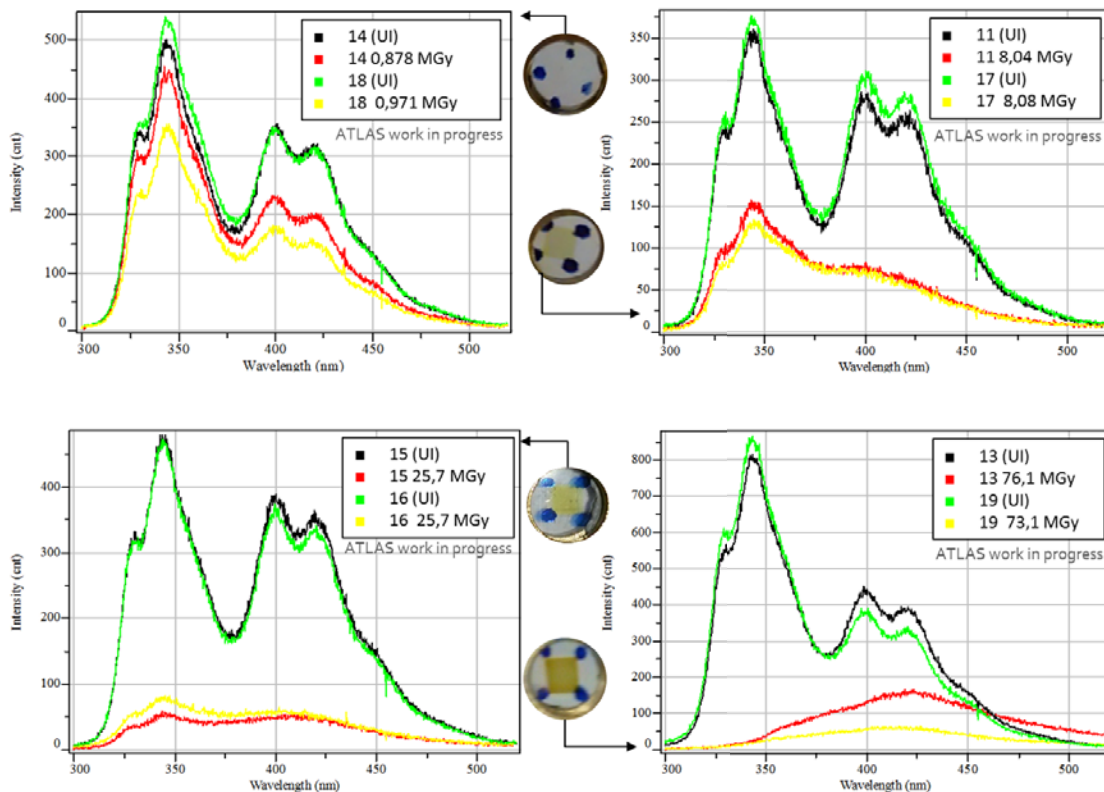


Figure 2: Fluorescence spectra of 350 μm thin EJ200 samples after exposure to several doses of 6 MeV protons

The fluorescence spectra in the un-irradiated EJ260 samples showed a very small amount of fluorescence over the 450-500 nm region despite its wavelength of maximum emission being at 490 nm. It was realized that since backscattered fluorescence light was detected, a large component of the measured light could have been from the surface which could have had less interaction with the fluors. Hence, a large component of “un-shifted” base scintillation light was measured.

For doses of ~0.8-1 MGy, an overall intensity loss occurs, with a more distinct loss to fluorescence peaks at the higher emission regions of 375-500 nm. This wavelength range correlates with emission expected from the fluor dopants. At this dose, very minimal transmission losses were observed, although a feature indicating loss to absorption by the fluors occurred. At progressively higher doses, the fluorescence intensity is further decreased, with significant loss to base emission peaks and fluor emission peaks. At the 70-90 MGy dose range, a very weak signal is obtained with an additional peak feature appearing in some of the spectra. This peak feature could not be correlated to any particular damage effect and may be influenced by several factors such as sample thickness and irradiation dose rate.

In order to compare the effect of fluorescence loss against radiation dose for the different scintillator types, a ratio between the integrated spectra over 350-500 nm, for the irradiated and un-irradiated regions were computed. A crude exponential fit was implemented to the data in order to provide a rough visual guide of the overall trend. This plot is shown in figure 3. The different scintillators perform within a 20% variation of each other. EJ208 exhibits the least fluorescence ratio loss, with UPS923A scintillators performing comparably against it, particularly at the higher dose exposures. The TileCal scintillators perform well against loss at the low doses, but lose light much faster at higher doses. After 25 MGy, EJ200 performs on par with EJ208 and UPS923A.

The results for EJ260 are not a true performance indicator as a very small component of the wavelength-shifted fluorescence was measured. In the Tile Calorimeter however, scintillation light is collected by wavelength shifting optical fibers which then lead to photo-multiplier tubes. The fibers presently used, Y11 fibers from Kuraray, have an absorption range of 420-450 nm and peak at 430nm. EJ260 therefore will not couple well to these fibers.

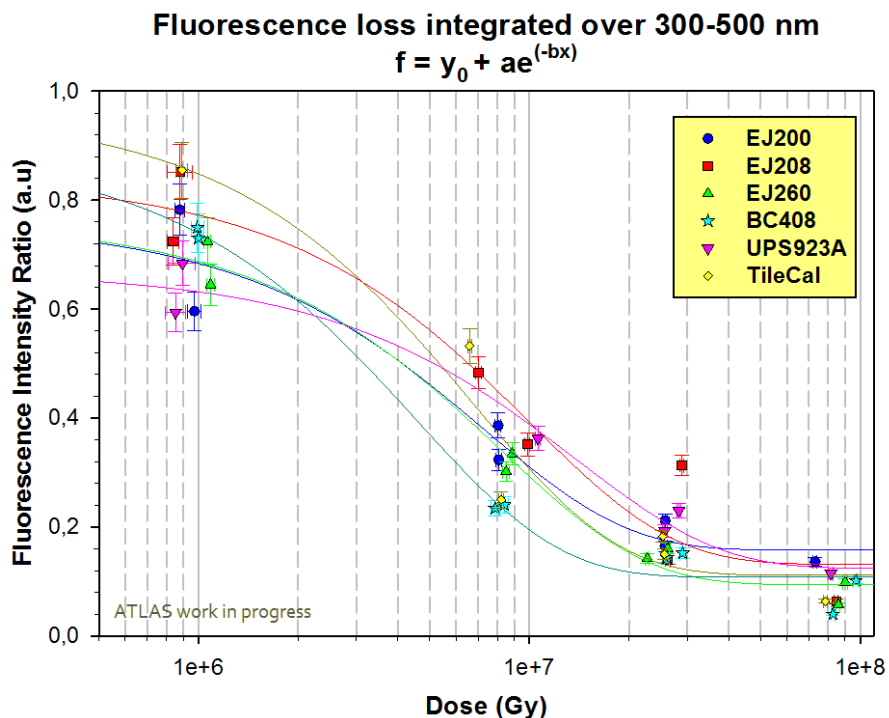


Figure 3: Ratio of fluorescence integrated over 300-500 nm for irradiated and un-irradiated regions of plastic scintillator samples.

5. Conclusion

The effect of 6 MeV proton induced radiation damage to the fluorescence capability of 350 μm thin PVT and PS based plastic scintillators was investigated. Fluorescence was measured off the surface of the samples using a 229 nm laser excitation. The following results were deduced:

- Fluorescence loss increases exponentially with increasing dose exposure.
- For doses below 1 MGy, a portion of the fluorescence arising from the added fluors is lost. Since a decrease in absorption corresponding to the fluors occurs for this dose as well, a bleaching-like effect may be the cause of damage to the fluors.
- As the dose exposure progresses to 8 MGy and above, fluorescence loss occurs for both the base and fluor emission regions. This ties in with Raman studies in [5], indicating that structural damage occurs to the polymer base. Colour centres or free radicals formed through the damage processes compete for absorption of base emitted light as well as some visible light over the lower blue region [5].
- At 70-90 MGy, minimal fluorescence over the fluor emission region is observed, whilst the base component of emission is lost. The different scintillator grades perform within a 20% variation of each other, with EJ208 exhibiting the least loss in fluorescence ratio.

A large component of the fluorescence light measured in this experiment was un-shifted light from scintillation off the polymer base since the geometry of the set-up minimised spatial interaction. Within the TileCal, scintillators employed are much larger and bulk effects play an important role in the scintillators performance. Whilst studying the thin samples give an indication of the finer damage mechanism at play, a study of the bulk effects is imperative for choosing the replacement candidate for the TileCal. Future work will therefore study the attenuation length and transmission of scintillation light in thick scintillators. Damage to the overall light loss in scintillator-fiber coupled systems will also be investigated. In addition, investigations using neutron irradiation are ongoing, and a new inorganic LYSO scintillation crystal is being added to the study.

Acknowledgments

The financial assistance of the National Research Foundation (NRF) and the DST-NRF Centre of Excellence in Strong Materials (CoE-SM) as well as the support of the University of the Witwatersrand towards this research is hereby acknowledged.

References

- [1] ATLAS Collaboration 2008 *The ATLAS Experiment at the CERN Large Hadron Collider* (IOP Publishing and SISSA)
- [2] Knoll G F 1999 *Radiation Detection and Measurement, Third Edition* (Michigan: John Wiley & Sons Inc.) chapter 8 pp 220-222
- [3] Zorn C 1993 A pedestrian's guide to radiation damage in plastic scintillators *Radiat. Phys. Chem.* **41** 37-43
- [4] Jivan H *et al* 2015 *Radiation hardness of plastic scintillators for the Tile Calorimeter of the ATLAS detector*, in Proceedings of SAIP2014, (University of Johannesburg), pp. 199 - 205. ISBN: 978-0-620-65391-6.
- [5] Jivan H *et al* 2015 Radiation hardness of plastic scintillators for the Tile Calorimeter of the ATLAS detector *J. Phys.: Conf. Ser.* **623** 012016
- [6] ELJEN Technology 2013 *Products: Plastic Scintillators* [Online]. Available: <http://www.eljentechnology.com/index.php/products/plastic-scintillators>.
- [7] Saint-Gobain 2015 *Plastic Scintillators Specifications* [Online]. Available: http://www.crystals.saint-gobain.com/Plastic_Scintillators.aspx.
- [8] ScintiTech 2014 *Products: Plastic Scintillators* [Online]. Available: <http://www.scintitech.com/CompanyPage.aspx?MenuId=39&MainId=3>.
- [9] Karyukhin A *et al* 1996 *Injection molding scintillator for ATLAS Tile Calorimeter* ATL-TILECAL-96-086, ATL-L-PN-86
- [10] Jivan H 2016 *Proton induced radiation damage studies on plastic scintillators for the Tile Calorimeter of the ATLAS detector* (Master's dissertation) [Online]. Available: <http://wiredspace.wits.ac.za/handle/10539/21672>

Estimation of jet-faked muon background in W-boson scattering at $\sqrt{s} = 13$ TeV with the ATLAS detector

Lucas Michael Henry McConnell

Supervised by: Dr A. Hamilton and Dr S. Yacoob

Department of Physics, University of Cape Town, South Africa

E-mail: lucas.mcconnell@cern.ch

Abstract. $W^\pm W^\pm \rightarrow W^\pm W^\pm$ is a rare Standard Model process which can be used to investigate the spontaneous symmetry breaking present in the Standard Model. Previous analysis, using $\sqrt{s} = 8$ TeV proton-proton collision data recorded by the ATLAS detector at the Large Hadron Collider, of events with two reconstructed same sign leptons ($e^\pm e^\pm, e^\pm \mu^\pm$, and $\mu^\pm \mu^\pm$) and two jets were analysed and $W^\pm W^\pm jj$ production cross sections were measured. First evidence for $W^\pm W^\pm jj$ production was observed to a significance of 4.5σ . Starting in 2015, analysis is underway to attempt to increase the significance for the measurements using $\sqrt{s} = 13$ TeV proton-proton collision data recorded by the ATLAS detector at the Large Hadron Collider. Since the process is very rare, it is dominated by various backgrounds, one of which is $t\bar{t}$ decay. In this presentation we discuss estimating the fake muon background coming from $t\bar{t}$ decay using Monte Carlo simulations.

1. The Standard Model of Particle Physics

The Standard Model [1, 2, 3, 4] of particle physics was developed in the latter half of the twentieth century. It describes how matter is comprised of point-like, basic building blocks called fundamental particles, and interacts via four fundamental forces. The Standard Model has successfully been tested many times and is widely regarded as the most accurate and stable [5] model of particle physics.

The Standard Model classifies the fundamental particles that make up matter into either lepton or quarks. Both leptons and quarks comes in three so-called generations, with the members of the first generation being the lightest and most stable, while those of the third generation are the heaviest and least stable. In ascending order of generation the leptons are: the electron and electron neutrino, the muon and muon neutrino, and the tau and tau neutrino. These particles possess half-integer spin and are known collectively as *fermions*.

The Standard Model describes three of the four fundamental interactions in nature. In increasing order of strength, these are the weak, electromagnetic, and strong forces. According to the Standard Model, the strong, weak, and electromagnetic forces result from the exchange of force-carrier particles. These force carriers possess integer spins and are collectively called *bosons*. Specific bosons are said to mediate a particular force. The strong force is mediated by the gluon, the electromagnetic by the photon, and the weak by the W and Z bosons.

A deficiency of the Standard Model is that it does not describe the gravitational interaction. Theories that seek to expand upon the Standard Model in order to incorporate gravity are said to be "beyond" the Standard Model.

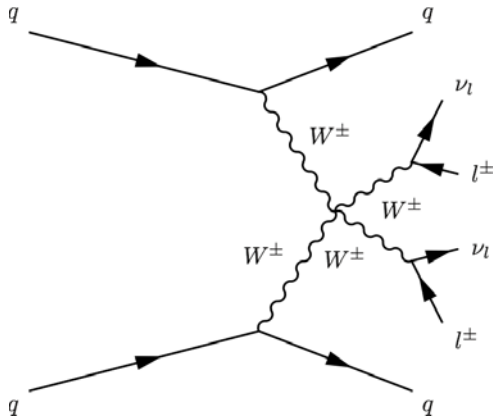


Figure 1: Feynman diagram showing the scattering of two same-sign W -bosons which subsequently decay leptonically.

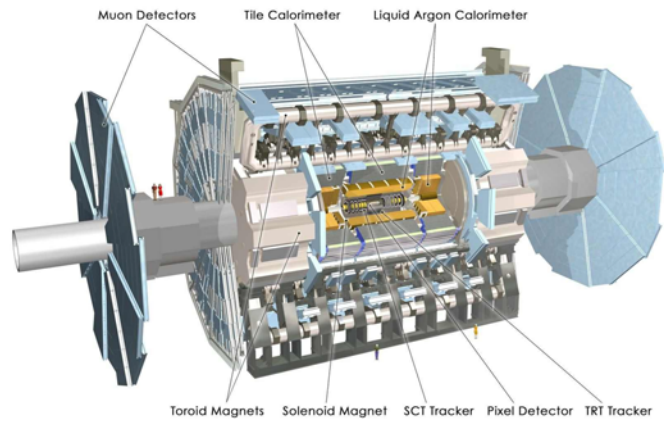


Figure 2: Cut-away view of the ATLAS detector showing its various components. [6]

2. The ATLAS Detector

Some of the experimental confirmation of the Standard Model has come from the European Organization for Nuclear Research (CERN) in Switzerland. In particular CERN is home to the largest and most powerful particle accelerator in the world: the Large Hadron Collider (LHC) [7]. The ATLAS (A Toroidal LHC Apparatus) detector [8] is one of the seven particle detectors at the LHC and is one of two general purpose detectors designed to take advantage of the unprecedented energy available at the LHC and investigate physical phenomena that involve high mass particles that were not previously observable at earlier low-energy accelerators. In particular the ATLAS experiment has been involved in the search for the Higgs boson [9], extra dimensions and dark matter particles [10]. ATLAS is 46 metres long, 25 metres in diameter and has a mass of about 7000 tonnes.

3. W-Boson Scattering

The scattering of W -bosons can be a useful process in the probing of electroweak symmetry breaking. Without a Higgs boson the longitudinally polarised amplitude of W -boson scattering violates unitarity when the WW centre-of-mass energy exceeds approximately 1 TeV [11, 12, 13]. With the discovery of the 125 GeV Higgs boson [9, 14], the high energy value of the cross-section again becomes unitarised within the Standard Model, giving insight as to whether it is the Standard Model Higgs boson.

The W -boson scattering can be either opposite-sign $W^\pm W^\mp$ or same-sign $W^\pm W^\pm$. The case of opposite-sign scattering is dominated by background contributions from *Quantum Chromodynamics* (QCD). This is however not the case for same-sign scattering, making it the preferable channel for analysis. Considering the leptonic decays of the W -boson, the distinctive experimental signature for this study is then two same-sign leptons ($e^\pm e^\pm, e^\pm \mu^\pm, \mu^\pm \mu^\pm$), along with two jets, and missing transverse energy from neutrinos. This is graphically represented in Fig (1).

First evidence for same-sign WW ($ssWW$) scattering using $\sqrt{s} = 8$ TeV proton-proton collision data was found with a significance of 4.5σ by ATLAS [15], while a similar analysis by the CMS experiment [16] found a significance of 2.0σ . These proceedings report on some of the work to increase the significance for the measurement using $\sqrt{s} = 13$ TeV proton-proton collision data recorded by the ATLAS detector.

4. Fake Lepton Background

Leptons coming from a W -boson are said to be prompt, while those those coming from the decay of a hadron are said to be non-prompt. Non-prompt leptons contribute to background in events selected for $ssWW$ measurement. This background is subsequently referred to in this note as the *fake lepton background*. The dominant contribution to the fake lepton backgrounds comes from the process $t\bar{t} \rightarrow WbWb \rightarrow l\nu b\bar{b}q\bar{q}$.

The degree to which leptons are *isolated* can be used to reduce the fake lepton background. Isolation is a measure of the number of particles produced in a cone in $\eta - \phi$ space, defined by $\Delta R = \sqrt{(\Delta\eta)^2 + (\Delta\phi)^2}$, with η being pseudorapidity and ϕ being the azimuthal angle, around the detector signature corresponding to the reconstructed lepton. “ $p_{Tcone20}$ ” is the sum of the transverse momenta of all tracks within a cone of $\Delta R = 0.20$, while “ $e_{Tcone20}$ ” is the sum of the transverse energy within a $\Delta R = 0.20$ centred on the lepton’s deposit in the calorimeter. Since hadrons are often produced in collimated flows, called jets, fake leptons are less likely to be isolated than prompt leptons. The primary goal of this work is to optimise the event selection criteria related to the lepton isolation to reduce the *fake lepton background*.

5. Results

The plots shown in Fig (3). display the isolation variables for muons with three different origins. The $t\bar{t}$ sample is produced using the *PowHeg-Box* event generator [17], while $ssWW$ sample is produced by the *Sherpa* event generator [18]. Using a $t\bar{t}$ sample as a background, reconstructed muons were matched to truth muons using the standard ATLAS Mone Carlo (MC) truth classifier tool. It was found that the majority of the background muons come from either W -bosons (63%) or b -mesons (12%), representing a prompt and non-prompt background respectively.

These backgrounds are plotted with the $ssWW$ sample. Note that the muons from the $ssWW$ and the prompt background muons are similarly isolated since both originate from W -bosons. The muons coming from b -mesons are less isolated, indicative of the muon having originated from a jet. A large fraction, 34%, of the reconstructed muons are unable to be truth-matched using the MC classifier tool.

6. Future Studies

Cuts motivated by the plots in Fig 3. suggest how the signal-to-background ratio may be optimised in analysis using experimental data.

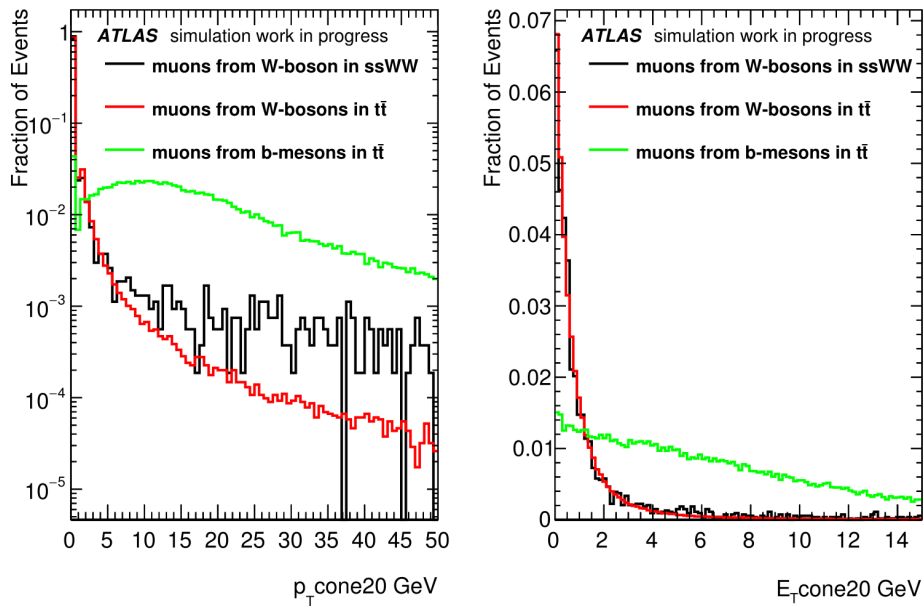


Figure 3: Simulation plots of the isolation variables for reconstructed muons with three different origins.

References

- [1] S. L. Glashow, *Nucl. Phys.* **22** (1961) 579
- [2] S. Weinberg, *Phys. Rev. Lett.* **19** (1967) 1264
- [3] A. Salam, *Conf. Proc. C* **680519** (1968) 367
- [4] G. S. Guralnik and C. R. Hagen and T. W. B. Kibble, *Phys. Rev. Lett.* **13** (1964) 20
- [5] M. Baak and R. Kogler, arXiv:1306.0571 [hep-ph].
- [6] ATLAS Collaboration, arXiv:1305.4551 [hep-ex].
- [7] L. Evans and P. Bryant (editors), *JINST* **3** (2008) S08001
- [8] ATLAS Collaboration, *JINST* **3** (2008) S08003
- [9] ATLAS Collaboration, *Phys. Lett.* **B716** (2012) 1
- [10] ATLAS Collaboration, *Phys. Lett.* **B710** (2012) 538
- [11] M. J. G. Veltman, *Acta Phys. Polon* **B8** (1977) 475
- [12] B. W. Lee and C. Quigg and H. B. Thacker, *Phys. Rev. Lett.* **38** (1977) 883
- [13] B. W. Lee and C. Quigg and H. B. Thacker, *Phys. Rev. Lett.* **D16** (1977) 1519
- [14] CMS Collaboration, *Phys. Lett.* **B716** (2012) 30
- [15] ATLAS Collaboration, *Phys. Rev. Lett.* **113** (2014), 141803
- [16] CMS Collaboration, *Phys. Rev. Lett.* **114**, 051801
- [17] S. Frixione, P. Nason, and C. Oleari, *JHEP* **0711** (2007) 070
- [18] T. Gleisberg, S. Hoeche, F. Krauss, M. Schonhrrtt, S. Schumann, et al., *JHEP* **0902** (2009) 007

Neutron irradiation and light transmission assessment of plastic scintillators of the TileCal section of the ATLAS detector.

J E Mdhuli¹, R Erasmus¹, Y U Davydov², H Jivan¹, S Liao¹, C Pelwan¹, E Sideras-Haddad¹, B Mellado¹, G Peters¹ and C Sandrock¹

¹University of the Witwatersrand, 1 Jan Smuts Avenue, Braamfontein 2000, Johannesburg.

²Joint Institute for Nuclear Research (JINR), Dubna, Russia.

E-mail: joyemmie@gmail.com

Abstract. Following the comparative study of proton induced radiation damage on various plastic scintillator samples from the ATLAS detector [1][3-5], a study on neutron irradiation and damage assessment on the same type of samples is currently being conducted. The samples were irradiated with different neutron fluxes produced in favourable nuclear reactions using the IBR-2 pulsed reactor at the Joint Institute for Nuclear Research (JINR) in Dubna. The MCNP 5 code was utilized in simulating the neutron transport for determining the dose rate. Light transmission tests were performed in order to assess the radiation damage on the scintillators. The first results of the effect of neutron irradiation on the transmission properties of a number of plastic scintillator materials is presented.

1. Introduction

The ATLAS detector is used to measure what happens in proton-proton collisions at the Large Hadron Collider (LHC) to find evidence of new physics. The tile calorimeter is part of the ATLAS detector, it is the hadronic calorimeter responsible for detecting hadrons, taus, and jets of quarks and gluons. The tile calorimeter consists of a central barrel and 2 extended barrels. Each barrel contains 64 modules that consists of a matrix of steel plates and plastic scintillators. The steel plates act as an absorber medium that converts the incoming jets into a shower of particles. The plastic scintillator tiles then absorb the energy of the particles and fluoresce to emit light. The light from the scintillators is passed through wavelength shifting optical fibres and is detected by photomultiplier tubes. The signal is further processed using readout electronics in order to digitize the data for further analysis [1][2].

Between the central barrel and extended barrels there is what is referred to as the Gap region. This region contains additional plastic scintillators that are radially distributed. During the first run of data taking, the scintillators in the gap region were exposed to a radiation environment of up to 10 kGy/year. It is predicted that during the high luminosity (HL)-LHC run time, the scintillators in the Gap region will sustain a significantly large amount of radiation damage and will require replacement during the phase 2 upgrade in 2018. This prediction has led to the comparative study of proton induced radiation damage on plastic scintillators conducted by H Jivan [1][3], C Pelwan [4] and S Liao [5].

With 2018 rapidly approaching, the comparative study of proton irradiated plastic scintillators

has been extended to study the effect of neutron induced radiation damage on plastic scintillators. In this paper, we report some of the results obtained from radiation damage induced by neutron irradiation.

Neutron interaction with matter makes the study more interesting since unlike with proton irradiation where the interaction with the plastics is through direct ionization, with neutron irradiation the interaction will be through indirect ionization. Neutron bombardment on materials creates a collision cascade within the material that results to point defects and dislocations. The collisions cause a massive transfer of kinetic energy to the lattice atom that has been displaced from its lattice site, becoming what is known as the primary knock-on atom (PKA). The knock-on atoms then lose energy with each collision and that energy therefore ionizes the material [6].

2. Scintillation Mechanism

The plastic scintillator samples that were studied are organic scintillators, these scintillators have a basic scintillation mechanism that involves Föoster energy transfer and self-absorption. They consist of one or two dopants. The scintillation mechanism of organic scintillators is determined by the characteristics of the benzene ring. An organic scintillator scintillates regardless of its crystal form, whether it be a liquid, a gas or imbedded in a polymer. The chemical bonds found within a benzene ring are: σ -bonds that are in the plane with bond angle 120° and are from sp^3 hybridization. The other chemical bonds found are π -orbitals which are out of plane and overlap. The π -electrons are completely delocalized.

Looking at the scintillation mechanism after the scintillator has absorbed the photon or excitation by ionization, the molecule will undergo vibrational relaxation to the S_{10} state. The S_{10} excited state radiatively decays to the vibrational sub-levels of the ground state. The lifetime of the S_{10} state is in the nanoseconds time range. The short lifetime allows for the fluorescence emission spectrum to be roughly a mirror image of the absorption spectrum, in other words, they have the same spacing. The emitted photons have less energy than the S_{00} - S_{10} phase transition and that's where the important Stokes shift is observed. There is no S_2 - S_0 emission, thus there is an internal non-radiatively de-excitation occurring within the scintillator taking place in the picoseconds time range and, the excited triplet state cannot decay to the ground state as a result angular momentum selection rules, it therefore results in a delayed fluorescence and phosphorescence [7]. This is clearly illustrated in figure 1.

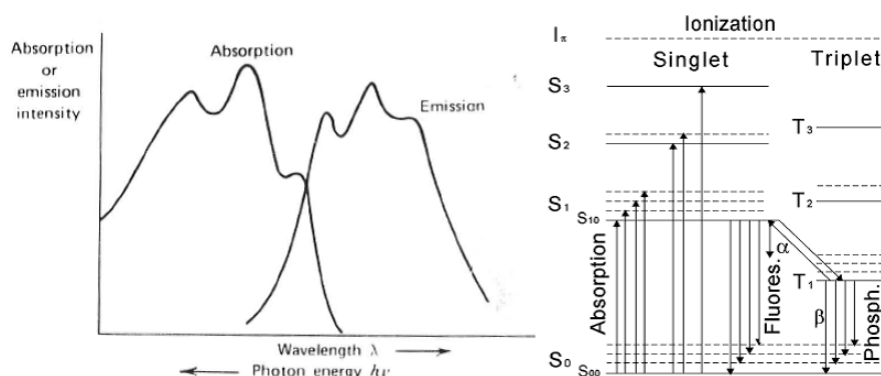


Figure 1. A fluorescence absorption and emission spectra (left) and scintillation mechanism for an organic scintillator (right) [7].

3. Experimental Details

Four plastic scintillator grades were under study, three of which were obtained from ELJEN technologies and one from Dubna. The three plastic scintillators obtained from ELJEN technologies are composed of a polyvinyl toluene base and 3% added organic fluors [1], the fourth plastic scintillator grade is the Kharkov (UPS923A) type manufactured by the Institute for Scintillation Materials (ISMA). The plastic scintillator grades under study are the EJ200, EJ208, EJ260 and the UPS923A.

Several samples of each plastic scintillator grade were cut and polished at the Dzhelapov Laboratory of Nuclear Problems (DLNP) at JINR. Sixteen samples were cut to dimensions 20 mm by 20 mm, with 6 mm thickness. Special sample holders were made to accommodate our samples due to their size. Channel 3 of the IBR-2 pulsed reactor at the Frank Laboratory of Neutron Physics (FLNP) in JINR was used to irradiate the samples [8]. The samples were subjected to irradiation with a beam of fast neutrons with energies ≥ 1 MeV for 337 hours, the length of the April Run 2016. The reactor was operating at an average power of 1875 kW. The samples were placed at three different positions from the reactor core to expose the samples to different neutron fluxes to achieve various doses. The neutron flux density ranged between $1 \times 10^6 \sim 7.7 \times 10^6$ $n/cm^2/s$.

Taking into account the reactor spectrum, the Monte Carlo N-Particle (MCNP) 5 [9] code was used to simulate neutron transport through plastic scintillators and to determine the dose rate. The Monte Carlo method is used to simulate statistical processes theoretically, in particular complex problems that cannot be solved/modelled using computer codes that use deterministic methods. Table 1 shows the neutron flux density, neutron fluences and doses at the various positions.

Table 1. Neutron flux density, neutron fluences and doses at the various positions.

Sample number	Flux density ($n/cm^2/s$)	Fluence (n/cm^2)	Dose (Gy)
1, 5, 12, 19	1.0×10^6	1.2×10^{12}	66
2, 6, 13, 20	3.6×10^6	3.6×10^{12}	199
3, 7, 14, 21	7.7×10^6	9.4×10^{12}	510

Light spectroscopy was conducted using the Varian Carry 500 spectrophotometer to characterize the optical properties of the irradiated samples due to the damage of the neutron irradiation. The light transmission of the samples was measured relative to the transmission in air over a laser wavelength range between 200-800nm. Transmission spectra were collected a few weeks after irradiation, control samples were left un-irradiated in order to gauge the transmission loss.

4. Light Transmission Results and Analysis

The light transmission spectroscopy results for each scintillator grade relative to the light transmission in air are shown below on the spectra on the left in Figures 2-5. In Figure 2, it is observed that at a wavelength of 400 nm the absorptive edge falls away completely for the EJ200 grade. Figure 3 shows the light transmission spectrum of the EJ208 grade. It is observed from the spectrum that the absorptive edge falls away at 385 nm. At the highest exposed neutron flux density, there is an increase in transmission. At neutron flux densities lower than 3.6×10^6 $n/cm^2/s$, there is a decrease in light transmission. We observe a relative increase in transmission above ~ 700 nm for samples EJ200 and EJ208. The transmission spectrum for the EJ260 is shown in Figure 4, it is observed that transmission starts to occur at wavelength 355 nm for a short wavelength range as seen from the mini peak on the spectrum. The absorptive edge

falls away completely at 460 nm. The overall transmission of the grade decreases with radiation damage. Figure 5 shows the transmission spectrum of the UPS932A grade, the absorptive edge for this grade falls off completely at 400 nm. It is observed that the overall transmission of the grade increases with increasing dose.

The transmission loss is observed at wavelength 450 nm as this corresponds to the peak absorption wavelength of the wavelength shifting optical fibres coupled with these scintillators within the Tile Calorimeter. We consider the transmission loss of the highest neutron flux density $7.7 \times 10^6 \text{ n/cm}^2/\text{s}$. We observe a 3.4% transmission loss for the EJ200, 3% transmission increase for the EJ208 and no transmission loss for the EJ260 as the sample absorbs light in the wavelength range from 400 nm to 460 nm. The UPS932A grade shows a 2.9% transmission increase. The transmission loss is clearly shown in Figures 2-5 on the spectra on the right.

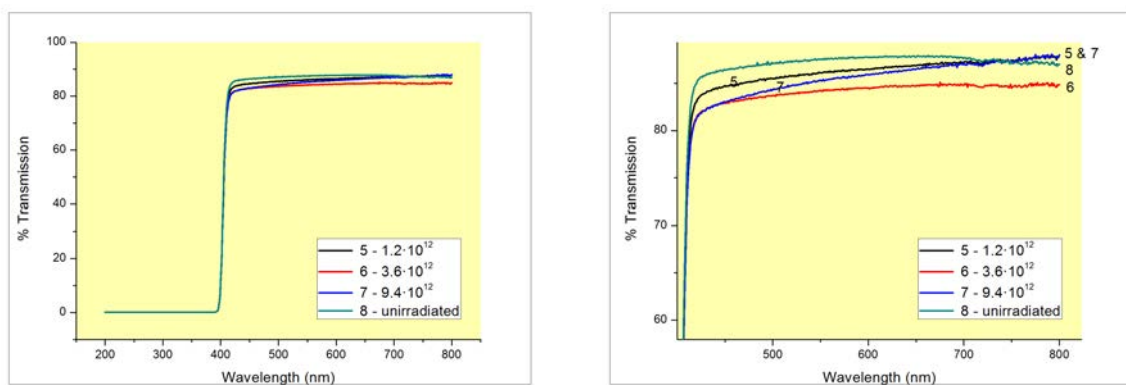


Figure 2. Left: Transmission spectrum for un-irradiated and irradiated samples for the EJ200 grade. Right: Enlarged spectrum at wavelength 400 800 nm.

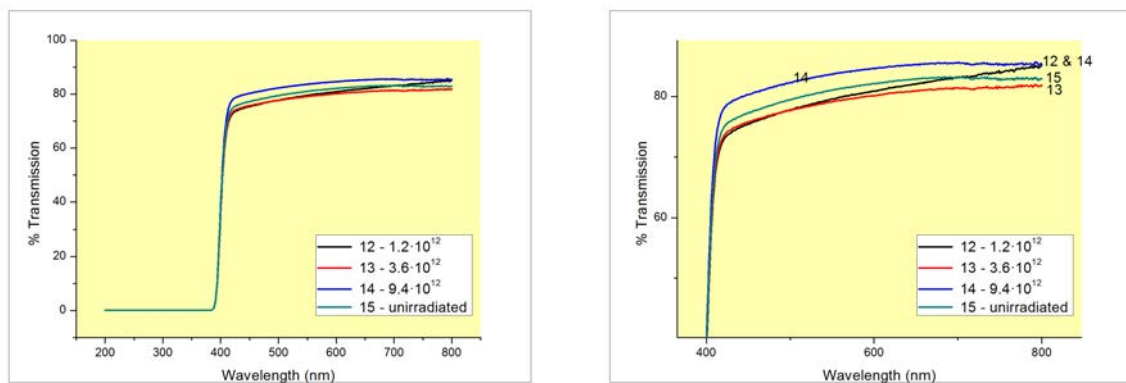


Figure 3. Left: Transmission spectrum for un-irradiated and irradiated samples for the EJ208 grade. Right: Enlarged spectrum at wavelength 400 800 nm.

5. Conclusion

From the results obtained in this study, neutron irradiation has indeed have an observable effect on the light transmittance of plastic scintillators. We considered the transmission loss at wavelength of approximately 450 nm which corresponds to the peak absorption wavelength of the

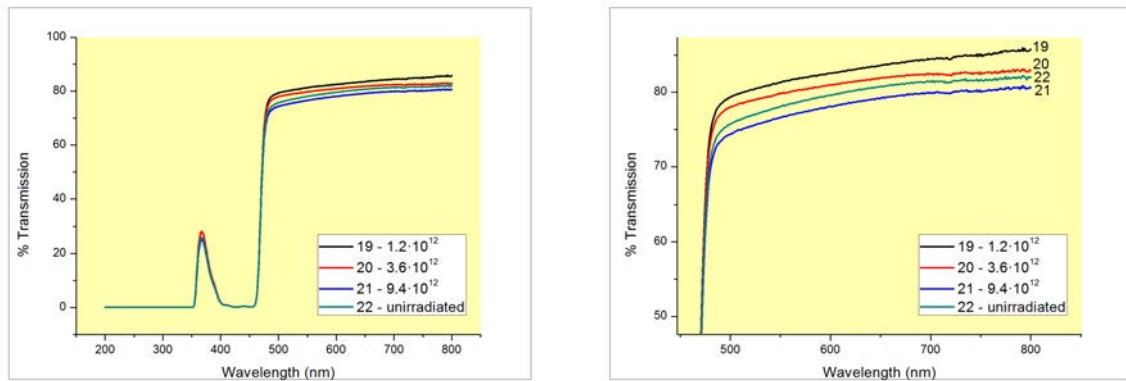


Figure 4. Left: Transmission spectrum for un-irradiated and irradiated samples for the EJ260 grade. Right: Enlarged spectrum at wavelength 460 800 nm.

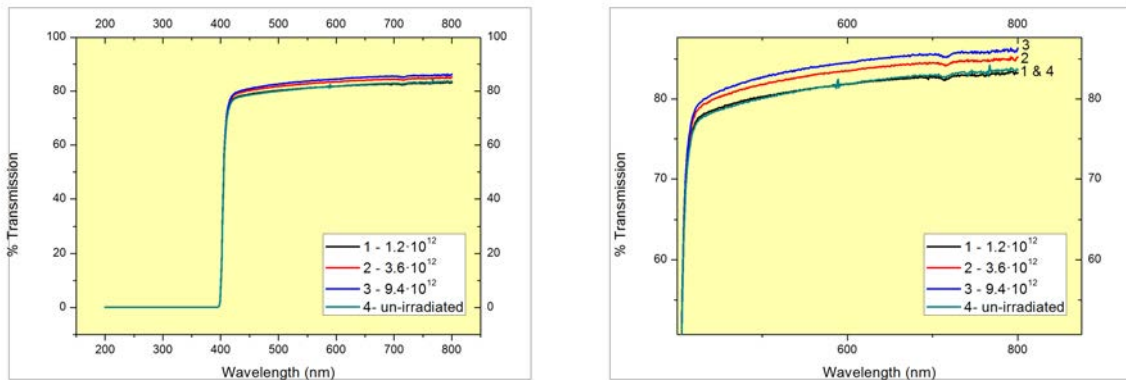


Figure 5. Left: Transmission spectrum for un-irradiated and irradiated samples for the UPS932A grade. Right: Enlarged spectrum at wavelength 400 800 nm.

wavelength shifting optical fibres coupled with these scintillators within the Tile Calorimeter. The EJ200 showed the highest transmission loss with a 3.8% loss whilst for the EJ260 no transmission occurs in the wavelength range of 400 460 nm. Unlike the EJ200 and EJ260, the EJ206 and the UPS932A have an increase in transmittance by 3% and 2.9% respectively. The overall transmission for the EJ200 and EJ260 decreases with exposure to radiation but there is no clear relationship between the neutron flux density and the light transmittance from the neutron flux densities under study. For the EJ208 and UPS932A, the highest neutron flux density shows an increase in transmittance. The highest neutron flux density shows an increase in light transmission whilst neutron flux density below $3.6 \times 10^6 \text{ n/cm}^2/\text{s}$ show that there is a transmission loss for the EJ208. The Kharkov grade shows transmission loss for the lowest neutron flux density, below $1.0 \times 10^6 \text{ n/cm}^2/\text{s}$ and an increase in transmission for neutron flux density above $3.6 \times 10^6 \text{ n/cm}^2/\text{s}$. No additional features were observed on the spectra due to radiation damage for all the grades compared to those observed in the proton irradiated samples [1].

All the results in this study are preliminary, they will be used as a guide in future studies. No conclusions can be made in this study on which plastic scintillator grade performed better under neutron radiation.

6. Upcoming Work

Light yield tests will be done next. Raman spectroscopy will also be performed to observe if any structural damage occurred from the radiation damage. More samples will be irradiated at higher exposure doses to study on how the plastic scintillators behave higher doses of radiation damage. A study on the thickness dependence of the plastic scintillators will also be conducted. This will focus on studying the relationship between the thickness and the transmittance of the sample after undergoing radiation damage.

The project aims to extend these studies to include radiation assessment damage of any component that processes the scintillating light and deteriorates the quantum efficiency of the Tilecal detector, namely, photomultiplier tubes, wavelength shifting optical fibres and readout electronics will also be exposed to neutron irradiation and the damage will be assessed in the same manner. The linear accelerator and the SAFARI-1 reactor will also be used to irradiated the samples under study.

Acknowledgements

We would like to acknowledge the technical staff at the Dzhelapov Laboratory of Nuclear Problems (DLNP) and Frank Laboratory of Neutron Physics (FLNP) at the Joint Institute for Nuclear Research (JINR) for all their assistance and allowing us to use their laboratories.

References

- [1] Jivan H, Erasmus R, Mellado B, Peters G, Sekonya K, Sideras-Haddad E. 2015. "Radiation hardness of plastic scintillators for the Tile Calorimeter of the ATLAS detector." *Journal of Physics conference series* **645**
- [2] Succurro A 2012. "The ATLAS Tile Hadronic Calorimeter performance in the LHC collision era." *Physcis Procedia* **37** 229 - 237.
- [3] Jivan H, Mellado B, Sideras-Haddad E, Erasmus R, Liao S, Madhuku M, Peters G, Solvyanov O. 2015. "Radiation hardness of plastic scintillators for the Tile Calorimeter of the ATLAS detector." *Journal of Physics conference series* **623**.
- [4] Pelwan C, Jivan H, Joubert D, Keartland J, Liao S, Peters G, Sideras-Haddad E. 2015. "Characterization of plastic scintillators using magnetic resonance techniques for the upgrade of the Tile Calorimeter in the ATLAS detector." *Journal of Physics conference series* **10** 645:012023
- [5] Liao S, Erasmus R, Jivan H, Pelwan C, Peters G, Sideras-Haddad E. 2015. "A comparative study of the radiation hardness of plastic scintillators for the upgrade of the Tile Calorimeter of the ATLAS detector." *Journal of Physics conference series* **10** 645:012021
- [6] Bisanti P 1986 "Magnetic properties of matter" *Turin:World Scientific* ed Borsa F, Tognetti V p 385-408
- [7] Chen M 2011 "Radiation detectors II: Scintillation detectors." [Online] Available: www.physics.queensu.ca/~phys352/
- [8] Bulavin M. 2015 Irradiation facility at the IBR-2 reactor for investigation of material radiation hardness *Nuclear Instruments and Methods* **B343** p26 - 29.
- [9] Los Alamos National Laboratory [Online] Available:<http://mcnp.lanl.gov/mcnp5.shtml> [Accessed 24 06 2017]

The K600 with CAKE and BaGeL

R. Neveling¹, F.D. Smit¹, P. Adsley^{1,2}, J.W. Brummer², J. Carter³,
 C. Aa. Diget⁴, H.O.U. Fynbo⁵, M. Freer⁶, N.J.H. Hubbarb⁴, D.G.
 Jenkins⁴, M. Kamil⁷, M. Khumalo⁷, M. Kohne², K.C.W. Li², P.Z.
 Mabika⁷, D.J. Marin-Lambarri^{1,7}, N.J. Mukwevho⁷, F. Nemulodi¹, P.
 von Neumann-Cosel⁸, P. Papka², L. Pellegrini^{1,3}, V. Pesudo^{1,7}, B.
 Rebeiro⁷, E. Sideras-Haddad³, G.F. Steyn¹, J.A. Swartz⁵, S.
 Triambak⁷, I.T. Usman³, C. Wheldon⁶, Tz. Wheldon⁶, J.J. van Zyl²

¹ iThemba Laboratory for Accelerator Based Sciences, Somerset West, South Africa

² Stellenbosch University, Department of Physics, Stellenbosch, South Africa

³ University of the Witwatersrand, School of Physics, Johannesburg, South Africa

⁴ University of York, Department of Physics, York, United Kingdom

⁵ Aarhus University, Department of Physics and Astronomy, Aarhus, Denmark

⁶ University of Birmingham, School of Physics and Astronomy, Birmingham, United Kingdom

⁷ University of the Western Cape, Department of Physics, Bellville, South Africa

⁸ Institute für Kernphysik, Technische Universität Darmstadt, Darmstadt, Germany

E-mail: neveling@tllabs.ac.za

Abstract. Medium energy hadronic scattering and reactions at very small scattering angles, including zero degrees, can be studied with low background and high energy resolution with the K600 magnetic spectrometer at iThemba LABS. Such measurements are notoriously difficult to perform, but highly sought after due to the advantage of being very selective to excitations with low angular momentum transfer. This simplifies the analysis of the many possible contributions to the spectra due to the complex nature of the nuclear interaction. The recent addition of coincident particle and gamma detection to the zero degree capability enhances the selectivity of such a facility, which opens up a host of new opportunities to be explored. The details of the new facility and capabilities thereof are described.

1. Introduction

The K600 magnetic spectrometer at the iThemba Laboratory for Accelerator Based Sciences (iThemba LABS), South Africa, is a kinematically corrected quadrupole dipole dipole (QDD) magnetic spectrometer for light ions. In recent years the capability to measure inelastically scattered particles and reactions at extreme forward angles that includes zero degrees was successfully developed [1], making it one of only two facilities worldwide (the other being at RCNP, Japan [2]) where high energy resolution is combined with zero degree measurements at medium beam energies.

The advantage of such measurements is the selectivity it provides to excitations with low angular momentum transfer. For this reason it represents a valuable experimental tool for research into a wide range of topics such as studies of the fine structure of giant resonances such as the giant dipole resonance (GDR) [3] and the giant monopole resonance (GMR) [4], pygmy dipole resonance (PDR) studies [5], finding and identifying cluster states [6], as well as

astrophysical investigations related to the Hot-CNO breakout process and type I X-ray bursts [7].

The selectivity of zero degree measurements can be improved through coincident decay measurements. For example, coincident gamma detection during inelastic alpha-particle scattering measurements at zero degrees is known to enable detailed spectroscopy of electric-dipole excitations below the particle threshold, allowing the PDR to be completely isolated from other multi-polarities [8].

While such measurements can in principle be performed with the existing infrastructure, various modifications and improvements were made to improve detection efficiencies. For example, the geometry of the 524 mm diameter sliding seal scattering chamber [1] is not optimized to accommodate ancillary detector systems, either Si detectors inside or high-purity germanium (HPGe) detectors outside. A new, smaller, 280 mm diameter scattering chamber was therefore designed and installed in 2014. This new scattering chamber presents substantially less material for gammas and charged particles to scatter from before reaching the ancillary detectors. Especially for detectors mounted outside the sliding seal scattering chamber the 50 mm thick Al walls 32 mm above and below the scattering plane presented a problem. The new scattering chamber has detachable shells, greatly improving operator access when working on internal detector setups. These detachable shells consists of only 3 mm thick Al for most of the azimuthal angle range. They can be replaced with flat sheets which will allow for a minimum separation of 50 mm between the target and any external detectors mounted on the scattering plane.

Coincident detection techniques are nothing new, nor is it the first time that such measurements are performed with the K600. However, the efficiency, granularity and also the fact that these measurements are made at zero degrees, all combine to make the facility unique. The new dedicated coincident charged particle decay detector system which can be mounted inside the new scattering chamber will be described in Section 2. A description of the coincident gamma decay detection system will be provided in Section 3. A summary and future outlook is presented in the last section.

2. Coincident charged particle decay detection

Charged particle decay products can be observed with the Coincidence Array for K600 Experiments (CAKE), which consist of five TIARA HYBALL MMM-400 double sided silicon strip detectors (DSSSDs) in a lampshade configuration, as shown in Fig. 1. Each of the 400 μm thick wedge-shaped DSSSDs consists of 16 rings and 8 sectors, and can be positioned at either forward or backward angles with the rings covering the polar angle range $114^\circ \leq \theta_{lab} \leq 166^\circ$. This results in coverage of $\sim 26\%$ of the decay particle solid angle for the case of inelastic α -scattering, where the recoil nucleus is practically stationary. The DSSSD's allows for the detection of protons up to 7 MeV and α -particles up to 28 MeV. The target-detector separation is ~ 100 mm which is sufficient for identification of protons and α 's through TOF measurements, as shown in Fig. 2.

For each focal-plane event all signals from CAKE within a time window of six μs are digitized in four 12-bit peak sensing VME Analog-to-Digital Converters (ADC). These are the 32-channel CAEN V785 models. Acquiring data in this manner yields both K600 singles as well as K600 + CAKE coincidence events. A beam pulse selector at the entrance of the cyclotron can be employed to ensure a sufficient time window for coincidence measurements. DSSSD rates of less than 5kHz per detector are routinely experienced. This rate is shared by the 24 active elements per detector, resulting in rates of only a few hundred Hz per active element. The typical energy resolution for the DSSSD's of ~ 60 keV (FWHM), determined with a ^{228}Th source, does not take into account target thickness effects during the coincidence measurement.

As an example where a better understanding of nuclear structure can be achieved through

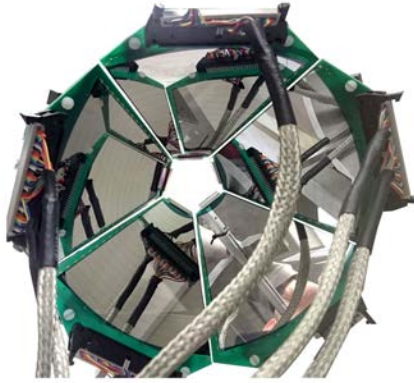


Figure 1. A picture of the Coincidence Array for K600 Experiments (CAKE).

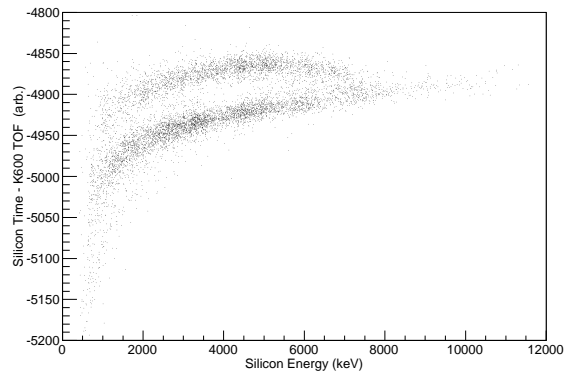


Figure 2. A particle identification (PID) plot of the time-of-flight (TOF) versus the energy of decay particles detected with CAKE. The top locus represent protons, and the bottom locus represents α -particles.

coincident decay measurements of charged particles at zero degrees, we consider clustering phenomena in light nuclei, in particular α -clustering. Light nuclei are expected to exhibit cluster-like properties in excited states with a low density structure. The Hoyle state, the 0_2^+ state at 7.654 MeV in ^{12}C , may be considered the prototype of a state that exhibits α -particle condensation [9], i.e. it is considered to have a 3α gas-like structure similar to a Bose-Einstein condensate consisting of three α particles all occupying the lowest $0S$ state. It is expected that equivalent Hoyle-like states should also exist in heavier $N\alpha$ nuclei such as ^{16}O . The measurement of particle decay widths of the 0_6^+ state in ^{16}O , presently considered to be a candidate for a Hoyle-like state, is required for a characterization of its cluster structure.

Inelastic α -particle scattering at zero degrees has the advantage that it only excites natural parity states, and particularly the 0^+ states. Such a measurement, coupled with coincident observations of the ^{16}O decay products, is therefore an ideal tool to measure the particle decay width of the 0_6^+ state in ^{16}O . An experiment was performed at iThemba LABS where the $^{16}\text{O}(\alpha, \alpha')$ reaction at 200 MeV was investigated [10]. A $^{nat}\text{Li}_2\text{CO}_3$ target was employed as the best non-gaseous compromise for an ^{16}O target. Coincidence data were extracted by gating on the prompt peak in the coincidence time spectrum, which yielded a random-to-real coincidence ratio of $\frac{1}{50}$. The coincidence matrix for all events with the target excitation energy as measured by the K600 on the horizontal axis and the energy of the charged particle decay as measured in CAKE on the vertical axis is shown in Fig. 3.

The facility was also successfully used to, amongst others, measure the proton decay branching ratios in unstable nuclei by means of the (p,t) reaction on a stable target [11]. Such measurements have astrophysical relevance due to the influence of the branching ratios on the calculation of breakout reactions in type 1 X-ray bursts.

3. Coincident gamma decay detection

The array referred to as the Ball of Germaniums and LaBr_3 detectors (BaGeL) was conceived to take advantage of the capability to perform high energy-resolution inelastic α scattering measurements at 0° . This makes it possible to pursue high-resolution spectroscopy of the low-

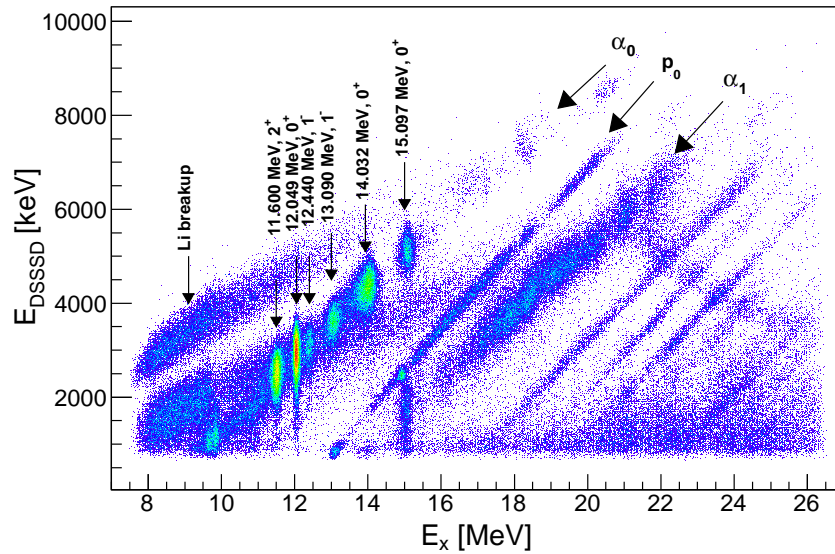


Figure 3. Two-dimensional coincidence matrix for inelastically scattered α -particles from a $^{nat}\text{Li}_2\text{CO}_3$ target summed over all CAKE channels. Three ^{16}O decay channels (α_0 , α_1 , p_0) are indicated, as well as prominent low spin states in ^{16}O . The indicated Li breakup locus appears prominently in the lower excitation energy region, and extends weakly into the α_0 decay channel. At higher excitation energies numerous proton decay channels from ^{12}C and ^{16}O are visible. A display threshold of >3 was used in plotting the data.

lying E1 strength through the $(\alpha, \alpha'\gamma)$ reaction.

BaGeL refers not only to the array of HPGe's that will be used in coincidence with the K600, but to the whole infrastructure designed to make coincident γ detection possible. This includes, amongst others, the necessary LN2 cooling and monitoring systems, which is designed to be independent of the existing systems of the AFRican Omnipurpose Detector for Innovative Techniques and Experiments (AFRODITE) array [12]. Furthermore, the design of BaGeL was made in such a way that it is highly flexible and configurable, making it easy to install a range of different detector systems for a wide range of geometries. This allows one to tailor detection capabilities to the experimental requirements, e.g. the high energy resolution capabilities of HPGe detectors or the high detection efficiencies of LaBr₃ detectors. The basic BaGeL support structure has a clamshell design as shown in Fig.4. The center of rotation for the two arms are 828 mm from the beam center, and during beam tuning the detectors in the 90° position can be removed to a perpendicular distance of 2045 mm away from the beam-line. This will ensure minimum neutron damage to sensitive HPGe detectors during beam tuning.

For the BaGeL commissioning run scheduled for October 2016 [13] it is envisaged that the eight HPGe Clovers (each with four crystals approximately 40 x 40 x 70 mm³ in size) available at iThemba LABS will be used. The expected γ -ray energy resolution is ~ 15 keV for the energy range of interest to PDR studies, which is 5-8 MeV. The absolute photo-peak efficiency for the array was calculated to be 0.6% for a target-detector separation of 170 mm for γ -rays of 6 MeV (assuming add-back). The currently available 12-bit CAEN ADCs are not optimum to exploit the high energy resolution capabilities of HPGe detectors. For this reason the collaboration acquired two 8-channel 16-bit Struck SiS3302 ADCs. Once these are fully commissioned more will be acquired to enable the full instrumentation of eight HPGe's with 16-bit ADCs.

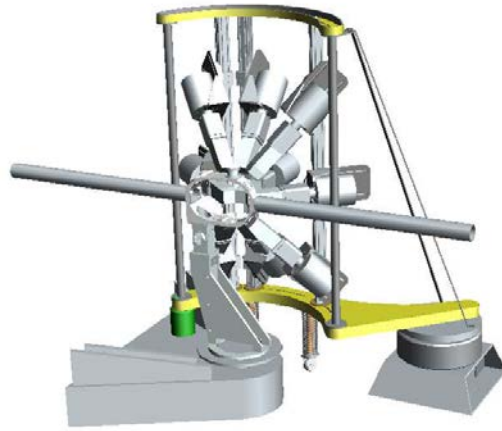


Figure 4. An illustration of the one arm of BaGeL on the beam-right side, instrumented with nine HPGe's. The particle beam enters the central scattering chamber from the right. The K600 is located on the left. Note however that for the near future the HPGe detectors will only be placed at backward angles.

4. Summary and outlook

During the past decade the constant developments of K600 magnetic spectrometer at iThemba LABS has helped to create a powerful facility that can be used to perform unique measurements in nuclear structure research. The developments to enable coincident decay particle measurement were already used to good effect in multiple experiments, and we are optimistic about the future of the BAGEL development.

At the same time we are looking ahead to further development of the facility. For particles below ~ 80 MeV in the focal plane the K600 is at present operated in a single scintillator trigger mode, due to the fact that the particles stop in the first scintillator in the focal plane. The resultant high trigger rate, mostly due to zero degree background (very low energy particles that do not penetrate beyond a mm into the scintillator), ultimately limits data acquisition rates and therefore potentially limits the scope of studies that could be performed. A new trigger scintillator that will consist of scintillating fibers was therefore designed. These scintillating fibers ($1.5 \times 1.5 \times 1800 \text{ mm}^3$) are much thinner than existing scintillators (thickness = 3.175 mm, 6.35 mm or 12.7 mm), which means that a trigger made by a coincidence signal of two scintillators will again be possible for particles of 80 MeV and below, in this way getting rid of the unwanted low energy background. The much improved light transport capabilities compared to existing scintillator trigger geometry (thickness $\times 100 \times 1000 \text{ mm}^3$) means that the scintillating fiber detector will be much more efficient than using a standard scintillator with dimensions $1.5 \times 100 \times 1000 \text{ mm}^3$.

Finally, in order to detect heavy ions in the focal plane a new position sensitive detector is required. This could also benefit the detection of low energy light ions (as well as 200 MeV α 's) since the thick Kapton vacuum exit window in front of the existing focal plane detectors limits the position resolution. Potential candidates include different geometries of cathode strip MWPC (Multi Wire Proportional Counter) detectors. Such a development, envisaged to start in the near future, is however dependent on manpower and financial restrictions.

Acknowledgements

This work was supported by the South African National Research Foundation (NRF), and financial support through the NRF Research Infrastructure Support Programme (Grant 86052) is gratefully acknowledged.

- [1] R. Neveling *et al.*, Nucl. Instr. and Meth. A 654 (2011) 29.
- [2] A. Tamii *et al.*, Nucl. Instr. and Meth. A 605 (2009) 326.
- [3] A. Tamii *et al.*, Phys. Rev. Lett. 107 (2011) 062502.
- [4] M. Itoh *et al.*, Phys. Rev. C 88 (2013) 064313.
- [5] A.M. Krumbholz *et al.*, Phys. Lett. B 744 (2015) 7.
- [6] J.A. Swartz *et al.*, Phys. Rev. C 91 (2015) 034317.
- [7] G.P.A. Berg *et al.*, J. Phys.: Conf. Ser. 387 (2012) 012003.
- [8] D. Savran *et al.*, Nucl. Instr. and Meth. A 564 (2006) 267.
- [9] P. Schuck *et al.*, J. Phys.: Conf. Ser. 413 (2013) 012009.
- [10] R. Neveling *et al.*, Project PR226, Research Proposal to the PAC of iThemba LABS, October 2013.
- [11] P. Adsley *et al.*, Project PR254, Research Proposal to the PAC of iThemba LABS, October 2015.
- [12] R. T. Newman *et al.*, proceeding of Balkan School on Nuclear Physics, 1-10 September 1998 (Istanbul, Turkey), Balkan Physics Letters, 82, (1998)
- [13] L. Pellegrini *et al.*, Project PR251, Research Proposal to the PAC of iThemba LABS, April 2015.

Tracking Electrons Produced by Compton Scatter within a Prompt Gamma Imaging Device

S W Peterson¹, M Hillebrand¹, D Mackin², E Draeger³, S Beddar², J Polf³

¹Department of Physics, University of Cape Town, Rondebosch 7700, South Africa

²Department of Radiation Physics, University of Texas MD Anderson Cancer Center, 1515 Holcombe Blvd, Houston, TX, USA

³Department of Radiation Oncology, University of Maryland School of Medicine, 22 South Greene St, Baltimore, MD, USA

Email: steve.peterson@uct.ac.za

Abstract. Proton therapy requires precise delivery of the accelerated particles to the cancerous tissue in order to maximize its considerable benefits. Unfortunately, there is no way to directly monitor the actual dose delivered to the patient. Prompt Gamma Imaging (PGI), specifically using a Compton camera, is a promising option for in vivo verification of the 3D dose distribution. A Compton camera relies on an incident gamma undergoing multiple Compton scatters within its multiple stages. The information (energy deposited and location) from the Compton scatters (2 or more) can be used to reconstruct a cone of origin. With a sufficient number of cones and appropriate image reconstruction techniques, a 3D image of the dose can be produced. Of course, the accuracy of the image reconstruction relies heavily on the quality of the data measured by the detector, specifically the energy and position of the detected electron. This work uses the Geant4 Monte Carlo toolkit to track the Compton electrons within the individual stages of the Compton camera in order to better understand the accuracy of the detected electron position and energy. The energy and range of the secondary electrons are broken down by scatter sequence order. Two detector configurations were investigated. The work provided some clear indications of the expected accuracy from the energy and position measurements of the electrons in a Compton camera.

1. Introduction

Proton therapy was first performed in South Africa more than 20 years ago at iThemba LABS in Somerset West. In the last 5-10 years, there has been a huge increase in the number of clinical proton therapy treatment facilities around the world due primarily to the decreasing cost of particle accelerators. Since the 1940s, the benefits of protons for the treatment of cancer have been well known. The basic advantage of proton radiation therapy is the way that protons interact with material, specifically a minimal entrance dose and a sharp increase in energy deposition near the end of the proton range. The lack of exiting protons has made it difficult to produce an actual image of the dose deposition within the patient; and the uncertainty in the dose delivery has made the need for an in-vivo dose verification system extremely important. A suggested method of dose verification is the use of the secondary gammas produced by proton-nucleus inelastic collisions in the patient [1]. These “prompt” gammas are produced during treatment at the location where the dose is deposited, making them an ideal candidate [2].

There are a number of ways to detect these prompt gammas, using both physically and electronically collimated devices [3-6], but this work concentrates on a device called a Compton camera. A Compton camera, originally developed for use in astronomy applications [7], relies on a particular gamma ray to interact two or more times within the detector, capturing energy and position data each time. This data can then be used to project the expected gamma creation position onto a cone. As more prompt gammas are detected, the intersection of the cones can be used to reproduce an image of the dose deposited within the patient. The advantage of this type of device would be a relatively compact system that could produce full three-dimensional pictures of the dose being deposited in the patient [8].

Several groups are working on developing a Compton camera for prompt gamma detection [4, 9-12], but this work will focus on understanding an existing solid-state system consisting of multiple detection stages composed of Cadmium zinc telluride, (CdZnTe) or CZT [13]. The reconstruction of useable images from a Compton camera relies heavily on the information (energy deposited and location) gathered from each Compton interaction. Any uncertainty in this data will result in difficulties in image reconstruction and consequently, reduced image quality. A primary source of position uncertainty has to do with the recorded position of electron produced during the Compton interaction.

This work uses the Geant4 Monte Carlo toolkit to track the Compton electrons within the individual stages of the Compton camera in order to better understand the accuracy of the detected electron position and energy. The energy and range of the secondary electrons are broken down by scatter sequence order while two different detector configurations were investigated. These results are used to make some estimation of the expected deviations in the energy and position measurements due to the electrons in the Compton camera.

2. Method

2.1. Compton Camera

2.1.1. *Basics.* The basic function of a Compton camera (CC) is to track an incident gamma as it undergoes multiple Compton scatters, recording the energy deposited (ΔE) and the position of each of the Compton interactions. There are two basic types of events, a double-scatter event where the gamma scatters once and is then absorbed, or a triple-scatter event where the gamma has two Compton interactions followed by a third position-recording event (Compton, photoelectric, or pair production). For double-scatter events, the initial energy (E_0) of the gamma is simply determined by

$$E_0 = \Delta E_1 + \Delta E_2, \quad (1)$$

where ΔE_1 and ΔE_2 is the energy deposited during the Compton and photoelectric interactions. For triple-scatter events, the initial energy is found using [14]

$$E_0 = \Delta E_1 + \frac{1}{2} \left(\Delta E_2 + \sqrt{\Delta E_2^2 + \frac{4\Delta E_2 m_e c^2}{1 - \cos \theta_2}} \right), \quad (2)$$

where θ_2 is the scattering angle of the second interaction, m_e is the mass of the electron and c is the speed of light. The scattering angle is determined by the positions (p_1, p_2, p_3) of the three interactions (see figure 1). The initial scattering angle (θ_1) can be determined by

$$\cos \theta_1 = 1 + m_e c^2 \left(\frac{1}{E_0} + \frac{1}{E_0 - \Delta E_1} \right). \quad (3)$$

The origin position of the gamma cannot be determine explicitly, but is restricted to the surface of the “cone-of-origin”, which has an opening angle θ_1 and apex p_1 . The axis of the cone is along the line containing the points p_1 and p_2 . This cone (along with many others) can then be used to produce an image of the original gamma distribution using an image reconstruction technique.

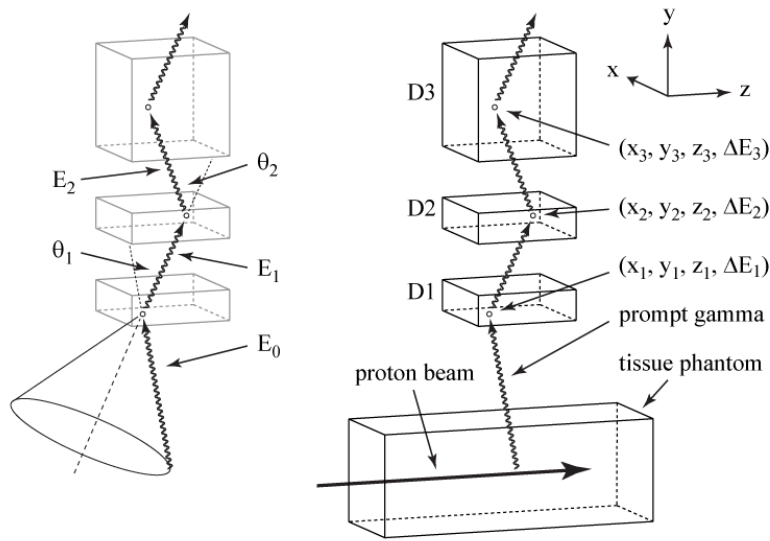


Figure 1. Diagram of the 3-stage Compton camera setup in parallel-plane geometry showing the Compton scatter angles (θ_1, θ_2) and the gamma ray energy (E_0, E_1, E_2) as it travels through the detectors (D1, D2, D3), as well as the projected code used to reconstruct the images. Figure reproduced from ref 4.

2.1.2. *Compton Electrons.* There are number of uncertainties that can hinder the effectiveness of a Compton camera, such as Doppler broadening and finite energy and spatial resolutions of the CC detectors. This work will look specifically at the impact of the recoil electron on the two measured quantities: deposited energy (ΔE) and interaction position (p). We are able to focus solely on the recoil electron by removing Doppler broadening from our simulations and using an “ideal” detector with infinite position and energy resolution.

2.1.3. *Detector Configuration.* Two different detectors were used for the work. First, the actual detector, the Polaris J detection system from H3D [15, 16] was used to determine the impact of the Compton electron in a realistic situation. Second, an “infinite” detector was used to explore specific features of the Compton electron.

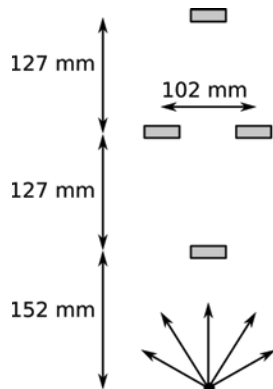


Figure 2. Configuration of the experimental Polaris J setup.

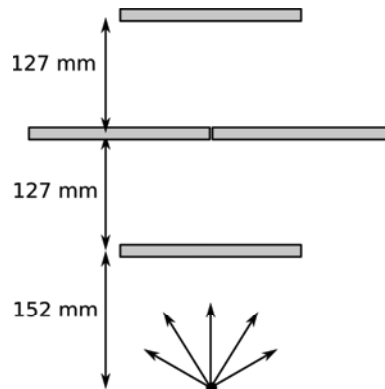


Figure 3. Configuration of the simulated “infinite” detector.

The Polaris J system [13] consists of four stages, each stage containing four CZT crystals, with two stages having 20 mm x 20 mm x 15 mm detector crystals, while the other two have 20 mm x 20 mm x 10 mm crystals. For this work, the four stages were arranged in a 1-2-1 configuration (as shown in figure 2) with a spacing of 5 inches (127 mm, center to center) between the three layers of detectors. The two middle detectors were each offset 2 inches (50.8 mm) from the CC axis, while the front and back detectors were placed in line with the CC axis. The CC was positioned 6 inches (152.4 mm) from the source. This configuration mimics the standard experimental setup used in previous work [13].

The infinite detector was composed of four 200 mm x 200 mm stages with the thickness varying from 5 to 25 mm. Each stage was simulated as a single CZT crystal and the four stages were arranged in a 1-2-1 configuration (as shown in figure 3) to mimic the Polaris J setup described above. This configuration was used in order to explore the Compton electron while saving computation time.

2.2. Monte Carlo

The simulations performed for this work used a previously developed Geant4 (v9.4.p01) model used for CC efficiency studies [4, 17], an image reconstruction study [8] and experimental comparisons [13]. The model has been expanded to look specifically at Compton electrons, but uses the same settings as previous work [4, 8, 13, 17]. An isotropic point source of 4.44 MeV gammas was used to produce the Compton scatters. The 4.44 MeV source was used to replicate one of the primary prompt gammas produced during proton irradiation. Only electrons produced during a triple-scatter event were tracked. An electron range cut of 0.01 mm was used (equivalent to an energy threshold of 44.4 keV) and each run started with 1×10^8 gammas. Escaped electrons were not tracked after they left the detector, although any energy deposited within a detector and the range of the electron was recorded. The electron energy deposition was recorded by scatter and also compared to the energy lost by the gammas. The Polaris J simulation required 1.1×10^{11} gammas.

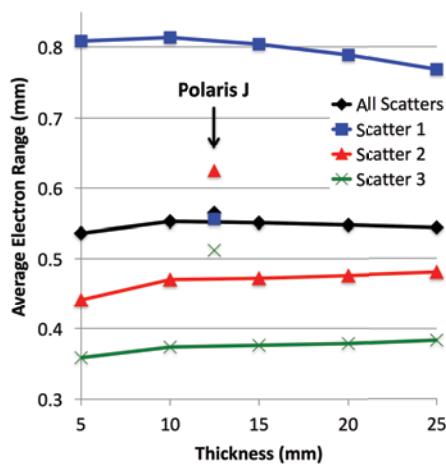


Figure 4. Average electron range for infinite detector at various thicknesses, with a breakdown by individual scatters. Average values for the Polaris J detector also included.

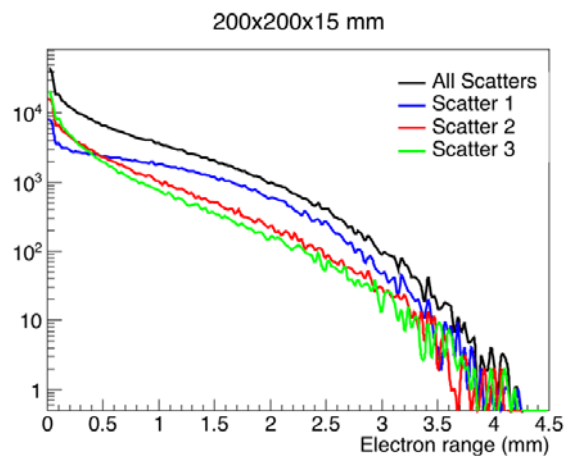


Figure 5. Histogram of the electron range broken down by scatter for the infinite detector with a 15 mm thickness. The y-axis (log scale) is the number of gammas at a given range.

3. Results and Discussion

3.1. Electron Range

Figure 4 shows the average electron range for the infinite detector at various thicknesses. The range of the electron for the first Compton interaction (Scatter 1) is significantly longer than for the other interactions, due to the higher incident gamma energy. The scatter angle of the Compton interaction will also impact the electron energy and range, but due to the geometry of the infinite detectors, the range of scatter angles for each scatter remains approximately the same, and thus will only have a smaller contribution on the electron range than the incident gamma energy. There is also a slight decrease in the range of the first scatter as thickness increases due to the fact that as thickness increases, the number of escaping electrons decreases (see Figure 6). Figure 5 shows the distribution of electron ranges for the 15 mm thick infinite detector. The first scatter consists primarily of electrons with long ranges in comparison to the second and third scatters. Figure 6 shows the sharp decrease in the number of escaping electrons with increasing thickness.

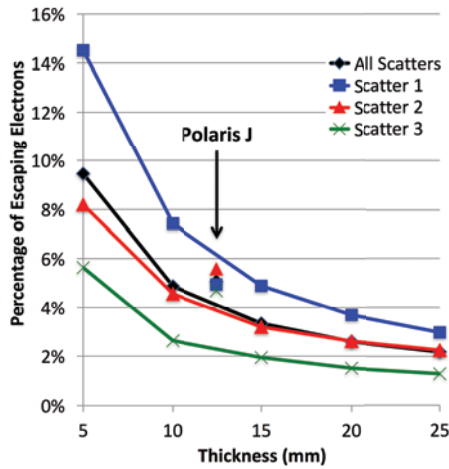


Figure 6. Percentage of Compton electrons that escape from the infinite detector broken down by scatter. Results from the Polaris J detector are also shown.

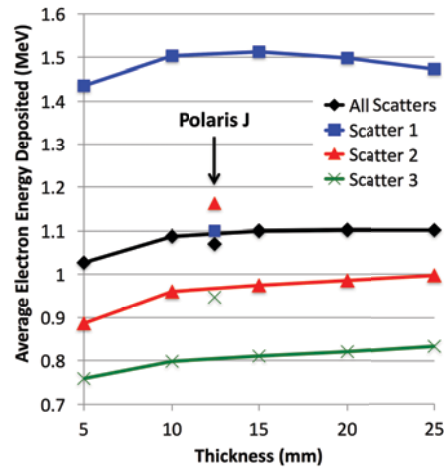


Figure 7. Average electron energy deposited in the infinite detector at various thicknesses, including the breakdown by individual scatters. Results from the Polaris J detector also shown.

3.2. Electron Energy Deposition

Figure 7 shows the average energy deposited by the electron in the infinite detector. Again, the first scatter has a much larger energy deposition and starts to decrease at the largest thicknesses due to the smaller number of escaping electrons while the second and third scatters are capturing more energy. Figure 8 shows the distribution of energy deposition for the 15 mm thick infinite detector (top panes). The top left shows the energy lost by the Compton gammas while the top right shows the energy deposited by the Compton electron. Notice a slight left-hand shift in the electron energy curve indicating a net loss of energy deposition, particularly at the high energies. For the 15 mm thick infinite detector, the average electron deposition for all scatters is 0.2 MeV below the expected value (energy lost by the Compton gammas).

3.3. Polaris J

Figures 4, 6, 7 show results from the simulated Polaris J Compton camera detector overlaid on the infinite detector results. In each figure, the Polaris J results show less deviation between the different scatter interactions while the overall values line up quite closely. In contrast to the infinite detector, the second scatter in the Polaris J detector produces the longest range (Figure 4) and the largest energy deposition (Figure 7) instead of the first scatter. The reason for this can be seen in Figure 8 (bottom panes). Notice the large bump in the energy deposition of the second scatters around 1.5 MeV, resulting in a higher average energy deposition and consequently, a higher average range. Because of the Polaris J detector geometry, a successful triple scatter interaction will have a very narrow angular window and due to the angular dependence of the Compton equation, will, consequently, have a very narrow energy acceptance window, resulting in the 1.5 MeV energy bump.

3.4. Deviations in Polaris J Measurements Due to the Compton Electron

The deviation in measured position by the Polaris J detector due to the path of the Compton electron is estimated to be 0.3 mm, which is roughly half of the simulated electron range, based on results from Figure 4. This assumption is likely an overestimation due to the fact that an electron path is not linear and does not take into account how the detector electronics capture the position of the interaction.

The deviation in measured energy deposition is estimated to be 0.2 MeV, which is the average energy difference between the expected energy lost by the gamma and the actual electron energy deposited.

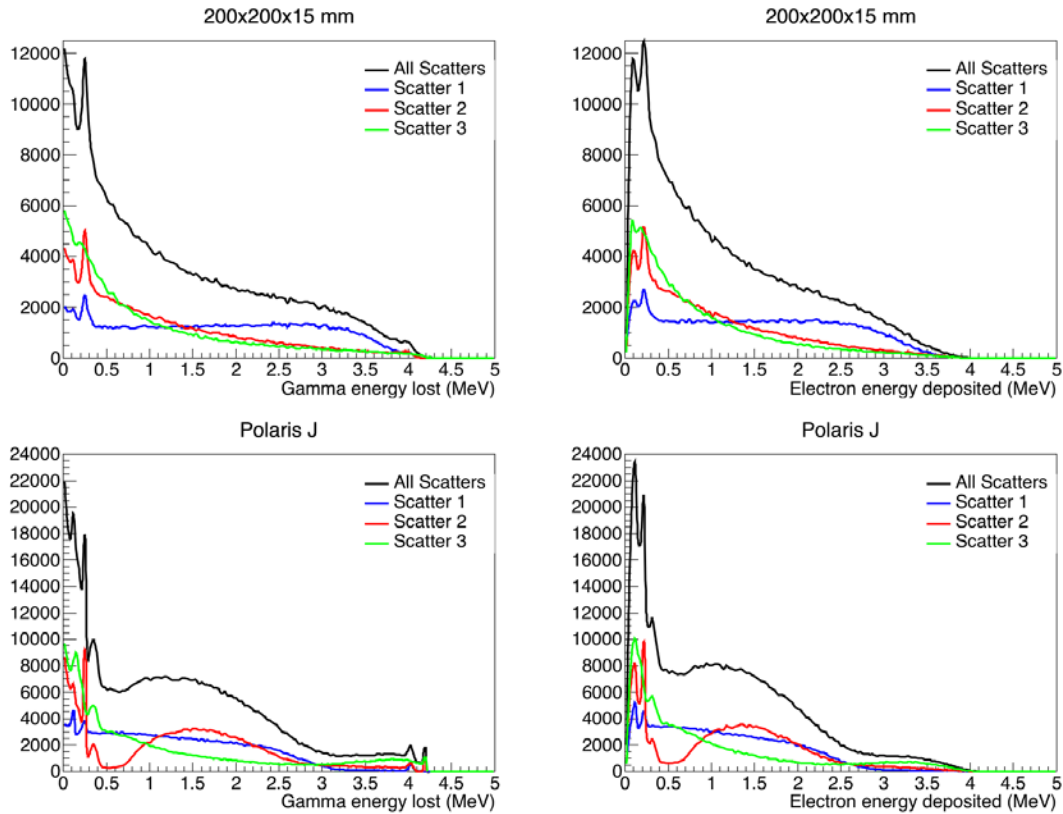


Figure 8. Histogram of the energy lost by the gamma (left panes) and the energy deposited by the electrons (right panes) for the 15 mm thick infinite detector (top panes) and the simulated Polaris J detector (bottom panes). The energy histograms are also broken down by scatter sequence number. The values on the y-axes are the number of gammas.

4. Conclusion

The Geant4-based Compton electron simulation estimated the deviations in the Polaris J detector to be 0.3 mm in position and 0.2 MeV in energy deposition for a 4.44 MeV gamma. The Compton electrons will certainly have an impact on a system that has stated resolutions of 1-2 mm and less than 0.1 MeV.

References

- [1] Min C, Kim C H, Youn M and Kim J 2006 Appl. Phys. Lett. 89 183517
- [2] Polf J C, Peterson S W, Ciangaru G, Gillin M and Beddar S 2009 Phys. Med. Biol. 54 731
- [3] Polf J, Peterson S W, et al. 2009 Phys. Med. Biol. 54, N519
- [4] Peterson S W, Robertson D and Polf J C 2010 Phys. Med. Biol. 55 6841
- [5] Verburg J M, Riley K, Bortfeld T and Seco J 2013 Phys. Med. Biol. 58 L37
- [6] Smeets J, et al. 2012 Phys. Med. Biol. 57 3371
- [7] Deleplanque M A, et al. 1999 Nucl. Instrum. Methods Phys. Res. A 430 292
- [8] Mackin D, Peterson S W, Beddar S, and Polf J 2012 Phys. Med. Biol. 57, 3537
- [9] Richard M, et al. 2012 IEEE Trans. on Nucl. Sci. 59, 1850
- [10] Seo H, et al. 2010 Nucl. Instrum. Methods Phys. Res. A 615 333
- [11] Kurusawa S, et al. 2012 Curr. App. Phys. 12 364
- [12] Hueso-González F, et al. 2014 JINST 9 P05002
- [13] McCleskey M, et al. 2015 Nucl. Instr. and Meth. Phys. Res. A 785 163
- [14] Kroeger R, Johnson W, Kurfess J, Philips B, and Wulf E 2002 IEEE Trans. Nucl. Sci. 49 1887
- [15] He Z, et al. 1999 Nucl. Instrum. Methods Phys. Res. A 422 173
- [16] Zhang F, He Z and Seifert C E 2007 IEEE Trans. Nucl. Sci. NS-54 843
- [17] Robertson D, Polf J C, Peterson S W, Gillin M T, and Beddar S 2011 Phys. Med. Biol. 56 3047

Investigating prompt gamma emission for a Carbon target using AFRODITE clover detectors

V Ramanathan¹, S Peterson¹, K Li², P Papka², E Lawrie³, K Lawrie³, J Kiener⁶, S Ouichaoui⁵, W Yahia-Cherif⁵, A Belhout⁵, P Jones³, D Moussa⁵, B Hinda⁷, S Damache⁸, A Chafa⁵, M Debabi⁵, K Raju M⁴, T Dinoko³ and D Bucher³

¹Department of Physics, University of Cape Town, Rondebosch, 7701, South Africa

²Department of Physics, University of Stellenbosch, Stellenbosch, 7599, South Africa

³iThemba LABS, National Research Foundation, Somerset West, 7129, South Africa

⁴Department of Physics, University of the Western Cape, Bellville, 7535, South Africa

⁵Université des Sciences et de la Technologie H.Boumediène (USHB), Algeria

⁶Centre de Spectrométrie Nucléaire et de spectrométrie de Masse (CSNSM), France

⁷Université de Boumerdes, Algeria

⁸Centre de Recherches Nucléaires (CRNA), Algeria

E-mail: viji07ra@gmail.com

Abstract. Over the last few decades remarkable progress has been made in radiotherapy treatment modalities towards effectively delivering a radiation dose to the planning target volume (PTV) while increasing the survival and reducing the side effects of cancer patients. Proton therapy has become an increasingly popular treatment modality due to its superior dose distribution. However, the advantage of proton beams cannot be fully utilized since no proper method is currently available to measure in-patient proton dose. The detection of secondary prompt gamma rays have been proposed as an in-situ method to determine the proton range since the location of the prompt gamma emission is strongly correlated with the proton depth dose profile. Previous work, using Monte Carlo simulations, has shown discrepancies with the production of prompt gamma data particularly in prominent elements found in tissue within the therapeutic range (50-250 MeV). The goal of this study is to investigate (using simulations and measurements) the prompt gamma emission for the element of carbon. Measurements using a thin target of natural Carbon at the energy 95 MeV were performed at iThemba LABS using the AFRODITE detector system. The experimental setup was then simulated using the Geant4 Monte Carlo toolkit and the results were compared to the measurements.

1. Introduction

The foremost goal of radiation therapy is precise targeting of the tumour volume with minimal exposure to surrounding normal healthy tissues. Proton therapy takes advantage of the steep dose fall-off at the end of the range of the protons in tissue, resulting in a significant reduction in dose to the organs at risk and precise dose conformity while increasing tumour control probability. However, the location of the distal fall-off (Bragg peak) is an uncertain parameter due to the various uncertainties in the treatment delivery.

In radiotherapy, sources of uncertainty are a recognized concern and are addressed by increasing the size of the treatment margins. While there are many possible uncertainties (organ

motion, set-up errors, imaging artifacts) [1], the most critical factor in proton therapy treatment is precisely knowing the range of the proton beam, allowing for more exact dose delivery. A dislocation of the Bragg peak due to these uncertainties can lead to either under-dosage or over-dosage in the treatment delivery. Therefore, in order to fully utilize the advantage of a proton therapy treatment beam it is important to verify the location of the Bragg peak. Due to the fact that treatment protons stop within the patient, secondary prompt gammas have been proposed as a technique for range verification. Although it has been shown that prompt gamma emission is well correlated with the proton Bragg peak [2, 3], Monte Carlo simulations have not been able to accurately reproduce the spectra for prompt gamma spectra produced by carbon [4, 5, 6]. Therefore, this study investigates the prompt gamma spectra from carbon using the AFRODITE (AFRican Omnipurpose Detector for Innovative Techniques and Experiments) detector system by comparing both simulated and experimental results.

2. AFRODITE Detectors

The AFRODITE detection system is a medium sized array that has the ability to detect both low and high energy photons with a reasonable efficiency by using escape suppressed n-type high purity Germanium (HpGe) clover detectors and p-type LEPS (Low Energy Photon Spectrometer) detectors. Each clover detector consists of four n-type separate coaxial HpGe crystals that are packed in the configuration of a four leaf clover and placed in the same cryostat. In order to optimize close packing, the high purity Germanium crystals are tapered at the front face providing a 41 mm X 41 mm square face. A Compton suppression shield (BGO- Bismuth Germanate) surrounds the cover and rejects the Compton-scattered gammas. The AFRODITE frame has the shape of a small rhombicuboctahedron with sixteen detector positions. The target chamber also consists of the same geometry with thin Krypton windows. The clover detectors and escape suppressors were supplied by EurisyS and Crismatec respectively. The diameter and length of the HpGe before shaping are 51 mm and 71 mm respectively. The solid angle of the detector (percentage of 4π) is 1.34% and the taper angle is 7% [7].

3. Geant4 model of AFRODITE detector system

Geant4 is an object oriented Monte-Carlo toolkit which is implemented in the C++ programming language [8]. It is used to simulate the interaction of particles with matter and it plays a major role in particle physics, nuclear physics, astrophysics and medical physics due to the versatility of the Geant4 code. The AFRODITE clover detector system was modelled using the Geant4 Monte-Carlo code (version 10.01.p03). The geometry of the germanium crystals, the BGO crystals, the rhombicuboctahedron shape target chamber, and the collimator were developed using CAD drawings. The complex geometry of the AFRODITE clover detector system was imported using the direct CAD model import interface, CADMesh [9, 10].

The Geant4 model of one crystal assembly with 16 BGO crystals shielding is shown in figure 1. In the Geant4 AFRODITE model, each BGO crystal is connected to a photo multiplier tube (PMT) but the PMTs were not included in the simulation studies. The Geant4 model of one of the clover detectors is shown in figure 2. For both the measurements and the simulations, eight clover detectors were used in the AFRODITE array. Four clovers were placed at 90° and the other four clovers were placed at 135° to the beam line.

4. Experiment

The measurements were carried out with the nuclear research division at iThemba LABS using the AFRODITE clover detector system. A proton beam of 95 MeV was used to hit a natural carbon target of thickness 8.40 ± 0.07 mg/cm². A thin target was selected to avoid multiple interactions. The target was prepared at iThemba LABS. An energy calibration was performed before the proton beam irradiation by using three standard gamma emitting sources, ¹⁵²Eu,

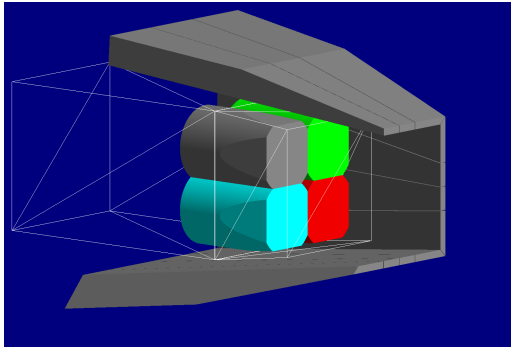


Figure 1. Geant4 model of the closely packed germanium crystals housed inside the Compton escape shielding

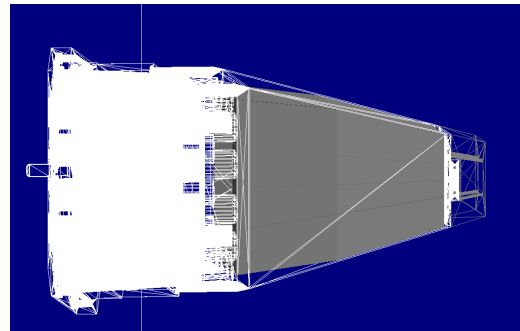


Figure 2. Geant4 model of one of the clover detectors

^{60}Co , and ^{137}Cs . In order to reproduce the distance between the target and the detectors, the gamma sources were placed at the target position. Aluminium (0.88 mm thickness) and Copper (1.21 mm) absorbers were used to reduce the counts from low energy X-rays, with the copper placed closest to the source followed by the aluminium. The data were collected for 30 minutes for each gamma emitting source in direct detection mode. These collected data sets were used to calibrate the energy by considering 17 photo peaks from the above gamma sources. The same data set was also used to determine the absolute detector efficiency for each high purity germanium crystal [11].

5. Simulation

5.1. Validation of AFRODITE model

In order to get accurate, reliable results from a Monte-Carlo model, validation of the model is a requirement. Therefore, the Geant4 model of the AFRODITE system was tested by using the standard gamma emitting source of ^{60}Co as used in the experiment. The Geant4 model of the AFRODITE detector system attempted to model the experimental setup as closely as possible. The standard gamma source was generated using the Geant4 General Particle Source package (GPS) and placed at the target position. The GPS package is able to describe the primary source particle with various spatial, spectral, and angular distribution specification. The source was modelled as an isotropic gamma source and was run with 1.5×10^9 histories.

5.2. Prompt gamma simulation

For the simulations of prompt gamma production, the Geant4 model of the AFRODITE detector was used as in the experimental setup. When using the Geant4 Monte-Carlo code, it is important to select a suitable physics list. The QGSP_BIC Physics list package was used. The thickness for the carbon target was optimized as 0.5 mm in order to decrease the simulation time and to improve statistics. The prompt gamma simulation required 1.2×10^{12} proton histories and 1.8×10^5 CPU hours.

6. Results and Discussion

6.1. Measurement of prompt gamma emission

Figure 3 shows the raw data from the 95 MeV proton bombardment of the carbon target as measured by the 4 clovers placed 90 degrees to the beam direction. This spectra include all backgrounds (room background, background radiations from empty frame with beam on

and beam off) measured during the experiment. All background radiation measurements were normalized according to the time acquisition and the integrated proton charge.

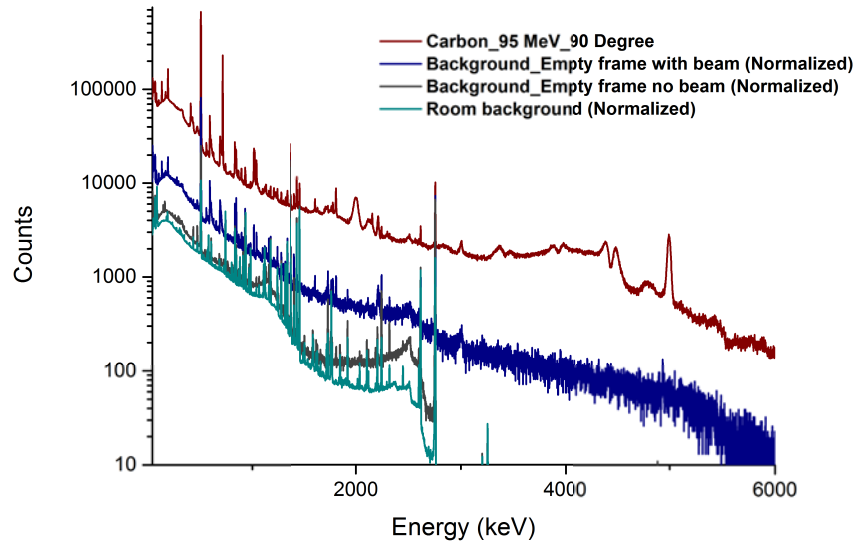


Figure 3. The red line shows the raw data for the 95 MeV proton bombardment of the carbon target, cyan color line is room background, the blue line indicates the background radiation from the frame with the beam on, and the gray line shows the background from the target frame with the beam off. These spectra were measured by the clovers placed at 90 degrees to the beam line. Normalization was done according to the time acquisition and the integrated proton charge.

6.2. Validation of Geant4 AFRODITE model

The Geant4 Monte-Carlo model of the AFRODITE detector system was validated by using the standard gamma emitting source of ^{60}Co as shown in figure 4. The simulated gamma spectrum was normalized against the experimentally obtained gamma spectra by comparing the number of gammas emitted by the gamma source (calculated from the source activity and the acquisition time) in the experiment and number of gamma histories used in the simulation. Both the experimental and simulated spectra have been Compton-suppressed.

Looking at the spectra in figure 4 the two major photo peaks as well as the Compton edge and back scattered peaks are aligned. Comparing the simulated and experimental spectra shows that the Geant4 AFRODITE model had a higher efficiency than the experiment since the simulated photo peaks were higher than the experimental photo peaks. Based on the total gamma production in the experimental and simulated spectra, the Compton shielding of the Geant4 model was determined to work about 15% better than actual Compton shielding detector.

6.3. Prompt gamma spectrum comparison

The prompt gamma energy spectrum was simulated and experimentally measured at 95 MeV. In order to make an absolute comparison between the experimental and simulated results, three primary factors were considered: the difference in the number of incident protons, the difference in the target thickness and the absolute detector efficiency correction factor. Each of these elements resulted in a correction to the simulated spectra. First, the difference in the number of incident protons was corrected by multiplying the simulated spectra by the ratio of the total number of protons from the experimental run to the total number of simulated protons. Next,

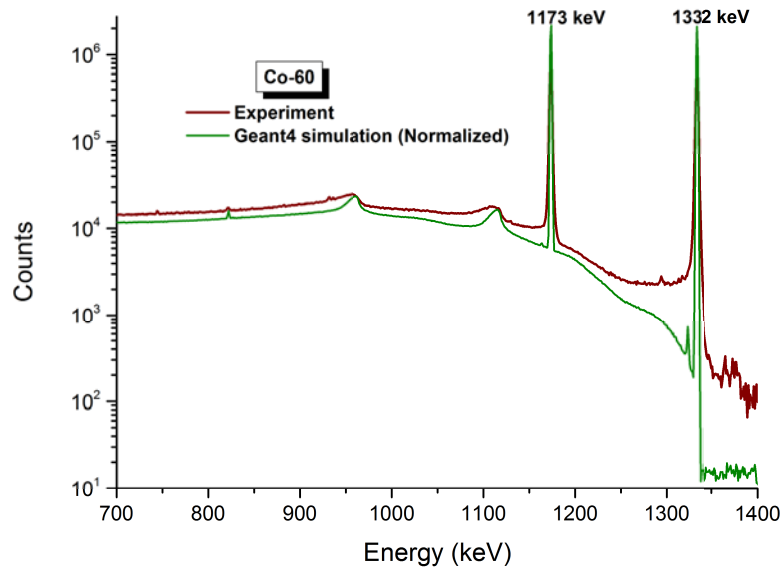


Figure 4. Comparison of the simulated and experimental gamma spectra from ^{60}Co for the AFRODITE clover detector system. The green line shows the simulated spectrum and red line shows the experimental spectrum. Normalization was done according to the number of gammas emitted by the source in the experiment and number of gamma histories in the simulation.

the difference in the target thickness was corrected by multiplying the simulated spectra by the ratio of the experimental target thickness to the simulated target thickness. Lastly, the difference in the absolute detector efficiency needed to be corrected for each crystal individually based in the absolute detector efficiency correction factors. The simulated spectra from each crystal was divided by its respective correction factor. The combination of these corrections provided a way to make an absolute comparison of the experimental and simulated spectra, as shown in figure 5.

Overall, the two spectra align quite well, showing good peak agreement along the energy scale, particularly for the 4.438 MeV peak. The spectra also agree reasonably well in the number of counts with two noticeable gaps (between 2.0 and 3.5 MeV and above 4.5 MeV) where the simulation spectra is higher than the experimental spectra. The stretches where the simulations spectra are higher could be a result of the historic overestimation of the prompt gamma production in Geant4 or possibly the timing settings of the simulated Compton suppression. The total gamma production (determined by summing the gamma counts up to 6.0 MeV) for the experimental and simulated spectra in Figure 5 reveals that the simulated results were 40% higher than the total measured gamma production values. Finally, looking more closely at the 4.438 MeV ^{12}C photo peak shows that the simulated peak is broader than the experimental peak.

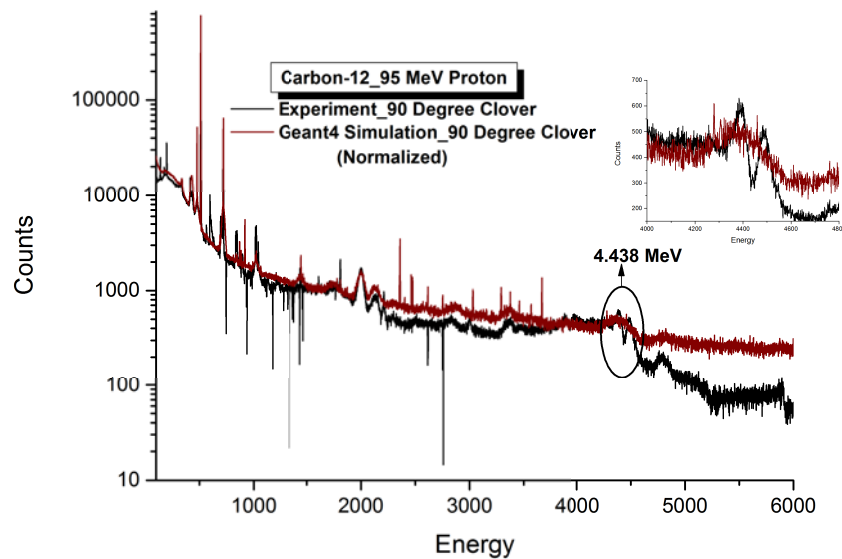


Figure 5. Gamma spectra comparison of the experimental and simulated results for a 95 MeV proton collision on the carbon target. The red line shows the corrected Geant4 simulated spectrum and the black line shows the experimental spectrum. Inset: Enlarged view of the 4.438 MeV gamma peak. Normalization was done according to the difference in the number of incident protons, the difference in the target thickness and the absolute detector efficiency correction factor.

7. Conclusion

The AFRODITE detector system was modelled using the Geant4 Monte-Carlo code (version 10.01.p03) and was validated by comparing to experimentally measured gamma spectrum using the standard gamma emitting source of ^{60}Co . This validation of the AFRODITE model led to the conclusion our Geant4 AFRODITE model had a slightly higher efficiency than the actual detector setup. The overall absolute gamma energy spectra from the 95 MeV experimental and simulation runs were compared and displayed a 40% overestimation for the total gamma production values. Comparison of the 4.438 MeV peak showed an unsatisfactory discrepancy in the shape of the simulated peak for the prompt gamma production from carbon. The Geant4 AFRODITE model will be used to further investigate these highlighted issues with the hadronic physics lists for prompt gamma production.

References

- [1] Min Hee PhD Thesis, Hanyang University, Seoul(KR), 2011
- [2] Min C, Kim C H, Youn M, and Kim J Applied Physics Letters, 89, 183517, 2006.
- [3] Polf J C, Peterson S, Ciangaru G, Gillin M, and Bedder S Physics in Medicine and Biology, 54, 731, 2009a.
- [4] Polf J C et al. Physics in Medicine and Biology, 54, N519-N527, 2009
- [5] Dedes G Physics in Medicine and Biology, 59, 7, 1747, 2014
- [6] Jeyasugiththan J and Peterson S W Physics in Medicine and Biology, 60, 19, 7617, 2015
- [7] Jones P M et al. Nucl. Instr. Meth. Phys. Res. A, 362, 556-560, 1995
- [8] Agostinelli S et al. Nucl. Instr. Meth. Phys. Res. A, 506, 250-303, 2003
- [9] Poole C M et al. Australasian Physical and Engineering Science in Medicine, 10.1007/s13246-012-0159-8, 2012
- [10] Poole C et al. IEEE Transactions on Nuclear Science, 99, 2012
- [11] Vijitha Ramanathan PhD Thesis, University of Cape Town, South Africa, 2017

Estimation of fake rate background in same sign $W^\pm W^\pm$ production at the LHC with ATLAS Detector

X. Thusini, Dr A. Hamilton, Dr S. Yacoob

Department of Physics, University of Cape Town, South Africa

E-mail: xolisile.octavia.thusini@cern.ch

Abstract. At the Large Hadron Collider, $W^\pm W^\pm$ boson scattering has been identified as a promising interaction for understanding of the Electroweak Symmetry Breaking. This is a rare Standard Model process with small cross-section. The previous measurements have found evidence for the process to a significance of 4.5σ using $\sqrt{s} = 8$ TeV proton-proton collision data recorded by the ATLAS detector. This paper aims at understanding the fake background in same sign $\ell^\pm \ell^\pm + E_T^{miss} + jj$ channel coming from the scattering of two W bosons with the same electric charge. The two W 's are required to decay leptonically with only electrons and muons in the final state. The background processes that can mimic the signature of same sign $\ell^\pm \ell^\pm + E_T^{miss} + jj$ are W +jet, $t\bar{t}$, single top or QCD multijet processes where one or two jets are mis-reconstructed as leptons. The main objective of this work is to understand non-prompt, fake, backgrounds coming from $t\bar{t}$ decay using Monte Carlo simulations.

1. Theoretical Background

The study of fundamental particles began in the first decade of 21st century when scientists started to observe new particles as a result of an increase in collision energies. The properties of these particles were not well explained till late 1970's when physicists of the time developed what became the Standard Model (SM) [1, 2, 3, 4, 5, 6] of particle physics. This is the only model that successfully describes the properties and interactions of the fundamental building blocks of nature at the smallest scales. The W boson is one of the SM particles responsible for weak interactions. It was discovered in 1983 at LEP collider [7, 8]. The W boson can be positively or negatively charged and has a mass of 80.385 ± 0.015 GeV.

In proton-proton collisions, same sign WW boson scattering can occur through non-resonance direct processes depicted in Figure 1 where both W bosons decay leptonically into $e\nu$ or $\mu\nu$. This is a rare Standard Model process with small cross-section that has not yet been observed, but previous measurements have found evidence for the process to a significance of 4.5σ by ATLAS experiment [9] and 2.0σ by CMS experiment [10]. The experimental signature of two same-signed leptons (electrons or muons), missing transverse energy, and two jets is used because of the relatively low background from diboson production, $t\bar{t}$ and $Z + jets$.

$$W^\pm W^\pm \rightarrow \ell^\pm \ell^\pm + E_T^{miss} + jj$$

This paper presents some of the ongoing work in understanding the backgrounds in the search for same sign WW boson scattering (ssWW) within the ATLAS experiment.

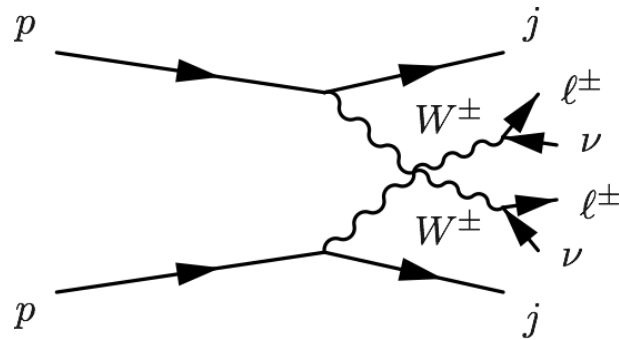


Figure 1. 1st order Feynman diagram of the same sign WW boson scattering.

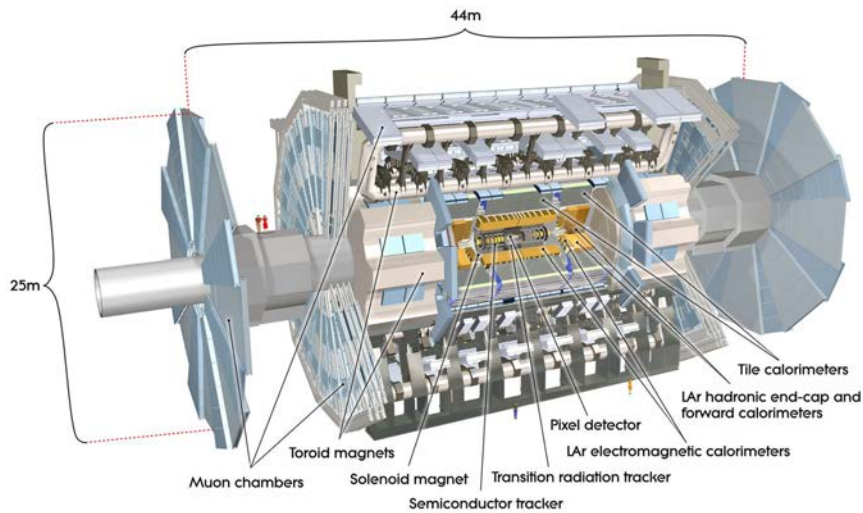


Figure 2. ATLAS detector and its subsystems[11].

2. The LHC and the ATLAS Experiment

In 2001, the LEP collider at the CERN was decommissioned so that the Large Hadron Collider (LHC) [12] could be installed in the 27km tunnel. The primary goal of ATLAS was to observe the SM Higgs particle. Inside the LHC tunnel, two beams of protons circulate in opposite directions and collide at four points instrumented with detectors. In the middle of 2015, the LHC started running in proton-proton collision mode at a centre of mass energy of 13 TeV and luminosity of about $1 \times 10^{34} \text{ cm}^{-2} \text{ s}^{-1}$. To date, the LHC has delivered approximately 8 fb^{-1} of data under these conditions.

ATLAS detector [11] is one of the general purpose experiments installed on the LHC. It is made up of cylindrical barrel region and end-cap region on either side, refer to Figure 2. Both barrel and end-cap are comprised of many subsystems that are classified into three sub-detectors; inner tracker, calorimeters and muon spectrometer. Each subsystem is designed to measure specific properties of the particles passing through it to identify the signature they leave in the detector. A particle is identified either by interacting directly with the detector or by its decay into particles which can be then interact directly. It is possible for the detector to misidentify a particle. These fake signatures contribute to the background in the search for ssWW. To better model the backgrounds, particle physicists rely on Monte Carlo numerical methods.

3. Event Generators and Detector Simulations

In particle physics experiments, Monte Carlo (MC) based event generators and detector simulations are critical for understanding the data produced. The event generators model the proton-proton collisions, while the detector simulations model the interaction of particles in the detector. The MC samples thus come with two pieces of information; the *truth* information including the list of particles produced in the event generator and the *reconstructed* (*reco*) information containing the signatures that were reconstructed with a detector simulation framework based on GEANT4 [13]. By comparing the *reco* to the *truth*, the MC samples can be used to estimate the amount of mis-modelling in the reconstruction of particle signatures.

To compare the *reco* to *truth*, each reconstructed object is required to have a corresponding truth object within a specified distance in $\eta - \phi$ space: $\Delta R = \sqrt{\Delta\eta^2 + \Delta\phi^2}$. ϕ is the azimuthal angle, $\phi = \arctan \frac{y}{x}$, measured in the xy -plane. At hadron colliders, scientists deal with very energetic products of the collision, in this highly relativistic regime changes in rapidity Δy are Lorentz invariant. Hence, the rapidity (y) which reduces to the pseudo-rapidity (η) when the particle mass can be neglected, is used as a co-ordinate in the yz -plane. Both these parameters are computed as follows: $y = \frac{1}{2} \ln \frac{E+p_z}{E-p_z}$, where E and p_z define the energy and momentum of the particle along the z -axis, respectively, and $\eta = -\ln \left(\frac{\theta}{2} \right)$.

The ATLAS standard comparison algorithm, called the ‘ATLAS MC Classification Tool’ was developed by the ATLAS analysis software group in order to classify reconstructed objects such as electrons, muons, taus and photons according to their truth origin or ancestry. However, this classification tool has some limitations, it failed to classify nuclei, some hadrons and neutrinos for a significant fraction of the semi-leptonic $t\bar{t}$ events that pass the $ssWW$ event selection criteria. Classification of these fake events is important for understanding the non-prompt background, coming from a decay of hadrons and not from a W boson. For these cases where the ATLAS tool failed to do the classification, a new tool called ‘My MC Truth Classification Tool’ has been developed.

The flow chart depicted in Figure 3 shows how both of these tools work. The ATLAS MC Classification Tool takes *reco* lepton and checks whether it has a truth particle associated with it. For the cases where this fails, My MC Truth Classification Tool takes the same lepton and return the list of all the closest *truth* particles within the cone size of $\Delta R = 0.2$. At the next stage it picks the particle with minimum ΔR from the list and checks if it belongs to the same decay chain as the other particles in the list, if it does the first generation is used as *origin*. The *type* depends on whether the list contain hadrons.

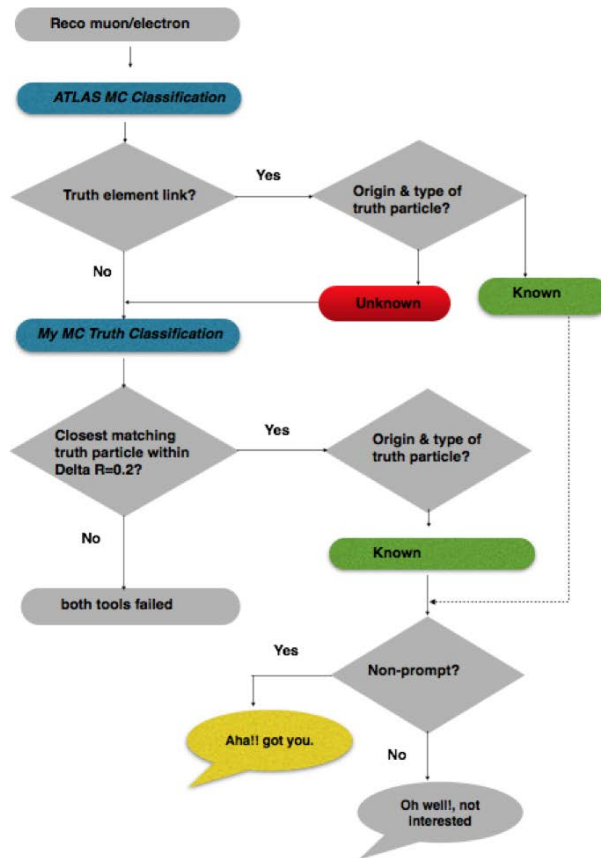


Figure 3. Flow of information between two classification tools.

4. My Truth MC Classification tool

Understanding the format of the event generator record is an important first step in classifying the truth origin of reconstructed signature as this may differ depending on the type of the generator. The decay chain from semi-leptonic $t\bar{t}$ event simulated by Sherpa event generator [14] is given in Figure 4. When there is hadronisation involved along the decay channel, it is more likely to reconstruct a lepton from hadron decay as a ‘real’ lepton, in this scenario a μ^- . This particular event illustrated in the diagram has two *reco* leptons, the first one is associated with *truth* e^- the second one has a μ^- as the closest *truth* match.

In addition to the non prompt background due to hadronisation, there are other classes of events that the ATLAS official tool classifies as two isolated leptons with opposite sign. When looking at the details of the truth record, the reason they pass the ssWW selection is that there is a photon conversion that is not property recorded by the tool.

5. Results and Discussion

Leptons originating from the underlying event are referred to as Background (Bkg) leptons. Mesons and baryons are hadrons, any lepton coming from these particles is non-isolated. The classification of truth particles for ATLAS standard tool is shown in Figure 5. However, other events failed the tool, indicated with red, this are the inputs in My MC Truth Classification tool, the distribution of truth origin as an output of this tool is shown in Figure 6.

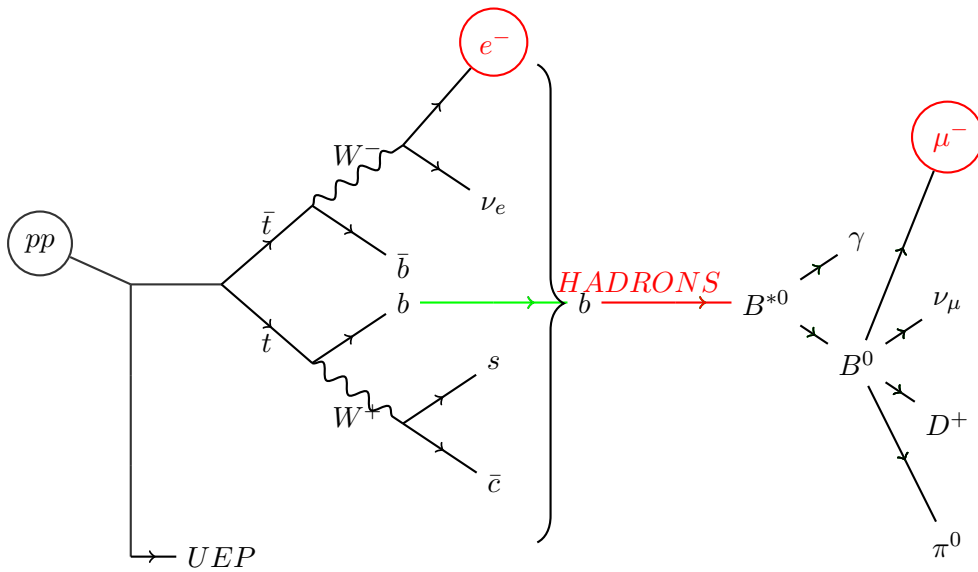


Figure 4. This diagram shows how $t\bar{t}$ event can end up being reconstructed with two same sign final state leptons, circled in red. One of these leptons, the μ^- , is a fake, or in this case non-prompt lepton; meaning that it come from a hadron and not from a W boson. UEP stands for underlying event particles and pp means proton-proton collision.

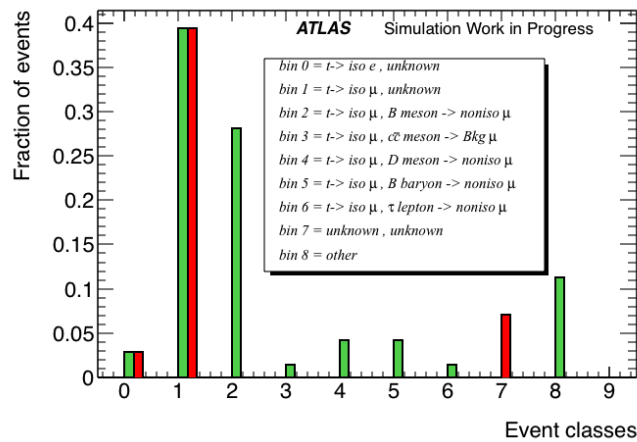


Figure 5. Different cases where $t\bar{t}$ events fake signal events with two leptons, electrons or muons, as defined by **ATLAS MC classification tool**. Each event is required to have two leptons, the plot shows the truth origin and type for both leptons. The unknowns are indicated in red, and are classified in My Truth MC Classification tool.

6. Conclusion

A new MC classifier tool has been developed to classify the truth origin of reconstructed signatures and to understand non-prompt background in $t\bar{t}$ production process. Preliminary results are summarised in figure 6 where we see that almost 40% of events which pass our selection are from an unknown source according to the standard ATLAS tool, and 27% from B meson decays. The events from unknown sources in figure 6 are further investigated using a cone matching algorithm and the results of this, summarised in figure 7, show that the dominant

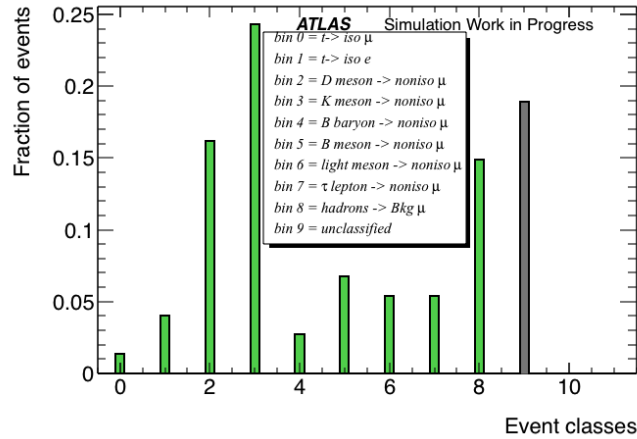


Figure 6. Truth origin and type of reconstructed leptons that failed ATLAS standard tool. These are the results from **My MC Truth Classification tool**. The case where both tools failed is marked in grey.

contribution is from D mesons. However 20% of these events remain unclassifiable. As future work, an understanding of this type of background will be used to optimise isolation and signal-to-background ratio for fake background studies in same sign WW production.

References

- [1] Glashow S.I. 1961 *Nucl. Phys.* **22** 579.
- [2] Weinberg S. 1967 *Phys. Rev. Lett.* **19** 1264.
- [3] Salam A. 1968 *Proceedings of the 8th Nobel Symposium* (Almqvist and Wiksell, Stockholm) 367.
- [4] Englert F., Brout R. 1964 *Physical Review Letters* **13** (9): 321 – 3.
- [5] Higgs P.W. 1964 *Physical Review Letters* **13** (16): 508 – 9.
- [6] Guralnik G.S., Hagen C.R., Kibble T.W.B. 1964 *Physical Review Letters* **13** (20): 585 – 7.
- [7] UA1 Collaboration 1983 *Physics letters B* **122** 103 – 16.
- [8] UA2 Collaboration 1983 *Physics letters B* **122** 476 – 85.
- [9] ATLAS Collaboration *Phys. Rev. Lett.* **113** 141803.
- [10] CMS Collaboration *Phys. Rev. Lett.* **114** 051801.
- [11] ATLAS Collaboration 2008 *JINST* **3** S08003.
- [12] Evans L. and Bryant P. (Eds.) 2008 *JINST* **3** S08001.
- [13] Agostinelli S. 2003 *Nucl. Instrum. Meth.* **A506** no. arXiv:1005.4568. CERN-PH-EP-2010-044, 250.
- [14] Gleisberg T., et al. 2009 *JHEP* **0902** 007.

Constraining hypothetical extensions to the Higgs sector at the LHC

Stefan von Buddenbrock^{a,1}, Nabarun Chakrabarty^b, Alan S. Cornell^c, Deepak Kar^a, Mukesh Kumar^c, Tanumoy Mandal^d, Bruce Mellado^a, Biswarup Mukhopadhyaya^b, Robert G. Reed^a and Xifeng Ruan^a

^aSchool of Physics, University of the Witwatersrand, Johannesburg 2050, South Africa.

^bRegional Centre for Accelerator-based Particle Physics, Harish-Chandra Research Institute, Chhatnag Road, Jhansi, Allahabad - 211 019, India.

^cNational Institute for Theoretical Physics; School of Physics and Mandelstam Institute for Theoretical Physics, University of the Witwatersrand, Johannesburg, Wits 2050, South Africa.

^dDepartment of Physics and Astronomy, Uppsala University, Box 516, SE-751 20 Uppsala, Sweden.

E-mail: ¹stef.von.b@cern.ch

Abstract. With Run 2 of the LHC currently under way at a record-breaking centre of mass energy of 13 TeV, new physics searches are becoming more feasible than ever before. In particular, the ATLAS and CMS collaborations are beginning to focus more on searches which may extend the Higgs sector of the Standard Model. Here it is shown that Run 1 data from both ATLAS and CMS hint at the existence of a new heavy scalar with a mass around 270 GeV. This work will also extend this idea by introducing a full Two-Higgs Doublet Model and outlining the potential Run 2 searches which could constrain the parameters of such a model, should it exist in nature. This will be presented in the context of searches for Higgs production in association with missing energy, leptons and large jet multiplicities. Some preliminary studies related to the rates and kinematic distributions of processes of interest are presented and their implications are discussed in the context of the ATLAS Z+MET search.

1. Introduction

The experimental discovery [1, 2] of the Standard Model (SM) Higgs boson (h) has finalised the minimal particle content which the SM requires. Most of what has been observed about this particle is consistent with what we expect in terms of its spin-parity [3, 4] and coupling strength to the SM particles [5]. There are, however, some measurements on the Higgs boson's properties which show deviations from what is expected in the SM.

The deviations which are considered here involve the following: distortions in the Higgs p_T spectra, di-Higgs resonance searches, VV resonance searches (where V is a weak vector boson – either Z or W^\pm), and enhancements of top associated Higgs production cross section. Due to space constraints, the reader is encouraged to read reference [6] for a review of these references.

This short paper explores the result of combining these deviations under the common hypothesis that a heavy scalar H exists with assumptions on its production mechanism and decay modes. As opposed to previous studies done on this topic (i.e. those in references [6] and [7]), this short paper first summarises the introduction of the model, and then focuses on

a particular final state with the data in mind – that is, two same flavour opposite sign (SFOS) leptons plus large missing energy. In section 2, an effective theory approach is taken to determine how well the hypothesis can explain data. The possible consequences of embedding H into a two Higgs doublet model (2HDM) are discussed in section 3, after which an interesting search channel is presented for this approach in section 4. The work is concluded in section 5.

2. The effective model

It can be argued that each of the afore-mentioned deviations can be explained by the existence of a heavy scalar:

- The boosted Higgs p_T spectra can be explained if the Higgs is a decay product of some heavy resonance H to give $H \rightarrow h + X$.
- Deviations around 300 GeV in the hh and VV searches could be due to the same resonance.
- Top associated H production is enhanced if the H couples weakly to the vector bosons. This idea has been explored in reference [8].

The most minimalistic way to model this hypothesis is to write down an effective Lagrangian which allows H to decay to the necessary final states which explain the deviations. Under the assumption that H is produced dominantly through gluon fusion (ggF), we can extend the SM by adding the following beyond SM (BSM) sectors to the SM Lagrangian [6]:

$$\mathcal{L}_{Hgg} = -\frac{1}{4}\beta_g \kappa_{hgg}^{\text{SM}} G_{\mu\nu} G^{\mu\nu} H, \quad (1)$$

$$\mathcal{L}_{HVV} = \beta_V \kappa_{hVV}^{\text{SM}} V_\mu V^\mu H, \quad (2)$$

$$\mathcal{L}_Y = -\frac{1}{\sqrt{2}} y_{ttH} \bar{t}tH - \frac{1}{\sqrt{2}} y_{bbH} \bar{b}bH, \quad (3)$$

$$\mathcal{L}_T = -\frac{1}{2}\lambda_{Hhh} Hhh - \frac{1}{2}\lambda_{h\chi\chi} h\chi\chi - \frac{1}{2}\lambda_{H\chi\chi} H\chi\chi, \quad (4)$$

$$\mathcal{L}_Q = -\frac{1}{4}\lambda_{HHhh} H^2 h^2 - \frac{1}{4}\lambda_{hh\chi\chi} h^2 \chi^2 - \frac{1}{4}\lambda_{HH\chi\chi} H^2 \chi^2 - \frac{1}{2}\lambda_{Hh\chi\chi} Hh\chi^2. \quad (5)$$

Here, Equation 1 describes an effective interaction between H and the gluon field in order to model ggF . It is multiplied by a dimensionless free parameter β_g , which controls the rate of H production. Similarly Equation 2 models the decay of $H \rightarrow VV$, controlled by the free parameter β_V . The decay of $H \rightarrow hh$ is brought about by the first term in Equation 4.

In order to model the $H \rightarrow h + X$ to explain the distortion in the Higgs p_T spectra, a massive scalar dark matter (DM) candidate χ has been introduced. The fourth term of Equation 5 allows for an $H \rightarrow h\chi\chi$ decay mode which allows for an $h + E_T^{\text{miss}}$ search channel.

Assuming that H can only decay to hh , VV and $h\chi\chi$, one can fix the former two's branching fractions against the data mentioned in section 1 and, in doing so, fix the latter by allowing it to saturate the remaining width. Then the free parameter β_g can be fixed by making a fit to the Higgs p_T spectra. This was done by generating Monte Carlo (MC) events in `MadGraph` [9] at leading order (LO), showering them in `Pythia 8.2` [10] and passing them through an appropriate analysis using the `Rivet` [11] framework. A χ^2 function was minimised to find the best fit value of β_g . This can be done for any value of m_H (the mass of H), so a scan was performed to find the best fit to all of the public Higgs p_T spectra simultaneously. The best fit result of this is shown in Figure 1. Note here that $m_\chi = 60 \text{ GeV} \simeq m_h/2$ in order to suppress the invisible branching fraction of the Higgs boson. The best fit point was at $m_H = 270 \text{ GeV}$, with $BR(H \rightarrow hh) = 0.030 \pm 0.037$, $BR(H \rightarrow ZZ) = 0.025 \pm 0.018$ and $BR(H \rightarrow WW) = 0.057 \pm 0.041$. The parameter β_g was best fit at the value of 1.5 ± 0.6 .

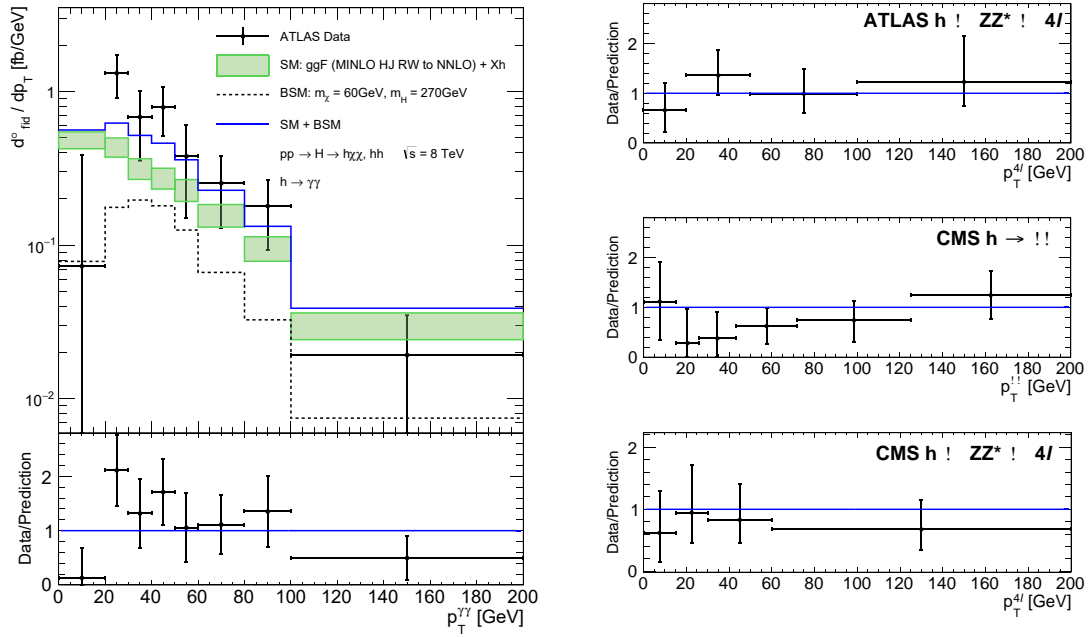


Figure 1. Fits to the $h \rightarrow \gamma\gamma$ and $h \rightarrow ZZ \rightarrow 4\ell$ p_T spectra for both ATLAS and CMS. On the left is the ATLAS $h \rightarrow \gamma\gamma$ spectrum, where the green blocks represent the NLO SM prediction as calculated using MINLO [12] reweighted to NNLO and normalised to the cross section computed in reference [13]. The contribution from other Higgs production modes is included. The black dotted line represents the Higgs p_T coming from $gg \rightarrow H \rightarrow h + X$, and the blue is a sum of the SM and BSM contributions. Due to space constraints, only the ratio plots are shown for the other channels (on the right).

This fit method can be done for any value of m_H in the range $[2m_h, 2m_t]$ – the lower bound is because we require $H \rightarrow hh$ to be an on-shell decay and the upper bound is to avoid a large $H \rightarrow t\bar{t}$ branching fraction. Doing a scan on mass points, the χ^2 for the hypothesis against the data is shown in Figure 2 (a). Interpolating between these points gives a minimised value at $m_H = 272_{-9}^{+12}$ GeV. This mass point corresponds to the best fit point for H mass hypotheses, with an error having a 1σ coverage. In Figure 2 (b), a test statistic of $\Delta\chi^2$ is used to measure the significance of this result. It can be seen from this plot that at 272 GeV, the local significance of the BSM hypothesis over the SM is around 3σ .

3. Extending the model

A local 3σ hint at a new ~ 270 GeV heavy scalar is a promising thought from an experimental point of view. There are, however, theoretical grievances with the effective model presented in section 2. For one, we have assumed that the three body decay of $H \rightarrow h\chi\chi$ dominates the width of H , where it would be far more natural if the two body decays were dominant. In addition to this, gauge invariance stipulates that the Lagrangian is incomplete. There are terms which arise from the gauge structures in the theory that have been omitted, some of which might influence the results presented here.

For this reason, the theory can be made more natural by introducing two theoretical modifications, as suggested in reference [7]. Firstly, we can easily make the assumption that H is the CP-even component of a 2HDM. 2HDMs are well motivated models which have no theoretical issues pertaining to unitarity, gauge invariance, etc. The ramifications of requiring

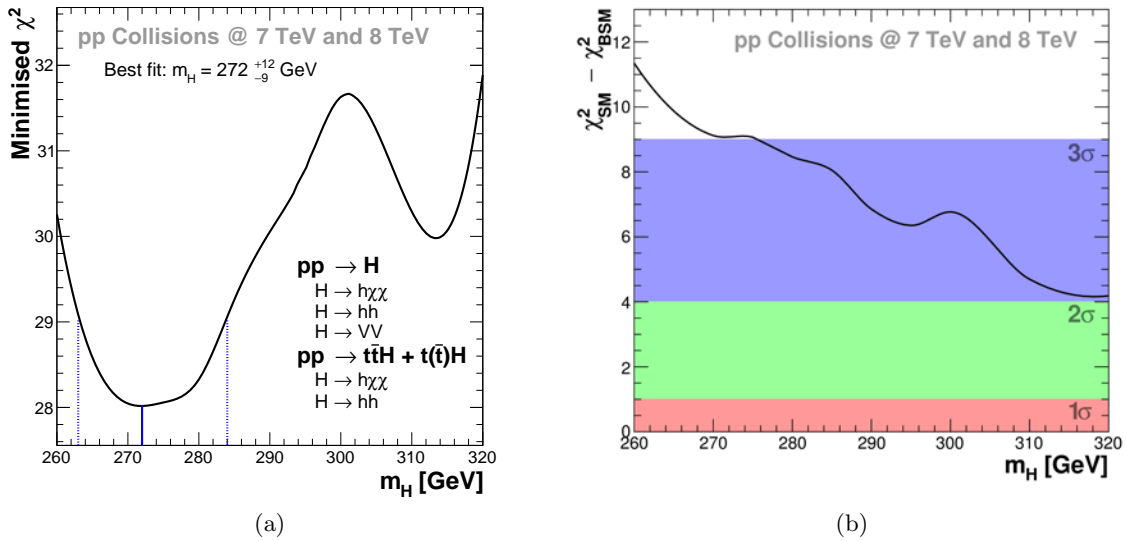


Figure 2. The results of a χ^2 calculation (a) and $\Delta\chi^2 = \chi^2_{\text{SM}} - \chi^2_{\text{BSM}}$ (b) as a function of the mass of H . These results were obtained by fitting to all p_T spectra, hh rates, VV rates and $t\bar{t}h$ rates. The free parameter β_g was marginalised for each value of m_H so as to minimise the χ^2 .

a 2HDM are that four new particles are introduced: the CP-even (scalar) H , the CP-odd (pseudoscalar) A , and two charged scalars H^\pm .

Secondly, we solve the issue of the dominant three body decay by introducing a singlet scalar S . We then postulate that H can decay to SS or Sh (in addition to hh , VV , etc.) and that S can decay invisibly to $\chi\chi$ as well as to SM particles. Doing this transforms the three body decay into a chain of two body decays – this is shown in Figure 3. S can take on a mass in the range $[m_h, m_H - m_h]$ so that decays of $H \rightarrow SS, Sh$ can be kept on-shell in most of the parameter space. The admixture of SS and Sh is controlled by the parameter a_1 , which is a ratio of the $H \rightarrow Sh$ and $H \rightarrow SS$ branching fractions.

4. $A \rightarrow ZH$: a potential search channel

As mentioned before, using a 2HDM introduces four new bosons to the theory. With some hints that H exists, one should also ask whether the model presented here can be used to make searches for the other new bosons too. Here a search channel for A is presented in the context of an ATLAS supersymmetry search.

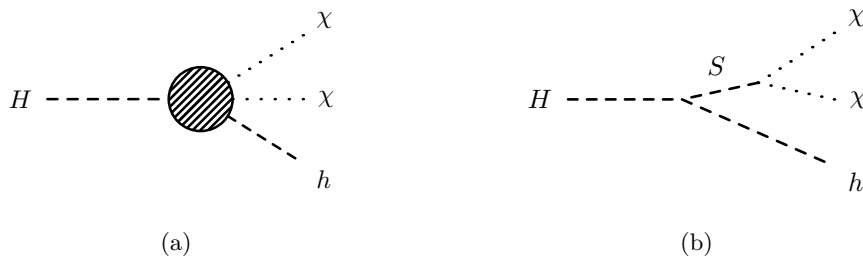


Figure 3. The effective decay of $H \rightarrow h\chi\chi$ (a) is replaced by a tree level decay process when the singlet scalar S is introduced (b).

Given that the model is embedding into a 2HDM, we find the following mixing terms in the Lagrangian of the theory:

$$\mathcal{L}_{V\phi\phi} \subset \frac{m_W}{v \cos \theta_W} \left[\sin(\beta - \alpha) Z_\mu (A \partial_\mu H - H \partial_\mu A) + \cos(\beta - \alpha) Z_\mu (A \partial_\mu h - h \partial_\mu A) \right], \quad (6)$$

where α and β are mixing angles, and v is the vacuum expectation value. For an SM-like H , we require that $\cos(\beta - \alpha) \sim 0$. This necessarily sets $\sin(\beta - \alpha) \sim 1$, meaning that the A - Z - H coupling is far stronger than the A - Z - h coupling. Therefore, if A is produced through ggF , we could expect a non negligible rate of $pp \rightarrow A \rightarrow ZH$ events, where $H \rightarrow SS, Sh$.

If S has a large branching fraction to $\chi\chi$, this should be a viable in Z +MET supersymmetry searches. These searches typically search for a $Z \rightarrow \ell\ell$ candidate with large missing energy

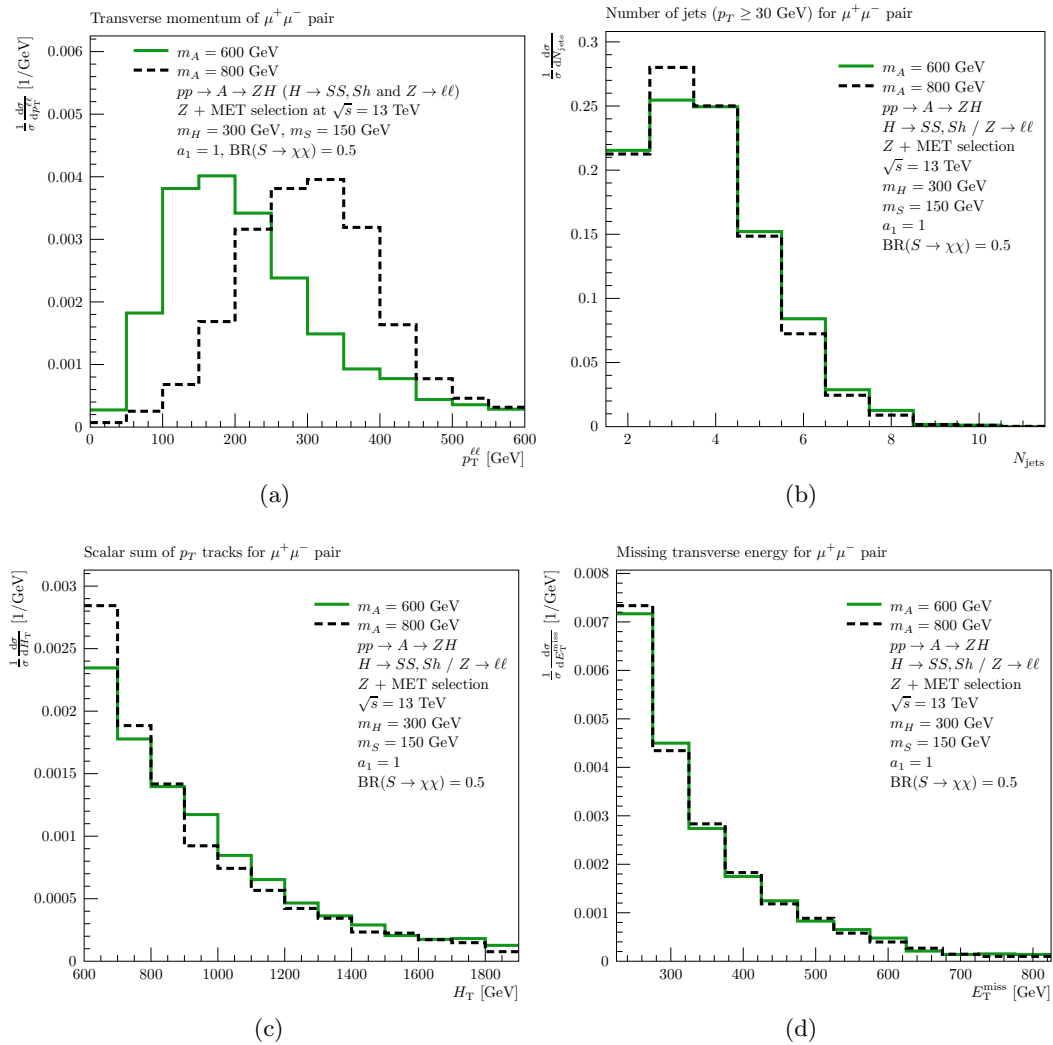


Figure 4. Sample distributions for $A \rightarrow ZH$ with the final state $\ell\ell + E_T^{\text{miss}} + X$. Events were generated in *Pythia 8.2* and analysed according to the Run 2 ATLAS Z +MET cuts [14] using *Rivet*. These show the di-lepton p_T (a), the jet multiplicity (b), the H_T – a scalar sum of jet and lepton p_T (c), the the missing transverse energy (d).

and jets. This final state could be predicted by certain supersymmetry models, but the model presented here could also predict this final state with $S \rightarrow \chi\chi$ or jets and $h \rightarrow$ jets.

In order to test the validity of this, a sample of $pp \rightarrow A \rightarrow ZH$ was simulated and decayed with $Z \rightarrow \ell\ell$ and $H \rightarrow SS, Sh$ in *Pythia 8.2*. S was given Higgs-like branching fractions as well as a 50% branching fraction to $\chi\chi$. m_A was considered at 600 GeV and 800 GeV, while m_H was fixed at 300 GeV, $m_S = 150$ GeV and $m_\chi = 60$ GeV. These events were selected and plotted using the ATLAS Run 2 Z+MET SRZ selection [14], where a 2.2σ excess was observed in data.

Some sample distributions from this procedure are shown in Figure 4 for the $Z \rightarrow \mu\mu$ channel. Here we see that the di-lepton p_T is a good discriminant in determining the effect of m_A , since a lower mass A predicts a softer spectrum which is arguably observed in the ATLAS data. The jet multiplicity is small compared to the supersymmetry models considered in reference [14], which is closer to what is seen in the data. The H_T and E_T^{miss} spectra shown resemble tails of a distribution rather than peaks, which is also close to what the data shows. The efficiencies for the events passing the cuts are 0.68% and 1.86% for $m_A = 600$ and 800 GeV, respectively (for both the $Z \rightarrow ee$ and $\mu\mu$ channels).

5. Concluding remarks

Under the assumption that various deviations observed in Run 1 of the LHC can be explained by the existence of a heavy scalar H , an analysis has been done to show that the data can be explained better by this hypothesis with a significance of 3σ over the SM. This approach has been expanded to fit with a 2HDM in association with a singlet scalar to resolve theoretical issues. Using this theory, a search channel has been presented for the pseudoscalar component of the 2HDM, A . A viable channel has been identified in the generic Z+MET supersymmetry searches.

While some tantalising results have been presented, it is noted here that much work is still needed to explain the theory fully. Since this work is data driven and can only progress when ATLAS and CMS publish more results, further studies will be done when these results are available.

References

- [1] Aad G *et al.* (ATLAS Collaboration) 2012 *Phys. Lett.* **B716** 1–29 (arXiv:1207.7214)
- [2] Chatrchyan S *et al.* (CMS Collaboration) 2012 *Phys. Lett.* **B716** 30–61 (arXiv:1207.7235)
- [3] Aad G *et al.* (ATLAS Collaboration) 2013 *Phys. Lett.* **B726** 120–144 (arXiv:1307.1432)
- [4] Chatrchyan S *et al.* (CMS Collaboration) 2013 *Phys. Rev. Lett.* **110** 081803 (arXiv:1212.6639)
- [5] The ATLAS and CMS Collaborations 2015 ATLAS-CONF-2015-044
- [6] von Buddenbrock S, Chakrabarty N, Cornell A S, Kar D, Kumar M, Mandal T, Mellado B, Mukhopadhyaya B and Reed R G 2015 (arXiv:1506.00612)
- [7] von Buddenbrock S, Chakrabarty N, Cornell A S, Kar D, Kumar M, Mandal T, Mellado B, Mukhopadhyaya B, Reed R G and Ruan X 2016 WITS-MITP-025, HRI-RECAPP-2016-003 (arXiv:1606.01674)
- [8] Farina M, Grojean C, Maltoni F, Salvioni E and Thamm A 2013 *JHEP* **05** 022 (arXiv:1211.3736)
- [9] Alwall J, Herquet M, Maltoni F, Mattelaer O and Stelzer T 2011 *JHEP* **06** 128 (arXiv:1106.0522)
- [10] Sjstrand T, Ask S, Christiansen J R, Corke R, Desai N, Ilten P, Mrenna S, Prestel S, Rasmussen C O and Skands P Z 2015 *Comput. Phys. Commun.* **191** 159–177 (arXiv:1410.3012)
- [11] Buckley A, Butterworth J, Lonblad L, Grellscheid D, Hoeth H, Monk J, Schulz H and Siebert F 2013 *Comput. Phys. Commun.* **184** 2803–2819 (arXiv:1003.0694)
- [12] Hamilton K, Nason P and Zanderighi G 2012 *JHEP* **10** 155 (arXiv:1206.3572)
- [13] Andersen J R *et al.* (LHC Higgs Cross Section Working Group Collaboration) 2013 (arXiv:1307.1347)
- [14] Aad G *et al.* (ATLAS Collaboration) 2015 Tech. Rep. ATLAS-CONF-2015-082 CERN Geneva URL <https://cds.cern.ch/record/2114854>

Division C – Photonics

Photobiomodulation of Isolated Lung Cancer Stem cells

A. Crous and H. Abrahamse

Laser Research Centre, University of Johannesburg, P.O. Box 17011, Doornfontein, Johannesburg, 2028, South Africa

Email: habrahamse@uj.ac.za

Abstract. Research has uncovered that one of the plausible reasons for cancer relapse is the existence of stem like cells, possessing cancer properties, called cancer stem cells (CSCs). Cancer research is highly focused on improving current cancer treatments. One method of targeted cancer therapy is Photodynamic therapy (PDT), where Low Intensity Laser Irradiation (LILI), along with a photochemical compound, is used. When implementing a mechanism by which CSCs are targeted, LILI might pose as a viable treatment option. Studies have shown that using high fluences of LILI (HF-LILI) can induce cell death in normal and neoplastic cells. Further investigations on cell death induced by HF-LILI of CSCs still needs to be explored. Lung CSCs were isolated using the stem cell marker CD 133 and were exposed to LILI at wavelengths of 636, 825 and 1060 nm at fluences ranging from 5 J/cm² to 40 J/cm². Post irradiation biochemical assays were conducted to monitor cellular responses including: viability, proliferation and cytotoxicity, after 24 hours incubation. Studies have indicated that LILI, when treating lung CSCs, can induce either a bio-stimulatory or bio-inhibitory effect depending on the wavelength and fluence used. This study indicated successful cell damage of lung CSCs when using HF-LILI, as well as, stimulation of ATP production, when using lower fluences of LILI.

1. Introduction

Cancer is the term used to describe a disease where there is abnormal proliferation of cells, which can affect any part of the body. Cancer is one of the primary diseases contributing to mortality rates globally. Lung cancer is the most commonly diagnosed cancer in both men and women [1]. Poor prognosis of lung cancer can be attributed to deficient treatment modalities and relapse caused by its metastatic capabilities [2]. Research have found that a subpopulation of tumour initiating cells referred to as cancer stem cells (CSCs) drive tumour genesis and relapse as it has been said to regenerate tumour formation after treatment thus being accountable for therapeutic resistance [3, 4]. This subpopulation of cells residing within a malignant tumour display a variety of stem-like properties; as they are clonal in origin, can regenerate and proliferate exponentially [5, 6]; as well as tumorigenic properties such as drug resistance, evading apoptosis, tumour initiation and metastatic potential [7]. CSCs reside within a niche that keeps them quiescent and enhance DNA repair, which contribute to their therapeutic resistance [8].

Normal lung tissue is maintained by stem cells (SCs) that are controlled by several pathways controlling these pulmonary precursors enabling them to develop into their different lineages. Abnormal pulmonary SC development can lead to lung CSCs arising from these lineages causing tumour formation [9]. CSCs have been identified and characterised using SC markers [10]. Promonin-1 (CD 133) is a gene encoding for a pentaspan transmembrane glycoprotein localized to membrane protrusions. It is an adult stem cell marker maintaining stem cell properties by suppressing differentiation. It is considered a primary marker for CSCs as its high expression is said to be an adverse prognostic factor [11].

Photobiomodulation is a form of phototherapy which uses Low Intensity Laser Irradiation (LILI) with wavelengths ranging from visible to near infrared light (600 – 1070 nm) which allows for optimal tissue penetration [12]. The effects seen are generated at a mitochondrial level where photobiological responses are generated from the intracellular chromophores causing different metabolic reactions depending on the wavelengths and energy output of the incident light [13]. Studies conducted on different cell lines found that when using LILI with low fluences (LF-LILI) ranging from 1 – 15 J/cm² and wavelengths of 600 nm – 700 nm it stimulated biological processes by increasing proliferation and viability [14-18], but have an inhibitory effect when using increased wavelengths of 800–830 nm and fluences larger than 10 J/cm² [15, 19,20]. An innovative therapy currently under investigation is photodynamic therapy (PDT), which uses the activation of a photo chemotherapeutic chemical by low level light emitting lasers. Reasons for new therapies being under investigation is to avoid current therapies failing to reject recurrence of cancer and having viewer side effects.

This exploratory study evaluated the effects of LF-LILI (5 – 20 J/cm²) and high fluence LILI (HF-LILI) (40 J/cm²), where different fluences were calculated through laser time exposure and output (mW), with wavelengths of 636 nm, 825 nm and 1060 nm on isolated lung CSCs. Biochemical analysis of irradiated lung CSCs included viability, proliferation and cytotoxicity.

2. Methodology

Lung CSCs were cultured in complete media consisting of Rosewell Park Memorial Institute 1640 medium (RPMI), with additional supplements consisting of 10% foetal bovine serum (FBS) and 1% antibiotics consisting of 0.5% penicillin/ streptomycin and 0.5% amphotericin B. Incubation took place at 37°C with 5% CO₂ in an 85% humidifying incubator.

Prior to irradiation lung CSCs were seeded at a number of 1×10^5 cells in culture plates of 35 mm in diameter along with 3 ml complete media and incubated for 24 hours allowing attachment to the culture dish. After 24 h incubation the culture dish was rinsed 3 times using Hanks Balanced Salt Solution (HBSS) and replaced with 3 ml complete media before placing the culture dish underneath a fibre optic irradiating the cells with a semiconductor diode laser in the dark with a fluence of 5 – 20 J/cm² and 40 J/cm². Control cells received no irradiation. This procedure was used for all wavelengths used of 636 nm, 825 nm and 1060 nm. All lasers were kept at a constant power output of 85 mW with a continuous pulse.

Post irradiation biochemical assays were conducted to monitor cellular responses including: viability, proliferation and cytotoxicity, after 24 hours incubation. Cell viability was determined using the dye exclusion test. Trypan blue is a diazo dye which is expelled by live cells which still have intact membranes. Cells undergoing cell death or damage will take up the dye when added to the cell suspension. Viability was measured as a percentage value. Cell proliferation only takes place in metabolically active cells. To measure cellular metabolism we looked at the amount of ATP present. This was measured using an ATP luminescent assay where the luminescent signal measured is proportional to the amount of ATP present. Cytotoxicity was calculated by measuring the amount of LDH in the media. LDH release indicates membrane damage and that cells are not metabolically active.

Statistical significant differences between groups were indicated as $p < 0.05$ (*), $p < 0.01$ (**) and $p < 0.001$ (***).

3. Results

All assay results are combined and indicated as stimulation (↑) or inhibition (↓) of viability and proliferation of lung CSCs and cytotoxicity as in increase (↑) in cell membrane damage that was statistically significant. Results indicated with an (↑/↓) were not statistically significant and (--) no difference was observed.

Table 1. Photobiostimulation or inhibition of lung CSCs at different irradiation levels.

		Viability	Proliferation	Cytotoxicity
636 nm	5 J/cm ²	↑	↑	---
	10 J/cm ²	↑	↑*	---
	20 J/cm ²	---	---	---
	40 J/cm ²	↓	↓*	↑*
825 nm	5 J/cm ²	↑	↑	---
	10 J/cm ²	↑*	↑**	---
	20 J/cm ²	---	---	---
	40 J/cm ²	↓***	↓*	↑*
1060 nm	5 J/cm ²	↑	↑	---
	10 J/cm ²	↑	↑	---
	20 J/cm ²	---	↑	---
	40 J/cm ²	↓	↓	↑*

4. Discussion and Conclusion

Potential outcomes of LILI on lung CSCs were explored in this study. There was an increase seen in both viability and proliferation when using LF-LILI on the lung CSCs. The increase in cell viability correlates with similar proliferation results seen. A statistical significance was seen when using LF-LILI at a wavelength of 825 nm and fluence of 10 J/ cm² for both viability and proliferation. Significant stimulation in proliferation was also seen when using a wavelength of 636 nm and 10 J/cm². No cytotoxicity was observed when using LF-LILI for all respective wavelengths. These findings are in accordance to similar studies conducted on SCs [14,18].

This indicates that photobiostimulation is achieved when irradiating lung CSCs with LF-LILI. When using HF-LILI of 40 J/cm² photobioinhibition is achieved as there was a decrease seen in proliferation when using wavelengths of 636 nm and 825 nm. Cytotoxicity results revealed that cell membrane damage was induced when irradiating lung CSCs with all respective wavelengths and HF-LILI of 40 J/cm². Similar results were seen in a study where replication inhibition was demonstrated [21].

The photobiomodulatory effects seen can be attributed to intracellular chromophores found in organelles such as the mitochondrion of a cell. The response triggered by LILI is due to these chromophores absorbing the light, having either a biostimulatory or bioinhibitory effect depending on the wavelength and fluence used. Photobiomodulation relies on specific parameters such as wavelength, fluence, power density, pulse structure, and treatment time when applied to biological tissue. This allows for targeting of specific light-absorbing molecules in specific tissues, operating on the principle of photochemistry, as opposed to photo thermogenesis. The light energy absorbed causes singlet state excitation of oxygen molecules, leading to triplet state excitation causing an energy transfer to ground state molecular oxygen (a triplet) to form the reactive species, singlet oxygen. Alternatively superoxide may be formed as a result of electron reduction. LILI operates at an exact wavelength of light, which

influences the depth of tissue penetration. Similar to normal cells, cancer cells also contain with intracellular chromophores. Different cellular chromophores are stimulated at different wavelengths. Therefore, the prediction can be made that in targeting cancerous cells, the outcome expected can be controlled by the wavelength as well as by the energy output that will lead to either stimulation or inhibition. The exact mechanism behind the stimulation of the light-absorbing molecules producing these two different effects is still being investigated [22,23].

Cell death studies conducted using lung cancer cells and PDT indicated that cell membrane damage and apoptosis was induced [2]. This type of photochemical therapy has shown to be a promising treatment for lung cancer. Further studies should include whether similar results are achieved when using PDT on lung CSCs as well as the mechanism behind the cell death induced.

References

- [1] World Health Organization (2015) Media Centre, Cancer. Available: <http://www.who.int/mediacentre/factsheets/fs297/en/>
- [2] Manoto SL, Sekhejane PR, Houreld NN, Abrahamse H. Localization and phototoxic effect of zinc sulfophthalocyanine photosensitizer in human colon (DLD-1) and lung (A549) carcinoma cells (in vitro). *Photodiagnosis Photodyn Ther* 2012;9:52–59.
- [3] Lu B, Chiou S, Deutsch E and Loric A (2011) Cancer Stem Cells *Journal of Oncology Article ID 269437*, doi:10.1155/2011/269437
- [4] Michael H (2009) Cancer Stem Cells: A Guide for Skeptics *Journal of Cellular Biochemistry* 106:745–749.
- [5] Baiguera S, Kaiathur M and Macchiarini P (2011) Cancer Stem Cells in Lung and Pleural Malignancies *CML Lung Cancer* 4(3):69-78.
- [6] Plaks V, Kong N and Werb Z (2015) The cancer stem cell niche: how essential is the niche in regulating stemness of tumor cells? *Cell Stem Cell* 16(3):225-38.
- [7] Mohr M, Zänker KS and Dittmar T (2015) Cancer (stem) cell differentiation: An inherent or acquired property? *Med Hypotheses* 85(6):1012-8.
- [8] Kosovsky, M. (2012) Culture and Assay Systems Utilized for Cancer Stem Cell Research. Available: http://www.flowcytometri.dk/literature/Kosovsky%202012%20BD%20ecm_cancer_stem_cell.pdf
- [9] Natarajan, T. G. and FitzGerald, K. T. (2007) Markers in normal and cancer stem cells. *Cancer Biomark* 3, 211–231.
- [10] Bin Bao, Aamir Ahmad, Asfar S. Azmi Shadan Ali, and Fazlul H. Sarkar (2013) Cancer Stem Cells (CSCs) and Mechanisms of Their Regulation: Implications for Cancer Therapy. *Curr Protoc Pharmacol* 14: Unit–14.25.
- [11] Qiu ZX, Zhao S, Mo XM and Li WM (2015) Overexpression of PROM1 (CD133) confers poor prognosis in non-small cell lung cancer. *Int J Clin Exp Pathol* 8(6):6589-95.
- [12] Huang, Y. Y., Chen, A. and Hamblin, M. (2009) “Low-level laser therapy: an emerging clinical paradigm *SPIE Newsroom*, doi:10.1117/2.1200906.1669.
- [13] Crous A. and Abrahamse H. (2016) Low intensity laser irradiation at 636 nm induces increased viability and proliferation in isolated lung cancer stem cells. *Photomedicine and Laser Surgery* 2015 Dec 21. doi:10.1089/pho.2015.3979.
- [14] de Villiers, J. A., Houreld, N. N. and Abrahamse, H., “Influence of low intensity laser irradiation on isolated human adipose derived stem cells over 72 hours and their differentiation potential into smooth muscle cells using retinoic acid,” *Stem Cell Rev* 7, 869–882 (2011).
- [15] Moore, P., Ridgway, T. D., Higbee, R. G., Howard, E. W. and Lucroy, M. D.’ “Effect of wavelength on low-intensity laser irradiationstimulated cell proliferation in vitro,” *Lasers Surg Med* 36, 8–12 (2005).
- [16] Fonseca, A. S., Moreira, T. O., Paixaõ, D. L., et al., “Effect of laser therapy on DNA damage,” *Lasers Surg Med* 42, 481–488 (2010).

- [17] Hu, W. P., Wang, J.J., Yu, C. L., Lan, C. C., Chen, G. S. and Yu, H. S., “Helium-neon laser irradiation stimulates cell proliferation through photostimulatory effects in mitochondria” *J Invest Dermatol* 127, 2048–2057 (2007).
- [18] Mvula, B., Mathope, T., Moore, T. J. and Abrahamse, H., “The effects of low level laser irradiation on human adipose derived stem cells,” *Laser Med Sci* 23, 277–282 (2008).
- [19] Abrahamse, H., Houreld, N. N., Muller, S. and Ndlovu, L (2010) Fluence and wavelength of low intensity laser irradiation affect activity and proliferation of human adipose derived stem cells,” *Medical Technology SA* 24, 9–14.
- [20] Chow, R. T., David, M. A. and Armati, P. J (2007) 830 nm laser irradiation induces varicosity formation, reduces mitochondrial membrane potential and blocks fast axonal flow in small and medium diameter rat dorsal root ganglion neurons: implications for the analgesic effects of 830 nm laser. *J Peripher Nerv Syst* 12, 28–39.
- [21] Ocana-Quero JM, Perez de la Lastra J, Gomez-Villamandos R and Moreno-Millan M. (1998) Biological effect of Helium-Neon (He-Ne) laser irradiation on mouse myeloma (Sp2-Ag14) cell line in vitro. *Lasers Medical Sciences* 13(3): 214-218
- [22] Wan-Ping H, Jeh-Jeng W, Chia-Li Y, Cheng-Che EL, Gow-Shing C and Hsin-Su Y (2007) Helium–Neon Laser Irradiation Stimulates Cell Proliferation Through Photostimulatory Effects in Mitochondria *Journal of Investigative Dermatology* 127: 2048–2057.
- [23] Abrahamse H. and Crous A. (2016) Biochemical responses of isolated lung cscs after application of low intensity laser irradiation. *Proceedings of SPIE 9695, Mechanisms of Photobiomodulation Therapy XI*, 96950J; doi:10.1117/12.2228902

Single-photon probing of plasmonic waveguides

Jason Francis and Mark Tame

School of Chemistry and Physics, University of KwaZulu-Natal, Durban, South Africa

Email: markstame@gmail.com

Abstract. Plasmonics is the study of the interaction of light and conduction electrons at metal-dielectric interfaces. Here, surface plasmon polaritons (SPPs) are hybrid photon-electron excitations that can be confined to subdiffraction scales. This feature affords enhanced coupling to emitter systems (e.g. quantum dots) to SPPs, making them suitable candidates for a wide range of on-chip quantum photonic components – most notably single-photon sources. This potential use of SPPs, along with the nonlinearity provided by emitter systems, opens up quantum plasmonics as a viable route to realising quantum information processing. In this setting, the excitation of single SPPs on waveguides via single photons and the confirmation of single-photon states upon output is an important goal. In our work we experimentally probe plasmonic waveguides with single photons and measure a second-order quantum correlation function of $g^{(2)}(0) = 0.10 \pm 0.02$. A value less than 0.5 is indicative of single-excitation states.

1. Introduction

Quantum plasmonics offers an alternative to a purely photonic realisation of quantum information processing. A major advantage it offers is the subdiffraction confinement of plasmonic modes such as SPPs and localised surface plasmons (LSPs) [1]. This allows enhanced coupling of single photons to emitter systems, such as nitrogen vacancy centres and quantum dots, by reducing the large size discrepancy between the modes [2-4]. This strong coupling makes on-chip single-photon and single-SPP sources possible [5]. Additionally, it can provide nonlinearity via the photon-blockade [6], where an emitter excited by a photon of a particular frequency cannot be further excited. This process has application in the development of active switches [7], which are useful for implementing controlled quantum logic gates.

To further motivate the suitability of SPPs for quantum information applications, several demonstrations have been made suggesting that photonic entanglement and quantum information can indeed be encoded in plasmonic states. It has been shown that polarisation-entangled photon pairs maintain entanglement after conversion to and from SPPs [8]. The same has been shown for photon-number statistics of single photons used to excite single SPPs [9].

As a first step in developing the capacity to explore further the quantum properties of single SPPs and their application to quantum information processing, we follow the lead of Di Martino *et al.* We couple single photons generated via spontaneous parametric down-conversion into SPP modes on plasmonic stripe waveguides and confirm single excitation states upon output by a measurement of the second-order correlation function at zero time delay $g^{(2)}(0)$.

1.1. Photon-number Statistics

Generally $g^{(2)}$ is a function of the time-delay τ between two measurements. At a fixed position it is a measure of the joint probability of detecting a photon at time t and another at some later time τ .

Equivalently for classical fields, it is a measure of the correlation between intensities. It can be measured at the two outputs of a beamsplitter, as in the Hanbury-Brown Twiss (HBT) intensity interferometer shown in the lower part of figure 1b. Classically it is given by [10]

$$g_{BB'}^{(2)}(\tau) = \frac{\langle I_B(t + \tau)I_{B'}(t) \rangle}{\langle I_B(t + \tau) \rangle \langle I_{B'}(t) \rangle}, \quad (1)$$

where I_B and $I_{B'}$ are the intensities measured by detectors B and B' respectively. For a 50:50 beamsplitter (1) can be written in terms of the input intensity I . Then at zero time-delay and after applying the Cauchy-Schwartz inequality, (1) becomes

$$g_{BB'}^{(2)}(0) = \frac{\langle [I(t)]^2 \rangle}{\langle I(t) \rangle^2} = g^{(2)}(0) \geq 1. \quad (2)$$

Thus $g^{(2)}(0)$ has a lower bound of 1 for classical light, while for photon-number states $g^{(2)}(0)$ takes the form [11]

$$g_{BB'}^{(2)}(0) = \frac{\langle \hat{n}(\hat{n}-1) \rangle}{\langle \hat{n} \rangle^2} = 1 - \frac{1}{n}, \quad (3)$$

where \hat{n} is the photon-number operator and n is the mean photon number. In the case of single-photon states $n = 1$ and so $g^{(2)}(0) = 0$. For $n = 2$, $g^{(2)}(0) = 0.5$, and so for a single-SPP excitation we expect a value less than 0.5 and ideally close to zero.

2. Experimental Details

To experimentally probe plasmonic waveguides a compound microscope stage was used. The stage was built to allow imaging of the waveguides as well as excitation of SPPs. SPPs could be excited using an alignment laser for the classical regime. A single-photon source, however, was used to excite single-SPPs. These two critical components are discussed in what follows.

2.1. Single-Photon Source

Spontaneous parametric down-conversion (SPDC) is a nonlinear optical process by which a photon of frequency ω_p from a pump beam is converted into a correlated photon-pair at lower frequencies and at particular angles relative to the pump. One photon of the pair is called the signal with frequency ω_s while the other is called the idler with frequency ω_i . The frequencies and angles of the output photons must satisfy the conservation of energy and momentum:

$$\omega_p = \omega_s + \omega_i \quad (4)$$

$$\vec{k}_p = \vec{k}_s + \vec{k}_i \quad (5)$$

where \vec{k}_p , \vec{k}_s , \vec{k}_i , are the pump, signal, and idler wavevectors respectively. This results in a conical region in which correlated photons are located on opposite sides of the pump.

In the single-photon source shown in figure 1a, a 3mm thick β -BaB₂O₄ (BBO) crystal is pumped with a 200mW continuous-wave laser of wavelength 405nm. A small percentage of pump photons undergo SPDC in the BBO crystal to produce photon-pairs with a half-opening angle 3° and a central wavelength of 810nm. A narrow wavelength band of correlated photon-pairs in arms 1 and 2 as shown, are selected by (810 ± 5) nm interference filters. These photons are then coupled into single-mode (SM) fibres. The smaller numerical aperture of these fibres acts to spatially select the centre of the down-conversion mode. This results in better correlated photon-pairs. Since the down-converted photons are

produced in pairs, a photon in arm 1 can be used to herald the arrival of a photon in arm 2. This effectively post-selects true single photons.

To measure $g^{(2)}(0)$, a HBT intensity interferometer is used and is shown in figure 1b. The single-mode fibre of arm 1 is connected to a multimode (MM) fibre through which heralding photons are decoupled and focused onto a single-photon avalanche diode detector (SPAD) A. The single-mode fibre on arm 2 which is also polarisation-maintaining (PM) is similarly connected to a multimode fibre. The heralded photons from this fibre is subject to the HBT interferometer such that we may measure correlations between photo-detections at SPAD detectors B and B'. The signals from each detector are sent to a counting module (CM) which then outputs the single-photon count rates at each detector and the coincidence rates between detectors to a PC. The coincidence rate is the number of detections in B and B' collectively that occur within 8 ns (the chosen coincidence window) of a detection in A.

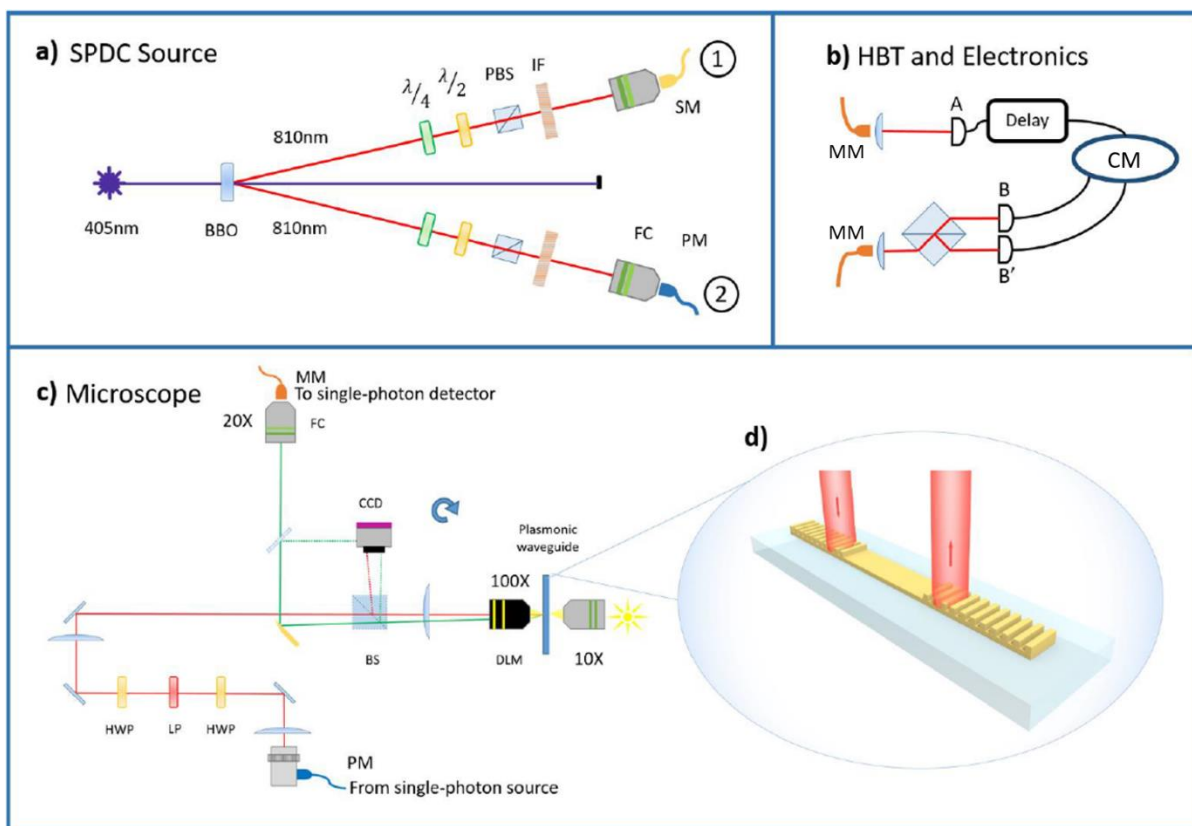


Figure 1. a) SPDC single-photon source showing all components. The waveplates are used for state tomography when the source is used to generate polarization-entangled photons. b) Hanbury-Brown Twiss setup with detectors and counting module needed for $g^{(2)}$ measurements. The signal from detector A is delayed to account for the length introduced by the microscope stage. The MM fibres shown are a fixture of the HBT setup, allowing it to be used with various other photon sources. The larger core of these fibres ensures a more efficient coupling to the SM fibres. c) Microscope used to probe the plasmonic waveguides. PM fibres were used to ensure minimal warping of the single photon polarisation and thus increase the number of photons available for SPP excitation. d) 3D diagram of the plasmonic waveguide supporting SPPs.

In the context of the experiment, $g^{(2)}(0)$ for single-photons can be expressed in terms of photon count rates as [9]

$$g^{(2)}(0) = \frac{N_{ABB'}N_A}{N_{AB}N_{AB'}}, \quad (6)$$

where each factor is a count rate with a subscript indicating at which detector. Two or more subscript letters represents coincidence rates between the indicated detectors. Ideally $N_{ABB'}$ should be zero, however we find that this is not the case due to detector dark-counts, background light, and a non-zero down-conversion linewidth. The measurement procedure was to record 12 sets of all count rates with an integration time of 5s using a LABVIEW program. We then calculate $g^{(2)}(0)$ using these count rates in equation (6). Typical count rates obtained: $N_A \sim 220000$ cps, $N_B \sim 120000$ cps, $N_{B'} \sim 140000$ cps, $N_{AB} \sim 4500$ cps, $N_{AB'} \sim 5500$ cps, $N_{ABB'} \sim 7$ cps.

To calculate $g^{(2)}$ as a function of the delay time τ , a variable delay must be introduced on either the signal from detector B or B'. The coincidence terms in equation (6) now become functions of τ . Varying τ and collecting count rates, $g^{(2)}(\tau)$ can be calculated in the same manner as described above for $g^{(2)}(0)$. A plot of $g^{(2)}(\tau)$ will exhibit a dip at $\tau = 0$. This alone does not indicate photon sub-Poissonian statistics, which is a signature of single-photon states. Instead we require only to demonstrate that $g^{(2)}(0) < 0.5$ to confirm single excitations [11].

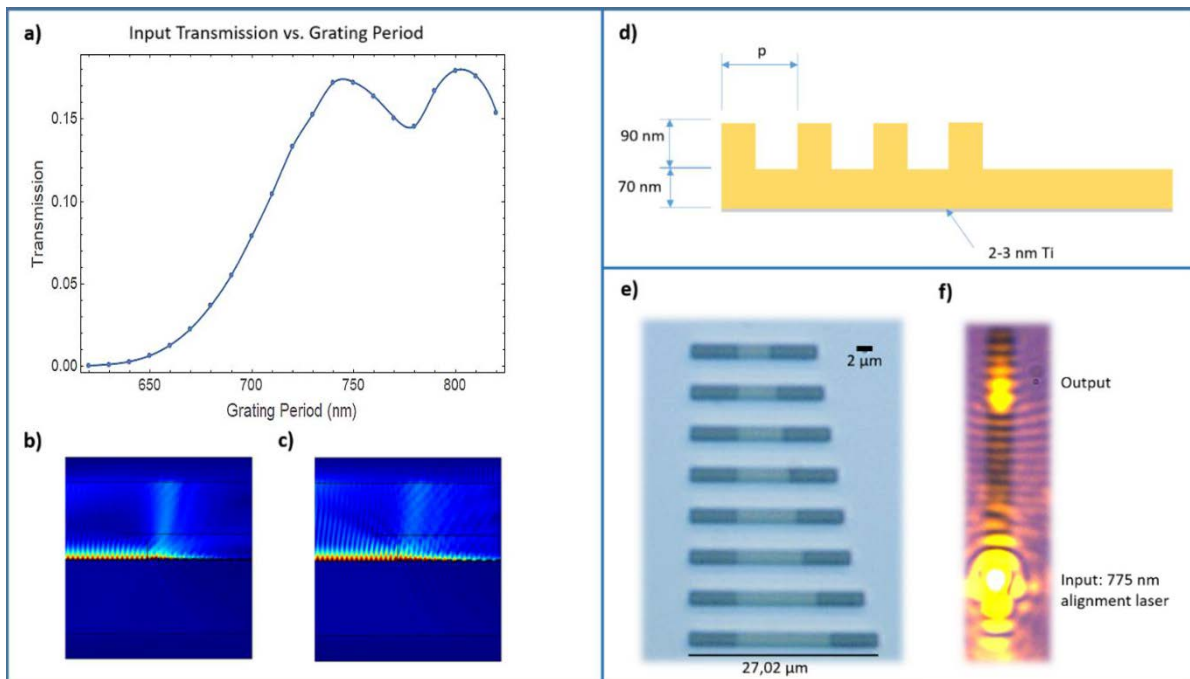


Figure 2. **a)** Plot of input grating efficiency as a function of the grating period. Peaks occur at 750 nm and 800 nm. **b)** Simulated electric field norm of SPP decoupled using a 740 nm grating. **c)** SPP decoupled using 800 nm grating. Note that the 740 nm period decouples the SPP more rapidly. **d)** Geometry of probed waveguides. **e), f)** Sample images obtained using the microscope setup - **f)** shows classical SPP excitation on the longest waveguide in **e)**.

2.2. Waveguide Structure and Probing Microscope

The structures probed were gold stripes $2 \mu\text{m}$ wide and 70 nm thick with a 90 nm high surface-relief diffraction grating at either end. They were fabricated in a two-stage electron-beam lithography and gold evaporation process onto a silica substrate. The first stage puts the flat waveguides onto the substrate

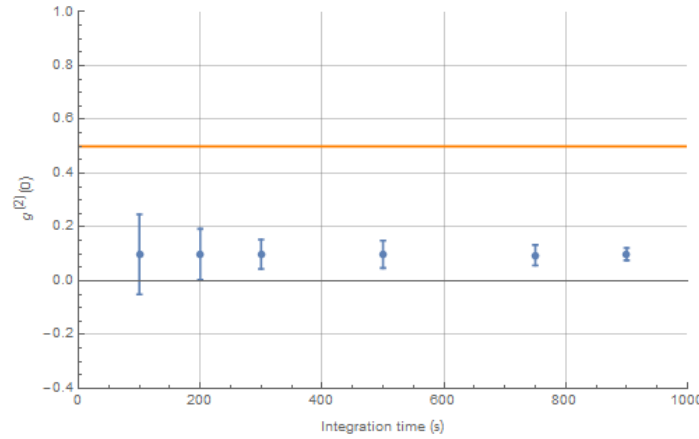


Figure 3. Single-SPP $g^{(2)}(0)$ values at increasing integration times.

while the second stage applies the gratings. A range of waveguide lengths and grating periods were fabricated. To estimate the optimal period for excitation by single photons of wavelength 810 nm , waveguides of different periods were simulated in COMSOL to obtain their input efficiencies. The resulting graph shown in figure 2a exhibits two peaks, one at 750 nm and another at 800 nm . The grating period chosen was 740 nm (the closest to 750 nm that was available). The 800 nm grating proved to decouple SPPs less efficiently in the experiment.

The microscope setup used to probe the plasmonic waveguides is shown in figure 1c. The most important constituent is the diffraction-limited microscope objective which allows us to adequately image the waveguides on the CCD camera, as well as focus the input beam to a spot size of roughly $2\text{ }\mu\text{m}$. The plasmonic chip containing a range of waveguides is mounted on a Thorlabs NanoMax XYZ translation stage to allow positioning. The input beam is injected via a PM fibre connected to a beam-collimator. To excite SPPs, the input grating of the chosen waveguide is positioned at the beam spot. Light can then be seen at the output grating when using a 775 nm alignment laser. A linear polariser is used to remove any elliptical character from the input, while the first half-wave plate can be used to maximise throughput. The second half-wave plate is used to rotate the polarization such that it is parallel to the SPP propagation direction to maximise the coupling. For more efficient measurements the beamsplitter is flipped out of the beam path and a D-shaped mirror is used to pick off the output and direct it to a fibre-coupler to which a SPAD detector or spectrometer may be connected.

Once the microscope stage is aligned and optimised using the alignment laser, the PM fibre on arm 2 of the single-photon source is connected via the beam-collimator. The MM fibre leading to the HBT interferometer is then connected to the output of the microscope setup. Due to the difference in wavelength between the alignment laser and the down-conversion photons, the alignment will require adjustment. This is easiest done with higher photon rates since plasmonic waveguides suffer great loss. Higher rates are achieved by using a wider (800 ± 20) nm interference filter on arm 2. The probing system is then optimised by increasing the count rate of output photons from the waveguide. Typical count rates obtained: $N_B \sim 4000\text{ cps}$, $N_{B'} \sim 4500\text{ cps}$, $N_{AB} \sim 110\text{ cps}$, $N_{AB'} \sim 120\text{ cps}$, $N_{ABB'} \ll 1\text{ cps}$.

To calculate the value of $g^{(2)}(0)$ for single-SPPs, count rates were recorded with 1 s integration time for 1.5 hours. Due to instability over long collection times, $g^{(2)}$ was obtained for zero delay only. As mentioned in the previous section, this is sufficient for confirming single excitations are present.

3. Results

A photonic $g^{(2)}(0)$ was obtained from each of the twelve sets of count rates. The average was taken to yield a value of $g^{(2)}(0) = 0.074 \pm 0.006$, which violates the classical lower bound of 1. In the SPP case, the records were grouped to obtain counts over a longer integration time. This was done to reduce error due to the low three-fold coincidence $N_{ABB'}$, which causes large fluctuations in the $g^{(2)}$ value. Figure 3 shows a plot of $g^{(2)}(0)$ at increasing integration times, clearly exhibiting the decrease in error.

The value at an integration time of 900 s is $g^{(2)}(0) = 0,10 \pm 0,02$. This value suggests single-excitation states upon conversion from photon to SPP.

4. Conclusion

The ability of single-SPPs to preserve the photon-number of their exciting photons has been demonstrated. A possible next step would be a more direct method to demonstrate the single-quanta nature of the excited SPPs. This can be achieved by using a plasmonic beamsplitter waveguide in place of the bulk one used in the HBT interferometer, allowing us to avoid conversion back into photons. We are now also in a position to explore coupling of SPPs to nitrogen vacancy centres for on-chip sources and switches, as well as waveguide fabrication using a newly installed atomic force microscope (AFM).

Acknowledgments

We acknowledge support from the South African National Research Foundation, the Centre for Scientific and Industrial Research, the National Institute for Theoretical Physics and the University of KwaZulu-Natal Nanotechnology Platform.

References

- [1] Maier S A 2007 *Plasmonics: Fundamentals and Applications* (Berlin: Springer)
- [2] Chang D E, Sørensen A S, Hemmer P R and Lukin M D 2006 Quantum optics with surface plasmons *Phys. Rev. Lett.* 97, 053002
- [3] Akimov A V et al. 2007 Generation of single optical plasmons in metallic nanowires coupled to quantum dots *Nature* 450, 402-406
- [4] Kolesov R et al. 2009 Wave-particle duality of single surface plasmon polaritons *Nature Phys.* 5, 470-474
- [5] Koenderink A F 2009 Plasmon nanoparticle array waveguides for single photon and single plasmon sources *Nano Lett.* 9, 4228-4233
- [6] Birnbaum K M et al. 2005 Photon blockade in an optical cavity with one trapped atom *Nature* 436, 87-90
- [7] Chang D E, Sørensen A S, Demler E A and Lukin M D 2007 A single-photon transistor using nanoscale surface plasmons *Nature Phys.* 3, 807-812
- [8] Altewischer E, van Exter M P and Woerdman J P 2002 Plasmon-assisted transmission of entangled photons *Nature* 418, 304306
- [9] Di Martino G et al. 2012 Quantum statistics of surface plasmon polaritons in metallic stripe waveguides *Nano Lett.* 12, 2504-2508
- [10] Thorn J J et al. 2004 Observing the quantum behaviour of light in an undergraduate laboratory *Am. J. Phys.* 72, 1210
- [11] Loudon R 2000 *The Quantum Theory of Light 3rd ed.* (Oxford: Oxford University Press)

Simulaser, a graphical laser simulator based on Matlab Simulink

C Jacobs¹, and W Koen¹

¹CSIR National Laser Centre, PO Box 395, Pretoria, South Africa, 0001

E-mail: cjacobs@csir.co.za

Abstract. We present a single-element plane-wave laser rate equation model and its implementation as a graphical laser simulation library using Matlab Simulink. Simulink's graphical interface and vector capabilities provide a unique layer of abstraction for numerical integration particularly well suited for laser simulation. Numerical integration of the coupled laser rate equations in Simulink enables simulation of laser dynamics for a range of intricate and novel laser cavity designs. In particular, simulation and real-world results will be compared for a dual crystal Ho:YLF oscillator with one of its two birefringent crystals rotated by 90° about the optical axis for efficient absorption of the incident unpolarised pump light.

1. Introduction

Solid-state laser gain dynamics can be fairly accurately modelled using coupled rate equations for inversion population and cavity photon density which is used extensively in the design and optimisation of solid-state lasers. The basic theory and derivation of both three and four level laser rate equations have been covered in detail by Siegman [1] and Koechner [2], with several expanded models presented in literature [3, 4]. As general analytic solutions don't exist, numerical integration and simulation are typically done using script-based computer programming like Matlab [5] or LAS-CAD [6].

In previous work [7] we presented a single-element plane-wave laser rate equation model with numerical simulations done using Matlab's ordinary differential equation solvers. Customising these Matlab scripts for multiple laser systems were complicated and time-consuming, and limited in the complexity of the laser cavity design. This same set of laser rate equations have been adapted and implemented in Matlab Simulink, providing a graphical programming environment with vector support to enable simulation of a variety of complicated laser system designs. In this proceeding we present the adapted rate equation model, its implementation as a Simulink laser library and a comparison between simulated and measured results obtained from a dual crystal Ho:YLF oscillator.

2. Laser rate equation model

Both four and three level solid-state laser systems can be approximated by a simplified two energy level scheme, given that the non-radiative transitions between different energy levels occur much faster than the primary laser transition, and that effective absorption and emission cross-sections are used to account for stark level splitting and level degeneracy. The upper laser level population density $N_2(t)$ and the cavity photon density $\Omega(t)$ as functions of time are then represented by the following coupled rate equations:

$$\frac{d\Omega}{dt} = \frac{cl_{crystal}}{l_o} (\Omega + 1) (\sigma_{laser}^{em} N_2(t) - \sigma_{laser}^{abs} N_1(t)) - \frac{\Omega}{\tau_c} \quad (1)$$

$$\frac{dN_2}{dt} = R_p - \frac{c\Omega(t)l_{crystal}}{V_{crystal}l_0} (\sigma_{laser}^{em} N_2 - \sigma_{laser}^{abs} N_1) - \frac{N_2}{\tau_2} \quad (2)$$

$$\text{with } R_p = \frac{\eta_{pump} P_{inc} (1 - e^{-(\sigma_{pump}^{abs} N_1 - \sigma_{pump}^{em} N_2) l_{crystal}})}{V_{crystal} h \nu_{pump}} \quad (3)$$

where R_p is the pump rate, N_1 is the ground manifold population density, σ^{em} and σ^{abs} are the effective emission and absorption cross-sections (at either the pump or laser wavelength depending on the subscript), τ_2 is the upper laser level lifetime, η_p the pump efficiency and $V_{crystal}$, $l_{crystal}$ and l_0 are the crystal volume, crystal length and corrected optical cavity length respectively. Furthermore, define c as the speed of light, τ_c as the cavity lifetime (equal to $2l_0/c\delta$ with δ the logarithmic round-trip loss including the output coupler) and ν_{pump} as the frequency of the pump light.

The coupled differential equations were carefully implemented in Simulink as shown in detailed block diagram form in Figure 1 and Figure 2. Simulink provides basic building blocks, such as a numerical integrator block to enable the construction of mathematical models. For readers unfamiliar with Simulink it helps to start at the integrator block and follow the signal wires to realise the block form version of a differential equation. The two differential equation block diagrams were each encapsulated in a Simulink subsystem (i.e. one gain medium block and one cavity mode block, as shown in Figure 3) with signals for simulated and spontaneous emission, and cavity photons connecting between them. Factors and terms were carefully grouped in order to confine input variables to either of the two subsystems (i.e. cavity length is only referenced in the ‘‘cavity mode’’ block). This was done in order to achieve logical separation and allow easy construction of novel resonator cavities containing multiple gain media blocks and cavity modes. Additionally, Simulink’s intrinsic vector-based signals were exploited to further this goal, essentially implementing multiple-coupled differential equations in the form:

$$\frac{d\Omega_i}{dt} = \frac{cl_{crystal,m}}{l_{o_i}} (\Omega_i + 1) (\sigma_{laser,i}^{em} N_{2,m}(t) - \sigma_{laser,i}^{abs} N_{1,m}(t)) - \frac{\Omega_i}{\tau_{c_i}} \quad (4)$$

$$\frac{dN_{2,m}}{dt} = R_{p,m} - \sum_j \frac{c\Omega_j(t)l_{crystal,m}}{V_{crystal,m}l_{0_j}} (\sigma_{laser,j}^{em} N_{2,m} - \sigma_{laser,j}^{abs} N_{1,m}) - \frac{N_{2,m}}{\tau_{2,m}} \quad (5)$$

Finally, the pump rate R_p was also vectorised to allow orthogonal polarisation components to be propagated throughout the subsystem blocks.

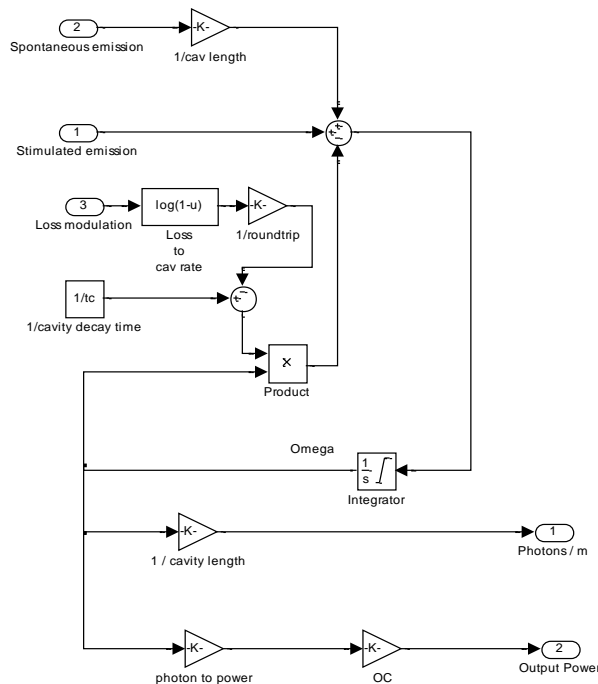


Figure 1. Block diagram for cavity photon density as per equation (4).

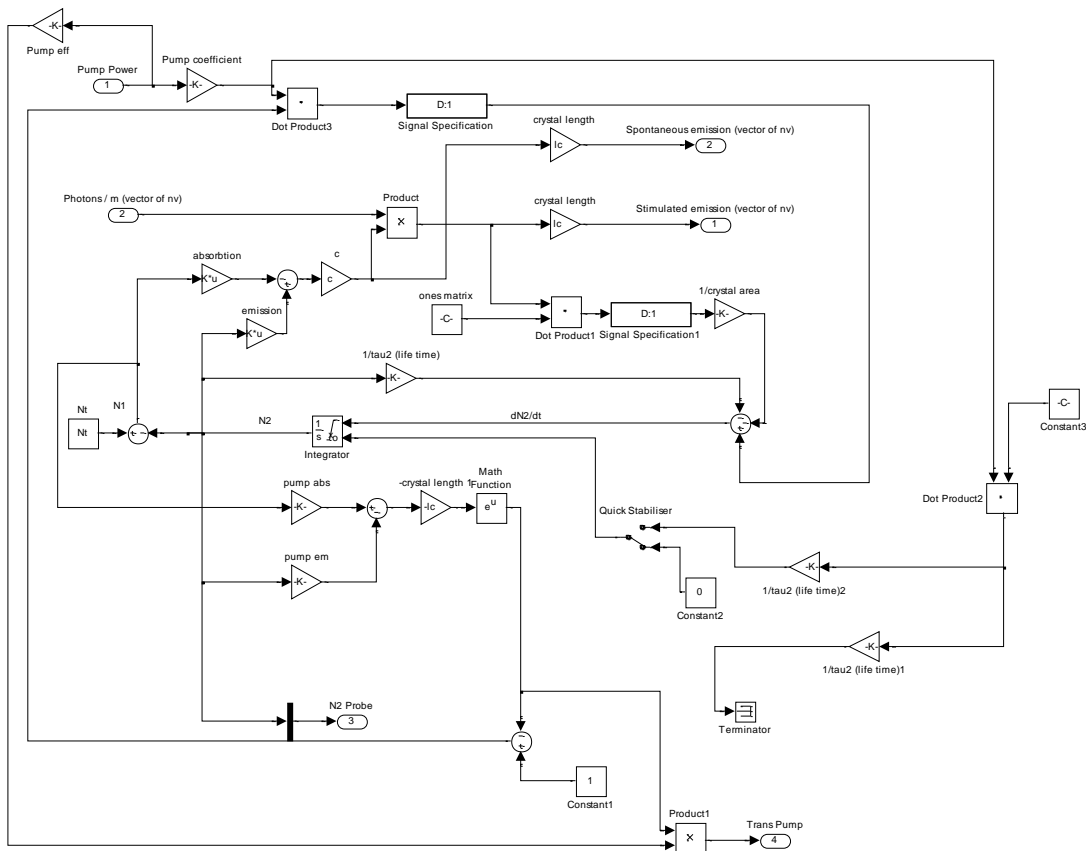


Figure 2. Block diagram for upper laser level population density as per equation (5).

3. Model validation

The combined subsystem blocks have been organised into a laser simulation Simulink library (“Simulaser”) as shown in Figure 3, together with additional blocks for diagnostics and Q-switching. The Simulaser library has been used to simulate several different laser designs at the CSIR National Laser Centre, though mostly classical single crystal, single cavity designs. For validation of the vectorised laser rate equation model, a recently developed dual-crystal Ho:YLF pulsed laser system [8] was simulated and used to determine the optimum mode size in the crystals.

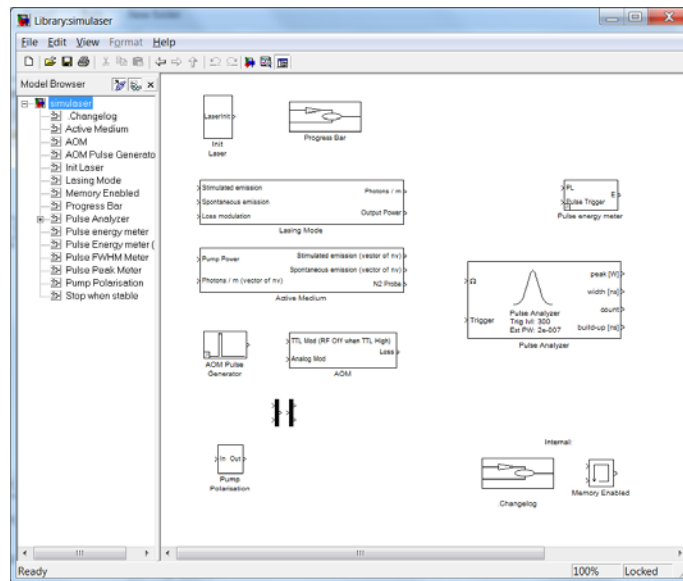


Figure 3. Simulaser block diagram library implemented in Matlab Simulink.

The Ho:YLF based laser was designed for high efficiency and required optimal absorption of the 84W unpolarised Tm-fibre laser pump light. Since Ho:YLF crystals are naturally birefringent (c-axis cut perpendicular to the optical axis), strong polarisation dependant absorption occurs which effectively polarises the transmitted pump beam after absorption in a single crystal. A second crystal with its c-axis rotated by 90° with respect to the first crystal strongly absorbs the remaining pump light making efficient use of the unpolarised pump. The Simulaser block diagram implementation of this dual crystal laser is shown in Figure 4. The 90° rotation of the gain media was achieved by rotating both absorption and emission cross-sections vectors supplied in the properties of the second crystal.

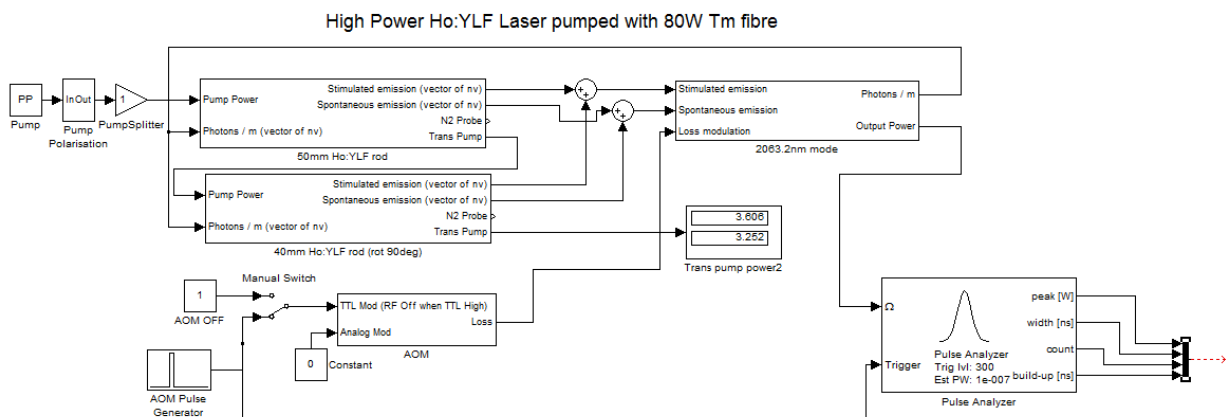


Figure 4. Dual-crystal Ho:YLF pulsed laser design implemented in Simulaser

4. Results and discussion

The simulation results for laser output power as a function of (a) mode radius in the crystals and (b) input pump power are shown in Figure 5. The maximum laser output power is achieved for mode sizes of 300 μm radius and below. However, below 300 μm the risk for optical damage increases considerably with less than 5% gain in output power. As such, the actual laser system was developed with a 300 μm pump and laser mode radius in both crystals. The laser was pulsed at 50 kHz and achieved a maximum of 45.1W average power with a slope efficiency of more than 66% (vs. incident pump power). The experimentally measured data of the laser in pulsed mode is also shown in Figure 5(b). The simulation results were in very good agreement with measured data, especially at high pump powers. The simulated continuous wave (CW) slope results provide an upper bound for pulsed performance. Simulated transmitted pump power through both crystals at full pump power equaled the experimentally measured transmitted power of 7.1 W.

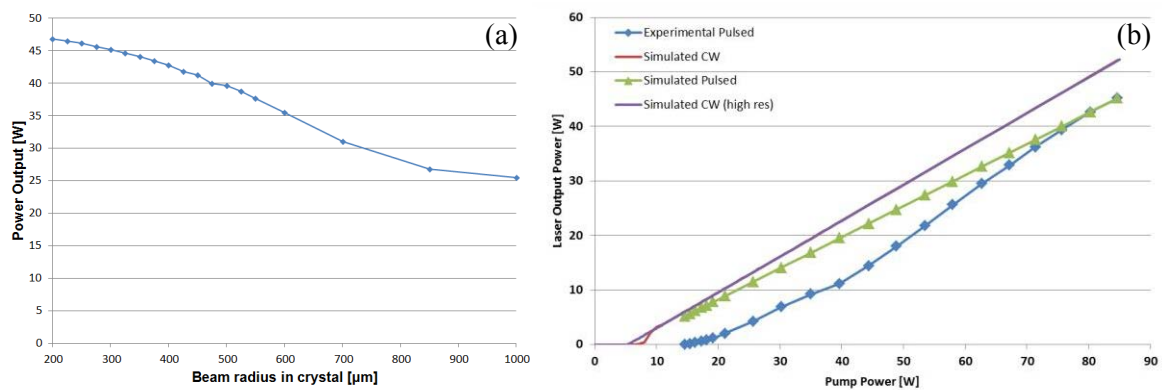


Figure 5. (a) Simulation results for laser output power as a function of laser mode radius in the crystal shows a steady increase in laser efficiency for smaller beam sizes. (b) Simulation results for laser output power in continuous wave and pulsed mode as compared to experimentally measured values for the actual laser in pulsed mode.

The output power discrepancies at lower pump powers are due to a number of factors including that model parameters (mode size, pump wavelength etc.) are best known at full power and that the model does not account for thermal lensing (the model assumes a perfect mode overlap between pump and laser mode that does not vary with pump power). Furthermore the model does not account for smaller pump sizes at low pump powers intrinsic to the operation of the Tm-fibre laser, the shift in pump wavelength with increasing pump power and the known water absorption loss around 40 - 50W of pump power (as the pump wavelength shifts through a water absorption line).

5. Conclusion

A novel, highly flexible and easy to use laser dynamic simulation library has been demonstrated by exploiting the graphical abstraction and vector capabilities of the Matlab Simulink numerical integration platform. The model's ability to simulate multi-mode/multi-gain media resonators was validated against measured results for a previously published efficient dual-crystal Ho:YLF oscillator [8]. The model was used to determine optimal laser cavity parameters such as the ideal laser mode size in the laser crystal. Measured and simulation results were in good agreement, especially at the high pump powers where simulation input parameters closely matched actual parameters.

References

- [1] A. E. Siegman, Lasers. University Science Books, 1986.
- [2] W. Koechner, Solid-state laser engineering, vol. 1. Springer, 2013.

- [3] T. Fan, "Optimizing the efficiency and stored energy in quasi-three-level lasers," *IEEE Journal of quantum electronics*, vol. 28, no. 12, pp. 2692–2697, 1992.
- [4] M. Schellhorn and A. Hirth, "Modeling of intracavity-pumped quasi-three-level lasers," *IEEE journal of quantum electronics*, vol. 38, no. 11, pp. 1455–1464, 2002.
- [5] "Matlab." [Online]. Available: <https://www.mathworks.com/>. [Accessed: 2016]
- [6] "LAS-CAD." [Online]. Available: <https://www.las-cad.com/>. [Accessed: 2016]
- [7] E. Bernhardi, C. Bollig, M. Esser, A. Forbes, L. Botha, and C. Jacobs, "A single-element plane-wave solid-state laser rate equation model," *South African Journal of Science*, vol. 104, no. 9–10, pp. 389–393, 2008.
- [8] W. S. Koen, C. Jacobs, O. Collett, and D. Esser, "Efficient Ho: YLF laser pumped by a Tm: fiber laser," in *Mid-Infrared Coherent Sources*, 2013, p. MW1C–6.

Nonlinear optical processes in two and multilevel atoms: a theoretical and numerical study

M Patel¹, G De Jager², Z Nkosi³ and K Govender⁴

^{1,3,4} Department of Electrical, Electronic and Computer Engineering, Cape Peninsula University of Technology, Symphony Way, Bellville, Cape Town, 7535, RSA

² Department of Electrical Engineering, University of Cape Town, Rondebosch, 7701, RSA

E-mail: ¹210230177@mycput.ac.za, ²Gerhard.DeJager@uct.ac.za, ³NkosiZ@cput.ac.za,

⁴GovenderK@cput.ac.za

Abstract. In this paper we report on the study of two-level and multilevel atoms interacting with one or more laser beams. The system is analyzed using the semi-classical approach where the dynamics of the atom is described quantum mechanically using Liouville's equation, while the laser is treated classically using Maxwell's equations. Firstly, we present results of a two-level atom interacting with a single laser beam and demonstrate Rabi oscillations between the two levels. We then examine the effects of laser modulation on the dynamics of the atom. The behaviour of the laser as it propagates through the atomic ensemble is studied by solving Maxwell's equations numerically. We study the nonlinear process called four-wave mixing that occurs when two or more pump beams, having different frequencies, interact with four different levels of a nonlinear medium. We make use of general energy levels in a diamond configuration. We present results of four-wave mixing for various detuning.

1. Introduction

Recently there has been a number of papers describing entangled photon pair generation using four-wave mixing in Rubidium atomic ensemble[1, 2, 3]. At the Cape Peninsula University of Technology an experiment is under development to investigate the properties of entangled photons generated by four-wave mixing in warm and cold Rubidium atoms. These atoms will be used for quantum key distribution in the future. In this paper we report on computational simulations of this process.

We report on the computational study of the interaction between laser beams and two and multilevel atoms. We use a semi-classical approach in which the dynamics of the atoms (described by the density matrix elements) are governed by the Von Neumann-Liouville equation,

$$i\hbar \frac{\partial \rho}{\partial t} = [\hat{H}, \hat{\rho}] + \text{relaxation terms} \quad (1)$$

while the laser beam is described by the wave equation derived from Maxwell's equations. The Hamiltonian of the total system is $\hat{H} = \hat{H}_0 + \hat{H}_I$, where \hat{H}_0 is the unperturbed Hamiltonian and \hat{H}_I is the interaction term. The relaxation terms contain the dissipative effects. We first discuss a two level atom interacting with a single laser beam and examine the dynamics of the populations and coherence terms of the density matrix elements. Thereafter we examine the behaviour of the laser beams as it propagates in multilevel atoms.

The overview of the paper is as follows: Section 2 describes the interaction of a two level atom with a single laser beam. Results showing the effects of a uniform and modulated laser beam are given. The study of the two-level atom is included to introduce basic ideas such as Rabi frequency, detuning and density matrix elements. Four-wave mixing is discussed in Section 3. Results are given for various parameters.

2. Laser-atom interactions

The interaction between a laser beam and a sample of stationary atoms having only two possible energy levels (separated in frequency by ω_0) has the following interaction Hamiltonian:

$$\hat{H}_I = -e\vec{E} \cdot \hat{\vec{D}} \cos \omega t \quad (2)$$

Here $-e\hat{\vec{D}}$ represents the dipole moment operator of the atom, \vec{E} is the electric field or amplitude of the laser beam and $\cos \omega t$ represents the time variation of the electric field of the laser beam where ω is the laser radian frequency. \hat{H}_I is then used in the Von Neumann Liouville equation to describe the time evolution of the density matrix elements of the system. The Von Neumann equation is used to derive the following equations for a two level atom (called Optical Bloch equations):

$$\frac{\partial \rho_{11}}{\partial t} = \frac{1}{2}i\Omega(\rho_{12} - \rho_{21}) + 2\gamma_{sp}\rho_{22} \quad (3)$$

$$\frac{\partial \rho_{12}}{\partial t} = \frac{1}{2}i\Omega(\rho_{11} - \rho_{22}) + [i(\omega_0 - \omega) - \gamma_{sp}]\rho_{12} \quad (4)$$

$$\frac{\partial \rho_{21}}{\partial t} = -\frac{1}{2}i\Omega(\rho_{11} - \rho_{22}) + [-i(\omega_0 - \omega) - \gamma_{sp}]\rho_{12} \quad (5)$$

$$\frac{\partial \rho_{22}}{\partial t} = -\frac{1}{2}i\Omega(\rho_{12} - \rho_{21}) - 2\gamma_{sp}\rho_{22} \quad (6)$$

where $\Omega = eE\langle D \rangle / \hbar$ is called the Rabi frequency and γ_{sp} represents a decay/de-coherence coefficient. ρ_{11} and ρ_{22} tells us the probability of the atom being in the ground and excited states, respectively. ρ_{12} and ρ_{21} are the interference terms of the atom indicative of superposition. We solve the above numerically.

2.1. Results

Results of the numerical solution of Equations 3-6 are given in Figures 1-2. Figure 1 corresponds to a uniform laser beam and Figure 2 deals with a modulated laser beam. In Figure 1, the blue curve represents ρ_{11} , the red curve ρ_{22} , the green curve ρ_{12} and the magenta curve ρ_{21} . The laser is switched on at $t = 0$ s with $\rho_{11} = 100\%$ and $\rho_{22} = 0\%$. Rabi oscillations are demonstrated in Figure 1A where $\omega_0 - \omega = 0$. In Figure 1B the laser is detuned i.e. $\omega_0 - \omega \neq 0$. The interference between Ψ_1 and Ψ_2 is decreased, where Ψ_i is the wave function corresponding to level i . A small dissipation is introduced in Figure 1C in the form of γ_{sp} . This results in the interference between Ψ_1 and Ψ_2 to decay to the point where the probability of superposition is close to 0%. The phase space plots in Figure 1D are related to Figures 1A-C: Rabi oscillation where the atom continues on the same path infinitely, (— black); laser detuning where the atom continues on the same path but at a different frequency to the Rabi frequency, (— purple); dissipation where the atom never follows the exact same path and diminishes at 0, (— orange).

The laser frequency, ω in the above equations, equations (3) to (6), is altered by including terms of modulation by means of a sinusoidal variation to the laser frequency. The modulated detuning is then

$$(\omega_0 - \omega) = \delta + D \sin(2\pi f_m t) \quad (7)$$

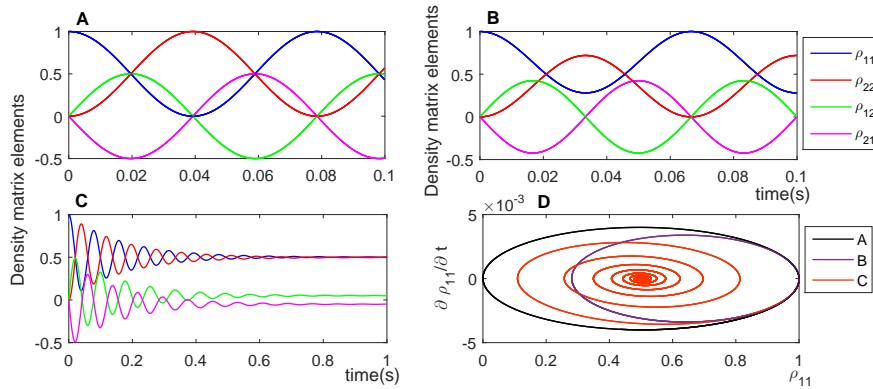


Figure 1. General features of a two-level atom interacting with a uniform laser beam. Plots A-C are the density matrix elements corresponding to (A) zero laser detuning demonstrating Rabi oscillation, (B) non-zero laser detuning, (C) zero detuning with added dissipation. Plot (D) shows the phase space plot, $\partial \rho_{11} / \partial t$ vs ρ_{11} for the above cases.

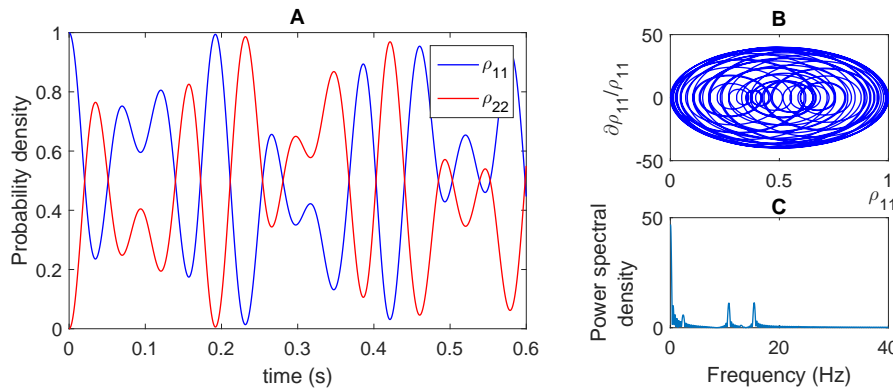


Figure 2. Two-level atom interacting with a laser beam where the modulated frequency is approximately equal to the Rabi frequency and the amplitude of modulation is small. The plots are: (A) time series; (B) phase space plot and (C) fast Fourier transform.

where δ has a fixed value, f_m is the modulation frequency and D represents the level of modulation. Making use of various parameters in equation (7) gives rise to interesting behaviour of the atomic dynamics. These are seen in Figure 2. The time series, Figure 2(A), shows an irregular curve. The phase space plot (B) shows that the atom deviates from the ground state from cycle to cycle - the path does not repeat itself. The atom behaves in a chaotic manner. In the Fourier spectra (C) there are three components that arise at 2.36 Hz, 10.72 Hz and 15.37 Hz, none of which appear at the Rabi frequency, $\Omega = 12.73$ Hz (ignoring the DC component at 0 Hz). These results show that the atom has tendencies to behave in a chaotic manner. Similar results have been seen by Pisipati et al. [4].

3. Nonlinear mixing in multilevel atoms

Next, we study the parametric process of four-wave mixing by having two pump beams, of different frequencies, interact with four levels of a hypothetical atom. Figure 3 shows the energy level structure where $|1\rangle$, $|2\rangle$, $|3\rangle$ and $|4\rangle$ are four relevant energy levels of the atom with $|1\rangle$ being the ground state and $|2\rangle$, $|3\rangle$ and $|4\rangle$ being excited states.

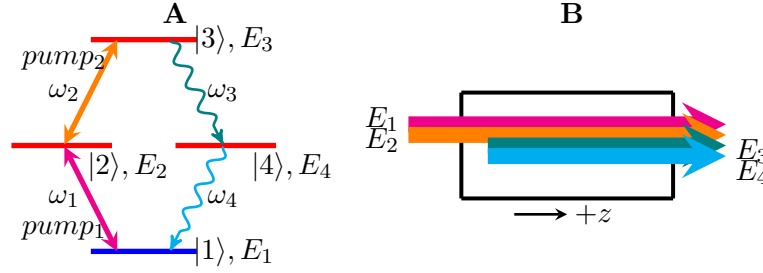


Figure 3. Four-wave mixing geometry. **A-** E_1 to E_4 are the corresponding energies of each level, ω_1 and ω_2 are the frequencies of two pump laser beams and ω_3 and ω_4 are the frequencies of two internally generated photons. **B-** E_1 and E_2 represent the electric fields of the pump beams and E_3 and E_4 represent the internally generated photons (these should not be confused with the energies).

In our analysis co-propagating beams, E_1 and E_2 , having different wavelengths are used as pumps beams. We investigate the production/variation of E_3 and E_4 across the longitudinal section of the sample. We assume that the pump laser beams are strong enough so that they do not get depleted as they propagate through the atomic ensemble. We also assume that all photons propagate in the positive z -direction. The atomic levels are assumed to be such that the photons of frequency ω_1 , ω_2 , ω_3 and ω_4 couple only transitions between $|1\rangle \leftrightarrow |2\rangle$, $|2\rangle \leftrightarrow |3\rangle$, $|3\rangle \leftrightarrow |4\rangle$ and $|4\rangle \leftrightarrow |1\rangle$, respectively, that is, they are very much detuned compared to the other transitions.

We now explain the derivation of the equation needed for predicting the electric fields, E_3 and E_4 . Further details of these derivations are provided in [5]. The behaviour of the electric fields E_3 and E_4 corresponding to frequencies ω_3 and ω_4 respectively are described by Maxwell's equations:

$$\frac{\partial}{\partial z} E_3(z) = i \frac{\omega_3}{2\epsilon c} \frac{N}{V} \mu_{34} \rho_{34}^{(3)} \quad (8)$$

$$\frac{\partial}{\partial z} E_4(z) = i \frac{\omega_4}{2\epsilon c} \frac{N}{V} \mu_{41} \rho_{41}^{(3)} \quad (9)$$

where $\rho_{ij}^{(3)}$ are the third order density matrix elements and are obtained from the master equation. These equations, equations (8) and (9), are derived from Maxwell's wave equation [6] where we have written the polarization in terms of $\rho_{34}^{(3)}$ and $\rho_{41}^{(3)}$.

The total Hamiltonian is

$$H = H_0 + H_I \quad (10)$$

where $H_I = -\hat{\mu} \cdot E$, $-\hat{\mu}$ is the dipole moment of the atom and E is the total electric field. The master equation (Liouville-von Neumann equation) that we solve is

$$\dot{\rho} = -\frac{i}{\hbar} [H'_I, \rho] + \text{relaxation terms} \quad (11)$$

where the interaction Hamiltonian term, H'_I , is in the interaction picture.

Making use of perturbation theory we let

$$\rho = \rho^{(0)} + \lambda \rho^{(1)} + \lambda^2 \rho^{(2)} + \dots \quad (12)$$

and expand and group terms by order to obtain the the population and coherence terms. The third order terms that are important for solving Maxwell's equation for the ω_3 and ω_4 terms are $\tilde{\rho}_{34}^{(3)}$ and $\tilde{\rho}_{41}^{(3)}$. The expansion for $\tilde{\rho}_{34}^{(3)}$ is

$$\begin{aligned} \tilde{\rho}_{34}^{(3)} = \frac{1}{(\Delta_{34} - i\Gamma_{34})} & \left[\frac{1}{\hbar^3} \frac{\mu_{21}\mu_{32}\mu_{14}\tilde{E}_1\tilde{E}_2\tilde{E}_4^*}{(\Delta_{42} + i\Gamma_{42})} \left(\frac{1}{(\Delta_{21} - i\Gamma_{21})} - \frac{1}{(\Delta_{41} + i\Gamma_{41})} \right) \right. \\ & + \frac{1}{\hbar^3} \frac{\mu_{34}|\mu_{14}|^2\tilde{E}_3|\tilde{E}_4|^2}{\gamma_{41}} \left(\frac{2\Gamma_{41}}{\Delta_{41}^2 + \Gamma_{41}^2} \right) - \frac{1}{\hbar^3} \frac{\mu_{21}\mu_{32}\mu_{14}\tilde{E}_1\tilde{E}_2\tilde{E}_4}{(\Delta_{21} - i\Gamma_{21})(\Delta_{31} - i\Gamma_{31})} \\ & \left. - \frac{1}{\hbar^3} \frac{\mu_{34}|\mu_{14}|^2\tilde{E}_3|\tilde{E}_4|^2}{(\Delta_{41} - i\Gamma_{41})(\Delta_{31'} - i\Gamma_{31})} \right] e^{-\omega_3 t} \end{aligned} \quad (13)$$

where Δ_{ij} represents the detuning between levels $|i\rangle$ and $|j\rangle$, Γ_{ij} represents the decay rate of the corresponding coherence ρ_{ij} and γ_{ij} represents the decay of the population ρ_{ii} . μ_{ij} are the matrix elements of the dipole moment μ in the basis $|1\rangle$, $|2\rangle$, $|3\rangle$ and $|4\rangle$. A similar equation is obtained for $\tilde{\rho}_{41}^{(3)}$. Equations for the fourth order terms which give the populations of each state as a function of detuning can be found in [7].

3.1. Results

We solve equations (8) and (9) numerically for various values of z and use updated values of $\tilde{\rho}_{34}^{(3)}$ and $\tilde{\rho}_{41}^{(3)}$ each time. We provide plots of the Rabi frequencies (which are proportional to the electric fields) of the emerging beams. Population values are also provided. Figures 4 and 5 show results of the population as a function of detuning of pump₁ (Δ_{21}) and pump₂ (Δ_{32}).

Figure 4 shows results for pump₁ (Δ_{21}) at a constant negative detuning as pump₂ (Δ_{32}) is varied. The atoms will not get excited from $|1\rangle \rightarrow |2\rangle$ easily due to the negative detuning of pump₁ (Δ_{21}). From the slight decrease in ρ_{11} we can assume that most of the atoms have remained in the ground state. As Δ_{32} decreases, corresponding to a smaller detuning, we see ρ_{22} decreasing slightly. This is because atoms have been excited from $|2\rangle \rightarrow |3\rangle$. At the same time ρ_{33} and ρ_{44} have increased by approximately the same amount. Note that ρ_{33} and ρ_{44} are shifted to the right relative to zero detuning to counteract the negative detuning of pump₁ beam in order to get maximum transfer of population to levels $|3\rangle$ and $|4\rangle$.

Figure 5 shows results for pump₂ (Δ_{32}) at a constant positive detuning as pump₁ (Δ_{21}) is varied. Plots for ρ_{11} and ρ_{22} show a decrease and increase in the populations at the respective levels as Δ_{21} decreases. We see that the plots for ρ_{33} and ρ_{44} have been shifted in the negative direction to counteract the positive detuning of the pump₂ beam in order to get maximum transfer of population to levels $|3\rangle$ and $|4\rangle$.

We note that spontaneously generated photons are directly proportional to the populations ρ_{22} , ρ_{33} and ρ_{44} . There are certain values of detuning for which there is maximum coherent beam intensity while the populations are away from their peak values.

4. Summary and Conclusion

We have investigated laser-atom interactions by first examining a two level atom interacting with a single laser beam where Rabi oscillations have been demonstrated. Dissipation effects show up as decay in the populations and de-coherence terms in the density matrix elements. Chaotic behaviour was also seen to occur when a modulated laser is used.

The analysis was extended to include the nonlinear process called four-wave mixing. One of the advantages of entangled photons generated in cold atoms via four-wave mixing is that they have better spectral characteristics and are better matched for absorption by the same type of atom. Various scenarios have been tested where one laser beam was kept constant while

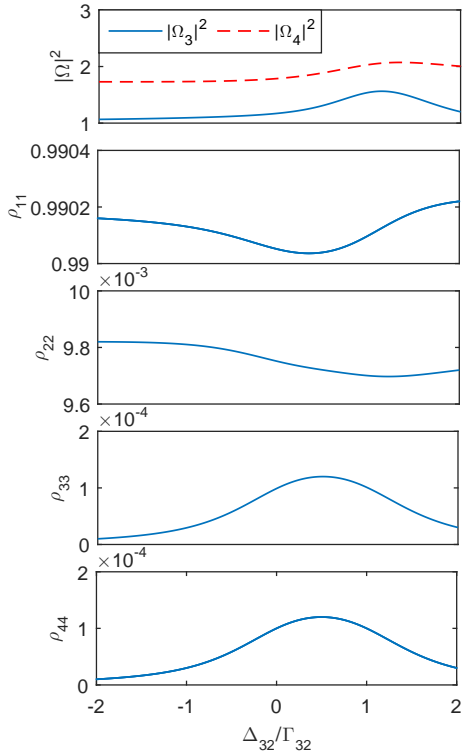


Figure 4. Plots from top to bottom are of Rabi frequency ($|\Omega|^2$) and populations (ρ_{11} , ρ_{22} , ρ_{33} and ρ_{44}) as the pump₂ beam is varied (Δ_{32}/Γ_{32}). Pump₁ beam is kept constant at a negative detuning (Δ_{21}).

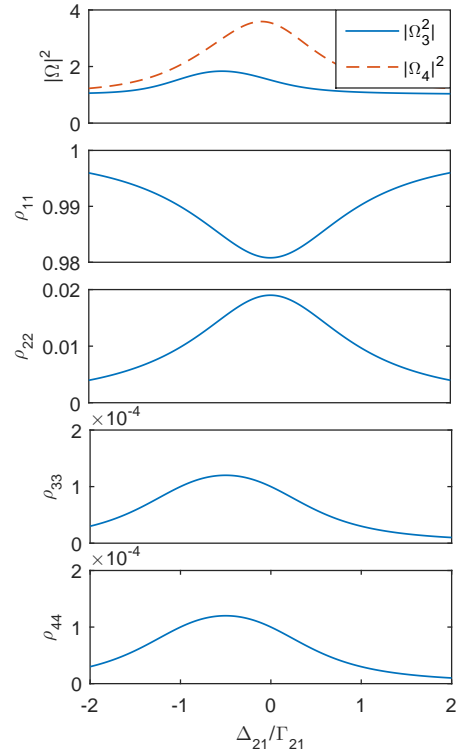


Figure 5. Plots from top to bottom are of Rabi frequency ($|\Omega|^2$) and populations (ρ_{11} , ρ_{22} , ρ_{33} and ρ_{44}) as the pump₁ beam is varied (Δ_{21}/Γ_{21}). Pump₂ beam is kept constant at a positive detuning (Δ_{32}).

the other was varied and vice versa. Maximum intensities of the coherent beams as well as populations were shown to be dependent on the laser detuning.

References

- [1] Srivathsan B, Gulati G K, Brenda C M Y, Maslennikov G, Matsukevich D and Kurtsiefer C 2013 *Phys. Rev. Lett.* **111**(12) 123602
- [2] de Melo N R and Vianna S S 2014 *J. Opt. Soc. Am. B* **31**
- [3] Jen H H and Chen Y C 2016 *Phys. Rev. A* **93**(1) 013811
- [4] Pisipati U, Almakrami I M, Joshi A and Serna J D 2012 *American Journal of Physics* **80**
- [5] Patel M, de Jager G, Wyngaard A and Govender K 2016 *Proc. Int Conf. Comp. Phys*
- [6] Grynberg G, Aspect A, Fabre C and Cohen-Tannoudji C 2010 *Introduction to Quantum Optics: From the Semi-classical Approach to Quantized Light* (Cambridge University Press)
- [7] Patel M 2017 *Numerical study of nonlinear spectroscopy and Four-Wave Mixing in two and multilevel atoms*. Master's thesis (Cape Peninsula University of Technology)

Applying the technique of ultrafast pump-probe spectroscopy on the main plant light-harvesting complex of spinach leaves

Asmita Singh, and Tjaart P J Krüger

Department of Physics, University of Pretoria, Pretoria, South Africa, 0002

E-mail: Tjaart.Kruger@up.ac.za

Abstract. The ultrafast transient dynamics of the main plant light-harvesting complex, LHCII, of spinach leaves were studied using transient absorption (TA) pump-probe spectroscopy. Explicitly, the excitation energy transfer (ET) processes within and amongst the protein-bound pigments (viz. chlorophylls (Chls) and carotenoids (Cars)) were investigated. These pigments are responsible for the absorption of solar photons and transfer the electronic excitation energy on ultrafast timescales to nearby complexes and eventually to a reaction center where charge separation is induced. We investigated differences in the ET kinetics that arise from exciting particular Cars preferentially. In particular, Lutein 1 and Neoxanthin were targeted using an excitation wavelength (λ_{ex}) of 489 nm, while Lutein 2 and Violaxanthin were excited specifically at 506 nm. Global analysis of the TA results was performed. The wavelength-dependent excitation study showed the ET dynamics to either be blue-shifted (λ_{ex} of 489 nm) or red-shifted (λ_{ex} of 506 nm) by ~ 5 nm. The general spectral (at the pigment peaks) and kinetic (species lifetimes) results were obtained. On average, the fluence was measured to be $\sim 10^{17}$ photons per cm^2 per pulse. A high excitation fluence induces the probability of singlet-singlet annihilation to occur, thus a surplus of molecules will relax back to the ground state. This work exhibits the successful application of the ultrafast pump-probe spectroscopic technique onto the LHCII of spinach leaves, preparing a local South African system to contend with international standards.

1. Introduction

Natural photosynthesis is a vital source for food production in nature and is the chief solar energy storing process known to exist on earth. Understanding the molecular mechanisms that underlie this process is necessary for sustainable future development, especially for solar energy production as an alternative to fossil fuel energy sources.

The photosynthetic light-harvesting (LH) apparatus of a plant is comprised of intricate networks of membrane-bound pigment-protein complexes. The photosystem-II (PSII) supercomplex houses the LHCII. LHCII, which naturally assumes a trimeric arrangement of three identical subunits, contains two main types of protein-bound pigments, viz. Chls and Cars [1]. These pigments capture the solar photons and transfer the electronic excitation energy on ultrafast timescales to neighbouring complexes and eventually to a reaction center (RC), where a charge separation is initiated [2, 3]. Plants are naturally able to protect themselves against the adverse effects of over-illumination through the process of non-photochemical quenching (NPQ). During NPQ excess energy is dissipated as heat via competing ET channels amongst the pigments [4]. Cars quench Chl triplet states in order to prevent the formation of reactive singlet oxygen, which is toxic to biological entities [5]. Understanding NPQ is a stepping-stone towards improving bio-inspired solar cell devices, particularly the role of Cars in quenching the Chl excited singlet states [6].

The light absorption region of Cars in higher plants is typically 400 nm – 500 nm, followed by excited ET to Chls *a* and *b*, thus increasing the spectral cross section for photosynthetic activity [7]. The individual ET dynamics can be studied through ultrafast spectroscopic techniques, such as transient absorption (TA) pump-probe (PP) spectroscopy. Pump pulses prompt the photoinduced processes, and the ET is typically probed with a white light continuum.

In the Car electronic structure, the excited-state manifold consists of two low-lying excited singlet states, viz. S_1 and S_2 . Transitions from the ground state (GS), S_0 , to S_1 are a one-photon symmetry forbidden transition due to S_0 and S_1 having the same electronic inversion symmetry. In contrast, the transition from S_0 to S_2 is strongly allowed and therefore typically observed in spectroscopic signals. Upon excitation, the S_2 state rapidly decays within a few hundred femtoseconds to the optically dark (i.e. nonradiative) S_1 state, which subsequently decays on a picosecond timescale to S_0 [7]. Due to the short lifetime of S_2 its excited state absorption (ESA) is not significant [8]. The decay of the strong negative ground state bleach (GSB), which is associated with the pump λ_{ex} , enables the estimation of the S_2 lifetime [9]. Therefore, it is necessary to exploit the structure and amplitude of the ESA of S_2 . In this study, we examined the TA signals of LHCII at two different λ_{ex} , exciting specific Cars, viz. 489 nm for Lutein 1 and Neoxanthin, and 506 nm for Lutein 2 and Violaxanthin.

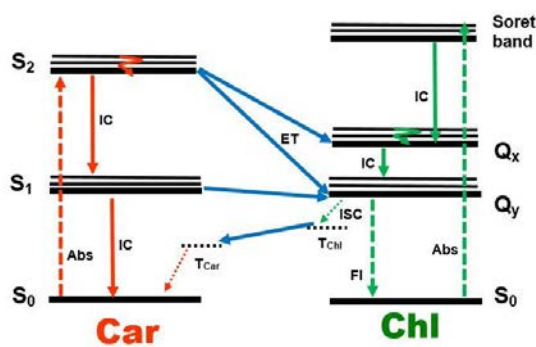


Figure 1: Simplified energy level diagram of the ET pathways between electronic excited states of Car and Chl pigment molecules, as well as the deactivation pathways within the molecules. Dotted lines show triplet states, whilst the solid lines denote singlet states. The Fl dashed arrow denotes a radiative process, solid blue is used for ET, and solid orange and green for non-radiative processes. Abs: absorption, Fl: fluorescence, IC: internal conversion, ISC: intersystem crossing.

2. Experimental

2.1. Sample preparation

Isolated LHCII trimers were prepared from PSII-enriched thylakoid membranes of spinach leaves [10, 11]. A buffer-detergent mixture (1.5 ml) consisting of 1.455 ml of 20 mM Hepes at pH 7.5 was added to 45 μ l of 1 % weight/volume β -DM detergent.

An Agilent Technologies Cary UV-Visible spectrophotometer was used to measure the LHCII sample's absorption spectrum, identifying pigment peak absorptions. Specifically, the exact sample concentration at the Q_y^2 peak of Chl *a* was found to be at an optimal optical density ($OD = \epsilon l C$) of 0.725/mm, using the Beer-Lambert law

$$I = I_0 e^{-\epsilon d C} \quad (1)$$

where I is the pump beam intensity after, and I_0 the intensity before the sample, ϵ the molar extinction coefficient [in $\text{dm}^3 \cdot \text{mol}^{-1} \cdot \text{cm}^{-1}$], d the path length and C the concentration of the sample [in $\text{mol} \cdot \text{dm}^{-3}$].

² Q_y transition: the longest-wavelength transition, invariably polarized along the y -axis of the molecule [12]

2.2. Experimental technique

The excited-state dynamics of isolated LHClI trimers was investigated by using the femtosecond TA PP spectroscopy laser facility of the National Laser Centre (NLC) at the Centre for Scientific and Industrial Research (CSIR) in Pretoria, South Africa.

The setup consists of a regenerative, 1 kHz amplified Ti:Sapphire solid-state laser (Clark – MXR, Inc. CPA 2110i). An optimal power of 1 W, with a pulse duration of 150 fs (corresponding to a transform-limited bandwidth of 7 nm) and central output peak wavelength of 775 nm was used. The CPA laser beam is split into two – one for the pump beam (30%) and one for the probe beam (70%). A non-collinear optical parametric amplifier (NOPA), pumped by the second harmonic (387.5 nm), is used to generate a pump pulse. Either a long-pass or short-pass filter at 500 nm was used outside the NOPA to narrow the spectral bandwidth for selective wavelength excitation. After prism compression, the pulse duration is ~30–40 fs, with a spectral FWHM bandwidth of 15 nm. A combination of neutral density filters were used to further tailor the pulse.

A 1 kHz mechanical chopper is used to distinguish between an excited state (pump-on) and an unexcited state (pump-off) for the pump pulse. This gives the difference in absorption (ΔA) of the sample. ΔA is probed with a broadband white-light beam, generated by a sapphire crystal. The probe pulse is delayed with respect to the pump pulse by using a 2 ns optical delay line. The pump and probe pulses overlap both spatially and temporally in the 1 mm path length cuvette that contains the prepared LHClI sample. The polarization of the pump pulse was set at the magic angle (54.7°) with respect to the probe pulse. Measurements were conducted at room temperature in aerobic conditions. To prevent photobleaching, small orthogonal vibrations were induced to the sample through the cuvette by using an amplifier.

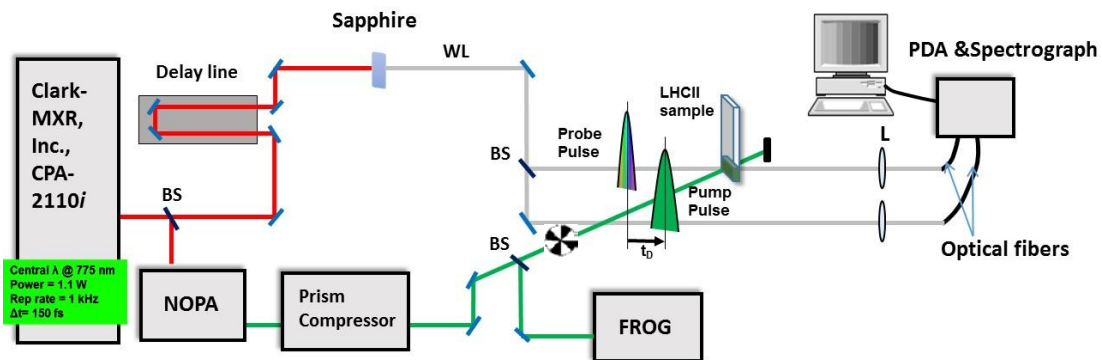


Figure 2: The TA PP spectroscopic setup used at the NLC. See text for detail.

The photoinduced OD changes are calculated as follows:

$$\Delta OD_\lambda = \Delta A_{\text{PumpON}} - \Delta A_{\text{PumpOFF}} = -\log\left(\frac{\left(\frac{I_\lambda^{\text{probe}}}{I_\lambda^{\text{ref}}}\right)_{\text{excited}}}{\left(\frac{I_\lambda^{\text{probe}}}{I_\lambda^{\text{ref}}}\right)}\right) \quad (2)$$

where $\left(\frac{I_\lambda^{\text{probe}}}{I_\lambda^{\text{ref}}}\right)_{\text{excited}}$ is a ratio of the pump and reference beam intensities at a specific wavelength λ , which is measured after the sample has been excited; whilst $\left(\frac{I_\lambda^{\text{probe}}}{I_\lambda^{\text{ref}}}\right)$ is the same ratio for an unexcited sample.

The nature of the TA PP data is complicated, and the subsequent interpretation after analysis is even more complex in terms of relating rate constants and results to literature. A number of factors such as the sample preparation process, unstable proteins after isolation, pigment ratios, temperature fluctuations, data measuring process, signal-to-noise ratios, sample refreshing rate, etc., all affect the quality of the data. By increasing the number of averages and reducing the focal beam spot sizes, and working in a dark, enclosed environment, the signal-to-noise ratio increased dramatically.

Time-resolved spectra were analyzed by fitting a model to estimate the rate constants of the various processes using kinetic parameters. We used the Glotaran [9] (Global and Target Analysis) freeware. Information of the ET mechanisms that occur in the LHCII trimer can be obtained from Global analysis in the form of rate constants for the various processes. The ET dynamics, which is typically seen from PP spectroscopy is termed Evolution Associated Difference Spectra (EADS), and decays sequentially with each species (τ) decaying into the subsequent one. For a three-compartmental model we therefore consider the scheme $\tau_1 \rightarrow \tau_2 \rightarrow \tau_3$.

3. Results and Discussion

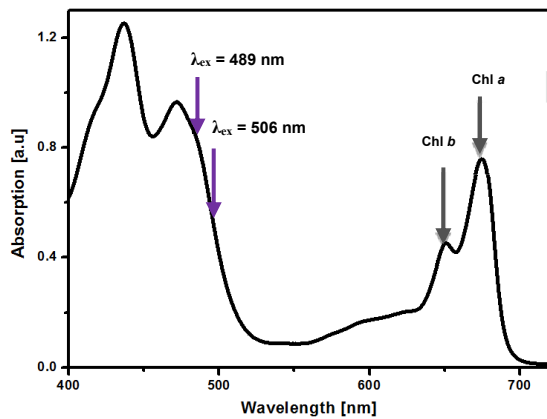


Figure 3: Measured absorption spectrum of LHCII. Chosen pump excitation wavelengths indicated with arrows – 489 nm and 506 nm. Q_y peak of Chl *a* measured as 0.725/mm. It is important to note that the excitation wavelength of 489 nm is relatively close to the peak of the Chl *b* Soret band, whereas 506 nm more specifically excites the Cars.

Two datasets were acquired from the TA PP measurements on LHCII, pumped at an excitation wavelength (λ_{ex}) of 489 nm and 506 nm, each with an intensity of 500 nJ/pulse. In both cases, a maximum of three kinetic parameters were fitted to the data, until the sequential model converged and a good dispersion fit (3rd order polynomial) was found for each dataset. According to the nature of the individual sample sets, various decay lifetimes were extracted from the data, ranging from a few 100 fs to a few ns – where the latter corresponds to typical fluorescence lifetimes.

The raw TA map upon excitation of LHCII at 506 nm is shown in figure 4(a), while figure 4(b) shows the line spectra at various time delays for the same dataset. The main features are the negative ground state bleach (GSB) around λ_{ex} of 506 nm, excited state absorption (ESA) (central $\lambda = 530$ nm), and GSB of Chl *b* (at 650 nm) and Chl *a* (at 673 nm).

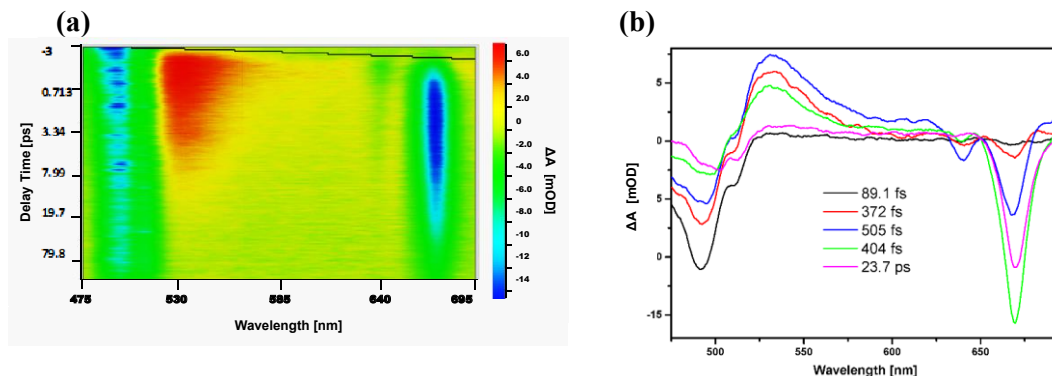


Figure 4: (a) Raw TA data of LHCII pumped at 506 nm with a pulse energy of 500 nJ. The dispersion fit is indicated by the black line. The negative blue/green sections indicate GSB, and positive red the ESA. (b) Spectral evolution (line spectra) of the sample at various delay times.

General trends are seen in the EADS of figure 5, demonstrating the excited ET at specific timescales. The three typical species lifetimes are: $\tau_1 \sim 500$ fs – 1.5 ps (black line), corresponding to a maximum

pump GSB and decay of the populated Car S₂-state to the other states (see figure 1) as well as maximum ESA. The second species (red) has a lifetime of $\tau_2 \sim 10$ ps, which corresponds to the fastest decay of the positive ESA band, denoting primarily ET from Car S₁ and Chl *b* to Chl *a* (GSB of the Q_y bands). The third lifetime (blue) has a characteristic lifetime of $\tau_3 \sim 600$ -700 ps and corresponds to relaxation of the Q_y-state of Chl *a*. Since the LHCII is isolated, it is no longer attached to a RC. Hence a surplus of energy remains at Chl *a*, which then results in values that are on the ns timescales and are typical of Chl *a* fluorescence.

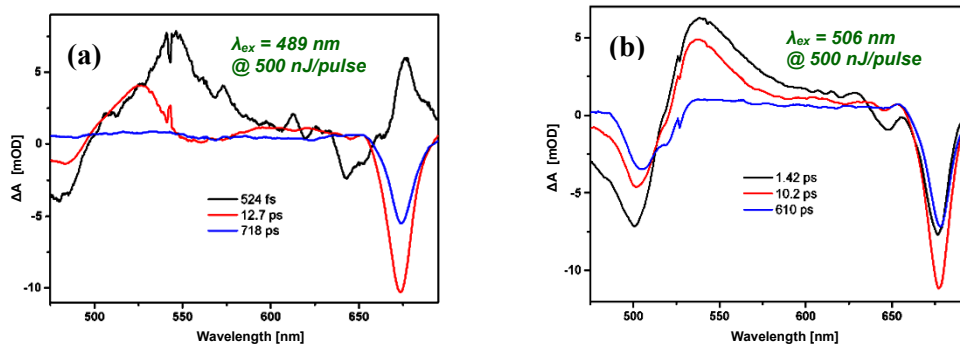


Figure 5: The Evolution Associated Difference Spectra (EADS) of the two LHCII samples investigated under different excitation wavelengths, (a) 489 nm and (b) 506 nm, each with a pulse energy of 500 nJ.

The Chl *b* bleach is stronger in figure 5(a) than in figure 5(b), which can be explained by the excitation in the blue region (489 nm) inferring a higher probability of exciting Chl *b* in the Soret region, as opposed to exciting only the Car region (506 nm). Thus, within the first few ps (τ_2), maximum ET occurs from the initially excited Chl *b* towards Chl *a*, as well as maximum ESA. The first lifetime of figure 5(a) has the structure of a coherent artefact, which arises around time zero as the supercontinuum probe traverses the sample [13]. Upon close inspection, there is a slight wavelength shift of ~ 5 nm towards the red for λ_{ex} 506 nm of all the bands, which corresponds to equilibrium of the energy before ET or de-excitation. The order of magnitude of the three EADS rate constants correspond to those found earlier in a similar study by Gradinaru, et al. in 2000 [8].

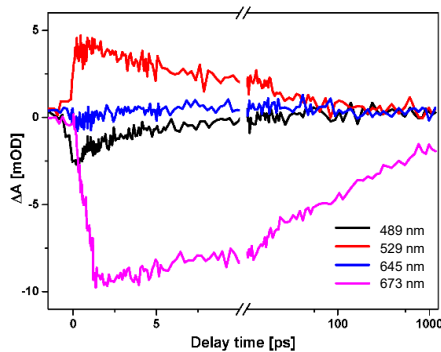


Figure 6: Difference intensity trace, after pumping with 500 nJ/pulse for λ_{ex} of 489 nm. At four characteristic wavelengths we see the following: 489 nm (decay of initially populated Car S₂ state), 529 nm (ESA, and population of Car S₁), 645 nm (Chl *b* peak), and 673 nm (Chl *a* peak).

Figure 6 shows that the decay of each species began around the same time. At first glance, it is apparent that the decay profiles of the λ_{ex} at 489 nm with 500 nJ/pulse excitation are noisy. The strong Chl *a* bleach at 673 nm has the longest rise time, suggesting that this bleach was the dominant processes.

The excitation fluence (number of photons per unit area per pulse) [14] was calculated using a beam diameter of 800 μm for λ_{ex} 489 nm and 506 nm, and pump power of 500 μW . On average, the fluence was measured to be $\sim 10^{17}$ photons per cm^2 per pulse. According to literature, at this order of magnitude we expect an increase in the singlet-singlet annihilation probabilities [15]. The difference is by and large attributed to the large beam diameter used, and one of the major future prospects is to reduce the focal spot sizes of both the pump and probe beams in the PP system. Hence, a high excitation fluence implies stronger change in absorbance signals, and a greater chance for singlet-singlet annihilation to occur.

4. Conclusion

This paper has highlighted some of the main spectral (at the pigment peaks) and kinetic (species lifetimes) results obtained for the various ET mechanisms amongst the Cars and Chls in the LHCII complex of spinach leaves. The wavelength dependent study, using a pulse energy of 500 nJ for the 489 nm and the 506 nm pump excitations exhibited a clear difference in the sample absorption and ET dynamics, as well as signal strengths (OD). The EADS showed that there is a difference in the ET dynamics between the Car region, and Chl *a* and *b* regions. Using different excitation wavelengths affect the lifetimes of processes, as well as the specific pigments that are targeted in this case. Global analysis gives the overall decay of a system as a whole (mixture of pure molecular states), from which specific elucidation of individual and intermediate states can be performed on the data as target analysis. High excitation fluence values infers a greater chance for singlet-singlet annihilation to occur, resulting in a larger number of molecules relaxing back to the GS. Nonetheless, the kinetic values obtained from this experiment for the various ET mechanisms amongst the Cars and Chls of the LHCII, are a good indication that the setup can be used for more sophisticated data acquisition experiments. In conclusion, the technique of ultrafast pump-probe spectroscopy was successfully applied to the LHCII of spinach leaves, preparing a local South African system to contend on an international platform.

Acknowledgments

The authors would like to extend their gratitude to the National Research Foundation (NRF) and the CSIR-NLC Rental Pool Program for financial assistance. A special vote of thanks to Attie Hendriks, Alexander Paradzah, Huzifa Elnour, and the rest of the Biophysics and Photonics research group at the University of Pretoria for their assistance and contributions to this work.

References

- [1] Liu Z, Yan H, Wang K, Kuang T, Zhang J, Gui L, An X, Chang W 2004 *Nature* **428** 287
- [2] Gradinaru C C, Kennis J T M, Papagiannakis E, van Stokkum I H M, Cogdell R J, Fleming G R, Nierderman R A, van Grondelle R 2001 *PNAS* **98** 2364–69
- [3] van Amerongen H, Croce R 2013 *Photosyn. Research* **116** 251-63
- [4] Xu P, Tian L, Kloz M, Croce R 2015 *Nature: Scientific Reports* **5** 1-10
- [5] Demmig-Adams B, Adams W W 2002 *Science* **298** 2149
- [6] Ruban A V, Berera R, Iliaia C, van Stokkum I H M, Kennis J T M, Pascal A A, van Amerongen H, Robert B, Horton P, van Grondelle R 2007 *Nature* **450** 575-9
- [7] Ostroumov E E, Mulvaney R M, Cogdell R J, Scholes G D 2013 *Science* **340** 52-6
- [8] Gradinaru C C, van Stokkum I H M, Pascal A A, van Grondelle R, van Amerongen H 2000 *J. Phy. Chem. B* **104** 9330-42
- [9] Snellenburg J J, Laptinok S P, Seger R, Mullen K M, van Stokkum I H M 2012 *J. Stat. Soft.* **49** 1-22
- [10] Van Roon H, van Breemen J F L, der Weerd F L, Dekker J P, Boekema E J 2000 *Photosyn. Research* **64** 155–66
- [11] von Leeuwen P J, Nieveen M C, van der Meent E J, Dekker J P, van Gorkom H J 1991 *Photosyn. Research* **28** 149-53
- [12] Blankenship R E, Molecular Mechanisms of Photosynthesis, Blackwell Science Ltd, Oxford 2002
- [13] Lebedev M V, Misochko O V, Dekorsy T, Georgiev N 2005 *J. Exp. & Theo. Phys.* **100** 272-82
- [14] Zaushitsyn Y, Jespersen K G, Valkunas L, Sundström V, Yartsev A 2007 *Phys. Review B* **75** 1952011-17
- [15] Schödel R, Hillmann F, Schrötter T, Voigt J, Irrgang K D, Renger G 1996 *Biophys. J* **71** 3370-80

Experimental characterisation of a metamaterial optical partial polariser in the quantum regime

S. A. Uriri, T. Tashima and M. S. Tame

School of Chemistry and Physics, University of KwaZulu-Natal, 4000, Durban, South Africa

E-mail: markstame@gmail.com

Abstract. Metamaterials have opened up many novel ways of controlling light, and in particular, controlling the polarisation of light. An important component in this respect is the polariser, which transmits light of one polarisation while blocking light of another polarisation. In our work, we experimentally probe and characterise a metamaterial polariser in the quantum regime. To do this, we prepare different polarisation-encoded single-photon states and send them through the metamaterial. We then perform quantum state tomography and obtain output states with a high fidelity to those expected ($\gtrsim 96\%$ on average). The transmission of vertically polarised light increases from 75% to 85% as the nanorod dimensions vary in the metamaterial. On the other hand, the metamaterials consistently transmit 99% of horizontally polarised light. The results are in full agreement with our theoretical predictions for an optical polarizer, in which we employ an analytical model for the metamaterial. Our study provides further evidence that metamaterials may be used for building compact optical components in on-chip quantum photonic systems.

1. Introduction

Plasmonic metamaterials are made from metallic nanostructures engineered with feature sizes smaller than the wavelength of interest [1]. They are able to achieve unusual optical responses that are not available in nature [2]. The metallic nanostructures in metamaterials, also known as ‘unit cells’, are usually arranged periodically in close range to each other, and their material and geometrical properties can be manipulated in order to change the bulk permittivity ϵ , permeability μ and other properties of the material. The unusual optical behaviour of metamaterials is due to the collective oscillations of the nanostructures in resonance with the incident light, *i.e.* a localised surface plasmon resonance [3, 4]. This plasmonic resonance gives metamaterials the ability to control and manipulate many different aspects of light.

Controlling the polarisation of light is an important process in many areas of science and technology, for example in communication [5], imaging [6, 7], and sensing [8]. Over the years, conventional optical polarisers have been made from birefringent materials [9], and from crystals or polymers [10]. Recently, the control of the polarisation of light using metamaterials has become possible. Shen *et al.* [11] have demonstrated an ultra-high efficiency metamaterial polariser, where light that is perpendicular to the principal axis is transmitted undisturbed, while light that is parallel is attenuated. Tam and Yan [12] have designed a plasmonic ultra-broadband polariser based on silver nanowire arrays where a broadband transmission was realised. Chin *et al.* [13] have shown that, with designed metamaterials mimicking anisotropic crystals, it is also possible to change the polarisation state of the field during the polariser operation.

In our work we experimentally probe and characterise a plasmonic metamaterial polariser in the quantum regime. We prepare different polarisation-encoded single-photon states and send them through the metamaterial. We then measure the output states of the metamaterial by performing quantum state tomography. An optical polariser that can control and manipulate the polarisation of light is an important component in quantum computing and quantum communication, where quantum information is encoded into the polarisation degree of freedom of single photons [14]. Due to the small size of the metamaterial it can be integrated with other optical components at the nanoscale in the design of an on-chip optical system. Along these lines, recently Asano *et al.* [15] used an optical metamaterial polariser to perform quantum state engineering, realising a quantum entanglement distillation protocol. Here, we extend this study by comparing the predictions of the expected theoretical response of the metamaterial using an analytical model to the experimental results obtained in the quantum regime.

2. Experimental setup

The experimental setup is shown in figure 1 (a), where type-1 spontaneous parametric down-conversion is used to generate pairs of single photons [16, 17]. A pump laser at 405 nm is rotated to vertical polarisation by a half-wave plate (HWP). The pump beam is then sent through a nonlinear BiBO crystal, which produces two ‘twin’ (idler and signal) photons polarised horizontally at a lower frequency (wavelength 810 nm). One photon is produced in arm A and the other in arm B. The optical axis of the BiBO is cut such that the two photons emerge at 3° from the initial pump direction. A single photon in arm A is used to herald the presence of another single photon in arm B. A qubit is encoded into the single photon in arm B using a quarter-wave plate (QWP) and HWP. Here, the polarisation states $|H\rangle$ and $|V\rangle$ are used as the orthogonal basis states of the qubit. This qubit is then sent through the plasmonic metamaterial (MTM).

Quantum state tomography is performed on the output of six different polarisation-encoded qubits sent through the metamaterial using a QWP, HWP and a polarising beamsplitter (PBS). This allows the density matrices to be reconstructed via projective measurements [18]. The output of our projective measurement is sent into fibre couplers and coincidence counts between

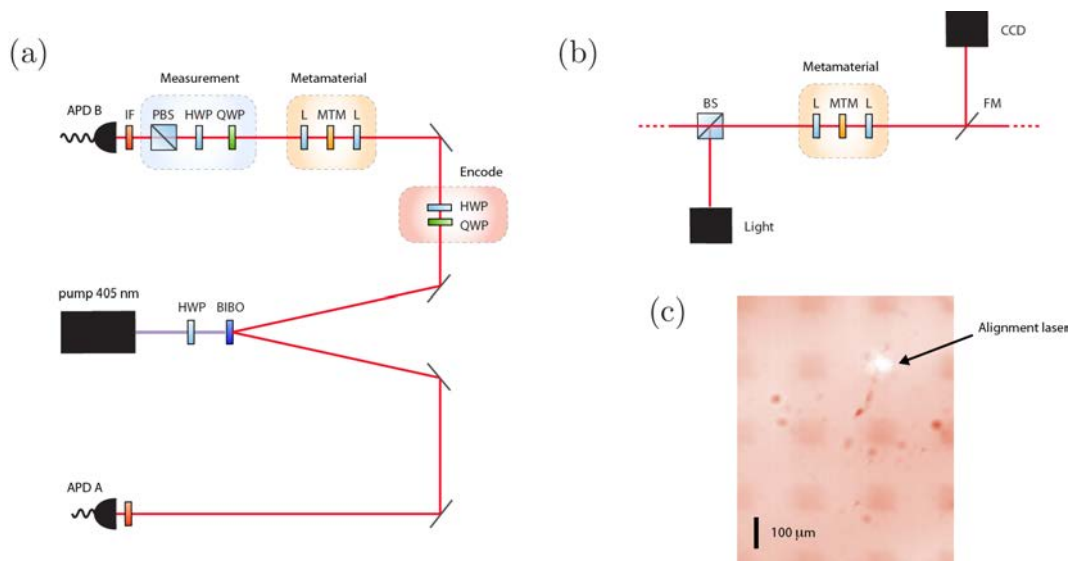


Figure 1: Overview of the experiment. (a) Experimental setup. Here, L is a convex lens, HWP and QWP are a half- and quarter-wave plate, BiBO is a nonlinear crystal, MTM is a metamaterial, PBS is a polarising beamsplitter and APD is an avalanche photodetector. (b) Telescope system for imaging the alignment laser and its position on different metamaterials. FM is a flip mirror. (c) Image of metamaterials with the alignment beam on a particular design.

arm A and B (8 ns window) are detected by silicon avalanche photodetectors and a coincidence counting unit. An interference filter (800 ± 20 nm) is placed in front of each fibre coupler to cut out photons of higher and lower frequencies corresponding to unwanted down-conversion processes and the pump beam. Figure 1 (b) shows the telescope system used to focus the single photons onto the metamaterial and CCD for imaging. Figure 1 (c) shows an image obtained from the CCD displaying the sample used with different metamaterial designs (each $100\mu\text{m} \times 100\mu\text{m}$). An alignment beam (785 nm) sent from the fibre coupler can be seen at one of the metamaterial designs. The telescope system is designed in such a way that the beam before and after the lenses is collimated and therefore the beam diameter of single photons traversing in the opposite direction will be roughly the same as that of the alignment beam. When single photons are used in the setup the beamsplitter and mirror in figure 1 (b) are flipped down.

3. Quantum state probing

The input probe states are encoded experimentally by using a QWP and HWP set at a particular angle (see encode box in figure 1 (a)). The unitary operations of the wave plates acting on the polarisation qubit of the single photon in arm B are given by

$$\hat{U}_{QWP}(q) = \frac{1}{\sqrt{2}} \begin{bmatrix} i - \cos(2q) & \sin(2q) \\ \sin(2q) & i + \cos(2q) \end{bmatrix}, \quad \hat{U}_{HWP}(h) = \begin{bmatrix} \cos(2h) & -\sin(2h) \\ -\sin(2h) & -\cos(2h) \end{bmatrix}. \quad (1)$$

By choosing the angles correctly [18] we obtain six different polarisation-encoded qubits

$$\begin{aligned} |H\rangle &= \begin{pmatrix} 1 \\ 0 \end{pmatrix}, |V\rangle = \begin{pmatrix} 0 \\ 1 \end{pmatrix}, |+\rangle = \frac{1}{\sqrt{2}} \begin{pmatrix} 1 \\ 1 \end{pmatrix}, \\ |-\rangle &= \frac{1}{\sqrt{2}} \begin{pmatrix} 1 \\ -1 \end{pmatrix}, |L\rangle = \frac{1}{\sqrt{2}} \begin{pmatrix} 1 \\ i \end{pmatrix}, |R\rangle = \frac{1}{\sqrt{2}} \begin{pmatrix} 1 \\ -i \end{pmatrix}, \end{aligned} \quad (2)$$

where $|H\rangle$, $|V\rangle$, $|+\rangle$, $|-\rangle$, $|L\rangle$ and $|R\rangle$ correspond to horizontal, vertical, diagonal, anti-diagonal, left- and right-circularly polarised single photons, respectively. We send these probe states through the metamaterial and perform quantum state tomography on the output states.

4. Theoretical prediction

Before discussing the results of probing the metamaterial in the quantum regime we describe the theory of transmission of light through them. For this we model the metamaterial as a periodic array of nanoparticles in a rectangular lattice with periods d_x and d_y . In the dipole approximation, each nanoparticle representing a unit cell of the metamaterial is modelled by a dipole with polarisability tensor α , which relates the dipole moment to the local electric field at the particle [19–21]. The plasmonic nanoparticles in this work are rod-like in shape and are well described as an ellipsoid with semi-axes a , b and c . This gives a diagonal polarisability tensor with non-zero elements [20]

$$\alpha_{ii} = 4\pi\epsilon_0 abc \frac{\epsilon_{au} - \epsilon_m}{3\epsilon_m + 3L_i(\epsilon_{au} - \epsilon_m)}, \quad (3)$$

where ϵ_0 is the free space permittivity, L_i ($i = x, y, z$) is a shape factor [20], $\epsilon_{au} = -22.842 + 1.8388i$ is the relative permittivity of gold and $\epsilon_m = (1.45)^2$ the relative permittivity of the surrounding medium (silica) at 810 nm. In our simulation, $a = \frac{l}{2}$, $b = \frac{w}{2}$, and $c = \frac{z}{2}$, where l is the length of the nanorod, w is the width and z is the height. The nanorods are fabricated by electron-beam lithography and gold deposition on a silica substrate [15]. The dimensions used are $d_x = d_y = 200$ nm for the period, $l = 95 - 110$ nm for the length, $w = 39 - 47$ nm for the width and $z = 30$ nm for the thickness. Each metamaterial in figure 1 (c) has a

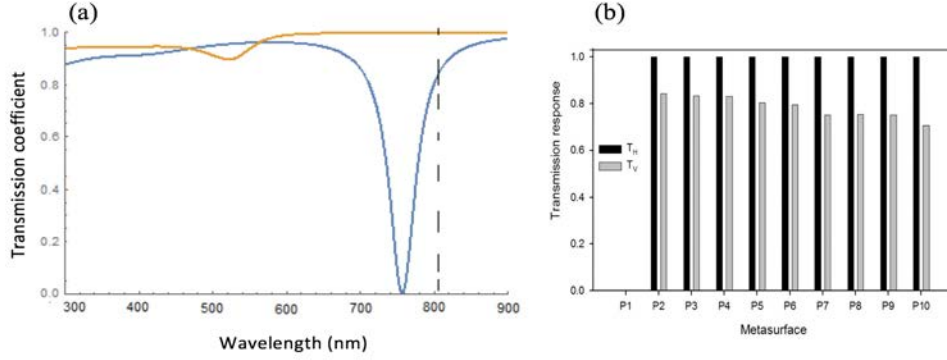


Figure 2: Theoretical and experimental transmission through metamaterials. (a) Theoretical transmission spectra for horizontally (orange line) and vertically (blue line) polarised light sent through a plasmonic metamaterial made of gold nanorods ($w = 39$ nm, $l = 110$ nm, $z = 30$ nm). The dashed line corresponds to 810 nm. (b) Transmission coefficients of horizontally (black) and vertically (grey) polarised single photons (at 810 nm) through different plasmonic metamaterials ($w = 39 - 47$ nm, $l = 110$ nm, $z = 30$ nm) obtained via experiment. Here, metamaterial design ‘P10’ has the dimensions used in (a) and design ‘P1’ is an empty slot on the sample.

different dimension chosen for the length and width of the nanorods used as unit cells, with a total square footprint of $100\mu\text{m} \times 100\mu\text{m}$. The transmission and reflection of light through this kind of nanoparticle periodic array are described in detail in Ref. [21] and given for light with normal incidence to the array and polarised in direction k as

$$R_k = \frac{i\mu_0\pi fc}{d_x d_y} \alpha_{kk}, \quad T_k = 1 + R_k. \quad (4)$$

Here, μ_0 is the free space permeability, f is the frequency of the propagating electromagnetic wave and c is the speed of light in a vacuum. With these equations at hand, we are able to model the transmission of single photons of horizontal and vertical polarisation through the different metamaterial designs shown in figure 1 (c), where the vertical axis of the single photons is oriented along the long axis of the nanorods. From the above theory, this means that the probability of transmitting a photon encoded in the state $|V\rangle$ through a metamaterial should decrease as the nanorod length in the metamaterial increases and width decreases. This is caused by a stronger plasmonic resonance of the nanorod. On the other hand, the transmission of a photon encoded in the state $|H\rangle$ is constant for all the metamaterial designs as the plasmonic resonance is weak along the width of the nanorod for the widths considered.

5. Experimental results

We now present our experimental results and compare them with results obtained via the theory outlined in the previous section. Figure 2 (a) shows the transmission for horizontally and vertically polarised light obtained from theory for a particular set of nanorod dimensions ($w = 39$ nm, $l = 110$ nm, $z = 30$ nm). A dashed line represents 810 nm, corresponding to the wavelength of our single photons. In figure 2 (b) we show the results from experimental probing of several metamaterials in our setup with different nanorod dimensions. The transmission response for $|H\rangle$ and $|V\rangle$ polarisation encoded photons were calculated using $T_H = \frac{T_{HM}}{T_{HS}}$ and $T_V = \frac{T_{VM}}{T_{VS}}$, respectively. Here, T_{HS} and T_{HM} are the transmission probabilities of the state $|H\rangle$ through the substrate (no metamaterial) and through the metamaterial, respectively. Similarly, T_{VS} and T_{VM} are the transmission probabilities of the state $|V\rangle$ through the substrate and metamaterial, respectively. As can be seen in figure 2 (b) that the transmission of the state $|V\rangle$ decreases from 85% to 75% as the nanorod dimensions vary in the metamaterial (length and thickness

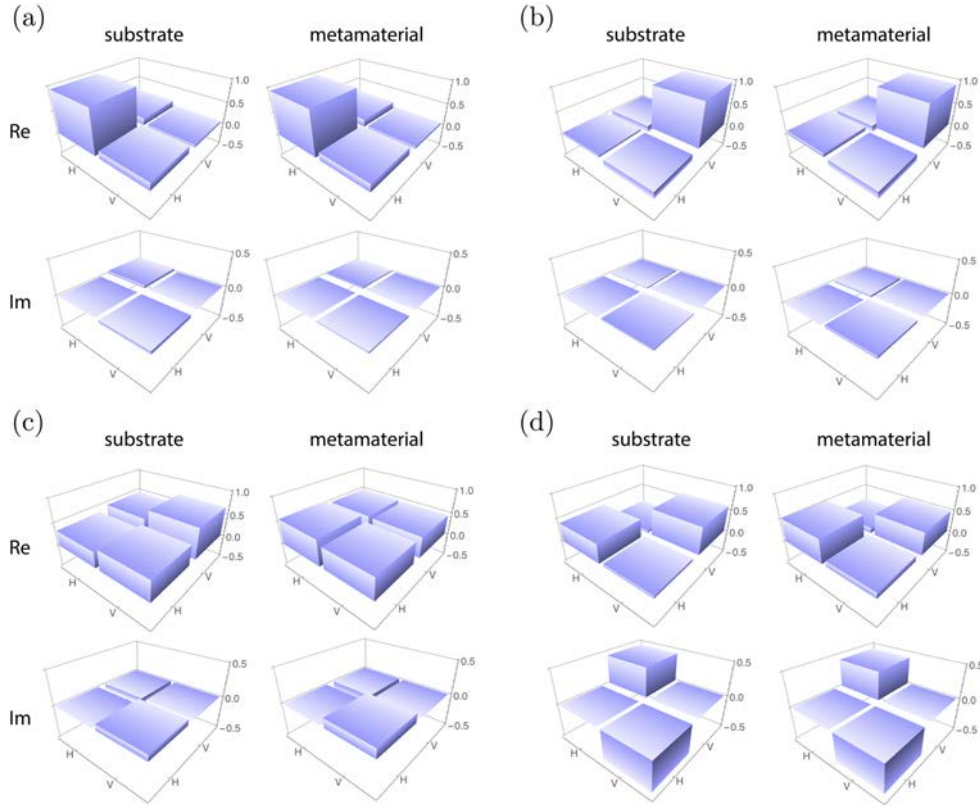


Figure 3: Quantum state tomography of probe states sent through the metamaterial and substrate. (a) Real and imaginary parts of the output state $\hat{\rho}_{exp}$ obtained from the state $|H\rangle$ sent through the substrate and metamaterial. (b) Real and imaginary parts of the output state for $|V\rangle$ sent through the substrate and metamaterial. The other panels show the output states for the following probe states: (c) shows $|+\rangle$ and (d) shows $|L\rangle$.

fixed, width decreases). On the other hand, the plasmonic metamaterials transmit $\sim 99\%$ of the state $|H\rangle$ compared to the bare substrate. In the experimental results in figure 2 (b), the metamaterial design ‘P10’ has nanorods with the same dimensions as those used in the theory for figure 2 (a). Considering the finite bandwidth of the single photons, the experimental results are in good agreement with the average transmission obtained from the theory. Also, the trend of our results generally agrees with the transmissions obtained by Asano et al. in Ref. [15], which reported transmissions from 11% to 41% for TV by classical FTIR for metamaterials with similar nanorod structures, but a different range of dimensions and thus transmission response.

In order to further investigate metamaterial P10 in the quantum regime we probe it with six polarisation-encoded single photon states: $|H\rangle$, $|V\rangle$, $|+\rangle$, $|-\rangle$, $|L\rangle$ and $|R\rangle$. The fidelity $F = \langle \psi | \hat{\rho}_{exp} | \psi \rangle$ and purity $P = tr(\hat{\rho}_{exp}^2)$ [22] were then calculated for the output states $\hat{\rho}_{exp}$ obtained using quantum state tomography [18]. Here, $|\psi\rangle$ is the ideal input quantum state and the fidelity provides a measure of the closeness of the output state to the ideal input state. The purity provides a measure of how close the output state is to a pure state. In figure 3 we show the real and imaginary parts of the density matrices for four different probe states ($|H\rangle$, $|V\rangle$, $|+\rangle$ and $|L\rangle$) sent through either the substrate or metamaterial P10. We obtained a fidelity of 0.960 ± 0.002 and a purity of 0.950 ± 0.007 for the probe state $|H\rangle$ transmitted through the substrate, and a fidelity of 0.97 ± 0.003 and a purity of 0.956 ± 0.007 for the state $|H\rangle$ transmitted through the metamaterial. The fidelity and purity of all six probe states are given in table 1.

One can see in figure 3 (a) and (b) that the $|H\rangle$ and $|V\rangle$ states are transmitted through the metamaterial in the same way as the substrate, although with fewer photons detected for $|V\rangle$

State	Fidelity		Purity	
	Substrate	Metamaterial	Substrate	Metamaterial
$ H\rangle$	0.960 ± 0.002	0.970 ± 0.003	0.950 ± 0.007	0.956 ± 0.003
$ V\rangle$	0.960 ± 0.002	0.928 ± 0.003	0.954 ± 0.004	0.925 ± 0.007
$ +\rangle$	0.940 ± 0.003	0.960 ± 0.002	0.946 ± 0.006	0.968 ± 0.005
$ -\rangle$	0.950 ± 0.003	0.910 ± 0.003	0.953 ± 0.006	0.987 ± 0.007
$ R\rangle$	0.924 ± 0.003	0.925 ± 0.003	0.912 ± 0.006	0.954 ± 0.006
$ L\rangle$	0.938 ± 0.003	0.929 ± 0.003	0.938 ± 0.002	0.934 ± 0.005

Table 1: Fidelity and purity for the single-photon probe states.

through the metamaterial. On the other hand, for the $|+\rangle$ and $|L\rangle$ states shown in figure 3 (c) and (d) the metamaterial acts as a partial polariser, balancing the ratio of the diagonal terms.

6. Summary

We experimentally characterised a plasmonic metamaterial optical polariser in the quantum regime and showed that the metamaterial behaves like a partial polariser, transmitting the horizontally polarised component of single photons undisturbed and part of the vertically polarised component. The experimental results are in agreement with the theory. The other metamaterials studied showed polarisation dependence for vertically polarised photons according to the dimensions of the nanorods used as unit cells. The transmission of horizontally polarised photons was essentially constant for all metamaterials. This study provides further evidence that metamaterials may be used as optical components in quantum photonic systems.

Acknowledgments

We acknowledge support from the National Research Foundation of South Africa (NRF).

References

- [1] Cai W and Shalaev V 2010 *Optical Metamaterials: Fundamentals and applications* (Dordrecht: Springer)
- [2] Barnes W L 2011 *Philos. Trans. R. Soc. London, Ser. A* **369** 3431-3433.
- [3] Huttler E and Fendler J H 2004 *Adv. Matter.* **16** 1685-1706
- [4] Tame M S, McEnery K R, Ozdemir S K, Lee J, Maier S A and Kim M S 2013 *Nature Phys.* **9** 329-340
- [5] Damask J N 2004 *Polarization optics in Telecommunications* (Dordrecht: Springer)
- [6] Fang N and Zhang X 2003 *Appl. Phys. Lett.* **82** 161
- [7] Fang N, Lee H, Sun C and Zhang X 2005 *Science* **308** 534-537
- [8] Chen T, Li S and Sun H 2012 *Sensors* **12** 2742-2765
- [9] Tyan R C et al. 1997 *J. Opt. Soc. Am. A* **14** 1627-1636
- [10] Land E H 1951 *J. Opt. Soc. Am.* **41** 957-963
- [11] Shen B, Wang P, Polson R and Menon R 2014 *Optica* **5** 356-960
- [12] Han C and Tam W Y 2015 *Appl. Phys. Lett.* **106** 081102
- [13] Chin J Y, Lu M and Cui T J 2008 *Appl. Phys. Lett.* **93** 251903
- [14] O'Brien J, Furusawa A and Vuckovic J 2005 *Nature Photon.* **3** 687-695
- [15] Asano M et al. 2015 *Sci. Rep.* **5** 18313
- [16] Hong C K and Mandel L 1986 *Phys. Rev. Lett.* **56**, 58-60
- [17] Burnham D C and Weinberg D L 1970 *Phys. Rev. Lett.* **25**, 84-87
- [18] James D F V, Kwiat P G, Munro W J, and White A G 2001 *Phys. Rev. A.* **64** 052312
- [19] Zhao Y and Alu A 2013 *Nano Lett.* **13** 1086 - 1091
- [20] Bohren C F and Huffman D R 1998 *Absorption and Scattering of light by small particles* (New York: John Wiley & Sons)
- [21] Alu A and Engheta N 2011 *Structured Surfaces as Optical Metamaterials* (New York: Cambridge University Press)
- [22] Nielsen M A and Chuang I L 2000 *Quantum Computation and Quantum Information* (Cambridge: Cambridge University Press)

Division D1 – Astrophysics

Existence of anti-Newtonian solutions in fourth-order gravity

Amare Abebe

Department of Physics, North-West University, Mmabatho 2735, Mafikeng, South Africa

E-mail: amare.abbebe@gmail.com

Abstract. We use the covariant consistency analysis formalism to show the existence of a class of perfect-fluid cosmological solutions, known as *anti-Newtonian universes*, in the context of modified gravity. There are no known linearized solutions in General Relativity, but the integrability conditions for such models in $f(R)$ gravity are presented.

1. Introduction

The phenomenological discovery that the Universe is currently undergoing accelerated expansion has attracted numerous theoretical alternatives to General Relativity (GR). Among such alternatives are fourth-order theories of gravity. Generally obtained by including higher-order curvature invariants in the Hilbert-Einstein action, or by making the action nonlinear in the Ricci curvature R or contain terms involving combinations of derivatives of R , these models attempt to address the shortcomings of GR in the infrared (IR) and ultraviolet (UV) ranges, i.e., very low and very high energy scales. The simplest, and perhaps most studied, of these models are the $f(R)$ models of gravitation. One advantage of such models is that they have enough freedom to explain early-universe inflation [1], late-time acceleration [2] and the cosmic evolution history in between [3, 4, 5]. As such freedom does not come without a cost, i.e., viable models should be constrained to conform with observational predictions and physically motivated mathematical restrictions, rigorous consistency analyses of the linearized field equations in such theories need to be made. Such initiatives have been undertaken in recent works [6, 7, 8, 9] for some classes of cosmological solutions with an underlying Friedman-Lemaître-Robertson-Walker (FLRW) background.

In GR, irrotational dust spacetimes have been studied as potential models for the description of gravitational collapse and late-time cosmic structure formation. The locally free gravitational field in such spacetimes is covariantly described by the gravito-electric and gravito-magnetic tensors, E_{ab} and H_{ab} , which, respectively, are responsible for the tidal tensor in the classical Newtonian gravitational theory and gravitational radiation in relativistic theories. Purely gravito-electric irrotational dust spacetimes are usually referred to as *Newtonian-like* or *quasi-Newtonian* universes, whereas those classes of irrotational dust universes with purely gravito-magnetic Weyl tensor are called *anti-Newtonian* universes. Consistency analyses of the general relativistic propagation and constraint equations arising from imposing external restrictions such as shear-free assumptions do generally show that such models suffer from severe integrability conditions [10, 11, 12, 13, 14] leading to the conclusion that there are no anti-Newtonian

spacetimes that are linearized perturbations of FLRW universes. Our present work shows that fourth-order gravitational theories, that generally assume non-vanishing anisotropic pressure and heat-flux terms, allow such solutions.

2. Linearized anti-Newtonian field equations

If we generalize the Hilbert-Einstein action by making the geometric contribution to the Lagrangian a generic function of the Ricci scalar, R , we obtain the $f(R)$ gravitational action

$$\mathcal{A} = \frac{1}{2} \int d^4x \sqrt{-g} [f(R) + 2\mathcal{L}_m] , \quad (1)$$

which, upon the application of the variation principle, yields the generalized Einstein field equations ¹

$$f' G_{ab} = T_{ab}^m + \frac{1}{2}(f - Rf')g_{ab} + \nabla_b \nabla_a f' - g_{ab} \nabla_c \nabla^c f' . \quad (2)$$

Here \mathcal{L}_m is Lagrangian for standard matter whose energy-momentum tensor (EMT) is given by

$$T_{ab}^m = \mu_m u_a u_b + p_m h_{ab} + q_a^m u_b + q_b^m u_a + \pi_{ab}^m , \quad (3)$$

where μ_m , p_m , q_a^m and π_{ab}^m are matter energy density, pressure, heat flux and anisotropic pressure respectively of matter, u^a is a normalized 4-velocity vector of fundamental observers, and h_{ab} is used to define the fully orthogonally projected covariant derivative operator $\tilde{\nabla}$. Eq. (2) shows that the standard Einstein field equations get modified due to the addition of the extra geometric terms ($f(R)$ and its derivatives) to the matter on the right hand side. These extra terms can be considered to make up the *curvature fluid* contributions to the EMT whose energy density, pressure, heat flux and anisotropic pressure are given by

$$\mu_R = \frac{1}{f'} \left[\frac{1}{2}(Rf' - f) - \Theta f'' \dot{R} + f'' \tilde{\nabla}^2 R \right] , \quad (4)$$

$$p_R = \frac{1}{f'} \left[\frac{1}{2}(f - Rf') + f'' \ddot{R} + f''' \dot{R}^2 + \frac{2}{3} \left(\Theta f'' \dot{R} - f'' \tilde{\nabla}^2 R \right) \right] , \quad (5)$$

$$q_a^R = -\frac{1}{f'} \left[f''' \dot{R} \tilde{\nabla}_a R + f'' \tilde{\nabla}_a \dot{R} - \frac{1}{3} f'' \Theta \tilde{\nabla}_a R \right] , \quad (6)$$

$$\pi_{ab}^R = \frac{f''}{f'} \left[\tilde{\nabla}_{(a} \tilde{\nabla}_{b)} R - \sigma_{ab} \dot{R} \right] , \quad (7)$$

where Θ and σ_{ab} are the expansion scalar and the shear tensor obtained from the full covariant derivative of u^a as follows:

$$\nabla_a u_b = -A_a u_b + \frac{1}{3} h_{ab} \Theta + \sigma_{ab} + \varepsilon_{abc} \omega^c . \quad (8)$$

Here $A_a = \dot{u}_a$ and $\omega^a = \varepsilon^{abc} \tilde{\nabla}_b u_c$ are the 4-acceleration and vorticity vectors. The angular brackets in Eq. (7) denote orthogonal projections of vectors and tensors. The volume element for the 3-rest spaces orthogonal to u^a is defined by ²

$$\varepsilon_{abc} = u^d \eta_{dabc} = -\sqrt{|g|} \delta_{[a}^0 \delta_b^1 \delta_c^2 \delta_{d]}^3 u^d \Rightarrow \varepsilon_{abc} = \varepsilon_{[abc]} , \quad \varepsilon_{abc} u^c = 0 , \quad (9)$$

¹ We have used the shorthands $f = f(R)$, $f' \equiv df/dR$, etc. Moreover, we use ∇ , $\tilde{\nabla}$ and an overhead dot $\dot{}$ to denote the full covariant derivative, the covariant 3-spatial derivative and differentiation with respect to cosmic time t , respectively.

² In this work, round brackets (ab) indicate symmetrization over the indices a and b whereas square brackets $[ab]$ denote anti-symmetrization over these indices.

where η_{abcd} is the 4-dimensional volume element such that

$$\eta_{abcd} = \tilde{\eta}_{[abcd]} = 2\varepsilon_{ab[cd]} - 2u_{[a}\varepsilon_{b]cd}. \quad (10)$$

We define the covariant spatial divergence and curl of vectors and tensors as

$$\text{div}V = \tilde{\nabla}^a V_a, \quad (\text{div}S)_a = \tilde{\nabla}^b S_{ab}, \quad (11)$$

$$\text{curl}V_a = \varepsilon_{abc} \tilde{\nabla}^b V^c, \quad \text{curl}S_{ab} = \varepsilon_{cd(a} \tilde{\nabla}^c S_{b)}^d. \quad (12)$$

Covariant spatial derivative operators acting on any scalar field ϕ obey the commutation relation

$$[\tilde{\nabla}_a \tilde{\nabla}_b - \tilde{\nabla}_b \tilde{\nabla}_a] \phi = 2\varepsilon_{abc} \omega^c \dot{\phi}, \quad (13)$$

and to linear order, the following differential relations apply:

$$[\tilde{\nabla}^a \tilde{\nabla}_b \tilde{\nabla}_a - \tilde{\nabla}_b \tilde{\nabla}^2] \phi = \frac{1}{3} \tilde{R} \tilde{\nabla}_b \phi, \quad (14)$$

$$[\tilde{\nabla}^2 \tilde{\nabla}_b - \tilde{\nabla}_b \tilde{\nabla}^2] \phi = \frac{1}{3} \tilde{R} \tilde{\nabla}_b \phi + 2\varepsilon_{dbc} \tilde{\nabla}^d (\omega^c \dot{\phi}), \quad (15)$$

where $\tilde{R} = \frac{6K}{a^2} = 2(\mu - \frac{1}{3}\Theta^2)$ is the 3-curvature scalar. $K = -1, 0$ or 1 depending on whether the Universe is *open*, *flat* or *closed* and $a = a(t)$ is the cosmological scale factor. μ is the energy density of the total cosmic fluid. Moreover, the curl of the spatial gradient of a scalar field is given by

$$\varepsilon^{abc} \tilde{\nabla}_b \tilde{\nabla}_c \phi = 2\omega^a \dot{\phi}. \quad (16)$$

Using the $(-+++)$ spacetime signature, the Riemann tensor is given by

$$R_{bcd}^a = \Gamma_{bd,c}^a - \Gamma_{bc,d}^a + \Gamma_{bd}^e \Gamma_{ce}^a - \Gamma_{bc}^f \Gamma_{df}^a \quad (17)$$

together with the Christoffel symbols, Ricci tensor and Ricci scalar respectively given as

$$\Gamma_{bd}^a = \frac{1}{2} g^{ae} (g_{be,d} + g_{ed,b} - g_{bd,e}), \quad R_{ab} = g^{cd} R_{cabd}, \quad R = R^a_a. \quad (18)$$

The Weyl conformal curvature tensor C_{abcd} is defined from the trace-free part of the Riemann tensor as

$$C^{ab}_{cd} = R^{ab}_{cd} - 2g^{[a} R^{b]}_{[c} R^d] + \frac{R}{3} g^{[a} R^{b]}_{[c} g^d]_{d]}, \quad (19)$$

and is usually split into its ‘‘gravito-electric’’ and ‘‘gravito-magnetic’’ parts, E_{ab} and H_{ab} , respectively given by

$$E_{ab} \equiv C_{agbh} u^g u^h, \quad H_{ab} = \frac{1}{2} \eta_{ae} g^h C_{ghbd} u^e u^d. \quad (20)$$

Now the *total* thermodynamic quantities of the matter-curvature fluid composition can be defined as

$$\mu \equiv \frac{\mu_m}{f'} + \mu_R, \quad p \equiv \frac{p_m}{f'} + p_R, \quad q_a \equiv \frac{q_a^m}{f'} + q_a^R, \quad \pi_{ab} \equiv \frac{\pi_{ab}^m}{f'} + \pi_{ab}^R. \quad (21)$$

Anti-Newtonian universes are special classes of irrotational dust spacetimes characterized by

$$p_m = 0, \quad A_a = 0, \quad q_a^m = 0, \omega_a = 0, \quad \pi_{ab}^m = 0, \quad E_{ab} = 0. \quad (22)$$

Putting all these together, the generalized propagation relations of the Einstein field equations for generic $f(R)$ gravitation describing anti-Newtonian universes can be given as [12, 15]

$$\dot{\mu}_m = -\mu_m \Theta, \quad (23)$$

$$\dot{\mu}_R = -(\mu_R + p_R)\Theta + \frac{\mu_m f''}{f'^2} \dot{R} - \tilde{\nabla}^a q_a^R, \quad (24)$$

$$\dot{\Theta} = -\frac{1}{3}\Theta^2 - \frac{1}{2}(\mu + 3p), \quad (25)$$

$$\dot{q}_a^R = -\frac{4}{3}\Theta q_a^R + \frac{\mu_m f''}{f'^2} \tilde{\nabla}_a R - \tilde{\nabla}_a p_R - \tilde{\nabla}^b \pi_{ab}^R, \quad (26)$$

$$\dot{\sigma}_{ab} = -\frac{2}{3}\Theta \sigma_{ab} + \frac{1}{2}\pi_{ab}^R, \quad (27)$$

$$\dot{\pi}_{ab}^R = 2\varepsilon_{cd(a} \tilde{\nabla}^c H_{b)}^d - (\mu + p_R) \sigma_{ab} - \tilde{\nabla}_{\langle a} q_{b)}^R - \frac{1}{3}\Theta \pi_{ab}^R, \quad (28)$$

$$\dot{H}_{ab} = -\Theta H_{ab} + \frac{1}{2}\varepsilon_{cd\langle a} \tilde{\nabla}^c \pi_{b)}^d. \quad (29)$$

The role of Eqs. (23)-(29) is to make sure that the covariant variables on some initial hypersurface S_0 are uniquely determined. The corresponding constraint relations

$$(C^1)_a := \tilde{\nabla}^b \sigma_{ab} - \frac{2}{3}\tilde{\nabla}_a \Theta + q_a^R = 0, \quad (30)$$

$$(C^2)_{ab} := \varepsilon_{cd\langle a} \tilde{\nabla}^c \sigma_{b)}^d - H_{ab} = 0, \quad (31)$$

$$(C^3)_a := \tilde{\nabla}^b H_{ab} + \frac{1}{2}\varepsilon_{abc} \tilde{\nabla}^b q_c^R = 0. \quad (32)$$

$$(C^4)_a := \tilde{\nabla}^b \pi_{ab}^R - \frac{2}{3}\tilde{\nabla}_a \mu + \frac{2}{3}\Theta q_a^R = 0, \quad (33)$$

put restrictions on the initial data to be specified and must remain satisfied on any hypersurface S_t for all comoving time t .

In GR, the evolution equations (23)-(29) decouple from the gradient, divergence and curl terms, forming ordinary differential evolution equations. As a result, anti-Newtonian cosmologies in GR are said to be *silent* models because the flowlines emerging from the initial hypersurface S_0 evolve separately from each other [11, 12, 14]. Interestingly, however, the non-vanishing of the curvature anisotropic pressure and total heat flux in Eqs. (24), (26), (28) and (29) shows that *anti-Newtonian solutions in $f(R)$ gravity are not silent* models. The curl terms in Eqs. (29) and (32) vanish if we apply the differential identities (13) and (14), the definitions (6) and (7) and the constraint Eq. (30), together with the irrotational, *i.e.*, $\omega^a = 0$ spacetime assumption. A consequence of these results is that the evolution and constraint equations for the gravito-magnetic Weyl tensor simplify as

$$\dot{H}_{ab} = -\Theta H_{ab}, \quad (34)$$

$$(C^{3*})_a := \tilde{\nabla}^b H_{ab} = 0. \quad (35)$$

The vanishing of the divergence of H_{ab} in the last equation is a necessary condition for gravitational radiation.

No new constraint equations have emerged as a result of the anti-Newtonian assumption (with the vanishing of the gravito-electric Weyl tensor). But in GR, this is not the case because Eq. (28) becomes a new constraint equation since the left-hand side of this equation identically vanishes. Integrability conditions arise as a result.

3. Integrability conditions in $f(R)$ gravity

Even if no new constraint equations emerge from the anti-Newtonian assumption, Eq. (33) is a modified constraint relation. If we take the curl of both sides of this equation and obtain an identity, we say that the constraint equation is *spatially consistent*. In fact, using our previous argument that the curl of a gradient (and hence also of a divergence) of an irrotational flow vanishes, we have

$$\begin{aligned} 0 &= \frac{f''}{f'} \varepsilon^{acb} \tilde{\nabla}_c \tilde{\nabla}^d \pi_{bd}^R - \frac{2}{3} \varepsilon^{acb} \tilde{\nabla}_c \tilde{\nabla}_b \mu + \frac{2}{3} \Theta \varepsilon^{acb} \tilde{\nabla}_c q_b^R \\ &= \omega^a \left\{ \frac{f''}{f'} \left[\frac{2}{3} \tilde{R} \dot{R} - \frac{4}{3} \dot{R} \Theta \right] - \frac{4}{3} \dot{\mu} - \left(\frac{\dot{R} f''}{f'^2} + \frac{2\Theta}{3f'} \right) \left[2 \left(f''' \dot{R} - \frac{1}{3} \Theta \right) \dot{R} + 2f'' \ddot{R} \right] \right\} = 0. \end{aligned} \quad (36)$$

Spatial consistency alone does not guarantee that the constraint equations are preserved under time evolution. A constraint equation is said to be *temporally consistent* if taking the time derivative of both sides of the equation results in an identity. Let us now study the evolution of Eq. (33):

$$\begin{aligned} 0 &= \left(\tilde{\nabla}^b \pi_{ab}^R \right)' - \frac{2}{3} \left(\tilde{\nabla}_a \mu \right)' + \frac{2}{3} \dot{\Theta} q_a^R + \frac{2}{3} \Theta \dot{q}_a^R \\ &= \tilde{\nabla}^b \dot{\pi}_{ab}^R - \frac{1}{3} \Theta \tilde{\nabla}^b \pi_{ab}^R - \frac{2}{3} \left(\tilde{\nabla}_a \dot{\mu} - \frac{1}{3} \Theta \tilde{\nabla}_a \mu \right) + \frac{2}{3} \dot{\Theta} q_a^R + \frac{2}{3} \Theta \dot{q}_a^R, \end{aligned} \quad (37)$$

where, in the second step, we have used the commutation relations

$$\left(\tilde{\nabla}_a \phi \right)' = \tilde{\nabla}_a \dot{\phi} - \frac{1}{3} \Theta \tilde{\nabla}_a \phi + \dot{\phi} A_a, \quad (38)$$

$$\left(\tilde{\nabla}_a S_{b\dots} \right)' = \tilde{\nabla}_a \dot{S}_{b\dots} - \frac{1}{3} \Theta \tilde{\nabla}_a S_{b\dots} \quad (39)$$

of temporal and spatial derivatives for scalar and tensor fields, respectively. The last expression in Eq. (37) can be further expanded using Eqs. (29), (35), (30) and (33) for the divergences of H_{cd} , σ_{ab} and π_{ab}^R and making use of the linearized vectorial identity

$$\tilde{\nabla}^b \tilde{\nabla}_{\langle a} V_{b \rangle} = \frac{1}{2} \tilde{\nabla}^2 V_a + \frac{1}{6} \tilde{\nabla}_a (\tilde{\nabla}^b V_b) + \frac{1}{6} \tilde{R} V_a. \quad (40)$$

The resulting equation reads

$$\Theta \dot{q}_a^R - \frac{1}{4} \tilde{\nabla}_a (\tilde{\nabla}^b q_b^R) + \frac{1}{4} \tilde{\nabla}^2 q_a^R + \frac{1}{2} (\mu + \Theta^2) q_a^R + \Theta \tilde{\nabla}_a p_R + \frac{2}{3} \Theta \tilde{\nabla}_a \mu = 0, \quad (41)$$

and acts as the necessary condition for the consistent evolution of the constraints in anti-Newtonian cosmologies with $f(R)$ gravity as the underlying theory of gravitation. Interestingly, this equation reduces to the simple result

$$\Theta \tilde{\nabla}_a \mu_m = 0 \quad (42)$$

when we take the limiting case of GR, *i.e.*, when $f(R) = R$. This is because all the curvature contributions to the thermodynamical quantities automatically vanish in GR. Eq. (42) implies that *there are no expanding linearized anti-Newtonian solutions* in GR, for if $\Theta \neq 0$ (expanding spacetime), $\tilde{\nabla}_a \mu_m = 0$ implies an FLRW background or $\mu_m = 0$ (vacuum spacetime), which contradicts the dust-universe assumption of anti-Newtonian cosmologies.

Let us now make one more simplification to Eq. (41); to do that, we use Eq. (26) to substitute for \dot{q}_a^R as well as Eq. (33). The resulting equation, after some algebraic manipulations, becomes

$$\tilde{\nabla}^2 q_a^R - \tilde{\nabla}_a (\tilde{\nabla}^b q_b^R) + \tilde{R} q_a^R + \frac{4f''}{f'^2} \mu_m \Theta \tilde{\nabla}_a R = 0. \quad (43)$$

Two interesting conclusions can be drawn from this consistency relation:

- For flat universes ($K = 0 = \tilde{R}$) universes, upon using Eq. (15) the condition (43) reduces to

$$\frac{f''}{f'^2} \mu_m \Theta \tilde{\nabla}_a R = 0 . \quad (44)$$

For a dust universe in $f(R)$, $\mu_m \neq 0$ and $f'' \neq 0$. As a result *flat, anti-Newtonian spacetimes in $f(R)$ gravity are either static ($\Theta = 0$) or spaces of constant Ricci curvature ($\tilde{\nabla}_a R = 0$).* No vacuum ($R = 0$) solution is allowed (this contradicts the dust-universe assumption).

- For closed and open universes ($K = \pm 1$), using the commutation (15) in (43) yields

$$\left[\frac{f'' \mu_m \Theta}{f'} \mp \frac{2}{a^2} \left(\dot{R} f''' - \frac{1}{3} \Theta f'' \right) \right] \tilde{\nabla}_a R \mp \frac{2f''}{a^2} \tilde{\nabla}_a \dot{R} = 0 . \quad (45)$$

This means that, provided $f'' \neq 0$, *any dust solution of Eq. (45) describes an anti-Newtonian universe.* Note that the case $f'' = 0$ is equivalent to GR (with or without a cosmological constant) and is, therefore, not an anti-Newtonian solution.

4. Conclusion

A linearized covariant consistency analysis of dust universes with vanishing gravito-electric part of the Weyl tensor in $f(R)$ gravity has been explored. The integrability conditions of such models for generic $f(R)$ gravitation actions have been presented. The solutions for such integrability conditions describe the existence of anti-Newtonian cosmological universes, which are known not to exist as solutions of General Relativity.

Acknowledgments

The author acknowledges the Faculty Research Committee of the Faculty of Agriculture, Science and Technology of North-West University for financial support to attend the *61st Annual Conference of the South African Institute of Physics.*

References

- [1] Starobinsky A A 1980 *Physics Letters B* **91** 99–102
- [2] Carroll S, Duvvuri V, Turner M and Trodden M 2004 *Physical Review D* **70**
- [3] De Felice A and Tsujikawa S 2010 *Living Rev. Rel* **13** 1002–4928
- [4] Capozziello S and De Laurentis M 2011 *Physics Reports*
- [5] Nojiri S and Odintsov S D 2011 *Physics Reports* **505** 59–144
- [6] Abebe A, Goswami R and Dunsby P *Physical Review D* 1–7 ISSN 1550-7998
- [7] Abebe A 2014 *Classical and Quantum Gravity* **31** 115011
- [8] Abebe A and Elmardi M 2015 *International Journal of Geometric Methods in Modern Physics* **12** 1550118
- [9] Abebe A, Momeni D and Myrzakulov R 2016 *General Relativity and Gravitation* **48** 1–17
- [10] Maartens R and Triginer J 1997 *Physical Review D* **56** 4640
- [11] van Elst H, Uggla C, Lesame W M, Ellis G F and Maartens R 1997 *Classical and Quantum Gravity* **14** 1151
- [12] Maartens R 1998 *Physical Review D* **58** 124006
- [13] van Elst H and Ellis G F 1998 *Classical and Quantum Gravity* **15** 3545
- [14] Wylleman L 2006 *Classical and Quantum Gravity* **23** 2727
- [15] Carloni S, Dunsby P and Troisi A 2008 *Physical Review D* **77** 024024

Calibration of statistical methods used to constrain pulsar geometries via multiband light curve modelling

M C Bezuidenhout¹, C Venter¹, A S Seyffert¹ and A K Harding²

¹ Centre for Space Research, North-West University, 11 Hoffman Street, Potchefstroom, 2531, South Africa

² Astrophysics Science Division, NASA Goddard Space Flight Center, 8800 Greenbelt Rd, Greenbelt, MD 20771, United States

E-mail: 23545496@nwu.ac.za

Abstract. Since its launch in 2008, the *Fermi* Large Area Telescope (LAT) has detected over 200 γ -ray pulsars above 100 MeV. This population of pulsars is characterised by a rich diversity of light curve morphologies. Researchers have been using both the radio and γ -ray light curves to constrain the inclination and observer angles for each of these pulsars. At first, this was done using a by-eye technique and later via statistical approaches. We have also developed two novel statistical approaches that place the radio and γ -ray data on equal footing despite their disparate relative flux errors. We chose eleven pulsars from the Second *Fermi* Pulsar Catalog, both old and young, and applied these new techniques as well as the by-eye technique to constrain their geometric parameters using standard pulsar models. We present first results on our comparison of the best-fit parameters yielded by each of the aforementioned techniques. This will assist us in determining the utility of our new statistical approaches, and gauge the overlap of the best-fit parameters (plus errors) from each of the different methods. Such a statistical fitting approach will provide the means for further pulsar magnetospheric model development using light curve data.

1. Introduction

Prior to the launch of the Large Area Telescope (LAT) aboard the *Fermi* mission in June 2008, fewer than ten pulsars had been detected in the γ -ray domain [1]. Since then the LAT has discovered¹ more than 200 new γ -ray pulsars, enabling multi-wavelength pulsar studies for the first time [2].

The simultaneous use of radio and γ -ray observations has, however, typically been complicated by the comparatively low γ -ray flux through the telescope, resulting in very disparate relative uncertainties on the respective data sets. This disparity renders traditional goodness-of-fit techniques ineffective, since the radio light curves (LCs) dominate every fit, leading some researchers to prefer so-called “by-eye methods” when attempting to jointly fit modelled LCs to observations in both domains (e.g., [3]). Other studies (e.g., [4,5]) have sought to address this problem by artificially inflating the errors on the radio data such that the radio

¹ <https://confluence.slac.stanford.edu/display/GLAMCOG/Public+List+of+LAT-Detected+Gamma-Ray+Pulsars>

and γ -ray observations carry roughly equal weight in determining the optimal fit to modelled data. These fitting methods have had limited success.

More recently, a method has been proposed for rendering the respective data sets comparable for the purposes of finding best-fit model parameters in both domains simultaneously [6]. The aim of this paper is to apply this method to eleven pulsars selected from the Second *Fermi* Pulsar Catalog [2] and compare the results to those found by other studies [4,5] as well as to what is found using by-eye fitting. Furthermore, a variation on the aforementioned fitting method is introduced here and applied to the same pulsars. Conclusions are drawn as to the utility of each of these fitting techniques.

2. Geometric pulsar models

This study uses an idealised picture of pulsars with vacuum retarded dipole magnetic field structures [7]. Here γ -ray emission is considered to originate from so-called acceleration gaps in the pulsar's magnetosphere where the density of the corotating plasma falls below the Goldreich-Julian charge density [8]. We use two geometric models that postulate the location of these acceleration gaps: the outer gap (OG, [9]) and two-pole caustic (TPC, [10]) models. For radio emission an empirical hollow-cone model [11] is assumed.

LCs are plots of a pulsar's intensity per unit solid angle. The tilt angle α and the observer angle ζ measured with respect to the pulsar's rotational axis are taken as free parameters, so that model LCs can be constructed using any viable (α, ζ) -pair; the fitting methods presented in this paper therefore aim to determine which combination of α and ζ best reproduce observed data in both radio and γ rays concurrently.

3. Fitting methods

The first approach used in this paper towards finding best-fit (α, ζ) combinations is simple by-eye fitting of modelled LCs onto observed data. For any given pulsar, modelled LCs for each parameter pair, and in both the γ -ray and radio domains, are successively constructed and superimposed on the pulsar's observed data. We make a qualitative decision as to whether or not the experimental data are satisfactorily reproduced by the LC realisation for a given (α, ζ) pair, and an inclusion contour is drawn for each pulsar. This is done twice per pulsar, once using each of the OG and TPC geometric models discussed in the previous section.

The best-fit parameters are taken to be in the centre of the contour, with the errors on this estimate comprising a square encompassing all of the contour. Note that in cases where two or more disconnected closed contours appear on the map, we study the LCs for the centre of each contour and choose the best fit among these.

This fitting method is, of course, rather subjective: applying the same method twice for the same pulsar using the same geometric model will produce two slightly differing answers. This is especially true when there are multiple (α, ζ) pairs plausibly replicating the observed data for a single pulsar. As such, this fitting method is not seen as an attempt at constraining pulsar geometries in and of itself, but rather as being a sanity check, or a basis for (qualitatively) judging the accuracy of more rigorous methods: if a statistical approach produces an answer far out of line with what by-eye fitting delivers, the former result is cast into doubt.

Considering the limitations of the by-eye fitting method, a more rigorous alternative is desired. This study uses a modified version of Pearson's χ^2 test statistic, defined by the equation

$$\chi^2 = \sum_{i=1}^{n_{\text{bins}}} \left(\frac{E_i - O_i}{U_i} \right)^2, \quad (1)$$

where E_i , O_i , and U_i refer to the modelled (expected) intensity, observed intensity, and uncertainty on the observed intensity in the i th bin of n_{bins} bins of the LC respectively.

Ideally the minimum value of χ^2 in either model would be approximately equal to the number of degrees of freedom, $N_{\text{dof}} = n_{\text{bins}} - n_{\text{parameters}} - 1$, specifying a good match between modelled and observed data. However, this rarely occurs for the models used in this study, with the minimum test statistic often being far larger than N_{dof} . This indicates that the models are still somewhat rough approximations of the real phenomena. In this light, in order for constraints to be drawn, X must be normalised such that its minimum value is N_{dof} . This approach works well for single-wavelength data sets, but breaks down when trying to find minima in two wavelengths simultaneously. In our case, the relative errors on the observed γ -ray data are much larger than they are on the radio data, so that the values of χ^2 are much smaller for the γ -ray domain than for the radio domain. Simply adding the test statistics of the γ rays and radio waves together therefore creates a combined χ^2 map which is very much radio-dominated.

Other studies [4,5] circumvented the problem of vastly differing χ^2 values on the γ -ray and radio datasets by artificially inflating the errors on the radio observations to match those of the γ -ray observations, both for MSPs [4] and for young and middle-aged pulsars with longer periods of rotation [5]. While this method invariably performs better than simple addition of the maps, different pulsars often require different degrees of radio error inflation, and in some cases these errors even need to be decreased to match the wide range of errors for different pulsar γ -ray LCs.

This study aims to consistently combine the respective χ^2 maps such that each dataset is considered on equal footing. Two methods are used to achieve this, the first being a scaling approach [6] and the second being a simple multiplication approach. In the χ^2 scaling method the dynamic ranges of the χ^2 maps for each waveband are equalised before adding them, forcing each domain to carry equal weight in the determination of the best concurrent fit. For a more detailed description of this approach, see Ref. [6]. At this stage no confidence contours have been implemented, as this is under investigation using a Monte-Carlo approach. The parameter constraints found using this method therefore do not yet have associated errors. The second approach followed by this study is simply multiplying the two χ^2 maps together for each (α, ζ) combination without any scaling. This method does not have confidence intervals yet either.

4. Results

We applied the three fitting methods described in the previous section to eleven pulsars selected from the Second *Fermi* Catalog [2]. Table 1 compares the parameter constraints obtained for the three fitting methods used in this study to what other studies [3,4] found for the same pulsars using the TPC model, while Table 2 makes the same comparison for the OG model. All angles are given in degrees.

Table 1. Best (α, ζ) fits — TPC model

Pulsar	Independent studies [4,5]	By-eye fitting	χ^2 scaling	χ^2 multiplying
J0030+0451	$(74 \pm 2, 55^{+3}_{-1})$	$(75 \pm 8, 59 \pm 6)$	(56,73)	(45,62)
J0205+6449	$(75 \pm 2, 86 \pm 2)$	$(75 \pm 6, 86 \pm 4)$	(77,84)	(78,84)
J0437-4715	$(35 \pm 1, 64 \pm 1)$	$(30 \pm 1, 65 \pm 1)$	(29,65)	(26,62)
J1124-5916	$(84 \pm 2, 89 \pm 2)$	$(79 \pm 9, 84 \pm 6)$	(87,75)	(78,84)
J1231-1411	$(26^{+3}_{-4}, 69 \pm 1)$	$(47 \pm 8, 75 \pm 3)$	(33,71)	(45,72)
J1410-6132	$(19^{+2}_{-4}, 6 \pm 2)$	$(20 \pm 3, 8 \pm 3)$	(10,20)	(10,20)
J1420-6048	$(52 \pm 2, 53 \pm 2)$	$(61 \pm 4, 53 \pm 5)$	(60,45)	(60,45)
J1513-5908	$(50 \pm 2, 54 \pm 2)$	$(50 \pm 8, 40 \pm 8)$	(55,46)	(55,46)
J1614-2230	$(80^{+8}_{-20}, 80^{+6}_{-4})$	$(85 \pm 5, 65 \pm 5)$	(36,74)	(48,83)
J1833-1034	$(55 \pm 2, 75 \pm 2)$	$(54 \pm 8, 78 \pm 4)$	(53,76)	(50,79)
J2229+6114	$(42 \pm 2, 55 \pm 2)$	$(53 \pm 5, 36 \pm 6)$	(46,60)	(45,59)

Table 2. Best (α, ζ) fits — OG model

Pulsar	Independent studies ^[4,5]	By-eye fitting	χ^2 scaling	χ^2 multiplying
J0030+0451	$(88_{-2}^{+1}, 68 \pm 1)$	$(85 \pm 2, 67 \pm 2)$	(85,68)	(56,73)
J0205+6449	$(73 \pm 2, 90 \pm 2)$	$(75 \pm 5, 86 \pm 4)$	(80,87)	(80,87)
J0437-4715	$(76 \pm 1, 46 \pm 1)$	$(62 \pm 3, 35 \pm 5)$	(27,63)	(27,63)
J1124-5916	$(83 \pm 2, 88 \pm 2)$	$(70 \pm 7, 86 \pm 4)$	(71,88)	(70,88)
J1231-1411	$(88 \pm 1, 67 \pm 1)$	$(82 \pm 4, 59 \pm 5)$	(33,71)	(45,72)
J1410-6132	$(87 \pm 2, 76 \pm 2)$	$(4 \pm 3, 7 \pm 3)$	(47,58)	(56,84)
J1420-6048	$(55 \pm 2, 57 \pm 2)$	$(57 \pm 7, 58 \pm 8)$	(62,45)	(58,56)
J1513-5908	$(60 \pm 2, 59 \pm 2)$	$(57 \pm 4, 44 \pm 5)$	(56,48)	(56,48)
J1614-2230	$(64_{-20}^{+8}, 88_{-5}^{+2})$	$(55 \pm 7, 86 \pm 4)$	(37,75)	(37,75)
J1833-1034	$(65 \pm 2, 87 \pm 2)$	$(58 \pm 9, 79 \pm 4)$	(87,65)	(87,57)
J2229+6114	$(75 \pm 2, 55 \pm 2)$	$(66 \pm 2, 41 \pm 2)$	(64,51)	(63,50)

As an example, we plot the best-fit LCs as predicted by each fitting method superimposed on the observed *Fermi* data for PSR J0030+0451 in Figure 1.

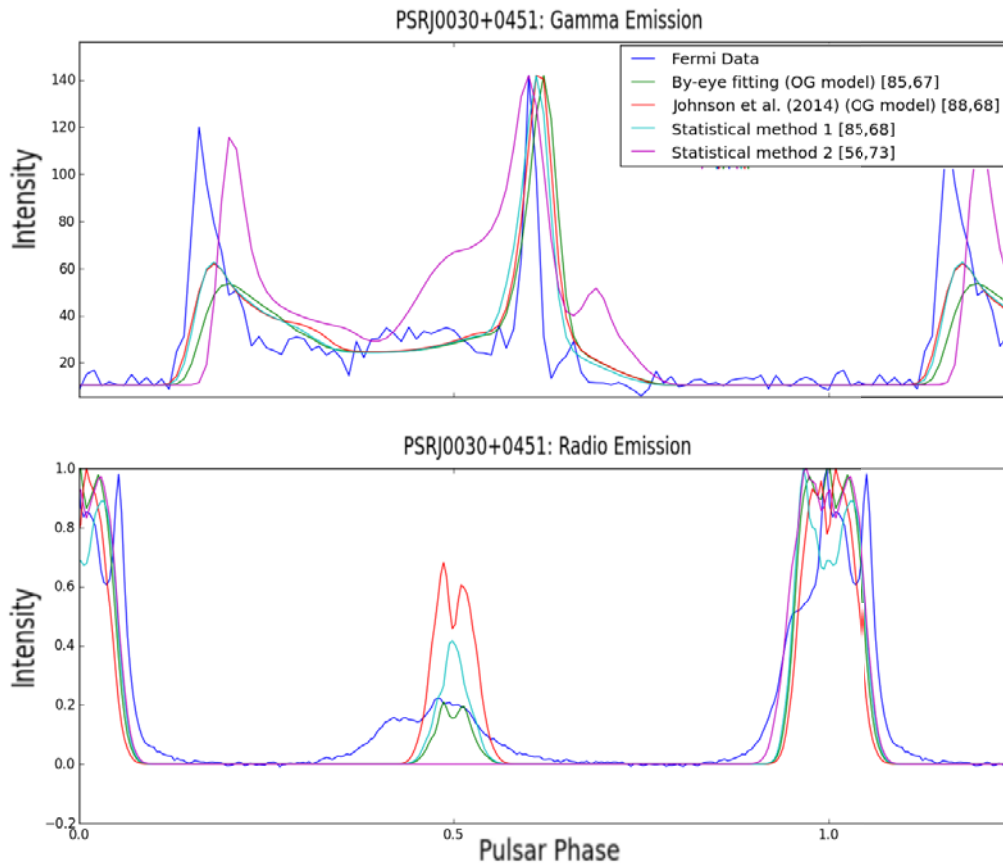


Figure 1. Best-fit LCs found using each fitting method for PSR J0030+0451. The observed *Fermi* LC is in dark blue, while the predicted LC found by Ref. [4] is in red, and the LCs as predicted using the by-eye fitting, χ^2 scaling (statistical method 1), and χ^2 multiplying (statistical method 2) techniques are in green, cyan, and pink, respectively. The constraint pair found using each method is indicated in square brackets in the legend.

One important effect discernible from Tables 1 and 2 is that different fitting methods often

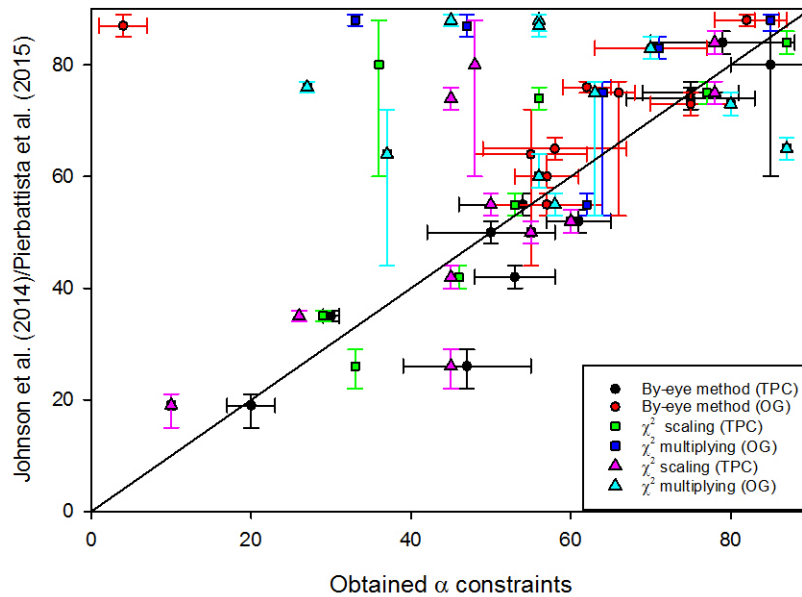


Figure 2. The constraints on α found independently via statistical techniques vs. those found in this study. For reference, a straight 45° line is shown corresponding to a perfect match of the constraint we found on α with that found independently.

produce inverted constraint pairs, i.e., if α and ζ were switched, the methods would be in much better accordance. This is expected, since LC predictions are very similar for similar values of the so-called impact angle, $|\beta| = |\zeta - \alpha|$, given the model assumption of symmetric emission from both magnetic poles.

In Figure 2 we plot the α constraints found in this work using by-eye fitting, χ^2 scaling, and χ^2 multiplying against those found by independent studies.

5. Conclusions

We relay the results of applying the by-eye fitting method to the eleven pulsars in question in the third column of Tables 1 and 2. Considering Table 1 first, we find that the constraints found in this study using the TPC model overlap with those found in the independent studies in five cases. In no case would inverting the (α, ζ) -pair have led to concurrence between the two methods. Looking at Table 2, using the OG model, four pulsars have an overlap of intervals. Again, inverting pairs would not have produced another match. However, the by-eye confidence intervals are fairly arbitrary, and a more lenient fitter might find significantly more overlap between these two fitting methods. The best-fit LCs found using this method also indicate that, for the most part, the by-eye fitting method is able to replicate observed LCs well, at least superficially. Taking into account the difficulties with subjectivity inherent to the by-eye fitting method, in the light of these comparisons this method seems to be a suitable basis for qualitatively judging the applicability of other, more rigorous fitting methods.

This study's second approach to LC fitting was the χ^2 scaling method, developed by Ref. [6], the results of which can be found in the fourth column of Tables 1 and 2. In the TPC model, only two constraints found by this method fall inside the confidence intervals of those found by the independent studies, although PSR J0030+0451 also qualifies if its α and ζ are switched. There are four overlaps between the by-eye fitting and χ^2 scaling constraints, and a further

three if pair inversion is taken into account. Considering the OG model constraints, there is just one overlap (or two with pair inversion) between the χ^2 scaling constraints and those of the independent studies; there are three overlaps with the by-eye fitting method. These comparisons are complicated by the fact that confidence intervals have not yet been implemented for the statistical methods. Even conservative errors would lead to quite a few more overlaps.

It seems clear that the χ^2 scaling fitting method is somewhat hit-and-miss. Some observations appear to be very well fit by this method, such as PSR J1420–6048 using the OG model, while others are quite poorly fit, such as PSR J2229+6114 in the TPC model.

For a blind statistical technique, the χ^2 scaling method seems to do an adequate fitting job, although it is still some way off being a rigorous alternative to by-eye fitting. It is not clear that the constraints found using this method match those found using the by-eye method significantly more frequently than those found using the artificial error inflation technique.

The results of the third fitting approach, novel to this paper, are presented in the fifth column in each of the tables of the previous section. Regarding the constraints found using the TPC model, as in Table 1, there are no pulsars for which the constraints found using the χ^2 multiplication technique is included in the confidence intervals of those found by the independent studies. There are five pulsars for which this method's constraints fall inside the errors of those obtained using by-eye fitting, and another if pair inversion is taken into account. Table 2 shows that in the OG model case there is one pulsar for which the χ^2 multiplying method constraints overlap with the independent studies' constraints (two with pair inversion), and one overlap with the by-eye fitting method's constraints.

Again, the constraints found using this method do not agree with the by-eye fitting method significantly better than those found using error inflation do. This fact is reflected in the best-fit LCs plotted using this method: the degree to which observed LCs are reproduced by this method is quite variable, sometimes qualitatively better and at other times worse than what is produced by error inflation. In many cases this fitting method produces best fits identical or at least close to that of the χ^2 scaling method. In this regard it is unclear which of these two statistical approaches produce better fits.

The most obvious avenue for the improvement best-fit LCs would be to employ more intricate geometrical models, although developing and implementing such models would be a long and arduous process. In the meantime, future study might focus on finding confidence contours in the χ^2 fitting techniques, or on developing new methods of combining the γ -ray and radio datasets altogether, perhaps with a different test statistic.

References

- [1] Thompson D J 2001 *AIP Conf. Series* **558** 103
- [2] Abdo A A et al. 2013 *Astrophys. J.* **208** 17
- [3] Seyffert A S, Venter C, Harding A K and Johnson T J 2011 *Proc. of The 56th Ann. SAIP Conf.* 531
- [4] Johnson T J et al. 2014 *Astrophys. J. Suppl. S.* **213** 1
- [5] Pierbattista M et al. 2015 *Astron. Astrophys.* **575** 1
- [6] Seyffert A S, Venter C, Harding A K, Allison J and Schutte WD 2016 *Proc. of The 61st Ann. SAIP Conf.* 350
- [7] Deutsch A J 1955 *Ann. d'Astrophys.* **18** 1
- [8] Goldreich P and Julian W H 1969 *Astrophys. J.* **157** 869
- [9] Cheng K S, Ho C and Ruderman M 1986 *Astrophys. J.* **300** 500
- [10] Dyks J and Rudak B 2003 *Astrophys. J.* **598** 1201
- [11] Story S A, Gonthier P L and Harding A K 2007 *Astrophys. J.* **671** 713

Isotropic energy and luminosity correlations with spectral peak energy for five long Gamma-Ray Bursts

Feraol F. Dirirsa^{1,*} and Soebur Razzaque¹ on behalf of the *Fermi*-LAT Collaboration

¹University of Johannesburg, Kingsway Campus, Auckland Park 2006, Johannesburg

E-mail: *fdirirsa@uj.ac.za

Abstract. We present a time-integrated spectral analysis of five long gamma-ray bursts (GRBs) with identified redshift and which triggered the *Fermi* satellite in 2015. Two bursts (GRB 150403A & GRB 150314A) are detected both by the *Fermi* Large Area Telescope (LAT) and Gamma-Ray Burst Monitor (GBM) while the other three sources (GRB 150727A, GRB 151027A & GRB 150301B) are detected only by the GBM. We describe the observable correlations of these bursts such as the intrinsic peak energy with the isotropic-radiated energy and luminosity in the source frame, to show their consistency with the global Amati/Yonetoku relation. We investigate the possibility that Band function, Power law (PL), Smoothly broken power law (SBPL) and Comptonized components may be present separately by fitting the prompt emission spectra in the keV-MeV energy range. At last, the intrinsic peak energy which is highly correlated to both the radiated isotropic energy (the Amati relation) and the peak luminosity (the Yonetoku relation) in the source frame is summarized.

1. Introduction

Gamma-ray bursts mostly emit radiation in the gamma rays which last for up to hundreds of seconds. Gamma radiation is tailed by the X-ray, optical and radio emission which last for a few days. Those bursts are the most luminous electromagnetic explosions in the Universe [1], with the highest isotropic equivalent radiated energy E_{iso} , up to 10^{54} erg [2]. For the long GRBs (duration of bursts > 2 s), observational correlations exist among the spectral peak energy E_{peak}^i of the prompt emission and its isotropic peak luminosity L_{iso} (so-called Yonetoku relation [3]) and isotropic radiated energy which was discovered by Amati et al. [4]. The key properties of GRBs prompt emission obtained from the time-integrated spectra of bursts with known redshift are still poorly understood. After measuring the redshift of GRB, one can correct for cosmological effects and infer its rest frame photon peak energy, E_{peak}^i of the νF_ν prompt spectrum. An open issue is that if these relations have a physical origin or they are due to instrumental selection effects (or biases) which were argued by many authors [5, 6, 7]. The investigation of GRB phenomenology with spectral energy correlations have relevant implications, both for the theoretical understanding of the prompt emission and for using GRBs as standard candles in cosmological studies.

In this work, we discussed the E_{iso} and L_{iso} correlations with E_{peak}^i for five long GRBs with identified redshift z detected by *Fermi* in 2015 (*Fermi*-2015). Our analysis is based on GRB time-integrated spectra. Since, the spectra of GRBs are in a wide energy range, it can usually be described by the Band function [8], which is a smoothly broken power law with a break break

energy. Below the breaking energy, the Band function reduces to a cut-off power law, while above the break energy, it is a simple power law. For the photon emission that covers large energy range, their spectra can be modelled by using a power law with exponential high-energy cut-off (Comptonized) or SBPL photon model. Using the parameters obtained from the best fit photon model, we have computed the E_{peak}^i , E_{iso} and L_{iso} to study the Amati relation ($E_{peak}^i - E_{iso}$) and Yonetoku relation ($E_{peak}^i - E_{iso}$). For the two *Fermi* LAT/GBM detected GRBs (GRB 150403A & GRB 150314A), we considered unbinned likelihood analysis using the pass 8 data [9] to determine the probability of photons coming from each event. Throughout the paper, we assume a flat-isotropic universe with $H_0 = 69.6 \text{ km s}^{-1} \text{ Mpc}^{-1}$, $\Omega_\Lambda = 0.714$ and $\Omega_m = 0.286$. Calculations of luminosity distances are done using the analytical approximation [10].

2. Sample and method of data analysis

We considered the GRBs detected by the *Fermi* satellite in 2015 with known redshift. In our sample, there are 5 long GRBs (observed duration > 2 s). Among these bursts, GRB 150403A & GRB 150314A are simultaneously detected by both LAT and GBM while the other three sources GRB 150727A, GRB151027A & GRB 150301B are triggered only by GBM as shown in Table 1. To analysis the LAT-detected GRBs with known redshift, we have selected the high energy data between 0.1 GeV and 30 GeV. The highest-energy (E_{max}) photon of the GRB 150314A is a ~ 0.62 GeV photon (with 97.8 % probability of being associated with GRB) and for the GRB 150403A, it is ~ 5.4 GeV (with 99.6 % probability) which are observed at ~ 81 s and ~ 632 s after the GBM trigger, respectively. The GBM light curve of both GRB 150314A and GRB 150403A shows a bright single pulse with a duration T_{90} [11] of about 10.7 s and 22.3 s with energy range computed between 50 and 300 keV, respectively. The GBM light curve of GRB 150301B consists of one main peak, the GRB 150727A light curve shows a FRED-like (fast-rise exponential-decay) pulse and the GRB 151027A light curve consists of three pulses with a duration T_{90} of about 13 s, 50 s, and 124 s, respectively as shown in Table 1.

Table 1. Data on *Fermi* LAT/GBM detected GRBs with known redshift.

GRB	z	T_{90} (s) ^f	Best on-ground location	# of HE photons ^l	Detectors
150314A	1.758 ^a	10.7	(RA, Dec)=125.40, 64.46 ^g	9	<i>Fermi</i> -LAT/GBM
150403A	2.06 ^b	22.3	(RA, Dec)=311.79, -62.76 ^h	6	<i>Fermi</i> -LAT/GBM
150301B	1.517 ^c	13	(RA, Dec)=89.157, -57.977 ⁱ	-	<i>Fermi</i> -GBM
150727A	0.313 ^d	50	(RA, Dec)=203.99, -18.355 ^j	-	<i>Fermi</i> -GBM
151027A	0.81 ^e	124	(RA, Dec)=272.491, 61.381 ^k	-	<i>Fermi</i> -GBM

^ade Ugarte Postigo A., et al., 2015, (GCN 17583)

^gAxelsson M., et al., 2015, (GCN 17576)

^bPugliese V., et al., 2015, (GCN 17672)

^hLongo F., et al., 2015, (GCN 17667)

^cLien Y., et al., 2015, (GCN 17515)

ⁱde Ugarte Postigo A., et al., 2015, (GCN 17523)

^dWatson M., et al., 2015, (GCN 18089)

^jCenko B., et al., 2015, (GCN 18076)

^ePerley A., et al., 2015, (GCN 18487)

^kMaselli A., et al., 2015, (GCN 18478)

^fThe time between accumulating 5% & 95% of the counts associated with the GRB

^lThe number of High Energy (HE) photons with probability $> 90\%$

2.1. Spectral analysis

For the time-integrated spectral analysis, data from the optimal sodium iodide (NaI) detectors were fitted together with bismuth germanate (BGO) detectors [12]. As in most of the previous spectral analysis of GRBs, we used SBPL, Power law function with an exponential high-energy cutoff [Comptonized (Comp)], Band function (Band) [8] and PL models. For the triggers

selection, the criterion adopted in Guiriec et al. [13] is implemented. To perform the spectral analysis, the recently released software RMFIT (*v3.3pr7*) [14] tool kits has been used. The NaI data from ~ 10 keV to ~ 915 keV and the BGO data from ~ 250 keV to ~ 10 MeV are used by cutting out the overflowing low and high-energy channels as well as the K-edge from ~ 30 to ~ 40 keV. The background in each of the GBM detectors was estimated by fitting polynomial functions to the light curves in various energy ranges before and after the source active time period. For GBM data, the background was fitted to the CSPEC data which cover a much longer time range, making the estimation of the background more reliable for long GRBs [15]. For GRB 151027A, GRB 150727A, GRB 150403A, GRB 150314A and GRB 150301B, the triggers (n0+n1+n3+b0), (n0+n3+n4+b0), (n3+n4+b0), (n0+n1+n2+n9+na+b0) and (n0+n3+n4+n6+n7+n8+b0+b1) are used for the time-integral analysis for the time section T_{90} [11] and T_{peak} (the time at high peak count rate), respectively.

3. Data analysis

The spectral parameters in Tables 2 and 3 have been obtained through the analysis of the time-integrated spectrum extracted from the GBM data by performing the software package RMFIT for the duration of T_{90} and T_{peak} in the ~ 10 keV to ~ 10 MeV energy range, respectively. The best spectral parameter values were estimated by optimizing the Castor C-statistic (hereafter C-stat), which is a likelihood technique that converges to χ^2 for a specific data set when there are enough counts. We have selected the best model by choosing the fit with the lowest C-stat value after each of the spectrum fitted with a Band, PL, SBPL and Comp models. Tables 2 and 3 show the results of these fits. Table 2 lists 5 long GRBs with their time integrated spectral parameters (columns 3, 4, and 7) and the time integrated isotropic radiated energy, computed in the rest frame in the 1 keV - 10 MeV energy range (L_{iso} , Column 5) and derived intrinsic peak-energy (E_{peak}^i , Column 6). Table 3 contains, the spectral analysis of five long GRBs for T_{peak} with the obtained parameters (columns 3, 4, and 5) and derived intrinsic peak luminosity, computed in the rest frame in the 1 keV - 10 MeV energy range (L_{iso} , column 6). Figures 1 and 2 show the Band spectrum fit of GBM data of GRB 150403A & GRB 150314A,

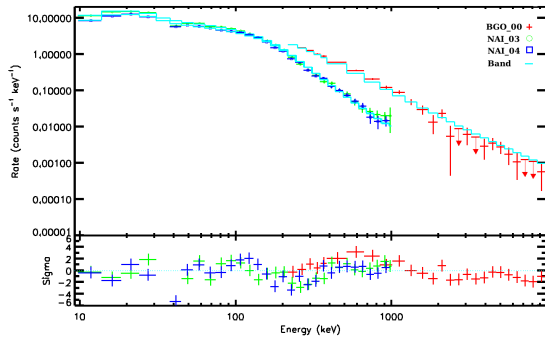


Figure 1. The time-integrated spectrum of GRB 150403A fitted by a Band function.

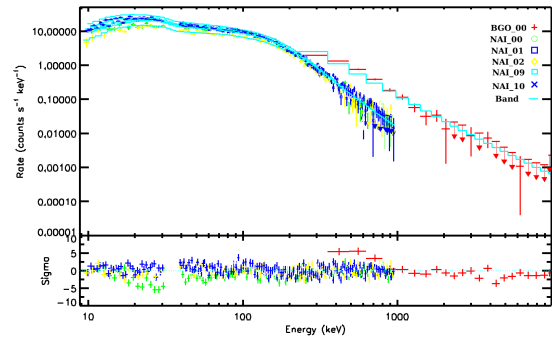


Figure 2. The time-integrated spectrum of GRB 150314A fitted by a Band function.

respectively. These bursts are detected by both the LAT and GBM. As shown in Tables 2 and 3, the GRB 150403A and GRB 150314A show a high band model component and their observed peak energies are the largest of the sample. In tables 2 & 3, the associated errors reported on E_{iso} , L_{iso} and E_{peak}^i was computed by properly weighing for data uncertainties [16] except for GRB 150314A, we assume 10% error in these measurements due to some statistical errors on the parameters.

Table 2. Results of the spectral fits for the duration of T_{90} and derived E_{iso} in the GRB rest frame.

GRB	T_{90} [sec.]	α /Index1	β /Index2	$E_{iso}/10^{52}$ [erg]	E_{peak}^i [keV]	E_{peak} [keV]	Model	C-stat/dof
151027A	-2.048 - 133.120	-1.47 ± 0.039	-	2.99 ± 0.365	592.6 ± 112.9	327.4 ± 62.4	Comp	866.55/430
		-1.46 ± 0.06	-1.98 ± 0.12	-	-	-	SBPL	863.56/429
		-1.66 ± 0.02	-	-	-	-	PL	908.54/431
150727A	0.003 - 50.177	-0.38 ± 0.20	-2.18 ± 0.21	0.32 ± 0.14	224.3 ± 37.7	170.8 ± 27.2	Band	1060.0/424
		-0.59 ± 0.12	-	-	-	220.8 ± 19.5	Comp	1066.6/425
		-0.58 ± 0.2	-2.19 ± 0.19	-	-	-	SBPL	1060.3/424
		-1.48 ± 0.02	-	-	-	-	PL	1191.3/426
150403A	-0.512 - 23.04	-0.77 ± 0.02	-2.04 ± 0.04	93.52 ± 4.46	1172.6 ± 43.1	383.2 ± 14.1	Band	438.65/315
		-0.88 ± 0.01	-	-	-	531.3 ± 13.4	Comp	550.79/316
		-0.87 ± 0.02	-1.99 ± 0.03	-	-	-	SBPL	434.55/315
		-1.37 ± 0.004	-	-	-	-	PL	4113.5/317
150314A	-2.912 - 11.424	-0.58 ± 0.01	-2.35 ± 0.04	87.4 ± 8.74	870.7 ± 87.1	315.7 ± 5.2	Band	1354.2/660
		-0.65 ± 0.008	-	-	-	367.6 ± 4.2	Comp	1467.6/661
		-0.73 ± 0.009	-2.25 ± 0.03	-	-	-	SBPL	1359.3/660
		-1.34 ± 0.003	-	-	-	-	PL	15663/662
150301B	-2.56 - 13.824	-1.13 ± 0.09	-2.21 ± 0.25	3.64 ± 0.97	498.85 ± 98.16	198.2 ± 39.0	Band	963.3/857
		-1.19 ± 0.06	-	-	-	244.3 ± 30.1	Comp	965.44/858
		-1.28 ± 0.06	-2.35 ± 0.29	-	-	-	SBPL	963.45/857
		-1.60 ± 0.02	-	-	-	-	PL	1043.3/859

Table 3. Results of the spectral fits for the duration of T_{peak} and L_{iso} in the GRB rest frame.

GRB	T_{peak} [sec.]	α	β	E_{peak} [keV]	L_{iso} [erg/s]	Model	C-stat/dof
151027A	0.002 - 1.792	-0.71 ± 0.096	-2.28 ± 0.19	170.0 ± 19.9	0.36 ± 0.096	Band	439.14429
		-0.83 ± 0.06	-	208.7 ± 14.7	-	Comp	448.7/430
		-0.96 ± 0.07	-2.46 ± 0.23	-	-	SBPL	439.06/429
		-1.52 ± 0.02	-	-	-	PL	664.73/431
150727A	4.096 - 6.144	-0.59 ± 0.31	-3.13 ± 3.58	273.3 ± 89.4	-	Band	402.16/426
		-0.58 ± 0.28	-	273.9 ± 65.2	0.0101 ± 0.0053	Comp	402.24/427
		-0.89 ± 0.21	-4.35 ± 5.42	-	-	SBPL	402.46/426
		-1.42 ± 0.056	-	-	-	PL	420.79/428
150403A	10.752 - 12.80	-0.66 ± 0.03	-2.14 ± 0.06	480.0 ± 26.4	20.55 ± 1.55	Band	338.08/294
		-0.79 ± 0.02	-	649.6 ± 24.6	-	Comp	424.79/295
		-0.77 ± 0.032	-2.08 ± 0.05	-	-	SBPL	339.86/294
		-1.38 ± 0.008	-	-	-	PL	1688.0/296
150314A	1.184 - 3.232	-0.296 ± 0.018	-2.4 ± 0.048	293.6 ± 5.6	22.2 ± 2.22	Band	1041.0/656
		-0.42 ± 0.01	-	352.3 ± 4.48	-	Comp	1159.7/657
		-0.49 ± 0.02	-2.32 ± 0.04	-	-	SBPL	1061.6/657
		-1.31 ± 0.004	-	-	-	PL	11083/658
150301B	1.536 - 3.584	-1.07 ± 0.12	-2.39 ± 0.53	211.7 ± 50.4	0.55 ± 0.203	Band	933.9/856
		-1.13 ± 0.009	-	249.4 ± 40.5	-	Comp	934.2/857
		-1.21 ± 0.098	-2.34 ± 0.37	-	-	SBPL	934.53/856
		-1.59 ± 0.03	-	-	-	PL	987.46/858

4. Correlation

4.1. Amati relation

In order to determine the strength and significance of $E_{peak}^i - E_{iso}$ correlation, we utilized a linear regression analysis using the Pearson's and Spearman's correlation. For this purpose we undertake a comparison between the Amati relation of the *Fermi*-2015 data analysis and the sample populations of 68 GRBs from Amati et al, 2008 (A2008) [17]. These data are shown in Figure 3. The computation of E_{iso} was determined in the rest-frame from 1 keV to 10 MeV energy range and the $E_{peak}^i = E_{peak}(1+z)$. The black dashed line is the best-fit power law that obtained by weighting each point by its error on both E_{peak}^i and E_{iso} for 5 *Fermi*-2015 GRBs.

The power law fit gives $E_{peak}^i[\text{keV}] = (338.6 \pm 78.0) (E_{iso}/10^{52}\text{erg})^{0.26 \pm 0.053}$ with the reduced $\chi_{red}^2 = 3.14$. The Spearman's rank correlation coefficient proved a high correlation value of $\rho_{sp} = 0.9$ with the chance probability $P_{sp} = 0.037$. Also, the Pearson's coefficient for this correlation is $\rho_p = 0.70$ with an extremely low value of the chance probability 4.34×10^{-12} . The combination of *Fermi*-2015 and A2008 data are also fitted together by power law. The best fit power law shown by magenta solid line results $E_{peak}^i[\text{keV}] = (93.1 \pm 6.23) (E_{iso}/10^{52}\text{erg})^{0.56 \pm 0.02}$ with the reduced $\chi_{red}^2 = 6.69$.

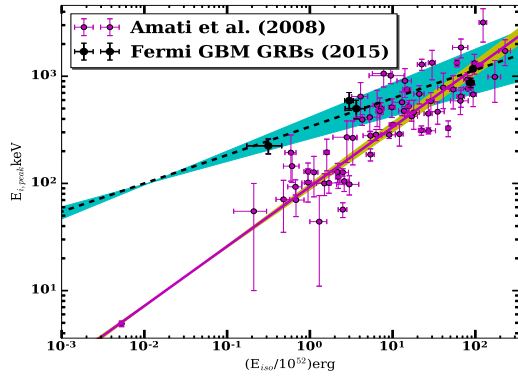


Figure 3. The $E_{peak}^i - E_{iso}$ relation. The black circles are our present results of five long *Fermi* GRBs. The data from A2008 [17] are shown by the magenta circles. Both results are plotted as E_{peak}^i at the rest frame of the GRBs and the E_{iso} is calculated using the T_{90} fluence.

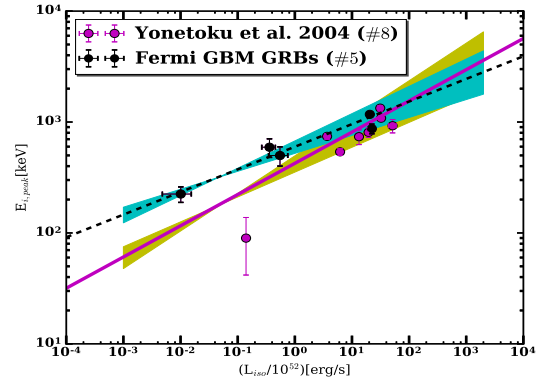


Figure 4. The $E_{peak}^i - L_{iso}$ relation. The black circles are our present results with five *Fermi* GRBs. The results of Yonetoku et al., 2004 (Y2004) [3] is also shown as the magenta circles. Both results are plotted as E_{peak}^i at the rest frame of the GRBs and the peak luminosity derived from the time T_{peak} flux.

4.2. Yonetoku relation

Another correlation among observable quantities is between E_{peak}^i and L_{iso} (Yonetoku correlation). In this correlation analysis, we computed the L_{iso} emitted at the 1-second peak of the light curve from 1 keV to 10 MeV band. In Figure 4, we have shown the plots of the peak luminosity as a function of intrinsic peak energy for both the data of *Fermi*-2015 GRBs and its combination with 8 GRBs in Yonetoku et al. 2004 (Y2004) [3]. In Y2004 data, the redshift of GRB 980326 and GRB 980329 are not precisely determined and only the upper limit of intrinsic peak energy has been reported for GRB 980703. Therefore, we can exclude these three bursts from our data analysis to avoid inaccurate result. When we adopt the power-law model to the $E_{peak}^i - L_{iso}$ relation, the best-fit function (magenta solid line) of 5 *Fermi*-2015 data is $E_{peak}^i[\text{keV}] = (598.4 \pm 76.9) (L_{iso}/10^{52}\text{ergs}^{-1})^{0.20 \pm 0.04}$ with the reduced $\chi_{red}^2 = 3.66$. The Spearman's rank correlation coefficient is 0.8 with chance probability 0.104. The best power-law fit (magenta solid line) for the *Fermi*-2015 data (black circles) together with Y2004 data (magenta circles) is $E_{peak}^i[\text{keV}] = (424.2 \pm 70.96) (L_{iso}/10^{52}\text{ergs}^{-1})^{0.28 \pm 0.06}$ with the reduced $\chi_{red}^2 = 8.3$. The Pearson's correlation coefficient is $\rho_p = 0.74$ with the chance probability $P_p = 0.0036$. The Spearman's rank correlation coefficient also gives $\rho_{sp} = 0.89$ with the chance probability $P_{sp} = 4.565 \times 10^{-5}$.

5. Discussion

We studied the time-integrated spectra of five *Fermi* GRBs by fitting time-integrated spectra over the duration of T_{90} and T_{peak} in the ~ 10 keV - ~ 10 MeV energy range, respectively. The spectral parameters obtained from this analysis are reported in Tables 2 and 3, where the Band function considered as adequately fitting GRB spectra. For the *Fermi*-2015 GRB observables, we found a high correlation of peak energy with isotropic radiated energy and the peak luminosity in the GRB source frame. For the *Fermi*-2015 data, there is a higher and tighter correlation between E_{peak}^i and E_{iso} . Their best-fit power law index is 0.26 ± 0.053 with the reduced $\chi_{red}^2 = 3.14$. This looks considerably tighter and more reliable than the relations suggested by the previous works [18, 19]. The best-fit power law index for the *Fermi*-2015 and A2008 joint data is 0.56 ± 0.02 with the reduced $\chi_{red}^2 = 6.69$, which has a similar result with the previous Amati [17] correlation (i.e. the index of the power-law ~ 0.57 and $\chi_{red}^2 = 7.2$). The Spearman's rank correlation coefficient also shows a high correlation between the observables E_{peak}^i and E_{iso} ($\rho_{sp} = 0.9$). As shown in Fig. 4, the *Fermi*-2015 and Y2004 data are poorly fitted by the power law with reduced $\chi_{red}^2 = 8.3$. This indicates that the fit has not fully captured the relationship between the observable. However, the Pearson's correlation coefficient ($\rho_p = 0.74$) and the Spearman's rank correlation coefficient ($\rho_{sp} = 0.89$) are indicating a positive strong correlation. For the $L_{iso} - E_{peak}^i$ correlation analysis, our results are limited by the small number of GRBs in the sample (i.e., 13 GRBs). To get a more reliable conclusion, the number of GRBs with well-determined redshifts and spectra needs to be significantly expanded.

Acknowledgments

The *Fermi*-LAT Collaboration acknowledges support for LAT development, operation and data analysis from NASA and DOE (United States), CEA/Irfund IN2P3/CNRS (France), ASI and INFN (Italy), MEXT, KEK, and JAXA (Japan), and the K.A. Wallenberg Foundation, the Swedish Research Council and the National Space Board (Sweden). Science analysis support in the operations phase from INAF (Italy) and CNES (France) is also gratefully acknowledged. The work presented in this paper was supported in part by an MWGR 2015 grant from the National Research Foundation with Grant No. 93273.

References

- [1] Piran T 1999 *Phys.Rept.* **314** 575
- [2] Amati L 2006 *MNRAS* **372** 233
- [3] Yonetoku D *et al.* 2004 *ApJ* **609** 935
- [4] Amati L *et al.* 2002 *A&A* **390** 81
- [5] Heussaff V, Atteia J L and Zolnierowski Y 2013 *A&A* **557** A100
- [6] Ghirlanda G *et al.* 2012 *MNRAS* **422** 2553
- [7] Nava L, Ghirlanda G and Ghisellini G 2009 *arXiv preprint arXiv:0902.1522*
- [8] Band D *et al.* 1993 *ApJ* **413** 281
- [9] Atwood W *et al.* 2013 *ApJ* **774** 76
- [10] Wright E L 2006 *ASP* **118** 1711
- [11] Ackermann M *et al.* 2010 *ApJ* **716** 2
- [12] Meegan C *et al.* 2009 *ApJ* **702** 791
- [13] Guiriec S *et al.* 2010 *ApJ* **727** L33
- [14] <http://fermi.gsfc.nasa.gov/ssc/data/analysis/rmfit/>
- [15] Guiriec S *et al.* 2015 *ApJ* **807** 148
- [16] Bevington J 1969 *McGrawHill* 36
- [17] Amati L *et al.* 2008 *ApJ* **390** 81
- [18] Dirirsa F F and Razzaque S 2015 *PoS(SSC2015)066*
- [19] Amati L 2005 *MNRAS* **372** 233

Integrability conditions for nonrotating solutions in $f(R)$ gravity

Maye Elmardi¹ and Amare Abebe²

¹ Astrophysics, Cosmology and Gravity Center, Department of Mathematics and Applied Mathematics, University of Cape Town, Rondebosch 7701, Cape Town, South Africa

² Department of Physics, North-West University, Mmabatho 2735, Mafikeng, South Africa

E-mail: maye.elmardi@acgc.uct.ac.za

Abstract. Several classes of cosmological models with irrotational fluid flows and where the underlying theory of gravitation is $f(R)$ -gravity are investigated. The integrability conditions describing a consistent evolution of the linearized field equations of shear-free dust universes are presented. We also derive consistency relations of models with more severe constraints, such as non-expanding spacetimes as well as those spacetimes with vanishing gravito-magnetic or gravito-electric components of the Weyl tensor.

1. Introduction

Among the most common generalizations to the General Theory of Relativity (GR) to explain current deficits in the energy budget of the universe, and hence to explain cosmic acceleration, are higher-order theories of gravity. Models that include functions of the Ricci curvature R in the Hilbert-Einstein action

$$\mathcal{A} = \frac{1}{2} \int d^4x \sqrt{-g} [f(R) + 2\mathcal{L}_m] , \quad (1)$$

where \mathcal{L}_m is the matter field Lagrangian, and result in fourth-order field equations are referred to as $f(R)$ -gravity theories [1, 2, 3, 4]. The generalized field equations arising from such action, obtained using the standard variational principle with respect to the metric g_{ab} , can be represented by

$$f'G_{ab} = T_{ab}^m + \frac{1}{2}(f - Rf')g_{ab} + \nabla_b \nabla_a f' - g_{ab} \nabla_c \nabla^c f' , \quad (2)$$

where G_{ab} and T_{ab}^m are the standard notations for the Einstein tensor and the energy-momentum tensor of standard matter. The extra terms on the right-hand side account for what is called the curvature-fluid energy-momentum tensor and identically vanish in GR. Here f is a shorthand for the $f(R)$ function and primes indicate derivatives with respect to R .

We assume the universe is filled with standard matter and curvature fluid sources and its total energy density, isotropic pressure, anisotropic pressure and heat flux terms are given, respectively, by [5, 6]

$$\mu \equiv \frac{\mu_m}{f'} + \mu_R , \quad p \equiv \frac{p_m}{f'} + p_R , \quad \pi_{ab} \equiv \frac{\pi_{ab}^m}{f'} + \pi_{ab}^R , \quad q_a \equiv \frac{q_a^m}{f'} + q_a^R , \quad (3)$$

where μ_m and μ_R stand, respectively, for the energy density of standard matter and curvature fluids, etc.

To linear-order perturbations around a Friedmann-Lemaître-Robertson-Walker (FLRW) background, the curvature fluid component are defined as

$$\mu_R = \frac{1}{f'} \left[\frac{1}{2}(Rf' - f) - \Theta f'' \dot{R} + f'' \tilde{\nabla}^2 R \right], \quad (4)$$

$$p_R = \frac{1}{f'} \left[\frac{1}{2}(f - Rf') + f'' \ddot{R} + f''' \dot{R}^2 + \frac{2}{3} \left(\Theta f'' \dot{R} - f'' \tilde{\nabla}^2 R \right) \right], \quad (5)$$

$$q_a^R = -\frac{1}{f'} \left[f''' \dot{R} \tilde{\nabla}_a R + f'' \tilde{\nabla}_a \dot{R} - \frac{1}{3} f'' \Theta \tilde{\nabla}_a R \right], \quad (6)$$

$$\pi_{ab}^R = \frac{f''}{f'} \left[\tilde{\nabla}_{\langle a} \tilde{\nabla}_{b \rangle} R - \sigma_{ab} \dot{R} \right], \quad (7)$$

where the overdot $\dot{}$ and $\tilde{\nabla}$ indicate time and covariant spatial derivatives. In the 1 + 3-covariant decomposition formalism, fundamental observers with 4-velocity vectors u^a slice spacetime into constant time and space hypersurfaces. We use u^a to define covariant time derivatives and the projection tensor $h_{ab} = u_a u_b + g_{ab}$ is used to define the fully orthogonally projected covariant derivative of tensors. We denote the orthogonally projected symmetric trace-free part of vectors and rank-2 tensors as

$$V^{(a)} = h_b^a V^b, \quad S^{(ab)} = \left[h^{(a} h^{b)}_d - \frac{1}{3} h^{ab} h_{cd} \right] S^{cd}, \quad (8)$$

and the volume element for the rest spaces orthogonal to u^a is given by [7]

$$\varepsilon_{abc} = u^d \eta_{dabc} = -\sqrt{|g|} \delta^0_{[a} \delta^1_b \delta^2_c \delta^3_{d]} u^d \Rightarrow \varepsilon_{abc} = \varepsilon_{[abc]}, \quad \varepsilon_{abc} u^c = 0, \quad (9)$$

where η_{abcd} is the 4-dimensional volume element with the properties $\eta_{abcd} = \eta_{[abcd]} = 2\varepsilon_{ab[c} u_{d]} - 2u_{[a} \varepsilon_{b]cd}$. In this work, brackets (ab) and square brackets $[ab]$ denote symmetrization and anti-symmetrization over the indices a and b . Covariant spatial divergence and curl of tensors are given as

$$\text{div} V = \tilde{\nabla}^a V_a, \quad (\text{div} S)_a = \tilde{\nabla}^b S_{ab}, \quad (10)$$

$$\text{curl} V_a = \varepsilon_{abc} \tilde{\nabla}^b V^c, \quad \text{curl} S_{ab} = \varepsilon_{cd(a} \tilde{\nabla}^c S_{b)}^d. \quad (11)$$

The full covariant derivative of u^a can be split into its irreducible parts as

$$\nabla_a u_b = -A_a u_b + \frac{1}{3} h_{ab} \Theta + \sigma_{ab} + \varepsilon_{abc} \omega^c, \quad (12)$$

where $A_a \equiv \dot{u}_a$, $\Theta \equiv \tilde{\nabla}_a u^a$, $\sigma_{ab} \equiv \tilde{\nabla}_{\langle a} u_{b \rangle}$ and $\omega^a \equiv \varepsilon^{abc} \tilde{\nabla}_b u_c$ are the acceleration, expansion, shear and vorticity (rotation) of the fluid flow. The *Weyl conformal curvature tensor* C_{abcd} is defined from the Riemann tensor R_{abcd}^a as

$$C^{ab}{}_{cd} = R^{ab}{}_{cd} - 2g^{[a} R^{b]}_{[c} R^d] + \frac{R}{3} g^{[a} R^b]_{[c} g^d]} \quad (13)$$

and can be split into its “gravito-electric” and “gravito-magnetic” parts, respectively, as

$$E_{ab} \equiv C_{agbh} u^g u^h, \quad H_{ab} = \frac{1}{2} \eta_{ae} g^{gh} C_{ghbd} u^e u^d. \quad (14)$$

E_{ab} and H_{ab} represent the free gravitational field, enabling gravitational action at a distance (tidal forces and gravitational waves), and influence the motion of matter and radiation through the geodesic deviation for timelike and null vector fields, respectively.

The linearised evolution equations in $f(R)$ gravity are given by [5, 8]:

$$\dot{\mu}_m = -(\mu_m + p_m)\Theta - \tilde{\nabla}^a q_a^m, \quad (15)$$

$$\dot{\mu}_R = -(\mu_R + p_R)\Theta + \frac{\mu_m f''}{f'^2} \dot{R} - \tilde{\nabla}^a q_a^R, \quad (16)$$

$$\dot{\Theta} = -\frac{1}{3}\Theta^2 - \frac{1}{2}(\mu + 3p) + \tilde{\nabla}_a A^a, \quad (17)$$

$$\dot{q}_a^m = -\frac{4}{3}\Theta q_a^m - \mu_m A_a, \quad (18)$$

$$\dot{q}_a^R = -\frac{4}{3}\Theta q_a^R + \frac{\mu_m f''}{f'^2} \tilde{\nabla}_a R - \tilde{\nabla}_a p_R - \tilde{\nabla}^b \pi_{ab}^R, \quad (19)$$

$$\dot{\omega}_a = -\frac{2}{3}\Theta \omega_a - \frac{1}{2}\varepsilon_{abc} \tilde{\nabla}^b A^c, \quad (20)$$

$$\dot{\sigma}_{ab} = -\frac{2}{3}\Theta \sigma_{ab} - E_{ab} + \frac{1}{2}\pi_{ab} + \tilde{\nabla}_{\langle a} A_{b\rangle}, \quad (21)$$

$$\dot{E}_{ab} + \frac{1}{2}\dot{\pi}_{ab} = \varepsilon_{cd\langle a} \tilde{\nabla}^c H_{b\rangle}^d - \Theta E_{ab} - \frac{1}{2}(\mu + p)\sigma_{ab} - \frac{1}{2}\tilde{\nabla}_{\langle a} q_{b\rangle} - \frac{1}{6}\Theta \pi_{ab}, \quad (22)$$

$$\dot{H}_{ab} = -\Theta H_{ab} - \varepsilon_{cd\langle a} \tilde{\nabla}^c E_{b\rangle}^d + \frac{1}{2}\varepsilon_{cd\langle a} \tilde{\nabla}^c \pi_{b\rangle}^d, \quad (23)$$

and propagate consistent initial data on some initial hypersurface S_0 uniquely along the (generally future-directed) reference timelike congruence. The initial conditions to be specified for the above evolution equations are restricted by the constraint equations

$$(C^1)_a := \tilde{\nabla}^b \sigma_{ab} - \frac{2}{3}\tilde{\nabla}_a \Theta + \varepsilon_{abc} \tilde{\nabla}^b \omega^c + q_a = 0, \quad (24)$$

$$(C^2)_{ab} := \varepsilon_{cd\langle a} \tilde{\nabla}^c \sigma_{b\rangle}^d + \tilde{\nabla}_{\langle a} \omega_{b\rangle} - H_{ab} = 0, \quad (25)$$

$$(C^3)_a := \tilde{\nabla}^b H_{ab} + (\mu + p)\omega_a + \frac{1}{2}\varepsilon_{abc} \tilde{\nabla}^b q^c = 0, \quad (26)$$

$$(C^4)_a := \tilde{\nabla}^b E_{ab} + \frac{1}{2}\tilde{\nabla}^b \pi_{ab} - \frac{1}{3}\tilde{\nabla}_a \mu + \frac{1}{3}\Theta q_a = 0, \quad (27)$$

$$(C^5) := \tilde{\nabla}^a \omega_a = 0, \quad (28)$$

$$(C^6)_a := \tilde{\nabla}_a p_m + (\mu_m + p_m)A_a = 0 \quad (29)$$

which must remain satisfied on any hypersurface Σ_t for consistency of the field equations.

2. Consistency analysis of irrotational spacetimes

Irrotational fluid flows have vanishing vorticity ($\omega_a = 0$). Imposing this vanishing vorticity condition on the evolution equations (15)-(23) results in Eq. (20) turning into a new constraint

$$(C^{6*})_a := \varepsilon_{abc} \tilde{\nabla}^b A^c = 0 \implies A_a = \tilde{\nabla}_a \psi \text{ for some scalar } \psi. \quad (30)$$

To check for temporal consistency, we propagate this constraint to obtain

$$\left(\varepsilon_{abc} \tilde{\nabla}^b A^c \right) \dot{} = 0, \quad (31)$$

which is an identity. Let us now take the curl of this constraint to check for spatial consistency:

$$\text{curl}(\text{curl}(A_a)) = \tilde{\nabla}_a \left(\tilde{\nabla}^2 \psi \right) - \tilde{\nabla}^2 \left(\tilde{\nabla}_a \psi \right) + \frac{2}{3} \left(\mu - \frac{1}{3}\Theta^2 \right) \tilde{\nabla}_a \psi = 0, \quad (32)$$

which is also an identity because for any scalar and vector field ϕ and V_a

$$\tilde{\nabla}^2 \left(\tilde{\nabla}_a \psi \right) = \tilde{\nabla}_a \left(\tilde{\nabla}^2 \psi \right) + \frac{1}{3} \tilde{R} \tilde{\nabla}_a \psi, \quad (33)$$

$$\text{curl}(\text{curl}V_a) = \tilde{\nabla}_a \left(\tilde{\nabla}^b V_b \right) - \tilde{\nabla}^2 V_a + \frac{2}{3} \left(\mu - \frac{1}{3}\Theta^2 \right) V_a. \quad (34)$$

2.1. Shear-free dust spacetimes

Pure dust spacetimes are characterised by $w = 0 = p_m$, $q_a^m = 0 = A_a$, $\pi_{ab}^m = 0$, and shear-free models are fluid flow models with $\sigma_{ab} = 0$. For such models, Eq. (21) turns into a new constraint

$$(C^{5d})_{ab} := E_{ab} - \frac{1}{2}\pi_{ab}^R = 0. \quad (35)$$

the temporal and spatial consistencies of which have to be checked. Unlike for shear-free dust spacetimes in GR, the electric component of the Weyl tensor does not vanish because of the non-vanishing contribution of the anisotropic pressure π_{ab}^R . But Eq. (25) shows that H_{ab} does vanish, leading to a modified constraint from Eq. (23)

$$(C^{6d})_{ab} := \varepsilon_{cd\langle a} \tilde{\nabla}^c E_{b\rangle}^d - \frac{1}{2}\varepsilon_{cd\langle a} \tilde{\nabla}^c \pi_{b\rangle}^d = 0, \quad (36)$$

which is an identity by virtue of Eq. (35). Moreover, Eq. (26) shows that q_a^R is irrotational and can, therefore, be written as the gradient of a some scalar field ϕ :

$$q_a^R = \tilde{\nabla}_a \phi. \quad (37)$$

Since from (24), $q_a^R = \frac{2}{3}\tilde{\nabla}_a \Theta$ we have, for irrotational and shear-free dust spacetimes,

$$\phi = \frac{2}{3}\Theta + C, \quad (38)$$

for some spatially constant scalar C . Using Eq. (6) in (37), an interesting integrability condition is obtained:

$$\frac{2}{3}f'\tilde{\nabla}_a \Theta + \left(f'''\dot{R} - \frac{1}{3}\Theta f''\right)\tilde{\nabla}_a R + f''\tilde{\nabla}_a \dot{R} = 0. \quad (39)$$

In the GR limit, i.e., $f = R$, $f' = 1$, $f'' = f''' = 0$, the above consistency relation leads to $\tilde{\nabla}_a \Theta = 0$, which is trivially true for the class of models under consideration. To check for temporal consistency of Eq. (35), let us take the time derivative of both sides of this equation to obtain

$$\dot{\pi}_{ab}^R + \frac{2}{3}\Theta\pi_{ab}^R - \frac{1}{2}\tilde{\nabla}_{\langle a} q_{b\rangle}^R = 0, \quad (40)$$

which, using Eqs. (6) and (7), yields

$$\left[\frac{3}{2}\left(\frac{f'''}{f'} - \frac{f''^2}{f'^2}\right)\dot{R} - \frac{\Theta f''}{6f'}\right]\tilde{\nabla}_{\langle a} \tilde{\nabla}_{b\rangle} R + \frac{3f''}{2f'}\tilde{\nabla}_{\langle a} \tilde{\nabla}_{b\rangle} \dot{R} = 0. \quad (41)$$

This implies that *irrotational shear-free dust spacetimes governed by $f(R)$ gravitational physics evolve consistently if Eq. (41) is satisfied*. Note that the GR limit of this equation is an identity since the left-hand side vanishes identically. Now the curl of the above equation gives

$$\left[\frac{3}{2}\left(\frac{f'''}{f'} - \frac{f''^2}{f'^2}\right)\dot{R} - \frac{\Theta f''}{6f'}\right]\varepsilon_{cda}\tilde{\nabla}^c\tilde{\nabla}_{\langle b}\tilde{\nabla}^d\rangle R + \frac{3f''}{2f'}\varepsilon_{cda}\tilde{\nabla}^c\tilde{\nabla}_{\langle b}\tilde{\nabla}^d\rangle\dot{R} = 0, \quad (42)$$

which is an identity since, for any scalar field ψ ,

$$\varepsilon_{cda}\tilde{\nabla}^c\tilde{\nabla}_{\langle b}\tilde{\nabla}^d\rangle\psi = \varepsilon_{cda}\tilde{\nabla}^c\tilde{\nabla}_{\langle b}\tilde{\nabla}^d\rangle\psi = \varepsilon_{cda}\tilde{\nabla}^c\tilde{\nabla}_b\tilde{\nabla}^d\psi = 0. \quad (43)$$

Thus, *all irrotational shear-free dust spacetimes in $f(R)$ -gravity are consistent*.

If we make a further restriction and turn off E_{ab} , a locally conformally flat metric is obtained. For this class of models a new linearized constraint emerges from Eq. (22):

$$\tilde{\nabla}_{\langle a} q_{b\rangle}^R = 0 = \left(\dot{R}f''' - \frac{1}{3}\Theta f''\right)\tilde{\nabla}_{\langle a} \tilde{\nabla}_{b\rangle} R + f''\tilde{\nabla}_{\langle a} \tilde{\nabla}_{b\rangle} \dot{R}, \quad (44)$$

and from Eq. (21) we get

$$\pi_{ab}^R = 0 = f'' \tilde{\nabla}_{\langle a} \tilde{\nabla}_{b \rangle} R . \quad (45)$$

For GR, $f'' = 0$ and an identity results. For $f'' \neq 0$, the equation leads to the constraint on the Ricci curvature: $\tilde{\nabla}_{\langle a} \tilde{\nabla}_{b \rangle} R = 0$. Using this and the relation

$$\left(\tilde{\nabla}_{\langle a} \tilde{\nabla}_{b \rangle} \psi \right) \cdot = \tilde{\nabla}_{\langle a} \tilde{\nabla}_{b \rangle} \dot{\psi} - \frac{2}{3} \Theta \tilde{\nabla}_{\langle a} \tilde{\nabla}_{b \rangle} \psi + \dot{\psi} \tilde{\nabla}_{\langle a} A_{b \rangle} , \quad (46)$$

in Eq. (44) leads to an identity. As a result, *linearised $f(R)$ field equations in irrotational and shear-free dust spacetimes with vanishing Weyl tensor are consistent.*

2.2. Dust models with divergence-free H_{ab}

A necessary condition for gravitational radiation is the vanishing of the divergence of a non-zero H_{ab} . If we prescribe this condition on the field equations, Eq. (38) generalizes to

$$\tilde{\nabla}_a \phi = \frac{2}{3} \tilde{\nabla}_a \Theta - \tilde{\nabla}^b \sigma_{ab} . \quad (47)$$

A subclass of such models, called “purely radiative” dust spacetimes, is a divergence-free E_{ab} . Such models in $f(R)$ gravity are constrained further as

$$\tilde{\nabla}_a \mu_m + f' \tilde{\nabla}_a \mu_R + f' \Theta q_a^R - \frac{3f'}{2} \tilde{\nabla}^b \pi_{ab}^R = 0 \quad (48)$$

as a result of Eq. (27). Purely radiative irrotational dust spacetimes in GR should be spatially homogeneous (with $\tilde{\nabla}_a \mu_m = 0$).

Models with vanishing gravito-electric component of the Weyl tensor are referred to as *anti-Newtonian* models because they are considered to be the most extreme of non-Newtonian gravitational models [9, 10, 11]. Although there are no anti-Newtonian solutions of linearized perturbations of FLRW in GR, it has been shown that such restrictions are conditional (of integrability conditions) in $f(R)$ gravity [11].

2.3. Non-expanding spacetimes

Here we want to explore the (in)consistencies that emerge assuming theoretical cases of a nonexpanding spacetime, i.e., $\Theta = 0$. One gets the evolution equation for matter heat flux

$$\dot{q}_a^m = \frac{w}{1+w} \tilde{\nabla}_a \mu_m , \quad (49)$$

and a new constraint arises from the Raychaudhuri equation (17)

$$(C^{6s}) := \tilde{\nabla}_a A^a - \frac{1}{2f'} (1+3w) \mu_m - \frac{1}{2} (\mu_R + 3p_R) = 0 . \quad (50)$$

It follows that dust models ($A_a = 0 = q_a^m$) have active gravitational mass $\mu + 3p = 0$. Since (15) implies $\mu_d(t) = \text{const}$, we notice that $\mu_R + 3p_R = \text{const}$, as well. From the definitions (4) and (5) for μ_R and p_R and the *trace equation*

$$3f'' \ddot{R} + 3\dot{R}^2 f''' + 3\Theta \dot{R} f'' - 3f'' \tilde{\nabla}^2 R - R f' + 2f - \mu_m + 3p_m = 0 , \quad (51)$$

we conclude that (2.3) implies

$$f - 2f'' \tilde{\nabla}^2 R = \text{const} . \quad (52)$$

Thus any nonrotating and noexpanding dust spacetime in $f(R)$ cosmology should have a gravitational Lagrangian that satisfies Eq. (52).

3. Conclusion

We have looked at the consistency relations of linearized perturbations of FLRW universes with irrotational fluid flows arising as a result of imposing special restrictions to the field equations. We have shown that linearized shear-free dust models have a vanishing gravito-magnetic component of the Weyl tensor. The case of vanishing full Weyl tensor in linearised $f(R)$ field equations has also been explored, as well as those models with purely gravito-magnetic spacetimes. A subclass of gravito-magnetic models are those in which the divergence of H_{ab} is zero, a necessary condition for emission of gravitational waves. In GR, it is known that these models are homogeneous dust FLRW universes. We have shown that the homogeneity condition is not necessary in $f(R)$ gravity. Lastly, we have derived an integrability condition for non-rotating and no-expanding dust spacetimes in $f(R)$ gravity.

Acknowledgments

ME acknowledges the hospitality of the Department of Physics of North-West University (Mafikeng) where most of this work was conducted. AA acknowledges the Faculty Research Committee of the Faculty of Agriculture, Science and Technology of North-West University for financial support to attend the 61st Annual Conference of the South African Institute of Physics.

References

- [1] Buchdahl H A 1970 *Mon. Notices Royal Astron. Soc.* **150** 1
- [2] Clifton T, Ferreira P G, Padilla A and Skordis C 2012 *Phys. Rep.* **513** 1
- [3] De Felice A and Tsujikawa S 2010 *Living Rev. Relativ.* **13** 3
- [4] Capozziello S and De Laurentis M 2011 *Phys. Rep.* **509** 167
- [5] Carloni S, Dunsby P and Troisi A 2008 *Phys. Rev. D* **77** 024024
- [6] Abebe A and Elmardi M 2015 *Int. J. Geom. Methods Mod. Phys.* **12** 1550118
- [7] Ellis G and van Elst H 1999 *Cosmological models Theoretical and Observational Cosmology* (Dordrecht: Kluwer) p 1
- [8] Maartens R 1998 *Phys. Rev. D* **58** 124006
- [9] Maartens R, Lesame W M and Ellis G 1998 *Class. Quantum Grav.* **15** 1005
- [10] Wylleman L 2006 *Class. Quantum Grav.* **23** 2727
- [11] Abebe A 2014 *Class. Quantum Grav.* **31** 115011

New calibration sources for very long baseline interferometry in the 1.4-GHz band

M K Hailemariam^{1,2}, M F Bietenholz², A de Witt², R S Booth¹

¹ Department of Physics, University of Pretoria, South Africa

² Hartebeesthoek Radio Astronomy Observatory (HartRAO), South Africa

E-mail: mekUNET@gmail.com

Abstract. We present new 1.6 GHz observations of 43 VLBI calibrator sources. Our goal was mainly to establish the suitability of the sources as calibrators for 1.4-GHz band VLBI observations. We used seven telescopes; ASKAP, ATCA, Ceduna, Hobart, Mopra and Parkes from Australia, and HartRAO from South Africa. We classified the sources into 4 categories according to their suitability as calibrators in the 1.4-GHz band by determining their angular size, total flux density and the fraction of the flux density in the central component. Of the 43 sources, we found that 38 sources fell in to the good or very good calibrator classes. On the basis of selected sources from our sample we found that 91% of the good calibrators at 8.4 GHz are also safe to use as calibrator in the 1.4-GHz band.

1. Introduction

Relatively few Very Long Baseline Interferometry (VLBI) calibrator sources are known in the Southern celestial Hemisphere especially in the 1.4-GHz band (1-2 GHz). This is mainly due to the smaller number of observing facilities in the south compared to in the north. There are different surveys underway to increase the number of calibrator sources in the Southern Hemisphere, but most of these surveys are focused on observations at frequencies higher than 2 GHz, for example 8.4 GHz and 2.3 GHz (e.g. [8, 11, 12]), and there are virtually no VLBI calibrator observations at frequencies < 2 GHz. The small number of known calibrator sources and antennas in the Southern Hemisphere makes VLBI observation more difficult.

New VLBI-capable telescopes are coming to the south, in particular operating at < 2 GHz. ASKAP (< 2 GHz only) and MeerKAT (< 2 GHz and higher frequencies) are the two telescope arrays currently being built by Australia and South Africa respectively ([2, 9]). The African VLBI Network (AVN) is another big project in Africa, which aims to use redundant large telecommunication antennas across the continent for radio astronomy [7]. Despite the increasing number of antennas in the Southern Hemisphere, the number of calibrator sources in the 1.4-GHz band, for VLBI observations are very few. The high demand for calibrator sources at frequencies < 2 GHz, especially in the future, is the major motivation to look for calibrator sources in the 1.4-GHz band.

Most VLBI observations rely on observations of calibrator sources. An ideal calibrator source would look the same on all observing baselines which implies that it has to be unresolved (point-like). A calibrator source should also be bright, so that it can be observed with high signal to noise ratio on all baselines, and have an accurately known position. Almost all calibrator

sources used for VLBI observations are Active Galactic Nuclei (AGN) [1, 10]. AGN are the active nuclei within galaxies thought to be due to accretion onto super massive black holes. These extra-galactic radio sources, AGN, are very distant objects and therefore, generally, have no discernible proper motions on the sky.

Our research involved the reduction and analysis of VLBI observations of 43 sources in the Southern Hemisphere, at 1.6 GHz (see section 2). We determined the suitability of these sources as calibrators at 1.6 GHz, and compare the results of our observations to other 8.4 GHz observations to see how safe it is to use known 8.4 GHz calibrator sources for 1.4-GHz band observations.

2. Data Selection and Observations

We selected our sample of 43 sources from the Radio Fundamental Catalog (RFC¹) of compact radio sources [1, 6, 10, 12, 13, 14, 15]. In the catalog, we found 1131 sources with declinations $< -30^\circ$ and that had only been observed at 8.4 GHz. Of these, we found 77 sources with a flux density > 500 mJy that are listed as suitable calibrator sources at 8.4 GHz. Among the 77 sources, we selected the 25 sources for which 8.4 GHz images are available and the brightest 9 of the remainder. In order to cover all Right Ascensions for our 24-hour observations we also included 7 sources listed in the RFC as non-calibrator sources. We finally added two additional sources, to use as fringe finders.

We observed the sources at 1.6 GHz, with total band width of 8 MHz, using seven antennas: ASKAP (single 12-m dish), ATCA, Ceduna, Hobart, Mopra and Parkes from Australia, and HartRAO from South Africa. The observations were carried out between 22 and 23 February 2015. We used the Astronomical Image Processing System (AIPS²) software to calibrate the data.

3. Results and Discussion

After the final calibration we did the imaging (i.e. inverse Fourier transform of calibrated visibility data) using the same software (AIPS) that we used for the data reduction. The resulting inverse Fourier transform of the sampled visibility is the convolution of the true brightness distribution and the dirty beam [3, 5]. To recover the true intensity distribution we used a deconvolution algorithm called CLEAN [4]. CLEAN is an iterative process which represents an estimate of the true sky brightness as a series of delta functions, called CLEAN components.

In Table 1, we list the total flux density (S_{CL}) for each of the sources we imaged, which is the sum of the flux densities of the CLEAN components in the image. We also list the peak brightness (B_P) and off-source rms brightness (B_{Orms}), which we use as an estimate of the brightness noise level of the images, for each of the sources we imaged. The average radius of the beams from our observations is 2.6 milliarcsecond (mas). The values of the B_P range from 118 mJy beam⁻¹ to 2720 mJy beam⁻¹ and B_{Orms} ranges from 2.2 mJy beam⁻¹ to 20.4 mJy beam⁻¹. The mean value of the image dynamic range (B_P/B_{Orms}) was 60, which is sufficient to determine whether or not the sources will make good calibrators. Images of some of the sources are shown in Figure 1

3.1. Core fraction

Next we calculated the core fraction and the radial extents of our sources to evaluate if they are compact enough to be used as calibrators. The core fraction, C , of a source is the ratio of the flux density in the unresolved core to the total flux density [11]. We define the core flux density as the sum of the CLEANed flux density within an angular radius of 2.5 mas from the brightest

¹ Available on the Web at <http://astrogeo.org/rfc/>

² <http://www.aips.nrao.edu>

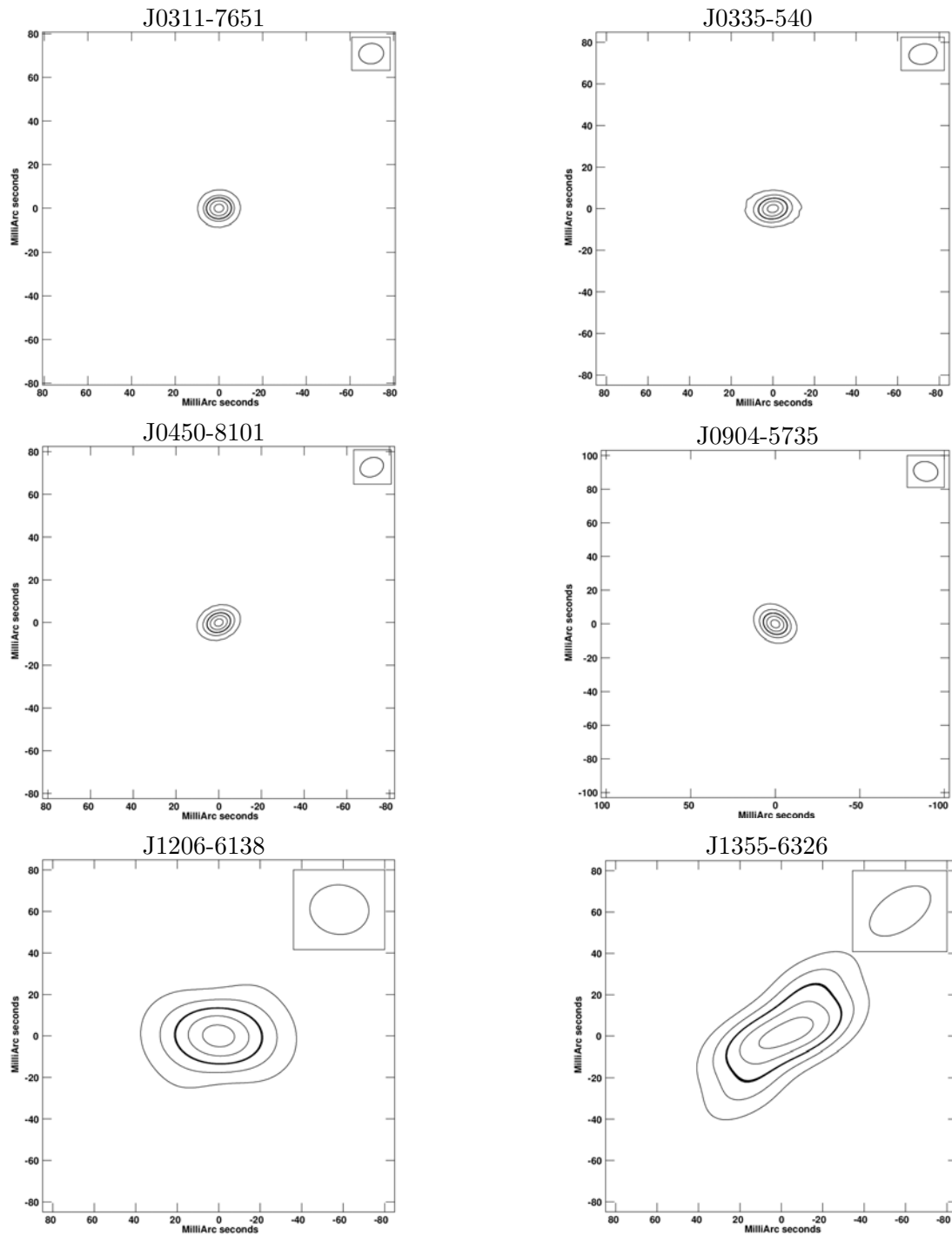


Figure 1. Contour plots of the brightness distribution as an example of compact (J0311-7651, J0335-540, J0450-8101, J0904-5735) and extended (J1206-6138, J1355-6326) sources in our sample. The contours are drawn at 10, 30, 50, 70 and 90 percent of the peak brightness with the 50 percent contour being darker than the rest. The FWHM of the convolving beam is shown in the upper right in each panel.

Table 1. Image Parameters: the peak brightness (B_P), the image off-source rms brightness (B_{orms}) and the total CLEAN flux densities (S_{CL})

Source (J2000 name)	B_P (Jy/beam)	B_{orms} (mJy/beam)	S_{CL} (mJy)	Source	B_P (Jy/beam)	B_{orms} (mJy/beam)	S_{CL} (mJy)
J0058-5659	361	6.3	369	J1424-6807	712	13.2	752
J0253-5441	678	16.1	687	J1427-4206	2000	2.3	2252
J0311-7651	486	9.6	498	J1512-5640	238	7.9	418
J0335-5430	260	5.5	281	J1515-5559	830	18.3	1020
J0450-8101	686	11.2	706	J1624-6809	1030	17.8	1060
J0529-7245	423	14.1	429	J1628-6152	367	5.2	400
J0743-6726	841	20.4	898	J1703-6212	467	5.2	566
J0904-5735	251	3.7	252	J1744-5144	2720	4.9	3650
J1038-5311	440	7.5	496	J1803-6507	469	6.2	489
J1041-4740	891	13.2	974	J1809-4552	226	4.1	263
J1051-5344	841	15.4	905	J1837-7108	723	13.9	755
J1101-6325	566	9.4	735	J1912-8010	536	16.2	550
J1107-6820	502	10.0	521	J1930-6056	527	9.9	660
J1112-5703	381	2.5	539	J1940-6907	795	13.4	830
J1131-5818	469	4.5	491	J2035-6846	118	2.4	121
J1145-6954	274	4.4	279	J2105-7825	260	5.2	265
J1151-6728	914	18.0	1080	J2147-7536	755	12.1	768
J1206-6138	134	2.2	232	J2152-7807	496	5.3	509
J1252-6737	430	4.3	298	J2303-6807	456	7.4	468
J1254-7138	470	10.5	487	J2336-5236	1190	19.8	1250
J1315-5334	178	3.0	218	J2356-6820	482	9.4	522
J1355-6326	285	17.6	728				

point in the image. An angular radius of 2.5 mas is representative of the resolution obtained in global baselines (and also of the maximum resolution we obtained in our observations). Only 7 of our sources have $C < 0.75$. This shows that most of our sources are largely dominated by the core or most of the flux density is concentrated in the central component. The values of C are listed in Table 2.

3.2. Radial extent

We calculated three types of radial extent measurements. The first one is the flux-weighted radial extent of the sources, which is given by

$$r_{wt} = \frac{\sum_i S_i r_i}{\sum_i S_i} \quad (1)$$

Where r_i is the radius from the brightest point of the i^{th} CLEAN component, and S_i its flux density. The flux weighted radial extent of the sources ranges from 0.41 to 5.36 mas, with a mean of 1.57 mas.

The second type of radial extent measurement is the 95 percent flux-density radius, $r_{95\%}$, which is the radius within which 95 percent of the flux density of the source is contained, also measured from the brightest point in the image. We determined $r_{95\%}$ by adding the flux densities of the CLEAN components in order of increasing radius until we get 95 percent of the S_{CL} . The $r_{95\%}$ ranges from 0.82 to 16.89 mas, with the mean equal to 4.13 mas.

Our third type of radial extent measurement, which is the half-width-at-half-maximum (HWHM) radius of a circular Gaussian whose Fourier transform was fitted directly to the visibilities by least squares (thus by passing the CLEAN deconvolution). The HWHM of the sources ranges from 0.3 mas to 12.8 mas, with the mean equal to 2.19 mas.

Finally, we take the mean of r_{wt} , $r_{95\%}$ and the HWHM for each source to get an average radius of r_{av} . We list the values of the r_{av} in Table 2.

4. Classification of Calibrator Quality

We determined whether our sources were suitable for use as calibrators by using r_{av} described in the previous section. We divided the sources into four groups, according to their calibrator quality, as follows:

- **Very Good (VG)**:- contains sources with core fraction $C \geq 0.8$ and average radius $r_{av} \leq 0.4$ mas. We have 31 sources in this group all of which have sufficient flux density on all baselines.
- **Good (G)**: contains sources which are not in the first group but which have $C \geq 0.5$ and $r_{av} \leq 6$ mas. They also have sufficient flux density on all baselines. We found seven of our sources in this group.
- **Intermediate (I)**: contains sources which are not in the first or the second group but which have $C \geq 0.5$ and $r_{av} < 8$ mas or $C > 0.3$ and $r_{av} < 0.6$ mas. We only have one source in this group. This source doesn't have sufficient flux density on HartRAO baselines.
- **Bad (B)**: contains sources which are not in the other three groups.

In addition to compactness and brightness, calibrator sources should have accurately known positions. Among our 43 sources, the 35 sources which are listed as calibrators³ (see Table 2) in the RFC, have accurately determined positions and are good calibrators at 8.4 GHz. Out of the 35 sources with accurate positions, 32 (91%) sources fell in to the good or very good calibrator classes. The remaining 8 sources, which are listed as non-calibrators⁴, have source positions with large uncertainties. It is important to classify not only the 35 sources but also the 8 sources, because we could get better positions for those 8 sources in future.

Table 2. The average radius, r_{av} , the core fraction, **C**, calibrator class of the sources (VG for Very Good, G for Good, I for Intermediate and B for Bad) and status of the sources in the rfc_2016b catalog (C- Calibrator and N- Non-calibrator)

Source	r_{av}	C	Class	RFC Status	Source	r_{av}	C	Class	RFC Status
J0058-5659	0.74	1.00	VG	C	J1424-6807	2.70	0.85	VG	N
J0253-5441	0.85	1.00	VG	C	J1427-4206	3.89	0.75	G	C
J0311-7651	1.50	0.91	VG	N	J1512-5640	12.96	0.16	B	C
J0335-5430	1.27	1.00	VG	C	J1515-5559	3.67	1.00	VG	C
J0450-8101	1.66	0.90	VG	C	J1624-6809	4.59	0.78	G	C
J0529-7215	0.70	1.00	VG	C	J1628-6152	1.62	1.00	VG	C
J0743-6726	1.79	1.00	VG	C	J1703-6212	2.35	0.92	VG	C
J0904-5735	1.10	0.96	VG	N	J1744-5144	9.30	0.43	B	C
J1038-5311	4.19	0.69	G	C	J1803-6507	0.98	1.09	VG	C
J1041-4740	1.88	1.00	VG	C	J1809-4552	2.32	1.00	VG	C
J1051-5344	5.22	0.76	G	C	J1837-7108	1.49	1.00	VG	C
J1101-6325	3.89	0.50	G	C	J1912-8010	1.30	1.00	VG	C
J1107-6820	1.72	1.00	VG	N	J1930-6056	6.06	0.88	G	C
J1112-5703	5.91	0.34	I	N	J1940-6907	1.54	1.00	VG	C
J1131-5818	1.78	0.93	VG	C	J2035-6846	0.76	1.00	VG	C
J1145-6954	1.15	0.85	VG	C	J2105-7825	1.59	1.00	VG	C
J1151-6728	5.08	0.86	G	C	J2147-7536	1.06	1.00	VG	C
J1206-6138	15.07	0.30	B	C	J2152-7807	1.10	1.00	VG	N
J1252-6737	1.84	1.00	VG	C	J2303-6807	0.61	1.00	VG	C
J1254-7138	1.36	0.89	VG	C	J2336-5236	1.27	1.00	VG	N
J1315-5334	3.44	0.80	VG	C	J2356-6820	1.55	1.00	VG	C
J1355-6326	19.30	0.13	B	N					

³ A source listed as calibrator in the RFC is a source which has 8 or more detections at both 2.3 and 8.4 GHz, and has position accuracy better than 25 nrad.

⁴ A source listed as non-calibrator in the RFC is a source which has at least 8 detections at either 2.3 or 8.4 GHz, and has position accuracy in the range [25, 500] nrad.

5. Summary and Conclusion

Our first interest in this research was to determine the suitability of our sources as calibrators for 1.4-GHz band observations. The two important properties we need from good calibrator sources are that they should be very bright and compact. Calibrator sources should also have accurately known positions. Among the 43 sources, we found that 38 sources are in the good or very good calibrator classes. Of the 38 sources 32 sources have accurately determined source positions in the RFC. Therefore, these 32 sources are good calibrators for global-array VLBI observations at 1.6 GHz.

After determining the suitability of the sources as calibrators, our second interest was to figure out how safe it is to use known 8.4 GHz calibrators for 1.4-GHz band observations. We found that 91% of the sources known to be good calibrators at 8.4 GHz are still good for 1.4-GHz band observations. This result is mainly important as the number of known calibrator sources in the 1.4-GHz band is very small, while there are many more known calibrator sources at 8.4 GHz observations from which we could get usable calibrator sources for 1.4-GHz band observations with 91% chance.

Acknowledgments

This research was supported by the National Space Science Program (NASSP), Hartebeesthoek radio Astronomy Observatory (HartRAO) and the National Research Foundation (NRF).

References

- [1] Beasley A J, Gordon D, Peck A B, Petrov L, MacMillan D S, Fomalont E B and Ma C 2002 *ApJS* **141** 13-21
- [2] Booth, R. S. and Jonas J. L 2012 *African Skies* **16** 101-04
- [3] Briggs D S, Schwab F R and Sramek R A 1999 *ASPC* **180** 127-149
- [4] Cornwell T, Braun R, Briggs D S 2004 *Synthesis Imaging in Radio Astronomy II, ASP Conference Series* **180** 151-70
- [5] Clark B G 1995 *ASPC* **82** 3-16
- [6] Fomalont E B, Petrov L, MacMillan D S, Gordon D and Ma C 2003 *AJ* **126** 2562-66
- [7] Gaylard M J, et al. 2011 *SAIP* 473-78
- [8] Hungwe F, Ojha R, Booth R S, Bietenholz M F, Collioud A, Charlot P, Boboltz D and Fey A L 2011 *MNRAS* **418** 2113-20
- [9] Johnston S, et al. 2008 *Experimental Astronomy* **22** 151-273
- [10] Kovalev Y Y, Petrov L, Fomalont E B and Gordon D 2007 *AJ* **133** 1236-43
- [11] Ojha R, et al. 2004 *AJ* **127** 3609-21
- [12] Petrov L, Phillips C, Bertarini A, Murphy T and Sadler E M 2011 *MNRAS* **414** 2528-39
- [13] Petrov L, Kovalev Y Y, Fomalont E B and Gordon D 2005 *AJ* **129** 1163-70
- [14] Petrov L, Kovalev Y Y, Fomalont E B and Gordon D 2006 *AJ* **131** 1872-79
- [15] Petrov L, Kovalev Y Y, Fomalont E B and Gordon D 2008 *AJ* **136** 580-85

Ultrahigh-energy neutrino events in current and future neutrino telescopes from nearby Gamma-Ray Bursts

Jessymol K Thomas, Reetanjali Moharana and Soebur Razzaque

Department of Physics, University of Johannesburg, P.O. Box 524, Auckland Park 2006, South Africa.

E-mail: jessymolkt@uj.ac.za

Abstract. Neutrino Astronomy has gained momentum after discovering cosmic neutrinos by the IceCube Neutrino Observatory at the south pole. A proposed upgrade of IceCube and planned future experiments will increase sensitivity to neutrino fluxes at very high energies ($> \text{PeV}$). We consider very high-energy neutrino flux from the Gamma Ray Bursts (GRBs) during the afterglow phase. We calculate this flux by modeling in details the observed afterglow data with standard afterglow theories for nearby long-duration GRBs within redshift 0.5. We also calculate neutrino events and corresponding upper limits from these GRBs for the future IceCube Gen-2 observatory.

1. Introduction

Gamma ray bursts are one of the most energetic transients and they have been proposed as sources of very high energy neutrinos. Ultra High Energy Cosmic Rays (UHECRs) are expected to be produced from shock acceleration in GRBs. These UHECRs can interact with low energy afterglow photons to produce very high energy neutrinos [1, 2]. We have modeled afterglow radiations of 17 nearby GRBs within redshift 0.5, and using the best fitted afterglow model parameters we have calculated expected neutrino flux and events from them. The synchrotron modeling of broadband spectral energy distribution (SED) at different time intervals and the temporal evolution of flux in different frequencies are done for all the 17 GRBs, using theories of blast wave evolution in the constant density interstellar medium (ISM) and in wind environment where the density decreases with distance from the center of the GRB (here after called as wind medium).

The high energy neutrino observatories such as IceCube, have recently successfully demonstrated the existence of astrophysical neutrino flux and this result is one of the driving consideration for the second generation detector at south pole, the IceCube-Gen-2 [3]. We have calculated neutrino fluence from individual GRBs in our sample, and by stacking fluence from all GRBs we have calculated neutrino events for the upcoming IceCube Gen-2 in both ISM and wind environment. We have also calculated upper limits for the stacked fluence of the IceCube Gen-2 observatory since no detection seems to be possible.

2. Synchrotron modeling of GRB afterglow

In the GRB explosions the afterglows follow the prompt emissions (< 2 s for short GRBs and > 2 s for long GRBs) and are produced by the synchrotron emission of accelerated electrons in

the GRB blastwave [4, 5]. Relativistic material ejected from GRB explosion drives a blastwave by accumulating surrounding medium. As the shock front propagates in the blast wave, a population of electrons gets accelerated to relativistic energies by a Fermi shock-acceleration mechanism. These electrons emit synchrotron radiations in a random magnetic field created (assuming some plasma instability) in the shock region. This synchrotron radiation is observed afterglows in all electromagnetic wavelengths. The synchrotron modeling of an afterglow spectrum is done for a power-law distribution of electrons with Lorentz factors γ as $n_e(\gamma) \propto \gamma^{-p}$ in the range $\gamma_{min} \leq \gamma \leq \gamma_s$. Here γ_{min} and γ_s are the minimum and maximum Lorentz factors, respectively and p the spectral index. Several breaks can appear in the electron spectrum due to efficient synchrotron cooling at high energies (γ_c) and synchrotron self-absorption at low energies. These breaks also give rise to breaks in the synchrotron spectrum, in the so-called slow-cooling ($\gamma_c > \gamma_{min}$) and fast-cooling regime ($\gamma_c < \gamma_{min}$) [5, 6, 7].

We have used afterglow data from gamma-ray to optical range which are detected by the Large Area Telescope (LAT) on board the Fermi Gamma ray Space Telescope, the Burst Alert Telescope (BAT), the X-ray Telescope (XRT) and the Ultraviolet/Optical Telescope (UVOT) of the Swift Gamma Ray Burst explorer and the data observed by other optical telescopes. The SEDs are taken for different time intervals from early time after T_{90} (duration of GRB prompt phase) to later times depending on the availability of data. The synchrotron modeling of the observed photon fluxes for the 17 GRB afterglows are done for both the ISM and wind media. We show in Fig. 1 and Fig. 2, as examples, the SEDs and light curves for GRB 150818A in the wind environment. Note that the blast wave model cannot explain well the light curve in Fig. 2 during the 100-500 s period, which reflects our still inadequate understanding of the afterglow emission models.

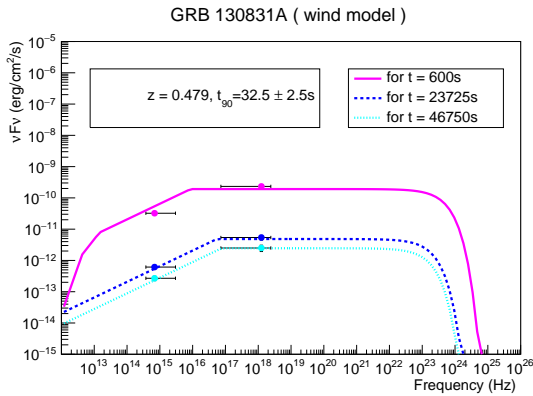


Figure 1. SEDs for GRB 130831A in wind medium at different times after T_{90} .

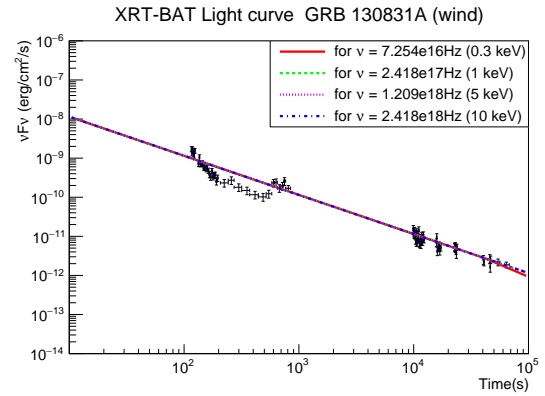


Figure 2. Swift-XRT light curves for GRB 130831A at different frequencies.

We have listed afterglow model parameters from our fits to 17 GRBs in Table 1 for the wind environment and in Table 2 for ISM. In these tables, E_{iso} is the isotropic-equivalent radiated gamma-ray energy within T_{90} , $E_{kin}(10^{55} \text{ erg})$ is the initial kinetic energy of the GRB blast wave in units of 10^{55} ergs, ϵ_e is the fraction of shock energy going to the relativistic electrons, ϵ_b is the fraction of shock energy going to the magnetic energy, $A_* \equiv \dot{M}_{-5}/v_8$, corresponding to a mass-loss rate of $\dot{M}_w = 10^{-5} \dot{M}_{-5} M_{\odot} \text{ yr}^{-1}$ in wind, with velocity $v_w = 10^8 v_8 \text{ cms}^{-1}$, by the progenitor star and n_0 is the number density of particles in the ISM.

3. Neutrino flux and events from GRBs

We have used the above modeled parameters for the afterglow radiation to calculate the neutrino flux and events from the GRBs by the upcoming IceCube Gen-2 neutrino telescope. In GRB

Table 1. WIND Model parameters

GRB	z	$T_{90}(s)$	$E_{iso}(erg)$	$E_{kin}(10^{55}erg)$	ϵ_e	ϵ_b	p	A^*
150818A	0.282	123.3±31.3	1×10^{51}	1×10^{-3}	6×10^{-3}	1×10^{-2}	2.14	0.1
130831A	0.479	32.5 ± 2.5	4.56×10^{51}	8×10^{-3}	9×10^{-3}	1×10^{-3}	2.0	1.0
130702A	0.145	15±1	7.8×10^{50}	7×10^{-4}	2×10^{-2}	5×10^{-2}	1.9	0.1
130427A	0.34	162.83±1.36	8.5×10^{53}	1.1	9×10^{-3}	1×10^{-4}	2.0	1.0
120714B	0.398	159 ± 34	4.51×10^{51}	4.5×10^{-3}	1×10^{-2}	1.2×10^{-3}	2.3	0.1
120422A	0.28	5.35±1.4	1.28×10^{51}	1.28×10^{-3}	3.5×10^{-2}	1×10^{-4}	2.4	1.0
111225A	0.297	106.8±26.7	2.88×10^{50}	2.88×10^{-4}	1×10^{-2}	1.45×10^{-2}	2.18	0.1
100316D	0.059	1300	9.81×10^{48}	9.8×10^{-6}	8×10^{-3}	1×10^{-4}	2.12	0.1
091127	0.49	7.1±0.2	1.60×10^{52}	1.6×10^{-2}	3×10^{-2}	5×10^{-3}	2.0	0.1
061021	0.346	46	4.06×10^{51}	4.06×10^{-3}	6×10^{-3}	4×10^{-3}	2.0	0.1
060614	0.125	102	8.4×10^{50}	8.4×10^{-4}	3×10^{-3}	2×10^{-3}	2.1	0.1
060512	0.443	8.6± 2	1.99×10^{50}	1.99×10^{-4}	5×10^{-2}	1×10^{-2}	2.18	0.1
060218	0.033	2100± 0.1	1.9×10^{49}	1.9×10^{-5}	1×10^{-2}	6.8×10^{-2}	2.27	0.1
051117B	0.481	8	2.77×10^{51}	2.77×10^{-3}	2×10^{-3}	3×10^{-4}	2.1	0.1
051109B	0.08	151	3.46×10^{48}	3.4×10^{-6}	2×10^{-2}	1×10^{-3}	2.0	0.1
050826	0.297	35± 8	3.39×10^{50}	3.39×10^{-4}	1×10^{-2}	5×10^{-3}	2.12	0.1
050803	0.422	85 ± 10	2.45×10^{51}	2.45×10^{-3}	2×10^{-2}	1×10^{-3}	2.0	0.1

Table 2. ISM Model parameters

GRB	z	$T_{90}(s)$	$E_{iso}(erg)$	$E_{kin}(10^{55}erg)$	ϵ_e	ϵ_b	p	n_0
150818A	0.282	123.3± 31.3	1×10^{51}	1×10^{-3}	1×10^{-3}	1×10^{-2}	2.02	1
130831A	0.479	32.5 ± 2.5	4.56×10^{51}	8×10^{-3}	3×10^{-3}	1×10^{-1}	2.0	0.01
130702A	0.145	15±1	7.8×10^{50}	7×10^{-4}	5×10^{-3}	8×10^{-2}	1.87	0.1
130427A	0.34	162.83±1.36	8.5×10^{53}	5×10^{-1}	1.2×10^{-3}	1×10^{-4}	2.0	1.0
120714B	0.398	159 ± 34	4.51×10^{51}	4.5×10^{-3}	2×10^{-3}	2×10^{-3}	2.28	1.0
120422A	0.28	5.35±1.4	1.28×10^{51}	1.28×10^{-3}	1×10^{-3}	1.3×10^{-2}	2.1	1.0
111225A	0.297	106.8±26.7	2.88×10^{50}	2.88×10^{-4}	4.5×10^{-3}	1.6×10^{-2}	2.19	1.0
100316D	0.059	1300	9.81×10^{48}	9.8×10^{-6}	1×10^{-3}	1×10^{-3}	2.12	0.1
091127	0.49	7.1±0.2	1.60×10^{52}	1.6×10^{-2}	1.2×10^{-2}	3.8×10^{-3}	2.0	0.1
061021	0.346	46±1	4.06×10^{51}	4.06×10^{-3}	4×10^{-3}	3×10^{-3}	2.0	0.1
060614	0.125	102	8.4×10^{50}	8.4×10^{-4}	2×10^{-3}	2×10^{-3}	2.18	1.0
060512	0.443	8.6± 2	1.99×10^{50}	1.99×10^{-4}	2×10^{-2}	3×10^{-2}	2.18	1.0
060218	0.033	2100	1.9×10^{49}	1.9×10^{-5}	1×10^{-2}	2×10^{-2}	2.27	0.14
051117B	0.481	8	2.77×10^{51}	2.77×10^{-3}	5×10^{-4}	1×10^{-3}	2.0	1.0
051109B	0.08	151	3.46×10^{48}	3.4×10^{-6}	2×10^{-2}	3×10^{-2}	2.1	1.0
050826	0.297	35±8	3.39×10^{50}	3.39×10^{-4}	4×10^{-3}	1×10^{-2}	2.14	1.0
050803	0.422	85±10	2.45×10^{51}	2.45×10^{-3}	7×10^{-3}	1×10^{-3}	2.0	1.0

blast waves, the low energy afterglow photons interacts with the UHECRs to produce muons, pions and kaons. Subsequently they decay to produce very high energy neutrinos. Due to neutrino oscillation during their propagation we expect 3 different neutrino flavors: muon neutrino, electron neutrino and tau neutrino and their anti neutrinos on the Earth. Here we have calculated the neutrino flux from pion and muon decay considering their production from Δ^+ resonance interaction $p\gamma \rightarrow \Delta^+ \rightarrow n\pi^+$ or $p\pi^0$, where n is neutron and p is proton. Subsequent decay channels for neutrino production are $\pi^+ \rightarrow \mu^+ + \nu_\mu \rightarrow e^+ + \nu_e + \nu_\mu + \bar{\nu}_\mu$.

3.1. Neutrino flux from GRBs

Using the synchrotron model parameters from the 17 GRBs we have modeled neutrino flux for all of them individually for different time intervals in terms of T_{90} . The neutrino flux from the proton-photon ($p\gamma$) interactions depends on the proper density of synchrotron photons in the blast wave frame and corresponding optical depth (efficiency) and the flux of cosmic-ray protons from the GRB blast wave. The photon spectrum in the blast wave can be expressed in terms of the differential proper density of the synchrotron photon $n'_\gamma(E'_\gamma)$ in the slow-cooling and fast-cooling regime [5, 1]. Here E'_γ is the photon energy in the blast wave frame and it is related to the observed synchrotron photon energy $h\nu$ as $E'_\gamma = h\nu(1+z)/\Gamma$, where Γ is the bulk Lorentz factor of the blast wave. The $p\gamma$ optical depth is $\tau_{p\gamma}(E'_\gamma) \approx E'_\gamma n'_\gamma(E'_\gamma) \sigma_{p\gamma} c t_{dyn}$, where t_{dyn} is the dynamic time. The optical depth as a function of the photon energy E'_γ can be converted to a function of the proton energy E'_p in the blast wave frame using the resonance energy for $p\gamma \rightarrow \Delta^+$ production as $E'_\gamma E'_p = 0.3 \text{ GeV}^2$. In the observer's frame $E_p = E'_p(1+z)/\Gamma$.

The $p\gamma$ opacity scales with the proton energy E_p in the slow-cooling regime as [9]

$$\tau_{p\gamma}(E_p) = \tau_{p\gamma}(E_{pl}) \times \begin{cases} \left(\frac{E_{ph}}{E_{pl}}\right)^{\frac{p}{2}-\frac{1}{2}} \left(\frac{E_p}{E'_{ph}}\right)^{\frac{p}{2}}; & E_p < E_{ph}, \\ \left(\frac{E_p}{E_{pl}}\right)^{\frac{p}{2}-\frac{1}{2}}; & E_{ph} < E_p < E_{pl}, \\ 1; & E_p > E_{pl}. \end{cases} \quad (1)$$

and in the fast-cooling regime as

$$\tau_{p\gamma}(E_p) = \tau_{p\gamma}(E_{pl}) \times \begin{cases} \left(\frac{E_p}{E_{pl}}\right)^{p/2}; & E_p < E_{pl}, \\ \left(\frac{E_p}{E_{pl}}\right)^{1/2}; & E_{pl} < E_p < E_{ph}, \\ \left(\frac{E_{ph}}{E_{pl}}\right)^{1/2}; & E_p > E_{ph}. \end{cases} \quad (2)$$

Here E_{pl} is the minimum proton energy corresponding to the break energy $h\nu_m$ in the afterglow synchrotron photon spectrum, corresponding to the electrons with minimum Lorentz factor γ_{min} . Similarly E_{ph} is the proton energy corresponding to the break energy $h\nu_c$ in the afterglow synchrotron photon spectrum, corresponding to the electrons with the cooling Lorentz factor γ_c . We refer the readers for details in [1] for equations and numerical values for these energies. The opacity value at the energy E_{pl} in the wind medium is,

$$\tau_{p\gamma}(E_{pl}) = 6.0(1+z)^{1/2} \epsilon_{b,0.1}^{1/2} A_*^2 t_2^{-1/2} E_{55}^{-1/2}, \quad (3)$$

where $t_2 = t/100$ and t is the time after the prompt emission. Similarly the opacity value at the energy E_{pl} for ISM is calculated as,

$$\tau_{p\gamma}(E_{pl}) = 0.7(1+z)^{-1/2} \epsilon_{b,0.1}^{1/2} n_0 t_2^{1/2} E_{55}^{1/2}. \quad (4)$$

The neutrino flux from the GRB afterglow is calculated from shock-accelerated cosmic-rays interacting with afterglow synchrotron photons as described above. We assume that cosmic-ray is dominated by protons and for calculation purpose we use a primary cosmic-ray flux and a pion flux, although those cannot escape directly the blast wave. The cosmic-ray spectrum, $n(E_p)$ or dN/dE , is a power-law of energy with index -2 , assumed to originate from Fermi acceleration. The normalization of the spectrum is done by integrating the differential spectrum $E(dN/dE)$ over the minimum and maximum energy range of protons and equating it to the total kinetic energy (dominated by protons) of the GRB blast wave [1]. The proton flux and is given as $J_P(E_p) = c/4\pi(R/d_l)^2 n(E_p)$, where d_l is the luminosity distance of the GRB. An intermediate pion flux, from $p\gamma$ interactions, can be calculated as $J_\pi(E_\pi) = J_p(E_p) \tau_{p\gamma}(E_p) f_{p \rightarrow \pi}(x)$, where $x = E_\pi/E_p$ and we took the average value of x as 0.2. We have calculated neutrino flux by assuming an average of $1/4^{th}$ energy of pion goes to one neutrino.

The neutrino flux for individual GRBs at time T_{90} for the ISM and wind environment are shown in Fig. 3 and Fig. 4, respectively and at $100 T_{90}$ for the ISM and wind environment are shown in Fig. 5 and Fig. 6, respectively.

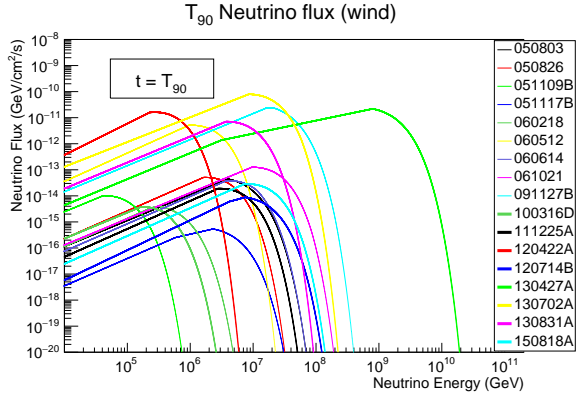


Figure 3. Neutrino flux calculated for T_{90} in the wind environment.

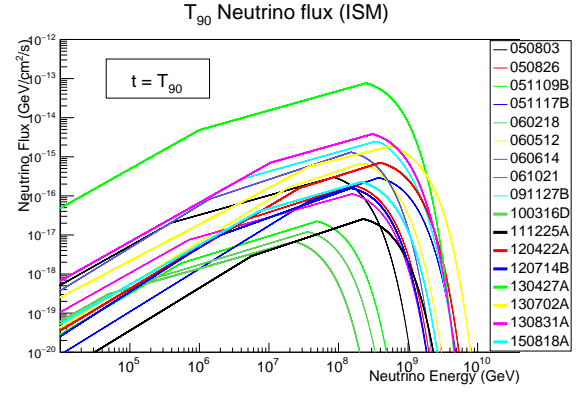


Figure 4. Neutrino flux calculated for T_{90} in the ISM.

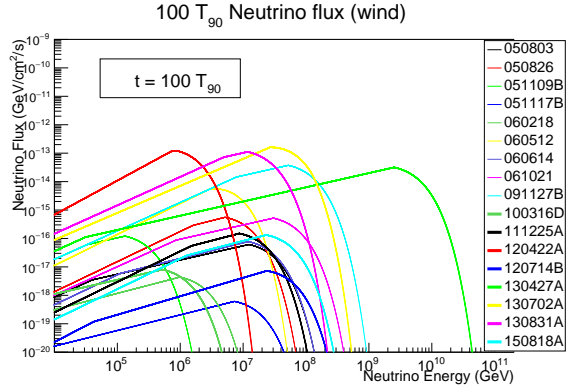


Figure 5. Neutrino flux calculated for $100 T_{90}$ in the wind environment.

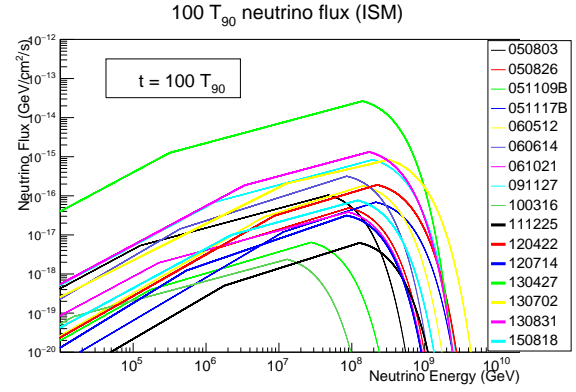


Figure 6. Neutrino flux calculated for $100 T_{90}$ in the ISM.

3.2. Neutrino events and fluence upper limit calculated for the IceCube Gen-2 .

The Neutrino observatories have made a significant progress in the study and research of Astrophysical Neutrinos. Out of the modeled 17 nearby long GRBs we have calculated the neutrino events and individual fluence from the 7 southern hemisphere GRBs which could be in the field of view of IceCube Gen-2. We also have stacked the fluence of all these 7 GRBs. Figures 7 and 8 show the neutrino fluence plots of the southern hemisphere GRBs for the IceCube Gen-2 in ISM and wind environment, respectively. In case of non-detection of neutrinos, the upper limits for the stacked fluence is also calculated. We calculated the neutrino events as,

$$N_{\nu} = \int_{E_{\nu,min}}^{E_{\nu,max}} \int_{T_{90}}^{100T_{90}} \frac{dN_{\nu}}{dE_{\nu}} A_{eff} dE_{\nu} dt_{90}, \quad (5)$$

where A_{eff} is the effective area for the IceCube Gen-2 [3], $E_{\nu,min} = 10^6$ GeV and $E_{\nu,max} = 10^9$ GeV. These upper limits on the stacked fluence for the 7 GRBs are also shown in Figs. 7 and 8.

Estimated neutrino fluence for IceCube corresponding to 468 long GRBs detected within 4 years (2011-2015) has been reported in Ref. [11], which gives an upper limit on the flux as $\approx 10^{-4}$ GeV cm $^{-2}$ sr $^{-1}$. This calculation considers both prompt and afterglow neutrino production in GRBs. Again IceCube Gen-2 has atleast one order of magnitude larger effective

area compared to IceCube [12]. Hence we have not done a precise neutrino event calculation for IceCube.

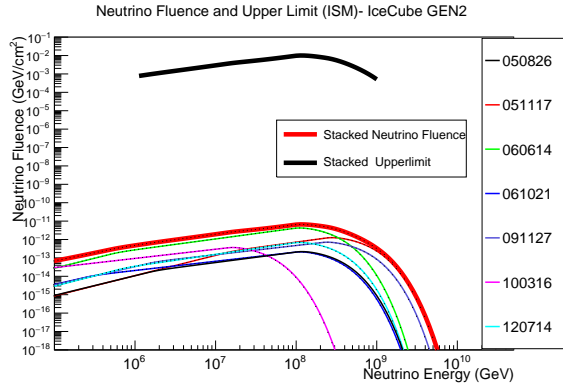


Figure 7. Neutrino fluence and upper limit calculated from time T_{90} to $100 T_{90}$ for IceCube Gen-2 in ISM.

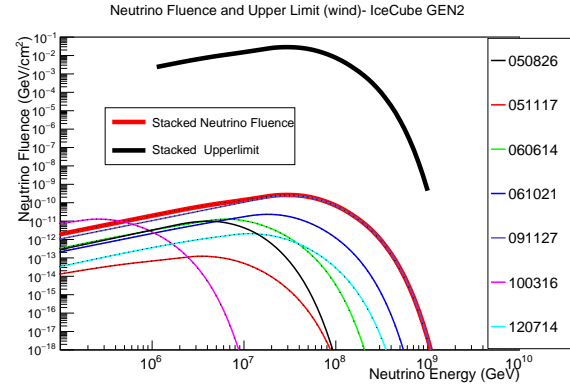


Figure 8. Neutrino fluence and upper limit from T_{90} to $100 T_{90}$ for IceCube Gen-2 in wind medium.

4. Discussion and conclusion

We have done a detailed study of afterglow radiations from a well defined set of 17 long nearby GRBs with redshift less than 0.5, which are the most promising GRBs for the neutrino detection. We have modeled the SED for different time intervals and the light curves for different frequencies of the afterglows of these GRBs. For this afterglow modeling we have used different data from LAT, XRT/BAT, UVOT/optical and other optical telescopes. We have obtained a set of reasonable model parameters for all these GRBs in both the constant density interstellar medium and wind environment.

We have calculated neutrino flux and fluence from the southern hemisphere GRBs for the IceCube Gen-2 neutrino observatory. Individual fluences for the 7 southern hemisphere GRBs are calculated and the stacked fluence of these GRBs are calculated. The number of neutrino events for the stacked fluence is very small and in such a case of non-detection we have calculated upper limit for these stacked fluences. Our calculations are useful to estimate sensitivity of new generation of neutrino telescopes for detecting very high energy (> 1 PeV) neutrinos from the afterglows of long-durations GRBs.

5. References

- [1] Razzaque S 2013, *Phys. Rev. D* **88** 103003
- [2] Waxman E and Bahcall J N 1997, *Phys. Rev. Lett.* **78** 2292
- [3] Aartsen, M G et al 2015, *PoS(ICRC2015)* 1148
- [4] Meszaros P and Rees M J 1997, *Astrophys.J.* **476** 23
- [5] Piran T 2005, *Rev. Mod. Phys.* **76** 1143
- [6] Thomas J, Moharana R, Razzaque S 2015, *Pos(HEASA2015)* 038
- [7] Thomas J, Moharana R, Razzaque S 2015, *Pos(SSC2015)* 073
- [8] Thomas J, Moharana R, Razzaque S 2015, *Pos(SAIP2015)*
- [9] Razzaque S, Yang L 2015, *Phys.Rev. D* **91** 043003
- [10] Hanson K 2015, in *VLVnT Workshop in La Sapienza (Rome, Italy)*
- [11] Brayeur L, 2015 Thesis, <https://inspirehep.net/record/1513509/files/LionelBrayeur-PhD-thesis.pdf>
- [12] Halzen F 2015, in *25th International Workshop on Weak Interactions and Neutrinos (Heidelberg, Germany)*

Long-term monitoring of TeV Blazars with the Watcher Robotic Telescope

J P Marais B van Soelen, R J Britto and P J Meintjes

Department of Physics, University of the Free State, Bloemfontein, 9301, South Africa

E-mail: MaraisJP@ufs.ac.za

Abstract. Blazars are known to show large-scale multi-wavelength variability on the order of sub-hours to years. This variability often manifests as rapid flares that can show correlation over a broad wavelength range. Since flares happen suddenly, rapid follow-up observations must be scheduled if a more detailed multi-wavelength observation campaign is to be started. We report on the long term optical photometric monitoring of a selection of known TeV blazars observed with the Watcher Robotic Telescope since May 2015 in the V, R and i' filters and present results of five well known sources: PKS 1510-089; AP Librae; PG 1553+113; PKS 2005-489 and PKS 2155-304. A reduction pipeline is currently in development to help identify potential sources for rapid follow-up multi-wavelength observations and provide optical light-curves to complement multi-wavelength observations. During the observation period PKS 1510-089 showed two outbursts and a $\Delta m_V = 1.7$ mag. Analysis with the Discrete Correlation Function between optical and γ -rays for PKS 1510-089 showed that all the flares are well correlated, suggesting a common origin for the optical and γ -ray emission. PKS 2155-304 showed a $\Delta m_V = 1$ magnitude difference and a steady increase in magnitude. PG 1553+113 exhibits an outburst with a total magnitude change of $\Delta m_V \sim 0.6$, while PKS 2005-489 shows a general magnitude increase toward the middle of the campaign and a decrease toward the end. No flare events were observed for AP Librae.

1. Introduction

Blazars are a class of Active Galactic Nuclei (AGN) which have a jet orientation which lies very close to the observer's line of sight ($\lesssim 10^\circ$) and they can be subdivided into Flat Spectrum Radio Quasars (FSRQ) and BL Lacertae objects (BL Lac). BL Lacs and FSRQs are characterized by their rapid multi-wavelength variability on the order of sub-hours to years, high polarization (radio to optical) and highly Doppler boosted emission from the jet. The Spectral Energy Distribution (SED) of blazars show a "double-humped" profile, with the low energy component (radio to UV/X-ray) produced by synchrotron radiation and high energy component (X-ray to γ -ray) produced by inverse Compton (IC) emission in the leptonic scenario [1] [2]. There is still some debate as to the origin of the high energy component, whether leptonic, hadronic or lepto-hadronic (see e.g. [3], [4] or [5]).

The Watcher Robotic Telescope, situated at the Boyden Observatory, South Africa is currently undertaking long-term observation of a selection of blazars detected with the High Energy Stereoscopic System (H.E.S.S.) telescope. The observational campaign began in December 2014. We present light-curves for five of these sources: PKS 1510-089; AP Librae; PG 1553+113; PKS 2005-489 and PKS 2155-304, from May (MJD = 57154) to November (MJD = 57335) 2015 in

the R, V and i' filters. In this short proceedings we analyse the long-term light-curves for these five sources to investigate their long-term variability. Aperture photometry was performed on *Fermi*-LAT ($0.1 \leq E_\gamma \leq 300$ GeV) data for PKS 1510-089 to investigate any correlation between its optical and γ -ray light-curves.

2. Data reduction pipeline and method

The goal of an automatic reduction pipeline is to reduce and analyse observational data with as little input by the user as possible. The reduction pipeline being developed in the Python Programming Language for the reduction of the Watcher Robotic Telescope data, uses output from various Python packages, such as `sep`, a module that uses `SExtractor` algorithms in Python to help analyse data [6], `pyRAF`, which allows Python programs to be executed in IRAF and `Astropy`, which reads the fits file headers during the IRAF reduction process [7] [8], allowing the pipeline to reduce long-term data with locally (daily) applicable bias, dark and flat files.

The reduction pipeline uses the output of the `Astropy` and `sep` modules as the input for `pyRAF`, which then performs the reduction and photometry with the standard IRAF `ccdred/ccdproc` and `daophot/phot` tasks. To ensure the quality of the data being reduced, the `sep` module is used to analyse the quality of the data and extracted sources. Frames are rejected if the background counts and total background noise (rms) is more than twice the average of all the data. This allows anomalous frames to be rejected, while still keeping the overall data quality approximately the same. Frames are also rejected if the eccentricity of the extracted sources are more than $e = 0.9$.

The data obtained from the Watcher Robotic Telescope was run through the reduction pipeline and photometric results obtained from the `daophot/phot` task. Differential photometry was performed using the method outlined in Everett and Howell [9]. The corrected magnitude is calculated by:

$$m = m_{\text{obs}} - \left(\langle m_i \rangle - \frac{1}{M} \sum_{j=1}^M \langle m_i \rangle_j \right). \quad (1)$$

Here m_{obs} is the observed instrumental magnitude per frame. The average instrumental magnitude of the N comparison stars, weighted by their variance, per frame is $\langle m_i \rangle$, M is the total the number of frames and $\langle m_i \rangle_j$ is the average magnitude of the comparison stars on frame j . The uncertainty in the corrected magnitude is determined by:

$$\sigma = \sqrt{\sigma_*^2 + \sigma_{\text{ens}}^2} \quad (2)$$

where σ_* is the error calculated by IRAF for the star and σ_{ens} is the ensemble error, given by

$$\sigma_{\text{ens}} = \left[\sum_{i=1}^N \left(\frac{1}{\sigma_{*i}^2} \right) \right]^{-\frac{1}{2}} \quad (3)$$

The Discrete Correlation Function (DCF) [10] was used to calculate correlations between the optical and γ -ray ($E_\gamma < 1$ GeV) flares in May and August 2015 and lower ($E_\gamma < 1$ GeV) and higher ($1 \leq E_\gamma \leq 300$ GeV) components of the flare detected by the LAT in August 2015 for PKS 1510-089.

3. Results and discussion

During the observation period PKS 1510-089 showed three flares detected in γ -rays, two of which were detected by the Watcher Robotic Telescope. The May 2015 flare was also detected

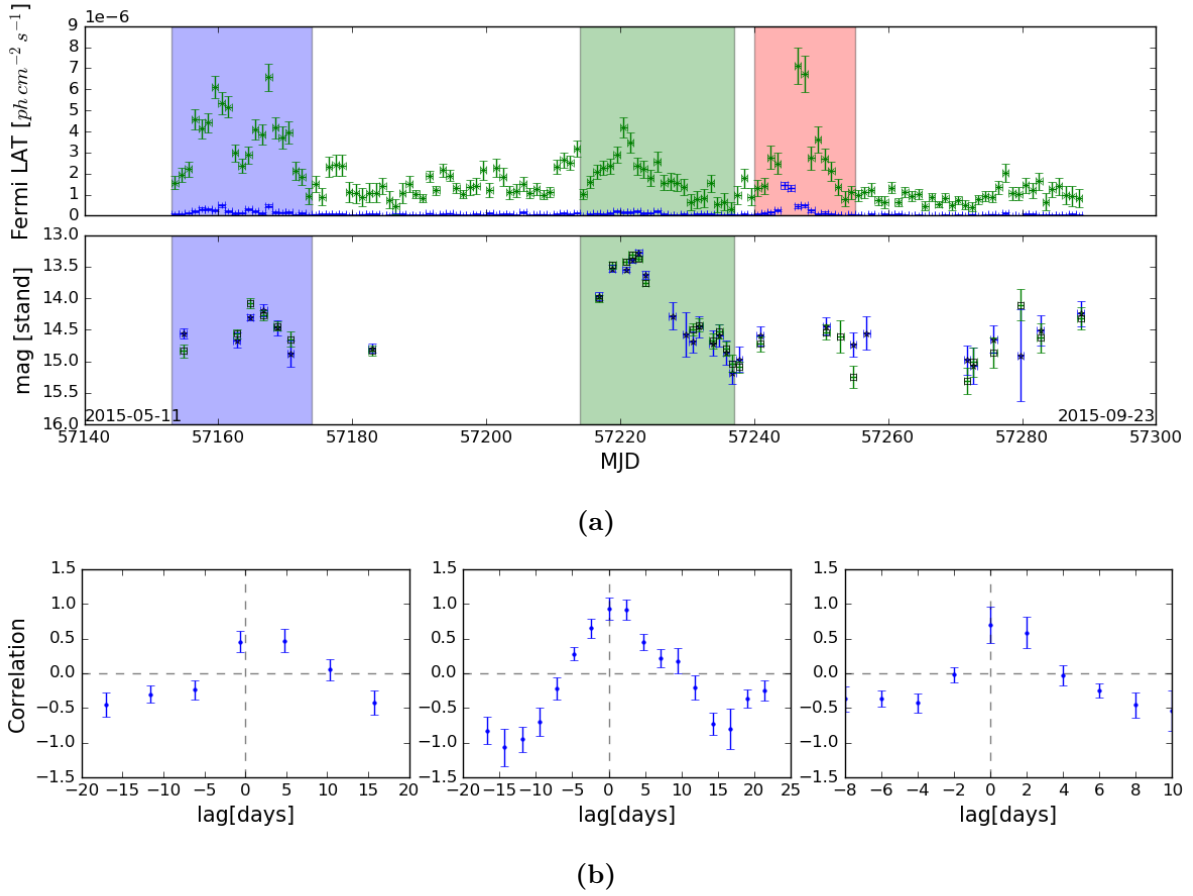


Figure 1: Light-curve and DCF for PKS 1510-089. Frame a) is the light-curve for PKS 1510-089. The top panel is the γ -ray light-curve from $E_\gamma < 1$ GeV (green crosses) and $1 \leq E_\gamma \leq 300$ GeV (blue plusses) emission. The green squares and blue stars are the R and V magnitudes respectively. Frame b) shows the correlations between the flares. Left and middle: May and July flares respectively. Correlations are calculated between $E_\gamma (< 1$ GeV) emission and R filter, right: August flare. Correlations are between the ($1 \leq E_\gamma \leq 300$ GeV) and ($E_\gamma \leq 1$ GeV) γ -ray emission.

by M.A.G.I.C. (Major Atmospheric Gamma Imaging Cherenkov) [11] and the July flare was detected by the 0.6m telescope of the Belgradchik observatory, situated in Bulgaria [12]. The light-curve and DCFs for the three flares are shown in figure 1. The third flare was not observed by Watcher, but was detected in γ -rays by *Fermi*-LAT. The first flare, in May 2015, had a $\Delta m_V \approx 1$ magnitude change with a maximum daily γ -ray flux of $F(E_\gamma < 1 \text{ GeV}) = (6.57 \pm 0.635) \times 10^{-6} \text{ ph cm}^{-2} \text{ s}^{-1}$.

The DCF calculations suggest a positive correlation with a lag of $\tau = 2.07 \pm 2.73$ days between the $E_\gamma < 1$ GeV emission and R filter. However, this ~ 20 day flare only has optical data every ~ 4 th day, so any information regarding short term correlation between the gamma-ray and optical emission should be treated with caution. The second flare in July 2015 showed a $\Delta m_V \approx 1.9$ with a maximum daily γ -ray flux of $F(E_\gamma < 1 \text{ GeV}) = (4.13 \pm 0.500) \times 10^{-6} \text{ ph cm}^{-2} \text{ s}^{-1}$. A DCF calculation showed a positive correlation with a $\tau = 1.19 \pm 1.19$ day lag between the γ -ray ($E_\gamma < 1$ GeV) emission and R filter. The third flare, in August, was not observed by Watcher, but a γ -ray flare was recorded with the LAT ($0.1 \leq E_\gamma \leq 300$ GeV). Maximum

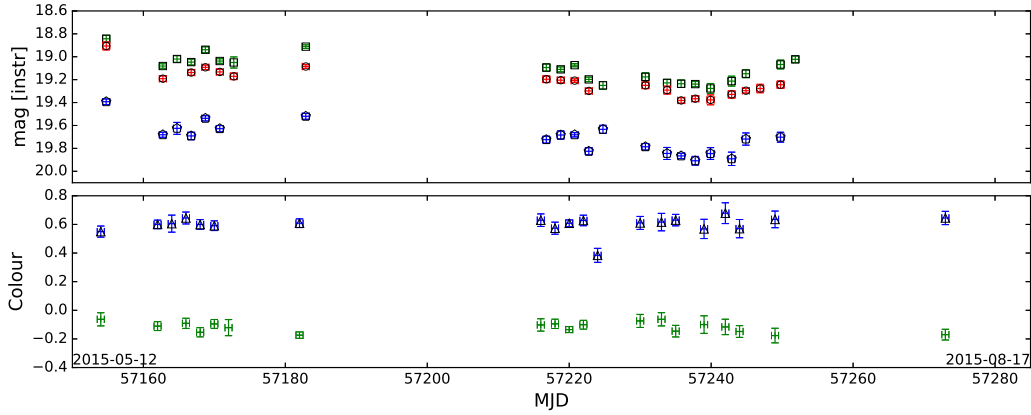


Figure 2: Light-curve for AP Lib. The light-curves show the data for the V (blue pentagons), R (green squares) and i' (red circles) filters in the top panels. The colour curves are shown in the bottom panels, with R-V (blue triangles) and R- i' (green pluses)

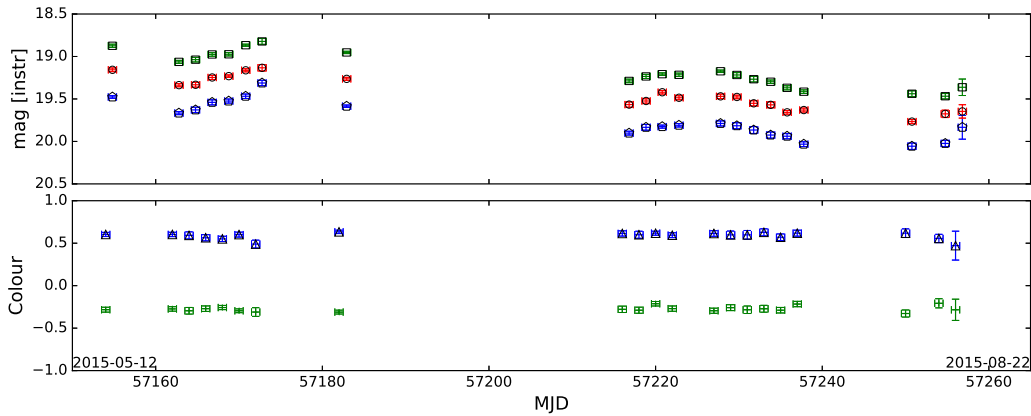


Figure 3: Light-curves for PG 1553+113. See figure 2 for description of symbols.

daily fluxes of $F(E_\gamma < 1 \text{ GeV}) = (7.125 \pm 0.864) \times 10^{-6} \text{ ph cm}^{-2} \text{ s}^{-1}$ and $F(E_\gamma > 1 \text{ GeV}) = (1.437 \pm 0.150) \times 10^{-6} \text{ ph cm}^{-2} \text{ s}^{-1}$ were recorded with the LAT. There was a lag of $\tau = 1 \pm 1$ days between the $1 \leq E_\gamma \leq 300 \text{ GeV}$ and $E_\gamma < 1 \text{ GeV}$ emission, calculated with the DCF.

AP Librae¹ showed a $\Delta m_V \approx 0.35$ magnitude change over the course of the observation campaign, with no sudden magnitude changes. Its R-V colour stayed constant (~ 0.6), but its R- i' colour varied slightly around ~ -0.1 . Its light-curve is shown in figure 2.

PG 1553+113 (figure 3) showed a overall decrease in magnitude with a $\Delta m_V \approx 1$ change. The R-V and R- i' colours stayed constant during the whole observation campaign with ~ 0.6 and ~ -0.2 respectively.

PKS 2005-489 showed a slight increase in magnitude toward the middle of the campaign, then a slight decrease toward the end, with an overall $\Delta m_V \approx 0.4$ magnitude change. The light-curve is shown in figure 4.

PKS 2155-304, shown in figure 5, displayed an overall magnitude increase during the campaign, with a $\Delta m_V \approx 1$ increase. It showed small variability ($\Delta m_R \approx 0.3$) in the R filter during the

¹ Please note that the instrumental magnitudes are used for AP Librae, PG 1553+113, PKS 20115-489 and PKS 2155-304.

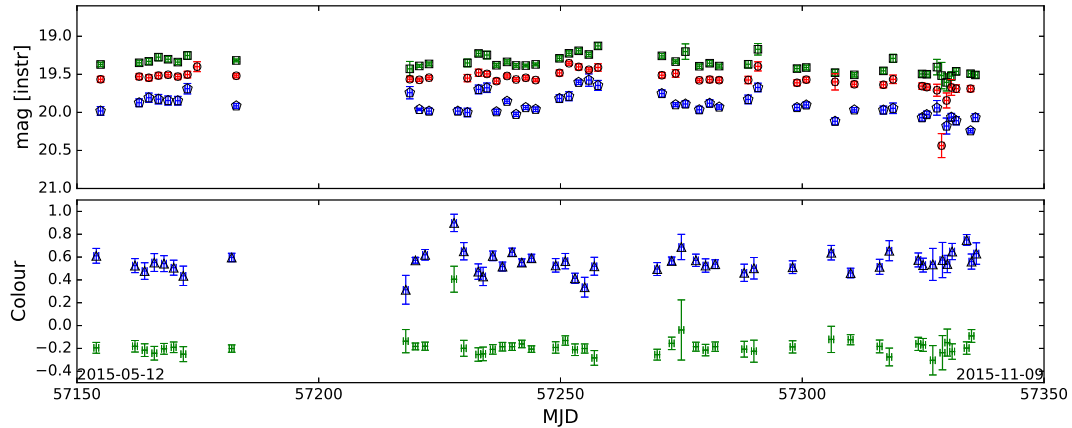


Figure 4: Light-curves for PKS 2005-489. See figure 2 for description of symbols.

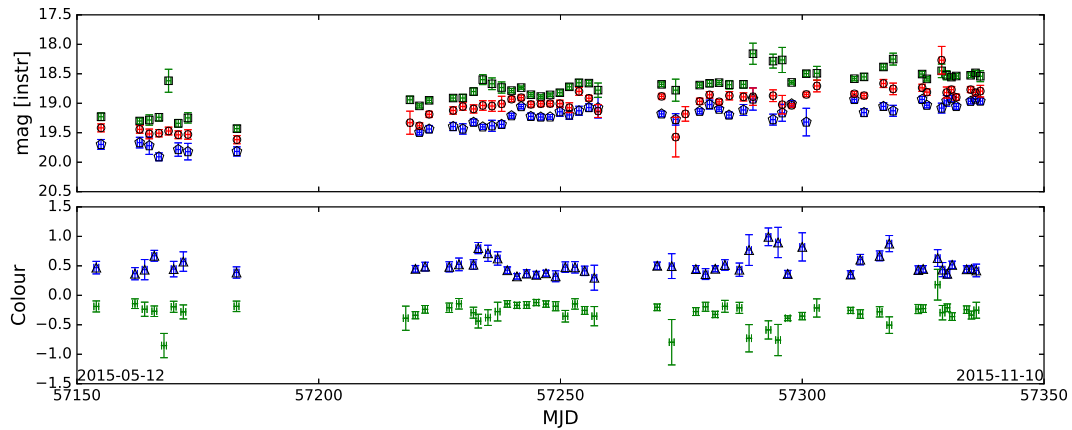


Figure 5: Light-curves for PKS 2155-304. See figure 2 for description of symbols.

middle of the campaign, but no corresponding change in magnitude was noted for the V and i' filters.

4. Conclusion

In this paper we presented light-curves on 5 well known TeV blazars observed with the Watcher Robotic Telescope for the period between May 2015 and November 2015. During this campaign, the FSRQ PKS 1510-089 ($z = 0.361$), which was discovered to be a TeV emitter in 2009 [13], experienced three flares during the observation period, two optical and γ -ray flares during May and July 2015 and a flare in August 2015 that was not detected by the Watcher Robotic Telescope, which was not observing the source during the flaring period. The August flare was detected *Fermi*-LAT in the $1 \leq E_\gamma \leq 300$ and $E_\gamma \leq 1$ GeV range.

AP Librae ($z = 0.049$), PG 1553+113 ($z = 0.43 - 0.58$); PKS 2005-489 ($z = 0.071$) and PKS 2155-304 ($z = 0.116$) are BL Lacs observed in the TeV range by H.E.S.S. [14]. The rapid flares of PKS 1510-089 hint that the emission during the flares originate from a small region in the jet and the small time lags between the γ -ray and optical emission has previously been shown to agree well with a Shock-in-Jet Model (see e.g. [15]). *Fermi*-LAT aperture photometry for AP Librae, PG 1553+113, PKS 2005-489 and PKS 2155-304 was also performed, but did not show any γ -ray

variability flaring events. The automatic reduction pipeline, currently in development, used to reduce the data and perform photometry, gave reasonable results, although more development and testing, under different conditions, still needs to be carried out. A more rigorous γ -ray analysis still need to carried out on the flares detected by the *Fermi*-LAT to explore the emission regions and conditions during the flares. The preliminary results show the importance of long-term monitoring and the rigorousness of the reduction pipeline.

Acknowledgments

The financial assistance of the National Research Foundation (NRF) towards this research, funded in part for the grant: Unique Grant No. 87919, is hereby acknowledged. Opinions expressed and conclusions arrived at, are those of the author and are not necessarily to be attributed to the NRF. This research has made use of the SIMBAD database, operated at CDS, Strasbourg, France. pyRAF is a product of the Space Telescope Science Institute, which is operated by AURA for NASA. We thank the Watcher Group for providing the optical data used in this analysis.

References

- [1] Beckmann V and Shrader C 2012 *Active Galactic Nuclei* Physics textbook (Wiley) ISBN 9783527410910 chapter 4 pp 116-120
- [2] Schneider P 2014 *Extragalactic astronomy and cosmology : an introduction*. (Berlin : Springer, 2014.) ISBN 9783642540820 chapter 5 pp 215-223
- [3] Cerruti M, Zech A, Boisson C and Inoue S 2011 *SF2A-2011: Proceedings of the Annual meeting of the French Society of Astronomy and Astrophysics* ed Alecian G, Belkacem K, Samadi R and Valls-Gabaud D pp 555–558
- [4] Böttcher M, Reimer A, Sweeney K and Prakash A 2013 *ApJ* **768** 54
- [5] Cerruti M, Zech A, Boisson C and Inoue S 2015 *MNRAS* **448** 910–927
- [6] Barbary K, Boone K and Deil C 2015 sep: v0.3.0 URL <http://dx.doi.org/10.5281/zenodo.15669>
- [7] Massey P and Davis L E 1992 *NOAO Laboratory*
- [8] Massey P 1997 *NOAO, Arizona, Tucson*
- [9] Everett M E and Howell S B 2001 *PASP* **113** 1428–1435
- [10] Edelson R A and Krolik J H 1988 *ApJ* **333** 646–659
- [11] Mirzoyan R and MAGIC Collaboration 2015 *The Astronomer's Telegram* **7542**
- [12] Bachev R 2015 *The Astronomer's Telegram* **7829**
- [13] HESS Collaboration *et al.* 2013 *A&A* **554** A107
- [14] Cerruti M 2011 *Proceedings of the 32nd International Cosmic Ray Conference* **8** 109
- [15] Spada M, Ghisellini G, Lazzati D and Celotti A 2001 *MNRAS* **325** 1559–1570

Graph theory and pulsar astronomy tie the knot: the use of labeled graph kernels in exploring the pulsar \dot{P} - P diagram

Jacques Maritz^{1*}, Elizabeth Maritz² and Pieter Meintjes¹

¹Physics Department, University of the Free State, 9300, South Africa

²Mathematics Department, University of the Free State, 9300, South Africa

E-mail: *maritzjm@ufs.ac.za

Abstract. In this paper we explore the dependency of pulsar population structures (seen in \dot{P} - P diagram) on the measurable characteristics of pulsars. We implement graph kernels for this investigation and it forms part of structure mining which is a domain of learning on structured data objects in machine learning. Among others, we implement one of the most powerful graph kernels that is based on random walks, and has been successfully applied to data mining projects in the field of astronomy. With instruments such as the SKA coming online in the near future, the quest continues to search for relationships between the different pulsar populations.

1. Introduction

Pulsars can be considered as stable cosmic clocks that serve the purpose of testing fundamental astrophysical theories and advancing computing technology [1]. However, the model describing the evolutionary path of pulsars on the \dot{P} - P diagram is incomplete and continuously undergoes upgrades in both complexity and completeness. The \dot{P} - P diagram describes the evolution of pulsars in the parameter space described by their spin-period (P), spin-down rate (\dot{P}), magnetic field (B) and characteristic spin-down age (τ_c), see Figure 1. The \dot{P} - P diagram is mostly populated by normal pulsars from where they evolve beyond the graveyard line to be reborn as isolated or binary millisecond pulsar systems (recycled pulsars).

The \dot{P} - P diagram is not just being populated via radio observations, but due to the fact that pulsars produce pulsed-emission across a large part of the electromagnetic spectrum, including optical, X ray and gamma ray, we can gather a wealth of information to try and understand the evolutionary path of pulsars on the \dot{P} - P diagram and clustering can accelerate this aim.

Graph clustering techniques are being used in machine learning and social network classification [3]. Specific graph kernels are also being used in photon event tracking seen in the latest Pass-8 Fermi data (<http://fermi.gsfc.nasa.gov/ssc/data/>). The new technique ultimately uses the three dimensional calorimeter readout and implements a Minimum Spanning Tree (MST) construction to minimize ghost signals and improve the event reconstruction process at GeV levels [4]. In earlier work, [5] proposed using the Minimum Spanning Tree algorithm to classify sources in gamma-ray bi-dimensional images where a photon's (or events) celestial coordinates represent a node in the graph and the edge is weighted by the angular distance

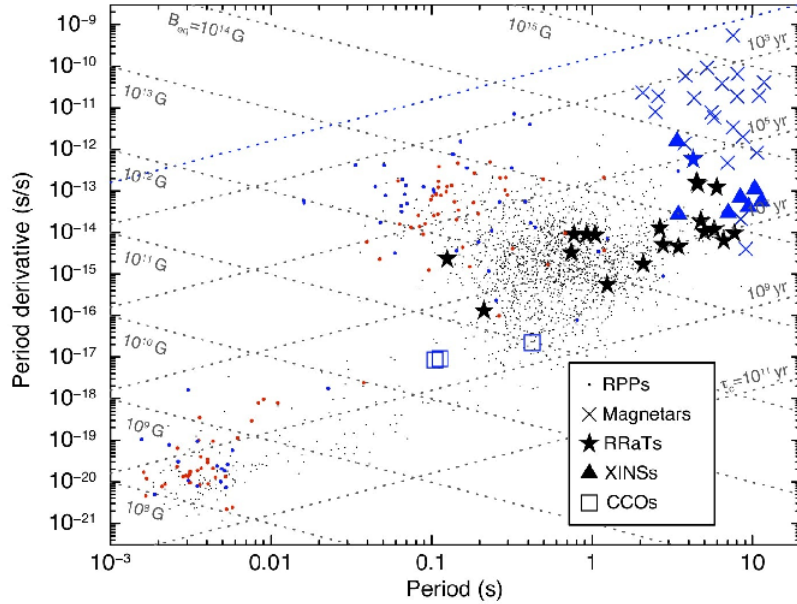


Figure 1. \dot{P} - P diagram illustrating the placement of isolated neutron star classes according to their characteristics, adopted from [2].

between the nodes. They applied this algorithm successfully to EGRET data of the Virgo field and detected several sources.

It needs to be stressed that graph kernels are highly application specific, i.e. when considering clustering applications on data we can use a specific kernel called the graph clustering kernel. In the next section we investigate the mechanism of graph clustering, after which we consider the application of graph clustering on the \dot{P} - P diagram via unsupervised machine learning.

2. Machine learning

There are two types of machine learning supervised and non-supervised. There are two main trends in machine learning. The first is the classification of objects with respect to a certain characteristic that they might or might not possess. Here we would start with a set of objects with predetermined outputs, i.e. a set of objects that are already classified in terms of either having a certain property, or not. The machine then uses this information, compares these objects and 'learns' what it is that makes them fall into one category or the other in terms of their similarity. The idea is to classify any new object according to what has been learned. The ultimate aim for classification is therefore *prediction*. The second is used for data that does not have clear-cut classifications, or perhaps we do not know what it is that we want to search for in terms of a classification. This then leads to clustering, which is simply grouping together elements that seem to demonstrate similar characteristics, without having to go into too much detail of what those characteristics are. The aim here is therefore *description*.

2.1. Graph kernels

We briefly define a graph and the concepts necessary to define some of the existing graph kernels.

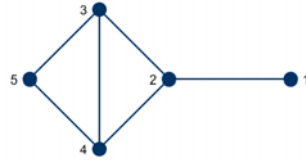


Figure 2. A graph G with adjacency matrix A in Equation 1.

A *finite graph* G consists of a set of vertices $V(G) = \{v_1, v_2, \dots, v_n\}$ with possible edges between them. The number of vertices in the graph is referred to as the *order* of the graph, in this case n . An edge is denoted by $e = v_i v_j$, meaning the link between vertices v_i and v_j . The set of edges of the graph is denoted by $E(G)$. We consider simple graphs with no loops (an edge from a vertex to itself) or multiple edges between vertices. If two vertices are joined by an edge, we refer to them as being adjacent. If two edges meet at a common vertex, they are also referred to as being *adjacent*. An edge meeting a vertex is *incident* to that vertex.

A *walk* in the graph refers to movement across the graph, starting at a vertex and moving along edges and across other vertices allowing for edges and vertices to be visited more than once. The *length* of the walk is simply the number of edges traversed. A *path* is a walk where no edges or vertices are visited more than once, and a *cycle* is a closed path, i.e. its initial vertex is also its end vertex.

We can describe the graph G by making use of an *adjacency matrix* A , which is an $n \times n$ matrix consisting of zeros and ones, depending on whether or not two vertices are adjacent. We therefore have the ij -th entry given as

$$[A]_{ij} = \begin{cases} 1 & \text{if } v_i v_j \in E(G), \\ 0 & \text{if } v_i v_j \notin E(G), \end{cases}$$

where $1 \leq i, j \leq n$.

Consider the graph G in Figure 2. For simplicity the vertices v_1, v_2, \dots, v_5 have been labeled using only values $1, 2, \dots, 5$. The adjacency matrix A of G is

$$A = \begin{bmatrix} 0 & 1 & 0 & 0 & 0 \\ 1 & 0 & 1 & 1 & 0 \\ 0 & 1 & 0 & 1 & 1 \\ 0 & 1 & 1 & 0 & 1 \\ 0 & 0 & 1 & 1 & 0 \end{bmatrix}. \tag{1}$$

The adjacency matrix of a graph contains valuable information, especially if we want to compare two graphs. The sum of the elements in each row or column gives that particular vertex's degree, i.e. its amount of adjacent vertices or neighbours. Also, the powers of the adjacency matrix, say A^4 , will give us the number of walks of length 4 in the graph, this can be found for each entry $[A]_{ij}$, that is, from vertex v_i to vertex v_j [6]. This concept is often used in what is called walk-based kernels, together with the idea of a direct product between graphs. To 'walk' on a direct product graph is therefore the same as walking on both graphs simultaneously [7–9]. An example of a direct product between graphs is given in Figure 3.

Graph-with-graph comparisons tend to fall under graph classification problems, while within-graph similarities are more used to cluster graphs.

2.2. Clustering

In terms of clustering or comparing vertices within a graph, we can make use of minimum spanning trees (MST), shared nearest neighbour (SNN), betweenness centrality, highly connected subgraphs, maximal clique enumeration and the kernel k -means, to name but a few.



Figure 3. An example of a direct product between two graphs G and H . If the graphs G and H have vertex sets $V(G)$ and $V(H)$, respectively, then the direct product graph of G and H has the vertex set $V(G) \times V(H)$, namely the set of ordered pairs consisting of vertices from G and H . Two vertices (u, u') and (v, v') in $G \times H$ are adjacent if and only if u is adjacent to v in the graph G and u' is adjacent to v' in the graph H .

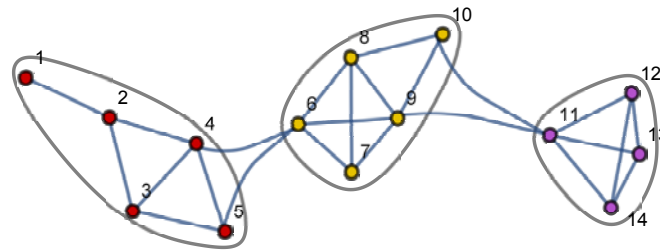


Figure 4. An example of graph clustering done on selected pulsars with respect to their dispersion measures. The lengths of the edges are not taken into consideration since they only represent connections between vertices.

In Figure 4 we have made use of a simple graph clustering based on the dispersion measure of each pulsar. A input threshold μ is specified whereby we form the graph structure. For this specific graph we choose $\mu = 10$ and vertices (pulsars) are adjacent if the difference between their dispersion measures are less than or equal to μ . On this graph we can then choose our method of clustering, depending on the similarities that we want to highlight. We now briefly discuss some of the methods of graph clustering.

A minimum spanning tree can be constructed from any connected weighted graph. A weighted graph is a graph where the edges have been assigned a numerical value which is referred to as its weight. A *tree* is a connected graph that contains no cycles. A *spanning tree* of a graph G is a subgraph of G consisting of all vertices of G . We construct a minimum spanning tree as follows. After choosing any vertex v to begin with, we use Prim’s algorithm (see also Kruskal’s algorithm) and we construct the tree T by using an incident edge that satisfies

- (i) it has the lowest weight,
- (ii) it has only 1 incidence with T .

We repeat this process until we have a tree T that contains all the vertices of the original graph, hence spanning. In order to cluster the graph, we start eliminating the maximum weighted edges from T . Since the tree T is a minimum spanning tree, the removal of any edge will result in a disconnected graph, the components of which would form the clusters.

Our aim is to make use of one or more of the existing clustering methods to investigate clustering of pulsars on the \dot{P} - P diagram. The main task will be to structure our data effectively

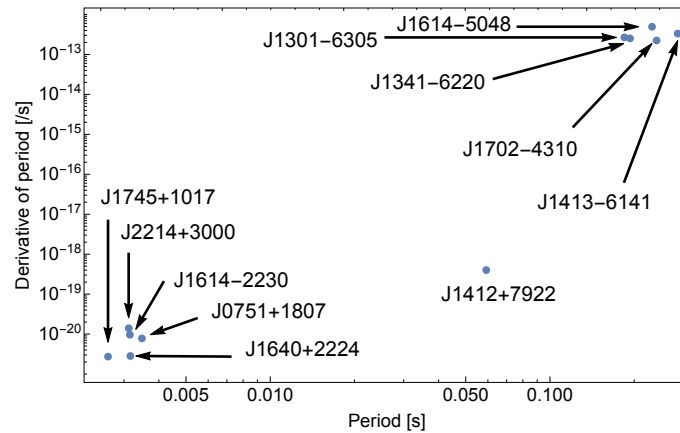


Figure 5. The pulsars in Table 1 plotted against period and period derivative.

in such a manner that the clustering methods could pick up more than just the standard clusters.

3. Application to \dot{P} - P diagram

To illustrate one of the most basic clustering methods using graph theory, we shall make use of eleven chosen pulsars and cluster them according to their respective distances on the \dot{P} - P diagram. The selection is obviously biased, but sufficient to test the algorithm.

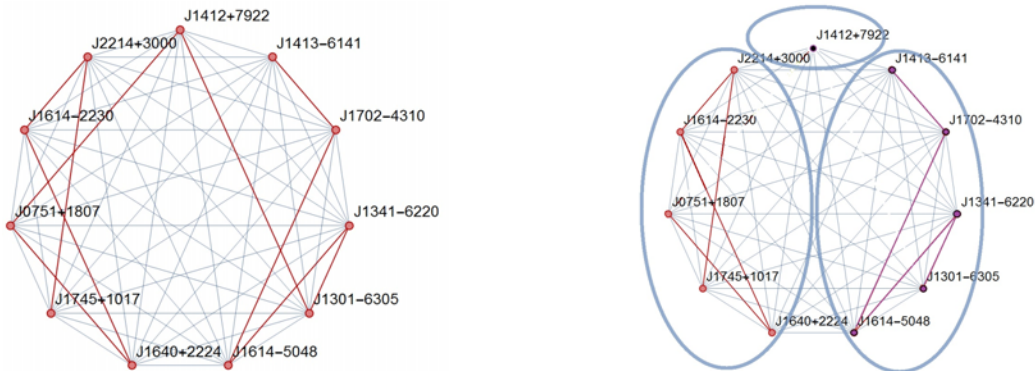
We form a complete graph of 11 vertices, that is, all vertices are adjacent to each other. Next, we assign weights to each edge in the graph according to the physical distances between its incident vertices (pulsars) on the \dot{P} - P diagram. We make use of a minimum spanning tree to cluster these pulsars. The pulsars that we have made use of can be found in Table 1. Their positions are plotted in Figure 5.

Now we construct a minimum spanning tree by choosing a vertex and adding edges according to the algorithm mentioned earlier. The spanning tree is shown in Figure 6a (bold edges).

For us to cluster these pulsars according to the spanning tree, we simply remove the heaviest weighted edges from the tree. For every edge we remove, we create a new clustering. If we remove the two heaviest edges from this specific tree, we find the clusters in Figure 6b, corresponding to our \dot{P} - P diagram in Figure 5.

Table 1. Pulsars and their \dot{P} - P coordinates used in our minimal working example.

PSR	P	Pdot
J2214+3000	0.003119	1.4×10^{-20}
J1614-2230	0.003151	9.62×10^{-21}
J0751+1807	0.003479	7.79×10^{-21}
J1745+1017	0.002632	2.73×10^{-21}
J1640+2224	0.003163	2.83×10^{-21}
J1412+7922	0.059198	4×10^{-19}
J1614-5048	0.231694	4.95×10^{-13}
J1301-6305	0.184528	2.67×10^{-13}
J1341-6220	0.19334	2.53×10^{-13}
J1702-4310	0.240524	2.24×10^{-13}
J1413-6141	0.285625	3.33×10^{-13}



(a) The spanning tree constructed from Table 1. (b) The spanning tree clusters formed

Figure 6. Spanning tree construction and clustering of a sample of pulsars

4. Discussion and Conclusions

In this paper we illustrated the usefulness and the adaptability of the graph cluster algorithm within the \dot{P} - P diagram by using pulsars with unique characteristics and clustered them accordingly. The MST results are in agreement with the clustering seen in Figure 5. The choice of threshold is problem specific. Optimizing the threshold can be done by several iterations using different threshold values. If the threshold is taken to high, the algorithm will simply allocate a cluster to each data point. For future work we are planning to cluster the entire up-to-date \dot{P} - P diagram using a well optimized clustering code.

Acknowledgments

The financial assistance of the South African SKA Project (www.ska.ac.za), and the National Research Foundation of South Africa.

References

- [1] Lorimer D R 2005 *Handbook of pulsar astronomy* (Cambridge, UK New York: Cambridge University Press) ISBN 978-0-521-82823-9
- [2] Turolla R, Zane S and Watts A L 2015 *Reports on Progress in Physics* **78** 116901 (*Preprint* 1507.02924)
- [3] Schaeffer S E 2007 *Computer Science Review* **1** 27 – 64 ISSN 1574-0137
- [4] Atwood W *et al.* 2013 *ArXiv e-prints* (*Preprint* 1303.3514)
- [5] Campana R *et al.* 2008 *Monthly Notices of the Royal Astronomical Society* **383** 1166–1174 (*Preprint* 0710.3691)
- [6] Samatova N F *et al.* 2013 *Practical Graph Mining with R* (Chapman & Hall/CRC) ISBN 143986084X, 9781439860847
- [7] Gärtner T, Flach P and Wrobel S 2003 *Conference on learning theory* pp 129–143
- [8] Ramon J and Gärtner T 2003 *Proceedings of the First International Workshop on Mining Graphs, Trees and Sequences* pp 65–74
- [9] Imrich W and Klavzar S 2000 *Product Graphs: Structure and Recognition* (John Wiley and Sons, New York, USA)

Constraining Lorentz Invariance violation using directional correlations of Gamma-Ray Bursts with IceCube cosmic neutrinos

Reetanjali Moharana¹ and Soebur Razzaque

Department of Physics, University of Johannesburg,
P. O. Box 524, Auckland Park 2006, South Africa

E-mail: reetanjalin@uj.ac.za

Abstract. A violation in Lorentz invariance (LIV) proposed in quantum gravity theories, delays the flight of extremely high energy gamma rays and neutrinos from their origin. Gamma ray bursts (GRBs) are one of the promising candidate sources of extremely energetic gamma rays and neutrinos at high redshift, as these particles propagate over long distances to develop any LIV induced propagation delays. Additionally GRBs are transient events, which gives a certain time stamp for gamma-ray emission to measure delays. With the recent discovery of astrophysical neutrino events by the IceCube observatory, a path is opened to search for Lorentz invariance at PeV energies. We use directional correlations of IceCube neutrino events and GRBs to constrain the LIV parameters at PeV energies from the observed time delay between the prompt gamma-ray and the neutrino events.

1. Introduction

IceCube Neutrino Observatory, the world's largest neutrino detector, has detected 54 neutrino events within 1347 days with energies between 20 TeV and 2.3 PeV [1][2]. Shower events, most likely due to ν_e or ν_τ charge current νN interactions and also due to neutral current νN interactions of all flavors, dominate the event list (39 including 3 events with 1–2 PeV energy) while track events, most likely due to ν_μ charge current interactions, constitute the rest. Among a total of 54 events about 21 could be due to the atmospheric neutrino ($9.0^{+8.0}_{-2.2}$) and muon (12.6 ± 5.1) backgrounds. A background-only origin of all 54 events has been rejected at a $6.5\text{-}\sigma$ level [2]. Therefore a cosmic origin of a number of neutrino events is robust. The track events have on average $\sim 1^\circ$ angular resolution, but the dominant, shower events have much poorer angular resolution, $\sim 15^\circ$ on average [2]. Searching for the sources of these events is now one of the major challenges in astrophysics. Pinpointing the astrophysical sources of these neutrinos is difficult, due to a large uncertainty in their arrival directions.

High energy cosmic rays (CRs) can interact with low energy photons and/or low energy protons to produce neutrinos and high energy gamma rays inside the source or while propagating to the Earth. Gamma Ray Bursts (GRBs) are promising candidates for producing neutrino by this process [4][5]. However a small violation in the Lorentz invariance (LI) can lead to time delay or advance in the detection of the neutrino event with respect to the GRB. The prospect

¹ Presently at Racah Institute of Physics, The Hebrew University, Jerusalem, Israel

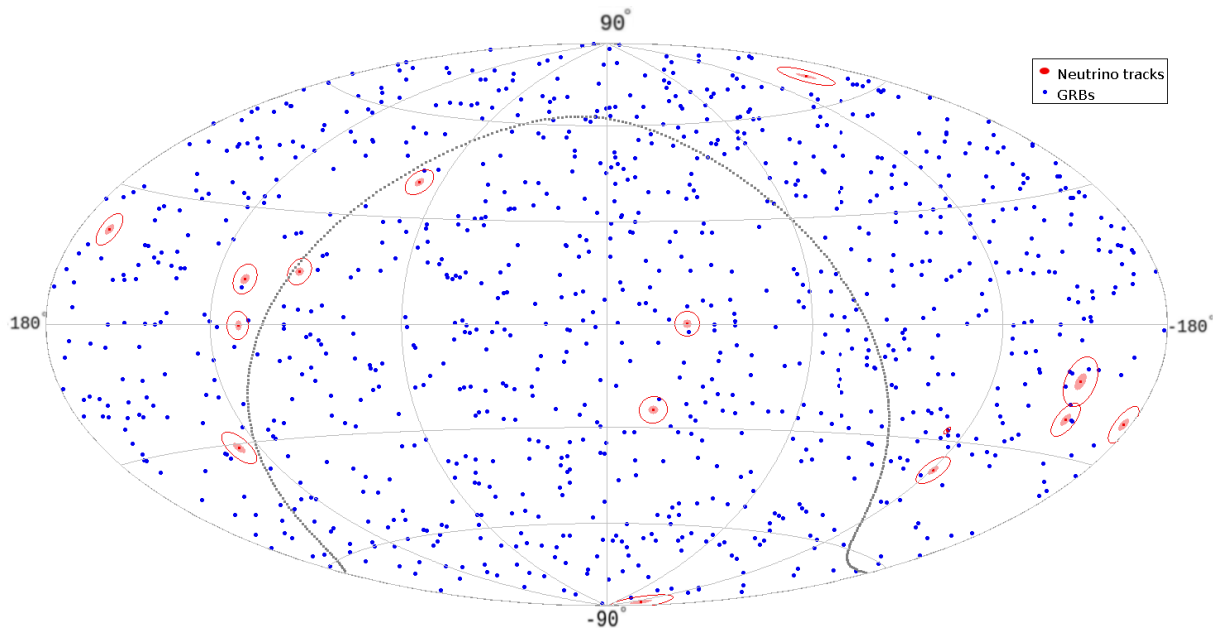


Figure 1. Sky map of total 15 neutrino track events, 13 from the IceCube 4 year HESE and the 2.6 up going event detected by IceCube [3] and one detected by ANTARES, with red dots and the red shaded area around the neutrino events shows the reported angular resolution while the red ellipses represent, three times the angular resolution in the equatorial coordinate. The Galactic plane is shown with the dotted gray line. The 1017 GRBs detected by *Swift* are shown with the blue dots.

of exploring the possible minute violation in LI with energetic gamma rays, neutrinos has been proposed earlier [6][7].

Here we have correlated the high energy neutrino events detected by IceCube and one event from the ANTARES [10] with the *Swift*² detected GRBs. Then we calculated the LIV parameter using the events that correlated with the GRBs.

2. High energy neutrino events and Gamma Ray Bursts

Out of all neutrino events we have considered only track events, as these kind of events leave a long muon track inside the detector which helps to reconstruct the arrival direction of the neutrino with better accuracy compared to shower events. With better angular resolution, muon track events can therefore give an idea of the location of the sources. This would help to claim for the sources. There are 14 track events in the 54 IceCube detected neutrino events, however two track events (event numbers 28 and 32) are coincident hits in the IceTop surface array and are almost certainly a pair of atmospheric muon background events [1]. Apart from the 54 events IceCube has also detected an up-going track event with an energy of 2.6 PeV [3]. In our analysis we have also included the ANTARES event having energy between 50 TeV to 100 TeV [10][11]. We have taken the energy of this event as 50 TeV with 10% of error due to lack of exact number. Now in total we have taken 15 high energy neutrino track events shown in the equatorial coordinate sky map, Fig. 1 along with their reported angular resolution and and with three times the angular resolution (outer ellipses).

The GRB catalogue used for correlation are selected from the swift detected GRBs within

² <http://swift.gsfc.nasa.gov/>

Table 1. The list of the GRBs that correlated with the detected high energy neutrino events.

Sources	Neutrino ID	Redshift	Δt [10^8 sec]
Known Redshift			
GRB 050724A	ANTARES event	0.257	3.19
GRB 070411A	IceCube 5	2.954	1.13
GRB 061110A	IceCube 44	0.758	2.27
Pseudo Redshift			
GRB 080915B	IceCube 23	0.124	1.05
GRB 090720A	IceCube 23	0.1518	0.8
GRB 110212A	IceCube 13	0.271	0.13
GRB 120913B	IceCube 23	0.006	0.2
GRB 130919A	IceCube 23	0.153	0.52
GRB 131202A	IceCube 18	0.4127	0.6
Assumed Redshift ($z=2.3$)			
GRB 050801A	IceCube 43		2.6
GRB 070809A	IceCube 43		2
GRB 080727A	IceCube 23,43		1.1, 1.7
GRB 120328A	IceCube 53		0.65

time period 2004 to 31 October 2014 ³. It contains a total 1017 GRBs. These GRBs are shown with blue dots on the skymap in figure 1. Out of these 1017 GRBs we found 14 correlated with the neutrino track events within three times the reported angular resolution ($\delta\gamma_i$), listed in table 1. We determined the number of correlations using the following method.

We mapped the Right Ascension and Declination (RA, Dec) of the GRBs and the neutrino events directions into unit vectors on a sphere as,

$$\hat{x} = (\sin \theta \cos \phi, \sin \theta \sin \phi, \cos \theta)^T,$$

where $\phi = RA$ and $\theta = \pi/2 - Dec$. The scalar product of the neutrino and GRB direction vectors ($\hat{x}_{\text{neutrino}} \cdot \hat{x}_{\text{GRB}}$) is therefore independent of the coordinate system. The angle between the two vectors

$$\gamma = \cos^{-1}(\hat{x}_{\text{neutrino}} \cdot \hat{x}_{\text{GRB}}), \tag{1}$$

is an invariant measure of the angular correlation between the neutrino event and the GRB directions [8][9]. We found the number of GRBs for which $3\delta\gamma_i$ is less than the separation γ , is 14.

3. Time Delay due to violation in Lorentz Invariance

We briefly mentioned above about the formalism of the LIV used in the present work. The details are discussed in [7]. For the particles with energies $E_\nu < \xi M_{pl}$, where M_{pl} is the Planck

³ https://swift.gsfc.nasa.gov/archive/grb_table/

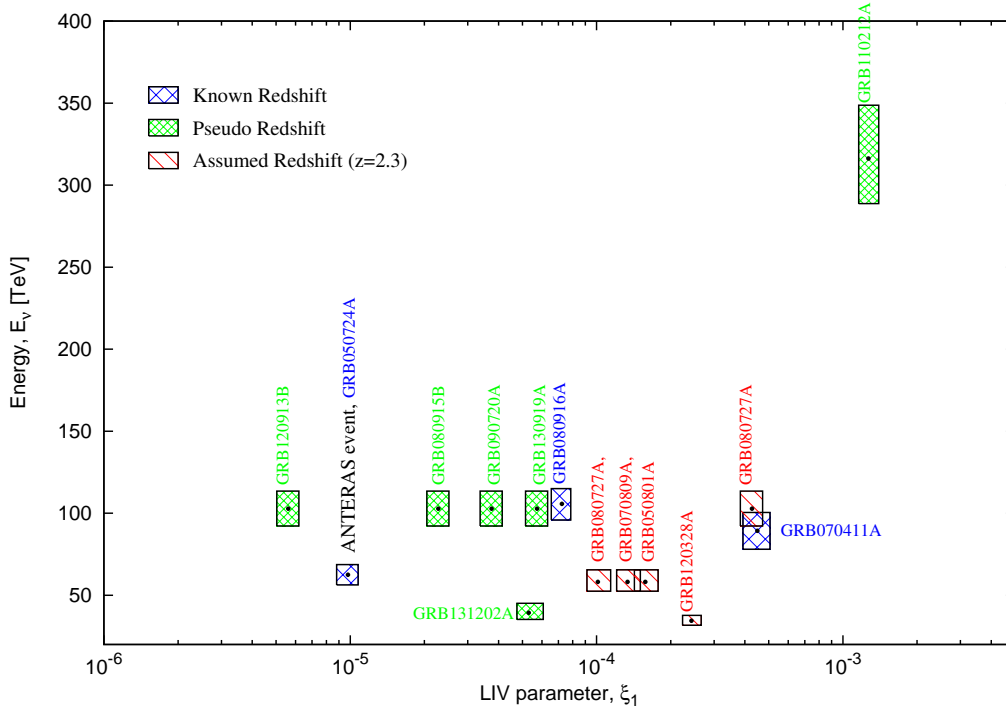


Figure 2. LIV parameter ξ_1 for different high energy neutrino events calculated for different GRBs which are correlated with the neutrino events, using the time delay of the neutrino events from the GRB. The red boxes are for GRBs that for which we have assumed the redshift to be 2.3, the green boxes represent the GRBs, for which we calculated the pseudo-redshifts according to [14], while the blue boxes are for GRBs with known redshifts.

mass, will have a dispersion relation,

$$E^2 - p^2c^2 - m^2c^4 \simeq \pm E^2 \left(\frac{E}{\xi_n M_{pl}} \right)^n. \quad (2)$$

As a result of this dispersion relation, the time needed for an ultra-relativistic particle to travel from a given sources to a given detector is, $t = t_0 + \Delta t$ [13], where t_0 is the time that would be predicted in classical space-time, and Δt is the time delay between photons and neutrinos from GRBs. The LIV time delay of a massless particle with an observed energy E_ν , emitted at redshift z is,

$$\Delta t = \frac{1}{H_0} \int_0^z \left(\frac{1+n}{2} \left(\frac{E_\nu}{\xi_n M_{pl}} \right)^n (1+z')^n \right) \frac{dz'}{\sqrt{\Omega_m(1+z')^3 + \Omega_\Lambda}}. \quad (3)$$

Where $H_0 = 71 \text{ km/sec/Mpc}$, $\Omega_m = 0.27$ and $\Omega_\Lambda = 0.73$ are the cosmological parameters evaluated at present. Here the leading LIV parameter ξ_n is corrected for order n, considering only lower order corrections, hence we have taken n=1 or 2. We have calculated this time delay factor for the 14 GRBs that correlated with the neutrino track events.

4. Results and Discussions

We have calculated the LIV parameters ξ_1 and ξ_2 for all the 14 GRBs correlated with the neutrino events. Out of 14 only 3 GRBs have known redshifts. We have calculated the pseudo

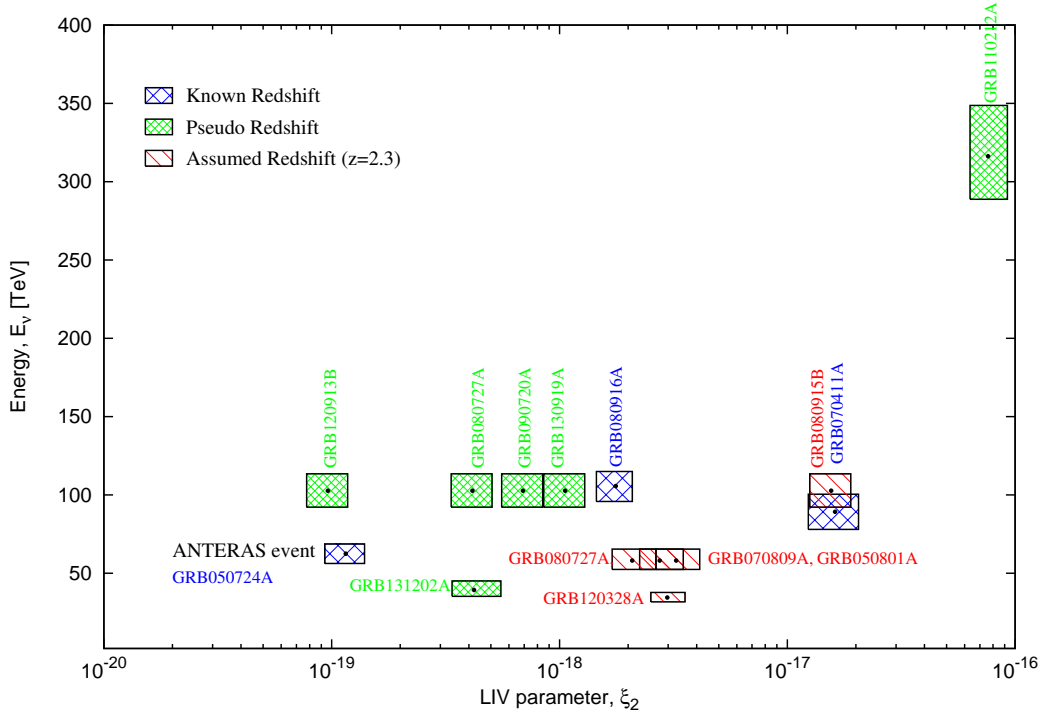


Figure 3. Similar to figure 2 but for LIV parameter ξ_2 .

redshift of the GRBs (6 GRBs) for which the peak energy, E_{peak} is the photons energy at the peak of the energy spectrum fitting the gamma-ray data in the 10 keV - 10 MeV range and S is the corresponding energy fluence (S) for the same energy range, is given publicly. The pseudo-redshift is calculated using the popular Amati relation [14], the correlation of the peak energy and isotropic energy. Particularly we have used the formula as in[15],

$$E_{peak} = 480 \left(\frac{4\pi D_L^2 S}{10^{51} \text{erg}} \right)^{0.7} \text{ keV.} \quad (4)$$

Where D_L is the luminosity distance of the GRBs. For the other GRBs we have taken an estimated value of redshift as 2.3, as the median redshift value of *Swift* [12]. The values of ξ_1 with respect to the neutrino track event energies are plotted in figure 2. The box represent the reported error in the energy of the events. The value of the LIV parameters ξ_1 varies from $5 \times 10^{-5} - 10^{-3}$ for GRB 120913B to GRB 110212A for the respective limits. The different category of GRBs that is known redshift, pseudo redshift and assumed redshift are shown with blue, green and red colored boxes respectively. A similar calculation shows that ξ_2 varies between $8 \times 10^{-20} - 9 \times 10^{-17}$.

The energy scale ($\xi_1 M_{pl}$) to explain the time delay corresponding to the ξ_1 limits is $10^{11} - 10^{13}$ GeV. This limit is not as constraining as earlier reported by *Fermi* detected gamma rays of energy GeVs for GRB 090510 and GRB 080916C [16][17] with limits $\xi_1 > 1.2$ and 0.1 respectively. However this is the first neutrino data analysis for the Lorentz invariance violation at TeV energy scale.

5. Summary

The IceCube neutrino observatory has detected at least 54 neutrino events within the 30 TeV–2 PeV energy range. The Origin of these events is still a puzzle for both particle physics and

astrophysics. On the other hand these high energy particles can probe exotic physics like a small violation in Lorentz invariance. Another high energy neutrino observatory ANTARES, has also detected a neutrino track event with an energy between 50 TeV to 100 TeV. Gamma ray bursts are promising sources for high energy neutrino. Assuming that, where GRBs correlated with the track events, assuming the neutrino events originate from the GRBs, we have calculated the LIV parameter. We found 14 times the track events correlated with the GRBs, and the result showed LIV parameter $\xi_1 M_{pl}$, to have lower limit as $10^{11} - 10^{13}$ GeV.

References

- [1] Aartsen M *et al.* (IceCube) 2014 *Phys.Rev.Lett.* **113** 101101
- [2] Halzen F 2015 Presentation *25th International Workshop on Weak Interactions and Neutrinos (Heidelberg, Germany)*.
- [3] Kopper C *et al.* 2015 *Proc. 34th Int. Conf. on Cosmic rays (The Netherlands)* PoS 1081
- [4] Waxman E and Bahcall J 1997 *Phys.Rev.Lett.* **78** 2292
- [5] Guetta D *et al.* 2004 *Astropart. Phys.* **20** 429
- [6] Amelino-Camelia G and Piran T 2001 *Phys. Lett. B* **497** 265
- [7] Jacob U and Piran T 2007 *Nature Physics* **3** p 87-90
- [8] Virmani A, Bhattacharya S, Jain P, Razzaque S, Ralston J P *et al.* 2002 *Astropart.Phys.* **17** p 489–495
- [9] Moharana R and Razzaque S 2015 *J. Cosmology and Astroparticle Phys.* JCAP08(2015)014
- [10] Dornic D *et al.* 2015 *Astronomer Telegram* -7987
- [11] Coleiro A 2017 Presentation *52nd Rencontres de Moriond on Very High Energy Phenomena in the Universe (La Thuile, Italy)*.
- [12] Krühler T *et al.* 2012 *AstroPhys. J* **758** 46
- [13] Amelino-Camelia G *et al.* 2015 *AstroPhys. J* **806** 269
- [14] Amati L 2006 *MNRAS* **372** p 233-245
- [15] Ghirlanda G, Ghisellini G and Lazzati D 2004 *em AstroPhys. J* **616** 331
- [16] Abdo A. A *et al.* 2009 *Nature* **462** 331
- [17] Abdo A. A *et al.* 2009 *Science* **323** 1688.

Investigating gamma-ray fluxes from globular clusters

H Ndiyavala^{1,2}, P Krüger¹, C Venter¹

¹Centre for Space Research, North-West University, 11 Hoffman Street, Potchefstroom, 2531, South Africa

²Department of Physics, University of Namibia, 380 Mandume Ndemufayo Avenue, Windhoek, 9000, Namibia

E-mail: hambeleleni.ndiyavala@gmail.com

Abstract. Globular clusters are large collections of old stars that are orbiting the core of a galaxy. Our Milky Way Galaxy has about 160 known clusters, with perhaps more to be discovered. We first accumulated the necessary parameters for 16 clusters and ran a numerical model that predicts the inverse Compton gamma-ray flux expected from each cluster. We also reanalysed data from 16 clusters observed by the H.E.S.S. very-high-energy (>100 GeV) gamma-ray telescopes. We confirmed the detection of Terzan 5 and found flux upper limits for the remaining 15 sources that were consistent with published results. We attempted to constrain some source parameters using X-ray and gamma-ray data. We lastly list the five most promising clusters for future observations by the Cherenkov Telescope Array.

1. Introduction

Globular clusters (GCs) are among the most ancient bound stellar systems in the Universe. GCs are tight groups of $10^4 - 10^6$ stars (e.g., [1]). They are thought to have formed during the early stages of galaxy formation. GCs are spherically distributed about the Galactic Centre with an average distance of ~ 12 kpc. They contain exotic stellar members such as black holes, millisecond pulsars, white dwarfs, and cataclysmic variables. The peculiar properties of these objects have been useful in diverse astrophysical disciplines such as cosmology, galaxy formation, stellar evolution, dynamics, as well as binary and variable stars [2, 3].

The *Fermi* Large Area Telescope (LAT), which is a gamma-ray satellite orbiting Earth, is continuously surveying the whole sky and has detected about a dozen GCs in the GeV band [4]. On the other hand, the ground-based Cherenkov telescope H.E.S.S., which is operating in a pointing mode, has only plausibly detected a single GC within our Galaxy, namely Terzan 5 [5]. Other Cherenkov telescopes could only produce upper limits in the very-high-energy (VHE) band for other Galactic GCs [6]. The future Cherenkov Telescope Array (CTA) will be about 10 times more sensitive than H.E.S.S. and is expected to see TeV emission from a few more GCs. GCs have also been detected in radio (e.g., [7]) and diffuse X-rays (e.g., [8–10]).

Our motivation is to study the detectability of 16 Galactic GCs¹ for H.E.S.S. and CTA, and to rank them according to their predicted TeV flux. In Section 2, we briefly discuss the model of Kopp et al. [12], after which follows excerpts of a parameter study to investigate the model's behaviour and to study the degeneracy between free parameters (Section 3). In Section 4 we

¹ We decided to revisit the 15 sources selected by Abramowski et al. [11] as well as Terzan 5, because new data and updated analysis methods have come available since that study was published.

present the results from reanalysing H.E.S.S. data on GCs. Section 5 includes a discussion on the parameters of Terzan 5 that we have constrained using multi-wavelength data; we then list the five most promising GCs for CTA based on their predicted VHE flux in Section 6. Our conclusions follow in Section 7. For more details, see Ndiyavala et al., *submitted*.

2. The leptonic transport and emission model for GCs

We used a multi-zone, steady-state, spherically symmetric model [12], that assumes pulsars are sources of relativistic leptons in GCs to calculate the particle transport (including diffusion and radiation losses) and to predict the spectral energy distribution (SED) expected from GCs for a very broad energy range by considering synchrotron radiation (SR), as well as inverse Compton (IC) emission. The Fokker-Planck type equation in Parker [13] prescribes the transport of charged energetic particles, i.e., electrons and positrons. Neglecting spatial convection, it is given by:

$$\frac{\partial n_e}{\partial t} = \kappa \nabla^2 n_e - \frac{\partial}{\partial E_e} (\dot{E}_e n_e) + Q, \quad (1)$$

where n_e is the electron density (per energy and volume) as a function of central radius r_s and particle energy E_e ; κ is the diffusion coefficient, \dot{E}_e denotes the radiation losses, and Q is the source term. In order to calculate the IC losses \dot{E}_{IC} , we consider blackbody soft-photon densities [14] due to the cosmic microwave background (CMB) and photons from stars with a temperature of $T_1 = 4\ 500$ K. For the stellar photons, we used the line-of-sight integral for the photon number density [12, 15],

$$n_{\varepsilon,j}(r_s, \varepsilon, T_1) = \frac{8\pi}{h^3 c^3} \frac{\varepsilon^2}{e^{\frac{\varepsilon}{k_B T_1}} - 1} \left(\frac{1}{2} \frac{N_{\text{tot}} R_\star^2}{R_c^2 \tilde{R}} \right) \int_{r'=0}^{r'=R_t} \hat{\rho}(r') \frac{r'}{r_s} \ln \left(\frac{|r' + r_s|}{|r' - r_s|} \right) dr', \quad (2)$$

where N_{tot} represents the total number of cluster stars, which can be written as $N_{\text{tot}} = M_{\text{tot}}/m$, with M_{tot} the total mass of the cluster and m the average stellar mass. Here, R_\star is the average stellar radius, R_c indicates the core radius² of the cluster, and $\tilde{R} = 2R_h - 2R_c/3 - R_h^2/R_t$, with R_h the half-mass radius³ and R_t the tidal radius⁴ of the cluster.

In the case of SR, we assumed a constant B -field to calculate the SR radiation losses. We considered Bohm diffusion

$$\kappa(E_e) = \frac{c}{3e} \kappa_B \frac{E_e}{B}, \quad (3)$$

with c being the speed of light and e the elementary charge. We also investigated diffusion coefficients of the form $\kappa(E_e) = \kappa_B (E_e/E_0)^\alpha$ where $E_0 = 1$ TeV and $\alpha = 0.6$ (e.g., [16]). Lastly we used a power-law particle injection spectrum:

$$Q(E_e) = Q_0 E_e^{-\Gamma} \quad (4)$$

between energies $E_{e,\text{min}} = 100$ GeV and $E_{e,\text{max}}$ is assumed to be ≤ 100 TeV. The value for the source strength or normalisation Q_0 were obtained using

$$\int E_e Q(E_e) dE_e = \eta \langle \dot{E} \rangle N_{\text{MSP}}, \quad (5)$$

with η the particle conversion efficiency i.e., the fraction of pulsar spin-down power that is converted to particle power, N_{MSP} the number of MSPs in the GC, and $\langle \dot{E} \rangle$ the average MSP spin-down power.

² The core radius is the distance from the centre of the cluster at which the apparent surface brightness of the cluster reduces by half.

³ The half-mass radius is the radius from the core including half of the total mass of the cluster.

⁴ The tidal radius is the distance from the cluster core beyond which the gravitational influence of the Galaxy is larger than that of the GC.

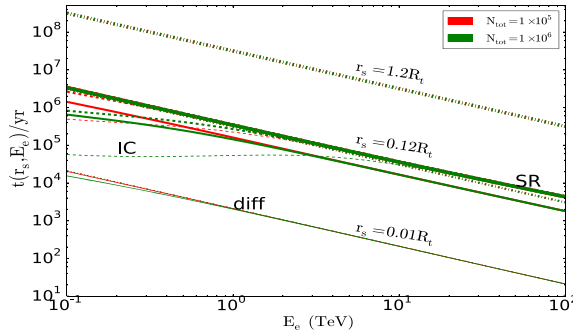


Figure 1: Timescales as a function of energy for diffusion (dotted lines), radiation losses (dashed lines), and the effective scale (solid lines). Thicker lines represent larger radii. The colours represent different values of N_{tot} as noted in the legend.

3. Parameter study

We have performed an extensive parameter study using our code. As an example, we present the effect of changing N_{tot} here. Figure 1 presents different timescales versus energy: Radiation ($\tau_{\text{rad}}^{-1} = \tau_{\text{IC}}^{-1} + \tau_{\text{SR}}^{-1}$, dashed lines, where $\tau_{\text{IC}} = E_e / \dot{E}_{e,\text{IC}}$ and $\tau_{\text{SR}} = E_e / \dot{E}_{e,\text{SR}}$), escape ($\tau_{\text{diff}} = r^2 / (2\kappa)$; dotted lines), and effective timescale ($\tau_{\text{eff}}^{-1} = \tau_{\text{rad}}^{-1} + \tau_{\text{diff}}^{-1}$); solid lines). The line thickness indicates different radii. The number density of stellar soft photons n_ϵ scales linearly with N_{tot} (see Eq. [2]). Therefore, so does the IC loss rate associated with the stellar component. This can be seen in Figure 1 at low energies. For a smaller N_{tot} , n_ϵ is lower and hence the IC loss rate drops. It therefore takes a longer time for the particles to lose energy. The IC cross section also drops as one goes from the Thomson regime at low energies to the Klein-Nishina regime at high energies. Therefore, the SR loss rate determines the effective timescale at high energies. At the smallest radii, diffusion dominates over radiation losses. At intermediate radii one can see the change in regime: for $r_s = 0.12 R_t$, with R_t the tidal radius, the SR timescale is only slightly lower than the diffusion timescale at the highest particle energies, and therefore determines the effective timescale in this case. At larger radii, n_ϵ rapidly declines (leading to smaller \dot{E}_{IC} and longer τ_{IC}) and SR losses dominate over diffusion (particle escape).

In Figure 2, at a fixed radius, the steady-state particle spectrum n_e is higher for a smaller value of N_{tot} (at low energies). This is because \dot{E}_{IC} is lower in this case. At large energies, this effect vanishes because SR cooling dominates and it is not a function of N_{tot} . At larger radii the effect of changing N_{tot} on the value of n_e is smaller, because n_ϵ and therefore \dot{E}_{IC} decreases rapidly with distance. One can see that there is a cutoff at higher energies due to SR. The cutoff energy becomes increasingly lower at larger radii since high-energy particles continue to lose energy due to SR. Furthermore, the overall level of n_e decreases with radius since it represents a particle density, and the volume scales as r_s^3 .

4. Reanalysis of H.E.S.S. data

H.E.S.S. searched for VHE signals from 15 GCs in their archival data [11] since many GC positions were covered by the H.E.S.S. Galactic Plane Survey [17] or lay in the same field of view (FoV) of other observed H.E.S.S. sources. The GC catalogue of [3] was used to select the 15 GCs which lay within 1.0° of the Galactic Plane [11]. The data runs furthermore should have passed the standard quality selection criteria. H.E.S.S. saw no significant excess emission above the estimated background for any of the 15 selected GCs. H.E.S.S. has accumulated more data since the previous analysis, and thus we decided to reanalyse the H.E.S.S. data to investigate whether we could find deeper flux upper limits which would be more constraining to our GC emission model. We compared our new results with those of the prior study [11], and found that

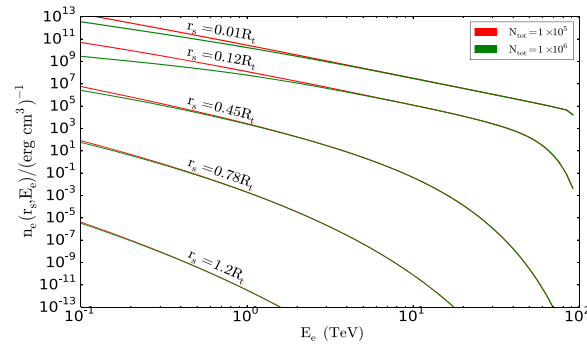


Figure 2: The steady-state particle spectrum as a function of particle energy E_e for different radii r_s .

our results on the 15 GCs were fully consistent with the earlier ones (we could not significantly detect any of the 15 GCs). We therefore decided to use the earlier published results to constrain our model parameters in what follows. We also performed a stacking analysis to search for a population of faint emitters. The total GC stack had an acceptance-corrected livetime of 644 hours of good quality data. Our new stacking upper limit was consistent with the published one [11]. We lastly studied Terzan 5, which is the only GC that has been plausibly detected at a significance of 5.3σ in the VHE band [5]. During our reanalysis of H.E.S.S. data, we confirmed the detection of Terzan 5 at a similar significance level.

5. Constraining model parameters via X-ray and gamma-ray data

We used diffuse *Chandra* X-ray and H.E.S.S. VHE gamma-ray observations to constrain cluster parameters for three sources (i.e., Terzan 5, 47 Tucanae, and NGC 6388) so as not to violate the data. As an example, we present the results for Terzan 5, using the structural parameters given in Table 1. Our model cannot reproduce the flat slope of the X-ray data. Hence, we postulate a new radiation component (see Venter et al., *in preparation*, who attribute this to cumulative pulsed SR from the individual MSP magnetospheres) to explain these data. We therefore treat the X-ray data as upper limits and our predicted SR component must lie below these. Figure 3 shows the predicted differential SED components of Terzan 5 (with gamma-ray [5] and X-ray [8] data overplotted) using three combinations of parameters: the blue lines represent the case for Bohm diffusion, $B = 5 \mu\text{G}$, $\Gamma = 1.8$, $Q_0 = 1.16 \times 10^{34} \text{erg}^{-1} \text{s}^{-1}$, $E_{e,\text{max}} = 100 \text{TeV}$; the red line represents the case for Bohm diffusion, $B = 1 \mu\text{G}$, $\Gamma = 1.8$, $Q_0 = 6.33 \times 10^{33} \text{erg}^{-1} \text{s}^{-1}$, $E_{e,\text{max}} = 20 \text{TeV}$; and the green line represents the case for $\kappa_0 = 0.7 \times 10^{-4} \text{kpc}^2/\text{Myr}$, $B = 2 \mu\text{G}$, $\Gamma = 2$, $Q_0 = 9.84 \times 10^{33} \text{erg}^{-1} \text{s}^{-1}$, and $E_{e,\text{max}} = 50 \text{TeV}$. We see that there are different parameters combinations that satisfy the observational constraints, indicating degeneracy between model parameters and the need for more low-energy data.

6. Ranking the GCs according to predicted VHE flux

We applied the model described in Section 2 to 15 non-detected GCs at TeV energies and to Terzan 5 using fixed parameters (see Table 1). We have used typical values for N_{MSP} , e.g., [18, 19], and N_{tot} values from Lang [1] and obtained distances d and structural parameters from Harris [2, 3]. We assumed Bohm diffusion, $\Gamma = 2.0$, and $B = 5 \mu\text{G}$ to produce SR and IC spectra for each individual cluster. From Figure 4 we can see that H.E.S.S. may possibly detect three GCs, i.e., Terzan 5 (orange), 47 Tucanae (blue), and NGC 6388 (green) if the telescope observes these sources for 100 hours. 47 Tucanae and NGC 6388 are currently not detected by H.E.S.S.; they were only observed for about 20 hours each. We note, however, that this flux

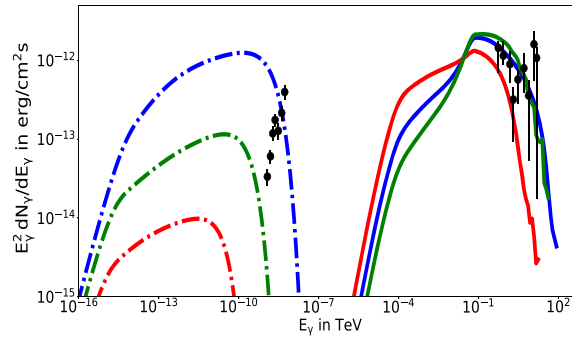


Figure 3: The SED for Terzan 5 indicating the predicted SR (integrated between $55' < r_s < 174'$ to match *Chandra* FOV, the dash-dotted lines) for the inner part of the source and IC (integrated over all r_s) components using combinations of parameters which do not violate the *Chandra* [8] and H.E.S.S. [5] data.

prediction and therefore ranking is very sensitive to the choice of parameters. The CTA will be 10 times more sensitive than H.E.S.S. and should therefore detect many more GCs (we find that more than half of the known Galactic population may be detectable, depending on observation time and model parameters). The five most promising GCs for CTA observations are NGC 6388, 47 Tucanae, Terzan 5, Djorg 2, and Terzan 10.

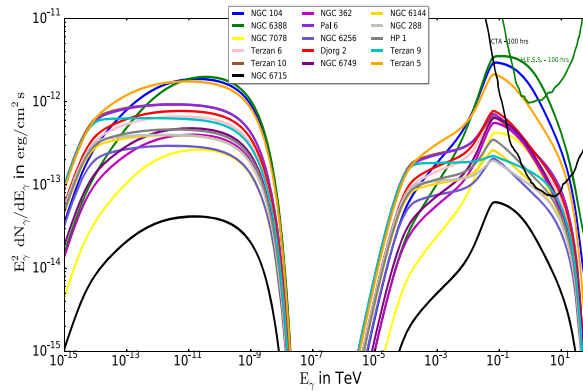


Figure 4: Predicted SED $E_\gamma^2 dN_\gamma/dE_\gamma$ in $\text{erg cm}^{-2}\text{s}^{-1}$ for 15 non-detected GCs and for Terzan 5. The two components represent the SR and IC spectra. The H.E.S.S. and CTA sensitivities (for 100 hours) are also shown.

7. Conclusion

We have briefly described an emission model that we applied to 15 GCs that have been observed, but not detected, in VHE gamma rays, as well as to Terzan 5. While the parameters of the individual GCs are uncertain (and sometimes degenerate), we noted that most of the flux predictions for the GCs are below the H.E.S.S. sensitivity limit, but that CTA may detect many more GCs (possibly tens of sources) because it will be 10 times more sensitive than H.E.S.S. Future multi-wavelength studies should allow us to constrain some parameters as well as discriminate between competing radiation models.

GC name	d (kpc)	N_{tot} (10^5)	N_{MSP}	Q_0 (10^{33} /erg/s)	R_c ($'$)	R_h ($'$)	R_t ($'$)
47 Tucanae	4.5	4.57	33	9.55	0.36	3.17	42.86
NGC 6388	9.9	5.81	180	52.1	0.12	0.52	6.21
NGC7078	10.4	4.13	25	7.24	0.14	1.00	21.5
Terzan 6	6.8	0.29	25	7.24	0.05	0.44	17.39
Terzan 10	5.8	0.38	25	7.24	0.9	1.55	5.06
NGC 6715	26.5	4.79	25	7.24	0.09	0.82	7.47
NGC 362	8.6	1.58	25	7.24	0.18	0.82	16.11
Pal 6	5.8	0.31	25	7.24	0.66	1.2	8.36
NGC 6256	10.3	0.21	25	7.24	0.02	0.86	7.59
Djorg 2	6.3	0.51	25	7.24	0.33	1.0	10.53
NGC 6749	7.9	0.24	25	7.24	0.62	1.1	5.21
NGC 6144	8.9	0.48	25	7.24	0.94	1.63	33.25
NGC 288	8.9	0.32	25	7.24	1.35	2.23	12.94
HP 1	8.2	0.48	25	7.24	0.03	3.1	8.22
Terzan 9	7.1	0.02	25	7.24	0.03	0.78	8.22
Terzan 5	5.9	8.0	34	6.33	0.10	0.72	13.27

Table 1: In this table we list structural parameters of the 16 GC. The first 15 parameters is taken from Table 1 in Venter et al. [19] and the parameters of Terzan 5 is taken from Harris [3]. The columns are cluster identification; distance in kpc; estimated number of stars [1]; number of MSPs; source strengths Q_0 ; core radius; tidal radius; and half-mass radius.

Acknowledgments

This work is based on the research supported wholly in part by the National Research Foundation of South Africa (NRF; Grant Numbers 93278, and 99072). The Grantholder acknowledges that opinions, findings and conclusions or recommendations expressed in any publication generated by the NRF supported research is that of the author(s), and that the NRF accepts no liability whatsoever in this regard.

References

- [1] Lang K R 1992 *Springer-Verlag Berlin Heidelberg New York: Astrophysical Data I. Planets and Stars*
- [2] Harris W E 1996 *AJ* **112** 1487–8
- [3] Harris W E 2010 *arXiv:1012.3224*
- [4] Nolan P L *et al.* 2012 *ApJS* **199** 31–76
- [5] Abramowski A *et al.* 2011 *A&A* **531** L18
- [6] Anderhub H *et al.* 2009 *A&A* **498** 83–7
- [7] Clapson A C, Domainko W, Jamrozy M, Dyrda M and Eger P 2011 *A&A* **532** A47
- [8] Eger P, Domainko W and Clapson A C 2010 *A&A* **513** A66
- [9] Eger P and Domainko W 2012 *A&A* **540** A17
- [10] Wu E M H *et al.* 2014 *ApJL* **788** L40
- [11] Abramowski A *et al.* 2013 *A&A* **551** A26
- [12] Kopp A, Venter C, Büsching I and de Jager O C 2013 *ApJ* **779** 126–37
- [13] Parker E N 1965 *Plan. SS* **13** 9–49
- [14] Zhang L, Chen S B and Fang J 2008 *ApJ* **676** 1210–17
- [15] Prinsloo P, Venter C, Büsching I and Kopp A 2013 *arXiv:1311.3791*
- [16] Moskalenko I V and Strong A W 1998 *ApJ* **493** 694–707
- [17] Gast H *et al.* 2011 *International Cosmic Ray Conference* **7** 158–61
- [18] Abdo A A *et al.* 2010 *A&A* **524** A75
- [19] Venter C and Kopp A 2015 *arXiv:1504.04953*

Variability in supersoft X-ray sources RX J0537.7-7034 and RX J0038.6+4020

M M Nyamai¹, A Odendaal¹, P J Meintjes¹ and A Udalski²

¹Department of Physics, University of the Free State, P.O BOX 339, Bloemfontein 9301, South Africa

²Warsaw University Observatory, Aleje Ujazdowskie 4, PL-00-478 Warsaw, Poland

E-mail: NyamaiMM@ufs.ac.za or miriamnyamai@gmail.com

Abstract. Using long term archival photometric observations from the MACHO (MASSive Compact Halo Objects) and OGLE (Optical Gravitational Lensing Experiment) projects, we find an orbital periodicity of 3.1 hrs for Large Magellanic Cloud (LMC) supersoft X-ray source RX J0537.7-7034. This establishes RX J0537.7-7034 as the supersoft X-ray source with the shortest orbital period. Long term light curves of combined MACHO and OGLE observations of RX J0537.7-7034 also show a steady fading in optical light. Timing analysis performed using *XMM-Newton* archival observations of the M31 transient supersoft X-ray source RX J0038.6+4020 (s2-26) reveal a 35.8 min periodic modulation in the X-ray data.

1. Introduction

Supersoft X-ray sources (SSSs) have been established as a distinct class of X-ray sources which emit most of their energy below 0.5 keV. These sources are characterised with high X-ray luminosities of $\sim 10^{36}$ - 10^{38} erg s⁻¹ but very soft X-ray spectra of low temperatures ($kT \sim 20$ -100 eV) corresponding to blackbody temperatures of $\sim 10^5$ - 10^6 K (see the most recent review of SSS by [1]). Utilizing the Stefan-Boltzmann relation between luminosity and temperature, it was established that the SSSs radii were of the order $R = 10^{10}$ cm, comparable to those of a white dwarf (WD) [2].

It has thus been suggested that the luminous supersoft sources consist of a WD accreting mass from a Roche-lobe filling companion star, with the material on the surface of the WD undergoing stable nuclear hydrogen burning [2]. In order to sustain the hydrogen burning on the surface of the WD, the accretion rate should be of the order $\sim 10^{-7}$ M_⊙ yr⁻¹, which is greater than the mass transfer rates in a related class of compact WD binary systems, namely cataclysmic variables (CVs, [3, 4]). This high mass transfer rate can only be possible if the donor star has a mass equal to or greater than that of the WD. With such a high mass ratio, the secondary Roche lobe shrinks, and mass transfer occurs rapidly on the thermal time-scale of the donor. The WD should also be massive enough to support continuous burning of hydrogen on its surface.

In binary systems, mass transfer occurs through two commonly known mechanisms: Roche lobe overflow or through stellar winds from the secondary star.

In this paper, we discuss optical and X-ray variability in SSSs RX J0537.7-7034 in the Large Magellanic Cloud (LMC) and RX J0038.6+4020 (s2-26) in M31. This paper is structured as

follows: In §2, a brief literature review of the sources is presented. Archival photometric data of RX J0537.7-7034 from the MACHO (MASSive Compact Halo Objects) and OGLE (Optical Gravitational Lensing Experiment) projects is presented in §3, together with an updated orbital ephemeris for this source. Timing analysis of *XMM-Newton* X-ray data of RX J0038.6+4020 (s2-26) is presented in §4, followed by the conclusions in §5.

2. RX J0537.7-7034 in the Large Magellanic Cloud and RX J0038.6+4020 (s2-26) in M31

ROSAT PSPC and *XMM-Newton* EPIC-pn spectra of RX J0537.7-7034 (hereafter RXJ0537) fitted with a blackbody model are characterised by a temperature between ~ 18 -57 eV and a bolometric luminosity of $(0.6-1.2) \times 10^{37}$ erg s $^{-1}$ with most of the X-ray energy emitted below 0.5 keV [5, 6]. The orbital period of RXJ0537 was first established as 3.5 hours, with the orbital ephemeris given by [7]

$$T_0 = \text{JD} (2451203.6392 \pm 0.0040) + (0.147275 \pm 0.0038)E \text{ days.}$$

RX J0038.6+4020 (hereafter s2-26) is also a ROSAT observed source classified as a supersoft X-ray source through hardness ratio criteria. The transient nature of the source in the X-ray waveband was established by three observations by the *Chandra* X-ray observatory from 2000 to 2001, since the source was only detected in one of these observations, i.e. in March 2001 [8]. No periodic modulations have been reported for this X-ray source yet.

3. MACHO and OGLE observations of RXJ0537

RXJ0537 was monitored by the MACHO project with observations performed with the 1.27-m Great Melbourne telescope at Mount Stromlo Observatory in Australia from 1992 to 2000. The MACHO project is a survey that was used to monitor the Large Magellanic Cloud (LMC) and Small Magellanic Cloud (SMC) for microlensing events [9]. This telescope provides CCD photometry in the ‘red’ band ~ 6300 -7600 Å and the ‘blue’ band ~ 4500 -6300 Å. The two-colour instrumental magnitudes were transformed to the standard Kron-Cousins *R* and *V* passbands.

RXJ0537 was also observed using the 1.3-m Warsaw telescope at Las Campanas Observatory, Chile as part of the OGLE project, which is still ongoing¹. The photometric observations of the OGLE project are taken in the *I* passband (~ 7000 -9000 Å). This project has been in operation since 1992 in phases I (1992-1995), II (1997-2000), III (2001-2009) and IV (2010 up to now). OGLE I was a pilot project and its observations were restricted to the Galactic Bulge. OGLE II observations provide an overlap with the MACHO data.

3.1. MACHO and OGLE light curves of RXJ0537

We show in figure 1 the light curves of RXJ0537 from both MACHO and OGLE observations. The observation dates were converted to Barycentric Julian Date in the Barycentric Dynamical Time (BJD_{TDB}) which corrects the arrival time of photons to the Solar system barycentre [10]. Note the slow decline in optical magnitude of the X-ray source.

3.2. Period analysis and folded light curve

Each light curve in the MACHO *V*-band, *R*-band and OGLE II, III, IV was analysed using the Starlink PERIOD package² which has analysis options including detrending the data, the task SCARGLE to create Lomb-Scargle (LS) periodograms [11, 12], and also the task FOLD to fold any data with a given period. The long-term fading was removed by subtracting a 2nd-order

¹ <http://ogle.astrouw.edu.pl/>

² www.starlink.rl.ac.uk/star/docs/sun167.htx/sun167.html

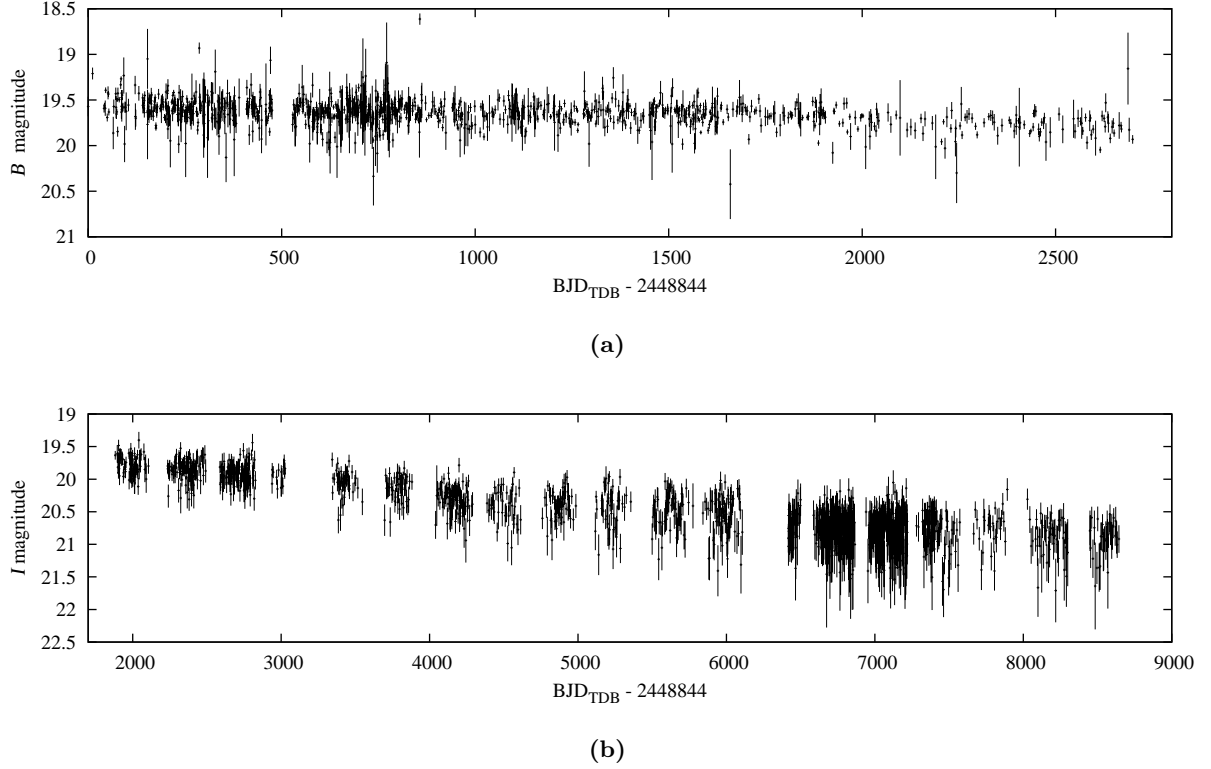


Figure 1: The optical light curve of RXJ0537 from MACHO project observations (top), and OGLE II, III and IV observations (bottom).

polynomial before getting periodograms from the light curves. The MACHO *V*-band, *R*-band and OGLE II and III periodograms showed a strong power peak at $P_{\text{orb}} = 0.1286836$ d. In the OGLE IV periodogram, the periodicity is hardly seen. Since a longer baseline enables one to obtain a more accurate value for the period, we decided to combine the detrended MACHO *R*-band and OGLE II+ III *I*-band light curves.

However, to compensate for the different filters of MACHO and OGLE, both these light curves were further detrended separately by subtracting the mean and dividing by the standard deviation, to yield light curves varying around 0, with a standard deviation of 1. Subsequently, the resulting MACHO and OGLE II+ III light curves were combined, removing the OGLE II points overlapping with MACHO, so as to yield a continuous light curve. The resulting periodogram is shown in figure 2 (a), exhibiting a very strong peak at $P_{\text{orb}} = 0.1286836 \pm 0.0000014$ d (3.08841 ± 0.00003 hrs) at a $\gg 99.99\%$ significance. The folded light curve is shown in figure 2 (b), exhibiting a quasi-sinusoidal orbital modulation. In order to constrain the time of minimum light, a sinusoid was fitted to the folded light curve, yielding the following updated ephemeris:

$$T_0 = \text{BJD}_{\text{TDB}} (2448844.3044 \pm 0.0075) + (0.1286836 \pm 0.0000014)E \text{ days}$$

where T_0 is the time of minimum light when the companion is closest to the observer.

3.3. Discussion

With the obtained orbital period and the radial velocity semi-amplitude of the He II $\lambda 4686$ emission-line of $K_1 = 115 \text{ km s}^{-1}$ [7], we estimate a small mass function of $0.020 M_{\odot}$ for

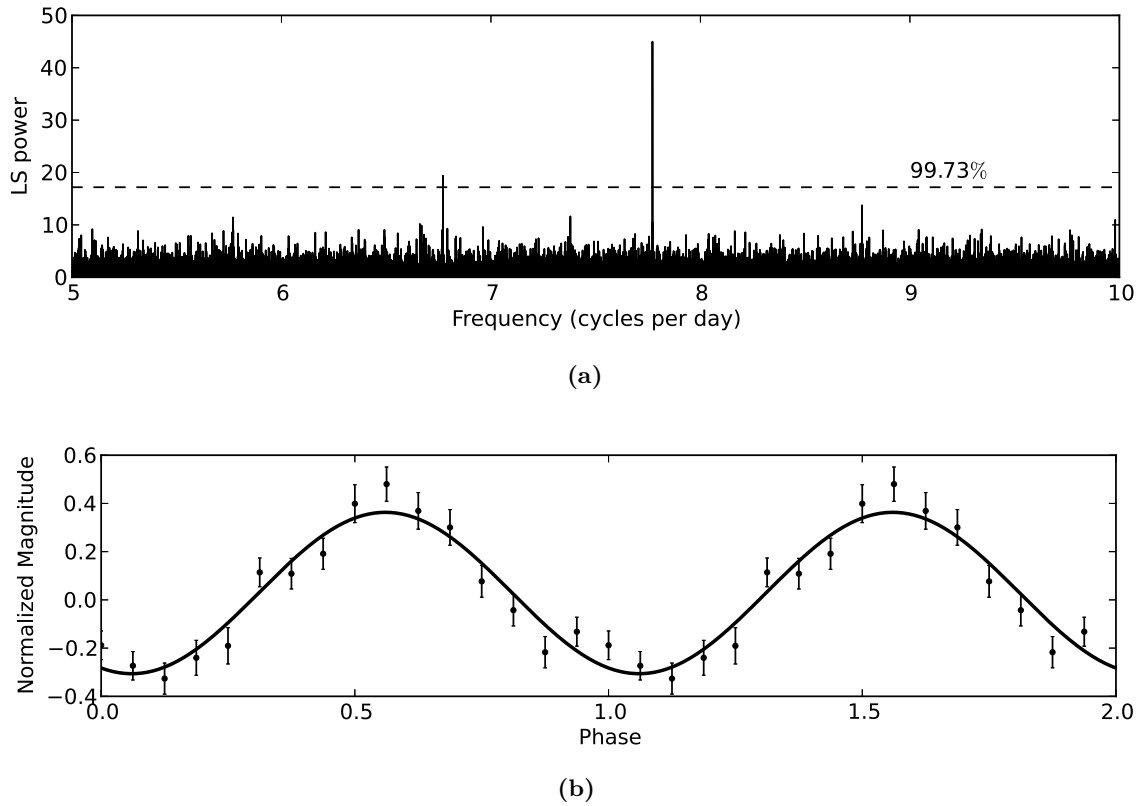


Figure 2: (a) Lomb-Scargle periodogram of RXJ0537 obtained from the combined MACHO and OGLE II+ III observations. The 99.73% significance level is indicated. Note the strong peak at $P_{\text{orb}} = 0.1286836$ d. (b) MACHO and OGLE II+ III orbital phase diagram of RXJ0537 folded on a period of $P_{\text{orb}} = 0.1286836$ d. The data have been averaged into 16 bins and fitted with a sinusoid with its period fixed at this value.

RXJ0537 implying a small mass donor star. In this case it has been assumed that the motion of the He II emission line represents the motion of the WD. However, this might not be the case if the emission line is due to the interaction of a wind from the accretion disc and that from the heated side of the donor. This would thus result in a significant underestimation of the mass function. In addition, when estimating the mass function, the semi-amplitude value of 115 km s^{-1} , which was derived by [7] with a corresponding period of 3.3 hrs was used. It is therefore possible that the used value of the semi-amplitude is slightly different from the one that would correspond with the derived period of 3.1 hrs.

The updated orbital period of 3.1 hrs of RXJ0537 confirms that this X-ray source is a very compact binary system and thus the masses of the two stars are not in the range of most known SSSs. Given that most known SSSs have mass ratios of $q \gtrsim 0.83$, where $q = M_{\text{donor}}/M_{\text{accretor}}$, the high mass transfer occurs when the Roche lobe of the donor star shrinks. This kind of mass transfer is very unstable and occurs on the thermal time-scale of the secondary star [2]. For binaries like RXJ0537 where the system is too small to host such a massive secondary, other methods of mass transfer like the wind-driven binaries should be considered [13]. The observed decline in the optical could be attributed to a decrease in mass transfer in the binary system.

Table 1: *XMM-Newton* observations of s2-26, with the Lomb-Scargle analysis results.

Observation ID	Start date time (UT)	Exposure time (ks)	Mean EPIC-pn counts/s	Period & error (mins)	Significance (%)
0402560101	2006-06-28 07:02:51	60.9	0.0060 ± 0.0041	-	-
0505760101	2007-07-24 17:28:34	58.9	0.0037 ± 0.0013	-	-
0511380101	2008-01-02 10:59:10	45.9	0.0044 ± 0.0011	35.8 ± 0.83	96.7

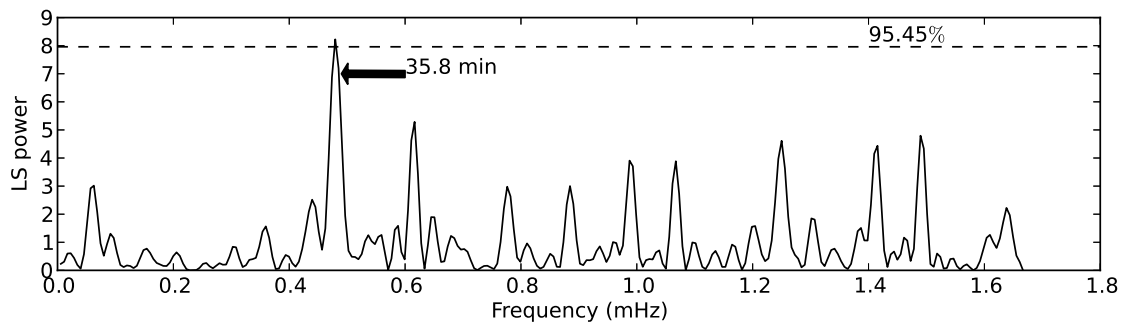


Figure 3: Lomb-Scargle periodogram of the EPIC-pn light curve from observation 0511380101 of s2-26, showing a significant peak of 35.8 mins. The 95.45% significance level is indicated. A light curve bin size of 300 s was used.

4. *XMM-Newton* observations of s2-26

4.1. Observations and timing analysis

s2-26 was observed by *XMM-Newton* in 2006, 2007 and 2008. The data was calibrated using standard data reduction procedures with SAS v. 12.0.1³ to produce EPIC-pn light curves in the energy range 0.15-2.5 keV. Every EPIC-pn light curve was detrended by subtracting a 2nd-order polynomial. Detrended light curves with different bin sizes were used to search for any form of variability. The SCARGLE task in the Starlink PERIOD package was used to create a Lomb-Scargle (LS) periodogram for each light curve. A periodicity of 35.8 min was evident in the observation performed in 2008, as shown in figure 3 and table 1.

The peak was also present when testing other bin sizes. The observations of s2-26 in 2006 and 2007 did not show any significant peaks. The mean EPIC-pn count rates for s2-26 did not show significant long-term variability between the three *XMM-Newton* observations performed in 2006, 2007 and 2008. This is contrary to what was reported by [8]. The ROSAT survey of M31 was done in 1991 and 1992, and *Chandra* observed it 9-10 years later. Given that this source was detected in *XMM-Newton* suggests that it has been active for close to 20 years.

4.2. Discussion

Periodic modulations on time-scales of minutes to hours have been reported previously in SSSs. CAL 83, which is the prototype of this class of binaries, has shown periodic pulsations of 1-300 mins from timing analysis of *XMM-Newton* data [14, 15]. A ~38.4 min period of CAL 83 reported from *Chandra* data timing analysis in [16], is interestingly close to the 35.8 min period

³ <http://www.cosmos.esa.int/web/xmm-newton>

in s2-26. The ~ 38.4 min period of CAL 83 has been associated with WD non-radial g -mode (internal gravity waves) pulsations [16]. Seismic waves in pulsating stars are classified depending on the restoring forces; g -modes, f -modes have gravity and negative buoyancy while p -modes are characterised with pressure gradient forces [17].

Non-radial pulsations have also been observed in dwarf novae [18], and it has been shown that novae undergo a supersoft X-ray phase on time-scales of up to 10 yrs [19]. X-ray data of these WD binaries have shown pulsations on time-scales of minutes. E.g. a strong ~ 41.7 min periodicity was reported in nova V1494 Aql [20], while a ~ 22.1 min modulation was found in V4743 Sgr [21]. The 35.8 min modulation in s2-26 reported here may have a similar origin.

5. Conclusions

An updated orbital ephemeris was presented for RXJ0537, with a slightly shorter period than reported before. The short orbital period of RXJ0537 and the observation of X-rays from this source present very interesting questions in terms of the accretion process that can drive very high mass transfer rates from the companion star. The process through which high mass transfer can occur in a WD binary system like RXJ0537 is still under investigation. RXJ0537 could probably represent a new class of transient supersoft X-ray sources and understanding it will contribute to a better understanding of binary evolution in general.

We found evidence of a 35.8 min modulation in X-ray data of supersoft X-ray source s2-26 which could be associated with g -mode oscillations, driven by instabilities due to thermonuclear reactions.

Acknowledgments

This work utilizes public data obtained by the MACHO project, jointly funded by the US Department of Energy, National Science Foundation through the Center for Particle Astrophysics at the University of California and Australian National University. M M Nyamai would like to thank Dr. Andrzej Udalski for providing us with the OGLE data. The financial assistance of the National Astrophysics and Space Science Programme (NASSP) towards this research is hereby acknowledged.

References

- [1] Kahabka P and van den Heuvel E P J 2006 *Compact stellar X-ray sources (Cambridge Astrophysics Series vol 39)* ed Lewin W H G and van der Klis M (New York: Cambridge University Press) chap 11, pp 461–474
- [2] Van den Heuvel E P J, Bhattacharya D, Nomoto K and Rappaport S A 1992 *A&A* **262** 97–105
- [3] Warner B 1995 *Cataclysmic Variable Stars* 28 (Cambridge University Press)
- [4] Hellier C 2001 *Cataclysmic Variable Stars-how and why they vary* (Springer Science & Business Media)
- [5] Kahabka A, Haberl F, Pakull M, Millar W C, White G L, Filipović M D and Payne J L 2008 *A&A* **482** 237
- [6] Orio M and Ögelman H 1993 *A&A* **273** L56–L58
- [7] Greiner J, Orio M and Schwarz R 2000 *A&A* **355** 1041–48
- [8] Di Stefano R *et al.* 2004 *ApJ* **610** 247–260
- [9] Alcock C *et al.* 1999 *The Astronomical Society of the Pacific* **111** 1539–58
- [10] Eastman J, Siverd R and Gaudi S B 2010 *The Astronomical Society of the Pacific* **122** 935–946
- [11] Lomb N R 1976 *Astrophysics and space science* **39** 447L
- [12] Scargle J D 1982 *ApJ* **263** 835–853
- [13] van Teeseling A and King A R 1998 *A&A* **338** 957–964
- [14] Odendaal A and Meintjes P J 2015 *Mem. S.A.It.* **86** 102
- [15] Odendaal A, Meintjes P J, Charles P A and Rajoelimanana A F 2014 *MNRAS* **437** 2948–56
- [16] Schmidtke P C and Cowley A P 2006 *AJ* **131** 600–602
- [17] Córscico A H 2009 *Boletín de la Asociación Argentina de Astronomía La Plata Argentina* **52** 317
- [18] Warner B and Woudt P 2005 *The Astronomical Society of the Pacific conference series* **334** 453
- [19] Orio M, Parmar P A N, Greiner J, Ögelman H, Starrfield S and Trussoni E 2002 *MNRAS* **333** L11–L15
- [20] Drake J J *et al.* 2003 *ApJ* **584** 448–452
- [21] Ness J U *et al.* 2003 *ApJ* **594** L127–L130

Identifying new narrow-line Seyfert 1 galaxies and white dwarfs from the second ROSAT all-sky survey catalogue

A Odendaal¹, T Boller², F Haberl² and P J Meintjes¹

¹Department of Physics, University of the Free State, P.O. Box 339, Bloemfontein, 9300, South Africa

²Max-Planck-Institut für extraterrestrische Physik, Giessenbachstraße, D-85748 Garching, Germany

E-mail: WinkA@ufs.ac.za

Abstract. The second ROSAT all-sky survey source catalogue (2RXS) has now been released. From the $\sim 135\,000$ sources in this catalogue, a selection of sources has been made with power law photon indices steeper than 3. This resulted in a sample of 1025 sources, representing the softest sub-sample of the 2RXS catalogue (ss2RXS). These selection criteria were chosen with the purpose of potentially identifying a new sample of narrow-line Seyfert 1 galaxies (NLS1s). However, there are also other sources with similar X-ray properties: mostly white dwarfs (WDs), but also some other bright stars. A conclusive distinction can be made between the different classes by means of optical spectroscopy, but in order to perform a pre-classification, existing archival data was utilized. A pre-classification system based on AllWISE infrared magnitudes and colours was developed, providing a reliable method of distinguishing NLS1s from WDs. We can thus obtain a preliminary classification for most of the unidentified sources in the ss2RXS sample, providing a basis for the planning of follow-up spectroscopic studies.

1. Introduction

Seyfert galaxies are mostly spiral galaxies, hosting an active galactic nucleus (AGN). Seyfert galaxies are classified as either Type 1, with both broad and narrow emission lines, and Type 2 with only narrow lines (e.g. [1, pp. 140-142]). The broad lines (full-width half maximum or $\text{FWHM} \sim 1000\text{-}10000 \text{ km s}^{-1}$) are formed in the broad line region (BLR), which is believed to be a region of rapidly moving clouds close to the black hole. The narrow lines ($\text{FWHM} \sim 300\text{-}500 \text{ km s}^{-1}$) are formed in the less dense, lower-velocity narrow line region (NLR) much further away from the black hole. The accretion disc is surrounded by a big dust torus. For Type 2, the AGN is observed from the side, with the BLR obscured by the torus. For Type 1, the observer looks more or less face on towards the disc, seeing both the NLR and BLR.

Narrow-line Seyfert 1s (hereafter NLS1s) form a subclass of Seyfert galaxies (e.g. [2]). The two general defining criteria for NLS1s are: (i) the broad components of the Balmer emission lines are narrower than in the classical broad-line Seyfert 1s (BLS1s), with $\text{FWHM}_{\text{H}\beta\text{br}} < 2000 \text{ km s}^{-1}$ (in fact, they are only slightly broader than the forbidden lines such as [O III], [N II] and [S II]), and (ii) the forbidden [O III] $\lambda 5007$ emission is quite weak, with the ratio $R_{5007} = \text{EW}_{[\text{O III}]} / \text{EW}_{\text{H}\beta}$ being smaller than 3 (EW=equivalent width) [3, 4]. NLS1s often exhibit strong Fe II emission,

e.g. the multiplets at 4570, 5190 and 5300 Å, anti-correlated with $EW_{[\text{OIII}]}$ and $\text{FWHM}_{\text{H}\beta\text{br}}$. It was also suggested that a more meaningful distinction can be made between NLS1s and BLS1s by using the strength of the Fe II $\lambda 4570$ blend between 4434 and 4684 Å, with $R_{4570} = EW_{\text{FeII}\lambda 4570}/EW_{\text{H}\beta} > 0.5$ for NLS1s [5].

AGNs are characterized by emission over an extremely wide range of energies in the electromagnetic spectrum, from radio to gamma-ray, including strong X-ray emission (e.g. [6, Chapter 14]). The X-ray spectra are usually fitted with a power-law, with typical values of the photon index Γ in the ~ 1.5 - 2.5 range (e.g. [7] and references therein). In figure 8 of [8], Γ is plotted versus $\text{FWHM}_{\text{H}\beta}$ for Seyfert 1s. Below a FWHM of 2000 km s^{-1} , the photon index rises from ~ 2.3 up to ~ 5 . This plot also illustrates that objects with photon indices above ~ 3 are almost exclusively NLS1s, making X-ray selection a very robust method to find new NLS1s.

NLS1s are thought to be quite young AGNs in their early evolutionary stages [9], harbouring low- or intermediate-mass black holes [10] accreting at rates as high as 10%-100% of the Eddington rate or even higher [11]. NLS1s thus represent an important link with the intermediate mass black holes, which have not been studied well so far. The very steep soft X-ray spectra of NLS1s are in fact due to their smaller black hole mass, and high accretion rates.

While for $\Gamma \gtrsim 3$ the BLS1s are not included in the sample, such a soft X-ray sample can also be expected to include another major source class, i.e. white dwarfs (WDs) (e.g. [12]). X-ray spectra of isolated WDs are characterized by very soft emission, which can be parametrized with blackbody models with typical temperatures of $kT \sim 20$ - 100 eV . Therefore, only the Wien tail of the spectrum is detected by the ROSAT PSPC, which cannot be distinguished from a steep power law due to insufficient energy resolution. This also applies to WDs in binaries, including interacting binaries like cataclysmic variables, where the accretion process is also associated with soft X-ray emission, and supersoft X-ray sources, where the nuclear burning of accreted hydrogen on the WD surface yields a high supersoft X-ray flux (e.g. [6, Chapter 10]).

In this paper, we describe the search for sources with unusually soft X-ray spectra, by utilizing the $\Gamma \gtrsim 3$ threshold in the second ROSAT all-sky survey source (2RXS) catalogue. In §2, a summary of the 2RXS catalogue is presented, together with a description of the selection of its softest sub-sample (the ss2RXS sample). In §3, the AllWISE infrared properties of confirmed NLS1s and WDs samples are described, followed by a discussion of how these properties can be used to distinguish NLS1s from WDs among unidentified sources in the ss2RXS sample. Our preliminary results for the ss2RXS sample is presented in §4, with the final conclusions in §5.

2. The 2RXS catalogue, and the selection of the ss2RXS sample

The 2RXS catalogue [13] is the second publicly released ROSAT catalogue of point-like sources detected during the ROSAT all-sky survey observations between June 1990 and February 1991, and contains $\sim 135\,000$ reliable source detections. The photon event files from the ROSAT all-sky survey have been re-analysed. The main goal was to create a catalogue of point-like sources, which is more reliable than the 1RXS catalogue [14, 15]. The reliability of detections was improved by an advanced detection algorithm and a complete screening process. With the publication of the 2RXS catalogue and its data products, the detailed science specific exploration is now available for the astrophysical community. The 2RXS is the deepest and most reliable X-ray all-sky survey catalogue before the launch of eROSITA.

New data products were created to allow timing and spectral analysis. Three different spectral models were fitted to the spectrum of each source: (i) a power law, (ii) an optically thin plasma emission model, and (iii) an optically thick blackbody model. The best-fit parameters for each model, with their associated errors, are also available in the released catalogue. The most interesting objects were listed in terms of their timing and spectral properties. The science themes include (i) AGN physics (timing and spectral properties down to the lowest fluxes, multi-wavelength properties, optical follow-up programmes with e.g. SDSS data); (ii) normal

galaxies (spectral properties, galaxy interactions); (iii) Galactic binaries, cataclysmic variables, neutron stars; (iv) timing properties from individual light curves of stars, and (v) search for ultra-soft X-ray emitters.

Following the motivation given in §1, a selection of sources was made from the main 2RXS catalogue, using the criteria of $\Gamma \geq 3$ for the power law fit, and the error in the best fit Γ -value also had to be smaller than 1.5. This yielded a sample of 1025 objects, representing the softest source sample from 2RXS (the ss2RXS sample).

3. AllWISE colours

It is well known that infrared colours provide a powerful method of distinguishing AGNs from other objects (see e.g. the work of [16]). Since the ss2RXS sample is expected to contain a substantial amount of NLS1s and WDs, a comparison of the infrared properties of known samples of these two classes was performed. The goal of this initial investigation was to evaluate the possibility of distinguishing between NLS1s and WDs by using only infrared properties.

3.1. The AllWISE colours of spectroscopically confirmed NLS1 and WD samples

The Sloan Digital Sky Survey (SDSS) provides photometric and spectroscopic data for a large fraction of the sky, making it a very powerful survey for identifying and studying large samples of sources from different object classes. The number of known NLS1s was increased by a factor of ~ 10 in 2006 with the publication of a sample of 2011 confirmed NLS1s from the spectroscopic sample of the SDSS Data Release 3 (DR3) [17, hereafter Z06]. In 2013, a new catalogue of 19 712 spectroscopically confirmed WDs was released, based on the SDSS DR7 [18, hereafter K13]. This catalogue consisted mainly of single WDs, but also included WDs with binary companions.

To date, the Z06 and K13 catalogues are the largest and most recent spectroscopically confirmed samples of NLS1s and WDs respectively. These samples were subsequently utilized as “training sets”. For each training set, a cross-correlation with the AllWISE catalogue [19] was performed with the CDS XMatch Service¹, using a search radius of 2 arcsec. It was found that 2006 of the 2011 Z06 NLS1s have AllWISE counterparts (i.e. 99.8%), while only 3022 of the 19 712 K13 WDs have AllWISE counterparts (15.3%).

The AllWISE catalogue contains not only the WISE $W1$, $W2$, $W3$ and $W4$ magnitudes, but also the 2MASS J , H and K magnitudes, for those cases where the source was also observed and detected with 2MASS. Various different combinations of colour-colour and colour-magnitude plots were calculated for the Z06 and K13 samples, and it was found that they are quite well separated on 4 of these plots: $K - W1$ vs. $H - K$; $K - W1$ vs. $W1$; $W1 - W2$ vs. $K - W1$ and $W1 - W2$ vs. $W1$ (figure 1). Only actual detections in each filter were used for these plots: if only upper limits were available, the source was not included. The colours of the Z06 NLS1s agree very well with the known colours of broad-line AGN candidates in general [16].

Each of the 8 scatter plots in figure 1 were subsequently converted to a continuous map, for easier visualization, and especially to enable the assignment of a numerical value to each ss2RXS candidate based on its position on these maps, as described in §3.2. Each map was created by including each source (i.e. each data point) as a normalized two-dimensional gaussian with its RMS width in each dimension equal to the error of the data point in that particular dimension, over the full relevant colour-colour or colour-magnitude parameter space. The map was then divided by the peak height of the distribution, to yield a “normalized” map where the value at a certain colour-colour or colour-magnitude combination represents the distribution’s “peak height fraction” (PHF) for that combination. This PHF is not an actual probability, but does provide a comparative numerical value with which to assess the relative chance of an unknown object belonging to either the NLS1 or WD class.

¹ <http://cdsxmatch.u-strasbg.fr/xmatch>

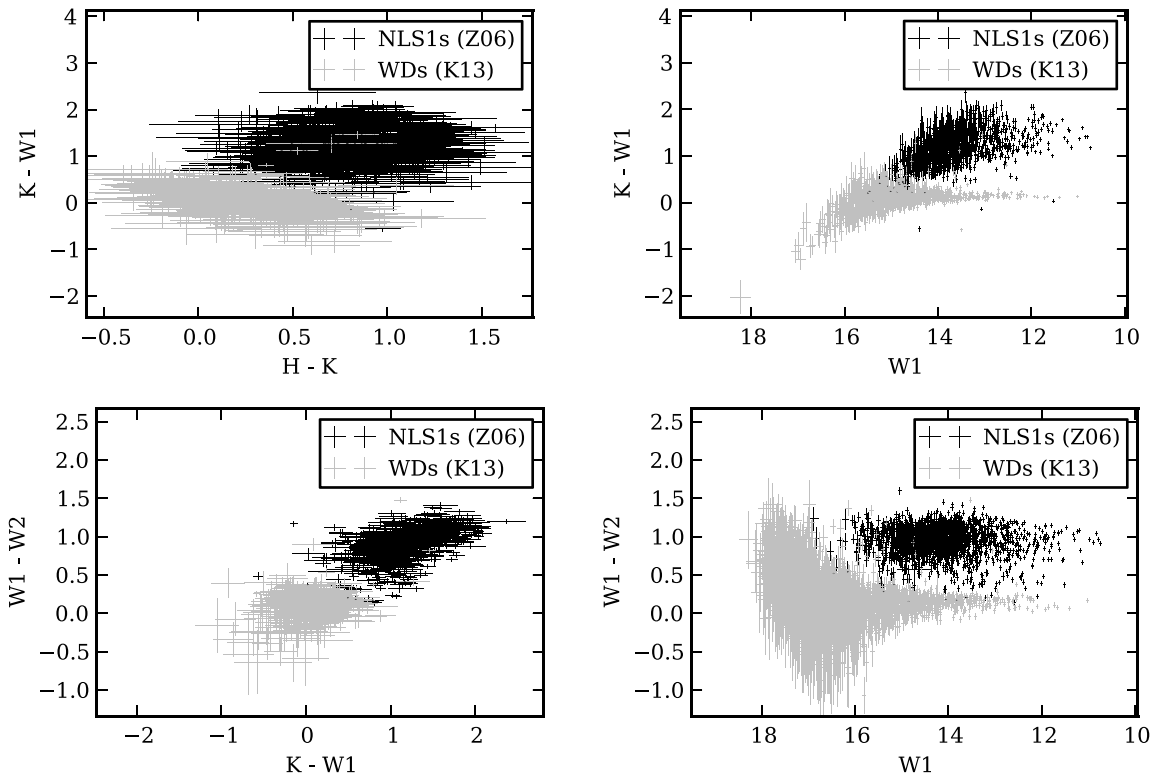


Figure 1. AllWISE colour-colour and colour-magnitude plots for the Z06 and K13 training samples. Note how each sample plots on a well defined region on each diagram, and how the two samples can be separated from each other quite well. Each data point represents one source.

3.2. Using AllWISE colours to distinguish NLS1s from WDs in the ss2RXS sample

One of the challenges in the identification of 2RXS sources with detections from other catalogues, is the relatively large positional error circle: the 1-sigma positional error for the ss2RXS sample is ~ 7 arcsec on average, but varies up to ~ 50 arcsec. Within this error circle, there are often several possible counterparts in e.g. the optical and infrared. Consequently, the AllWISE catalogue was queried for every ss2RXS source, and each AllWISE detection within a 5-sigma error radius around that source was stored in the ss2RXS database.

For each potential AllWISE counterpart, its detected magnitudes were used to calculate a mean $NLS1_{PHF}$ and mean WD_{PHF} associated with its position on the NLS1 and WD continuous maps respectively. It was mentioned previously that 99.8% of the Z06 NLS1s were detected by AllWISE. Among these, the source was detected without exception in both the $W1$ and $W2$ bands, and in the vast majority of cases in the $W3$ and $W4$ bands as well. This is to be expected, since AGN have significant emission over almost the whole electromagnetic spectrum. Therefore, one can expect that, for $\sim 99.8\%$ of NLS1s, the position of the source can be located on at least the $W1 - W2$ vs. $W1$ map, implying that a value for $NLS1_{PHF}$ can indeed be determined.

On the other hand, only 15.3% of the K13 WDs were detected with AllWISE. Among this 15.3%, every single one was detected in $W1$, but some not in $W2$, and most of them not in $W3$ and $W4$. This implies that most WDs will not be detected by AllWISE, and for some of those detected, the calculation of a WD_{PHF} value might not be possible. However, this does yield the very useful conclusion that, if an infrared source with an $NLS1_{PHF}$ indicating NLS1 membership is not present near a certain ss2RXS source, that ss2RXS source is highly unlikely to be an NLS1, and belongs to a different class, possibly being a WD.

4. The nature of the ss2RXS sample: preliminary results

In addition to the cross-match with AllWISE described in the previous section, all potential counterparts within a 5-sigma positional error circle of each ss2RXS source were extracted from the following catalogues, and stored in the ss2RXS database: the *XMM-Newton* Serendipitous Source Catalogue, 3XMM-DR4 [20], the *XMM-Newton* slew survey catalogue, XMMSL1 [21], the *Chandra* Source Catalog, Release 1.1 [22], the 1SXPS *Swift* X-ray telescope point source catalogue [23], the Second ROSAT PSPC Catalog², the ROSAT HRI Pointed Observations³, the CDS Simbad Astronomical Database [24], the catalogue of Quasars and Active Galactic Nuclei [25], the updated catalogue of Spectroscopically Identified White Dwarfs of McCook+ (2008) [26], the SDSS DR7 WD catalogue (K13), and also the SDSS DR3 NLS1 catalogue (Z06).

The following procedure was then carried out for each of the 1025 sources in the ss2RXS sample: The 2RXS position, as well as all the potential counterparts from the different catalogues, together with their associated error circles, were overplotted in the Aladin Sky Atlas [27]. Firstly, the positions of any detections with other X-ray missions were considered, since the (mostly) more accurate X-ray positions from the *XMM-Newton*, *Chandra* and *Swift* catalogues enable a more accurate identification of the correct optical/infrared counterpart.

Then, together with the other X-ray detections, the positions and properties of the nearby entries from all the other catalogues mentioned above were scrutinized, with special consideration of the NLS1_{PHF} and WD_{PHF} values of the nearby AllWISE counterparts, and a series of judgements were made for the source. If a specific counterpart for the ss2RXS source could be identified from a certain catalogue with a high degree of certainty, a flag was set in the ss2RXS database indicating this counterpart. Flags were also set to indicate whether the ss2RXS source is already known as a NLS1, a WD, or a different type. For the unidentified sources, the available information was used to perform a pre-classification as being most likely a NLS1, WD or neither.

It was found that 40 sources in the ss2RXS sample are already listed as NLS1s in the Z06 catalogue, while 83 are already known as WDs. There are 370 sources with confirmed classifications as other source types, the vast majority of which are known stars with very bright optical and infrared magnitudes, the latter being brighter than 9 magnitudes in the *W1* filter (clearly outside of the NLS1 and WD regions in figure 1). However, although these bright stars make out a substantial fraction of the total ss2RXS sample, we consider it unlikely that a significant amount of the remaining unidentified sample consist of bright stars, since (i) stars with these magnitudes are mostly well documented already, and (ii) the unidentified ss2RXS sources were not observed to coincide with such bright optical and infrared objects.

Among the remaining 532 sources, a further 370 are not in the Z06 NLS1 catalogue, but are highly likely to be NLS1s. Among these, 182 are already known in general as Seyfert 1s. Another 91 sources are considered likely to be new WD candidates. For the remaining 71 unidentified sources, insufficient information was available to perform a reliable prediction at this stage. As explained in §1, figure 8 of [8] shows that Seyfert 1s with $\Gamma \gtrsim 3$ are almost exclusively NLS1s. Even though BLS1s can be expected to have similar infrared colours to NLS1s (e.g. [16]), it is therefore very unlikely that the ss2RXS sample contains BLS1s, and the vast majority of the 182 known Seyfert 1s mentioned here can be considered to be NLS1s.

The estimates obtained from this preliminary analysis provide a basis from which to perform follow-up studies of the 370 new NLS1 candidates, and 91 new WD candidates. Although correlations with several large catalogues have been performed, a detailed literature study of these 461 candidates will be performed to discern whether a few of them might already have been identified elsewhere. Where necessary, spectroscopic follow-up studies with SALT (the Southern African Large Telescope) and the 1.9-m telescope at the SAAO (South African Astronomical Observatory) are planned to confirm the pre-classification, and to investigate the new source

² <http://cdsarc.u-strasbg.fr/viz-bin/Cat?IX/30>

³ <http://cdsarc.u-strasbg.fr/viz-bin/Cat?IX/28A>

properties. The new NLS1s thus identified will be investigated by studying available multi-wavelength data, in combination with the spectral and variability information available in 2RXS, to further constrain the properties of this fascinating class. For those sources where a large 2RXS positional error circle and no other X-ray detections made counterpart identification impossible, follow-up pointings with *XMM-Newton* are planned to obtain more accurate X-ray positions.

5. Conclusion

A sample of 1025 sources with very soft X-ray spectra (the ss2RXS sample) were selected from the 2RXS catalogue. This sample was expected to contain a significant number of new NLS1 and WD candidates. By means of a rigorous analysis of the AllWISE detections of confirmed NLS1s and WDs, it has been shown that NLS1s can be successfully distinguished from WDs (and also very bright stars) on the basis of infrared colours and magnitudes. By visually screening each of the 1025 sources individually, utilizing the infrared selection method, as well as cross-correlations with other catalogues, it was found that there are potentially 370 new NLS1 candidates, and 91 new WD candidates, within the ss2RXS sample. This initial analysis and pre-classification provides a starting point for further follow-up studies of the unidentified soft 2RXS sources.

Acknowledgments

A Odendaal would like to thank the Max-Planck-Institut für extraterrestrische Physik for their hospitality and the funding provided to visit the institute to work on this research project, as well as the DST-NRF (SA-GAMMA) and the NRF KIC grant (UID 97171) for supplementary financial assistance. The authors also thank the two anonymous reviewers for their comments.

References

- [1] Ghisellini G 2013 *Radiative Processes in High Energy Astrophysics (Lecture Notes in Physics vol 873)* (Heidelberg: Springer)
- [2] Komossa S 2008 *Revista Mexicana de Astronomía y Astrofísica (Serie de Conferencias vol 32)* ed Benítez E *et al.* pp 86–92
- [3] Osterbrock D E and Pogge R W 1985 *ApJ* **297** 166–176
- [4] Goodrich R W 1989 *ApJ* **342** 224–234
- [5] Véron-Cetty M P, Véron P and Gonçalves A C 2001 *A&A* **372** 730–754
- [6] Seward F D and Charles P A 2010 *Exploring the X-ray Universe* (New York: Cambridge University Press)
- [7] Ishibashi W and Courvoisier T J L 2010 *A&A* **512** A58
- [8] Boller T, Brandt W N and Fink H 1996 *A&A* **305** 53–73
- [9] Mathur S, Kuraszekiewicz J and Czerny B 2001 *New Astronomy* **6** 321–329
- [10] Peterson B M *et al.* 2000 *ApJ* **542** 161–174
- [11] Boroson T A and Green R F 1992 *ApJS* **80** 109–135
- [12] Fleming T A, Snowden S L, Pfeffermann E, Briel U and Greiner J 1996 *A&A* **316** 147–154
- [13] Boller T, Freyberg M J, Trümper J, Haberl F, Voges W and Nandra K 2016 *A&A* **588** A103
- [14] Voges W *et al.* 1999 *A&A* **349** 389–405
- [15] Voges W *et al.* 2000 *VizieR Online Data Catalog* **9029**
- [16] Edelson R and Malkan M 2012 *ApJ* **751** 52
- [17] Zhou H, Wang T, Yuan W, Lu H, Dong X, Wang J and Lu Y 2006 *ApJS* **166** 128–153
- [18] Kleinman S J *et al.* 2013 *ApJS* **204** 5
- [19] Cutri R M *et al.* 2014 *VizieR Online Data Catalog* **2328**
- [20] XMM-Newton Survey Science Centre C 2013 *VizieR Online Data Catalog* **9044**
- [21] Saxton R D, Read A M, Esquej P, Freyberg M J, Altieri B and Bermejo D 2008 *A&A* **480** 611–622
- [22] Evans I N *et al.* 2010 *ApJS* **189** 37–82
- [23] Evans P A *et al.* 2013 *VizieR Online Data Catalog* **9043**
- [24] Wenger M *et al.* 2000 *A&AS* **143** 9–22
- [25] Véron-Cetty M P and Véron P 2010 *A&A* **518** A10
- [26] McCook G P and Sion E M 1999 *ApJS* **121** 1–130
- [27] Bonnarel F, Fernique P, Bienaymé O, Egret D, Genova F, Louys M, Ochsenbein F, Wenger M and Bartlett J G 2000 *A&AS* **143** 33–40

Investigating the hot gas in active brightest cluster galaxies

A.L. Ratsimbazafy¹, S.I. Loubser¹

¹Centre for Space Research, North-West University, Potchefstroom 2520, South Africa

E-mail: Ando.Ratsimbazafy@nwu.ac.za

Abstract. We investigate a crucial phase in the cooling–feedback cycle in the star forming Brightest Cluster Galaxies (BCGs) by looking at the optical emission line properties of the reheated gas that ultimately causes the cycle to repeat. We investigate the source(s) of ionisation of the gas as single dominant ionisation mechanism can reproduce the observed emission lines, and it is possible that a mixture of the heating mechanism(s) applies to the nebula(e). To identify the dominant ionisation processes, excitation sources, morphology and kinematics of the hot gas, more line ratios over the entire optical wavelength range are necessary. For this purpose, the spatially–resolved spectra over the entire optical wavelength range for eight nearby, active BCGs in X–ray luminous groups and clusters have been obtained with the Southern African Large Telescope (SALT). The sample was chosen to have H α detections – a strong indication of star formation activity, as well as existing data from X–ray regime available. The fundamental gas properties such as electron density, gas temperature, metallicity and several abundances were derived using the spectral features across the long wavelength range. The present optical sample will be combined with the other multi–wavelength data to form a complete view of the different phases (hot and cold gas and young stars) and how they interact in the processes of star formation and feedback detected in central galaxies in cooling flow systems, as well as the influence of the surrounding intracluster medium (ICM). Here we present our preliminary results on one of those eight BCGs, Hydra A, which shows the complexity and spatial variation of the ionisation mechanisms in the nucleus.

1. Introduction

Brightest Cluster Galaxies (BCGs) are massive early-type galaxies with high luminosities, and diffuse and extended structures. They dominate the central locations in clusters. An unknown number fraction of these galaxies is very active. This challenges our point of view of most massive early–type galaxies in clusters which are believed to be “red and dead”. Moreover, BCGs located at the centres of cool-core clusters show signs of activity, such as the presence of a small fraction of young stars, radio sources, emission–line nebulae, excess UV light, far–infrared emission from warm dust, and molecular hydrogen. Various star formation histories have been found in BCGs located in the centres of X–ray luminous clusters (e.g. in Ref [1]).

In the centre of the cool–core clusters, the hot intracluster gas is dense enough that it should cool quickly, leading to cooling flow that condenses and form stars. The cooling flows are in reality much smaller than predicted, as revealed by the X–ray observations. This is referred to as the “cooling flow problem”. The central cluster galaxies often host radio–loud AGN which may account for the necessary heating to counteract radiative cooling. Other mechanisms have

also been proposed to explain where cooling flow nebulae obtain their energy: fast shocks, self-irradiation by the cooling hot gas, turbulent mixing layers etc. The dense core of a galaxy cluster represents a unique environment, where the hot ICM is cooling most rapidly, feedback from the AGN is most effective, and the BCG dominates the mass. This represents one of the few places in the Universe where large-scale cooling and feedback processes can be readily observed. Gas accretion models in the centres of clusters have received a lot of attention lately, e.g. the “cold-gas accretion model” which has emerged as a useful framework for interpreting various observed properties of elliptical galaxies as well as BCGs in the centres of clusters.

This project is concerned with the optical emission line properties of the reheated gas that ultimately causes the cooling-feedback cycle to repeat. The heating source(s) in BCGs currently remains uncertain as no proposed heating mechanism reproduces all the emission-line properties within the optical wavelength ranges previously observed. A single dominant mechanism may not apply to all BCG nebulae, and there may be a mixture of heating mechanisms acting within a single nebula. Thus to get more information, which will enable the dominant mechanism(s) to be identified, we measured more line ratios over the entire optical wavelength range.

2. SALT & Gemini Observations and Data reduction

Our overall sample of eight targets has been selected from the literature to have H α detections and strong indications of star formation activity and observed with the SALT telescope. Each one of them has been analysed and modelled in detail. The SALT data were supplemented with existing long-slit data from Gemini/GMOS. The SALT data was obtained with the Robert Stobie Spectrograph (RSS) using PG0900 grating, with a 1.5” slit. However, the B600 grating was used on Gemini with two different central wavelength settings: 461 and 466 nm with a slit width of 0.75”. The properties and the details of the long-slit observations with SALT and Gemini telescopes are given in Table 1 and Figure 1 for Hydra A.

The details of the SALT data reductions were given in [2]. The telluric absorption features contaminating our red spectra were not corrected. The basic Gemini data reductions, which are similar to the SALT reduction, were performed with the Gemini-specific GMOS data reduction package implemented in the standard IRAF package. The spectra were binned so that each bin in the red frame had a minimum signal-to-noise ratio (S/N) of 30. The same bins were then extracted from the blue frames to ensure identical spatial locations of the bins in the blue and red frame. This delivered a S/N ratio of minimum 20 in the blue bins. Both SALT and Gemini spectra have different pixel scales. The same spatial bins were extracted in both the SALT and Gemini data, by taking the different pixels scale into account.

The emission lines and absorption lines were fitted simultaneously by adapting the fitting code GANDALF [3]. This code accurately separates the stellar continuum and absorption lines from the ionised gas emission. First, the emission line regions were masked, and it fits the spectrum using a set of best-fitting stellar templates in the library. The emission line mask is then lifted and with the stellar kinematics fixed, it reassesses the stellar continuum by simultaneously fitting a number of Gaussian emission-line templates consisting of recombination and forbidden lines.

3. Emission line analysis

3.1. Diagnostic diagrams

Standard diagnostic diagrams (BPT) [4] rely on the line ratios $I([\text{O III}]\lambda 5007)/I(\text{H}\beta)$ versus $I([\text{N II}]\lambda 6584)/I(\text{H}\alpha)$, $I([\text{S II}]\lambda\lambda 6717,6731)/I(\text{H}\alpha)$ or $I([\text{O I}]\lambda 6300)/I(\text{H}\alpha)$. These diagrams can be constructed for emission line galaxies to separate ionisation from AGN and star formation. Kewley et al. [5] used a combination of photoionisation and stellar population synthesis models to place a theoretical upper limit on the location of star forming galaxies (H II regions) on the BPT diagram. Thus, the galaxies above the Kewley’s criterion are defined as purely AGN. The AGN branch is generally associated with two populations of sources: the LINERs (low

α_{J2000}		09h18m05.7s
δ_{J2000}		-12d05m44s
z		0.055
$E(B-V)_{gal}$	(mag)	0.042
Exp. time with SALT	(seconds)	7317 R
Pixel scale with SALT	(arcsec/pix)	0.12
Resolution with SALT	($\text{\AA}/pix$)	0.95
Exp. time with Gemini	(seconds)	3600 B
Pixel scale with Gemini	(arcsec/pix)	0.14
Resolution with Gemini	($\text{\AA}/pix$)	0.91

Table 1: Hydra A properties, and the details of the long-slit observations with SALT and Gemini telescopes. The rest-frame coverage is $\sim 5000\text{--}7500 \text{ \AA}$ for the red (R), and $\sim 3500\text{--}5800 \text{ \AA}$ for the blue (B).

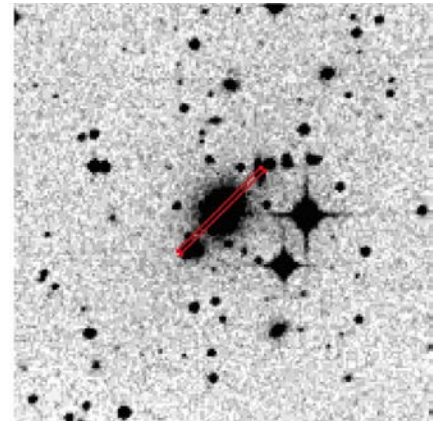
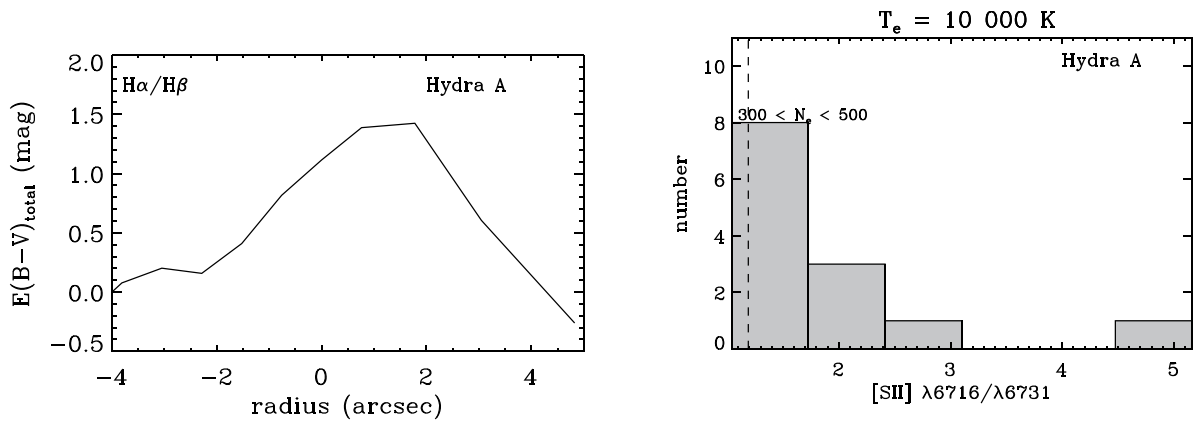


Figure 1: ESO/DSS 5 x 5 arcmin image of Hydra A with slit placement overlaid.



(a) The total extinction using $H\alpha/H\beta$ ratio. (b) Distribution of the line ratios for density. The total number of bins measured was 13.

Figure 2: Total extinction and electron density in Hydra A. The density of the gas in the centre of the galaxy is highlighted by the vertical dashed line.

ionisation emission) and Seyferts (high ionisation emission) regions. Kauffmann et al. [6] revised the Kewley's criterion to a curve below which purely H II regions exist. Thus, the area between the curves contains the composite objects.

The total extinction was derived using $H\alpha/H\beta$ relative strength ratios (in the red frames) and the dust extinction law given by [7] (see Figure 2a). We show three BPT diagrams for Hydra A in Figure 3. Different frames were added, taken at different conditions (notably seeing). This can account for a maximum of ~ 1 arcsec spread in the data points, nevertheless, a clear trend can be seen as the bins are located further from the nucleus of the galaxy. The centre of the galaxy shows LINER-like line ratio whereas the whole galaxy is classified as composite by looking at the $[N II]$ diagram. It is important to note that AGN-like line ratios can also be caused by other heating mechanisms, and the ionisation regions require more detailed modelling to disentangle the complex combination of AGN feedback, photoionisation from hot stars, and other mechanisms.

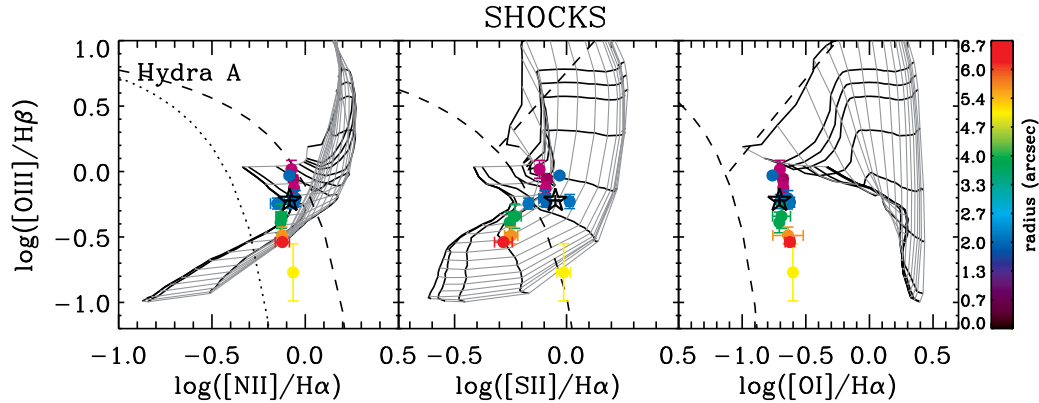


Figure 3: BPT diagrams based on $[\text{N II}]\lambda 6584/\text{H}\alpha$ (left), $[\text{S II}]\lambda\lambda 6717, 6731/\text{H}\alpha$ (middle) and $[\text{O I}]\lambda 6300/\text{H}\alpha$ (right). The black star indicates the measurement across the whole galaxy (one single extracted spectrum). The demarcation by the dashed and dotted lines separates H II regions, composites and AGN as defined by [5] and [6] (see text). The model predictions for ionisation by shocks are indicated by the grids. These model predictions are from [9] with solar metallicity, pre-shock magnetic fields B from 0.001 to 100 (dark lines), and shock velocity of V from 200 to 1000 km s^{-1} (light lines – slow to fast shocks: from left to right for $[\text{S II}]$ and $[\text{O I}]$ diagrams, and the opposite for $[\text{N II}]$ or precisely from top to bottom lines) and the densities n_e is 100 cm^{-3} .

3.2. Electron density and temperature

The most common means of estimating the electron density uses two emission lines of the same element which have different thresholds for collisional excitation. Doublet line ratios such as $I([\text{S II}]\lambda 6716)/I([\text{S II}]\lambda 6731)$ are very useful measures of electron densities in a low-ionisation scenario. These densities, n_e , are very weakly dependent on electron temperature. The density equation are iteratively solved using a technique originally developed by [8], applied with the NEBULAR package in STSDAS, layered on the IRAF environment.

Electron temperature can similarly be measured from the $I([\text{S II}]\lambda 4068 + [\text{S II}]\lambda 4076)/I([\text{S II}]\lambda 6716 + [\text{S II}]\lambda 6730)$ ratios (depending on the ionisation scenario), and is also very weakly dependent on electron density. We show the distribution of the $[\text{S II}]$ line ratios for the density in Figure 2b. The line-emitting gas in nucleus (marked by the dashed line in the plot) has densities between 300 and 500 cm^{-3} (assuming $T_e \sim 10\,000 \text{ K}$).

3.3. Oxygen lines and shocks

The $[\text{O III}]\lambda 4363$ line can be used as an indicator for shocks. Measurements of $[\text{O III}]\lambda 4363$ and He II recombination line at 4686 \AA can rule out shocks as a major ionising mechanism and point toward hot stars as the primary ionising agent in the ISM. The ratio indicative of the presence/absence of shocks is given by the ratio between the $[\text{O III}]\lambda 4363$ and the sum of $\lambda\lambda 4959$ and 5007 lines, often called R_{OIII} .

Most shock models predict this ratio to be between 0.05–0.07, e.g. in Ref [10]. Photoionisation models predict smaller R_{OIII} values because the $[\text{O III}]$ -emitting gas is cooler. At a temperature of 10 000 K, R_{OIII} is found to be about 0.005 in low density gas. We found that at the centre of Hydra A R_{OIII} does not fall into that above limit, which strongly indicates that shocks are not the dominant ionisation process. Figure 4a illustrates the radial variation of the R_{OIII} ratio.

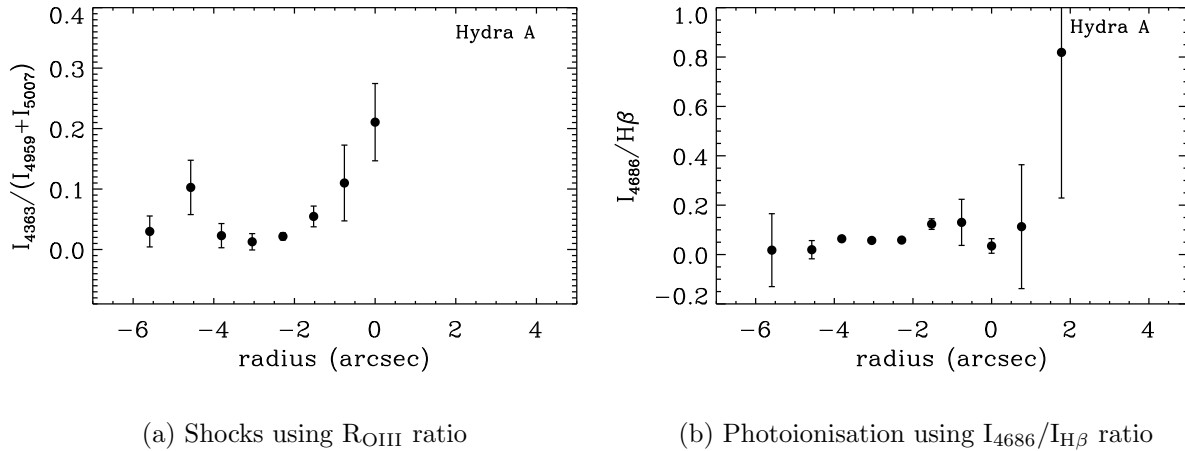


Figure 4: Model independent shocks and photoionisation.

3.4. Helium recombination lines

Our blue and red spectra contain the He II recombination line at 4686 Å and He I recombination lines at 6678 Å, 5876 Å (in red spectra) and 4471 Å (in blue spectra). He I line at 6678 Å is very weak and blended by the [S II] doublet and [N II]λ6583. The most reliable measurement to be used in this case is $I_{4686}/I_{H\beta}$ in the blue spectra. The presence of a non-negligible He II recombination line for this galaxy indicates that there is harder photoionisation near the nucleus than its edge. Figure 4b demonstrates the radial variation of the He II recombination line for Hydra A.

4. Sources of ionisation

There are several possible sources of ionisation of the hot gas in the cool-cores of galaxy clusters. The most popular ideas have been: (a) the central AGN, (b) young stellar populations, (c) X-rays from the ICM, (d) heat conduction from the ICM to the cold filament, (e) shocks and turbulent mixing layers, and (f) collisional heating by cosmic rays. In Figure 3 we show our line measurements with model predictions for shocks of various speeds and magnetic field strengths from [9]. The shock models cover the same range in [N II]/Hα and [S II]/Hα data, but overpredict [O I]/Hα. These low ionisation ratios match the centre of galaxy by slow shocks ($v \sim 200\text{--}300 \text{ km s}^{-1}$) and its edge by much faster shocks ($v \sim 400\text{--}550 \text{ km s}^{-1}$).

We show other ionisation mechanisms compared to our data in Figure 5. The first panel is the model expectations for a dust-free AGN by [11], assuming a solar and a twice solar metallicities and n_e of 100 cm^{-3} . The model with a twice solar metallicity accurately predicts the [N II]/Hα ratios, but underpredicts the [S II]/Hα and [O I]/Hα ratios. However, a model with a solar metallicity is a better fit to the data. The second panel is the model prediction for collisional ionisation by cosmic rays [12]. This model produces very low [O III]/Hβ ratios. The third panel is the model expectation for the heat conduction along the boundary between the hot ICM and the cool filaments from [13]. This model fails to produce the observed ratios. Thus, cosmic rays and conduction cannot be the dominant source of ionisation in Hydra A. It is likely, however, that a combination of ionisation processes, such as shocks and AGN, are responsible for heating the gas, and is currently studied in more detail in the model independent results in sections 3.3 and 3.4.

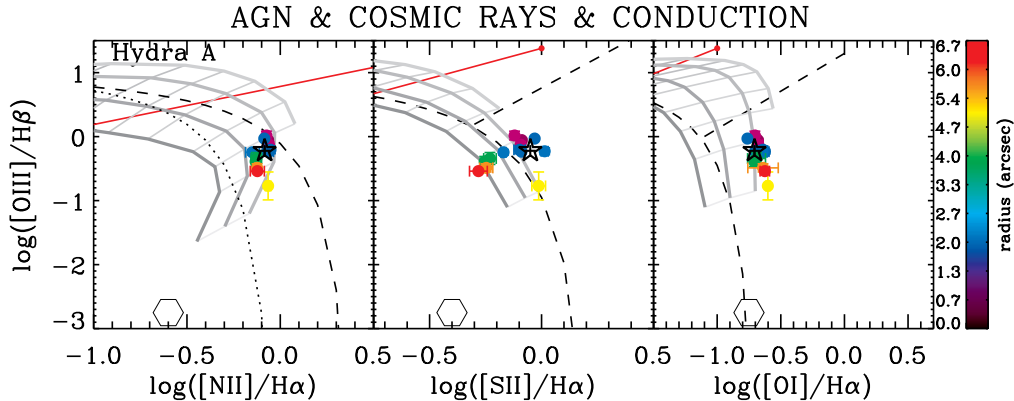


Figure 5: Similar to Figure 3, but with photoionisation by a dust-free AGN model predictions overlaid. A model with $Z = 2Z_{\odot}$ (in the left plot) and $Z = Z_{\odot}$ (in the middle and right plots), and $n_e = 100 \text{ cm}^{-3}$. The grids of photoionisation are taken from [11]. From left to the right, the power-law spectral indices of $\alpha = -2, -1.7, -1.4$ and -1.2 are indicated by the curved lines. From top to the bottom, the lines represent the ionisation parameter of $\log U = -4, -3.3, -2.6, -2, -1.3, -0.60$ and 0 . The parameter increases with $[\text{O III}]\lambda 5007/\text{H}\beta$. The conduction line (red line) is from [13] and corresponds to different initial conditions. The collisional ionisation by cosmic rays prediction is also overlaid, and indicated by a hexagon (using model predictions by [12]).

5. Conclusion

We present SALT and Gemini data for Hydra A, as part of a larger project to study eight star forming BCGs in detail, for which data has been collected mostly on SALT during a two year period. This data enables us to measure all the emission lines (with amplitude-to-noise ratio > 2) in the optical wavelength range. Our initial calculations of the hot gas properties illustrate a variety of gas kinematics and ionisation mechanisms as well as a change in hot gas properties further from the galaxy nucleus. Here, we present some preliminary results from the model independent measurements and from photoionisation models from the literature by using the BPT diagrams.

Placing the hot gas ionisation mechanisms into context with all available data from X-ray (ICM) through radio should allow for a more robust solution to this long-standing problem, while combining the hot gas kinematics with deep X-ray and radio studies may shed new light on the motions of this gas.

References

- [1] Loubser S. I., et al. 2016 *MNRAS* **456** 1565
- [2] Loubser S. I., Ratsimbazafy A. 2015 in *proceedings of SALT Science Conference PoS (SSC2015)* **015**
- [3] Sarzi M., et al. 2006 *MNRAS* **366** 1151
- [4] Baldwin J. A., Phillips M. M., Terlevich R. 1981 *PASP* **93** 5
- [5] Kewley L. J., Dopita M. A., Sutherland R. S., Heisler C. A., Trevena J. 2001 *ApJ* **556** 121
- [6] Kauffmann G., et al. 2003 *MNRAS* **346** 1055
- [7] Calzetti D., Armus L., Bohlin R. C., Kinney A. L., Koornneef J., Storchi-Bergmann T. 2000 *ApJ* **533** 682
- [8] De Robertis M. M., Dufour R. J., Hunt R. W. 1987 *JRASC* **81** 195
- [9] Allen M. G., Groves B. A., Dopita M. A., Sutherland R. S., Kewley L. J. 2008 *ApJS* **178** 20-55
- [10] Dopita M. A., Sutherland R. S. 1996 *ApJS* **102** 161
- [11] Groves B. A., Dopita M. A., Sutherland R. S. 2004 *ApJS* **153** 75
- [12] Ferland G. J., et al. 2009 *MNRAS* **392** 1475
- [13] Boehringer H., Fabian A. C. 1989 *MNRAS* **237** 1147

Correlation study of multi-wavelength transient emission of selected CRTS cataclysmic variables

H Szegedi, A Odendaal and PJ Meintjes

Department of Physics, University of the Free State, PO Box 339, Bloemfontein, 9300, South Africa

E-mail: szegedih@ufs.ac.za

Abstract. A sample of cataclysmic variable systems, showing high levels of transient emission, have been identified in the Catalina Real-Time Transient Survey archive. This study involved the identification of rapidly varying transient sources which met the criteria for intensive multi-wavelength follow-up studies. The selection criteria are discussed, as well as the PSF photometry process that was used to obtain light curves for the selected sample. The follow-up studies will be aimed at better understanding the processes driving thermal and non-thermal transient phenomena in several disc-fed and disc-less cataclysmic variable sources. Further optical observations will include photometric observations with the UFS/Boyden 1.5-m telescope at the Boyden Observatory and spectroscopic observations with the SAAO 1.9-m telescope, located at the South African Astronomical Observatory (SAAO).

1. Introduction

The Catalina Real-Time Transient Survey (CRTS) is aimed at discovering sources that undergo transient variations in brightness, e.g. cataclysmic variables (CVs), supernovae and blazars [1]. It provides a detailed survey that includes extremely faint sources of up to 20 magnitudes. The CRTS makes use of three dedicated telescopes which, combined, cover $\sim 30000 \text{ deg}^2$ of sky in the declination range of $-75^\circ < \delta < 65^\circ$. The telescopes run separate sub-surveys which are known as the Catalina Schmidt Survey (CSS), the Mount Lemmon Survey (MLS) and the Siding Spring Survey (SSS), respectively [2]. The CRTS started operating in 2007 and has since identified more than 1300 CV candidates, making it the largest sample of CVs from a single survey to date. Due to the survey's success, it is the ideal database to mine for sources that show high levels of transient emission, e.g. the CVs.

CVs are close binary systems in which a Roche lobe filling low-mass star (secondary) transfers matter to a white dwarf (WD) primary [1, 3]. These are compact systems, with a separation of $\sim 1 R_\odot$ between the binary components, and with orbital periods (P_{orb}) of a few hours or less [4]. The intensity of the WD's magnetic field determines the accretion process. CVs where the primary has a weak magnetic field ($B_\star < 1 \text{ MG}$), are known as non-magnetic CVs (NMCVs) and material is accreted via an accretion disc. If the primary has a strong magnetic field, then the CV is either an Intermediate Polar (IP) ($B_\star \sim 1 - 10 \text{ MG}$) or a Polar ($B_\star \sim 10 - 150 \text{ MG}$) [5]. Polars channel material towards the magnetic poles and IPs accrete material via a disrupted accretion disc and an accretion stream to the primary's poles.

Many CVs exhibit dramatic outbursts, which are classified according to the outburst recurrence time and magnitude range. These outbursts are essentially caused by either runaway

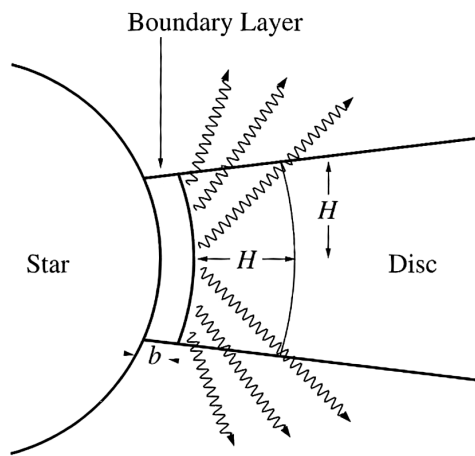


Figure 1. Schematic illustration of an optically thick boundary layer. The secondary's Roche lobe overflow is accreted by the WD with a weak magnetic field (Adopted from [8, p. 156, Fig. 6.2].

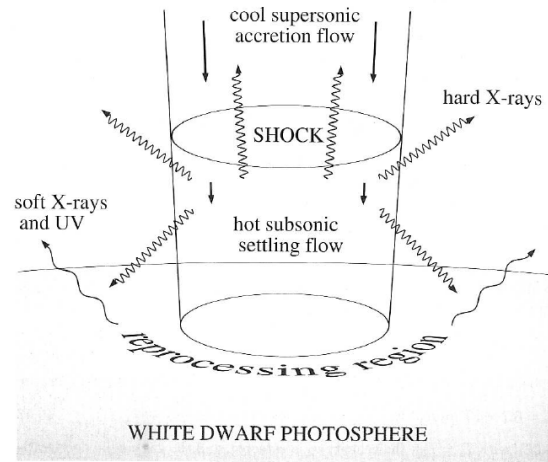


Figure 2. Schematic illustration of the accretion column typically seen in a Polar. The WD has a strong magnetic field causing accretion material to channel through the magnetic poles. (Adopted from [8, p. 178, Fig. 6.11].

thermonuclear burning of the accreted material on the WD's surface, as in classical novae (CNe) and recurrent novae (RNe), or a release of gravitational energy caused by a temporary increase in the mass transfer rate of the accretion disc, as in dwarf novae (DNe) [6]. The vast majority of these eruptive systems are NMCVs, as outbursts in magnetic CVs are rare events. V1500 Cyg (novae outburst in 1975) [7], and GK Per (dwarf nova outburst in 2015) [8], are two magnetic CVs who exhibited such eruptive behaviour. In a fourth class of systems, the so-called nova-likes, large eruptions as in novae or DNe have not been observed.

The most common CV type detected is DNe, since most CVs accrete material onto the WD via an accretion disc [2]. During an outburst, a DN shows a typical increase in brightness of 2 - 5 magnitudes. The outburst can last for a few days and recurs on a timescale of days to years [6]. DNe are sub-divided into three distinct types, namely U Gem, Z Cam and SU UMa stars. SU UMa stars occasionally have superoutbursts which last ~ 5 times as long as an ordinary outburst. The knowledge gained from monitoring CVs and studying the physical processes related to gravitation, viscosity and magnetic fields, will contribute to the understanding of e.g. planet formation and larger accreting systems, such as Active Galactic Nuclei (AGNs).

CVs emit energy almost across the whole electromagnetic spectrum [9]. The regions where the strongest emission occurs in non-magnetic and magnetic CVs are illustrated in figure 1 and figure 2, respectively. In NMCVs, the accretion disc often dominates the luminosity of the system, making the primary and secondary almost invisible in the optical spectrum. The boundary layer, which is the transition region between the accretion disc and the WD, is the region where particles decelerate to match the surface velocity of the WD. Soft X-rays and extreme ultraviolet (EUV) emission are detected from this region when the boundary layer is optically thick [6]. An optically thin boundary layer emits hard X-rays. Infrared radiation comes from the outer regions of the disc. In magnetic CVs, high energy radiation, such as hard X-rays, are emitted from a region in the accretion column where supersonic accretion flow produces a stand-off shock. Soft X-rays and ultraviolet radiation are emitted where the hot subsonic settling flow interacts with the WD's photosphere. Radio emission is also observed due to synchrotron

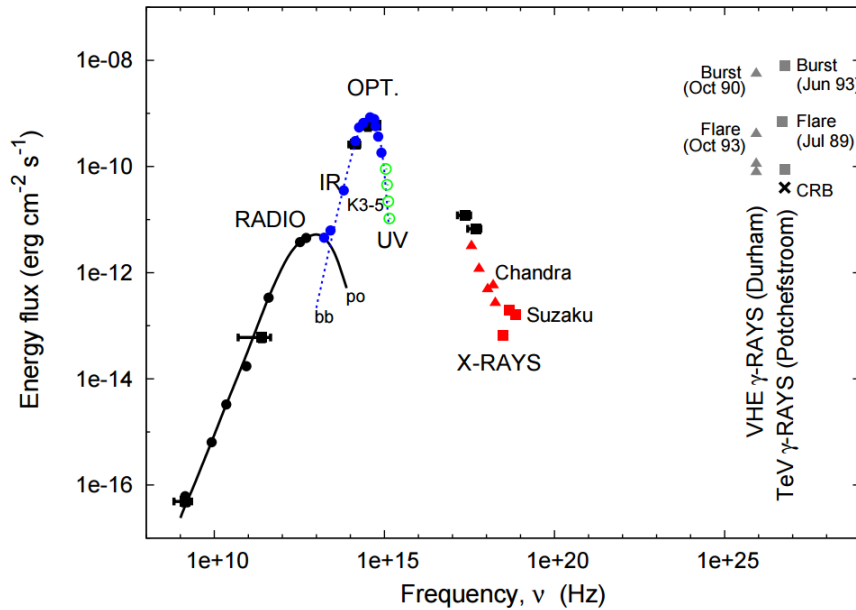


Figure 3. SED of AE Aqr (Adopted from e.g. [9, p. 645, Fig. 4]).

or cyclotron radiation (e.g. [2]). A fascinating magnetic CV in its propeller phase, AE Aqr, is one of a few CVs to date that have been studied from radio to TeV gamma-rays [11]. Figure 3 shows the spectral energy distribution (SED) of AE Aqr. Multi-wavelength studies are therefore essential to fully understand the different processes in these systems.

For this study in general, the parameters we want to determine are the orbital periods and WD spin periods, the accretion rate, and particularly the fraction of accretion power that may be channelled into non-thermal flares or outbursts. A sample of CVs, showing high levels of transient emission, have been identified in the CRTS. In the following sections, the selection criteria for the sample are discussed, as well as the necessary photometric process to obtain accurate light curves for the CRTS data. The light curves of three DN SU UMa sources are also presented.

2. Selection criteria

The criteria used to select CV candidates from the CRTS database for further study were: 1.) they were observed for more than a year by the CRTS, and 2.) exhibit variability of more than 2 magnitudes. In order to perform follow-up studies of the sample, which includes optical photometric observations with the UFS/Boyden 1.5-m telescope at the Boyden Observatory, the sources must have a V magnitude less than 19 and a declination less than +30°.

The light curves provided by the CRTS only provide a rough estimate of a source's variability, as they were produced by an aperture photometry pipeline [2]. Part of the CRTS photometric processing included transforming unfiltered magnitudes to standard (Johnson) V magnitudes using Landolt photometric standards. Aperture photometry is not the ideal photometric process to apply on all the sources as some of the sources are in crowded fields. One of the key factors of the selection criteria was to identify rapidly varying transient sources that have the potential to be selected for intensive multi-wavelength follow-up studies. We therefore preferred to produce light curves by applying point spread function (PSF) photometry and differential photometry on the available CRTS fits files. This enabled us to get a better idea of the sources' variability and to obtain a more accurate magnitude range.

3. PSF photometry

The Image Reduction and Analysis Facility (IRAF) package is freeware that is mainly used for general image processing (reduction and analysis) of astronomical data [13]. It includes packages to do accurate photometric processing. A Python- and PyRAF-based script was developed which automated PSF photometry in IRAF. The standard routines of the DAOPHOT package were used. By automating PSF photometry, the PST package in DAOPHOT automatically identifies stars to create a PSF. The problem with the CRTS data is that some of the stars in the images are saturated and cannot be used to create a PSF. This was overcome by setting a maximum detection value in the DAOFIND package to ensure that the saturated stars were not identified and used to create a PSF.

A differential photometry method largely based on the method described by Everett and Howell [14] was included in the automated script. For the purpose of differential photometry, three comparison stars were chosen near the source. Another pitfall of the CRTS data is that the source is not centred in the images and have an extreme positional shift between frames. This limited the number of comparison stars that could be used for differential photometry, as the chosen comparison stars are not in the field of view for all the frames. The script was programmed to identify the comparison stars that were visible in most of the frames and that had the lowest corrected magnitude variance values. This helped to eliminate the possibility that the chosen comparison stars are also variable stars and ensured that the best differential photometry results were obtained.

Figure 4 shows the light curves (with error bars) obtained for SSS J202948-155437, CSS J163121+103134 and CSS J152614+081802. All three sources are classified as SU UMa DNe and show prominent outbursts. During quiescence, the sources vary by ~ 1 magnitude, which is a clear indication that there must be other processes at hand that cause variability, other than the release of gravitational energy. This lower magnitude range variability is visible when the light curves are compared to the reference lines (dashed lines) included in the plots. The error bars are extremely small, indicating the high degree of accuracy associated with the PSF photometry process. All three sources are included in the sample and further observations will assist in narrowing down the causes of variability.

The sample of sources that was selected for intensive multi-wavelength follow-up studies is discussed in the next section.

4. The sample from CRTS

The CRTS CV sample that was chosen for the multi-wavelength follow-up study is given in table 1. The CV classifications and the orbital periods P_{orb} were obtained from the Outburst catalogue of cataclysmic variables [15], accessible through the CDS Vizier website [16]. The V magnitudes are the values specified by the CRTS [1]. CDS Vizier was also used to determine in which wavelengths the CVs have been observed or detected. This is for an indication of how extensive the multi-wavelength studies can potentially be.

5. Prospects for future work

Optical observations of the sample will be undertaken, and other archives, e.g. GALEX, WISE, XMM-Newton and Fermi, will be investigated in an attempt to match outbursts detected by CRTS. The new observations will include photometric observations with the UFS/Boyden 1.5-m telescope at the Boyden Observatory, and spectroscopic observations with the SAAO 1.9-m telescope, located at the South African Astronomical Observatory (SAAO). The increased sensitivity of instruments, such as the currently constructed MeerKAT, will increase the number of radio detections in CVs. In the near future, we wish to utilise MeerKAT, more specifically ThunderKAT (The HUNt for Dynamic and Explosive Radio transients with MeerKAT), to help us better understand the processes causing non-thermal outbursts in the system.

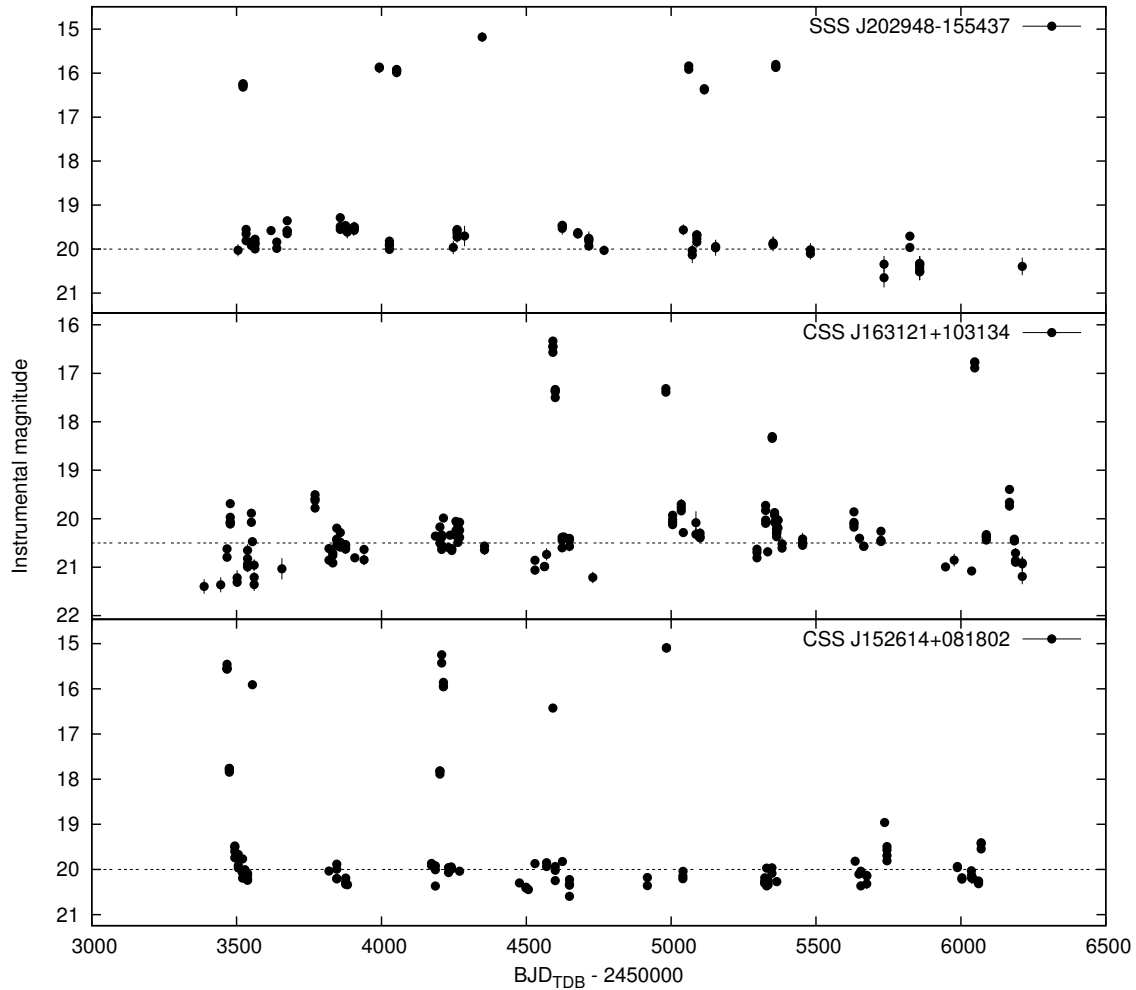


Figure 4. Light curves of three SU UMa CVs. The dashed lines at instrumental magnitudes 20 and 20.5 in the respective plots are only reference lines. Error bars are included for all the data points, but are smaller than the plotted data points in most cases.

Table 1. The sample of CRTS CVs selected for intensive multi-wavelength follow-up studies. The last column specifies in which wavebands the sources have been detected, namely Radio (R), Infrared (IR), Optical (V), Ultraviolet (UV) and X-ray (X).

CRTS Name	Type	P_{orb} (h)	V_{mag}	Detected emission
MLS J022733+130617	Polar	3.79	16.5 - 18.4	IR, V, UV
CSS J034515-015216	DN	1.68	15.5 - 18.6	IR, V
CSS J054558+022106	DN	2.88	14.6 - 16.4	IR, V
CSS J103947-050658	IP	1.57	16.4 - 20.2	IR, V, X
CSS J152614+081802	DN SU UMa	1.78	12.6 - 17.7	IR, V, UV, X
CSS J162147-225310	IP	3.56	15.6	R, IR, V, X
CSS J163121+103134	DN SU UMa	1.5	14.1 - 18.1	IR, V, UV
SSS J202948-155437	DN SU UMa	1.5	13 - 17.9	IR, V
CSS J233003+303301	Non-DN	—	16.6 - 18.3	IR, V, UV, X

Acknowledgments

The financial assistance of the National Research Foundation (NRF) towards this research is hereby acknowledged. This research has made use of the SIMBAD database as well as the VizieR catalogue access tool, CDS, Strasbourg, France.

References

- [1] Drake A J *et al.* 2009 *ApJ* **696** 870–884
- [2] Breedt E, Gänsicke B T, Drake A J, Rodríguez-Gil P, Parsons S G, Marsh T R, Szkody P, Schreiber M R and Djorgovski S G 2014 *MNRAS* **443** 3174–3207
- [3] Szkody P and Gänsicke B T 2012 *Journal of the American Association of Variable Star Observers (JAAVSO)* **40** 563–571
- [4] Hellier C 2001 *Cataclysmic Variable Stars - How and why they vary* (Chichester: Praxis Publishing Ltd)
- [5] Singh K P 2015 *Recent Trends in the Study of Compact Objects (RETCO-II): Theory and Observation (Astronomical Society of India Conference Series vol 12)* pp 29–34
- [6] Warner B 1995 *Cataclysmic Variable Stars* vol 28 (Cambridge: Cambridge University Press)
- [7] Stockman H S, Schmidt G D and Lamb D Q 1988 *ApJ* **332** 282–286
- [8] Yuasa T, Hayashi T and Ishida M 2016 *MNRAS* **459** 779–788
- [9] Giovannelli F 2008 *Chinese Journal of Astronomy and Astrophysics Supplement* **8** 237–258
- [10] Frank J, King A and Raine D J 2002 *Accretion Power in Astrophysics* 3rd ed (Cambridge: Cambridge University Press)
- [11] Meintjes P 2015 *The Golden Age of Cataclysmic Variables and Related Objects - III (Golden2015)* p 7
- [12] Meintjes P J, Oruru B and Odendaal A 2012 *Mem. S.A.It.* **83** 643–650
- [13] Tody D 1980 *Conference on Applications of Digital Image Processing to Astronomy (SPIE vol 264)* ed Elliott D A pp 171–179
- [14] Everett M E and Howell S B 2001 *PASP* **113** 1428–1435
- [15] Coppejans D L, Kording E G, Knigge C, Pretorius M L, Woudt P A, Groot P J, Van Eck C L and Drake A J 2016 *MNRAS* **456** 4441–4454
- [16] Genova F *et al.* 2000 *A&AS* **143** 1–7

Emission modelling of numerical hydrodynamical simulations with application to active galactic nuclei jets

IP van der Westhuizen, B van Soelen and PJ Meintjes

Department of Physics, University of the Free State, Bloemfontein, 9301, SA

E-mail: vanderwesthuizenip@ufs.ac.za

Abstract. Active Galactic Nuclei, such as quasars and blazars, are highly variable over intra-day to year time scales. The regions that produce this variability have been the topic of many recent studies, especially in the investigation of correlation between multi-wavelength components from radio to gamma-rays. In this study a simulation of an idealistic relativistic hydrodynamical jet propagating through a uniform background medium is presented. This simulation is created with the use of the numerical code PLUTO ver 4.2 which uses high resolution shock capturing algorithms to evolve the fluid dynamic partial differential equations with time. In order to investigate possible causes of variable emission in the simulation a post processing emission code is developed to compute intensity maps of the hydrodynamic computational environment. The code is designed to model the synchrotron self-absorption spectrum in the radio regime for each cell. This emission is calculated using the emission and absorption coefficients, which are then integrated along a fixed line of sight to produce simulated intensity maps of the relativistic jet. Using the intensity maps we can investigate regions of variable emission as well as the respective time scales on which they occur. In this paper we present the initial results and intensity maps produced by the emission code as well as the planned future development of the project. The tools which are being developed for this hydrodynamic model can be applied to a range of other transient sources, such as X-ray and γ -ray binaries, to investigate the different emission components produced by such sources.

1. Introduction

Observational studies of jets from Active Galactic Nuclei (AGN) have revealed a complex system of both stationary and moving emission regions inside AGN sources [1]. These emission regions have been associated with shock fronts inside the relativistic jet and produce variability on both short, intra-day, as well as longer time-scales. AGN sources emit radiation over a wide range of the electromagnetic spectrum, from radio to gamma rays, with low energy region of the spectrum being dominated by synchrotron radiation produced by relativistic electrons inside the jet [2].

In order to investigate the production and propagation of shock fronts and other structures inside highly relativistic jets that may lead to the observed characteristics many studies have turned to numerical simulations using fluid dynamics to evolve jet-like environments with time [3]. Such simulations have revealed complex interaction between the relativistic jet material and the surrounding medium as well as the internal structure [4, 5]. The physical characteristics, such as the density, velocity and pressure, calculated by hydrodynamic simulations are, however, not directly related to the emission we receive from these sources. In order to produce emission

Table 1. Variables used in the set up of the initial conditions for the preliminary RHD jet simulation.

Parameter		Value (arbitrary units)
Lorentz factor	Γ	10
Density ratio	η	10^{-3}
Jet density	ρ_b	0.1
Ambient density	ρ_{am}	100
Mach number	M_b	3.0
Adiabatic index	γ_{ad}	5/3

maps from the numerical simulations, that are comparable to observational data, the emission mechanisms of such sources as well as the relativistic effects must be taken into account [2].

In this paper we present the results of ideal numerical hydrodynamic simulations of a relativistic jet evolved using the PLUTO open source code. We also present intensity maps calculated by a radiative code which computes emission based on properties of each computational cell and integrates the calculated emission along a user defined line of sight. In section 2 we will discuss the numerical environment used to run the relativistic hydrodynamic (RHD) simulations, while section 3 will focus on the emission modelling of these simulations. Section 4 summarizes the current results followed by a conclusion in section 5.

2. Numerical simulation of relativistic outflows

A RHD simulation of an AGN jet can be achieved by setting up a fluid environment on a structured mesh grid. On this mesh grid quantities such as density, pressure and velocity are assigned to each cell. The environment can then be evolved with time by numerically solving the fluid dynamical conservation equations. In this study we considered an ideal relativistic outflow, with no viscosity, injected into a uniform medium. For this simulation the magnetic field was considered to be dynamically unimportant and we, therefore, chose a purely relativistic hydrodynamic solver. To calculate the internal energy density of the fluid the ideal caloric equation of state was used,

$$e = \frac{p}{\rho(\gamma_{ad} - 1)}, \quad (1)$$

where e is the internal energy, p is the pressure, ρ is the density and $\gamma_{ad} = C_p/C_v$ is the adiabatic index of the fluid [5].

The 3D environment of the simulation was set up on a Cartesian mesh grid consisting of $64 \times 64 \times 64$ length units. The units of the simulation was chosen as arbitrary to avoid large truncation errors, which may occur if the computed values are very small. Initially a uniform rest background medium was assigned to the grid, while a nozzle was defined on the $z = 0$ boundary to inject relativistic outflow material into the computational domain. The radius of the nozzle was set to 1 length unit and less dense jet material was injected at a steady rate with $\Gamma = 10$. The density of the injected material was normalized such that $\Gamma\rho_{jet} = 1$. For the environment we assumed a pressure matched (PM) model to collimate the outflow material. The pressure of the medium was chosen such that the injected material was supersonic. A complete list of the initial parameters for the simulation is given in table 1. The environment was evolved numerically with time using PLUTO *ver 4.2* Open source code [6]. This grid base code is designed for supersonic flows containing contact discontinuities and uses high resolution

shock capturing schemes. The code was set up to use piecewise parabolic interpolation along with the HLLC Riemann solver [7] and characteristic trace time stepping. The simulation was run on the UFS high performance cluster (HPC) at a resolution of 8 points per unit length.

3. Post-processing emission modelling

In order to produce emission maps of the numerically simulated environment post-processing emission modelling code is being designed in Python. The code determines the synchrotron emission (j_ν^{sy}) and absorption (α_ν^{sy}) coefficients for each cell based on a delta-approximation model [8] given by

$$j_\nu^{sy} = \frac{4}{9} \left(\frac{q^2}{mc^2} \right)^2 u_B \nu^{\frac{1}{2}} \nu_0^{-\frac{3}{2}} n \left(\sqrt{\frac{\nu}{\nu_0}} \right), \quad (2)$$

$$\alpha_\nu^{sy} = \frac{2p+2}{9 m\nu^2} \left(\frac{q^2}{mc^2} \right)^2 u_B \nu_0^{-1} n \left(\sqrt{\frac{\nu}{\nu_0}} \right), \quad (3)$$

where,

$$\nu_0 = \frac{3qB}{4\pi mc} \quad (4)$$

Here q is the charge of the radiating particle (assumed to be electrons), m is the mass of the radiating particle, c is the speed of light, u_B is the magnetic field energy density, ν is the frequency in the co-moving frame and $n(\gamma)$ is the particle spectrum [2]. To calculate the coefficients it was assumed that the jet material had a power law particle distribution with spectral index $p = 2$. The magnetic field energy density was assumed to be proportional to the energy density of the fluid with,

$$u_b = \epsilon_B e \quad (5)$$

where $\epsilon_B = 10^{-3}$ is the B-field equipartition parameter based on [9].

Next the code transforms the coefficients from the co-moving frame to an observer frame with regard to the user defined angle as,

$$j_\nu^{sy} = \frac{j_\nu^{sy'}}{(\Gamma[1 - \beta \cos(\psi)])^2}, \quad (6)$$

where j_ν^{sy} is the emission coefficient in the observer frame, $j_\nu^{sy'}$ is the emission coefficient in the co-moving frame, Γ is the Lorentz factor, β the magnitude of the velocity in units of c and $\cos(\psi)$ is the angle between the observer and the velocity of the fluid.

The post-processing code finally determines the change in intensity dI_ν for each cell following

$$\frac{dI_\nu}{ds} = j_\nu^{sy} - \alpha_\nu^{sy} I_\nu, \quad (7)$$

and integrates this change along a user defined line of sight to produce a 2D intensity map. This is illustrated in figure 1.

4. Results

The simulation was run until the head of the outflow crossed the computational domain. Figure 2 displays 2D slices of the xz -plane at the origin, showing the density, pressure and velocity distributions. From these results we note that the outflow remains collimated and highly relativistic throughout the simulation similar to the simulations produced by [4, 5].

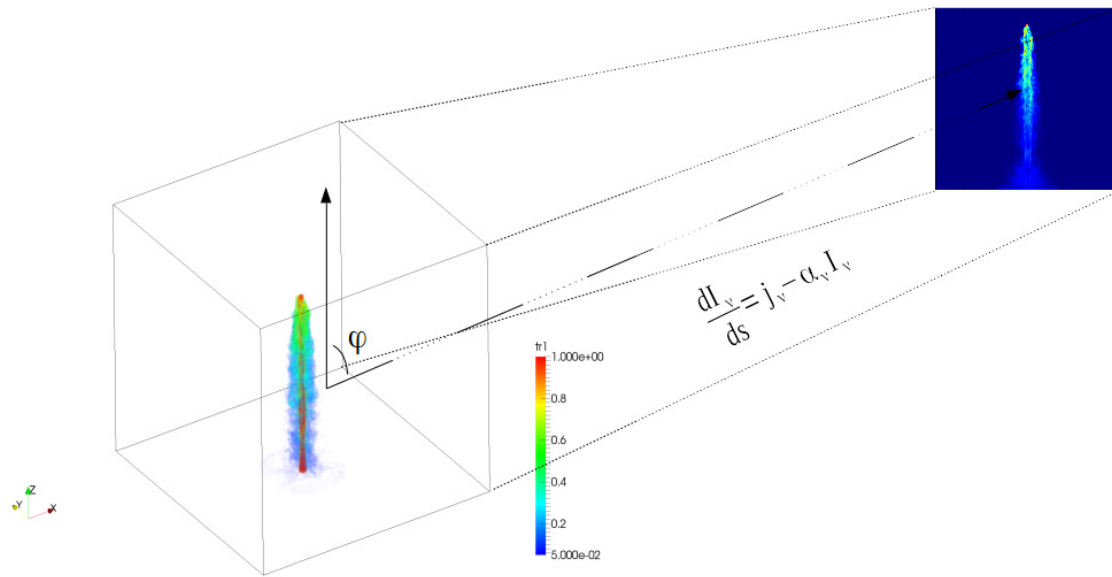


Figure 1. The emission from the 3D fluid dynamic simulation is projected onto a 2D image plane by numerically integrating the change in intensity along a line of site.

Figure 3 displays the calculated intensity maps for three different angles with regards to the propagation direction of the jet. The emission was calculated for a frequency of 12 GHz in the observer frame. In these figures we note that the bow wave structure seen in the density and pressure plots has negligible emission compared to the other structures of the jet. Both the cocoon and the relativistic beam of the jet are initially faint, but increase in brightness with an increase in the z direction closer to the head of the jet. The emission map is dominated by emission at the working surface as well as hotspot regions on the boundary of the relativistic beam. We also note the occurrence of individual asymmetric emission regions close to the head of the jet.

As the viewing angle, ψ , changes from edge-on ($\psi = 90^\circ$) to head-on ($\psi = 0^\circ$) the maximum intensity increases due to Doppler boosting of the fluid moving toward the observer. For example the hotspot regions present in the edge-on system are less prominent at a $\phi = -30^\circ$. This indicates that these regions are located in the cocoon of the jet and are moving at lower velocities compared to the relativistic beam. For the head-on system we obtain a ring type structure with emission of an order of magnitude larger than the edge-on system. The origin of the ring structure is still unknown and further investigation is required to rule out all numerical effects.

5. Discussion and conclusions

A 3D numerical simulation of a relativistic outflow was created and evolved with time using the PLUTO code. The simulation shows a collimated central beam with little deceleration surrounded by an outer cocoon. Intensity maps were computed for the simulation at 12 GHz with a delta approximated synchrotron model. The formation of individual asymmetric emission regions was shown for steady injection model. This suggests that bright emission components can form and propagate in AGN jets without the presence of perturbations in the injection of the outflow. Using these results we will be able to study the propagation of these emission regions further and compare the results to observational data such as [1]. The emission code is still under development with continuous testing and optimization. Future improvements include the addition of a high energy component through an inverse-Compton model, SED modelling, including time of arrival effects and flux calculations. Jet like outflows have been associated with

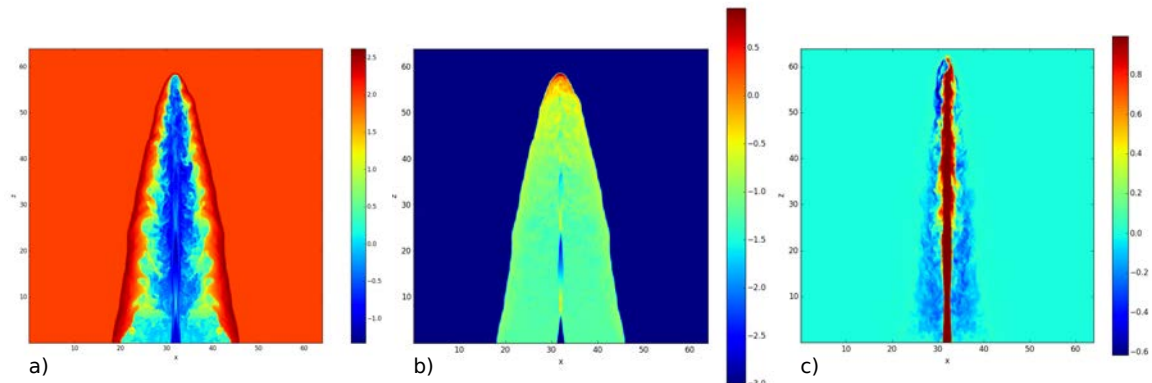


Figure 2. Two dimensional visualizations of the simulation through the xz -plane of the jet, showing a) the density, b) the pressure and c) the velocity component in the z direction. Logarithmic scales are shown for the density and pressure plots in arbitrary units, while the velocity plots have a linear scaling in units of c .

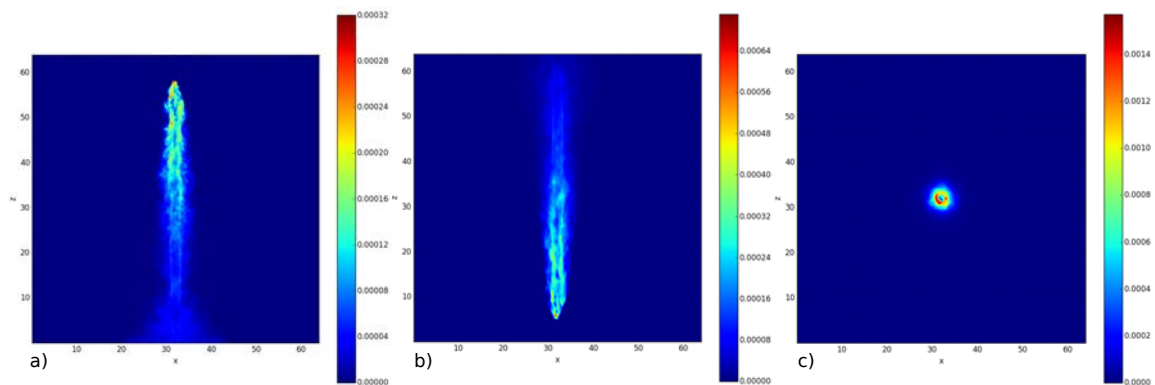


Figure 3. Intensity maps calculated at 12 GHz for different viewing angles a) $\psi = 90^\circ$ b) $\psi = -30^\circ$ c) $\psi = 0^\circ$

many sources such as micro-quasars, young stellar objects (YSO), gamma-ray bursts (GRB's) and X-ray binaries. The code that is being developed for this project can be applied to these sources in future studies.

References

- [1] Lister M L, *et al.* 2009 MOJAVE: Monitoring of jets in active galactic nuclei with VLBA experiments. V. Multi-epoch VLBA images *ApJ* **137** 37183729
- [2] Böttcher M 2011 Modeling the spectral energy distributions and variability of blazars *2011 Fermi & Jansky: Our Evolving Understanding of AGN (preprint arXiv:1205.0539)*
- [3] Toro E F 2009 *Riemann Solvers and Numerical Methods for Fluid Dynamics: A Practical Introduction Third Edition* (Berlin: Springer) Chapter 1 pp 1-40
- [4] Rossi P, Mignone A, Bodo G, Massaglia S and Ferrari A 2008 Formation of dynamical structures in relativistic jets: the FRI case *A&A* **488** 795-806
- [5] Martí J M, Müller E, Font J A, Ibáñez J M and Marquina 1997 Morphology and dynamics of relativistic jets *ApJ* **479** 151-163

- [6] Mignone A, Bodo G, Massaglia S, Matsakos T, Tesileanu O, Zanni C and Ferrari A 2007 PLUTO: a numerical code for computational astrophysics *ApJ* **170** 228-42
- [7] Mignone A and Bodo G 2006 An HLLC Riemann solver for relativistic flows - II. Magnetohydrodynamics *MNRAS* **368** 1040-54
- [8] Böttcher M, Harris D E and Krawczynski H, 2012 *Relativistic Jets from Active Galactic Nuclei*, Weinheim, Germany: Wiley-VCH Verlag GmbH & Co. KGaA Chapter 3 pp 39-80
- [9] Böttcher M and Dermer C 2010 Timing signatures of the internal-shock model for blazars *ApJ* **711** 445-460

A comparative timing analysis of *Suzaku* X-ray data of the nova-like variable system AE Aquarii.

HJ van Heerden and PJ Meintjes

Department of Physics, University of the Free State, Bloemfontein, South Africa

E-mail: vanheerdenhj@ufs.ac.za

Abstract. The nova-like cataclysmic variable system AE Aquarii shows strong emission in the X-ray regime. Previous studies using data from *Ginga*, *ASCA*, *XMM-Newton*, *Suzaku*, *Chandra* and *Swift* were used to characterise the soft and hard X-ray components. The soft component was found to be multi-thermal whereas the hard component could possibly be non-thermal. Additional timing analysis of predominantly the soft X-ray data was used to update the white dwarf (WD) spin ephemeris, with discrepancies however still reported between different ephemerides determined at different epochs and data sets. For this study a comparative timing analysis of the available *Suzaku* data was considered. The timing analysis results was used in conjunction with results from previous studies to compare the current most accurate and expected spin period for the WD as calculated by [14] and [5] to confirm the WD ephemeris. A very accurate WD ephemeris is critical for other studies, such as a possible correlation that has been reported between the WD spin period and possible pulsar-like emission towards higher energies. This study however found that the timing analysis results are highly dependant on the type of analysis process, and recommends further studies on the selection criteria of timing analysis processes to be used in similar and future timing analysis studies.

1. Introduction

The unique nova-like magnetic cataclysmic variable star AE Aquarii consists of a fast rotating white dwarf (WD) primary star, and a K2-K5 type evolved secondary star [1]. The WD is in the ejector state, wherein a propeller mechanism drives the in-falling matter from the secondary star away from the WD in the form of interacting blobs [1]. The primary and secondary components orbit the centre of mass of the system at a $P_{\text{orb}} = 9.88$ h [2, 3], with the highly magnetized WD ($B_1 \sim 10^6$ G) [4] having a spin period of $P_{\text{spin}} \approx 33$ s. The WD is also spinning down at a rate of $\dot{P}_{\text{spin}} = 5.64 \times 10^{-14}$ s s^{-1} , resulting in a spin-down luminosity of $-\dot{\Omega}\Omega = 6 \times 10^{33} I_{50} \text{erg s}^{-1}$ [5]. This large spin down power is ~ 120 times greater than the inferred accretion luminosities derived from UV [6] and X-ray emission [7]. This spin down power could act as a reservoir that drives non-thermal particle acceleration [8], explaining the radio synchrotron and possible high

energy (γ -ray) emission [9, 10].

The discovery of the WD spin pulsations in *Einstein* data [11] led to further studies utilising data from *ASCA*, *XMM-Newton*, *Chandra*, *Swift* and *Suzaku* to detect, define and model the soft and hard X-ray emission components from the system. The soft X-ray emission (≤ 10 keV) has been shown to be multi-thermal [12, 13], while the hard X-ray emission (≥ 10 keV), could best be described through non-thermal emission from accelerated electrons, as inferred from a power-law model fit [12]. Correlations between the pulsations in the soft X-ray and the lower hard X-ray (10-25 keV) *Suzaku* data were also found [12]. The very strong 33 s pulsations in the soft X-ray data from *ASCA*, *XMM-Newton* and *Chandra* were used to update the WD spin ephemeris [14]. It was found that an additional $\dot{P}_{\text{spin}} = 2.0(1.0) \times 10^{-15} \text{ s s}^{-1}$ term, explained as a modest increase in the accretion torques spinning down the WD, best fitted the discrepancy between the analysis and the earlier de Jager [5] ephemeris. Another ephemeris containing a \ddot{P} term was also proposed by [14], but was found to be inconsistent with the proposed models. Timing analysis of *Suzaku* data [12] correlated to measured results [14]. However a multi-wavelength campaign using optical, UV, X-ray (*Swift*) and gamma-ray (MAGIC) telescopes conducted in 2012 [15, 16], found a phase-offset to the proposed ephemeris by [14], but it has to be noted that the \dot{P} version of the Mauche [14] ephemeris was used.

Because a very accurate WD ephemeris is critical for other studies, such as a possible correlation that have been reported between the WD spin period and possible pulsar-like emission towards higher energies, a comparative timing analysis of the available (0.2-12 keV) *Suzaku* soft X-ray instrument (XIS) data will be considered. The timing analysis results will be used in conjunction with results from previous studies to compare the current most accurate and accepted ephemerides for the WD as calculated by [14] and [5] to update and confirm the WD ephemeris.

This study utilised data from *Suzaku*. Additional information on the telescope and mission is available at <http://heasarc.gsfc.nasa.gov/docs/suzaku/>.

2. *Suzaku* XIS data analysis

Suzaku observed AE Aquarii on three separate occasions during October of 2005, 2006 and 2009. Although the 2005 (ID 400001010) and 2006 (ID 400001020) datasets were previously studied [12], they were revisited in addition to the 2009 dataset (ID 404001010). The datasets had on-source observation lengths of 180 ks, 96 ks and 299 ks respectively. Timing analysis of the XIS data were performed using "XSELECT" (Version 2.4c) available in the "Heasoft" (Version 6.15.1) software package available from the HEASARC site at <http://heasarc.gsfc.nasa.gov/>, the time-series analysis package "Period" (Version 5.0-2) available in the "Starlink" (Version 2015B) package, as well as custom Matlab scripts.

To utilize the latest available calibration data files, the raw uncleaned datasets were used. These datasets were run through the *Suzaku* "AE pipeline" (Version 1.1.0).

The filtered and calibrated datasets timing data were then corrected from telescope time to TDB (barycentric dynamic time) using "aebarycen" with source coordinates of RA = 310.038175 and Dec = -0.87085. Source and background (1 second resolution) light-curves were then extracted from the cleaned and time corrected datasets using "XSELECT", with the background data used to subtract the sky soft X-ray background from the source light-curves. The XIS instrument has 4 detectors, i.e. xis0, xis1, xis2 and xis3. Xis0, xis2 and xis3 are front illuminated (FI) CCD detectors, while xis1 is a back illuminated (BI) CCD detector. The recommendation is to combine the FI data to boost the signal to noise and thus reduce the uncertainty. The combined FI and singular BI data were then examined using standard FFT techniques to check signal strength and correlations between FI and BI data. A clear correlation was found between the FI and BI periodograms, with the only difference at the signal power levels, as can be seen in Figure 1. With the clear indication that the measured signal of the FI and BI detectors are the same, the FI and BI light-curves were combined incoherently with the errors recalculated as the *mean error*/ \sqrt{n} where n is the number of contributing values per bin (Figure 2).

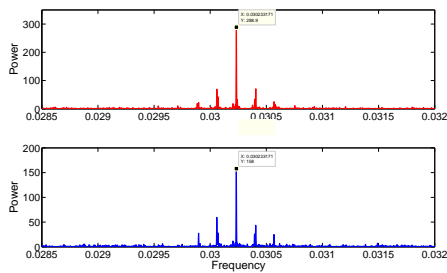


Figure 1. FFT periodograms of FI (top) and BI (bottom) data filtered between 0.0285 and 0.032 cycles per second. The side lobes are uncorrected residuals of the satellite orbital motion.

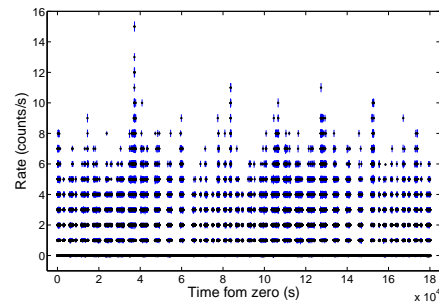


Figure 2. Incoherently combined light-curve for all XIS detectors for the 2005 dataset. The errors are scaled according to the combining process from the original errors in the count rates.

The final combined light-curves were analysed using the following process. The combined light-curves were entered into the "Period" package. The light-curves were detrended using "Period-Detrend.option[M]". Lomb-Scargle periodograms were produced in "Period-Period" using a frequency selection of 0.01 Hz to 0.1 Hz with test for significance enabled over 200 iterations. Using "Period-Peaks" the clear 33 second period and error values were determined for the three data-sets. The determined periods for each dataset were used to fold the corresponding light-curve. Regression analysis was thereafter performed on the folded curves to determine the best fit parameters for the following equation:

$$y = B + A \sin(2\pi(x - t_0)/P) \tag{1}$$

With y the rate, B the shift in the rate, A the amplitude, P the test period, x the folded time vector and t_0 the shift in the time. See Figure 3, Figure 4 and Figure 5 for the folded light-curves as well as the best fit regression models. See Table 1 for the best fit parameter values.

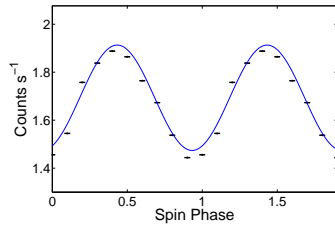


Figure 3. Folded light-curve for 2005 data for $P_{spin} = 33.07625245 \pm 0.001518$

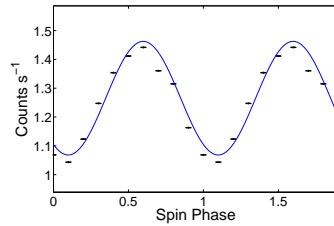


Figure 4. Folded light-curve for 2006 data for $P_{spin} = 33.07660634 \pm 0.002834$

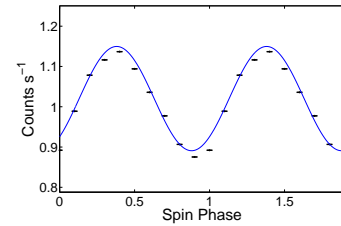


Figure 5. Folded light-curve for 2009 data for $P_{spin} = 33.07720393 \pm 0.000913$

Table 1. Best fit parameters for folded light-curves.

Parameters	2005	2006	2009
T0 (BJD)	2453674.45021604965	2454033.76738751408	2455121.26481127436
A (counts/s)	0.21956 ± 0.0002371	0.19724 ± 0.0002832	0.12943 ± 0.0003190
B (counts/s)	1.69354 ± 0.0001684	1.26540 ± 0.0002003	1.02024 ± 0.0002257
$t_0(s)$	6.03997 ± 0.047043	11.52168 ± 0.007249	4.31722 ± 0.095284
$P_{spin}(s)$	33.0762524 ± 0.001518	33.0766063 ± 0.002834	33.0772039 ± 0.000913

O-C diagrams were calculated using equations based on the results obtained by [5] and [14]. Figure 6 shows the three predicted ephemeris curves for the WD spin period with the de Jager et al (1994) ephemeris forming the baseline (black line). The blue dotted line is the predicted Mauche (2006) ephemeris with the additional \dot{P} term, while the red dashed line is the predicted Mauche (2006) ephemeris with the additional \ddot{P} term. The WD P_{spin} values determined in this study are included in Figure 7 (Green points). In addition the WD P_{spin} (black point) as determined by [12] is included as reference.

3. Discussion

The main focus of this study was to do a comparative timing analysis, and based on the significance of the results, to either update or confirm the WD spin ephemeris. The technique used to determine the WD spin period was a model independent approach

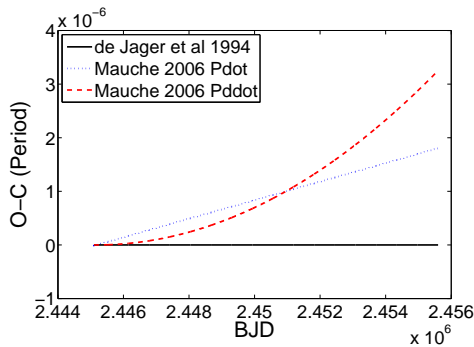


Figure 6. O-C diagram for the WD spin period showing the three different ephemeris models relevant to this study, with the de Jager et al (1994) [5] ephemeris (black line) forming the baseline. The blue dotted line is the predicted Mauche (2006) [14] ephemeris with the additional \dot{P} term, while the red dashed line is the predicted Mauche (2006) [14] ephemeris with the additional \ddot{P} term.

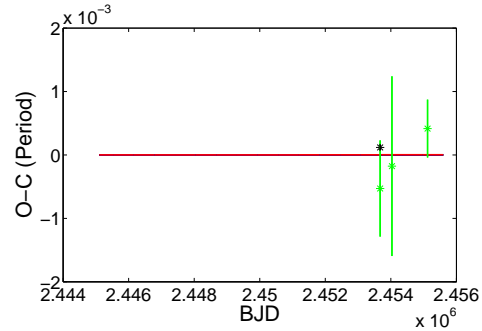


Figure 7. O-C diagram for the derived WD spin period showing the three different ephemeris models relevant to this study with the de Jager et al (1994) [5] ephemeris forming the baseline. The determined O-C derived spin periods and errors for the 2005, 2006 and 2009 datasets are indicated in green. In addition the O-C derived WD spin period and error for the combined 2005 and 2006 datasets investigated by [12] is indicated in black.

and only considered the data and standard time series analyses. The resultant WD spin period values, although compatible within error with the currently proposed WD spin ephemeris models, are not accurate enough to give a clear indication to which model is the unique model describing the evolution of the WD spin the best. The WD spin value as determined by [12] is not compatible within error with any of the three models, but does indicate a stronger spin-down rate. The technique used by [12] follows an epoch folding analysis as described in [17].

The trend of the WD spin period, based on the mean values of each dataset used, as determined in this study, does show a spin-down, but it is very dramatic, with a required spin-up in an epoch preceding this study to fit the general trends of the model ephemerides. This however would be unrealistic as the expected mechanisms in the system is dissipative, with the WD being in a long term spin-down phase. There are a couple of possible explanations for the results: Either the time series analysis technique is, although robust, too inaccurate in relation to the model requirements, or there might be an inherent variability in the WD spin period, or both. A recent study by [18] found that the secondary star is not tidally locked and has various starspots. This means that the mass transfer in the system is most probably variable in nature. This can result in variable accretion and rotational torque moments on the WD. The interactions between internal and external stellar structures might lead to a small variation in the WD spin-down rate, analogous to star-quakes experienced in pulsars but on a very small scale.

4. Conclusion

Based on the results and indicative inconsistencies between various studies and proposed models of the WD spin ephemeris, a new approach is required for the data analysed in this and similar studies. The analysis technique might have to be a lot more model dependant, such as used by [14], in that deviations in the model is determined and examined using the data in conjunction with the models.

The possible variation in the WD spin needs to be examined in greater detail, and new and extensive studies need to be conducted using both new observations as well as all available archival data. The analysis techniques must also be tested and standardised using Monte-Carlo simulations to exclude inconsistencies due to varying analysis methodologies. With Astrosat (India's first dedicated multi-wavelength space observatory) that was launched in September 2015, with its very large sensitivity range, applications can be made to study the emission from AE Aquarii in greater detail, thus facilitating the refinement of the models describing the system, specifically the evolution of the WD.

References

- [1] Wynn G A, King A R and Horne K 1997 *Mon. Not. R. Astron. Soc.* **286** 436-46
- [2] Welsh W F, Horne K and Gomer R 1995 *Mon. Not. R. Astron. Soc.* **275** 649-70
- [3] Friedjung M 1997 *New Astron.* **2** 319-22
- [4] Meintjes P J and Venter L A 2005 *Mon. Not. R. Astron. Soc.* **360** 573-82
- [5] de Jager O C, Meintjes P J, O'Donoghue D and Robinson E L 1994 *Mon. Not. R. Astron. Soc.* **267** 577-88
- [6] Eracleous M, Horne K, Robinson E L, Zhang E, Marsh T and Wood J 1994 *Astrophys. J.* **433** 313-31
- [7] Eracleous M, Halpern J and Patterson J 1991 *Astrophys. J.* **382** 290-300
- [8] de Jager O C 1994 *Astrophys. J. Suppl. S.* **90** 775-82
- [9] Meintjes P J, Raubenheimer B C, de Jager O C, Brink C, Nel H I, North A R, van Urk G and Visser B 1992 *Astrophys. J.* **401** 325-36
- [10] Meintjes P J 1994 *Astrophys. J.* **434** 292-305
- [11] Patterson J, Branch D, Chincarini G and Robinson E L 1980 *Astrophys. J.* **240** L133-36
- [12] Terada Y, Hayashi T, Ishida M, Mukai K, Dotani T, Okada S, Nakamura R, Naik S, Bamba A and Nakamura K 2008 *Publ. Astron. Soc. Jpn.* **60** 387-97
- [13] Oruru B and Meintjes P J 2012 *Mon. Not. R. Astron. Soc.* **421** 1557-68
- [14] Mauche C W 2006 *Mon. Not. R. Astron. Soc.* **369** 1983-87
- [15] López-Coto R et al 2013 *33rd International Cosmic Ray Conference* [icrc2013-0397]
- [16] Aleksić J et al 2014 *Astron. Astrophys.* **568** 8-17
- [17] Larsson S 1996 *Astrophys. J. Suppl. S.* **117** 197-201
- [18] Hill C A, Watson C A, Shahbaz T, Steeghs D and Dhillon V S 2014 *Mon. Not. R. Astron. Soc.* **444** 192-207

Solving the radiative transfer equation for maser environments

R van Rooyen¹ and DJ van der Walt²

¹ SKA South Africa, 3rd Floor, The Park, Park Road, Pinelands, 7405, Western Cape, South Africa

² Department of Space Physics, North-West University, Potchefstroom Campus, 11 Hoffman Street, Potchefstroom, 2531

E-mail: ruby@ska.ac.za

Abstract. The study of astrophysical maser formation provides a method for probing the chemical composition of the sources they are observed in. In order to understand the pumping mechanisms and physical characteristics of masers, suitable models must contain expressions for each level population from which an inverse function that will cause the mean line intensity to move away from black body form can be derived. Central to this is obtaining numerically consistent solutions to the population density distributions of the maser molecules. The “masers” package is developed in Python and implements the escape probability approximation method. It solves the level population problem for non-LTE statistical equilibrium using molecular data and parameters describing the physical environment. It extends existing radiative transfer software by providing a reasonably fast, stable algorithm that deals with the solution method’s inherent sensitivity to oscillations and multiple valid outcomes; allows different maser geometries for calculation; includes the contribution of interacting background radiation fields, as well as other sources of opacity such as line overlap.

1. Introduction

Determining the level population distribution in an arbitrary situation is the central problem in modelling spectral line emission in general and maser radiation in particular. In essence this consists of a two part solution: Solve the rate-equation problem for the populations of the energy levels under conditions that will produce an inversion. Then, calculate the amplification of the maser radiation through the medium sustaining the inversion.

The escape probability approximation method separates population density calculations from the line radiation in the radiative transfer, RT, equation [1]. This is one of the most implemented methods for solving the RT equation and software implementing this method for the study of thermal line emission are readily available. Care should be taken however, since obtaining numeric solutions under conditions causing inversion in maser environments are a little more tricky. In this paper we present easily overlooked numerical failures found during a study investigating physical conditions to investigate population inversion leading to formaldehyde masers.

2. Theory and Calculation

Applying the escape probability to the rate equations, the level populations calculation can be expressed as presented in Equation 2.7.1 from [1].

$$\begin{aligned} \frac{dn_i}{dt} = & - \sum_{j < i} \left\{ A_{ij} \beta_{ij} [n_i + W \aleph_{ij} (n_i - n_j)] + C_{ij} \left[n_i - n_j \exp \left(\frac{-h\nu_{ij}}{kT} \right) \right] \right\} \\ & + \sum_{j > i} \frac{g_j}{g_i} \left\{ A_{ji} \beta_{ji} [n_j + W \aleph_{ji} (n_j - n_i)] + C_{ji} \left[n_j - n_i \exp \left(\frac{-h\nu_{ji}}{kT} \right) \right] \right\} \end{aligned} \quad (1)$$

where $N_i = g_i n_i$, g_i is the statistical weight of level i , N_i represents the number density in level i , W is the dilution factor and \aleph_{ij} the photon occupancy number at transition frequency ν_{ij} .

To obtain the matrix equation, rewrite the parameters of Equation 1, grouping all populating and depopulating levels and substitute the radiative and collisional components

$$\begin{aligned} R_{ij} &= \begin{cases} A_{ji} \beta_{ji} (1 + X_{ji}) & i < j \\ A_{ij} \beta_{ij} \left(\frac{g_i}{g_j} \right) X_{ij} & j > i \end{cases} \\ R_{ii} &= - \sum_{i \neq j} R_{ji} \\ \tilde{C}_{ij} &= C_{ji} \\ \tilde{C}_{ii} &= - \sum_{i \neq j} C_{ij} \end{aligned}$$

Thus obtaining the form:

$$\mathbf{Q}\mathbf{x} = \mathbf{b}$$

where $\mathbf{b} = [0, \dots, 0, 1]^T$, $x_i = \frac{n_i}{n_{mol}}$ the normalised fractional population density with n_{mol} the total population density of the molecule and $\mathbf{Q} = \mathbf{R} + \tilde{\mathbf{C}}$.

The equation can be solved using iterative methods, such as LU-factorization or the singular value decomposition (SVD). The required initial solution is obtained by calculating the level population at local thermal equilibrium (LTE).

3. Masers Python Package

3.1. Implementation

The **masers** package solves for statistical equilibrium given some parameters to describe the physical environment. The most basic parameters that must be provided are the density of the cloud, the abundance of the maser molecule, various temperatures, and the column density. To calculate the optical depth, the anticipated size and geometry of the cloud must also be provided, as well as any and all diffuse background radiation components that may interact with the line emission.

Since the solution of the radiative transfer equation is dependent on the molecular level populations, molecular rate and collision coefficients must also be provided. These coefficients are obtained from the molecular data files in the Leiden LAMBDA database [2], <http://home.strw.leidenuniv.nl/~moldata>.

During development, we used the RADEX non-LTE excitation and radiative transfer code [3], available from the Leiden website, for comparison and verification; note that both methods solve the rate equations iteratively. Iterative methods are sensitive to oscillation and multiple valid solutions since the solution of the previous iteration is used as the initial estimate for the next iteration and the process is repeated until the input estimate and calculated solution have reached some convergence criteria.

Numerical stability is evaluated by calculating the optical depth and excitation temperature for formaldehyde molecular data [4], gas kinetic temperature $T_k = 300$ K, H_2CO fractional abundance $X_{H_2CO} = 5 \times 10^{-7}$, specific column density $\frac{N_{col}}{\Delta v} = 10^6, 10^9, 10^{12} \text{ cm}^{-3}\text{s}$ respectively

and $T_{BB} = 30$ K as blackbody radiator, private communication Prof van der Walt. The equilibrium solution for total density ranging from 10^3 – 10^{12} cm^{-3} is calculated using a convergence limit of $|x_n - x_{n-1}|/x_{n-1} < 10^{-3}$, with x_n and x_{n-1} is the level populations calculated during the current and previous evaluation.

Possible convergence criteria includes using population densities or excitation temperature calculations, via the relation $\frac{n_u}{n_l} = \frac{g_u}{g_l} \exp(\frac{-h\nu}{kT_{ex}})$. The effect of choosing either convergence criteria for the parameters above was inspected for specific column density $\frac{N_{col}}{\Delta v} = 10^{12}$ cm^{-3}s . The `masers` implementation uses the population densities calculated at each iteration. `RADEX` evaluates the average difference between the excitation temperature calculated from the previous solution compared to the calculation of the current solution (from source code). Inspection of excitation temperature calculation as convergence criteria showed sensitivity to oscillating solutions, Figure 1, caused by catastrophic cancellation due to the difference of small numbers in the denominator of the excitation temperature calculation, $T_{ex} \propto [\ln(x_l g_u) - \ln(x_u g_l)]^{-1}$. `RADEX` minimises this by only selecting certain levels to evaluate convergence (from source code).

Excitation temperature values computed at all iterations over total density range are shown in the top graph of Figure 1. The centre and bottom graphs shows the effect carried forward and amplified in the optical depth and level population calculations. The red line in the bottom graph shows the population densities for the lower level of the transition as they were calculated over iterations, while the blue line shows the population densities for the upper transition level. Slight step functions show the total density steps, but the population densities clearly show oscillating behaviour around $n_{H_2} = 10^6$ – 10^8 cm^{-3} .

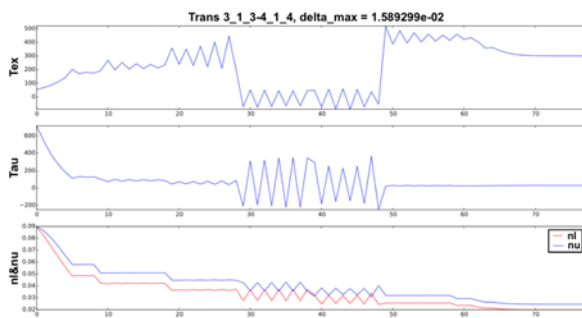


Figure 1. Oscillating behaviour seen in convergence evaluation using excitation temperature evaluation. The convergence results are seen in the 4_{14} – 3_{13} transition showing 80 iterations over total density range $n_{H_2} = 10^6$ – 10^8 cm^{-3} and specific column density $\frac{N_{col}}{\Delta v} = 10^{12}$ cm^{-3}s .

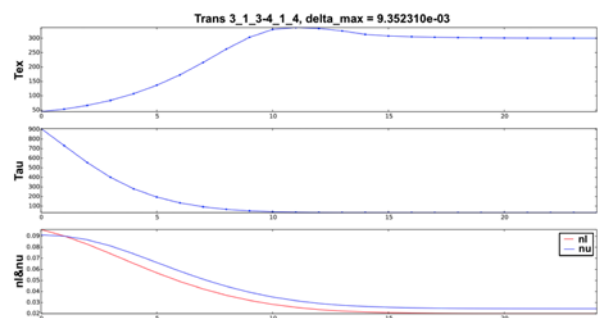


Figure 2. A ratio of 9.5:0.5 means that only 5% is given to the new calculation, pulling the iterative solution close to the previous behaviour. This “memory” stabilizes the iterative calculation by ensuring it is not independent, but is influenced by the previous results.

Oscillating behaviour is only pronounced at lower transition levels and the solutions were found to become more stable if the next iteration is given some “memory” of the previous solutions. This was done using a running average calculation, $x_n = c_1 \times x_n + c_2 \times x_{n-1}$ where $c_1 \leq 1$ and $c_2 \leq 1$ are some weighting coefficients with $c_1 + c_2 = 1$. The larger the coefficient for the previous solution x_{n-1} the “longer” the memory of the solution is. For `masers` this “memory” was found to be fairly large with $x_n = 0.05 \times x_n + 0.95 \times x_{n-1}$ providing solutions under all simulated conditions. It should be noted that a “long memory”, $c_2 \rightarrow 1$, requires a more stringent convergence limit. For `masers` this is found to be $|x_n - x_{n-1}|/x_{n-1} < 10^{-7}$ to obtain solutions shown in Figure 2.

Lastly, the calculation of optical depth between the 2 implementations is also found to be significant. The `masers` solver applies the large velocity gradient, LVG, definition for the escape

probability calculation [1]. When results are compared to solutions obtained from RADEX care must be taken to ensure no large negative optical depth values. For thermal radiative transfer calculations the optical depth is always expected to be positive, thus RADEX substitutes the turbulent medium escape probability calculation for $|\tau| \geq 7$ (from source code). This escape probability calculation requires the computation of $\sqrt{\tau}$, which fails for maser regions when inversion causes the optical depth to be negative [3].

Stabilising masers against the highlighted numerical sensitivities provides a robust solver to use during the inspection of maser pumping parameter space. Figure 3 shows the improvement at selected levels known to cause numerical failures in RADEX. The top row shows results from the masers solver, while the bottom row shows results from the RADEX code. The four columns show Tex, log10(Tex), Tau, log10(Tau) for selected transition levels $1_{10-1_{11}}$ and $12_{1_{11}}-11_{1_{10}}$.

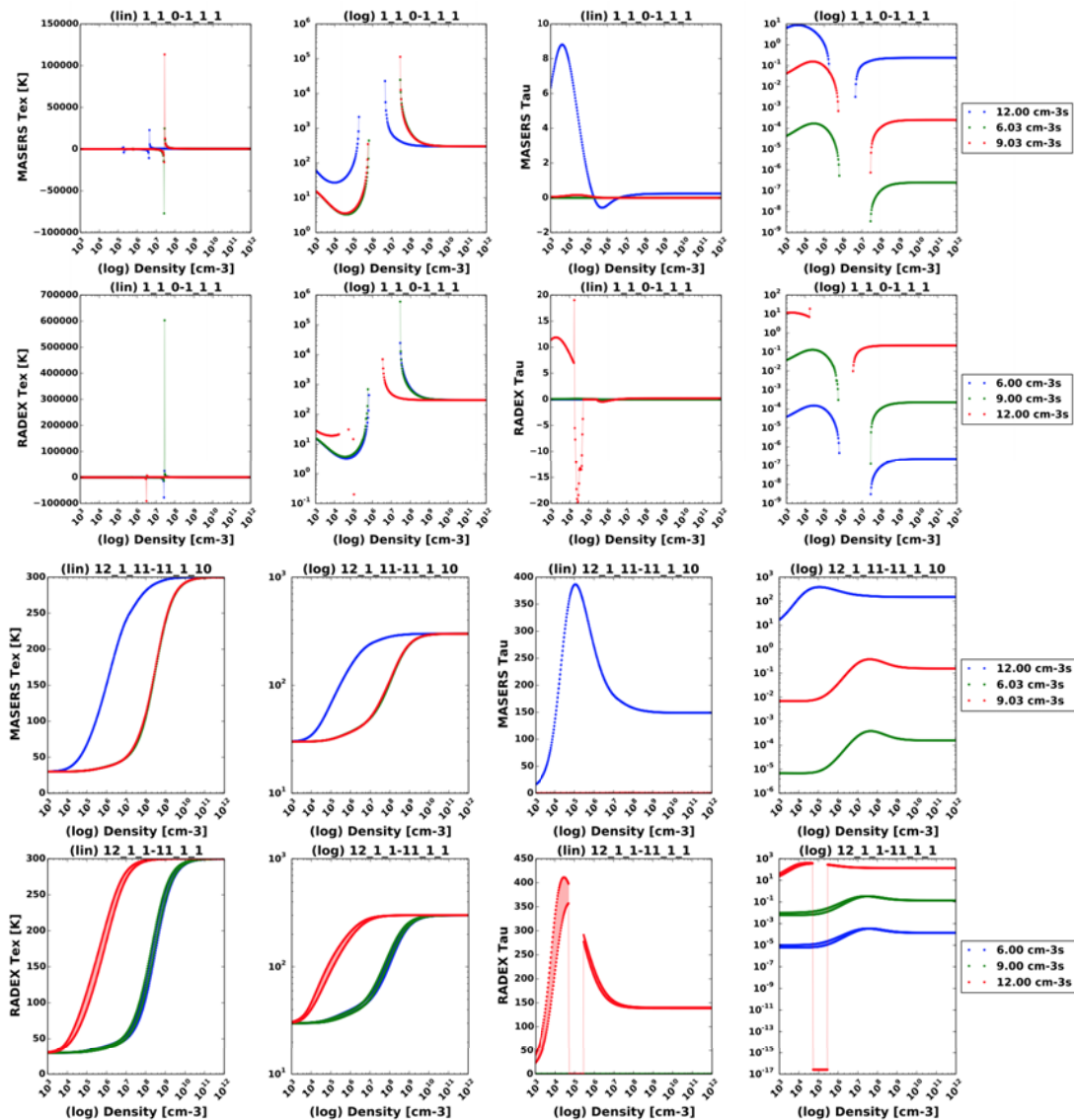


Figure 3. The first and third rows show results from the masers solver with colour scales showing specific molecular column density $\frac{N_{col}}{\Delta v} = 10^6$ (green), 10^9 (red), 10^{12} (blue) for all H_2CO transitions. The second and last rows show results obtained from the RADEX solver with specific molecular column density $\frac{N_{col}}{\Delta v} = 10^6$ (blue), 10^9 (green), 10^{12} (red) for all H_2CO transitions.

3.2. Verification

Following methodology suggested by Prof van der Walt, in a private communication, the basic functionality of the `masers` software could be verified. This methodology describes the inspection of the pumping and inversion of H_2CO masers in star-forming region G37.55+0.20, specifically looking at the optical depth calculation for the 4.8 GHz maser associated with the $1_{10}-1_{11}$ transition as a function of the specific column density.

Assuming fractional molecular density $X_{H_2CO} = 5 \times 10^{-7}$ and electron temperature $T_e = 10^4$ K, Figure 4 shows example calculations of the following three physical environments:

- $n_{H_2} = 4.4 \times 10^5 \text{ cm}^{-3}$, $T_d = 100$ K, $T_k = 300$ K, $w_d = 0.1$ and no H_{II} region,
- $n_{H_2} = 10^4 \text{ cm}^{-3}$, $T_k = 20$ K, $w_{H_{II}} = 0.1$, $EM = 6 \times 10^9 \text{ cm}^{-6} \text{ pc}$ and no dust,
- $n_{H_2} = 10^4 \text{ cm}^{-3}$, $T_d = 100$ K, $w_d = 0.1$, $T_k = 300$ K, $w_{H_{II}} = 0.1$, $EM = 6 \times 10^9 \text{ cm}^{-6} \text{ pc}$.

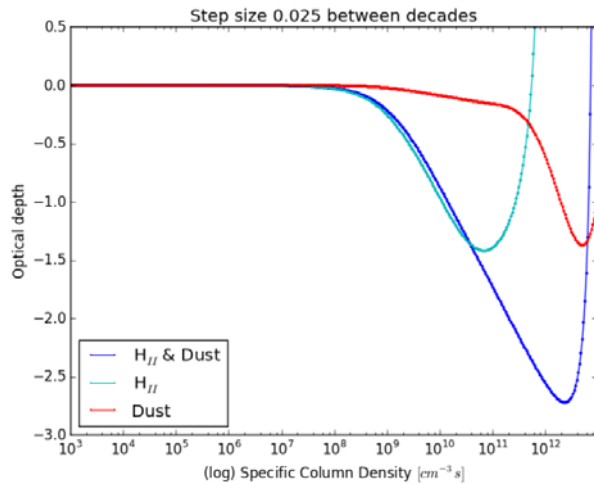


Figure 4. Three examples showing variation of optical depth calculation of the $1_{10}-1_{11}$ transition. Physical parameters were kept constant over the range of specific column density values, showing the maximum optical depth identified.

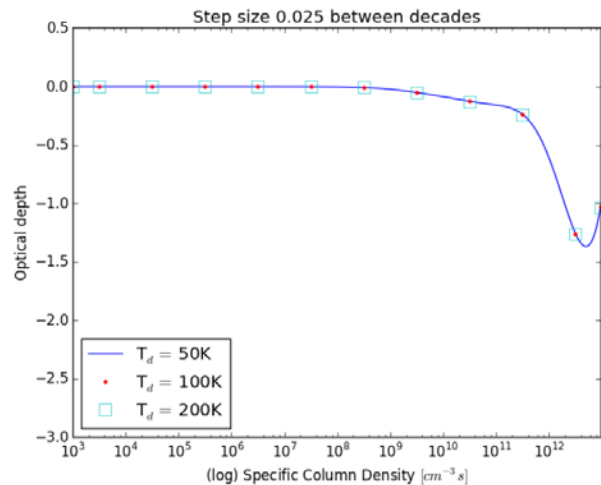


Figure 5. These results indicates that the inversion is unrelated to the dust temperature, which suggests that radiative pumping by the dust infrared radiation field is not significant for the maser.

Similarly, Figure 5 shows results for optical depth calculation with dust temperatures using $T_d = 50, 100, 200$ K, given $n_{H_2} = 4.4 \times 10^5 \text{ cm}^{-3}$, $T_k = 300$ K, $w_d = 0.1$ and no H_{II} region.

Numerical results obtained were compared to results obtained by Prof van der Walt using independent numerical code solving the rate equations using Heun's method.

3.3. Pumping

Applying the `masers` software to investigate the pumping of the H_2CO maser in G37.55+0.20 as described in [5] showed good comparison between results. Both methods showed that collisional excitation with H_2 as well as radiative excitation by the free-free radio continuum radiation from a nearby ultra- or hyper-compact H_{II} region can invert the $1_{10}-1_{11}$ (4.8 GHz) transition.

Collisional excitation Figure 6 shows the optical depth of $1_{10}-1_{11}$ transition as a function of H_2CO specific column density over range $10^8-10^{14} \text{ cm}^{-3} \text{ s}$ and $T_k = 140, 180, 220, 260, 300$ K, $n_{H_2} = 4 \times 10^5, 2.6 \times 10^5, 1.6 \times 10^5, 1.3 \times 10^5, 7.5 \times 10^4 \text{ cm}^{-3}$. Visual comparison shows results are duplicate of those shown in Fig 1 presented in [5].

Radiative excitation via the dust continuum emission The dependence of optical depth on the specific column density is shown in Figure 7, for $T_k = 180$ K, $n_{H_2} = 1.3 \times 10^5 \text{ cm}^{-3}$, $w_d = 1.0$ and $T_d = 0$ K (no dust), 100, 180 K. Comparison shows results are duplicate of those shown in Fig 3 presented in [5].

Radiative excitation through the free-free continuum emission from an ultra- or hyper-compact H_{II} region is shown in Figure 8 using emission measure of the H_{II} region $EM = 10^{10} \text{ pc cm}^{-6}$, as well as $T_e = 10^4$ K, $w_{H_{II}} = 1.0$, $T_k = 140, 180, 220, 260, 300$ K, and $n_{H_2} = 4 \times 10^5, 2.6 \times 10^5, 1.6 \times 10^5, 1.3 \times 10^5, 7.5 \times 10^4 \text{ cm}^{-3}$. Comparison shows results are duplicate of those shown in Fig 6 presented in [5].

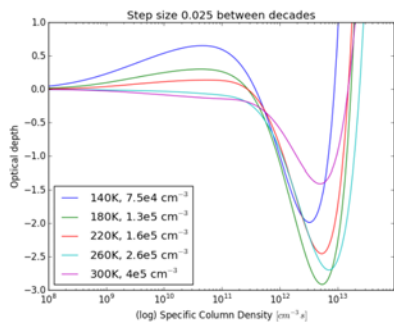


Figure 6. Effect of collisions on the level populations in the absence of radiation fields.

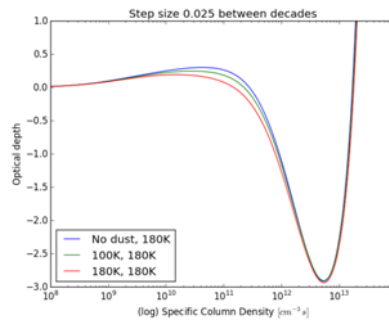


Figure 7. Optical depth as a function of specific column density.

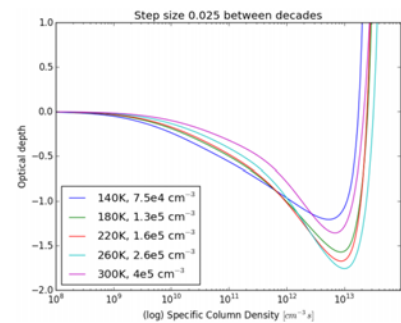


Figure 8. Free-free emission has a significant effect on the inversion.

4. Summary

The paper highlights various reasons why standard matrix inversion methods used in the calculation of thermal line transfer models need to be more robust to ensure good results in the stimulated maser environments used to model maser pumping schemes.

Verification could be achieved through personal communication with Prof van der Walt who has independent software for solving the rate equations using Heun's method.

Validation of the implementation is followed by comparison between the results obtained with the `masers` package to results published in [5]. Visual comparison of graphs showing results of example parameters inspecting the pumping of the H_2CO maser in G37.55+0.20 shows good agreement.

References

- [1] Elitzur M 1992 *Astronomical masers* (Kluwer Academic Publishers) ISBN 0-7923-1217-1 PB
- [2] Schöier F L, van der Tak F F S, van Dishoeck E F and Black J H 2005 *A&A* **432** 369–79
- [3] van der Tak F F S, Black J H, Schöier F L, Jansen D J and van Dishoeck E F 2007 *A&A* **468** 627–35
- [4] Wiesenfeld L and Faure A 2013 *MNRAS* **432** 2573–8
- [5] van der Walt D J 2014 *A&A* **562** A68

The contribution of photons from the circumstellar disc to gamma-gamma absorption in PSR B1259-63

B van Soelen¹ and I Sushch^{2,3}

¹ Department of Physics, University of the Free State, 9300, Bloemfontein, South Africa

² Centre for Space Research, North-West University, 2520, Potchefstroom, South Africa

³ Astronomical Observatory of Ivan Franko National University of Lviv, vul. Kyryla i Methodia, 8, UA-79005 Lviv, Ukraine

E-mail: vansoelenb@ufs.ac.za

Abstract. The gamma-ray binary system PSR B1259-63, consists of a Be star and a pulsar, and is one of only a few known high mass binary systems where the spectral energy distribution, in the νF_ν representation, peaks in the gamma-ray regime. It is also the only very high energy emitting gamma-ray binary where the nature of the compact object is known. Near periastron, the pulsar passes through the circumstellar disc that surrounds the Be star companion. Observations around periastron show a local minimum in the TeV gamma-ray flux, when the seed photon energy density, and hence the inverse Compton flux, should be highest. This discrepancy may be explained through gamma-gamma absorption. The contribution of the photons from the circumstellar disc surrounding the Be star significantly modifies the gamma-gamma absorption and may significantly modify the very high energy light curve.

1. Introduction

The binary system which consists of the pulsar PSR B1259-63 and the Be type star LS 2883, is part of a growing number of high-mass binaries which produce the peak of their non-thermal emission at gamma-ray energies. These sources are collectively referred to as gamma-ray binaries (see [1] for a review of these systems). PSR B1259-63 is a 48 ms pulsar in a ~ 3.4 year orbit around the Be companion star (LS 2883), which is surrounded by a circumstellar disc [2, 3, 4]. Of the known Very High Energy (VHE) emitting gamma-ray binaries, PSR B1259-63/LS 2883 is the only system where the nature of the compact object is identified as a pulsar via radio pulsations, while arguments in favour of both pulsars and blackholes have been put forward for the other systems (e.g. [5, 6]).

In PSR B1259-63/LS 2883 the non-thermal emission is believed to originate from particles accelerated in the shock that occurs between the pulsar and stellar wind (e.g. [7, 8]) and this emission has been detected from radio to gamma-rays (see e.g. [9, 10] and references therein). At the highest energies, the TeV gamma-rays detected by H.E.S.S. [11, 12] can be produced through inverse Compton scattering of seed photons from the optical star. However, the high energy density of optical photons also provides a high number of photons for gamma-gamma absorption, which may decrease the observed gamma-ray emission. Dubus [13] previously considered this effect for the then known gamma-ray binaries, including a comparison to H.E.S.S. observations of PSR B1259-63/LS 2883, where the author considered the effect of the optical photons originating from the star, and did not investigate whether the emission from the circumstellar

disc surrounding LS 2883 would have an important effect. The latter was briefly discussed in [14], where it was shown that the disc might significantly contribute to gamma-gamma absorption.

The spectra of Be stars are known to have an excess of emission at infrared (in comparison to B stars) due to free-free emission from the circumstellar disc (see [15] for a review of Be stars) and this is clearly detected from LS 2883 [16]. The circumstellar disc appears to always be present in this system as indicated by the strong H α emission line which has been observed around periastron [9, 10, 17]. In this proceedings contribution we further investigate the influence the circumstellar disc will have on the gamma-gamma absorption.

2. Gamma-gamma absorption

Pair production of an electron-positron pair can occur in the scattering of two photons if the combined energy of the photons is high enough. A gamma ray with an energy ϵ_γ must interact with a photon with an energy ϵ which is greater than or equal to the threshold energy (i.e. $\epsilon \geq \epsilon_{\text{th}}$) which is given by

$$\epsilon_{\text{th}} = \frac{2}{\epsilon_\gamma(1 - \mu)}, \quad (1)$$

where $\mu = \cos(\theta)$, θ is the angle of interaction, and the energies of the photons are normalized to the electron rest-mass energy ($m_e c^2$), i.e. $\epsilon = h\nu/m_e c^2$. The minimum threshold occurs for a head-on collision ($\mu = -1$), and for a 1 TeV gamma-ray photon this will require photons with a threshold frequency of,

$$\nu \approx 6.3 \times 10^{13} \left(\frac{h\nu_\gamma}{1 \text{ TeV}} \right)^{-1} \text{ Hz} \quad (2)$$

which is within the mid-infrared regime.

The gamma-gamma optical depth can be calculated from

$$\tau_{\gamma\gamma} = \int_0^l \int_0^{4\pi} \int_{\frac{2}{\epsilon_\gamma(1-\mu)}}^\infty n_{\text{ph}}(\epsilon, \Omega) \sigma_{\gamma\gamma}(\epsilon, \epsilon_\gamma, \mu) (1 - \mu) d\epsilon d\Omega dx, \quad (3)$$

where the photon number density $n_{\text{ph}}(\epsilon, \Omega)$ is determined from the disc and star, and $\sigma_{\gamma\gamma}$ is the gamma-gamma cross-section. The cross-section is expressed as

$$\beta = \sqrt{1 - \frac{2}{\epsilon\epsilon_\gamma(1 - \mu)}}, \quad (4)$$

as

$$\sigma_{\gamma\gamma}(\beta) = \frac{3}{16} \sigma_T (1 - \beta^2) \left[(3 - \beta^4) \ln \left(\frac{1 + \beta}{1 - \beta} \right) - 2\beta(2 - \beta^2) \right], \quad (5)$$

where σ_T is the Thomson cross-section.

3. Stellar and circumstellar disc photons

The photon number density in equation (3) is determined from the photons originating from the circumstellar stellar disc and star. Below we briefly outline how we determine this contribution.

3.1. Circumstellar disc

The circumstellar disc has been modelled under the assumption that the disc has a single temperature ($T_{\text{disc}} = 19800 \text{ K}$), a radius $R_{\text{disc}} = 50R_\star$, a constant opening angle ($\theta_{\text{disc}} = 1^\circ$), and the density of the disc decreases with distance, r , as

$$\rho = \rho_0 \left(\frac{r}{R_\star} \right)^{-n}, \quad (6)$$

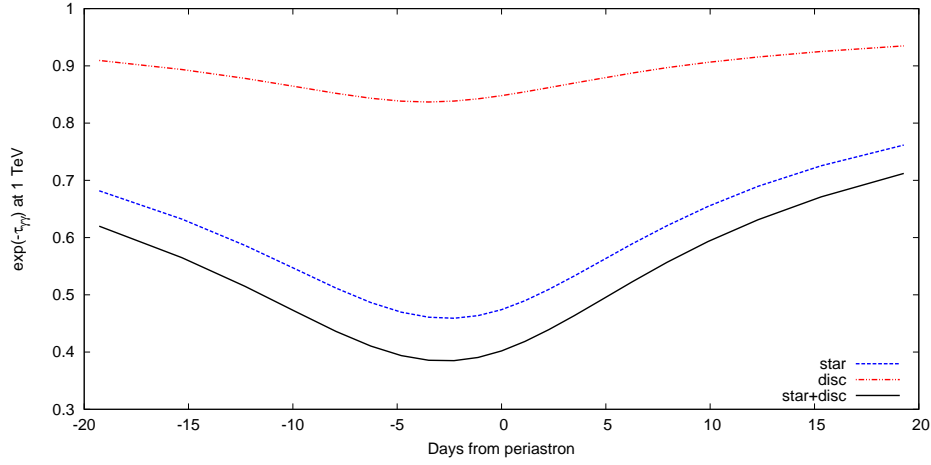


Figure 1. Extinction of a 1 TeV gamma ray due to gamma-gamma absorption resulting from photons that originate from the star (blue dashed line), the circumstellar disc (red double-dotted dashed line) and the combined effect (black solid line).

where R_* is the radius of the star and ρ_0 is the density of disc at the surface of the star [18]. The photon number density from the disc in every direction is calculate from

$$n_{\text{ph}}(\nu) = \frac{mc}{h^2\nu} B_\nu (1 - e^{-\tau_\nu}) \quad [\text{cm}^{-3} \text{ster}^{-1}], \quad (7)$$

where $B_\nu(T_{\text{disc}})$ is Planck's function and τ_ν is the optical depth through the disc. Following the method outlined in [18] the optical depth can be calculated from

$$\tau_\nu = \int X_\lambda X_* R_*^{-1} \left(\frac{r}{R_*} \right)^{-2n} ds \quad (8)$$

where X_λ is a wavelength dependent term which is a function of the disc temperature and the Gaunt factors (equation 5 in [18]) and the integration is along a line-of-sight through the disc. The remaining free parameters (n and X_*) are found by fitting the free-free model to observational data and here we have used the same parameters as in [16].

3.2. Stellar photons

The stellar photons have been modelled assuming the star is a blackbody emitter with a temperature of $T_* = 33\,000$ K. The attenuation of stellar photons due to absorption in the disc is calculated by decreasing the stellar component by $\exp(-\tau_\nu)$ if the line-of-sight passes through the disc.

4. Results

The gamma-gamma opacity around periastron for PSR B1259-63/LS 2883 has been calculated assuming that the gamma rays originate at a point source at the position of the pulsar. Here the binary parameters have been calculated assuming a mass of $1.4 M_\odot$ for the pulsar, that LS 2883 has a mass of $M_* = 31 M_\odot$ with a radius of $R_* = 9.2 R_\odot$, the system has an orbital period of $P = 1236.7$ d and the eccentricity is $e = 0.87$. The extinction for a 1 TeV gamma-ray photon is shown in figure 1. As expected, the gamma-gamma absorption due to the disc is lower than that for the star but may still result in a decrease of more than 10 per cent at TeV energies. The combined contribution of both the stellar and disc photons results in an absorption of ≈ 60 per cent a few days before periastron.

5. Discussion & Conclusion

The light curve observed at TeV energies from PSR B1259-63/LS 2883 shows an apparent dip near periastron [12]. If the gamma rays are produced by inverse Compton scattering, it is expected that the emission should peak at periastron due to the increase in the seed photon density or remain constant around periastron in the case of saturation. This has led to a number of possibilities, which have included the suggestions of hadronic models [19] which are, however, in contradiction to the inferred location of the circumstellar disc, and the introduction of variable adiabatic cooling around periastron [20, 21]. The gamma-gamma opacity was also investigated by [13] who showed an absorption of 40 percent of the VHE flux (above 380 GeV) near periastron for a stellar temperature of $T_{\star} \approx 27\,000$ K. However, the newer estimate for the stellar spectral type suggests a higher temperature ($T_{\star} \approx 33\,000$ K) [3]. This significantly increases the number of photons and increases the gamma-gamma opacity. The effect of the circumstellar disc was also not considered.

Here we have shown that the increase in the temperature of star, plus the addition of the circumstellar disc increases the gamma-ray absorption to a maximum of approximately 60 per cent near periastron for a 1 TeV photon. For gamma rays originating close to the pulsar this will result in a significant effect on the observed light curve. While this alone is not sufficient to explain all the details of the H.E.S.S. observations around periastron, we argue that gamma-gamma absorption will have a significant effect and must be included when attempting to model the VHE emission from this binary system, as well as others that include a Be companion.

References

- [1] Dubus G 2013 *A&ARv* **21** 64
- [2] Johnston S, Manchester R N, Lyne A G, Nicastro L and Spyromilio J 1994 *MNRAS* **268** 430
- [3] Negueruela I, Ribó M, Herrero A, Lorenzo J, Khangulyan D and Aharonian F A 2011 *ApJ* **732** L11
- [4] Shannon R M, Johnston S and Manchester R N 2014 *MNRAS* **437** 3255
- [5] Massi M, Ribó M, Paredes J M, Garrington S T, Peracaula M and Martí J 2004 *A&A* **414** L1
- [6] Massi M and Jaron F 2013 *A&A* **554** A105
- [7] Tavani M and Arons J 1997 *ApJ* **477** 439
- [8] Dubus G 2006 *A&A* **456** 806
- [9] Chernyakova M *et al.* 2014 *MNRAS* **439** 432
- [10] Chernyakova M *et al.* 2015 *MNRAS* **454** 1358
- [11] H.E.S.S. Collaboration 2013 *A&A* **551** A94
- [12] Romoli C *et al.* 2015 *The 34th International Cosmic Ray Conference* (The Hague: Netherlands) **PoS(ICRC2015)** 873
- [13] Dubus G 2006 *A&A* **451** 9
- [14] Sushch I and Böttcher M 2014 *JHEAp* **3** 18
- [15] Rivinius T, Carciofi A C and Martayan C 2013 *A&A Rev* **21** 69
- [16] van Soelen B, Meintjes P J, Odendaal A and Townsend L J 2012 *MNRAS* **426** 3135
- [17] van Soelen B, Väisänen P, Odendaal A, Klindt L, Sushch I and Meintjes P J 2016 *MNRAS* **455** 3674
- [18] Waters L B F M 1986 *A&A* **162** 121
- [19] Chernyakova M, Neronov A, Lutovinov A, Rodriguez J and Johnston S 2006 *MNRAS* **367** 1201
- [20] Khangulyan D, Hnatic S, Aharonian F and Bogovalov S 2007 *MNRAS* **380** 320
- [21] Kerschhaggl M 2011 *A&A* **525** A80

Analysis of the rich optical iron-line spectrum of the x-ray variable I Zw 1 AGN 1H0707–495

H Winkler, B Paul

Department of Physics, University of Johannesburg, PO Box 524, 2006 Auckland Park, Johannesburg, South Africa

E-mail: hwinkler@uj.ac.za

Abstract. Thirty years ago the optical counterpart of the x-ray source 1H0707–495 was discovered to be a 15th magnitude broad-line Seyfert galaxy with a rich Fe II emission line spectrum typical of the AGN subclass sometimes referred to as the I Zw 1 objects after their progenitor. This object became the subject of much interest and investigation just over five years ago when it was shown to have undergone dramatic x-ray luminosity variations. This paper presents an extensive series of medium resolution spectra recorded at the 1.9 m telescope at Sutherland in January 2016. Through co-adding the spectra, we are able to achieve a signal-to-noise hitherto not achieved for this object, allowing us to resolve individual Fe II lines and measure their relative strengths and profiles to a degree of accuracy not previously available for this AGN. We provide possible physical interpretations of our measurements and investigate links between the spectral evidence collected in this study and the known x-ray behaviour.

1. Introduction

The advent of x-ray astronomy and subsequent systematic searches of the optical counterparts of x-ray-bright sources led to the identification of a significant number of these with active galactic nuclei (AGN). Optical spectroscopy revealed the x-ray source 1H0707–495 to be linked to a galaxy of magnitude $V = 15.7$ mag at redshift $z = 0.041$ with a rich emission line spectrum with broadened features indicative of Seyfert type 1 class [1]. The spectrum distinguished itself from that of other AGN identified in the discovery paper through its uncharacteristically strong Fe II emission spectrum, no obvious narrow forbidden lines and the fact that the Balmer lines were not as broad. This type of spectrum has subsequently been recognized as a Seyfert/AGN subclass of its own, referred to as narrow line Seyfert 1 (NLS1) [2], and, when the iron-line spectrum is exceptionally prominent, as I Zw 1 type object after the sub-class prototype of that name.

As with other AGN, the objects associated with the I Zw 1 sub-class are believed to consist of a central massive black hole surrounded by an accretion disk illuminating nearby fast-moving gas. However the exact mechanisms generating their characteristic spectra are not properly understood. It is not even clear why the spectra of some broad-line Seyfert galaxies display no iron emission lines whatsoever, while there are other AGN such as Markarian 231 where the iron spectrum completely dominates the blue part of the spectrum (see e.g. [3]).

1H0707–495 has in the more recent past been frequently observed in other wavelength regimes, particularly in x-rays [4], where strong variability has been detected. This contrasts with optical luminosity variations that are quite moderate by comparison (e.g. [5]).

2. Observations and spectral calibration

Optical spectroscopic observations of 1H0707–495 were carried out with the 1.9 m telescope at the Sutherland station of the South African Astronomical Observatory in January 2016. We used the medium resolution reflection grating with 600 lines/mm corresponding to a dispersion of 100 Å/mm, and set the slit width to 150 μm, translating to 0.9 arcsec in the field of view. The grating angle was adjusted to obtain a wavelength range $\lambda\lambda$ 3600–6400 Å on the detector.

Two sets of spectra were collected. The first set, obtained during the night 13–14 January under dark sky conditions, consisted of four exposures totaling 3600 s. The second set (three exposures totaling 3000 s) was recorded on the night 19–20 January with a bright moon up (lunar phase = 0.81). The CCD images obtained were processed using standard procedures: i) the frame bias was subtracted; ii) intrinsic pixel sensitivity differences and throughput variations along the slit were corrected using flatfield images obtained from illumination by a smooth-spectrum lamp; iii) cosmic ray blemishes on the images were removed by manually identifying affected pixels and smoothing these using neighbouring pixels.

The wavelength calibration was effected by means of argon calibration spectra recorded before and after each spectrum of 1H0707–495. The resultant plots of wavelength versus pixel position were fitted by means of third-order polynomials, which were then applied to the galaxy spectrum. The sky background was determined by averaging the recorded (and similarly wavelength calibrated) spectrum in two strips 15 CCD channels on either side of the galaxy – no evidence of an extended galaxy halo could be detected in these strips. The sky spectrum was then subtracted from the preliminary object spectrum to obtain the non-contaminated spectrum of the AGN. The noise levels of the three spectra of 19 Jan are significantly higher than for those of 13 Jan due to the bright moonlit sky later in the week.

Conditions were not photometric on both nights, and the seeing also not stable, meaning that absolute spectrophotometric calibration was not possible. Nonetheless, spectra of the spectrophotometric standard star LTT 2415 [6] were recorded and, together with the standard Sutherland atmospheric extinction correction, used to determine the relative spectral flux calibration, so that it becomes possible to determine emission line ratios (but not absolute line fluxes). No corrections were applied for telluric absorption as the significant telluric lines all fall outside the observed wavelength range.

The seven individual spectra for 1H0707–495 were finally combined to obtain the high signal-to-noise spectrum illustrated in figure 1.

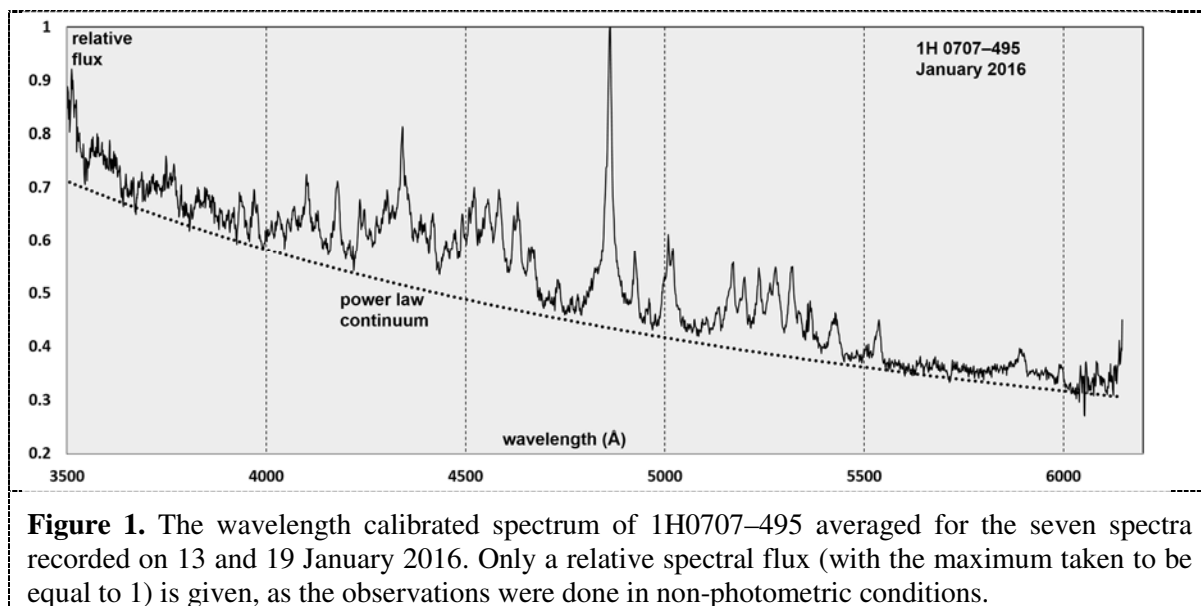


Figure 1. The wavelength calibrated spectrum of 1H0707–495 averaged for the seven spectra recorded on 13 and 19 January 2016. Only a relative spectral flux (with the maximum taken to be equal to 1) is given, as the observations were done in non-photometric conditions.

3. Spectral analysis

3.1. General spectral characteristics

The January 2016 spectrum of 1H0707–495 still closely resembles the discovery spectrum of Remillard et al. [1], confirming that the I Zw 1 classification still applies. While a fraction of the photons recorded in the spectrum originate from integrated host galaxy starlight generated far from the nucleus, that component is not distinguishable in figure 1. There is also no sign of interstellar absorption features at $\lambda\lambda$ 3934/67 Å (Ca II) and $\lambda\lambda$ 5889/96 Å (Na I) that can be conspicuous in similar iron-rich AGN spectra.

The overall shape of the continuum is well fitted by a power law spectrum $F_\lambda \propto \lambda^\gamma$ with a spectral index $\gamma = -1.5$ (also shown in figure 1). This agrees closely with the estimate from UV-optical spectra from previous studies [7].

3.2. The Fe II spectrum

We then introduce the Fe II spectral templates computed by Véron-Cetty et al. [8] and Kovacevic et al. [9], and compare this with the observed spectrum (with the power law subtracted) in figures 2 and 3. The former template was determined empirically from a spectrum of I Zw 1, while the latter is based on theoretical calculations of iron ion transition probabilities, with the full width at half maximum (*FWHM*) adjusted to 800 km s⁻¹.

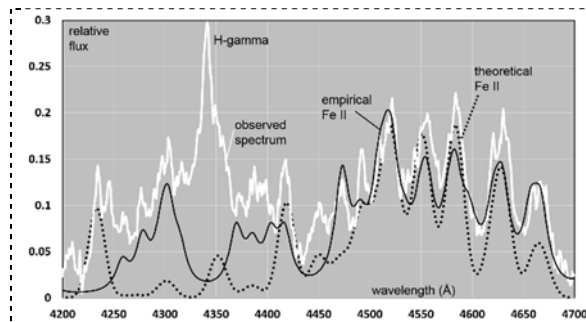


Figure 2. Fit of the observed Fe II emission bands near 4500 Å.

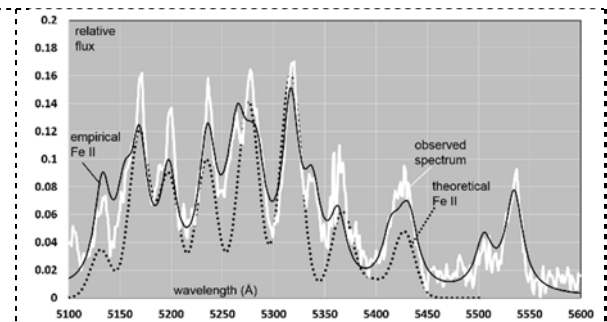


Figure 3. Fit of the observed Fe II emission bands near 5300 Å.

While most of the peaks in the templates match actually measured peaks, neither of the templates fit the observed spectra satisfactorily.

3.3. The H-beta emission profile

The H-beta emission line has been fitted by the superposition of two commonly applied profile functions (see figure 4). The first of these is a comparatively narrow Gaussian component with a *FWHM* corresponding to 800 km s⁻¹, which is identical to the width most suited to fitting the Fe II emission line spectrum.

The broader of the H-beta components was best fitted by a Lorentzian profile shifted bluewards from the other component by 120 km s⁻¹, and with a *FWHM* of 2600 km s⁻¹. While the Gaussian component has a greater peak height, the total flux ratio of the Lorentzian H-beta fraction to the Gaussian fraction is 3.7. There is an additional bump in the red wing of the line (near 4850 Å), which may be due to a further component in H-beta or another feature related to the iron line spectrum.

3.4. Forbidden line spectrum

Figure 5 displays the part of the spectrum containing the characteristic AGN nebular lines [O III] 4959 Å and 5007 Å. While these clearly are exceptionally weak, small peaks corresponding to these features are clearly visible with wavelengths almost consistent with redshift of the H-beta peak.

These peaks have been fitted with Gaussian profiles, maintaining their theoretically known peak ratio of 1:3. The width thus obtained for these forbidden lines only correspond to *FWHM* ~ 400 km s⁻¹. We

measure the flux ratio of the (total) H-beta line to the [O III] 5007 Å line, a commonly used indicator of the nature of the AGN activity [10], to be 42:1. This is exceptionally high (by comparison, the ratio rarely exceeds 10:1 in type 1 Seyfert galaxies), and points to possible fundamental differences in the nuclear structure of 1H0707–495.

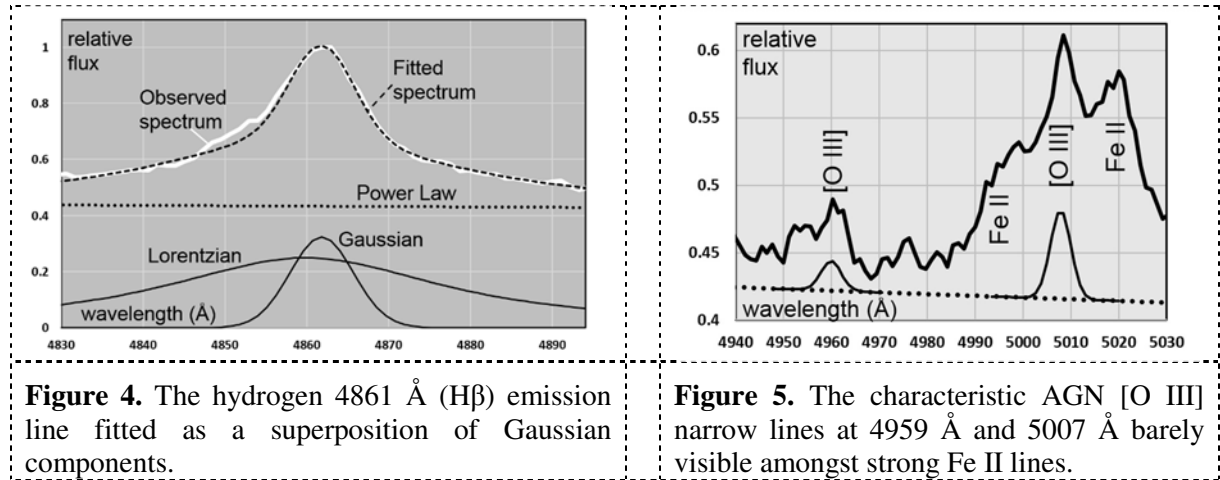


Figure 4. The hydrogen 4861 Å (H β) emission line fitted as a superposition of Gaussian components.

Figure 5. The characteristic AGN [O III] narrow lines at 4959 Å and 5007 Å barely visible amongst strong Fe II lines.

No further common Seyfert forbidden lines (e.g. [O II] 3727 Å) could be identified in the spectrum.

3.5. Further emission line characteristics

We make the following further observations about our 1H0707–495 spectrum.

No obvious changes could be confirmed between our data and previously published spectra of this object (e.g. [7]). This includes the discovery spectrum [1] measured at least 30 years before us. We also did not find any evidence of short term variability, our two sets of spectra taken six days apart in essence looking identical to each other.

With the exception of H-alpha, the spectral range observed covers the Balmer series of hydrogen. One clearly sees the emission lines from H-beta to H-epsilon in our spectrum. The relative strength of the bluest of the lines confirms that reddening due to dust in the line of sight must be low.

In addition to these and the Fe II emission we can confirm a relatively strong emission feature with peaks corresponding to the Na I doublet at $\lambda\lambda$ 5889/5896 Å. The wavelengths of other peaks always match one of the wavelengths catalogued in the extensive catalogue of emission lines identified in by Véron-Cetty et al. in I Zw 1 [8].

Even though this is not evident from figures 2 and 3, the complete spectrum of I Zw 1 (used to determine the Véron-Cetty et al. [8] Fe II template) actually matches the spectrum of 1H0707–495 presented in this paper exceptionally well (compare our figure 1 to figure 6 in that paper [8]). We mention here some minor differences, namely that the emission feature at \sim 3885 Å (probably Fe II) and some emission (possibly a blend of Fe II and Fe II) in the red wing of H-gamma.

Other than that, however, the spectra practically match each other.

4. Discussion and conclusion

We now compare the spectral characteristics of 1H0707–495 with those of other objects associated with the I Zw 1 class.

As discussed in the previous section, 1H0707–495 can truly be considered as a ‘near-twin’ to the prototype I Zw 1 itself. IRAS 07598+6508 is another relatively bright and well-studied representative of the I Zw 1 class of AGN [11], though its Fe spectrum is stronger compared to the Balmer lines, and the individual emission lines are wider.

SDSS J120011–020452 has also been shown to have exceptionally weak Seyfert forbidden lines [12], with only [O II] 3727 Å previously detected and no sign of [O III] 4959/5007 Å. There is also a

strong Na I absorption feature due to interstellar material in the SDSS J120011–020452 host galaxy that we do not see at all in 1H0707–495.

The spectrum of the I Zw 1 AGN 1H0707–495 that we have presented in this paper confirm this to be an object of substantial interest, and invites further optical spectroscopy (in addition to the considerable recent studies of this AGN in x-rays). The project leading to the current paper plans the collection of a further 3-4 sets of spectra at approximately yearly intervals, to determine whether any small spectral changes can be detected, and if so which spectral lines are varying. Combining all the spectra with a total integration time amounting to 6-8 hours would reduce the noise in the spectral data sufficiently to discover hitherto undetected weak features in the spectrum and perform one of the most detailed analyses of the emission line properties in I Zw 1 objects. The comparison of this spectrum with the few high quality spectra available for similar objects of this class will hopefully enable us to gain a much better understanding of the structure of the nuclear regions in this type of AGN.

Acknowledgements

The paper is based on data collected with the telescopes at the South African Astronomical Observatory. We thank SAAO for the allocation of telescope time.

References

- [1] Remillard R A, Bradt H V, Buckley D A H, et al. 1986 *Astrophys. J.* **301** 742
- [2] Osterbrock D E, Pogge R W 1985 *Astrophys. J.* **297** 166
- [3] Veilleux S, Trippe M, Hamann F, et al. 2013 *Astrophys. J.* **764** 15
- [4] Fabian A C, Zoghbi A, Wilkins D, et al. 2013 *Mon. Not. Roy. Astron. Soc.* **419** 116
- [5] Winkler H 1997 *Mon. Not. Roy. Astron. Soc.* **292** 273
- [6] Bessell M S 1999 *Publ. Astron. Soc. Pac.* **111** 1426
- [7] Leighly K M, Moore J R 2004 *Astrophys. J.* **611** 107
- [8] Véron-Cetty M-P, Joly M, Véron P 2004 *Astron. Astrophys.* **417** 515
- [9] Kovačević J, Popović L Č, Dimitrijević M S 2010 *Astrophys. J. Suppl.* **189** 15
- [10] Winkler H 1992 *Mon. Not. Roy. Astron. Soc.* **257** 677
- [11] Véron-Cetty M-P, Joly M, Véron P, et al. 2006 *Astron. Astrophys.* **451** 851
- [12] Rahman N, Winkler H 2014 *Proceedings of the South African Institute of Physics 2013 Annual Conference*, Richards Bay 368

Division D2 – Space Science

Automated scheduling for a robotic astronomical telescope

D Maartens^{1,2}, P Martinez³ and R van Rooyen⁴

¹ Southern African Large Telescope, Observatory Road, Observatory, Cape Town 7935

² South African Astronomical Observatory, Observatory Road, Observatory, Cape Town 7935

³ SpaceLab, University of Cape Town, Rondebosch, Cape Town 7700

⁴ SKA South Africa, 3rd Floor, The Park, Park Road, Pinelands, 7405, Western Cape, South Africa

E-mail: dsm@salt.ac.za

Abstract. Scheduling related to science instruments is typically more complex and quite different from the standard, application-related scheduling problems which are routinely solved in industry. For instance, the problem requires making choices which impact other choices later and contains many interacting complex constraints over both discrete and continuous variables. Furthermore, the set of applicable constraints is particular to a science project, while new types of constraints may be added as the fundamental problem changes.

The aim of this project is to design and develop a more general scheduling strategy to deal with the eccentricities of astronomy scheduling. Resulting on a strawman implementation of such an automated scheduler for optical photometers such as the Alan Cousins Automatic Photometric Telescope (APT).

1. Introduction

The Alan Cousins Automatic Photometric Telescope (APT) is a 0.75-m automatic photoelectric telescope commissioned in mid-2000. The sole science driver for the APT is photometry, used mainly for the long-term monitoring of variable stars. In addition, there is the potential for target-of-opportunity (TOO) observations such as gamma ray bursts and solar eclipse observations. Ultimately the APT is expected to be fully robotic. Some advance toward this goal has been made. The next phase is the development of an automated scheduler that will generate a pool of viable observations for each night of observation.

Astronomy projects are complex, often consisting of inseparably connected constraints, requiring long-term planning as well as short-term optimisation [1]. While one aspect of scheduling focuses on optimising resource utilisation as the goal, conditions can change significantly during an observing session, leading to schedule breakage. In addition, science observing may require prompt follow-up observations that arise during an observation session. These issues give rise to the need for a scheduling system that is capable of recovering from periods of bad observational conditions and of integrating newly added observations during operation [2].

Planning and scheduling are distinctly different activities. Planning is not only concerned with setting up an observation plan for a telescope and/or instruments but it also entails planning, carried out by the observatory, on scheduling the observations to achieve some

objective. Scheduling requires planning information to assess temporal assignment of observations to best achieve an execution plan. Observing has to deal with the dynamic conditions during execution of an observation and best choice selection based on available observation plans [3].

Considering the three distinct time scales that fundamentally makes up astronomical scheduling, we will describe the problem using a design that contains three stages. Implementation of the stages as distinct modules are not always required, but all modules should incorporate the criteria for good scheduling.

2. Scheduler Design

The three criteria for a “good schedule” are (a) fairness, (b) efficiency, and (c) sensibility. A fair schedule balances time allocations between users such that they all share good and bad observing times equitably. An efficient schedule is one that maximises instrument utilisation and strives to match observations with required conditions. A sensible schedule is one that attempts only those observations that are possible under the current observing conditions [4]. Optimisation aims of the various criteria are represented through the stages of the design which are connected by an objective function representing a per observation rank calculation based on constraints. An observation specifies both hard constraints and soft preferences. The scheduling problem is to synthesise a schedule that satisfies all hard constraints and achieves a good score according to an objective function based on the soft preferences [5].

2.1. Planning

Longer term planning deals with scheduling over the observation season, given the approved science projects. The main aim of this section is the fair distribution of time among users/partners, as well as maximising scientific return.

Optimisation for long term planning is mainly driven by the aims of the observatory and are restricted by the constraints of the telescope. Observations can, and usually do, conflict. Longer term plans allow for better resolution of these conflicts to achieve optimal scientific output.

Intermittent re-planning allows for the re-evaluation of observatory performance, which in turn allows for the re-evaluation of parameters or change of optimisation function. Furthermore, over the lifetime of the observatory, other constraints may be required such as new instrumentation or change in operations.

The optimisation strategy for planning ignores dynamic conditions and assumes (a) problem-free execution of each observation, (b) perfect knowledge of the time duration needed for each observation, and (c) perfect fore-knowledge of the weather throughout the night.

Given the complexity and size of the search space for long term scheduling, it is obvious that this type of scheduling cannot be done in real time, therefore the focus does not have to be on time-efficient algorithms.

2.2. Scheduling

This is the more traditional form of scheduling, focused on optimising the use of the observatory, minimising overhead and maximising science output.

Setting up a pool of observations available for execution based on a subset from the planning section allows for the efficient use of telescope time and instrumentation setup. While planning decreases the number of observations to consider based on best choice and other fixed constraints, setting up a selection of viable observations is composed of a large number of complex, heterogeneous constraints over both continuous and discrete variables. Even relatively simple schedules have to deal with geometric constraints, precedence constraints, mutual exclusion constraints and temporal constraints, all in the same problem [2].

Non-scorable observations are subject to their own unique scheduling rules. Such observations are fixed observations that must be scheduled at a specific date and time regardless of the possible score. The only goal here is to make certain everything actually gets on the schedule, given its individual constraints. Optimisation of other observations happens around these observations and will generally result in a less-optimal solution.

2.3. Observations

Executing observations are an extremely time-constrained activity, leaving little time for peripheral actions. Only minimal optimisation must be done in order to ensure efficiency and sensibility.

The scheduler can generate a pool of observations available to the executioner based on predicted values—duration of the night, observation plan, etc. The executioner must continually process short term viability based on constant updates that can include added observations, constraints, or weather conditions.

Given a set of observations to perform; a date and time to perform them, a description of the environment; and the objective function; select the observation that maximises the objective function and satisfies all the constraints.

3. Constraint Evaluation using Merit Functions

Operational parameters may be general to astronomy or unique to an observatory, instrument, observation mode, etc. Other influences will depend on observatory policies and procedures such as those related to long-term projects, or compensations for time loss due to TOO observations or similar programs.

The most complex part of an observation request are the constraints on the observation. Some of these constraints are explicitly given by astronomers, while others are implicit, due to the nature of instrument/telescope [1].

In order to decide which observation, n , to carry out, the rank is defined as [6]:

$$R(n) = f(n) \cdot \prod_{x=1}^{x=X} v_x(n) \cdot \frac{\sum_{m=1}^{m=M} \varepsilon_m(n)}{M} \quad (1)$$

For any observation constrained by X hard limits and M soft preferences: $f(n)$ is a measure of fairness, $\varepsilon_m(n)$ measures of efficiency and $v_x(n)$ Boolean veto functions as measures of sensibility.

Observatory time must be shared equitably between projects. The fairness function evaluates how fair doing a particular observation is based on the project's time allowance. The time allocated by partners is thus a form of observatory accounting and when share values drop below a reasonable number, the system must give higher preference to that partner [7].

The veto function has to prevent observations being carried out that are not possible at the current time due to a number of Boolean constraints.

$$\prod_{x=1}^{x=X} v_x(n) = v_1(n) \cdot v_2(n) \cdot \dots \cdot v_X(n), \quad (2)$$

where $v_x(n)$ describes the constraint limits.

The purpose of the efficiency merits is to decide which observation to carry out at any given moment in time considering observatory policy, scientific expectation and observing conditions [6].

$$\sum_{m=1}^{m=M} \varepsilon_m(n) = \beta_1 \varepsilon_1(n) + \beta_2 \varepsilon_2(n) + \dots + \beta_M \varepsilon_M(n), \quad (3)$$

where $\varepsilon_m(n)$ describes the constraint equations, each with an optional weighting factor β_m .

3.1. Astronomical Veto Functions

Astronomical constraints that can be considered as “hard” constraints, are generally related to observational limits.

Target brightness evaluation is based on the instrument sensitivity limits related to the source target properties. The brightness of the object must be low enough not to saturate the instrument, but high enough to be a viable observation.

$$v(\text{magnitude}) = 1 \in [\text{noise limit}, \text{brightness limit}] \quad (4)$$

Lunar phase and elevation not only influence sky brightness calculations but also determines a hard limit to observational “brightness” conditions and can be defined in terms of Lunar illumination as a percentage of the surface illumination (PLI).

$$\text{Lunar brightness} = \begin{cases} \text{dark, if PLI} < 0.4 \\ \text{grey, if PLI} < 0.7 \\ \text{no constraint, True} \end{cases} \quad (5)$$

$$\begin{aligned} v(\text{dark}) &= 1, \text{ if dark} \\ v(\text{grey}) &= 1, \text{ if dark} \cup \text{grey} \\ v(\text{any}) &= 1, \text{ if dark}^c \cap \text{grey}^c \end{aligned}$$

It is only worthwhile to consider a target for observation if that target will be visible during the observation session. For an optical telescope, this means selecting a sequence of observations starting at some time after sunset, N_{start} , and ending before sunrise, N_{end} .

$$v(\text{visible}) = 1 \forall h_{\text{target}} > \text{horizon} \in (N_{start}, N_{end}) \quad (6)$$

3.2. Astronomical Efficiency Functions

General constraints can be used to optimise the observation scheduling. The strictness of application of these “soft” preferences depends on the observation. To allow the flexibility and fuzziness that is required by astronomical observations, soft constraints are defined using merit functions using simple parameters that can be adjusted to make the constraint more, or less, stringent.

Airmass (Figure 1) can be used to assign lower weighting as the targets get closer to the horizon, thereby favouring observations at higher elevation:

$$\varepsilon_h(\text{airmass}) = \frac{1}{(z(h))^\alpha}, \quad (7)$$

for some observatory related airmass model, z .

The target must be a specific angular distance from the Moon. Separation angles may be dependent on the observation wavelength with different criteria between longer and shorter wavelengths, or brightness of target and comparator pair (Figure 2). It is advised that the separation angle be chosen as narrow as possible since very strict phase and angle requirements may drastically reduce the time period in which the observation can be carried out, and hence a lower probability that it would be successfully completed.

$$\varepsilon(\text{separation}) = \left(\frac{\theta(\text{target}, \text{Moon}) - a}{b} \right)^c \quad (8)$$

For a separation distance θ and separation limit a . Parameters b and c is used to shape the strictness of the merit.

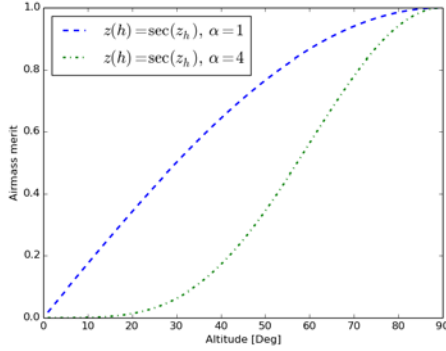


Figure 1. Using the homogeneous plane-parallel atmosphere approximation, the airmass model is given by the secant of the zenith angle. The merit scales the strictness of the airmass model using steepness parameter α .

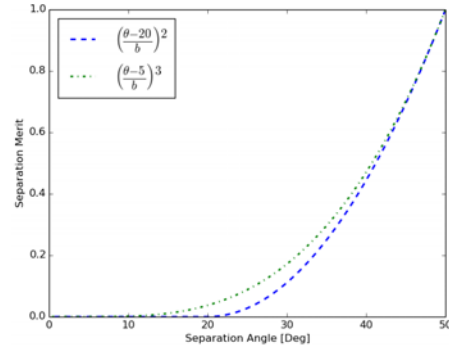


Figure 2. Separation angles merit allows for softer limits as targets approach solar system objects, thus improving the probability of observation.

For a Southern hemisphere observatory at latitude, ϕ and an object with declination δ , the minimum and maximum elevation angles are calculated:

$$E_{min}(horizon) = \begin{cases} -90^\circ - (\phi - \delta), & \text{if transit during observation period} \\ \min\{E(N_{start}), E(N_{end})\}, & \text{otherwise} \end{cases},$$

$$E_{max}(horizon) = \begin{cases} 90^\circ + (\phi - \delta), & \text{if transit during observation period} \\ \max\{E(N_{start}), E(N_{end})\} & \text{otherwise} \end{cases}$$

A positional merit can thus be defined as Equation 9 and shown in Figure 3.

$$\varepsilon(altitude) = \frac{h - \max\{E_{min}(horizon), E_{min}(limits)\}}{\min\{E_{max}(limits)\} - \max\{E_{min}(horizon), E_{min}(limits)\}}, \quad (9)$$

where h is the current altitude of the target; $E_{min}(horizon)$ the minimum pointing angle and $E(limits)$ some instrument specific pointing restrictions.

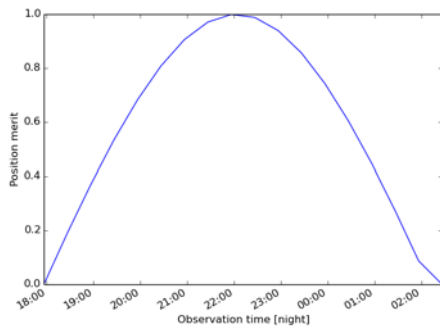


Figure 3. The current merit favours higher sky location during positional merit evaluation.

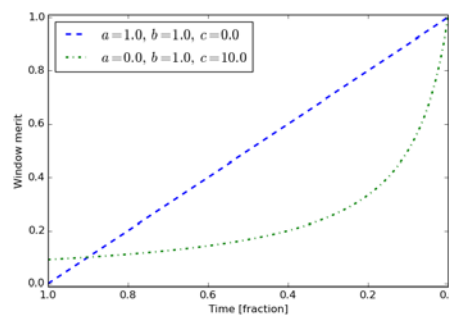


Figure 4. Merit increases as the fractional time remaining of the target observation window decreases.

In addition to the target altitude, Figure 4 shows a window merit that increases the selection weight as the target observation window shortens [8].

$$\varepsilon(window) = -a \times t_r + \left(\frac{b}{1 + c \times t_r} \right), \quad (10)$$

where $t_r = \frac{\Delta t_{target}}{\Delta t_{visible}}$ is the ratio of the target observation window over observation time remaining. The parameters a, b, c in this merit are only used to control the steepness of the rise.

To describe preferences related to the observation target's rise and set times, the start and terminate merits—shown in Figure 5—controls the rank evaluation as these boundaries approach.

$$\varepsilon(\text{boundary}) = \tanh\left(c \times \frac{\Delta t}{\sigma}\right), \quad (11)$$

relaxed by the gradient σ as time approaches the start and terminate boundary and Δt some buffer around the rise and set times.

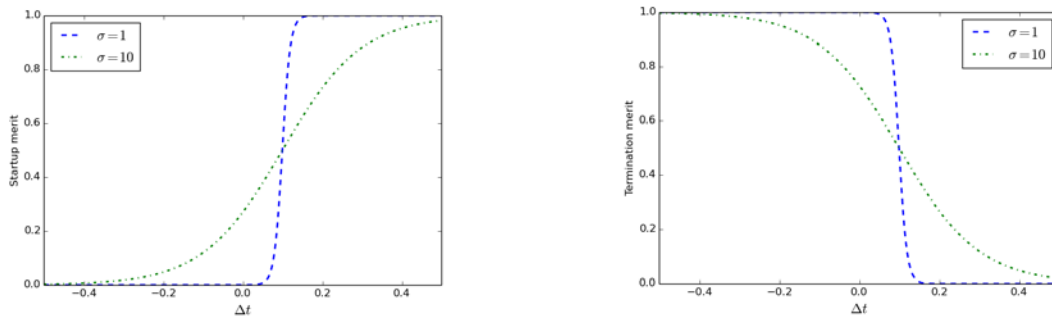


Figure 5. (Left) Merit indicating strictness to start observation at rise time. (Right) Merit indicating strictness to end observation before set time.

4. Summary

Planning and scheduling generally refer to off-line processing, while observing requires good solutions with minimal computation time. For each of these stages, we can define the problem input as consisting of the set of observations that have been requested, the constraints peculiar to the instrument/environment, and the optimisation of the objective function [4].

Maximum science efficiency is achieved by executing the programmes with highest scientific value first, under the required observing conditions. Additionally, maximised scientific use of telescope time is obtained by having appropriate programmes ready for execution under a broad range of observing conditions.

Fuzzy choices are essential for astronomical observation scheduling and is achieved by representing constraints as merit functions with a strictness parameter associated to each.

References

- [1] Frank J and Kürklü E 2003 Sofia's choice: Scheduling observations for an airborne observatory *Proceedings of the 13th International Conference on Automated Planning and Scheduling (ICAPS-03)* pp 226–35
- [2] Gómez de Castro A I and Yáñez J 2003 *Astronomy & Astrophysics* **403** 357–67
- [3] Wall M B 1996 *A genetic algorithm for resource-constrained scheduling* Ph.D. thesis Massachusetts Institute of Technology
- [4] Denny R B 2004 Dispatch scheduling of automated telescopes *The Society for Astronomical Sciences 23rd Annual Symposium on Telescope Science* vol 23
- [5] Swanson K, Bresina J and Drummond M 1994 Robust telescope scheduling *Proc. In i-SATRAS* vol 94 pp 347–50
- [6] Steele I A and Carter D 1997 Control software and scheduling of the Liverpool robotic telescope *Telescope Control Systems II* vol 3112 pp 222–33
- [7] Kubánek P 2008 *Genetic algorithm for robotic telescope scheduling* Master's thesis University of Granada
- [8] Granzer T 2004 *Astronomische Nachrichten* **325** 513–8

Near-Earth Object Avoidance Mitigation: Profiting One Rock at a Time

G C MacLeod¹

¹Research Fellow, Hartebeesthoek Radio Astronomy Observatory,

E-mail: gord@hartrao.ac.za

Abstract. Several Near Earth Object (NEO) avoidance mitigation concepts have been investigated. A simplified metrical analysis methodology is presented to demonstrate the viability and added benefits of methods. In particular an associated cost/additional benefits analysis (benefits beyond Earth protection) is presented. Nuclear weapons remain the clear method of choice to deflect a NEO, but it has little economic value beyond that. Other NEO avoidance mitigation methods offer potentially greater economic return and may warrant development. More research is required to create objective, measurable criteria for each NEO avoidance method. Saving the Earth one rock at a time might be profitable.

1. Introduction

Sixty-six million years ago a 10 km wide asteroid struck the Earth causing a massive extinction event, wiping out the dinosaurs and ultimately allowing humanity to rise from the ashes some 200,000 years ago [1]. Asteroids continue to strike the Earth today. Below are graphs, taken from Nelson [2], of the frequency of asteroid strikes versus diameter (figure 1) and energy (figure 2) to emphasise the impact of potential asteroid collisions.

As of 23 March 2016 the National Aeronautics and Space Administration (NASA) reports that there are 13,705 Near Earth Objects, or NEOs, greater than 140 m in diameter, of these 710 are larger than 1 kilometer in diameter. Any one of these can cause great damage if it struck the Earth; even smaller ones can. On 15 February 2013 a small 20-m in diameter asteroid exploded about 30 km above Chelyabinsk, Russia with the energy of 20 to 30 times more energy than that of the nuclear weapon unleashed over Hiroshima in 1945. The high altitude explosion limited damages to about \$30 million or more and injured ~1,500 people. There was no reported detection before it entered the atmosphere. On Halloween and Christmas Eve 2015 a comet and an asteroid, 600 m and 1,100 m in diameter, passed uncomfortably close to Earth. Each, had they impacted, would have caused massive devastation. Worse still the Halloween comet was detected only 21 days before its nearest approach leaving Earth defenses, whatever they are, helpless to respond.

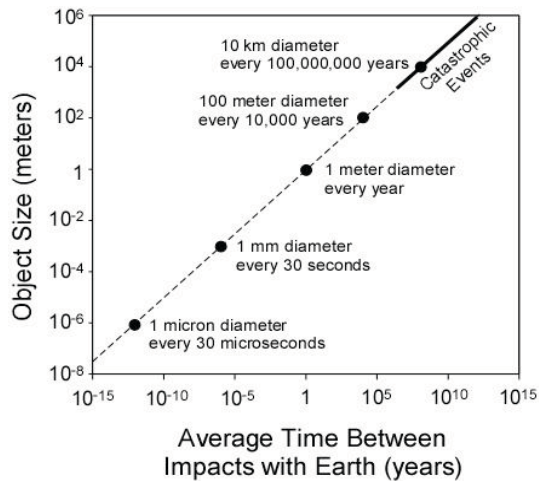


Figure 1: Average time between impacts of asteroid strikes vs diameter [2].

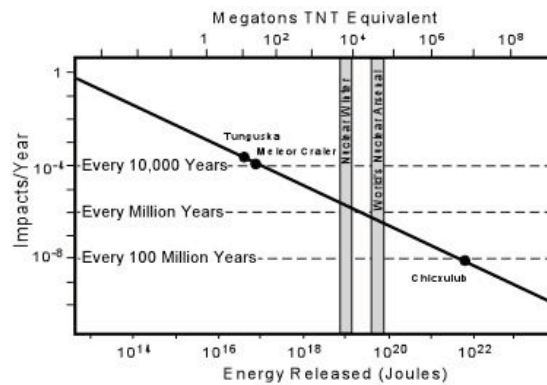


Figure 2: Impacts per year vs Energy Released [2].

What are the various methods devised to save us from a celestial encounter? Lamb [3] listed 10 possible asteroid avoidance mitigation strategies in no particular order; his 1st was the nuclear option and his 10th simply evacuate the predicted impact area. His methods for Earth protection are:

- Nuclear Device (ND) - launch a nuclear device(s) to knock the NEO off course even at close range,
- Kinetic Impactor (KI) - launch a weighted object to knock the NEO off course,
- Solar Paint (SP) - paint a portion of the NEO white and another black and it will drift off course,
- Solar Sail (SS) - attach a solar sail to the NEO and let the solar winds move it,
- Solar Net (SN) - encase the NEO in a mesh net; it will act like a solar sail,
- Solar Mirrors (SM) - station mirrors in orbit about the NEO and use focused sunlight to move it,
- Rocket Engine (RE) - attach a rocket engine and drive it away from the Earth,
- Gravity Tractor (GT) - rendezvous a large, heavy spacecraft with the NEO and use gravity to pull it,
- Robotic Miners (RM) - place robotic mining equipment on NEO and expel fragments providing push,
- Evacuation - evacuate the potential impact zone.

Using Wikipedia [4] another variation of the rocket engine was found: the Ion Beam shepherd (IB) gently pushes the NEO out of orbit from a small spacecraft. Only the first two options, nuclear weapons and kinetic impactors, seem plausible at this time [5]. The nuclear option is the only current technology available to deflect large NEOs [6].

There are 70 space agencies of which 13 have launch capabilities and only 3 countries are currently capable of human space flight, USA, Russia, and China [7]. Only two agencies have set up specific programmes relating to Earth Protection, they are: NASA and the European Space Agency (ESA). Such programmes are in their infancy in Russia and other countries. If nuclear weapons are the only option at present then Earth protection is left to only 7 nations with both miniaturised nuclear warheads and launch capabilities. One possibility to increase the number of organizations capable of protecting Earth is by identifying technologies with non-military applications but with alternative economic benefits. Below simplified metrics of the various NEO avoidance mitigation strategies as it relates to economics is presented.

2. Metrical Analysis of Mitigation Methods

Excluding evacuation, there are 10 possible NEO avoidance methods mentioned above. In order to compare each method a simple metric is created below where we try to answer 2 questions: "Can we build it?" and "Will it work?". A second set of metrics to compare associated costs and additional

benefits of each method is also presented. Associated costs are a measure of the total costs relating to the method from development through to successful completion of mission. Additional benefits are a measure of the benefits from the development to implementation not relating to actually protecting the Earth from catastrophe, e.g. new industrial opportunities, new technologies, etc.

For each metric there are a series of questions asked, each requiring a score from 1 to 10 (from bad to good, hard to easy, etc.). In table 1 the metrics, groups of questions, and how they are scored are presented. Note that this list is by no means complete or demonstrative of the topics but serves as a starting point for further development.

Table 1: List of questions asked for each metric and how each are scored.

“Can we do it?”		
C1	Does the tech exist?	1=none, 10=all
C2	How mature is the tech?	1=new, 10=mature
C3	How easy is it to prepare?	1=hard, 10=easy
C4	Time to develop?	1=long, 10=none
C5	Do resources exist to do it?	1=none, 10=all
“Will it work?”		
W1	How long will it take to succeed?	1=decades, 10=hours
W2	Will it be effective?	1=no, 10=completely
W3	Are there risks to failure?	1=significant, 10=none
W4	Is it proven tech?	1=no, 10=completely
Associated Costs		
AC1	Development costs	1=high, 10=low
AC2	Capital expenses	1=high, 10=low
AC3	Operational costs	1=high, 10=low
AC4	Maintenance costs	1=high, 10=low
AC5	Impact of economies of scale	1=high, 10=low
Additional Benefits		
AB1	Is it prestigious?	1=low, 10=high
AB2	Is there human capital development involved?	1=low, 10=high
AB3	Are there alternative economic uses?	1=low, 10=high
AB4	Are there technology spinoffs?	1=low, 10=high
AB5	Are there opportunities for private investment?	1=low, 10=high

For metrics representing “Can we do it?” and “Will it work?” a simple average is calculated. Economies of scale decrease the costs of capital, operations, and maintenance, and hence it is accorded greater weight. Likewise development costs are inherently expensive up-front costs and also afforded a greater weight. The score for associated costs is determined by

$$\text{Score} = (\text{AC1} + \{[(\text{AC2} + \text{AC3} + \text{AC4}) / 3] + \text{AC5}\} / 2) / 2. \tag{1}$$

Likewise if there are opportunities for private funding the weighted benefits are increased; it is naively accorded equal weight to the sum of the others. As with the metrics used, these weights and the relationships of each, have to be better determined. The score is calculated using

$$\text{Score} = [(AB1 + AB2 + AB3 + AB4) / 4 + AB5] / 2. \tag{2}$$

The scores listed in tables 2 & 3 are guestimates based on present technology, future planning and present business practices. They should not be seen as exact in any way and are used merely for presentation purposes; they are best guestimates by the author.

Table 2: Score for each avoidance mitigation method. Note that the two-letter initials of each method are used for identification.

	Can we do it?					Score	Will it work?				Score
	C1	C2	C3	C4	C5		W1	W2	W3	W4	
ND	9	9	7	7	10	8.4	10	9	7	8	8.5
KI	9	10	7	3	10	7.8	5	6	7	6	6
GT	5	3	3	3	7	4.2	3	4	3	3	3.25
SS	7	4	4	3	5	4.6	6	6	5	4	5.25
SP	7	5	3	3	7	5	4	4	5	2	3.75
SN	7	5	5	3	7	5.4	4	4	5	2	3.75
SM	7	5	6	4	7	5.8	6	6	6	5	5.75
RE	5	5	4	3	3	4	4	4	4	3	3.75
RM	5	3	4	3	6	4.2	3	7	3	5	4.5
IB	5	3	4	3	6	4.2	3	6	3	5	4.25

Table 3: Score for each avoidance mitigation method estimated for Associated Costs and Additional Benefits. Note that the two-letter initials of each method are used for identification.

	Associated Costs					Score	Additional Benefits					Score
	AC1	AC2	AC3	AC4	AC5		AB1	AB2	AB3	AB4	AB5	
ND	8	7	9	7	6	7.4	1	1	1	1	1	1
KI	8	5	6	7	2	6.0	3	3	1	3	1	1.75
GT	3	3	3	4	2	2.8	7	7	3	5	5	5.25
SS	4	4	4	4	5	4.3	5	4	3	5	5	4.625
SP	4	4	3	4	1	3.2	3	4	1	3	1	1.875
SN	4	4	5	5	3	3.9	3	4	1	3	1	1.875
SM	4	4	6	6	3	4.1	5	4	1	5	3	3.375
RE	3	3	3	3	5	3.5	7	8	4	5	8	7
RM	3	2	2	2	10	4.5	7	10	10	7	10	9.25
IB	4	3	3	3	5	4.0	5	6	4	5	5	5

Graphical representations of each set of metrics, "Can we do it?" versus "Will it work?" and "Associated Costs" versus "Additional Benefits" are presented in figure 3 and 4 respectively.

Figure 3 is divided into four areas:

- Sci-Fi – Solutions with little or no technology developed or tested.
- Not practical – Options that will demonstrate limited success.

- R&D required – Systems that can work but require significant development.
- Functional – Workable solutions with mature technologies.

Only 3 avoidance mitigation systems fall into “Functional”: solar mirrors, kinetic impactors, and nuclear weapons. Based on the scoring above the nuclear option is the best method at present. However, this has political consequences making it a difficult choice especially if these weapons are put in space for faster response time. Utilising kinetic impactors is politically more palatable but is presently only demonstratively capable of stopping small NEOs detected years before potential impact. The Double Asteroid Redirect Test (DART) mission scheduled for 2022 will study the effectiveness of the kinetic impactor method [8]. Solar mirrors are found in the Functional area of figure 3; this is suited to situations where we have significant advanced warning (years). The rest are largely in the realm of science fiction and require significant development to prove viability.

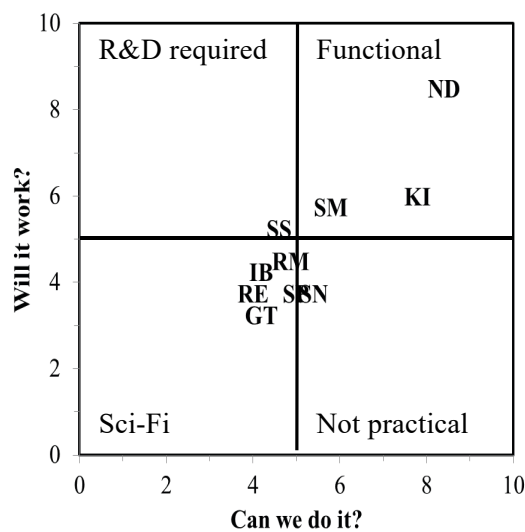


Figure 3: Metrical analysis of each mitigation system as it pertains to “Can we do it?” vs. “Will it work?”

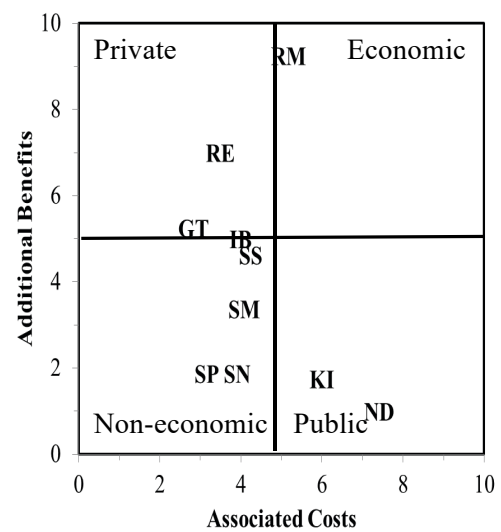


Figure 4: Cost/Benefit analysis of each mitigation system.

The Cost/benefit analysis presented in figure 4 provides insight into where funding for various asteroid avoidance mitigation systems might come, public versus private funding or a combination. Private investments flow into projects that create economic rent and a financial return to the investors. Public funding typically is used in projects for the public good, like defense where arguably there is no direct return on investment. Several of the proposed mitigation systems appear to be non-economic or expensive with little return on investment. The kinetic impactor (KI) and nuclear device (ND) options have little added benefits and would require public funding. Only robotic mining falls into the economic category; a few others (e.g. RE, GT, and IB) might be worth studying for private funding. Each appears to have economic spinoffs worth investing in.

Robotic mining (RM) is rated, in this scorecard, the best in terms of additional benefits and private investors might consider it. The weakness of RM is its associated costs; further investigation is required to determine if economies of scale, Research & Development (R&D) and decreasing space transport costs will make this an attractive investment. The American space agency (NASA) is proposing retrieving an asteroid and placing it in a lunar orbit where astronauts can practice mining it amongst other things. To give context to the potential of mining asteroids, the estimated worth of the metallic asteroid 3554 Amun (orbiting between Earth and the Sun) may be \$20 Trillion dollars in precious metals [9]. It might just be very profitable saving the Earth one rock at a time!

Earth protection can be greatly enhanced if the number of organizations and people is substantially increased. Even if nuclear devices are the only answer, only a handful of countries would be capable of launching defensible measures and increasing this number is not in Earth's best interest. The survival of the human race can be increased by increasing the number of people and solutions available. In order for other NEO avoidance mitigation techniques to be developed, and increase Earth's chances of survival, alternative economic benefits may encourage development. As stated above many of the avoidance systems mentioned here have no additional benefits (benefits beyond saving the Earth). The development of rocket engines for new spacecraft offers investors significant economic return resulting from technology to be developed for new engine designs. Whereas robotic mining (RM) has significant upside economic opportunities, if instead of simply ejecting matter from the NEO, and change its course, this material is mined for valuable resources [10].

3. Conclusions

Several NEO avoidance mitigation concepts have been investigated. A simplified metrical analysis methodology is presented to determine the viability of each and if they might attract investment for non-Earth defense reasons. In particular an associated cost/additional benefit analysis (benefits beyond Earth protection) is presented. Nuclear weapons remain the clear method of choice to deflect a NEO, but it has little economic value beyond that. Other NEO avoidance mitigation methods offer potentially greater economic return, e.g. robotic mining, and may warrant private investor development. More research is required to create objective, measurable criteria for each NEO avoidance mitigation method. Saving the Earth one rock at a time might be profitable.

4. Acknowledgements

I wish to thank the creators of Google and Wikipedia for these resources contributing to this report.

5. Bibliography

- [1] Renne P R, Deino A L, Hilgen F J, Kuiper K F, Mark D F, Mitchell III W S, Morgan L E, Mundil, R, Smit J 2013, *Science*, 339, 684
- [2] Nelson S A, "Meteorites, Impacts and Mass Extinctions", http://www.tulane.edu/~sanelson/Natural_Disasters/impacts.htm, Tulane University, 1 December 2014
- [3] Lamb R, "10 Ways to Stop an Asteroid", *Space*, <http://news.discovery.com/space/asteroids-meteors-meteorites/top-10-asteroid-deflection-130130.htm>, 30 Jan 2013
- [4] Wikipedia 2016a, https://en.wikipedia.org/wiki/Asteroid_impact_avoidance
- [5] Ahrens T J, Harris A W 1992, *Nature*, 360, 429
- [6] Bruck-Syal M, Dearborn D S P, Schultz P H 2013, *Acta Astronautica*, 90, 103
- [7] Wikipedia 2016b, https://en.wikipedia.org/wiki/List_of_government_space_agencies
- [8] Cheng A F, Michel P, Reed C, Galvez A, Carelli I 2012, European Planetary Science Congress, Vol. 7 EPSC2012-935-1 2012
- [9] Lewis R S 1997, "Mining the Sky: Untold Riches from the Asteroids, Comets, and Planets", Pegasus Books Group, ISBN 0201328194
- [10] Eubanks T M 2015, George Marshal U., "Asteroid Mining: Thinking Outside the Sphere", presented at "Asteroid Day Talk" at George Madison University, DOI: 10.13140/RG.2.1.4042.3527, 30 June 2015

Cosmic ray ground level enhancements: Power of the pulse shape

O. Ogunjobi, R.D. Strauss

Center for Space Research, School for Physical and Chemical Sciences, North-West University, Potchefstroom, 2520 South Africa

E-mail: olakunle.ukzn@gmail.com

Abstract. Ground level enhancements (GLEs) of the cosmic-ray intensity have been observed seventy-one times over the past seven decades. GLEs are due to sudden increases in the intensity of solar energetic particles associated with large eruptive episodes. GLEs have been, controversially, divided into two distinct categories, gradual (classical) and impulsive events. Recent findings also argue that some GLEs are too impulsive to be accelerated in the eruptive episodes. Here we investigate this hypothesis by studying the time profiles of nine GLEs, which were observed with excellent data coverage of the associated solar eruptions. Results show that, when characterized solely on their time profile (i.e. pulse shape), GLEs do not separate into two distinct classes, but rather form a continuous distribution between these two extremes. Preliminary modelling results indicate that the interplanetary transport conditions may alter the GLE pulse shape in such a way as to obscure any source information by the time it reaches Earth. This implies that the shape of the GLE profile is, perhaps, a powerful indicator of propagation conditions between Sun and Earth.

1. Introduction

Ground level enhancements (GLEs) are sudden increases in the cosmic ray intensity as observed at Earth. Ground-based cosmic ray (CR) observations started with the observation of a GLE on 28 February 1942. Since then, GLEs have been observed seventy-one times by ground-based neutron monitors. This is possible due to large solar eruptive episodes that originate primarily from the western longitudes on the surface of the Sun. In other words, these GLEs are the result of solar eruptive episodes that produce atmospheric showers of secondary particles that can reach ground level, provided that the incoming particle energy is ≥ 500 MeV per unit charge, or rigidity ≥ 1 GV. Relativistic protons produced from these solar energetic particles (SEPs) events represent a direct sample of matter from some of the most energetic processes in the solar system, particularly, solar flares and coronal mass ejections (CMEs). Solar flare are enormous explosions which occur in the solar corona, while CMEs represent vast structures of plasma and magnetic fields that are expelled from the Sun into the heliosphere.

The relationship between flares and CMEs, and their role in accelerating particles to relativistic energies during major solar events remains an exigent scientific challenge. Previous studies e.g [1] classify SEPs, albeit controversially, into two distinct classes, impulsive and gradual events. Flares in the low solar corona are relatively short-lived and have a narrow range of solar longitudes (about one Earth radii, R_E) that are magnetically well-connected to

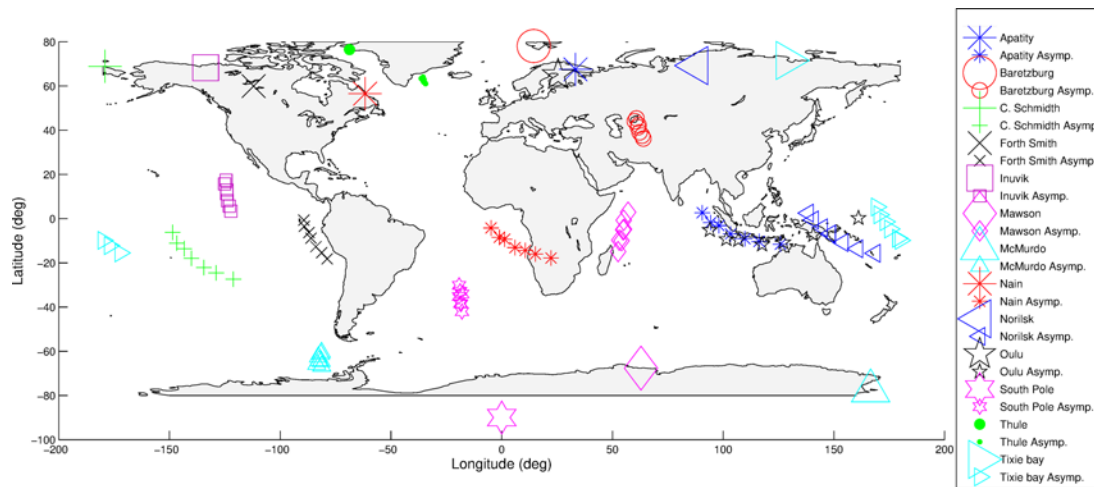


Figure 1. Geographical locations of the contributing neutron monitors with geomagnetic cut-off rigidity below 1 GV (large markers) and the corresponding asymptotic viewing directions (small markers).

the observer. [1] and others also attribute particle acceleration to flare processes such as wave-particle interactions following magnetic reconnection. Conversely, CMEs develop more gradually at distances beyond about four R_E , which is much larger than the Sun, and should therefore have shock fronts that are widely extended in heliolatitude and longitude. So, it is expected to associate the impulsive GLE events with acceleration in solar flares, and gradual GLE events in CME shock fronts. The classification of gradual versus impulsive events are mostly based only on the time profile (pulse shape) of the GLE event as observed by a number of neutron monitors.

Impulsive events, according to [1], are characterized by high $^3\text{He}/^4\text{He}$ ratios (>0.1), high Fe charge states (~ 20), high Fe/O ratios and low particle fluxes, while the composition of the gradual events is more characteristic of the composition of the solar wind or interplanetary medium. Hence, this supports the inference that impulsive SEP events contain particles that were accelerated in the corona, likely by solar flares, while the more gradual events originate more likely from the acceleration in the bow shocks of CMEs.

At energies of a few MeV per nucleon, space observation of impulsive and gradual events can be distinguished by compositional signatures. For GLEs, as observed primarily by ground-based neutron monitors, the signatures of the composition and ionization state are lost. However, GLEs observed with Earth's neutron monitors have the advantage of being sensitive to the arrival direction of the particles, which gives an indication of the anisotropy of the event. For vertical arrival at a neutron monitor, the particles must have come from a so-called asymptotic direction in space before they penetrated the geomagnetosphere [2]. This directional sensitivity explains why a given GLE can display an impulsive character on one set of neutron monitors, but only show up as gradual on others.

We show in Figure 1 the asymptotic cone of acceptance for all neutron monitors used in this study. The large symbols indicate the position of the neutron monitor, while the smaller symbols show the asymptotic position for rigidities of 1 - 5 GV. Note the highest rigidity point is closest to the station. Also, because only stations with a cut-off below 1 GV are used, all the monitors are located in the polar regions. For an anisotropic SEP event, the looking direction (asymptotic cone) will be different for different neutron monitor stations, and as such, they will measure different intensities.

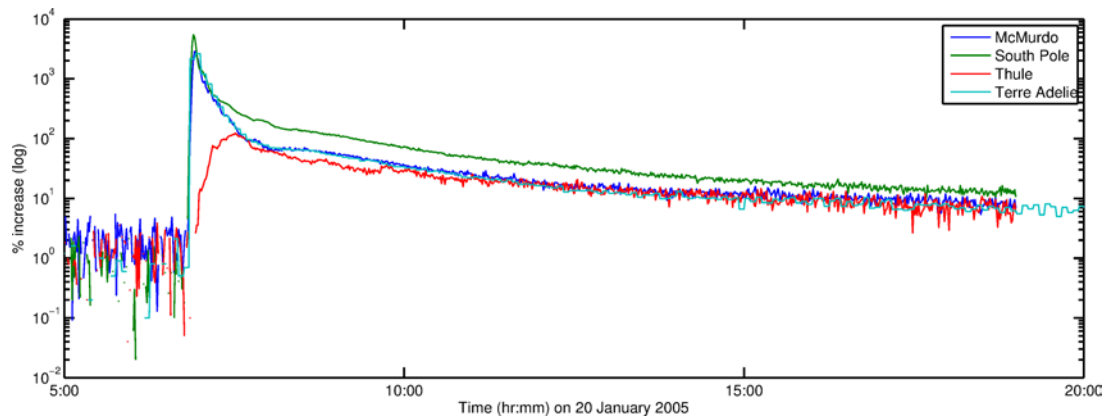


Figure 2. Time-intensity profile of GLE 69 showing both of impulsive and gradual characteristics.

Figure 2 illustrates this directional sensitivity of the neutron monitor network on the very large GLE 69 of 20 January 2005. It was such that three neutron monitors (South Pole, Terre Adelie and McMurdo) saw an extremely impulsive increase, reaching the peak intensity in ~ 5 minutes, while Thule saw a much longer rise time of ~ 30 minutes. A third group of stations observed two consecutive peaks (not shown here). [3] interpreted this structure as indicating two injection/acceleration mechanisms, namely a fast, short-lived solar flare, and a slower, longer-lived bow shock of the CME. This was not consistent with the generally accepted idea that the slow rising-stations merely observed a filling-in effect from the directions that were viewed by the fast-rising ones. Earlier, [4] investigated all the impulsive GLEs over the entire time span, and demonstrated that these events typically extend to higher energies than the more gradual ones. The authors, [4], further noted that the fastest rising peak coincided well with high-energy gammas produced by particles slamming into the dense matter of the low corona while the rate of decrease shows an evidence of kink at ~ 1 hour. This is a natural explanation for the first, impulsive peak to recede below the second, gradual one at this time as presented in Figure 2.

Furthermore, the concept of impulsive versus gradual GLEs for large GLE 42 on 29 September 1989 was put in perspective by [5]. At the peak intensity the difference between impulsive and gradual is about a factor of 3, while for GLE 69 this difference is at least a factor of 30. This means that GLE 42 was much less anisotropic than GLE 69. The solar activity associated with GLE 69 was in the well-connected region at $\sim 65^\circ$ W, while for GLE 42 it was invisible behind the western limb and could only be inferred indirectly at $\sim 120^\circ$ W. This longitude would have been so poorly connected that particles that might have been accelerated in the highly anisotropic first beam in the lower corona, could not have reached Earth. The combination of all available observations from ~ 40 neutron monitors show, however, that these variations are qualitatively different from the true impulsive and gradual peaks, and [3] ascribed them as due to fluctuations in the direction of the heliospheric magnetic field. It has been suggested in other studies e.g [5], that the knowledge of pulse shapes or time profile of GLEs is required to determine the fidelity of impulsive and gradual events, and how to interpret its physical meaning.

In this paper, the average pulse shapes of selected nine (9) GLEs were simultaneously determined. The maximum amplitude, the time-to-maximum, half decay time from the maximum intensity, and the heliolongitude of the asymptotic cone of acceptance of each of the 9 events were studied.

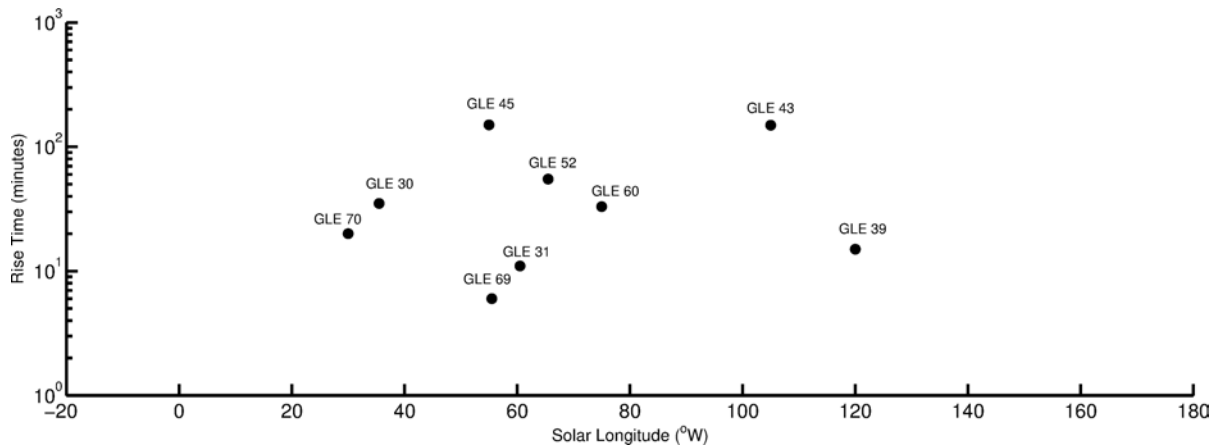


Figure 3. The relationship between the rise time of the selected 9 GLEs and the solar longitude of their associated solar events.

2. Observation and analysis of the time profile of selected 9 GLEs

The data base, which contains all available ground level neutron monitors observation, of all 71 GLEs since 1942 has been described by [6]. In this study, only 9 GLEs (30, 31, 39, 43, 45, 52, 70, 60 and 69) are used. These GLEs under study have amplitude much more than 10% and it is a subset of all available 71 GLEs. The peculiarities and differences between the intensities of secondary solar particles occurring between different neutron monitor stations during the selected 9 GLEs can be interpreted on the basis of their asymptotic directions of viewing. Here we used only the stations with cut-off rigidity below 1 GV in order to eliminate any energy/rigidity dependence. Also we study the time (pulse shapes) of the selected 9 GLEs simultaneously, to determine how to differentiate between impulsive and gradual ones, and how to, eventually, interpret its physical meaning. In doing this, it is important to see if the GLEs are magnetically well connected to Earth.

To determine the rise times of each event, the beginning of the event was taken as the earliest time for which a statistically significant increase could be visually inspected from the intensity-time profile. The time of maximum was generally easy to read off, but was sometimes complicated when the profile lingered around the maximum intensity, or when it even show multiple peaks. [9] hypothesised that multiple peaks found in some GLEs could be due to two different injections or a probable swing in magnetic field direction.

Figure 3 displays the rise time of the events as function of heliolongitude. The distribution is centered on the heliolongitude that connects to Earth via the nominal Parker spiral magnetic field, corresponding to 60° W [7]. This corroborates the study by [8], which showed that the hardest spectra, at energies below the GLE cutoff, originated from the region around 60° W. Although [9] recently reported a weak correlation with longitude. No clear distribution is evident from Figure 3 and we are unable to confirm that the so-called “fast-risers” (i.e. GLEs with short rise times) are always magnetically connected to Earth.

Figure 4 shows the relationship between the rise and decay times (to 50% of the peak intensity) of all the GLEs. The full line on the plot is the best-fit linear regression. This shows that, on average, the decay time is about twice as long as the rise time. The main result of this analysis is that GLEs do not separate into two distinct categories of impulsive and gradual events. The rise times show a continuous range from 5 to 160 minutes. Effort is underway to interpret these results in terms of a particle transport model, with initial results presented in [10].

Irrespective of the step taken when determining the rise times in Figures 3 and 4, we note that

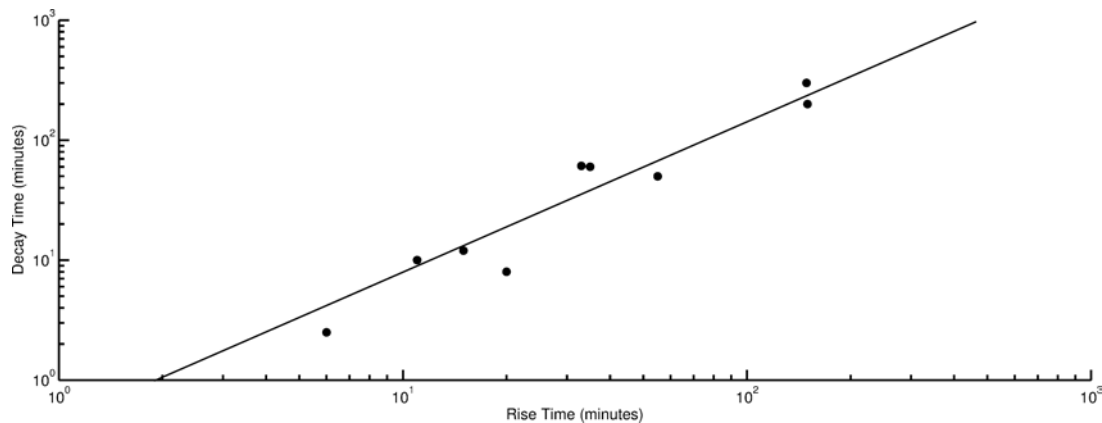


Figure 4. The relationship between the rise and decay time of the selected 9 GLEs. The thick line is the best-fit linear regression.

the beginning of the event may be difficult to be interpreted physically or in terms of modeling. This is due to the obvious anisotropic direction of propagation of the solar particle and due to the disparities in the counting rates recorded between different contributing neutron monitors. In order to correct this problem, we apply the measure of central tendency by averaging over viewing direction. This will provide us with cosmic ray fluxes which can better compared with model solutions.

Figure 5 shows the average time-profile recorded by all the contributing neutron monitors during each of the selected events. Note that the ninth GLEs (GLE 69) has been represented in Figure 2. The use of the average time-profile (in Figure 5), however, has eliminated some of the limitations such as the large uncertainty in the time-profile as measured by different stations. Based on the average, the selected events do not have strong anisotropic like distributions. They are, in fact, isotropic. These isotropic observations fulfil all the necessary assumptions of our ongoing transport model. Interpretations of the present observation in terms of the propagation of a gyro-tropic distribution of SEPs transport model is underway.

3. Summary

The main result of the paper is that there is no clear distinction of GLEs in impulsive and gradual classes, but rather a continuous range between these extremes. On average, the decay time is about twice as long as the rise time for the 9 selected GLE events, with a good linear correlation between these two quantities.

Acknowledgments

The concept behind this work originated from the late H. Moraal, it was expanded by O. Ogunjobi and R.D. Strauss with the purpose of interpretation in terms of a more realistic transport model for GLEs. The GLE database is available at ftp://cr0.izmiran.rssi.ru/COSRAY!/FTP_GLE/ (hosted by E. Eroshenko), <https://gle.oulu.fi/>, as well as http://usuarios.geofisica.unam.mx/GLE_Data_Base/. This work is based on the research supported in part by the National Research Foundation (NRF) of South Africa (grant no. 106049). Opinions expressed and conclusions arrived at are those of the authors and are not necessarily to be attributed to the NRF. OO acknowledges the support of the post-doctoral programme of the North-West University in South Africa. *This paper is dedicated to the memory of the late Harm Moraal.*

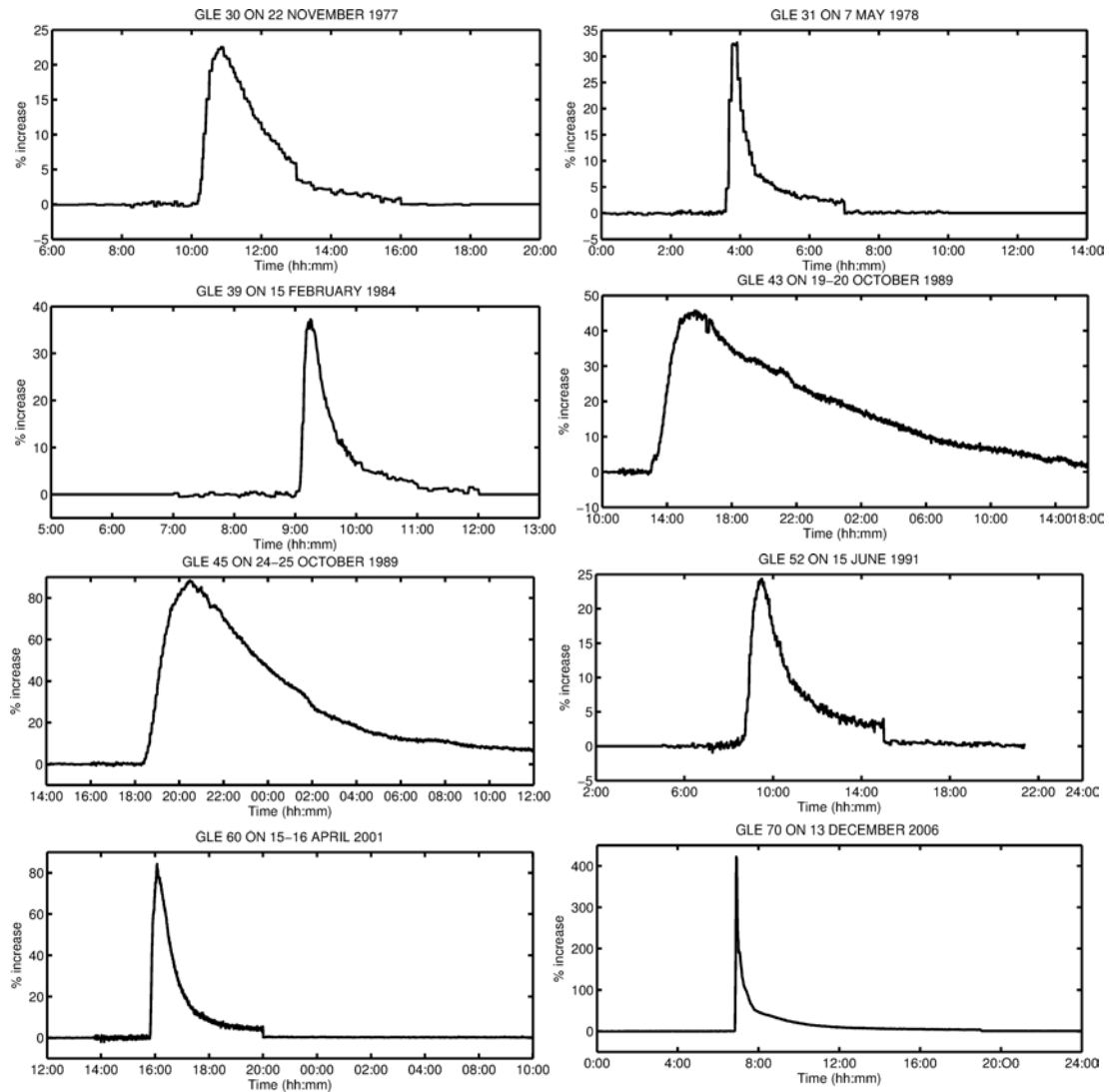


Figure 5. Average time-profile recorded by all the contributing neutron monitors during each event.

References

- [1] Reames D 1999 *Space Sci. Rev.* **90** 41
- [2] Shea M and Smart D 1990 *Solar Phys.* **127** 297
- [3] McCracken K, Moraal H and Stoker P 2008 *J. Geophys. Res.* **113** A12101
- [4] McCracken K, Moraal H and Shea M 2012 *Astrophys. J.* **761** 101
- [5] Moraal H 2013 *Space Sci. Rev.* **176** 299
- [6] Moraal H and McCracken K 2012 *Space Sci. Rev.* **171** 85
- [7] McCracken K and Palmeira R 1960 *J. Geophys. Res.* **65** 2673
- [8] Van Hollebeke M A I, Ma Sung L S and McDonald F 1975 *Solar Phys.* **41** 189
- [9] Mewaldt R A, Looper M, Cohen C, Haggarty D, Labrador A, Leske R, Mason G, Mazur J and Von Rosenvinge T 2012 *Space Sci. Rev.* **171** 97
- [10] Strauss R D, Ogunjobi O, Moraal H, McCracken K G and Caballero-Lopez R A 2017 *Sol. Phys.* **292** 51

Ionospheric characterisation of the South Atlantic Magnetic Anomaly using a mobile ship-based dual-frequency GPS Ionospheric Scintillation and Total Electron Content Monitor

Annelie Vermeulen¹, Pierre J Cilliers^{1,2}, Peter Martinez¹

¹SpaceLab, Department of Electrical Engineering, University of Cape Town, Rondebosch, Cape Town, 7700, South Africa

²South African National Space Agency (SANSA) Space Science, Hermanus, 7200, South Africa

E-mail: ¹ani@entropy.co.za or spacelab@uct.ac.za, ²pjcilliers@sansa.org.za

Abstract. This project proposes the novel use of a mobile geodetic-grade dual-frequency GPS Ionospheric Scintillation and Total Electron Content Monitor (GISTM), located on board the polar research vessel SA Agulhas II, to characterise the ionosphere over the South Atlantic Magnetic Anomaly (SAMA) during voyages through this area of the South Atlantic Ocean. It is shown that a 10° elevation cut-off is sufficient to tolerate ship roll angles of up to 20° to avoid multipath from the ocean surface. Preliminary ship-based scintillation results show increased S_4 counts, as well as extremely high σ_ϕ counts, compared to a stationary GISTM at Hermanus, South Africa.

1. Ionospheric Scintillation

Ionospheric Scintillations are rapid fluctuations in both the phase and amplitude of trans-ionospheric radio signals resulting from variations in electron density along the ray path [1]. Scintillation measurements are traditionally done using dedicated dual-frequency GPS receivers at static locations. Ionospheric scintillation affects GPS signals in two ways: Amplitude scintillation presents as an abrupt severe fade in signal strength while phase scintillation is characterised by rapid changes in the carrier wave phase; both of these can lead to loss of lock, increase in position errors and GPS outage [2].

SANSA operates several of these specialised receivers throughout Southern Africa as well as at Marion Island, Gough Island, and in Antarctica at the SANAE IV research station. The SAMA is a region of the Earth where the magnetic field is up to 60% weaker than at comparable latitudes [3]. It is of interest due to increased levels of precipitation of high energy particles into the ionosphere over this region during geomagnetic storms. However, the majority of the SAMA lies beyond the reach of these fixed land-based sensors [4]. The geographical extent of the South Atlantic Magnetic Anomaly is shown in Figure 1. The approximate coverage that these (and other) static stations provide of the Southern Oceans can be seen in Figure 2.

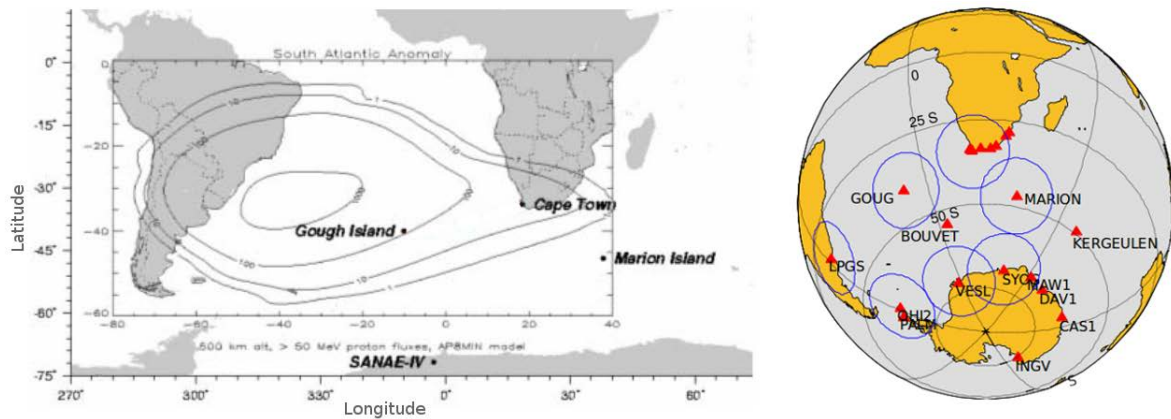


Figure 1: (Left) The South Atlantic Magnetic Anomaly as defined in terms of the ≥ 50 MeV proton flux particles at 500km altitude during a geomagnetic storm [5].

Figure 2: (Right) Approximate coverage of existing fixed GISTM stations. These are calculated using a 350km ionospheric pierce point (IPP) height and an elevation of 10° [5].

2. The SA Agulhas II route and GISTM

The SA Agulhas II ice-breaking polar research vessel sails from Cape Town to Antarctica/South Georgia in December–February, Marion Island in April–May, and Gough Island/Tristan da Cunha in August–October. A plot of the typical locations of the SA Agulhas II at various times of the year is shown in Figure 3.

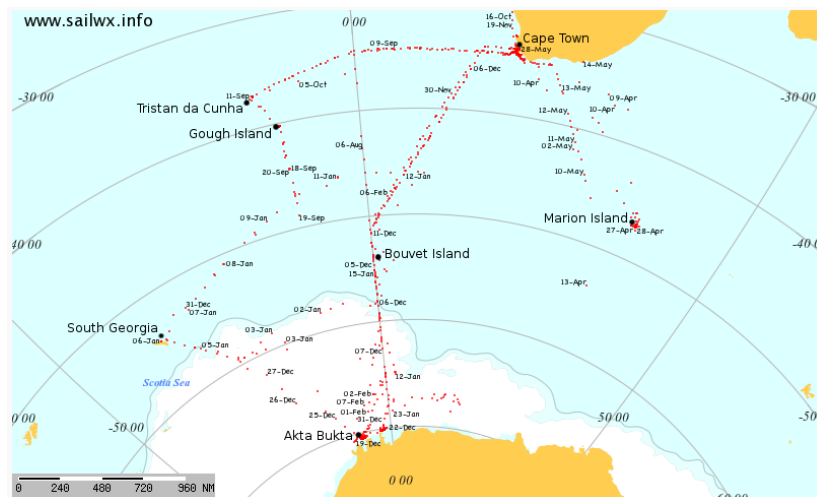


Figure 3: The various routes of the SA Agulhas II between May 2013 and Feb 2016.[6]

The multi-frequency multi-constellation NovAtel GISTM unit was installed on board the SA Agulhas II in 2012 (see Figure 4). It has enabled the first terrestrial measurements of scintillation from new locations within the SAMA region [3],[5]. In this research, the amplitude (S_4) and phase scintillation (σ_ϕ) indices from L1 signals recorded at 50 Hz during the SA Agulhas II voyages in the periods 28 June 2014 – 13 October 2014 and 18 December 2014 – 10 February 2016 will be analysed for the first time. Only GPS satellites ($PRN \leq 32$) will be used.



Figure 4: The SA Agulhas II polar research vessel, pictured at Akta Bukta in Antarctica in February of 2015, is equipped with a NovAtel GISTM receiver in the Crow's Nest. The grey dome antenna is located at the very top of the mast, providing an unobstructed view of the sky.

3. Negative Horizon and Ship Roll Tolerances

The open ocean has no urban canyons or environmental obstructions which may cause multipath. The only potential source of multipath GPS signals is the ocean surface itself. A hard-coded limitation in the GISTM receiver software resulted in only data for ray paths with elevations $\geq 10^\circ$ being recorded. The 37.8 m height of the GISTM antenna (above mean sea level) and taking the radius of the Earth at 6378 km produces a negative horizon elevation angle of 0.2° as seen in Figure 5. The antenna to horizon distance is 22.219 km.

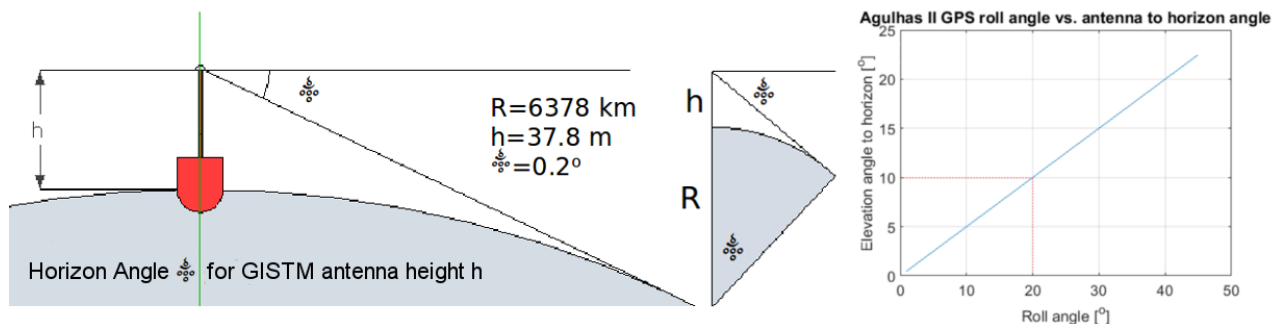


Figure 5: The relation between the roll angle and the elevation angle of the horizon for the SA Agulhas II.

The motion of the vessel includes translation (point A to B), vibration and the 3 axial movements (roll, pitch and yaw). The roll motion is most likely to incur occasional multipath if the roll angle is large enough. Roll angles of up to 20° off vertical can be tolerated by the 10° GISTM cut-off without incurring multipath (see Figure 5). It is rare for the SA Agulhas to experience rolling beyond this limit. The motion effect on the scintillation data due to waves and vibration will be studied in future work.

4. Preliminary Results

The thresholds for significant scintillation can be expressed in terms of the amplitude (S_4) and phase (σ_ϕ) scintillation indices, or the number of scintillation events above a given threshold in a given time. The levels of ionospheric scintillation which may give rise to GPS navigation errors and outages have been reported in several studies ([2],[7],[8],[9]). The benchmark levels for significant scintillation have been shown to be dependent on the particular receiver technologies

[10]. In high-latitude regions phase scintillation is more frequent and intense than amplitude scintillation [9]. In most cases scintillation levels of $S_4 \leq 0.2$ and $\sigma_\phi \leq 0.2$ are considered to be insignificant in terms of impact on GPS navigation [8]. In this study, scintillation is quantified in terms of the number of S_4 and σ_ϕ -events with intensity above 0.2 in a 10-minute period. This allows a clear distinction between background noise levels and significant increases in scintillation counts. S_4 and σ_ϕ values ≥ 1 are suppressed to remove outliers.

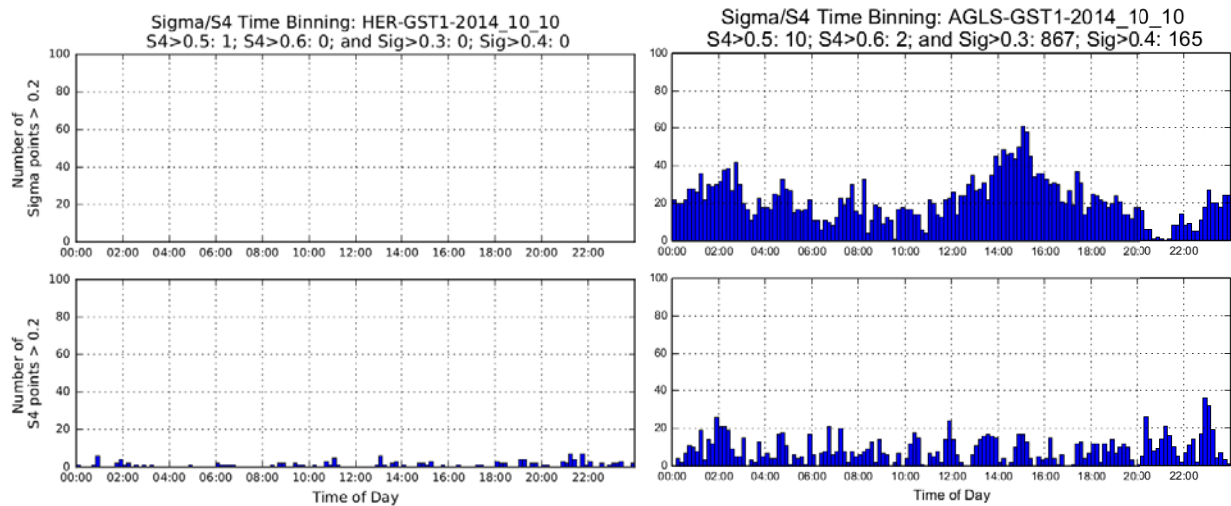


Figure 6: Histogram of S_4 and $\sigma_\phi \geq 0.2$ counts recorded on 10 October 2014 at Hermanus (left) and on board the SA Agulhas II (right). Time is in UT.

Figure 6 shows a comparison of S_4 and σ_ϕ values ≥ 0.2 counts recorded on 10 October 2014 on board the SA Agulhas II with similar counts recorded in Hermanus on the same date. The SA Agulhas II results clearly show the high background level of scintillation above the threshold of 0.2. The higher background levels may be a result of the motion of the SA Agulhas II affecting the scintillation observations.

A significant increase in the σ_ϕ (phase) ≥ 0.2 counts is visible in the SA Agulhas II data during the period 14:00-16:00 UT, while there was no change at Hermanus. This indicates that the likely cause of the increase may be a precipitation event over the SAMA which was not observed from Hermanus.

An increase in the σ_ϕ without a concurrent increase in S_4 is in line with typical results for high latitude regions.[9]

5. Conclusions

A 10° elevation cut-off on the GISTM is shown to be sufficient to prevent multipath from the horizon up to roll angles of 20° while the ship is in the open ocean. Preliminary results indicate that the motion of the ship may be responsible for higher background level of phase scintillation. The increase in σ_ϕ during the period 14:00-16:00 UT on 10 October 2014 may indicate a precipitation event over the SAMA.

This work is in the early phase. Future work will include investigating the extent of the ship's motion effect on scintillation data, as well as attempting to identify scintillation events in the SAMA region by comparing the SA Agulhas II data to the stationary receiver on Gough Island.

Acknowledgments

Thanks to Jon Ward (SANSA) and Jan Vermeulen for their assistance with scripts for correcting and processing the raw GISTM data. We acknowledge the support of the National Research Foundation (NRF) for the research funding of the National Equipment Programme which includes the GISTM unit on the SA Agulhas II used in this research through Grant SNA14073083260 to SANSA. We acknowledge the support of the Department of Environmental Affairs (DEA) for the installation and maintenance of the GISTM on board the SA Agulhas II as part of the South African National Antarctic Program (SANAP). This student is partially funded by an NRF Innovation Masters Bursary.

References

- [1] Kintner, P., Humphreys, T., and Hinks, J., 2009. GNSS and Ionospheric Scintillation: How to Survive the Next Solar Maximum. *InsideGNSS*, July/Aug, pp.22-30.
- [2] Doherty, P.H., Delay, S.H., Valladares, C.E., and Klobuchar, J.A., 2003. Ionospheric scintillation effects on GPS in the equatorial and auroral regions. *Navigation*, 50(4), pp.235-245.
- [3] Korte, M., Manda, M., Linthe, H.J., Hemshorn, A., Kotze, P., and Ricaldi, E., 2009. New geomagnetic field observations in the South Atlantic Anomaly region. *Annals of Geophysics*, 52, pp.65-81
- [4] van der Merwe, S.J., 2011. Characterisation of the Ionosphere over the South Atlantic Anomaly by using a ship-based dual-frequency GPS receiver. MEng Dissertation, University of Pretoria.
- [5] Cilliers, P.J., Mitchell, C.N., and Opperman B.D.L., 2006. Characterization of the Ionosphere over the South Atlantic Ocean by Means of Ionospheric Tomography using Dual Frequency GPS Signals Received On Board a Research Ship. *Proceedings of NATO Information Systems Technology (IST) Panel Specialists Meeting on Characterising the Ionosphere (Fairbanks: RTO-MP-IST-056)*, pp.28.1-28.18.
- [6] SA Agulhas II Route Map. Accessed May 2016, <http://www.sailwx.info/shiptrack/shipposition.phtml?call=ZSNO>
- [7] Basu, S., Groves, K.M., Basu, S. and Sultan, P.J., 2002. Specification and forecasting of scintillations in communication/navigation links: current status and future plans. *Journal of Atmospheric and Solar-Terrestrial Physics*, 64(16), pp.1745-1754.
- [8] Carrano, C.S., Groves, K.M. and Griffin, J.M., 2005, May. Empirical characterization and modeling of GPS positioning errors due to ionospheric scintillation. In *Proceedings of the Ionospheric Effects Symposium*, Alexandria, VA, pp.1-9.
- [9] Ngwira C. M., McKinnell L. A., Cilliers P. J., 2010. GPS phase scintillation observed over a high-latitude Antarctic station during solar minimum. *Journal of Atmospheric and Solar-Terrestrial Physics*, 72, pp.718-725.
- [10] Skone, S., Knudsen, K. and De Jong, M., 2001. Limitations in GPS receiver tracking performance under ionospheric scintillation conditions. *Physics and Chemistry of the Earth, Part A: Solid Earth and Geodesy*, 26(6-8), pp.613-621.

Division E – Education

Teaching students problem solving with the ‘light bulb effect’ cognitive diagrammatic representation

C Albers, D Clerk and D Naidoo

School of Physics, University of the Witwatersrand, Private Bag 3, WITS 2050

E-mail: claudia.albers@wits.ac.za

Abstract. A diagrammatical representation of the cognitive processes required, for solving Physics problems, is used to teach students in Physics I major, at the University of the Witwatersrand, about problem solving by empowering them metacognitively, with the help of a cognitive process diagrammatic representation called ‘the light bulb effect’. After a teaching session on ‘the light bulb effect’ students answer a questionnaire with a problem that is new to them, and then are invited to reflect on their cognitive process by describing those processes in their own words and drawing a ‘light bulb effect’ diagram that represents their cognitive processes. Analysis of responses shows that most students find it easy to describe their cognitive processes after the session and also that students find the session helpful.

1. Introduction

Problem solving ability is one of the most challenging teaching endeavours and yet it is one that is of great importance in physics. True problem solving is a creative process which requires the problem solver to create a path to the solution that is not initially obvious [1]. Problems arise in real life and in physics. In physics, it is used as a learning strategy through which students get the opportunity to practice the principles and concepts they are learning [2]. It is usually only in the process of solving a problem that the true meaning and implication of principles and concepts can be achieved. However, it is usually difficult to teach students the necessary creative processes required for problem solving as most students believe that the required procedure is that of simply remembering the correct path previously demonstrated by a teacher. The student usually obtains this perception from the logical manner in which a teacher presents the solution to a problem in class. This presentation is done with none of the false starts, restarts and rethinking that are usually necessary to create a solution when the problem is a real problem [3]; that is, a problem that the problem solver has never encountered before. Students thus have a tendency to give up when confronting a problem for which they do not have an immediate solution in their memories [2]. But teaching students about the problem solving process, which requires metacognitive monitoring, has been shown to have a positive impact in students’ ability to engage in the required creative problem solving process [4, 5]. Since metacognition involves knowledge and regulation of one’s cognitive processes [6], teaching students about the cognitive processes involved in problem solving and how their cognitive structures form and create meaning should lead to better problem solving performance. The aim of this study is to demonstrate that it is possible to teach students the metacognitive skills involved in problem solving with the aid of the ‘light bulb effect’ diagrammatic representation [7].

The cognitive processes involved in problem solving may be defined as “meaning creation processes” [7]. Incoming stimuli cause neurons or groups of neurons called neural networks to emit

signals in reaction to the stimuli. These signals are interpreted by the cognitive system through cognitive structures or cognitive tools that are also made up of neural networks. The cognitive tools grow and change over long periods of time and are what Piaget and Garcia [9] call schema. The development of these cognitive tools or structures is called learning and is a long term process. The cognitive process of creating meaning happens over very short periods, usually within seconds or minutes, and is what Piaget and Garcia [9] call ‘assimilation’, whilst “accommodation” is the term they use in reference to changes in the cognitive structures or tools. There are three dimensions involved in a cognitive process: the area of content, the level of complexity and time. A student’s cognitive structures or tools may be more developed in an area of content, such as in Newton’s laws rather than in electrostatics. When neural structures grow in complexity they are able to deal with more abstract processes. For example, a cognitive process, involving arithmetic is more concrete, and therefore less complex than one involving algebra. Students’ neural structures need to have developed to the point that they can deal with the abstractness of an algebraic manipulation in order to deal with a problem that requires that level of complexity. It takes time for neural structures to grow in complexity and it takes time for a student to produce meaning in a certain area of content. If the problem is less complex than the students’ structures the meaning will emerge much faster than if the problem is far more complex than the cognitive structures that the student has developed up to that point in time [8].

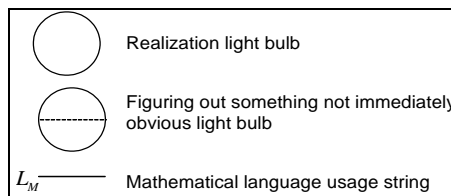


Figure 1. Three diagrammatic problem solving cognitive process representation elements

The ‘light bulb effect’ was used in 2015 to identify possible processes involved in physics problem solving and to determine which of these processes make a problem more or less difficult for students [7]. In this diagrammatic representation, straight lines, called ‘strings’ and circles, called ‘bulbs’, are used to represent different cognitive processes and are linked in a diagram that attempts to represent a complete problem solving process. The strings denoted processes that should have become familiar to the students as a result of use during their school education. The bulbs symbolized processes that would be novel to most students. The two bulb elements and an example of a string element are shown in Figure 1. Each of the string elements were accompanied by a code comprising of a letter and a subscript [7]. Diagrams were assigned levels according to the number of bulbs they contained, so for example a diagram with one bulb was a level 1 (L1) diagram.

<p>The motion of a particle, moving along a straight line is described by the following equation:</p> $x = (2.3 \text{ m.s}^{-1})t + (4.8 \text{ m.s}^{-2})t^2$ <p>where x refers to the particle’s position, which is measured in metres, and t refers to time, which is measured in seconds.</p> <p>(a) What is the particle’s initial position at time $t = 0$? (b) What is the particle’s initial speed?</p> <p>Given: $s = v_o t + \frac{1}{2}at^2$ $v = v_o + at$</p>	<div style="text-align: right;"> <p style="text-align: right;">(a)</p> </div> <hr/> <div style="text-align: right;"> <p style="text-align: right;">(b)</p> </div>
---	---

Figure 2. Parts (a) and (b) of Question 2, in the Problem Solving skills test, with the corresponding cognitive process diagrams, appearing on the right.

2. Method and Analysis

In order to demonstrate how the ‘light bulb’ diagrams were used to represent the cognitive processes involved in the solution of a problem, figure 2 shows parts (a) and (b) of question 2 in the Problem Solving skills test, used in 2015, as well as the diagrams representing the cognitive processes they required.

There were two possible diagrams for part (b) because it was discovered after examining the students’ test solutions that some students knew and used calculus instead of going through the ‘light bulb’ process or realization, they would use if calculus was unknown to them. The realization required was that the given expression matched the given equation so that the initial speed could be identified.

Overall, it was possible to conclude that the student performance in questions that required a L1 cognitive process was lower than in the questions where the required cognitive process was at L0 [7], in agreement with the fact that bulbs represent less known processes to the students.

At the beginning of the second semester in 2015, after lectures on Coulomb’s law, the students in Physics I major were given a special presentation on how the brain works and the Light Bulb representation used to analyse the Problem Solving skills test. They were also given feedback on their performance in the test using the analysis previously discussed [7]. During the course of the presentation on how the brain works they were told that at birth the brain is wired already so that stimuli coming in through the senses are connected to certain parts of the brain and over time more and more of these wired connections are used so that networks build up. Then with age and as learning progresses these networks grow larger and more complex. The students were given the following example: When you go to friend’s house for the first time it is sometimes not easy to locate it, you may need to consult the map, count the number of streets and look at the numbers once you get to the right street, whilst feeling uncertain, and it may take a long time to find the right house but as you visit the same friend over and over it becomes easier and takes less time, and you feel more confident. You have now built up a pathway in your brain that helps you find your friend’s house. Then as you continue to visit this friend you get to know the neighbourhood where your friend lives better and so the initial pathway becomes a complex network with you knowing where is the nearest petrol station or local grocery store. Because of this you can now solve more complex problems. Initially the problem was getting to your friend’s house on time, later it may be getting to your friend’s house on time whilst buying bread and filling up with petrol nearby.

The students were encouraged not to give up when solving a difficult problem. The following example was given to them to this effect: Solving a type of problem where there is something you have never encountered before is like standing on the edge of a cliff. You see another cliff on the other side. Between the cliffs there is a very deep canyon which you need to cross - you see no way of crossing. But as you stand there and think about the known paths you took to reach this point and demand of your brain that a way across be found, suddenly, a light bulb rises from the bottom of the canyon, which opens up into a bridge and you walk across triumphantly.

At the end of the session the students were given the Light Bulb Questionnaire. Question 1 in the questionnaire, shown in Figure 4, was a problem that used their recently acquired knowledge of Coulomb’s law but also required a certain realization that the forces between all charges along the sides of the square and Q cancel except for q at the top left and $2q$ at the bottom right..

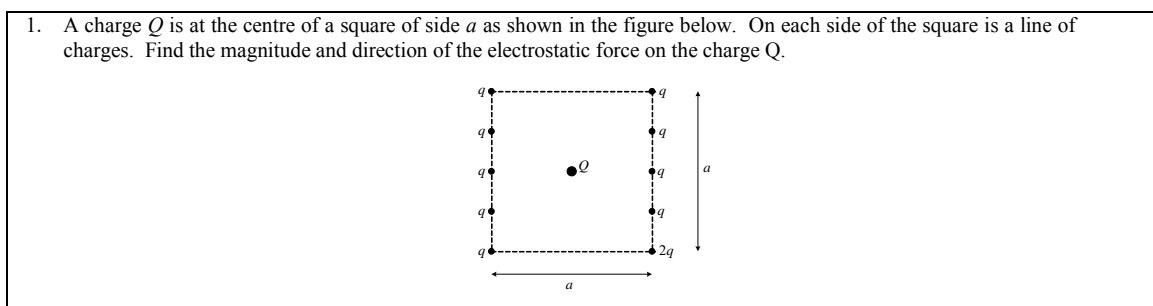


Figure 4. Question 1 in the Light Bulb questionnaire showing a Coulomb’s law problem

The remaining Light Bulb Questionnaire questions are shown in Figure 5.

2.	(a) How many realization or figuring light bulbs would you need to represent the cognitive processes needed to solve this problem?
	(b) Describe the process behind each light bulb in your own words:
3.	Draw the cognitive process diagram associated to the big problem in question 1.
4.	(a) Did you find this teaching session on problem solving helpful?
	(b) Explain why:

Figure 5. Questions 2 to 4 in the Light Bulb Questionnaire

3. Results

Thirty student responses to the Light Bulb questionnaire have been analysed, 27 responses to question 1 showed that students had achieved the intended realization, i.e. all charge contributions except two, cancel. Responses to question 2(a) are summarized in Table 1. Twenty three students thought there were more than 1 light bulb, responses ranged between 2 and 11 light bulbs.

Table 1. Student responses to question 2(a) in the Light Bulb Questionnaire.

Number of students	Number of light bulbs
4	1
23	More than 1
3	No answer

The responses to question 2(b) where students were asked to describe the process behind each light bulb in their own words are summarised in Table 2. All the students who responded could describe their cognitive processes and 20 described ‘string’ processes as bulb processes.

Table 2. Student responses to question 2(b) in the Light Bulb Questionnaire.

Number of students	Answer
17	Described correct realization process
25	Could describe their own cognitive processes
20	Perceived string processes as figuring out light bulbs
11	Described both language and mathematical processes as bulb processes
7	Described mathematical and geometric processes as bulb processes
3	Described understanding language as a bulb processes
4	Described only the intended realization as a bulb process
5	Did not answer

Table 3. Examples of student responses to question 2(b) in the Light Bulb Questionnaire.

Response Category	Response
I. Correct realization described as a light bulb (LB)	Figure out that charges q cancel out with the exception of the q at the top and the $2q$ at the bottom on opposite ends
II. Described understanding language as a LB	*Usually we are given charges with a certain magnitude however in the above problem we are given charges with magnitude q unknown and understanding the given statement about the problem is very important (1st bulb). Hence I felt uncertain on how to solve the problem.
III. Described both understanding language and using mathematics as LBs	Matter of understanding English, physics law, use of mathematical geometry and answering in the form of English physics relationship

Some examples of student responses to question 2(b) are shown in Table 3. The response in the first row is given by a student who described only the intended realization as a light bulb (LB). The response in the row below was made by a student who described the intended realization as a LB but also thought that understanding language was a LB. The last response was given by a student who thought that both language and mathematical processes were LBs.

Table 4: Student responses to question 3, in the Light Bulb Questionnaire

Number of students	Response
14	Drew a diagram with only 1 light bulb
1	Drew a diagram with 0 light bulbs
7	Drew a diagram with more than 1 light bulb ranging from 2 to 7
7	Did not answer

Of the 23 students who answered question 3, 22 used realization light bulbs as they had been shown in the presentation. Only 1 student did not, he/she simply made a list of his/her light bulb processes. The number of students drawing diagrams with different numbers of diagrams in response to question 3 is shown in Table 4.

Twenty seven students answered question 4 and 24 said that ‘yes’ they had found the session helpful. One student said ‘a little’ and 2 students said ‘no’. Both the student who said ‘a little’ and one who said ‘no’ in response to question 4(b) wrote that there was something that they had missed in the session. The other student, who said ‘no’, wrote that he/she didn’t think the realization process can be forced or learnt. This student, had the correct realization for question 1, was one of the 4 who in answer to question 2(a) gave 1 as the number of light bulbs needed and also, was one of the 14 who drew a Light Bulb cognitive process diagram with only 1 realization Light Bulb, so perhaps he/she already had the necessary metacognitive skills before the session. Some typical responses to question 4(b) were:

- Very helpful. I never understood why I could 'jam' in some problems, but its just my brain not recognizing the language used
- Realising that the more you use neurological pathways the easier it is to use it. That the only way to create a new pathway is to keep on trying
- Because in a way it gave me an idea or method to do problems and never give up until the bulb glows

In this teaching session students were taught that string processes were processes that were known to them and realization or figuring out processes (bulb processes) were processes that were new to them. But as can be seen from Table 2, many students described string processes as bulb processes. This was probably because these string processes had not developed to the required and expected complexity. For this reason, at the beginning of 2016, Physics I major students were again given a teaching session, a worksheet containing part of the Problem Solving Skills test, and a questionnaire containing a Dimensional Analysis problem instead of the Coulomb problem in the 2015 version, but otherwise the same as the 2015 version. However, this time they were taught that they could use bulbs inserted within strings to represent a string that had to be used at a higher level than usual from the student’s perspective. The results from the 10 responses that have been analysed so far are shown in Table 5.

Since all 10 students responded, we see that only 7 students were able to describe their cognitive processes as compared to the 2015 group, where all 25 students were able to do so. Only 1 student drew a bulb at the connection point whilst 8 drew bulbs inside strings. This indicates that students clearly understood that if a string processes was not yet well known it required a realization or figuring out process to use it in solving the problem. The fact that only 1 student used the connection

bulb showed that the students focus on the string processes, such as language and algebra, again highlighting the degree of complexity they still needed to develop for these processes.

Table 5. Student responses to questions in the Light Bulb Questionnaire, in 2016.

Number of students	Answer
9	Used the correct realization in solving the problem
7	Could describe their own cognitive processes
3	Described the intended realization
1	Drew diagrams with bulbs at the connection points
8	Drew diagrams with bulbs inside strings
10	Drew diagrams that demonstrated the principles they were taught in the session

4. Discussion and Conclusion

It is encouraging that in the 2015 sample of 30 responses, most students thought that the session was helpful and all who gave an answer (25) could describe their cognitive processes. The fact that so many students, 20, described ‘string’ processes as bulb processes suggested that their cognitive tools had not developed enough complexity for their use to be easier. This indicates more learning needs to occur in these areas. The fact that so many could describe their cognitive processes and from the mainly positive responses to question 4 means that metacognitive understanding was imparted in the session to the majority of these thirty students. Even though metacognitive understanding was clearly also imparted in 2016, the results show that less students learnt to describe their cognitive processes. So it can be concluded that giving the students a test and giving them feedback thereafter, showing them how the ‘light bulb’ representation works, as was done in 2015, is the superior way of using the “light bulb effect’ for teaching students about the cognitive skills involved in problem solving.

References

- [1] D. Gil-Perez, A. Dumas-Carre, M. Caillot and J. Martinez-Torregrosa 1990 Paper and pencil problem solving in the physical sciences as a research activity *Studies in Science Education* **18** 137-151
- [2] R. M. Garrett 1986 Problem-solving in science education *Studies in Science Education* **13** 70-95.
- [3] M. Martinez 1998 What is problem solving? *Phi Delta Kappan* **79** 132, retrieved from <http://www.questia.com/PM.qst?a=o&se=gglsc&d=5001331555>.
- [4] K. Teong 2003 The effect of metacognitive training on mathematical word-problem solving *Journal of Computer Assisted Learning* **19** 46-55
- [5] T. Gok 2010 The general assessment of problem solving processes and metacognition in physics education *Eurasian Journal of Physics and Chemistry Education* **2** 110-122
- [6] J. Flavell 1976 Metacognitive aspects of problem solving *The nature of intelligence* ed L.B. Resnick (New Jersey: Lawrence Erlbaum Associates) pp 231-236
- [7] C. Albers, D. Clerk and D. Naidoo The light bulb effect: University students’ problem solving cognitive processes in a physics problem solving skills test *Proceedings of the 62nd Annual Conference of the South African Institute of Physics (Port Elizabeth, South Africa, 28 June-3 July, 2015)* accepted
- [8] C. Von Aufschnaiter and S. von Aufschnaiter 2003 Theoretical Framework and Empirical Evidence of Students’ Cognitive Processes in Three Dimensions of Content, Complexity, and Time *Journal of Research in Science teaching* **40**(7) 616-648
- [9] J. Piaget and R. Garcia 1991 *Toward a Logic of Meanings*. (Hillsdale, New Jersey: Lawrence Erlbaum Associates)

The development of views on the nature of science of learners in a science enrichment programme

VM Baloyi¹, WE Meyer¹ and E Gaigher²

¹Department of Physics, University of Pretoria, Private bag X20, Hatfield, Pretoria, South Africa, 0028, South Africa

² Department of Science, Mathematics and Technology Education, University of Pretoria, Private bag X20, Hatfield, Pretoria, South Africa, 0028

E-mail: vonani.baloyi@up.ac.za

Abstract. This paper presents results of the study conducted with a group of 82 grade 10 applicants to a science enrichment programme offered by a university in South Africa. The Views on the Nature of Science (VNOS) questionnaire composed of eleven open-ended questions was used in examining learners' views on seven aspects of the nature of science (NOS). A follow up study was performed on the same group of learners two years later. This group included learners that had attended the science enrichment course (the experimental group) as well as the learners that had not done so (the control group). This study provided the opportunity to investigate the effect of attending the science enrichment course on the learners' views on the NOS. The follow-up study showed that the view on NOS of both groups improved over the period. Although the score in the VNOS test of both groups improved, the improvement for the experimental group was statistically significant. In addition, the results in the post test also differed by a statistically significant amount between the two groups. Interestingly, the understanding of the social and cultural embeddedness, did not improve in either the control or the experimental group.

1. Introduction

The understanding of the nature of science (NOS) is an important part of scientific literacy [1, 2, 3]. Abd-El-Khalick and Boujaoude [4] argue that a scientifically literate person should develop an understanding of science concepts and the relationship between science and technology. Other research studies show that the teaching of NOS from elementary through post-secondary science education improves students' enjoyment of science; interest in science classes and careers; curiosity in learning about science [5].

Many learners in different parts of the world have poor conceptions of NOS [6]. Research shows that effective teaching of NOS cannot be accomplished as the majority of science teachers in the United States (US) are harbouring uninformed conceptions of NOS [7]. This may be related to teacher-centred instruction methods which teachers have developed from their own experiences as students [8].

In many South African schools, teacher-centred instruction occurs, which does not promote the development of a better understanding of different features of NOS [9]. After the 1994 first democratic elections, the government's reconstruction and development programme led to the introduction of new Curriculum 2005 (C2005) policy guided by principles of outcomes-based education [10] in 1998, which was later reviewed to become the Revised National Curriculum Statement for General and

Education Training (Grades R- 9) and the National Curriculum Statement for grades 10 – 12 [11]. Further curriculum review led to the National Curriculum Assessment Policy Statement [12] which still promoted the development of science process skills, application of scientific knowledge in real-life problems and acknowledging the relationship between science, society and technology [12].

The current study was undertaken at a South African university that hosts a science enrichment programme for senior secondary school pupils. The enrichment programme, presented by the Faculty of Natural and Agricultural Sciences, uses an inquiry based approach in a three year programme from grade 10 to 12 to help learners develop a better understanding and appreciation of science. During the programme, the students visit the University on one Saturday every month during the school semester and for a week during the July holiday. In the first year of the programme, learners are exposed to the various departments in the faculty and participate in inquiry-based activities which provide them with hands-on opportunities to learn and experience science. During the second year, the learners are assigned to a specific department, where they participate in a project lead by senior students and staff from that department. The aim of the project is to allow students to experience what scientists really do, how research is done and showing the various opportunities that exists in the various sciences. The activities varied widely between departments, but were generally hands on mini-research projects, not directly related to the work done at school, but rather extending the work to new aspects that are not part of the standard school curriculum. In some cases the projects included aspects of actual research done in the department. The NOS was not explicitly taught during the programme.

Every year, schools in the area are invited to nominate up to two candidates for the programme. From these, approximately 50 learners are selected on the basis of their grade 9 marks as well as a short essay they have to write on why they enjoy science. Measures are also in place to ensure that the group was well balanced as far socio-cultural background gender is concerned, and generally only one student per school was selected.

This study reports on the development of the understanding of NOS amongst a cohort of participants in the enrichment programme and compares their performance with that of a group of their peers, which were proposed, but not selected for the programme.

1.1. Inquiry based learning

Inquiry has been defined diversely across the literature. Broadly, it may be defined as scientific investigations that encourage classroom practices such as posing questions which focus at knowledge attainment and development [13]. The inquiry-based approach to science education has recently been extended by the Next Generation Science Standards in the USA at high school level, to include interdisciplinary inquiry in teaching [14]. Learning through inquiry enables students to construct their own knowledge by building connections between their existing knowledge and new experiences [15].

1.2. Nature of science

Nature of science (NOS) is a construct used by many researchers to refer to epistemological beliefs in science education. NOS focuses on the philosophical assumptions that underpin science knowledge [16] such as values, improvement, theoretical developments, how agreements are reached within the scientific community, and the distinctive features of scientific knowledge. This study will be informed by Lederman's [17] description of NOS as the epistemology of science or science as a way of knowing. The differences which have been and are still occurring among the historians of science, philosophers of science, scientists and science educators with regard to the specific definition of NOS are irrelevant to high school learners [18]. In addition, there is a level of consensus on features of NOS that can be accessible to high school learners [19]. The seven NOS aspects include that scientific knowledge is tentative; empirical; theory-laden; requires imagination and creativity; influenced by social and cultural values; based on observation and inferences; and described by scientific theories and laws and developed in the absence of a universal scientific method.

Table 1. Questions in the modified VNOS form C questionnaire

Nr	Text
2	What in your view is science? What makes science (or a scientific discipline such as physics, biology, etc) different from other disciplines of inquiry (e.g. religion, philosophy)? [Empirical and tentative nature]
3	What is an experiment? [Empirical nature]
4	Does the development of scientific knowledge require experiments? Give an example to explain your position. [Empirical and tentative nature]
5	After scientists have developed a scientific theory (e.g. atomic theory, evolution theory), does the theory ever change? <ul style="list-style-type: none"> • If you believe that scientific theories do not change, explain why. Illustrate your answer with examples. • If you believe that scientific theories do change: <ul style="list-style-type: none"> (a) Explain why theories change? (b) Explain why we bother to learn scientific theories? Illustrate your answer with examples. [Tentative nature]
6	Is there a difference between a scientific theory and a scientific law? Illustrate your answer with an example. [Difference between theory and law.]
7	Science textbooks often represent the atom as a central nucleus composed of protons (positively charged particles) and neutrons (neutral particles) with electrons (negatively charged particles) orbiting that nucleus. How certain are scientists about the structure of the atom? What specific evidence do you think scientists used to determine what an atom looks like? [Theory and law, scientific models]
8	It is believed that about 65 million years ago the dinosaurs became extinct. A number of hypotheses were formulated by scientists to explain the extinction. <ul style="list-style-type: none"> • A: One hypothesis, formulated by one group of scientists, suggests that a huge meteorite hit the earth 65 million years ago and led to a series of events that caused the extinction. • B: Another hypothesis, formulated by another group of scientists, suggests that massive and violent volcanic eruptions were responsible for the extinction. How are these different conclusions possible if scientists in both groups have access to and use the same set of data to derive their conclusions? [Observations and inferences, tentative nature, imagination and creativity.]
9	Some people claim that science is infused with social and cultural values. That is, science reflects the social and political values, philosophical assumptions, and intellectual norms of the culture in which it is practised. Others claim that science is universal. That is, science transcends national and cultural boundaries and is not affected by social, political, and philosophical values, and intellectual norms of the culture in which it is practiced. <ul style="list-style-type: none"> • If you believe that science reflects social and cultural values, explain why. Illustrate your answer with examples. • If you believe that science is universal, explain why. Illustrate your answer with examples. [Social and cultural embeddedness].
10	Scientists perform experiments/investigations when trying to find answers to the questions they set for themselves. Do scientists use their creativity and imagination during their investigations? <ul style="list-style-type: none"> • If yes, then at which of the three stages of the investigations do you believe scientists use their imagination and creativity: (i) planning and design, (ii) data collection, (iii) after data collection? Please explain why scientists use imagination and creativity. Provide examples if you can. • If you believe that scientists do not use their imagination and creativity, please explain why. Provide examples if you can. [Imagination and creativity].
11	A person interested in botany collected specimens from Table Mountain and from the Drakensberg. Based on their specimens and his extensive field notes, he developed the concept of altitudinal zonation, which describes how plant species found at sea level differ significantly from those found at high elevations. Would you describe this person's work as science? Please explain. [Scientific method].
12	You decide to inventory the birdhouses in your neighbourhood as an after-school project. During this inventory, you locate a total of 34 birdhouses, only 14 of which are being used by nesting birds. The others are currently unoccupied. You decide that you would like to know why some of the birdhouses are occupied and others are not. How would you conduct this study? [Scientific method]

2. Methodology

The study is located in the positivist paradigm, using a mixed methods approach. For this study learners' views of NOS were assessed using a modified open-ended Views of the Nature of Science (VNOS Form C) questionnaire adapted from Lederman et al. [20]. The questionnaire contains eleven open-ended questions that examine the aforementioned aspects of the NOS, summarized in Table 1. The VNOS Form C questionnaire has been validated and used regularly in research [20], and minor adaptations were made to make it more relevant to South African learners. Learners wrote pre- and post-tests and follow up interviews were conducted to validate the data found through the open-ended questionnaire [17]. The response to each question was scored on a scale of 0 to 4 (0 represents naïve, 1 represents partially naïve, 2 represents moderate, 3 represents partially informed, 4 represents informed) and results analysed quantitatively. Descriptions of NOS aspects by Schwartz, Lederman and Crawford [21] were used as a guide during the scoring process. In this study, qualitative data was transformed into quantitative data, followed by the analysis of the final data [22].

The pre-test was performed before the students were informed of the outcome of the selection process, but was only evaluated afterwards. The post test was performed during the university's open day, where participants were invited and offered a meal voucher. The entire group of applicants to the university's science enrichment program was evaluated. Of these, 82 learners consisting of thirty-two males and fifty females wrote both the pre and the post test. Only these students were included in this study.

At the beginning of the study, the participants in this study were minors with an age range of between 14 and 16, therefore parents and legal guardians gave written consent for their children to participate in this study and results published anonymously. Participation in the study was voluntarily and participants were free to withdraw at any time. Permission was granted by the ethics committee of the university prior to the commencement of this study.

3. Results

Figure 1 shows the VNOS scores obtained for each question by the control and experimental groups at the start of the study (a) and at the end of the study (b). At the start of the study, for most questions, there was no significant difference between the scores obtained by the control and experimental groups. A possible exception is Q4 ("Are experiments required", where the control group did 40% worse, however, according to a t-test, the difference is not statistically significant ($p = 0.10$). The average score of the control group was 5% lower than that of the experimental group ($p = 0.22$). We can therefore conclude that, even though the experimental group was selected on merit from the group of applicants, there was no significant difference between the scores obtained in the VNOS test by the two groups before the study.

Figure 1(b) shows the VNOS scores for the control and experimental groups per question, as

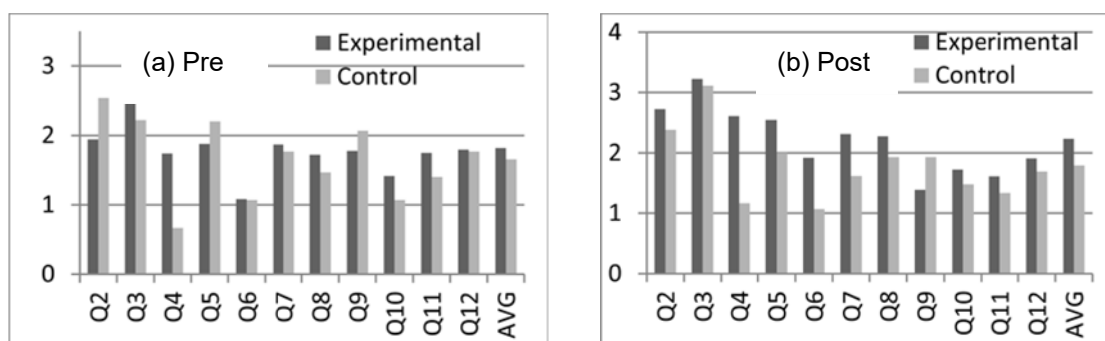


Figure 1. Scores obtained by students in the modified VNOS questionnaire (a) before and (b) after the two year period.

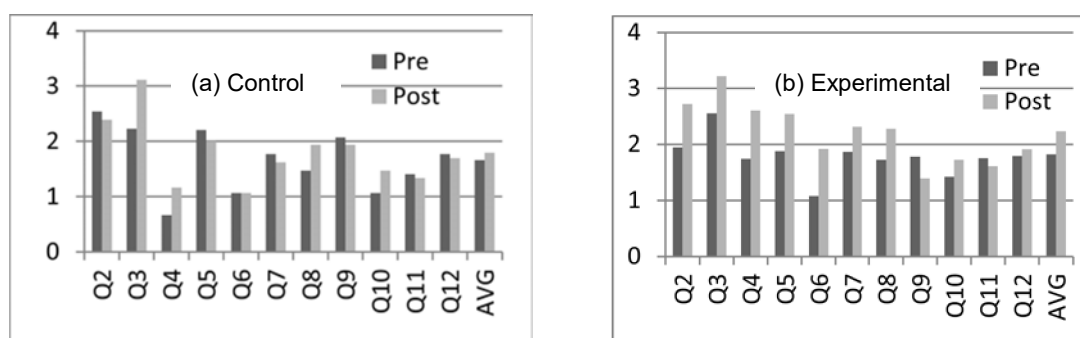


Figure 2. Scores obtained by students in the modified VNOS questionnaire for (a) the control (left) and (b) the experimental (right) groups in the pre- and post-tests.

obtained after the study. In all but one question (Q9, Social and cultural influence) the experimental group scored better than the control group. In Q9, the control group scored 14% better, but this was not statistically significant ($p = 0.27$). The experimental group scored considerably better in Q4 (“Are experiments required”, 36%, $p = 0.01$), and the average score was 11% better ($p = 0.03$).

Figure 2 shows average VNOS scores for the experimental and control groups obtained in the pre- and post-tests. As seen in Figure 2(a), the control group showed improved scores in 4 questions and reduced scores for 6 questions, none of which were statistically significant. The average score improved by 4%, but again this was not statistically significant ($p = 0.58$). For the experimental group, the increase in the average score was significant (13%, $p = 0.002$). The scores in 9 questions improved and only two scores decreased. For question 2 the improvement was statistically significant ($p = 0.004$), while the improvement in questions 3, 4, 6 and 7 was substantial with $p = 0.04$, 0.02, 0.01, 0.01, respectively). Again Q9 was the notable exception to the rule.

4. Discussion

From the results of the pre-test, it seems that there was no statistical significant difference between the control and the experimental group. This was expected, as the selection process did not deliberately select students on the basis of their knowledge of NOS. We can therefore assume that the control and experimental groups were approximately equal at the start of the study, and that any differences in the groups at the end of the study could be attributed to the experimental group’s participation in the science enrichment programme.

The control group showed no significant improvement in their VNOS scores after two years. However, the experimental group showed a statistically significant improvement, and, in the post test, scored better than the control group in all but one question, with a statistically significant (11%, $p = 0.03$) higher average score. This is strong evidence that the science enrichment programme contributed significantly to the participant’s understanding of NOS. Specifically the students showed a strong improvement in their understanding of the empirical and tentative nature, the difference between theories and laws, as well between observations and inferences. Interestingly, there was a decrease in both groups understanding that science is embedded in social and cultural background. Although not statistically significant, this aspect could be worth while investigating further.

The significant improvement in the average VNOS score of the experimental group compared to the control was unexpected, as NOS was not explicitly taught. Implicit approaches are believed not to encourage students to reflect on science activities thus they cannot develop informed views of NOS [7, 23]. The finding in the current study differs from that of Bell et al. [24] in that there were students in the experimental group who showed significantly more informed views of NOS.

5. Conclusion

We conclude that the participation of the grade 10 learners in the science enrichment programme enhanced their understanding of the nature of science, even though NOS was not explicitly taught. As far as individual aspects are concerned, the largest effect was observed in the answers to the question

“are experiments required”. A possible exception was the learners’ understanding of the social and cultural embeddedness of science, in which a slight decrease was observed. Given the wide variety of cultural backgrounds of learners in South Africa, this point may be worth further investigation.

The results in the current study should not be generalized to the entire grade 10 population of South Africa, as only the best students from each school participated.

Acknowledgements

Funding was provided by the Sasol Inzalo Foundation and the National Research Foundation of South Africa (Grant specific unique reference number (UID) 76938).

References

- [1] Anderson R D 2007 Inquiry as an organizing theme for science curricula *Handbook of Research on Science Education* ed KS Abell and NG Lederman (Mahwah, NJ: Lawrence Erlbaum Associates, Inc) pp.807-830
- [2] Roberts D A 2007 Scientific literacy *Handbook of research on science education* ed KS Abell and NG Lederman (Mahwah, NJ: Lawrence Erlbaum Associates, Inc) pp.729-780
- [3] Lederman N G 2007 Nature of science: Past, present, and future *Handbook of research on science education* ed KS Abell and NG Lederman (Mahwah, NJ: Lawrence Erlbaum Associates, Inc) pp. 831-880
- [4] Abd -El-Khacik F and Boujaoude S 1997 *J. Research Sci. Teach.* **34** 673
- [5] Clough M P 2011 *Sci. Teach.* **78** 56
- [6] Abd-El-Khalick F 2006 Over and over again: College students' views of Nature of Science *Scientific Inquiry and Nature of Science: Implications for Teaching, Learning and Teacher Education* ed LB Flick and NG Lederman (Dordrecht, The Netherlands: Springer)
- [7] Abd-El-Khalick F and Lederman N G 2000 *Int. J. Sci. Educ.* **22** 665
- [8] McDermott L C, Shaffer P S and Constantinou C P 2000 *Phys. Educ.* **35** 411
- [9] Dekkers P 2006 *Afr. J. Math. Sci. Tech. Educ.* **10** 81
- [10] Department of Education 2002 *Revised National Curriculum Statement* (Pretoria: Government Printer)
- [11] Department of Education 2006 *National Curriculum Statement* (Pretoria: Government Printer)
- [12] Department of Education 2012 *Curriculum and Assessment Policy Statement: Physical Sciences Grade 10 – 12* (Pretoria: Government Printer)
- [13] Blanchard M R, Annetta L A and Southerland S A 2008 *Investigating the effectiveness of inquiry-based versus traditional science teaching methods in middle and high school laboratory settings* Paper presented at the annual conference of the National Association for Research in Science Teaching, Baltimore, MA.
- [14] National Research Council 2012 *A Framework for K-12 Science Education Practices, Crosscutting Concepts, and Core Ideas* (Washington, DC: National Academy Press)
- [15] Berge O and Slotta J D 2005 *Learning technology standards and inquiry-based learning* Paper presented at the meeting of the Information Science and IT Education Joint Conference, Arizona.
- [16] Smith C and Wenk L 2006 *J. Res. Sci. Teach.* **43** 747
- [17] Lederman N G 1992 *J. Res. Sci. Teach.* **29** 331
- [18] Abd-El-Khalick F and Lederman N G 2000 *J. Res. Sci. Teach.* **37** 1057
- [19] Abd-El-Khalick F, Bell L and Lederman N G 1998 *Sci. Educ.* **82** 417
- [20] Lederman N G, Abd-El-Khalick F, Bell R L and Schwartz R S 2002 *J. Res. Sci. Teach.* **39** 497
- [21] Schwartz R S, Lederman N G and Crawford B A 2004 *Sci. Educ.* **88** 610
- [22] Caracelli V J and Greene J C 1993 *Educ. Eval. Policy Anal.* **15** 195
- [23] Akerson V L and Abd-El-Khalick F 2003 *J. Res. Sci. Teach.* **40** 1025
- [24] Bell R, Blair L, Crawford B and Lederman N G 2003 *J. Res. Sci. Teach.* **40** 487

Understanding of vector addition and subtraction by first year university students: graphical versus algebraic methods

E Carleschi

Department of Physics, University of Johannesburg, PO Box 524, Auckland Park 2006, South Africa

E-mail: ecarleschi@uj.ac.za

Abstract. The understanding of vector addition and subtraction in two-dimensions by first year university students was investigated for both the graphical representation (where vectors are represented as arrows) and the algebraic notation (using unit vectors \hat{i} and \hat{j}) in a generic mathematical context. In particular, students enrolled in the 2016 first semester module General Physics for Earth Sciences at the University of Johannesburg were given tests dealing with vectors in one- and two-dimensions. Questions in these tests were structured in such a way to probe students capabilities in manipulation of vectors for different relative orientations (with aligned and/or opposing x - and y -components) for both graphical and algebraic methods. Students' performance shows that difficulties are mostly found in the use of the graphical representation, while the average performance in the algebraic format was excellent. Some of the trends include scores being comparatively higher for addition than for subtraction of vectors. For one-dimensional vectors the performance in both addition and subtraction improves when vectors point in the same direction, as opposed to when they are opposite. No such pattern is observed for two-dimensional vectors. For subtraction of vectors in one-dimension, the score is definitively worse when the vector to be subtracted points in the negative direction, because of the incapability to properly account for the negative sign given by the vector direction and the task of subtracting the same vector. Interestingly, the average performance for vector subtraction is found to be higher in two-dimensional than in one-dimensional vectors. Follow-up interviews were carried out in order to identify students' most common misconceptions.

1. Introduction

Vectors constitute a fundamental building block for any introductory physics course at university level. Vector concepts are used in topics such as motion, forces, momentum and torque, and therefore need to be properly mastered by students. Vectors are generally taught in two different representations: the graphical method (where vectors are represented as arrows in a Cartesian reference frame) and the algebraic method, where vectors are identified by means of unit vectors \hat{i} and \hat{j} in the two-dimensional case. While the arrow representation is certainly pedagogically relevant, as it poses the accent on the directional component of a vector as a mathematical object and it helps the students to visualise physical quantities in the real space, the algebraic notation is also important as it allows for a more immediate representation of vectors in three or more dimensions, and it is useful in calculations involving vectors. Both representations

are therefore necessary and complementary to each other, and it is important to understand students' perception of both.

There have been several studies dedicated to the understanding of vectors by students, and most of them have focused on the graphical representation of vectors [1, 2, 3]. Others have reported some partial comparison of the performance of students in the graphical and algebraic methods [4, 5, 6], even though the results were somewhat ambiguous [6], or different types of questions were given to different students [5], making the comparison of the results more difficult.

This study aims at gathering further insight into students' understanding of vector concepts and vector addition and subtraction in a generic mathematical context by directly comparing the students' performance in manipulating vectors in the graphical and algebraic method. This was done by means of two carefully designed tests designed to probe addition and subtraction of vectors. These tests were given to exactly the same student population, so that a one-to-one comparison of the answers could be performed. The outcome of the present investigation is in agreement with the findings reported in the literature [4, 5, 6].

2. Method

Students' understanding of vector concepts was probed by means of two tests, focusing on the addition and subtraction of vectors in one- and two-dimensions. These tests were written by 23 first year students representing the 2016 intake for the first semester course named General Physics for Earth Sciences (or PHYG01A) in the Faculty of Science at the University of Johannesburg. This is an algebra-based introductory physics course intended for students majoring in geology, geography and environmental management. The author of this paper is the lecturer of the course. It is acknowledged that the class size is rather small in terms of statistical sample, but the author's plan is to extend this investigation to larger first year physics classes at the University of Johannesburg. The tests were written by the students in class under supervision. Students were expected to work alone, and were allowed to complete the tests at their own pace.

Vectors are the second topic in the PHYG01A syllabus. They were dealt with in detail in class over a time span of 10 single lectures, which roughly takes up the first two and a half weeks of the semester. These tests were given to the students right at the end of the third week, just after the topic of vectors was completed in class. Based on the material covered during lectures, students were expected to know how to add and subtract vectors using the graphical method, as well as the algebraic method.

Both tests were set in such a way to probe the capability of adding and subtracting vectors with different relative orientations. It is important to note that the same orientation pattern was used in both tests for the graphical and the algebraic method (as it will be clarified in the following), in order to allow for a direct comparison of the performance of the students.

3. Test on one-dimensional vectors: students' performance and analysis

The test on vectors in one-dimension was composed of 32 questions, out of which 16 were meant to probe vector addition and subtraction in the graphical method, while the other 16 questions dealt with the algebraic method. Each question counted for one mark towards the overall score.

In order to obtain a more systematic understanding of student difficulties, questions probed addition and subtraction in the following four possible configurations: $\vec{A} + \vec{B}$, $\vec{A} - \vec{B}$, $-\vec{A} + \vec{B}$ and $-\vec{A} - \vec{B}$. For each configuration, combinations of vectors pointing in the same and in opposite directions were used. This resulted in four kinds of questions, as shown in figure 1 for $\vec{A} - \vec{B}$: $+(p) - (p)$, i.e. a vector in positive direction minus a vector in positive direction (a); $+(n) - (n)$, i.e. negative minus negative (b); $+(p) - (n)$, i.e. positive minus negative (c); $+(n) - (p)$, i.e. negative minus positive (d). The same orientation pattern was used for the other

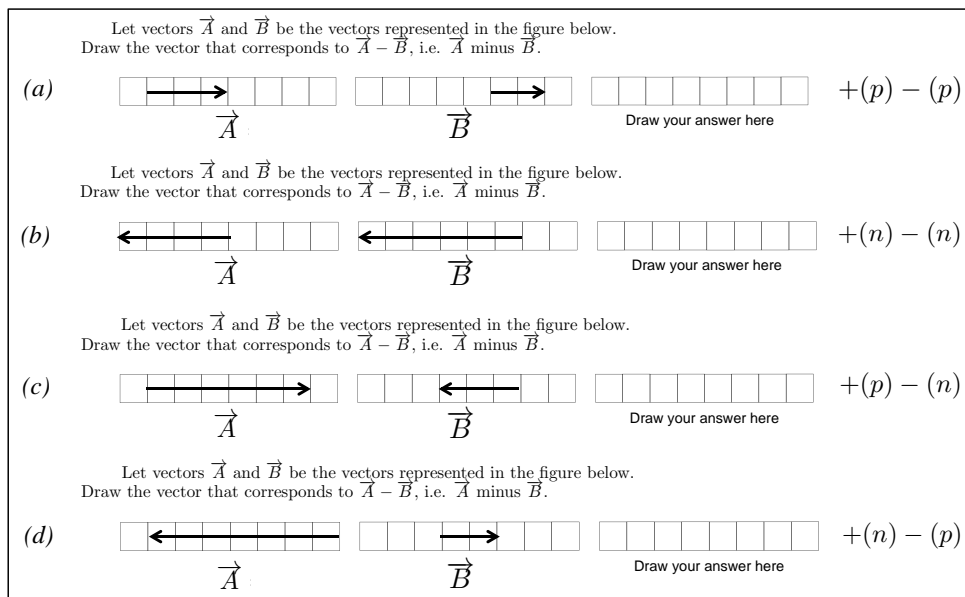


Figure 1. Examples of questions for one-dimensional vectors in the arrow format for $\vec{A} - \vec{B}$, exploiting different relative orientations between vectors \vec{A} and \vec{B} . A one-dimensional grid was assigned to vectors \vec{A} and \vec{B} separately, and students were asked to draw their answer in an empty grid. Question were reiterated in symbol and word format (e.g., \vec{A} minus \vec{B}) in order to better ensure that the students were not simply misreading the operation and making unnecessary mistakes.

three configurations, making the number of possible combinations to add up to 16.

Specific operations and relative orientations were also accounted for in the algebraic method, in order to obtain the one-to-one correspondence between graphical and algebraic methods, as mentioned above. The order in which questions were asked in the test was shuffled, to avoid students being able to find out the underlying structure of the test.

This is an example of the algebraic method, corresponding to the graphical situation shown in figure 1 (a), i.e. $+(p) - (p)$:

Consider vectors $\vec{A} = 5\hat{i}$ and $\vec{B} = 4\hat{i}$. What is $\vec{A} - \vec{B}$? Answer:

Students' performance in this test is shown in Table 1. The comparative analysis of the results allows to extract the following trends:

- (i) The performance in the algebraic method is excellent, with an overall average score of 93%, which is much higher than the performance in the graphical method. This does not depend upon whether addition or subtraction was tested.
- (ii) The overall best performance in the graphical method was scored for $\vec{A} + \vec{B}$ (average of the four same-type questions = 84%), while the worst for $\vec{A} - \vec{B}$ (average = 30%). In particular the lowest score was obtained for the subtraction of vectors of the type $+(p) - (n)$. Follow-up interviews helped to clarify the reason behind this. Most of the students were confusing the negative sign given by the vector direction with the task of subtracting the same vector, and did not understand that both contributions (the negative sign and the subtraction) had to be properly accounted for. This indicates that students' difficulties associated to

Table 1. Class performance in the test on one-dimensional vectors for both graphical and algebraic methods. The difference score (graphical-algebraic) is shown in the last column.

		graphical (%)	algebraic (%)	difference (%)
$\vec{A} + \vec{B}$	$+(p) + (p)$	87	95	-8
$\vec{A} + \vec{B}$	$+(n) + (n)$	96	91	+5
$\vec{A} + \vec{B}$	$+(p) + (n)$	70	100	-30
$\vec{A} + \vec{B}$	$+(n) + (p)$	83	95	-12
$\vec{A} - \vec{B}$	$+(p) - (p)$	39	95	-56
$\vec{A} - \vec{B}$	$+(n) - (n)$	52	86	-34
$\vec{A} - \vec{B}$	$+(p) - (n)$	13	95	-82
$\vec{A} - \vec{B}$	$+(n) - (p)$	17	86	-69
$-\vec{A} + \vec{B}$	$-(p) + (p)$	87	100	-13
$-\vec{A} + \vec{B}$	$-(n) + (n)$	48	90	-42
$-\vec{A} + \vec{B}$	$-(p) + (n)$	13	76	-63
$-\vec{A} + \vec{B}$	$-(n) + (p)$	30	90	-60
$-\vec{A} - \vec{B}$	$-(p) - (p)$	61	100	-39
$-\vec{A} - \vec{B}$	$-(n) - (n)$	48	95	-47
$-\vec{A} - \vec{B}$	$-(p) - (n)$	43	100	-57
$-\vec{A} - \vec{B}$	$-(n) - (p)$	22	90	-68

the presence of a negative sign depend on the direction of the vectors as well. Surprisingly in fact the average score for $-\vec{A} + \vec{B}$ and $-\vec{A} - \vec{B}$ was 44%, definitively higher than for $\vec{A} - \vec{B}$.

- (iii) Focusing on the relative orientation between vectors in the graphical method, scores were definitively higher when vectors point in the same direction, than when they are opposite. This is consistent across the four different configurations. Interviews revealed that the most common misconception is that opposing arrows are always “acting against each other” (and it does not matter which mathematical operation, addition or subtract, is asked for), and the task is to find which one “wins” in this competition. This is effectively equivalent to always adding vectors, which obviously leads to mistakes.

4. Test on two-dimensional vectors: students’ performance and analysis

The test on two-dimensional vectors was again composed of 32 questions, evenly split between the graphical method and the algebraic notation, keeping the usual one-to-one correspondence between the two. Each question counted for one mark towards the overall score. In this second test only addition ($\vec{A} + \vec{B}$) and subtraction ($\vec{A} - \vec{B}$) were probed, for situations where the two vectors were either aligned in both dimensions, or where they were aligned in one dimension but opposed in the other. The aim was to probe whether the same pattern of mistakes encountered by students in the one-dimensional case persisted in two-dimensions. If this was the case, then we would expect questions with vectors having one opposite component to score significantly less than when both components are aligned.

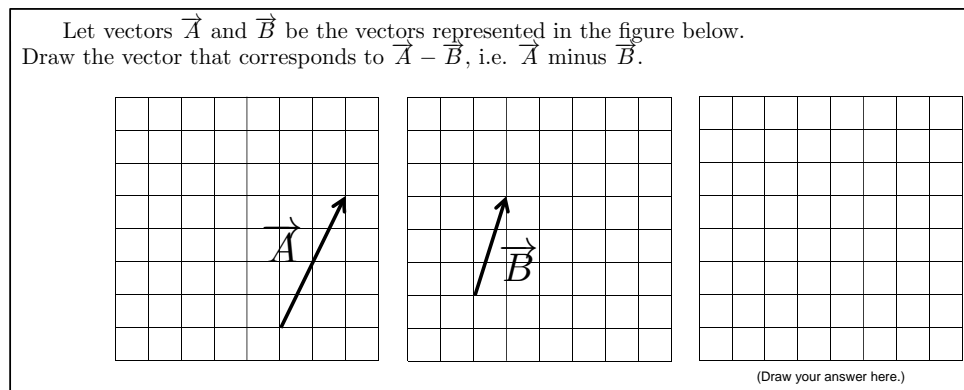


Figure 2. Example of two-dimensional question in the arrow format.

Table 2. Class performance in the test on two-dimensional vectors for both graphical and algebraic methods. The difference score (graphical-algebraic) is shown in the last column. “+” and “-” indicate the orientation of vector components A_x , A_y , B_x and B_y .

	A_x	A_y	B_x	B_y	graphical (%)	algebraic (%)	difference (%)
$\vec{A} + \vec{B}$	+	+	+	+	59	91	-32
$\vec{A} + \vec{B}$	-	-	-	-	59	91	-32
$\vec{A} + \vec{B}$	+	-	+	-	45	95	-50
$\vec{A} + \vec{B}$	-	+	-	+	50	100	-50
$\vec{A} - \vec{B}$	+	+	+	+	41	95	-54
$\vec{A} - \vec{B}$	-	-	-	-	32	95	-63
$\vec{A} - \vec{B}$	+	-	+	-	59	86	-27
$\vec{A} - \vec{B}$	-	+	-	+	55	95	-40
$\vec{A} + \vec{B}$	+	+	+	-	59	95	-36
$\vec{A} + \vec{B}$	-	-	+	-	73	100	-27
$\vec{A} + \vec{B}$	-	+	+	+	73	91	-18
$\vec{A} + \vec{B}$	-	+	-	-	50	95	-45
$\vec{A} - \vec{B}$	+	+	+	-	59	90	-31
$\vec{A} - \vec{B}$	-	-	+	-	55	95	-40
$\vec{A} - \vec{B}$	-	+	+	+	42	86	-41
$\vec{A} - \vec{B}$	-	+	-	-	32	86	-54

Figure 2 shows an example of how a two-dimensional question in the arrow format was asked. Vectors \vec{A} and \vec{B} were drawn in two different two-dimensional grids, and the students were expected to draw the final answer in a third grid. For the particular example reported in this figure both x - and y -components of the vectors are positive (please note that students were informed of this convention). The equivalent question asked in the algebraic format was as follows:

Consider vectors $\vec{A} = 2\hat{i} + 3\hat{j}$ and $\vec{B} = 3\hat{i} + 8\hat{j}$. What is $\vec{A} - \vec{B}$? Answer:

Students' performance in this second test is shown in table 2. From these results the following considerations can be drawn:

- (i) The score for the algebraic method is very high, with an average score of 93% over the 16 questions that were asked; this is the same as the average score in the one-dimensional case.
- (ii) As far as the graphical method is concerned, scores were lower than the algebraic one, and in particular slightly higher for addition than for subtraction; interestingly, this does not depend upon the relative orientation of the components. In short, students did not seem to perform better when vectors were aligned as in the one-dimensional case.
- (iii) Again for the graphical method, the direct comparison of the scores in one- and two-dimensions for vector subtraction $\vec{A} - \vec{B}$ specifically, shows that surprisingly students scored higher in two-dimensions. The average score in two-dimensions was in fact 47% against a 30% scored in one-dimension. Again, post-test interviews were found to be a very important tool in order to understand this finding. The scenario that emerged is the following: students have a very strong perception of the direction for one-dimensional vectors (in other words a vector is perceived as being either positive or negative); this leads to them facing the task of subtracting vectors with some kind of "preconception" (for example that opposing arrows are always in competition) on what the outcome should be. This spacial awareness is much weaker in two dimensions; students are then more free from preconceptions and able to apply the procedure for vector subtraction more successfully.

5. Concluding remarks

In conclusion, first year students' understanding of vector concepts was investigated for both the graphical and the algebraic methods of vector representation. Students were given two tests to probe their capability to add and subtract one- and two-dimensional vectors with different relative orientations. In general, the score in the algebraic method type questions was averaged above 90%, while the performance in the graphical method was far less successful. As far as the graphical method is concerned, students generally performed better in the addition than in the subtraction of vectors. But while the score for one-dimensional vectors is higher if vectors are aligned, there is no such trend for two-dimensional vectors. Having to deal with aligned or opposite vector components does not clearly impact on the correctness of the final answer.

Interestingly, the scores for subtraction of vectors in the graphical method were higher in two-dimensions as opposed to the one-dimensional case. From post-test interviews this can be understood by considering the weaker perception of space and vector direction that students have for the two-dimensional case. Giving a post-test to the same students, which should be structured in a similar way to the first one and should follow one-to-one and class consultation on the issues raised from the first test, would help understand how addressing such issues explicitly would improve class performance. An interestingly follow-up of this study could then be the investigation of the relationship between students' perception of space and performance in vector graphical manipulation, and how the two affect each other in both one- and two-dimensions.

References

- [1] Nguyen L and Meltzer D E 2003 *Am. J. Phys.* **71** 630
- [2] Flores S, Kanim S E and Kautz C H 2004 *Am. J. Phys.* **72** 460
- [3] Shaffer P S and McDermott L C 2005 *Am. J. Phys.* **73** 921
- [4] Barniol P and Zavala G 2014 *Phys. Rev. ST Phys. Educ. Res.* **10** 010121
- [5] Heckler A F and Scaife T M 2015 *Phys. Rev. ST Phys. Educ. Res.* **11** 010101
- [6] Knight R D 1995 *Phys. Teach.* **33** 74

Termites in our Tests? The role of stigmergy in our examination system

Douglas Clerk, Deena Naidoo and Claudia Albers

School of Physics, University of the Witwatersrand, Private Bag 3, WITS, 2050

E-mail: Douglas.Clerk@wits.ac.za

Abstract. This study is inspired by perceived shortcomings in the ‘problem-solving’ abilities of undergraduate physics students. A detailed analysis of student performance in examinations in relation to the type of question being answered - for a first year physics course for engineering students - has been undertaken. The data collected show that firstly, there is empirical evidence in support of these perceptions. Secondly, evidence has also emerged that there is a favoured question-type that can explicitly be taught and relatively easily mastered, and which typically makes up a sufficiently large fraction of an examination, that students can pass without having to demonstrate any real problem-solving ability. What students need to demonstrate instead is a well-developed ability to expedite routine operations at various levels of complexity – which by definition does not amount to problem-solving. It is possible that this bias has become established *stigmergically* via a feedback process sometimes called ‘backwash’, to which candidates, examiners and instructors have all been party. Candidates learn what kind of questions to expect, examiners learn what kind of questions candidates can be expected to answer, and instructors learn what kind of question-answering skills need to be taught - by traces left by these agents in the system’s environment. The third outcome of the study has been the emergence of a taxonomy of question-types typically set in physics examinations.

1. Introduction and rationale

Problem-solving is an educational outcome of extraordinary importance. Jonassen [1] for example, rates it as “the most important cognitive goal of education”. Martinez [2] states that “the most important kinds of human activities involve accomplishing goals without a script”. Given this wide recognition of its great importance, one would imagine that problem-solving would surely have been pursued as an educational goal with considerable vigour and hence, success. However this seems not to be the case: Gil-Perez, Dumas-Carré, Caillot, & Martinez-Torregrosa [3] regard the “abundance of literature” on problem-solving as evidence not only for “the relevance of problem-solving to the learning of science”, but they also see it as “evidence of a general failure of students at problem-solving tasks”. The rationale being, that if there were no ‘problem’ with problem-solving, there would not have been such a great abundance of literature concerning it. Apart then from ‘tea-time talk’ amongst disgruntled lecturers, there is thus considerable literature support for the view that problem-solving lacks general success as a learning outcome, for example: “On routine problems – that is, problems that are like those they have already learned to solve – they excel; on non-routine problems – i.e., problems that are not like any that they have solved in the past – they fail. Similar examples can be found in other academic domains, including reading and writing” [4].

This lack of success of problem-solving as an educational outcome is somewhat curious and indeed, of some concern. Hence, we have set out to shed some light on the situation and attempt to suggest a

mechanism for what is at play. This study examines the role of the examination system, in the development – or perhaps the *failure* to develop – of problem-solving competencies in students of physics. Three questions come readily to mind, the first being *what* is ‘problem solving’? The other two serve as our research questions: is there empirical evidence of a deficiency in problem-solving abilities among our students - and if so, what could be causing the deficiency? These questions have been addressed by an on-going analysis of examination and test questions in physics, and of the marks (grades) students typically achieve when answering them, spanning now several years.

The first of the three questions above concerns our working definitions – without which further debate could prove to be futile. Apart from a dictionary, the obvious place to look for such definitions is of course the literature. This has proved to be something of a ‘problem’ as explicit definitions are not always given in the literature. This fact has itself been commented on – for example: “researchers into paper and pencil problem solving do not generally raise the question of what constitutes a problem” [3]. Where the question is raised, there is sometimes significant – but usually *not* exact – agreement with our own understanding. We have been able then to select a sub-section of the relevant literature (see below) in which the given definitions are not only explicit, but are also both clear and succinct, *and* which resonate well with our own understandings; and we develop our own working definition based on those, as follows:

Tasks in physics – both for training and assessment - can often be performed by means of an algorithmic process. An algorithm - here defined as a series of instructions to be followed sequentially in the performance of some task (i.e. a procedural ‘script’) - can be learnt, and could thus become a routine task such as those referred to above by Mayer [4]. Note here that Mayer does not make the same semantic distinctions as we do: he refers to both routine and non-routine tasks as ‘problems’. Nevertheless the claim he makes supports our findings and, in a later publication, Mayer [5] does show that he is at least *aware* of ‘our’ meaning.

Any student then expediting such a learnt algorithm in response to an examination question might indeed be ‘performing well’ - in the sense that good grades would be awarded for their efforts - but would not be problem-solving as, by our chosen definition, a task is not a ‘problem’ if its algorithm is already known. This follows the views of authors such as Adams & Weiman [6], Bodner [7], and Martinez [2]. Problem-solving occurs not when the student generates the answer to a question by expediting a familiar, pre-fabricated algorithm, but rather, when the student *constructs* the necessary algorithm. Hence, our central working definition becomes: ***A problem is a task with a cryptic algorithm*** – i.e. an algorithm not initially known to the solver but that *becomes* known during the course of and through the process of solving the problem. The point of ‘problem-solving’ is then to discover the algorithm.

Evidence exists – both in the literature, [3, 4] and in empirical form - from this study at least - that the problem-solving deficiency referred to here is indeed real. We also suggest a possible causal mechanism, known as ‘backwash’ which is documented in the literature [8, 9]. It consists of a feedback, or perhaps more accurately, a feed-*forward* loop in which past assessment influences current and future teaching, learning, and assessment. Backwash has been quite extensively researched in the learning of languages but less so in physics, although the continuing demand for past examination papers suggests that it is very much alive and well as a contributing factor.

2. Theoretical Framework

A theoretical framework provides an ontological and epistemological context within which to design and conduct research, and hence to interpret findings [10]. In educational research generally, such a framework must of necessity be somewhat complex and must draw on several sources, as it involves complex issues where effects usually arise from multiple causes, and where we deal with, as Redish [11] says, “a strongly interacting many-body system in which observations change the system in uncontrollable ways” – i.e. a *complex* system.

What is of concern in this study is essentially a pattern of learnt behaviour, both individually and collectively – hence, constructivism as a theory of learning would broadly underpin the research. We

are interested in the collective behaviour of individuals in society when learning to cope with a difficult situation – i.e. that occasioned by ‘high-stakes’ examinations – which we see as any examination with significant consequences [12] for the examination candidate. A candidate’s need to perform well varies in intensity depending on how high the ‘stakes’ are. Indeed failure can have life-altering consequences for the candidate, and hence would also be of some importance to the instructor and also the examiner. There is thus high pressure on all agents acting within the system towards the achievement of ‘successful’ outcomes. We believe that what we describe here is a negative and unintended consequence of this pressure [12, 13].

We draw thus on the theoretical perspectives of constructivism, metacognition and the basics of complex systems theory, to suggest that students and instructors, being agents acting within a complex system, will construct a ‘*meta-knowledge*’ that allows them to make sense of and act successfully within that system – in short: knowledge of how to pass an examination and what it *means* to do so. This strongly suggests a link with metacognition, as the meta-knowledge is not *subject* knowledge. Rather, it is knowledge about how to learn the discipline in such a way that one can satisfy the requirements of the examination system – i.e. that which a student would need to know in order to be a successful strategic learner [15].

The active construction of knowledge in and by the mind of the learner involves the production of viable explanations for our experiences for better navigation through what we commonly call ‘reality’. Ideally, the mental models that we thereby create [16] would as far as possible need to be a true reflection of that reality, in order to function as reliable navigational tools. This knowledge is not constructed in isolation hence it is necessary also to recognise the strong input of the social environment in the construction of this knowledge. The meta-knowledge here considered would be constructed as a *collective* ‘effort’ within a community – that comprising principally the students, instructors and examiners of physics; and also, but more peripherally, the various other stakeholders.

Collective efforts within any system require some mechanism of coordination between the various agents and we are informed therefore also by *stigmergy*, as the agents in the system both make and sense ‘signs’ in the environment of that system, that influence the behaviour of other agents [17, 18, 19]. These signs, we believe, consist on the one hand of the discernible patterns of question-types found in the examination papers and on the other, of the performances – reflected in their marks (grades) - of the examination candidates who answer them.

3. Methodology

Our basic aim was to assess the extent to which examination questions typically require students to work in ‘algorithmically unfamiliar territory’ and to compare their performance in such questions with that in other types of questions, in particular ones involving familiar algorithms. This we did by identifying essentially what it is that the student would need to do in order to produce the answer to a given question, and then to assess the average performance of the students for each question. This approach has allowed us to identify several question-types typically asked in (our) physics examinations and hence, to assess how the students perform when answering each of the various question-types.

In order to link student performance with question-type, we recorded the marks awarded to each student for each individual question on a spread-sheet (see Figure 1 below). This allowed the convenient calculation of an average mark for each question, to indicate the group performance. Data was thus captured from examinations given to a first year course in ‘general’ physics for engineering students. We base our claims here on the data from both the mid-year and the final examination results of 2012 and 2013. We present below a sample spreadsheet for a class test, showing a selection of the data to illustrate the capture and analysis of the data.

Question:	1		2		3		4				
Sub-section:	a	b	a	b	a	b	a	b			
Sub-sub-section								i	ii	iii	Total:
Out of:	10	8	1	7	8	4	3	3	4	2	50
Student #	4	8	1	7	7	2	3	3	4	2	41
Student #	2	1	1	0	2	0	1.5	3	0	2	12.5
Student #	4	0	0	2	1	1	1.5	0	2	0	11.5
Student #	5	8	1	2	5	0	3	3	0	0	27
Student #	10	5	1	4	3	0	3	3	4	2	35
Student #	10	8	1	2	1	0	3	3	2	0	30
Student #	10	5	1	3	1	1	3	3	4	0	31
Student #	4	8	1	4	7	1	3	3	4	2	37
count:	832	832	832	832	832	832	832	832	832	832	
Sum:	4957	3829	665	3111	3146	845	2399	2222	2524	728	
Average:	6	5	1	4	4	1	3	3	3	1	
Average %:	60	58	80	53	47	25	96	89	76	44	
Recall & Present:	1	1	4	1	2	1	4	1	1	1	
Intuitive/Interpretive:	2	1		3	1	3			2	3	
Familiarity:	3	3		1	3	1		4	3	2	
Complexity:	2	2		3	2	2		0	2	2	
Topic:	Optics	Optics	Fluids	Fluids	Waves	Waves	Thermal	Thermal	Thermal	Thermal	

Figure 1: Sample spreadsheet illustrating types of data emerging from study.

Limitations of space allow the marks of only eight of the original class of more than eight hundred students to be shown, but the averages shown are calculated from the full data set.

A five point typology coding scale – see Figure 1 - was used, ranging from zero to four.

The following points illustrate their use in this study:

- Two questions (question 2a and question 4a) were rated ‘4’ for recall – this means that the questions were *pure* ‘recall-and-present’ questions. The blanks in the blocks below indicate that there was no computation involved, hence the familiarity or complexity of an algorithm was simply ‘not applicable’, as was the use of ‘physics intuition’. Both questions yielded very high averages – eighty percent and ninety-six percent respectively.
- Three questions (2a, 3b and 4biii) were coded ‘3’ for ‘physics intuition’. Two of the three yielded failing averages, one of which was the lowest average – twenty five per cent - in the data set. This question-type has stood out both for its relative rarity and the extremely poor performances usually associated with it.
- Question 4b (i) was a computation and was rated a ‘4’ for algorithmic familiarity and a ‘0’ for complexity, and yielded the second highest average of eighty nine per cent. All other ‘algorithmic’ questions were given lower familiarity ratings and also yielded poorer performances.

4. Outcomes & Results

A taxonomy of question types was thus established by considering what the student would need to *do* to produce an answer to a given question - as follows:

a) Recall: either *recall-and-present* – such as laws, definitions and sundry ‘bookwork’; or else *recall-and-use* where material is recalled and then utilised during the production of other parts of the answer - see ‘computations’ below.

b) Intuitive/interpretive (questions): using a previously constructed mental model - largely *qualitatively* - to make a judgement or prediction, or else to explain something - sometimes called ‘physics intuition’.

c) Computations: – questions involving mathematical operations, being either ‘routine operations’ or ‘novel problems’ - which mark the two ends of the same continuum; and constituting one dimension of the “difficulty” of the problem-solving process. In a routine operation the algorithm is recalled and used, in a novel problem the algorithm is discovered and constructed during the solving process.

Further we note that:

- As we have reported before [20], several of these taxonomic types often feature as *elements* in a question, rather than being the sole attribute of a single question.
- The ‘routine operation’ emerges as the clear favourite question-type by a considerable margin (see Figure 2 below) and,
- Students perform reliably well when dealing with familiar algorithms – i.e. in routine operations - even where the algorithm is quite complex (see Figure 3 below).

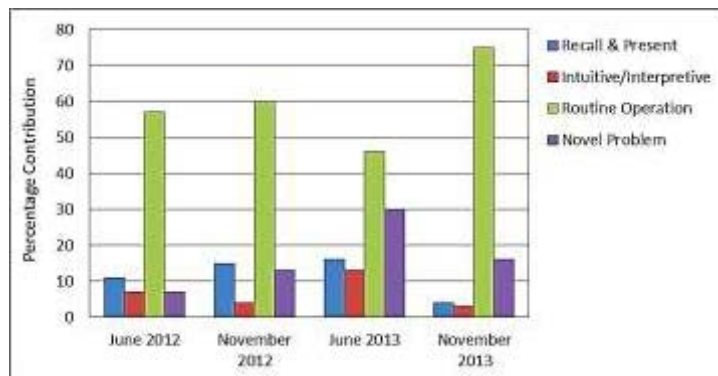


Figure 2: Percentage contribution to examination marks by question type.

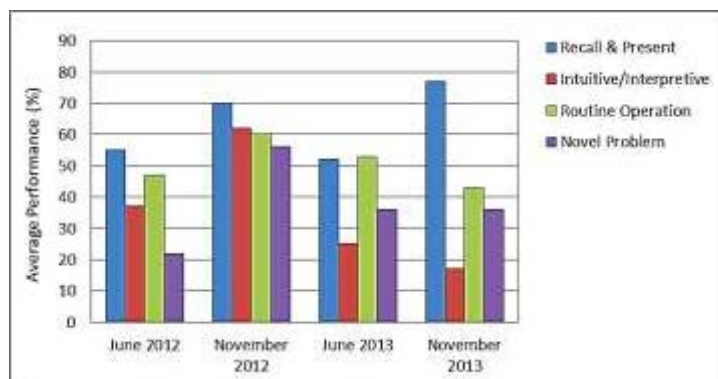


Figure 3: Average performance – as percentage - by question type.

5. Concluding discussion

It was thus possible for students to pass any of these examinations in the almost complete absence of true problem-solving. To support this claim we point out that in the papers analysed, 60% to 70% of the marks were allocated to questions demanding only a working knowledge of some routine operation. The majority of the students who passed would have scored between 50% and 70% - i.e. within the same range. Students who achieve anything up to 70% thus provide no evidence that they are capable of much other than performing routine operations. Given the widely agreed importance of problem-solving as a learning outcome [1], there is surely something amiss with this situation.

Backwash feeds the message into the system that routine operations are the dominant question-type and that a candidate can expect to pass an examination knowing almost nothing else. The medium of this ‘message’ is essentially stigmergic – consisting of the patterns discernible in the examination questions and the performances of the candidates answering those questions. These patterns are analogous to the pheromone trails left in the environment by foraging ants or nest-building termites.

Motivation for teachers to maximise their pass rates above and beyond the ‘satisfaction of a job well done’ is provided by the ‘performativity’ ideology of educational management now prevalent in most countries [21, 22] in which target metrics (e.g. pass and distinction rates) that should serve as management tools, indicating the achievement of more fundamental learning outcomes [23] become instead, goals in their own right that instructors and examiners must strive to achieve, or face sanction.

Given the definitional vagueness concerning what constitutes problem-solving found in the literature, [3] instructors could well be teaching routine operations under the impression that this amounts to the teaching of problem-solving. As good pass rates can be achieved by teaching routine operations and not much else, we suggest that this may be why the ability to solve true – i.e. novel – problems is so underdeveloped. If we exclude true problem-solving from our examination system, we in effect exclude it from our *de facto* curriculum. This omission may be a significant, but under-recognised ingredient in the education ‘crisis’ from which our country is currently suffering.

A parallel analysis of the South African school-leaving (physics) examination since 2008 reveals that here also, routine operations are the dominant question-type [24]. Unfortunately data for student performance *per question* are not available for these examinations.

References

- [1] D. H. Jonassen, (2010) *The 11th International conference on Education Research New education paradigm for learning and instruction*, , pp. 1–15.
- [2] M. E. Martinez, *Phi Delta Kappan*, vol. 79, no. 8, pp. 605–609, 1998.
- [3] D. Gil-Perez, a. Dumas-Carré, M. Caillot, and J. Martinez-Torregrosa, *Stud. Sci. Educ.*, vol. 18, no. 1, pp. 137–151, 1990.
- [4] R. E. Mayer, *Instr. Sci.*, vol. 26, pp. 49–63, 1998.
- [5] R. E. Mayer, *International Encyclopedia of Education*, 2010, pp. 273–278.
- [6] W. K. Adams and C. E. Wieman, *AIP Conf. Proc.*, vol. 883, pp. 18–21, 2007.
- [7] G. M. Bodner, *Univ. Chem. Educ.*, 2003.
- [8] L. Cheng, *Language and Education*, vol. 11, pp. 38–54, 1997.
- [9] Q. Xie and S. Andrews, *Language Testing*. 2012.
- [10] L. Mack, *Polyglossia*, vol. 19, pp. 5–11, 2010.
- [11] E. F. Redish, *Proc. Int. Sch. Phys. Enrico Fermi Course CLVI*, p. 63, 2004.
- [12] N. Noddings, *Theory Res. Educ.*, vol. 2, no. 3, pp. 263–269, 2004.
- [13] G. J. Cizek, *Educ. Meas. Issues Pract.*, vol. 20, pp. 19–27, 2001.
- [14] T. G. Lewis, *Cogn. Syst. Res.*, vol. 21, pp. 7–21, 2013.
- [15] J. B. Biggs, *Teaching for quality learning at university: what the student does.*, 2003, pp. 11–33.
- [16] D. Clerk and M. Rutherford, *Int. J. Sci. Educ.*, vol. 22, no. 7, pp. 703–717, 2000.
- [17] F. Heylighen, *Cognition*, pp. 1–23, 2011.
- [18] F. Heylighen, in *Lewis, Ted & Marsh, Leslie (eds), Human Stigmergy: Theoretical Developments and New Applications (Studies in Applied Philosophy, Epistemology and Rational Ethics*, 2015, pp. 1–43.
- [19] H. Van Dyke Parunak, *Proc. 2nd Int’l Conf. Environ. Multi-Agent Syst. II (E4MAS ’05)*, vol. 3830, no. 2005, pp. 163–186, 2006.
- [20] D. Clerk, D. Naidoo, and S. Shrivastava, *Book of Abstracts, 57th Annual Conference of the South African Institute of Physics.*, 2011, p. 85.
- [21] S. J. Ball, *J. Educ. Policy*, vol. 18, no. 2, pp. 215–228, Apr. 2003.
- [22] S. J. Ball, *Br. J. Educ. Stud.*, vol. 60, no. March, pp. 17 – 28, 2012.
- [23] J. Hennessy and P. M. McNamara, *English Teaching: Practice and Critique*, vol. 12, no. 1, pp. 6–22, 2013.
- [24] D. Clerk and D. Naidoo, *Proceedings of the 18th Annual Meeting of the Southern African Association for Research in Mathematics, Science and Technology Education*, 2010, pp. 142 – 147.

Student difficulties in vectors: foothold ideas

Ignatius John

Department of Physics, Cape Peninsula University of Technology, Cape Town, South Africa - 7530

johni@cput.ac.za

Abstract. This investigation was conducted with the aim of developing a research based teaching strategy in vectors for non-major physics students. The study reports the explanations used by 132 first year university students to answer five questions without context in two dimensions. The two angled analysis of the methods and explanations used for answering the five questions show lack of understanding of basic vector concepts and inappropriateness in the methods used to solve the problems. The findings indicate that the majority of students used one method and reasoning in all questions irrespective of its suitability and thus answered a few questions correctly and others incorrectly. This paper describes the methods used by students and the productive foothold ideas identified.

1. Introduction

To understand many physics concepts, at any level, it is vital to have a good understanding of vectors. The vectors are introduced, in first year university courses and high schools, by the definition of vectors and scalars. After that the distance and displacement followed by speed and velocity are discussed as examples. This is followed by describing the motion of an object to a distance in one direction and then to another direction, thereafter to find the distance between the initial position and final position to define the resultant displacement. This is easily done by the method of head to tail method rather than parallelogram method. Thus the first step in the introduction of the resultant is done using the method of head to tail followed by parallelogram (without much emphasis in the latter).

Nguyen and Meltzer [1] investigated the understanding of vector addition presented in graphical format, in terms of magnitudes and directions. The seven question set used in the study, a few of them were presented with grid and others without grid, requested explanations for the answers provided. They found that majority of the students were unable to perform vector additions correctly. Hawkins, Thompson and Wittmann [2] investigated the vector addition skills of students using interviews. They used two dimensional graphical vector questions to obtain different solutions and found that most of the students used only one method to answer all questions irrespective of the suitability. Flores, Kanim and Kautz [3] used two dimensional questions and interviews in their studies and found that students lack the ability to reason vectors after traditional instructions. They suggested that modifications in the instruction could improve the student understanding of vector additions. Shaffer and McDermott [4] found that students were able to solve vector problems better without the real life situations. Barniol and Zavala [5] investigated the effect of context and position of vectors in two dimensions. They found that the student responses are contextually dependent. In a similar note, Southey and Allie [6] investigated the student responses in different vector contexts: force, displacement and momentum. They found that additions of different physical vectors are not perceived as the same by majority of students. From these studies it is evident that students have difficulties, however, it is not clear that the

reason for these difficulties at a fundamental level is addressed in the instruction. The present study tries to identify the methods and reasoning used by students while solving simple one and two dimensional problems without any physical context. The absence of physical context in the study enabled us to focus on the fundamental aspects in vectors to identify the “ideas” that helped the “correct” students to come to the acceptable answer. The result can be interpreted using the “knowledge in pieces” perspective.

2. Methodology

The present study is trying to probe the aspects in vectors by analysing the student responses to a single situation in which no physical contextual changes were made but only the direction. A questionnaire consisted of five questions was used in the study. All questions were presented in graphical representation and each question consisted of two vectors of different magnitudes and directions. Of the five, four were in two dimensions and the last was in one dimension orientated in the same direction. Thus the study is trying to answer the following questions:

1. What are the methods used by students in answering the questions, namely the parallelogram method, head to tail method or resolution of components method or any other method?
2. While answering the questions, did they use graphical methods in the process or used some other familiar “concepts” from their prior knowledge?
3. What are the ideas used by the students to answer each question irrespective of its correctness?

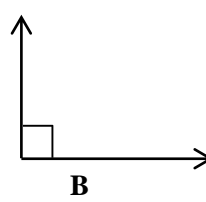
2.1. Instrument

A five question instrument was used in the probe. Each question consisted of two vectors of different magnitudes. While keeping one of the vectors with the same magnitude and horizontal direction in all five questions, the direction of the second vector was changed in each question i.e. the angle between the vectors changed between 0° and 180°. The two vectors were connected tail to tail in all questions, except the last one. All questions were presented graphically without a grid and the possible answers to the resultant vector were given as options. The students were requested to choose one of the given options and explain in detail the reason for choosing the particular option. The answer to the resultant was always related to the previous question and answer, except the first. The first question asked for the magnitude of the resultant vector of two vectors acting perpendicular to each other. The following two questions had the angle between the vectors was changing between 0° and 90°, and the fourth question formed an angle greater than 90°. In the last question both vectors were parallel to each other. The format of a question is shown in Figure 1. The full questionnaire is presented in Figure 2.

For the five questions below, choose the resultant of the two vectors. Circle the BEST ANSWER of the given options and explain your reasons: $\vec{A} = 3 \text{ units}$ and $\vec{B} = 4 \text{ units}$

1. The resultant $\vec{R}_1 = \dots$

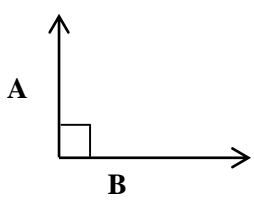
A. 1 unit	B. 3 units	C. 4 units
D. 5 units	E. 7 units	F. none of the above



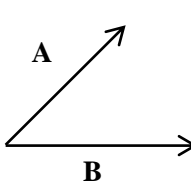
Explain your answer.....

Figure 1: Format of a question used in the study.

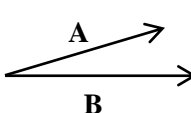
For the five questions below, choose the resultant of the two vectors. Circle the BEST ANSWER of the given options and explain your reasons: $\vec{A} = 3$ units and $\vec{B} = 4$ units

1.  The resultant $\vec{R}_1 = \dots$
 A. 1 unit B. 3 units C. 4 units
 D. 5 units E. 7 units F. none of the above

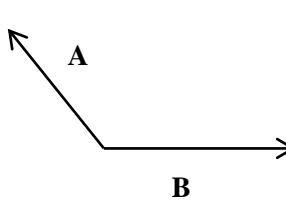
Explain your answer.....

2.  The resultant $\vec{R}_2 = \dots$
 A. smaller than \vec{R}_1 B. bigger than \vec{R}_1
 C. equal to \vec{R}_1 D. none of the above

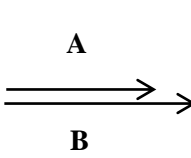
Explain your answer.....

3.  The resultant $\vec{R}_3 = \dots$
 A. smaller than \vec{R}_2 B. bigger than \vec{R}_2
 C. equal to \vec{R}_2 D. None of the above

Explain your answer.....

4.  The resultant $\vec{R}_4 = \dots$
 A. smaller than \vec{R}_1 B. bigger than \vec{R}_1
 C. smaller than \vec{R}_2 D. bigger than \vec{R}_2
 E. none of the above

Explain your answer.....

5.  The resultant $\vec{R}_5 = \dots$
 A. smaller than \vec{R}_4 B. equal to \vec{R}_4
 C. bigger than \vec{R}_4 D. bigger than \vec{R}_3
 E. smaller than \vec{R}_1 F. bigger than \vec{R}_1
 G. None of the above

Explain your answer.....

Figure 2: The questionnaire used in the study.

The test was conducted during a physics lecture period, as a weekly formative assessment. Students were told that they may use any type of explanation, in terms of either textual or graphical or a combination of both. A few students completed the test in fifteen minutes and others took more than 20 minutes.

2.2. Sample

The cohort consisted of 132 first year university students registered for various courses in the Science Faculty (non-physics major). All these students passed Physical Science (a combination of Physics and Chemistry) in Grade 12 and vectors were part of their syllabus in high school. The majority of the students were from rural schools, aged about 18 years, and for whom English is second or third language. The students received instruction on vectors and kinematics at the university before the test.

3. Result

The data was captured in a spread sheet that consisted of ten main columns (5 x 2). The answer to each question was recorded as two parts in each column: (i) the forced choice responses and (ii) the written responses.

3.1 Forced Choice Responses

Majority of the students answered questions 1 and 5 correctly. 94% chose the answer 5 units in Q1 and 84% chose the answer 7 units in Q5. The reason given by all students for Question 1 was the same with the Pythagoras theorem being stated as the reason. The two reasons for question 5 were: “sum” of two vectors and vectors are in the “same direction”. Since the majority of them answered these questions correctly, with acceptable reasoning, no further analysis was done on these two responses. Thus the questions 3, 4 and 5 was analysed in detail. Figure 3 shows the full responses of the cohort. The first set of three bars shows that each of the questions were answered correctly by almost half of the students. However, only 10% of the students answered all questions correctly.

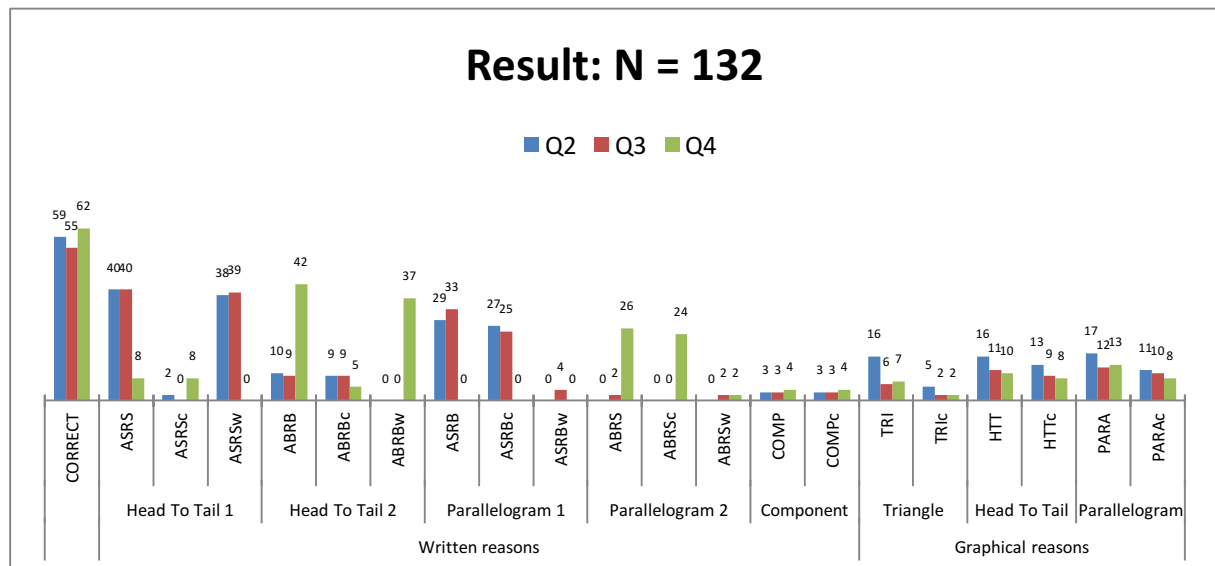


Figure 3: Student reasoning responses for the three questions: the two versions of head to tail, parallelogram and component method are presented including graphical reasons.

3.2 Free Writing Response

The majority of students used different written reasons to explain their answers. However, they did not use any method consistently or did not apply any method appropriately in all three questions. Instead

they used different reasoning without properly analysing the situation at hand. Some used only words to explain and others used words and drawings; the drawings they used were also different from question to question. Thus the free writing responses provided by students were divided into two categories: Written reasons (WR) and Graphical reasons (GR), as shown in Figure 3. The blue, red and green bars represent the number of responses for questions 2, 3 and 4 respectively.

3.2.1. Reasoning in Words (WR)

The analysis of free writing responses revealed that most of the students were familiar with the head to tail method. The different explanations in words they used were categorised into five reasoning categories: (i) when the angle is small, the resultant is small (ASRS) (ii) when the angle is big, the resultant is big (ABRB) (iii) when the angle is small, the resultant is big (ASRB) (iv) when the angle is big, the resultant is small (ABRS) and (v) resolution of components (COMP).

The first two reasoning can be related to head to tail method and the third and fourth can be related to parallelogram method. Of the 40 students who used the category ASRS, almost all of them answered Q2 and Q3 incorrectly (ASRS_w); however, the few who used this category in Q4 answered it correctly (ASRS_c). Of the 42 students who used the category ABRB in Q4, most of them answered incorrectly (ABRB_w), while a few who used this category in Q2 and Q3 answered all correctly (ABRB_c). The subscripts c and w represent the correct and wrong answers respectively.

A fifth of the cohort used the category ASRB in Q2 and Q3. Of this, more than 80% answered these questions correctly (ASRB_c). However, none of them used this category in Q4. The category ABRS used by a few students in Q4; all answered correctly.

All students who used the components reasoning (COMP) answered all questions correctly although this group was very small in number.

3.2.2. Graphical Reasoning (GR)

An average of 10% of students used written reasons and graphical reasons in combination for their reasoning. The graphical reasons are subdivided to three categories: closed Triangle (TRI), head to tail (HTT) and parallelogram (PARA). More than 70% of the students who used correct graphical methods, HTT and PARA, answered all questions correctly and those who used TRI explanation (which itself is an incorrect method) answered most of the questions incorrectly.

4. Discussion

The general features of all questions used in this probe were the same. All questions were presented in graphical form, in which the vectors were connected tail to tail in two dimensions. The only variation in each question was the angle between the two vectors. Since the vectors were connected tail to tail, it would have been easier to answer these questions by employing the parallelogram method in all cases. However, it was interesting to note that most of the students used head to tail method rather than parallelogram or components method. Even though, most of them were familiar with head to tail method, they were unable to use this method correctly in all situations. In general, students who used only the written explanation in all three questions did not answer all of them correctly. For example, the idea of “angle small resultant small” and “angle big resultant big” are correct if used in the head to tail method and incorrect if used in the parallelogram method. Similarly, the idea “angle small resultant big” and “angle big resultant small” are correct if used in the parallelogram method and incorrect if used in the head to tail method. In summary the students who used the head to tail method (ASRS, ABRB) answered incorrectly and the students who used the parallelogram method (ASRB, ABRS) answered correctly and all students who used the components method answered all questions correctly. The reason for this phenomenon may be attributed to the majority of college physics (and high school) textbooks introducing scalars and vectors using the concepts of distance and

displacement. While doing so, it is reasonable to start with two displacements, one after the other and ask for the distance between the initial position and final position to determine the resultant displacement. Thereafter, the parallelogram method (may be followed by components method) is introduced but not emphasis. This initial process may be strongly embedded in the minds of the students as the best method, although, this method may not work efficiently in the context of forces. These variations in context and misunderstanding or partial understanding of different methods used in different contexts and the confusion between them can be explained using the framework of the 'knowledge in pieces' perspective.

Thus from the study we can argue that the students who used the parallelogram method and the component method performed significantly better than the students who used the head to tail method. This was evident both in terms of the written explanations and graphical explanations. Thus the parallelogram method and component method seems to be the productive foothold ideas in understanding vectors. These results have huge teaching implications. At this stage, it can be suggested that introducing vectors with forces in two dimensions using the parallelogram method and component methods may be a better strategy to introduce vector addition. Furthermore, the context in which students frame these questions needs to be ascertained by investigating if they use a mathematical or a physical context.

Future research is considered to include a post test after the feedback and with more than two vectors.

References

- [1] Nguyen N and Meltzer D. E 2003 Initial understanding of vector concepts among students in introductory physics courses, *Am. J. Phys.*, vol. 71, no. 6, pp. 630–638.
- [2] Hawkins J. M, Thompson J. R, and Wittmann M. C 2009 Students' Consistency of Graphical Vector Addition Method on 2-D Vector Addition Tasks, *AIP Conf. ...*, vol. 1179.
- [3] Flores S, Kanim S. E, and Kautz C. H Student use of vectors in introductory mechanics, *Am. J. Phys.*, vol. 72, no. 4, p. 460.
- [4] Shaffer P. S and Mcdermott L. C 2005 A research-based approach to improving student understanding of the vector nature of kinematical concepts, *Am. J. Phys.*, vol. 73, no. 10, pp. 921–931.
- [5] Barniol P and Zavala G 2009 Investigation of Students' Preconceptions and Difficulties with the Vector Direction Concept at a Mexican University.
- [6] Southey P and Allie S 2014 Vector Addition in Different Contexts Follow up Interviews, *AIP Conf. Proc.*, pp. 243–246.
- [7] John I and Allie S 2013 DC circuits: Context dependence of student responses, *Phys. Educ. Res. ...*, vol. 202, no. 1, pp. 202–205.

Physical models: A crucial link between reality and mathematical models

M Lemmer¹ and R Gunstone²

¹ School of Physical and Chemical Sciences, North-West University, Potchefstroom, South Africa

² Faculty of Education, Monash University, Clayton, Australia

miriam.lemmer@nwu.ac.za

Abstract. Physics describes real-life phenomena with the aid of models; mathematical modelling is a prime goal of physicists. All models, even abstract mathematical models, are embedded in real life experiences and Physics students should learn to look at the world through this lens and to handle modelling cycles with ease. Major processes of a modelling cycle are mathematical modelling of a physical system followed by mathematical processing from which the outcome is interpreted and validated in the physical system. It is argued here that it is crucial to pay attention during physics instruction to understanding of physical models (that incorporate physical systems) as an initial phase in the modelling process. Physical models involve simplifications of real life situations and the assumptions, features and limitations of physical systems; conceptual understanding of physics concepts, relations, basic principles, laws and theories and the ability to translate between various representations thereof as well as application of scientific causal, proportional and analogical reasoning. Research-based problems that students encounter when physics tuition commences with mathematical models or when these are directly build onto real life situations without sufficient attention to physical models are discussed. Teaching strategies to circumvent these problems are proposed.

1. Introduction

The central place of models and modelling in the evolution of the discipline of physics (and of science more generally) has been widely recognized by physicists. For example [1], writing for the International Commission on Physics Education, notes that “One of the main goals of physics is to develop plausible conceptual models, as they are called, in terms of which various physical phenomena can be described and explained” (p.14). The centrality of models and modelling has also been very commonly described by historians of physics (and science) (e.g. [2]), scholars of the philosophy of physics (and science) (e.g. [3]), and scholars of the nature of physics/science (e.g. [4]).

In physics, a “model” can be a physical and/or a mathematical and/or conceptual representation of a system of ideas, events or processes. Models are critical for the ways in which physicists seek to identify and understand patterns in our world. Models which also enable predictions are of greater epistemological value, and those that enable precise (mathematical) predictions are, in most areas of physics, the most highly valued (see [3] among many examples). In this paper, we use the term “modelling” to describe the constructing of and/or the using of appropriate models.

Our core purposes in this paper are about the learning of physics, and the ways models and modelling might be better considered in the development of student understanding. In such learning contexts, it can often be helpful to categorize models as “mental” models (that is the ways individuals represent

complex ideas, events or processes in their thinking about these); “expressed models” (that is an explicit statement by an individual via word, speech, diagram, etc of their mental model); and “consensus models” (that is an expressed model that has been subject to testing by physicists and consensus reached that the model has merit [5] because of its fit with data, its congruence with explanations of related phenomena, its transferability, and its power to enable questions, predictions and experiments [6]).

Central to our core purposes here is the discrimination between “reality”, “physical models”, and “mathematical models”, and the ways these are relevant to learners’ development of the concepts and relationships of physics. Our use of these terms is quite conventional. Nevertheless, it is appropriate to be clear as to this use. We also illustrate this use by reference to a specific example across the three.

Here “reality” is used to refer to the direct experiences that learners have with their world, relevant ways in which learners interact with their world (so “reality” is variable across any given group of learners). In the broad area of Newtonian mechanics then, “reality” will include the alternative conceptions (sometimes labelled intuitive conceptions or, unfortunately, misconceptions) that a learner has constructed through the everyday ways they have moved objects with forces they apply or seen others move objects, and any specific experiences in science/physics laboratories during their formal education. Alternatively, we could have described our meaning for “reality” as being the mental models held by a student as they enter our classroom. To emphasize this point, we use the term “real world” rather than “reality” from this point. We use “physical model” to refer to the core explanatory (conceptual) framework that physics has developed for a group of observations, phenomena, events (in the terms used above, the current “consensus” model). For the broad area of Newtonian mechanics, this can be expressed as “if the motion of an object changes [accelerates], then there must be a resultant force acting on the object”. A “mathematical model” then is the precise quantification (mathematization) of the physical model – in the case of Newtonian mechanics, “ $F = ma$ ”.

Our motivations for writing this paper are twofold:

- 1) To argue the central place of models in physics, and therefore in physics learning
- 2) To describe and justify an ongoing research programme focussed on models and physics learning.

In a manner consistent with the northern European construct of *didactics* (e.g. [7]), this research programme takes two significantly interrelated beginning points – the discipline of physics and the learner of physics.

2. Theoretical framework

Models and modelling are central in the discipline of physics and thus should also be in the learning and teaching of physics (e.g. [8, 9]). Models describe key characteristics of observed phenomena, events or processes by using scientific representations in order to make explanations and testable predictions. Essential components of a model are the target phenomenon or system, and assumptions and simplifications used to focus on relevant features and representations that depict scientific concepts, relations and principles in ways that create a model with explanatory and predictive power.

Modelling is the “dynamic process of constructing and using models” [9]. This is widely recognized in the content development of physics; it is also critical to students’ conceptual development in physics. [10] added to the elements of construction and deployment in the practice of modelling also the evaluation and revision thereof. They further emphasized that students should understand the nature and purpose of models that guide and motivate the practice of physics.

Since [8] advocated modelling as instructional method it has developed into an efficient approach towards meaningful science learning in which students’ existing mental models are re-constructed systematically and intentionally towards the consensus models of the scientific theory (mathematized scientific models) [6].

Working from constructivist and socio-cultural theories, [6] derived six criteria for pedagogical usefulness of teaching models: The models must be intelligible, plausible and fruitful to students; contain meaningful causal mechanisms; bring to the fore and address students’ conceptual difficulties; engage students effectively; advance students’ understanding of consensus models and also the nature, purpose, assumptions and limitations of all models. Conceptual refinement instructional approaches can

guide students in refining and advancing their experiential resources towards a conceptual understanding of generalized physics principles and laws before formalising it as mathematical expressions and representations ([11]).

Modelling cycles intended to promote students' understanding of consensus scientific models have been proposed (e.g. [12, 13]). Most modelling cycles distinguish between each of the real world, physical models and mathematical models and describe *translation processes* between them. Physical models are abstracted from real world situations through processes of *simplification* and structuring representations. Integration of mathematics knowledge aids in translating physical models into mathematical models, a process called *mathematization*. Conversely, mathematical models are *interpreted* in physical models and the results are *validated* in the real world. It is important to realise that modelling cycles are structured pedagogical tools that help advance students' understanding, but are not necessarily chronological and are not identical for each student in a given context of physics.

3. Differences between real world and physical models

Although authors of proposed modelling cycles recognize that scientific models are embedded in the Real World, these cycles tend to focus more on construction of mathematical models than the development of physical models from real world situations. In this section we argue that many of students' conceptual difficulties reported by physics education researchers (refer to [14] for many examples) may result from differences in how learners perceive concepts, solve problems, explain events and apply reasoning in their real world as compared to the way physicists do these tasks when using physical models. A physical model can be perceived as an encoding of a target system that is embedded in a complex real world situation.

Other Physical models differ in various aspects from everyday observations and descriptions of situations in the real world, as we have categorized and structured in table 1. Features of the real world conceptions follow from literature reported over several decades of Physics Education Research, (e.g. many references in [14]), and we compared features thereof with physical models that we have deduced from knowledge and experience of teaching physics content. An example referred to in the table is that physics concepts are uniquely defined, usually in relation to previously defined concepts, while concepts in everyday life are often perceived as contextually or functionally related. While physicists seek an underlying framework of principles and laws that explains various phenomena, students' intuitive explanations and reasoning depend on the situation or event. We now illustrate the ways beginning students derive concepts and intuitive explanations and reasoning – “alternative conceptions” – from their everyday experiences by considering the case of normal reaction.

4. The difficulties we know beginning physics students have with normal reaction

The term “normal reaction” itself leads some students to construct alternative conceptions. If the term “normal” is not explicitly linked with the mathematical concept of orthogonality, then a meaning can be constructed that there is somewhere an “abnormal” force. Unless the matter is explicitly considered with students, many will make most unfortunate links with Newton's Third Law through the term “reaction”, and conclude that gravity and normal reaction for a book on a table are an action-reaction pair. (This incorrect construction is also made by some teachers, and even the occasional school physics textbook writer.) Other alternative conceptions common in beginning physics students are: in any system that a physicist would describe as in ‘equilibrium’ there are no forces of any form (crudely, ‘no motion means no force’); the only force involved with a book on a table is gravity, the book remains at rest because the table is just “rigid” or “in the way”; when the book is placed on a rigid table nothing about the table changes so it makes no sense to even think about forces; gravity exerts the same force on everything (and so there is no mystery in the table being able to support either one book or many books); gravity must be stronger than any upward force or the book would float. Also a significant difficulty, although hardly an alternative conception, is a common tendency to not see the need to describe a force in terms of what object exerts the force and what object the force is exerted on (e.g. [15, 16, 17]).

Table 1. Some differences between real world and physical models.

	Real world	Physical model
Concepts and relations	Different meanings can be attached to a concept name. Concepts are related on basis of observable or functional correspondences.	Concepts are uniquely defined. Concepts are related mathematically to other concepts.
Problem solving	Focus on what seems to be relevant. Contextual features of the problem setting play a role, sometimes only these.	Consider concepts, principles and representational formats of a specific physical system (model of reality).
Explanations of events or phenomena	Social and cultural views and situational aspects are taken into account.	Scientific principles, theories or laws are used; these are independent of situational aspects, including social and cultural views.
Findings/Results	Findings may depend on the situation or context.	Results are required to be repeatable, valid and reliable and independent of context.
Representations	Realistic diagrams of phenomena or events (i.e. reproductions of the reality).	There are multiple scientific acceptable representations of events, e.g. diagrams, graphs, mathematical expressions, etc.
Reasoning	Intuitive cause-effect and analogical reasoning.	All of causal, proportional, analogical, mathematical reasoning are used.

5. A modelling framework to discuss, explore and explain physics students’ difficulties in understanding consensus models

Because of the difficulties that students experience in translating between real world situations and physical models we argue that physical models provide an important connection between students’ mental models derived from real world experiences and the mathematical models that are the endpoint learning goals of these students. A modelling cycle is suggested in figure 1 followed by a brief example of implementation in a sequence on normal reaction.

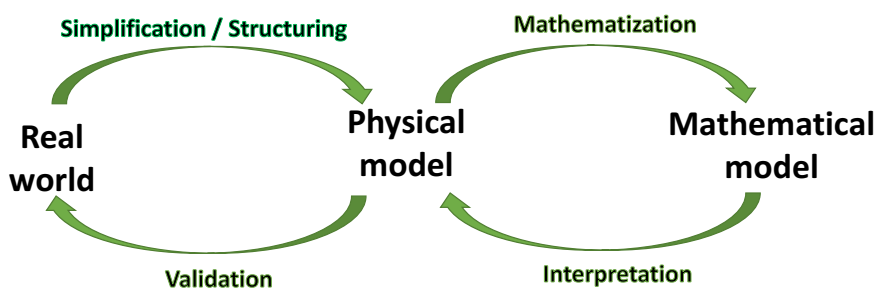


Figure 1. Proposed modelling cycle.

This modelling cycle is derived from literature described in the theoretical framework above. For example, the cycle of [12] involves transfer between the physical and mathematical models with the aid of the processes of mathematization and interpretation. [13] also focused on integration of physics and mathematics, but argued that this transfer should be perceived as a continuum. Their physical-mathematical model “can be used on its own as well as connected to the ‘world’ ” [13:496] using the processes of simplification/structuring and validation. However, we propose that the transfer between the real world and physical models is on an equal footing with the transfer from physical to mathematical models (as depicted in Figure 1) and perceive this first cycle also as a continuum (unlike [13]). The processes that connect the real world with physical models (simplification / structuring a physical model from the real world, validation of findings from the physical model in real world situations) are often

neglected in physics instruction ([15], [19]), resulting in learning difficulties such as those on normal reaction discussed above and addressed below.

6. A brief example of the application of the Modelling Framework to the development of student understanding via connections between the real world and the physical model

Our example is, again, the concept of normal reaction. The approach outlined here has been evolving over many years in the teaching of the second author, and of a high school science teacher. Its early forms derived much from the work of [16], and is discussed in [18]. Versions close to its current form exist, as used with BSc (biology majors) preparing to teach integrated science to Grade 10 ([17]) and with Grade 10 science classes ([15]). It has also been used in undergraduate physics. Research has shown the same broad student difficulties before undergraduate instruction in this topic (e.g. [20]).

The beginning point is a book on a horizontal table and the question “why doesn’t the book fall?”. This Real world situation is placed in front of the students, and throughout the following discussion is considered only in terms of book and table. That is, the whole system of book/table/floor/ building/ earth is simplified to the limited system of book/table. As a further simplification, only this situation is considered, and the vector nature of force is only addressed via terms “up”, “down”, “push”, “pull”.

A range of related real situations is used to seek to reveal the ways students already make sense of their real world, and to challenge these ideas. These include: a volunteer has one arm horizontal, one book is placed on the hand (figure 2 left), the sensory consequence described and class explanations briefly discussed, then several books are placed on the hand (figure 2 right); similar use of one book and several books suspended from a strong rubber band; volunteers of obviously different weight successively sit on the same chair; a metre ruler is supported at each end by bricks and increasing numbers of books placed in the middle (figure 3). This latter situation is particularly powerful as a direct illustration of what physically happens to a (rigid) table when a book is placed on it.

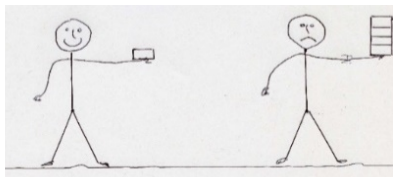


Figure 2. Sensory experience of holding one and more books on the hand.

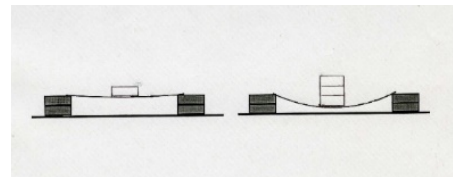


Figure 3. Illustration of the effect of an increasing number of books on a metre ruler.

This set of experiences is used to lead to the Physical Model of a system of an object placed on another object and remaining stationary while being acted on by gravity: distortion resulting in a force opposite to the gravitational force. It is noted that the initial case of the book on the table is as yet not explained (there is as yet no evidence of distortion of that table). Discussion quite quickly leads to most students accepting that if one could actually show distortion in the table, then this situation too is explained by the same Physical Model. That demonstration is surprisingly easy for many tables (so one chooses the initial table with care!). Unless the table has a stabilising feature (e.g. metal frame), the distortion is shown clearly by (i) placing a mirror in the middle of the table, (ii) shining a bright beam of light (e.g. slide projector) onto the mirror at an angle, so a reflection appears on a side wall, and (iii) leaning on the table and showing the image of the light beam being displaced. It is useful to explore with students how they predict the beam will move when the table is lent on at either side of the mirror – this makes engagement with the observation stronger and more cognitively meaningful.

In this example, the more difficult matter in developing student understanding is helping students simplify and structure as they move from their Real World to the Physical Model. The further shift to the Mathematical Model is relatively much easier. Indeed, aspects of the initial experiences described above also show that increased gravity force results in increased force in the opposite direction in order to continue the stationary state. The more precise quantification that is the final Mathematical Model is relatively clear by using rubber bands or springs where there is a linear relationship between extensions

and upwards force. The completion of the sequence is to work back to the Real World and to explain the initial experiences in terms of both the Physical Model and the Mathematical Model.

7. Conclusions and implications for physics instruction

Ignoring physical models and trying to connect mathematical models directly to real life problems often results in students' alternative conceptions. To a considerable extent this is because no attempts are made to link/bridge/reconcile the Reality of the student that is brought to the study of physics with the Physical Model that is central to the mathematical model the physicist has developed.

Students should obtain first-hand experience with analysing differences between real world, physical and mathematical models when doing experiments and solving problems. Physics instructors should carefully introduce, motivate and explain the construction and use of models to their students, constantly revise and refine their understanding until the students are enculturated in physics.

References

- [1] French A P 1997, 1998 *Connecting Research in Physics Education with Teacher Education* (Vol 1) eds A Tiberghien, E L Jossem, *et al.* Accessed 26 April 2016 at <http://iupap-icpe.org/publications/teach1/ConnectingResInPhysEducWithTeacherEduc.pdf>.
- [2] Krieger M H 1987 *Am. J. Phys.* **55** 1033–38.
- [3] Bunge M 1973 *Philosophy of Physics* (Dordrecht: Reidel).
- [4] Lederman N, Abd-El-Khalick F and Schwartz R 2015 *Encyclopedia of Science Education* ed R Gunstone (Dordrecht: Springer) pp 704-708.
- [5] Gilbert J K, Boulter C and Rutherford M 1998 *Int. J. Sci. Educ.* **20** 83–97; **20** 187-203.
- [6] Hart C 2008 *Res. Sci. Educ.* **38** 529-544.
- [7] Fischler H 2011 *The Professional Knowledge Base of Science Teaching* eds D Corrigan, J Dillon *et al.* (Dordrecht: Springer) pp 31-50.
- [8] Hestenes D 1987 *Am. J. Phys.* **55** 440.
- [9] Zwickl B M, Hu D, Finkelstein N and Lewandowski H J 2015 *Phys. Rev –Phys. Educ. Res.* **11** 1–12.
- [10] Swartz C V, Reiser B J, Davis E A, Keyon L, Acher A, Fortus D, Swartz Y, Hug B and Krajcik J 2009. *J. Res. Sci. Teach.*, **46** 632-654.
- [11] Lemmer M 2011 *AJRMSTE* **15** 4–17.
- [12] Redish E F and Kuo E 2015 *Sci. & Educ.* **24** 561–590.
- [13] Uhdén O, Karam R, Pietrocola M and Pospiech G 2012 *Sci. & Educ.* **21** 485-506.
- [14] Duit R 2009 Bibliography – STCSE: Students' and teachers' conceptions and science education www.ipn.uni-kiel.de/aktuell/stcse/stcse.html.
- [15] Gunstone R and Mitchell I 1998 *Teaching Science for Understanding* eds J Mintzes, J Wandersee *et al.* (San Diego: Academic Press) pp 133-163.
- [16] Minstrell J 1982 *Phys. Teach.* **20** 10-14.
- [17] Gunstone R 1994 *The Content of Science* eds P J Fensham, R F Gunstone *et al.* (London: Falmer Press) pp 131-146.
- [18] Champagne A, Gunstone R and Klopfer, L (1985). *Cognitive structure and conceptual change* eds L.H.T. West and A.L. Pines (New York: Academic Press) pp 163-187.
- [19] Reif F 2008 *Applying cognitive science to education: thinking and learning in scientific or other complex domains* (Cambridge, Mass: MIT Press).
- [20] Hake R R 1999 *Am. J. Phys.* **66** 64-74.

Shoestring Practicals and the Teaching of Problem Solving

Douglas Clerk, Deena Naidoo and Claudia Albers

School of Physics, University of the Witwatersrand, Private Bag 3, WITS 2050
Johannesburg, South Africa

E-mail: Deena.Naidoo@wits.ac.za

Abstract. Traditional “recipe-based” practical exercises may have a high degree of outcome predictability, but, because they absolve the student of a great deal of thinking, such exercises have a low degree of value as learning experiences. Practical exercises could instead become problem solving activities, where the student must devise a method as well as generate an answer to a question. The student is given prior warning only of the broad outcome of the task. A common objection to this sort of exercises is that realistically, it can only be performed by students after the relevant ‘theory’ has been covered. This can present a difficulty for service courses where prohibitively large groups of students would have to perform the same practical exercise simultaneously. In addition economic and logistic obstacles, such as the cost of purchasing large quantities of laboratory equipment, and problems of storage can be seen as prohibitive. In this paper, two exercises are presented that are potentially good learning experiences and can easily be performed by first year Physics students without detailed procedural instructions as problem solving activities compared to traditional ‘cookbook’ practical exercises. Furthermore the apparatus for these exercises is cheap to acquire and relatively easy to store, hence the objection mentioned above becomes invalid.

1. Introduction

Practical work is something of a ‘sacred cow’ in science education – its necessity is taken as axiomatic, its efficacy as guaranteed. A closer look at laboratory programmes might, however, reveal something less than optimal. The American Association of Physics Teachers [1] recognises five goals of the introductory physics practical:

- I. The Art of Experimentation:** The introductory laboratory should engage each student in significant experiences with experimental processes, including some experience designing investigations.
- II. Experimental and Analytical Skills:** The laboratory should help the student develop a broad array of basic skills and tools of experimental physics and data analysis.
- III. Conceptual learning:** The laboratory should help students master basic physics concepts.
- IV. Understanding the Basis of Knowledge in Physics:** The laboratory should help students to understand the role of direct observation in physics and to distinguish between inferences based on theory and on the outcomes of experiments.
- V. Developing Collaborative Learning Skills:** The laboratory should help students develop collaborative learning skills that are vital to success in many lifelong endeavors.

It is difficult to see how the traditional ‘cookbook’ practical can achieve any of these goals as they effectively absolve the student of the necessity to think. For example, in order for students to learn to design an investigation they reason, ponder, reason, reflect and apply themselves – the cookbook exercise requires none of these - all the student has to do is follow a set of instructions. Students find this type of exercise not only unchallenging [2, 3] but also unedifying: according to constructivist wisdom, “conceptual understanding is not so much an outcome of experimental work as a prerequisite for its successful operation” [4].

The first-year practical programme at the School of Physics, University of the Witwatersrand is a case in point. For reasons that have more to do with logistics than with good instructional practice, in any one week a student will perform a practical exercise which is allocated according to a roster. In the following week, the next exercise will be performed and so on. There is seldom any connection between the practical exercise being performed and the physics theory being taught at any given time of the year except by coincidence. The practical programme becomes essentially independent of the theoretical programme. This makes it absolutely necessary that students are given detailed instructions - literally a recipe to follow – as they may not necessarily have any relevant theoretical background when performing a given exercise. In some cases they perform a practical at the beginning of the year and only deal with the relevant theory at the end. In other cases, the converse will apply and students will be performing exercises at the end of the year where the theory is covered at the beginning and is for all intents and purposes long forgotten.

The given reason for this state of affairs is that in order to guarantee that all students perform any practical exercise shortly after the theory has been dealt with, they would of necessity need to all be doing the same exercise at the same time. As some of our service courses cater for large groups of students (approaching 1000 in some years in the case of engineering) - the sheer quantity of equipment needed; the expense of acquisition and the space needed for its storage are both regarded as prohibitive. Hence, the roster system currently and historically in force. The problem here is that didactic considerations are being knowingly sacrificed for logistic considerations – there is no claim of any didactic advantage to be gained from the roster system, merely that there is no other economic way of doing it.

In this paper we argue that this may not necessarily be the case. There exist several practical exercises – perhaps enough for an entire curriculum and if not, for at least part of one – that require apparatus that is so cheap and compact that all students, even in large groups, *can* do them simultaneously. Acquisition and storage of the apparatus is not a problem – in fact a significant portion of it is generic equipment that would be in stock anyway, such as metre sticks, retort stands, clamps etc. We present here two of these exercises as examples. Each of these exercises has what we like to call a high ‘*didactic payload*’ – in other words, they have good potential as learning activities. In particular, there is good potential for these exercises to achieve the goals of practical work according to the American Association of Physics Teachers [1]. In addition, the added possibility exists of using the practical exercise as a way of teaching problem-solving which is not possible with the ‘cookbook’ exercise.

2. General considerations

When a practical exercise is performed in the absence of a recipe – i.e. where the devising of a method is part of what the student has to *do* – two things are essential: The students must be *au fait* with the relevant theory and students *must* prepare for the exercise. In the absence of these two requirements, the exercise becomes worse than a cookbook practical. Most university lecturers would probably maintain that any student not *au fait* with theory already covered and unwilling to do preparation should not be at university anyway.

Exercise 1: The measurement of the track separation of a laser disc.

Suitability: Any first year physics courses involving physical optics.

In this exercise the student is faced with the instruction to measure the track separation of a laser disc. Most students are familiar with CD's and DVD's and should have an idea that the track separation is very small and might wonder what sort of instrument they will be using to measure such a small separation. Provided that diffraction and the diffraction grating has been dealt with in lectures and in tutorials, the student - with luck and some judiciously dropped hints from the lecturer and maybe some creative 'googling' - should come across the idea that the laser disc is in fact a diffraction grating. At this point the student can figure out that measuring the separation of the interference maxima can lead to the calculation of the line separation of any diffraction grating and hence the track separation of the laser disc. Hereafter all that remains is the logistics of actually taking the measurements.

The procedure is as follows: First the student needs to 'calibrate' the laser - i.e. establish the wavelength of the laser light. This is necessary as the lasers being used are likely to be laser pointers and the wavelength is unlikely to be obtainable from a label. For this purpose, a standard diffraction grating, the laser to be used and some metre sticks - as well as sundry stands and clamps are all that's required.

The laser is shone through the diffraction grating as shown - note that the metre stick is actually used as a screen to make measuring separations between maxima more convenient:

Once the diffraction angle is known, the wavelength of the laser light can be calculated:

$$m\lambda = d \sin \theta \Rightarrow \lambda = \frac{m\lambda}{d}$$

where d is the line separation of the diffraction grating and m is the order number of the interference maxima.

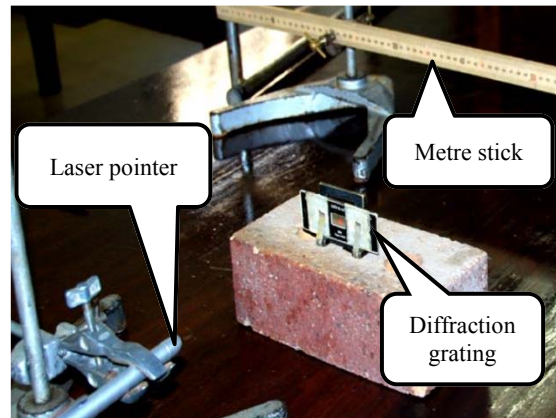


Figure 1. Laser disc track separation experiment – measuring the laser light wavelength.

At this point the diffraction grating is replaced with the laser disc. Here, the student is faced with a problem to solve: the disc is backed with a reflective layer and will not transmit the laser light. There are two solutions to this problem: either remove the reflective layer or place the metre stick acting as the screen just behind the laser. The latter is preferable as you can re-use the laser disc several times.

In the photograph shown in Figure 2, the bright spot above the '50' on the metre stick is the central maximum of the pattern reflected back onto the stick.

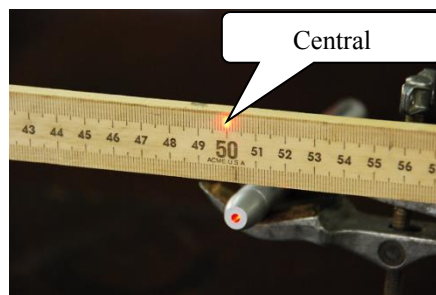


Figure 2. Laser experiment – diffraction pattern central maximum.

Once again, the diffraction angle is determined as before using the measured separation between two interference maxima (again sensibly zero and one), and the distance between the laser disc and the metre stick and then the track separation is determined from:

$$m\lambda = d \sin \theta \Rightarrow d = \frac{m\lambda}{\sin \theta}.$$

The value typically obtained by first year students, working in the complete absence of a recipe, is close to the ‘book’ value of $1.6 \mu\text{m}$ [5].

The cost of the apparatus is minimal: most of the items needed are already in stock in a properly equipped physics laboratory – the only item not usually part of standard stock would be the laser discs. We have never had any problem obtaining enough of these at no cost at all. The existing stock of lasers might need to be increased, but laser pointers can be bought for as little as R35.00. Better quality laser pointers will cost about R200.00 but even this is hardly prohibitive. Storage of the items between exercises is also no problem as they are compact and take up very little space.

Exercise 2: The collision apparatus.

Suitability: any first year physics course involving two dimensional projectile motion and conservation of momentum.

A curved ramp is clamped to a laboratory bench so that a ball bearing rolling down the ramp leaves its lower end horizontally – see photograph:

A plumb bob hangs from the end of the ramp so that the point vertically below the end can be marked on a sheet of paper on the floor.

The simplest exercise is to roll a ball bearing down the ramp and determine the speed with which it leaves the end of the ramp. As before, the student would be faced with the instruction to do so and no recipe to follow. The only measurements needed are the height through which the ball falls and the horizontal distance between the point directly below the end of the ramp and the point of impact of the ball on the floor. This point of impact is marked by placing carbon paper over the sheet of paper on the floor, business side down. The impact of the ball on the carbon paper will make a dot on the sheet of paper. Both of these distances can be measured with sufficient accuracy with a metre stick. The time in flight is calculated from the (vertical) height (h) through which the ball falls:

$$h = \frac{1}{2}gt^2 \Rightarrow t = \sqrt{\frac{2h}{g}}$$

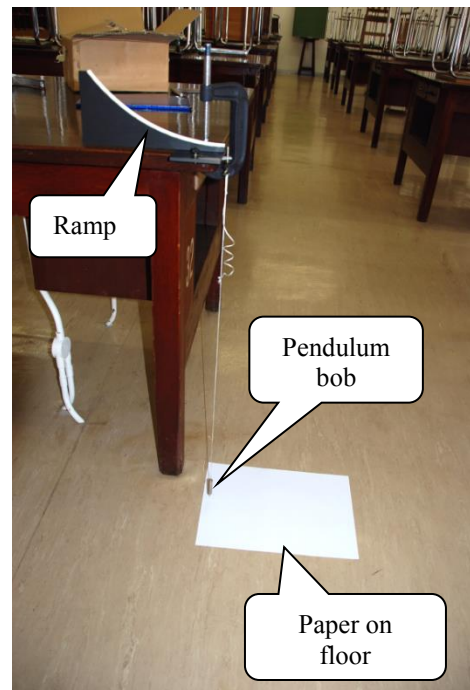


Figure 3. Collision experiment apparatus.

Assuming negligible air resistance, the horizontal acceleration can be assumed to be zero and hence the initial horizontal speed can now be calculated from the time in flight and the range (s) of the ball using: $v_o = s/t$.

A more ambitious (and follow-up) exercise would be to demonstrate conservation of linear momentum in two dimensions. For this a second ball bearing is placed on a special holder at the end of the ramp. – see figure 4 below. The apparatus can be set so that the rolling ball strikes the stationary ball a glancing blow, after which the two balls fall to the paper below. The landing points of the two balls are marked using carbon paper as described before. An example of a typical result is shown in figures 4 and 5 below:

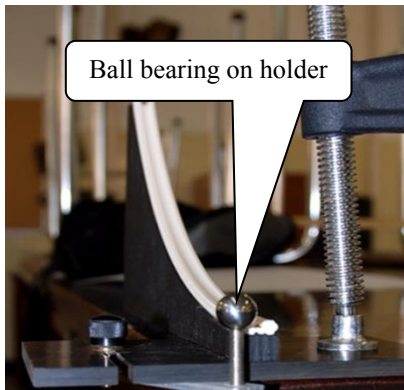


Figure 4. Second ball-bearing on holder.

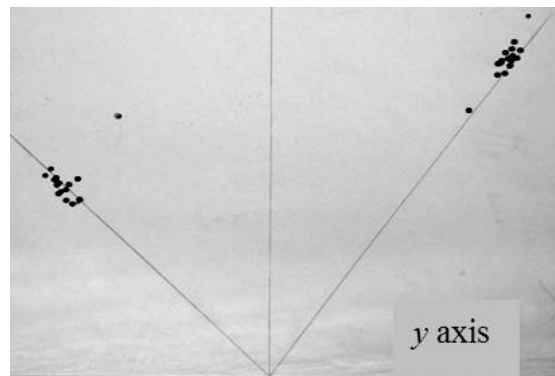


Figure 5. Collision experiment; ball bearing landing points on the floor.

If the bottom edge of the sheet is regarded as the y axis, then the line up the centre of the sheet is the x axis. The x and y components of the ranges of the two balls can now be measured on the paper and hence their initial horizontal velocities – and hence their momenta immediately after the collision. The y -components of the momenta can be summed and shown to equal zero, and the x components can be summed and compared to the momentum of the moving ball just prior to the collision – its velocity having been determined in the earlier phase of the exercise. Another possibility would be to compare the loss of gravitational potential energy as the ball rolls from the top to the bottom of the ramp with the gain in mechanical kinetic energy. There will be a mismatch between these quantities as some of the lost potential energy becomes rotational kinetic energy. Reconciling the gain in rotational kinetic energy with the mismatch could be tricky as there is no guarantee that the ball does not slip at any point as it rolls down the ramp. There is also a question of precisely where the ramp, which is ‘U’ shaped in cross section, supports the ball. These problems can be minimised by judicious design and construction of the apparatus – or choice of ball bearing. Whatever the case, this could be a very nice introduction to rotational kinetic energy. The ramp – which is essentially the major part of the apparatus not normally resident in any laboratory – can be easily and cheaply constructed. They can also be bought from a laboratory supply, but the whole point is to cut costs so that large quantities can be procured. The workshop staff at The Wits School of Physics estimate that the cost of making one ramp, ready to use is less than R50.00.

3. Conclusion

With these two exercises it becomes possible to require the students to do two things not usually required in a practical exercise: firstly, the students must figure out for themselves how to perform the required procedure. This forces them literally to solve a problem as they are not simply following instructions that somebody else has provided. Secondly, they can be required as part of the exercise to write a description of their procedure in the form of a set of instructions that somebody else could follow in replicating their exercise – i.e. they can be made to construct an algorithm for performing the exercise. As these two requirements are the essence of problem-solving, this changes the practical exercise from a ‘cookbook’ exercise into a problem-solving exercise.

Faced with the limited didactic efficacy of ‘cookbook’ practicals, we should be looking for better alternatives for our first (and other) year programmes. Some exercises do exist which are not prohibitively expensive and could therefore be done by all students of even quite large groups simultaneously. With some effort it should be possible to devise a large enough collection of such ‘shoestring experiments’ that at least a portion of a first year practical programme could be run as problem solving exercises that were directly linked to the theoretical programme. A question we need to address is ‘what stops us?’ One answer to this could be that there is a shortage of research data to support what we are proposing here. Three issues arise from this: the first is that a logical next step would be a proper evaluation of this type of practical exercise. The second is that supporting research data *does* exist – Allie *et al.* [6], report that this form of practical is used at the Physics Department of the University of Cape Town and ‘*has greatly enhanced the overall learning experience of our students.*’ Thirdly, it may not be useful to take the attitude that in the absence of ‘hard’ data, we should not proceed. After all, given a programme to train runners that effectively absolved the trainees of the need to run – would we *really* insist on hard research data before we started looking for a better option?

Another – potentially unpopular - answer to the question that must be considered very carefully: perhaps we don’t want to change existing programmes for purely emotional reasons. All the effort and expense that went into creating them in the first place – and the fact that they now allow teaching staff to operate in something of a comfort zone that they will be understandably reluctant to leave. If there is any validity in this answer, we need to think very carefully about what we are doing and about possibly making some changes.

Although these simple experiments do place student in “real” problem-solving situations, they may not however be easily acceptable by teaching staff. For example, during a tea room discussion, a colleague suggested that there is a danger that the ‘shoestring’ practical would, because of its low budget image, reduce the motivation of students to perform properly during practical exercises. Our answer to this is twofold:

- There is no necessity to tout these exercises as being in any way inferior to the more conventional exercises involving ‘big-budget’ equipment.
- Historically, the performance of students during conventional practical exercises has in fact sometimes been ‘suboptimal’ – an example being the widespread use of ‘recycled’ measurements during laboratory exercises in the first author’s own first year of physics in 1971.

References:

- [1] American Association of Physics Teachers, 1998 Goals of the Introductory Physics Laboratory *American Journal of Physics* **66** 483 – 485
- [2] Belcher J W 2001 *Studio Physics at MIT* MIT Physics Annual
- [3] Hanson D and Wolfskill T 2000 Process workshops-a new model for instruction. *Journal of Chemical Education* **77**(1) 120-130
- [4] Solomon J 1992 *Getting to Know about Energy in School and Society* (London: Falmer Press)
- [5] Jones E R and Childers R L 1993 *Contemporary College Physics* (Addison-Wesley Reading, Massachusetts)
- [6] Allie S, Buffler A, Kaunda L and Inglis M 1997 Writing-Intensive Physics Laboratory Reports: Tasks and Assessment, *The Physics Teacher* **35** 399 – 405

Division F – Applied Physics

Dose perturbations of unilateral Ti prosthesis in the dosimetry of 6 MV photon beam

N Ade and F.C.P. du Plessis

Medical Physics Department, University of the Free State, PO Box 339, Bloemfontein 9300, South Africa
E-mail: leroinicholson@yahoo.ca

Abstract. During irradiation of malignancies in the hip region with external megavoltage photon beams, the presence of metallic prostheses could partially shield the beam at the target and alter the dose distribution. This may cause a dramatic difference in treatment outcome. This study investigates the magnitude of 6 MV photon beam dose perturbations caused by unilateral titanium prosthesis and were measured with Gafchromic EBT2 film in a pelvic phantom made out of nylon slices. Dose perturbations were measured and compared using absorbed dose distributions for a range of field sizes between 3×3 and 10×10 cm². The magnitude of these perturbations was quantified as dose correction factors, DCFs which is defined as the ratio of the dose influenced by the prosthesis and the unaltered beam. A DCF of unity marks the margin between dose enhancement (where $DCF > 1.0$) and dose reduction (where $DCF < 1.0$). DCFs above unity were observed on the proximal (beam entry) side of the prosthesis while DCFs below unity occurred in the distal region (behind the prosthesis). For the studied field sizes maximum DCFs ranged between 1.251 ± 0.003 and 1.269 ± 0.013 . Minimum DCFs ranged between 0.744 ± 0.007 and 0.801 ± 0.012 . The DCFs on the proximal side of the prosthesis drop off rapidly with distance from the proximal nylon-prosthesis interface. The results of the study indicate that at the nylon-prosthesis interface, about 25% of dose enhancement is due to electron backscatter from the prosthesis and at least 20% of dose reduction behind the prosthesis is due to photon attenuation.

1. Introduction

A growing number of patients requiring external beam radiotherapy (EBRT) for malignancies in the pelvic region have metal implants such as hip prostheses [1]. The presence of metal implants during megavoltage photon radiotherapy could partially shield the beam at the target and alter the absorbed dose distribution [1-4]. This may cause a dramatic difference in treatment outcome [2]. It is believed that there is a decrease in tumour control due to a reduced target dose from beam attenuation by the prosthesis [3] or a rise in complication rates due to the local dose perturbations caused by implants [2]. The extent of dose perturbations is affected by factors such as the size, mass density, atomic composition and design of the prosthesis as well as beam energy. It is understood that the scientific understanding and approach of medical dosimetry for the presence of metal implants during EBRT is challenging [3-6]. Various implant materials include stainless steel, cobalt-chromium-molybdenum (Co-Cr-Mo) and titanium (Ti) [4-8]. The selection of an implant material is influenced by factors such as corrosion, fatigue resistance and mechanical strength [8]. Various experimental and Monte Carlo studies are available on photon beam dose perturbations of prostheses [1-11]. However, most of the

reports are limited to beam attenuation behind the prosthesis measured in water or plastic phantoms containing the prosthesis.

This study aims to investigate 6 MV photon beam dose perturbations of Ti prosthesis in front and behind the prosthesis using Gafchromic film measurements in a novel pelvic phantom. The newly designed phantom consists of a stack of nylon slices with a built-in unilateral Ti prosthesis.

2. Materials and methods

2.1. The novel pelvic phantom and film calibration

The phantom employed in this work is a locally fabricated pelvic phantom with an in-built Ti hip prosthesis and was designed for film dosimetry. Figure 1 shows the novel symmetrical phantom consisting of a stack of 25 Nylon 12 slices (each slice is 1.0 ± 0.1 cm thick) of which some are fitted with Ti discs to form a unilateral Ti prosthesis. Nylon 12 is a polymer with formula $[(CH_2)_{11}CONH]_n$. The pelvic phantom contains bony structures including the spinal cord and pelvic bone constructed from tissue-equivalent substitutes. The components and material compositions (% by mass) of the tissue-equivalent substitutes include²⁹: Araldite GY-6010 epoxy resin (36.4), Jeffamine T-403 hardener (14.6); silicon dioxide (25.5) and calcium carbonate (23.5). The diameter of the Ti disc in the plane of measurement considered in this study is 2.7 ± 0.1 cm. A thin layer of tissue material (nylon) located between the prosthesis and bone defines the bone-prosthesis interface.

All irradiation measurements reported in this study are from exposures of a single batch of Gafchromic® EBT2 films (Lot #: 01201501) in a 6 MV photon beam produced by a Philips SL75 linear accelerator. Before dose perturbation measurements, film calibrations were performed for conversion of optical density (OD) to dose in related approaches as reported in literature [13] using a rational calibration function of the type [14]:

$$X(D) = A + [B/(D - C)] \quad (1)$$

where $X(D)$ is the film response (OD) at dose D , and A , B and C are parameters that can be fitted to the calibration data using a least square optimization method. Calibration was performed by placing five 10×4 cm² film pieces horizontally (one at a time) inside a 30×30 cm² RW3 slab phantom at 10 cm depth on the central axis of a 10×10 cm² 6 MV beam at 100 cm source-to-phantom surface distance. The film pieces were irradiated to dose values between 0 and 245 cGy. Irradiated films were digitized using an Epson Perfection V330 Photo flat-bed document scanner 24 hours post exposure to allow for polymerization.

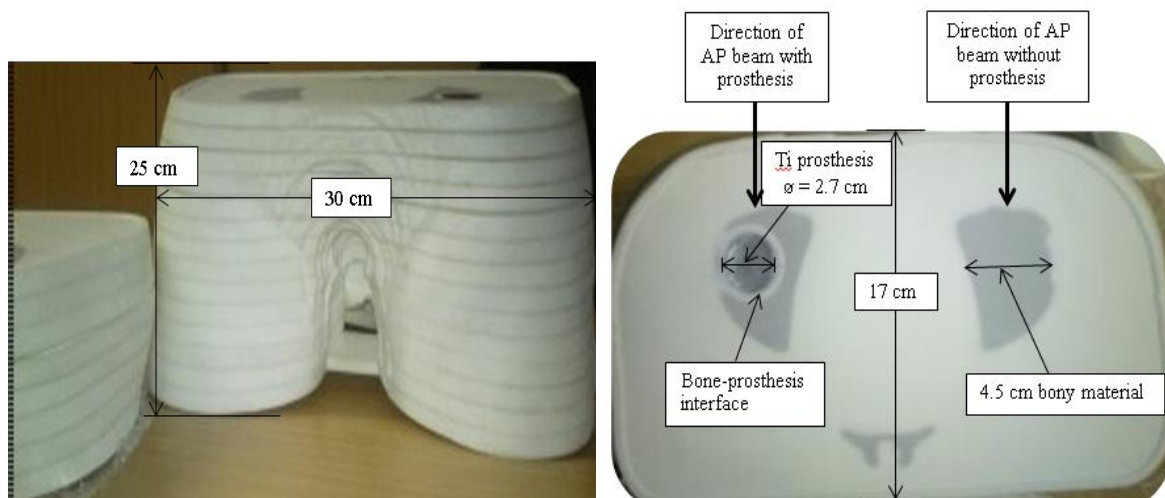


Figure 1. Picture of novel pelvic phantom (Left) with unilateral Ti prosthesis (Right). The figure on the right shows the measurement plane and the beam directions incident on the phantom.

2.2. Dose perturbation measurements

Perturbations in absorbed dose distributions due to the presence and influence of the Ti prosthesis were measured and compared using dose maps and profiles for a range of field sizes. The pelvic phantom was placed in the supine position and dose distributions were acquired using single anterior-posterior (AP) (figure 1) beams for field sizes of 3×3 , 5×5 and 10×10 cm². The measurements were acquired with and without the prosthesis by fitting cut EBT2 film pieces from a single batch (Lot #: 01201501) in the phantom. That is, as the phantom is symmetrical measurements were taken on the left side (with the prosthesis) and on the right side (without the prosthesis). Each fitted film piece covered only half (left or right side) of the measurement plane. Hence for the three field sizes studied, six pieces of film were used for the 6 MV beam and each film piece was irradiated separately. Employing a 100 cm source-to-axis distance (SAD) for each field size, an absorbed dose of 300 cGy was delivered at isocentre to each film fitted in the phantom at a depth of 8.5 cm from the surface to the centre of the phantom. The magnitude of dose perturbations caused by the prosthesis on measured dose distributions was quantified as dose correction factors, DCFs (enhancement and reduction) which is defined as the ratio of the dose influenced by the prosthesis and the unaltered beam.

3. Results and Discussion

3.1. Film calibration

Film images were digitized as raw 48-bit RGB (16 bits per colour) and saved as tagged-image-file format (TIFF) image files in a related approach as reported elsewhere [13]. Digitized images were then processed employing the 16 bits red channel of the scanned RGB images. Calibration curves for the red channel are shown in figure 2 with points corresponding to the measured mean OD at the corresponding dose. Superimposed on these points is the fitted rational function (1) with fitting coefficients of $A = 0.794$, $B = -149.260$ and $C = -255.068$.

3.2. Dose distribution measurements

Figures 3(a) – (e) show 6 MV photon beam dose distributions measured with Gafchromic EBT2 films in the pelvic prosthesis phantom for a 10×10 cm² field. In these figures the dose maps measured with (figure 3(a)) and without (figure 3(b)) the prosthesis, are displayed. For each dose image the beam is directed from the positive z-axis. The colour palette (figure 3(c)) shows the dose variation on the maps. The profiles for the dose maps displayed in figures 3(a) and (b), just before the beam enters the prosthesis (proximal side) and just after it exits the prosthesis (distal side) are presented in figures 3(d) and (e), respectively. The horizontal lines drawn through the dose images show where the profiles were extracted. It could be observed on the dose maps and profiles that the dose increases at the nylon-prosthesis interface on the proximal side and decreases (attenuates) in the distal region of the prosthesis. The dose escalation is due to electron backscatter from the prosthesis and the dose decrease is due to beam attenuation just after the beam exits the prosthesis [15]. The dose increase depicted by the peak and attenuation depicted by the dip in figures 3(d) and (e) (green curves) are indicated by the purple bands, respectively. The dip indicated by blue band in figure 3(d) shows beam attenuation by bone for the case of no prosthesis (red curve). The dose increase and attenuation were also observed for the 5×5 cm² and 3×3 cm² images and profiles.

Figures 4(a) and (b) show 6 MV depth dose curves for 5×5 cm² and 3×3 cm² fields, respectively obtained from the dose maps. Regions consisting of nylon (white), bone (blue), and prosthesis (purple) as indicated in these figures show where the photon beam pass through when directed on the phantom. Shown on figures 3(a) and (b) for the 10×10 cm² field are areas (vertical lines drawn through the images) where the depth dose curves were extracted. The influence of the prosthesis on the depth dose curves are noticeable as its presence causes significant dose modification (red lines) compared to the case with no prosthesis (blue lines). Similar to the observation made in figures 3(d) and (e), figures 4(a) and (b) show that there is dose enhancement on the proximal side of the prosthesis and dose reduction in the distal region when compared to the case with no prosthesis.

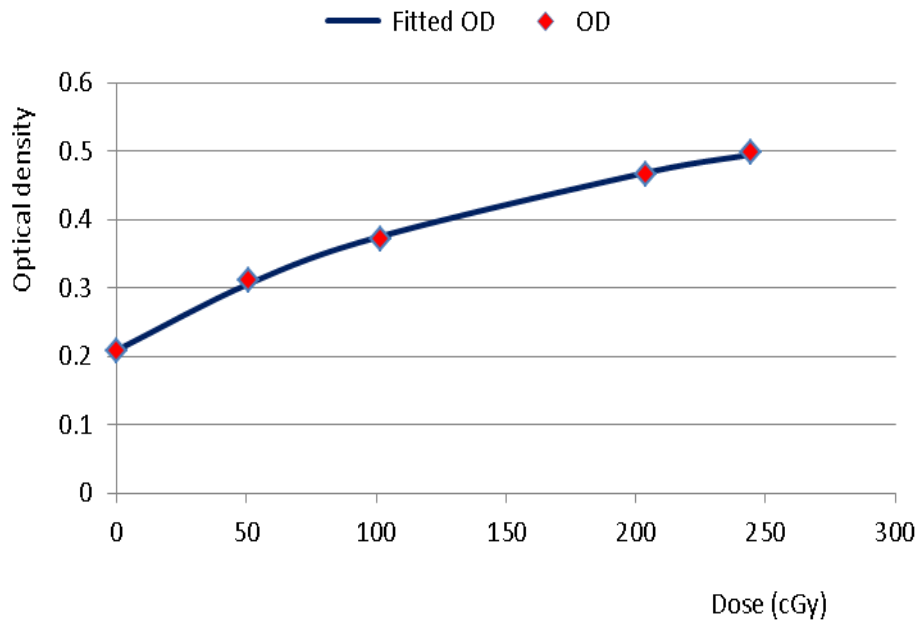


Figure 2. Red channel calibration curves for Gafchromic EBT2 film

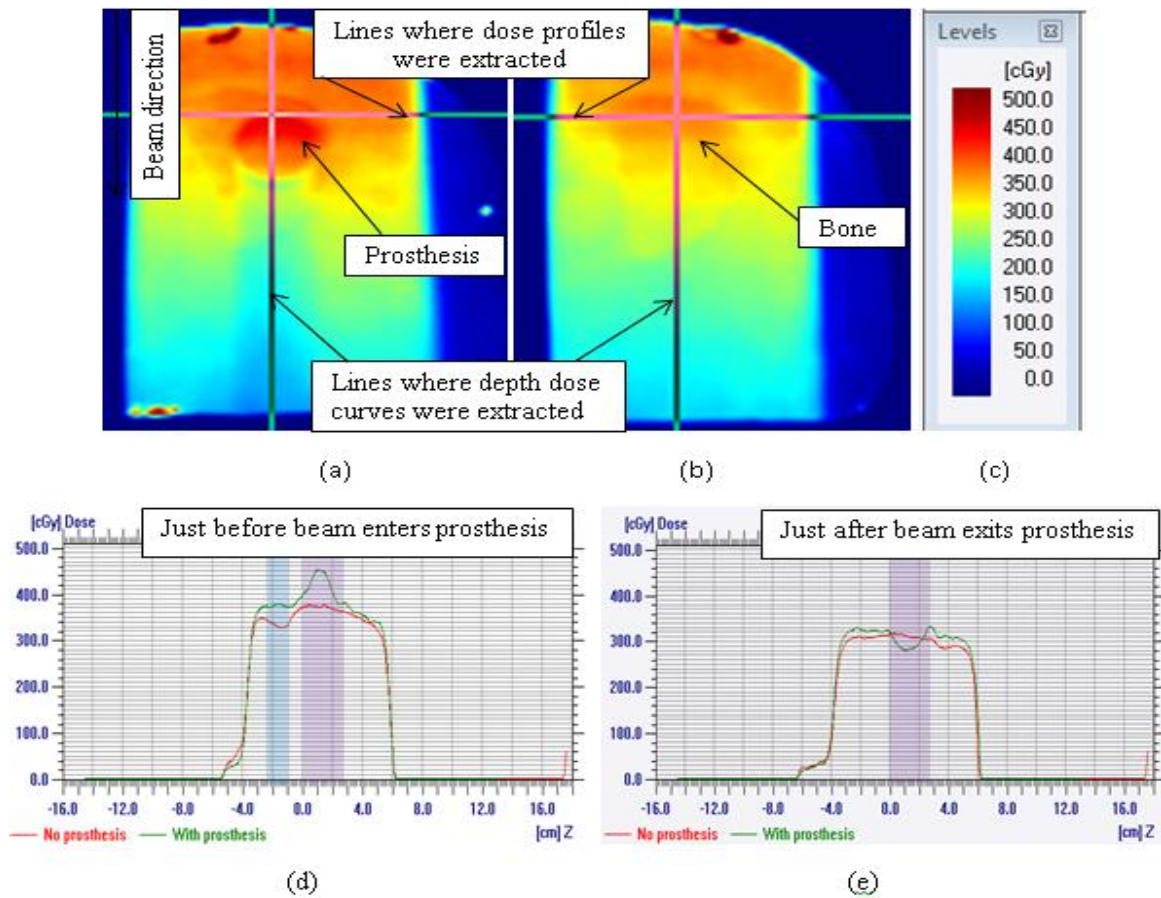


Figure 3. 6 MV beam dose distributions measured with Gafchromic film for a 10x10 cm² field.

3.3. Quantification of dose perturbation measurements

The extent of dose perturbations observed on the proximal and distal sides of the Ti prosthesis was quantified as dose correction factors DCFs (defined in section 2.2), calculated along the depth dose curves shown by the green lines in figures 4(a) and (b). A DCF of unity marks the margin between dose enhancement (where $DCF > 1.0$) and dose reduction (where $DCF < 1.0$) so figures 4(a) and (b) show that DCFs > 1.0 occur inside the prosthesis and on its proximal side while DCFs < 1.0 occur on the distal side of the prosthesis, primarily due to beam attenuation by the prosthesis.

For the studied 6 MV beam, maximum DCFs of 1.251 ± 0.003 , 1.269 ± 0.013 and 1.265 ± 0.10 (i.e., dose enhancements of $25.1 \pm 0.3\%$, $26.9 \pm 1.3\%$ and $26.5 \pm 1.1\%$) which usually occurred on the beam entry side of the implant in the phantom (excluding the implant) were computed for 3×3 , 5×5 and 10×10 cm² fields, respectively. Similarly, minimum DCFs of 0.790 ± 0.013 , 0.744 ± 0.007 and 0.801 ± 0.012 (i.e. dose reductions of $21.0 \pm 1.3\%$, $25.6 \pm 0.7\%$ and $19.9 \pm 1.2\%$) which typically occurred on the beam exit side of the implant were obtained for 3×3 , 5×5 and 10×10 cm² fields, respectively. The values quoted for the maximum and minimum DCFs for each field size are the averages of at least the six largest or lowest values and the errors are the standard deviations of the average values. The implant also receives a higher dose from the photon beam. This observation could be due to the long range of more energetic electrons generated in the beam proximal to the implant.

The range of backscattered electrons is relatively short. As displayed in table 1, the DCFs fall off quickly with distance from the nylon-prosthesis proximal interface. For instance, for the 10×10 cm² field it changes from 1.180 at 0.1 cm from the interface to 1.007 at 0.5 cm. The trend shown in table 1 has also been reported elsewhere [2,7,16]. The relatively short range of backscattered electrons suggests that the energy of backscattered electrons is rather low [16].

The perturbation effects of prostheses are well reported in literature, though with considerable variation from one study to the other. Also, most reports are restricted to photon attenuation on the transmission side of the implant. For a Ti alloy attenuations which ranged from 0.26-0.28 and 0.17-0.20 at a depth of 10 cm in a water phantom were reported by Sibata et al. [8] for 15×15 cm² 6 MV and 18 MV photon beams, respectively. The results presented in this study indicate that the dose enhancement on the proximal side of the prosthesis shows a marginal variation with field size. A slight change of dose increase with field size has also been reported [11,16]. For various materials evaluated in photon beams from 6-24 MV the dose enhancement remained constant with field size between 4×4 and 20×20 cm² [16]. The field size independence of the DCF is ascribed to electron transport [16].

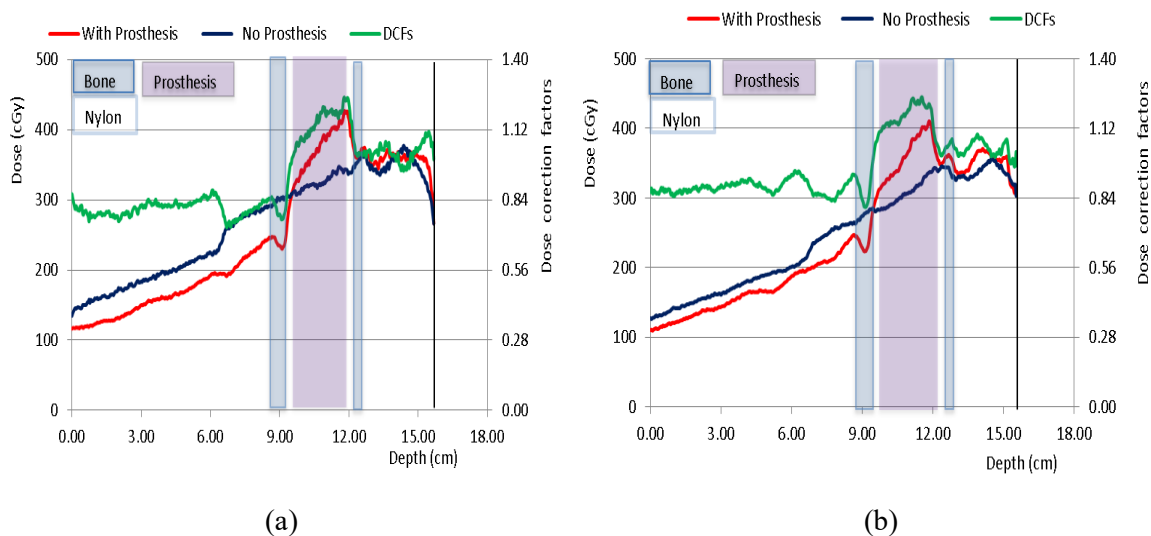


Figure 4: Variation of 6 MV photon beam depth dose data with and without prosthesis for (a) 5×5 cm² and (b) 3×3 cm² fields. Dose correction factors with depth are shown by the green curve.

Table 1. Variation of DCFs with distance from the proximal nylon-prosthesis interface for a range of field sizes.

Distance (cm)	$3 \times 3 \text{ cm}^2$	$5 \times 5 \text{ cm}^2$	$10 \times 10 \text{ cm}^2$
0.1	1.204	1.240	1.180
0.2	1.135	1.221	1.085
0.3	1.069	1.155	1.017
0.5	1.015	1.025	1.007

4. Conclusions

In this study 6 MV photon beam dose perturbations of unilateral Ti prosthesis have been measured in a pelvic prosthesis phantom using Gafchromic EBT2 films. For the studied field sizes, the magnitude of dose enhancement ranged between $25.1 \pm 0.3\%$ and $26.9 \pm 1.3\%$ at the nylon-prosthesis interface on the proximal side of the prosthesis. Similarly, dose attenuations between $19.9 \pm 1.2\%$ and $25.6 \pm 0.7\%$ were observed in the distal region of the prosthesis. The degree of dose enhancement showed a marginal variation with field size, the dose reduction increased at the $5 \times 5 \text{ cm}^2$ field and varied only slightly for the 3×3 and $10 \times 10 \text{ cm}^2$ fields. DCFs were found to drop off with distance from the proximal interface of the prosthesis. The presentation suggests that significant alteration in absorbed dose distribution by hip prosthesis during radiation therapy could affect clinical outcome.

Acknowledgements

This research and the publication thereof is the result of funding provided by the Medical Research Council of South Africa in terms of the MRC's Flagships Awards Project SAMRC- RFA-UFSP-01-2013/HARD.

References

- [1] Wieslander E and Knöös T 2003 *Phys. Med. Biol.* **48** 3295.
- [2] Reft C, Alecu R, Das IJ, Gerbi BJ, Keall P, Lief E, Mijnheer BJ, Papanikolaou N, Sibata C and Van Dyk J 2003 *Med Phys.* **30** 1162.
- [3] Spezi E, Palleri F, Angelini A L, Ferri A and Baruffaldi F 2007 *J Phys Conf Ser.* **74** 021016.
- [4] Carolan M, Dao P, Fox C and Metcalfe P 2000 *Australas Radiol.* **44** 290.
- [5] Keall PJ, Siebers J V, Jeraj R and Mohan R 2003 *Med Dosim.* **28** 107.
- [6] Fattahi S and Ostapiak OZ 2012 *J Appl Clin Med Phys.* **13** 3347.
- [7] Mesbahi A and Nejad FS 2007 *Radiat Med – Med Imaging Radiat Oncol.* **25** 529.
- [8] Sibata CH, Mota HC, Higgins PD, Gaisser D, Saxton JP and Shin KH 1990 *Int J Radiat Oncol Biol Phys.* **18** 455.
- [9] Chatzigiannis C, Lymperopoulou G, Sandilos P, Dardoufas C, Yakoumakis E, Georgiou E and Karaikos E 2011 *J Appl Clin Med Phys.* **12** 3295.
- [10] Erlanson M and Franzén L 1991 *Int J Radiat Oncol. Biol Phys.* **20** 1093.
- [11] Biggs PJ and Russell MD 1998 *Int J Radiat Oncol Biol Phys.* **14** 581.
- [12] Jones AK, Hintenlang DE and Bolch WE 2003. *Med Phys.* **30** 2072.
- [13] Fuss M, Sturtewagen E, De Wagter C and Georg D 2007 *Phys Med Biol.* **52** 4211.
- [14] Lewis D, Micke A, Yu X and Chan MF 2012 *Med Phys.* **39** 6339.
- [15] Ding GX and Yu CW 2001 *Int J Radiat Oncol Biol Phys.* **51** 1167.
- [16] Das IJ and Kahn FM 1997 *Med Phys.* **16** 367.

Radiation Shielding Analysis and Optimisation for the MinPET Kimberlite Sorting Facility using the Monte Carlo Calculation Code, MCNPX

EM Chinaka^{1,2}, Z Zibi³, J van Rooyen², SH Connell¹, MN Cook¹

¹ The University of Johannesburg, Auckland Park, South Africa

² The Nuclear Energy Corporation of South Africa (Necsa), Pelindaba, South Africa

³ The Technology Innovation Agency (TIA), Pretoria, South Africa, formerly Necsa

E-mail: Eric.Chinaka@necsa.co.za

Abstract. Radiation shielding calculations, analysis and optimization process carried out in order to design shielding for a Mineral-Positron Emission Tomography (MinPET) facility are presented. PET is a nuclear imaging technique commonly used in diagnostic medicine. The technique is based on the detection of 511 keV coincident and co-linear photons produced from the annihilation of a positron (produced by a positron emitter) and a nearby electron. This technique is currently being developed for mineral detection and quantification, particularly diamonds in kimberlite rocks through the MinPET facility. The facility is aimed at improving diamond mining through the early detection of the diamond bearing rocks. High energy photons are produced via bremsstrahlung when a high energy, 40 MeV 5mA, electron beam impinges on a high density target - tungsten. The resultant high energy photon beam is used to irradiate the candidate rock, activating the naturally occurring non-positron emitting isotope ¹²C, producing a positron emitting isotope ¹¹C via a photo-nuclear (γ, n) reaction. The resultant high intensity and high energy radiation field (which includes both photons and neutrons up to 40 MeV) requires appropriate shielding to protect personnel and the environment around the facility. A Monte Carlo based radiation transport code, MCNPX, was used to model the MinPET facility including the electron accelerator, the irradiation chamber and the proposed shield. Shielding calculations were performed, applying the theory of interaction of radiation with matter together with the modeling and the radiation transport calculation capabilities of MCNPX. The calculations were applied to determine the types, optimum combinations and thickness of shielding materials. About 1.6 m of shielding composed of lead, iron, wax and boron carbide combined in the shield matrix were found to be sufficient to drop dose rates to acceptable levels on the personnel side of the shield, where several meters of concrete would have been required.

1. Introduction

MinPET is a revolutionary technology that is expected to improve diamond mining and sorting by introducing efficiency in the usage of equipment, energy and water. The technique is based on the detection of 511 keV coincident and co-linear photons produced from the annihilation of a positron (produced by a positron emitter) and a nearby electron. The technique is popularly used in diagnostic medicine and is now being developed for use in the mining sector and in particular the identification of diamond from kimberlite rocks. The current diamond extraction process involves the crushing of candidate rocks several times to small pieces, typically to a few

millimeters in diameter exposing the diamonds to the surface. Physical separation techniques are then applied to extract the diamond particles. It has been noted however, that only a small fraction of the crush actually contains significant quantities of diamond particles[1]. The crushing process is energy, equipment and water intensive.

In the MinPET technique, the rocks are only crushed to manageable sizes, equivalent to the “first crush”. A high energy photon beam at least 23 MeV, is used to irradiate the rocks thus activating the naturally occurring, non-positron emitting ^{12}C , producing a positron emitting ^{11}C via a photo-nuclear reaction namely $^{12}\text{C}(\gamma, n)^{11}\text{C}$. A 40 MeV electron beam, incident on a tungsten target is used to produce the high energy photon beam through bremsstrahlung.

The high energy photons, the resultant neutrons from the (γ, n) reaction and products from other $^{12}\text{C}(*,*)^{11}\text{C}$ processes due to the interaction of photon beam with rock constituents, the primary electrons from the accelerator and the γ -rays from resultant radioactive products all create a high energy, mixed radiation field in and around the MinPET facility. The need for an appropriate shield to protect personnel and the environment around the facility cannot be over emphasised.

A Monte Carlo radiation transport code, MCNPX was used to model the facility and together with radiation transport theory, calculations were carried out to developed an optimum shield for this facility.

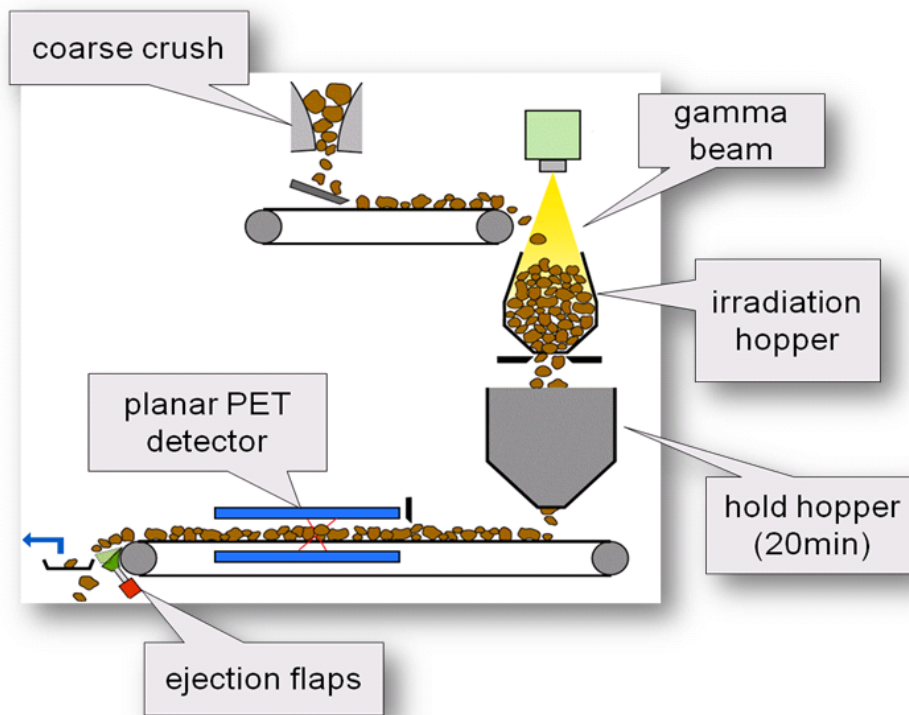


Figure 1. The MinPET process flow

2. The MinPET Facility

Figure 1 shows the process flow in the MinPET facility. Kimberlite rocks are coarse crushed, “the first crush”, and carried by a conveyor belt to the irradiation chamber. A photon beam

is directed towards the irradiation chamber so that activation can take place. The activated rocks are then fed into a holding chamber where they are held for 20 mins, enough time to allow unwanted short lived activated products, which may interfere with the detection signal, to decay away. The proposed shield should cover the accelerator, the irradiation and the holding chambers, excluding the detection system. It has been determined that the irradiation process does not yield long lived activation products, hence it is not necessary at this stage to design a shield that covers the detection system. This reduces the cost of the shield. It must be noted at this stage, that a static system was modelled, due to MCNPX limitations. In reality, the rocks are continuously fed into the two chambers and into the detection system by the conveyor belts. However, this static system sufficiently approximates the dynamic system from a radiological point of view.

3. MinPET Facility simulation

MCNPX version 2.7.e with ENDF/B-7.0 cross-section data (2008) was used for the shielding calculations. First, a simple model of the facility was developed and the geometry was plotted using a graphic application, Vised X, for debugging purposes especially to check the relative positions of the irradiation chamber, the electron beam and the tungsten target.

4. Source Term Characterisation

The first step in the development of a shield is source term characterization. This process was carried out to determine the type of radiation sources and the energy distribution, including the respective directions of radiation particles. The results of the MinPET facility source term characterisation are shown in Figures 2 - 3. Figure 2 (left) shows the variation of photon flux with energy at different polar angles around the accelerator and Figure 2 (right) shows the variation of the photon flux with energy at different axial positions from the accelerator. A positive sign represents a position above the accelerator and negative means below. It is assumed here that the radiation produced, is symmetric around the azimuthal angle because the beam is un-polarised.

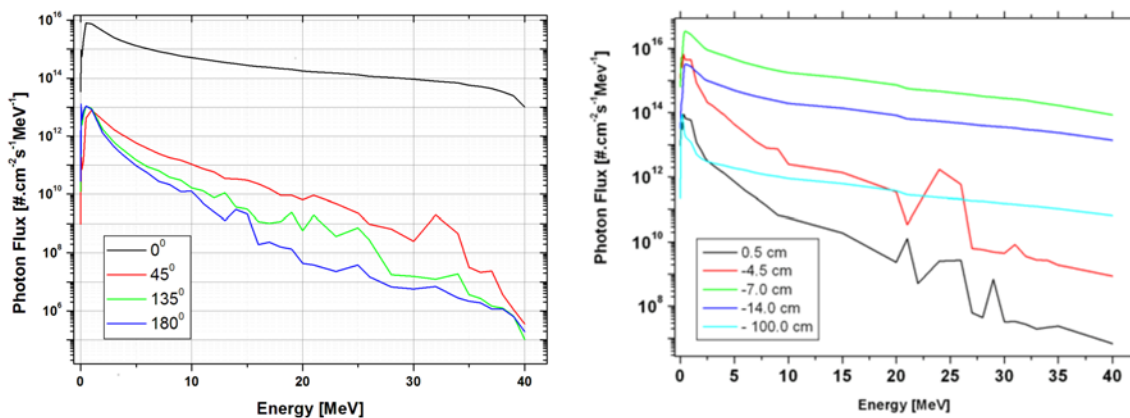


Figure 2. Photon flux at various polar angles and at different axial positions

A mesh tally was set up around the facility to further ascertain the levels of radiation dose produced by the MinPET and the mesh tally results are shown in figure 4.

5. Radiation Transport

Ionising radiation can be in the form of electrically charged particles such as alpha particles, beta particles, protons and heavy ions or uncharged particles and radiation quanta such as neutrons,

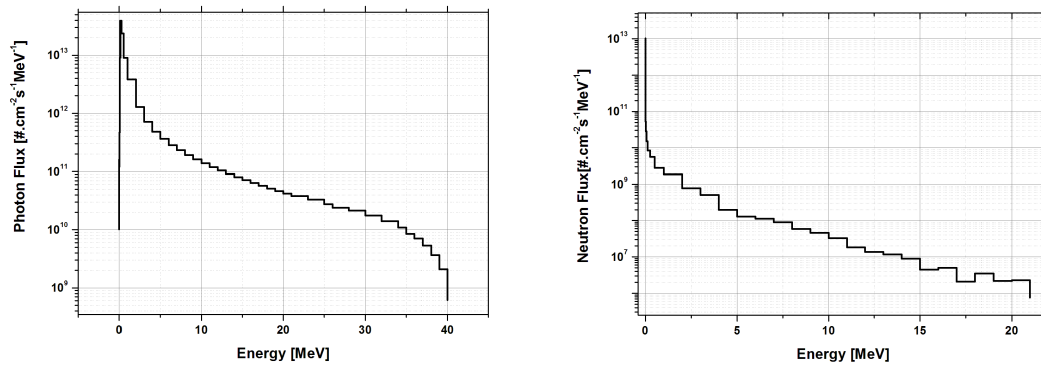


Figure 3. Total photon and neutron flux in the irradiation chamber

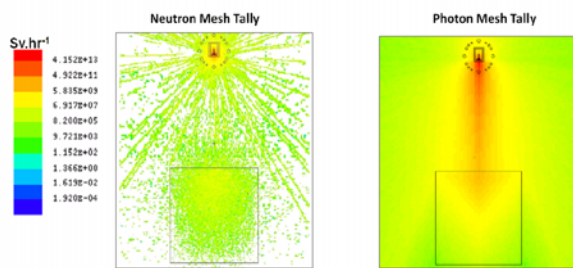


Figure 4. Neutron and photon mesh plots in the MinPET

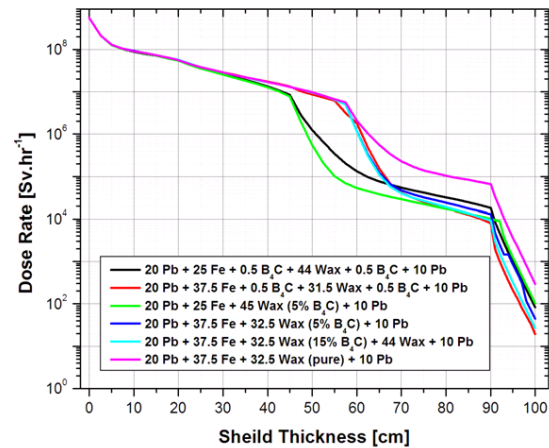


Figure 5. Dose rates for six different shield configurations.

gamma radiation and X-rays [2]. Charged particles do not present major shielding problems because they lose large amounts of energy in each interaction as they interact with matter and as a result, charged particles are characterized by short ranges in matter [3]. However it is important to note that charged particles may produce secondary electromagnetic radiation i.e. bremsstrahlung photons, which contribute to the radiation field.

Neutrons and photons are the most difficult radiation types to shield and are therefore the center of focus in this paper. Neutral particles generally move between points of interaction in straight lines. Their mean free path (mfp) and hence the range of neutral ionising radiation is much longer than those of charged particles. Neutral particles cause ionisation indirectly and ultimately transfer their energy to charged particles which then cause the direct ionisation [4].

6. Interaction of Radiation with Matter

To design nuclear systems, one needs to understand the way in which radiation interacts with matter [5]. A study of neutron scattering kinematics and dynamics [6], [7], [8], [9], [10], [11] shows that the isotope ^{56}Fe has a high cross section for neutron inelastic scattering at high neutron

energies and the isotope ^1H has a very high energy-lowering elastic scattering cross-section at relatively low neutron energies. Furthermore, the isotope ^1H has a high cross-section for neutron capture, albeit with a subsequent production of highly ionising photons. Any neutron capture reaction (n, γ), for that matter introduces secondary ionising photons. However the isotope, ^{10}B , produces very low energy photons in the $^{10}\text{B}(n, \alpha)^7\text{Li}$ reaction hence its introduction into the radiation shield helps to suppress the production of the high energy photons.

Ionising photons are “killed” off by using high atomic number Z and high density materials within the shield. A beam of monochromatic photons moving through an absorber (shield) displays a characteristic exponential reduction of the number of photons travelling along the original direction [7] , [12].

7. Shielding Scheme

From the principles of neutron and photon shielding it can be seen that the effective and optimal shield should contain the following materials:

- (i) **Lead** – to attenuate gamma rays (high Z , high ρ) and begin to slow down fast neutrons.
- (ii) **Iron** – to attenuate high energy neutrons (via inelastic scattering).
- (iii) **Wax** – to further attenuate and absorb neutrons slowed down by iron to within the cross-section group of ^1H (wax is rich in ^1H).
- (iv) **Boron carbide (B_4C)** - used on its own or mixed with wax. The isotope ^{10}B suppresses the production of high energy secondary photons. Ammonium pentaborate can be used as alternative.

8. Shield Optimisation

Six different shield configurations were developed as detailed in figure 5. The graph shows the total dose rate as a function of distance from the internal surface of the shield to the external surface for each configuration. All six configurations show a considerable reduction of dose rates within 100 cm. Due to space constraints in the MinPET facility, the shield was restricted to about 100 cm.

By considering the results in figure 5 the best shield configuration in this study contains 20cm lead, 37.5 cm iron, 31.5 cm wax flanked by 0.5 cm strips of B_4C and finally 10 cm lead in laminar sheets.

9. Shield Effectiveness

Figure 6 shows the reduction of neutron and photon dose rates hence the effectiveness of the selected shield configuration. It can be seen that the internal space has high dose rates, in the order of $10^{17} \text{ Svhr}^{-1}$ and in the external environment the dose rates go down, in the order of 10^1 Svhr^{-1} for photons and 10^2 Svhr^{-1} for neutrons.

10. MinPET proposed shield

Figure 7 shows the proposed shield for the MinPET facility. The shield forms a 200 cm by 200 cm by 200 cm (internal dimensions) room with walls about 100 cm thick. Figure 7 (A) shows the full cross section of the room and Figure 7 (B) shows the cross-section of one side the shield wall.

11. Conclusions

The study shows that the operation of the MinPET activation system produces very high radiation doses around it and a properly designed shield is a necessity. Although the proposed shield structure in figure 7 is very effective, it reduces the photon dose more

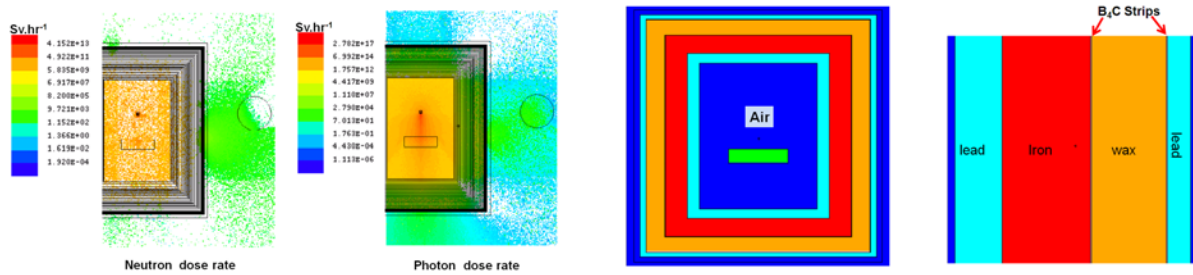


Figure 6. Mesh plots showing the reduction of dose rates from the interior going through the shield **Figure 7.** Proposed Shield for the MinPET Facility

considerably, relative to neutron dose. Neutrons are more penetrating than photons with the same energy. The resultant dose given in section 9 above are still too high considering the annual dose limits prescribed in the ICRP [13],[14]. These are 1 mSv/year for the public and 20 mSv/year for regulated occupational exposure (this is effectively 20 μ Sv/hour for the latter case). Considering these minimum dose limits, the shield must be made somewhat thicker beyond the 100 cm limit considered here. This adjustment increases the cost of producing the shield but it will reduce the dose rates to the required few μ Sv/hour range.

12. Acknowledgments

The authors acknowledge the support of the National Research Foundation (NRF).

References

- [1] Ballestrero S 2009 *Proceedings of the 12th International Conference on Nuclear Reaction Mechanisms* 589–602
- [2] Wentz C A 1988 *Safety, Health and Environmental Protection*
- [3] Kohl R D Z and Lukens H R 1961 *Radioisotope Applications Engineering*
- [4] Martin A and Harbison S A 1979 *An Introduction to Radiation Protection 2nd ed*
- [5] Lamarsh J R and Baratta A J 2001 *Introduction to Nuclear Engineering*
- [6] Martin J E 2006 *Physics for Radiation Protection - A handbook 2nd ed*
- [7] Lilley J S 2001 *Nuclear Physics: Principles and Applications*
- [8] Lamarsh J R 1972 *Introduction to Nuclear Reactor Theory*
- [9] van Rooyen T J *Transport and Shielding of Ionising Radiation*
- [10] Hebert A 2009 *Applied Reactor Physics*
- [11] Dorschel V S and Steuer J 1966 *The Physics of Radiation Protection*
- [12] Leroy C and Rancoita P G 2004 *Principles of Radiation Interaction in Matter and Detection*
- [13] Locharh I Bogdevitch E G 2009 *Annals of ICRP, ICRP Publication 111 39 No. 3* 19 –23
- [14] Valentin J 2007 *Annals of ICRP, ICRP Publication 103*

Using Geant4 to create 3D maps of dosage received within a MinPET diamond sorting facility

MNH Cook and SH Connell

University of Johannesburg, Johannesburg, South Africa

E-mail: martin@minpet.co.za

Abstract. The MinPET project aims to locate diamonds within kimberlite by activating carbon within kimberlite, then using Positron Emission Tomography (PET) to image carbon density. Although calculations suggest that long-term activation is not significant, modelling is required to determine the dose received by workers operating close to recently activated material at different positions within a hypothetical MinPET sorting unit. Two modelling techniques are deployed to investigate received dose. The first is a full simulation of energy absorbed, using the CERN Geant4 particle tracking toolkit. The results for this are validated against a numerical computation of the attenuation of outgoing radiation. The result is a set of 3-dimensional dosage maps. These can be used to set guidelines around where and for how long workers could operate, and to identify areas that need additional radiation shielding. The techniques developed are not limited to MinPET, and could prove useful for any situation requiring the simulation of dose received by workers operating near radioactive material.

1. Introduction

The MinPET project [1] images locked diamonds within coarsely crushed kimberlite (± 10 cm rocks), using Positron Emission Tomography (PET). The kimberlite is irradiated with high energy gamma rays, producing the unstable ^{11}C isotope via a photonuclear reaction. This beta decays, and the positron annihilation leads to back-to-back collinear 511 keV photons. These are detected in coincidence by two planes of position sensitive detectors above and below the kimberlite. A 3D carbon density image is created by back-projecting the lines of response. Because the signal from oxygen-15 (with a 2 minute half-life) dominates early on, irradiated material is held for 20-30 minutes before it goes to the detectors. At this point, the carbon-11 starts to dominate, due to its longer 20 minute half-life.

One of the concerns for an industrial scale MinPET plant is the radiation exposure of workers. The shielding requirements for the irradiation system have already been investigated in [2]. This included radiation shielding calculations, analysis, and optimisation with the aid of the MCNPX Monte Carlo code. The conclusion was that a 1.6 m thick shielding matrix of lead, iron, wax and boron carbide adequately shielded personnel from the irradiation system. If the accelerator, irradiation system and hold hopper were buried underground away from personnel, these requirements would be less stringent. The hold hoppers where kimberlite is stored can also be shielded.

It therefore remains to quantify the radiation hazard posed by activated material after the 20-30 minute point. Two scenarios we are especially interested in understanding are the dose received by workers near the conveyor belt at time of detection, and near a discarded pile of mine

tailings. Two numerical techniques have been developed to calculate the exposure given by a particular geometry of radioactive material. The first uses an attenuation model to arrive at an integral that can be solved numerically. This technique only applies to rectangular cuboid bodies of material. The results of this are compared to a full Monte Carlo physics simulation that is more accurate, but far more computationally intensive. The second technique can, however, be applied to any geometry.

2. MinPET Activity Levels

A series of irradiations were performed at the 100 MeV electron accelerator at Aarhus University [3]. These identified two isotopes that are of concern over time scales greater than 20 minutes, namely carbon-11 and sodium-24.

Assuming a 0.2% CO₂ concentration in kimberlite, at run-of-mine MinPET specifications (feed rate of 700 tons/hour and 1s irradiation with a 1m² footprint photon beam from a 40 MeV optimally converted electron bremsstrahlung beam [4]), the combined oxygen and carbon activity is 33.9 Bq/g at the 29 minute mark. Each beta decay leads to two positron annihilation photons, so this is equivalent to a photon rate of 67.8 Hz/g. The measured sodium-24 concentration in our Aarhus sample, extrapolated to MinPET conditions, was 1.01 Bq/g.

3. Attenuation Model

3.1. General Case

The intensity of a mono-energetic photon beam passing through a material can be described using a linear attenuation constant, μ_L , as follows:

$$\frac{I}{I_0} = e^{-\mu_L x} \quad (1)$$

This does not capture the full story however, as once a photon interacts with an atom, all of its energy does not always disappear into the medium. Photons interact with the medium predominantly via pair production, the photoelectric effect and Compton scattering [5]. These can leave the primary photon with some energy, and can also release charged particles which are then free to interact further. One way of quantifying this is with a mass energy-absorption coefficient μ_{en} (see, for example, [6]). This attempts to quantify the energy absorbed by a material through which photons are passing. If, at each step dx , the material absorbs an energy dE given by $dE = E\mu_{en}dx$, then the energy that is not yet absorbed follows an exponential decay of the form of equation (1). We shall refer to the attenuation constant simply as μ , which is a function of both the photon energy and the material being traversed.

Given the specific activity S_A (presumed measured in Bq.m⁻³) of a radioactive isotope, and a photon energy E_γ , our goal is to find the overall energy incident on an object near some radioactive material per unit time. This will allow a radiological assessment of risk, to a person, in the proximity of the source. Using equation (1), the energy incident per unit time (dP) on a small surface area centred at point Q due to a small volume element dV centred at point P is

$$dP = \frac{d\Omega(P, Q)}{4\pi} dV S_A E_\gamma e^{-\mu l(P, Q)} \quad (2)$$

where $d\Omega$ is the solid angle subtended by the small area and l is the path length travelled by the radiation through the material. To find the total power incident on a target, we integrate over the volume of radioactive material, and over the solid angle subtended by the object. If the target is small or far away, then l does not change much for different points on the target, and $l(P, Q) \approx l(P)$. The integral over $d\Omega$ collapses to the total solid angle subtended by the target, Ω . We further simplify by considering a spherical target of radius r . The solid angle subtended

by a sphere is $\Omega = 2\pi(1 - \sqrt{1 - r^2/R^2})$, where R is the distance to the sphere, and thus the total power incident on the target due to a volume V is

$$P = \frac{S_A E_\gamma}{2} \int_V dV \left(1 - \sqrt{1 - \frac{r^2}{R^2}} \right) e^{-\mu l} \quad (3)$$

3.2. Rectangular Cuboid Volume

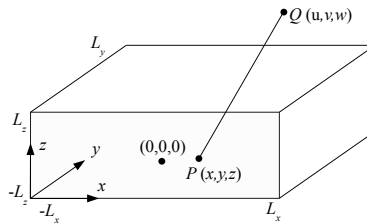


Figure 1. Rectangular geometry in attenuation model

In the case of a cuboid volume, with coordinates as shown in figure 1, the path length l can be expressed in terms of R : $l = R \left(\frac{L_z - z}{w - z} \right)$. The power will now be given by

$$P = \frac{S_A E_\gamma}{2} \int_{-L_x}^{L_x} dx \int_{-L_y}^{L_y} dy \int_{-L_z}^{L_z} dz \left(1 - \sqrt{1 - r^2/R^2} \right) e^{-\mu \left(\frac{L_z - z}{w - z} \right) R} \quad (4)$$

where $R^2 = (x - u)^2 + (y - v)^2 + (z - w)^2$. This integral does not have a readily available analytic solution and is calculated numerically.

An additional complication arises because equation (4) assumes that the photons passes through the upper z face. In the general case, an extra step is required at each point of the integral, that tests which face of the cuboid is intersected by the line joining P and Q . The coordinates of the term in the exponential can then be rotated appropriately.

4. Monte Carlo Simulation

In order to get results in more complex geometries, a full simulation is needed to individually track particles from emission to target impact. The toolkit of choice is the Geant4 framework [7][8], created at CERN.

In order to compare results to the attenuation model, we first find the effective energy attenuation within kimberlite of Geant4 simulations. Photons are fired out from the centre of a large sphere, and the energy that makes it to a certain radius is graphed against the radius. This is fitted with an exponential decay in figure 2. 511 keV and 1369 keV are the energy levels from the PET isotopes and sodium respectively. 100 keV was included as a lower energy comparison. The fit is relatively good, with only small divergences at high and low energy. This validates the treatment of energy loss with a simple exponential attenuation. From the slope of the exponential fits in figure 2, the effective Geant4 energy attenuation constants are $9.352 \pm 0.002 \text{ m}^{-1}$ for 1369 keV, $12.804 \pm 0.004 \text{ m}^{-1}$ for 511 keV and $26.37 \pm 0.02 \text{ m}^{-1}$ for 100 keV.

The full Geant4 simulation consists of an activated kimberlite volume and a human phantom (sphere of water that makes up the target). We will use a water sphere of radius 0.5 m. This has the same frontal surface area as a standing person, approximated as 1.7 m tall and 50 cm wide. If more accuracy is desired, a more realistic shape can easily be created, but the advantage of a sphere is that the results are directly comparable to those from the attenuation model, for cross-checking. The sphere is placed at a succession of positions on a three dimensional grid.

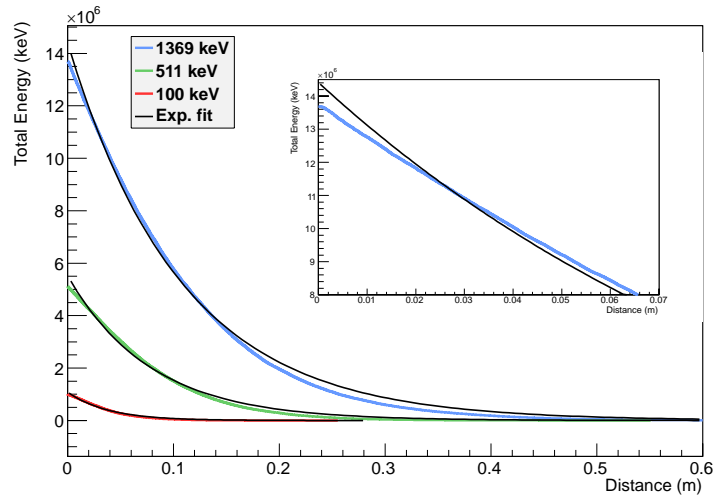


Figure 2. Difference between Geant4 simulation and simple attenuation model. Coloured lines show simulated data from Geant4. Inset shows magnification of lower radius region for 1369 keV.

5. Results

5.1. Comparison between Attenuation Model and Geant4 Simulation

An example geometry was created with a kimberlite cuboid 2 m high, 4 m wide and 6 m long. A 0.5 m radius spherical target was then moved along a horizontal plane at a height of 0.6 m above the cuboid, and the energy deposited was calculated using both the attenuation model and the Geant4 simulation. The attenuation model was integrated numerically using the Vegas algorithm from ROOT [9]. The Geant4 simulation fired 1 000 000 particles for each data point and recorded the energy that hit the target. The results are shown in figure 3. The agreement is quite good. The major qualitative difference is that the Geant4 simulation is not as smooth, as it is a stochastic Monte Carlo simulation.

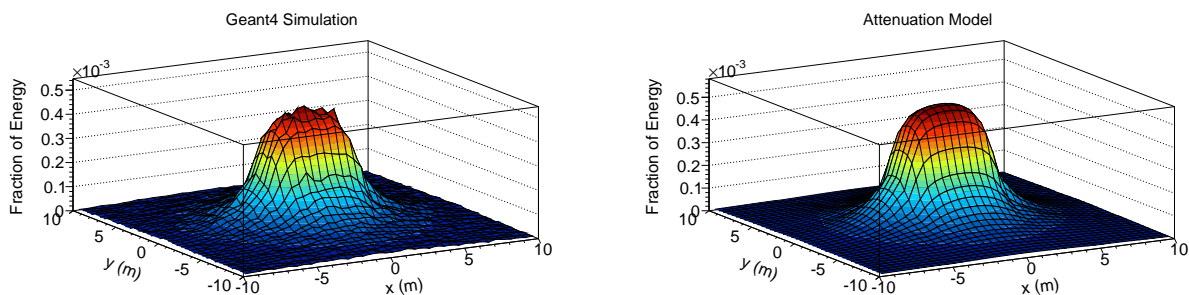


Figure 3. Fraction of activity reaching target in Geant4 simulation and attenuation models.

Small non-statistical differences between the models are observed at small distances. This is to be expected, because the derivation of equation 3 relied on the assumption that the target is small compared to the distance between the target and the source.

5.2. Kimberlite on Belt

We now investigate a body of material moving on a conveyor belt at the time of detection. The kimberlite can be approximated as a rectangular cuboid of material, and is therefore a candidate for the numerical integral technique. We will consider a 20 m long kimberlite stream, 1 m wide and 10 cm tall, using the 67.8 Hz/g photon rate from section 2. We assume a packing density of 0.7 for kimberlite, which is approximated by using kimberlite which is 30% air by volume.

Figure 4 shows the activity absorbed by the target as a function of the position of the centre of the target. The conveyor belt extends from $x = -10$ m to $x = 10$ m, and from $y = -0.5$ m to $y = 0.5$ m. The edge of the target is 5 cm from the belt at its closest, and the centre of the target is 30 cm above the belt. This approximates a worker standing at various positions next to the conveyor belt. Both the activity in Bq/cm^3 and the gamma attenuation constant are multiplied by 0.7 to take the packing density into account.

The activity that hits the target when there is a 5 cm horizontal gap between the belt and the target, i.e. a 105 cm horizontal distance between centre of belt and centre of target, is 2.40×10^5 photons/s. Considering a photon energy of 511 keV and a gamma radiation quality factor of 1 [5], this corresponds to $70.8 \mu\text{Sv/h}$. At a distance of 1 m, this has already fallen to 7.50×10^4 photons/s or $22.1 \mu\text{Sv/h}$. Workers would have to spend six hours a day for 118 days at a distance of 5 cm, to reach the 50 mSv level set in the IAEA safety guide relating to radioactive material in mining [10]. Workers could be employed full time at a distance of 1 m. The kimberlite will be more active at the time of detection if the carbon dioxide concentration is substantially greater than 0.2%. In this case, worker access should be more limited. It is not anticipated that workers would need to spend significant time periods at the side of the belt.

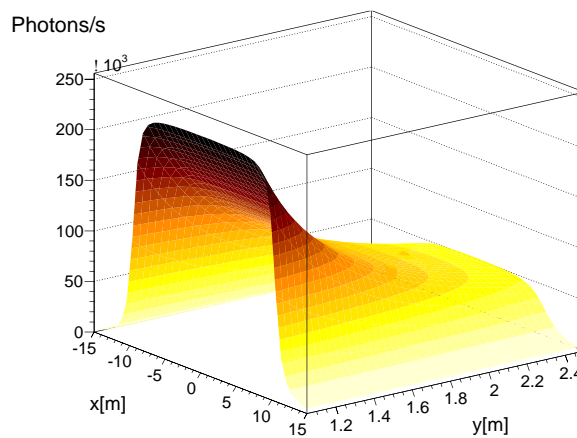


Figure 4. Activity at different points along the side of a $20 \text{ m} \times 1 \text{ m}$ conveyor belt carrying kimberlite 10 cm deep. Positions quoted are for the centre of a water target, relative to the centre of the belt.

5.3. Tailings

To reproduce a pile of tailings, a Geant4 simulation of a trapezoid was made, with a base side length of 6 m and a top diameter of 4 m, 2 m high. Only the ^{24}Na was considered, as all other isotopes have died away when several hours have passed. We use the worst case scenario of 1.01 Bq/g. Again, we model a 0.7 packing density by simulating kimberlite with 30% air content, and multiplying the activity per cm^3 by 0.7.

According to the Geant4 simulation, the fraction of the energy that reaches the target is 2.72×10^{-4} . This means that 24 hours after irradiation, the target receives an energy dose of

6.54×10^{-8} J/s, taking into account the fact that sodium decays are associated with the release of gamma rays at three different energies, 472 keV, 1369 keV and 2754 keV. This is equivalent to about $23.5 \mu\text{Sv/h}$. After 72 hours, this has dropped to $2.55 \mu\text{Sv/h}$. According to the ALARA principle of as little exposure as possible, preferably humans should not be too close to the tailings during the first day. A worker could, however, work full time near a one day old 6 m wide tailings pile and not exceed the IAEA guidelines for one year exposure.

6. Conclusions

We have explored two techniques for finding position specific radiation exposures due to specific geometries of radioactive material. The results for each are in close correspondence. The attenuation model is quick to calculate, and is useful for simple geometries such as cuboids. Calculating the graph shown took seconds on a personal computer. The Geant4 simulation is far more powerful, as it can simulate any geometry, and can easily be extended to include layers of shielding etc. The downside is that it is far more computationally intensive. A single (x, y) point from figure 3, with one million events, took 5 minutes to compute on a personal computer. The University of Johannesburg's cluster computer [11] was therefore used to generate the graph of activity as a function of position.

In both scenarios considered, it is clear that the radiation dose levels to workers in a MinPET plant would be acceptable, in the context of a well-controlled radiation producing facility.

References

- [1] Ballestrero S, Bornman F, Cafferty L, Caveney R, Connell S, Cook M, Dalton M, Gopal H, Ives N, Lee C A, Mampe W, Phoku M, Roodt A, Sibande W, Sellschop J P F, Topkin J and Unwucholaa D A 2010 Mineral-PET: Kimberlite sorting by nuclear-medical technology *12th International Conference on Nuclear Reaction Mechanisms* ed Cerutti F and Ferrari A (Varenna, Italy) pp 589–602
- [2] Chinaka E M, Zibi Z, van Rooyen J, Connell S H and Cook M *To appear in the these conference proceedings of the 2016 South African Institute of Physics Conference*
- [3] Tchonang M, Cook M, Bornman F, Connell S and Ballestrero S 2013 Elemental Analysis of Kimberlite and Associated Country Rock *Proceedings, 58th Annual Conference of the South African Institute of Physics (SAIP 2013)* ed Botha R and Jili T pp 502–506 ISBN 9780620628198 URL <http://events.saip.org.za/getFile.py/access?resId=0&materialId=9&confId=32>
- [4] Cook M 2014 *Remote Detection of Light Elements Using Positron Emission Tomography* (PhD Thesis : University of Johannesburg)
- [5] Leo W 1994 *Techniques for Nuclear and Particle Physics Experiments: A How-to Approach* (Springer) ISBN 9783540572800 URL <http://books.google.co.za/books?id=hDEbAQAAIAAJ>
- [6] Seltzer S 1993 *Rad. Res.* **136** 141–70
- [7] Agostinelli S *et al.* 2003 *Nuclear Instruments and Methods A* **506** 250–303
- [8] Allison J, Amako K, Apostolakis J, Araujo H, Dubois P *et al.* 2006 *IEEE Trans.Nucl.Sci.* **53** 270–8
- [9] Brun R and Rademakers F 1997 *Proceedings AIHENP'96 Workshop, Lausanne, Sep. 1996, Nucl. Inst. & Meth. in Phys. Res. A* **389** 81–86 see also <http://root.cern.ch/>.
- [10] International Atomic Energy Agency 2002 Management of radioactive waste from the mining and milling of ores series No. WS-G-1.2
- [11] University of Johannesburg cluster. URL <http://physics.uj.ac.za/clusters>

A genetic algorithm approach to enhancing the performance of a PET detector array

MNH Cook, SH Connell

University of Johannesburg

E-mail: martin@minpet.co.za

Abstract. The MinPET project aims to locate diamonds within kimberlite by activating carbon within kimberlite, then using Positron Emission Tomography (PET) to image carbon density. Distinguishing small diamonds from the background depends crucially on the accurate reconstruction of detector hit positions. This is subject to two kinds of errors: local errors, where the position of a hit within a particular detector is not accurately constructed from the incoming photomultiplier tube signals, and global errors, where the internal parameters that describe the physical location and orientation of detector pixels do not accurately match reality. Because of the large number of detectors in a full MinPET unit, there are too many parameters involved to feasibly adjust them by hand. We have therefore developed a custom genetic algorithm that iteratively evolves detector parameters in order to optimise the image quality. Results are presented from before and after the optimisation is performed, indicating that image accuracy and resolution are improved. This algorithm could be employed periodically in an industrial setting to automatically correct for detector movements or calibration drift.

1. Introduction

The MinPET project [1] images locked diamonds within coarsely crushed kimberlite (± 10 cm rocks), using Positron Emission Tomography (PET). The kimberlite is irradiated with high energy gamma rays, producing the unstable ^{11}C isotope via a photonuclear reaction. This beta decays, and the positron annihilation leads to back-to-back colinear 511 keV photons. These are detected in coincidence by two planes of position sensitive detectors above and below the kimberlite. A 3D carbon density image is created by back-projecting the lines of response formed by coincident events from opposite detector arrays.

A laboratory scale detector system has been created, with two arrays of pixelated scintillation crystals paired to position sensitive photomultiplier tubes. Fast electronics are utilised with good timing resolution, mostly eliminating any random background arising from separate positron annihilations being detected within the same coincidence time window. There is still a background present due to non-diamond positron annihilation events however. This is due both to homogeneously distributed carbon throughout the kimberlite, and oxygen-15, which is inevitably also produced in the irradiation process. Image fidelity is further degraded by Compton scattering, both within the kimberlite and the detectors. This leads to falsely reconstructed lines of response. The energy resolution is not sufficient to completely eliminate this by only accepting 511 keV photons.

The ability of the technique to differentiate small diamonds from this background depends crucially on the resolution of the detectors. This implies firstly that the detectors must accurately

reconstruct the positions of detected hits, and secondly that the detectors' orientation and position are accurately described within software. We employ a genetic algorithm approach to optimising various detector parameters, to improve performance in both of these areas. We refer to the optimisation of position reconstruction within each detector as "local", as opposed to "global" optimisation, which involves the relative position of detectors with respect to each other. Inspiration for this approach was taken from the track-based alignment procedure used in the ATLAS Transition Radiation Tracker [2], where detector elements are aligned so as to improve the matching of the reconstructed to known physics behaviour.

2. Detector system

The detector system consists of 16 Hamamatsu R2486 photomultiplier tubes (PMTs), with 16 crossed wire anodes coupled for each direction over a voltage divider network, furnishing two x and two y signals. Each scintillation crystal is a 1 cm thick, 5 cm diameter disk-shaped BGO ($\text{Bi}_4\text{Ge}_3\text{O}_{12}$) crystal that is further divided into individually wrapped 5 mm segments (or "pixels"). The detectors are split into an upper and a lower plane to allow coincidence detection.

The crossed wire anodes from the PMTs furnish two voltages for each of x and y , denoted x_a, x_b, y_c and y_d . These are amplified, and are passed to a spectroscopy amplifier. This has a slower output that integrates the incoming signal size to produce a shaped output, and a fast output for timing information. The fast outputs from the upper and lower detector planes are used to determine coincidence, which is then used to gate the data acquisition. In this manner, only coincident events are recorded, allowing a high event rate.

3. Genetic algorithm

Both local and global optimisation as described above are difficult tasks. Firstly, they need to find the global optimum, ruling out simple minimisation strategies which can get stuck in local minima. Secondly, they involve a very large parameter space. As we shall see below, local optimisation is within a 11-dimensional space, and global optimisation involves 6 parameters per detector plus another 10 collective parameters. Finally, the optimisation landscapes are highly chaotic due to statistical noise. This is shown in figure 1, which is a two-dimensional slice of the global optimisation landscape, showing how the detector system performs as the x and y position of one of the detectors is varied. The optimisation technique cannot rely on derivatives in a landscape of this nature.

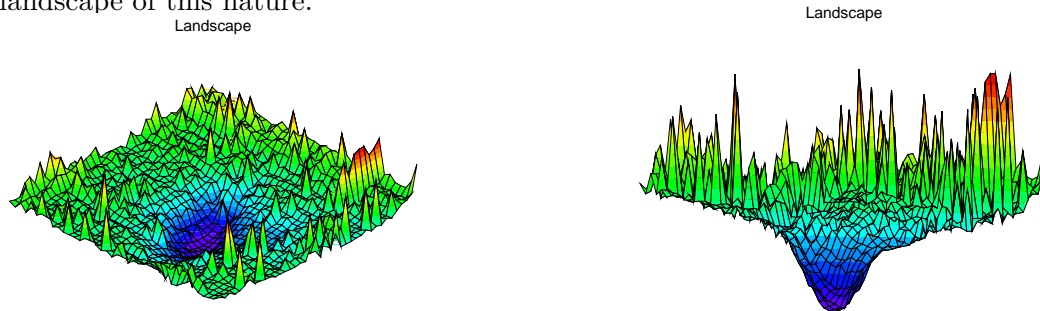


Figure 1. Detector performance as a function of x, y position of one detectors (lower is better).

Due to the badly-behaved and poorly quantified nature of the optimisation landscape, we have created a custom genetic algorithm. Genetic algorithms are an example of evolutionary algorithms, which are inspired by biological evolution. Evolutionary computation has found increasing use in physics whenever the solution space has made more traditional approaches difficult. Examples include fields as diverse as astronomy and astrophysics ([3], [4]), heat transfer optimisation [5], event selection in high energy physics [6], spectrum fitting in X-ray fluorescence

[7], nuclear reactor design [8] and many others. Reference [9] contains an example where, as in our case, a genetic algorithm was used for image calibration.

In the biological analogy, “individuals” are points in parameter space, and their coordinates are their “genes”. A scoring function is defined that evaluates a given individual in terms of how well the detector system performs when calibrated according to the parameters that define that individual. The optimisation proceeds iteratively in “generations”, where the individuals within each generation are randomly generated from the previous generation, favouring parents with good scores. Genetic algorithms are highly robust, they are able to find global minima, they do not need derivatives and they require no assumptions about the structure of the landscape.

The MinPET genetic algorithm is built on the GALib framework [10], and its basic flow is shown in figure 2. In each generation, pairs of individuals are selected as parents, with a probability determined by their score. Offspring are then created from these parents by one of cloning, crossover or mutation. Cloning directly copies a single parent, in order to preserve a good solution. Crossover is the analogue of sexual reproduction, where genes are swapped between individuals. This allows the algorithm to explore different combinations of existing genetic information, and can break out of local minima to find new minima. Mutation takes a single individual and randomly perturbs each of its parameters. This allows the exploration of a given local minimum. A crossover and a mutation are shown in figure 3. The probability of crossover, mutation or cloning is dependent on the distance in parameter space between the parents, tuned such that parents from different local minima are more likely to create offspring via small mutations, reducing the probability that their offspring are kicked out of their respective minima. After two new individuals are created, there is a random chance of a mutation, randomly varying the individual, in order to introduce new genetic information into the population.

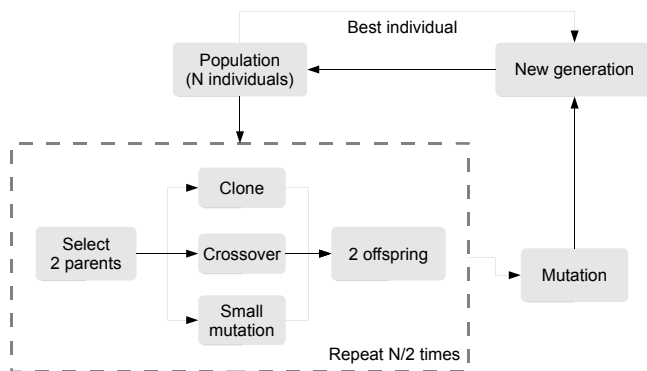


Figure 2. Flowchart of MinPET genetic algorithm.

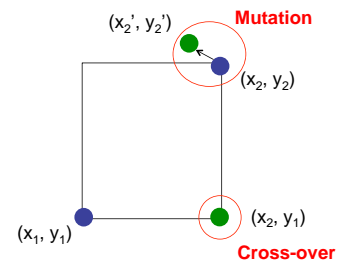


Figure 3. Example of a crossover and a mutation.

4. Local optimisation

The output signals from the crossed-wire anodes, x_a , x_b , y_c and y_d , are discussed in section 2 above. Once these are suitably linearly calibrated and amplified, the position of the hit is given by the ratio of the signals:

$$x = \left(\frac{x_a}{x_a + x_b} - 0.5 \right) \times d, \quad y = \left(\frac{y_c}{y_c + y_d} - 0.5 \right) \times d \quad (1)$$

where d is the diameter of the detector. This reconstruction, however, can be significantly distorted, as can be seen in the left side of figure 4. Reconstructed hits can be up to 6 mm from

their true positions.

In order to improve performance, we introduce a series of parameters to adjust the reconstructed position. These consist of an overall scaling factor, a rotation around the origin, and parameters proportional to x^2 , y^2 , x^3 , y^3 , xy^3 and yx^3 . These were selected in order to correct for defects noticed in the reconstructed pixel locations, including an expansions of points near the centre, incorrect rotations, and asymmetries between x and y directions observed in some detectors.

Our initial approach to scoring the results relied on employing a 2D peak-finding algorithm to locate each pixel peak, then calculating a chi-squared for the deviation of each peak from the actual pixel position. This was however too unstable when the image was severely distorted and when adjacent pixels were not clearly separated. It was also too computationally expensive. An alternate scoring function was therefore defined as

$$S_{\text{local}} = \sum_{i \in H} \frac{(\mathbf{h}_i - \mathbf{p}_i)^2}{|H|} \quad (2)$$

where H is the set of all detector hits, $|H|$ is the number of hits, \mathbf{h}_i is the measured position of hit i adjusted according to the current parameter values and \mathbf{p}_i is the actual position of the closest pixel centre to \mathbf{h}_i .

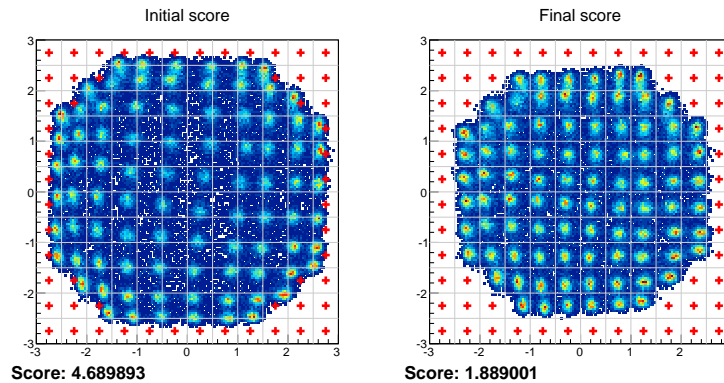


Figure 4. Example detector pixel reconstruction before and after optimisation. Grey lines demarcate pixel boundaries. Red crosses denote pixels that should be empty. Axes are in cm.

Figure 5 shows an example of how the scores of a population migrate with successive generations for a detector. As generations go by, the population moves closer together, and there is an overall trend toward better scores.

The optimisation procedure was applied to each detector in turn, with a population size of 500 and 250 generations. In order to judge the effectiveness of the procedure, a sodium-22 point source was moved along a straight path through the detector array at a series of different positions, and the FWHM of the point source in the back-projected PET image was measured. This test was repeated for the best known parameters before the optimisation, and the same parameters with their values after optimisation. The genetic algorithm was able to reduce the FWHM by an average of 10% in the direction of movement, 6% in the vertical direction and 15% in the perpendicular direction, a substantial improvement.

5. Global optimisation

Global optimisation proceeds by varying detector element positions and orientations so as to improve the sharpness of the reconstructed image of a point source. Our initial approach was to

fit a three-dimensional gaussian to the point source peak, and evaluate the standard deviations along each axis. This did not yield good results, firstly because of computational complexity, and secondly because the point source peaks often did not resemble a gaussian closely. We therefore introduce a new method to quantify peak sharpness, S , defined as:

$$S_{\text{global}} = \sum_{(i,j,k) \in W} V(i, j, k)^2 \quad (3)$$

where $V(i, j, k)$ is a three-dimensional histogram that stores the sum of the tubes passing through the voxel labelled by coordinates i, j and k . The summation extends over a window W around the point source coordinates. By taking the square of the voxel counts, the score is increased both by sharpening the peak corresponding to the point source, as well as ensuring that as many tubes as possible pass through the fitting window W . In a sense the score can be thought of as a χ^2 fit for a flat background, and a good, sharp peak is one that fits this flat background as badly as possible. Minimisation proceeds by evaluating the inverse, $1/S$.

For a single point source in one position, some nonsensical solutions will give rise to good scores, such as all detectors placed exactly on top of each other. We therefore insist on covering the whole volume between the detector by sending a series of point sources on different constant velocity trajectories on a conveyor belt through the detectors. The algorithm simultaneously optimises all data sets, with the global score defined as the average of the individual track scores defined in equation 3. In order to form a point source image, each line of response's position must be extrapolated back in time based on the velocity and its time stamp. This is highly dependent on accurately quantifying the velocity. This was measured as accurately as possible, then included as a parameter in the optimisation.

The total set of parameters to be optimised is thus as follows:

- The belt velocity
- 3D rotation of the detector system relative to the conveyor belt
- 3D position and 3D rotation of lower detector array relative to upper detector array
- 3D position and 3D rotation of each detector (16 in total)

This corresponds to a total of 106 parameters. Optimising in a 106 dimensional space is not feasible, so we rather proceed in an iterative hierarchical fashion. The algorithm optimises each set of parameters in the list above separately while holding the remaining parameters constant. The parameters for a specific detector are optimised one by one, while keeping the other detectors stationary. The whole procedure is then repeated in a second iteration.

Figure 6 shows the change in global score as this procedure is followed. The optimisation parameters varied according to stage (more effort was put into the collective coordinates), with between 100 and 200 generations, and a population between 35 and 50. These numbers are limited by computational cost, where a back-projected 3D PET image must be created for each of a series of data sets, in order to evaluate each individual in each generation.

When the overall effect on image fidelity was examined, there were mixed results. While the overall orientation was improved, the algorithm had a bias towards moving all the detector elements closer to one another, in effect zooming out the entire image. An overall zoom factor improves the score as defined in equation 3. The next step would therefore be to use a known configuration of point sources to fix the scale, combining the distance between known and reconstructed points with the existing score.

6. Conclusions and discussion

We developed a custom genetic algorithm that successfully optimises detector parameters. Optimisation leads to significant improvements in the reconstruction of detected positions from

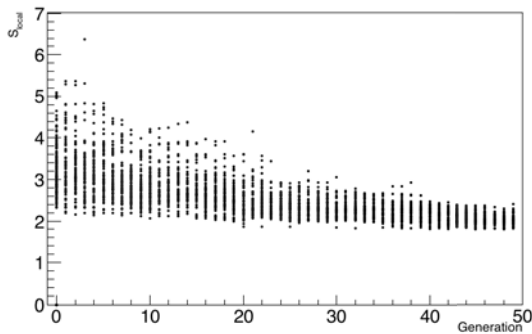


Figure 5. Change of score with local optimisation. Each dot represents the score of one individual in a given generation.

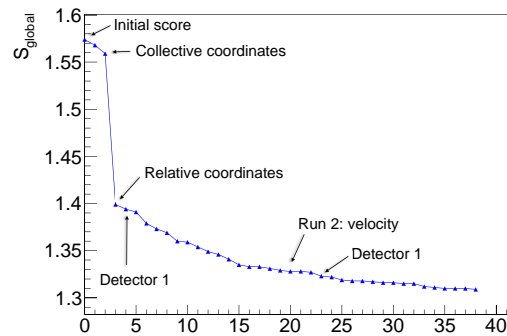


Figure 6. Change of score with global optimisation. The x axis shows successive optimisation stages.

detector signals. The procedure also showed promise for the accurate calibration of the position and orientation of detector elements. Further work is needed to remove a bias toward reducing the overall length scale.

This optimisation approach could easily be automated, and regularly deployed in an industrial setting as part of standard operating procedure, in order to keep a deployed MinPET system optimally configured. This would combat performance degradation due to calibration drift and detector element movement due to impacts and vibration.

References

- [1] Ballestrero S, Bornman F, Cafferty L, Caveney R, Connell S, Cook M, Dalton M, Gopal H, Ives N, Lee C A, Mampe W, Phoku M, Roodt A, Sibande W, Sellschop J P F, Topkin J and Unwucholaa D A 2010 Mineral-PET: Kimberlite sorting by nuclear-medical technology *12th International Conference on Nuclear Reaction Mechanisms* ed Cerutti F and Ferrari A (Varenna, Italy) pp 589–602
- [2] Bocci A and Hulsbergen W 2009 *ATL-INDET-PUB-2007-009*
- [3] Rajpaul V 2012 ArXiv:1202.1643 [astro-ph.IM] (*Preprint* 1202.1643)
- [4] Gutiérrez J A G, Cotta C and Fernández-Leiva A J 2012 *CoRR* abs/**1202.2523**
- [5] Gosselin L, Tye-Gingras M and Mathieu-Potvin F 2009 *International Journal of Heat and Mass Transfer* **52** 2169 – 2188 ISSN 0017-9310 URL <http://www.sciencedirect.com/science/article/pii/S0017931008006534>
- [6] Teodorescu L and Sherwood D 2008 *Computer Physics Communications* **178** 409–419
- [7] Brunetti A 2013 *Computer Physics Communications* **184** 573 – 578 ISSN 0010-4655 URL <http://www.sciencedirect.com/science/article/pii/S0010465512003438>
- [8] Pereira C M and Lapa C M 2003 *Annals of Nuclear Energy* **30** 555 – 565 ISSN 0306-4549 URL <http://www.sciencedirect.com/science/article/pii/S0306454902001068>
- [9] Dickens T P 1998 Image-calibration transformation matrix solution using a genetic algorithm *Industrial Applications of Genetic Algorithms* ed Freeman L M and Karr C L (Boca Raton, FL, USA: CRC Press, Inc.) 1st ed ISBN 0849398010
- [10] Wall M 2007 GAlib, A C++ Library of Genetic Algorithm Components <http://lancet.mit.edu/ga/> accessed: 2013-10-30

A method for examining water absorption in sand using fast neutron radiography

G C Daniels^{1,2}, V Dangendorf², A Buffler³, K Tittlemeier²

¹Pelindaba Laboratories for Accelerator and Beamline Science, The South African Nuclear Energy Corporation (Necsa), South Africa

²Physikalisch Technische Bundesanstalt (PTB), Braunschweig, Germany

³Department of Physics, University of Cape Town, South Africa

E-mail: Graham.Daniels@necsa.co.za

Abstract. Water concentration in porous media is an important aspect when inferring the structural integrity of the building framework. A need has arisen to determine this water content. Experiments were conducted at the PTB cyclotron making use of a 6.6 MeV fast neutron beam and fast neutron radiography to follow the uptake of water through porous media. The observed benefit of fast neutrons is the ability to interrogate thicker samples. From the resulting radiographs, the presence of water absorbed as well as the rate of absorption is shown.

1. Introduction

The water content available in high strength concrete and sand is important in buildings where knowledge of the structural integrity is essential. Slowing of the cracking process in concrete can be better understood when the water content within dense mixtures is known [1]. Water content within the pores of a concrete structure has a direct relation to its strength and effective safe lifetime. Testing the sample for porosity, sorptivity and water retention capability is a traditionally destructive processes and does not allow for quick testing on site [2].

Thermal neutron radiography has been used to examine the porosity and presence of water in a sample of prepared concrete and sand [3]. Due to the attenuation of thermal neutrons by hydrogen, thermal neutron radiography was used to determined the amount of water absorbed [4].

Sample thickness limits the thermal neutron radiography technique, due to the penetration depth of the thermal neutrons and compromises the achievable contrast as the sample thickness grows. Fast neutrons have a higher penetration capability through dense materials than thermal neutrons but a lower attenuation for lighter elements (hydrogen and oxygen). Fast neutron radiography has been used in this investigation to examine the water absorption in thick samples of a porous sand medium in order to infer the volume of water absorbed.

2. Experiment

The investigation was carried out at Physikalisch-Technische Bundesanstalt (PTB) in Braunschweig, Germany, making use of the PTB cyclotron which produces a 6.6 MeV fast neutron beam via the $D(^9\text{Be},n)$ reaction. The beam flux was approximately 10^8 neutrons

$s^{-1}cm^{-2}$ with the sample and detector placed 1.2 m away from the source of neutrons. The TRION fast neutron radiography system [6] was used to conduct the radiography. Figure 1 shows the experimental setup for the sample, with regular dehydrated sand placed in a water tray. The sand was dehydrated in a microwave oven and placed in the setup shown. Water was allowed to drip into the tray following the path indicated in Figure 1, subsequently being absorbed by the sand, this process was imaged via fast neutron radiography.

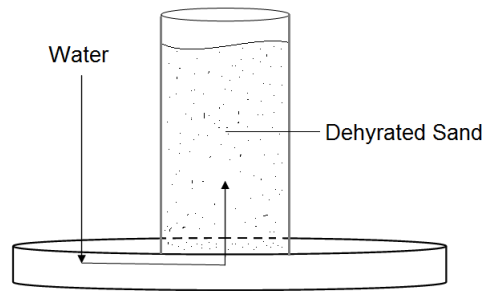


Figure 1. Experimental setup of water absorption experiment

The sample has a cross sectional thickness of 8.7 cm. To qualify the amount of water absorbed, the mass of the sand is recorded before and after being placed in water. The images were acquired in intervals of 12s during absorption.

3. Results

The radiographs in Figure 2 shows the absorption of water and areas of stratification forming. The fast neutrons can examine thicker samples, yielding different information about the bulk with a higher resolution over this thickness. Using the measured radiographs, Figure 2, a method of comparing the attenuation coefficient of the dry and wet areas is applied to infer the presence of water. Three regions of interest (RoI) are defined on the radiographs, highlighted in Figure.2, with the attenuation coefficient being calculated at these regions.

The attenuation coefficient for a single attenuating sample is calculated using Beers Law adapted for radiography [7], represented by equation 1,

$$I = I_0 e^{-\mu x} \tag{1}$$

where I_0 is the flat field radiograph taken without the investigating sample present, I is the radiograph with the investigating sample present, μ and x being the attenuation coefficient and thickness of the sample, respectively. For each RoI in Figure 2 we apply equation 1, to obtain the attenuation coefficient of the water sand mixture (sand alone is also calculated in this manner). Each image is corrected for the effects of dark current and read-out noise [8][9]. As fast neutrons have a higher probability of interaction with lighter elements (low Z materials), than heavier elements (high Z materials) [10], an increase in μ for the water sand mixture, compared to that of sand, illustrates an increased presence of water in the RoIs. This is illustrated in Figure 3 for each RoI, as a function of time.

Figure 3 shows the moving water front through the sample by the increased presence of water in the RoI's.

The water/sand system has a mix of attenuating material, each one effecting the complexity in the calculation of the attenuation coefficient. Using the technique by Anderson *et al* [11], the increase in the water thickness (designated by α) is calculated using equation 2,

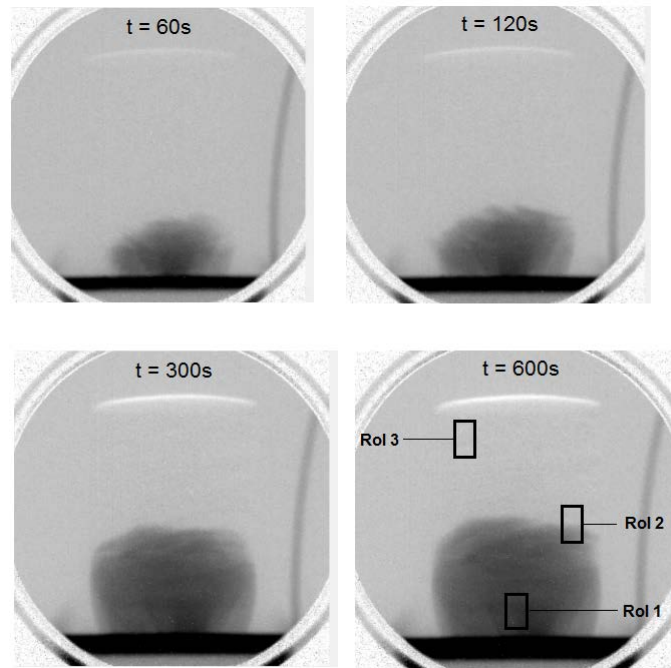


Figure 2. Fast neutron radiographs of the absorption of water in a column of sand taken at specified times.

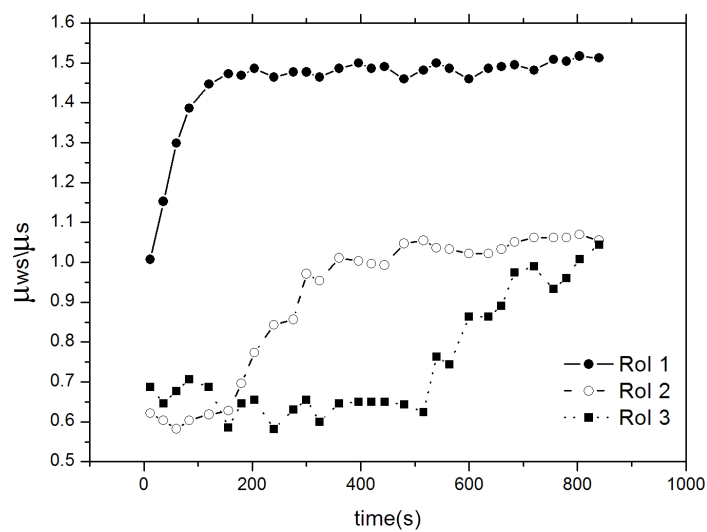


Figure 3. Attenuation coefficient of the water sand mixture μ_{ws} relative to the attenuation coefficient of sand, μ_s , as a function of time.

$$\alpha = \frac{\log \frac{I_{ws}}{I_s}}{\log \frac{I_w}{I_s}} \quad (2)$$

where I_{ws} is the intensity from the composite water/sand radiograph with I_w and I_s being the intensities from the water alone and sand alone, respectively. The results for the 3 RoI's are plotted in Figure 4.

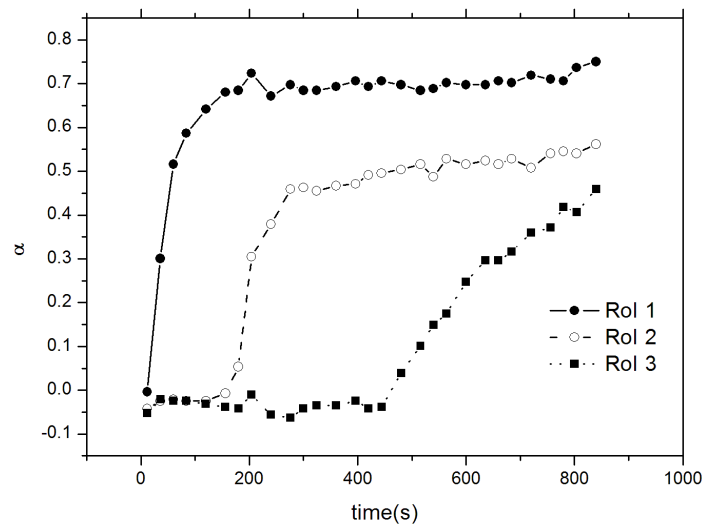


Figure 4. Water thickness as a factor of sand thickness over time.

Similarly to the results achieved and represented in Figure 3, the trend of the water contribution (α) increases faster in RoI 1 than the other contributing regions. There is a clear relation in the data represented in Figure 3 and Figure 4 with a fast initial growth, indicative of a fast absorption rate that plateaus after around 240s as the RoI's begin to saturate.

4. Conclusions

The results represented in Figure 3 and Figure 4, assist in inferring the amount of water absorbed and the amount of water present in a structure, at a given time, when compared to the dry sample. The water being absorbed through the sand and the different thicknesses of water due to the increase in α , is calculated from the resulting fast neutron radiographs, which enables one to analyse thicker samples.

References

- [1] Zhutovsky S, Kovler K and Bentur A 2002 Efficiency of lightweight aggregates for internal curing of high strength concrete to eliminate autogenous shrinking *Materials and Structures*.
- [2] Korshunov DA and Sidorenko MV 1992 Methods for determining the strength of concrete *Materials and Structures* **25** 29-33.
- [3] deBeer FC, le Roux JJ and Kearsley EP 2005 Testing the durability of concrete with neutron radiography *Materials and Structures A* **542** 226-231.
- [4] deBeer FC, Strydom WJ and Griesel EJ 2004 The drying process of concrete: a neutron radiography study *Applied Radiation and Isotopes A* **61** 617-623.
- [5] Kaestner A, Lehmann E and Stampanoni M 2008 Imaging and image processing in porous media research and Advances in Water Resources *NIM*.
- [6] Mor I, Vartsky D, Bar D, Feldman G, Goldberg MB, Katz D, Sayag E, Shmueli I, Cohen Y, Tal A, Vagish Z, Bromberger B, Dangendorf V, Mugai D, Tittelmeier K and Weierganz M 2009 THigh spatial resolution fast-neutron imaging detectors for pulsed fast-neutron transmission spectroscopy *JINST*.
- [7] Harms AA and Wyman DR 1986 *Mathematics and Physics of Neutron Radiography* (Dordrecht: D.Reidel Publishing Company).
- [8] Lanza RC, Shi S and McFarland EW 1996 A Cooled CCD Based Neutron Imaging System for Low Fluence Neutron Sources *IEEE Transactions on Nuclear Science* **43**.
- [9] Satija R, Jacobson DL, Arif M and Werner SA 2004 In situ neutron imaging technique for evaluation of water management systems in operating PEM fuel cells *Journal of Power Sources* **129** 238-245.
- [10] McLane V 2012 *Neutron Cross Sections* vol 2 (London: Academic Press).
- [11] Andersson P, Sunden EA, Svard SJ and Sjostrand H 2012 Correction for dynamic bias error in transmission measurements of void fraction *Review of Scientific Instruments* **83**.

Effect of atmospheric turbulence on entangled photon field generated by partially coherent pump beam

Stuti Joshi¹, Yaseera Ismail¹ and Francesco Petruccione^{1,2}

¹University of KwaZulu-Natal, Private Bag X54001, Durban 4000, South Africa

²National Institute for Theoretical Physics, KwaZulu-Natal, South Africa

E-mail: joshis@ukzn.ac.za

Abstract. The propagation of two-photon fields from down-conversion of a partially coherent Gaussian Schell-model pump beam in turbulent atmosphere is reported. The results show that the spatial coherence of the pump beam affects the detection probability of the photon pair at two different positions. It is also found that the detection probability of the entangled photon is less susceptible to atmospheric turbulence, if a partially coherent pump beam produces the field.

1. Introduction

Entanglement received attention over the years owing to its potential applications in quantum communication [1] and information processing [2]. Spontaneous parametric down-conversion (SPDC) [3] is one of the convenient sources of entangled photon fields. These photons are entangled in position, momentum and polarization. In previous studies, the pump beam was considered to be spatially fully coherent. Recently, Jha and Boyd [4] showed theoretically that the spatial coherence properties of the pump field were entirely transferred to the down-converted two-photon field.

Of late, the effect of atmospheric turbulence on the entangled photon fields produced by the down-conversion of the fully spatially coherent pump has been reported [5, 6]. However, the effect of atmospheric turbulence on the entangled photon fields produced by a partially coherent pump beam has not been reported yet. Recently, a theoretical model for the influence of atmospheric turbulence on entangled photon fields produced by partially coherent dark hollow beam has been reported [7]. It has been shown that the detection probability of the entangled two-photon fields is higher and less susceptible to turbulence if the field is produced by a lower mode of partially coherent pump beam.

In the present paper, we have theoretically studied the influence of atmospheric turbulence on the entangled photon fields produced by spatially partially coherent pump beam. It is well known that the spatially partially coherent light is less sensitive to phase distortion and less affected by atmospheric turbulence than spatially fully coherent light. We show that the photon field produced by spatially partially coherent pump beam (PCPB) is less affected by atmospheric turbulence than the photon field produced by the spatially fully coherent pump beam (FCPB).

2. Theoretical Background

A generic situation to study the effect of atmospheric turbulence on the coincidence counts of the two-photon fields is represented in figure (1). The signal-idler photons produced by SPDC are detected in coincidence by detectors D_1 and D_2 respectively. The two-photon field can be expressed as [8],

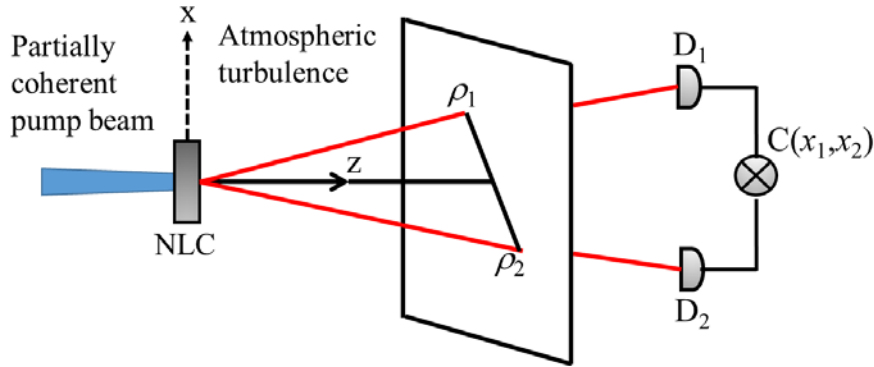


Figure 1. Schematic setup that could be used to study the influence of atmospheric turbulence on the coincidence counts. The pump beam is partially spatially coherent.

$$|\psi\rangle = \iint dq_s dq_i \Gamma(q_s, q_i) \hat{b}_s^\dagger(q_s) \hat{b}_i^\dagger(q_i) |0, 0\rangle, \quad (1)$$

where, \hat{b}_s^\dagger and \hat{b}_i^\dagger are the creation operators for signal (s) and idler (i) with the corresponding transverse wave-vectors q_s and q_i respectively. The vacuum state is denoted by $|0, 0\rangle$ and $\Gamma(q_s, q_i)$ describes the phase-matching and perfect energy conservation in the SPDC process,

$$\Gamma(q_s, q_i) = A \int dq_p U(q_p) \delta(q_p - q_s - q_i) \tilde{\zeta}(q_s, q_i), \quad (2)$$

where $U(q_p)$ is the pump field and $\zeta(q_s, q_i)$ is defined as,

$$\tilde{\zeta}(q_s, q_i) = \text{sinc}\left(\frac{\Delta q L}{2}\right) \exp\left(-i \frac{\Delta q L}{2}\right), \quad (3)$$

and A is the integral constant, L is the crystal length. The positive electric field component of the signal and idler photon at the detection plane after propagation through an arbitrary optical system is given by [8],

$$E_\alpha^+ = \int dq_\alpha H_\alpha(x, q_\alpha) \exp(-i\omega_\alpha t) \hat{b}_\alpha^-, \quad \alpha = s, i, \quad (4)$$

where, $H_\alpha(x, q_\alpha)$ is the response of the signal (idler system), ω_α the frequency and t is the time photons take to reach the detector. The detection probability of signal photon at x_1 and idler photon at x_2 is given by [8],

$$C(x_1, x_2) = \langle \psi | \hat{E}_s^+(x_1) \hat{E}_i^+(x_2) \hat{E}_i^-(x_2) \hat{E}_s^-(x_1) | \psi \rangle. \quad (5)$$

Substituting equations (1)-(4) into equation (5) and considering the crystal is illuminated by a partially coherent pump beam and the two photon field is propagated through a turbulent atmosphere, we have,

$$C(x_1, x_2) = A \iiint \iiint W(x'_1, x''_1, x'_2, x''_2) \langle h_s(x_1, x'_1) h_s^*(x_1, x''_1) h_i(x_2, x'_2) h_i^*(x_2, x''_2) \rangle, \quad (6)$$

$$dx'_1 dx''_1 dx'_2 dx''_2$$

where $h_s(x, x')$ is the spatial Fourier transform of $H_s(x, q_s)$ and similarly for the idler system. The Cross-spectral density (CSD) of the photon field is expressed as,

$$W(x'_1, x''_1; x'_2, x''_2) = \iint \langle U_p(x) U_p^*(x_0) \rangle \eta(x + x'_1, x + x'_2) \eta^*(x_0 + x''_1, x_0 + x''_2) dx dx_0, \quad (7)$$

where $\eta(x, x')$ is the Fourier transform of $\tilde{\zeta}(q_s, q_i)$ and

$$h_\alpha(x, x') = \left(-i \frac{k_\alpha}{2\pi z} \right)^{1/2} \exp \left[i \frac{k_\alpha}{2z} (x - x')^2 + \phi_\alpha(x, x') \right], \quad \alpha = s, i, \quad (8)$$

where k_α is the wavenumber, z is the distance between nonlinear crystal and detectors and $\phi_\alpha(x, x')$ is the phase turbulence due to scattering for a Kolmogorov atmosphere model and is given by [7],

$$\langle \exp[\phi_\alpha^*(x_1, x'_1) + \phi_\alpha(x_2, x'_2)] \rangle = \exp \left[- \frac{(x_1 - x_2)^2 + (x_1 - x_2)(x'_1 - x'_2) + (x'_1 - x'_2)^2}{\rho_\alpha^2} \right], \quad (9)$$

where, $\rho_\alpha = (0.55 C_n^2 k_\alpha^2 z)^{-3/5}$ ($\alpha = s, i$). C_n^2 , describes the turbulence level. Within the paraxial approximations, we have assumed $k_s \approx k_i \approx k_p / 2$ and $\Delta q = |q_s - q_i|^2 / (2k_p)$, k_p is the wavenumber of the pump. Using the approximation $\text{sinc}(\Delta q L / 2) \approx \exp[-\gamma L \sqrt{\Delta q^2} / 2]$, the CSD is given by,

$$W(x'_1, x''_1; x'_2, x''_2) = \frac{4\pi k_p}{L \sqrt{\gamma^2 + 1}} \left\langle U_p \left(-\frac{x'_1 + x'_2}{2} \right) U_p^* \left(-\frac{x''_1 + x''_2}{2} \right) \right\rangle \times \exp \left[-\frac{(x'_1 + x'_2)^2 k_p}{4L(\gamma + i)} - \frac{(x''_1 + x''_2)^2 k_p}{4L(\gamma - i)} \right], \quad (10)$$

For the special case of partially coherent pump field of Gaussian-Shell model type the correlation of the field is represented as [9],

$$\langle U(x'_1) U^*(x'_2) \rangle = S_0 \exp \left[-\frac{x_1'^2 + x_2'^2}{4\sigma^2} \right] \exp \left[-\frac{(x'_2 - x'_1)^2}{2\delta^2} \right], \quad (11)$$

where, S_0 is a constant, σ is the beam width and δ is the spatial coherence length of the pump beam. Substituting equations (7)-(11) into equation (6) we get,

$$C(x_1, x_2) = \left(\frac{4\pi k_p}{L(\gamma^2 + 1)} \right) S_0 \left(\frac{k_p}{4\pi z} \right)^2 \iiint \exp \left[-\frac{(x'_1 + x'_2)^2 + (x''_1 + x''_2)^2}{16\sigma^2} \right] \exp \left[-\frac{(x''_1 + x''_2 - x'_2 - x'_1)^2}{2\delta^2} \right] \times \exp \left[-\frac{(x'_1 + x'_2)^2 k_p}{4L(\gamma + i)} - \frac{(x''_1 + x''_2)^2 k_p}{4L(\gamma - i)} \right] \exp \left[-\frac{ik_p}{4z} \left((x_1 - x_1'')^2 - (x_1 - x_1')^2 + (x_2 - x_2'')^2 - (x_2 - x_2')^2 \right) \right] \times \exp \left[-\frac{(x'_1 - x''_1)^2 + (x'_2 - x''_2)^2}{\rho^2} \right] dx'_1 dx'_2 dx''_1 dx''_2. \quad (12)$$

3. Results and Discussion

The theoretical results are shown in figures (2)-(4). The effect of atmospheric turbulence (C_n^2) on the coincidence count rate (in arbitrary units), when one detector was fixed ($x_2=0$) and other was moved (x_1) in the transverse direction, was plotted using equation (12) for FCPB and PCPB. The wavelength

of the pump beam was assumed to be 405 nm, $L=0.7$ mm and $\sigma=10$ mm. Figures (2a), (3a) and (4a) show the influence of weak ($C_n^2 = 10^{-14} \text{m}^{-2/3}$) and strong turbulence ($C_n^2 = 5 \times 10^{-14} \text{m}^{-2/3}$) on the coincidence count rate when the pump beam is considered to be partially coherent ($\delta = 0.5 \text{mm}$). While figures (2b), (3b) and (4b) are plotted when the pump beam was considered to be fully coherent ($\delta = \infty$).

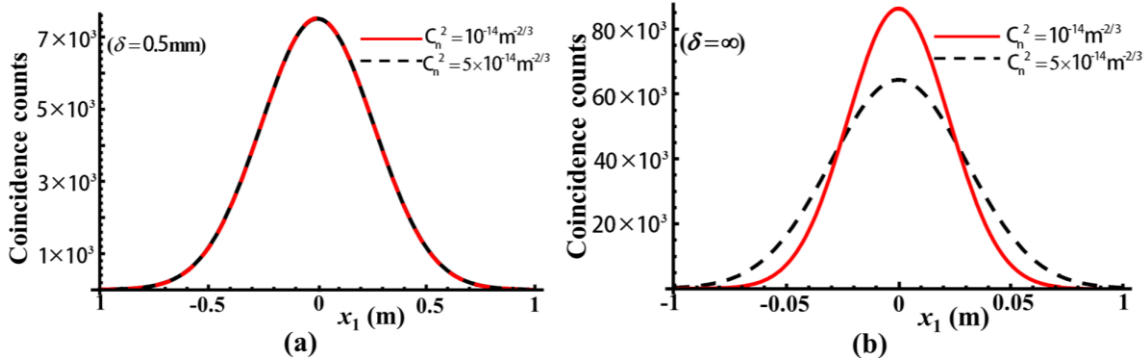


Figure 2. The effect of varying turbulence on the coincidence counts rate of two-photon entangled field at $z=1$ km. (a) partially coherent pump beam (b) fully coherent pump beam.

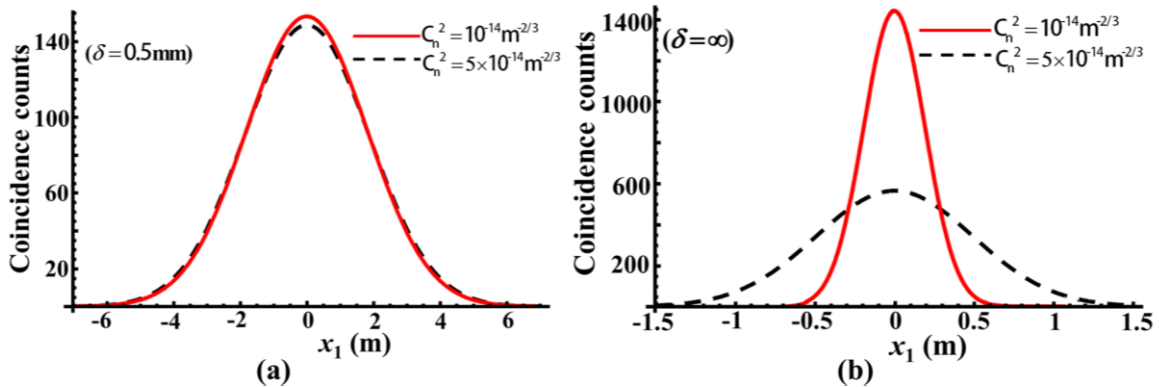


Figure 3. The effect of varying turbulence on the coincidence counts rate of two-photon entangled field at $z = 7$ km. (a) partially coherent pump beam (b) fully coherent pump beam.

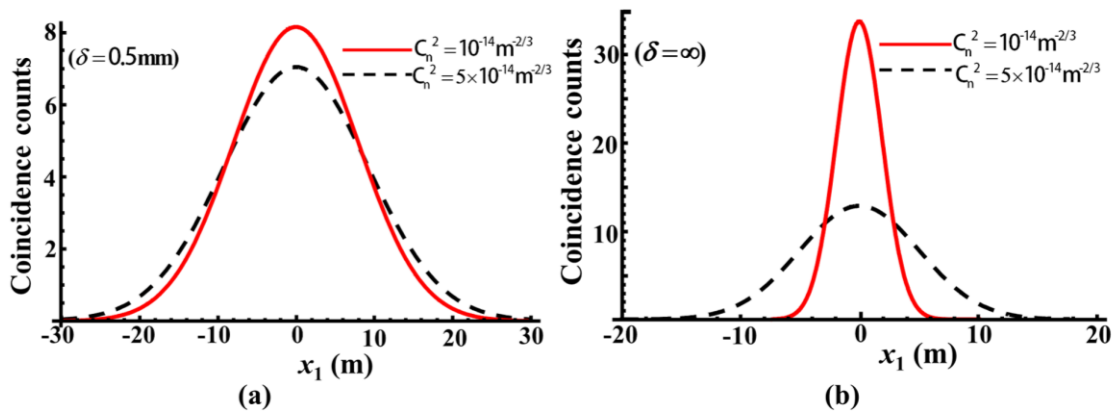


Figure 4. The effect of varying turbulence on the coincidence counts rate of two-photon entangled field at $z=30$ km. (a) partially coherent pump beam (b) fully coherent pump beam.

When the propagation distance was small, $z=1$ km, the detection probabilities for both the values of C_n^2 was almost the same when the entangled field was generated by PCPB (figure (2a)). This means the effect of atmospheric turbulence on the detection probabilities was negligible at this distance. On the other hand, there was a difference in the detection probabilities for two different values of C_n^2 when the crystal was illuminate by a FCPB (figure (2b)). As the propagation distance increased (figure (3a) and figure (4a)), the difference in the detection probabilities for two different values of C_n^2 was very small for PCPB. On the other hand, when we considered FCPB the difference of the detection probabilities for two different values of C_n^2 increased with the increase in the propagation distance (figures (3b) and figure (4b)). It can therefore be concluded that the detection is more stable when the entangled photons are generated by the PCPB.

It can be seen from figures (2)-(4) that the spreading of coincidence counts is almost the same for $C_n^2 = 10^{-14} \text{ m}^{-2/3}$ and $C_n^2 = 5 \times 10^{-14} \text{ m}^{-2/3}$ when PCPB was considered while the spreading of coincidence counts for $C_n^2 = 10^{-14} \text{ m}^{-2/3}$ and $C_n^2 = 5 \times 10^{-14} \text{ m}^{-2/3}$ are different for FCPB. In other words, the diffraction broadening (λ/δ) dominates over broadening caused by atmospheric turbulence for PCPB. On the other hand, in the case of FCPB the broadening in coincidence counts was caused by the atmospheric turbulence. The decrease in the coherence therefore results in lowering the normalized variance of the intensity or the scintillation. In addition, the wandering effect becomes smaller just due to broadening.

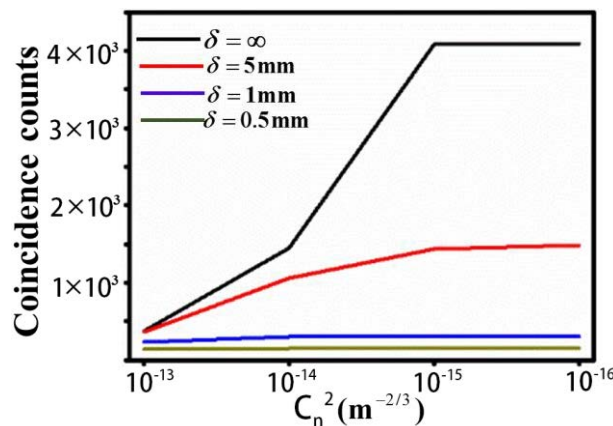


Figure 5. Change in the coincidence counts at a fixed points ($x_1=0$ and $x_2=0$) versus refractive-index structure parameter. $\sigma=1$ cm, $z=7$ km.

In figure (5), we illustrated the effect of pump coherence on the coincidence counts where coincidence counts at two fixed points ($x_1=0$ and $x_2=0$) were shown as a function of atmospheric turbulence. For the less coherent pump beam, the coincidence counts remain almost constant with the decrease in the atmospheric turbulence strength. As the coherence length increases to $\delta=5$ mm it maintains an almost constant value of coincidence counts until turbulence strength increases to a point where atmospheric turbulence effect dominates over the coherence effect. For weak turbulence, FCPB ($\delta = \infty$) has constant coincidence counts, which decrease with the increase in the turbulence strength.

4. Conclusion

We have obtained an expression for the coincidence count rate for entangled photon fields generated by the process of spontaneous parametric down-conversion. The effect of atmospheric turbulence on the detection probabilities depends on the spatial coherence property of the pump beam. It is concluded that the photon fields generated by PCPB is more robust for the change in atmospheric

turbulence. Present work provides new insights into the nature of SPDC emission by considering pump beam partially coherent and have application in free-space quantum communication.

Acknowledgment

This work is based on research supported by the South African Research Chair Initiative of the Department of Science and Technology and National Research Foundation.

References

- [1] Gisin N, Ribordy G, Tittel W, and Zbinden H 2002 *Rev. Mod. Phys.* **74** 145
- [2] O'Brien J L 2007 *Science* **318** 1567
- [3] Burnham D C, and Weinberg D L 1970 *Phys. Rev. Lett.* **25** 84
- [4] Jha A K, and Boyd R W 2010 *Phys. Rev. A* **81** 013828
- [5] Gopaul C, and Andrews R 2007 *New J. Phys.* **9** 94
- [6] Semenov A, and Vogel W 2010 *Phys. Rev. A* **81** 023835
- [7] Qiu Y, and She W 2012 *Appl. Phys. B* **108** 683
- [8] Saleh B E, Abouraddy A F, Sergienko A V, and Teich M C 2000 *Phys. Rev. A* **62** 043816
- [9] Wolf E 2007 *Introduction to the Theory of Coherence and Polarization of Light* (Cambridge University Press)

Volume determination of irregular objects by hydrostatic weighing at NMISA

B Ndlovu and R T Mautjana

National Metrology Institute of South Africa, Private Bag X 34, Lynnwood Ridge, Pretoria, 0040, South Africa

Email: bndlovu@nmisa.org

Abstract. Accurate volume determination of irregular objects can be complex because there are no standard formulae to be applied. Various techniques based on Archimedes' principle where the buoyancy force exerted by a fluid on a submerged object is equated to the weight of the object may be applied. One technique is the water displacement method which is not very accurate. The other is by weighing a submerged object in a fluid of known density. At NMISA the volumes of the OIML-shaped stainless steel mass pieces (50 g to 1 kg) have been measured using the automated volume comparator VC1005 (VC) which weighs in the FC-40 fluid. The results were validated against the previous measurements that were done at KRISS. The volumes of the mass pieces were measured to an average agreement of greater than 99.998%. These measurements led to the determination and confirmation of densities of the mass pieces which is critical for high accuracy mass measurements. The density results show improved measurement uncertainties for NMISA. The current work demonstrates a new achievement of high accuracy volume and density measurements for South Africa by the hydrostatic weighing method. This paper presents the volume and density results found for 50 g to 1 kg mass pieces using the VC.

1. Introduction

The volume of a regular object can accurately be determined by measuring the object's dimensions to apply a formula. However, when it comes to irregular objects, measuring dimensions is not always possible. Various techniques that are based on Archimedes' principle can be used for volume and density determination of irregular objects. Archimedes' principle states that the buoyancy force on an object that is submerged in a fluid is equivalent to the weight of the displaced fluid [1]. The buoyancy force F_B exerted by a fluid of density ρ_f on a submerged volume V_0 is given by

$$F_B = V_0 \rho_f g \quad (1)$$

where g is the gravitational acceleration.

Figure 1 shows a summary of three volume determination techniques that are based on Archimedes' principle [2]. In technique (a) the object is submerged in water by a thin suspension wire and this creates a weight difference ΔW on a balance which then enables the determination of the object's volume by $V_0 = \frac{\Delta W}{\rho_f}$. Technique (b) shows the water displacement technique where a rise in the water level is equivalent to the volume of the object. Technique (c) shows the liquid overflow technique in which the fluid displaced by the object is collected on a graduated container to read of the volume of the object directly.

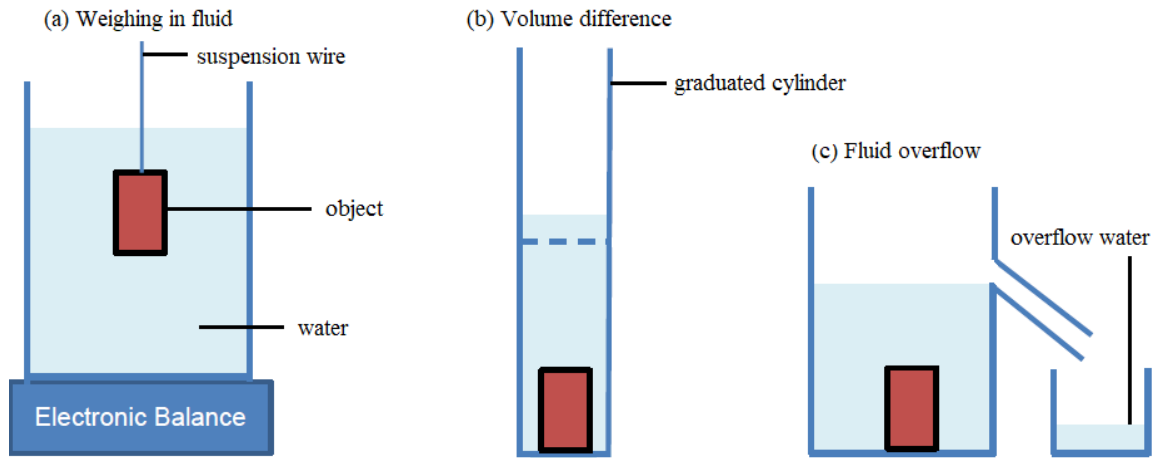


Figure 1: Schematic representation of (a) suspension, (b) liquid level and (c) overflow techniques for volume determination of solids [2].

This paper discusses the volume determination of irregular objects by hydrostatic weighing at the National Metrology Institute of South Africa (NMISA). The automated volume comparator VC1005 (VC) is used for volume and density determination of objects ranging from 1 g to 1 kg. The repeatability of weighing in liquid and temperature-stability on this system is critical in performing high accuracy measurements. The improved accuracy as indicated by smaller uncertainties at NMISA would mean improved accuracy for the South African volume and density measurements through dissemination from the national standards.

2. The volume determination

The VC works by performing comparisons between two objects (reference and test) to detect the difference in volume. When an object of mass m and volume V balances a reference mass piece of mass m_c and volume V_c in a fluid of density ρ_f , the net force equation in the vertical direction which considers the downward weight due to the object and the upwards buoyancy due to the fluid can be written as

$$mg - \rho_f Vg = m_c g - \rho_f V_c g. \quad (2)$$

For a weight taken at a temperature of 20 °C, the conventional mass m_c is defined as the mass of a reference of density 8000 kg/m³ that the weight would balance in air density of 1.2 kg/m³ [3]. Setting $V_c = \frac{m_c}{\rho_c} = \frac{m_c}{8000}$ and $\rho_f = \rho_{air} = 1.2$ in Equation (2), this definition may be expressed mathematically as

$$m = m_c \left(1 - \frac{1.2}{8000} \right) + V(1.2). \quad (3)$$

The weighing equation that is used for calculating the volume difference ΔV between the reference and test mass pieces, in terms of the conventional masses, is given by

$$\Delta V = \frac{(m_{ct} - m_{cr}) \left(1 - \frac{1.2}{8000} \right)}{\rho_f - 1.2} - \frac{B\Delta m_w}{\rho_f - 1.2} \quad (4)$$

where: m_{ct} and m_{cr} are the conventional masses for the test and reference respectively,

$$\Delta m_w = m_{wt} - \frac{m_{wr1} + m_{wr2}}{2} \text{ is the drift-eliminated weighing difference,}$$

$B = \left(1 - \frac{\rho_{air}}{\rho_{bw}}\right)$ is the balance correction factor,

ρ_{air} is the air density and ρ_{bw} is the density of the balance's internal weights.

The volume $V_t(20)$ of the test object at 20 °C is then determined using the volume difference by

$$V_t(20) = \frac{V_r [1 + \alpha_r (T_{av} - 20)] + \Delta V}{1 + \alpha_t (T_{av} - 20)} \quad (5)$$

where: α_r and α_t are the thermal expansion coefficients of the reference and test since the measurements are performed at temperature T_{av} ,

V_r is the volume of the reference mass [4]. In the next section we discuss the experimental details and set-up of the VC.

3. Experimental details

The volumes of the OIML-shaped stainless-steel mass pieces (50 g, 100 g, 200 g, 500 g and 1 kg), shown in Figure 2, were determined using the VC. The front view of the NMISA's VC with the side view of the fluid bath is shown in Figure 3.



Figure 2: OIML-shaped weights.

The VC system is mounted on top of a stable granite table to minimize vibrations. The VC consists of the outer and inner fluid baths. The outer bath is filled with sterilized distilled water to prevent the build-up of micro-organisms and contaminants inside. This water provides some sort of fluid gradient from the dense FC-40 in the inner bath to the outside air which minimizes the risk of the inner glass cracking due to the heavy FC-40. The mass pieces are submerged in the FC-40 fluid for weighing. The FC-40 electronic fluid is a fluorinert colourless liquid that is thermally stable and single-phase liquid over a temperature range of -57 °C to 165 °C which makes it suitable for relatively constant temperature measurements as in this current work [5]. Prior to measurements the fluid density has to be determined to ensure the correct density which is about 1.87 g/cm³ is recorded. Fluid calibration for density may be performed using internal weights of the VC or using the calibrated external mass pieces, with the latter being more accurate.

The turntable inside the fluid bath has four loading positions. The mass pieces are loaded using the loading arm which can move up or down. Figure 4 shows a schematic representation of the experimental set-up of the apparatus. The weighing pan inside the fluid bath hangs from the comparator. Close to this weighing pan is a temperature sensor connected outside to a Thermometer Readout. This ensures that the fluid temperature is measured close to where the weighing occurs. A

ClimaLog was used to measure the air temperature (T), pressure (P) and relative humidity (RH) for calculating the air density. The measured data is then collected onto the computer software ComVol for processing where the data for the reference and test objects to be measured are also stored.



Figure 3: The front view (left) of the VC1005 and the side view (right) of the fluid bath on the right.

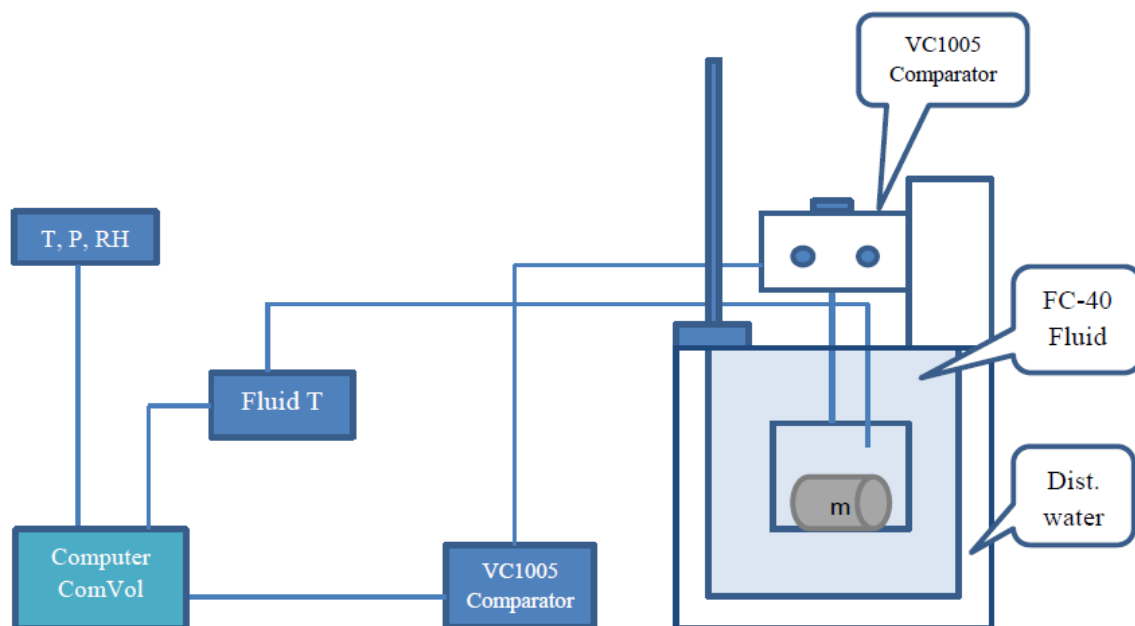


Figure 4: Schematic representation of the VC1005 experimental set-up.

The reference and test weights of the same nominal mass and known conventional masses were loaded across each other on the turntable positions. Weights were thermally stabilized in the fluid for a minimum of two hours before performing measurements.

4. Results and discussion

The mass pieces used in this current work were previously calibrated for mass and density at Korea Research Institute of Standards and Science (KRISS) in the year 2010. The volumes V of the weights

by KRISS were calculated from the calibration certificates using the measurement results of mass m and density ρ , as per the formula $V = m / \rho$. The calculated volumes from KRISS measurements were used to validate the results found. The associated volume uncertainties $u(V)$ for KRISS were

determined by the relation $\left(\frac{u(V)}{V}\right)^2 = \left(\frac{u(m)}{m}\right)^2 + \left(\frac{u(\rho)}{\rho}\right)^2$ where $u(m)$ and $u(\rho)$ are the

uncertainties in mass and density certificates respectively [7]. The measured volumes with the calculated uncertainties (K=2) that were found by NMISA and KRISS are shown in Table 1. The accredited calibration and measurement capabilities (CMCs) for NMISA solid weights density calibrations [6] are shown in Table 2 which also shows the density results of NMISA and KRISS. The

agreement between the results was calculated using the relation $y = \left(1 - \frac{|x_1 - x_2|}{(x_1 + x_2)/2}\right) \times 100\%$ [8].

Table 1: Volumes measured at NMISA with VC1005 and calculated volumes from KRISS results.

Nominal mass (g)	NMISA 2016		KRISS 2010		Agreement of results (%)
	Measured Volume (cm ³)	Calculated Uncertainty (cm ³)	Calculated Volume (cm ³)	Calculated uncertainty (cm ³)	
50	6.244 41	0.000 50	6.244 69	0.000 78	99.996
100	12.490 02	0.000 50	12.489 85	0.000 84	99.999
200	24.980 12	0.000 50	24.979 52	0.001 28	99.998
500	62.444 93	0.000 71	62.444 49	0.002 89	99.999
1 000	125.843 33	0.001 12	125.842 07	0.005 54	99.999

Table 2: Densities measured at NMISA with VC1005 and at KRISS.

Nominal mass (g)	NMISA 2016			KRISS 2010		Agreement of results (%)
	Measured Density (kg/m ³)	Calculated Uncertainty (kg/m ³)	Accredited CMC (kg/m ³)	Density (kg/m ³)	Uncertainty (kg/m ³)	
50	8007.16	0.32	8.00	8006.80	1.00	99.996
100	8006.38	0.32	5.00	8006.49	0.54	99.999
200	8006.37	0.16	5.00	8006.56	0.41	99.998
500	8007.05	0.09	5.00	8007.11	0.37	99.999
1 000	7946.40	0.07	5.00	7946.48	0.35	99.999

It can be seen in Table 1 and Table 2 that the volume and density determined by NMISA in year 2016 are in agreement with those determined by KRISS in year 2010 with an average percentage agreement of greater than 99.998%. There is significant improvement in the density uncertainties compared to the currently accredited CMCs for NMISA. Graphical representation of densities in Figure 5 shows good overlap between NMISA's and KRISS' results.

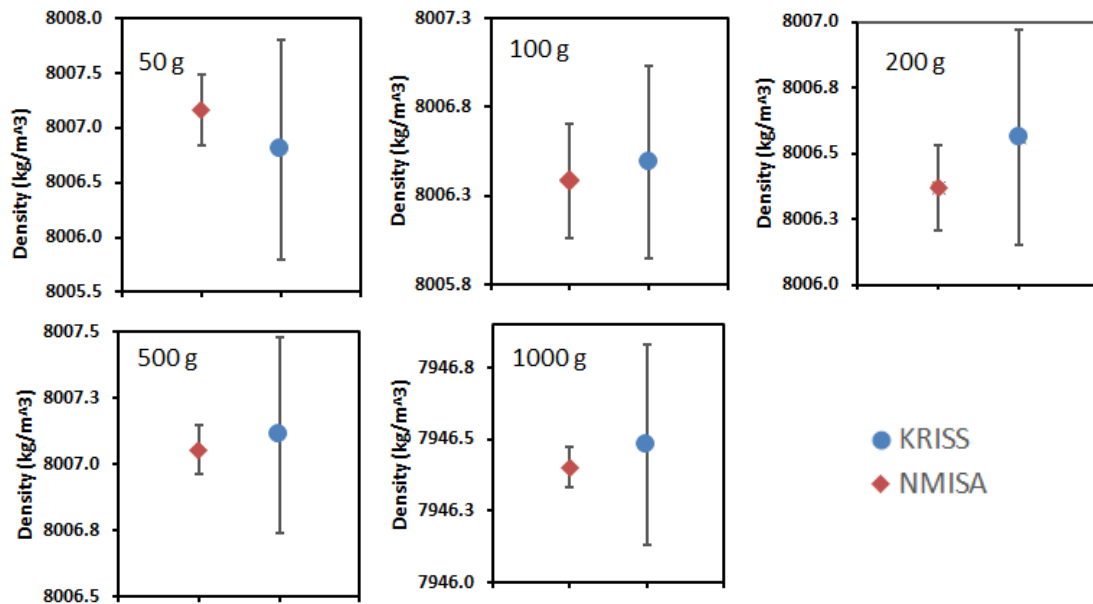


Figure 5: Graphical representation of the measured densities.

5. Conclusions

We have accurately measured the volumes and densities of weights ranging from 50 g to 1000 g using the automated volume comparator VC1005. The results for density show a significant improvement on the accredited measurement uncertainties for NMISA. Through this work, we have demonstrated a new achievement of high accuracy volume and density measurements for South Africa by the hydrostatic weighing method. Moreover, NMISA's results for volume and density are in agreement with the results that were found by KRIS.

References

- [1] Young H D, Freedman R A and Ford A L 2007 **University Physics** vol 1 (San Francisco: Pearson education) p 456-75
- [2] Hughes S W 2005 Archimedes revisited: a faster, better, cheaper method of accurately measuring the volume of small objects **Phys. Edu.** vol. **40** 468-74
- [3] International Organization of Legal Metrology 2004 **OIML R111-1** ed 2004 (E) p 6
- [4] Mettler Toledo 2009 **Operating instructions Volume Comparator VC1005** vol Ver 2.9
- [5] 3M Fluorinert Electronic Liquid FC-40 2010. Available: http://multimedia.3m.com/mws/media/648880/fluorinert-electronic-liquid-fc-40.pdf?fn=prodinfo_FC40.pdf. [Accessed June 2016]
- [6] South African National Accreditation System 2014. Available: <http://www.sanas.co.za/schedules/calibration/1605-06-2014.pdf>. [Accessed June 2016]
- [7] JCGM 2008 **Guide to the Expression of Uncertainty in Measurement** 1st ed. p 63
- [8] <http://www2.phy.ilstu.edu/~wenning/slh/Percent%20Difference%20Error.pdf> [Accessed June 2016]

A High Speed OCT System Developed at the CSIR National Laser Centre

Ameeth Sharma, Ann Singh, Ted Roberts, Rocky Ramokolo, Hencharl Strauss
CSIR, National Laser Centre, P.O Box 395, Pretoria, 0001

E-mail: asharma@csir.co.za

Abstract. Light-based techniques continue to gain momentum in different spheres of diagnostic and therapeutic applications due to their non-invasive, non-contact properties. One such technique is Optical Coherence tomography (OCT). Since first being reported by Huang in 1991, OCT has made significant strides in different fields such as dermatology, ophthalmology, polymer characterisation and biometrics. The type of OCT system employed can be a simple, cost effective solution or a complex, highly specific and fast system depending on the application. As part of a larger project, we have designed and built a high speed OCT system that can image a large surface area (25 by 25 mm) to a depth of 11 mm (sample dependant). Resultant 3-D images (512 x 512 x 2048 pixels) are acquired in less than 3 seconds. The heart of the system is a 200 kHz swept laser source and two-axis galvanometer based scanner. Signal acquisition is made possible through a high-speed analogue-to-digital converter capable of speeds greater than 1GS/s. This paper will give an overview of the system design and the specifications that have been obtained.

1. Introduction

OCT is a non-invasive, non-contact, optical imaging technique that is able to yield sub-surface morphology (2D or 3D) of scattering samples in situ and in real time. OCT is often described as the optical analogue to ultrasound and uses the technique of low coherence interferometry to compensate for the high speed of the backscattered light. The technique was first demonstrated by Huang in 1991 [1] and later for a different configuration by Fercher [2]. Since then, it has been applied extensively to biomedical applications, especially ophthalmology, dermatology and cardiology [3-6]. Many other applications also exist in material science, artwork, biometrics etc. [7-10].

2. Basic theory

The OCT technique involves a broadband (low coherence length) light source, which is split between a sample and a reference mirror (reference path). When the difference between the distance travelled by the light for the sample and the reference paths is within the coherence length of the light source, then interference will occur at the detector. OCT measures the echo time delay and intensity of backscattered light.

The process starts by acquiring an A-scan as shown in figure 1, below. The A-scan provides information about the reflective or scattering properties of the sample as a function of depth at a fixed position (point) of the sample. The light source can be linearly scanned across a sample to obtain a

cross-sectional image (B-scan), which is collection of successive A-scans. The collection of successive B-scans results in a volumetric image.

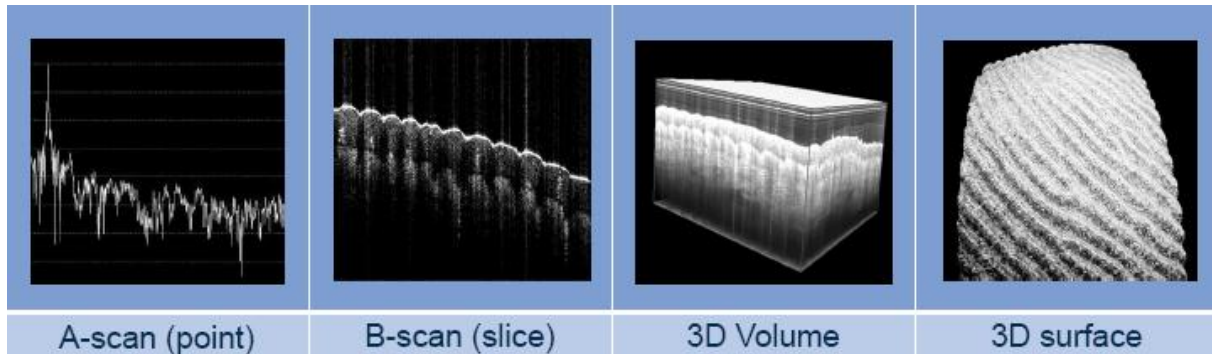


Figure 1. Imaging progression from an A-scan to a 3D surface image.

There are different configurations of OCT but all are based on the same principle. These configurations are Time Domain (TD) OCT and Fourier Domain (FD) OCT. TD OCT involves scanning the reference mirror back and forth to match different depths in the sample to within the coherence length of the light source. Fourier Domain (FD) uses a fixed reference mirror and measures the spectral response of the resultant interferogram. The interferogram is encoded in optical frequency space and undergoes a Fourier transform to yield the reflectivity profile of the sample. FD OCT can be further divided into Spectral Domain (SD) OCT and Swept Source (SS) OCT. Spectral Domain (SD) requires a broadband light source for illumination and separates the spectral components with a spectrometer. Swept Source (SS) OCT uses a light source which probes the sample with different optical frequencies sequentially (swept source). The power is then measured with a single photo detector.

OCT systems operate at different wavelengths (depending on the application) either in the infrared (800-900 nm) or in the near infrared (NIR) band (1250–1350 nm). The NIR wavelengths are preferable when imaging non-transparent tissue due to the better penetration depth. Ophthalmology is performed at 800-850 nm due to the transparent nature of the eye in this band. High-resolution applications require shorter wavelengths. Longer wavelengths are considered for samples with higher scattering properties.

3. System design

The design of an OCT system involves the design of the optical system (light source to detector) and the data acquisition system (detector to digital data/image). A few factors need to be considered when building an OCT system. These are briefly described below:

a. The type of OCT system is the first design choice. TD OCT is the simplest and easiest to implement but the moving reference mirror mechanism makes it slow. FD OCT systems are faster but implementation is more complicated with more computation required to obtain an OCT image. The SD OCT system is also known to suffer some signal to noise ratio (SNR) degradation that is not prominent in SS OCT systems. SD OCT systems are usually developed in the 800 nm band, due to the availability of high speed line scan cameras at these wavelengths but is unsuitable for skin tissue. SS OCT operates at 1.3 μm due to the available swept source light sources and uses a single photo detector. It has other advantages over the TD and SD configurations including lower noise and does not suffer from SNR drop-off, due to the narrow bandwidth of the light source.

b. The light source firstly depends on the choice of OCT system. The wavelength band of the chosen light source is an important specification and is determined by the application. The scan rate is also important when considering a SS OCT system.

c. The type of detector is dependent on the type of OCT system and application. The sensitivity, detection band and speed are important criteria. The resolution of the detector arrays in the SD OCT systems should also be considered. Low noise amplification usually accompanies the detector to improve the signal to noise ratio..

c. The Field of View (FOV) determines the area that is to be imaged. When building an OCT system, this is determined by the properties of the scan lens. The FOV also depends on the range of the scanning system (e.g. galvanometer).

d. Sensitivity is another parameter that has an effect on the contrast of the resultant images. The choice of photo-detector and digitisation electronics determines the sensitivity.

e. Resolution is dependent on the centre wavelength and other properties as described in the theory section.

f. Scan rate refers to the speed with which the 2D cross sections can be imaged. B-scan profiles of intensity versus depth are affected by the chosen configuration. For an SD OCT system, the scan rate is determined by the camera speed of the detection spectrometer whereas in SS OCT, it is determined by the sweep rate of the swept laser source and the speed of the scanning system. SS OCT systems are known to provide the highest scan rates. There is a tradeoff between the high scan rate and sensitivity. However fast scan rates are required for applications where motion artifacts affect the resultant images, such as in cardiovascular imaging and fingerprint acquisition etc.

g. The speed and resolution of the data acquisition system is important and is determined by the choice of electronic components (e.g. analogue to digital converter). The configuration of the data acquisition system may vary slightly depending on the type of OCT system and the target application.

4. Optical system design

The first design choice is the type of OCT system. Our requirement was to build a high speed OCT system to capture images of skin tissue within a few seconds. Based on the literature review, this could be achieved through a SS OCT system at 1.3 μm . A fiber-coupled, 200 kHz swept source laser (Thorlabs SL1310V1-20048) with a custom built Michelson interferometer with fibre coupled detector was used. The fiber coupled sample arm feeds into a large area scan lens, such that the light can be directed to the sample to be imaged. The reference arm is also fiber coupled and directed towards a mirror. This setup is shown in figure 2.

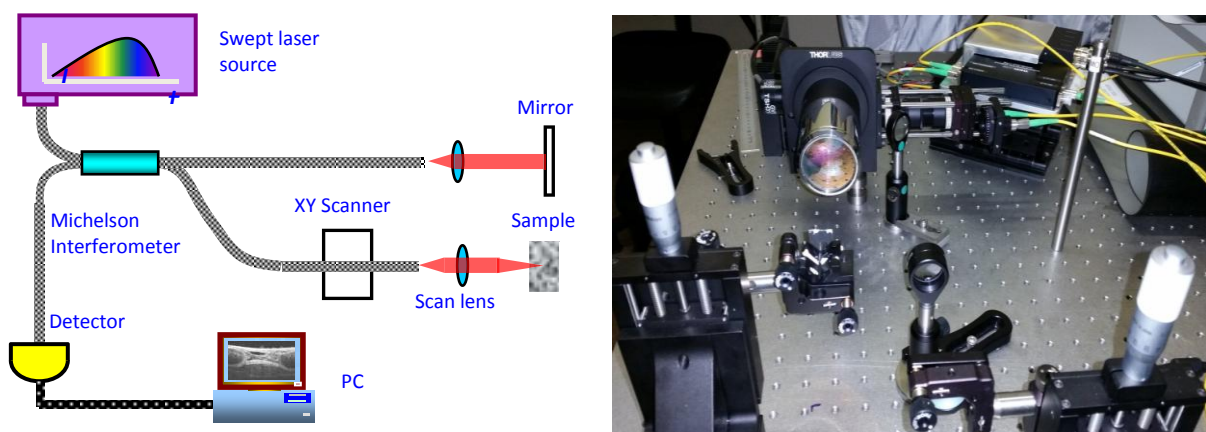


Figure 2. Optical layout of SS OCT system and a photograph of the initial test setup in the laboratory.

5. Data acquisition system design

Speed and resolution of the data acquisition are important when considering data capture in a SS OCT system. The main component is high-speed analogue to digital converter (ADC), which converts the

detector signal to digital data for storage. A layout and interconnections between all the main components in the data acquisition system is given in figure 3. The system can be divided into three main sections: the PC, the Scanner and the Optical interface. The high speed PC houses the digital to analogue converter (DAC) card for the scanner control and synchronisation, the ADC card, which interfaces mainly with the laser and optical detector. The scanner includes the XY galvanometer and the power supplies and driver electronics. The optical interface includes the laser interface and the photodiode detector. The swept laser source provides two main signals i.e. the DAQ trigger and the DAQ k-clock. The rising edge of the digital DAQ trigger signal indicates the time for the next A-scan and the k-clock trigger, trigger the capture of samples within a single A-scan. As the laser sweeps in wavelength, the k-clock trigger rising edge indicates the time at which the laser has swept to the next wavelength increment. The bottom right plot in figure 3 shows the laser output signals involved. The A-scan trigger (DAQ trigger) occurs at 200 kHz and K-clock trigger occurs at ~ 1 GHz.

The framestart signal is generated by the DAC and triggers the capture of successive B-scans. The top right plot in figure 3 indicates how the fast (X) and slow (Y) axes are controlled to rasterise the sample surface. The signals are generated by the DAC and synchronised in software. The framestart signal is delayed to compensate for the change in direction of the fast axis and to allow for both axes to stabilize into a linear motion. The fast axis is scanned at 180 Hz.

The high bandwidth signal from the detector is captured by the analogue to digital card (ChA) which can sample at rates up to 1.8 GHz. The ADC is optimised for high-speed data capture and uses an Auto-DMA mode, which captures data continuously to onboard dual port memory and simultaneously streams the acquired data to the PC memory at a slower rate. Capturing data in a SS OCT system also involves some data processing, in particular, an inverse Fast Fourier Transform (FFT) is required. The ADC card used has a field programmable gate array (FPGA) which allows the real time computation of the FFTs This is done via the software interface.

These two features along with the ability to be triggered externally for both A- and B-scans ensure that all large volumetric scans can be captured in under 3 seconds without any data loss. At 12-bit resolution, the resultant data file size is ~ 1 GB. The software interface, which generates the scanner control signals and synchronises them with the data capture, is coded in LabVIEW.

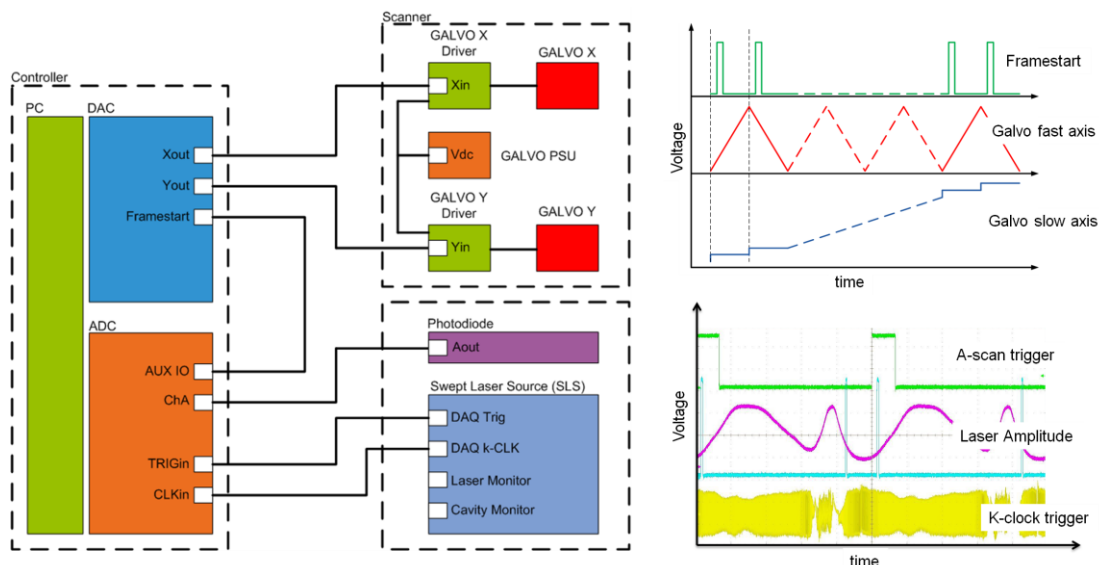


Figure 3. Schematic layout of the data acquisition system and the different timing and scanner control signals.

6. Mechanical system design

The prototype system was integrated into a custom-built enclosure after initial tests were performed in a lab setup. The enclosure was fitted with wheels for easy mobility. Figure 4 below, shows a schematic of the system layout.

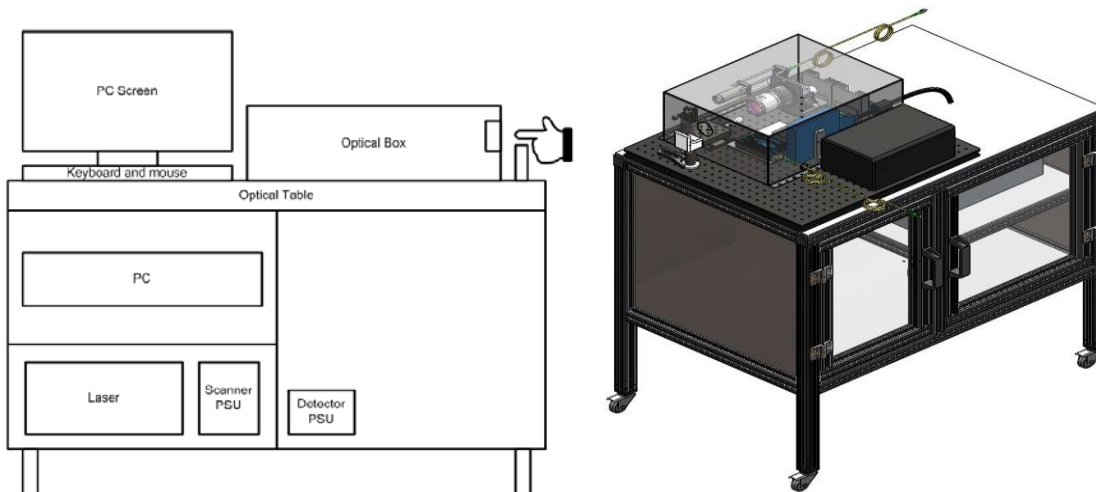


Figure 4. A schematic layout and 3D model of the integrated system in the trolley enclosure.

The top of the trolley has an optical breadboard on which the optical, opto-mechanical components, XY scanner and some electronics are fitted and housed in a shielded box. The ‘optical box ‘shields the components against dust and electromagnetic interference and has a port for the electrical and optical fiber connections and a port for the laser output beam. The swept source laser and power supplies for the scanner and detector are installed on the lower level. The PC, which is connected to the laser source and optical box, is installed on the second level with the mouse, PC screen and keyboard on top, next to the optical box.

7. System specifications

The system specifications are summarised in table 1 below and a photograph of the system built into the mechanical enclosure is shown in figure 5.



Figure 5. A photograph of the system.

Table 1. Summary of system specifications.

OCT system type	Swept source
Laser scan rate	200 kHz
Centre wavelength	1310 nm
Bandwidth	104 nm
Max. image area	25 mm x 25 mm
Max. image depth	11 mm
Area resolution	512 x 512 pixels
Depth resolution	2048 pixels
ADC Sampling rate	1 GHz
ADC voltage range	+/- 400 mV
B-scan rate	180 Hz
3D image capture time	2.8 s
File size (12 bit)	1 GB
Data transfer rate	2500 Mb/s

8. Conclusions

A swept laser source OCT system has been built and tested at the CSIR National Laser Centre (NLC), which involved the design and integration of an optical system as well as a high-speed data acquisition and control system. The prototype was constructed and installed into a mobile enclosure. Initial results have indicated that the system provides valid 3D image data, at adequate resolutions, for numerous applications. Our partners at CSIR Modelling and Digital Science (MDS), have confirmed that the speed of the data acquisition system is comparable with other systems available worldwide [11,12] for biometric applications (3D fingerprint acquisition) where larger areas and higher speeds are required. Research is ongoing in this application area and a future paper will provide a description of the system test results.

Acknowledgments

The authors would like to acknowledge the Department of Science and Technology (DST) for funding this joint project between the CSIR NLC and CSIR MDS. The authors would also like to acknowledge the technical assistance provided by Gary King, who assisted with the laboratory setup and Corrie van der Westhuizen, who designed and built the mechanical enclosure and trolley.

References

- [1] Huang D, Swanson EA, Lin CP, Schuman JS, Stinson WG, Chang W, Hee MR, Flotte T, Gregory K, Puliafito CA and Fujimoto JG 1991 Optical coherence tomography *Science* **254** 1178–1181
- [2] Fercher AF, Hitzenberger CK, Kamp G and El-Zaiat SY 1995 Measurement of intraocular distances by backscattering spectral interferometry *Opt. Commun.* **117(1-2)** 43–48
- [3] Hamdan R, Gonzalez RG, Ghostine S and Caussin C 2012 Optical coherence tomography: From physical principles to clinical applications *Archives of Cardiovascular Disease* **105** 529-534
- [4] Verga N, Mirea DA, Busca I, Poroschianu MN, Zarma SF, Grinisteanu L, Anica A, Gheorghe CA, Stan CA and Verga M, R. Vasilache 2014 Optical Coherence Tomography In Oncological Imaging *Romanian Reports in Physics* **66(1)** 75–86
- [5] Gabriele ML, Wollstein G, Ishikawa H, Kagemann L, Xu J, Folio LS and Schuman JS 2011 Optical coherence tomography: history, current status, and laboratory work *Invest Ophthalmol Vis Sci* **52** 2425–2436
- [6] Abtahian F and Jang IK 2012 Optical coherence tomography: basics, current application and future potential *Current Opinion in Pharmacology* **12** 583–591
- [7] Ju MJ, Lee SJ, Min EJ, Kim Y, Kim HY, and Lee BH 2010 Evaluating and identifying pearls and their nuclei by using optical coherence tomography *Opt. Express* **18(13)** 13468–13477
- [8] Chang S, Larin KV, Mao Y, Almuhtadi W and Flueraru C Fingerprint 2011 Spoof Detection Using Near Infrared Optical Analysis *State of the art in biometrics*, Intechopen, Croatia 57–84
- [9] Khutlang R, Singh A and Nelwamondo FV 2015 Segmentation of Forensic Latent Fingerprint Images Lifted Contact-less from Planar Surfaces with Optical Coherence Tomography *CFSE 2015: The 7th IEEE International Workshop on Computer Forensics in Software Engineering*, Taichung, Taiwan
- [10] Larin KV and Cheng Y 2006 Artificial fingerprint recognition by using optical coherence *Appl. Opt.* **45 (36)** 9238-9245
- [11] Okabe Y, Sasaki Y, Ueno M, Sakamoto T, Toyoda S, Kobayashi J and Ohmi M 2013 High-Speed Optical Coherence Tomography System Using a 200-kHz Swept Light Source with a KTN Deflector *Optics and Photonics Journal* **3(2)** 190-193
- [12] Drexler W, Liu M, Kumar A, Kamali T, Unterhuber A et al 2014 Optical coherence tomography today: speed, contrast, and multimodality *J. Biomed. Opt.* **19(7)** 071412

Spark Plasma Sintering of 2507 Duplex Stainless Steel Reinforced with TiC

R Sule¹, PA Olubambi², I. Sigalas¹, JKO Asante³, SW Maseko⁴

¹School of Chemical and Metallurgical Engineering, DST/NRF Centre of Excellence, University of the Witwatersrand, Johannesburg, South Africa

²Department of Chemical Engineering, University of Johannesburg, Johannesburg, South Africa

³Department of Physics, Institute for Nano-Engineering Research, Tshwane University of Technology, Pretoria, South Africa

⁴Department of Chemical, Metallurgical and Materials Engineering, Institute for Nano-Engineering Research, Tshwane University of Technology, Pretoria, South Africa.

E-mail: Rasidi.sule@wits.ac.za, richysule@yahoo.com

Abstract. As technological development is advancing towards the use of powder metallurgical (PM) processed stainless steels for automotive and structural applications, 2507 duplex stainless steel have gained considerable scientific attention and technological interest due to potential benefit associated with their unique properties such as corrosion and oxidation resistance and good formability. However, application of this material is hindered by its low mechanical strength and poor anti-friction properties resulting from the elongated porosity which acts as stress concentration sites that could lead to premature and brittle failure at a relatively lower load. These drawbacks can be improved using appropriate technology. Effort was made in this study to reinforce 2507 stainless steel with TiC particles and consolidate with spark plasma sintering (SPS). A relative density of 99.7% and Vickers hardness of 289.7 HV was obtained for 2507 DSS sintered at 1000 °C. The hardness value of 2507 stainless steel containing 10 vol%TiC was found to be 296.03 HV. The microstructure of the material produced was investigated using SEM.

1. Introduction

Technological developments of advanced materials for better industrial applications are ongoing. Powder metallurgy is one of the methods used in synthesizing these material composites as in processed steels for automotive and structural applications [1,2]. Powder metallurgy gives good densification, low cost net-shaping, relatively low-temperature processing, high material utilization (95%) and the ability to tailor microstructures for specific applications [3].

One such material, 2507 duplex stainless steel, has gained considerable scientific attention and technological interest due to its unique properties such as corrosion resistance, oxidation resistance and good formability. These properties are attributed to the relative high Cr (25 wt%), Ni (7 wt%) and Mo (4 wt%) contents as compared to other steels [4]. Typically, 2507 duplex stainless steel finds

applications in hostile environment such as in desalination plants, oilrig structures, firefighting systems, chemical process industries, among others [4]. The Fe component has a mixed microstructure of austenite and ferrite in 50/50 ratio.

However, Duplex 2507 stainless steel, in temperatures above 250 °C, forms intermetallic phases, becomes brittle and compromises its useful mechanical and physical properties such as corrosion resistance and hardness [5]. In order to improve duplex 2507 properties, and possibly enhance its temperature limitation, various attempts such as adding ceramics particulates have been undertaken [6, 7]. Among the materials of choice, Titanium Carbide (TiC), Titanium Nitride (TiN) and Titanium Carbo-Nitride (TiCN) have emerged as good reinforcements to austenitic stainless steels due to their excellent properties - high hardness, low density, high melting temperature, high modulus, excellent wear and corrosion resistance, good wettability and stability in steel melt [8]. In addition, TiC particles are thermodynamically stable in an iron alloy matrix at the low sintering temperatures, with practically negligible (0.5–1%) solubility [9]. This limited solubility might have resulted in the formation of the (Fe, Cr)-rich precipitates at the interface which contributed to the improved strength of the component [9]. However, homogeneous mixing and fabrication of ceramics and steel powders into useful material composite has been a daunting task due to surface contamination of impurities [10] and the creation of unwanted pores that affect densification [7] of the final composite product [1].

Lin and Xiong [11] investigated the microstructure and mechanical properties of 316L stainless steel reinforced with TiC prepared by microwave sintering and warm compaction. They reported that the relative density, hardness and abrasive properties of 316L stainless steel could be improved by using 5 wt.% TiC particles as reinforcements in composites towards a maximum relative density of 94.8%.

Spark Plasma Sintering (SPS) brings some exceptional advantages into the sintering of materials due to its unique features [12]. The accurate control of sintering temperature as well as high temperature up ramp speed makes SPS a promising technique for producing highly dense materials with controlled grain growth [12]. Li *et al.* [12] reported on rapid fabrication of *in-situ* TiC particulates reinforced Fe-based composites by spark plasma sintering. They obtained a maximum relative density of 99.2% at the following sintering consolidation: applied heating rate from room temperature was about 80 °C/min until sintering temperature of 1150 °C, holding time and pressure of 5 minutes and 30 MPa in vacuum, respectively.

In the present study, attempt to reinforce 2507 duplex stainless steel powder of average size 3 – 40 μm with TiC powder (2 - 15 μm) of different compositions (10, 15 and 20 vol.%) was undertaken. The objectives were to check for good sinterability, densification and hardness of the composites. Two sintering consolidation temperatures used were 1000 °C and 1100 °C.

2. Materials and methods

2.1. Feed stock powder and characterization

Dry elemental mixing of the powders were performed with 3 stainless steel balls (9.5 mm diameter) in a Turbula T2F mixer at a rotating speed of 72 rpm for a period of 4 hours. The High Resolution Scanning Electron Microscope (HRSEM Joel 7600F) equipped with Energy Dispersion X-ray (EDX) was used to check the homogeneity of the powder mixture.

2.2. Consolidation and characterization of sintered samples

The powder mixtures were consolidated by Spark Plasma Sintering (HPD 25, FCT System GmbH, Germany) furnace. The powders were loaded into a graphite die 30 mm diameter and a sintered sample thickness obtained was 5 mm. A minimum load of 10 kN (14.1 MPa) was applied to establish good electrical contact between the powder particles and the die assembly. The consolidation was carried out under a vacuum of 0.56 mbar. The mixed powders were uniaxially pressed at 50 MPa.

2.3. Characterization of the sintered samples

The densities were measured using the Archimedes's principle method. Samples for analysis were cut in a plane perpendicular to the pressing direction, hot mounted and grinded using different sizes of silicon carbide paper ranges from 120 to 1200 grit. The samples were then polished using 3 μm diamond suspensions on a polishing cloth for 5 minutes at a speed of 300 rpm. The final polishing was done with 1 μm diamond paste. The microstructure investigation was performed on the polished surface using HRSEM equipped with EDS analysis. Microhardness measurements were made on the as-polished specimens using the Vickers microhardness tester at 100 g load for 15 s. The samples' surfaces were indented randomly at five different positions for each sample and the average hardness values were recorded. The fracture surface of 2507 stainless steel containing TiC was analysed to evaluate the sinterability of material and TiC bonding into the matrix.

3. Results and discussion

Figure 1 shows the SEM micrograph of 2507 stainless steel powder particles. The starting powders revealed spherical shape and agglomerates of smaller particles. The micrograph also shows that the powder particles size ranged from 3 μm to 40 μm .

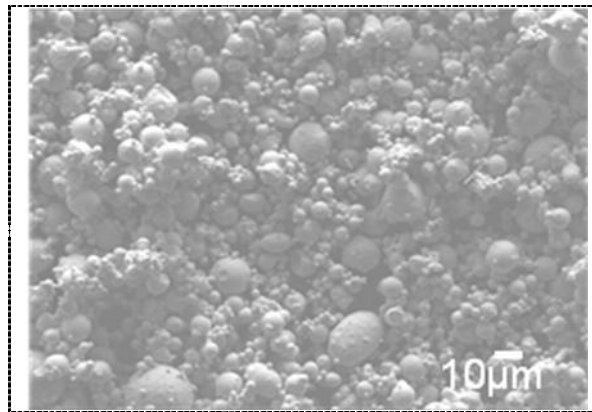


Figure 1. SEM micrograph of 2507 stainless steel powder

Figure 2 shows the SEM micrograph of the as-received TiC powder particles. The particles were jagged and large fractured irregular surface. Also seen in the micrograph are inherent pores created because of the high reaction heat released during the powders' formulation.

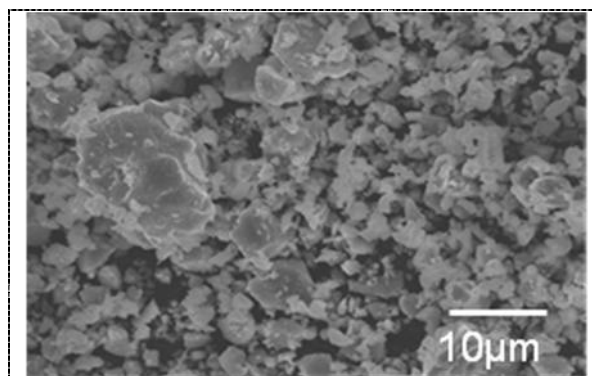


Figure 2. SEM micrograph of TiC powder

Sintering of crystalline materials can occur by several mechanisms such as surface diffusion, lattice diffusion, grain boundary diffusion and dislocation motion. All these processes are temperature dependent. An increase in temperature would cause the diffusion of atoms and this would result in necking as well as shrinkage (densification) [13]. Table 1 summarizes the relative density of the neat 2507 stainless steel and that with the TiC composites. A relative density of 99.7% was obtained for as-received – neat - 2507 sample at both sintered temperatures at 1000 °C and 1100 °C. The high densification could be ascribed to the spherical shape and size as well as the enhanced activation of plasma which resulted in large quantity of necking and welding of constituents [14]. Good sintering was therefore achieved for the neat 2507 stainless steel.

The increasing content of TiC particles reduced the relative density of 2507 DSS/TiC composite samples, sintered at both temperatures. The reduction was due to the low specific weight of the TiC particles [7] and the formation of micro-voids in the constituents (spherical dimples - see figure 4). However, for the same composite, increase in temperature, produced higher densification because of grain size expansion and the reduction of pore volume/void size.

Table 1. Results of the relative densities and microhardness of sintered sample

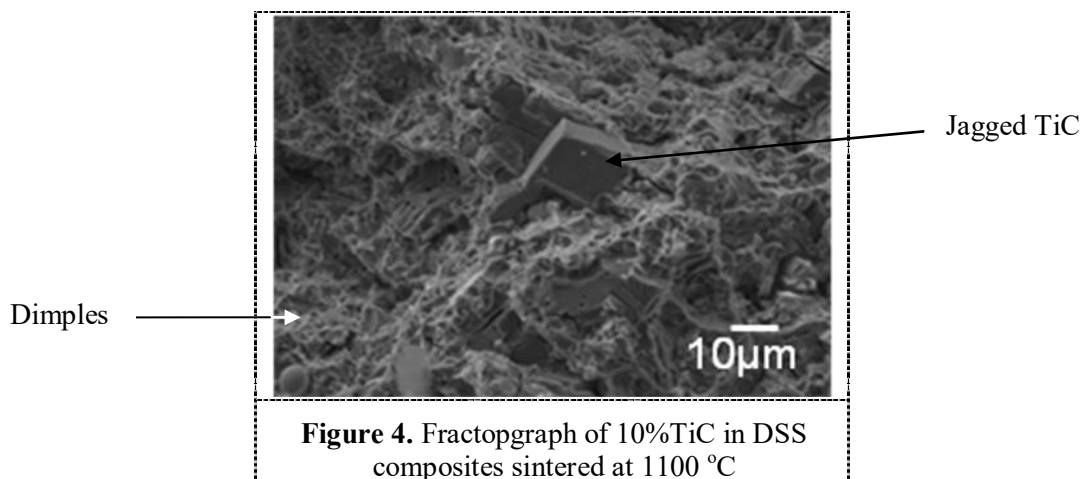
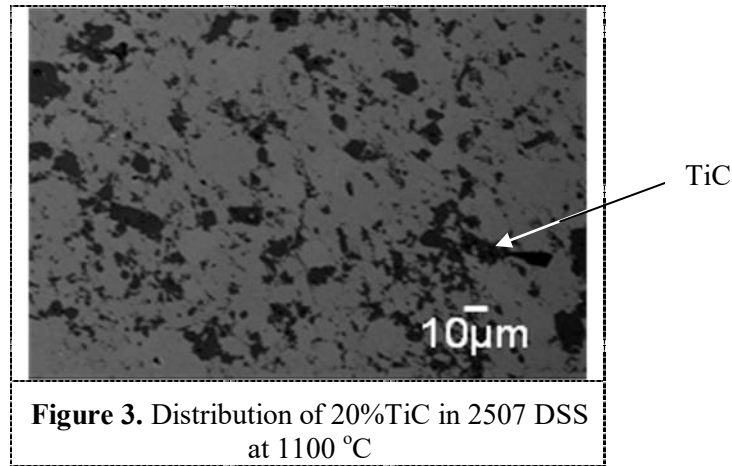
Sample vol.%	Consolidation condition (temperature) at 50 MPa, heating ramp rate 100°C/min and holding time of 5 min	Density (%)	Microhardness (HV)
2507 DSS	1000°C	99.7	289.7±0.2
2507-10TiC	1000°C	97.3	281.7±0.5
2507-15TiC	1000°C	95.5	266.9±0.7
2507-20TiC	1000°C	93.2	259.1±1.2
2507 DSS	1100°C	99.7	289.7±0.2
2507-10TiC	1100°C	98.3	296.3±0.3
2507-15TiC	1100°C	97.6	281.4±0.6
2507-20TiC	1100°C	94.7	279.9±0.8

Figure 3 shows the SEM micrograph of 2507 stainless steel matrix reinforced with 20 vol% TiC sintered at 1100 °C with holding time of 5 minutes. The image shows the composites have a uniform distribution of the hard but less dense TiC (dark patches in Figure 3) within the matrix without cracks.

The measured microhardness of the neat 2507 stainless steel samples was 289.7±0.2 HV. The value did not change for the sintered temperatures at 1000 and 1100 °C. Measured microhardness value, however, decreased with TiC content additions at a particular sintering temperature; and this could be due to the reduction in their densities value. This is contrary to Lin and Xiong [10] reported result. They found that the hardness of composites of TiC in 316L stainless steel increase with increasing TiC content. Possible reason for the present result could be due to the jagged shape of the TiC powder and the sintering temperatures used. Clearly, (see the indicated ‘inert’ TiC in Figure 4) there was not adequate sintering of the composites at the chosen consolidation parameters – temperatures, uniaxial pressure and dwell time – that should have been increased. However, the hardness value of the composite matrix with addition of 10 vol.% TiC, increased from 281.7 (at 1000 °C) to 296.3 HV (at 1100 °C). This indicated 1100 °C to be better sintering temperature than 1000 °C. Furthermore, measured values of the other composites also showed about 5% (15 vol% TiC) to 8% (20 vol% TiC) microhardness increase from sintering temperatures of 1000 to 1100 °C. The increased hardness is attributed to possible segregation of impurity elements (N and C) from the bulk to the surface resulting in the formation of harder nitrides and carbides.

Figure 4 shows the fractograph of 2507 stainless steel reinforced with 10 vol% TiC sintered at 1100 °C and hold for 5 min. The fractograph reveals dimple structure – a sign that reveals microvoids in the

intra- and inter-bonding of the components. Some sections of the figure also show physical (other than metallurgical) bonding between the matrix and TiC indicating incomplete sintering at 1100 °C.



4. Conclusion

A processing technique was developed to incorporate different TiC compositions homogeneously into the 2507 stainless steel matrix and consolidated by Spark Plasma Sintering. Composite hardness does not just increase with increasing TiC content but depends on factors such as sintering temperature, powder size and shape, composite densification and perhaps a critical vol.% of the TiC in the matrix. The 2507 DSS-10 vol.%TiC consolidated at 1100°C was found the hardest (296.3 HV) and best dense composite (relative density of 98.3%).

References

- [1] Abenojar J., Velasco F., Bautista A., Campos M., Bas J.A., Torralba J.M., Atmosphere Influence in Sintering Process of Stainless Steels Matrix Composites Reinforced with Hard Particles, *Composites Science and Technology*, **63** (2003), 69-79
- [2] Pellizzari M., Fedrizzi A., Zadra M., Spark Plasma Co-Sintering of Hot Work and High Speed Steel Powders for Fabrication of a Novel Tool Steel with Composite Microstructure, *Powder Technology*, **214** (2011), 292-99.
- [3] Kurga N., Effects of sintering atmosphere on microstructure and mechanical property of sintered powder metallurgy 316L stainless steel. *Materials Design*, **52** (2013) 995-998.

- [4] Stainless T. M. R., Practical Guidance for the Fabrication of Duplex Steel, 3rd ed. International Molybdenum Association (IMOA), (2014), 4, London.
- [5] Brühl S. P, Charadia R, Sanchez C., Staia M. H., Wear Behavior of Plasma Nitrided AISI 420 Stainless Steel', *International Journal of Materials Research*, **99** (2008), 779-86.
- [6] Gowtam D.S., Ziyauddin M., Mohape M., Sontakke S.S. , Deshmukh V.P., . Shah A.K., In Situ TiC-Reinforced Austenitic Steel Composite by Self-Propagating High Temperature Synthesis, *International Journal of Self-Propagating High-Temperature Synthesis*, **16** (2007), 70-78.
- [7] Lee J., Euh K., Oh J. C., Lee S., Microstructure and Hardness Improvement of TiC/Stainless Steel Surface Composites Fabricated by High-Energy Electron Beam Irradiation, *Materials Science and Engineering: A*, **323** (2002), 251-59.
- [8] Li B., Liu Y., Li J., Cao H., He L., Effect of Sintering Process on the Microstructures and Properties of in situ TiB₂-TiC Reinforced Steel Matrix Composites Produced by Spark Plasma Sintering, *Journal of Materials Processing Technology*, **210** (2010), 91-95.
- [9] Pagounis E., Lindroos V.K., Processing and properties of particulate reinforced steel matrix composites. *Materials Science and Engineering A*, **246** (1998), 221-234
- [10] Cheng F., Kwok C., Man H., Laser surfacing of S31603 stainless steel with engineering ceramics for cavitation erosion resistance. *Surface and Coatings Technology*, **139**(1) (2001), 14-24.
- [11] Lin S., Xiong W., Microstructure and abrasive behaviors of TiC-316L composites prepared by warm compaction and microwave sintering. *Advanced Powder Technology*, **23**(3) (2012) 419-425.
- [12] Li B., Liu Y., Cao H., He L., Li J., Rapid Fabrication of in situ TiC Particulates Reinforced Fe-Based Composites by Spark Plasma Sintering, *Materials Letters*, **63** (2009), 2010-2012.
- [13] De Jonghe L.C, Rahaman M.N., Sintering of Ceramics, Handbook of Advanced Ceramics, Somiya et al. (Eds) (2003), 187-264.
- [14] Suárez M., Fernández A., Kessel H.U, Hennicke J., Menéndez J.L., Kirchner R., Torrecillas R., Kessel T., *Challenges and Opportunities for Spark Plasma Sintering: A Key Technology for a New Generation of Materials* INTECH Open Access Publisher, (2013).

Comparison of measurement results obtained from three different calibration systems for performing accelerometer calibration

M L Temba, V Tyalimpi

National Metrology Institute of South Africa, Acoustics, Ultrasound and Vibration Laboratory, Private Bag X34, Lynnwood Ridge, 0040, South Africa

Abstract. The vibration laboratory of the National Metrology Institute of South Africa (NMISA) has recently acquired new low frequency exciters, in replacing the old low frequency exciters. These exciters are to be used with the secondary vibration calibration system to disseminate measurement in low frequency ranges down to 0.2 Hz, on the secondary level. A study wherein the calibration results (from the three different laboratory systems) were compared has been undertaken in order to establish how well the new secondary system performed. Calibration measurement results from three different laboratories that used different calibration methodologies, i.e. methods in compliance to ISO 16063-11 and ISO 16063-21 standards, and systems were compared. A transducer that was calibrated at SPEKTRA and at NMISA using the primary calibration method was used as the transfer standard to compare with the results obtained using the new secondary setup. The results showed that the new secondary system performed quite well, with its results agreeing with those from the other laboratories, at primary level, to within at least 90%. This was illustrated by the values of the Pearson correlation coefficient r and the p -values.

1. Introduction

When re-calibrating an accelerometer for sensitivity and phase response as a function of frequency, the resonance frequency of the transducer should be included in the range of frequencies to be tested. This can be a challenge to the calibration laboratories that try to perform a calibration with minimised measurements uncertainty in a cost effective manner.

Two categories of accelerometer calibration applicable to vibration measurements; primary and secondary, were utilized. By definition, primary calibration provides direct traceability of a measurement to international recognised fundamental or derived units for physical quantities [2]. Secondary calibration, in contrast, uses a reference transducer, which itself has been calibrated and traceable to a primary standard [3]. It therefore, follows that secondary calibration will have uncertainties of measurement that are larger than primary calibrations, since every step in the calibration chain adds to uncertainty of measurement (UOM).

Recently the secondary vibration laboratory of the Acoustics, Ultrasound and Vibration has acquired a full medium frequency vibration system in replacement of an aging system they had. This new vibration system has brought a great improvement as it covers a wider frequency range of 3 Hz to 10 kHz, better than the previous system that could only cover ranges from 10 Hz to 10 kHz.

Additionally, two low frequency exciters (horizontal APS 113 and vertical APS 113, see Figure 1) were purchased to improve the laboratory capability in covering the low frequencies ranges. The two

exciters couple with the medium frequency system, expanding the frequency range in order to make measurements from 0.2 Hz up to 200 Hz, overlapping with the medium frequencies.

Two low frequency accelerometers were selected for the experiment, in order to verify and commission the low frequency exciters used with the medium vibration system. The measurement results obtained from the manufacturer SPEKTRA on both accelerometers were considered and compared to the measurement results obtained from the NMISA primary and secondary laboratories, in the range of 0.2 Hz up to 63 Hz.

2. Transfer Standards

Two back-to-back capacitive accelerometers (listed in Table 1) coupled with power amplifier units were selected to be used for the work. Accelerometer B forms part of the low frequency exciters recently acquired, with A already in use as a low frequency standard in the primary laboratory. Both accelerometers were initially calibrated by SPEKTRA before they were supplied to NMISA.

Table 1. Accelerometers used for the comparison, with B used as a transfer standard for A.

<i>Accelerometer</i>	<i>Lab ID</i>	<i>Manufacturer</i>	<i>Model Number</i>	<i>Serial Number</i>
<i>A</i>	VS-STD-08	PCB	3701G2FA3G	8790
<i>B</i>	VS-STD-21	PCB	3701G2FA3G	8973

Accelerometer B, was used as reference standard (REF) on the secondary system (Horizontal APS 113, Figure 1) while accelerometer A was used as the unit under Test (UUT). Various combinations of inter-calibration were used to verify the system using the low frequency exciters in the horizontal configuration.

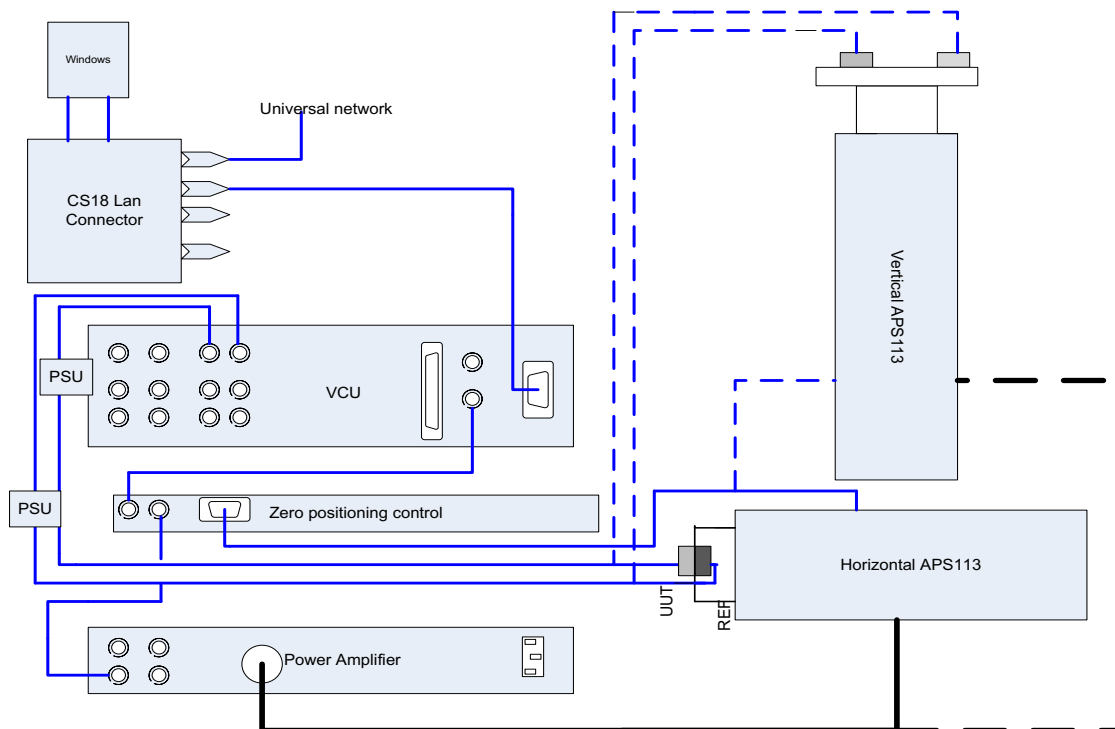


Figure 1. Secondary calibration system schematic.

3. Calibration System

Discussion about accelerometer calibration often refers primarily to the measurement of voltage sensitivity over a certain frequency range. The most commonly used way to calibrate accelerometer sensitivity is by comparison to a reference transducer, generally another accelerometer designed to have stable low noise sensitivity in the conditions of calibration. This secondary method is performed by back-to-back measurements, typically as a stepped sinusoid across an appropriate frequency range. The UUT is mounted in a back-to-back arrangement against a reference accelerometer and both sensors are subjected to a common mechanical excitation (see Figure 2). Since the motion input is assumed the same for both devices, the ratio of their outputs is also the ratio of their sensitivities, and the UUT sensitivity can be expressed by the following equation:

$$S_{uut} = S_{ref} \cdot \left(\frac{U_{uut}}{U_{ref}} \right) \cdot \left(\frac{G_{ref}}{G_{uut}} \right) \quad (1)$$

where:

S_{uut} is the UUT sensitivity in mV/g, mV/(m· s⁻²), pC/g or pC/(m· s⁻²),

S_{ref} is the reference transducer sensitivity in mV/g, mV/(m· s⁻²), pC/g or pC/(m· s⁻²),

U_{ref} is the reference channel output voltage in mV,

U_{uut} is the UUT channel output voltage in mV,

G_{uut} is the UUT conditioner gain in mV/mV or mV/pC,

G_{ref} is the reference conditioner gain in mV/mV or mV/pC.

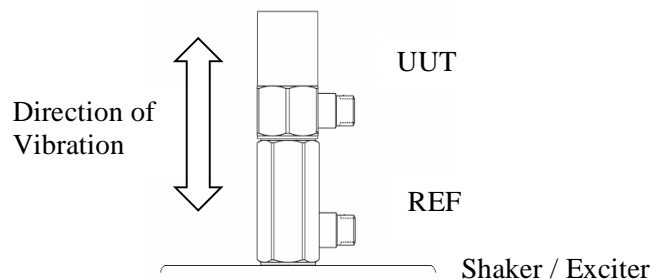


Figure 2. The back-to-back accelerometer calibration setup.

Accelerometer calibrations in the primary laboratories are performed using the primary calibration methods, with laser interferometry, in compliance with ISO 16063-11 method number three (Sine approximation method) [2]. The transducer is exposed to the sinusoidal acceleration which is applied by means of an electrodynamic vibration exciter. The output of the transducer is compared to the acceleration measured with the laser vibration meter on the exciter's surface.

4. Calibration results

4.1. SPEKTRA results

As per ISO 17025 requirement and best metrology practice, all new measurable equipment purchased shall be supplied with a calibration supporting documents, as such the selected accelerometers that were used for the exercise had calibration certificates from the supplier. These results are identified as SPEKTRA results (see Figure 3).

4.2. NMISA Primary vibration laboratory results

Upon receiving any system or measuring equipment from supplier, the system needs to be verified and calibrated as part of the system commissioning and maintenance procedure. The two accelerometers

(VS-STD-08 and VS-WSTD-21) were also verified in the primary laboratory. The VS-STD-08 results obtained from primary calibration were also considered for the exercise (see Figure 4).

4.3. NMISA Secondary vibration laboratory results

The secondary vibration laboratory used the CS18 medium frequency system coupled with the new low frequency vibration exciter and VS-WSTD-21, as the reference standard, in calibrating VS-STD-08. The results obtained are used for the performance comparison of the system and are illustrated in Figure 5.

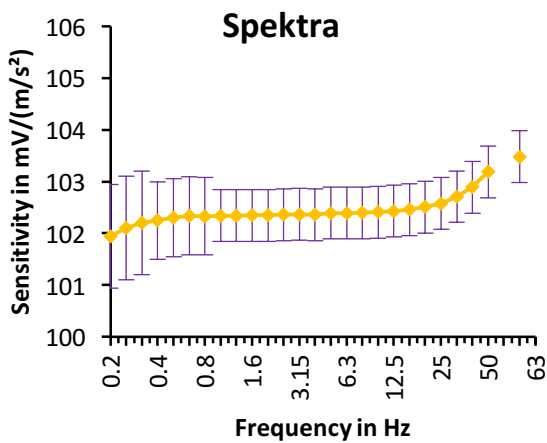


Figure 3. VS-STD-08 sensitivity values from a SPEKTRA calibration certificate plotted against frequency, with uncertainties overlaid as error bars.

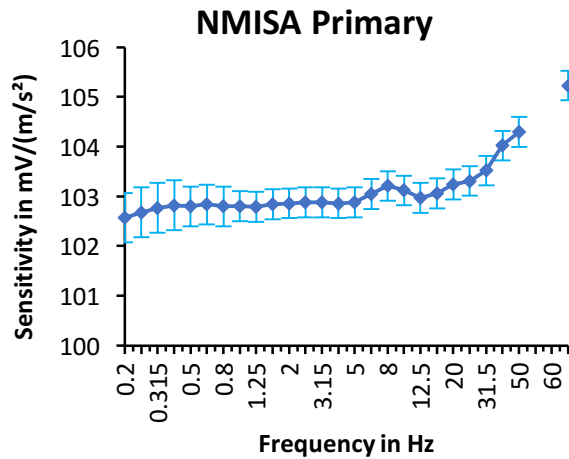


Figure 4. VS-STD-08 sensitivity values from a NMISA primary vibration laboratory calibration certificate plotted against frequency, with uncertainties overlaid as error bars.

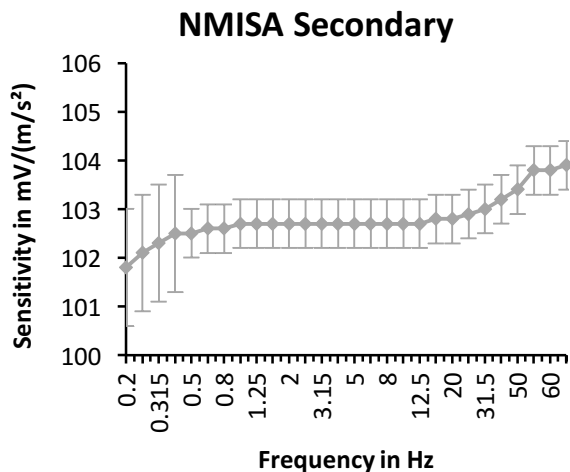


Figure 5. VS-STD-08 sensitivity values from a NMISA secondary vibration laboratory calibration certificate plotted against frequency, with uncertainties overlaid as error bars.

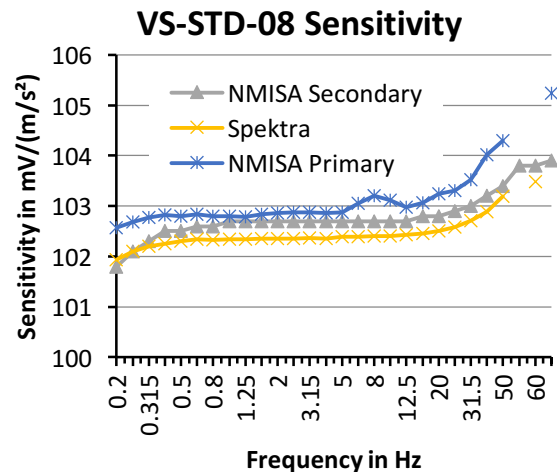


Figure 6. Sensitivities of the VS-STD-08 accelerometer plotted as a function of frequency, obtained from three different laboratories; SPEKTRA, NMISA primary and secondary vibration laboratories.

Figure 6 illustrates overlaid graphs of sensitivity measurements of the vibration’s laboratory standard accelerometer VS-STD-08 from the three laboratories plotted against frequency. The results from the SPEKTRA and NMISA primary vibration laboratory are illustrated with the blue and yellow graphs respectively. The grey graph represent the results obtained from the NMISA secondary vibration laboratory. For this set of results, a laboratory working standard accelerometer VS-WSTD-21, traceable to SPEKTRA, was used as a transfer standard.

4.4. Correlation

Results from the three laboratories were then plotted against one another to try and establish any linear relationship between the results obtained from the different laboratories. Figures 7 to 9 illustrate such relationships. Equation (2) was used to calculate the Pearson correlation coefficient r between a pair of data from the three laboratories.

$$r = \frac{\sum_{i=1}^n (x_i - \bar{x})(y_i - \bar{y})}{\sqrt{\sum_{i=1}^n (x_i - \bar{x})^2} \sqrt{\sum_{i=1}^n (y_i - \bar{y})^2}} \quad (2)$$

The r values between the results of the VS-STD-08 from the NMISA secondary laboratory and those from SPEKTRA and NMISA primary laboratory were found to be 0.96 and 0.90, respectively, an indication of a very strong linear relationship between the datasets. A significance test was performed on the r values to establish confidence that these values were indeed significantly different from zero ($p < 0.001$).

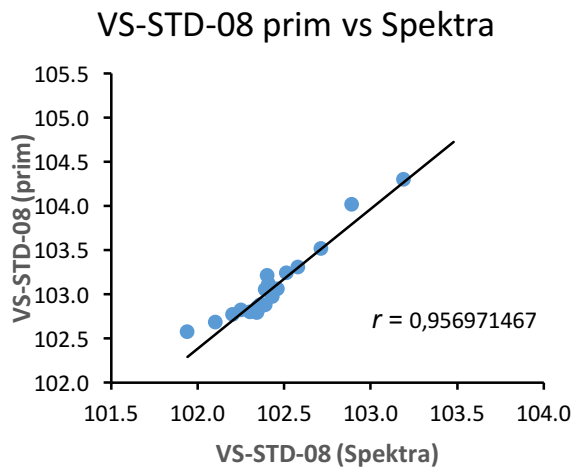


Figure 7. A comparison of VS-STD-08 sensitivity measurements from SPEKTRA and NMISA primary vibration laboratory with the correlation coefficient r displayed.

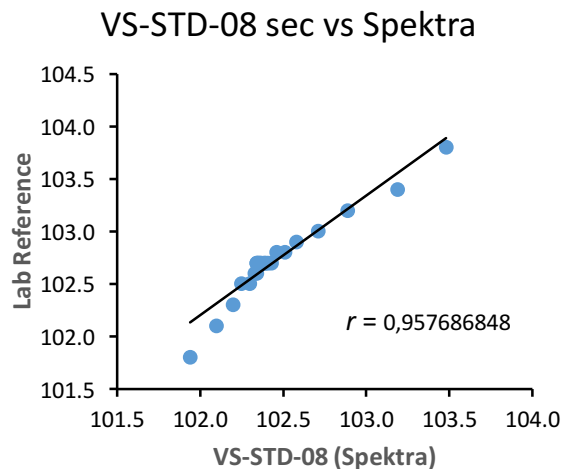


Figure 8. A comparison of VS-STD-08 sensitivity measurements from SPEKTRA and NMISA secondary vibration laboratory with the correlation coefficient r displayed.

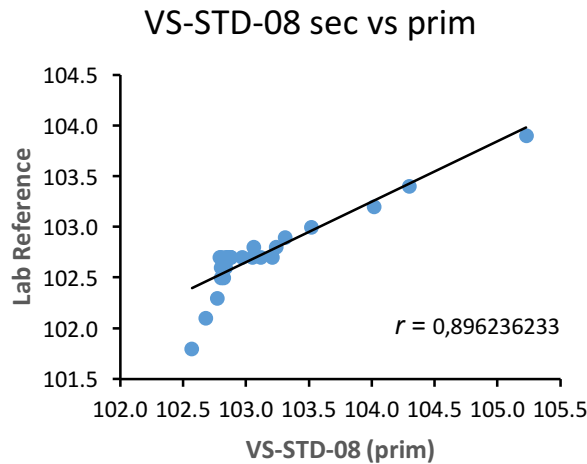


Figure 9. A comparison of VS-STD-08 sensitivity measurements from NMISA primary and secondary vibration laboratories, with the correlation coefficient r displayed.

5. Discussion and conclusion

A vibration laboratory standard accelerometer was calibrated in three different laboratories. Figure 6 shows a similar trend observed from all three graphs with the difference less than 1.5% between the furthest points. This agreement is further emphasised by the correlation coefficients displayed on Figures 7, 8 and 9. The correlation results indicated that the strength of association between the variables is very high ($r \geq 0.90$), and that the correlation coefficients are significantly different from zero ($p < 0.001$). This linear relationship is also visually observed on these figures. The deviations observed at lower frequencies (or lower sensitivity values) could be attributed to the transverse motion due to the different mounting techniques of the three different systems.

From the exercise, two objectives were attained. The low frequency results from the three laboratories using different systems and methods; SPEKTRA, NMISA Primary vibration laboratory using a primary calibration method and NMISA secondary laboratory using a back-to-back method, were found to be comparable. The verification of the newly acquired low frequency exciter coupled to the medium vibration system has been successfully achieved. Based on this work, the low frequency measurements capability in the range of 0.2 Hz to 63 Hz from the secondary vibration laboratory was assessed and approved by South African National Accreditation System (SANAS) for accreditation.

Therefore, the back to back method is a valid method to be used in the secondary laboratories, for low frequency measurements, with the results comparable to those of the primary laboratories.

References

- [1] Davis, K.E. 2001. "Vibration - Performing back to back calibration." Test and Measurements. Conference Digest.
- [2] ISO 16063-11. 1999. "Methods for the calibration of vibration and shock transducers - Part 11: Primary vibration calibration by laser interferometry."
- [3] ISO 16063-21. 2003. "Methods for the calibration of vibration and shock transducers - Part 21: Vibration calibration by comparison to a reference transducer."

How local conditions affect solar irradiance and photovoltaic module performance in South Africa

H Winkler

Department of Physics, University of Johannesburg, PO Box 524, 2006 Auckland Park, Johannesburg, South Africa

E-mail: hwinkler@uj.ac.za

Abstract. Solar power generation efficiency is not only a function of the detector technology and configuration, but also depends on the amount, spectral distribution and angular profile of sunlight at ground level. This paper reviews some common techniques used to estimate the solar photon field at its interface with the detector. It examines the suitability of the associated light transmission and scattering models from a physical perspective under atmospheric conditions representative of the dry South African western plateau (where most local solar power stations are planned to be sited). The article concludes with a presentation of a simple ground-level spectral irradiance model formulation specific to South African condition that is readily adaptable to site conditions. Applied to the configuration and spectral responsiveness of a solar device this model is expected to yield better estimates of electricity generation than many internet-based tools commonly used for this purpose.

1. Introduction

South Africa is witnessing a massive growth in its solar energy generation capacity. This is manifested both by the construction of large solar power stations, as well as small scale installations such as rooftop photovoltaic modules and solar heaters [1].

Much research effort has been directed towards the achievement of greater energy solar conversion efficiency in the employed technologies, as well as improving the cost efficiencies. In comparison, relatively little work has focused on the determination of the available ground-level radiation and its spectral properties. The effect that these factors have on the determination of the energy yield of a solar power device is often not fully appreciated. The characteristics of the ground-level solar radiation are determined by the interplay between the solar photons and the atmosphere. The nature of the latter is to a significant degree location dependent, and also exhibits seasonal trends.

Atmospheric models used in solar irradiance calculations therefore need to be adapted to local circumstances, and this has only been done on a limited scale in South Africa. This paper seeks to summarize the main factors to be considered, and suggests parameters considered suitable for use in local irradiance modeling.

2. Theory

The solar irradiance measured at ground level is a function of both the solar zenith angle ζ (i.e. the angle the solar beam makes with the vertical), the height h of the site above sea level and the composition of the atmosphere above the site.

First and foremost, the zenith angle, in conjunction with a module tilt angle, determines the so-called cosine losses of the incident radiation [2]. Other physical parameters significant for such a study are summarized in the following sub-sections.

2.1. Airmass

The airmass m [3] represents the relative atmosphere traversed by the unscattered solar beam to reach ground level. It is measured in units of the equivalent of the medium crossed along the vertical path from the outer atmosphere to sea level. Therefore if the solar zenith angle is 0° at sea level, then $m = 1$. It is easy to show geometrically that for other zenith angles the airmass may be approximated by

$$m \cong \sec \zeta$$

The formulation above requires the assumption that we make a local ‘flat Earth’ approximation, as otherwise the Earth curvature causes this expression to gradually diverge from the true airmass with increasing ζ . For locations above sea level, the amount of atmosphere above the site is smaller. The fraction of atmosphere compared to the sea level atmosphere is sufficiently accurately described by the pressure ratio p/p_0 , where p is the site atmospheric pressure and p_0 is the corresponding quantity at sea level. A good approximation of the atmospheric pressure as a function of h (when measured in meters) is given by the barometric formula

$$p = p_0 \exp(-h/8400) .$$

2.2. Optical thickness

The optical thickness indicates the degree to which a beam of light is attenuated when traversing a medium. If σ is the solar irradiance at the top of the atmosphere and the transmitted fraction is given by ϕ , then the direct beam irradiance I recorded at the solar power generating site is

$$I(\lambda) = \sigma(\lambda)\phi(\lambda, m) = \sigma(\lambda) \exp(-m\tau(\lambda))$$

The factor τ is a measure of the atmospheric turbidity, and is referred to as the optical depth. It turns out that this factor is the algebraic sum of the partial optical depths for each of the constituents accounting for atmospheric light beam attenuation:

$$\tau(\lambda) = \tau_R(\lambda) + \tau_O(\lambda) + \tau_G(\lambda) + \tau_W(\lambda) + \tau_A(\lambda)$$

where the subscripts represent Rayleigh scattering, ozone, other gases, water vapour and aerosols respectively, and these quantities may further be designated as follows [4].

- The Rayleigh optical thickness is strongly wavelength dependent, with $\tau_R(\lambda)$ very nearly proportional to λ^{-4} and the quantity otherwise only dependent on near-constant atomic parameters.
- The ozone optical thickness $\tau_O(\lambda)$ is very high at the violet end of the optical spectrum, but relatively insignificant at other wavelengths. It is a function of the atmospheric ozone concentration, which undergoes annual oscillations with an overall downward trend.
- The near-constant trace gas optical thickness $\tau_G(\lambda)$ includes the contributions due to spectral absorption by atmospheric gases such as N_2 , O_2 , CO_2 and CH_4 . Only very few of these transitions are in the spectral range to which photovoltaic modules are sensitive.
- The water vapour optical thickness $\tau_W(\lambda)$ is a function of the amount of water vapour above a site, which is strongly dependent on meteorological conditions.
- The aerosol optical thickness $\tau_A(\lambda)$ depends on the particle type, size and optical properties in addition to the particle concentration. It is frequently parameterized in the form $\tau_A = \beta\lambda^{-\alpha}$, where β becomes a measure of the concentration, while α , which ranges between 0 and 4, becomes an indicator of the other aerosol properties. There have been determinations of representative α

values for common aerosol types, but these are associated with considerable uncertainty [5]. Atmospheric aerosols depend on processes and conditions at the sources of generation, as well as meteorological factors, and therefore this term is the most difficult to model. This term is as a result also the greatest contributor to uncertainty in the scattered light contribution.

2.3. Scattered light

In addition to photons from the direct solar beam, photovoltaic modules also receive a fraction of their incoming radiation from skylight, i.e. from photons deflected by scattering events elsewhere in the sky. This component is referred as the diffuse irradiance. The characteristics of this diffuse component thus also depend on local conditions.

The number of scattering events depends on the optical thickness for each attenuating process. In addition, one needs to look at the distribution of the angle of deflection for the scattering process. We can here differentiate between scattering due to small particles, and that involving larger particles.

When the scattering centre is significantly smaller than the wavelength, the beam experiences Rayleigh scattering for which the distribution of the scattering angle θ is described as follows:

$$\Phi_R(\theta) \propto (1 + \cos^2 \theta)$$

When however the particle size becomes comparable to the wavelength, the scattering process is referred to as Mie scattering, and the angular distribution probability is determined by the Henyey-Greenstein function [6]

$$\Phi_A(\lambda, \theta) \propto \frac{1 - g(\lambda)^2}{(1 + g(\lambda)^2 - 2g(\lambda)\cos\theta)^{3/2}},$$

where the asymmetry factor g depends on the particle type, but is normally in the range $0 < g < 1$.

3. PV module calibration procedures

Photovoltaic modules are rated according to illumination tests usually performed under laboratory conditions. In order to standardize the testing, the convention has been adopted to approximate the insolation conditions on the module as follows.

- The spectral distribution of the incident light should match what has become known as the AM1.5 spectrum, which has been adopted as a standard by the American National Renewable Energy Laboratory (NREL). It is supposed to approximate the sea level solar spectrum for an airmass 1.5 solar beam under typical conditions for that country.
- Furthermore, the total radiative power incident on the module should amount to 1 kW m^{-2} at a 90° angle to the surface.
- The PV module must be maintained at a temperature of 25°C throughout the test.

In practice it is practically impossible to reproduce the spectral characteristics of the solar spectrum in a laboratory. Hence lamps with different types of spectra are used, which must then be periodically calibrated against measurements of real sunlight, to ensure that the lamp calibrations can provide a realistic total (rather than spectral) measure of the power converted to electricity by the module.

4. Parameters appropriate for South African conditions

The irradiation of solar modules in South African conditions differs from the calibration environment in the following important respects. The local latitudes are such that the solar zenith angle near mid-day is smaller than for the northern mid-latitudes where the biggest concentrations of solar power installations are found. Much of South Africa also sits on a plateau, and large parts of the country are considered semi-arid as a result of low cloud frequencies. The vast oceanic areas to the west, east and south of the country contribute to overall lower concentrations of aerosols associated with fires, dust and human activity.

4.1. The characteristic airmass

The solar airmass is constantly varying with the changing solar position throughout the day, and the solar track across the sky is seasonally dependent. It is possible to determine a characteristic (daylight) solar airmass at a location by tracing the solar zenith angle as a function of time, and determine the median value of ζ over successive fixed time intervals. Multiplying this with the site relative zenith airmass (given by p/p_0), this leads to this representative site airmass value. Table 1 lists these values in the fourth column for a series of sites of interest, together with their geographical latitudes and altitudes above sea level. The first such site is the city of Washington in the USA, which is included here for comparison purposes. Then the table lists the three major South African urban centres. The final six rows in Table 1 present six of the new South African solar power plants (chosen to provide a wide spread in regional location and latitude).

Utilising the airmass values determined in this manner is slightly misleading for the type of analysis being carried out here. Crucially, the total amount of solar power collected is in most circumstances significantly lower when the Sun approaches the horizon (i.e. when ζ approaches 90°). This is particularly the case when photovoltaic technologies are employed that do not involve tracking the solar part. Even when this is the case though, the total light reaching the solar module becomes less at high zenith angles due to the greater atmospheric light losses.

If we analyse the case where PV modules are placed horizontally, the angle θ that the normal to the PV module makes with the solar beam becomes identical to ζ . If we ignore the decreasing transmissivity of the atmosphere at high ζ , and only apply the so-called cosine losses resulting from a misalignment of the module with the Sun, we find that the amount of solar energy collected is then equal to $\cos\theta$. It is therefore far more appropriate to introduce a weighting factor equal to $\cos\theta$ in our calculation of the average airmass. The weighted average airmass m_{weighted} was therefore determined using the formula

$$m = \frac{p}{p_0} \sec \left[\frac{\int_{\text{year}} \zeta(t) \cos\theta(t, \theta = \zeta) dt}{\int_{\text{year}} \cos\theta(t, \theta = \zeta) dt} \right].$$

This value has also been calculated for all the sites in Table 1, and is given there in the final column. It is probably not surprising that the value of this quantity for Washington DC amounts to almost exactly 1.5, which explains the choice of the AM1.5 model for the United States.

Table 1. Latitude and altitude for selected sites, together with average and weighted airmasses.

Site	Latitude ($^\circ$)	Altitude (m)	$(p/p_0)\sec\langle\zeta\rangle$	m_{weighted}
Washington DC, USA	+38.889	9	1.923	1.502
Johannesburg CBD	-26.198	1732	1.364	1.104
Cape Town CBD	-33.930	27	1.806	1.433
Durban CBD	-29.859	8	1.732	1.390
Soutpan Solar (Limpopo)	-22.992	827	1.480	1.206
RustMo Solar (Marikana)	-25.738	1223	1.443	1.169
Kathu Solar	-27.601	1142	1.481	1.195
Khi Solar (Upington)	-28.540	839	1.549	1.247
Ilanga Lethemba (De Aar)	-30.595	1253	1.505	1.205
Vredendal Solar	-31.634	110	1.743	1.392

The South African sites however have significantly lower weighted average airmasses, due to their more equatorial latitudes and because of the high altitude of the South African plateau. This confirms that the AM1.5 is not the optimal spectral representation for South African conditions. A solar spectrum corresponding to $m \sim 1.25$ would be more typical of the irradiance experienced.

4.2. Ozone layer differences

The thickness of the ozone layer varies seasonally, with a minimum being recorded annually during the spring. Furthermore, the ozone concentration is also a function of latitude. In the polar regions of the southern hemisphere the layer can become particularly depleted, a phenomenon that has been termed the “ozone hole”.

The ozone optical depth is therefore often lower in South Africa than it would be in some northern hemisphere countries. This discrepancy is however only of minor significance, as the ozone mainly affects the light at the shortest wavelengths, which is in any case less likely to traverse the atmosphere, and also corresponds to that part of the spectrum to which a photovoltaic device is least sensitive.

4.3. Water vapour

Water vapour concentration in the atmosphere is strongly variable. It tends to be higher at tropical latitudes. While this is also true at high altitude over South Africa, humidity is low compared to other localities at ground level at most of the sites at which solar farms have been constructed – these are for obvious reasons preferentially set up in the most sunny and dry places.

Another factor worth noting when discussing the role of water vapour in solar energy is that the water vapour optical depth is highly wavelength dependent, and mainly affects the infrared. Most photovoltaic modules however do not absorb significant amounts of light from that part of the spectrum, as the really strong water vapour absorption features are all found redwards of 1 micron.

Because of this, and due to the strong variability, no quantification of any systematic differences in water vapour concentration over South Africa as opposed to conditions resulting in the AM1.5 spectrum will be attempted here.

4.4. Aerosols over southern Africa

Previous atmospheric studies have determined that aerosol loading over South Africa is low compared to other parts of the world [7,8,9]. Solar power stations have usually been constructed in the country’s interior, away from urban areas. At such locations atmospheric aerosol loading is generally only affected by dust at ground level and by seasonal biomass burning smoke residue at greater altitudes. In particular, aerosol turbidity due to the burning of vegetation occurs at the end of the winter dry season. It is only then that a higher aerosol optical depth is appropriate for irradiance calculations in South Africa.

The aerosols also play a crucial role in determining the diffuse irradiance. The fraction of the diffuse spectrum due to Rayleigh scattering is a function of solar position and height above sea level only. This is reproduced to a high degree of accuracy over time, and the scattered radiation from any particular part of the sky, at any specific time can be determined well using the Rayleigh scattering function. The diffuse fraction related to aerosols is however far more variable, depending not only on the concentration, but also on the aerosol scattering properties, such as the asymmetry factor g . A highly reliable South African solar irradiance model would need to incorporate that aspect.

4.5. The South African optimal ground level solar spectrum

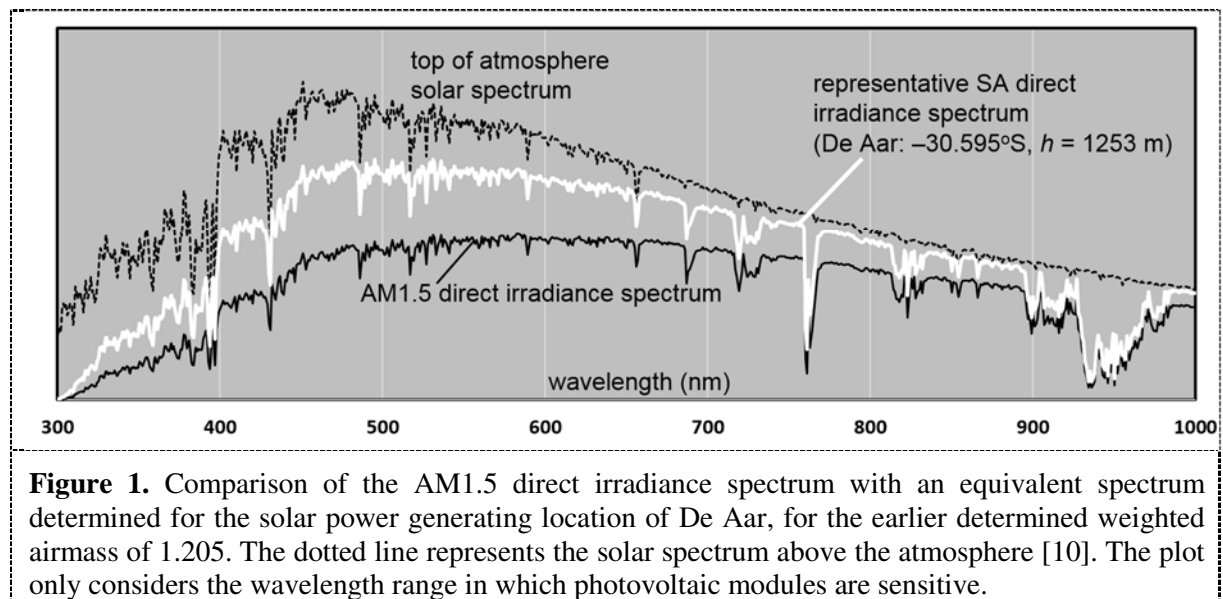
As an illustration, this paper presents a concrete example of a representative South African ground-level solar spectrum. It has been determined for the central town of De Aar, near which numerous solar power stations are being constructed, and for which typical aerosol concentrations and optical properties have been previously derived with some confidence [9].

Figure 1 displays the direct irradiance spectrum for $m = 1.205$ earlier tabulated as best describing that site, with $\beta = 0.021$ [8,9] and other transmittances as in [4]. Also plotted there is the direct irradiance part of the AM1.5 spectrum as well as the solar irradiance at the top of the atmosphere. The much greater

direct irradiance for De Aar is striking, and corresponds to a far higher solar yield for concentrated solar power technologies, which only process direct sunlight.

If a module spectral response function resembling an ideal PV cell (proportional to λ and zero beyond a cutoff set at 1 μm) is used, the comparative power increase achieved through illumination by a hypothetical AM1.205 lamp relative to the AM1.5 standard lamp was determined to be 34%.

For photovoltaic modules one must however also include the diffuse light contribution, i.e. the scattered radiation manifesting itself as skylight. This diffuse contribution increases with greater direct beam attenuation due to Rayleigh and aerosol scattering, the end result being that the global AM1.5 spectrum used for module characterization does not differ from the typical South African total irradiance spectrum by as much as figure 1 suggests.



5. Conclusion

PV modules in South Africa slightly exceed their suggested power ratings. The relative improvement factor is however much dependent on the time of measurement, module tilt, the presence and nature of module tracking mechanisms and current aerosol and water vapour characteristics. The projected solar installation power yield at a specific time and place can only be determined with confidence through calculation and projection of the appropriate ground-level solar spectrum onto a particular device. The mere crude application of the PV module power rating will produce a far less reliable energy yield.

References

- [1] Walwyn D R, Brent A C 2015 *Renewable and Sustainable Energy Reviews* **41** 390
- [2] Chang T P 2009 *Solar Energy* **83** 1274
- [3] Kasten F, Young A T 1989 *Applied Optics* **28** 4735
- [4] Gueymard C A 2001 *Solar Energy* **71** 325
- [5] Dubovik O, Holben B, Eck T F, et al. 2002 *J. Atmos. Sciences* **59** 590
- [6] Kocifaj M 2012 *Solar Energy* **86** 3575
- [7] Formenti P, Winkler H, Fourie P, Piketh S, Makgoba B, Helas G and Andreae M O 2002 *Atmospheric Research* **62** 11
- [8] Power H C, Willmott C J 2001 *Int. J. Climatology* **21** 579
- [9] Winkler H, Formenti P, Esterhuysen D J, Swap R J, Helas G, Annegarn H J and Andreae M O 2008 *Atmos. Environment* **42** 1169
- [10] Gueymard C A 2004 *Solar Energy* **76** 423

*Division G – Theoretical and
Computational Physics*

Probing quark gluon plasma in pA collisions

D M Adamiak^{1,2}, W A Horowitz¹

¹Department of Physics, University of Cape Town, Private Bag X3, Rondebosch 7701, South Africa

E-mail: ² daniel.m.adamiak@gmail.com

Abstract. We present novel predictions for the suppression of high momentum particles in high multiplicity proton-nucleus (pA) collisions at LHC. Shocking recent data from LHC demonstrates that high multiplicity pA collisions show signatures of the formation of a quark-gluon plasma (QGP), thought previously to only result from nucleus-nucleus collisions. Our work provides a new test of this QGP creation hypothesis.

We generate our predictions by first computing the initial spectrum of high momentum quarks and gluons using leading order (LO) perturbative quantum chromodynamics (pQCD). These LO pQCD predictions use both the usual parton distribution functions (PDFs) and nuclear PDFs, which encapsulate the modifications of the usual PDFs by the presence of multiple nucleons in a nucleus. We find that our results consistently describe the $p\bar{p}$ data at Fermilab, across multiple orders of magnitude in centre of mass energy \sqrt{s} , and over many orders of magnitude in transverse momentum. Next we implement state-of-the-art LO pQCD energy loss including radiative and collisional modes through a dynamical QGP medium. Finally, the particles are fragmented into hadrons and compared to the spectrum of high momentum particles in minimum bias pp collisions for future comparison with experimental data.

1. Introduction

Experiments from RHIC[1] and Cern[2] reveal a new state of matter that allow us to probe quantum chromo-dynamics (QCD). This state of matter is the quark-gluon-plasma (QGP). It occurred micro-seconds after the big-bang[3] and arises due to the emergent, many-body physics of QCD[4]. Successfully predicting and understanding QGP will give us an insight into these processes.

The primary mechanism by which we will investigate QGP is that of parton pair production on near the edge of the QGP medium[5]. When partons are pair-produced, by conservation of momentum, they scatter back-to-back. One parton escapes the QGP quickly and forms a jet largely unmitigated by the presence of a medium. The second parton has to travel through medium, where it undergoes radiative[6] and collisional[7] energy loss via interactions with the medium, eventually forming a jet with much lower energy than the first. These two jets may be compared, where the energy loss between the two may be used to deduce properties of the medium.

There are two prerequisites to performing energy-loss calculations. The first is that any and all non-energy-loss effects need to be under good theoretical control in order to not conflate between disparate effects. In particular, since there is strong evidence of QGP in nucleus nucleus collisions[8], the nuclear effects of interacting partons that arise from nuclei need to be taken

into account. To the end of setting up this good theoretical control, careful analysis of proton anti-proton and proton nucleus collisions are presented.

The second prerequisite is that energy-loss calculations can only be performed for partons with known momenta. Therefore it is critical to obtain the spectra for the outgoing partons in these collisions. These spectra are also known as the partonic contributions to the total cross-section.

In this work we satisfy these two conditions, laying the groundwork for exploration into energy-loss, not only in nucleus nucleus collisions, but proton nucleus and proton proton collisions as well.

2. Leading Order pQCD Calculations

Using formulae derived from perturbative QCD (pQCD), we intend to calculate the inclusive spectra of charged hadron production from proton anti-proton and proton nucleus collisions. We also intend to lay the groundwork for energy-loss calculations that can be used to determine the presence of QGP in collider experiments.

This is done by calculating the differential cross-section of charged hadron production from these collisions, which has the following structure

$$\text{cross-section} = \text{PDF} \times \text{partonic cross-section} \times \text{energy-loss} \times \text{fragmentation}$$

where the terms on the right-hand side each describe a phase in the collision. The PDF (parton distribution function) describes partons incoming from their respective hadrons. The partonic cross-section describes the probability of them interacting in a particular way, e.g. the likelihood of two gluons scattering into a quark anti-quark pair. After the parton scattering, the outgoing partons may then lose energy in the presence of a medium and it is this aspect of collisions by which we aim to probe the QGP. Finally, the outgoing partons fragment into hadrons.

It is vital to get the PDF and partonic cross-section correct in isolation, because they feed directly into the energy-loss and fragmentation. In other words, it would be impossible to discern effects due to energy-loss in isolation until we have a comprehensive understanding of all the non-energy-loss effects present in these heavy-ion collisions. To that end, we need to study collisions where we do not expect energy-loss or the presence of a medium. Proton anti-proton collisions serve this purpose. We also need to study nuclear effects, the difference in behaviour of partons that come from nuclei as opposed to single protons. The study of proton nucleus collisions serve this.

More details of each constituent to the cross-section are given in the next section.

2.1. $p\bar{p}$ collisions

Using Mathematica, we calculate the inclusive differential cross-section for production of a charged hadron h at a rapidity y from an proton anti-proton ($p\bar{p}$) collision. The expression for this cross-section, derived using pQCD, is given in [9]

$$\begin{aligned} \frac{d\sigma^{AB \rightarrow h+X}}{dq_T^2 dy} &= K(\sqrt{s}) J(m_T, y) \int \frac{dz}{z^2} \int dy_2 \sum_{\langle ij \rangle \langle kl \rangle} \frac{1}{1 + \delta_{kl}} \frac{1}{1 + \delta_{ij}} \times \\ &\times \left\{ x_1 f_{i/A}(x_1, Q^2) x_2 f_{j/B}(x_2, Q^2) \left[\frac{d\hat{\sigma}^{ij \rightarrow kl}}{d\hat{t}}(\hat{t}, \hat{u})_{k \rightarrow h} D(z, \mu_F^2) + \frac{d\hat{\sigma}^{ij \rightarrow kl}}{d\hat{t}}(\hat{u}, \hat{t})_{l \rightarrow h} D(z, \mu_F^2) \right] \right. \\ &\left. + x_1 f_{j/A}(x_1, Q^2) x_2 f_{i/B}(x_2, Q^2) \left[\frac{d\hat{\sigma}^{ij \rightarrow kl}}{d\hat{t}}(\hat{u}, \hat{t})_{k \rightarrow h} D(z, \mu_F^2) + \frac{d\hat{\sigma}^{ij \rightarrow kl}}{d\hat{t}}(\hat{t}, \hat{u})_{l \rightarrow h} D(z, \mu_F^2) \right] \right\} \end{aligned} \quad (1)$$

where y_1 and y_2 are the rapidities of the final-state partons, k and l . The momentum fractions of the incoming partons are given by $x_1 = \frac{p_T}{\sqrt{s}}(e^{y_f} + e^{y_2})$ and $x_2 = \frac{p_T}{\sqrt{s}}(e^{-y_f} + e^{-y_2})$. z is a parameter equal to the ratio of the energy of the quark, f , to hadron h . \sqrt{s} is the root center of mass energy, the energy in the rest frame of the interaction. Present are the differential cross-sections of parton interactions, $\frac{d\sigma}{dt}$ and the Mandelstam variables, \hat{t}, \hat{u} . Also present are the parton distribution functions[10][11], f and fragmentation functions[12][13], D . J is the Jacobian of the change between pseudo-rapidity and rapidity, given by

$$J(m_T, y) = \left(1 - \frac{m^2}{m_T^2 \cosh^2 y}\right)^{-1/2} \quad (2)$$

where m is the mass of the outgoing hadron and m_T is the transverse mass of the outgoing hadron. The sum over i, j, k, l is a sum over every possible interaction, where i, j, k, l stand for labels of the different partons (quarks, anti-quarks and gluons). The constant, K , is the ratio of the experimental cross-section to the leading order cross-section. It was found by Eskola and Honkanen[9] that K was a function only of \sqrt{s} and encapsulates the next-to-leading order contributions.

Intuitively, what is being described by this integral, is that the probability of h being formed at momentum q_T , is equal to the sum over every possible interaction that could form h with momentum q_T .

2.2. pA collisions

Using Mathematica, we calculate the differential cross-section for the production of charged hadrons for proton-nucleus (pA) collisions. We use the same calculation as for $p\bar{p}$ collisions, except one of the parton distribution functions of eq[1] are replaced with the nuclear parton distribution function[14] to indicate that the associated parton forms part of a larger nucleus, rather than a mere proton. These nuclear parton distribution functions encapsulate the nuclear effects that arise from involving nuclei in the collision.

2.3. Modification to extract partonic contributions

We now modify our calculation so that we can calculate the individual contribution to the total cross-section from each parton to serve as an input into future energy-loss calculations. The modification is quite simple. Examining eq[1], we eliminate the fragmentation functions, since these are used to tell us about the formation of hadrons. This leaves us with a calculation concerning the production of partons.

The second modification is that, rather than summing over all the partons, we record the contribution due to each parton separately. Our calculation then looks like

$$\begin{aligned} \frac{d\sigma^{AB \rightarrow k+X}}{dq_T^2 dy_f} &= \int dy_2 \sum_{\langle ij \rangle \langle kl \rangle} \frac{1}{1 + \delta_{kl}} \frac{1}{1 + \delta_{ij}} \times \\ &\times x_1 f_{i/A}(x_1, Q^2) x_2 f_{j/B}(x_2, Q^2) \left[\frac{d\hat{\sigma}^{ij \rightarrow kl}}{d\hat{t}}(\hat{t}, \hat{u}) \right] \end{aligned} \quad (3)$$

where, once again, i, j, k, l represent each of the participating partons where we now save the result for the k outgoing partons individually.

3. Results

3.1. $p\bar{p}$ cross-section

In order to verify that eq[1] is valid, we compute the cross-section at $\sqrt{s} = 630$ GeV and compare to data.

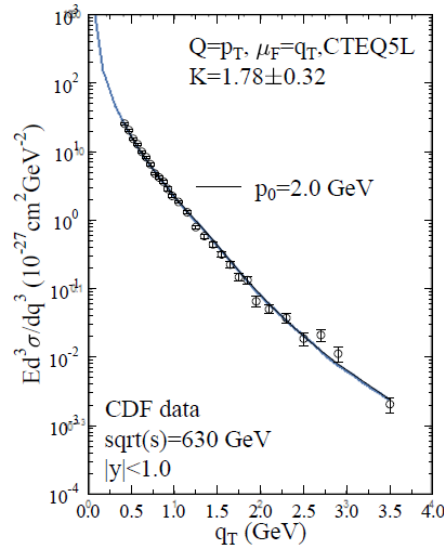


Figure 1. Differential cross-section of charged hadron production of a $p\bar{p}$ collision at $\sqrt{s} = 630$ GeV. The blue line is our calculation, the black line (over-lapping with the blue line) is the prediction from fig[5] of [9], where the data are taken.

Our calculation shows strong agreement with data and agrees with the prediction from [9] within numerical precision.

3.2. pA cross-section

In order to verify our understanding of the nuclear effects in scattering cross-section we calculate the differential cross-section of pA collision at $\sqrt{s} = 5.02$ TeV and compare with data from ALICE[15]

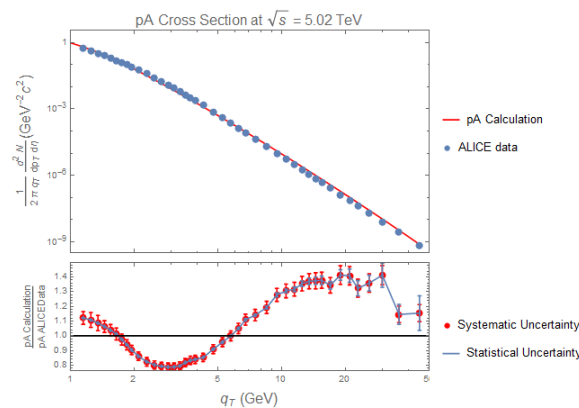


Figure 2. (Top) Plotted is the minimum bias inclusive differential cross-section of charged hadron production. The red line is our calculation, the blue points are data from ALICE. (Bottom) A ratio of our calculation to the data with systematic and statistical uncertainties.

We find that our calculation agrees with the data to within 40 percent. This is a strong agreement for a QCD calculation.

3.3. Partonic contribution

To serve as a critical input into energy loss calculations we find it useful to extract the partonic contributions from the above calculated cross-sections as calculated in eq[3]. As an example, we calculate the partonic contribution of a $p\bar{p}$ collision at $\sqrt{s} = 5.02$ TeV.

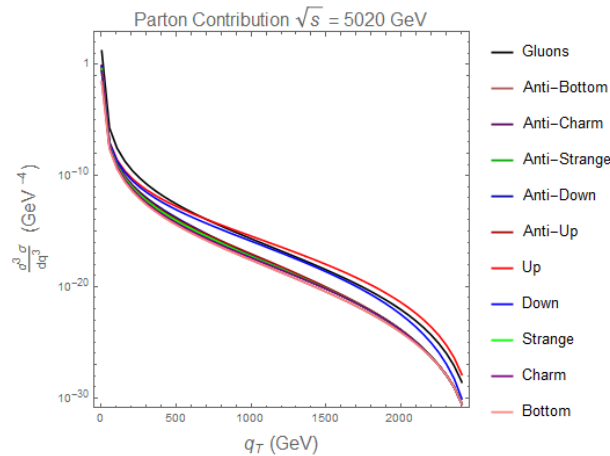


Figure 3. Spectra of each parton and their contribution to the total differential cross-section

4. Discussion

The goal of this work was to establish good theoretical control over the non-energy loss processes that occur in collisions. Figure 1 shows that we can accurately predict the result of $p\bar{p}$ collisions. This demonstrates an understanding of the partonic processes, the interaction between partons in these collisions, as well as the fragmentation process into hadrons. Figure 2 shows that we are able to predict the result of pA collisions. Since the only effects we included into our calculation that differ from the $p\bar{p}$ calculation are the nuclear effects and the fact that we have such strong agreement with data, indicate that we have good theoretical control over the nuclear effects.

We have also demonstrated the ability to extract the partonic contribution to the cross-section. We have confidence in this result because, in the absence of energy-loss (such as in $p\bar{p}$ collisions), the partonic contribution serves as a direct input into the fragmentation process, which gives the total differential cross-section of fig 1.

5. Outlook

The techniques of pQCD have shown to be apt when it comes to the prediction of differential cross-sections of charged hadron production. We have confidence that non-energy-loss effects are under good control. The stage is set to perform energy-loss calculation to probe the presence of a QGP. The most obvious avenue to do this is for AA collisions, but recent research suggests that high-multiplicity cuts of pp and pA collisions show characteristics of possessing a medium [16]. This presents the perfect opportunity to apply energy-loss calculations to pp and pA collisions, where the presence of QGP has not been confirmed, but could serve as a new probe into this medium.

6. Acknowledgments

I would like to thank the Harry Crossley foundation for supporting me financially throughout this endeavor.

References

- [1] Miklos Gyulassy and Larry McLerran. Quark-gluon plasma. new discoveries at rhic: Case for the strongly interacting quark-gluon plasma. contributions from the rbrc workshop held may 14-15, 2004 new forms of qcd matter discovered at rhic. *Nuclear Physics A*, 750(1):30 – 63, 2005.
- [2] Thomas Ullrich, Bolek Wysouch, John W. Harris, and Urs Achim Wiedemann. The quark matter 2012 introductory overview of quark matter 2012. *Nuclear Physics A*, 904:3c – 10c, 2013.
- [3] K. Kajantie and Hannu Kurki-Suonio. Bubble growth and droplet decay in the quark-hadron phase transition in the early universe. *Phys. Rev. D*, 34:1719–1738, Sep 1986.
- [4] The Frontiers of Nuclear Science, A Long Range Plan. 2008.
- [5] Miklos Gyulassy, Peter Levai, and Ivan Vitev. Jet quenching in thin plasmas. *Nucl. Phys.*, A661:637–640, 1999.
- [6] Magdalena Djordjevic and Marko Djordjevic. Generalization of radiative jet energy loss to non-zero magnetic mass. *Phys. Lett.*, B709:229–233, 2012.
- [7] Magdalena Djordjevic. Collisional energy loss in a finite size QCD matter. *Phys. Rev.*, C74:064907, 2006.
- [8] Julia Velkovska. What have hard probes taught us about the quarkgluon plasma as measured in cms? *Nuclear Physics A*, 932:17 – 24, 2014. Hard Probes 20136th International Conference on Hard and Electromagnetic Probes of High-Energy Nuclear Collisions.
- [9] K. J. Eskola and H. Honkanen. A Perturbative QCD analysis of charged particle distributions in hadronic and nuclear collisions. *Nucl. Phys.*, A713:167–187, 2003.
- [10] M Dittmar, S Forte, A Glazov, S Moch, S Alekhin, Guido Altarelli, J Andersen, R D Ball, J Blmlein, Helmut B Bttcher, T Carli, Marcello Ciafaloni, D Colferai, A Cooper-Sarkar, Gennaro Corcella, L Del Debbio, G Dissertori, J Feltesse, A Guffanti, C Gwenlan, J Huston, G Ingelman, M Klein, J I Latorre, T Lastoviicka, G Lastoviicka-Medin, L Magnea, A Piccione, J Pumplin, V Ravindran, B Reisert, J Rojo, Agustin Sabio Vera, Gavin P Salam, F Siegert, A M Stasto, H Stenzel, C Targett-Adams, R S Thorne, A Tricoli, J A M Vermaseren, and A Vogt. Introduction to parton distribution functions. 2005.
- [11] H. L. Lai, J. Huston, S. Kuhlmann, J. Morfin, Fredrick I. Olness, J. F. Owens, J. Pumplin, and W. K. Tung. Global QCD analysis of parton structure of the nucleon: CTEQ5 parton distributions. *Eur. Phys. J.*, C12:375–392, 2000.
- [12] D de Florian and D Milstead. 17. fragmentation functions in e e-, ep and pp collisions.
- [13] Bernd A. Kniehl, G. Kramer, and B. Potter. Fragmentation functions for pions, kaons, and protons at next-to-leading order. *Nucl. Phys.*, B582:514–536, 2000.
- [14] K. J. Eskola, H. Paukkunen, and C. A. Salgado. EPS09: A New Generation of NLO and LO Nuclear Parton Distribution Functions. *JHEP*, 04:065, 2009.
- [15] K. Aamodt et al. Suppression of Charged Particle Production at Large Transverse Momentum in Central Pb-Pb Collisions at $\sqrt{s_{NN}} = 2.76$ TeV. *Phys. Lett.*, B696:30–39, 2011.
- [16] Georges Aad et al. Centrality and rapidity dependence of inclusive jet production in $\sqrt{s_{NN}} = 5.02$ TeV proton-lead collisions with the ATLAS detector. *Phys. Lett.*, B748:392–413, 2015.

Density functional theory on a lattice: Self-consistent Hartree plus exchange approximation.

Kossi Amouzouvi and Daniel Joubert

National Institute for Theoretical Physics, School of Physics and Mandelstam Institute for Theoretical Physics, University of the Witwatersrand, Johannesburg, Wits 2050, South Africa.

E-mail: kossi@aims.edu.gh

Abstract. Within an ensemble density functional theory formulation for a finite chain single band Hubbard Hamiltonian we define a "Hartree plus exchange" approximation that can be solved exactly in a self-consistent framework. In this formulation we exclude a small "correlation" term. Comparison of the results for a short Hubbard chain with the exact values show that the discontinuity in the Kohn-Sham potential is reproduced well and that the approximate total energy is a good approximation of the exact total energy. The results suggest that it is possible to find a good approximate solution for a Hubbard chain of any length and opens the way for solving interesting models such as Hubbard defect chains in a numerically simple and reliable way.

1. Introduction

In the mid 1960's Kohn with Hohenberg [1] and Sham [2] established the formal basis of Density Functional theory (DFT), a well known powerful formulation nowadays widely used by chemists and material scientists. DFT is formally exact, but the exact form of all the density functionals in the formalism, including the exchange-correlation energy, is not known. In practical applications the exchange-correlation term is approximated and unfortunately there is no systematic way to develop approximations to the exact density functionals. This has led to a confusing multitude of approximations in the literature. Approximations that have been used with success include 1) the venerable Local Density Approximation (LDA) [2–4] which is based on the properties of the homogeneous electron gas, 2) Generalized Gradient Approximations (GGA) [5, 6] where the exchange-correlation functional expression includes the gradient of the density, 3) Hybrid functionals [7–9] which include a contribution from exact exchange. Many other approximations have been proposed for many-electron systems whose spatial coordinates belong to a continuum. A systematic examination of the properties of approximations are hampered by the almost impossible task of finding exact solutions for models of real systems. Lattice DFT [10, 11] is one of the interesting ways to investigate density functionals. Here the finite chain single band Hubbard Hamiltonian has been used since it is possible to determine the exact interacting density and eigenenergies for a range of models. For example, the exact Kohn-Sham (KS) potential for this model can be studied as a function of electron number, which allows an investigation of a spatially independent discontinuity of the functional derivative of the exchange-correlation potential at integer particle numbers.

In Section 2, we summarise some important background of Lattice-DFT functionals combined with an ensemble DFT formalism necessary to fully explore the properties of density functionals.

In Section 3 we introduce the approaches we used to probe the Hartree plus exchange approximation and the consequent KS potential as functions of the number of electrons in the lattice. We then present results followed by their analysis in Section 4 which leads us to the conclusion in Section 5.

2. Background

The simplest Hubbard Hamiltonian [12, 13] for a finite chain single band of length l that contains n_e electrons can be written as

$$\hat{H} = \hat{t} + \hat{u} + \hat{v}. \quad (1)$$

In Eq.(1), $\hat{t} = -t \sum_{\substack{1 \leq i, j \leq l \\ j=i \pm 1}} \sum_{\sigma=\uparrow, \downarrow} c_{j\sigma}^\dagger c_{i\sigma}$, $\hat{u} = u_0 \sum_{1 \leq i \leq l} \hat{n}_{i\uparrow} \hat{n}_{i\downarrow}$ and $\hat{v} = \sum_{1 \leq i \leq l} \sum_{\sigma=\uparrow, \downarrow} v_i \hat{n}_{i\sigma}$ are the kinetic,

the spin-correlation and the external potential operators respectively. At zero temperature, the ground state wavefunction ψ^0 , solution of the Schrödinger equation $\hat{H}\psi^i = E_i\psi^i$, helps to determine the ground state site-density $n_i^0 = \langle \psi^0 | \sum_{\sigma} \hat{n}_{i\sigma} | \psi^0 \rangle$ and the ground state energy

$E_0 = \langle \psi^0 | \hat{H} | \psi^0 \rangle$. If the ground state energy of a system that exchanges particles with a particle reservoir satisfies the convexity condition [14–16], $E_0(n_e) - E_0(n_e - 1) \leq E_0(n_e + 1) - E_0(n_e)$, it leads to the simple two state ensemble $\Gamma_\alpha[v] = (1 - \alpha) |\psi^0[n_e, v]\rangle \langle \psi^0[n_e, v]| + \alpha |\psi^0[n_e + 1, v]\rangle \langle \psi^0[n_e + 1, v]|$ where α ($1 - \alpha$) is the probability of finding the system in the state $\psi^0[n_e + 1]$ ($\psi^0[n_e]$). For a system in a state with $N = n_e + \alpha$ electrons, where n_e is an integer, the expectation value of any observable \hat{O} is $\langle O \rangle = Tr \{ \Gamma_\alpha[v] \hat{O} \}$ where Tr is the trace of the product of the two operators. In the KS framework [2], we map the interacting system onto a fictitious non-interacting system with Hamiltonian $\hat{H}_{KS} = \hat{t} + \hat{v}^{KS}$, with potential v^{KS} , unique up to a constant, which reproduces the exact interacting electronic (site-) density of the interacting ground state. The ground state energy can be partitioned as

$$\begin{aligned} E_0(N) &= Tr \{ \Gamma_\alpha H \} \\ &= T_{KS} + E_{HX} + E_C + Tr \{ \Gamma_\alpha [v^{KS}] \hat{v} \} \end{aligned} \quad (2)$$

where the last expression follows since $\Gamma_\alpha[v^{KS}]$ and $\Gamma_\alpha[v]$ yield the same ground state density by construction. For historical reasons we call E_{HX} the Hartree plus exchange energy term and E_C the correlation energy, while T_{KS} is the kinetic energy of the non-interacting Kohn-Sham system. In Eq. (2),

$$\begin{aligned} T_{KS} &= Tr \{ \Gamma_\alpha [v^{KS}] \hat{T} \}, \\ E_{HX} &= Tr \{ \Gamma_\alpha [v^{KS}] \hat{u} \}, \\ E_C &= Tr \{ \Gamma_\alpha [v] (\hat{T} + \hat{u}) \} - Tr \{ \Gamma_\alpha [v^{KS}] (\hat{T} + \hat{u}) \} \end{aligned}$$

and the Kohn-Sham potential is

$$\hat{v}^{KS} = \hat{v}^{HX} + \hat{v}^C + \hat{v}$$

where v^{HX} is the functional derivative of E_{HX} and v^C this of E_C . The correlation energy E_C is expected to make a small contribution to the total energy as confirmed below and in the

Hartree plus exchange approximation we set this term to zero with the resultant approximate Kohn Sham potential

$$\hat{v}^{KS} = \hat{v}^{HX} + \hat{v}. \quad (3)$$

It is useful to define $\tilde{E}_{HXv} = \tilde{E}_{HX} + Tr \{ \Gamma_\alpha [\tilde{v}^{KS}] \hat{v} \}$ so that $E_0 = \tilde{T}_{KS} + \tilde{E}_{HXv} + \tilde{E}_C$ i.e. $\tilde{E}_C = E_0 - [\tilde{T}_{KS} + \tilde{E}_{HXv}]$. This definition of \tilde{E}_C is exact for the exact DFT equations and is an approximation of the correlation energy in the Hartree plus exchange approximation.

3. Method

For any allowed number of electrons for a finite lattice, fractional or integer, we start by solving the exact interacting Hubbard Hamiltonian numerically and then we solve the KS equation self-consistently to obtain the exact KS potential v^{KS} . This gives us the exact results to which approximations can be compared. Using Eq. (3) it is possible to solve the Hartree plus exchange approximation within the Kohn-Sham formulation. We first perform an exact diagonalization of an initial KS Hamiltonian with an approximate potential v_0^{KS} . Using perturbation theory we compute $\frac{\partial \phi^0}{\partial v^{KS}}$ from which we determine $\frac{\partial n^0}{\partial v^{KS}}$ and \tilde{v}_0^{HX} . Finally we obtain a new KS potential v_1^{KS} using Eq. (3). This process is repeated until a self-consistent approximate KS potential \tilde{v}^{KS} is obtained. From now on, let us consider a lattice of 4 sites with a flat external potential $v = (1, 1, 1, 1)^T$. We choose this potential to highlight the site dependence of the exchange-correlation potential. For this model we are interested on the KS potential for electron number N in the range $1 \leq N \leq 8$. Let us set in arbitrary units the hopping term t to be 1 while the on-site coulomb potential u is set to 2.

All the results discussed in this paper were calculated with code written in Octave [17].

4. Results and analysis

The exact KS potential shows a site independent discontinuity at integer particle numbers (Figure 1) if we compare the potential as we approach an integer particle number from below or above. The approximate KS potential (Figure 2) reproduces the shape and the discontinuity observed for the exact potential. In Figure 3 and Figure 4 we notice a shift of the approximate potential with respect to the exact one. The Hartree plus exchange potential has the form

$$v_i^{HX}(N) = (1 - \alpha)v_i^{HX}[n_e, v^{KS}(N)] + \alpha v_i^{HX}[n_e + 1, v^{KS}(N)] + E_{HX}(n_e + 1) - E_{HX}(n_e) \quad (4)$$

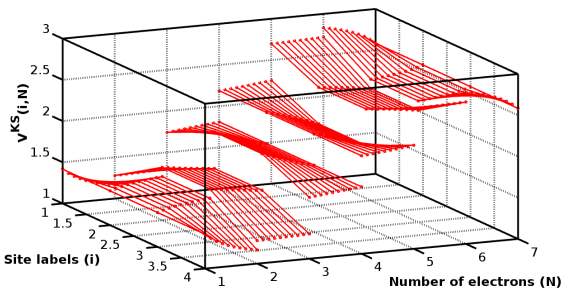


Figure 1. Exact KS potential v^{KS} as a function of particle number for a finite chain.

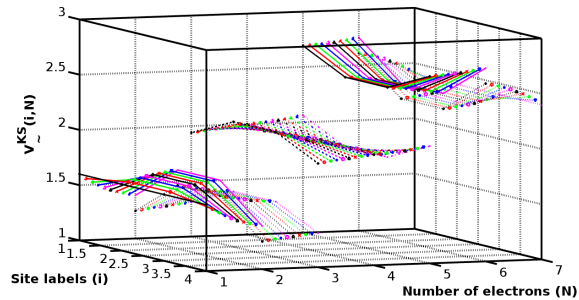


Figure 2. Approximate KS potential \tilde{v}^{KS} as a function of particle number for a finite chain.

where n_e is an integer and $n_e \leq N \leq n_e + 1$. The first two terms describe the shape of the potential and the last two terms are particle number dependent site independent constants. These constants change when N passes through an integer and give rise to a site independent discontinuity in the potential at integer particle numbers.

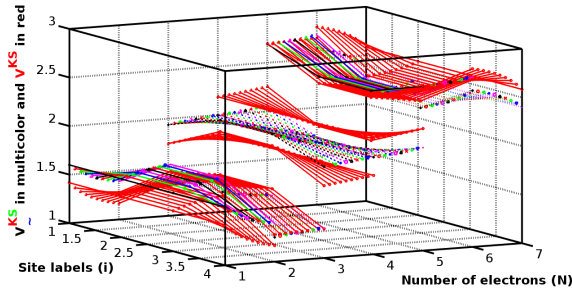


Figure 3. 3D plot of the exact and the approximate KS potentials.

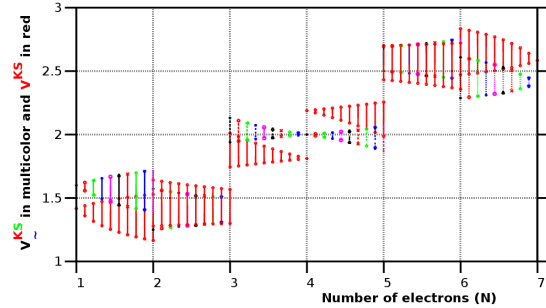


Figure 4. 2D plot of the exact and the approximate KS potentials.

The maximum percentage error between the exact and approximate kinetic energies is less than 0.26% while for the Hartree plus exchange energy it is 1.09%. This is interesting since it reveals the similarity between ϕ^0 and $\tilde{\phi}^0$, the exact and approximate KS ground state wavefunctions. Figure 5 shows the maximum and minimum, over all the sites, percentage error in the ground state density. The highest percentage error is 3.12%. The difference between the curves in Figure 6 gives an indication of the size of E_C . The correlation energy decreases at high filling while it reaches its maximum around a filling of 3. The overall behaviour shows that

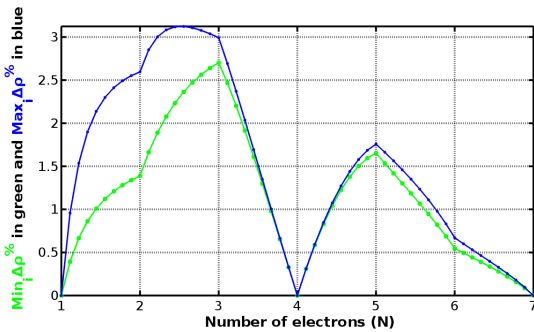


Figure 5. Maximum and minimum density percentage error.

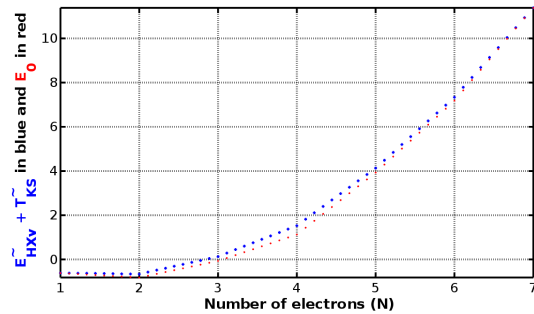


Figure 6. Correlation energy.

the correlation energy makes a relatively small contribution to the total energy of the system.

5. Conclusion and Outlook

We have performed a self-consistent calculation of the Hartree plus exchange approximation, a new DFT approximation applied to the Hubbard model. We found that the approximate KS potential has a similar shape and discontinuity at integer particle numbers when compared to exact results. The correlation energy, estimated by the difference between the exact and approximate total energies (Figure 6) makes a small contribution to the total energy. From the similarity between the exact and approximate electronic densities, we confirm that the approximate KS potential has a shape which closely follows that exact potential. Future work

includes an attempt to include correlations by using a Jastrow factor to map the KS wave function onto the interacting wave function.

Acknowledgment

The first author acknowledges a Deutscher Akademischer Austauschdienst (DAAD) bursary.

References

- [1] Hohenberg P and Kohn W 1964 *Phys. Rev.* **136**(3B) B864–B871
- [2] Kohn W and Sham L J 1965 *Phys. Rev.* **140** A1133
- [3] von Barth U and Hedin L 1972 *Journal of Physics C: Solid State Physics* **5** 1629
- [4] Rajagopal A K and Callaway J 1973 *Phys. Rev. B* **7**(5) 1912–1919
- [5] Langreth D C and Perdew J P 1980 *Phys. Rev. B* **21**(12) 5469–5493
- [6] Perdew J P, Burke K and Wang Y 1996 *Phys. Rev. B* **54**(23) 16533–16539
- [7] Lee C, Yang W and Parr R G 1988 *Phys. Rev. B* **37**(2) 785–789
- [8] Becke A D 1993 *The Journal of chemical physics* **98** 5648–5652
- [9] Perdew J P, Burke K and Ernzerhof M 1996 *Phys. Rev. Lett.* **77**(18) 3865–3868
- [10] Schönhammer K, Gunnarsson O and Noack R 1995 *Phys. Rev. B* **52** 2504
- [11] Schönhammer K and Gunnarsson O 1987 *Journal of Physics C: Solid State Physics* **20** 3675
- [12] Hubbard J 1963 *Proceedings of the royal society of london a: mathematical, physical and engineering sciences* vol 276 (The Royal Society) pp 238–257
- [13] Essler F H, Frahm H, Göhmann F, Klümper A and Korepin V E 2005 *The one-dimensional Hubbard model* (Cambridge University Press)
- [14] Joubert D P 2012 *The Journal of chemical physics* **136** 174113
- [15] Sagvolden E and Perdew J P 2008 *Phys. Rev. A* **77** 012517
- [16] Perdew J P, Parr R G, Levy M and Balduz Jr J L 1982 *Phys. Rev. Lett.* **49** 1691
- [17] John W Eaton David Bateman S H and Wehbring R 2015 *GNU Octave version 4.0.0 manual: a high-level interactive language for numerical computations* URL <http://www.gnu.org/software/octave/doc/interpreter>

First-principles studies of transition metal defects in a MoS₂ monolayer

N F Andriambelaza¹, R E Mapasha¹ and N Chetty^{1,2}

¹Department of Physics, University of Pretoria, Pretoria 0002, South Africa

²National Institute for Theoretical Physics, Johannesburg 2000, South Africa

E-mail: arinala.f@gmail.com

Abstract. Density functional theory (DFT) implemented within the Vienna *ab-initio* simulation package (VASP), have been used to study the effects of transition metal defects (Rhenium (Re) and Tantalum(Ta)) on the thermodynamic stability and electronic properties of a MoS₂ monolayer. Calculations are performed using the projector augmented wave method (PAW) with the Perdew-Burke-Ernzerhof (PBE) for the exchange-correlation interactions. Our results show that Ta_{Mo} is a thermodynamically stable *p*-type defect whereas Re_{Mo} is a *n*-type with high cost of energy. To reduce the high energy cost of Re_{Mo} in a MoS₂, co-doping was considered. Our studies show that the co-doping of acceptors and donors to be accessible, the acceptors should dominate the donors. The variation of donors and acceptors in a MoS₂ monolayer tune the magnetic moment on and off. Our results indicate that combination of *p*-type (Ta) and *n*-type (Re) doped MoS₂ monolayers are promising materials for various electronic applications.

1. Introduction

Since its discovery, graphene has attracted considerable attention due to its unique electronic structure, high carrier mobility and exceptional strength [1]. Although it is a promising material for nanoelectronic devices, the absence of band gap inhibits its direct application. For this reason, researchers became interested in exploring other kind of two dimensional (2D) materials. The transition metal dichalcogenides (TDMCs) such as MoS₂, WS₂, MoSe₂, WSe₂, etc, are wide band gap semiconductors and are thermodynamically stable 2D materials [2]. Several studies have reported that MoS₂ monolayer has a band gap of about 1.90 eV experimentally [3] and of about 1.67 eV theoretically [4, 2]. Xu *et al.* reported that MoS₂ exhibits an excellent carrier mobility and desirable optical properties. These interesting properties make MoS₂ a suitable candidate for nanoelectronic devices [5].

During the synthesis of MoS₂ monolayer, point defects and impurities appear in the samples [6] just like in any materials. The presence of these defects are known to greatly alter the properties of pristine MoS₂ monolayer. It was reported that presence of the *p*-type and *n*-type defects causes semiconductor to metal transition in a MoS₂ system. Noh *et al.* reported that Rhenium (Re) impurities exist naturally in a MoS₂ monolayer and are *n*-type defects [7]. The valence band maximum (VBM) and conduction band minimum(CBM) states of a pristine MoS₂ monolayer are derived mainly from Mo 4*d* orbitals. This was shown by atomic resolution transmission electron microscopy [8]. In most studies of defects in a MoS₂ monolayer, Mo site is chosen in order to examine the influence of defects on the VBM and CBM states.

The widely studied *p*-type defect in MoS₂ is the Niobium (Nb) substituting Molybdenum (Nb_{Mo}). Dolui *et al.* reported that the presence of Nb_{Mo} has low formation energy and introduces impurity states above the VBM whose origin is the hybridisation of Nb and Mo *d* orbitals [9]. Lu *et al.* reported that the formation energy for Ta_{Mo} is lower than that of Nb_{Mo}. However, its electronic and magnetic properties have not been explored extensively [10]. Therefore, Tantalum (Ta) which is below Nb on the periodic table is also worth of investigation as an isolated defect (Ta_{Mo}) to learn how its interaction with MoS₂ influences the electronic and magnetic properties of MoS₂ monolayer.

In this paper, we examine the effect of Ta acceptor and Re donor defects on the thermodynamic stability and electronic properties of a MoS₂ monolayer. We also examine Ta and Re co-doping on MoS₂ monolayer. This will be to study the interaction of an acceptor (Ta) and donor (Re) defects on the stability and electronic properties of the system. We further identify Ta-Re configurations that have ferromagnet characteristics and low formation energy which will be important in spintronic application devices.

2. Methodology

In this work, density functional theory (DFT) [11] as implemented in the Vienna *ab-initio* simulation package(VASP) [12] is employed to perform ab initio calculations on the electronic and magnetic properties of monolayer MoS₂ doped with Re and Ta impurities. All calculations are carried out using the projector augmented wave (PAW) pseudopotential and generalized gradient approximation (GGA) exchange correlation parameterized by Perdew, Burke, and Ernzerhof (PBE) [13]. A 5×5 hexagonal supercell with 75 atoms (25 Mo atoms and 50 S atoms) and having a vacuum region of 15 Å is employed to suppress the influence of neighboring layers. A kinetic energy cutoff of 250 eV for plane wave expansion and 2×2×1 k-point mesh are used. The atomic structures were relaxed until the Hellmann-Feynman forces were less than 0.02 eV/Å. The formation energies (E_{form}) of a particular dopant is defined as :

$$E_{form} = E_{tot}[MoS_2 + D] - E_{tot}[MoS_2] + \mu_{host} - \mu_D \quad [6] \quad (1)$$

where $E_{tot}[MoS_2+D]$ is the total energy of the MoS₂ monolayer with the substitutional atom D (Re or Ta), $E_{tot}[MoS_2]$ is the total energy of the pristine MoS₂ monolayer. μ_D and μ_{host} , are respectively the chemical potentials of the substitutional atom D (Re or Ta) and the host atom (Mo or S). All the chemical potentials are calculated by using the reference (stable) phase of each element. The orthorhombic structure is chosen for the sulphur and body center cubic (bcc) for Mo. μ_D is obtained from DFT total energies of a Ta bcc metal and Re hexagonal structure per atom.

3. Results and discussion

Before discussing the effect of dopant on a MoS₂ monolayer, let us analyse the electronic properties of the pristine MoS₂ monolayer. The top view and side view of a MoS₂ monolayer are shown in (Fig. 1). It can be seen that each of the S atom is bonded covalently to the three Mo atoms. Each Mo atom is coordinated with six S atoms, three of them make the top surface and other three to the bottom S layer. The band gap obtained using GGA functional for the pristine is 1.65 eV. This value is in good agreement with the experimental value of 1.90 eV and the previous theoretical results found in references [4, 2]. The VBM is mainly constituted from the hybridisation of Mo 4d and S 3p orbitals, whereas the CBM is mainly due to Mo 4d orbitals. The pristine of MoS₂ monolayer is a non-magnetic material in nature, since the spin up states are invertibly symmetric to spin down states for the entire plot. In the next section, we examine the effects of Ta and Re atoms on the electronic properties of a MoS₂ monolayer.

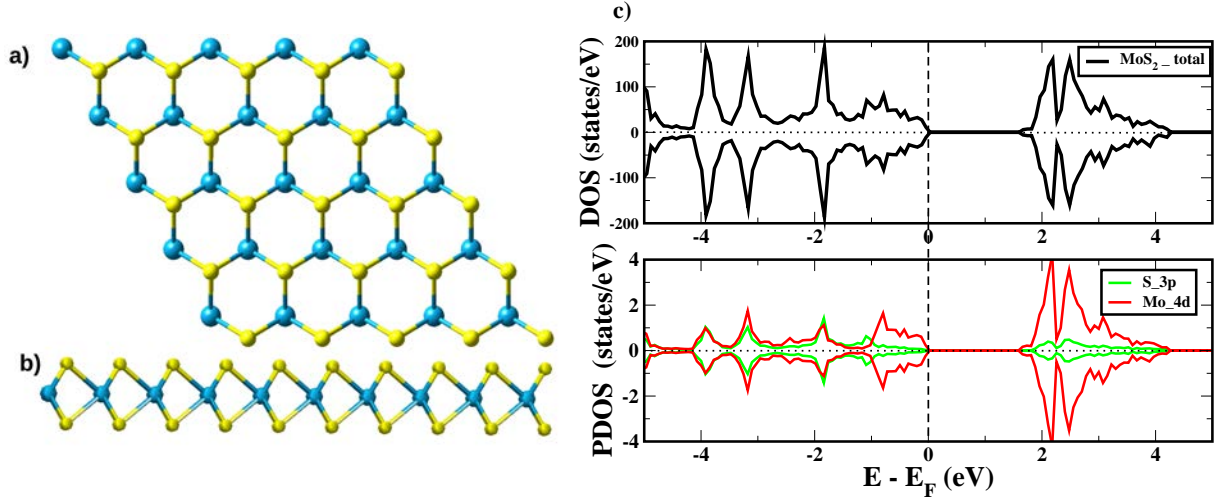


Figure 1. (a) Top view and (b) side view of a 5×5 MoS₂ monolayer. Blue spheres indicate Mo atoms and light yellow spheres indicate S atoms. (c) The total DOS and Projected DOS for a pristine MoS₂ monolayer. The positive DOS and PDOS values refer to majority spins, while the negative ones are for minority. The dashed line indicates the Fermi energy.

3.1. Ta substitution

Firstly, we analyse Ta atom(s) substituting Mo atom(s). The number of Ta dopants considered ranges between one and three (Ta_{*x*} where $x = 1\text{Mo}, 2\text{Mo}$ and 3Mo) on a single hexagonal ringlike in a MoS₂ monolayer. When examining the structures, we found that the insertion of Ta atom in a MoS₂ monolayer affects the bond lengths. The relaxed Ta-S bonds for Ta_{1Mo}, Ta_{2Mo} and Ta_{3Mo} are 2.41, 2.46 and 2.47 Å respectively. The Mo-S bond length for the relaxed MoS₂ monolayer is 2.42 Å which is in good agreement with references [2, 9]. Therefore, we realise that the induced strain in Ta_{1Mo} is small, however in Ta_{2Mo} and Ta_{3Mo}, it is significantly large. This should have a significant effect on the other properties.

Table 1. Formation energies E_{form} (eV) and magnetic moments $m(\mu_B)$ of Ta and Re defects in a MoS₂ monolayer.

Type of doping	E_{form} (eV)	$m(\mu_B)$
Ta _{1Mo}	-0.43	0.01
Ta _{2Mo}	-0.97	0.00
Ta _{3Mo}	-1.73	0.00
Re _{1Mo}	2.18	1.00
Re _{2Mo}	4.02	0.00
Re _{3Mo}	5.73	1.00
Ta _{1Mo} Re _{1Mo}	0.09	0.01
Ta _{2Mo} Re _{1Mo}	-0.38	0.01
Ta _{1Mo} Re _{2Mo}	2.10	0.98

The relative stability of our defects is determined using the formation energies calculated using Eq.1. Table.1 shows that the formation energies of Ta_{Mo} (Ta_{1Mo}, Ta_{2Mo} and Ta_{3Mo}) are all negative. We realised that E_{form} becomes more energetically favourable when the number of defects increases. The negative formation energies indicate that the corresponding substitutional

reactions can occur spontaneously under favourable conditions. Ding *et al.* have reported that

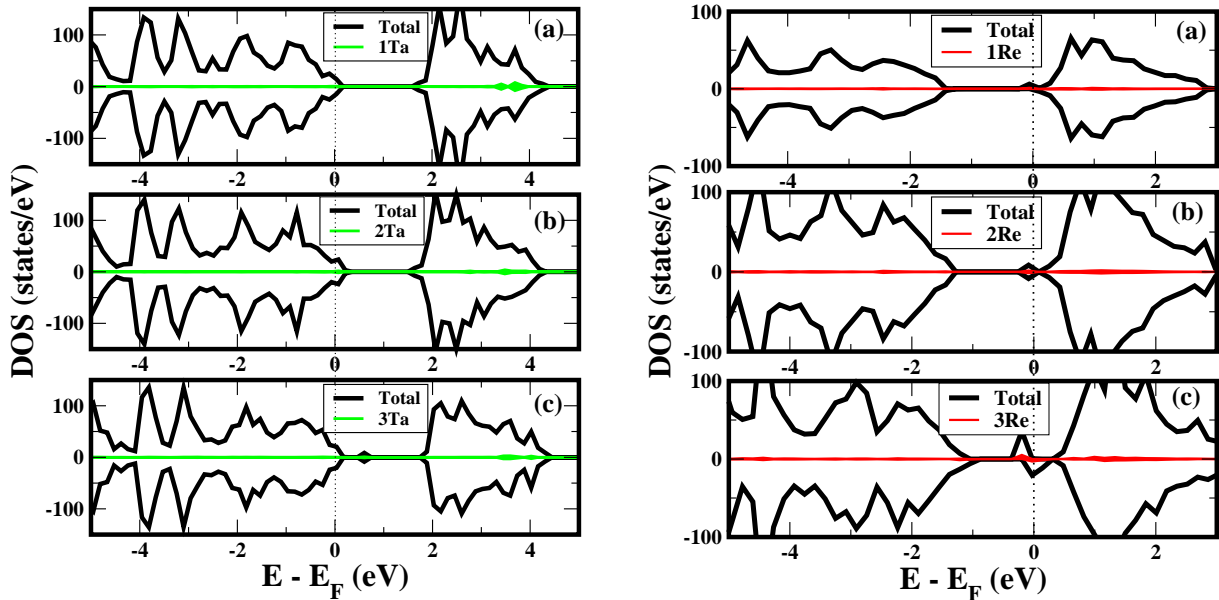


Figure 2. The Total DOS for a 5×5 supercell of (a) Ta_1Mo , (b) Ta_2Mo , (c) Ta_3Mo , (d) Re_1Mo , (e) Re_2Mo and (f) Re_3Mo . The positive DOS values refer to majority spins, while the negative ones are for minority. The dashed line indicates the Fermi energy.

Fig. 2 shows the density of states (DOS) plots for Ta_1Mo (Fig. 2(a)), Ta_2Mo (Fig. 2(b)) and Ta_3Mo (Fig. 2(c)). We found that the effect of Ta substituting Mo is to shift the Fermi level into the valence band. This shift is an indication that Ta_1Mo , Ta_2Mo and Ta_3Mo systems have deficiency of electrons compared to MoS_2 . Therefore, Ta_MMo systems are *p*-type defects in a MoS_2 monolayer and can act as an electron trap. In a Ta_3Mo DOS, we also noted an extra non-spin polarised impurity states at 0.47 eV above the VBM within the band gap. These exotic impurities states are relative deep, and therefore will unlikely be ionised at room temperature [14]. Fig. 2 also shows that in all cases, the minority spin is aligned to the majority spin revealing that the systems are non-magnetic (see Table.1). Nevertheless, Ta defect is energetically stable and can be a suitable *p*-type dopant for MoS_2 monolayer.

3.2. Re substitution

The formation energies of Re defect configurations, Re_1Mo , Re_2Mo and Re_3Mo , are shown in Table.1. They are all positive indicating that the cost of substituting Mo with Re is energetically expensive. We further found that when the number of Re dopants in the system increases, i.e Re_3Mo , the system gradually becomes more energetically unstable. The DOS of Re_1Mo , Re_2Mo and Re_3Mo are shown in Fig. 2(a), Fig. 2(b) and Fig. 2(c) respectively.

For Re_1Mo system, we found that the induced defect state is near but at 0.25 eV below the CBM. This state is formed by hybridisation of the Re 5d orbitals with the Mo 4d orbitals. The creation of Re_1Mo add an electron into the system, resulting in shifting the Fermi level into the CB. This reveals that Re_1Mo system is a *n*-type. The DOS of Re_1Mo (Fig.2(d)) also shows that the majority spin and minority spin are asymmetric leading the system been magnetic with a magnetic moment of $1\mu_B$. This is in good agreement with reference [9].

The substitution of two Re dopants induces non-spin polarised states at 0.19 eV below the CBM. This system is non-magnetic in nature. This might be due to the effect of pairing of localised electrons each contributed by defect. However, the introduction of three Re defects for the Re_3Mo system induces spin-polarised states in the gap around 0.3 eV below the CBM. A magnetic moment of $1\mu_B$ in this defective system is noted. The half metallic character is also noted in Re_3Mo as the Fermi level crosses only the spin down states. The systems that are half metallic ferromagnet have a future application in the spintronic technology.

Since the intrinsic defects are inefficient to create a n -type MoS_2 monolayer [9], our results indicate that Re is a plausible for a n -type dopant in MoS_2 although highly expensive to form.

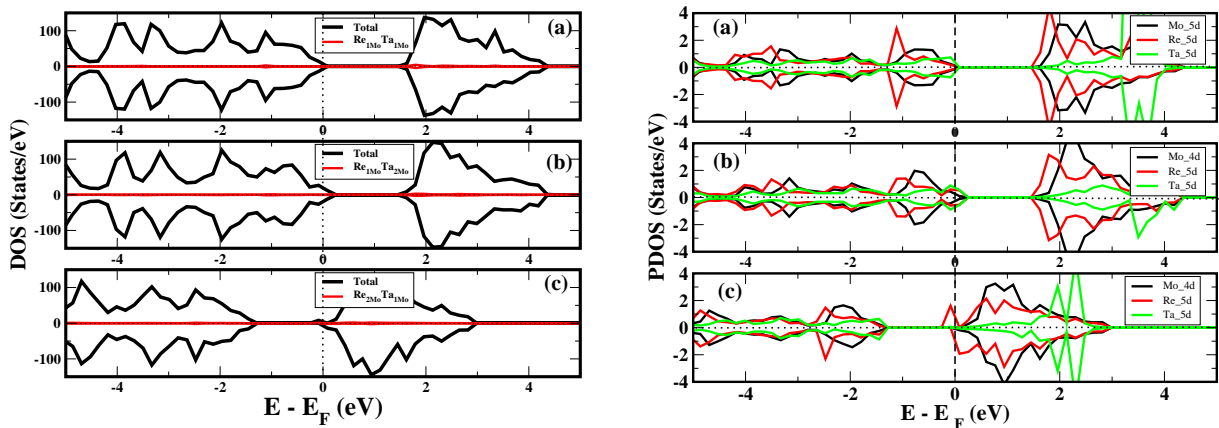


Figure 3. The total DOS(left) and Projected DOS(right) for (a) $\text{Ta}_1\text{MoRe}_1\text{Mo}$, (b) $\text{Re}_1\text{MoTa}_2\text{Mo}$ and (c) $\text{Re}_2\text{MoTa}_1\text{Mo}$. The dashed line indicates the Fermi energy.

3.3. Re and Ta co-doping

Lastly, we examine the co-doping of the Re and Ta dopants in a MoS_2 monolayer. It has been reported that Re exists spontaneously during the synthesis of the MoS_2 samples and an n -type device was characterised. We model the interactions of naturally existing Re defects with Ta dopants in a MoS_2 system. This will be to give an explanation of how the unintentional donors can be controlled by acceptors in a MoS_2 monolayer.

Substitution around the ringlike hexagonal is considered by varying the number of dopants. The three possible defects denoted as $\text{Re}_1\text{MoTa}_1\text{Mo}$, $\text{Re}_1\text{MoTa}_2\text{Mo}$ and $\text{Re}_2\text{MoTa}_1\text{Mo}$ are considered. Table.1 shows that the formation energies of these defects are higher than that of isolated acceptors (Ta) doping but lower than that of donors (Re) doping. The relatively low formation energy for $\text{Re}_1\text{MoTa}_1\text{Mo}$ of 0.09 eV albeit positive, do not rule out the possibility of synthesising this material at an ambient conditions. The substitution of a second acceptor making $\text{Re}_1\text{MoTa}_2\text{Mo}$ system yields a low formation energy of -0.38 eV. However two donors and one acceptor $\text{Re}_2\text{MoTa}_1\text{Mo}$ is a problem because the formation of this system is endothermic. For such defects to be easily accessible under ambient conditions, acceptors should always dominate the donors.

For the first case of $\text{Re}_1\text{MoTa}_1\text{Mo}$, the DOS is quite similar to the pristine (Fig. 3(a)). Since Re has one electron more and Ta has one electron less compared to Mo, those two excess electrons compensate each other. Therefore, the compensation does not alter much the electronic behaviour of the MoS_2 monolayer. But for $\text{Re}_1\text{MoTa}_2\text{Mo}$, we observe that the Fermi level is shifted deeper into the VB. This is to ensure that $\text{Re}_1\text{MoTa}_2\text{Mo}$ behave as n -type material. The system is, however, non-spin polarised with no magnetic moment obtained.

In the case of $\text{Re}_{2\text{Mo}}\text{Ta}_{1\text{Mo}}$, impurities states appear near the CBM. They are originated from 5d orbital of Re (Fig. 3(a)). The Fermi level is shifted closer to the CBM which indicates that $\text{Re}_{2\text{Mo}}\text{Ta}_{1\text{Mo}}$ has a p -type behaviour. After the compensation of one electron from Re and one from Ta, there is still one unpaired electron in the system which makes the system ferromagnetic with a magnetic moment of $1\mu_B$.

4. Conclusion

We have successfully studied the electronic properties and the thermodynamic stability of a MoS_2 monolayer doped with Re and Ta atoms using DFT approximation. We considered isolated doping along a single hexagonal ringlike in a 5×5 supercell of MoS_2 monolayer. We found that Ta atom doping is thermodynamically stable (exothermic) for all possible defect configurations. Ta doping also show a p -type features in MoS_2 monolayer. For Re doping, the formation energies are positive (endothermic) for all defect configurations considered. For $\text{Re}_{1\text{Mo}}$ and $\text{Re}_{3\text{Mo}}$ the system show ferromagnetic features with a magnetic moment of about $1\mu_B$. The DOS analysis of Re doping possess n -type characteristics. In trying to control or lower the high formation energy of Re doping co-doping of Ta with Re was also considered. This was to combine donors (Re) with acceptors (Ta) in a MoS_2 monolayer. Three configurations were investigated $\text{Ta}_{1\text{Mo}}\text{Re}_{1\text{Mo}}$, $\text{Re}_{1\text{Mo}}\text{Ta}_{2\text{Mo}}$ and $\text{Re}_{2\text{Mo}}\text{Ta}_{1\text{Mo}}$. $\text{Re}_{\text{Mo}}\text{Ta}_{2\text{Mo}}$ is the most energetically favourable configuration whereas $\text{Re}_{2\text{Mo}}\text{Ta}_{1\text{Mo}}$ is the least. For a co-doping to be releasable under ambient conditions, acceptors should dominate the donors. Our results suggest that these systems might be useful in various electronic and spintronic devices applications.

Acknowledgments

The authors would like to thank the University of Pretoria for computational resources and financial support. We also thank R.C. Andrew and E. Igumbor for useful discussions.

References

- [1] Geim A K and Novoselov K S 2007 *Nat. Mater.* **6** 183–191
- [2] Ding Y, Wang Y, Ni J, Shi L, Shi S and Tang W 2011 *Phys. B* **406** 2254–60
- [3] Izyumskaya N, Demchenko D O, Avrutin V, Özgür Ü and Morkoç H 2014 *Turk. J. Phys.* **38** 478–496
- [4] Faraji M, Sabzali M, Yousefzadeh S, Sarikhani N, Ziashahabi A, Zirak M and Moshfegh A 2015 *RSC Adv.* **5** 28460–66
- [5] Xu M, Liang T, Shi M and Chen H 2013 *Chem. Rev.* **113** 3766–98
- [6] Komsa H P and Krasheninnikov A V 2015 *Phys. Rev. B* **91** 125304
- [7] Noh J Y, Kim H and Kim Y S 2014 *Phys. Rev. B* **89** 205417
- [8] Lin Y C, Dumcenco D O, Komsa H P, Niimi Y, Krasheninnikov A V, Huang Y S and Suenaga K 2014 *Adv. Mater.* **26** 2857–61
- [9] Dolui K, Rungger I, Pemmaraju C D and Sanvito S 2013 *Phys. Rev. B* **88** 075420
- [10] Lu S C and Leburton J P 2014 *Nanoscale Res. Lett.* **9** 1–9
- [11] Kohn W and Sham L J 1965 *Phys. Rev.* **140** A1133
- [12] Hafner J 2008 *J. Comput. Chem.* **29** 2044–78
- [13] Perdew J P, Burke K and Ernzerhof M 1996 *Phys. Rev. Lett.* **77** 3865
- [14] Freysoldt C, Grabowski B, Hickel T, Neugebauer J, Kresse G, Janotti A and Van de Walle C G 2014 *Rev. Mod. Phys.* **86** 253

Small $(q - 1)$ expansion of the Tsallis distribution and study of particle spectra at LHC

Trambak Bhattacharyya¹, Jean Cleymans¹, Arvind Khuntia², Pooja Pareek², Raghunath Sahoo²

¹ UCT-CERN Research Centre and Department of Physics, University of Cape Town, Rondebosch 7701, South Africa;

² Discipline of Physics, School of Basic Sciences, Indian Institute of Technology Indore, M.P. 452020, India;

E-mail: trambak.bhattacharyya@uct.ac.za

Abstract. The fact that in most of the fits to the hadronic spectra the Tsallis q parameter is close to 1, enables us to expand the Tsallis distribution in the Taylor's series of $(q - 1)$. Tsallis thermodynamics has been studied with the help of this expansion and the particle spectra have been fitted. Also, the effect of the inclusion of the collective flow in Tsallis distribution has been investigated.

1. Introduction

The transverse momentum distributions of hadrons at high energies is very often described by the Tsallis distribution [1]. The PHENIX and STAR collaborations [2, 3] at the Relativistic Heavy Ion Collider (RHIC) at BNL and by the ALICE, ATLAS and CMS collaborations [4, 5, 6, 7, 8] at the Large Hadron Collider (LHC) at CERN have made extensive use of this non-extensive distribution. The Tsallis distribution has been very successful in explaining the experimental transverse momentum distribution, longitudinal momentum fraction distribution as well as the rapidity distribution of hadrons from e^+e^- as well as p - p collisions [9, 10, 11, 12, 13, 14, 15]. Here we use a thermodynamically consistent form of the Tsallis distribution, described in detail in [16, 17].

The relevant thermodynamic quantities can be written as integrals over the following distribution function:

$$f = \left[1 + (q - 1) \frac{E - \mu}{T} \right]^{-\frac{1}{q-1}}. \quad (1)$$

Although the q and the T parameter were shown to be consistent for all the particle species [15, 17], the studies [18, 19] leave ample room to scrutinize this conclusion.

2. Review of Tsallis thermodynamics and its application to high-energy physics

The entropy density, s , particle number density, n , energy density, ϵ , and the pressure, P in Tsallis thermodynamics are given by [17],

$$\begin{aligned} s &= -g \int \frac{d^3p}{(2\pi)^3} [f^q \ln_q f - f], \quad n = g \int \frac{d^3p}{(2\pi)^3} f^q, \\ \epsilon &= g \int \frac{d^3p}{(2\pi)^3} E f^q, \quad P = g \int \frac{d^3p}{(2\pi)^3} \frac{p^2}{3E} f^q. \end{aligned} \quad (2)$$

where g is the degeneracy factor. The \ln_q function appearing in Eq. 2 is often referred to as q logarithm and is defined by

$$\ln_q(x) \equiv \frac{x^{1-q} - 1}{1 - q}.$$

The first and second laws of thermodynamics lead to the following two differential relations:

$$d\epsilon = T ds + \mu dn, \quad (3)$$

$$dP = s dT + n d\mu. \quad (4)$$

where, $s = S/V$ and $n = N/V$ are the entropy and particle number densities, respectively (V is the volume).

It is seen that if we use f^q instead of f to define the thermodynamic variables, the above equations satisfy the thermodynamic consistency conditions which require that the following relations are satisfied:

$$T = \left. \frac{\partial \epsilon}{\partial s} \right|_n, \quad \mu = \left. \frac{\partial \epsilon}{\partial n} \right|_s, \quad n = \left. \frac{\partial P}{\partial \mu} \right|_T, \quad s = \left. \frac{\partial P}{\partial T} \right|_\mu. \quad (5)$$

The first equality in Eq. 5, in particular, shows that the variable T appearing in Eq. 1 can indeed be identified as a thermodynamic temperature and is more than just another parameter. It is straightforward to show that these relations are indeed satisfied [17].

Based on the above expressions the particle distribution can be rewritten, using variables appropriate for high-energy physics as

$$\frac{dN}{dp_T dy} = \frac{gV}{(2\pi)^2} p_T m_T \left(1 + (q-1) \frac{m_T}{T} \right)^{-\frac{q}{q-1}} \quad (6)$$

at chemical potential $\mu = 0$ and rapidity $y = 0$.

3. Taylor expansion of the Tsallis distribution and thermodynamic variables

In all fits to the experimental data (transverse momentum spectra, for example) the value of q is very close to 1 and hence, for analytical simplicity, we can expand the Tsallis distribution in a Taylor's series of $(q-1)$. The Taylor's expansion is given by (up to order $(q-1)^2$) [20]:

$$\begin{aligned} & \left[1 + (q-1) \frac{E-\mu}{T} \right]^{-\frac{q}{q-1}} \simeq e^{-\frac{E-\mu}{T}} \left\{ 1 + (q-1) \frac{1}{2} \frac{E-\mu}{T} \left(-2 + \frac{E-\mu}{T} \right) \right. \\ & \left. + \frac{(q-1)^2}{2!} \frac{1}{12} \left[\frac{E-\mu}{T} \right]^2 \left[24 - 20 \frac{E-\mu}{T} + 3 \left(\frac{E-\mu}{T} \right)^2 \right] \right\} \end{aligned} \quad (7)$$

The thermodynamic variables keeping up to $O(q - 1)$ of the expansion in Eq. 7 are calculated below:

3.1. Number density

The particle density in Tsallis thermodynamics is given to first order in $(q - 1)$ by the following expression:

$$n \approx n^B + (q - 1)n^1 \quad (8)$$

where n^B is the standard Boltzmann result for the particle density:

$$n^B = \frac{g}{2\pi^2} e^{\frac{\mu}{T}} T^3 a^2 K_2(a), \quad (9)$$

with $a \equiv m/T$, and the first order expression in $q - 1$ is given by

$$n^1 = \frac{ge^{\frac{\mu}{T}} T^3}{4\pi^2} \left[-6a^2 K_2(a) - 2a^3 K_1(a) - 4a^2 b K_2(a) + 3a^3 K_3(a) + a^4 K_2(a) + a^2 b^2 K_2(a) - 2a^3 b K_1(a) \right]. \quad (10)$$

where K_n are the modified Bessel's function of second kind.

3.2. Energy density

$$\begin{aligned} \epsilon &\approx \epsilon^B + (q - 1)\epsilon^1; & \epsilon^B &= \frac{ge^{\frac{\mu}{T}} T^4}{2\pi^2} (3a^2 K_2(a) + a^3 K_1(a)) \\ \epsilon^1 &= \frac{ge^{\frac{\mu}{T}} T^4}{4\pi^2} \left[9a^3 K_3(a) + 4a^4 K_2(a) + a^5 K_1(a) \right. \\ &\quad \left. + 2b \left(3a^2 K_2(a) + a^3 K_1(a) - 3a^3 K_3(a) + a^4 K_2(a) \right) b^2 \left(3a^2 K_2(a) + a^3 K_1(a) \right) \right]. \end{aligned} \quad (11)$$

3.3. Pressure

Finally, the pressure is given by

$$\begin{aligned} P &\approx P^B + (q - 1)P^1; & P^B &= \frac{ge^{\frac{\mu}{T}} T^4 a^2 K_2(a)}{2\pi^2} \\ P^1 &= \frac{ge^{\frac{\mu}{T}} T^4}{4\pi^2} \left[a^4 K_2(a) + 3a^3 K_3(a) - 2a^3 b K_3(a) + a^2 b^2 K_2(a) + 2a^2 b K_2(a) \right]. \end{aligned} \quad (12)$$

4. Description of the experimental data

In Fig. 1 we show fits to the transverse momentum distribution of π^+ in p - p collisions at 900 GeV. For the Tsallis distribution (solid line) the parameters $T = 70.8$ MeV, $q = 1.1474$. The volume parameter V corresponds to a spherical radius of 4.81 fm. For the Boltzmann distribution (dashed line) the parameters $T = 150.2$ MeV, while the radius used to determine the volume was fixed at a value of 2.65 fm. For the fit using the Boltzmann distribution and the first order term in $(q - 1)$ (dashed-dotted line) the values are $T = 138.4$ MeV, $q = 1.035$ while the radius is given by 2.80 fm. In the last case corresponding to Boltzmann plus first and second orders in $(q - 1)$ (dotted line) one has $T = 121.2$ MeV, $q = 1.065$ and a radius of 3.09 fm. As is well-known and evident, the fit using the Tsallis distribution is very good.

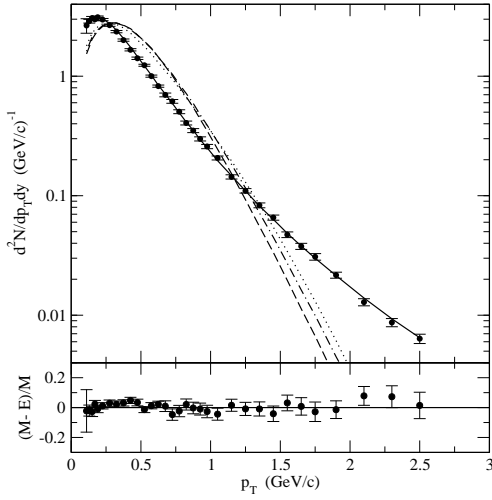


Figure 1. Fits to the normalized differential yields of π^+ as measured by the ALICE collaboration in p - p collisions at $\sqrt{s} = 0.9$ TeV [5] fitted with the Tsallis (solid line) and Boltzmann distributions (dashed line). Also shown are fits with the Tsallis distribution keeping terms to first (dash-dotted line) and second order in $(q - 1)$ (dotted line). The lower part of the figure shows the difference between model (M) and experiment (E) normalized to the model (M) values.

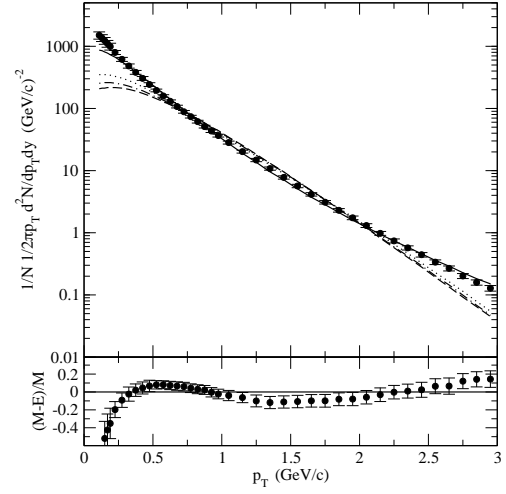


Figure 2. Fits to the normalized differential π^- yields as measured by the ALICE collaboration in $(0 - 5)\%$ Pb-Pb collisions at $\sqrt{s_{NN}} = 2.76$ TeV [6] fitted with the Tsallis (solid line) and Boltzmann distributions (dashed line). Also shown are fits with the Tsallis distribution keeping terms to first (dash-dotted line) and second order in $(q - 1)$ (dotted line). The lower part of the figure shows the difference between model (M) and experiment (E) normalized to the model (M) values.

In Fig. 2 we show fits to the normalized differential π^- yields in $(0 - 5)\%$ Pb-Pb collisions at $\sqrt{s_{NN}} = 2.76$ TeV as measured by the ALICE collaboration [6] with the Tsallis (solid line) and Boltzmann distributions (dashed line). Fits with the Tsallis distribution keeping terms to first order (dash-dotted line) and second order in $(q - 1)$ (dotted line) are also shown. The lower part of the figure shows the difference between the Tsallis distribution (M) and experiment (E). It is clear that the best fit is achieved with the full Tsallis distribution, whereas, using the Boltzmann distribution the description is not good. Successive corrections in $(q - 1)$ improve the description. There is a clear deviation at very low transverse momentum (below 0.5 GeV) and also at higher values above 2.75 GeV.

5. Inclusion of Flow to First Order in $(q - 1)$

With a view to see whether the inclusion of flow could improve the description of the transverse momentum distributions obtained in Pb-Pb collisions, we have included a constant flow velocity, v . We use the following ansatz (in cylindrical polar coordinates) for introducing flow inside our calculations:

$$p^\mu = (m_T \cosh y, p_T \cos \phi, p_T \sin \phi, m_T \sinh y) \quad (13)$$

$$u^\mu = (\gamma \cosh \zeta, \gamma v \cos \alpha, \gamma v \sin \alpha, \gamma \sinh \zeta) \quad (14)$$

where $(\zeta)y$ is the (space-time)rapidity of particles (fluid-element) and v is the velocity of fluid. Now, to include flow inside the Tsallis distribution, we replace $E \rightarrow p^\mu u_\mu$. The dot product

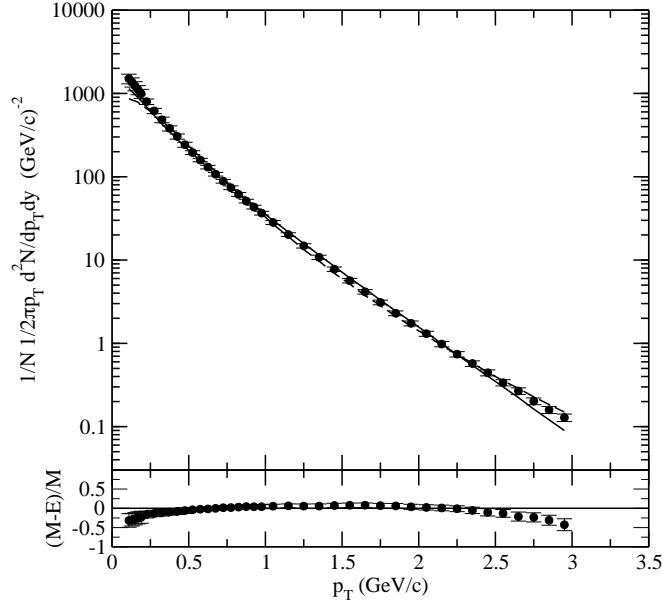


Figure 3. Fits to the normalized differential π^- yields as measured by the ALICE collaboration in (0 – 5)% Pb-Pb collisions at $\sqrt{s_{NN}} = 2.76$ TeV [6]. The fit with the Tsallis distribution including flow keeping terms to first order in $(q - 1)$ (dashed line). The flow velocity is fixed at $v = 0.609$, with $T = 146$ MeV, $q = 1.030$ and the radius of the volume is $R = 29.8$ fm. The solid line is the Tsallis distribution without flow as given in Fig. 2. The lower part of the figure shows the difference between model (M), i.e. Tsallis with flow up to first order in $(q - 1)$, and experiment (E) normalized to the model (M) values.

then becomes,

$$p^\mu u_\mu = \gamma m_T \cosh(y - \zeta) - \gamma v p_T \cos(\phi - \alpha) \quad (15)$$

Now putting Eq. 15 in a Taylor's expansion of Eq. 6 up to $\mathcal{O}(q - 1)$ and integrating over ϕ and ζ , for space-like freeze-out surfaces, the invariant yield is given by the following formula

$$\begin{aligned} \frac{1}{p_T} \frac{dN}{dp_T dy} &= \frac{gV}{(2\pi)^2} \left\{ 2T[rI_0(s)K_1(r) - sI_1(s)K_0(r)] - (q - 1)Tr^2I_0(s)[K_0(r) + K_2(r)] \right. \\ &+ 4(q - 1)TrsI_1(s)K_1(r) - (q - 1)Ts^2K_0(r)[I_0(s) + I_2(s)] \\ &+ \frac{(q - 1)}{4}Tr^3I_0(s)[K_3(r) + 3K_1(r)] - \frac{3(q - 1)}{2}Tr^2s[K_2(r) + K_0(r)]I_1(s) \\ &\left. + \frac{3(q - 1)}{2}Ts^2r[I_0(s) + I_2(s)]K_1(r) - \frac{(q - 1)}{4}Ts^3[I_3(s) + 3I_1(s)]K_0(r) \right\} \quad (16) \end{aligned}$$

where

$$r \equiv \frac{\gamma m_T}{T}; \quad s \equiv \frac{\gamma v p_T}{T}. \quad (17)$$

$I_n(s)$ and $K_n(r)$ are the modified Bessel functions of the first and second kind. In this formula, the freeze-out surface has been considered to be space-like and so the integration over the freeze-out surface turns out to be trivial. For a more detailed treatment of the freeze-out surface in this context, readers are referred to Ref. [21].

The comparison between model and experiment is quite good with notable deviations at small values of the transverse momentum p_T and again above values of 2.5 GeV (see Fig. 3). These could easily be attributed to the coarse way of treating transverse flow. More detailed investigations have been carried out in [18].

6. Summary and Conclusion

Fits to the particle spectra using the Taylor's expansion are limited to certain ranges of transverse momentum. This may be attributed to the fact that there are certain constraints on the values q , E and T take for these expansions to be valid. Hence, we need to carry out more rigorous treatments to find out exact analytical forms of the Tsallis thermodynamic variables.

Acknowledgments

TB acknowledges the support of IIT Indore, India.

References

- [1] Tsallis C 1988 *J. Statist. Phys.* **52** 479
- [2] Abelev B I *et al.* (STAR collaboration) 2007 *Phys. Rev. C* **75** 064901
- [3] Adare A *et al.* (PHENIX collaboration) 2011 *Phys. Rev. D* **83** 052004
- [4] Aamodt K *et al.* (ALICE collaboration) 2010 *Phys. Lett. B* **693** 53
- [5] Aamodt K *et al.* (ALICE collaboration) 2011 *Eur. Phys. J C* **71** 1655
- [6] Abelev B *et al.* (ALICE collaboration) 2012, *Phys. Rev. Letts.* **109** 252301
- [7] Khachatryan V *et al.* (CMS collaboration) 2010 *J. of High Eng. Phys.* **02** 041
- [8] Aad G *et al.* (ATLAS collaboration) 2011 *New J. Phys.* **13** 053033
- [9] Bediaga I, Curado E M F and Miranda J M de 2000 *Physica A* **286** 156.
- [10] Wilk G and Włodarczyk Z 2015 *Acta Phys. Polon. B* **46** 1103
- [11] Ürmössy K, Barnaföldi G G and Biró T S 2011 *Phys. Lett. B* **701** 111
- [12] Ürmössy K, Barnaföldi G G, and Biró T S 2012 *Phys. Lett. B* **718** 125.
- [13] Khandai P K, Sett P, Shukla P and Singh V 2013 *Int. Jour. Mod. Phys. A* **28** 1350066
- [14] Li B -C, Wang Y -Z and Liu F -H 2013 *Phys. Lett. B* **725** 352
- [15] Marques L, Cleymans J and Deppman A 2015 *Phys. Rev. D* **91** 054025
- [16] Cleymans J and Worku D 2012 *J. Phys. G* **39** 025006
- [17] Cleymans J and Worku D 2012 *Eur. Phys. Jour. A* **48** 160
- [18] Tang Z, Xu Y, Ruan L, van Buren G, Wang F and Xu Z 2009 *Phys. Rev. C* **79** 051901(R)
- [19] Biró T S, Pürselli G and Ürmössy K 2009 *Eur. Phys. J. A* **40** 325
- [20] Bhattacharyya T, Cleymans J, Khuntia A, Pareek P and Sahoo R 2016 *Eur. Phys. J A* **52** 30
- [21] Ürmössy K and Biró T S 2010 *Phys. Lett. B* **689** 14

Quantum Boltzmann evolution of the Quark-Gluon Plasma

William Grunow^{1,2}, André Peshier¹

Department of Physics, University of Cape Town, Rondebosch 7700, South Africa

E-mail: ²William.Grunow@alumni.uct.ac.za

Abstract. The rapid equilibration of the Quark-Gluon Plasma, produced in nucleus-nucleus collisions in a far-from-equilibrium initial state, seems to be difficult to understand theoretically. One reason could be that almost all existing approaches based on the relativistic Boltzmann equation neglect quantum-statistics features of the quarks and gluons. Against this background, we put forward a novel Monte-Carlo method to solve the Boltzmann equation, with quantum effects included.

1. Introduction

Recent heavy-ion experiments have confirmed the existence of a deconfined plasma of quarks and gluons, the Quark Gluon Plasma (QGP) [1, 2]. The rapid (≤ 1 fm) onset of hydrodynamical flow of the QGP requires rapid thermalization of the plasma; this is contrasted with the Color Glass Condensate (CGC) picture which is a model of the initial conditions where the incoming nuclei are saturated with gluons up to a saturation scale Q_s . How this rapid thermalization of the QGP occurs is a matter of much theoretical interest. It has been suggested by [3] that if the initial conditions are dense enough, and number changing processes in early times suppressed enough, that a transient Bose-Einstein condensate could develop. The development of a condensate could significantly influence the dynamics of the plasma [4]. Whether or not the condensate is kinetically able to form in the time constraints is currently unknown. Initial applications of kinetic theory have neglected quantum effects, these classical models not only do not thermalize rapidly enough, but also drive the system to a Maxwell-Boltzmann type equilibrium, precluding the formation of a condensate. We thus want to study the kinetic theory of the QGP without neglecting quantum effects.

2. The Boltzmann equation

To study the thermalization of the QGP and see if the rapid formation of a Bose-Einstein condensate is kinetically allowed we turn to the Boltzmann equation. The Boltzmann equation is a way of describing the evolution of the distribution function of a non-equilibrium system, and reads,

$$\frac{d}{dt}f(\mathbf{x}, \mathbf{p}, t) = \mathcal{C}[f(\mathbf{p}, t)] - \mathbf{v}\nabla f(\mathbf{x}, \mathbf{p}, t), \quad (1)$$

where $f(\mathbf{x}, \mathbf{p}, t)$ is the distribution function. The $\mathbf{v}\nabla f(\mathbf{x}, \mathbf{p}, t)$ term describes the flow of matter through space, for the purposes of this paper we will assume a spatially isotropic distribution

function, and thus this term shall be zero. We will further assume momentum isotropy so that the distribution function is only a function of the magnitude of the momentum. $\mathcal{C}[f(\mathbf{p}), t]$ is the so-called collision term which is a functional that describes the interaction between different particles, for bosons, for a binary elastic interaction this term reads

$$\begin{aligned} \mathcal{C}[f(\mathbf{p}, t)] = & \frac{1}{2E_p} \int \frac{d^3p_2}{(2\pi)^3 2E_2} \frac{1}{\nu} \int \frac{d^3p_3}{(2\pi)^3 2E_3} \int \frac{d^3p_4}{(2\pi)^3 2E_4} |\mathcal{M}_{p_1 p_2 \rightarrow p_3 p_4}|^2 \\ & \times [f(p_3)f(p_4)(1+f(p))(1+f(p_2)) - f(p)f(p_2)(1+f(p_3))(1+f(p_4))] \\ & \times (2\pi)^4 \delta^4(p + p_2 - p_3 - p_4). \end{aligned} \quad (2)$$

This expression details the rate at which particles are scattered into, and out of a particular momentum state, by summing every kinetically allowed scattering event weighted by the quantum mechanical amplitude (\mathcal{M}^2) for such a particular scattering to occur and the Bose enhancement factors (the $(1+f)$ terms). The Bose enhancement factors are absent in the classical formulation. Most existing approaches, like [5] perform a classical approximation.

It is readily checked that the Bose-Einstein distribution,

$$f_{\text{BE}}(p) = \frac{1}{e^{\beta E(p)} - 1}, \quad (3)$$

satisfies

$$\mathcal{C}[f_{\text{BE}}(p)] = 0, \quad (4)$$

and thus is a fixed point of the Boltzmann equation.

The Bose enhancement terms strictly increase the rate at which scatterings occur, which could lead to a more rapid thermalization.

The Boltzmann equation is a non-linear functional equation and has no general analytic solution, and we resort to either applying simplifying assumptions to the model we study or rely on a numerical solution which we detail now.

3. Numerical solution of the Boltzmann equation

To solve the Boltzmann equation, we use a Monte Carlo algorithm inspired by [5], we improve upon it by not making the aforementioned approximation, albeit using a different method. This was done by [6] as well, although using a different, more computationally expensive method than what we will perform.

The idea behind our algorithm is as follows, the Boltzmann equation describes the scattering of particles into new momentum states, so once an initial distribution is specified, we draw an ensemble of N particles from this distribution, calculate the probability that each unique particle pair will interact in some timestep Δt , (there are $\frac{N(N-1)}{2}$ such pairs), “roll the dice” to determine which particle pairs interact and update the momentum of the scattered particle. This specifies a new ensemble which is a representation of the new distribution function, at $t + \Delta t$.

An ensemble of finitely many samples is going to have fluctuations, possibly large, which limits the quality of the approximation of the distribution function, this can be overcome by averaging over ensembles, the fluctuations average out, and we can extract a better approximation of the distribution function.

With this in mind, instead of only performing the scattering step once, we roll the dice multiple times to get many different ensemble representations of the new distribution function, which we can reconstruct from the ensembles. We detail how we reconstruct the distribution function is presented in the following section.

The details of how the interaction probability of a pair of particles is calculated can be found here [6].

Position space is discretized into cells, only particles within a single cell can interact. We've only considered a single cell at this point. Having multiple cells will allow us to reintroduce the flow term into the Boltzmann equation.

3.1. Reconstruction of the distribution function

Our algorithm requires the ability to reconstruct a distribution function from a given ensemble.

A typical technique to extract a probability distribution from an ensemble is to bin the data into a histogram and interpolate an approximation of the function. This approach is, however, not desirable in this context as the reconstructed distribution function should conserve energy and accurately replicate the slope of, in particular, the Bose-Einstein distribution at small momenta (where the contribution from Bose enhancement is expected to be largest). This approach was taken by [6], and they required a very large number of particles work.

Instead, we smear each particle in the ensemble into a Gaussian-like “basis” function(chosen to satisfy the criteria above), and the combination of these basis functions gives an approximation of the true distribution function. This procedure also has a physical justification in the uncertainty principle, where the width of the basis function corresponds to the uncertainty.

We found the most effective radial distribution functions given by the following form,

$$R(p; \mu, \sigma) = \frac{2}{\sigma\sqrt{\pi}} \text{Erf} \left(\frac{\mu}{\sigma} \right) \exp \left(-\frac{p^2 + \mu^2}{\sigma^2} \right) \sinh \left(\frac{2p\mu}{\sigma^2} \right), \quad (5)$$

where the parameters σ and μ control the width and the peak of the curve respectively. Energy conservation constrains one of the parameters, we specify the width based upon the average separation between particles in momentum space, which specifies the value of the peak.

Once the width σ is specified the position of the peak, μ , is specified (by energy conservation) by

$$\frac{\mu}{\text{Erf} \left(\frac{\mu}{\sigma} \right)} = E \quad (6)$$

when smearing a particle with energy E .

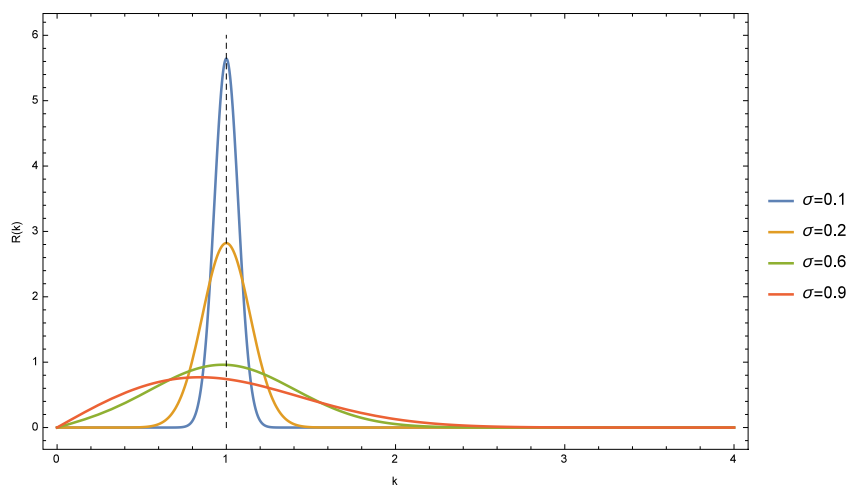


Figure 1: Here we see how the basis functions look for various values of the width parameter, the original particle had a momentum specified by the dashed line.

Here we show a couple of examples of reconstructions done by this technique,

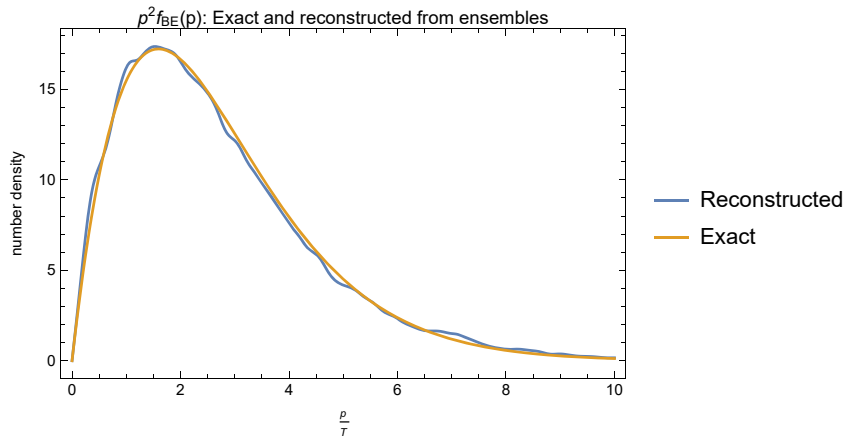


Figure 2: A reconstruction of the radial Bose-Einstein distribution, the reconstruction was done with 500 ensembles of 64 particles.

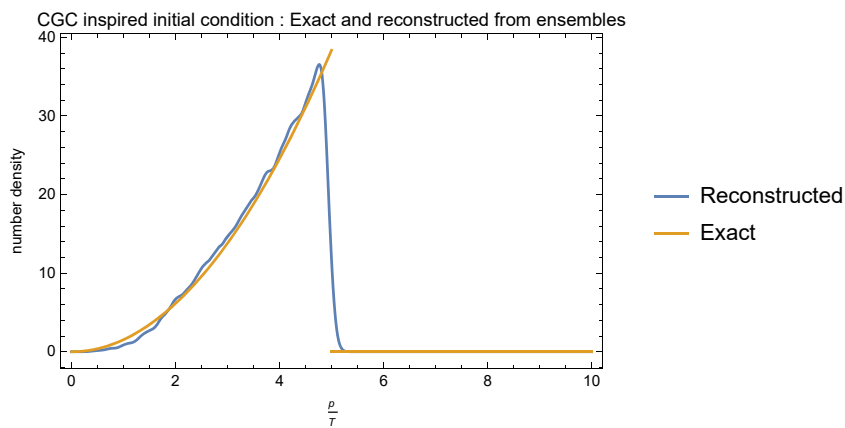


Figure 3: A reconstruction of a radial Fermi-like distribution (inspired by the CGC), the reconstruction was done with 500 ensembles of 64 particles.

this shows both the ability to accurately reconstruct the Bose-Einstein distribution, especially getting the small momentum behaviour correct, and that it generalises to another distribution, the same parameters are used for the reconstruction of both distributions.

4. Preliminary results

Whilst a full simulation has not yet been carried out, we present some preliminary results. We considered the effect that adding quantum fluctuations would have on the scattering rate of binary gluons, in particular the dominant t-channel exchange process,

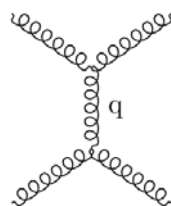


Figure 4: Feynman diagram for t-channel binary gluon scattering

with the corresponding regulated cross-section

$$\frac{d\sigma}{dt} = \frac{9\pi\alpha_s}{(t - m_D^2)^2} \quad (7)$$

We compute the interaction likelihoods of this process on an ensemble of 64 particles drawn from a Bose-Einstein distribution for both the quantum case(inclusion of Bose enhancement) and the classical case(no Bose enhancement)

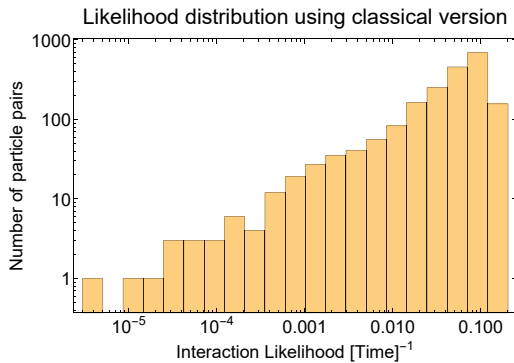


Figure 5: Calculation of the interaction likelihoods 100 particle pairs using the classical algorithm, the scattering time will be dominated by the largest interaction likelihood, in this case $0.1s^{-1}$

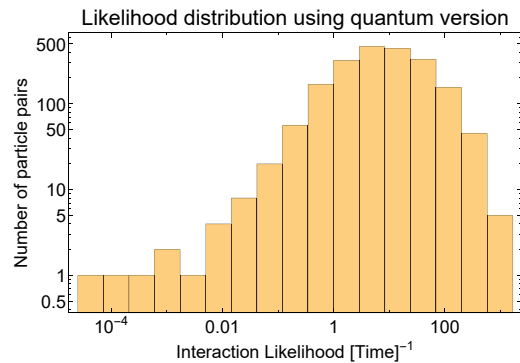


Figure 6: Calculation of the interaction likelihoods 100 particle pairs using the quantum algorithm, the scattering time will be dominated by the largest interaction likelihood, in this case $100s^{-1}$

By looking at the most likely interactions in each case, we see an increase in the interaction rate in the quantum case by 2-3 orders of magnitude. This is a promising result, whether it is enough to see rapid thermalization is yet to be seen.

5. Conclusion

We develop a numerical algorithm to solve the Boltzmann equation with quantum effects included; this required the development of a novel way of reconstructing a distribution function from a representative ensemble. We hope that this can be used in the near future to investigate the kinetics of Bose-Einstein condensate formation in the QGP. The high interaction rates generated when including quantum effects requires a very short timestep, so detailed studies using this code have not yet been done. There are some obvious numerical optimisations to be done, for instance, the parallelization of the calculation of interaction probabilities. The next features to be developed would be a robust technique for detecting the presence of a condensate, an implementation of a running coupling, the inclusion of number changing processes and the reintroduction of the flow term.

References

- [1] Müller B and Nagle J L 2006 *Annu. Rev. Nucl. Part. Sci.* **56** 93–135
- [2] Aamodt K, Abelev B, Quintana A A, Adamova D, Adare A, Aggarwal M, Rinella G A, Agocs A, Salazar S A, Ahammed Z *et al.* 2010 *Physical review letters* **105** 252302
- [3] Blaizot J P, Gelis F, Liao J F, McLerran L and Venugopalan R 2012 *Nucl. Phys.* **A873** 68–80 (*Preprint* 1107.5296)
- [4] Peshier A and Giovannoni D 2016 *J. Phys. Conf. Ser.* **668** 012076 (*Preprint* 1511.02571)
- [5] Xu Z and Greiner C 2005 *Phys. Rev.* **C71** 064901 (*Preprint* hep-ph/0406278)
- [6] Scardina F, Perricone D, Plumari S, Ruggieri M and Greco V 2014 *Phys. Rev.* **C90** 054904 (*Preprint* 1408.1313)

Energy loss of open strings with massive endpoints in AdS/CFT

W. A. Horowitz¹ and A. Andrianaivalomahefa²

¹Department of Physics, University of Cape Town, Private Bag X3, Rondebosch 7701, South Africa

²Department of Mathematical Sciences, University of Durham, Durham, DH1 3LE, UK

E-mail: ¹wa.horowitz@uct.ac.za and ²arnaud@aims.ac.za

Abstract. We propose a novel AdS/CFT construction for a heavy quark in an $\mathcal{N} = 4$ SYM theory. Using our new AdS/CFT heavy quark Lagrangian, in which we couple massive endpoints to the usual open string, we compute the stopping distance and differential energy loss for heavy quarks traversing a strongly-coupled $\mathcal{N} = 4$ SYM plasma. We discuss the implications of our new holographic results for heavy-ion physics.

1. Introduction

We wish in heavy ion physics to characterize theoretically and confirm experimentally the non-trivial, emergent, many-body properties of quantum chromodynamics (QCD) at energy scales above the expected deconfinement temperature, at which the relevant degrees of freedom for the theory change from the usual hadronic matter we experience in everyday life to something new, and at nearly zero baryon chemical potential. Experimentally, the field uses colliders to smash nuclear matter together at enormous speeds, the Relativistic Heavy Ion Collider (RHIC) located at Brookhaven National Laboratory in the USA and at the Large Hadron Collider (LHC) located at CERN in Switzerland. The particle species used at these colliders tend to be protons and large nuclei such as gold and lead. On the theoretical side, perturbative quantum chromodynamics (pQCD), lattice QCD (lQCD), and the AdS/CFT conjecture are the three main tools used to derive predictions to be compared with data.

That both pQCD and AdS/CFT are concurrently used reflects the current uncertainty in some of the basic properties of the quark-gluon plasma (QGP) produced in these heavy ion collisions. In particular, it is not clear experimentally or theoretically what, if any, small parameter exists for the description of the QGP at temperatures not far above $\Lambda_{QCD} \sim 180 \text{ MeV} \sim 10^{12} \text{ K}$. An enormous amount of progress has been made for high momentum observables using both the assumption that the usual coupling in the QCD Lagrangian, evaluated at the temperature of the plasma, is small: $g(T) \ll 1$ [1–17]. On the other hand, a large swath of low momentum data is better described under the naive assumption that the 't Hooft coupling is large: $\lambda \equiv g^2 N_c \gg 1$ [18–31].

Since in science we seek a consistent picture of the processes we observe in nature, we'd like to resolve the current, seeming paradoxical picture of heavy ion collisions into a unified understanding. There are essentially two paths to this unification: 1) a successful application of

weak coupling techniques to low momentum observables or 2) a successful application of strong coupling techniques to high momentum observables. Fascinating recent work has shown promise for the first direction of research [32–37]. We will, however, follow the latter path.

The main phenomenological obstacle faced when comparing high momentum observable predictions from AdS/CFT to data is all research so far has shown that in a strong coupling theory the particles are stopped by the plasma very rapidly [38–41]. Perhaps, it is possible that this very short stopping distance (and thus large energy loss) is due to using an AdS/CFT analog for QCD objects that is not accurate. For example, there are puzzling aspects to using the usual AdS/CFT construction for heavy quarks [42]; e.g., in the presence of a plasma, the mass of the heavy quark *decreases*. Perhaps a more natural construction for a heavy quark in AdS/CFT exists which will simultaneously solve the puzzling aspects of heavy flavor and also yield energy loss results more similar to data.

2. Weighing the string endpoints

We propose to extend the finite endpoint momentum work [43] to allow string endpoints to have both finite momentum and finite mass. We therefore hope to provide an additional connection between heavy ion physics and AdS/CFT; our finite mass endpoint construction should naturally apply to the open heavy flavor physics measured at RHIC and LHC.

The simplest Poincaré invariant action that includes finite momentum and finite mass at the string endpoints may be written as

$$S = -\frac{1}{4\pi\alpha'} \int_M d\tau d\sigma \sqrt{-h} h^{ab} \partial_a X^\mu \partial_b X^\nu G_{\mu\nu} + \frac{1}{2} \int_{\partial M} d\xi \left(\frac{1}{\eta} \dot{X}^\mu \dot{X}^\nu G_{\mu\nu} - \eta m^2 \right), \quad (1)$$

where ∂M is the boundary of the worldsheet M and $G^{\mu\nu}$ is the metric of the target spacetime. Here h refers to the determinant of auxiliary worldsheet metrics h_{ab} and η is auxiliary field defined at ∂M . The dots denote differentiation with respect to ξ , which is an independent parametrization of the worldsheet boundary. The first term in our action Eq. 1 is the usual Polyakov action describing a bosonic string. The second term is nothing but the action for a relativistic point particle of mass m .

We may find the equations of motion due to Eq. 1 by varying the action with respect to the coordinates X^μ :

$$\begin{aligned} \delta S = & \int_M d\tau d\sigma \partial_a (P^a_\mu \delta X^\mu) - \int_M d\tau d\sigma (\partial_a P^a_\mu) \delta X^\mu + \int_M d\tau d\sigma P^a_\lambda \partial_a X^\mu \Gamma^\lambda_{\rho\nu} (\delta X^\rho) \\ & + \int_{\partial M} d\xi \frac{d}{d\xi} (p_\mu \delta X^\mu) - \int_{\partial M} d\xi (\dot{p}_\mu) \delta X^\mu + \int_{\partial M} d\xi p_\lambda \dot{X}^\mu \Gamma^\lambda_{\rho\mu} \delta X^\rho, \end{aligned} \quad (2)$$

where we defined the worldsheet and endpoint momenta as

$$P^a_\mu := -\frac{1}{2\pi\alpha'} \sqrt{-h} h^{ab} \partial_b X^\nu G_{\mu\nu}; \quad p_\mu := \frac{1}{\eta} \dot{X}^\nu G_{\mu\nu}. \quad (3)$$

Applying the two dimensional version of Stokes' theorem over the surface term on the string worldsheet in Eq. 2 gives

$$\int_M d\tau d\sigma \partial_a (P^a_\mu \delta X^\mu) = \int_{\partial M} dn^a \epsilon_{ab} P^b_\mu \delta X^\mu = \int_{\partial M} d\xi \dot{n}^a \epsilon_{ab} P^b_\mu \delta X^\mu,$$

where $n^a(\xi)$ parametrizes the normal to the worldsheet boundaries and ϵ_{ab} is an antisymmetric symbol with $\epsilon_{\tau\sigma} = 1$. Then by extremizing the string action and after relabelling some dummy indices, the bulk and boundary equations of motion read, respectively as

$$\partial_a P^a_\mu - \Gamma^\lambda_{\mu\nu} \partial_a X^\nu P^a_\lambda = 0; \quad \dot{p}_\mu - \Gamma^\lambda_{\mu\nu} \dot{X}^\nu p_\lambda = \dot{n}^a \epsilon_{ab} P^b_\mu. \quad (4)$$

Now let us spend a few moments to discuss on the dynamics of the endpoints. A key result in the study of [43] shows that the free string endpoint motion is no longer purely transverse when the endpoints have non-vanishing momentum. Thus the endpoints are driven in such a way that their velocity is pointing at least partially in the same direction as the tangent to the string at the worldsheet boundary. Our massive endpoints move at velocity $v < 1$.

Furthermore we have the following identity

$$\dot{n}^a \epsilon_{ab} P_\mu^b \pm \frac{\eta}{2\pi\alpha'} p_\mu = 0, \quad (5)$$

which shows that we can separate the motion of the endpoints from that of the interior of string. This separation of motion is actually a direct consequence of the finite endpoint momenta.

Next, by substituting Eq. 5 into Eq. 4, it is straightforward to show – by means of a change of variable – that the endpoints’ equation of motion describes a timelike geodesic on the spacetime boundary. Finally, in the rest of this work we shall assume a configuration of strings that prevents a snap-back as the 4-point momentum p^μ vanishes. Indeed we will argue that the endpoint momenta are going to vanish as the string crosses the black hole horizon.

3. Falling strings on spacetime geodesics

The metric of the asymptotic AdS₅ part of the 10-dimensional dual geometry can be written as

$$ds^2 = \frac{L^2}{z^2} \left[-f(z)dt^2 + \frac{1}{f(z)}dz^2 + d\vec{x}^2 \right], \quad f(z) = 1 - \left(\frac{z}{z_h} \right)^4. \quad (6)$$

Here L is the AdS curvature radius, (t, \vec{x}) corresponds to 4-dimensional Minkowski coordinates and z denotes the inverse radial coordinate. Thus the spacetime boundary is located at $z = 0$, while the black hole horizon is at $z = z_h$. The temperature of the field theory equals the Hawking temperature of the black hole in the interior of the asymptotic AdS₅ [44]. The AdS/CFT dictionary provides us with a relation between the background temperature and the horizon radius such that $T = 1/(\pi z_h)$.

In the gravity dual, adding a fundamental representation quark in $\mathcal{N} = 4$ SYM is tantamount to adding a D7 brane [42] that fills a transverse S^3 and extends along the radial direction from the boundary of the asymptotic AdS₅ up to some depth z_* . The dual description of probe quark moving through the plasma involves classical open IIB strings whose endpoints are attached to the D7 brane. One can think the string as an holographic representation of the colour field between a quark-antiquark pair.

Again we restrict our attention to the motion of the string in the x - z plane of the asymptotic AdS₅ geometry. We are also interested in a string configuration with an initial pointlike state and no component of the initial velocity along the radial direction. Let us assume that the string is created at some coordinate $z = z_*$, then extends while the endpoints follow timelike geodesics until it ultimately falls into the black hole.

The proper time τ at the worldsheet boundary can be chosen to parametrize the endpoints path. Geodesic equations with respect to the t and x coordinate system in the asymptotic AdS₅ background read

$$\frac{d^2t}{d\tau^2} + \frac{z^2}{L^2 f(z)} \frac{d}{dz} \left(\frac{L^2}{z^2} f(z) \right) \frac{dz}{d\tau} \frac{dt}{d\tau} = 0, \quad \frac{d^2x}{d\tau^2} + \frac{z^2}{L^2} \frac{d}{dz} \left(\frac{L^2}{z^2} \right) \frac{dz}{d\tau} \frac{dx}{d\tau} = 0, \quad (7)$$

respectively, with the constraint

$$G_{\mu\nu} \frac{dX^\mu}{d\tau} \frac{dX^\nu}{d\tau} = -f(z) \left(\frac{dt}{d\tau} \right)^2 + \frac{1}{f(z)} \left(\frac{dz}{d\tau} \right)^2 + \left(\frac{dx}{d\tau} \right)^2 = \zeta. \quad (8)$$

Here $\zeta = 0, -1$ for null or timelike geodesics corresponding to massless and massive endpoints respectively. However, we would like a smooth approach to find the limiting case of a lightlike geodesic, that is by setting $m = 0$ everywhere in our results. Notice that since any monotonic function $\tau'(\tau)$ is equivalently a good parameter for the geodesic, then, physically it does not make any difference to parametrize paths by τ or τ' . In order to exhibit the mass term, let us parametrise the geodesics by $\tau' = \tau/m$. Working out the geodesic equations we obtain

$$\frac{dx}{dt} = \frac{h_2}{h_1} f(z), \quad \frac{dz}{dt} = f(z) \left[1 - \frac{m^2 + (h_2 z/L)^2}{(h_1 z/L)^2} f(z) \right]^{1/2}, \quad (9)$$

where h_1, h_2 are constants of integration. It follows that

$$\frac{dx}{dz} = \frac{v}{f(z_*)} \left[1 - \frac{m^2 + (h_2 z/L)^2}{(h_1 z/L)^2} f(z) \right]^{-1/2}. \quad (10)$$

where v is the initial velocity of the endpoints along the x direction and $h_2/h_1 = v/f(z_*)$. Notice that the results of [43] for massless string endpoints are correctly recovered by setting $m = 0$. Furthermore we can solve for the h_1, h_2 constants from the initial pointlike conditions that yields

$$\frac{dx}{dz} = \frac{v}{f(z_*)} \left[1 - \frac{-v^2 + f(z_*) + (vz/z_*)^2}{(f(z_*)z/z_*)^2} f(z) \right]^{-1/2}. \quad (11)$$

Eq. 11 does not explicitly depend on the endpoint mass. In fact, this parameter is encoded in the initial conditions of our string. To recover the results for massless endpoints we just use the appropriate initial conditions for the massless case, namely $v = \sqrt{f(z_*)}$, which corresponds to the speed of light along the x -direction and at constant depth z_* in the Schwarzschild-AdS₅ geometry. Since the endpoints are now massive and follow timelike geodesics, they move with initial velocity $v < \sqrt{f(z_*)}$.

4. Maximal stopping distance

Recall first that the velocity of the endpoints vanishes when they cross the horizon. In principle, we will integrate Eq. 11 from $z = z_*$ to $z = z_h$ to find the distance travelled by the string endpoints, but this expression is difficult to find analytically. However, we can estimate the stopping distance by means of a reasonable approximation. The idea consists of assuming the endpoints move at an approximately constant depth $z = z_*$ and constant velocity $v \approx 1$ for a long time compared to z , before plunging rapidly into the horizon. Integrating Eq. 11 in the limit $z_* \ll z_h$ under this assumption yields

$$\Delta x \approx v \frac{z_h^2}{z_*} \frac{\sqrt{\pi} \Gamma(\frac{5}{4})}{\Gamma(\frac{3}{4})}. \quad (12)$$

One may easily recover the massless limit in [43] by taking $v = 1$. Since $v < 1$, then the string with massless endpoints goes *further* than the massive one provided that both endpoints start at the same depth $z = z_*$.

In particular, we find that

$$\Delta x = v \Delta x_0 = v \left(\frac{2}{\pi^2} \right)^{1/3} \frac{\Gamma(\frac{5}{4}) \Gamma(\frac{1}{4})^{1/3}}{\Gamma(\frac{3}{4})^{4/3}} \left[\frac{1}{\sqrt{\lambda}} \frac{E_0}{T^4} \right]^{1/3}, \quad (13)$$

where in the last equality we used the equation $T = 1/(\pi z_h)$ furnished by the AdS/CFT dictionary, and Δx_0 is the result for massless string endpoints [43], λ is the 't Hooft coupling, and E_0 is the initial energy of the quark.

5. Heavy-quark energy differential loss in AdS/CFT

We want to compute how quickly the endpoints' energy decreases as the string approaches the horizon. If we assume again that the string endpoints quickly swoop down to the black hole after evolving for a relatively long time at radius $z \approx z_*$ with constant velocity v , we find

$$\frac{dE}{dz} \approx -\frac{\sqrt{\lambda}}{2\pi} \frac{1}{z^2 \sqrt{1 - \frac{f(z)}{f(z_*)}}}. \quad (14)$$

By comparing Eq. 14 with [43], the massive string endpoints lose approximately the same energy as the massless endpoints, with respect to z . Notice however that we also did an overestimation here.

To read off the energy loss by the quark in field theory, we need to compute the energy loss of the endpoints as they move ahead in the x direction. This is done by means of a chain rule in Eq. 14 and using the geodesic equation, which gives

$$\frac{dE}{dx} \approx -\frac{1}{v} \left(\frac{\sqrt{\lambda} f(z_*)}{2\pi z^2} \right) \approx -\frac{1}{v} \left(\frac{\sqrt{\lambda}}{2\pi} \frac{1}{z^2} \right), \quad (15)$$

where in the last step we assumed $z_* \ll z_h$. By taking $v \rightarrow 1$, we recover one of the main results from [43]. Notice that since the additional factor $v < 1$ the string endpoints lose more energy along a timelike geodesic than a lightlike one.

6. Discussion

In this proceedings we generalized the work of Ficnar and Gubser [43] to allow strings with *both* finite endpoint mass and momentum. Our results are completely consistent with those of Ficnar and Gubser: we recover all their results when we take our endpoint masses to 0. Additionally, our results are quite sensible: 1) the endpoint stopping distance Δx for a massive quark is reduced by a factor of $v < 1$ when the heavy quark starts at the same z depth as the massless quark and 2) the differential energy loss dE/dx is similarly enhanced by a factor of $1/v > 1$ in the massive case compared to the massless case.

From the work of this proceedings, one may improve the modelling of strong-coupling open heavy flavor energy loss calculations used in heavy ion phenomenology.

Naïvely one expects a massive particle *of the same momentum* as a massless particle to propagate further before stopping. We leave checking such an expectation for future work.

Acknowledgments

The authors wish to thank the South African National Research Foundation and SA-CERN for support.

References

- [1] Gyulassy M, Levai P and Vitev I 2002 *Phys. Lett.* **B538** 282–288 (*Preprint nucl-th/0112071*)
- [2] Vitev I and Gyulassy M 2002 *Phys. Rev. Lett.* **89** 252301 (*Preprint hep-ph/0209161*)
- [3] Wang E and Wang X N 2002 *Phys. Rev. Lett.* **89** 162301 (*Preprint hep-ph/0202105*)
- [4] Majumder A, Wang E and Wang X N 2007 *Phys. Rev. Lett.* **99** 152301 (*Preprint nucl-th/0412061*)
- [5] Dainese A, Loizides C and Paic G 2005 *Eur. Phys. J.* **C38** 461–474 (*Preprint hep-ph/0406201*)
- [6] Armesto N, Cacciari M, Dainese A, Salgado C A and Wiedemann U A 2006 *Phys. Lett.* **B637** 362–366 (*Preprint hep-ph/0511257*)
- [7] Wicks S, Horowitz W, Djordjevic M and Gyulassy M 2007 *Nucl. Phys.* **A784** 426–442 (*Preprint nucl-th/0512076*)
- [8] Majumder A, Nonaka C and Bass S A 2007 *Phys. Rev.* **C76** 041902 (*Preprint nucl-th/0703019*)
- [9] Zhang H, Owens J F, Wang E and Wang X N 2009 *Phys. Rev. Lett.* **103** 032302 (*Preprint 0902.4000*)

- [10] Vitev I and Zhang B W 2010 *Phys. Rev. Lett.* **104** 132001 (*Preprint* 0910.1090)
- [11] Schenke B, Gale C and Jeon S 2009 *Phys. Rev.* **C80** 054913 (*Preprint* 0909.2037)
- [12] Young C, Schenke B, Jeon S and Gale C 2011 *Phys. Rev.* **C84** 024907 (*Preprint* 1103.5769)
- [13] Majumder A and Shen C 2012 *Phys. Rev. Lett.* **109** 202301 (*Preprint* 1103.0809)
- [14] Horowitz W A and Gyulassy M 2011 *Nucl. Phys.* **A872** 265–285 (*Preprint* 1104.4958)
- [15] Buzzatti A and Gyulassy M 2012 *Phys. Rev. Lett.* **108** 022301 (*Preprint* 1106.3061)
- [16] Horowitz W A 2013 *Nucl. Phys.* **A904-905** 186c–193c (*Preprint* 1210.8330)
- [17] Djordjevic M and Djordjevic M 2014 *Phys. Lett.* **B734** 286–289 (*Preprint* 1307.4098)
- [18] Teaney D, Lauret J and Shuryak E V 2001 *Phys. Rev. Lett.* **86** 4783–4786 (*Preprint* nucl-th/0011058)
- [19] Kolb P F, Heinz U W, Huovinen P, Eskola K J and Tuominen K 2001 *Nucl. Phys.* **A696** 197–215 (*Preprint* hep-ph/0103234)
- [20] Hirano T and Tsuda K 2002 *Phys. Rev.* **C66** 054905 (*Preprint* nucl-th/0205043)
- [21] Kolb P F and Heinz U W 2003 (*Preprint* nucl-th/0305084)
- [22] Teaney D 2003 *Phys. Rev.* **C68** 034913 (*Preprint* nucl-th/0301099)
- [23] Hirano T and Gyulassy M 2006 *Nucl. Phys.* **A769** 71–94 (*Preprint* nucl-th/0506049)
- [24] Hirano T, Heinz U W, Kharzeev D, Lacey R and Nara Y 2006 *Phys. Lett.* **B636** 299–304 (*Preprint* nucl-th/0511046)
- [25] Romatschke P and Romatschke U 2007 *Phys. Rev. Lett.* **99** 172301 (*Preprint* 0706.1522)
- [26] Song H and Heinz U W 2008 *Phys. Rev.* **C77** 064901 (*Preprint* 0712.3715)
- [27] Schenke B, Jeon S and Gale C 2011 *Phys. Rev. Lett.* **106** 042301 (*Preprint* 1009.3244)
- [28] Shen C, Heinz U, Huovinen P and Song H 2011 *Phys. Rev.* **C84** 044903 (*Preprint* 1105.3226)
- [29] Gale C, Jeon S, Schenke B, Tribedy P and Venugopalan R 2013 *Phys. Rev. Lett.* **110** 012302 (*Preprint* 1209.6330)
- [30] Bzdak A, Schenke B, Tribedy P and Venugopalan R 2013 *Phys. Rev.* **C87** 064906 (*Preprint* 1304.3403)
- [31] Casalderrey-Solana J, Liu H, Mateos D, Rajagopal K and Wiedemann U A 2011 (*Preprint* 1101.0618)
- [32] Molnar D and Gyulassy M 2002 *Nucl. Phys.* **A697** 495–520 [Erratum: *Nucl. Phys.*A703,893(2002)] (*Preprint* nucl-th/0104073)
- [33] Lin Z w and Ko C M 2002 *Phys. Rev.* **C65** 034904 (*Preprint* nucl-th/0108039)
- [34] Bzdak A and Ma G L 2014 *Phys. Rev. Lett.* **113** 252301 (*Preprint* 1406.2804)
- [35] Orjuela Koop J D, Adare A, McGlinchey D and Nagle J L 2015 *Phys. Rev.* **C92** 054903 (*Preprint* 1501.06880)
- [36] He L, Edmonds T, Lin Z W, Liu F, Molnar D and Wang F 2016 *Phys. Lett.* **B753** 506–510 (*Preprint* 1502.05572)
- [37] Lin Z W, He L, Edmonds T, Liu F, Molnar D and Wang F 2015 Elliptic Anisotropy v_2 May Be Dominated by Particle Escape instead of Hydrodynamic Flow (*Preprint* 1512.06465) URL <https://inspirehep.net/record/1410941/files/arXiv:1512.06465.pdf>
- [38] Morad R and Horowitz W A 2014 *JHEP* **11** 017 (*Preprint* 1409.7545)
- [39] Casalderrey-Solana J, Gulhan D C, Milhano J G, Pablos D and Rajagopal K 2014 *JHEP* **10** 19 [Erratum: *JHEP*09,175(2015)] (*Preprint* 1405.3864)
- [40] Horowitz W A 2015 *Phys. Rev.* **D91** 085019 (*Preprint* 1501.04693)
- [41] Moerman R W and Horowitz W A 2016 (*Preprint* 1605.09285)
- [42] Karch A and Katz E 2002 *JHEP* **06** 043 (*Preprint* hep-th/0205236)
- [43] Ficnar A and Gubser S S 2014 *Phys. Rev.* **D89** 026002 (*Preprint* 1306.6648)
- [44] Witten E 1998 *Adv. Theor. Math. Phys.* **2** 505–532 (*Preprint* hep-th/9803131)

Are we gauging the pressure correctly?

G Jackson and A Peshier

Department of Physics, University of Cape Town, Rondebosch 7700, South Africa

E-mail: JCKGRE003@myuct.ac.za

Abstract. Thermodynamic properties of the quark-gluon plasma have been the subject of active investigation over the past decades. Monte Carlo lattice calculations have made great progress; in particular for the gluons, which form the first steps to full QCD. Nonetheless, ‘artifacts’ of this coarse-grained approach lead to uncertainties near the transition temperature, which are closely related to the divergences encountered in continuum perturbation theory. The latter must first be regularised and then renormalised, which we propose to do by comparing to the QCD trace anomaly. Fixing the analytic results at a semi-perturbative temperature, we find the bulk properties tend towards the free limit more gradually than has been presented in recent lattice findings.

1. Introduction

At sufficient energy densities, of about $1 \text{ GeV}/\text{fm}^3$, quantum chromodynamics (QCD) predicts that ordinary nuclear matter melts into a deconfined state of quarks and gluons. Heavy-ion collisions at RHIC and LHC are expected to probe this phase in the vicinity of the crossover temperature $T_c \sim 200 \text{ MeV}$ and part of the program to understand these experiments is pinpointing the equation of state. Although not physically realised, asymptotic freedom of QCD provides a rigorous limit for which the plasma is ‘weakly coupled’. In this (high temperature) regime, well-defined approximations can be made and serve as a benchmark for theoretical statements.

The pressure, which is related to the thermodynamic potential $-pV$, is a quantity of central importance for statistical physics. Knowing the temperature dependence, one derives the entropy density $s = \partial p / \partial T$ and energy density $e = Ts - p$. Lattice gauge theory has been the long-standing approach to calculate equilibrium properties of QCD near T_c , and has revealed that interactions remain ‘strong’ for $T_c < T \lesssim 4T_c$. Recent studies in the quenched limit have obtained the equation of state for values $T \in [0.7, 1000]T_c$, thus affording a comparison with perturbation theory [1]. For an ideal gluon gas, the Stefan-Boltzmann pressure is

$$p_{\text{SB}} = d_g \frac{\pi^2}{90} T^4,$$

where $d_g = 16$ is the gluon degeneracy factor.

Interactions, built into QCD via the parameter α make the pressure deviate from its free value. By virtue of the momentum dependence of the coupling constant $\alpha(q)$ for large arguments ($q \gg \Lambda$, which we define later), perturbation theory can be used. This remains true at high temperatures, where the average momentum \bar{q} is similar to the temperature, $\bar{q} \sim T$ (in

equilibrium). Let the pressure be represented as an expansion in powers of α , with

$$p(T; \alpha) = p_0(T) + p_1(T) + p_2(T) + \dots, \quad (1)$$

where $p_n(T) \sim \mathcal{O}(\alpha^n)$. The normalisation is set by $p_0(T) = p(T; 0) = p_{\text{SB}}$ and yields an upper bound $p_{\text{SB}} \geq p(T; \alpha)$.

The lowest order $\mathcal{O}(\alpha)$ diagrams give a negative correction to the pressure, which may also be related to an ‘excluded volume’ for gluons. For certain graphs of order $\mathcal{O}(\alpha^n)$, $n \geq 2$, the direct evaluation gives $p_n = \infty$. Such *non-analytic* behaviour stems from the long ranged nature of the (gauge) force, and is well known from the classical Coulomb gas [2]. The remedy is to resum infinitely many diagrams, giving a term of order $\mathcal{O}(\alpha^{3/2})$ in Eq.(1). After this, at order $\mathcal{O}(\alpha^2)$, a term $\alpha^2 \log(\alpha)$ occurs and requires 3-loop diagrams to be screened [3]. Furthermore, the $\mathcal{O}(\alpha^2)$ formula compels the use of the coupling $\alpha(\mu)$, where μ is a renormalisation scale appearing in a manner such that $\partial p(T; \alpha(\mu)) / \partial \mu$ is higher order than the approximation used.

The perturbative expansion for $p(T; \alpha)$ is known through order $\mathcal{O}(\alpha^{5/2})$, beyond which the serious infrared difficulties of QCD prohibit further progress [4]. Nevertheless, asymptotic formulae can be useful when truncated to a finite number of terms. A *fixed order* calculation becomes precise¹ in the limit $\alpha \rightarrow 0$, for which purpose we shall study

$$p(T; \alpha(2\pi T)) = p_{\text{SB}} \left\{ 1 + c_1 \alpha + c_{3/2} \alpha^{3/2} + \alpha^2 (c_2 + c'_2 \log(\alpha)) + c_{5/2} \alpha^{5/2} + \mathcal{O}(\alpha^3) \right\}. \quad (2)$$

The term $\mathcal{O}(\alpha^3)$ contains a last perturbative piece, see [5], and a non-perturbative coefficient. Since the asymptotic expansion does not converge, it is particularly sensitive to this last coefficient – which has been ‘fit’ to the lattice data [1]. To avoid this aspect, we simply use Eq. (2), with the *known* coefficients (and the canonical scale $\mu = 2\pi T$), to argue our case.

2. Renormalising via $w(T)$

Although $p(T)$ may be obtained on the lattice [6], it is more convenient to calculate the *interaction measure* (also called trace anomaly),

$$w(T) := e(T) - 3p(T) = \text{Tr } \Theta, \quad (3)$$

where $\Theta^{\mu\nu}(T)$ is the energy momentum tensor, equal to $\text{diag}(e, p, p, p)$ in the local rest frame. It thus follows that $w(T) \geq 0$ and this is indeed met by (2), reproducing the fact that $p(T)/p_{\text{SB}}$ is a smoothly *increasing* function of T .

For a conformal theory, the equation of state $e(T) = 3p(T)$ is true even for fully interacting systems. Therefore, $w(T) \neq 0$ can only arise for a system with an additional scale, other than T and V . This is indeed the case for QCD, where the energy scale Λ enters as a pole in α , for example the 2-loop formula

$$\alpha(\mu) \simeq \frac{4\pi}{11t} \left\{ 1 - \frac{102 \log t}{121t} \right\}, \quad \text{with } t = \log(\mu^2/\Lambda^2).$$

To clarify this point, note that from (3) we may express

$$w(T) = T \frac{d}{dT} \left\{ \frac{p(T)}{T^4} \right\}. \quad (4)$$

Hence, for a ‘fixed’ coupling, $p(T; \alpha)/T^4$ is constant and thus $w(T) = 0$. In order to obtain a non-zero $w(T)$, it is necessary to renormalise, i.e. specify how α in Eq.(2) depends on T . To

¹ Here we mean that the absolute error tends to zero, usually as $\sim \exp(-1/\alpha)$, although the sign may (and does in this case) depend on the level of truncation.

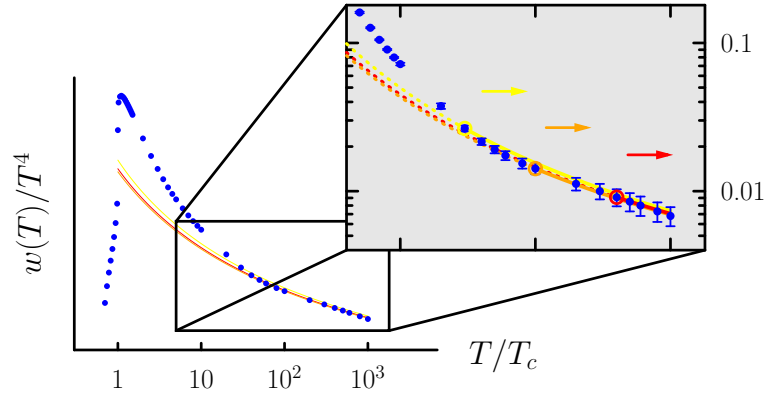


Figure 1. The interaction measure as a function of temperature as calculated on the lattice [1]. The inset focuses on $T \gtrsim 5T_c$, and shows the perturbative result for $w(T)$ with the renormalisation points circled in yellow, orange and red ($T_\star = \{30, 100, 400\}T_c$ respectively). For $T > T_\star$ as shown by the arrows, the formulae consistently agrees with the lQCD data.

this end, we choose the popular scale $\mu = 2\pi T$ and use the 2-loop formula for the coupling. Applying (4) to Eq.(2) yields a model for $w(T)$. Our idea is then to fix the residual scale Λ , by directly matching the perturbative formula to the lattice value, viz. $w(T_\star) = w_\star^{\text{lQCD}}$. Since the lattice results are calculated in units of T_c , the single free parameter in our comparison is the ratio $\lambda = \Lambda/T_c$.

Fig. 1 shows the results for $w(T)$, using a semi-perturbative T_\star to fix the value of λ . Testing the scheme at $T_\star = \{30, 100, 400\}T_c$ consistently gives $\lambda \simeq 0.5$. Provided that $\alpha(T_\star)$ is sufficiently small² at the determined value for λ , approximations for $w(T)$, where $T \gg T_\star$, should (and do) corroborate the lattice values. Below T_\star , there is no reason to expect that $p(T; \alpha)$ should converge and the shape of $w(T)$ for temperatures $T \gtrsim 2T_c$ has been understood in terms of quasiparticles [7]. The pressure in Eq.(2) is then specified, having adjusted λ in our scheme to w^{lQCD} .

One of the principle challenges in lattice QCD, is taking the continuum limit (which is, not by coincidence, the same limit that Λ emerges). By computing $w(T)$, one avoids having to subtract the zero point contribution to $p(T)$ or $e(T)$. From the interaction measure (4), given as a function of T , the pressure can be reconstructed, up to an integration constant,

$$\frac{p(T)}{T^4} = \frac{p(T_0)}{T_0^4} + \int_{T_0}^T \frac{d\tau}{\tau} \left\{ \frac{w(\tau)}{\tau^4} \right\}. \quad (5)$$

This integral method depends on $w(T)$ over a range of values for T . In particular, the area bounded by the interaction measure over all temperatures gives the normalisation of $p(T)$ [presuming that $p(T) \rightarrow 0$ at zero temperature]. With information on $w(T)$ only at a discrete set of values for T , Eq.(5) is at best a Riemann sum, and dependent on extrapolation to ‘endpoints’ $T = 0$ or $T = \infty$, depending on whether $T \gtrsim T_0$. Furthermore, $p(T)/T^4$ receives a large numerical contribution near the peak value of $w(T)/T^4$, at about $T/T_c \simeq 1.1$.

² Characterising α as ‘small’ depends on the nature of the asymptotic series.

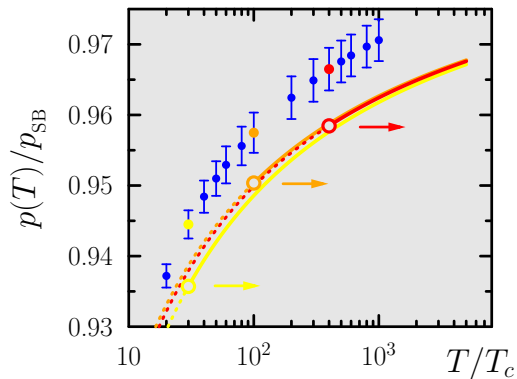


Figure 2. The pressure as a function of temperature (in units of the free value) for $n_f = 0$. Shown as blue points are the lattice data [1]. The yellow, red and orange curves are obtained by renormalising according to $w(T)$, Fig. 1. Solid lines indicate $T_* < T$, where the approximation schemes *should* converge. Evidently there is a systematic discrepancy of $\sim 1\%$ with the lattice data.

3. Reason for concern

Given the precision of pure gauge IQCD data, we now point out a discrepancy that has so far escaped notice. The previous section outlined two approaches to calculating the pressure $p(T)$,

- (i) using a truncated asymptotic formula, i. e. Eq.(2),
- (ii) by means of (5), from $w(T)$ determined on the lattice [1].

Shown in Fig. 2 is $p(T)$ at large temperatures $T > 10T_c$ according to these two distinct methods. Evidently they disagree at about 1% of the free limit and, more urgently, the values for $p(T_*)$ fail to match at the renormalisation point. Method (i) appears to give robust predictions for $T_* < T$, but systematically *underestimates* the lattice values.

This failure is actually crucial to resolve because it emerges from a well-defined limit, in which theoretical descriptions *should* be under control. The perturbative analysis of the QCD trace anomaly indicates a slower approach of the $p(T)$ to the free limit [and similarly for $e(T)$ and $s(T)$]. Our conclusion may seem of little consequence for phenomenology of heavy-ion collisions. However, an uncertainty of one percent in $p(T)/p_{SB}$ can translate into an order of magnitude in the temperature T/T_c (see Fig. 2). This casts aspersions on hydrodynamic simulations, where the equation of state is needed to evolve $\Theta^{\mu\nu}$ prior to freeze-out.

References

- [1] Borsányi S, Endrödi G, Fodor Z, Katz S D and Szabó K K, *JHEP* **1207** (2012) 056 (*Preprint* hep-lat/1204.6184)
- [2] Kardar M, 2007, *Statistical Physics of Particles*, (Cambridge University Press)
- [3] Arnold P B and Zhai C X, *Phys. Rev. D* **50** (1994) 7603 (*Preprint* hep-ph/9408276)
- [4] Linde A D, *Phys. Lett. B* **96** (1980) 289
- [5] Kajantie K, Laine M, Rummukainen K and Schröder Y, *Phys. Rev. D* **67** (2003) 105008 (*Preprint* hep-ph/0211321)
- [6] Endrödi G, Fodor Z, Katz S D and Szabó K K, *PoS LAT* **2007** (2007) 228 (*Preprint* hep-lat/0710.4197)
- [7] Peshier A, Kämpfer B, Pavlenko O P and Soff G, *Phys. Rev. D* **54** (1996) 2399

Partition function zeros of adsorbing self-avoiding walks

EJ Janse van Rensburg

Department of Mathematics & Statistics, York University, Toronto, Ontario, M3J 1P3, Canada

E-mail: rensburg@yorku.ca

Abstract. Partition function or Fisher zeros play a fundamental role in the theory of phase transitions in models in classical statistical mechanics. In this paper the properties of partition function zeros in a square lattice self-avoiding walk model of polymer adsorption are presented. Some results constraining the distribution of zeros in the complex plane, based on mathematical results on the distribution of polynomial zeros, are presented. Numerical results on the distribution of zeros are shown, based on approximate enumeration of square lattice walks using the GAS algorithm.

1. Introduction

Partition function zeros in the complex plane (also called *Fisher zeros* [1]) provide a mathematical mechanism which explains phase transitions in models in classical statistical mechanics. In the thermodynamic limit, Fisher zeros accumulate in the complex plane in patterns which create an *edge singularity* at the critical point on the real axis where a phase transition occurs.

There is a significant literature devoted to the study of partition function zeros and the edge-singularity in models of lattice spin systems. These models include the Ising model [2, 3], the q -state Potts model [4–7], the van der Waal gas and ideal Bose gas [8]. In contrast, far less is known about the partition function zeros in models of lattice clusters, including models of the self-avoiding walk (see figure 1).

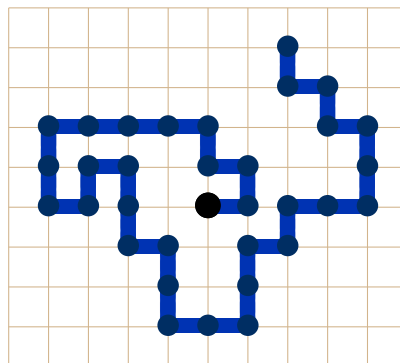


Figure 1: A self-avoiding walk from the origin in the square lattice.

Exact enumeration of self-avoiding walks in the square lattice in reference [9] to lengths $n = 28$ was used to determine partition function zeros, and to study the relation between the leading partition function zero and the thermodynamic properties of the model. Similar work in the cubic lattice is reported in references [10, 11]. The partition function zeros in a bond fluctuation model of polymer adsorption was considered in reference [12]. In this last study chains in two dimensions of length up to 1536 were generated and the distribution of partition function zeros was examined.

In this paper a study similar to that of reference [12] is reported. In particular, some theoretical properties of partition function zeros in adsorbing lattice walks in the square lattice are examined, and some numerical data in support of these properties are presented.

2. Adsorbing walks

Denote the d -dimensional hypercubic lattice by \mathbb{L}^d and let c_n be the number of self-avoiding walks from the origin length n in \mathbb{L}^d (see figure 1). Since $d^n \leq c_n \leq 2d(2d-1)^{n-1}$ in \mathbb{L}^d , it follows that c_n grows exponentially with n , and it is known that the limit

$$\lim_{n \rightarrow \infty} \frac{1}{n} \log c_n = \log \mu_d \tag{1}$$

exists [13]. The number $\kappa_d = \log \mu_d$ is the *connective constant* of the lattice \mathbb{L}^d , and μ_d is the hypercubic lattice *growth constant* of c_n , namely $c_n = \mu_d^{n+o(n)}$ [14].

The half lattice \mathbb{L}_+^d is defined by

$$\mathbb{L}_+^d = \{\vec{v} \in \mathbb{L}^d \mid v_d \geq 0\}, \tag{2}$$

where $\vec{v} = (v_1, v_2, \dots, v_d)$ is a vertex in \mathbb{L}^d . A self-avoiding walk from the origin in the half lattice \mathbb{L}_+^d is a *positive walk*. The number of positive walks of length n is denoted by c_n^+ . Naturally, $c_n^+ \leq c_n$. It is known that

$$\lim_{n \rightarrow \infty} \frac{1}{n} \log c_n^+ = \lim_{n \rightarrow \infty} \frac{1}{n} \log c_n = \log \mu_d. \tag{3}$$

See, for example, reference [15].

The boundary of the half lattice \mathbb{L}_+^d is the $(d-1)$ -dimensional hypercubic lattice given by

$$\partial\mathbb{L}_+^d = \{\vec{v} \in \mathbb{L}_+^d \mid v_d = 0\}, \tag{4}$$

and it is equivalent to \mathbb{L}^{d-1} . A model of *adsorbing (positive) walks* is obtained by weighing vertices of a positive walk with the weight or *activity* a whenever the walk returns to or visits the boundary $\partial\mathbb{L}_+^d$. This assigns a weight a^v to each positive walk making v visits to $\partial\mathbb{L}_+^d$. Notice that, by convention, the first vertex at the origin is not a visit. A *positive* or *adsorbing walk* with visits weighted by a^v is shown in figure 2.

If $c_n^+(v)$ is the number of positive walks of length n and with v visits in the adsorbing boundary $\partial\mathbb{L}_+^d$, then the partition function and limiting free energy of adsorbing walks are given by

$$A_n^+(a) = \sum_{v=0}^n c_n^+(v) a^v \quad \text{and} \quad \mathcal{A}^+(a) = \lim_{n \rightarrow \infty} \frac{1}{n} \log A_n^+(a). \tag{5}$$

Existence of the limiting free energy $\mathcal{A}^+(a)$ was shown in reference [15], and it is known that $\mathcal{A}^+(a)$ is a non-decreasing convex function of $\log a$. Moreover, there is a critical point a_c^+ in the model, defined by $\mathcal{A}^+(a) = \log \mu_d$ if $a \leq a_c^+$ and $\mathcal{A}^+(a) > \log \mu_d$ if $a > a_c^+$. The critical point a_c^+ is the *adsorption critical point* in the model, and it is a singular point in the free energy $\mathcal{A}^+(a)$.

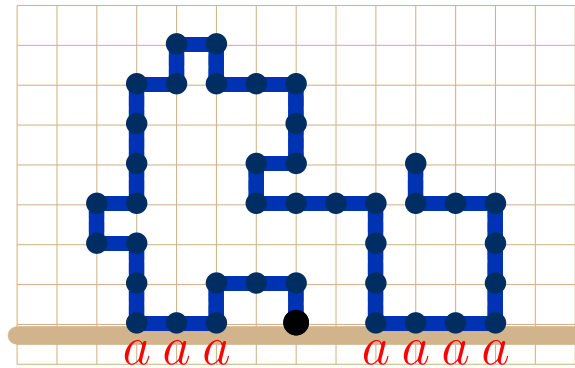


Figure 2: A positive or adsorbing self-avoiding walk in the half square lattice. This positive walk steps from the origin (in the boundary of the half lattice), and each vertex (other than the first vertex at the origin) where the walk returns to or visits the boundary is weighted by an activity a .

3. Partition function zeros

Partition function zeros are the (complex valued) roots of $A_n^+(a)$. Since $A_n^+(a)$ is a polynomial of degree n , there are n zeros $\{a_j\}$, and $A_n^+(a)$ factors as

$$A_n^+(a) = C_n \prod_{j=1}^n (a - a_j) \tag{6}$$

where C_n is the (positive) coefficient of a^n in equation (5) (it depends on n). Notice that C_n is the number of walks in \mathbb{L}^{d-1} , since the coefficient of a^n is the number of walks with every vertex in $\partial\mathbb{L}_+^d$. Taking logarithms and dividing by n , and letting $n \rightarrow \infty$, gives the limiting free energy of the model, namely

$$\mathcal{A}^+(a) = \lim_{n \rightarrow \infty} \frac{1}{n} \log A_n^+(a) = \log \mu_{d-1} + \lim_{n \rightarrow \infty} \frac{1}{n} \sum_{j=1}^n \log(a - a_j), \tag{7}$$

in particular since $\log \mu_{d-1} = \lim_{n \rightarrow \infty} \frac{1}{n} \log C_n$. Taking derivatives to $\log a$ gives the *energy density* and *specific heat* of the adsorbing walk.

3.1. The distribution of partition function zeros

The distribution of partition function zeros may be examined by defining the functions

$$\begin{aligned} \nu_n(\rho) &= \#\{\mathcal{A}^+(a) \text{ zeros } a_k \mid (1-\rho) \leq |a_k| \leq \frac{1}{1-\rho}\} \\ \alpha_n(\theta, \phi) &= \#\{\mathcal{A}^+(a) \text{ zeros } a_k \mid \theta < \mathfrak{A}rg a_k \leq \phi\}. \end{aligned} \tag{8}$$

That is, $\nu_n(\rho)$ is the number of zeros of $\mathcal{A}^+(a)$ in the annulus $(1-\rho) \leq |a| \leq \frac{1}{1-\rho}$ in the a -plane (where $\rho \in (0,1)$), and $\alpha_n(\theta, \phi)$ is the number of zeros a_k with complex principal arguments $\mathfrak{A}rg a_k$ greater than θ and less than or equal to ϕ .

The theorem by Hughes and Nikeghbali [16] is useful in providing bounds on $\nu_n(\rho)$, while the angular distribution of zeros can be examined using the classical theorem of Erdős and Turán [17]. Let $\zeta_d = \log \frac{\mu_d}{\mu_{d-1}}$, then, if $\zeta_d < \rho < 1$, then Hughes and Nikeghbali's theorem implies that

$$0 < 1 - \frac{1}{\rho} \zeta_d \leq \liminf_{n \rightarrow \infty} \frac{1}{n} \nu_n(\rho) \leq \limsup_{n \rightarrow \infty} \frac{1}{n} \nu_n(\rho) \leq 1. \tag{9}$$

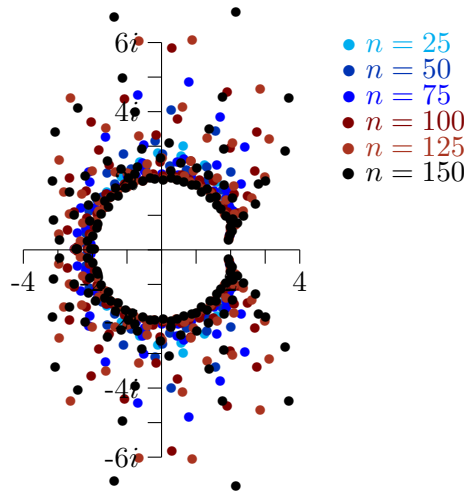


Figure 3: Partition function zeros of the partition function $A_n^+(a)$ of adsorbing self-avoiding square lattice walks. The data shown are for walks of length $n \in \{25, 50, 75, 100, 125, 150\}$.

The theorem by Erdős and Turán similarly shows that there is a constant C_0 so that, if $\zeta_d < \rho < 1$, then

$$\limsup_{n \rightarrow \infty} \left| \frac{1}{2\pi}(\phi - \theta) - \frac{1}{n} \alpha_n(\theta, \phi) \right| \leq \sqrt{\frac{1}{2} C_0 \zeta_d}. \quad (10)$$

These results strongly suggest that partition function zeros are distributed in an annular region in the complex plane, and that the angular distribution is asymptotically fairly even.

3.2. Numerical results

Numerical data were collected on adsorbing walks using the GAS algorithm [18] which was implemented for adsorbing walks in reference [19]. These simulations produced estimates of $c_n^+(v)$ for $0 \leq v \leq n \leq 500$ in the microcanonical ensemble. Combining these data as in equation (5) produces estimates of the partition function $A_n^+(a)$. Zeros of $A_n^+(a)$ were obtained to high accuracy by deflating the polynomials in Maple 17 [20]. In figure 3 the partition function zeros for adsorbing square lattice walks are shown.

Finite size approximations to the free energy can be computed from the partition function zeros using equation (7). Similarly, the energy density \mathcal{E}^+ and specific heat \mathcal{C}^+ are given by

$$\mathcal{E}^+(a) = \lim_{n \rightarrow \infty} \frac{1}{n} \sum_{j=1}^n \frac{1}{a - a_j}, \quad \text{and} \quad \mathcal{C}^+(a) = \lim_{n \rightarrow \infty} \frac{-1}{n} \sum_{j=1}^n \frac{1}{(a - a_j)^2}. \quad (11)$$

In figure 4 finite size approximations to the excess free energy $\mathcal{A}^+(a) - \log \mu_d$, energy density and specific heat, are plotted for $n \in \{60, 125, 250, 500\}$. Notice the sharp peak in the specific heat curves, and that these curves intersect close to a common point at $\log a_c^+$ in the graph. For values $\log a < \log a_c^+$ the curves decrease with increasing n , and for $\log a > \log a_c^+$ the curves increase with increasing n . This intersection is therefore a good estimate of the critical adsorption activity in the model. By calculating it for $(n, 2n)$ and $n \in \{100, 110, 120, \dots, 250\}$ a set of estimates of a_c^+ is obtained (see equation (58) in reference [19]). Taking the average to find the best estimate gives

$$a_c^+ = 1.764(16), \text{ in } \mathbb{L}_+^2. \quad (12)$$

This estimate can be compared to the best estimate $a_c^+ = 1.77564$ in the square lattice using exact enumeration methods [21] and $a_c^+ = 1.779$ in reference [19].

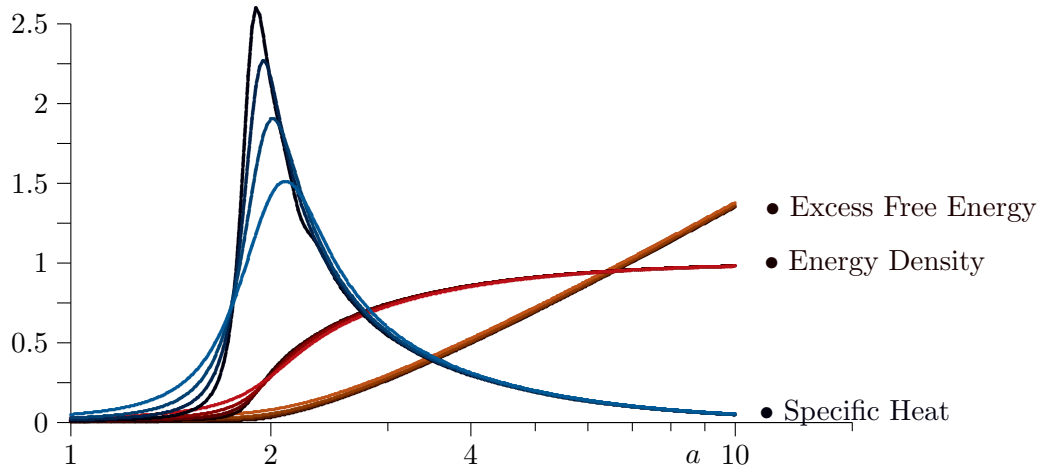


Figure 4: The excess free energy, energy density and specific heat of adsorbing walks as a function of a on a log-linear scale for walks of length $n \in \{60, 125, 250, 500\}$.

3.3. The cumulative angular distribution function

A cumulative angular distribution function $\mathcal{Q}_n(\phi)$ of partition function zeros (of $A_n^+(a)$) around the origin in the complex a -plane is defined by using the function $\alpha_n(\theta, \phi)$ defined in equation (8):

$$\mathcal{Q}_n(\phi) = \frac{1}{n} \alpha_n(-\pi, \phi). \tag{13}$$

$\mathcal{Q}_n(\phi)$ is a non-decreasing step-function which increments in steps of height $\frac{1}{n}$ each time an increase in ϕ includes new zeros in the interval $(-\pi, \phi]$, and with $\mathcal{Q}_n(-\pi) = 0$ and $\mathcal{Q}_n(\pi) = 1$. In other words, $\mathcal{Q}_n(\phi)$ is the fraction of partition function zeros with principal argument in the interval $(-\pi, \phi]$.

The cumulative angular distribution function $\mathcal{Q}_n(\phi)$ is plotted in figure 5 for $n \in \{60, 125, 250, 500\}$. It increases with ϕ , except near $\phi = 0$ where it has a slight flattening (this is for zeros close to the positive real axis in the a -plane). This flattening becomes less pronounced as n increases. In the limit the data suggest a straight line increasing from 0 at $\phi = -\pi$ to 1 at $\phi = \pi$. That is, the cumulative distribution function apparently converges such that $\lim_{n \rightarrow \infty} \mathcal{Q}_n(\phi) = \frac{1}{2\pi} \phi + \frac{1}{2}$. This implies that the limiting angular distribution is given by $\lim_{n \rightarrow \infty} \frac{1}{n} \alpha_n(\phi, \theta) = \frac{1}{2\pi} (\phi - \theta)$ (this remains unproven).

4. Conclusions

In this paper I report on some aspects of partition function zeros in a self-avoiding walk model of two dimensional adsorbing polymers. The data in figure 5 suggest strongly that the angular distribution of zeros, in the limit as $n \rightarrow \infty$, is uniform. Algebraic results in equations (9) and (10) constraining the distribution of partition function zeros were determined, and tested numerically by examining the distribution of partition function zeros. It is found that a positive density of zeros is distributed in an annulus with center at the origin in \mathbb{C} and that the angular distribution is bounded in the sense that $\lim_{n \rightarrow \infty} \frac{1}{n} \alpha_n(\theta, \phi)$ approaches zero as $\theta \nearrow \phi$ (and the numerical data in figure 5 suggest that it is uniform).

In section 3.2 the partition function zeros are estimated from numerical data obtained by sampling adsorbing self-avoiding walks in the square lattice using the GAS algorithm [18]. The free energy is approximated in terms of the partition function zeros, and in figure 4 the excess free energy, energy density and specific heat are plotted. The specific heat curves intersect in a point approximating the critical adsorption activity a_c^+ , giving the estimate in equation (12).

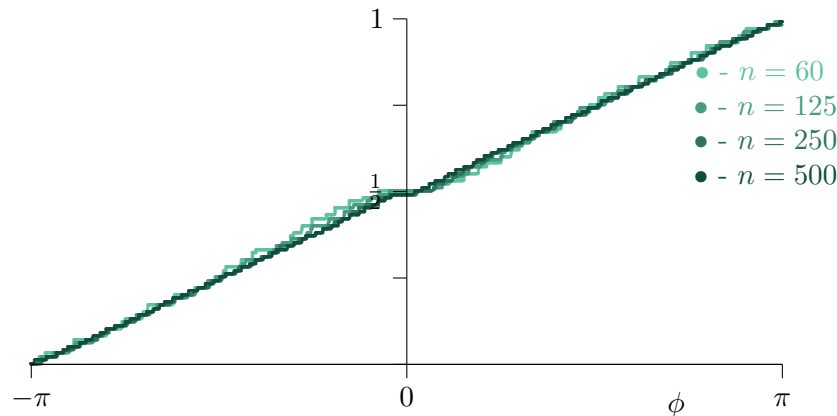


Figure 5: The cumulative distribution function $\frac{1}{n}\alpha_n(-\pi, \phi)$ of the principal arguments of partition function zeros in the complex plane for finite values of n . These data are for $n \in \{60, 125, 250, 500\}$ and appear to converge to the line $\frac{1}{2\pi}\phi + \frac{1}{2}$ as $n \rightarrow \infty$.

Acknowledgements

EJJvR acknowledges support from NSERC(Canada) in the form of a Discovery Grant.

References

- [1] Fisher M 1965 *The nature of critical points* (University of Colorado Press)
- [2] Lu W and Wu F 1998 *Physica A: Stat Mech Appl* **258** 157–170
- [3] Lu W and Wu F 2001 *J Stat Phys* **102** 953–970
- [4] Kim S Y and RJ C 1998 *Phys Rev E* **58** 7006–7012
- [5] Kim S Y and Creswick R 1998 *Phys Rev Lett* **81** 2000–2003
- [6] Kim S Y and Creswick R 2001 *Phys Rev E* **63** 066107
- [7] Kim S Y 2004 *Phys Rev E* **70** 016110
- [8] van Dijk W, Lobo C, MacDonald A and Bhaduri R 2013 *arXiv 1303.4770*
- [9] Lee J 2004 *J Korean Phys Soc* **44** 617–620
- [10] Lee J, Kim S Y and Lee J 2010 *J Chem Phys* **133** 114106
- [11] Lee J, Kim S Y and Lee J 2012 *Phys Rev E* **86** 011802
- [12] Taylor M and Luettmer-Strathmann J 2014 *J Chem Phys* **141** 204906
- [13] Hammersley J 1957 *Proc Camb Phil Soc* **53** 642–645
- [14] Broadbent S and Hammersley J 1957 **53** 629–641
- [15] Hammersley J, Torrie G and Whittington S 1982 *J Phys A: Math Gen* **15** 539–571
- [16] Hughes C and Nikeghbali A 2008 *Compositio Mathematica* **144** 734–746
- [17] Erdős P and Turán P 1950 *Ann Math* **51** 105–119
- [18] Janse van Rensburg E and Rechnitzer A 2009 *J Phys A: Math Theo* **42** 335001
- [19] Janse van Rensburg E 2016 *J Stat Mech: Theo Expr* **2016** 033202
- [20] Maplesoft *Maple 17* (A division of Waterloo Maple Inc. (Waterloo, Ontario))
- [21] Beaton N, Guttmann A and Jensen I 2012 *J Phys A: Math Theo* **45** 055208

Next-to-leading order electron-quark scattering

GJ Kemp¹ and WA Horowitz²

¹Department of Pure and Applied Mathematics, University of Johannesburg, P.O. Box 524, Auckland Park 2006, South Africa

²Department of Physics, University of Cape Town, Private Bag X3 Rondebosch 7701, South Africa

E-mail: gkemp@uj.ac.za & wa.horowitz@uct.ac.za

Abstract. We compute the differential cross section for massless $2 \rightarrow 2$ scattering between a quark and an electron in a t-channel photon exchange at next to leading order in the $\overline{\text{MS}}$ renormalisation scheme. Specifically, we show that the result is UV and IR finite. Lastly we explore the role of disconnected contributions to the square of the scattering amplitude.

1. Introduction

We compute the differential cross section for massless $2 \rightarrow 2$ scattering between a quark and electron in a t-channel photon exchange at next to leading order (NLO) in the $\overline{\text{MS}}$ renormalisation scheme. We couple the quarks to an abelian $U(1)$ gluon field and compute the NLO calculation in this coupling. We explicitly demonstrate the cancelation of IR-divergences and explore the presence and need for disconnected contributions to amplitude, \mathcal{M} and to the amplitude squared $|\mathcal{M}|^2$. To the best of our knowledge, this calculation has not yet appeared in the literature.

One of the aims of this work is to demonstrate that the cross section at NLO in the coupling is finite. Treatment of the UV divergences are well understood in the context of renormalised perturbation theory. However, there seems to be some controversy involving IR divergence.

Whenever massless particles are present in a theory, one is forced to deal with IR divergences. IR divergences in the vertex correction are indeed cancelled by those arising in real emission processes according to the Bloch-Nordsieck (BN) and Kinoshita-Lee-Nauenberg (KLN) prescriptions [1, 2, 3, 4]. However, there are still real absorption processes to take into account, reintroducing IR divergences. Following KLN, one searches for additional degenerate processes to render the overall process finite. It has been proposed, in the context of the Drell-Yan process and QED electron scattering, to consider contributions from processes involving disconnected gluons and photons [5, 6]. Interference between these disconnected and connected diagrams at the amplitude level can yield connected contributions at the level of the amplitude squared. While this approach works and the result is again finite, it also lead to disconnected diagrams contributing to the amplitude squared. Indeed, processes involving any number of disconnected photons may contribute to $|\mathcal{M}|^2$ at the same order of the coupling. To the best of our knowledge this issue has not yet been resolved using the standard techniques of perturbative quantum field theory.

In section 2 we present our results for the leading order and NLO vertex correction. We use dimensional regularisation to regulate all divergences with $\epsilon \equiv 4 - d$. Section 3 deals with the real emission process where we present our results for the soft, collinear and soft and collinear

real emission processes. Section 4 demonstrates that adding these processes leads to a finite result. Section 5 then explores the issue regarding the disconnected diagrams. Lastly, we only present the divergent pieces of our calculations. We have also computed the finite pieces and are available upon request.

2. $2 \rightarrow 2$ scattering at NLO

We compute the following diagrams

$$\begin{array}{c}
 \begin{array}{c} q \xrightarrow{p_i} \xrightarrow{p_f} q \\ \downarrow \gamma \\ e^- \xrightarrow{q_i} \xrightarrow{q_f} e^- \end{array}
 +
 \begin{array}{c} q \xrightarrow{p_i} \xrightarrow{p_f} q \\ \downarrow \gamma \\ e^- \xrightarrow{q_i} \xrightarrow{q_f} e^- \end{array}
 +
 \begin{array}{c} \text{self-energy} \\ \text{diagram} \end{array}
 \end{array}
 \quad (1)$$

for deep elastic scattering. Because the photon momentum in the t-channel exchange is spacelike, it is possible to boost into a frame where energy is conserved. Below, we first compute the leading order diagram, followed by the vertex correction at NLO.

2.1. Leading order

The leading order \mathcal{M}_0 amplitude from the LSZ formula in the $\overline{\text{MS}}$ scheme is

$$\mathcal{M}_0 = \frac{R_{\overline{\text{MS}}}^q R_{\overline{\text{MS}}}^e e^2}{t} \bar{u}(p_f) \gamma^\mu u(p_i) \bar{u}(q_f) \gamma_\mu u(q_i), \quad (2)$$

where t is a Mandelstam variable. The differential cross section $d\sigma_0 \propto |\mathcal{M}_0|^2 d\Pi_{LIPS}$, where where the spin averaging has already been included in $|\mathcal{M}_0|^2$. The Lorentz-invariant phase space volume element, $d\Pi_{LIPS}$, contains an overall momentum conserving delta function which we use of to evaluate our integrals. The $R_{\overline{\text{MS}}}$'s are the residues of the respective two-point functions. In the $\overline{\text{MS}}$ scheme, the residues are no longer trivial and may be determined from the particle's self energy [7]. In our boosted frame, $E_{q_i} = E_{q_f}$, and so the δ -function in $d\Pi_{LIPS}$ may be split up into a spatial part and the temporal part $\delta(E_{p_i} - E_{p_f})$. Using the δ -functions to evaluate the integrals, the leading order differential cross section is

$$\left(\frac{d\sigma}{d\Omega} \right)_0 = \frac{(R_{\overline{\text{MS}}}^q R_{\overline{\text{MS}}}^e)^2 e^4}{16E_{q_i}^4 |v_{p_i} - v_{q_i}|} \left[2 \left(\frac{\tilde{s}}{\tilde{t}} \right)^2 + 2 \left(\frac{\tilde{u}}{\tilde{t}} \right)^2 - \epsilon \right] \left(\frac{E_{p_i}}{2\pi} \right)^{2-\epsilon}, \quad (3)$$

where $\tilde{s}, \tilde{t}, \tilde{u}$ are Mandelstam variables with unit norm.

2.2. Vertex correction

The amplitude for the vertex correction is

$$\mathcal{M}_{v.c.} = R_{\overline{\text{MS}}}^q R_{\overline{\text{MS}}}^e \frac{\bar{u}(q_f) \gamma^\mu u(q_i) e^2}{t} g^2 \bar{u}(p_f) \gamma^\rho \int \frac{d^d k}{(2\pi)^d} \frac{(\not{p}_i - \not{k}) \gamma_\mu (\not{p}_f - \not{k})}{(p_i - k)^2 k^2 (p_f - k)^2} \gamma_\rho u(p_i). \quad (4)$$

After integrating with respect to the gluon momentum k and some algebra

$$\mathcal{M}_{vc} = \mathcal{M}_0 \frac{\alpha_g}{4\pi} \left[-\frac{8}{\epsilon_{ir}^2} - \frac{4}{\epsilon_{ir}} \left(2 + \log(\tilde{X}) \right) + \frac{2}{\epsilon_{uv}} + \frac{\pi^2}{6} - 8 - 3 \log(\tilde{X}) - \log^2(\tilde{X}) \right], \quad (5)$$

where $\tilde{X} \equiv 4\pi \tilde{\mu}^2 / (-te^\gamma)$, γ is the Euler number, $\tilde{\mu}$ is a scale introduced to make coupling g dimensionless and $\alpha_g \equiv \tilde{g}^2 / 4\pi$. Lastly, we denoted a positive ϵ by ϵ_{uv} and a negative ϵ by ϵ_{ir} .

In the $\overline{\text{MS}}$ -bar scheme, the UV-divergence is subtracted out by the counterterm and the scale $\tilde{\mu}$ is redefined so that $\tilde{X} = \mu^2/(-t)$. To the relevant order in g

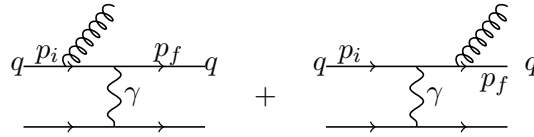
$$R_{\overline{\text{MS}}}^q = \frac{1}{1 - \frac{\alpha_g}{2\pi} \frac{1}{\epsilon_{ir}}} \approx 1 + \frac{\alpha_g}{4\pi} \frac{2}{\epsilon_{ir}}. \quad (6)$$

Thus, expanding $R_{\overline{\text{MS}}}^q$, following the steps in section 2 and simplifying, we obtain

$$\left(\frac{d\sigma}{d\Omega}\right)_{\text{virtual}} = \left(\frac{d\sigma}{d\Omega}\right)_0 \left[1 + \frac{\alpha_g}{2\pi} \left[-\frac{8}{\epsilon_{ir}^2} - \frac{1}{\epsilon_{ir}} \left(6 + 4 \log\left(\frac{\mu^2}{t}\right) \right) + \text{finite} \right] \right]. \quad (7)$$

3. Real emssion (bremsstrahlung)

The real contributions will fall into two pieces. One will be soft gluon emission from the incoming and outgoing quark lines integrated over all angles, and the other will be from hard collinear gluon emission. For the latter, we treat the case for which the final state gluon is collinear with both incoming and outgoing quark lines. The diagrams are



$$\quad (8)$$

3.1. Soft bremsstrahlung

Neglecting the terms that are $O(k)$ in the numerator, the soft bremsstrahlung amplitude (sb) is

$$\mathcal{M}_{sb} = \mathcal{M}_0 g \left[\frac{2p_i \cdot \epsilon}{(p_i - k)^2} + \frac{2p_f \cdot \epsilon}{(p_f + k)^2} \right]. \quad (9)$$

The Lorentz-invariant phase space has an extra final state gluon factor and in the soft gluon approximation, we neglect the gluon momentum in the δ -function. This leads to the following expression for soft bremsstrahlung differential cross section

$$\left(\frac{d\sigma}{d\Omega}\right)_{sb} = \left(\frac{d\sigma}{d\Omega}\right)_0 \int g^2 \frac{2p_i \cdot p_f}{(p_i \cdot k)(p_f \cdot k)} \frac{d^{d-1}k}{(2\pi)^{d-1} 2\omega_k}. \quad (10)$$

Following [3] in evaluating the integral over all angles and from zero up to some small cutoff gluon energy, E_{cut} , we find

$$\left(\frac{d\sigma}{d\Omega}\right)_{sb} = \left(\frac{d\sigma}{d\Omega}\right)_0 \frac{\alpha_g}{2\pi} \left[\frac{8}{\epsilon_{ir}^2} + \frac{4}{\epsilon_{ir}} \log\left(\frac{\mu^2}{\rho E_{cut}^2}\right) + \text{finite} \right], \quad (11)$$

where $\rho = t/E_{p_i}^2$.

3.2. Hard collinear bremsstrahlung

We consider the final state degeneracy for which the final state gluon is collinear with outgoing quark. According to KLN we also must consider the initial state degeneracy. To account for this, we double our final result.

Beginning from (8), and making use of collinear approximations the hard collinear bremsstrahlung (hcb) differential cross section is

$$\left(\frac{d\sigma}{d\Omega}\right)_{hcb} = \left(\frac{d\sigma}{d\Omega}\right)_0 \frac{\alpha_g}{2\pi} \left[\frac{1}{\epsilon_{ir}} \left(8 \log\left(\frac{E_{cut}}{E_{p_i}}\right) + 6 \right) + \text{finite} \right], \quad (12)$$

where ‘finite’ depends on the parameter δ - a small angular cutoff below which the detector cannot distinguish between a quark and a quark plus gluon.

4. The final result is finite

In this section, we show that the total differential cross section is independent of ϵ_{ir} and thus finite as $d \rightarrow 4$. Firstly, the $1/\epsilon_{ir}^2$ terms cancel straightforwardly. Thus, we only have to show that the $1/\epsilon_{ir}$ terms cancel. For $\rho = t/E_{p_i}^2$, we find

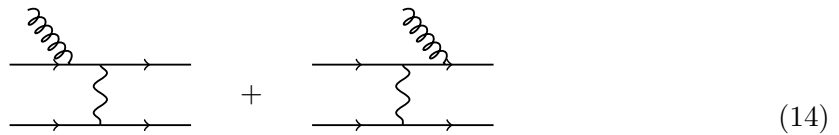
$$\frac{\alpha_g}{2\pi} \frac{1}{\epsilon_{ir}} \left[-6 - 4 \log\left(\frac{\mu^2}{t}\right) + 4 \log\left(\frac{\mu^2}{\rho E_{cut}^2}\right) + 8 \log\left(\frac{E_{cut}}{E_{p_i}}\right) + 6 \right] = 0. \quad (13)$$

5. Disconnected cross sections

In this section, we demonstrate how to cancel the IR-divergences that result from the absorption of a soft gluon by each quark. We reproduce the results of [5, 6] but in the context of our calculation. Searching for additional degenerate processes, we are lead to Feynman diagrams featuring a single disconnected gluon line contributing to \mathcal{M} . In so doing, we obtain contributions to $|\mathcal{M}|^2$ from diagrams with disconnected gluon lines. It is not yet clear if this issue may be resolved using standard techniques of perturbative quantum field theory.

We note that very soft massless particles have broad wave packets. It is thus possible for a disconnected gluon's wave packet to overlap with the particles participating in the scattering experiment. Secondly, one can usually rely on the Cluster Decomposition principle to argue that disconnected diagrams need not be considered [8]. However, one can show that the interference between two well-separated collections of fields in a Green's function decays as e^{-mR} , where R is the spacelike separation between the two sets of fields and m is the smallest mass in the theory [9]. For massless particles, this suggests that it is possible to have interference.

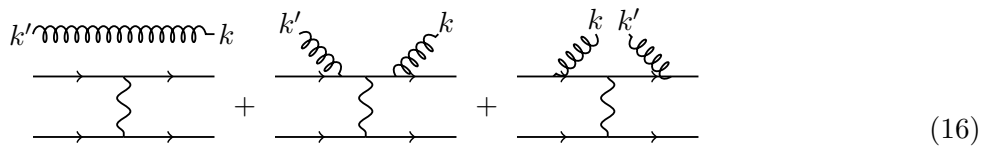
The absorption diagrams we compute are



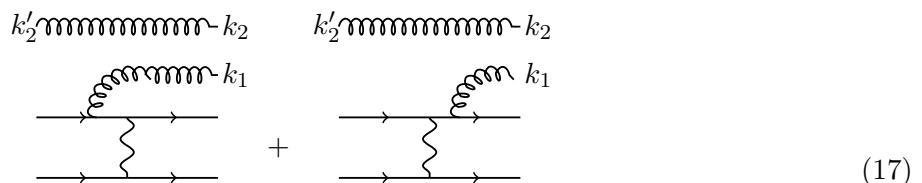
The result of this process is the same as the real emission process in section 3.1,

$$|\mathcal{M}_{sb}|^2 = |\mathcal{M}_0|^2 g^2 \frac{2p_i \cdot p_f}{(p_i \cdot k)(p_f \cdot k)}. \quad (15)$$

Once again, we have IR divergences that presumably need cancelling. Now consider the $3 \rightarrow 3$ processes



There are additional diagrams that ultimately evaluate to zero in the massless limit. The first diagram is equal to $\mathcal{M}_0(2\pi)^3 2\omega_k \delta^{(3)}(k - k')$. At the level of the amplitude squared, interference between the first diagram and the second two higher order diagrams produces connected contributions to $|\mathcal{M}|^2$ at order $e^4 g^2$. These ultimately lead to $-2|\mathcal{M}_{sb}|^2$. KLN states that we should continue to search for additional degenerate processes at $O(e^4 g^2)$. It turns out there are such processes in the degenerate $3 \rightarrow 4$ scattering amplitude,



with two additional diagrams having k_1 and k_2 swapped. Again, interference occurs between these diagrams to produce a connected contribution to $|\mathcal{M}|^2$. The interference turns out to be $|\mathcal{M}_{sb}|^2$, precisely what is required to cancel the infrared divergences.

It only remains for us to explain (or explain away) the additional disconnected terms in $|\mathcal{M}|^2$. For example, in (16), the leading order e^4 contribution to $|\mathcal{M}|^2$ features a completely disconnected gluon line. Indeed, one can have any number of disconnected gluon lines and still be at the same order in the coupling.

6. Discussion

We have computed the differential cross section for massless $2 \rightarrow 2$ scattering between a quark and electron in a t-channel photon exchange at next to leading order (NLO) in the $\overline{\text{MS}}$ renormalisation scheme. We considered the abelian gluon case, and, using dimensional regularisation, we have shown that the cross section is finite. We have also computed (but not shown) the finite pieces to the individual processes. We have briefly explored the role of disconnected diagrams to the amplitude-squared in the context of our specific calculation. We have explained that by opening the Pandora's box of disconnected diagrams, one could, in principle, have to sum an infinite number of disconnected diagrams, all contributing to the amplitude squared at the same order in the coupling.

Acknowledgments:

WH would like to thank SA-CERN and the NRF. GK would like to thank SA-CERN and the UJ GES Postdoc Fellowship.

References

- [1] Kinoshita T 1962 Mass singularities of Feynman amplitudes *J. Math. Phys.* Volume **3** Number 4 pages 650-677
- [2] Lee T D and Nauenberg M 1964 Degenerate systems and mass singularities *Phys. Rev.* **133** B1549
- [3] Contopanagos H F 1990 Smooth massless limit of QED *Nucl. Phys. B.* **343** 571
- [4] Gastmans R, Verwaest J and Meuldermans R 1976 Dimensional regularization in massless QED *Nucl. Phys. B.* **105** 454
- [5] Akhoury R, Sotiropoulos M G and Zakharov V I 1997 The KLN theorem and soft radiation in gauge theories: abelian case *Phys. Rev. D.* **56**, 377
- [6] Lavelle M and McMullan D 2006 Collinearity, convergence and cancelling infrared divergences *JHEP* **0603** 026
- [7] Srednicki M 2007 *Quantum Field Theory* Cambridge University Press
- [8] Weinberg S 1995 *Quantum Theory of Fields, Volume 1, Foundations* Cambridge University Press
- [9] Brown L S 1994 *Quantum Field Theory* Cambridge University Press

Evolution of quark masses and flavour mixings in 5D for an $SU(3)$ gauge group

Mohammed Omer Khojali¹, A. S. Cornell²

National Institute for Theoretical Physics; School of Physics and Mandelstam Institute for Theoretical Physics, University of the Witwatersrand, Wits 2050, South Africa

E-mail: ¹khogali11@gmail.com, ²alan.cornell@wits.ac.za

Abstract. The evolution of the Cabibbo-Kobayashi-Maskawa matrix elements, the Jarlskog invariant and the quark mixings are derived for the one-loop renormalisation group equations in a five-dimensional model for an $SU(3)$ gauge group compactified on an S_1/Z_2 orbifold. In this work we have assumed that there is a fermion doublet and two singlets located at the fixed points of the extra dimension. This work builds on earlier works of gauge couplings and Yukawa coupling evolutions, which pointed to some interesting phenomenology in this toy model of gauge-Higgs unification.

1. Introduction

The Standard Model (SM) of particle physics is believed to be an effective low energy theory for a number of reasons, where one of these reasons is to try and understand the fermion mass hierarchy and quark mixings [1]. In the SM there is a hierarchy of the quark masses belonging to various generations of the up-type quark masses (m_t, m_c, m_u) and also the down-type quark masses (m_b, m_s, m_d) [2]:

$$m_t \gg m_c \gg m_u, \quad m_b \gg m_s \gg m_d. \quad (1)$$

In gauge theories, the renormalisable fermion masses come from mass terms such as $\bar{f}Mf$ and also arise from Yukawa terms like $\bar{f}Yf\Phi$. For these Yukawa terms, once the Higgs doublet acquires a vacuum expectation value, all the SM fermions acquire a mass, where this mass is proportional to their Yukawa couplings [3]:

$$Y_{t,c,u} = \frac{m_{t,c,u}}{v} \quad Y_{b,s,d} = \frac{m_{b,s,d}}{v}. \quad (2)$$

$Y_{t,c,u}$ and $Y_{b,s,d}$ are the nontrivial Yukawa couplings eigenvalues, v is the vacuum expectation value of the Higgs field, where this value can be fixed from the measurement of the W boson mass:

$$v = \frac{2M_W}{g} \simeq 246\text{GeV}. \quad (3)$$

In the standard electroweak model with three quark families, the quark sector contains ten free parameters, six quark masses and also four flavour mixing parameters [4]. In order to look into the dynamics of fermion mass and flavour mixing we need to extend the SM. We expected that

any new physics beyond the SM shall appear above the $M_Z \sim 91.2$ GeV scale. In order to build a mass model of quarks at the high energy scale, one can use the Renormalisation Group Equations (RGEs). We need this technique to fill in the space between the predictions of the model at $\mu \gg M_Z$ and the experimental ones at $\mu \leq M_Z$ [5]. We are using these RGEs in order to study the asymptotic behaviour of the Lagrangian parameters, such as Yukawa couplings for both up-type quarks and down-type quarks and also the mixing angles θ_{12} , θ_{13} and θ_{23} [6]. In order to compute the running of quark masses above the M_Z scale we are going to use the quark masses and the mixing parameters, which are obtained at the M_Z scale to determine the Yukawa couplings Y_u and Y_d . After doing this, we need to solve the RGEs of the Yukawa couplings, in order to get the running of the quark masses at any energy scale [5]. In order to diagonalise the quark mass matrices, one can use an unitary matrix as follows [3, 7]:

$$u_L = (U_{u_L})u'_L, \quad u_R^c = (U_{u_R^c})^\dagger u'_R, \quad d_L = (U_{d_L})d'_L, \quad d_R^c = (U_{d_R^c})^\dagger d'_R. \quad (4)$$

However, this will lead to the following:

$$(U_{u_R^c})^\dagger Y_u (U_{u_L}) = \text{diag}(y_u, y_c, y_t), \quad (5)$$

$$(U_{d_R^c})^\dagger Y_d (U_{d_L}) = \text{diag}(y_d, y_s, y_b), \quad (6)$$

or equivalently we can diagonalise the quark mass matrices appearing in the Lagrangian of Yukawa interactions by using the bi-unitary transformation [3, 4]:

$$(U_{u_L})^\dagger M_u (U_{u_R^c}) = \text{diag}(m_u, m_c, m_t), \quad (7)$$

$$(U_{d_L})^\dagger M_d (U_{d_R^c}) = \text{diag}(m_d, m_s, m_b). \quad (8)$$

We use this bi-unitary transformation in order to change all our quark fields from their flavour eigenstate basis to the basis of mass eigenstates [4]. Let us assume that we are working in the basis where the Yukawa couplings for the up-type quark Y_u is diagonal, as appears in Eq. (5), then the mass eigenstates of the down-type quark are connected to their weak eigenstates by the Cabibbo-Kobayashi-Maskawa (CKM) matrix V_{CKM} [5]:

$$V_{CKM}^\dagger Y_d Y_d^\dagger V_{CKM} = \text{diag}(l_d^2, l_s^2, l_b^2). \quad (9)$$

For the other way around, that is, if we are working in the basis in which the Yukawa coupling for the down-type quarks are diagonal, then the mass eigenstates of the up-type quark are given by:

$$V_{CKM}^\dagger Y_u Y_u^\dagger V_{CKM} = \text{diag}(k_d^2, k_s^2, k_b^2). \quad (10)$$

Furthermore, we can build the Yukawa couplings for the down-type quarks from their eigenvalues and also from the CKM matrix [5].

There are many ways to look at the quark mass hierarchy and flavour mixings; we shall investigate an $SU(3)$ gauge group compactified on an S^1/Z_2 orbifold which has size $R^{-1} = 1$ TeV, 5 TeV and 20 TeV. In this paper we assume that the fermion doublet and the two singlet are located at the fixed points of the extra-dimension, the quark masses and the flavour mixings are derived at one-loop level [8].

2. The evolution of CKM matrix in 5 dimension for an $SU(3)$ gauge group

The SM of particle physics has been very successful in describing most of the particle phenomenology known to date [9], but it possesses some problems whose solution could imply physics beyond the SM. The SM is not like QCD and QED, it is the theory which violates parity

(P), time reversal (T) and charge conjugation (C). The C and P separately are not a good symmetry of the SM, but the combination CP, in the case of only one family of matter fields, or even if we have two families, is a good symmetry. Since we have three families in the SM, CP is not a good symmetry. All of the SM Lagrangian is invariant under CP transformations, except the part where the CKM matrix appears.

In order to study the CKM matrix, let us start with $\bar{u}_{iL}\gamma^\mu d_{iL}$ and express it in terms of mass eigenstates.

$$\bar{u}_{iL}\gamma^\mu d_{iL} = \bar{u}'_{hL}(U^{uL})_{hi}\gamma^\mu(U^{dL})_{ij}^\dagger d'_{jL} = (U^{uL})_{hi}(U^{dL})_{ij}^\dagger \bar{u}'_{hL}\gamma^\mu d'_{jL}, \quad (11)$$

because in the above equation the two matrices are different, when we compute the product of two unitary matrices we still get a unitary matrix. This unitary matrix is called the CKM matrix

$$(U^{uL})_{hi}(U^{dL})_{ij}^\dagger \equiv V_{hj}. \quad (12)$$

In order to parameterise the quark sector's flavour mixing we need the CKM matrix [10], and it has 9 parameters. Let us see how the CKM can be parameterised in terms of these 9 parameters[11]:

$$V = \begin{pmatrix} e^{i\tau_1} & 0 & 0 \\ 0 & e^{i\tau_2} & 0 \\ 0 & 0 & e^{i\tau_3} \end{pmatrix} V_{st} \begin{pmatrix} e^{i\sigma_1} & 0 & 0 \\ 0 & e^{i\sigma_2} & 0 \\ 0 & 0 & e^{i\sigma_3} \end{pmatrix}. \quad (13)$$

V_{st} is the standard parametrisation and it is given by:

$$V_{st} = \begin{pmatrix} 1 & 0 & 0 \\ 0 & c_{23} & s_{23} \\ 0 & -s_{23} & c_{23} \end{pmatrix} \begin{pmatrix} c_{13} & 0 & s_{13}e^{i\delta} \\ 0 & 1 & 0 \\ -s_{13}e^{-i\delta} & 0 & c_{13} \end{pmatrix} \begin{pmatrix} c_{12} & s_{12} & 0 \\ -s_{12} & c_{12} & 0 \\ 0 & 0 & 1 \end{pmatrix}, \quad (14)$$

where $c_{ij} \equiv \cos\theta_{ij}$, $s_{ij} \equiv \sin\theta_{ij}$ [12]. From the standard parameterisation in Eq. (14). The CKM matrix has the following form [13]

$$V_{st} = \begin{pmatrix} c_{12}c_{13} & s_{12}c_{13} & s_{13}e^{-i\delta} \\ -s_{12}c_{23} - c_{12}s_{23}s_{13}e^{i\delta} & c_{12}c_{23} - s_{12}s_{23}s_{13}e^{i\delta} & s_{23}c_{13} \\ s_{12}s_{23} - c_{12}c_{23}s_{13}e^{i\delta} & -c_{12}s_{23} - s_{12}c_{23}s_{13}e^{i\delta} & c_{23}c_{13} \end{pmatrix}. \quad (15)$$

From the experimental point of view we know that $\sin\theta_{13} \ll \sin\theta_{23} \ll \sin\theta_{12} \ll 1$, and we can express this hierarchy using the Wolfenstein parametrisation [14]:

$$\sin\theta_{23} = \frac{|V_{cb}|}{\sqrt{|V_{ud}|^2 + |V_{us}|^2}}, \quad (16)$$

and

$$\sin\theta_{12} = \frac{|V_{us}|}{\sqrt{|V_{ud}|^2 + |V_{us}|^2}}. \quad (17)$$

The RGEs for the CKM matrix beyond the R^{-1} scale is given as follows [15]:

$$16\pi^2 \frac{dV_{i\gamma}}{dt} = 12S(t) \left[\sum_{\sigma,j \neq i} \frac{k_i^2 + k_j^2}{k_i^2 - k_j^2} l_\sigma^2 V_{i\sigma} V_{j\sigma}^* V_{j\gamma} + \sum_{j,\sigma \neq \gamma} \frac{l_\gamma^2 + l_\sigma^2}{l_\gamma^2 - l_\sigma^2} k_j^2 V_{j\sigma}^* V_{j\gamma} V_{i\sigma} \right], \quad (18)$$

where the energy scale parameter $t = \ln(\mu/M_Z)$ and $S(t) = M_Z R e^t$. As we mentioned earlier, our renormalisation point is the Z boson mass. Furthermore, we can introduce the Jarlskog

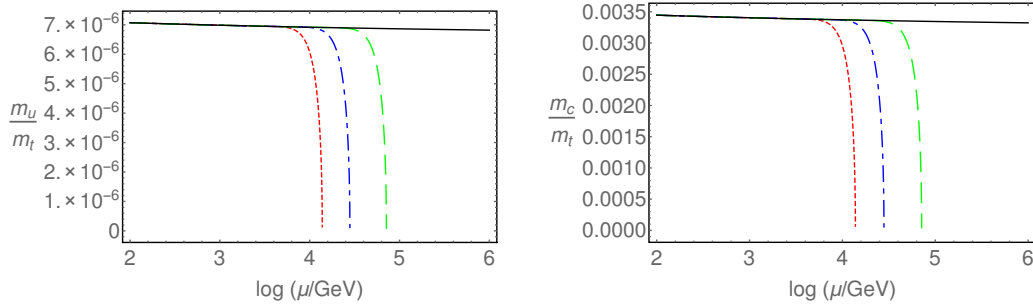


Figure 1. Evolution of the mass ratio for three different values of the compactification radius we have used: 4 TeV (dotted red line), 8 TeV (dot-dashed blue line), 20 TeV (dashed green line); as a function of the scale parameter t . In the left panel is the evolution of the mass ratio m_u/m_t , and the right panel is the evolution of the mass ratio m_c/m_t .

rephasing-invariant parameter J , which is crucial to measuring CP violation, and it is given through the unitarity properties of V_{CKM} , as [4]:

$$\text{Im}(V_{k\alpha}V_{l\beta}V_{k\beta}^*V_{l\alpha}^*) = J \sum_{m,\delta} (\varepsilon_{klm}\varepsilon_{\alpha\beta\delta}), \quad (19)$$

where the subscript (k, l or m) runs over the (u, c, t) quarks and the subscript (α, β or δ) runs over the (d, s, b) quarks. In particular, in this paper, we are using the following J to present the CP violation phenomena

$$J = \text{Im}(V_{cs}V_{tb}V_{cb}^*V_{tb}^*). \quad (20)$$

Thus, one can write its square as:

$$J^2 = |V_{tb}|^2|V_{cs}|^2|V_{ts}|^2|V_{cb}|^2 - \frac{1}{4} \left(1 - |V_{tb}|^2 - |V_{cs}|^2 - |V_{ts}|^2 - |V_{cb}|^2 + |V_{tb}|^2|V_{cs}|^2 + |V_{ts}|^2|V_{cb}|^2 \right). \quad (21)$$

For completeness, the independent parameters of V_{CKM} are $|V_{ud}|$, $|V_{us}|$, $|V_{cd}|$ and $|V_{cs}|$ and they take the following initial values:

$$|V_{ud}| = 0.9738, \quad |V_{us}| = 0.2196, \quad |V_{cd}| = 0.224, \quad |V_{cs}| = 0.996. \quad (22)$$

We can define the RGE invariant quantity in the hierarchical limit $m_b \gg m_s$ [16]:

$$R_{23} = \sin(2\theta_{23}) \sinh \left[\ln \left(\frac{m_b}{m_s} \right) \right]. \quad \Rightarrow \quad R_{23} = \sin \theta_{23} \cos \theta_{23} \left(\frac{m_b}{m_s} \right). \quad (23)$$

3. Numerical Results

In FIG.1 we present the evolution of the mass ratio for the one-loop calculation for three different compactification scales: $R^{-1} = 4$ TeV, 8 TeV and 20 TeV. We expect new physics to come into play when we reach our cut-off. The cut-off for our effective theory when $t = 4.1400, 4.4475, 4.8538$ for $R^{-1} = 4$ TeV, 8 TeV, 20 TeV respectively. In the left panel we present the evolution of m_u/m_t ; in this case one can see that the SM (the black solid line) behaves like λ^8 , where $\lambda \sim 0.22$. Through the numerical analysis of the one-loop calculation, we observe that when the fifth dimension contributions switch on, the mass ratio m_u/m_t decreases whenever the energy increases, and this creates a significant change of order of λ^8 . In the right panel we are showing the evolution of m_c/m_t , in this case we see that the SM behaves like λ^4 , and when the fifth

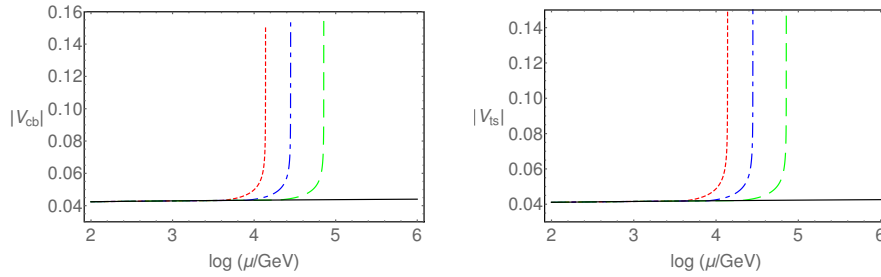


Figure 2. The evolution of the CKM elements for three different values of the compactification radius we have used: 4 TeV (dotted red line), 8 TeV (dot-dashed blue line), 20 TeV (dashed green line); as a function of the scale parameter t . In the left panel is the evolution of the CKM element $|V_{cb}|$, and the right panel is the evolution of CKM element $|V_{ts}|$.

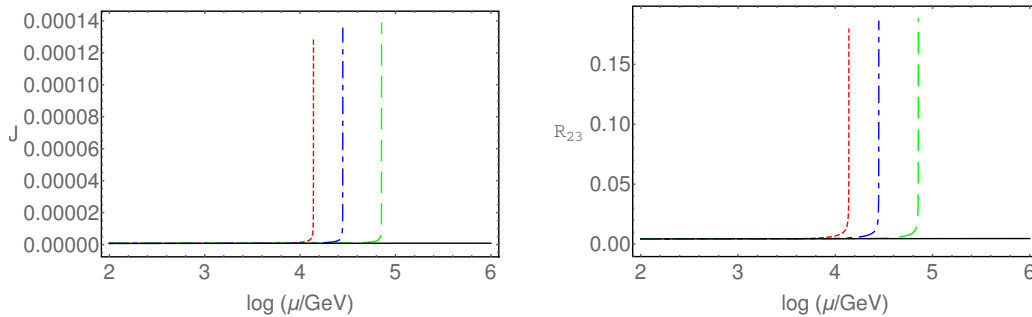


Figure 3. In the left panel is the evolution of the Jarlskog rephasing-invariant parameter; the right panel is the evolution of R_{23} , for three different values of the compactification radius: 4 TeV (dotted red line), 8 TeV (dot-dashed blue line) and 20 TeV (dashed green line); as a function of the scale parameter t .

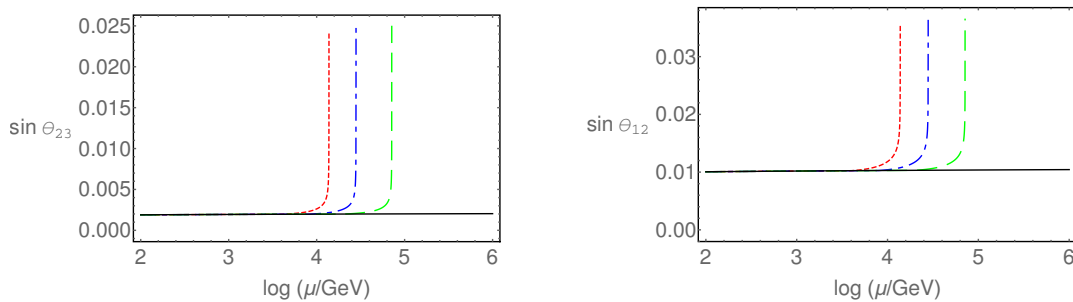


Figure 4. Left panel is the evolution of $\sin \theta_{23}$; the right panel is the evolution of $\sin \theta_{12}$, for three different values of the compactification radius: 4 TeV (dotted red line), 8 TeV (dot-dashed blue line), 20 TeV (dashed green line), as a function of the scale parameter t .

dimension KK-modes become kinematically accessible the mass ratio m_c/m_t decreases with increasing energy, and in this case the change is of the order of λ^4 .

In FIG.2 we plot the evolution of the CKM parameters, in the left panel we plot $|V_{cb}|$ and in the right panel $|V_{ts}|$. We see that once the fifth dimension contributions switch on, one can see that there are new contributions coming from the fifth dimension. Accordingly the evolution of the CKM parameters $|V_{cb}|$ and $|V_{ts}|$ are rapidly increasing, this significant increase is of order of λ^2 .

In FIG.3, left panel, we plot the Jarlskog invariant parameter. As we mentioned earlier, this gives us a good indication of the amount of CP violation in the quark sector. As can be seen, once the fifth dimension contributions are reached, the value of the Jarlskog invariant increases sharply until we reach the cutoff. In the right panel we present the evolution of the renormalisation invariant R_{23} ; this quantity describes the relationship between the mixing angles ($\sin \theta_{23}$ and $\cos \theta_{23}$) and the mass ratio (m_b/m_s) as it appears in Eq. (23). This renormalisation invariant quantity starts to increase rapidly when the fifth dimension contributions switch on. This rapid increase causes increases in the mixing angles, which is suppressed by the mass ratio m_b/m_s ; similarly, in FIG.4, in the left panel, we present the evolution of the mixing angle $\sin \theta_{23}$, and in the right panel we plot the evolution of the mixing angle $\sin \theta_{12}$. After, the fifth dimension is switched on, the mixing angles $\sin \theta_{23}$ and $\sin \theta_{12}$ increase rapidly. However, this increase is suppressed by $|V_{cb}|$ and $|V_{us}|$ respectively, as is shown in Eq. (16) and Eqs (17).

4. Conclusion

In conclusion, in this paper we derived the one-loop RGEs in a five-dimensional gauge-Higgs unification model for an $SU(3)$ gauge group by assuming that the fermion doublet and the two singlets are located at the fixed points of the fifth dimension. We test the evolution of the mass ratios m_u/m_t , m_c/m_t , the CKM elements $|V_{cb}|$, $|V_{ts}|$, the Jarlskog rephasing-invariant, R_{23} and the evolution of the mixing angle $\sin \theta_{23}$ and $\sin \theta_{12}$. We observed that when the fifth dimension KK-modes become kinematically accessible all the previous physical observables evolution change rapidly.

Acknowledgments

We gratefully acknowledge the valuable discussions and advice provided by Aldo Deandrea and Giacomo Cacciapaglia (Université Lyon 1, France). This work is supported by the National Research Foundation (South Africa).

References

- [1] N. Arkani-Hamed, S. Dimopoulos and G. R. Dvali, Phys. Lett. B **429**, 263 (1998) [hep-ph/9803315].
- [2] A. Abdalgabar and A. S. Cornell, J. Phys. Conf. Ser. **455**, 012050 (2013) [arXiv:1305.3729 [hep-ph]].
- [3] D. Falcone, Int. J. Mod. Phys. A **17**, 3981 (2002) [hep-ph/0105124].
- [4] H. Fritzsch and Z. z. Xing, Prog. Part. Nucl. Phys. **45**, 1 (2000) [hep-ph/9912358].
- [5] Z. z. Xing, H. Zhang and S. Zhou, Phys. Rev. D **77**, 113016 (2008) [arXiv:0712.1419 [hep-ph]].
- [6] A. S. Cornell, A. Deandrea, L. X. Liu and A. Tarhini, Phys. Rev. D **85**, 056001 (2012) [arXiv:1110.1942 [hep-ph]].
- [7] P. H. Chankowski and S. Pokorski, Int. J. Mod. Phys. A **17**, 575 (2002) [hep-ph/0110249].
- [8] M. O. Khojali, A. S. Cornell and A. Deandrea, arXiv:1602.07441 [hep-th].
- [9] John F. Donoghue, Dynamics of the Standard Model, London, 2nd edition, July 1994.
- [10] A. S. Cornell and L. X. Liu, Phys. Rev. D **83**, 033005 (2011) [arXiv:1010.5522 [hep-ph]].
- [11] N. Cabibbo, Phys. Rev. Lett. **10**, 531 (1963).
- [12] M. Kobayashi and T. Maskawa, Prog. Phys. **49**, 652 (1973).
- [13] L.L. Chau and W.Y. Keung, Phys. Rev. Lett. **53**, 1802 (1984).
- [14] L. Wolfenstein, Phys. Rev. Lett. **51**, 1945 (1983).
- [15] K.S. Babu, Z.Phys.C - Particles fields **35**, 69-75 (1987).
- [16] L. X. Liu and A. S. Cornell, PoS KRUGER **2010**, 045 (2010) [arXiv:1103.1527 [hep-ph]].

Short Path Length Energy Loss in the Quark Gluon Plasma

Isobel Kolbé, W. A. Horowitz

Department of Physics, University of Cape Town, Private Bag X3, Rondebosch 7701

E-mail: isobel.kolbe@cern.ch

Abstract. High Energy Particle Physics collider experiments at the Relativistic Heavy Ion Collider (RHIC) in the USA and the Large Hadron Collider (LHC) in Geneva, Switzerland, are probing the most fundamental properties of matter by accelerating a range of particles, from protons to Lead nuclei, to relativistic speeds and causing them to collide. The decay products of these violent collisions can be studied in detail and have revealed that a new state of matter in which the constituents of nucleons, quarks and gluons, exist in a deconfined state, creating what appears to be a perfect fluid called the Quark Gluon Plasma (QGP). The QGP only exists for a few femto seconds and is therefore extremely difficult to characterize. The manner in which a highly energetic particle loses energy as it traverses the QGP has proven to be an effective probe of the QGP, but recent results in smaller colliding systems such as proton-lead (pPb) have brought into question our understanding of perturbative Quantum Chromodynamical (pQCD) descriptions of energy loss, particularly in small systems of QGP. We present a short separation distance correction to the well-known (static scattering centre) DGLV (Djordjevic, Gyulassy, Levai, Vitev) pQCD energy loss calculation, revealing a number of shortcomings and problematic assumptions. We also investigate the feasibility of a similar small system correction in the (dynamical scattering centre) thermal field theory formalism.

1. Introduction

For decades now, particle physicists have explored the fundamental properties of the universe by colliding various nuclei at ever increasing energies in order to probe their constituent particles - quarks and gluons. In recent years, evidence has arisen of the production of a new state of matter, the Quark - Gluon Plasma (QGP), in which the quarks contained within nucleons and other hadrons become deconfined [1]. The QGP offers unique insight into the structure of the most fundamental building blocks of matter as well as an opportunity to study the physics of many body non-abelian gauge theories.

High momentum particles produced along with the QGP can be used as tomographic probes in a phenomenon known as jet-quenching, in which high-momentum particles lose energy as they traverse the QGP. The physics of jet-quenching is complex, but the same phenomenon of energy loss affects all the particles of the QGP, resulting in a reduction of the cross section of charged hadrons seen in nucleus-nucleus (AA) collisions as compared to proton-proton (pp) collisions (if scaled appropriately). Such studies have met with great success in AA collisions, leading to the rise of a number of perturbative quantum chromodynamical (pQCD) energy loss formalisms that have evolved to provide a very detailed description of the energy-loss mechanisms [2, 3, 4, 5] in the QGP.

However, new analyses of experimental data [6, 7, 8, 9, 10, 11] have shown that there is evidence for collective behaviour even in small colliding systems previously thought to be too small to create a QGP. If a QGP does exist in these smaller colliding systems, a clear understanding of the energy loss mechanisms in small systems is of crucial importance, because current energy loss models rely heavily on the assumption that the system is large compared to the debye screened length of the scattering centres. Mathematically, relaxing the assumption that the system is large in the GLV (Gyulassy, Levai, Vitev) formalism amounts to relaxing the assumption that the distance between scattering and radiation is large compared to the inverse debye mass. That is, the present calculation is an *all* separation distance generalization of the DGLV (Djordjevic, GLV) [12] energy loss for a massive quark traversing a static medium.

The large separation distance assumption led to a mathematical simplification through the exponential suppression of certain terms at the amplitude level. We present here the energy loss formula obtained by retaining terms that are exponentially suppressed due to $1/\mu_D \ll \Delta z$. Alarmingly, upon numerical evaluation of the energy loss formula, we find that the correction term dominates at high (~ 100 GeV) parton energies.

2. Setup

For the present calculation we follow precisely the setup of the DGLV calculation [12]. The details of the current calculation can be found in [13], but will not be discussed at length. For clarity, we treat the transverse momentum eikonal parton produced at an initial point (t_0, z_0, \mathbf{x}_0) inside a finite QGP, where we have used \mathbf{p} to mean transverse 2D vectors, $\vec{\mathbf{p}} = (p_z, \mathbf{p})$ for 3D vectors and $p = (p^0, \vec{\mathbf{p}}) = [p^0 + p^z, p^0 - p^z, \mathbf{p}]$ for four vectors in Minkowski and light cone coordinates respectively. As in the DGLV calculation, we consider the target to be a Gyulassy-Wang Debye screened potential [14] with Fourier and color structure given by

$$\begin{aligned} V_n &= V(\vec{\mathbf{q}}_n) e^{-i\vec{q}_n \cdot \vec{x}_n} \\ &= 2\pi\delta(q^0) v(\mathbf{q}_n, q_n^z) e^{-i\vec{q}_n \cdot \vec{x}_n} T_a(R) \otimes T_a(n). \end{aligned} \quad (1)$$

The color exchanges are handled using the applicable $SU(N_c)$ generator $T_a(n)$ in the d_n dimensional representation of the target or $T_a(R)$ in the d_R dimensional representation of the p_T parent parton.

In light cone coordinates the momenta of the emitted gluon, the final p_T parton, and the exchanged medium Debye quasiparticle are

$$\begin{aligned} k &= \left[xP^+, \frac{m_g^2 + \mathbf{k}^2}{xP^+}, \mathbf{k} \right], \\ p &= \left[(1-x)P^+, \frac{M^2 + \mathbf{k}^2}{(1-x)P^+}, -\mathbf{k} \right], \\ q &= [q^+, q^-, \mathbf{q}], \end{aligned} \quad (2)$$

where the initially produced p_T particle of mass M has large momentum $E^+ = P^+ = 2E$ and negligible other momentum components. Notice that we include the Ter-Mikayelian plasmon effect with an effective emitted gluon mass m_g [12, 15]. See Fig. 1 for a visualization of these momenta.

A shorthand for energy ratios will prove useful notationally. Following [12] we define $\omega \approx xE^+/2 = xP^+/2$, $\omega_0 \equiv \mathbf{k}^2/2\omega$, $\omega_i \equiv (\mathbf{k} - \mathbf{q}_i)^2/2\omega$, $\omega_{(ij)} \equiv (\mathbf{k} - \mathbf{q}_i - \mathbf{q}_j)^2/2\omega$, and $\tilde{\omega}_m \equiv (m_g^2 + M^2x^2)/2\omega$.

We will also make the following assumptions: 1) the eikonal, or high energy, approximation, for which E^+ is the largest energy scale of the problem; 2) the soft (radiation) approximation

$x \ll 1$; 3) collinearity, $k^+ \gg k^-$; 4) that the impact parameter varies over a large transverse area; and, most crucially for this letter, 5) the large formation time assumption $\omega_i \ll \mu_i$, where $\mu_i^2 \equiv \mu^2 + \mathbf{q}_i^2$.

Note that the above approximations, in addition to allowing us to systematically drop terms that are small, permit us to 1) (eikonal) ignore the spin of the p_T parton; 2) (soft) assume the source current for the parent parton varies slowly with momentum $J(p-q+k) \approx J(p+k) \approx J(p)$; 3) (collinearity) complete a separation of energy scales

$$E^+ \gg k^+ \gg k^- \equiv \omega_0 \sim \omega_{(i\dots j)} \gg \frac{(\mathbf{p} + \mathbf{k})^2}{P^+}; \tag{3}$$

and 4) take the ensemble average over the phase factors, which become $\langle e^{-i(\mathbf{q}-\mathbf{q}')\cdot\mathbf{b}} \rangle = \frac{(2\pi)^2}{A_\perp} \delta^2(\mathbf{q} - \mathbf{q}')$.

In the original DGLV calculations [12], the large formation time played only a minor role. However, when considering short separation distances between the scattering centers, the large formation time assumption naturally increases in importance.

With the above approximations, we reevaluated the 10 diagrams contributing to the $N = 1$ in opacity energy loss amplitude [12] without the additional simplification of the large separation distance $\Delta z \gg 1/\mu$ assumption.

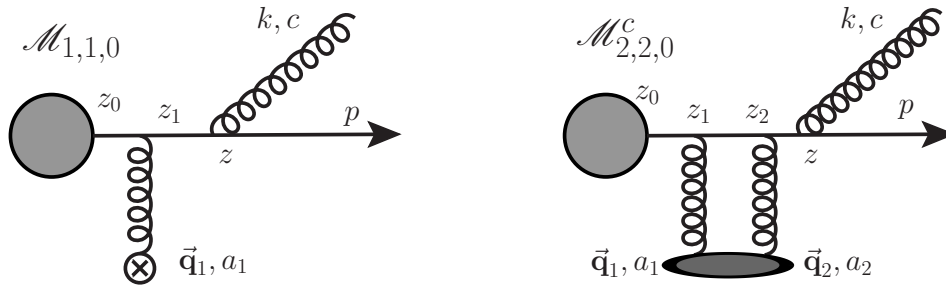


Figure 1: $\mathcal{M}_{1,1,0}$ (left hand panel) and $\mathcal{M}_{2,2,0}^c$ (right hand panel) are the only two diagrams that have non-zero short separation distance corrections in the large formation time limit. $\mathcal{M}_{2,2,0}^c$ is the double Born contact diagram, corresponding to the second term in the Dyson series in which two gluons are exchanged with the single scattering center.

3. Calculation and Results

The $N = 1$ in opacity energy loss derivation that was originally performed by DGLV evaluated 10 diagrams and utilized the large separation distance approximation $\Delta z \gg 1/\mu$ to neglect terms proportional to $\exp(-\mu\Delta z)$. Although we retained such terms in our reevaluation of the 10 diagrams in question, the large radiated gluon formation time approximation, $\omega_i \ll \mu_i$, allowed for a further simplification. As a result, only 2 of the 18 new small distance correction pole contributions are suppressed. We show the two diagrams with non-zero contributions at the amplitude level $\mathcal{M}_{1,1,0}$ and $\mathcal{M}_{2,2,0}^c$ in the large formation time approximation in Fig. 1.

The full result for these two amplitudes under our approximation scheme is then

$$\begin{aligned} \mathcal{M}_{1,1,0} &\approx -J(p)e^{ipx_0}2gT_{a_1}ca_1 \int \frac{d^2\mathbf{q}_1}{(2\pi)^2}v(0, \mathbf{q}_1)e^{-i\mathbf{q}_1 \cdot \mathbf{b}_1} \\ &\times \frac{\mathbf{k} \cdot \boldsymbol{\epsilon}}{\mathbf{k}^2 + m_g^2 + x^2M^2} \left[e^{i(\omega_0 + \tilde{\omega}_m)(z_1 - z_0)} - \frac{1}{2}e^{-\mu_1(z_1 - z_0)} \right] \end{aligned} \quad (4)$$

$$\begin{aligned} \mathcal{M}_{2,2,0}^c &\approx J(p)e^{i(p+k)x_0} \int \frac{d^2\mathbf{q}_1}{(2\pi)^2} \int \frac{d^2\mathbf{q}_2}{(2\pi)^2} e^{-i(\mathbf{q}_1 + \mathbf{q}_2) \cdot \mathbf{b}_1} \\ &\times igT_{a_2}T_{a_1}ca_2a_1v(0, \mathbf{q}_1)v(0, \mathbf{q}_1) \frac{\mathbf{k} \cdot \boldsymbol{\epsilon}}{\mathbf{k}^2 + m_g^2 + x^2M^2} \\ &\times \left[e^{i(\omega_0 + \tilde{\omega}_m)(z_1 - z_0)} + e^{-\mu_1(z_1 - z_0)} \left(1 - \frac{\mu_1 e^{-\mu_2(z_1 - z_0)}}{2(\mu_1 + \mu_2)} \right) \right]. \end{aligned} \quad (5)$$

The double differential single inclusive gluon emission distribution is given by [12]

$$d^3N_g^{(1)}d^3N_J = \frac{d^3\vec{\mathbf{p}}}{(2\pi)^3 2p^0} \frac{d^3\vec{\mathbf{k}}}{(2\pi)^3 2\omega} \times \left(\frac{1}{d_T} \text{Tr}\langle |\mathcal{M}_1|^2 \rangle + \frac{2}{d_T} \Re \text{Tr}\langle \mathcal{M}_0^* \mathcal{M}_2 \rangle \right), \quad (6)$$

from which the energy loss, given by the energy-weighted integral over the gluon emission distribution $\Delta E = E \int dx x dN_g/dx$, can be calculated from the amplitudes.

The main analytic result of our letter is then the $N = 1$ first order in opacity small distance generalization of the DGLV induced energy loss of a high- p_T parton in a QGP:

$$\begin{aligned} \Delta E_{ind}^{(1)} &= \frac{C_R \alpha_s L E}{\pi \lambda_g} \int dx \int \frac{d^2\mathbf{q}_1}{\pi} \frac{\mu^2}{(\mu^2 + \mathbf{q}_1^2)^2} \int \frac{d^2\mathbf{k}}{\pi} \\ &\times \int d\Delta z \bar{\rho}(\Delta z) \left[-\frac{2(1 - \cos\{(\omega_1 + \tilde{\omega}_m)\Delta z\})}{(\mathbf{k} - \mathbf{q}_1)^2 + m_g^2 + x^2M^2} \left(\frac{(\mathbf{k} - \mathbf{q}_1) \cdot \mathbf{k}}{\mathbf{k}^2 + m_g^2 + x^2M^2} - \frac{(\mathbf{k} - \mathbf{q}_1)^2}{(\mathbf{k} - \mathbf{q}_1)^2 + m_g^2 + x^2M^2} \right) \right. \\ &+ \frac{1}{2}e^{-\mu_1\Delta z} \left\{ \left(\frac{\mathbf{k}}{\mathbf{k}^2 + m_g^2 + x^2M^2} \right)^2 \left(1 - \frac{2C_R}{C_A} \right) \left(1 - \cos\{(\omega_0 + \tilde{\omega}_m)\Delta z\} \right) \right. \\ &\left. \left. + \frac{\mathbf{k} \cdot (\mathbf{k} - \mathbf{q}_1)}{(\mathbf{k}^2 + m_g^2 + x^2M^2)((\mathbf{k} - \mathbf{q}_1)^2 + m_g^2 + x^2M^2)} (\cos\{(\omega_0 + \tilde{\omega}_m)\Delta z\} - \cos\{(\omega_0 - \omega_1)\Delta z\}) \right\} \right]. \end{aligned} \quad (7)$$

The small separation distance correction shown in the last four lines of Eq. 7 has the properties we expect: 1) the correction goes to zero as the separation distance becomes large, $\Delta z \rightarrow \infty$ (or, equivalently, as the Debye screening length goes to 0, $\mu \rightarrow \infty$) and 2) the correction term vanishes as the separation distance vanishes, $\Delta z \rightarrow 0$, due to the destructive interference of the LPM effect.

We investigated the importance of the short separation distance correction term in Eq. 7 numerically to produce Figs. 2a, 2b and 2c. The numerical results use the same values as [12]: $\mu = 0.5$ GeV, $\lambda_{mfp} = 1$ fm, $C_R = 4/3$, $C_A = 3$, $\alpha_s = 0.3$, $m_{charm} = 1.3$ GeV and $m_{bottom} = 4.75$ GeV, and the QCD analogue of the Ter-Mikayelian plasmon effect was taken into account by setting $m_{gluon} = \mu/\sqrt{2}$. As in [15], kinematic upper limits were used for the momentum integrals such that $0 \leq k \leq 2x(1-x)E$ and $0 \leq q \leq \sqrt{3E\mu}$. This choice of k_{max} guarantees that the final momentum of the parent parton is collinear to the initial momentum of the parent parton and that the momentum of the emitted gluon is collinear to the momentum of the parent parton.

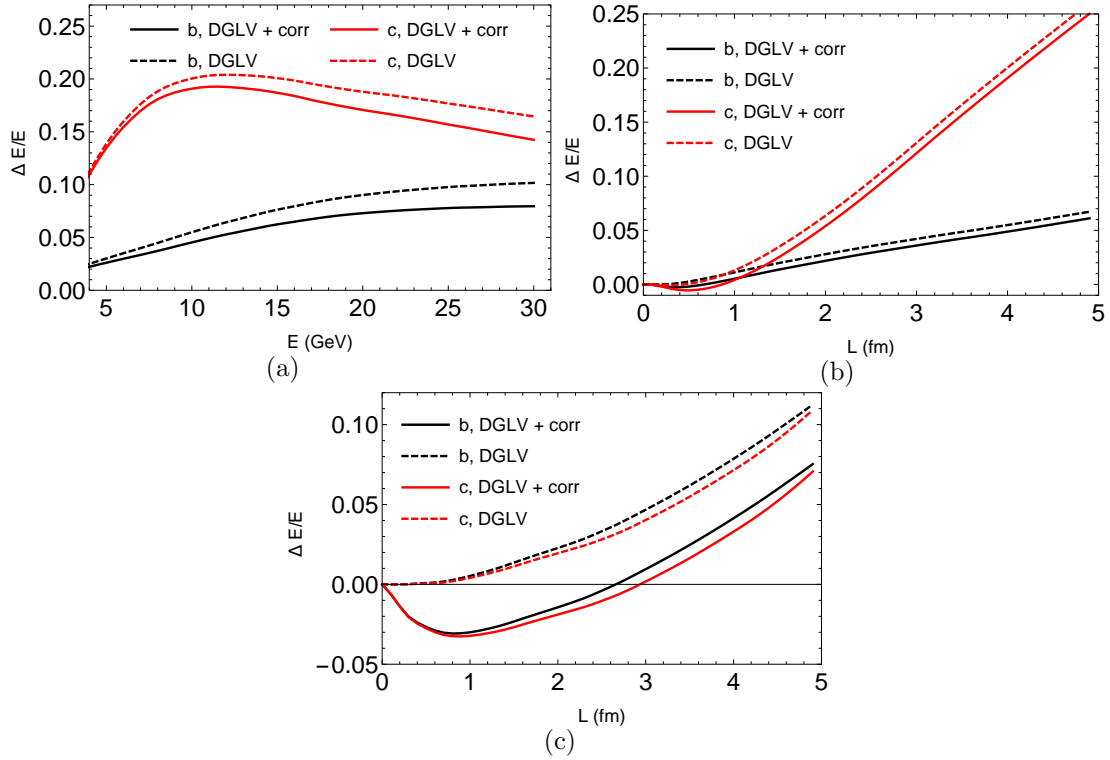


Figure 2: Fractional energy loss of charm and bottom quarks in a QGP with $\mu = 0.5$ GeV and $\lambda_{mfp} = 1$ fm for (a) fixed path length $L = 4$ fm, (b) fixed energy $E = 10$ GeV, and (c) fixed energy $E = 100$ GeV. In the figures, “DGLV” dashed curves are computed from the original $N = 1$ in opacity large separation distance DGLV formula while “DGLV + corr” solid lines are from our all separation distance generalization of the $N = 1$ DGLV result, Eq. 7.

The fraction of momentum carried away by the radiated gluon, x , was integrated over from 0 to 1. The distribution of scattering centers, although originally assumed to be exponential in [12] in order to account for the rapidly expanding medium, was here assumed to have the form of a unit step function, since an exponential distribution biases towards short separation distance scattering, lending excessive weight to contributions from short separation distance terms. The choice of a step function distribution reduces the effect of the correction terms by $\sim 10\%$ at low (~ 10 GeV) parton energies and $\sim 50\%$ at higher (~ 100 GeV) energies as compared to results using an exponential distribution.

In Fig. 2a we show the fractional energy loss of charm and bottom quarks of varying energy propagating through a 4 fm long static QGP brick. We note that the present calculation amounts to an energy *gain* compared to the DGLV result.

In Fig. 2b we plot the fractional energy loss of charm and bottom quarks of energy $E = 10$ GeV for path lengths up to 5 fm. The integration over all separation distances (even in the DGLV calculation) results in the non-zero effect seen here even for large path lengths and is therefore not surprising, albeit unexpected.

Our most important result is shown in Fig. 2c, which presents the fractional energy loss of 100 GeV charm and bottom quarks propagating up to 5 fm through a QGP. The small distance “correction” term dominates over the leading DGLV result for the first ~ 3 fm of the path.

4. Conclusions

An asymptotic analysis of Eq. 7, following [16], reveals that the correction term dominates because it scales as $E \log E$ while the large separation distance term grows much slower, as $\log E$. This dominance is difficult to reconcile with experimental data and suggests that the large formation time assumption is invalid in the DGLV approach

Since all energy loss formalisms, GLV, BDMPS-Z-ASW, AMY, and HT (see [1] and references therein) exploit the large formation time approximation, we are faced with a need to reassess the applicability of the large formation time assumption in any description of energy loss. Deriving expressions in the other formalisms that do not rely on either the collinear or large formation time approximations might also be formidable. Lastly, the factorization of the production of the hard parton from the scattering will demand careful consideration in finite media, particularly since the behaviour of a Debye screened scattering centre near the edge of a thermalized medium is unclear.

5. Acknowledgments

The authors wish to thank the SA-CERN Collaboration, the South African National Research Foundation (NRF), and the National Institute for Theoretical Physics (NITheP) for their generous support. The authors also wish to thank CERN for the hospitality extended to them during the completion of part of this work. Finally, the authors wish to thank Miklos Gyulassy, Ulrich Heinz, and Carlos Salgado for valuable discussions.

References

- [1] Majumder A and Van Leeuwen M 2011 *Prog. Part. Nucl. Phys.* **66** 41–92 (*Preprint* 1002.2206)
- [2] Armesto N, Cacciari M, Dainese A, Salgado C A and Wiedemann U A 2006 *Phys. Lett.* **B637** 362–366 (*Preprint* hep-ph/0511257)
- [3] Horowitz W A 2013 *Nucl. Phys.* **A904-905** 186c–193c (*Preprint* 1210.8330)
- [4] Burke K M *et al.* (JET) 2014 *Phys. Rev.* **C90** 014909 (*Preprint* 1312.5003)
- [5] Djordjevic M, Djordjevic M and Blagojevic B 2014 *Phys. Lett.* **B737** 298–302 (*Preprint* 1405.4250)
- [6] Khachatryan V *et al.* (CMS) 2015 *Phys. Rev. Lett.* **115** 012301 (*Preprint* 1502.05382)
- [7] Aad G *et al.* (ATLAS) 2016 *Phys. Rev. Lett.* **116** 172301 (*Preprint* 1509.04776)
- [8] Adare A *et al.* (PHENIX) 2016 *Phys. Rev. Lett.* **116** 122301 (*Preprint* 1509.04657)
- [9] Aad G *et al.* (ATLAS) 2015 *Phys. Lett.* **B748** 392–413 (*Preprint* 1412.4092)
- [10] Abelev B B *et al.* (ALICE) 2014 *Phys. Lett.* **B728** 25–38 (*Preprint* 1307.6796)
- [11] Collaboration C (CMS) 2015
- [12] Djordjevic M and Gyulassy M 2004 *Nucl. Phys.* **A733** 265–298 (*Preprint* nucl-th/0310076)
- [13] Kolbe I and Horowitz W A 2016 *J. Phys. Conf. Ser.* **668** 012107 (*Preprint* 1509.06122)
- [14] Gyulassy M and Wang X n 1994 *Nucl. Phys.* **B420** 583–614 (*Preprint* nucl-th/9306003)
- [15] Wicks S, Horowitz W, Djordjevic M and Gyulassy M 2007 *Nucl. Phys.* **A784** 426–442 (*Preprint* nucl-th/0512076)
- [16] Gyulassy M, Levai P and Vitev I 2001 *Nucl. Phys.* **B594** 371–419 (*Preprint* nucl-th/0006010)

Phenomenology of additional scalar bosons at the LHC

Mukesh Kumar^{a,1}, Stefan von Buddenbrock^{b,2}, Nabarun Chakrabarty^{c,3}, Alan S. Cornell^{a,4}, Deepak Kar^{b,5}, Tanumoy Mandal^{d,6}, Bruce Mellado^{b,7}, Biswarup Mukhopadhyaya^{c,8}, Robert G. Reed^{b,9} and Xifeng Ruan^{b,10}

^a National Institute for Theoretical Physics; School of Physics and Mandelstam Institute for Theoretical Physics, University of the Witwatersrand, Johannesburg, Wits 2050, South Africa.

^b School of Physics, University of the Witwatersrand, Johannesburg, Wits 2050, South Africa.

^c Regional Centre for Accelerator-based Particle Physics, Harish-Chandra Research Institute, Chhatnag Road, Jhusi, Allahabad - 211 019, India.

^d Department of Physics and Astronomy, Uppsala University, Box 516, SE-751 20 Uppsala, Sweden.

E-mail: ¹mukesh.kumar@cern.ch, ²stef.von.b@cern.ch, ³nabarunc@hri.res.in, ⁴alan.cornell@wits.ac.za, ⁵deepak.kar@cern.ch, ⁶tanumoy.mandal@physics.uu.se, ⁷bruce.mellado@wits.ac.za, ⁸biswarup@hri.res.in, ⁹robert.reed@cern.ch, ¹⁰xifeng.ruan@cern.ch

Abstract. The confirmation of the Higgs boson in Run I data at the Large Hadron Collider (LHC) and the deviations from the Standard Model (SM) (which are strictly not statistically significant excesses at this stage) in recent Run II data can be considered suggestive of scenarios beyond the SM. We pursue a study in a minimal model which is an extension of a scalar doublet in the SM known as two-Higgs doublet model (THDM). Following earlier suggestions two real scalars χ and S have been introduced in the THDM where χ is treated as a candidate for dark matter. χ does not receive any vacuum expectation value (vev) in the model whereas the Higgs-like scalar S acquires vev . This allows small mixing between the CP -even scalars of the THDM, h , H and S . In this study the mass spectrum of new scalars is taken to be $2m_h < m_H < 2m_t$, $m_\chi < m_h/2$, $m_h \lesssim m_S \lesssim m_H - m_h$, $m_A > 2m_t$ and $m_H^\pm < m_A$, where m_h and m_t is masses of the SM Higgs and top-quark respectively, m_H , m_A and m_{H^\pm} are the masses of the heavy CP -even scalar H , CP -odd scalar A , and charged Higgs H^\pm , respectively. A partial list of potential search channels at the LHC has been provided with possible phenomenological consequences. The expected phenomenology and constraints on parameters are also discussed in a model-independent approach .

1. Introduction

After the confirmation of the Higgs boson (h) in Run I data at the Large Hadron Collider (LHC) [1, 3, 2, 4, 5, 6], it is pragmatic to move forward in searches of physics beyond the Standard Model (BSM). In this context we already have well-defined models with a rich particle spectrum which shall be supplemented through observed deviations in the experimental data. Some of the deviations in Run I data at the ATLAS and CMS, namely, the deviation in transverse momentum (p_T) spectrum of the Higgs boson in $h \rightarrow \gamma\gamma$ and $h \rightarrow ZZ \rightarrow 4l$ [7, 8, 9, 10] channel has been addressed in Ref. [11] by corroborating other source of deviations in heavy scalar

searches through di-Higgs boson production [12, 13, 14, 15] and in associated production of top-quarks [16, 17, 18, 19]. A deviation noted as a non statistically significant excess in the di-photon channel around 750 GeV [20, 21] in early data of Run II at the LHC¹ also provides hints of new physics BSM where it could be assumed to arise through a scalar or pseudo-scalar resonance around this mass.

These deviations can be explained by introducing a particle spectrum BSM in an effective theory as well as in a proper model by considering the appropriate sources of constraints in the theory and known limits on parameter space in that particular model. It is evident that this new particle spectrum comes with new phenomenology and helps in not only explaining the observed data but also in searches beyond a particular model(s). In this proceeding we intend to address the phenomenology of scalars BSM, assuming the particle spectrum of two-Higgs doublet model (THDM) in addition with other real singlets χ and S introduced in Refs. [24, 25].

2. The Model

Before moving towards the phenomenological implications of the additional scalars BSM, we first discuss the particle spectrum and parameters introduced in a model dependent as well as in a model independent approach. A simple extension of the SM is known as the THDM with one more additional scalar doublet, where this additional scalar doublet transform under the SM gauge symmetries similar to the Higgs field in the SM. After spontaneous electroweak symmetry breaking, five physical Higgs particles are left in the spectrum of THDM, two CP -even states, H (heaviest) and h (lightest), one CP -odd scalar, A , and one charged Higgs pair, H^\pm . The ratio of the two vacuums (v_1, v_2) of corresponding doublets is a free parameter of the theory, $\tan\beta = v_2/v_1$ in addition with the masses of the scalars² and the mixing angle α between h and H . Based on different choices of symmetries and couplings to fermions different types of THDM is available, *viz.*, Type-I, Type-II, Lepton-specific or Flipped THDMs. For more details of this model we refer the Refs. [26, 27].

In a model-independent approach i.e. *via* an effective theory the authors of Refs. [11, 24, 25] introduced three real scalars H ,³ χ - introduced as a dark matter (DM) candidate whose signature is a source of missing energy in the colliders, and S - a Higgs-like real singlet scalar. In these studies, it is found necessary to fit all data that the heavier H should have a large branching ratio in the channel $H \rightarrow h\chi\chi$, where h is the Standard Model (SM) Higgs boson. However, this explanations can also be accommodated by introducing the on-shell participation of S in the decay of $H \rightarrow Sh, S \rightarrow \chi\chi$. To achieve the fittings, the free parameters of the theory are fixed by considering various observed limits in VV ($V = W^\pm, Z$) resonance searches [28, 29, 30] and the DM constraints.

As an extension to this model-independent approach, it is interesting to add χ and S in a THDM as a model-dependent scenarios. In that case all new parameters of interactions among these scalars follow the constraints from THDM with few additional parameters in the theory. The details of this model can be found in Ref. [25], where χ does not acquire vacuum expectation value (vev) while S acquires vev in result there is small mixing between h, H and S is considered to obtain hHS coupling which should respect the bounds from the Higgs data.

¹ Note the earlier reference [20, 21] is deprecated and now replaced with [22, 23] where the deviations, though they remain, have nonetheless diminished with more data and a more careful analysis.

² It is to be noted that the two CP -even scalars h and H may have different interpretations in terms of masses in comparison to the SM Higgs boson. In our case we assume the lighter h to aligned with the SM Higgs boson.

³ H may not be same as THDM heavier CP -even scalar. The difference is also noticed since in this approach it is considered to be a real singlet scalar while in THDM it is a part of doublet which appear after spontaneous electroweak symmetry breaking.

3. Phenomenology

In this section we discuss the phenomenology associated with the scalars introduced in previous sections which is useful in explaining the observed data in experiments as well as to provide hints for searches at particular energy and parameter choices in the colliders like the LHC. The observed final states are highly dependent on the choice(s) of masses of these scalars after production rates *via* gluons, quarks or gluons and quarks.

Following the results of Ref. [11], we consider following mass ranges for THDM scalars with additional real scalars χ and S to explain the phenomenology:

- (a) Light Higgs: $m_h = 125$ GeV (assuming as the SM Higgs),
- (b) Heavy Higgs: $2m_h < m_H < 2m_t$,
- (c) CP -odd Higgs: $m_A > (m_H + m_V)$, where ($V = W^\pm, Z$),
- (d) Charged Higgs: $(m_H + m_V) < m_{H^\pm} < m_A$,
- (e) Additional scalars χ, S : $m_\chi < m_h/2$ and $m_h \lesssim m_S \lesssim (m_H - m_h)$.

Based on these masses we can study the branching fractions of THDM scalars into the SM particles and additional scalars χ and S as listed in Table 1 with following production channels:

- (a) $gg \rightarrow h, H, A, S$,
- (b) $pp \rightarrow tH^-(\bar{t}H^+), tH^-\bar{b} + \bar{t}H^+b, H^+H^-, H^\pm W^\pm$.

A partial list of interesting searches are summarised in Table 2 which leads striking signatures of clean final states involving the scalars introduced in this proceedings. Mostly we discussed leptonic final states with missing energy signatures through the decays of heavy scalars. The same-sign leptonic channels provides prominent signatures for any new physics models beyond the SM. Apart from these search list

- (1) It is interesting to constrain the parameter space of THDM and associated parameters with χ and S by explaining the distortion in the p_T spectrum of the Higgs boson in $h \rightarrow \gamma\gamma$ and $h \rightarrow ZZ \rightarrow 4l$ channels as in Ref. [11]. Also the consequences of introducing S to explain the large branchings in the effective theory due to $H \rightarrow h\chi\chi$ can be understood in both model independent and dependent approaches by allowing $H \rightarrow hS$ and $S \rightarrow \chi\chi$.
- (2) The first LHC data at $\sqrt{s} = 13$ TeV observed a deviation in the $\gamma\gamma$ final state peaked at the invariant mass around 750 GeV [20, 21] (but later moderated by the ATLAS [22] and CMS [23]) with the best fit width of the resonance as 45 GeV. Here according to our parameter choice that resonance could be a CP -odd scalar A . And further based on the choices of mass and width of this possible resonance the model parameters can be constrained.

A few analyses of interesting final states with selected leptonic signatures are discussed in the Ref. [25] by considering $H \rightarrow 4W \rightarrow 4l$ with missing energy and associated H production with top quarks and decays as $t(t)H \rightarrow 6W \rightarrow l^\pm l^\pm l^\pm + X$. With this note we summarise our work in the next section.

4. Summary

In this proceedings we discuss the phenomenology of the scalars beyond the Standard Model. These scalars are introduced in a model independent way as an effective theory and also in a model dependent approach - considering the two-Higgs doublet model. A logical way of introducing χ and S has been discussed. A list of search strategies has been drawn up based on

Table 1: List of possible decay modes of 2HDM scalars to the SM particles and additional scalars based on the mass choices of all scalars as described in the text. Note that we are not interested in $h \rightarrow \chi\chi$ decay, instead we prefer $S \rightarrow \chi\chi$ decay mode. In the final states of all decay we consider W^\pm , $Z \rightarrow$ leptonic decay modes.

S. No.	Scalars	Decay modes
D.1	h	$bb, \tau^+\tau^-, \mu^+\mu^-, s\bar{s}, c\bar{c}, gg, \gamma\gamma, Z\gamma, W^+W^-, ZZ$
D.2	H	D.1, hh, SS, Sh
D.3	A	D.1, $t\bar{t}, Zh, ZH, ZS, W^\pm H^\mp$
D.4	H^\pm	$W^\pm h, W^\pm H, W^\pm S$
D.5	S	D.1, $\chi\chi$

Table 2: A list of potential search channels arising from the addition of the new scalars presented in this proceedings. This list is by no means complete, but contains clean search channels (mostly leptonic) which could make for striking signatures in the LHC physics regime. Note that in the mass ranges we are considering, H almost always decays to SS or Sh , where S and h are likely to decay to W s or b -jets.

Scalar	Production mode	Search channels
H	$gg \rightarrow H, Hjj$ (ggF and VBF)	Direct SM decays as in Table 1 $\rightarrow SS/Sh \rightarrow 4W \rightarrow 4\ell + \text{MET}$ $\rightarrow hh \rightarrow \gamma\gamma b\bar{b}, b\bar{b}\tau\tau, 4b, \gamma\gamma WW$ etc. $\rightarrow Sh$ where $S \rightarrow \chi\chi \implies \gamma\gamma, b\bar{b}, 4\ell + \text{MET}$
	$pp \rightarrow Z(W^\pm)H$ ($H \rightarrow SS/Sh$)	$\rightarrow 6(5)l + \text{MET}$ $\rightarrow 4(3)l + 2j + \text{MET}$ $\rightarrow 2(1)l + 4j + \text{MET}$
	$pp \rightarrow t\bar{t}H, (t + \bar{t})H$ ($H \rightarrow SS/Sh$)	$\rightarrow 2W + 2Z + \text{MET}$ and b -jets $\rightarrow 6W \rightarrow 3$ same sign leptons + jets and MET
H^\pm	$pp \rightarrow tH^\pm$ ($H^\pm \rightarrow W^\pm H$)	$\rightarrow 6W \rightarrow 3$ same sign leptons + jets and MET
	$pp \rightarrow tbH^\pm$ ($H^\pm \rightarrow W^\pm H$)	Same as above with extra b -jet
	$pp \rightarrow H^\pm H^\mp$ ($H^\pm \rightarrow HW^\pm$)	$\rightarrow 6W \rightarrow 3$ same sign leptons + jets and MET
	$pp \rightarrow H^\pm W^\pm$ ($H^\pm \rightarrow HW^\pm$)	$\rightarrow 6W \rightarrow 3$ same sign leptons + jets and MET
A	$gg \rightarrow A$ (ggF)	$\rightarrow t\bar{t}$ $\rightarrow \gamma\gamma$
	$gg \rightarrow A \rightarrow ZH$ ($H \rightarrow SS/Sh$)	Same as $pp \rightarrow ZH$ above, but with resonance structure over final state objects
	$gg \rightarrow A \rightarrow W^\pm H^\mp$ ($H^\mp \rightarrow W^\mp H$)	$6W$ signature with resonance structure over final state objects

recent observed excesses in ATLAS and CMS data, a sketch has been suggested incorporating the mass spectrum of the introduced scalars. In most of the cases we considered the leptons with missing energy final states with a significant number of same-sign leptons make the searches to be clean and striking.

Here it is also important to summarise the present constraints on the two-Higgs doublet model parameters from Run-I data at the LHC. In Ref. [31] a summary of exclusion limits were presented for several searches on additional heavy Higgs bosons in physics BSM. In the case of THDM, two benchmark scenarios Type-I and Type-II were considered. The Type-I (II) THDM is generally constrained to $\cos(\beta - \alpha) \lesssim 0.5(0.2)$, $m_H \lesssim 380(\approx 380)$ and $\tan\beta \lesssim 2$ (all) of the heavy Higgs boson. These constraints have been obtained by considering the decay channels

$A/H/h \rightarrow \tau\tau$, $H \rightarrow WW/ZZ$, $A \rightarrow ZH(l\bar{l}b\bar{b})$ and $A \rightarrow ZH(l\bar{l}\tau\tau)$. We hope that our work towards this direction in Run-II data will show interesting features.

References

- [1] F. Englert and R. Brout, Phys. Rev. Lett. **13**, 321 (1964)
- [2] P. W. Higgs, Phys. Rev. Lett. **13**, 508 (1964)
- [3] P. W. Higgs, Phys. Lett. **12**, 132 (1964)
- [4] G. S. Guralnik, C. R. Hagen and T. W. B. Kibble, Phys. Rev. Lett. **13**, 585 (1964)
- [5] ATLAS Collaboration (G. Aad *et al.*) Phys.Lett. **B716**, 1 (2012)
- [6] CMS Collaboration (S. Chatrchyan *et al.*), Phys.Lett. **B716**, 30 (2012)
- [7] G. Aad *et al.* [ATLAS Collaboration], JHEP **1409**, 112 (2014) [arXiv:1407.4222 [hep-ex]].
- [8] G. Aad *et al.* [ATLAS Collaboration], Phys. Lett. B **738**, 234 (2014) [arXiv:1408.3226 [hep-ex]].
- [9] V. Khachatryan *et al.* [CMS Collaboration], Eur. Phys. J. C **76**, no. 1, 13 (2016) [arXiv:1508.07819 [hep-ex]].
- [10] CMS Collaboration, (2015), CMS-PAS-HIG-14-028
- [11] S. von Buddenbrock *et al.*, arXiv:1506.00612 [hep-ph].
- [12] G. Aad *et al.* [ATLAS Collaboration], Phys. Rev. D **92**, 092004 (2015) [arXiv:1509.04670 [hep-ex]].
- [13] CMS Collaboration, (2014), CMS-PAS-HIG-13-032
- [14] V. Khachatryan *et al.* [CMS Collaboration], arXiv:1510.01181 [hep-ex].
- [15] V. Khachatryan *et al.* [CMS Collaboration], Phys. Rev. D **90**, 112013 (2014) [arXiv:1410.2751 [hep-ex]].
- [16] G. Aad *et al.* [ATLAS Collaboration], Phys. Lett. B **740**, 222 (2015) [arXiv:1409.3122 [hep-ex]].
- [17] G. Aad *et al.* [ATLAS Collaboration], Phys. Lett. B **749**, 519 (2015) [arXiv:1506.05988 [hep-ex]].
- [18] G. Aad *et al.* [ATLAS Collaboration], Eur. Phys. J. C **75**, no. 7, 349 (2015) [arXiv:1503.05066 [hep-ex]].
- [19] V. Khachatryan *et al.* [CMS Collaboration], JHEP **1409**, 087 (2014) [JHEP **1410**, 106 (2014)] [arXiv:1408.1682 [hep-ex]].
- [20] The ATLAS collaboration, "Search for resonances in diphoton events with the ATLAS detector at $\sqrt{s} = 13$ TeV," ATLAS-CONF-2016-018.
- [21] CMS Collaboration, "Search for new physics in high mass diphoton events in 3.3 fb^{-1} of proton-proton collisions at $\sqrt{s} = 13$ TeV and combined interpretation of searches at 8 TeV and 13 TeV," CMS-PAS-EXO-16-018.
- [22] M. Aaboud *et al.* [ATLAS Collaboration], Phys. Lett. B **775**, 105 (2017) doi:10.1016/j.physletb.2017.10.039 [arXiv:1707.04147 [hep-ex]].
- [23] V. Khachatryan *et al.* [CMS Collaboration], Phys. Rev. Lett. **117**, no. 5, 051802 (2016) doi:10.1103/PhysRevLett.117.051802 [arXiv:1606.04093 [hep-ex]].
- [24] M. Kumar *et al.*, arXiv:1603.01208 [hep-ph].
- [25] S. von Buddenbrock *et al.*, arXiv:1606.01674 [hep-ph].
- [26] J. F. Gunion, H. E. Haber, G. Kane and S. Dawson, "The Higgs Hunter's Guide".
- [27] G. C. Branco, P. M. Ferreira, L. Lavoura, M. N. Rebelo, M. Sher and J. P. Silva, Phys. Rept. **516**, 1 (2012) doi:10.1016/j.physrep.2012.02.002 [arXiv:1106.0034 [hep-ph]].
- [28] G. Aad *et al.* [ATLAS Collaboration], JHEP **1601**, 032 (2016) [arXiv:1509.00389 [hep-ex]].
- [29] G. Aad *et al.* [ATLAS Collaboration], Eur. Phys. J. C **76**, no. 1, 45 (2016) [arXiv:1507.05930 [hep-ex]].
- [30] V. Khachatryan *et al.* [CMS Collaboration], JHEP **1510**, 144 (2015) [arXiv:1504.00936 [hep-ex]].
- [31] CMS PAS HIG-16-007, "Summary results of high mass BSM Higgs searches using CMS run-I data," The CMS Collaboration.

Quantum corrections to the kink-antikink potential

Z Lee, H Weigel

Physics Department, Stellenbosch University, Matieland 7602, South Africa

E-mail: 16578996@sun.ac.za, weigel@sun.ac.za

Abstract. We estimate the one loop quantum correction to the kink-antikink potential by computing the vacuum polarization energy as a function of the kink-antikink separation. This energy is calculated from scattering data for fluctuations about the static kink-antikink configuration. To construct a well-defined quantum theory for these fluctuations an additional constraint must be implemented.

1. Introduction

Non-linear field theories may produce classical solutions that have a localized energy density. These solutions are called solitons or solitary waves [1]. In many cases these solitons have particle properties. The most prominent example is the Skrymion as a model for baryons [2, 3]¹. In these identifications the integrated energy density is the mass of the particle. Typically this integral overestimates the actual mass of the particle because quantum corrections are omitted. This is not problematic when investigating properties of a single particle. However, the quantum corrections may become important when comparing configurations with different particle numbers as it occurs, for example, when computing binding energies of compound objects. The leading quantum correction to the soliton energy is the vacuum polarization energy (VPE). The VPE is the renormalized sum of the shifts of the zero point energies of the quantum fluctuations due to their interaction with the background configuration generated by the soliton. Being a quantum field theory calculation a proper renormalization must be applied. In the present study we therefore calculate the VPE of the soliton-antisoliton potential in a renormalizable model with a quartic self-interaction in one time and one space dimensions.

2. VPE and spectral method

The calculation of the VPE from scattering data is by now a well established endeavor in the framework of spectral methods [5]. To apply these methods we call the soliton solution to the field equation $\phi_0(x)$. Then we introduce time dependent fluctuations $\eta(x, t) = \eta_\omega(x)e^{-i\omega t}$ and linearize the full field equation. This gives rise to a relativistic wave-equation

$$\omega^2 \eta_\omega(x) = \left[-\frac{d^2}{dx^2} + U[\phi_0(x)] \right] \eta_\omega(x), \quad (1)$$

where $U[\phi_0(x)]$ is the potential for the fluctuations generated by the background soliton. This wave-equation is a standard problem in potential scattering [6]. The background polarizes the

¹ For a recent review see Ref. [4].

quantum fluctuations $\eta_\omega(x)$ in two aspects. First, it creates bound states with energies ω_j and second, the density of the scattering states is distorted. The scattering states have energies $\omega = \sqrt{k^2 + m^2}$ where k is the momentum and m the mass of the fluctuating field. Then the distortion of the density of scattering states is measured by the derivative of the scattering phase shift $\delta(k)$. Weighting the contribution from the scattering states to the VPE accordingly yields

$$E_{\text{vac}} = \sum_j \frac{\omega_j}{2} + \sum_{p=\pm} \int_0^\infty \frac{dk}{2\pi} \sqrt{k^2 + m^2} \left. \frac{d\delta_p(k)}{dk} \right|_{\text{renorm.}}, \quad (2)$$

since in one space dimensions there are two scattering channels when the potential is reflection invariant. These two channels are characterized by symmetric ($p = +$) and anti-symmetric ($p = -$) wave-functions when $x \rightarrow -x$.

Renormalization is accomplished in two steps. First the divergent contributions to the momentum integral in Eq. (2) are identified from the Born series. They are subtracted under the integral and added back to the VPE as Feynman diagrams. In the second step the divergences of the Feynman diagrams are removed with the help of standard counterterms whose coefficients are universal for a fixed renormalization scheme. For the current problem with boson quantum fluctuations in one space dimension this procedure is quite simple because only the first order tadpole diagram is divergent. This diagram is local and can be fully removed under renormalization. Applying Levinson's theorem to the formal expression and integrating by parts yields the VPE

$$E_{\text{vac}} = \frac{1}{2} \sum_j (\omega_j - m) - \sum_{p=\pm} \int_0^\infty \frac{dk}{2\pi} \frac{k}{\sqrt{k^2 + m^2}} [\delta_p(k) - \delta_p^{(1)}(k)], \quad (3)$$

where $\delta_p^{(1)}(k)$ is the Born approximation to the phase shift in channel p .

3. Kink-antikink configuration

To be specific we consider the ϕ^4 model in one space and one time dimension. This model is defined by the Lagrangian

$$\mathcal{L} = \frac{1}{2} \partial_\mu \phi \partial^\mu \phi - \frac{\lambda}{4} \left[\phi^2 - \frac{m^2}{2\lambda} \right]^2 \quad (4)$$

where λ is a coupling constant. The corresponding field equation contains a static solution, the so-called *kink*, $\phi_0(x) = (m/\sqrt{2\lambda}) \tanh(mx/2)$. The antikink solution is obtained by spatial reflection. These solutions build the soliton-antisoliton (or kink-antikink) configuration

$$\phi_R(x) = \frac{m}{\sqrt{2\lambda}} \left[\tanh\left(\frac{m}{2}(x - R)\right) - \tanh\left(\frac{m}{2}(x + R)\right) + 1 \right], \quad (5)$$

for which we want to compute the potential as a function of the fixed separation $2R$. There are classical and VPE contributions.

The classical potential is obtained by substituting the parameterization, Eq. (5) into the Lagrangian, integrating over the coordinate x [7] and subtracting twice the kink mass:

$$V_{\text{cl}}(R) = \frac{2m^3}{\lambda} \left[Rm + \frac{3}{\tanh(Rm)} - \frac{2 + 3Rm}{\tanh^2(Rm)} + \frac{2Rm}{\tanh^3(Rm)} - 1 \right]. \quad (6)$$

To compute the VPE contribution we need to solve Eq. (1) for $U[\phi_R(x)]$. However, this does not lead to a well-defined quantum theory for the fluctuations as can be seen from the following

argument. When the kink and antikink are widely separated, *i.e.* $R \rightarrow \infty$, each possesses the translational zero mode $\omega^2 = 0$ as well as the breather bound state with energy $\omega^2 = 3m^2/4$ [1]. When reducing R , the two zero mode solutions split with one bound state energy squared turning negative. This produces an imaginary energy eigenvalue [9] and must be avoided. We do so by recalling that the distance R is fixed and no fluctuations in this direction should be admitted. This induces the constraint $\int_{-\infty}^{\infty} dx \eta_{\omega}(x)z(x) = 0$ with

$$z(x) = N \frac{d}{dR} \phi_R(x) \quad \text{and} \quad N^{-2} = \int_{-\infty}^{\infty} dx \left(\frac{d}{dR} \phi_R(x) \right)^2. \quad (7)$$

This constraint turns the wave-equation into an integro-differential equation that describes a non-local interaction

$$-\eta_{\omega}''(x) = k^2 \eta_{\omega}(x) - \left(U[\phi_R(x)] - m^2 \right) \eta_{\omega}(x) + z(x) \int_{-\infty}^{\infty} dy \left[z(y) \left(U[\phi_R(y)] - m^2 \right) - z''(y) \right] \eta_{\omega}(y). \quad (8)$$

Here primes denote the derivative with respect to the spatial coordinate. Since $z(x)$ vanishes asymptotically, this equation represents a well-defined scattering problem from which phase shifts and their Born approximations can be computed. We also note that the constraint only affects the symmetric ($p = +$) channel. It does not take effect for large separation R where $z(x)$ parameterizes two independent translational vibrations that, by construction, are orthogonal to the remaining fluctuations.

4. Scattering data

To compute the phase shift $\delta_+(k)$ in the symmetric channel from the integro-differential equation (8) we introduce $u(x) = U[\phi_R(x)] - m^2$ and parameterize $\eta_{\omega}(x) = e^{\nu_S(x)} \cos[kx + \delta_S(x)]$. This leads to coupled differential equations²

$$\begin{aligned} \frac{d\delta_S(x)}{dx} &= -\frac{1}{k} c(x) \left[u(x)c(x) - \alpha z(x) e^{-\nu_S(x)} \right] \\ \frac{d\nu_S(x)}{dx} &= -\frac{1}{k} s(x) \left[u(x)c(x) - \alpha z(x) e^{-\nu_S(x)} \right], \end{aligned} \quad (9)$$

where $c(x) = \cos[kx + \delta_S(x)]$ and $s(x) = \sin[kx + \delta_S(x)]$. Furthermore α is a Lagrange multiplier that is iteratively adjusted such that $\int_{-\infty}^{\infty} dx z(x)c(x)e^{\nu(x)} = 0$. This system of equations is solved with the initial conditions $\delta_S(0) = 0$ and $\nu(0) = 0$ for a given value k . Then $\delta_+(k) = \lim_{x \rightarrow \infty} \delta_S(x)$. In the antisymmetric channel we similarly parameterize $\eta_{\omega}(x) = e^{\nu_A(x)} \sin[kx + \delta_A(x)]$. Since the constraint is not active in that channel, the wave-equation simplifies to an ordinary differential equation

$$\frac{d\delta_A(x)}{dx} = -\frac{u(x)}{k} \sin^2[kx + \delta_A(x)]. \quad (10)$$

The initial condition $\delta_S(0) = 0$ then produces $\delta_-(k) = \lim_{x \rightarrow \infty} \delta_A(x)$. The Born approximations $\delta_{\pm}^{(1)}(k)$ are similarly obtained from the linearized versions of equations (9) and (10) with $\alpha = 0$ since in the renormalization process we need to resemble the full Feynman diagram³.

As it is the case for the scattering data, *cf.* Eqs. (9) and (10), the bound state wave-functions are either symmetric or antisymmetric under spatial reflection. Of course the discrete sum (\sum_j)

² The two functions are related by $c(x)d\nu_S(x)/dx = s(x)d\delta_S(x)/dx$ [8].

³ Of course, formally we could compute the diagram subject to the constraint, but this would unnecessarily complicate matters.

Table 1. Bound state energies in the symmetric ($\omega_j^{(+)}$) and antisymmetric ($\omega_j^{(-)}$) channels for various values of the separation distance R .

bound state	$R = 0.25$	$R = 0.5$	$R = 0.75$	$R = 1.0$	$R = 3.0$	$R = 4.0$
$\omega_1^{(+)}$	0	0	0	0	0	0
$\omega_2^{(+)}$	—	1.905	1.719	1.592	1.723	1.731
$\omega_1^{(-)}$	1.815	1.350	0.927	0.606	0.012	0.002
$\omega_2^{(-)}$	—	—	1.999	1.955	1.740	1.733

in Eq. (3) comprises these channels. We obtain the bound state energies by first constructing a set of basis states via implementing boundary conditions on the non-interacting solutions ($U \equiv m^2$) at a distance L representing spatial infinity. Within this basis we compute matrix elements of the operator on the right-hand-side of Eq. (1) and find its eigenvalues. Those below m^2 are the bound state energies (squared). Since the bound state wave-functions decay exponentially at large x , the corresponding energies are not sensitive to the particular value of L as long as it is large enough. For the symmetric channel with the constraint we diagonalize the operator from Eq. (1) after sandwiching it between the projector $\mathbb{1} - |z\rangle\langle z|$. Note that this always causes a zero mode to appear for the solution, $|z\rangle$ that is annihilated by the projector.

With these solutions to the constraint wave-equation we compute the VPE from Eq. (3) for distinct values of the distance R . Subtracting twice the VPE of a single (anti)kink yields the leading quantum correction to the kink-antikink potential as a function of R .

5. Results

To produce numerical results we redefine the field and the coordinates such that $m = 2$ and $\lambda = 2$.

In table 1 we list the bound state energies as a function of the kink-antikink separation R that result from the wave-equation (8). A zero mode always appears in the symmetric channel because of the projection. As $R \rightarrow \infty$ the lowest bound state, $\omega_1^{(-)}$ in the anti-symmetric channel also turns into a zero mode. In the same limit the second bound state, $\omega_2^{(-)}$ approaches the breather energy at $\sqrt{3}m/2$.

We also note that the resulting phase shift for the constraint scattering problem reproduces Levinson's theorem

$$\delta_+(0) = \left(n_+ - \frac{1}{2}\right)\pi \quad \text{and} \quad \delta_-(0) = n_-\pi \quad (11)$$

for scattering in one space dimension [10, 11]⁴. Here n_+ and n_- are the number of bound states in the symmetric and anti-symmetric channels, respectively. Note that n_+ also counts the zero mode from the constraint. This statement can readily be verified for $R = 0.5$ for which we plot the phase shifts in figure 1.

In figure 2 we compare our main result for the quantum energy of the kink-antikink system relative to the quantum energy of two independent kinks

$$V_{\text{vac}}(R) = E_{\text{vac}}(R) - 2E_{\text{vac}}^{(\text{kink})} \quad (12)$$

to the classical counterpart from Eq. (6). While the latter is indeed known to be attractive we find that the quantum correction is repulsive. However, in magnitude it is not enough to

⁴ A formal proof of the theorem for non-local interactions is presented in Ref. [12].

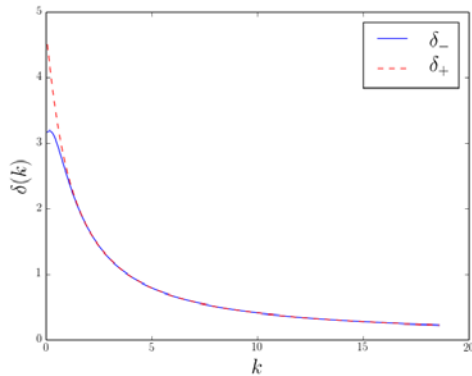


Figure 1. (color online) Phase shift in the symmetric (δ_+) and antisymmetric (δ_-) channels for separation distance $R = 0.5$.

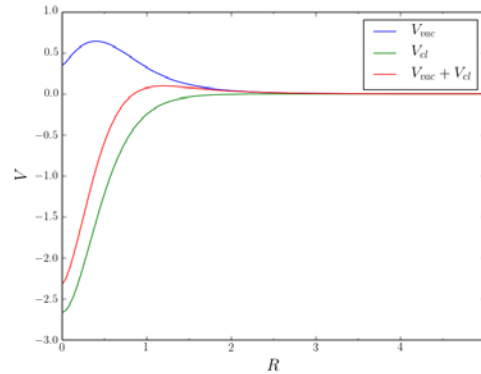


Figure 2. (color online) Quantum correction to kink-antikink potential as a function of the separation R defined in Eq. (12). Also shown is the classical potential from Eq. (6).

turn the whole potential into being repulsive. On the contrary, we find that (in absolute value) the VPE is significantly smaller than the classical potential. This, of course, is consistent with the VPE being a mere correction. Nevertheless, we see from figure 2 that the total potential $V_{cl}(R) + V_{vac}(R)$ produces a small barrier at an intermediate distances. Hence the quantum corrections indeed have the potential to stabilize a classically unstable configuration.

Though we have circumvented the fundamental problem of dealing with imaginary frequencies by introducing a constraint, this leads to an inconsistency that still needs to be resolved. A closer look at figure 2 shows that V_{vac} approximates 0.36 in the limit $R \rightarrow 0$. This is actually the trivial configuration which has zero VPE so that $V_{vac} \rightarrow -2E_{vac}^{(kink)}$ which in our units is 0.94. In this limit the non-zero result for the VPE originates purely from the constraint.

6. Conclusion and open problems

We have estimated the one-loop quantum correction to the kink-antikink potential. This is a prototype calculation of quantum corrections that require the comparison of soliton energies for different particle numbers. This will eventually shed more light on the predictions for classically stable configurations with large particle numbers such as nuclei [13], for example.

We observe that the quantum correction mitigates the strong attraction seen in the classical kink-antikink potential. Our findings are consistent with the VPE being just a correction to the classical energy. Interestingly enough, though, the quantum correction produces a mild repulsion at intermediate separation suggesting that these corrections stabilize a classically unstable configuration.

We have already mentioned the inconsistency of our VPE result for the trivial configuration $R \rightarrow 0$. We note that $\phi_R(x)$ is actually not a solution to the field equations and therefore a static source term in the wave-equation (1) must be added. Currently we investigate how this source term contributes to the kink-antikink potential. There may be both, a direct contribution and an indirect one as a modification of the constraint may turn out inevitable.

Acknowledgments

This project is supported in part by the NRF (South Africa) under grants 77454 and 109497. Z.L. appreciates a NITheP bursary.

References

- [1] R. Rajaraman, *Solitons and Instantons*, North Holland, 1982.
- [2] T. H. R. Skyrme Int. J. Mod. Phys. A **3** (1988) 2745. Article reconstructed by I. Aitchison.
- [3] G. S. Adkins, C. R. Nappi, and E. Witten, Nucl. Phys. B **228** (1983) 552.
- [4] H. Weigel, Lect. Notes Phys. **743** (2008) 1.
- [5] N. Graham, M. Quandt, and H. Weigel, Lect. Notes Phys. **777** (2009) 1.
- [6] R. G. Newton, *Scattering Theory of Waves and Particles*. Springer, New York, 1982.
- [7] T. Sugiyama, Prog. Theor. Phys. **61** (1979) 1550.
- [8] F. Calegero, *Variable Phase Approach to Potential Scattering*. Acad. Press, New York and London, 1967.
- [9] N. Graham and R. L. Jaffe, Phys. Lett. B **435** (1998) 145.
- [10] G. Barton, J. Phys. A **18** (1985) 479.
- [11] N. Graham, R. L. Jaffe, M. Quandt, and H. Weigel, Annals Phys. **293** (2001) 240.
- [12] Z. Q. Ma and A. Y. Dai, J. Phys. A **21**, (1988) 2085.
- [13] D. T. J. Feist, P. H. C. Lau, and N. S. Manton, Phys. Rev. D **87** (2013) 085034.

Two-Higgs doublet model and the LHC

Chuene Mosomane

National Institute for Theoretical Physics: School of Physics and Mandelstam Institute for theoretical Physics, University of Witwatersrand, Wits 2050, South Africa

E-mail: cjmosomane@gmail.com

Abstract. The discovery of a 125 GeV Higgs boson at the Large Hadron Collider (LHC) in 2012, which has properties as expected in the Standard Model (SM), was a major milestone for particle physics. More recently the ATLAS and CMS experiments have reported several excesses in the search for di-Higgs boson resonances. In these proceedings, we shall review the study of the general two-Higgs doublet model (2HDM) together with the Inert doublet model (IDM). The SM Higgs boson can also be realised within the Inert Doublet Model (IDM); a version of the two Higgs doublet model (2HDM), with an unbroken Z_2 symmetry under which one of the $SU(2)$ is the SM Higgs doublet (with one being the SM Higgs boson), and the second $SU(2)$ doublet transforms non-trivially with no vacuum expectation value, and does not interact with fermions. The 2HDM is a model which goes beyond the SM; it has a richer particle spectrum. The most general potential of a 2HDM is Lorentz invariant and renormalizable, containing 14 free parameters, with the most general Yukawa Lagrangian.

1. Introduction

The discovery of the Higgs boson is a milestone in particle physics and an extraordinary success of the LHC machine and the ATLAS and CMS collaborations [1]. The existence of the Higgs boson ensures unitarity in the scattering of longitudinal polarised W bosons, which allows the introduction of the gauge bosons (W^\pm, Z^0) and the quarks masses without breaking the gauge symmetry of the theory through the Higgs mechanism [2]. The underlying idea of this mechanism is the introduction of a complex scalar field into the theory, whose ground state acquires a non-zero vacuum expectation value (vev). The potential of the Higgs field does not share the same symmetry as the full Lagrangian of the theory, and hence the symmetry is spontaneously broken by the vev of the Higgs field. Due to the Goldstone theorem [3], which implies that a spontaneously broken local symmetry leads to massless Goldstone bosons whose degrees of freedom are then eaten up by the gauge bosons, only one degree of freedom of the Higgs field remains as a physical particle in the theory. This is the Higgs boson whose mass is a parameter in the theory [4]. Despite its great success in explaining all available data the SM has several inadequacies for the fermions and mass spectrum. It does not contain any dark matter particles [5], the SM also does not explain the strong CP problem [6]. These deficiencies led particle physicists to explore theory Beyond the SM (BSM). The two Higgs doublet model (2HDM) predicts more physical scalars such as a charged scalar, two neutral scalars and a pseudoscalar. We shall also discuss the Inert doublet model (IDM), which is a 2HDM with an unbroken Z_2 symmetry under which one of the doublets transform non-trivially, and all other SM fields are invariant.

2. 2HDM

The SM (with only one scalar field) has been a triumphant achievement in particle physics in terms of explaining the laws of nature, it has been regarded as having inadequacies and incomplete because there are phenomena that it doesn't explain (such as the darkmatter candidate and the baryonic-asymmetry of the universe). This gives us the impetus to investigate more complete theories that better address these questions, these are what we consider Beyond the SM (BSM). The 2HDM is a BSM theory which answers some of these questions, such as CP-violation etc. The motivation behind the 2HDM is that when breaking the electroweak symmetry does nature only allow for one scalar field, where by adding another scalar doublet to the SM we observe some interesting properties, such as the production of additional Higgs particles, sources of CP-violation and Flavour Changing Neutral Currents (FCNCs). We shall write the 2HDM Lagrangian which requires it to be renormalisable and Lorentz invariant.

$$\mathcal{L}_{2HDM} = (D_\mu \Phi_1)^\dagger (D^\mu \Phi_1) + (D_\mu \Phi_2)^\dagger (D^\mu \Phi_2) - V(\Phi_1 \Phi_2), \quad (1)$$

where the covariant derivative in the standard notation is given by:

$$D_\mu = \partial_\mu + ig \frac{\tau^i}{2} \cdot W_\mu^i + i \frac{g'}{2} Y B_\mu, \quad (2)$$

and the τ^i are the Pauli matrices and the Y is the hypercharge. The potential is:

$$\begin{aligned} V = & m_{11}^2 \Phi_1^\dagger \Phi_1 + m_{22}^2 \Phi_2^\dagger \Phi_2 - (m_{12}^2 \Phi_1^\dagger \Phi_2 + h.c) \\ & + \frac{\lambda_1}{2} (\Phi_1^\dagger \Phi_1)^2 + \frac{\lambda_2}{2} (\Phi_2^\dagger \Phi_2)^2 + \lambda_3 (\Phi_1^\dagger \Phi_1) (\Phi_2^\dagger \Phi_2) + \lambda_4 (\Phi_1^\dagger \Phi_2) (\Phi_2^\dagger \Phi_1) \\ & + \left[\frac{\lambda_5}{2} (\Phi_1^\dagger \Phi_2)^2 + \lambda_6 (\Phi_1^\dagger \Phi_1) (\Phi_1^\dagger \Phi_2) + \lambda_7 (\Phi_2^\dagger \Phi_2) (\Phi_1^\dagger \Phi_2) \right]. \end{aligned} \quad (3)$$

The 2HDM potential exhibits two CP-conserving neutral minima $\langle \Phi_1 \rangle$ and $\langle \Phi_2 \rangle$ of the form:

$$\langle \Phi_1 \rangle = \begin{pmatrix} 0 \\ \frac{v_1}{\sqrt{2}} \end{pmatrix}, \quad \langle \Phi_2 \rangle = \begin{pmatrix} 0 \\ \frac{v_2}{\sqrt{2}} \end{pmatrix},$$

with v_1 and v_2 being the vev's of the scalar doublet fields. In order for the doublets Φ_a to have their minima at $\langle \Phi_a \rangle$, the minimisation conditions apply, the end result gives us the following expressions

$$m_{11}^2 = m_{12}^2 \frac{v_2}{v_1} - \frac{\lambda_1}{2} v_1^2 - (\lambda_3 + \lambda_4 + \lambda_5) \frac{v_2^2}{2}, \quad (4)$$

$$m_{22}^2 = m_{12}^2 \frac{v_1}{v_2} - \frac{\lambda_1}{2} v_1^2 - (\lambda_3 + \lambda_4 + \lambda_5) \frac{v_1^2}{2}. \quad (5)$$

Introducing eight fields ϕ_a^\pm , ρ_a , and η_a ($a = 1, 2$) the doublets may be expanded around the minima, taking the form:

$$\Phi_a = \begin{pmatrix} \Phi_a^\pm \\ \frac{1}{\sqrt{2}}(v_a + \rho_a + i\eta_a) \end{pmatrix}, \quad a = 1, 2.$$

Inserting the scalar fields into the 2HDM potential generates terms that are linear in the two fields ρ_a . The expansion of the scalar fields into the 2HDM potential generates terms that are bilinear in the fields ϕ_a^\pm , ρ_a and η_a . Since these bilinear terms contribute to the propagators of

the eight fields, they give rise to the mass terms. All bilinear terms in the 2HDM potential can be transformed into the explicit form of non-diagonal mass-squared matrices given by,

$$\mathcal{M}_\rho^2 = -(\rho_1, \rho_2) \begin{pmatrix} m_{12}^2 \frac{v_2}{v_1} + \lambda_1 v_1^2 & -m_{12}^2 + \lambda_{345} v_1 v_2 \\ -m_{12}^2 + \lambda_{345} v_1 v_2 & m_{12}^2 \frac{v_2}{v_1} + \lambda_2 v_2^2 \end{pmatrix} \begin{pmatrix} \rho_1 \\ \rho_2 \end{pmatrix}, \quad (6)$$

$$\mathcal{M}_\eta^2 = \frac{m_A^2}{v_1^2 + v_2^2} (\eta_1, \eta_2) \begin{pmatrix} v_2^2 & -v_1 v_2 \\ -v_1 v_2 & v_1^2 \end{pmatrix} \begin{pmatrix} \eta_1 \\ \eta_2 \end{pmatrix}, \quad (7)$$

$$\mathcal{M}_{\phi^\pm}^2 = [m_{12}^2 - (\lambda_4 + \lambda_5) v_1 v_2] (\phi_1^-, \phi_2^-) \begin{pmatrix} \frac{v_2}{v_1} & -1 \\ -1 & \frac{v_1}{v_2} \end{pmatrix} \begin{pmatrix} \phi_1^+ \\ \phi_2^+ \end{pmatrix}. \quad (8)$$

To have physical propagating particles in the 2HDM, we shall consider the eigenstates with specific masses. This can be achieved by diagonalising the mass-squared matrices in Eq (6-8). The fields ϕ_i^\pm, ρ_i and η_i in the gauge basis are transformed into physical fields. The massless particles G^0 and G^\pm are the three Goldstone bosons of the 2HDM and are “eaten” up to give the W^\pm, Z^0 gauge bosons. The remaining five physical particles H^0 (heavy) and h^0 (lighter) are the CP-even, A^0 is a CP-odd and the H^\pm are the charged Higgs:

$$h^0 = \rho_1 \sin \alpha - \rho_2 \cos \alpha, \quad (9)$$

$$H^0 = -\rho_1 \cos \alpha - \rho_2 \sin \alpha, \quad (10)$$

$$H^\pm = \phi_1^\pm \sin \beta + \phi_2^\pm \cos \beta, \quad (11)$$

$$A^0 = \eta_1 \sin \beta - \eta_2 \cos \beta, \quad (12)$$

where the parameter α is a mixing angle between the CP-even scalars (h^0, H^0) and the parameter β is a rotational angle that diagonalises the mass-squared matrices of the charged Higgs and the pseudoscalars and is defined as; $\tan \beta = v_2/v_1$. The mass matrices Eq. (5-7) are diagonal in this basis; therefore these corresponding fields are referred to as the mass basis of the 2HDM potential. The tree-level masses of the particles in the mass basis are given by

$$m_{H^0}^2 = \frac{1}{2} \left[\mathcal{M}_{11}^2 + \mathcal{M}_{12}^2 + \sqrt{(\mathcal{M}_{11}^2 - \mathcal{M}_{22}^2)^2 + 4(\mathcal{M}_{12}^2)^2} \right], \quad (13)$$

$$m_{h^0}^2 = \frac{1}{2} \left[\mathcal{M}_{11}^2 + \mathcal{M}_{12}^2 - \sqrt{(\mathcal{M}_{11}^2 - \mathcal{M}_{22}^2)^2 + 4(\mathcal{M}_{12}^2)^2} \right], \quad (14)$$

$$m_{H^0}^2 = v^2 \left(\frac{m_{12}^2}{v_1 v_2} - \lambda_5 \right), \quad m_{G^0}^2 = 0, \quad (15)$$

$$m_{H^\pm}^2 = v^2 \left(\frac{m_{12}^2}{v_1 v_2} - \frac{\lambda_4 + \lambda_5}{2} \right), \quad m_{G^\pm}^2 = 0, \quad (16)$$

where $\mathcal{M}_{11}, \mathcal{M}_{12}, \mathcal{M}_{22}$ are the mass-squared matrices and the λ_4, λ_5 are the quartic couplings.

3. Yukawa Lagrangian

In the SM, diagonalising the mass matrix automatically diagonalises the Yukawa interactions, therefore, there are no tree-level FCNC. A general 2HDM introduces the possibility of having FCNCs at tree-level. However, in general Yukawa interactions (Y_1 and Y_2) will not be simultaneously diagonalised, and thus the Yukawa couplings will not be flavour diagonal. The

interaction of the fermions and scalar bosons of the 2HDM is determined by the form of the Yukawa Lagrangian. The transformation from a general to a flavour-conserving 2HDM can be achieved naturally by imposing a discrete or continuous symmetries on the Higgs doublets Φ_1 and Φ_2 [7]. Imposing these discrete symmetries will suppress FCNCs at tree-level with the same quantum numbers, i.e those that potentially mix, and couple only to the same Higgs doublet. The 2HDM will have four different model types and can be summarised in the table 1.

Table 1. Natural flavour conservation models. The superscript i is a generation index.

Models	Type I	Type II	(Leptonic-specific)	(Flipped)
u_R^i	Φ_2	Φ_2	Φ_2	Φ_2
d_R^i	Φ_2	Φ_1	Φ_2	Φ_1
e_R^i	Φ_2	Φ_2	Φ_1	Φ_2

We can write the Yukawa Lagrangian that conserves the FCNCs as follows:

$$\begin{aligned} \mathcal{L}_Y = & \bar{Q}_{L,i}(Y_{u,1}^{ij}\tilde{\Phi}_1 + Y_{u,2}^{ij}\Phi_2)u_{R,j} + \bar{Q}_{L,i}(Y_{d,1}^{ij}\Phi_1 + Y_{d,2}^{ij}\tilde{\Phi}_2)d_{R,j} \\ & + \bar{L}_{L,i}(Y_{l,1}^{ij}\Phi_1 + Y_{l,2}^{ij}\tilde{\Phi}_2)l_{R,j} + h.c, \end{aligned} \quad (17)$$

with $\tilde{\Phi}_i = -i[\Phi_i^\dagger \tau_2]^T$, $i = 1, 2$ and $Y_{u,1}^{ij}$ being the 3×3 Yukawa matrices. The (u_R, d_R) represent the right handed up-quark and down-quark, the l_R represent the right handed lepton, and the $(\bar{Q}_{L,i}, \bar{L}_{L,i})$ are the left handed quarks and left handed leptons. The coupling constants of the Yukawa interaction can be summarised as follows[8]:

4. Inert doublet model

The IDM is introduced to allow for the possibility of several mirror families of fermions. In the IDM the Higgs doublet Φ_2 does not couple to matter and the vev is zero, leaving the Z_2 symmetry unbroken. The scalar spectrum consists of the SM-like Higgs obtained from Φ_1 and one charged and two neutral states from Φ_2 (inert scalars). The scalar potential is the same as in Eq. (2) with $m_{12}^2 = 0$. The asymmetry phase $\langle \phi_1^0 \rangle = v/\sqrt{2}$ and $\langle \phi_2^0 \rangle = 0$ corresponds to a sizeable region of parameter space, and the scalar masses are as follows:

$$m_h^2 = \lambda_1 v^2, \quad m_S^2 = m_{22} + \frac{(\lambda_3 + \lambda_4 + \lambda_5)v^2}{2}, \quad (18)$$

$$m_+^2 = m_{22}^2 \frac{\lambda_3 v^2}{2}, \quad m_A^2 = m_{22} + \frac{(\lambda_3 + \lambda_4 + \lambda_5)v^2}{2}. \quad (19)$$

The $m_+^2 = m_-^2$ is the mass-squared matrix for the charged Higgs boson and it is the same, the Φ_2 can be produced at colliders through their couplings to the electroweak gauge bosons, subjected to the Z_2 symmetry. In addition they also participate in the cubic and quartic Higgs couplings:

$$\begin{aligned} V_{int} = & \frac{\lambda_2}{2} \left(H^+ H^- + \frac{S^2 + A^2}{2} \right)^2 + \lambda_3 \left(vh + \frac{h^2}{2} \right) \left(H^+ H^- + \frac{S^2 + A^2}{2} \right) \\ & + \frac{\lambda_4 + \lambda_5}{2} \left(vh + \frac{h^2}{2} \right) S^2 + \frac{\lambda_4 - \lambda_5}{2} \left(vh + \frac{h^2}{2} \right) A^2. \end{aligned} \quad (20)$$

Assuming the mass hierarchy $m_{\pm}^2 > m_A^2 > m_S^2$, the dominant decay of $A \rightarrow S f \bar{f}$, where A is a CP-odd scalar and f is fermion and S (singlet scalar) appears as missing energy. The decay pattern and the ratios of the neutral scalars can be examined at the LHC. We would observe S with mass ≈ 50 GeV. In this case S could be observed as a resonance through $pp \rightarrow S \rightarrow VV$ modes, with $V = ZZ, W^+W^-$; it also alters the coupling strength of the known interaction in the theory[8].

5. Phenomenology of the 2HDM at the LHC

We shall also discuss the phenomenology of the 2HDM particle spectrum. We are interested in studying the production and the decay of CP-even scalars (and the couplings), the Heavy Higgs and lighter Higgs as summarised in Table 2. In this proceedings we shall concern ourselves with the CP-even scalars. The phenomenology of h is similar to that of the SM Higgs boson coupling. The vector boson coupling constants for the lighter Higgs boson, hZZ and hW^+W^- , are given by the SM Higgs boson times $\sin(\beta - \alpha)$, similarly HZZ and HW^+W^- are proportional to $\cos(\beta - \alpha)$; these vertices are the most important for our phenomenology. The scalars h and H thus share the Higgs field vev and strength of the coupling of the W^+W^- and ZZ to scalar fields. Furthermore the decay of the Higgs boson in the 2HDM depends on the model for the Yukawa interaction and also when $\sin(\beta - \alpha) = 1$ the decay pattern of h is almost the same as that of the SM. Therefore the production of H can vary over a large range. In Figure 1, we have conducted a general search for an additional heavy Higgs boson, $H \rightarrow \gamma\gamma$, in a mass range between $2m_h < m_H < 2m_t$ [9]. The analyses are performed in a combination of 50000 events category; we showed the energy scales in GeV against the number of events which is the normalized differential cross-sections.

Table 2. Couplings of h^0 and H^0 to gauge bosons pairs:

$\cos(\beta - \alpha)$	$\sin(\beta - \alpha)$
HW^+W^-	hW^+W^-
HZZ	hZZ
ZAh	ZAH
$W^\pm H^\mp h$	$W^\pm H^\mp H$
$ZW^\pm H^\mp h$	$ZW^\pm H^\mp h$
$\gamma W^\pm H^\mp h$	$\gamma W^\pm H^\mp h$

6. Conclusion

In this proceedings we discussed the particle spectrum that arises because of electroweak symmetry breaking in the 2HDM. There are many possibilities for the decay branching ratios of these particles. We briefly reviewed the 2HDM, which is an extension of the SM with an additional scalar doublet. In particular we have studied the IDM, which is obtained by setting one of vevs to zero. The ongoing searches at the LHC rely on specific production and decay mechanisms that occupy only a part of the complete parameter space[?]. The study of the IDM is done by imposing several constraints on the exploration of the Higgs sector, where the main constraint comes from the discovery of the resonance 125 GeV by ATLAS and CMS. In the context of 2HDM, this resonance might be interpreted as the h and H . In the $H \rightarrow \gamma\gamma$, the final state particles can be very precisely measured and the reconstructed mass m_H is excellent

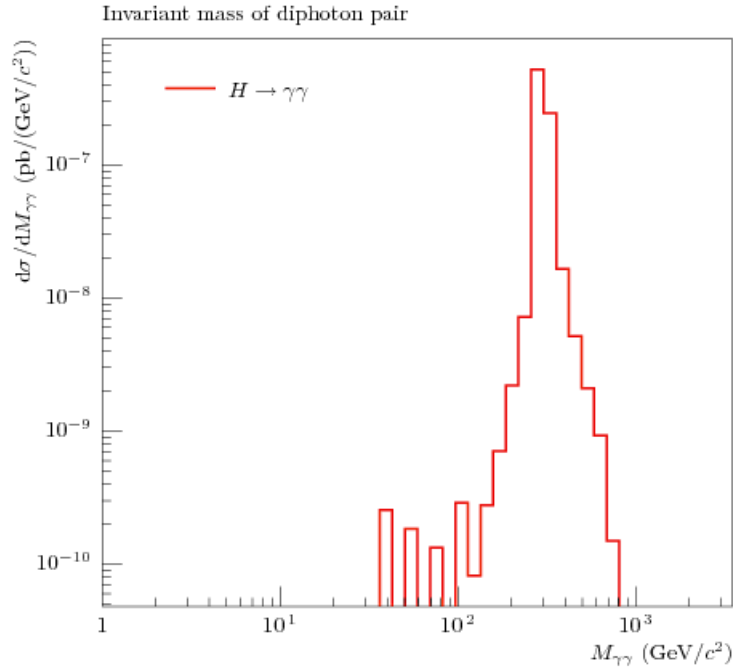


Figure 1. Left: Invariant mass of the kinematic fit in the process $H \rightarrow \gamma\gamma$ in 2HDM with $m_H \approx 300\text{GeV}$

as shown in Fig.1. Currently, we can make a demonstration of how the phenomenology of the 2HDM particle spectrum could be observed at the LHC using some Monte-Carlo simulators.

Acknowledgements

I would like to thank the National Research Foundation of South-Africa for funding this project, my co-supervisor Deepak Kar, my supervisor Alan Cornell for his encouragements and dedicated time to this project and also the Wits HEP group.

References

- [1] Chatrchyan S, *et al.* [CMS Collaboration], Phys. Lett. B **716**, 30 (2012) [arXiv:1207.7235 [hep-ex]].
- [2] Chang J, Cheung K, Tseng P. Y and Yuan T. C, [arXiv:1206.5853 [hep-ph]].
- [3] Lynn B. W, and Starkman G. D, Phys. Rev. D **96**, no. 6, 065006 (2017) [arXiv:1509.06199 [hep-ph]].
- [4] Biswas A and Lahiri A, [arXiv:1412.6187 [hep-ph]].
- [5] Robbins G, Mahmoudi F, Arbey A, and Boudaud M, arXiv:1710.03658 [hep-ph].
- [6] Agrawal P and Howe K, [arXiv:1710.04213 [hep-ph]].
- [7] Barroso A, Ferreira P. M, Santos R, Sher M and Silva J. P, arXiv:1304.5225 [hep-ph].
- [8] Branco G. C, Ferreira P. M, Lavoura L, Rebelo M. N, Sher M [arXiv:1106.0034 [hep-ph]].
- [9] Kumar M, arXiv:1603.01208 [hep-ph].

Wilson lines and color-neutral operators in the color glass condensate

J M Alcock-Zeilinger¹ and H Weigert²

Department of Physics, University of Cape Town, Private Bag X3, Rondebosch 7701, South Africa

E-mail: ¹judy.zeilinger@gmail.com, ²heribert.weigert@uct.ac.za

Abstract. Color-neutral operators (singlets) are useful in high energy QCD to construct Wilson line correlators. In this proceedings we describe an algorithm that allows us to systematically construct all singlets for a given Fock-space configuration. In particular, we exemplify this algorithm with the singlets of the $3q + 3\bar{q}$ -algebra.

1. Introduction

Confinement is a phenomenon of QCD, that is to this day theoretically not well understood in the sense that it is unclear, what feature of QCD forces color-charged objects to be confined. However, the consequences of confinement are very clear: all objects that carry color charge (i.e. quarks and gluons) are necessarily bound together in color-neutral states such as baryons or mesons. It is thus of paramount importance to understand color-neutral states, so-called *singlet-states* in order to perform QCD calculations on physically meaningful objects.

The study of singlets becomes even more relevant when considered in the high-energy limit of QCD. In this regime, all interactions between a projectile and a target occur (to a good approximation) exclusively via Wilson lines. This is due to the fact that the target is highly Lorentz contracted and thus acts as an essentially static but extremely localized color source, allowing us to make a no-recoil approximation, [1].

We begin our discussion with an explanation of why the study of singlets is so significant in this branch of physics. In many places, we will do so by summarizing results of [1]; we have used the same diagrammatic notation as [1] in order to make a comparison easier. Beyond this section, the diagrammatic notation will be modified to better suit our purposes.

Wilson line correlators can carry singlets into singlets. This is easiest seen when considering the dipole correlator; this example is described in detail in [1], we will therefore only give a brief summary here. The contribution of the dipole interaction with a target via a Wilson line to the total cross section is described in the absolute value of the square of the difference between the state in which an interaction takes place, and the state which describes no interaction with the

target,

$$\left| \begin{array}{c} \text{interaction} \\ \text{no interaction} \end{array} \right|^2 = \left(\begin{array}{c} \text{interaction} \\ \text{no interaction} \end{array} \right) \cdot \left(\begin{array}{c} \text{interaction} \\ \text{no interaction} \end{array} \right); \quad (1)$$

in the above diagrams, the blue line represents an interaction with the target, while the dashed line indicates that no interaction with the target has occurred. Thus, in the “no-interaction”-diagrams, the Wilson lines (represented by arrows) are gauge equivalent to the unit. Once the brackets in eq. (1) are multiplied out, keeping in mind that the transverse momentum is integrated over, we can observe the following simplification,

$$\begin{aligned} \left| \begin{array}{c} \text{interaction} \\ \text{no interaction} \end{array} \right|^2 &= \begin{array}{c} \text{interaction} \\ \text{no interaction} \end{array} - \begin{array}{c} \text{interaction} \\ \text{no interaction} \end{array} - \begin{array}{c} \text{interaction} \\ \text{no interaction} \end{array} + \begin{array}{c} \text{interaction} \\ \text{no interaction} \end{array} \\ &= \underbrace{\text{tr}(U_y^\dagger U_y U_x^\dagger U_x)}_{=\text{tr}(\mathbf{1})} - \underbrace{\text{tr}(U_y U_x^\dagger)}_{\text{tr}(U_y^\dagger U_x) = (\text{tr}(U_y U_x^\dagger))^\dagger} - \underbrace{\text{tr}(U_y^\dagger U_x)}_{\text{tr}(U_y U_x^\dagger) = (\text{tr}(U_y U_x^\dagger))^\dagger} + \underbrace{\text{tr}(\mathbf{1})} \\ &= 2 \cdot \begin{array}{c} \text{interaction} \\ \text{no interaction} \end{array} - \left\{ \begin{array}{c} \text{interaction} \\ \text{no interaction} \end{array} + \left(\begin{array}{c} \text{interaction} \\ \text{no interaction} \end{array} \right)^\dagger \right\} \end{aligned}$$

The first term in the above sum does not include an interaction with the target, and is thus of no particular interest to the discussion at hand. However, each of the terms in the curly braces includes one interaction: it is important to note that the $q\bar{q}$ -dipole is explicitly in a singlet state before as well as after the interaction. Thus, the eikonal interaction in this situation did not destroy the “singlet-ness” of the dipole, even though each quark has experienced a color rotation. This feature of Wilson lines, that they leave singlets in tact, can also be observed in higher point correlators, [2].

In the case of a $q\bar{q}$ -dipole, there exists only one possible singlet. For two $q\bar{q}$ -dipoles, the situation becomes more interesting, since there are two possible singlets that can be formed, [1],

$$\frac{1}{d_f} \} \quad \text{and} \quad \frac{1}{\sqrt{d_A}} \}$$

In an evolution equation such as the JIMWLK-equation, all of these singlets have to be considered simultaneously, as the Wilson line correlators may map one singlet into the other. Thus, the JIMWLK-evolution of two $q\bar{q}$ -dipoles is governed by the following correlation matrix,

$$\mathcal{A}(Y) := \begin{pmatrix} \frac{1}{d_f^2} & \frac{1}{d_f \sqrt{d_A}} \\ \frac{1}{d_f \sqrt{d_A}} & \frac{1}{d_A} \end{pmatrix} (Y); \quad (2)$$

the evolution of this correlation matrix is discussed in [1].

In order to determine the JIMWLK-evolution of any n -point correlator it is of utmost importance to know all possible singlet states for the corresponding Fock space constituents. In [3], we will present

- (i) a counting argument determining the number of singlets
- (ii) an algorithm which allows one to construct all singlets in a particular basis.

In this proceedings, we will illustrate the methods discussed in [3] by means of a concrete example.

The singlet operators of a particular configuration in Fock space do not represent independent degrees of freedom; we will exhibit this by means of an example in section 3. In order to effectively study the JIMWLK evolution of these operators, one usually performs a parameterization of the correlation matrix $\mathcal{A}(Y)$ as

$$\frac{d}{dY}\mathcal{A}(Y) = \left(\frac{d}{dY}\mathcal{A}(Y)\right)\mathcal{A}(Y)^{-1}\mathcal{A}(Y) =: -\mathcal{M}(Y)\mathcal{A}(Y),$$

provided $\mathcal{A}(Y)$ is invertible¹. This equation can then be integrated to yield

$$\mathcal{A}(Y) = \mathcal{P}_Y \exp \left\{ - \int_{Y_0}^Y dY' \mathcal{M}(Y') \right\} \mathcal{A}(Y_0),$$

for some initial rapidity Y_0 . The Ansatz

$$\mathcal{M}(Y) = \frac{1}{2} \int d\mathbf{u} d\mathbf{v} (G_{Y,uv} \bar{\nabla}_u^a \bar{\nabla}_v^a + \dots),$$

where truncation after the first term is referred to as the *Gaussian Truncation*, [1], allows us to write each component (singlet) of $\mathcal{A}(Y)$ as an exponential with the functions G in the exponent. This parameterization therefore allows us to formulate the evolution equation in terms of elements of the tangent space rather than the singlet space itself, where the functions G now represent the *independent* degrees of freedom. However, to make sure that these independent degrees of freedom accurately represent the properties of the singlet algebra, the latter has to be studied in more detail. In this proceedings, we exhibit the fact that the Wilson line correlators are not independent degrees of freedom by means of an example. In particular, we will present all Wilson line correlators of the $3q + 3\bar{q}$ -algebra and take a coincidence limit between two Wilson lines, section 3. In future work, we will use coincidence limits such as the one presented in this paper in order to impose constraints on the functions G .

At this point, we note that the interesting behaviour of the n -point correlators in coincidence limits stems from the fact that the interaction is eikonal, that is localized and only via Wilson lines. A general n -point correlator for non-eikonal interactions does not exhibit any special behaviour when local coincidence limits are considered. For example, Figure 1 depicts a $q\bar{q}$ -dipole interacting with a target t (indicated by the gray box) via the exchange of gluons:

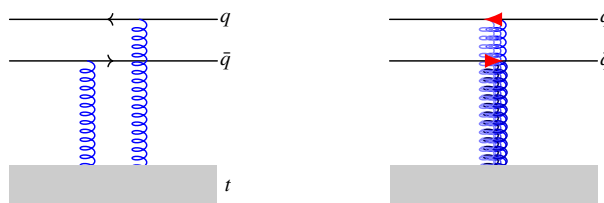


Figure 1. At low energies (*left* picture), the interaction of the $q\bar{q}$ -dipole with the target t happens at no particular point in the x^- -direction. At high energies (*right* picture), the target t is extremely Lorentz contracted, localizing the interaction at a particular point along the x^- -axis.

¹ Since the correlation matrix becomes the unit matrix if all Wilson lines are set to unity, and one expects a smooth departure from unity as the Wilson lines smoothly vary from $\mathbb{1}$, it is physically plausible to assume that $\mathcal{A}(Y)$ is invertible, at least in some neighbourhood of the unit matrix.

In a low-energy interaction therefore, a coincidence limit between the $q\bar{q}$ -pair does not reveal new information, since the interaction between the dipole and the target is not localized in the x^- -direction, unlike the high-energy counterpart.

2. Construction of general singlets and birdtrack notation

We assume a familiarity of the reader with the representation theory of $SU(N_c)$ over an all-quark algebra by means of Young projection operators, see [4, 5] and other standard textbooks. This is known as the *theory of invariants*, which utilizes the the Young projection operators to classify all irreducible representations of $SU(N_c)$. This topic recently received a more modern treatment when Cvitanović, [6], reformulated the theory of invariants in terms of birdtracks, which were originally developed by Penrose and MacCallum, [7]. In this formalism, symmetrizers (resp. anti-symmetrizers) are represented as empty (white) (resp. filled in (black)) boxes over the lines representing the tensor indices which they (anti-) symmetrize. For example,

$$\begin{array}{|c|c|} \hline 1 & 2 \\ \hline \end{array} : \quad \mathbf{S}_{12}T^{ab} = \begin{array}{|c|c|} \hline \square & \square \\ \hline \end{array} T^{ab} = \frac{1}{2} \left(\text{---} + \text{X} \right) T^{ab} = \frac{1}{2} \left(T^{ab} + T^{ba} \right),$$

where \mathbf{S}_{12} denotes the symmetrizer over the 1st and 2nd tensor index of T . In this way, the Young projection operator corresponding to the following Young tableau Θ can be written as

$$\Theta = \begin{array}{|c|c|c|} \hline 1 & 3 & 4 \\ \hline 2 & 5 & \\ \hline \end{array} \quad \mapsto \quad Y_\Theta = \alpha_\Theta \cdot \begin{array}{c} \text{---} \\ \text{---} \\ \text{---} \\ \text{---} \\ \text{---} \\ \text{---} \end{array}$$

where Y_Θ denotes the Young projection operator corresponding to the Young tableau Θ , and α_Θ is the normalization constant needed to ensure the idempotency of Y_Θ , which can be obtained from the *hook length formula*, [6, 4, 8].

We will show in [3] that *any* singlet for *any* Fock-space configuration (such as $m q + \bar{m} \bar{q} + n g$) is equivalent to a singlet in the $k q + k \bar{q}$ -algebra, where $k = k(N_c) \in \mathbb{N}$ is a N_c -dependent parameter, for a particular value of N_c . Therefore, it suffices to analyse the singlets of $SU(N_c)$ over an algebra of the same number of quarks and anti-quarks.

The singlets of such an $m q + m \bar{q}$ -algebra are obtained by *reshaping* the basis elements of the algebra of invariants of the $m q$ -algebra, [3]. A particularly useful basis to choose for this process is that of Hermitean Young projection operators and transition operators, which we constructed in [9], as this basis will yield *orthogonal* singlet states, [3]. For example, the Hermitean Young projection operators and transition operators for the $3q$ -algebra are given by

$$\underbrace{\begin{array}{c} \text{---} \\ \text{---} \\ \text{---} \end{array}, \quad \frac{4}{3} \cdot \begin{array}{|c|c|} \hline \square & \square \\ \hline \end{array}, \quad \frac{4}{3} \cdot \begin{array}{|c|c|} \hline \square & \square \\ \hline \end{array}, \quad \begin{array}{|c|} \hline \square \\ \hline \end{array}}_{\text{projection operators}}, \quad \underbrace{\sqrt{\frac{4}{3}} \cdot \begin{array}{|c|c|} \hline \square & \square \\ \hline \end{array}, \quad \sqrt{\frac{4}{3}} \cdot \begin{array}{|c|c|} \hline \square & \square \\ \hline \end{array}}_{\text{transition operators}}$$

giving the following singlet states for the $3q + 3\bar{q}$ -algebra,

$$\zeta_1 \begin{array}{c} \text{---} \\ \text{---} \\ \text{---} \\ \text{---} \\ \text{---} \\ \text{---} \end{array}, \quad \zeta_2 \begin{array}{c} \text{---} \\ \text{---} \\ \text{---} \\ \text{---} \\ \text{---} \\ \text{---} \end{array}, \quad \zeta_2 \begin{array}{c} \text{---} \\ \text{---} \\ \text{---} \\ \text{---} \\ \text{---} \\ \text{---} \end{array}, \quad \zeta_3 \begin{array}{c} \text{---} \\ \text{---} \\ \text{---} \\ \text{---} \\ \text{---} \\ \text{---} \end{array}, \quad \zeta_2 \begin{array}{c} \text{---} \\ \text{---} \\ \text{---} \\ \text{---} \\ \text{---} \\ \text{---} \end{array}, \quad \text{and} \quad \zeta_2 \begin{array}{c} \text{---} \\ \text{---} \\ \text{---} \\ \text{---} \\ \text{---} \\ \text{---} \end{array} \quad (3)$$

$$\text{with} \quad \zeta_1 = \frac{6}{(N_c + 2)(N_c + 1)N_c}, \quad \zeta_2 = \frac{3 \cdot \theta(N_c - 2)}{(N_c^2 - 1)} \quad \text{and} \quad \zeta_3 = \frac{6 \cdot \theta(N_c - 3)}{(N_c - 2)(N_c - 1)N_c},$$

where the top three lines denote the quark lines, and the bottom three lines denote the anti-quark lines.

3. Wilson line correlators and coincidence limits

As mentioned previously, we are interested in the behaviour of Wilson line correlators. These are constructed as

$$\langle S_1 | \mathbf{U} | S_2 \rangle,$$

where $|S_1\rangle, |S_2\rangle$ are singlet states, $\langle S_1| = |S_1\rangle^\dagger$, and

$$\mathbf{U} = U_{x_1} \otimes \dots \otimes U_{x_n} \otimes U_{y_m}^\dagger \otimes \dots \otimes U_{y_1}^\dagger$$

is a tensor product of Wilson lines $U_{x_i} \in \text{SU}(N_c)$ with x_i being the x^+ -coordinate of the i^{th} quark in the singlet. We will denote Wilson lines U_{x_i} by red arrowheads pointing from right to left and $U_{y_j}^\dagger$ by red arrowheads pointing from left to right, suppressing the explicit coordinate dependence, for example

$$U_{x_1} \otimes U_{x_2} \otimes U_{y_1}^\dagger \rightarrow \begin{array}{c} \leftarrow \leftarrow \\ \rightarrow \rightarrow \end{array}.$$

Returning to the $3q + 3\bar{q}$ -example with singlet states (3), we can form a *correlation matrix* including each Wilson line singlet correlator as (where we have neglected the normalization factors for brevity)

$$\bar{\mathcal{A}}(Y) := \begin{pmatrix} \text{Diagram 1} & \text{Diagram 2} & \text{Diagram 3} & \text{Diagram 4} & \text{Diagram 5} & \text{Diagram 6} \\ \text{Diagram 7} & \text{Diagram 8} & \text{Diagram 9} & \text{Diagram 10} & \text{Diagram 11} & \text{Diagram 12} \\ \text{Diagram 13} & \text{Diagram 14} & \text{Diagram 15} & \text{Diagram 16} & \text{Diagram 17} & \text{Diagram 18} \\ \text{Diagram 19} & \text{Diagram 20} & \text{Diagram 21} & \text{Diagram 22} & \text{Diagram 23} & \text{Diagram 24} \\ \text{Diagram 25} & \text{Diagram 26} & \text{Diagram 27} & \text{Diagram 28} & \text{Diagram 29} & \text{Diagram 30} \\ \text{Diagram 31} & \text{Diagram 32} & \text{Diagram 33} & \text{Diagram 34} & \text{Diagram 35} & \text{Diagram 36} \end{pmatrix}.$$

When a coincidence limit between the Wilson lines acting on the top two quarks is taken, that is

$$U_{x_1} \otimes U_{x_2} \otimes U_{x_3} \otimes U_{y_3}^\dagger \otimes U_{y_2}^\dagger \otimes U_{y_1}^\dagger \xrightarrow{x_1 \rightarrow x_2} U_{x_1} \otimes U_{x_1} \otimes U_{x_3} \otimes U_{y_3}^\dagger \otimes U_{y_2}^\dagger \otimes U_{y_1}^\dagger,$$

then many of the Wilson line correlators in Eq (3) vanish, revealing a block-diagonal form, [3],

$$\bar{\mathcal{A}}(Y) = \begin{pmatrix} \text{Diagram 1} & \text{Diagram 2} & \text{Diagram 3} & \text{Diagram 4} & \text{Diagram 5} & \text{Diagram 6} \\ \text{Diagram 7} & \text{Diagram 8} & \text{Diagram 9} & \text{Diagram 10} & \text{Diagram 11} & \text{Diagram 12} \\ \text{Diagram 13} & \text{Diagram 14} & \text{Diagram 15} & \text{Diagram 16} & \text{Diagram 17} & \text{Diagram 18} \\ \text{Diagram 19} & \text{Diagram 20} & \text{Diagram 21} & \text{Diagram 22} & \text{Diagram 23} & \text{Diagram 24} \\ \text{Diagram 25} & \text{Diagram 26} & \text{Diagram 27} & \text{Diagram 28} & \text{Diagram 29} & \text{Diagram 30} \\ \text{Diagram 31} & \text{Diagram 32} & \text{Diagram 33} & \text{Diagram 34} & \text{Diagram 35} & \text{Diagram 36} \end{pmatrix} \xrightarrow{x_1 \rightarrow x_2} \begin{pmatrix} \text{Diagram 1} & 0 & 0 & 0 & 0 & 0 \\ \text{Diagram 7} & \text{Diagram 8} & 0 & 0 & 0 & 0 \\ \text{Diagram 13} & \text{Diagram 14} & \text{Diagram 15} & 0 & 0 & 0 \\ 0 & 0 & 0 & \text{Diagram 22} & \text{Diagram 23} & \text{Diagram 24} \\ 0 & 0 & 0 & \text{Diagram 28} & \text{Diagram 29} & \text{Diagram 30} \\ 0 & 0 & 0 & \text{Diagram 34} & \text{Diagram 35} & \text{Diagram 36} \end{pmatrix}. \tag{4}$$

This example exhibits that the various Wilson line correlators in $\bar{\mathcal{A}}(Y)$ do not represent independent degrees of freedom - they vanish *simultaneously* as certain coincidence limits are considered. As was said previously, coincidence limits of correlation matrices such as in Eq. (4) are used to impose constraints on the functions G , which represent the independent degrees of freedom of the correlation matrix. It is clear that a complete set of constraints on the G 's can however not be extracted from merely studying the coincidence limits of the singlet operators in one basis, but rather requires a study of these limits in *all* possible bases, and perhaps also an entirely different analysis of these singlets. In [3], we will give an expression of $\bar{\mathcal{A}}(Y)$ for the $3q + 3\bar{q}$ -algebra in an alternate basis and discuss coincidence limits in this basis.

The algorithm giving all singlet states generates them in a particular basis, namely that of Hermitean Young projection operators and transition operators. While we do not (yet?) have a generic way of changing bases, having a counting argument for the dimension of the singlet algebra allows us to discern whether a different basis acquired by some other means is complete, and thus fit for an analysis of the singlet algebra.

References

- [1] Marquet C and Weigert H 2010 New observables to test the color glass condensate beyond the large- N_c limit *Nucl. Phys. A* **843** 68–97 (*Preprint* 1003.0813)
- [2] Weigert H 2005 Evolution at small x_{bj} : the color glass condensate *Prog. Part. Nucl. Phys.* **55** 461–565 (*Preprint* hep-ph/0501087)
- [3] Alcock-Zeilinger J M and Weigert H 2016 Singlets (in preparation)
- [4] Tung W K 1985 *Group Theory in Physics* (Singapore: World Scientific)
- [5] Fulton W and Harris J 2004 *Representation Theory - A First Course* (New York, USA: Springer)
- [6] Cvitanović P 2008 *Group Theory: Birdtracks, Lie's and Exceptional Groups* (Princeton, USA: Univ. Pr.)
- [7] Penrose R and MacCallum M A H 1972 Twistor theory: an approach to the quantisation of fields and space-time *Phys. Rept.* **6** 241–316
- [8] Sagan B 2000 *The Symmetric Group - Representations, Combinatorial Algorithms, and Symmetric Functions* 2nd ed (New York, USA: Springer)
- [9] Alcock-Zeilinger J M and Weigert H 2016 Compact hermitean Young projection operators and transition operators (in preparation)